SPAWAR

Systems Center
San Diego

TECHNICAL DOCUMENT 2989
March 1998

Proceedings of the 1997 Battlespace Atmospherics Conference 2–4 December 1997

K. D. Anderson
J. H. Richter

TECHNICAL DOCUMENT 2989
March 1998

Proceedings of the 1997 Battlespace Atmospherics Conference 2–4 December 1997

K. D. Anderson
J. H. Richter

Systems Center
San Diego

Space and Naval Warfare Systems Center
San Diego, CA 92152–5001

SPACE AND NAVAL WARFARE SYSTEMS CENTER
San Diego, California 92152–5001

H. A. Williams, CAPT, USN
Commanding Officer

R. C. Kolb
Executive Director

ADMINISTRATIVE INFORMATION

These proceedings were prepared for the Office of Naval Research by the Propagation Division, Space and Naval Warfare (SPAWAR) Systems Center, San Diego.

Released under authority of
J. H. Richter, Head
Propagation Division

SB

PROCEEDINGS OF THE 1997 BATTLESPACE ATMOSPHERICS CONFERENCE

2-4 DECEMBER 1997

CONFERENCE CHAIRS

Dr. Juergen H. Richter and Kenneth D. Anderson

TECHNICAL COMMITTEE

Gail Anderson, Kenn Anderson, Dr. Walter Bach, Dan Dockery, Dr. Juergen Richter,

Dr. David Rogers, Dr. Scott Sandgathe, Dr. Richard Shirkey, Paul Tattelman

EXECUTIVE COMMITTEE

K. Anderson, S. Campbell, L. MacPherson, J. Richter, and N. Vorce.

Until 1995, Battlefield Atmospherics Conferences were hosted annually by the Army's Atmospheric Sciences Laboratory (ASL) at White Sands, NM. These conferences, while primarily addressing Army concerns, had Navy, Air Force, and international participation. With the incorporation and move of ASL into the Army Research Laboratory, the Army could not host this widely recognized conference in 1996. DDR&E recommended that it become a tri-service event to be hosted by each of the three U.S. services in succession, whereby each service would be responsible for the conference 2 years in a row. The Navy was selected for 1996 and 1997, with the Space and Naval Warfare Systems Center, San Diego (SSC San Diego, formerly NRaD) as host. The conference name was changed to *Battlespace* Atmospherics Conference to reflect the broader concerns of all service branches. The 1996 Battlespace Atmospherics Conference (BAC '96) was held from 3-5 December 1996. BAC '97 was held from 2-4 December 1997. The conference objective is to enhance cooperation and coordination in all aspects of atmospheric effects assessment between the U.S. military services, the civilian community, and other nations. BAC '97 had about 150 participants from all U.S. service branches, NOAA, academia, and industry as well as representatives from eight other countries (Australia, Canada, France, Germany, Israel, Norway, Russia, and the United Kingdom). A total of 85 papers and 4 posters were presented. The topics covered a broad range of atmospheric sciences including model development, experiments, sensor and sensing technique development, modeling and simulation, tactical decision aids, and operational issues.

The Battlespace Atmospheric Conferences are unclassified. All DoD agencies, industry and academia, are welcome; attendance by foreign nationals is encouraged. The U.S. Air Force (Air Force Research Laboratory) will host the next two Battlespace Atmospheric Conferences.

Juergen Richter and Kenn Anderson

Chairmen, BAC '96 and BAC '97

Contents

Meteorological Measurements & Modeling 1, Chair: Steve Payne

Atmospheric Sensing 2, Chair: Dr. David Rogers

Meteorological Measurements & Modeling 2, Chair: Dr. Richard Shirkey

EO Propagation Measurements & Modeling 1, Chair: Gail Anderson

Radio Propagation Measurements & Modeling 1, Chair: Dan Dockery

QUANTITATIVE VS QUALITATIVE TACTICAL DECISION AIDS: IS THERE A DIFFERENCE?

Richard Shirkey
Army Research Laboratory
Information Science and Technology Directorate
Battlefield Environment Division
WSMR, NM 88002-5501

ABSTRACT

With the plethora of weapons systems available on the battlefield the warfighter, from commander to foot soldier, needs to be able to determine which system to use and how that system will be affected by the weather. The Integrated Weather Effects Decision Aid (IWEDA) transforms raw weather data into weather intelligence to display environmental effects on weapon systems and operations. IWEDA employs a data base constructed by querying weapon system operators regarding the applicability of a given system under specific weather conditions and is therefore rule-based. This approach does not take advantage of current physics-based Tactical Decision Aids (TDAs). To examine the differences, a study has been undertaken using both rule-based and physics-based TDAs for a limited number of sensors and weather conditions.

1. INTRODUCTION

The commander and soldier of today's Army has a wide selection of weapons to chose from to engage the enemy. However not all weapons work well in all weather conditions: each weapon is dependent upon its associated sensor, which in turn is affected by the natural environment and the components of the battlefield environment. These non-uniform obscurant sources include aerosols and particulates such as clouds, rain, snow, fog, dust, smoke and chaff. Their attenuation effects on the propagation of natural and man-made electromagnetic energy impact target acquisition and weapon systems. There are a number of decision aids that can aid the warfighter with this problem that fall into two distinct categories: those that contain targets and provide range for acquisition (quantitative) and those that do not (qualitative). Examples of quantitative Tactical Decision Aids (TDAs) that provide range information relevant to target acquisition under various weather conditions are ACQUIRE[1], EOTDA[2], ORACLE[3], and TARGAC[4]. A qualitative TDA that provides information relevant to system selection, but not target acquisition, under various weather conditions is the Integrated Weather Effects Decision Aid (IWEDA)[5]. Quantitative TDAs are usually constructed by applying an in-depth knowledge of physics coupled with criteria for determination of an observer's ability to classify a target[3,6], e.g. detection, recognition, identification, under given visibility conditions. In contradistinction to quantitative TDAs, qualitative TDAs do not provide information concerning probability of acquisition, but rather rely upon operators of the weapon systems to provide information concerning their weapons systems performance under different weather conditions; this information is subsequently coded into "rules" for system usage.

The study contained herein compares the qualitative rule-based IWEDA TDA with the physics-based TDAs EOTDA, ORACLE, and TARGAC. Wavelength ranges were constrained to the visual (0.4 - 0.9 μm) and infrared (8.0 - 12.0 μm) bands.

2. TARGET ACQUISITION MODELS

Target acquisition models require information regarding the target/background contrast[7,8], the atmospheric illumination[9] and transmission[10,11], and the sensor performance[1,3]. Some models require direct input of derived quantities (e.g. illumination of 7500 cd/m^2), whereas others will contain sub-models to compute such quantities (e.g. date + time of day + location + atmospheric conditions = illumination of 7500 cd/m^2). Of the three quantitative models discussed here ORACLE requires derived input; the EOTDA and TARGAC compute such quantities. All three of these models will predict the range for target acquisition at a given probability and acquisition level (detection, recognition, identification).

2.1 The Army Integrated Weather Effects Decision Aid - IWEDA

IWEDA displays a graphical analysis of how weapons systems will perform, given different weather conditions. It combines data from the Gridded Met Database and a set of 505 rules to evaluate the effectiveness of user-defined weapons systems for user-defined periods often up to 24 hours determined by the Battlescale Forecast Model[12] forecast area. IWEDA is arranged in a hierarchy, the basic building block of which is the system. A group of systems is called a mission; a system often contains one or more subsystems, and the subsystems may often have one or more components. IWEDA thus allows for the determination of weather impacts from operations or missions at the highest level, down to systems, subsystems, and components at the lowest level. For user-defined missions, systems, subsystems, and components, the effects - favorable (green), marginal (amber), and unfavorable (red) - and the time periods are shown on weather effects matrices (WEMs). Knowledge bases containing critical weather values are prepared for the systems, subsystems, and components operated by specific individual units. Currently IWEDA stores information on 71 systems, 55 of which are friendly, 16 of which are threat. Following the completion of a series of setup options, IWEDA applies expert system technologies to provide the user with weather impact information in the form of color-coded WEMs overlaid on terrain maps.

2.2 The Air Force Electro-Optical Tactical Decision Aid - EOTDA

The EOTDA predicts the performance of air-to-ground weapon systems and direct view optics (DVOs) based on environmental and tactical information. Tactical information includes time over target, target location and characteristics, sensor specification and height, and background characteristics. The software supports systems in three regions of the spectrum: visible (0.4 - 0.9 μm); laser (1.06 μm); and IR (8.0 - 12.0 μm). The visible (TV) includes low-light devices and DVOs. Performance is expressed primarily in terms of maximum detection or lock-on range, with the results being displayed in alphanumeric and graphic formats. The EOTDA is self-

contained in-so-far as the user does not need to input derived quantities, although detailed information about weather conditions are required.

2.3 The Army Target Acquisition Model - TARGAC

As with the EOTDA, the Electro-Optical Systems Atmospheric Effects Library[13] target acquisition model TARGAC was designed to be a self-contained program that would enable the user to predict the atmospheric effects on the ability of electro-optical sensors to detect and/or recognize a target. In fact TARGAC and EOTDA utilize many of the same sub-models and harmonization efforts have been performed[14]. TARGAC calculates ranges as a function of the probability of detection and recognition for a variety of sensors, including DVOs, image intensifiers, silicon televisions, and thermal imagers; output is displayed in alphanumeric format.

2.4 British Aerospace Visual Performance Model - ORACLE

Unlike EOTDA and TARGAC, ORACLE requires that detailed derived physical quantities, such as the level of illumination, the contrast, the extinction coefficient, etc., be entered for target acquisition. ORACLE also generates target acquisition probabilities in a different fashion than either EOTDA or TARGAC. ORACLE's probabilities are a function of time and accumulate with successive 330 ms glimpses. Thus both acquisition probabilities and times to reach a certain probability can be obtained, where successive fixations are not directed at the same point in space. Target parameters such as range may be varied not only to extract detection ranges for a particular target, but also systematically, between successive glimpses, in order to simulate closing range acquisition. By altering background characteristics (clutter, luminance, sky-to-ground ratio) one is able to simulate ground (or sea)-to-ground, ground-to-air, or air-to-ground conditions. Output is displayed in alphanumeric and graphical formats.

3. SCENARIO

3.1 Parameters

In order to minimize the environmental effects on the target acquisition routines, certain parameters were kept constant and the overall scenario was simplified as much as possible. Only DVOs and IR/thermal devices were considered; the probability level for identification/recognition/ lock-on acquisition was fixed at 90%. The parameters are presented in Table 1. While it may not make sense to have freezing temperatures at the time and location chosen, for the purposes of this study it was not relevant. The weather conditions chosen were

Table 1. Parameters for the Study

Parameter	Value
Latitude	0 degrees
Longitude	0 degrees
Date	21 June 1997
Time	1200 hrs
Fog type	Moderate Radiation[15]
Temperature	80 degrees* or 0 degrees+
Relative Humidity	80%
Wind Speed	3 m/s
Target	Tank: OD paint* or idling+
Background	Live Vegetation* or Snow+
Clutter level	Low
* visible λ	+ thermal λ

determined by the IWEDA rules and fall into three categories: 1) clear with varying visibilities, 2) overcast with rain/snow with varying visibilities, and 3) no clouds with fog/blowing dust with varying visibilities. The visibilities used and the weather conditions chosen (rain, snow, fog, dust) may be found in Tables 2 through 5 below. A horizontal path was assumed in all cases. Shadows were not considered.

The target chosen was a T62 tank against a background of either live vegetation or snow. The time of year and day and the location were arbitrary choices. For summer conditions a muggy day was chosen with a gentle breeze; for fog scenarios the wind speed was set to zero and for blowing sand the wind speed was set to 15 m/s.

In the visual, sensor types were chosen as generic DVOs or TV; for IR wavelengths generic FLIRS were used.

3.2 Caveats

There are a number of items to keep in mind when comparing the IWEDA results to the TDA results. IWEDA was not originally designed for target acquisition and the quantitative TDA values do not always agree with observations[15]. During the course of this study both the EOTDA and TARGAC routines produced occasional non-physical results. Also the target acquisition routines EOTDA and TARGAC do not account for different precipitation intensities[4,16], thus, for the same visibilities, the ranges do not vary for drizzle, light rain or moderate rain, or light and moderate snow. Further the apparent acquisition range agreement of ORACLE with TARGAC is not entirely fortuitous. As ORACLE requires the user to input values rather than calculating them, the IR extinction coefficients were calculated by using the XSCALE[17] routine and illumination values were calculated using ILUMA[9]; both XSCALE and ILUMA are resident in TARGAC. Further, the sky-to-ground ratio and the temperature differences required as input to ORACLE were taken from the TARGAC output. Finally, without examining each model in detail it is not possible to ascertain if all of the input conditions are treated equally and that the identification, recognition, and lock-on acquisition criteria used in the three routines are equivalent.

4. RESULTS AND DISCUSSION

Care must be taken in performing a comparison between the qualitative IWEDA TDA and the quantitative TDAs EOTDA, ORACLE and TARGAC (for the following discussion we will refer to EOTDA, ORACLE and TARGAC as the quantitative TDAs). As currently configured IWEDA is rule based. These rules have been obtained from Army field manuals and by requesting that operators of weapon systems, intelligence officers, and staff weather officers provide information concerning when the system is impacted by the atmosphere/weather. This information has been subsequently coded up into a knowledge data base such that when queried IWEDA will inform the user when a weapon system is marginal or unfavorable via qualitative information - red/amber/green "stop light" charts. As an example, if the visibility is less than

1000 m then weapon system A may be unfavorable (red); weapon system B might be marginal under the same conditions (amber). This is in contradistinction to the quantitative TDAs which would be run for the same weather conditions, but would return the actual range that sensor A or B could detect the target at for a given probability level of either detection, recognition or identification. To mitigate this disparity the following methodology was used for comparison to the IWEDA stop light charts. Range values for acquisition of a target (T62 tank) against the background (live vegetation/snow) were computed using the quantitative TDAs for varying illumination conditions determined by cloud cover, and varying weather conditions of rain, fog, snow, blowing dust or clear. Once the ranges had been computed for all cases, then the clear day case (visibility 40 km, no significant weather) was used as a baseline in the two separate wavelength regions (visible and thermal). Red, amber or green were then assigned to range values by taking a percentage of the baseline case. Green was greater than or equal to 60% of the baseline value; amber was chosen to fall between 60% and 20% of the baseline value; and red was less than or equal to 20% of the baseline value.

Results may be found in Tables 2 through 5. Within these tables the ranges associated with ORACLE identification, EOTDA lock-on, and TARGAC recognition are indicated by OR Id, EO Lo, TG Rec, respectively. Tables 2 and 3 present results in the visible and IR respectively, using IWEDA rules as input: i.e. for a DVO operating in light snow with a visibility of 3 km, IWEDA would return an amber value; the IWEDA visibility and snow condition were then used along with the other parameters listed in Table 1 as input to the quantitative TDAs which all returned ranges less than 20% of the baseline value, resulting in a red condition. In Tables 4 and 5 the definition of weather type[18,19] was used to determine visibilities rather than the IWEDA rules. These visibilities, in conjunction with the weather types, then determined the IWEDA condition and were also used as input for the qualitative TDAs to determine the acquisition ranges. The visibility for blowing sand was chosen through the author's experience living in the southwest U.S. Thus, for the large part, actual meteorological definitions and empirical values were used for Tables 4 and 5. In Tables 2 through 5 colors are delineated as follows: green is underlined; amber is in *italics*; and red appears shaded.

Inspection of the tables show that at visual wavelengths, using DVOs, the results from IWEDA and the TDAs compare favorably. Slight discrepancies are noted, but nothing significant. In the light snow case in Table 3 the amber condition returned by IWEDA can easily be explained using the meteorological definition of light snow[18]: visibility of 1,100 yards (1 km) *or more*. However the results in the IR are not as favorable. Discrepancies may be found for the cases where there is no weather, or fog or blowing dust exist in conjunction with low visibilities, or when snow is present. In the case where no snow is present it would appear that the operators, from whom the IWEDA rules have been partially derived, have biased the rules toward meteorological visibilities as opposed to using IR "visibilities" employing the IR sensor itself. In the cases where snow is present, IWEDA does not sufficiently take into account the possible significant differences in temperature that may be found between, say, an idling tank on a snowy background.

Table 2. Visible Wavelength Sensors - IWEDA Rules						
TYPE	**Visibility (km)**	**Weather Condition**	**IWEDA**	**OR Id (km)**	**EO Lo (km)**	**TG Rec (km)**
DVO/TV	1.5	none	***Amber***	**0.3**	**0.3**	**0.2**
DVO/TV	5.0	none	***Amber***	***0.6***	***1.0***	***0.7***
DVO/TV	unlimited	none	**Green**	**1.3**	**2.3**	**1.7**
DVO/TV	3.0	light rain	***Amber***	**0.3**	**0.5**	**0.3**
DVO/TV	3.0	moderate rain	**Red**	**0.3**	**0.5**	**0.3**
DVO/TV	3.0	light snow	***Amber***	**0.3**	**0.5**	**0.3**
DVO/TV	3.0	moderate snow	**Red**	**0.3**	**0.5**	**0.3**
DVO/TV	3.0	drizzle	**Red**	**0.3**	**0.5**	**0.3**
DVO/TV	3.0	fog	**Red**	***0.5***	**0.5**	***0.6***
DVO/TV	3.0	blowing sand	**Red**	**0.3**	***0.7***	**0.3**
DVO/TV	5.0	light rain	***Amber***	***0.4***	***0.8***	***0.4***
DVO/TV	5.0	moderate rain	***Amber***	***0.4***	***0.8***	***0.4***
DVO/TV	5.0	light snow	***Amber***	***0.4***	***0.8***	***0.4***
DVO/TV	5.0	moderate snow	***Amber***	***0.4***	***0.8***	***0.4***
DVO/TV	5.0	drizzle	***Amber***	***0.4***	***0.8***	***0.4***
DVO/TV	5.0	fog	***Amber***	***0.5***	***1.0***	***0.8***
DVO/TV	5.0	blowing sand	***Amber***	**0.3**	***1.0***	***0.4***

KEY
100 % > **Green** ≥ 60 %
60 % > ***Amber*** > 20 %
20 % ≥ **Red** > 0 %

Table 3. Infrared Wavelengths - IWEDA Rules						
TYPE	**Visibility (km)**	**Weather Condition**	**IWEDA**	**OR Id (km)**	**EO Lo (km)**	**TG Rec (km)**
IR/Thermal	2.0	none	**Red**	*0.7*	1.4	1.0
IR/Thermal	4.0	none	***Amber***	0.8	1.4	1.0
IR/Thermal	unlimited	none	Green	1.2	1.4	1.2
IR/Thermal	3.0	light rain	**Red**	*0.6*	0.3	*0.7*
IR/Thermal	3.0	moderate rain	**Red**	*0.5*	0.3	*0.7*
IR/Thermal	3.0	light snow	**Red**	1.2	1.6	1.2
IR/Thermal	3.0	moderate snow	**Red**	1.2	1.6	1.2
IR/Thermal	3.0	drizzle	**Red**	*0.5*	0.3	*0.7*
IR/Thermal	3.0	fog	**Red**	1.3	1.2	0.9
IR/Thermal	3.0	blowing sand	**Red**	1.2	*0.8*	1.3
IR/Thermal	4.0	light rain	***Amber***	*0.6*	0.3	*0.7*
IR/Thermal	4.0	moderate rain	***Amber***	*0.5*	0.3	*0.7*
IR/Thermal	4.0	light snow	***Amber***	1.4	2.3	1.3
IR/Thermal	4.0	moderate snow	***Amber***	1.4	2.3	1.3
IR/Thermal	4.0	drizzle	***Amber***	*0.5*	0.3	*0.7*
IR/Thermal	4.0	fog	***Amber***	1.5	1.4	0.9
IR/Thermal	4.0	blowing sand	***Amber***	1.5	*0.8*	1.3

KEY
100 % > Green ≥ 60 %
60 % > *Amber* > 20 %
20 % ≥ **Red** > 0 %

Table 4. Visible Wavelength Sensors - Meteorological/Empirical						
TYPE	**Visibility (km)**	**Weather Condition**	**IWEDA**	**OR Id (km)**	**EO Lo (km)**	**TG Rec (km)**
DVO/TV	7.0	light rain	**Green**	*0. 4*	*1.0*	*0.5*
DVO/TV	4.0	moderate rain	***Amber***	**0.3**	*0.7*	*0.4*
DVO/TV	3.0	light snow	***Amber***	**0.3**	**0.5**	**0.3**
DVO/TV	1.5	moderate snow	**Red**	**0.3**	**0.3**	**0.3**
DVO/TV	8.0	drizzle	**Green**	*0.5*	*1.2*	*0.6*
DVO/TV	4.0	fog	***Amber***	*0.5*	*0.8*	*0.7*
DVO/TV	7.0	blowing sand	**Green**	*0.4*	*1.3*	*0.5*

Table 5. Infrared Wavelength Sensors - Meteorological/Empirical						
TYPE	**Visibility (km)**	**Weather Condition**	**IWEDA**	**OR Id (km)**	**EO Lo (km)**	**TG Rec (km)**
IR/Thermal	7.0	light rain	**Green**	*0.6*	**0.3**	*0.7*
IR/Thermal	5.0	moderate rain	**Green**	*0.5*	**0.3**	*0.7*
IR/Thermal	3.0	light snow	**Red**	**1.8**	**1.6**	**1.5**
IR/Thermal	1.5	moderate snow	**Red**	**1.8**	**1.0**	**1.5**
IR/Thermal	8.0	drizzle	**Green**	*0.5*	**0.3**	*0.7*
IR/Thermal	5.0	fog	**Green**	**1.4**	**1.4**	**1.0**
IR/Thermal	7.0	blowing sand	**Green**	**1.5**	**1.0**	**1.3**

KEY
100 % > **Green** ≥ 60 %
60 % > ***Amber*** > 20 %
20 % ≥ **Red** > 0 %

5. FUTURE WORK

It is necessary to keep in mind that IWEDA was never designed to deal with target acquisition per se. However it is apparent that further examination and refinement of the IWEDA rules are necessary, particularly at IR wavelengths. Examination of methodologies to couple the rules more closely to IR "visibilities" is underway as are ways to provide further refinement when significant temperature differences between target and background exist. Current plans are to couple IWEDA to an existing TDA so that when IWEDA is invoked an actual acquisition range is returned for a given target, coupled to a given system, sensor and current forecast weather conditions.

REFERENCES

1. "ACQUIRE Range Performance Model for Target Acquisition Systems," Version 1 User's Guide, U.S. Army CECOM Night Vision and Electronic Sensors Directorate Report, Ft. Belvoir, VA, May 1995.

2. Gouveia, M., DeBenedictis, D., Freni, J., Halberstam, I., Hamann, D., Hilton, P., Hodges, D., Hoppes, D., Oberlatz, M., Odle, M., Touart, C., Tund, S-L., "Electro-Optical Tactical Decision Aid (EOTDA) User's Manual," Version 3.1, U.S. Air Force Phillips Laboratory Technical Report PL-TR-94-2174(I), Hanscom AFB, MA, June 1994.

3. Hinton, J.L., "The BAe SRC Visual Performance Model ORACLE An Overview," British Aerospace Sowerby Research Centre Report JS 12138, Bristol, UK, July 1992.

4. Gillespie, P., "TARGAC Technical Description and User's Guide," U.S. Army Research Laboratory Technical Report ARL-TR-273-3, Adelphi, MD, April 1995.

5. Sauter, D., "The Integrated Weather Effects Decision Aid (IWEDA): Status and Future Plans," in Proceedings of the 1996 Battlespace Atmospherics Conference, 3-5 December 1996, Naval Command, Control and Ocean Surveillance Center RDT&E Division Technical Document 2938, San Diego, CA, December 1996.

6. Johnson, J., "Analysis of Image Forming Systems," in Proceedings of the Image Intensifier Symposium, Ft. Belvoir, VA, October 1958.

7. Hering, W., and Johnson, R., "The FASCAT Model Performance Under Fractional Cloud Conditions and Related Studies," U.S. Air Force Geophysics Laboratory Technical Report AFGL-TR-84-0168, Hanscom AFB, MA, 1983.

8. Johnson, K., "Technical Reference Guide for TCM2," Georgia Technical Research Institute, Atlanta, GA, 1991.

9. Duncan, L., Sauter, D., Miller, A., EOSAEL 87, Volume 21, "Natural Illumination Under Realistic Weather Conditions, ILUMA", U.S. Army Atmospheric Sciences Laboratory Technical Report ASL-TR-0221-21, White Sands Missile Range, NM, October 1987.

10. Heaps, M. and Johnson R., "An Empirical Algorithm for the Vertical Structure of Atmospheric Extinction", U.S. Army Atmospheric Sciences Laboratory Technical Report ASL-TR-0142, Whites Sands Missile Range, NM, 1983.

11. Kneizys, F.X., Shettle, E., Abreu, L., Chetwynd, J., and Anderson, G. "Users Guide to LOWTRAN 7, U.S. Air Force Geophysics Laboratory Technical Report AFGL-TR-88-0177, Hanscom AFB, MA, 1988.

12. Henmi, T., Dumais, R., "Description of the Battlescale Forecast Model (BFM)", U.S. Army Research Laboratory Technical Report ARL-TR-1032, White Sands Missile Range, NM, January 1998.

13. Shirkey, R.C., L.D. Duncan, F.E. Niles, EOSAEL 87, Volume 1, Executive Summary, U.S. Army Atmospheric Sciences Laboratory Technical Report ASL-TR-0221-1, White Sands Missile Range, NM, 1987.

14. Gillespie, P., private communication, 1997.

15. Dreksler, S., "Electro-Optical Tactical Decision Aid Sensor Performance Model Evaluation", Naval Research Laboratory Technical Report NRL/MR/7543--94-7216, Monterey, CA, April 1995.

16. Touart, C., Gouveia, M., DeBenedictis, D., Freni, J., Halberstam, I., Hilton, P., Hodges, D., Hoppes, D., "Electro-Optical Tactical Decision Aid (EOTDA) User's Manual", Version 3, Technical Description, Appendix A, , U.S. Air Force Phillips Laboratory Technical Report PL-TR-93-2002 (II), Hanscom AFB, MA, January 1993.

17. Fiegel, R.P., "Natural Aerosol Extinction Module, XSCALE", U.S. Army Research Laboratory Technical Report ARL-TR-273-1, Adelphi, MD, 1994.

18. Aerographer's Mate 3 & 2, Bureau of Naval Personnel Rate Training Manual, NAVPERS 10363-D, Millington, TN, 1971.

19. Quantitative Description of Obscuration Factors for Electro-Optical and Millimeter Wave Systems, Military Handbook DOD-HDBK-178(ER), July 1986.

Battlespace Atmospheric Conference
2- 4 December 1997

Interactive Multisensor Analysis Training

Sandra K. Wetzel-Smith
NCCOSC RDT&E Division
Code D301 BLDG BK-328, Room 212A
53560 Hull Street
San Diego, CA 95112-5001
(619) 553-7693 (553-0477 - FAX)
skw@nosc.mil

Wayne H. Wilson, PhD
Photon Research Associates, Inc
5720 Oberlin Drive
San Diego, CA 92121
(619) 455-9741 (455-0658 - FAX)
whw@photon.com

Abstract

The Interactive Multisensor Analysis Training (IMAT) system is designed to teach the complex interactions among onboard systems, environment and threat to the operational users of advanced weapons and sensor systems. Users need an intuitive but not necessarily scientific understanding of the physical principles which underlie the tactical use of their sensors and the effect of the environment in which they are used. The IMAT system employs multidimensional graphics, animations and scientific visualization methods to illustrate complex physical and environmental interactions. The system has been effectively applied in the context of tactical oceanography. During the past year a component to the IMAT system addressing electromagnetic sensors has been implemented and is being used for training purposes in the context of ASW surface surveillance. Subjects covered by the training system includes sensors, behavior of radio-wave emissions, refractivity and its dependence on weather and lower boundary layer conditions, frequency in range-dependent environments and boundary interactions. Sensor positioning and settings, environmental conditions and target characteristics can all be modified interactively in order to illustrate to the trainee specific instructional points and to generate "what-if" scenarios. The IMAT system allows the instructor to demonstrate optimal sensor employment in support of tactical battlespace management. This paper describes the IMAT system and its use as an effective training system for electromagnetic concepts.

INTRODUCTION

The development of atmospheric propagation models and supporting databases has a significant impact on the use of current and future naval sensor/targeting systems. These models must provide realistic and accurate representations of the target/environment/sensor in order to ensure that operational fleet users have access to comprehensive and complete knowledge of their tactical environmental situation. The development of these models and databases should not be generated in isolation without regard to the their eventual use by non-technical users (i.e. fleet personal) but should recognize the context, including training, in which they should and will be used. The concurrent development of training systems for fleet personal to utilize these databases and models must be addressed in parallel with this R&D in order to ensure that operators and tactical commanders understand and can perform complex tasks with them.

It has become evident over the last decade that target/environment/sensor issues are critical with respect to tactical training. A number of factors are responsible for this situation. First, the naval tactical situation has shifted from an open ocean environment to a littoral one. This shift introduces a significantly more complex and dynamic environment with respect to the tactical situation. Second, the application of low observable technology has reduced target signatures to levels at or below environmental clutter. This requires a fundamental understanding of the effect of the environment on target sensing. Third, the use of obscurants, which affect electromagnetic propagation, can dramatically affect target detection and classification. The knowledge of the existence and effects of these obscurants by the tactical commander can allow tactical control of local areas. Fourth, associated with low observable technology is the recognition that passive tactics, either by the target and/or the sensor, can fundamentally affect the tactical situation. And fifth, it has been recognized that no single sensor or phenomenology is adequate to address either existing and future target/environment issues. This issue will require the use of multisensors, multiplatforms, and multiphenomenology in order to control the local tactical situation.

TRAINING

The successful use of many advanced weapon and sensor systems in a complex tactical environment has historically required years of course work and operational experience for any single individual to achieve true tactical proficiency. In most cases these individuals do not have or need the scientific or technical background to understand the complex system operation, the impact of the environmental variability on propagated signals or the target's vulnerability to critical threat detection and prosecution. Experience has shown that individuals who become top performers have been those who were able to derive the best tactical solutions through sophisticated reasoning - what observers might call a "sixth sense" - based on the individual's exposure to a wide variety of environmental and tactical situations. Close examination of these top performers reveals that the key to their success is that they have developed conceptual understanding of the complex interrelationships between their sensor systems, the environmental effects, and the targets of interest. This conceptual understanding frequently does not involve an in-depth scientific or mathematical understanding of how a particular subsystem works but rather how that subsystem interacts with the other components of the problem. The recognition that

achieving top performance requires the individual to understand and perform complex cognitive tasks and not rote memorization of "standard" scenarios has lead to the development of IMAT. This training curriculum concentrates on providing the operator with a conceptual basis of his systems and how they interact with the environment and targets.

The key issue in developing the required level of conceptual understanding is how the three major areas interrelate, namely,

1. The target - the source of the signal in passive applications and a reflector of energy in active applications
2. The environment - the medium through which signals propagate
3. The sensor - where signal from the threat is received, and also the *source* of the signal in active applications

The IMAT system has been developed over the last decade in recognition of these concepts and is being used as both a classroom instructional aid and a student tool for conveying the required conceptual understanding of complex concepts. It enhances the traditional courses that rely on memorization of facts, procedures and rules. Initial development and implementation of IMAT has achieved significant success in the instruction of acoustics and tactical oceanography. Over the last year enhancement of the system with respect to electromagnetics have been addressed with an initial training capability scheduled for this year.

SCIENTIFIC VISUALIZATION

The key to the development and use of IMAT has been the application of the appropriate levels of training technology and instructional design in teaching complex technological concepts. The appropriate levels are based on a number of considerations with respect to the desired operator or user performance achievements. These considerations include:

- Level of abstraction - physical cause-and-effect relationships may not be readily apparent, but are the outcome of many subtle interactions. Electromagnetic propagation through a complex refractive environment is a good example.
- Continuity - many physical phenomena and their effects are described as discrete points on a continuum, and by presenting these points in progression, students can develop a feel for the trend and flow of the entire system.
- Non-linearity - the more complex the mathematics needed to describe an effect, the more difficult it is to produce a simple "rule" to understand the process.
- Dynamic state - understanding the *progression* of a scenario over time is often impossible by examining a series of stand-alone snapshots. A basis of understanding built on instances rather than animation can constrain later performance in rapidly evolving mission situations.

- Simultaneity - the extent of concurrency that must be taken into account. With sensors, threats and environment all acting simultaneously, each major influence must be understood fundamentally *and* as part of the entire scenario.
- Interactivity - Electromagnetic propagation provides an excellent example of the need to understand the interplay of factors, with dozens of variables in hundreds of combinations.
- Conditionality - although principles may be applied universally in scientific or mathematical terms, practical uses in a warfare environment are likely to be highly contextualized. This becomes difficult when complex subject matter has been reduced to a set of heuristics for ease of teaching. The application of range-independent heuristics to a range-dependent refractivity environment is an example.

Each of these considerations is important in teaching sensor system operation, tactical employment, team integration and crew coordination. The development of IMAT and its current curriculum was developed by understanding these considerations and the fact that the traditional methods of teaching based on detailed mathematical and physical explanations have failed to impart the desired level of performance based on the average operator's education and experience. The recognition that advanced scientific visualization techniques could provide a framework, wherein the interrelations between the various components of the problem could be presented in order to convey the complex concepts needed to understand and perform each task is a fundamental aspect of IMAT.

The key to any scientific visualization is the transformation of mathematical and data representations such as wavefronts, propagation, and climatological/environmental databases into a useful and informative context with which the student can identify or recognize. Electromagnetic propagation, for example, involves differences in wavelength, transmission paths, boundary reflections, absorption, scattering, and frequency shifts and understanding the multivariate outcome, difficult even for a knowledgeable scientist or engineer, is likely to be impossible for a novice sensor operator.

Over a period of time the IMAT system has developed, based on feedback from the training schools and operational use, a visualization system which employs a multi-use concept display that provides three-dimensional representations of cause-and-effect relationships. Complex mathematical formulae are transformed into visualizations of physical or abstract concepts. Using IMAT, students and instructors may now display a wide range of scenarios that reflect the input of climatological/environmental databases and sensor and target characteristics. Easy-to-use computer interfaces allow on-the-fly classroom simulation of "what-if" scenarios, mission replays and decision analysis.

IMAT SOFTWARE AND HARDWARE

The various IMAT software modules used for modeling targets, the environment and the sensors and the supporting databases are based on community standard codes and databases and therefore incorporate the latest assessment of the state of knowledge of the environmental/physical factors effecting the tactical problem. The system has, by virtue of assessing the performance of sensor systems against targets in different environmental scenarios, been able to recommend upgrades to community models and/or databases for use by the fleet.

Central to the IMAT development effort, and partially responsible for its success, has been the philosophy of using commercial-off-the-shelf (COTS) equipment and modular software. Currently versions of the IMAT system reside on various Silicon Graphics workstations and Pentium PCs.

ELECTROMAGNETIC INSTRUCTION

IMAT's oceanographic and acoustic software has been developed over the last decade in response to the considerations discussed above. It has been implemented in a form and format that has improved the efficiency of training in these areas. In 1996, in response to fleet requirements, the first electromagnetic models, displays and curriculum were implemented following the same structure as the oceanography/acoustics portions. The goal of the electromagnetic enhancements was to introduce a range of concepts from refractivity and its dependence on temperature, pressure, and humidity in the atmosphere, to propagation, including range-dependent refractivity, terrain and polarization effects. Based on initial response to the system, continuing development has and will provide additional mission-specific predictive capabilities, such as the ability to compute signal excess and probability of detection.

In order to provide a perspective of the structure of IMAT and the implementation of its training paradigm, the following paragraphs describe those electromagnetic modules within the current system in the order in which they are is presented to the student. These brief examples are not meant to be comprehensive or to cover all areas of the electromagnetic instruction course. They are meant to illustrate those areas that the IMAT team has recognized as key to the development of an operator's conceptual understanding of the use of electromagnetics in a tactical context.

Environment and Refractivity Profiles The environmental profiles shown in Figure 1 are used to introduce the student to the important environmental factors which influence the shape of a refractivity profile and hence the propagation of electromagnetic energy through the atmosphere. In this example, the duct is a result of significant changes in the water vapor pressure over a small change in altitude. The concept of a modified refractivity (M) unit profile is also introduced. This profile is used because it is easier to determine duct boundaries and because it corrects for the earth's curvature.

Ray Tracing A common misconception held by novice operators is that electromagnetic energy travels in straight lines through the atmosphere. One of the displays used early in the instruction shows how electromagnetic energy is actually refracted. This display, shown in

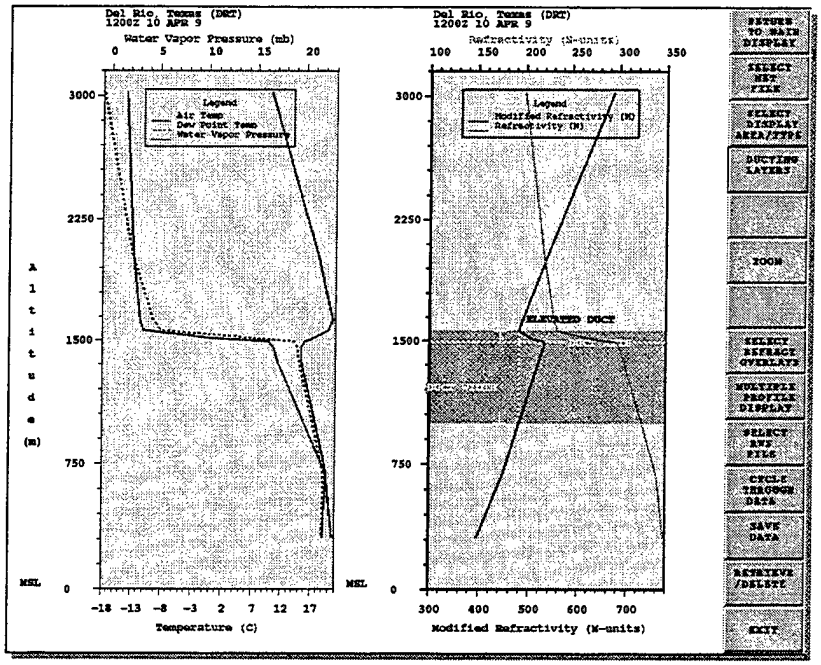

Figure 1. Environment and Refractivity

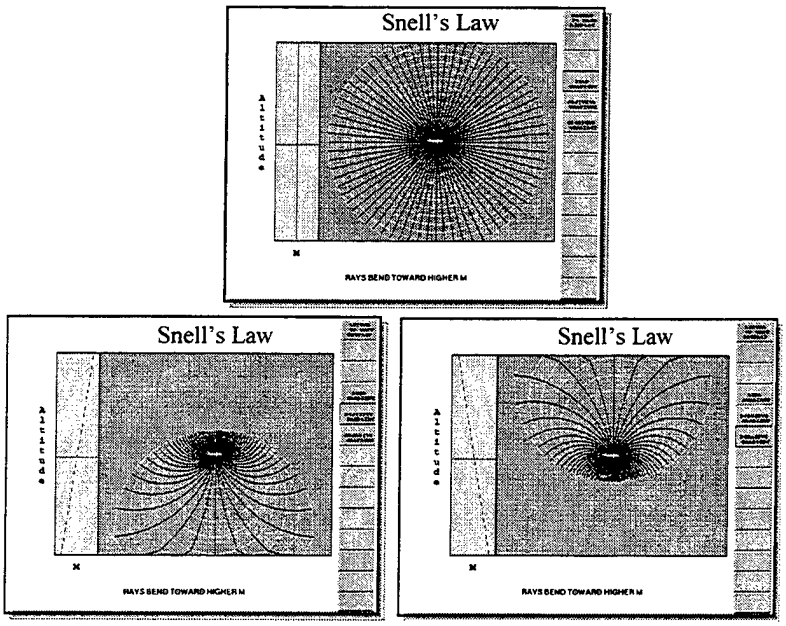

Figure 2. Snell's Law

Figure 2, allows the instructor to choose a constant, a positive, or a negative gradient profile segment. The student can then watch an animation where wave fronts spread from a source and the resultant ray paths are drawn.

Figure 3, shows how the choice of coordinate system affects the presentation of the data: in this case, one ray: a ray traveling straight out from an emitter in a curved earth system is seen as a curved ray in a flat earth system. Finally, a ray trace model and its display are introduced (Figure 4). For ray tracing, IMAT uses the multiple-profile ray-tracing program (MPP), a model adapted from underwater acoustics, which is range-dependent in both refractivity and terrain height. In this figure, a standard atmosphere profile and the associated ray paths are shown in the top

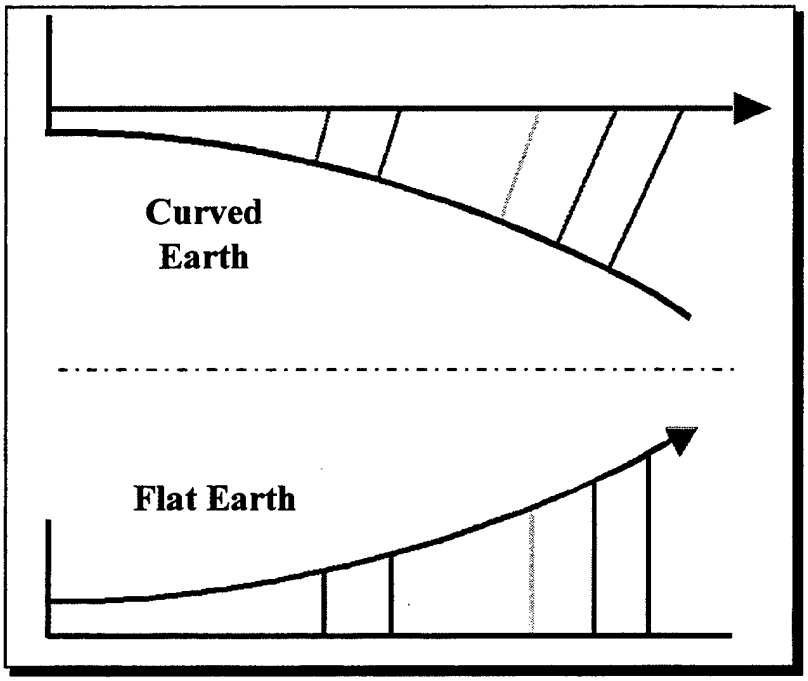

Figure 3. Curved vs. Flat Earth

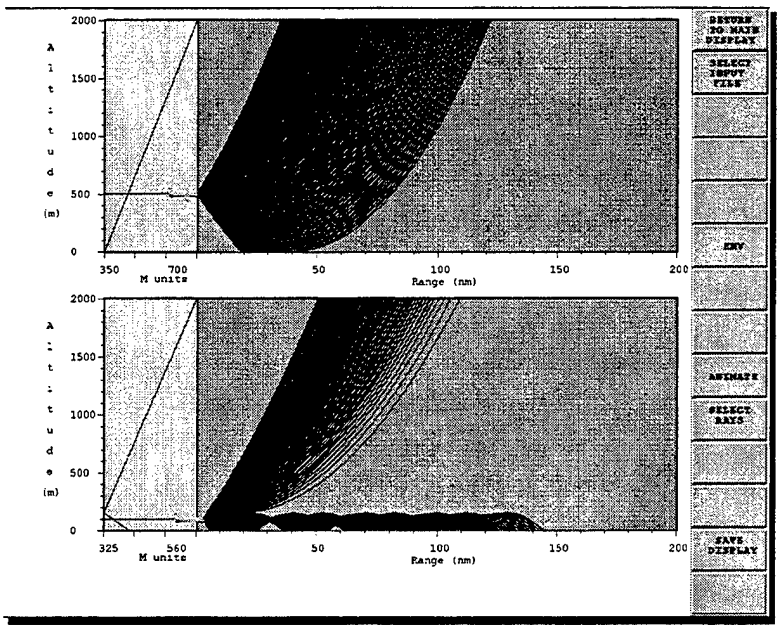

Figure 4. Ray tracing - Standard Atmosphere vs. Surface-based duct

picture. As expected, the rays bend towards higher M-unit values. The bottom picture shows the same projected ray fan for a transmitter in a surface duct. Figure 5 shows three frames of an animation demonstrating sensitivity of ray paths to transmitter height relative to a duct. These concepts provide to students connectivity between the environment, placement of a transmitter, and propagation paths.

Path Loss While a ray trace model provides insight into potential ray paths, a propagation model is needed to contribute the path loss term in the passive and active radar equations. IMAT currently uses a Navy standard propagation model, TPEM, to predict propagation loss for almost any sensor-target geometry in environments that reflect range-dependence in terrain type, terrain height, and refractivity. Other propagation models, such as RPO and VTRPE, are also available for use, depending on the degree of fidelity or computation speed required. Figure 6 shows propagation loss as a function of range and altitude in a range-dependent environment. Phenomena such as Lloyd's mirror and diffraction due to terrain features can be seen. This illustrates a tactically-relevant concept to the student that is normally counter-intuitive: that energy bends around corners and could be exploited there.

Both propagation loss and ray trace models offer dynamic as well as static displays. The following variables can currently be animated, in the propagation loss model:

- Frequency
- Source position in range and altitude
- Time (diurnal or seasonal effects)
- Antenna Tilt

Background Land/Sea Modeling High-fidelity physics-based simulations have proven to be a powerful means of evaluating radar concepts and augmenting experimental development programs. With the advent of deterministic background scene generation, simulations can now actually "fly" the sensor in specific geographic environments. Full time-domain simulations, however, tend to be complex and generally do not provide real-time end-to-end performance measures.

Computationally efficient frequency-domain radar modeling techniques are being developed and will enable simulations to be conducted in real time using physics-based deterministic background scenes. The outputs of these simulations will drive simulated operational radar displays, such as PPIs. Signal and clutter and spectral characteristics are derived directly from the background scene and convolved with the radar sensor front end (antenna radiation pattern, transmitter power, etc.).

Clutter Modeling Clutter maps showing the radar cross-section of sea and land surfaces are generated combining highly-detailed information about the surfaces with range-dependent propagation between the sensor and surface.

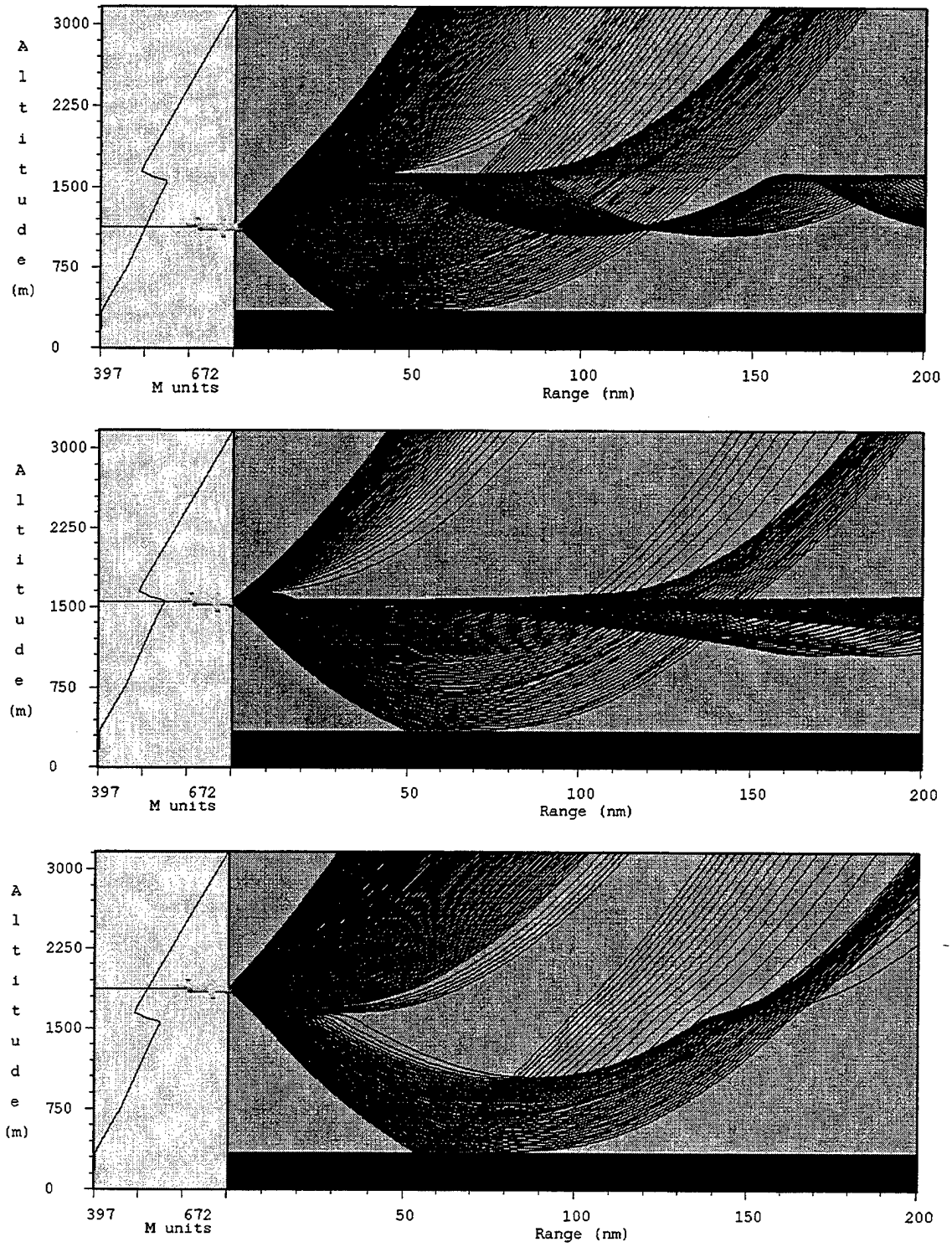

Figure 5. Ray trace, Del Rio Profile

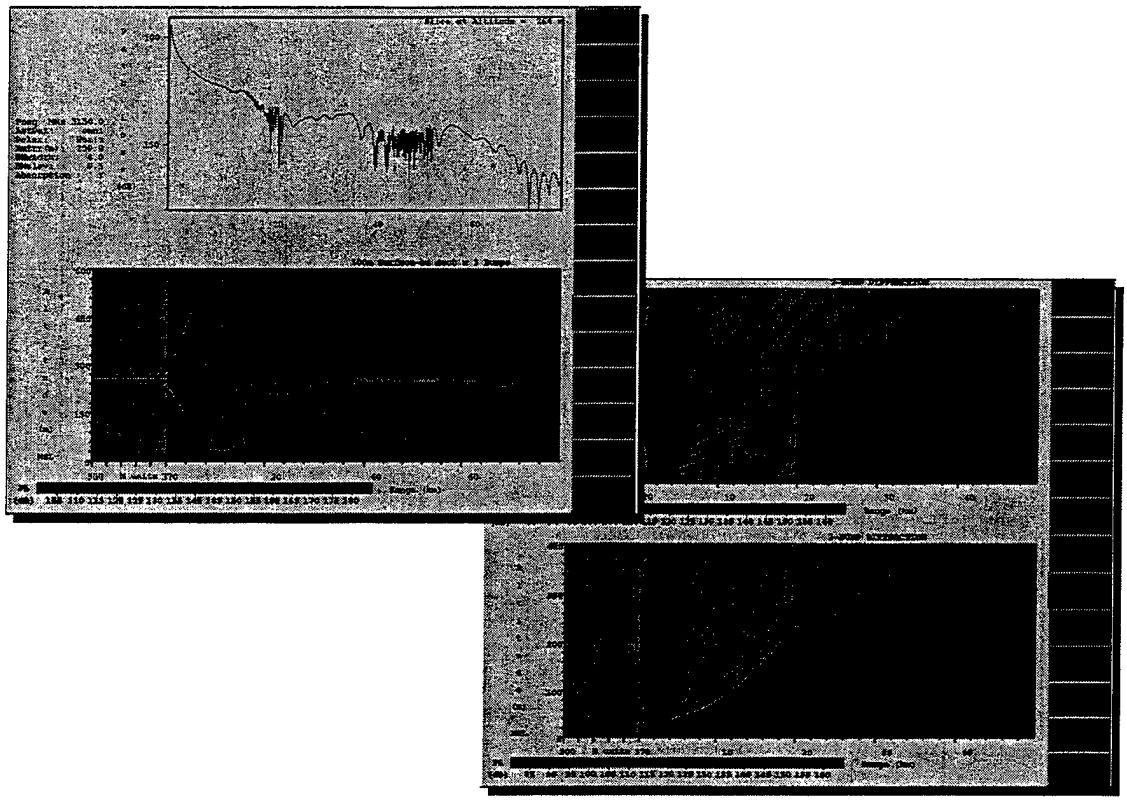

Figure 6. Propagation over a wedge

Conclusions

The IMAT system has been demonstrated to provide significant improvements in the performance of operators and tactical commanders in tactical situations. The continued enhancements of the system with respect to phenomenologies such as electromagnetics and optics in both the atmosphere and ocean will provide a consistent training-modeling environment for all Naval tactical situations. The fundamental premise of the IMAT system that the whole problem, spanning target, environment and sensor issues, must be factored into the training process is being incorporated into all phases of the IMAT curriculum. The enhancements with respect to electromagnetics have followed and will continue to follow this premise.

MODTRAN4 VS. HISTORIC CODES: POTENTIAL SENSOR SYSTEMS IMPACT OF IMPROVED PHYSICS

G.P. Anderson*, J.H. Chetwynd
PL/Geophysics Directorate, 29 Randolph Rd., Hanscom AFB, MA 01731
617-377-2335, Fax 377-8900, 'ganderson@plh.af.mil'
A. Berk, L.S. Bernstein, P.K. Acharya
Spectral Sciences, Inc., 99 S. Bedford St., Burlington, MA 01803
H.E. Snell
Atmospheric and Environmental Research, Inc., 840 Memorial Dr., Cambridge, MA 02139
E.P. Shettle
Naval Research Laboratory, Washington, D.C. 20375

ABSTRACT

The new MODTRAN4 band model, with its Correlated-*k* Beer's Law algorithm, can efficiently and correctly calculate the scattering and absorption signatures of realistic molecular, aerosol and cloudy environments in the lower and middle atmosphere. The current approach for molecular scattering accommodates line overlap and partial correlations between both molecular species and the solar irradiance, while maintaining internal band model spectral resolution at either 2 (1 cm^{-1} binning) or 15 cm^{-1}. This new level of evolution and validation will permit improved syntheses, analyses and detection of total (direct plus scattered) solar and thermal energy components for clouds, aerosol decks, plumes and other realistic non-clear sky conditions.

Validation is provided through two avenues. The first involves direct comparisons with line-by-line calculations, as exemplified by FASE (the line-by-line algorithm jointly developed from FASCODE by DoD and DOE) which provides the molecular standard for layer effective optical depths, single scattering albedos, and transmittances. This enables the MODTRAN4 algorithm to be refined for more flexible spectral resolution plus efficient and accurate determination of those layer quantities necessary for multiple scattering applications; e.g. DISORT. The second validation step centers on comparisons against a variety of measurements, mostly airborne visible and IR up-welling radiances, including both clear and clouded skies. Finally, comparisons of the new MODTRAN4 approach against those associated with LOWTRAN 7 and previous versions of MODTRAN can provide an assessment of the potential impact on sensor simulations, particularly in regard to hypothetical Tactical Decisions Aids (TDA's) in the 3-5 and 8-12 um range.

1. INTRODUCTION

With the development of MODTRAN4 (Bernstein, et al., 1996), a flexible tool for radiative energy budget calculations is now available. While this version of MODTRAN is grounded in the prior series of AF radiative transfer band model (BM) algorithms (LOWTRAN, Kneizys, et al., 1980, 1983, 1988, through MODTRAN3, Berk et al., 1989, 1995), it is distinct in its ability to employ Beer's law ($T_\nu = \exp(-k_{\nu,i}\, n_i)$) to describe local layer transmittances for input to the radiance calculations. While this capability is not always necessary, it allows appropriate handling of multiple scattering (m.s.) using existing monchromatic (e.g. non-BM) algorithms (DISORT, Stamnes et al., 1988, and Isaacs et al., 1987). MODTRAN4, while maintaining the basic 2 cm^{-1} spectral resolution, can now complement the m.s. routines by introducing a Correlated-*k* (CK) capability which is expressly compatible with these Beer's law formulations. MODTRAN4 also provides greatly improved predictive capabilities under cloudy and/or heavy aerosol loading conditions in both the visible and IR. It now allows the explicit definition of water and ice cloud vertical profiles and spectral data, either by scaling and combining default clouds or by redefining entirely new model clouds with micro-layering options (Berk et al., 1997). Similar aerosol options have recently been added (Anderson et al, 1997), with flexibility on layering and optical properties, including

NOVAM (Navy Oceanic Vertical Aerosol Models, Gathman and Davidson, 1993). To complement the extensive additions in user-based options, a stand-alone Mie scattering code has also been provided (Shettle and Longtin, private communication).

This combination of improvements should permit rapid identification of atmospheric contaminants and/or signatures in window regions as well as accurate spectral radiance calculations in the presence of clouds for both thermal and solar spectral regimes. In the regions of molecular opacity, where weighting functions peak in the atmosphere, it is expected that MODTRAN4 can play a role in very quick 'primitive' retrievals, avoiding the large number of line-by-line (LBL) calculations necessary for initiating derivative (perturbation) matrices (Anderson et al., 1993). While the error estimates and residuals associated with a 2 cm^{-1} resolution algorithm will be slightly larger than those associated with LBL retrievals, the speed advantage for image processing might warrant this initial approach.

Of more recent concern is the impact of these new MODTRAN4 capabilities as potential replacements for existing embedded systems algorithms. For instance, tactical decision aids (TDA's, e.g. broad-band Mid Wave IR (3-5 um) and IR (8-12 um) systems) may rely upon look-up tables generated from historic band models, perhaps predicated on LOWTRAN calculations over relatively short paths. Hypothetically, these tables may then have been employed to infer transmittances and radiances for arbitrary line-of-sight configurations that exceed the range over which the original tables were presumed valid and beyond the assumptions internal to the TDA logic. The requirements for such extended ranges necessitate reexamining the assumptions for accuracy and applicability. For long-path applications where objects must be discriminated against backgrounds and where assessment of lock-on ranges may be critical, very rapid calculations against 'realistic' weather scenarios can now be supported by MODTRAN4.

2. BACKGROUND

Spectrally uniform treatment of the atmospheric radiative transfer (RT) problem has been approached through two different techniques - very high resolution line-by-line (LBL) algorithms and lower resolution band models (BM). Each has its advantages and specific applications. However, if commonality and validation of a specific set of RT approaches are to be mutually maintained, then these codes must be continually reevaluated against both measurements and other models.

2.1 FASE: FASE (FASCODE for the Environment, Snell et al, 1995) is a full LBL atmospheric radiation code, grounded in the original USAF FASCODE (Fast Atmospheric Signature Code, Smith et al, 1978) line-shape decomposition algorithm (Clough and Kneizys, 1979). The Department of Energy Atmospheric Radiation Measurement Program (ARM) and the AF Geophysics Directorate jointly supported FASE, which now envelops both agencies important upgrades. In particular, DOE/ARM, through provision of their FASCODE-based LBL code, LBLRTM (Clough, 1993), has supplied: new H_2O and CO_2 continua, code vectorization, improved line shape sampling, and expanded maximum spectral ranges. The non-LTE and laser options originally available in FASCODE have been reacquired and augmented. The shared common elements from MODTRAN (Berk et al., 1989, Anderson et al, 1993) evolution (as subsequently described), include more flexible cloud (and eventually aerosol) optical properties. Two exclusive FASE capabilities center on (1) incorporation of recent CFC cross-sections (Varanasi and Nemtchinov, 1994), requiring the development of a pseudo-line data base (Toon, private communication); and (2) access to the ultraviolet Schumann/Runge (S/R) O_2 band system as a temperature-dependent cross-section (Minschwaner et al, 1992). Both options will eventually be ported to MODTRAN.

2.2 LOWTRAN (obsolete): LOWTRAN 7 (Kneizys et al., 1988) was the last version of the LOWTRAN series, a low-resolution (20 cm^{-1}) BM and computer code for predicting atmospheric transmittance and background radiance from 0-50,000 cm^{-1}. This code was based on LOWTRAN 6 and its predecessors (Kneizys et al, 1983) but employed an entirely new band model approach. Separate band models and band model absorption parameters developed by Pierluissi and Maragoudakis (1986) were used to develop

analytic transmission functions, replacing numerical tables used in all previous LOWTRAN codes. These new models were developed with and based on degraded LBL spectra and validated against laboratory measurements, when available. A critique of LOWTRAN 7 was published by AGARD (Advisory Group for Aerospace Research & Development, Kneizys et al, 1990). It must be emphasized that the LOWTRAN sequence of radiative transfer codes, while extremely valuable for their time, are now obsolete. Transmittance calculations, run at the same spectral resolution, often differ from FASCODE by more than 10-20% over narrow spectral ranges, even in the bands of interest for TDA applications. Not only are the transmittances now inadequate, but the radiance algorithms (Minschwaner et al, 1993) and all other applications, including the geometry (Gallery et al, 1985), have been improved dramatically since the release of MODTRAN.

More importantly, however, even when LOWTRAN and MODTRAN give comparable results for similar configurations, the flexible LOWTRAN mode that provided this agreement may *not* be typical of how the code was embedded into active systems. In most cases, LOWTRAN was actually further parameterized in order to fit the application criteria. For instance, again, hypothetically and simplistically, a standard 5 km path could have been chosen, against which to calculate a set of look-up tables (LUT's) for a broad-band filter application (e.g. 3-5 um). The data in the LUT's could then be extrapolated to other paths and lines-of-sight using a secant scaling approximation. For paths that approximately matched the LUT formulation, this assumption is reasonably appropriate, given the accuracy of LOWTRAN itself. In the extreme, for a horizontal path extrapolation from 5 to 150 km, such a primitive LOWTRAN-based algorithm could fail by 30% or more, with no simple predictive means for correcting the error. See Figure 1 a/b. Figure 1a depicts the transmittance failure of a hypothetical LOWTRAN-based TDA (3-5 um), based on a 5 km horizontal path calculated at 10 km altitude, extrapolated to 150 km. The comparable MODTRAN-based run provides the correct solution for the 150 km path. Figure 1b is a similar calculation for an 8-12 um hypothetical TDA, but at 5 km altitude, diminishing the impact of ozone (9.6 um band) upon the results. In both cases, the LOWTRAN predictions show significantly lower transmittance than is actually encountered, leading to potentially false interpretations. Actual TDA's may not show this extreme failure mode; this is only a demonstration of the possibilities. A careful evaluation of the assumptions inherent in real TDA's need to be examined for these phenomena. If true, one proposed solution is to design new systems directly around MODTRAN4. This will be discussed later.

Figure 1a/b: Hypothetical LOWTRAN-based TDA's for 3-5 and 8-12 um spectral ranges. The paths transmittances have been scaled from 5 km range tabulated calculations to 150 km. In each case, the actual 'full path' MODTRAN4 results (upper curves) are more transparent, both spectrally and band-integrated. These values demonstrate extremes for the failure mode. MODTRAN4, if embedded in a similar TDA formulation, is expected to reproduce the correct (more transparent) results.

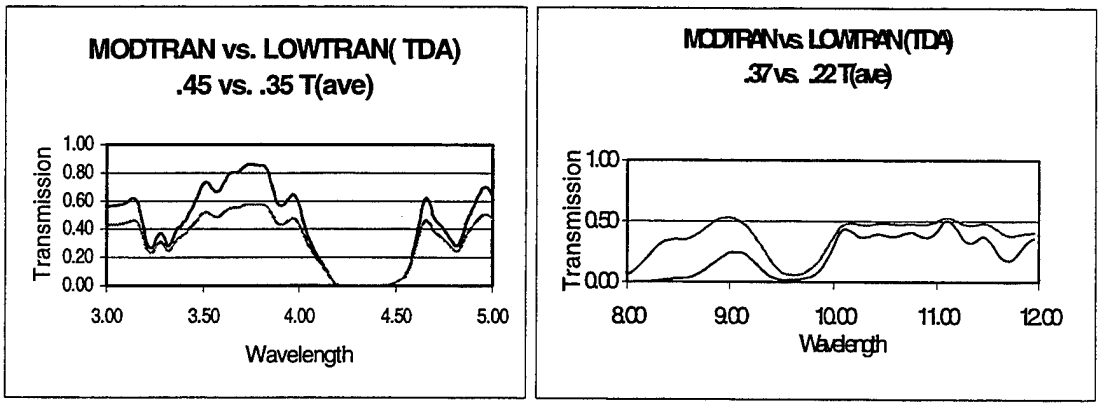

2.3 MODTRAN: MODTRAN (Moderate Resolution Transmittance Model), a 2 cm^{-1} resolution BM, is derived directly from the HITRAN spectroscopic database (Rothman et al., 1992, 1997), with transmittance

calculations independent from LBL formulations. An example of MODTRAN accuracy in transmittance, relative to FASCODE, is presented in Figure 2. The path approximately corresponds to a 150 km horizontal path, as might be required for the next generation of TDA's. Note that the resolution is that of MODTRAN, 2 cm^{-1}. A typical 8-12 um TDA is configured with a broadband filter over a large portion of this spectral range, between 833 and 1250 cm^{-1}.

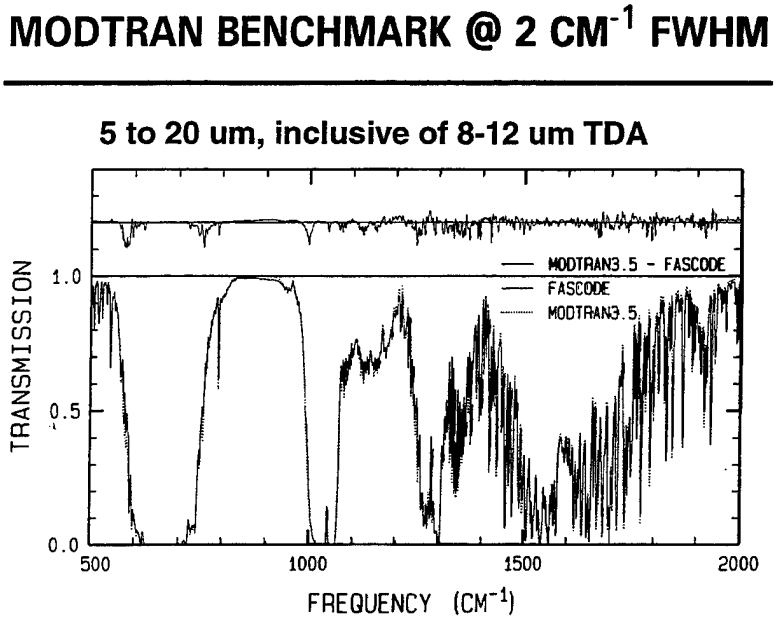

Figure 2: FASCODE and MODTRAN3.5 (equivalent to MODTRAN4) transmittances over the IR spectral range for a 150 km path length. The strong ozone signature near 1000 cm^{-1} (9.6 um) would be minimized for lines of sight in the troposphere. The agreement is, in general, excellent, and when further spectrally degraded to typical TDA resolutions (in this case, 8-12 um), the RMS residuals fall to less than 3%.

MODTRAN4 has been made fully compatible with the current multiple scattering algorithms by the addition of a Correlated-*k* (CK) approach (Bernstein et al, 1993, Lacis and Oinas, 1991, and as discussed more fully below) for the layer-specific opacities. This allows reasonably rapid analyses of solar and thermal scattering contributions in the presence of both molecular and realistic particulate environments, covering the spectral range from the visible into the far-IR. For further efficiency in the visible and near-IR spectral ranges, a 15 cm^{-1} version of the CK algorithm is also undergoing testing. The UV spectral range is independent of the CK technique because the primary absorbers are already described by cross sections (O_2, O_3, SO_2, and NO_2). While this broader resolution works well in the UV/Vis, it begins to fail in the MWIR (Figure 3) in the presence of strong and/or overlapping molecular absorption features from different species. In advance of the of the CK version of MODTRAN, an intermediate code (MODTRAN3.7, Berk et al, 1997) has been placed into full release. It employs a new spectroscopic adjustment to the binning algorithm for the band model parameters plus important variations for cloud, aerosol and solar input (Anderson and Acharya, 1997) options.

The synergistic feedback and validation of FASE and MODTRAN are critical to the joint maintenance of the paired codes. They represent over 20 years of historic radiative transfer coding evolution with a commitment to remaining "state-of-the-art."

Figure 3: A comparison of MODTRAN4 'default' band model databases in the 3-5 um range for a 150 km path range. Note that when the molecular band absorption is strong, the percent difference (upper curve) can be relatively large. The spectral band-integrated transmittances for the two cases are close, 0.41 and 0.43, for 1 and 15 cm^{-1} resolution, respectively. The 15 cm^{-1} BM tends to yield slightly more transparent results. A similar calculation for the 0.5-1.7 um spectral range (visible and near-IR) yielded identical band-averaged transmittances of 0.64, suggesting that, for the resolutions of many instruments in this spectral range, the 15 cm^{-1} BM may provide sufficient accuracy.

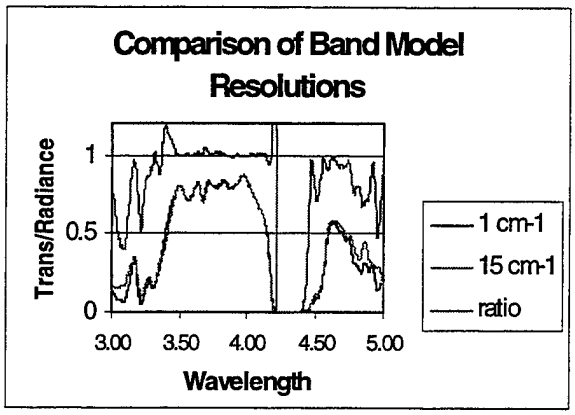

3. ADDITION OF A CORRELATED-*k* CAPABILITY TO MODTRAN

Addition of a CK capability to MODTRAN (Bernstein et al., 1995) provides an accurate and fast means for evaluation of the effects of clouds and heavy aerosol loading on retrievals (both surface properties and species concentration profiles) and on atmospheric radiative heating/cooling calculations. These radiative transfer computations require coupling the effects of gaseous molecular absorption due primarily to water vapor, carbon dioxide, and ozone, with particulate multiple scattering due to volcanic aerosols, ice crystals, and water droplets. In order to adapt a band model approach for use in scattering calculations it is necessary to express the band model transmission function in terms of a weighted sum of Beer's law exponential terms. Thus, a method for determining the weighing factors and monochromatic absorption coefficients for the MODTRAN band model is required. An abbreviated discussion of the CK approach as tailored for integration into MODTRAN is given below; for a more complete discussion of the CK method the reader is referred to Lacis and Oinas (1991).

For simplicity, consider the problem of determining the average transmittance, as defined by Beer's law, for a homogeneous path over a finite spectral interval. The generalization to inhomogeneous paths is straightforward. The path transmittance can be exactly determined through evaluation of:

$$T(u) = \frac{1}{\omega_2 - \omega_1} \int_{\omega_1}^{\omega_2} d\omega \ \exp(-k(\omega)u) \quad ,$$

where ω is frequency, $k(\omega)$ is the monochromatic absorption coefficient, and u is absorber column density. The basis of the CK approach is that evaluation of T(u) by integration over frequency can be replaced by an equivalent integration over the distribution of absorption coefficient values f(k) in the spectral interval

$$T(u) = \int_0^{\infty} dk\, f(k) \exp(-ku) \quad .$$

The distribution function f(k) is not smooth or monotonic; it generally consists of a series of sharp spikes which reflects the sharp line structure of $k(\omega)$. It then becomes more computationally convenient to work with the smooth and monotonic cumulative probability distribution function

$$g(k) = \int_0^{k} d'k\, f(k') \quad .$$

Note that k(g) is given by the inverse of g(k), $k(g) = g^{-1}(k)$.

The MODTRAN band model for a single species is based on four parameters: (1) the integrated line strength S in a spectral interval $\Delta\omega$ ($\Delta\omega$ = 1 cm^{-1} in MODTRAN); (2) the effective number of equivalent lines n (non-integer values of n are acceptable) in the interval; (3) the average pressure broadening Lorentz line width γ_L; and (4) the Doppler line width γ_D. These parameters are determined directly from the 1997 HITRAN parameter line compilation (Rothman et al., 1997). A parallel version of the CK databases is maintained at 15 cm^{-1} resolution to permit more rapid calculations of solar radiance/irradiance, as demonstrated in Figure 3.

4. MODTRAN4 AND TDA APPLICATIONS

As noted, a major limitation to the development of fully general real-time engagement simulations is the lack of real-time and realistic models for the atmospheric effects and target plume emissions. Just such a real-time atmospheric attenuation model for the 3-5 um wavelength region, based on MODTRAN4, is under development. This work is intended (at a minimum) to port 3-5 um weather effects into a Tactical Decision Aid (TDA) for a tailored application with ranges extending to 150 km. However, the basic approach is general and can be readily adapted to other simulation problems (i.e., other wavelength regions, path scenarios, contaminant emissions, etc.).

A key aspect of the approach is its use of the CK approximation which enables the transmittance for a finite spectral interval to be described by a weighted sum of just a few exponential terms (i.e., Beer's Law). The determination of the weighting factors and effective monochromatic absorption coefficients is complicated but readily implemented within MODTRAN4, as previously described. The CK approach has a number of important computational advantages over the traditional BM approach in earlier versions of MODTRAN. For instance, the TDA application requires an ability to treat "segmented" paths (e.g., portions of a line-of-sight across changing 'weather' volumes) simply by adding the adjacent monochromatic CK optical depths.

For this experimental 3-5 um TDA, MODTRAN4 is used to establish a species and altitude dependent matrix of effective monochromatic absorption coefficients. The spectral database of absorption coefficients need only be determined once since it does not depend (to first order) on the simulation scenario. The TDA is compatible with a 3D simulation grid (i.e., where the weather varies within the simulated spatial volume) and will return the path transmittance, as in Figure 4. Prediction or measurement, where the available height/pressure and horizontal grids determine the scale size of the 'segments' or voxels, can define the actual weather. In this case the smallest voxel elements were defined by the NCAR-Pennsyvania State mesoscale model, MM5, 1997.

In the first tests of this approach, MODTRAN4 was found to be sufficiently fast in producing the voxel transmittances and integrating them along the path. The resulting transmittances could then be coupled with additional components and incorporated into a computer simulation where the weather columns were defined by different temperature/pressure/constituent profiles and potential cloud content.

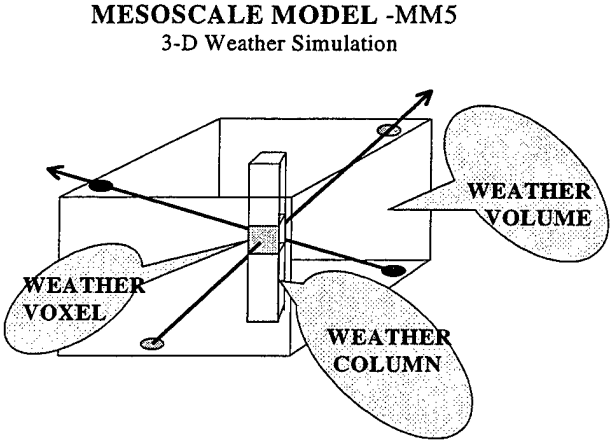

Figure 4: MM5 simulation of a mesoscale scenario for a region of order 150 km on a side. The horizontal spatial resolution of the model will determine the vertical column resolutions, and the voxels, themselves, will be defined by the vertical resolution. MODTRAN4 will be able to piecewise integrate across the voxel elements as determined by the line-of-sight. Two viewing geometries are presented in the figure.

5. CONCLUSIONS

MODTRAN4 with a Correlated-*k* implementation provides enhanced capabilities for scaling pre-calculated transmittances. This improvement relates to the direct implementation of Beer's law, where the average transmittance is the product of path-segment transmittances and for total paths not requiring spherical geometry (e.g. viewing and solar angles less than 65°; note: this latter limitation is only temporary). In such cases, the transmittances can be converted back to equivalent optical depths, permitting the scaling to be 'corrected' by the ratios of the secants of the path trajectories. Thus, arbitrary path segments defined by different temperatures, pressures, and mixing ratios, can now be convolved (in both transmittance and radiance) without recourse to the 'full-path' requirements of the original MODTRAN band models. Preliminary analyses show that such convolutions match the 'full path' results when the paths are identical, preserving the older validations. The improvement arises when longer paths, horizontal gradients or heavy aerosol and cloud content impact the line-of-sight. MODTRAN4 will continue to be tested for applications related to Tactical Decision Aids, in particular, and any other scenarios that might relate to measurements within the UV to the far-IR spectral ranges.

6. REFERENCES

Anderson, G.P., J.H. Chetwynd, P.K. Acharya, A. Berk, L.S. Bernstein, E.P. Shettle, S.G. Gathman, Addition of NOVAM (Navy Oceanic Vertical Aerosol Models) to MODTRAN in Support of OMPS, Report to NPOESS, 1997.

Anderson, G.P., J.H. Chetwynd, A. Berk, L.S. Bernstein, P.K. Acharya, An Algorithm for Hyperspectral Remote Sensing: Solar and Thermal Regimes, Optical Society of America, *Proceedings of Optical Remote Sensing of the Atmosphere*, Sante Fe, Feb 10-14, 1997.

Anderson, G.P., P.K. Archarya, Support to Assess Techniques for Ozone Monitoring: Solar Irradiance Upgrades, Report to NPOESS, 1997.

Anderson, G.P., Kneizys, F.X., M.L. Hoke, L.W. Abreu, E.P. Shettle, 'MODTRAN2: Suitability for Remote Sensing", *Proc. of SPIE, 1954, Remote Sensing*, 1993.

Berk, A., L.S. Bernstein and D.C. Robertson, *MODTRAN: A Moderate Resolution Model for LOWTRAN7*, PL-TR-89-0122, PL/GPOS, Hanscom AFB, MA (1989).

Berk, A., "Upgrades to the MODTRAN Layer Cloud/Rain Models," Report. No. SSI-SR-56, Spectral Sciences, Inc., 99 S. Bedford St., Burlington, MA, 1995.

Bernstein, L. S., A. Berk, D. C. Robertson, P. K. Acharya, G. P. Anderson, and J. H. Chetwynd, "Addition of a Correlated-*k* Capability to MODTRAN," Proceeding of the 1996 IRIS Targets, Backgrounds, and Discrimination Meeting, 1996.

Bernstein, L.S., A. Berk, P.K. Acharya, D.C. Robertson, G.P. Anderson, J.H. Chetwynd, L.M. Kimball, "Very Narrow Band Model Calculations of Atmospheric Fluxes and Cooling Rates Using the MODTRAN Code," *J. Atm. Sci.*, 53, 2887-2904, 1996.

Clough, S.A. and F.X. Kneizys, Convolution Algorithm for the Lorentz Function, *Appl. Opt., 18*, 2329, 1979.

Clough, S.A., Radiative Transfer Model Development in Support of the Atmospheric Radiation Measurement Program, *Proceedings of the 3rd Atmospheric Radiation Measurement (ARM) Science Team Meeting*, CONF-9303112, Norman, OK, 1993.

Gallery, W.O., Kneizys, F.X., and Clough, S.A., **Air Mass Computer Program for Atmospheric Transmittance Radiance Calculations: FASCATM**, AFGL-TR-83-0065, 1983.

Gathman, S.G. and K. L. Davidson, *The Navy Oceanic Vertical Aerosol Model*, TR 1634, Naval Command Control and Ocean Surveillance Center, RDT&E Division, San Diego, CA, 1993.

Isaacs, R. G., W. C. Wang, R. D. Worsham, and S. Goldenberg, "Multiple Scattering LOWTRAN and FASCODE Models," *Applied Optics, 26*, 1272-1281, 1987.

Kneizys, F.X., Shettle, E.P., Gallery, W.O., Chetwynd, J.H., Abreu, L.W., Selby, J.E.A., Fenn, R.W., McClatchey, R.A., **Atmospheric Transmittance/Radiance: Computer Code LOWTRAN 5**, AFGL-TR-80-0067, AD A058643, 1980.

Kneizys, F.X., Shettle, E.P., Gallery, W.O., Chetwynd, J.H., Abreu, L.W., Selby, J.E.A., Clough, S.A., Fenn, **Atmospheric Transmittance/Radiance: Computer Code LOWTRAN 6**, AFGL-TR-83-0187, AD A137796, 1983.

Kneizys, F.X., Shettle, E.P., Chetwynd, J.H., Abreu, L.W., Anderson, G.P., Gallery, W.O, Selby, J.E.A., Clough, S.A.., **Users Guide to LOWTRAN 7**, AFGL-TR-88-0177, 1988.

Kneizys, F.X., G.P. Anderson, E.P. Shettle, L.W. Abreu, J.H. Chetwynd, J.E.A. Selby, W.O. Gallery, S.A. Clough, LOWTRAN 7: Status, Review, and Impact for Short-to-Long Wavelength Infrared Applications, in Atmospheric Propagaton in the UV, Visible, IR and mme-wave Region and Related Systems Aspects, AGARD-CP-454, 13-1 to 13-11, Copenhagen, 1990.

Lacis, A. A., and V. Oinas, "A description of the Correlated K Distribution Method for Modeling Nongray Gaseous Absorption, Thermal Emission, and Multiple Scattering in Vertically in Homogeneous Atmospheres," *J. Geophys. Res., 96*, 9027 - 9063, 1991.

Minschwaner, K., G.P. Anderson, L.A. Hall, and K. Yoshino, Polynomial Coefficients for Calculating O_2 Schumann-Runge Cross Sections at 0.5 cm^{-1} Resolution, *J. Geophys. Res., 97*, 10103-10108, 1992.

Minschwaner, K., G.P. Anderson, L.A. Hall, R.J. Thomas, D. Rusch, A. Berk, J. Conant, Scattered Ultraviolet Radiation in the Upper Stratosphere, II: Modeling and Analysis, *J. Geophys. Res.,100*, 11165-11172, 1995.

MM5; see http://weather.met.psu.edu/mm5/MM5about.html, 1997.

Pierluissi, J.H. and C.E. Maragoudakis, Molecular Transmission Band Models for LOWTRAN, AFGL-TR-86-0272, AD A180655, 1986.

Rothman, L.S., et al., The HITRAN Molecular Database: Editions of 1991 and 1992, *J. Quant. Spectrosc. Radiat. Transfer, 48*, 469-507, 1992.

Rothman, L.S., A. McCann, HITRAN 1996, Phillips Laboratory/Geophysics Directorate, Hanscom AFB, MA., Released on CD-ROM, June 1996.

Shettle, E.P. (NRL) and D.R. Longtin (OptiMetrics, Inc.), private communication, 1997.

Smith, H.J.P., D.J. Dube, M.E. Gardner, S.A. Clough, F.X. Kneizys, L.S. Rothman, *FASCODE- Fast Atmospheric Signature Code (Spectral Transmittance and Radiance)*, AFGL-TR-78-0081, 1978.

Snell, H.E., G.P. Anderson, J.Wang, J.-L. Moncet, J.H. Chetwynd, S.J. English, Validation of FASE (FASCODE for the Environment) and MODTRAN3: Updates and Comparisons with Clear-Sky Measurements, The European Symposium on Satellite Remote Sensing, Conference on Passive Infrared Remote Sensing of Clouds and the Atmosphere III, *Proceedings of SPIE*, Paris, France, 1995.

Stamnes, K., S. C. Tsay, W. J. Wiscombe, and K. Jayaweera, "Numerically Stable Algorithm for Discrete-Ordinate-Method Radiative Transfer in Multiple Scattering and Emitting Layered Media," *Applied Optics, 27*, 2502-2509, 1988.

Toon, G., JPL, Private Communication.

Varanasi, P., V. Nemtchinov, Thermal Infrared Absorption Coefficieints of CFC-12 at Atmospheric Conditions, *JQSRT, 51*, 679-687, 1994.

DEVELOPMENT AND USE OF ELECTROMAGNETIC PARABOLIC EQUATION PROPAGATION MODELS FOR U.S. NAVY APPLICATIONS

G. Daniel Dockery

The Johns Hopkins University Applied Physics Laboratory
Johns Hopkins Road
Laurel, MD 20723-6099
Phone: (240)228-5461; Fax: (240)228-5494
Email: g.d.dockery@jhuapl.edu

Introduction

The U.S. Navy began working to understand and predict low-elevation electromagnetic (EM) propagation in the troposphere 50 years ago (e.g., Ref. 1). The review article by Hitney, et al (Ref. 2) provides several references documenting progress in modeling EM propagation and its impact on ship's systems performance through the early 1980s. At that point, practical methods for representing propagation included geometric optics (ray-tracing), normal mode waveguide theory, and spherical-earth multipath and diffraction models (Ref. 3). Each of these methods has well-documented limitations in accuracy and/or applicability relating to allowable frequencies, diffraction effects, terrain modeling, and restrictions in refractivity complexity. These restrictions have often severely limited the utility of such models for high fidelity applications, such as predicting the radar detection of low-altitude anti-shipping missiles (ASMs).

The development of efficient numerical solutions of the parabolic wave equation (PWE) offered a major breakthrough in EM propagation modeling by allowing accurate calculations for realistically complicated refractive environments. The PWE is a "forward-scatter," "narrow angle" approximation to the full Helmholtz wave equation (Refs. 4 & 5), and inherently includes effects due to spherical-earth diffraction, atmospheric refraction, and surface reflections (i.e., multipath). Advanced PWE models may also include impedance boundaries, rough surfaces, complicated antenna patterns, irregular terrain, atmospheric absorption, and/or other scattering phenomena (e.g. Refs. 4 through 10). PWE-based methods result in less complicated propagation models in the sense that direct numerical evaluation of the wave equation eliminates the need to use different approximations & algorithms for different geometries (e.g., "multipath interference," "transition" & "diffraction" regions), or for different frequency regimes (e.g., surface-wave formulation for HF and simple Fresnel reflection theory for higher frequencies). Nor is there a need to express the solution as a complicated sum of normal or coupled modes.

For these reasons, PWE methods have become the preferred propagation modeling approach for many U.S. Navy applications covering a wide range of frequency and propagation geometry for radar, communication, weapon, and electromagnetic support measures (ESM) systems. PWE models are currently used in trade-off studies and design evaluations (Ref. 11), analyses of experiments and at-sea tests (Refs. 12, 13, 14, & 15), operational performance assessment (Refs. 16, 17, & 18), and mission planning programs (Ref. 19). It is also likely that they will be used in acceptance testing and other phases of the Navy's acquisition process in the near future.

The considerable propagation modeling capability that currently exists within the Navy's EM community is due largely to the cooperation and interaction that has occurred among various laboratories, including (but not limited to) the SPAWAR Systems Center San Diego (SSC-SD) (formerly Naval Command, Control, and Ocean Surveillance Center RDT&E Division, NRaD), the Johns Hopkins University Applied Physics Laboratory (JHU/APL), Naval Postgraduate School (NPS), the Naval Research Laboratory's Monterey contingent (NRL/Monterey), and Rutherford Appleton Laboratories in the United Kingdom (RAL). The productive interchanges between these organizations are typified by two PWE workshops hosted by SSC-SD in San Diego, CA in 1989 and RAL in Abington, UK in 1992, as well as by the Electromagnetic Propagation Workshop held at JHU/APL in Laurel, MD (Ref. 20). Similar, less-

organized exchanges have taken place at certain NATO AGARD (Advisory Group on Aerospace Research & Development) symposia and other forums focused on propagation. On these occasions, ideas, calculations, and algorithms were presented and discussed openly among the participating groups, and many comparisons between models and approaches were performed. The net result has been a merging of approaches and accelerated progress in propagation model development for the Navy. It is hoped and expected that such cooperation between these laboratories will continue in the future.

The above-mentioned activities have produced a number of different PWE-based models, in various versions, over the last several years, resulting in occasional confusion regarding pedigree, accuracy, features & capabilities, and validation & verification. Generally, the various models have been developed for different applications, which in turn have different requirements for computation speed, model features and accuracy, and it is important to understand these attributes when selecting a model for a particular use. Unfortunately, the applications for which models have been certified or validated are sometimes forgotten or ignored, resulting in misapplication of these models.

The purpose of this paper is to present some historical perspective on the development and use of PWE-based tropospheric propagation models within the Navy, as well as to address some application, standardization and certification issues. Current thrust areas in model development and application are also mentioned.

General Characteristics of PWE Models

Before continuing, it is helpful to briefly describe some of the general characteristics of PWE codes that set them apart from other propagation modeling techniques. The PWE is an initial-value problem amenable to numerical solution using marching methods that begin at or near the antenna of interest and march out in range and/or altitude. It is thus necessary to specify an initial field solution at a reference range (or altitude), as well as boundary conditions in the other dimension. The most common type of PWE model marches in range, calculating the field along a vertical strip during each range step. It is also possible to march in altitude using an initial solution specified in range at a reference altitude (Ref. 21). As described below, there are at least two popular numerical methods for solving the PWE, but they both involve stepping in range (or altitude) and require the same kind of initial solution and boundary conditions.

In contrast to some other types of propagation models (e.g., geometric optics and spherical earth diffraction models), PWE methods naturally produce a range-height grid of calculated values; this characteristic has both advantages and disadvantages. The primary advantages are (1) the user can examine many different trajectories through the output data matrix without rerunning the model, and (2) the data for range-height color-modulated plots (e.g., Fig. 3) are an automatic by-product. However, if any of the system or environmental parameters are changed (e.g., frequency, antenna height, antenna pointing direction, refractive conditions, etc.), the model must be executed again with the new parameters. Furthermore, one cannot simply go to a downrange point and calculate a value; the model must "march" to that point from the beginning. For this reason, speed comparisons between PWE and other methods should be made in the context of a particular type of application. For example, although PWE codes can be quite fast, they generally remain too computationally burdensome for use in a time-step tracking simulation in which the modeled antenna pointing direction is changing frequently. On the other hand, other types of models often take substantially longer than PWE-based codes to calculate a large grid of values for range-height plots. In any case, the PWE approach is at present the only method capable of handling realistically complicated atmospheric conditions.

The two most popular methods of evaluating the PWE are the Fourier Split-Step solution (FSS) and implicit finite difference (IFD) equations. The former method employs an approximate solution to the PWE in the Fourier Transform domain (spatial frequency space), while the latter converts the PWE to a system of coupled difference equations which is solved via matrix inversion techniques. Both methods solve for field values at a given range and up to the maximum altitude based on the field values at the

previous range. Generally, the stability of the FSS algorithm allows the use of larger range increments (which means fewer steps) than the IFD approach, but it is easier to implement complicated boundary shapes and conditions with IFDs. While there are situations in which the IFD method is desirable, the FSS has thus far been the most successful, particularly in the EM microwave regime where propagation distances are typically thousands of wavelengths. Most frequently-used PWE models in the U.S. Navy community are of the FSS variety.

Other typical features for PWE codes include (1) the use of a Leontovich impedance boundary condition to represent the conductivity, permittivity, and fine-scale roughness of the earth's surface, and (2) calculation of an initial solution using the Fourier transform relationship between an elevation-plane antenna radiation pattern and a line-source distribution (Refs. 5 and 22). Also, many PWE developers have recently gravitated toward the use of algorithms based on Ref. 23 for representing propagation over terrain.

Perhaps the greatest "danger" associated with PWE models is that when they fail, they often do so in an unremarkable way that may go unnoticed, particularly by less-experienced users. For this reason, developers expend substantial effort to include checks for inappropriate input parameters and accumulating errors. PWE codes have progressively become more robust over the past several years, and numerical problems are relatively rare except when a major new capability is first implemented.

History of Electromagnetic PWE Modeling in the U.S. Navy

Electromagnetic propagation was described using parabolic wave equations as early as the 1940s by Fock (Ref. 24), but practical solutions were possible only for very simple atmospheric and surface boundary conditions. In 1973, however, Hardin & Tappert introduced a numerical method for directly solving the PWE using a Fourier Transform, or "spectral," technique called the Fourier Split-Step (FSS) solution (Refs. 25 & 26). Ironically, Tappert first applied this method to EM propagation in the ionosphere, but circumstances soon caused him to focus on underwater propagation (Ref. 27), and while FSS PWE solutions rapidly became popular in the acoustic propagation community, they did not resurface (no pun intended) for EM problems until almost 10 years later.

As previously mentioned, an alternative numerical method for solving PWEs is to apply an implicit finite difference (IFD) scheme which approximates the wave equation's partial derivatives with difference equations. This method was applied to EM wedge diffraction in 1968 by Popov (Ref. 28). The underwater community was using IFD PWE methods for larger-scale propagation problems by 1981 (Refs. 29 & 30), and through the years, the dialogue between proponents of IFD and FSS methods for acoustic propagation has been quite lively. IFD techniques have been, and still are, occasionally revisited for certain types of EM propagation applications (Ref. 31).

The FSS PWE model was introduced for tropospheric EM propagation in 1983 by Dr. Ko et al (Ref. 32); this model was called the Electromagnetic Parabolic Equation (EMPE) program and was based on an existing acoustic propagation code. EMPE initially allowed only perfectly conducting surfaces to be specified and had a number of other limitations. Subsequently, improved models were developed, including later versions of EMPE, which modeled more general surface boundaries and user-supplied antenna patterns. PWE models were also developed in other countries (Refs. 33 & 34).

EMPE was used with considerable success in post-test analyses and reconstructions of Navy tests beginning in 1984. These analyses used high-resolution, range-dependent refractivity information collected during test events, in conjunction with EMPE and radar system models, to explain observed system performance. This procedure permitted for the first time a quantitative analysis, including refractive effects, that relates measured performance to specified performance. Performance specifications are typically generated assuming standard, 4/3-earth refractive conditions, and observed performance can be substantially enhanced or degraded relative to these specifications by non-standard refractive conditions.

By the late 1980s, dozens of Navy tests had been analyzed using EMPE, and the considerable success of those analyses caused U.S. Navy sponsors, most notably the AEGIS Shipbuilding Program, to encourage the development of a PWE-based propagation model by SSC-SD, which is the U.S. Navy's designated laboratory for propagation model development. SSC-SD undertook this task and developed a PWE code called RPE (Radio Parabolic Equation) (Ref. 35), which was later replaced by a "hybrid" PWE-geometric optics model, RPO (Radio Physical Optics) (Ref. 36). A PWE model called PC Parabolic Equation Model (PCPEM) was also developed by RAL in the U.K. in this time frame.

RPO is a blend of PWE, geometric optics, flat-earth, and PWE-initialized geometric optics models, with the choice of model depending on position, refractive condition, and other parameters. RPO was designed with speed as well as accuracy goals in order to satisfy the Navy's requirement for a shipboard propagation model to support rapid at-sea propagation assessments. As a result, some compromises in fidelity were made to allow for rapid computation. RPO development has been supported at various stages by the Office of Naval Technology (ONT, now combined with ONR), the Office of Naval Research (ONR), and the Naval Oceanographer's Office. RPO has gone on to become the "Navy Standard" propagation model for operational applications involving over-water paths and surface-based systems. Interpretation of this "Navy certification" is discussed further below.

EMPE, which was developed by The Johns Hopkins University Applied Physics Laboratory (JHU/APL), was licensed to be sold commercially in 1987 by the original developers. In 1988, a research & development version of EMPE was renamed TEMPER (Tropospheric Electromagnetic Parabolic Equation Routine) to distinguish it from the commercial code. TEMPER is the program that continues to be JHU/APL's advanced propagation code in support of Navy projects. In 1989, the mixed Fourier Transform (MFT) was developed for the PWE split-step solution and implemented in TEMPER (Ref. 4). This new solution rigorously incorporated an impedance boundary into the transform, permitting HF surface-wave calculations and accurate implementation of rough surface impedance algorithms. Further improvements to the MFT decreased computation time and increased numerical stability (Ref. 5).

The need to represent propagation over land as well as sea was well established by the late 1980s in connection with littoral naval missions. Initially, the primary situation of interest for the surface Navy involved propagation from a shipboard system toward and over coastal terrain. More recently, Navy interest has expanded to include over-land propagation from higher altitude systems, such as surveillance aircraft. Propagation over land presents the challenge of specifying a lower boundary for the PWE that varies in height, roughness, conductivity and permittivity with range. Several approaches to this problem have been investigated by JHU/APL, SSC-SD, the Naval Postgraduate School (NPS), and Rutherford Appleton Laboratories (RAL) in the United Kingdom (e.g., Refs. 6, 7, 8, 37, & 38).

In response to the above need, SSC-SD developed the Terrain Parabolic Equation Model (TPEM) (Ref. 6), the terrain mapping portion of which is based loosely on work published by Beilis and Tappert in Ref. 23. JHU/APL has been investigating the rigorous incorporation of the surface impedance into this type of terrain-mapping algorithm (referred to hereafter as linear shift mapping, LSM) (Ref. 39), while also experimenting with the other approaches described in Ref. 37. TEMPER currently has two alternative methods for representing terrain: (1) the impedance-modified LSM just mentioned, and (2) a knife-edge method which simply inserts a perfectly conducting knife-edge at each range with height equal to the terrain height at that range. These two methods give very similar results in "shadowed" regions where diffraction dominates, but have different surface reflection characteristics. Comparisons between different terrain algorithms, including the TEMPER knife-edge and TPEM Beilis-Tappert methods, were performed for the 1995 EM Propagation Workshop (Ref. 20). These comparisons also included the hybridized Terrain Parabolic Equation Model (TERPEM) developed by RAL (see Fig. 3).

SSC-SD is currently working on a hybrid PWE model, called APM (Advanced Propagation Model) which combines the capabilities of RPO and TPEM in a relatively fast code. As with RPO, minor compromises in accuracy are made in the interest of speed. APM uses hybrid techniques, similar to those

in RPO, for propagation over land as well as sea, as long as the specified antenna height is below 100 m. For higher antennas, APM reverts to a full-PWE mode. The expectation is that APM will replace both RPO and TPEM in the Navy's Oceanographic and Atmospheric Master Library (OAML).

Although there has been very good interchange of ideas throughout the community of laboratories working on propagation, an especially useful relationship has developed between SSC-SD and JHU/APL. With the encouragement of the AEGIS Shipbuilding Program, JHU/APL has delivered advanced algorithms, such as the previously mentioned mixed Fourier transform, to SSC-SD for evaluation and potential incorporation in their operational and R&D models. The MFT is now resident in TPEM and the APM prototype. The two organizations have also exchanged model source codes for mutual evaluation and testing. These collaborative efforts have resulted in rapid advancement of Navy propagation models. Fig. 1 summarizes the chronology of, and relationship between, the various models discussed above.

Classes of Applications for Propagation Models

As stated in the previous discussion, there currently exists a number of PWE-based propagation models in the Navy engineering community, including RPO, TPEM, APM, and TEMPER in various versions. These models exhibit different strengths and weaknesses which are to some extent a function of their intended applications. In order to better match models to needs, the following five categories are identified:

Operational Assessment: This type of application includes propagation models embedded in tactical decision aids (TDAs), mission planners and performance assessment tools. In such applications, propagation models are typically required to execute rapidly over large domains and for the full range of parameters (frequency, polarization, antenna height & beamwidth, etc.) associated with U.S. Navy sensor and communications systems. Furthermore, these models must be very robust in the sense that operation by inexperienced users will not result in errors or other numerical problems. The limitations on execution time and memory associated with shipboard use often force some compromises in model capability and/or accuracy.

Engineering Design: Propagation models are used to realistically simulate nominal and stressing natural environments in which to test new system designs. These simulated environments may influence selection of frequency, polarization, antenna pattern characteristics, operating bandwidth, power margin, etc. In this application, execution speed is usually less of an issue, but fidelity and capability requirements can be quite severe. The features of the propagation model may be tailored to emphasize fidelity in a particular risk area, such as antenna sidelobe control, monopulse operation, or surface scattering. Thus, models may be frequently modified to address particular features of the system under design, and to interface with detailed system simulations developed as part of the design process. In these situations, configuration control becomes difficult.

In addition to being a design tool, propagation models are also used by government teams to evaluate contractor proposals and designs. The model requirements for this use are essentially the same as above.

Test Performance Evaluation: Use of propagation models in post-test reconstruction and analysis has become relatively common, particularly for low-elevation tests where refraction, diffraction, and multipath are very important effects. For this application, the model must be able to accurately incorporate measured environmental data, including complicated, range-varying refractivity, sea-state and terrain characteristics. Although accuracy is important, uncertainties and variabilities in nature, as well as limitations in environmental data collection, will typically result in uncertainties of several dB in propagation predictions. For this reason, it is capabilities such as surface roughness and terrain that are the stressing requirements for propagation models, rather than speed and absolute accuracy.

Acquisition: There is a move afoot in the U.S. Navy to rely more on modeling and simulation, and less on actual field testing, for acceptance tests and demonstration tests of new or upgraded systems. In this role, a propagation model may end up embedded in, or providing data to, an advanced distributed simulation (ADS). How this connection to an ADS is approached has a large impact on the execution speed and interface requirements for the model. As a "run-time" participant in an ADS, execution speed would be critical, but as discussed above, the use of PWE models in time-step simulations is not usually practical. More likely, many propagation calculations would be performed in advance, and tables of the resulting data would be made available to the ADS members. In this case, speed is somewhat less of an issue (although a great number of off-line runs might be required to construct the tables), but accuracy remains very important. An error of a few dB may determine whether or not a system is accepted by the Navy.

Research: A number of organizations use research-oriented PWE models to investigate particular aspects of EM propagation and to examine methods for improving computation speed and numerical accuracy. Some examples of less-well-understood propagation effects currently under study are multiple surface scattering, terrain cover (grass, trees, etc.), surface-wave contributions and 3-dimensional scattering. Computational areas under investigation include "transparent" boundary conditions, non-local surface boundary conditions, and hybrid techniques involving mixtures of PWE, normal mode, geometric optics, and analytic methods. Models used for research purposes tend to be very accurate, but not necessarily fast or user-friendly. They are also continuously evolving, making them poor candidates for configuration control. Advances in propagation modeling resulting from these studies are eventually incorporated in more "production-like" codes.

Although some PWE models can serve in more than one of these applications, it should be clear that no single model will be suitable for all of them. The requirements for the different applications are diverse, particularly with regard to speed and accuracy. A matrix of desirable characteristics versus application type is shown in Fig. 2.

Model Verification, Validation and Certification

For certain of the above types of applications, the U.S. Navy has an understandable desire to use only models that have been suitably validated and certified. Unfortunately, these terms have come to have different meanings to different organizations, resulting in confusion and the misapplication of some propagation models. It is important to realize that certification of a model is inevitably relative to some specified range of applications.

For the purposes of this discussion, "verified" means that the model has been demonstrated to execute its functions correctly, without consideration of whether or not its algorithms provide the required accuracy or capabilities. "Validation" means that, within its stated limitations, the model is providing accurate results; i.e., it's generating the correct answers. Finally, "certification" means that the model has gone through some formal approval process, and evidence of verification and validation are usually partial requirements for this approval. "Independent verification and validation" (IVV) refers to having verification/validation performed by an independent party, typically for the purpose of providing unbiased evidence of V&V to a certifying committee.

Certification

Currently, the best-known certification process for Navy propagation models is acceptance into the Oceanographic and Atmospheric Master Library (OAML), which is maintained by the Commander of the Naval Meteorological and Oceanographic Command (CNMOC) (Ref. 40). OAML's objective has been to maintain a library of certified models and databases for use by the operational U.S. Navy. Examples of operational uses include the Tactical Environmental Support System (TESS), and Geophysics Fleet Mission Program Library (GFMPL), both of which are presently deployed in the fleet. The models and databases in TESS and GFMPL reside in OAML. The RPO model is OAML certified,

and the next-generation model, APM, was recently submitted as well. RPO underwent OAML certification because it was intended for use in a planned upgrade to TESS.

In contrast to operational uses, the engineering and R&D applications involve the use of models that are NOT currently being certified by OAML. Acceptance into OAML, which results in a certain degree of configuration control, would be problematic for such models because they are frequently being modified for specific, detailed applications, and improved based on research and testing. On the other hand, there is an important need for configuration control in operational applications, where the users are less likely to understand the differences between various models.

Although the OAML certification process includes IVV (Ref. 40), IVV has yet to be performed for an OAML EM propagation model. For example, in lieu of IVV, the RPO model was evaluated by a CNMOC Independent Model Review Panel (CIMREP), comprised of propagation experts, most of whom were familiar with RPO. This panel documented the strengths and weaknesses of RPO and recommended that the model be accepted into OAML without awaiting IVV (Ref. 41). Thus, for practical reasons, OAML certification does not necessarily imply that IVV has been conducted for that model. Furthermore, OAML certification would not generally benefit engineering or R&D models. Presently, the primary functions of OAML regarding EM models are: (1) configuration control of distributed operational models, (2) documentation of capabilities and limitations, and (3) distribution of models to requesting organizations.

In addition to OAML, there are a few other efforts to standardize and/or certify models for Navy use. The AEGIS Program Executive Office (PEO SC/AP) has a model certification office (PMS-400B30M), which maintains the AEGIS Simulation/Simulator Catalog (Ref. 42). In the AEGIS process, "authentication" represents PEO SC/AP acknowledgement of the legitimacy of a model for AEGIS applications, and results in its inclusion in the catalog. Validation is an additional step that is tailored to the application planned for the model, and is handled on a case-by-case basis. TEMPER is included in the AEGIS catalog, but has yet to go through the validation stage.

The Program Executive Officer for Theater Air Defense, PEO(TAD), also contains a modeling and simulation office, PEO(TAD)MS, one of the goals of which is to identify and certify models appropriate for use in an advanced distributed simulation (ADS). PEO(TAD)MS attempts to be consistent with the Department of Defense Modeling and Simulation Office (DMSO). Specific procedures for PEO(TAD)MS certification have yet to be established, but will almost certainly include compliance with the ADS High-Level Architecture (HLA). For PWE models, this may simply require the development of HLA-compliant "servers" to provide pre-calculated propagation data to the ADS.

So, what is the status of propagation model certification in the Navy? OAML certification means documentation and distribution of operational models. AEGIS certification means ensuring that a model is appropriate for AEGIS applications, with validation being an additional, unspecified procedure. PEO(TAD)MS certification will emphasize architectural suitability for use in an ADS. None of the above "certifications" necessarily guarantee the suitability or accuracy of a propagation model for the applications described in the previous section. Thus, the certification status of a model is often of little help in determining its suitability. It is generally more useful to consider the features, capabilities and validation status of candidate models.

Validation

Within the Navy community, PWE models have undergone extensive, but informal, verification and validation testing as they were developed. The most common type of tests have been numerous comparisons with more rigorous, less flexible models, like normal-mode codes, as well as other PWE codes. The SSC-SD normal-mode model, MLAYER, has become the defacto benchmark program in the U.S. Navy EM propagation community (Refs. 4 and 22). In regions where propagation can be described

by a limited number of modes (i.e., near and beyond the radio horizon), MLAYER gives excellent results for horizontally homogeneous refractive environments (Ref. 43).

TEMPER, RPO, TPEM and other models were frequently compared at various stages during their development. Although such comparisons have happened informally and continuously over the past several years, the most fruitful activity has occurred at the previously mentioned PWE Workshops and the EM Propagation Workshop (Ref. 20). Fig. 3 provides an example of the comparisons carried out during this workshop; the case shown is for propagation over a mixed land-sea path as calculated by TEMPER and RAL's TERPEM. Comparisons of this type have ultimately exhibited the accuracy and limitations of the participating models, and essentially formed the basis for the CIMREP recommendation to accept RPO into OAML. TEMPER has also emerged as a high-fidelity reference standard for U.S. Navy PWE models.

Comparisons with measured data have been conducted by the respective developing organization for some models. Extensive experimental campaigns were executed in the late 1980s to validate TEMPER (Ref. 12), and more recently, RPO and TPEM have been shown to compare favorably with measured data (Refs. 6, 13, and 20). These comparisons, in conjunction with successful reconstruction of low-altitude radar system performance during Navy tests, have established high confidence in PWE-based propagation models.

Considerations for Selecting EM Propagation Models

In this author's opinion, selection of an EM propagation model for a particular application should be based on each candidate model's demonstrated accuracy, robustness, computational speed and features. Unfortunately, there does not presently exist a centralized or certified record of these attributes, and the burden of making an informed choice falls to the potential user. One could argue with some justification that RPO is the only "certified" U.S. Navy PWE model, but RPO's features support only over-water, low-antenna-height applications, and the model's accuracy has been certified only for operational, rather than engineering or research, uses.

Without addressing details regarding specific applications, some general guidelines can be recommended on model application; the discussion is limited to models that have been developed under U.S. Navy sponsorship. TEMPER is currently the highest fidelity U.S. Navy EM PWE model, and is used as a baseline for less rigorous models. TEMPER is also used in high-fidelity engineering design and post-test reconstruction tasks, as well as to investigate new rough-surface algorithms and HF surface-wave propagation. This model has the fewest restrictions on antenna height, antenna patterns, surface characteristics, and steep-angle propagation, though very large computation times can result for large problem domains. The TEMPER algorithms that have been shown to provide new or improved capabilities to PWE models are passed on to SSC-SD for incorporation in their propagation codes.

RPO is suitable for over-water, surface-based system calculations, when it is acceptable to sacrifice a little accuracy in return for reduced execution times. This suggests its use for over-water calculations in shipboard environmental assessment programs, such as TESS, where the uncertainties in atmospheric data are considerable and computation speed is important. RPO may be used for some types of engineering studies provided polarization, surface roughness, and near-surface field effects are not important to the study. There are also some limitations on antenna pattern representation in RPO; the model's limitations are adequately discussed in the OAML documentation.

TPEM is a full-PWE model emphasizing over-land propagation, and will often have similar execution times to TEMPER. The steepness of scattered energy from terrain features is limited in return for containing execution time to some degree. Also in the interest of simplicity, there are limitations to the land characteristics that can be specified. TPEM can be used in moderately high-fidelity engineering applications where fine-scale roughness on land, and high-angle scattering from land are not important (as is often the case).

The forth-coming APM model will combine RPO and TPEM with a considerable number of improvements to both. Over-land calculations will be hybrid, as they are in RPO, for sufficiently low antenna heights, and improved polarization and roughness models will be incorporated into the over-water portion as well. APM attempts to maintain the rapid execution times realized with RPO while retaining fidelity up to at least TPEM's level. Antenna heights larger than 100 meters will cause APM to revert to a full-PWE mode. Although future testing is needed to establish the level of accuracy obtained by APM, it will certainly be suited to operational applications, and will likely be appropriate for some engineering tasks as well.

The existing Navy EM propagation models have been developed within a community of Navy laboratories which have endeavored to stay abreast of each model's capabilities and limitations via both formal and informal interchanges. There is general consensus among the model developers regarding the range of suitable applications of each model, and potential users can access this information by contacting these developers. However, for the time being at least, users cannot rely on a U.S. Navy certification process to indicate which model to use.

References

1. "Symposium on Tropospheric Wave Propagation," Naval Electronics Laboratory (now SSC-SD), Report 173, July 1949.

2. H. V. Hitney, J. H. Richter, R. A. Pappert, K. D. Anderson, and G. B. Baumgartner, Jr., "Tropospheric Radio Propagation Assessment," Proc. IEEE, Vol. 73, No. 2, p. 265, 1985.

3. G. B. Baumgartner, Jr., H. V. Hitney, and R. A. Pappert, "Duct Propagation for the Integrated-Refractive-Effects Prediction System (IREPS)," IEE Proc., Vol. 130, No. 7, Part F, p. 630, 1983.

4. J. R. Kuttler and G. D. Dockery, "Theoretical Description of the Parabolic Approximation/Fourier Split-Step Method of Representing Electromagnetic Propagation in the Troposphere," Radio Science, Vol. 26, No. 2, p. 381, 1991.

5. G. D. Dockery and J. R. Kuttler, "An Improved Impedance-Boundary Algorithm for Fourier Split-Step Solutions of the Parabolic Wave Equation," IEEE Trans. Ant. Prop., Vol. 44, No. 12, p. 1592, 1996.

6. A. E. Barrios, "A Terrain Parabolic Equation Model for Propagation in the Troposphere," IEEE Trans. Ant. Prop., Vol. 42, p. 90, 1994.

7. M. F. Levy, "Parabolic Equation Modeling of Propagation Over Irregular Terrain," Electron. Lett., Vol. 26, No. 15, p. 1153, 1990.

8. R. J. McArthur, "Propagation Modeling Over Irregular Terrain Using the Split-Step Parabolic Equation Method," Proc. IEE Int. Conf. Radar, Brighton, U.K., 12-13 Oct. 1992, p. 54.

9. H. V. Hitney, "A Practical Tropospheric Scatter Model Using the Parabolic Equation," IEEE Trans. Ant. Prop., Vol. 41, No. 7, p. 905, 1993.

10. M. F. Levy, "Modelling of Rough Surface Effects with the Matched Transform PE," AGARD Conference Proceedings 582: Remote Sensing: A Valuable Source of Information, p. 13-1, 1996.

11. E. R. Thews, et al, "A Study of US Navy Radars' Performance in the Near-Shore Environment," Record of the 43rd Annual Tri-Service Radar Symposium, 24-26 June 1997, Boulder, CO.

12. G. D. Dockery and G. C. Konstanzer, "Recent Advances in Prediction of Tropospheric Propagation Using the Parabolic Equation," Johns Hopkins APL Tech. Dig., Vol. 8, No. 4, p. 404, 1987.

13. K. D. Anderson, "Radar Detection of Low-Altitude Targets in a Maritime Environment; Vol. 1: Final Analysis," Naval Command, Control, and Ocean Surveillance Center, RDT&E Center Technical Report 1630, November 1993.

14. J. Goldhirsh, et al, "Propagation Measurements and Modeling at C Band for Over-the-Water, Line-of-Sight Propagation Links in the Mid-Atlantic Coast," Radio Science, Vol. 26, No. 3, p. 671, 1991.

15. J. Stapleton and S. Kang, "Direct Measurement of Microwave Propagation Effects," AGARD Conference Proceedings 582: Remote Sensing: A Valuable Source of Information, p. 12-1, 1996.

16. W. L. Patterson, "Overview of the Electromagnetic Propagation Assessment Systems Developed at the Naval Command, Control, and Ocean Surveillance Center, RDT&E Division," Proceedings: Electromagnetic/Electro-Optics Prediction Requirements & Products Symposium, 3-5 June 1997, Monterey, CA, p. 227.

17. G. D. Dockery and E. R. Thews, "The Parabolic Equation Approach to Predicting Tropospheric Effects in Operational Environments," AGARD Conference Proceedings No. 453: Operational Decision Aids for Exploiting or Mitigating Electromagnetic Propagation Effects, p. 18-1, 1989.

18. G. C. Konstanzer, et al, "SEAWASP: Real-Time Assessment of AN/SPY-1 Performance Based on In-Situ Shipboard Measurements," Proceedings: Electromagnetic/Electro-Optics Prediction Requirements & Products Symposium, 3-5 June 1997, Monterey, CA, p. 87.

19. S. A. Fast, "The Electromagnetic Propagation Server (EMPS)," Proceedings: Electromagnetic/Electro-Optics Prediction Requirements & Products Symposium, 3-5 June 1997, Monterey, CA, p. 257.

20. R. Paulus, Proceedings of the Electromagnetic Propagation Workshop, NRaD (now SSC-SD) Technical Document 2891, December 1995.

21. M. F. Levy, "Horizontal Parabolic Equation Solution of Radiowave Propagation Problems on Large Domains," IEEE Trans. Ant. Prop., Vol. 43, No. 2, p.137, 1995.

22. G. D. Dockery, "Modeling Electromagnetic Wave Propagation in the Troposphere Using the Parabolic Equation," IEEE Trans. Ant. Prop., Vol. 36, No. 10, p. 1464, 1988.

23. A. Beilis and F. D. Tappert, "Coupled Mode Analysis of Multiple Rough Surface Scattering," J. Acoust. Soc. Am., Vol. 66, No. 3, p. 811, 1979.

24. V. A. Fock, "Solution of the Problem of Propagation of Electromagnetic Waves Along the Earth's Surface by Method of Parabolic Equations," J. Phys. USSR, Vol. 10, No. 1, p. 13, 1946.

25. R. H. Hardin and F. D. Tappert, "Applications of the Split-Step Fourier Method to the Numerical Solution of Nonlinear and Variable Coefficient Wave Equations," SIAM Review, Vol. 15, p. 423, 1973.

26. F. R. DiNapoli and R. L. Deavenport, "Numerical Methods of Underwater Acoustic Propagation" in Ocean Acoustics, J. A. DeSanto, Ed., New York: Springer-Verlag, 1977.

27. F. D. Tappert, "The Parabolic Approximation Method" in Wave Propagation and Underwater Acoustics, J. B. Keller and J. S. Papadakis, Eds., Lecture Notes in Physics, Vol. 70, Heidelberg: Springer-Verlag, 1977.

28. A. V. Popov, "Solution of a Parabolic Equation of Diffraction Theory by a Finite Difference Method," USSR Comp. Math and Math. Phys., Vol. 8., p. 282, 1968.

29. D. Lee, et al, "Finite-Difference Solution to the Parabolic Wave Equation," J. Acoust. Soc. Amer., Vol. 70, p. 795, 1981.

30. D. Lee and S. T. McDaniel, "Ocean Acoustic Propagation by Finite Difference Methods," Comp. Math. Applic., Vol. 45, No 5, 1987.

31. M. F. Levy, "Diffraction Studies in Urban Environment with Wide-Angle Parabolic Equation Method," Elect. Letters, Vol. 28, No. 16, p. 1491, 1992.

32. H. W. Ko, J. W. Sari, and J. P. Skura, "Anomalous Microwave Propagation Through Atmospheric Ducts," Johns Hopkins APL Tech. Dig., Vol. 4, No. 2, p. 12, 1983.

33. K. H. Craig, "Propagation Modelling in the Troposphere: Parabolic Equation Method," Electronics Letters, Vol. 24, No. 18, p. 1136, 1988.

34. M. Fournier, "'Etude de la Propagation dans une Atmosphere Inhomogene dans les Directions Horizontale et Vertical par la Method de L'Equation Parabolique," AGARD Conference Proceedings No. 453: Operational Decision Aids for Exploiting or Mitigating Electromagnetic Propagation Effects, p. 21-1, 1989. (In French).

35. F. J. Ryan, "RPE: A Parabolic Equation Radio Assessment Model," AGARD Conference Proceedings No. 453: Operational Decision Aids for Exploiting or Mitigating Electromagnetic Propagation Effects, p. 19-1, 1989.

36. H. V. Hitney, "Hybrid Ray Optics and Parabolic Equation Methods for Radar Propagation Modeling," Proc. IEE Int. Conf. Radar, Brighton, U.K., 12-13 Oct. 1992, p. 58.

37. D. J. Donohue and J. R. Kuttler, "Modeling Radar Propagation Over Terrain," Johns Hopkins APL Tech. Dig., Vol. 18, No. 2, p. 279, 1997.

38. R. Janaswamy, "A Curvilinear PE Approach to EM Propagation Predictions Over Terrain," Proceedings: Electromagnetic/Electro-Optics Prediction Requirements & Products Symposium, 3-5 June 1997, Monterey, CA, p. 241.

39. D. J. Donohue, "Propagation Modeling Over Terrain by Coordinate Transformation of the Parabolic Wave Equation," Proc. 1996 IEEE Ant. Prop. Int. Symp., July 1996, Baltimore, MD, p. 44.

40. "Oceanographic and Atmospheric Master Library (OAML) Configuration Management Plan," OAML-CMP-44, Naval Oceanographic Office, May 1993.

41. R. L. Haney, "Technical Review of the Radio Physical Optics (RPO) Model," Final CIMREP Report to CNMOC, 1 June 1995.

42. "AEGIS Simulation/Simulator Catalog," PEO SC/AP, October 1996.

43. G. B. Baumgartner, "XWVG: A Waveguide Program for Trilinear Tropospheric Ducts: Computer Program for Calculating the Signal Levels of EM Waves Propagating Over Sea Water," NOSC (now SSC-SD) Technical Document 610, 30 June 1983.

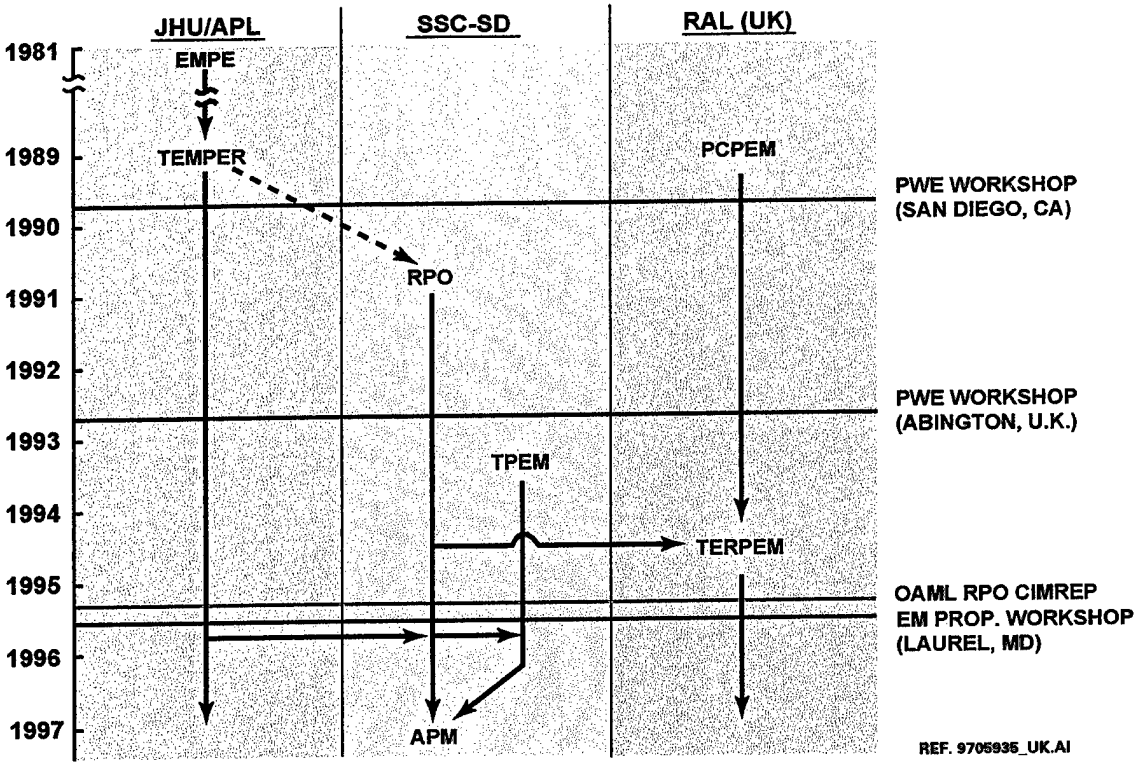

Figure 1. U.S. Navy EM PWE Model History.

	Accuracy	Comp. Speed	Flexibility	Config. Control	Robustness	User Interface
Operational Assessment	M	H	L	H	H	H
Engineering Design	H	M	H	M	M	M
Test Perf. Evaluation	M	L	L	M	M	M
Acquisition/ Procurement	H	H	L	H	H	M
Research	H	L	H	L	L	L

Figure 2. Matrix of propagation model attributes and applications.
(H = high, M = medium, L = low importance)

9800239_UK.AI

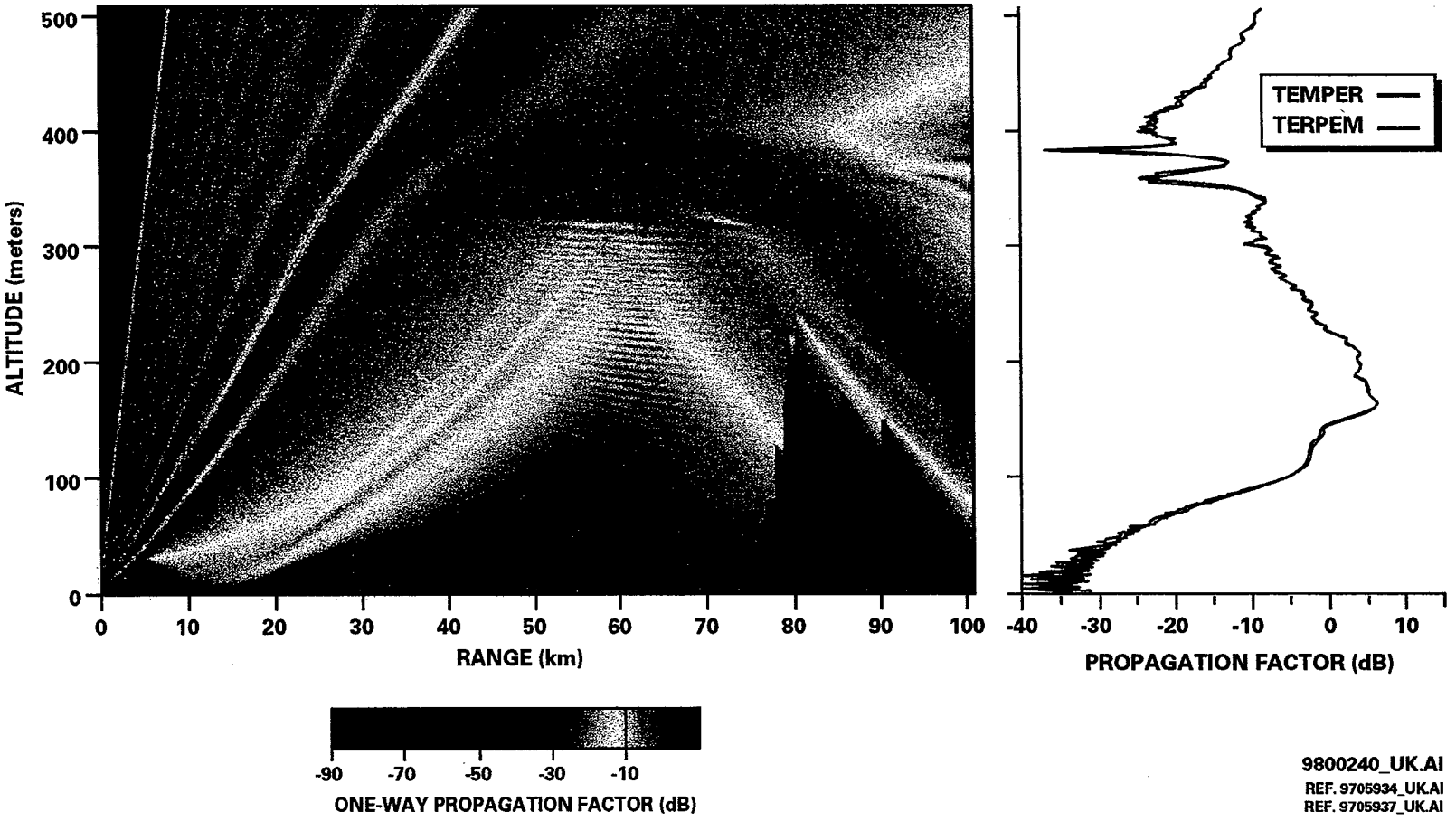

Figure 3. EM Workshop Case 9: 3GHz, 10-m Antenna, 400-m Surface Duct over Terrain, Range = 100km

ARMY FORCE XXI WEATHER OPERATIONS ARCHITECTURE

Richard J. Szymber
U.S. Army Research Laboratory
Information Science and Technology Directorate
Battlefield Environment Division

Wayne L. Stram
U.S. Army Intelligence Center and Fort Huachuca
Directorate of Combat Developments
Requirements Division

Commander, USAIC&FH
ATTN: ATZS-CDS-W
Fort Huachuca, AZ 85613
Ph: 520-538-0723
Fax: 520-538-0708
E-mail: szymberr@huachuca-emh1.army.mil

1. INTRODUCTION

The U.S. Army Intelligence Center and Fort Huachuca, Directorate of Combat Developments (DCD), Architecture Team and Weather Team have developed an Army weather architecture for the 2005 timeframe based on envisioned Army weather support requirements and capabilities. The weather architecture is patterned after the DCD series of Force XXI intelligence architectures. The architecture describes the connectivity between the weather sensing/observing systems, weather processing/forecasting systems and centers, and Army Battle Command System (ABCS) information systems and communications systems involved in the Army weather support function. Details on these systems, their interconnections, and associated concept of operations can be found in Szymber (1997), Szymber and Corbett (1996), and Szymber and Cogan (1994), and are not repeated here.

2. WEATHER ARCHITECTURE OVERVIEW

The weather operation architecture (2003-2005) for a major regional conflict (war) is overviewed in figure 1. As figure 1 shows, Army weather support and operations extend from the front lines of the battlefield all the way back to the Continental United States (CONUS). The weather architecture revolves around the Integrated Meteorological System (IMETS). The IMETS, or any Army tactical weather system, is very dependent on communications to receive and disseminate weather information. Fine-scale/high resolution forecast model output, imagery, and other data/products must be transmitted to multiple IMETS over broadband broadcasts to avoid overloading tactical communications pipes from the highest to the lowest levels on the battlefield.

3. WEATHER ARCHITECTURE BY ECHELON

Specific Army weather architectures for the 2005 timeframe were developed by echelon, starting at the largest theater-size picture (figure 1) and working down from Echelons Above Corps (EAC) to Brigade. The EAC weather architecture is depicted in figure 2. The Corps weather architecture is described in figure 3. Figure 4 shows the Division weather architecture. The Aviation Brigade weather architecture is pictured in figure 5 and the Brigade architecture in figure 6.

All of the communications systems/linkages and information systems/services shown in figures 1-6 comprise the Area Common User System (ACUS) or eventually what will be the Warfighter Information Network (WIN). The main components of the ACUS or WIN depicted in these figures are: Global Broadcast Service (GBS); Local Area Networks (LANs) and Wide Area Network (WAN); Combat Net Radio (CNR); ABCS information systems (e.g., the All Source Analysis System (ASAS) and IMETS); and information services such as SIPRNET. The ACUS/WIN consists of the tactical internet at brigade and below. The minimum data rate for WIN is 128 kbps per user channel. More details on WIN can be found at www.gordon.army.mil/dcd.

The primary communications path from CONUS to the theater battlefield is via GBS, and from theater back to CONUS via SIPRNET. The primary means of communications for in-theater dissemination across the battlefield is through a combination of GBS, WANs, LANs, and CNR. The WAN is internal to the echelon and connects all the LANs. The LANs are internal to the Tactical Operations Centers (TOCs) and Command Posts (CPs). CNR is mainly used to transmit weather observational data.

The GBS will provide a one way transmission of broadband high-volume common user information available from National and in-theater sources directly to the Force XXI warfighter in the battlespace. The major GBS components are: user Ground Receive Terminals (GRTs) and Tactical Injection Point (TIP) mobile terminals in theater; CONUS fixed-site Primary Injection Point (PIP) Joint Broadcast Management Center and National information platforms/providers such as the Air Force Weather Agency (formerly the Air Force Global Weather Center (AFGWC)); and satellites. The GBS PIP provides the National to theater broadcast of AFWA (AFGWC) global/theater weather databases and products to IMETS. The PIP will have a minimum 94Mbps data uplink, of which approximately 64 kbps is the weather data. The IMETS will be connected to the GRT via the LAN. The Army requires 27 GRTs per Division. The GBS TIP provides in-theater dissemination/broadcast of IMETS' tactical/local weather data/forecasts and tailored products to other IMETS, to other users, and down to brigade level. IMETS will be connected to the TIP via the WAN. There will be one TIP per Division, Corps, and EAC with a minimum 6Mbps data uplink, of which about 64 kbps is the IMETS data.

4. SUMMARY

Army weather support operational and systems architectures for the Force XXI time period of 2003-2005 have been developed by echelon for aviation brigade, brigade,

division, corps, and echelons above corps/joint task force. These weather supporting concept diagrams depict the "big picture" high level view of the operational warfighting context/environment representative of a major regional conflict. The architectures help to define weather information requirements and support system interoperability. Specifically, they describe the systems, communications and interconnections supporting the weather warfighting function, and define the physical connection between components, the identification and location of key nodes, networks, and systems/platforms. The Army weather operation architecture can be applied in the development of Army weather doctrine, concept of operations, requirements and capabilities. It directly supports the command, control, computers, and intelligence (C4I) for the warrior concept and the Army Enterprise Strategy.

REFERENCES

Szymber, R. J., 1997: "Owning the Weather: Weather Support to Force XXI." Military Intelligence, Volume 23, Number 1, pp. 42-45, January-March 1997. US Army Intelligence Center and Fort Huachuca, Fort Huachuca, AZ.

Szymber, R. J. and J. L. Cogan, 1994: "Owning the Weather Battlefield Observations Framework." Proceedings of the 1994 Battlefield Atmospherics Conference, pp. 449-460, 29 November-2 December 1994. US Army Research Laboratory, Battlefield Environment Directorate, White Sands Missile Range, NM.

Szymber, R. J. and M. F. Corbett, 1996: "The Integrated Meteorological System (IMETS) Weather Supporting Concept." Proceedings of the 1996 Battlespace Atmospherics Conference 3-5 December 1996, Technical Document 2983, pp. 57-66, December 1996. Naval Command, Control and Ocean Surveillance Center, RDT&E Division, San Diego, CA.

ABBREVIATIONS AND ACRONYMS

ACT: Analysis Control Team
ACUS: Area Common User System
ADA: Air Defense Artillery
AFATDS: Advanced Field Artillery Tactical Data System
AFGWC: Air Force Global Weather Center
AI: Area of Interest
AO: Area of Operations
ARTY: Artillery
ASAS: All Source Analysis System
ATCCS: Army Tactical Command and Control System
AVN: Aviation
BCE: Battlefield Coordination Element
BDE: Brigade
BN: Battalion
BTFD: Battlefield
BTOC: Brigade TOC
CDR: Commander
CGS: Common Ground Station
CMDS: Commands
CP: Command Post
CSSCS: Combat Service Support Control System

CTOC: Corps TOC
DIV: Division
DS: Direst Support
DTOC: Division TOC
DTSS: Digital Topographic Support System
EAC: Echelons Above Corps
EN or ENG: Engineer
FA: Field Artillery
FCE: Fire Control Element
FDC: Fire Direction Center
FLT: Flight
FS: Fire Support
FSE: Fire Support Element
FSO: Fire Support Officer
G2: Intelligence Officer (General Staff level)
G3: Operations Officer (General Staff level)
GBS: Global Broadcast Service
GEO: Geostationary
GND: Ground
GRP: Group
GRT: Ground Receive Terminal
IC: Intelligence Center
IMETS: Integrated Meteorological System
LAN: Local Area Network
LNO: Liaison Officer
MET: Meteorological
METSAT: Meteorological Satellite
MI: Military Intelligence
MITT: Mobile Integrated Tactical Terminal
MMS: Meteorological Measuring System
MNVR: Maneuver
MSN: Mission
OPS: Operations
PIP: Primary Injection Point
PLNS: Plans
PMO: Provost Marshall Officer
PYSOP: Psychological Operations
RGR: Ranger
RGT: Regiment
RWS: Remote Workstation
S2: Intelligence Officer (Staff level)
S3: Operations Officer (Staff level)
SF: Special Forces
SIPRNET: Secret Internet Protocol Router Network
SMS: Semi-automatic Meteorological Station
SOAR: Special Operations Army
SOF: Special Operations Forces
TAC: Tactical CP
TCS: Tactical Control System
TGT: Targeting Officer
TIP: Tactical Injection Point
TOC: Tactical Operations Center
TUAV: Tactical Unmanned Aerial Vehicle
WAN: Wide Area Network
WS: Workstation
WX: Weather

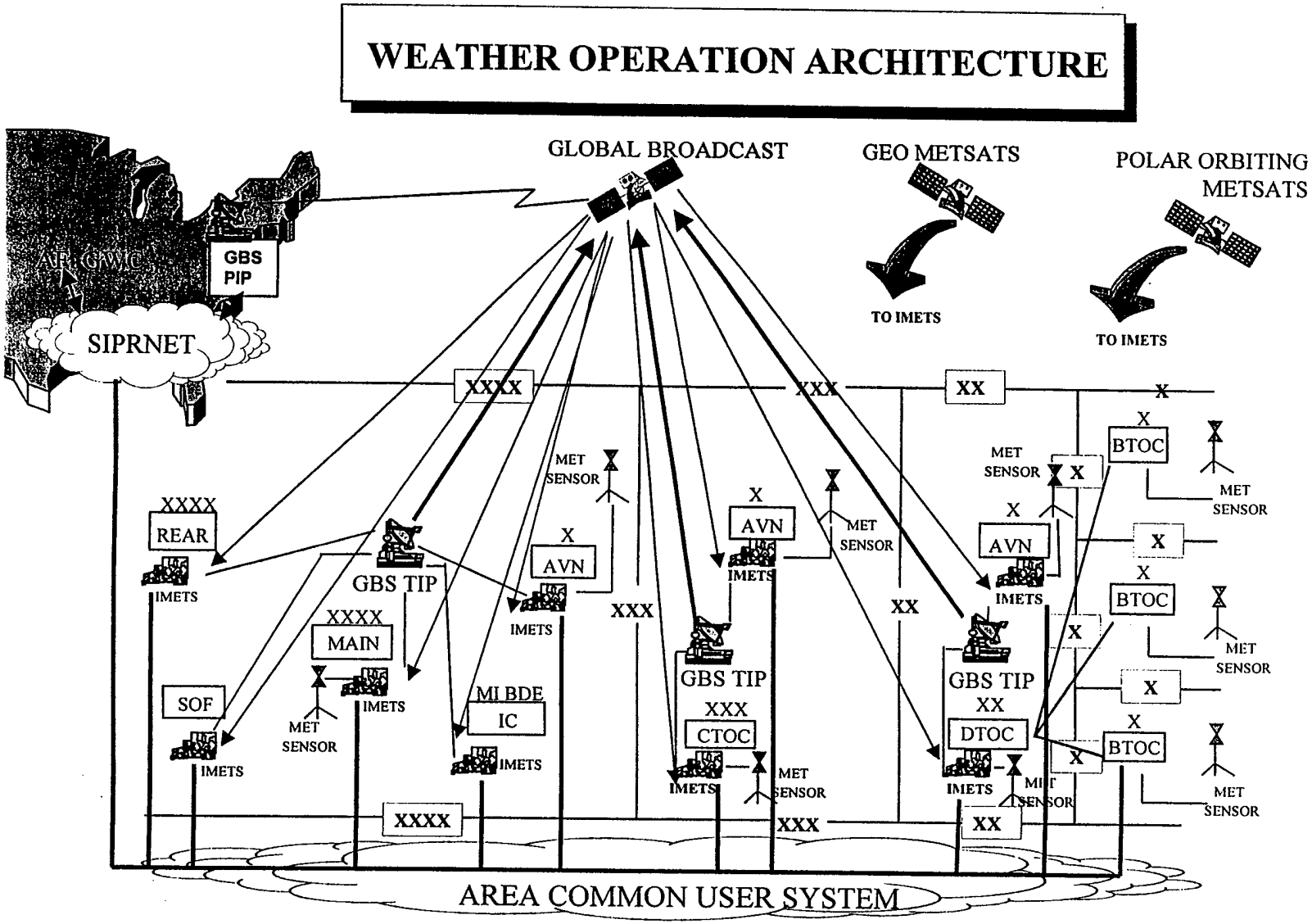

Figure 1. Overview of Army Force XXI (2005) weather architecture.

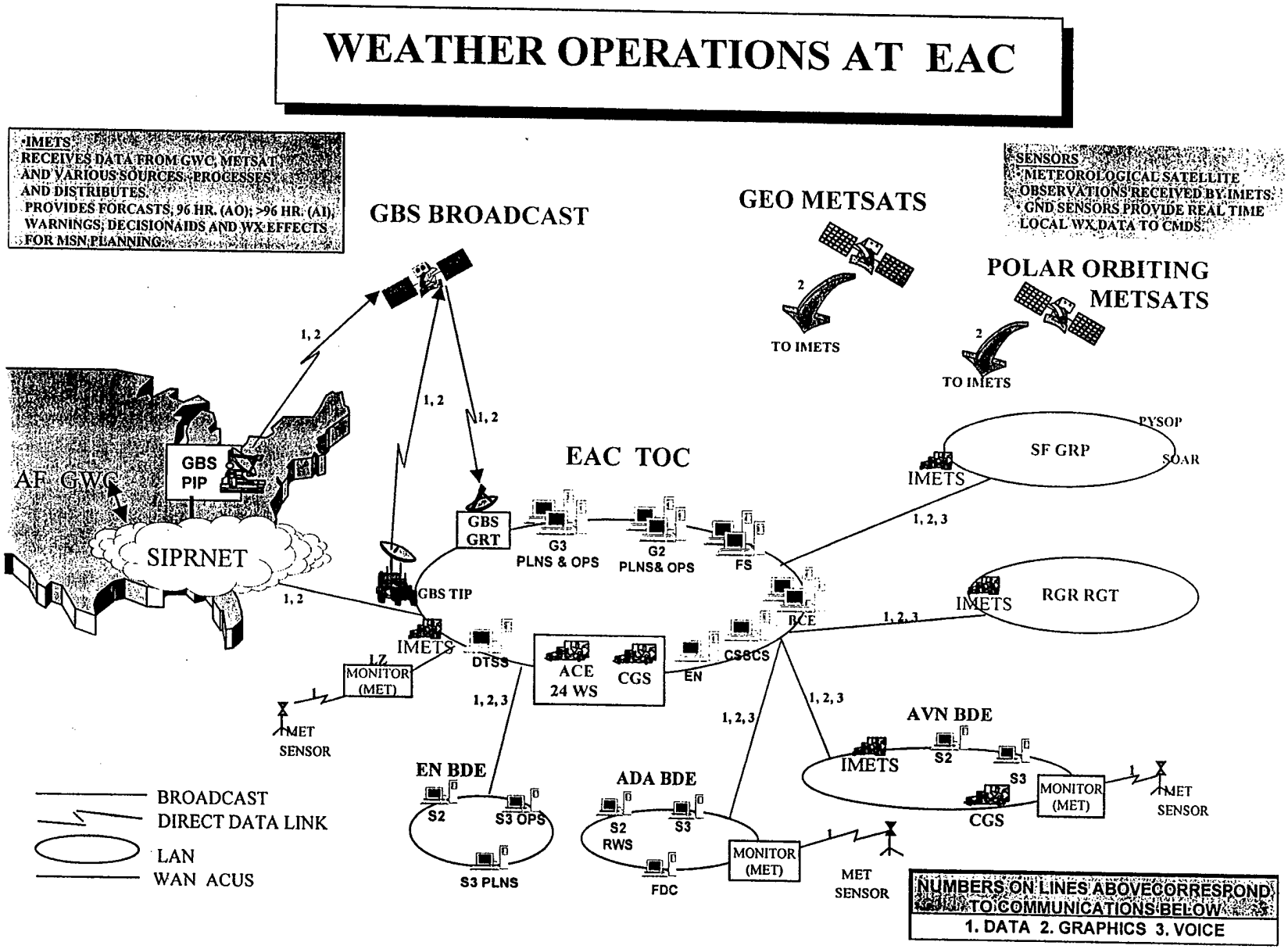

Figure 2. EAC weather architecture (2005).

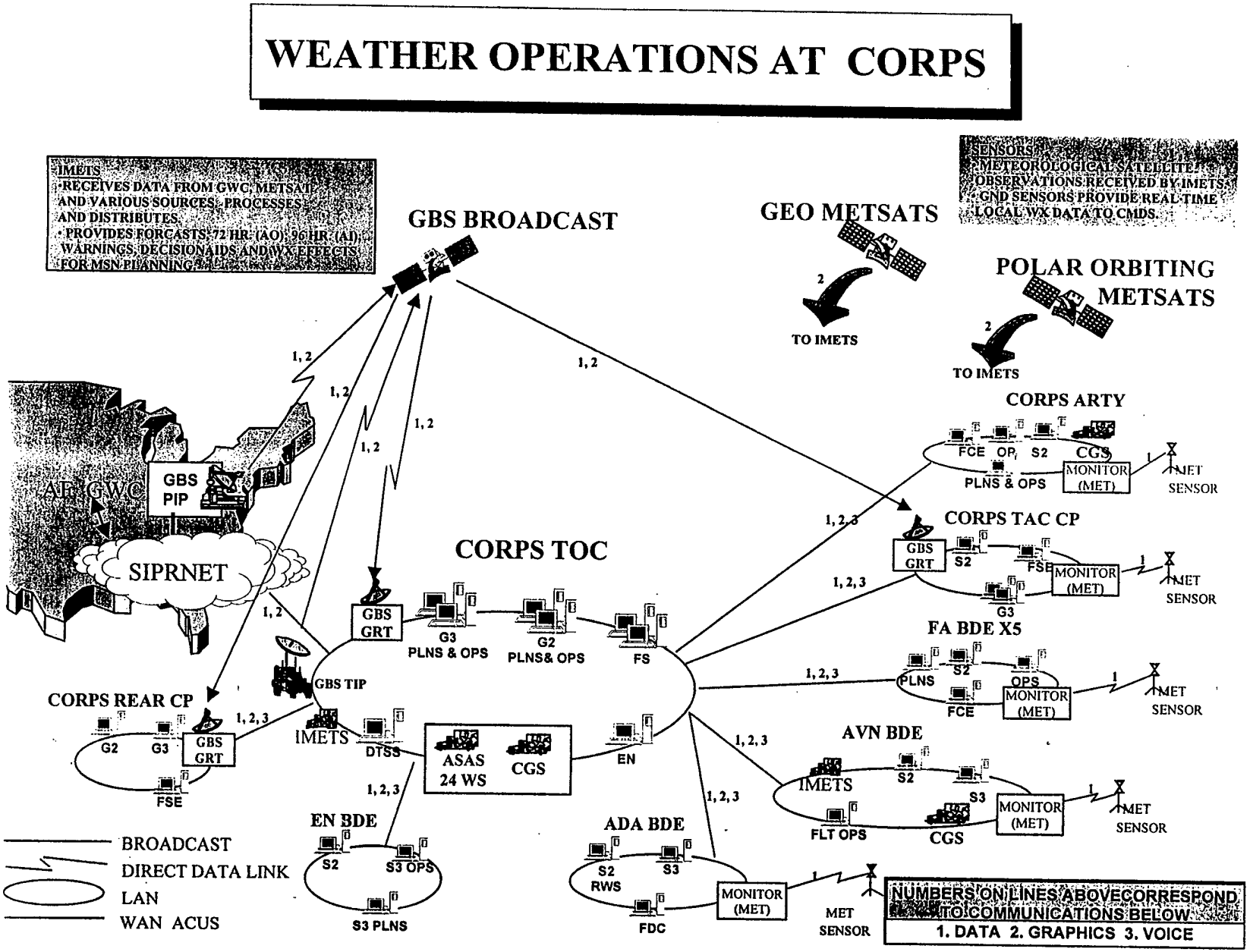

Figure 3. Corps weather architecture (2005).

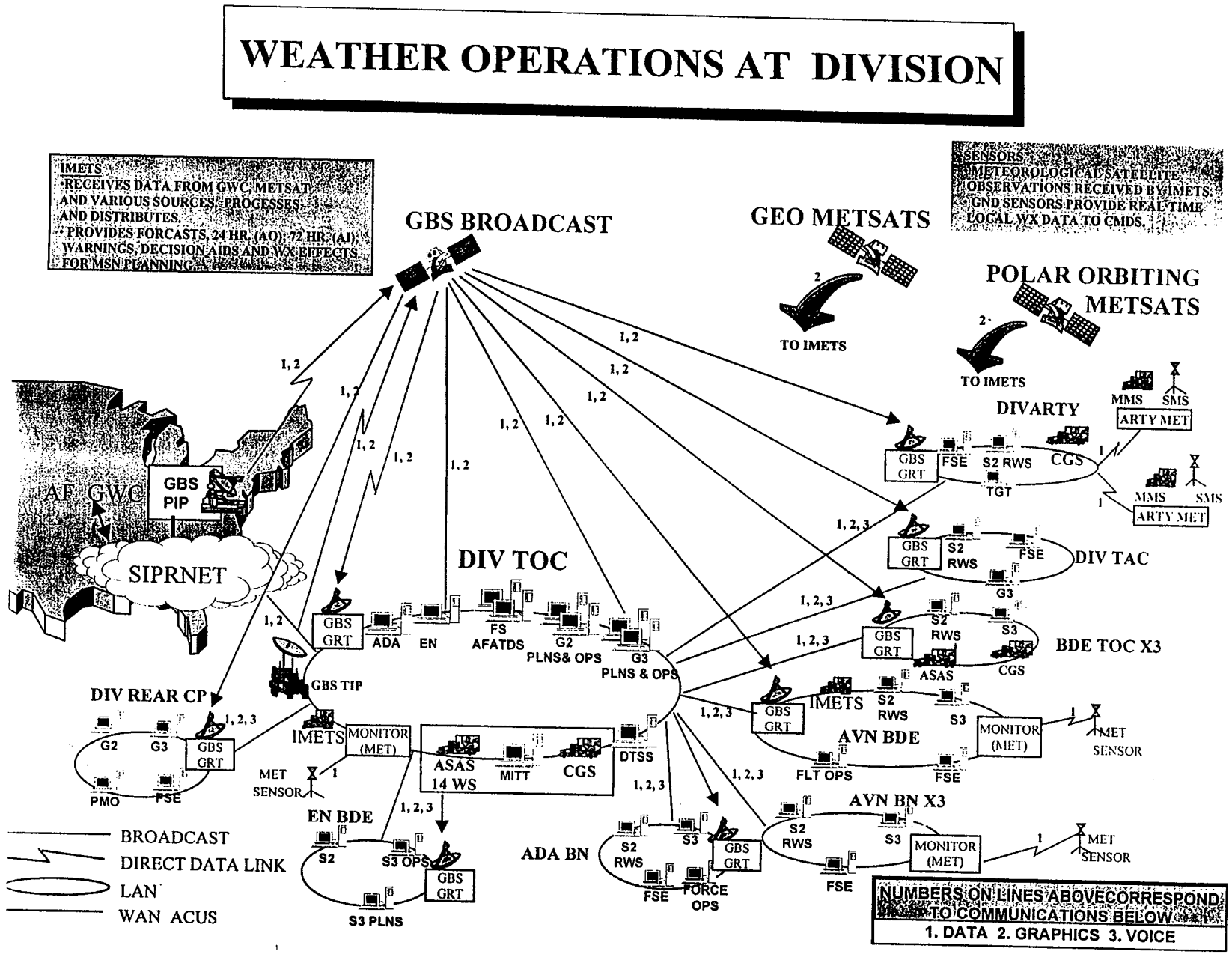

Figure 4. Division weather architecture (2005).

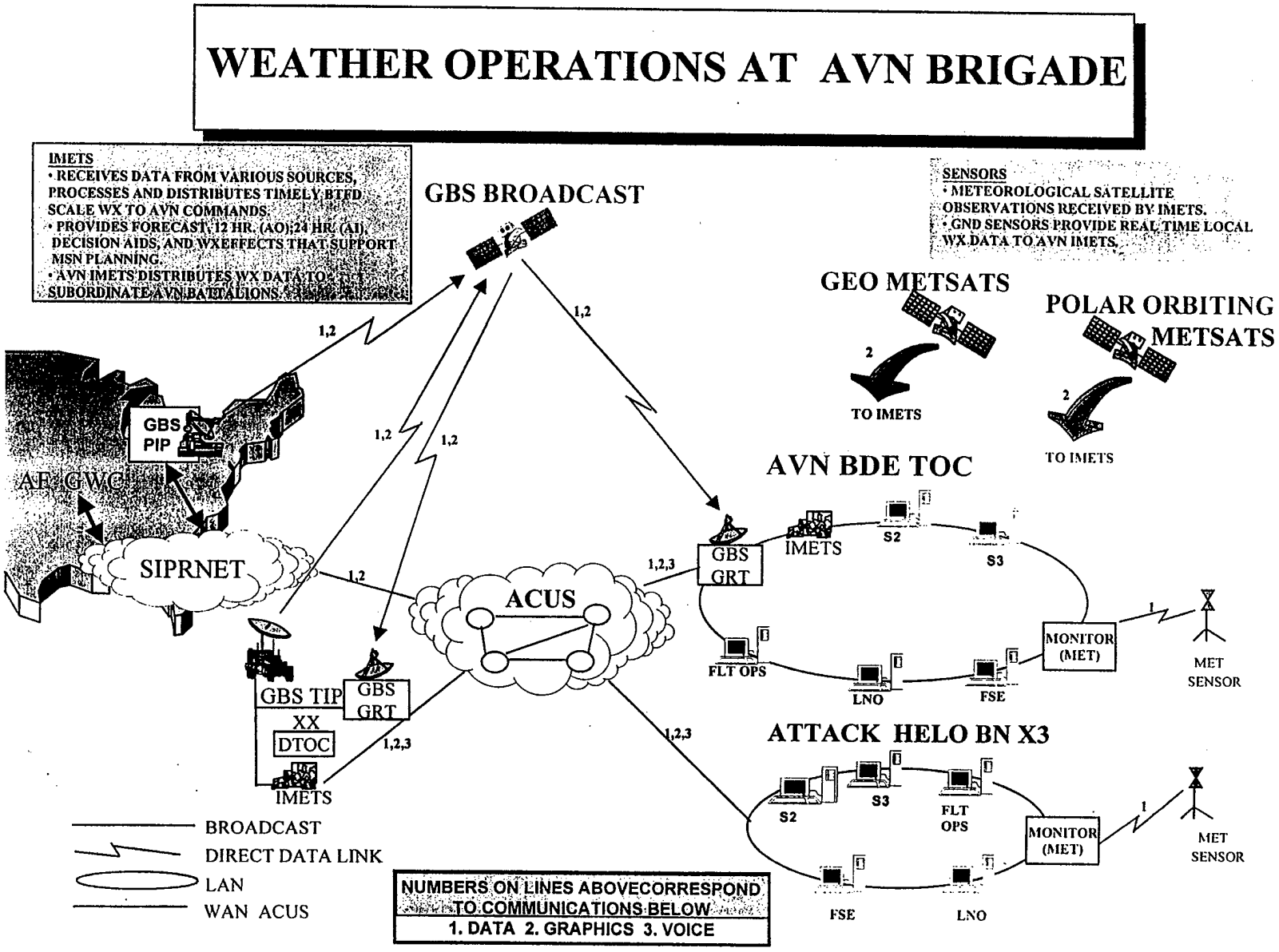

Figure 5. Aviation Brigade weather architecture (2005).

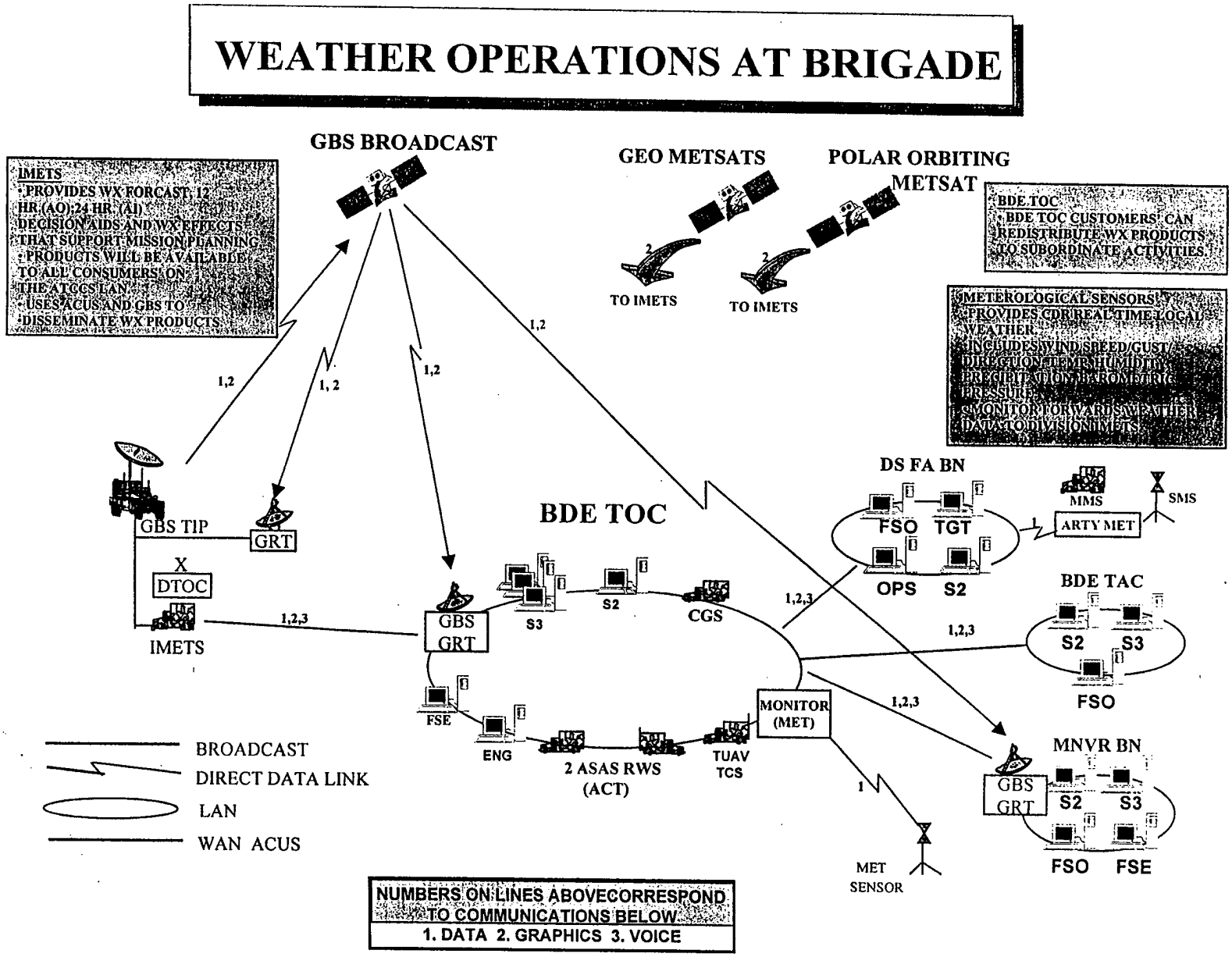

Figure 6. Brigade weather architecture (2005).

IWEDA FOR BRIGADE TASK FORCE XXI: ASSESSMENT AND LESSONS LEARNED

David P. Sauter
U.S. Army Research Laboratory
White Sands Missile Range
NM 88002
Ph: 505-678-2078 Fax: 505-678-8766
E-mail: dsauter@arl.mil

The Integrated Weather Effects Decision Aid (IWEDA) is automated software to provide detailed information in terms of how, when, where, and why weather affects weapon systems (as well as their subsystems and components) and operations. In order to provide a common horizontal (i.e., within echelon) and vertical (i.e., at a higher or lower echelon) depiction of these impacts, IWEDA was integrated into the client/server architecture for the Army's Advanced Warfighting Experiment (AWE) Brigade Task Force XXI (TFXXI) - held at the Army's National Training Center (Ft. Irwin, CA) during March 1997. IWEDA was installed on all of the Army's Battlefield Functional Areas (BFAs) such that a common tool could be used to query and visualize weather impacts on the weapon systems of interest. The Integrated Meteorological System (IMETS) was used to ingest and process raw weather data into the required IWEDA database tables. The various BFA clients could then query IMETS and retrieve the latest weather data to run IWEDA locally. Some of the lessons learned from the AWE include the requirement for a dynamic rule editor to allow editing of the default rule set; the capability for the clients to have IWEDA database tables automatically retrieved from the IMETS server; and additional training on IWEDA for the clients before the next AWE. Feedback and lessons learned from the second TFXXI exercise (Division AWE at Ft. Hood in November 1997) will be summarized in the presentation and paper.

I. INTRODUCTION

As presented and described at prior Battlespace Atmospheric Conferences, IWEDA has proven itself as a useful tool for providing the commander with the environmental effects on his weapon platforms. In a matter of a few years, IWEDA has evolved from a primitive PC based tool with crude map graphics and a cumbersome and time consuming manual entry of the environmental parameter values to a relatively sophisticated Unix/XWindows application with automated meteorological data retrieval (with the exception of 4 parameters) and a realistic display over a digital map background. The next step in the evolution of IWEDA was (and is) to integrate the software into the Army's command and control architecture to demonstrate the utility of the program in a tactical environment. The remainder of this paper will discuss this integration in more detail.

II. TASK FORCE XXI INITIATIVE

With the advent of the computer and the continual advancement in capabilities (along with a decrease in weight, size, and cost), the Army has long recognized the potential for its use on the battlefield. As a result, the Task Force XXI initiative will lead to the milestone of the Army's first digitized division in the year 2000. In preparation for this digitized division, a brigade level exercise was held at the National Training Center in March 1997 (Brigade Task Force XXI) and was followed up by the Division Advanced Warfighting Experiment (DAWE) at Ft. Hood in November 1997. All of the command and control functional areas participated and included intelligence, logistics, maneuver control, air and missile defense, and field artillery. In addition to demonstrating the interoperability of the software applications among these functional areas (as opposed to "stove pipe" systems that cannot communicate between each other), a primary goal of these endeavors was to determine the utility of the various command and control software packages to the commander. As a result, numerous test and evaluation personnel were present during these exercises to collect data and analyze the results. Some of these assessments for IWEDA follow.

III. IWEDA ASSESSMENTS

Although the Brigade Task Force XXI exercise and the DAWE provided excellent opportunities to learn not only how the software would perform in a tactical environment (i.e., with tactical comms, fielded equipment, 24 hour operation, etc.) but also what utility the operators saw in the application, in reality, there was little feedback for IWEDA from operators other than the staff weather officers (SWOs). IWEDA resided on all battlefield functional area (BFA) systems, but as a weather client on these other servers, was not exercised to the extent that the "native" applications were. Unfortunately, all client software seemed to suffer from this problem. It became apparent that operators of the various BFAs were kept busy simply learning the native applications on their system. As a result, feedback for IWEDA from the non-weather community was limited. Until a more regimented and broad training program is initiated within the Army, this problem is likely to persist.

Within the weather community, the overall feedback on IWEDA was that it provided useful information about weather effects. A number of suggestions for improvement were provided by the weather officers or Army Research Laboratory (ARL) personnel on site during the exercises. Several of these suggestions were related to the user interface and will not be discussed further. Many of these suggested changes have already been made to IWEDA. Some of the more significant requirements include:

• Dynamic rule editor. Within different units of the Army, there may exist different critical environmental threshold values for the same weapon system. As a result, the default rule as a part of the installed IWEDA may not necessarily be the value that the user wants to have fire a marginal or unfavorable impact. To satisfy this requirement, a dynamic rule editor has been developed that will allow the SWO to view and modify any of the existing fields of the approximately 500 IWEDA rules. The SWO can revert to the default rule set at any point with a

simple mouse click. This software enhancement is currently being tested in-house within ARL. Near term improvements to this application will include the capability to save different rule sets by name (for future retrieval and use) and the addition of new systems not currently included in the IWEDA inventory.

• Automatic retrieval of the IWEDA database from the weather server. Due to a lack of training of IWEDA on the majority of the BFA systems, it was observed that the operators would not always click on the "Refresh Weather Data" button within the IWEDA application. Failing to do so would result in a stale weather effects database residing on the client's system, i.e., although the database as maintained by the SWO may only be 6 hours old, it could be 24 hours or older on the other BFAs. Software has been written at ARL for the client to automatically check the status of the database on the weather server every 30 minutes, and if more recent than on the client, to be retrieved.

• Disabling of IWEDA by the SWO. If, for whatever reason, the SWO determines that the IWEDA database as made available to the clients is invalid, he needs some way of disabling the IWEDA on the clients. ARL has included a flag in the IWEDA database for this purpose. This flag will be checked every 30 minutes, and if set to disabled, will disable the client's IWEDA and display an appropriate message to the user.

In addition to the requests for software enhancements as detailed above, a number of observations and assessments were made. These include:

• IWEDA is only as good as the input data provided by ARL's Battlescale Forecast Model (BFM). The BFM is a high resolution mesoscale forecast model that runs in a tactical environment. It is typically run twice a day and forecasts a number of meteorological parameters required by IWEDA out to 24 hours over a battlescale area (up to 500 km by 500 km and up to approximately 20,000 ft). During the Brigade TFXXI exercise, it became apparent that the BFM was experiencing difficulty in predicting surface temperatures and wind velocities under certain circumstances (these problems have since been resolved). As IWEDA is highly dependent on these meteorological parameters, weather effects as predicted by the application could be erroneous. As a result, ARL has added a switch on the weather server to allow the SWO to manually disable IWEDA in the event this happens in the future.

• The tactical internet/DCE provided fairly reasonable means of transferring the required IWEDA database tables to the clients within the echelon. Within an echelon (e.g., division or brigade), the various BFA systems are interconnected via a local area network (LAN). The LAN provided a very reliable architecture for passing information from one system to another. Coupled with this was a commercial distributed computing environment (DCE) software package. The DCE software provided the protocols for the actual distribution of data among BFAs and was used by the clients to retrieve the IWEDA database from the weather server. Due to the distances between higher and lower echelons, however, a LAN architecture is not possible for inter-echelon communication. In the case, Mobile Subscriber Equipment (MSE) was used to relay information. MSE is a tactical communication system providing secure circuit and packet switch communications for wire and mobile tactical subscribers at Echelons Corps and Below

(ECB). MSE has a much smaller bandwidth than a LAN and due, in part, to the amount of information trying to be passed over it, was not nearly as reliable as the within echelon comms. In fact, the weather officer at the brigade level during the NTC exercise estimated that he was successful in retrieving the IWEDA database from the division via MSE only 10% of the time.

• The Command Post Exercise (CPX) environment (DAWE) is not conducive to meaningful application of IWEDA. During the November DAWE, wargames were played with "canned" (i.e., archived) weather data. This, in combination with the battle being scripted for most of the DAWE, led to very limited use of IWEDA. Depending on the tempo and whether or not slated objectives were being met, weather could be "turned off" at any point such that there would be no weather effects (regardless of what the archived data was). The NTC exercise which occurred in real time with real weather was much more conducive for use of IWEDA in planning and execution.

• Maintaining IWEDA as a client on a variety of hardware and software platforms is time consuming. Two hardware platforms (Sun and Hewlett Packard), two commercial relational database packages (Informix and Oracle), two DCE packages, and different versions of operating systems led to ARL having to maintain and install 5 different versions of IWEDA for a total of 6 systems! Needless to say, this, coupled with the dynamic environment of trying to meet deadlines associated with the Task Force XXI exercise milestones, resulted in a significant amount of time and resources being committed that could have otherwise been spent on software development. As a result, IWEDA project members within ARL have decided to explore the feasibility of rewriting IWEDA as a Java application. This would hopefully simplify things in the long term of only having to maintain a single IWEDA binary. Questions remain to be answered regarding the impact on the weather server and interfacing with the client map server to name two.

• At echelons where there is no weather server, the IWEDA database will need to reside on another BFA system. Doctrinally the weather server (i.e., the Integrated Meteorological System or IMETS) is located at corps, division, separate brigade, and with special operation forces. Obviously there is a requirement for information regarding weather impacts on weapon systems at all echelons. Although echelons not served by an IMETS could, in theory, retrieve the IWEDA database tables from another echelon via MSE, as demonstrated during the Brigade Task Force XXI exercise, this is not a reliable method. Considering that there can be dozens of systems at an echelon not served by IMETS, it is entirely unfeasible to expect MSE to provide the database tables to all machines in a timely matter. However, if the IWEDA database tables can be provided to a single system (hopefully via a high bandwidth satellite link) at the echelon not served by an IMETS, this system could act as an IMETS surrogate to distribute the required tables within the echelon over the existing LAN.

IV. SUMMARY

Task Force XXI experiments and exercises and paving the way for the Army's First Digitized Division in the year 2000. Task Force XXI provides a valuable benchmark for ARL to evaluate IWEDA in terms of current status, performance in a tactical environment, and required

enhancements. Additional training on client applications for the BFA operators is necessary before a valid evaluation of IWEDA can be made on systems other than the IMETS. ARL will continue to explore alternatives to the current client server architecture (DCE) to determine whether or not they may provide a feasible method to lessen the burden of installing and maintaining IWEDA on the numerous BFA systems.

DIRECT: Dynamic IWEDA Rule Editor and Database Control Tool

Mario A. Torres
U.S. Army Research Laboratory
White Sands Missile Range
NM 88002-5501
Ph: (505) 678-4657 Fax: (505) 678-8766
E-mail: atorres@arl.mil

ABSTRACT

In our efforts to expand the weather intelligence capability for the battlespace commander through decision-aid software packages, the U.S. Army Research Laboratory (ARL) has developed a software utility designed to complement the existing Integrated Weather Effects Decision Aid (*IWEDA*). This new software package, the Dynamic *IWEDA* Rule Editor and Database Control Tool (*DIRECT*), is a graphical user interface tool designed to assist the staff weather officer (SWO) in editing, deleting, and creating weather impact rules which are stored in a database and utilized by *IWEDA*. *DIRECT* gives *IWEDA* the added capability to provide detailed and up-to-date information that is essential for mission planning. With *DIRECT*, the SWO can directly maintain the "how, when, where, and why" of weather effects on weapons and operations.

DIRECT includes an easy-to-use X-Windows-Motif based graphical user interface that contains direct links to information stored under the Informix relational database management system. All information displayed by *DIRECT* is "true-data," extracted explicitly from the database and presented in an easy-to-read and -edit format. In addition to providing the SWO with the explicit knowledge of weather impacts on a system-by-system basis, *DIRECT* also gives him the capability to change default values to tailor weather rules to best fit the unit he is supporting. As a precautionary measure, the original default values can be reset in the database at any time. This paper presents details of *DIRECT*'s purpose and application and illustrates the "look and feel" of its graphical user interface. Feedback from preliminary in-house testing and SWO recommendations are included.

1. INTRODUCTION

IWEDA software transforms raw weather data into weather intelligence for the battlespace commander. ARL is currently fielding the *IWEDA* System to provide detailed weather effects information for various weapons systems and their subsystems and components. Simply, *IWEDA* provides an SWO with an easy-to-use tool to discern and illustrate the "how, when, where, and why" of weather effects on weapons systems. However, the SWO could not previously modify *IWEDA*'s weather impact rules, which are stored in a database. An SWO may

wish to manipulate the weather impact rules for a system that is believed to be outdated, incomplete, or inconsistent with mission demands. By having the capability to manipulate weather impacts, the SWO has the flexibility to provide the commander and the soldier with mission-critical, up-to-date information. ARL's new software program, *DIRECT*, has been designed to allow easy manipulation and review of weather impact rules used by *IWEDA*.

DIRECT Version 0.2 provides the user with the following capabilities:

- a graphical user interface to query the database for systems, subsystems, components, and their respective rules;
- dynamic queries of weather impact rules beginning at any level (systems, subsystems, or components);
- a list of the systems, subsystems, and components in their hierarchical structure;
- a review of available weather impact rules in the database;
- the ability to edit, save, reset, or delete individual weather impact rules on a per-item basis from the database;
- a global default reset of user-definable weather impact rules; and
- a simple graphical user interface interaction, requiring no database management skills.

This paper briefly describes how to use *DIRECT* to edit the weather impact rules located in the *IWEDA* database and gives the reader (and potential user) a basic feel for *DIRECT*'s capabilities and its functionality.

2. SOFTWARE GOALS

The *IWEDA* software package has been operational in the field for over 2 years as an essential component of the Integrated Meteorological System (IMETS) in support of the Army's Brigade Task Force XXI. SWOs participating in these exercises have provided invaluable feedback on how to improve the system and its operations. In essence, *DIRECT* is a materialization of a user requirement to provide a fast and simple method for editing weather impact rules used by *IWEDA*.

DIRECT's software goals are to provide an easy-to-use graphical user interface to *IWEDA*'s Informix database by:

- having the capability to edit, delete, and create weather impact rules directly in the database;
- giving the user a "quick-view" of the rules contained in the database in a simple-to-understand format; and
- eliminating the requirement of users to have Structured Query Language (SQL) and/or database administration skills.

3. CURRENT SOFTWARE CAPABILITIES

DIRECT is currently available to operate under the Army's Common Operation Environment (COE), which consists of a Sun computer platform with Solaris Operating System and a properly installed *IWEDA* database with an Informix dB engine. Upon execution of *DIRECT*, the user can view and edit weather impact rules at any one of three levels: systems, subsystems, or components (see figure 1), the topmost level being systems, followed by subsystems and then components. Selecting of any of these three levels executes a "direct" query to the Informix database, and the results of the query are displayed as a list of all available items for that particular level, as illustrated in the left-hand column of figure 2. From this initial list, the user can display subitems of an available list item by pointing at the item and clicking the right mouse button. Figure 2 illustrates this concept and shows the subsystem available for the F-16 aircraft system (the Maverick) along with the components of that subsystem. The user can view the weather impact rules in the database for the available "Editable Items" by pointing at an item and clicking the left mouse button.

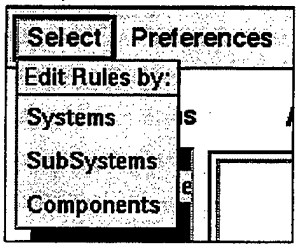

Figure 1. The Weather impact levels

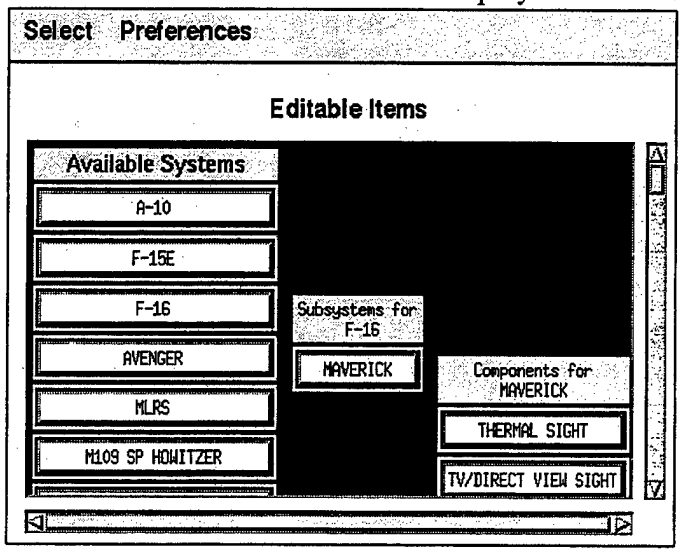

Figure 2. Menu of available systems

When the user chooses an item to view, information from various tables in the database are joined to compose an easy-to-read list of "Available Weather Impact Rules" for the item. Each rule is displayed in row format, and each row contains eight columns with corresponding parameters. Figure 3 displays columns 1 through 5, and figure 4 displays columns 6 through 8. The first column in each row displays the parameter name (i.e., Freezing Rain) and its rule number ([56]). The second column contains the operand. The third column gives a number, condition, or fraction, depending on the type of rule. The fourth column is a one-

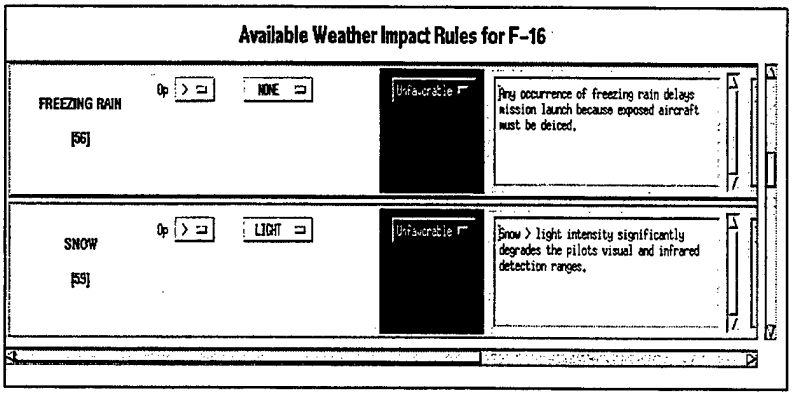

Figure 3. Columns 1 through 5 of the available weather impact rules screen

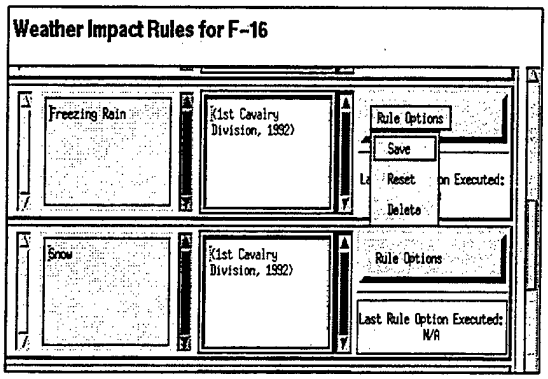

Figure 4. Columns 6 through 8 of the available weather impact rules screen.

word, color-coded weather impact, such as Marginal (yellow) or Unfavorable (red), and the fifth column shows the full weather impact statement. The sixth column displays a condensed weather impact (figure 4). The seventh column displays the rule source, and the eighth column is a menu with three rule options: Save, Reset, and Delete. A user can choose any of these options to execute for that particular rule; that is, after a rule has been edited, the user can save the changes, reset the rule to default values, or delete the rule from the database. A rule can be reset individually, or all of the rules can be reset from a default set of tables contained in the database.

Figure 5 shows a full screen capture that contains all of the above-explained capabilities. All information is displayed on one simple-to-read screen. The buttons and their actions are intuitive, and rule interpretation is simple and straightforward. For instance, an available weather impact rule for the F-16 aircraft would read: "*Freezing rain greater than none is unfavorable.*" This, of course, is also easily interpreted from the full impact window, which reads: *"Any occurrence of freezing rain delays mission launch because exposed aircraft must be deiced."*

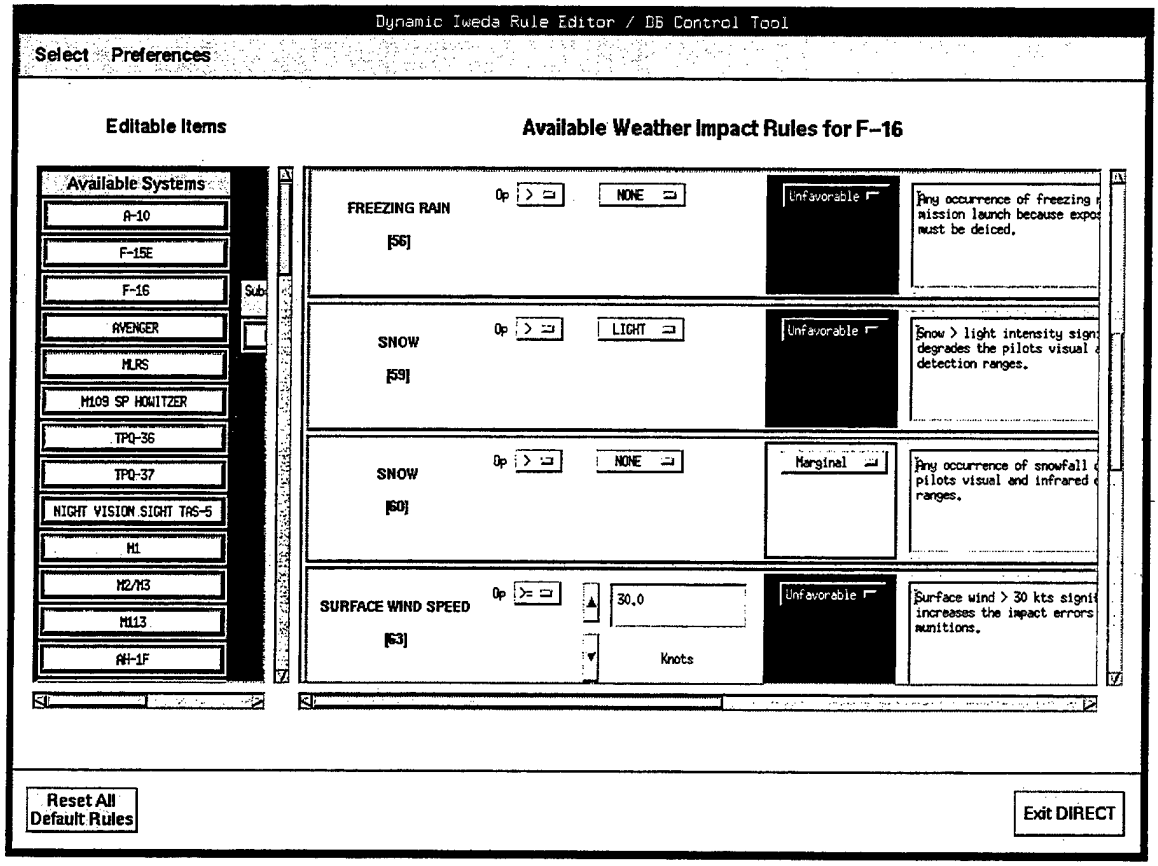

Figure 5. Full screen composite of figures 1 through 4.

4. FUTURE SOFTWARE ENHANCEMENTS

As with *IWEDA*, ARL expects *DIRECT*'s capability to increase and improve with subsequent releases. Some of the planned enhancements will allow the user to:

- create new rules for existing systems (currently, users can only edit existing rules);
- add new systems and their rules (to help when the default set of systems is expanded and new weather impacts become available);
- save modified rule sets as uniquely named databases (to allow different users to save their own sets of rules or have various sets for different missions); and
- highlight a modified rule (in *IWEDA*) with alternate font or color (to alert the *IWEDA* user that an activated weather impact rule is an edited rule and different from a default rule).

User feedback is invaluable and always welcomed at ARL. All comments, suggestions, and bug reports may be directed to the author of this paper via e-mail.

5. EVALUATION RESULTS AND SUMMARY

DIRECT provides many key benefits to the *IWEDA* user. *DIRECT* gives users the requested flexibility to manipulate the weather impact rules used by *IWEDA*, and *DIRECT* is an easy-to-use graphical user interface to a complicated database of weather impact rules. *DIRECT* facilitates the viewing, editing, and deleting of rules from the database, and it eliminates the need for knowledge of SQL to edit rules in the database tables. Evaluators of *DIRECT* affirm its ease of use and believe it to be a valuable asset to the *IWEDA* System. They point out that interaction with the database and all necessary queries are fast and complete.

With *DIRECT*'s versatility, the SWO can quickly modify weather impacts rules used by *IWEDA*. *DIRECT* gives the SWO the added capability to tailor weather intelligence output, which is essential for mission planning and operations. With *DIRECT* and *IWEDA*, the battlespace commander is one step closer to "owning the weather" in the battlefield.

Weather Impact Decision Aids - IR and NVG Model Validation

Dana Madsen*, Stan Heckman, Timothy Hiett, Paul Tattelman,
Guy Seeley, Steve Ayer, Steve Luker, Ralph Hoar, Jim Andersen
Air Force Research Laboratory
29 Randolph R&D
Hanscom AFB, MA 01731
617-377-2963, FAX -2984
madsen@plh.af.mil

The Air Force Research Laboratory manages the Weather Impact Decision Aids (WIDA) program that develops software to predict the influence of the weather and other environmental parameters on the operational performance of Electro-Optical (EO) sensors used in air-to-ground munitions, navigation systems, and night vision goggles (NVGs). Key products under development include the Infrared (IR) Target-Scene Simulation Software (IRTSS) to provide target area scenes for pilot situational awareness prior to a mission, the Target Acquisition Weather Software (TAWS) to provide an EO targeting replacement for the currently-operational EO Tactical Decision Aid (EOTDA), the NVG Operations Weather Software (NOWS) for environmental performance impacts, and the Weather Automated Mission Planning Software (WAMPS) for automating weather impacts into the mission planning process. Unique measurement facilities have been established to evaluate EO target and background signature models in the IR (3-5 and 8-12 micron) and near-IR (0.7-0.9 micron) wavebands. EO data and imagery, along with supporting meteorological and geophysical data, are collected for systematic model validation. Experiments have been conducted at a fixed site at Hanscom AFB for nearly three years. A mobile van has been equipped to conduct IR and NVG experiments at several sites at Otis ANGB, Cape Cod, MA. Data from both of these facilities is used for model development and an extensive validation of model performance under a variety of target/background types and weather conditions. In addition, IRTSS-predicted IR scenes are being validated against actual cockpit video provided by the Eglin AFB 46th Test Wing. This presentation will provide a brief overview of the WIDA program, followed by a description of our very unique data collection facilities and model validation efforts.

1.0 Introduction

The AFRL Weather Impact Decision Aids (WIDA) program is developing technologies that translate meteorological parameters into bottom-line impacts on weapon and navigation sensors in the IR (8-12 micron and 3-5 micron), visible, NVG, and laser wavebands. This translation process packages data best understood by a meteorologist into a form readily assimilated by the warfighter. WIDA efforts, targeted at the force and unit levels, span multiple wavebands, including the 8-12 micron IR and the NVG wavebands. Four software products are under development as follows:

- The *IR Target-Scene Simulation Software (IRTSS)* provides "through-the-sensor" weather-impacted target scene visualizations for mission planning and enhanced aircrew situational awareness. It currently operates in the 8-12 micron IR waveband but is being extended to the 3-5 micron, TV, and NVG wavebands.

- The *Night Vision Goggles (NVG) Operations Weather Software (NOWS)* provides NVG performance predictions, including predicted detection ranges of ground targets and aircraft and predicted horizon visibility. NOWS has been developed by TASC Incfor AFRL.

- The *Target Acquisition Weather Software (TAWS)* is being developed as a joint Air Force/Navy, Windows95/NT-based replacement to the Electro-Optical Tactical Decision Aid (EOTDA) for providing predicted detection and lock-on ranges in the IR (8-12 micron

and 3-5 micron), TV, NVG, and laser wavebands. It will include upgraded physics, support for new sensors in the 3-5 micron IR and NVG wavebands, modern software technology, and IRTSS-based scene visualization.

- The *Weather Automated Mission Planning Software (WAMPS)* is aimed at providing force-level mission planners using automated mission planning systems with weather impact guidance. WAMPS will provide guidance for hundreds of targets at a time up to 72 hours out in the mission planning process.

The above software products are being developed around a core set of WIDA physics models covering the IR (8-12 micron and 3-5 micron), NVG, visible, and laser wavebands. Using these core physics models in both force-level products (WAMPS) and unit-level products (IRTSS, NOWS, TAWS) ensures consistent weather impact guidance across the chain of command.

To date, work on the physics models has focused on the 8-12 micron IR and the NVG wavebands. The 8-12 micron IR waveband is characterized by several models which have been integrated to produce "through-the-sensor" target-scene visualizations based on forecast weather in that waveband. Inherent background radiances are derived from the Smart Weapons Operability Enhancement (SWOE) Interim Thermal Model (ITM)[1]. Inherent target radiances are derived from the Thermal Contrast Model version 2 (TCM2).[2] MODTRAN[3] and an interpolator developed by TASC for AFRL[4] are used to apply atmospheric propagation effects to inherent radiances. An AFRL-developed sensor performance model accounts for sensor characteristics including field of view, resolution, and detectivity. These physics models form the basis of IR support in IRTSS, TAWS, and WAMPS.

The NVG waveband is characterized by several models which have been integrated to produce NVG performance predictions. The Solar-Lunar Almanac Code (SLAC)[5] is used for computing solar and lunar positions. Atmospheric optical properties, direct and diffuse lunar and twilight radiance, and atmospheric transmission and path radiance are provided by the Fast Atmospheric SCATtering (FASCAT) model.[6,7,8] NOWS includes a rudimentary urban illumination model based on a parametric model developed by Garstang.[9] Parameters derived from these three models are used to compute target, background, and shadow inherent and apparent radiance. Finally, a sensor performance model based on the Army Night Vision and Electronic Sensors Directorate (NVESD) 1994 version of the Image Intensifier Code[10] is used to compute target

---

[1] G. Koenig. Smart Weapons Operability Enhancement Program Final Report, Annex D, SWOE Models. Technical Report, Army Cold Regions Research and Engineering Laboratory, 1994.

[2] L. Blakeslee and L. Rodrigues. Technical Reference Guide for TCM2. USAF Wright Laboratory Technical Report WL-TR-94-1063, 1994.

[3] Alexander Berk, Lawrence S. Bernstein, and David C. Robertson. MODTRAN: A Moderate Resolution Model for LOWTRAN7. Air Force Geophysics Laboratory Technical Report GL-TR-89-0122, 1989.

[4] P. D. Hestand and M. M. Gouveia. Atmospheric Effects Interpolation Algorithm Technical and Software Description. Technical Report, TASC, 1995.

[5] J. A. Bangert. A Portable Computer Source-Code Module for Computing Accurate Times of Lunar and Solar Phenomena. U.S. Naval Observatory, Astronomical Applications Department Technical Report, 1996.

[6] W. S. Hering. An Operational Technique for Estimating Visible Spectrum Contrast Transmittance. Technical Report, Air Force Geophysics Laboratory Technical Report AFGL-TR-81-0198, University of California, San Diego, Scripps Instituion of Oceanography, Visibility Laboratory, 1981.

[7] W. S. Hering. Analytic Techniques for Estimating Visible Image Transmission Properties of the Atmosphere. Air Force Geophysics Laboratory Technical Report, AFGL-TR-83-0236, University of California, San Diego, Scripps Instituion of Oceanography, Visibility Laboratory, 1983.

[8] W. S. Hering and R. W. Johnson. The FASCAT Model Performance Under Fractional Cloud Conditions and Related Studies. Air Force Geophysics Laboratory Technical Report, AFGL-TR-84-0168, University of California, San Diego, Scripps Instituion of Oceanography, Visibility Laboratory, 1984.

[9] R. H. Garstang. Model for Artificial Night-Sky Illumination. Astronomical Society of the Pacific, v. 97, pp 364-375, 1986.

[10] J. E. Rice. Documentation and Technical User's Guide for the Night Vision Laboratory Image Intensifier Computer Code. US Army MERADCOM Technical Report OMI-82-024, Optimetrics, Inc, 1982.

detection ranges at a user-specified detection probability or probability of target detection at a user-specified range.

The WIDA program includes an extensive effort aimed at validating and upgrading the physics models described above. This is crucial to ensuring that warfighters receive accurate weather impact guidance for mission planning. Validation capabilities and results for the IR and NVG models are described below.

2.0 IR Model Validation Efforts

The WIDA IR model validation effort is ensuring the accuracy of the physics models in IRTSS, TAWS, and WAMPS under varied weather conditions at multiple geographic locations. The validation effort consists of three parts. A fixed Hanscom test site has allows model evaluation in a well-understood scenario with detailed meteorological and environmental data in all weather conditions. A mobile validation trailer provides the capability to systematically characterize IRTSS modeling of complex geographic scenes and long atmospheric path lengths under varied geographic and weather scenarios. Finally, comparison of IRTSS imagery to cockpit video collected from air-to-ground missions provides a bottom-line validation of the complete IR model suite in an operational setting. Validation at the Hanscom test site and cockpit video comparisons are described below; IR data collected with the mobile platform is currently being analyzed. Validation has been focused on IRTSS, since IRTSS is very mature. TAWS and WAMPS will use the same physics models.

2.1 Hanscom AFB Test Site

Figure 1 shows the fixed Hanscom AFB test site that has been operating for nearly three years under all weather conditions. It consists of an 8-12 micron FLIR, a 3-5 micron PRISM, a suite of environmental sensors, and a simple test target against a grass background. The simple target and extensive instrumentation provide a well-documented scenario for in-depth evaluation and update of IR thermal, radiance, and sensor models. This setup supports two experiment scenarios: viewing of the test target and viewing surrounding features (forests, buildings, etc.). To date, analysis of Hanscom data has focused on 8-12 micron IR target modeling. Initially, detailed evaluations of the target thermal model (TCM2) were carried out. As the IRTSS software has matured, it has become possible to test the entire IR model suite through end-to-end comparisons of IRTSS imagery with FLIR video of the test target. Results from these efforts show a favorable comparison of IRTSS with truth.

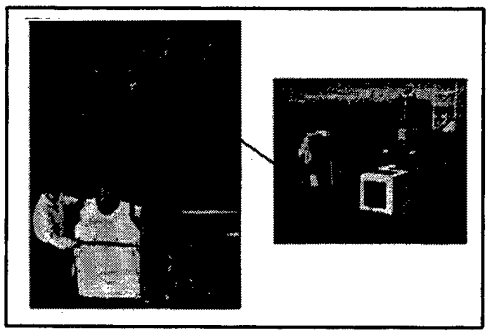

Figure 1: Hanscom AFB IRTSS test site. At left is the 8-12 micron FLIR looking down on the test target and meteorological instruments. At right is a close-up of the test target.

The test site allows concurrent collection of IR video and detailed environmental data. The 8-12 micron imager is the FLIR 2000 imager manufactured by FLIR Systems, Inc. It has a 28 degree x 15 degree wide field of view and a 7 degree by 3.75 degree narrow field of view. The image footprint has 350 x 343 active infrared pixels. The sensor is AC-coupled, meaning that it does not capture absolute scene radiance information. This does introduce difficulties in end-to-end comparisons of FLIR video with IRTSS imagery which are only partially resolved with in-scene calibration targets. FLIR imagery is logged on a time-lapse Super-VHS videocassette recorder and is digitized once per minute.

Environmental data are collected by a variety of instruments at intervals of one minute or less. A Vaisala Milos 500, situated in the target area, captures measurements of solar and IR radiation, relative humidity, temperature, dewpoint, wind speed and direction, atmospheric pressure, rainfall presence and amount, and soil moisture. A Campbell weather station, also in the target area, measures temperatures of test target plates, soil temperature, and air temperature at heights of 5 cm, 1m, and 3m. An HSS, Inc. present weather sensor logs daytime visual range, precipitation type and amount, and presence of haze or fog. A TPQ-11 cloud profiling radar operating at 35 GHz measures height and relative thicknesses of most cloud types up to 62,000 feet. Finally, closed-circuit television (CCTV) cameras capture images of the test target and sky to facilitate later data interpretation.

The test target is a rectangular box offering a simple geometry for thermal and radiance model evaluation. The target is constructed of styrofoam insulation and ¼-inch thick aluminum plates treated with Camouflage Chemical Agent Resitant Coating (CARC). One side of each plate firmly abuts the styrofoam substrate, and thermistors have been epoxied to both surfaces. Two of the plates are connected for evaluation of thermal conductance models. Spectral propoerties of CARC are well understood.

In each experiment episode, environmental data are gathered for a three-day initialization period, followed by concurrent IR image and environmental data collection. The initialization period provides past environmental history required for thermal model stabilization. Image and environmental data are stored according to a well-defined and documented format[11] based on the ISO9660 and UniData netCDF[12] standards. The enormous data volume has necessitated development of an automated software system for systematically assessing model performance under varied weather conditions.

Initially, data analysis focused on the TCM2 thermal model used for target characterization. This was chosen in part because the IRTSS software had not matured sufficiently to support integrated testing of the entire IR model suite. Thermistors attached to the test target allow quantitative analysis.

Results from analysis of two months of data indicate that TCM2 can predict temperatures within a few Kelvins (K) of truth and correctly predict contrasts of less than 1K 84% of the time. Most of the error arises from the convection code, which assumes that cooling of a target plate by the wind has no dependence on the direction of the wind. Mass transfer is usually handled with an error of less than 1K but occasionally yields very large errors. The sporadic nature of these errors complicates correction efforts. Conduction code accounts for approximately 10% of the error in the TCM2 model. The radiative transfer code shows no significant errors. Figure 2 shows a representative plot of observed versus predictive temperatures for a six-day period. The

[11] T. Hiett. A User's Guide to the ACT/EOS Validation Experiment Level-2 Data Set. USAF Phillips Laboratory Technical Report PL-TR-95-2136, 1995.
[12] R. Rew, G. Davis, and S. Emmerson. NetCDF User's Guide. Unidata Program Center, 1993.

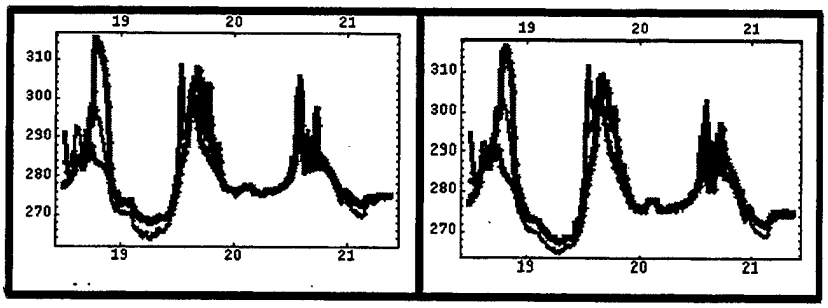

Figure 2: Representative plot of observed temperatures versus TCM2-predicted temperatures for a six-day period.

underpredicted temperature on day 3 arises from convection code errors resulting from an east wind on a west-facing target.

Recent analysis efforts have focused on integrated evaluation of the full IR model suite through end-to-end comparison of IRTSS imagery with FLIR target video over extended time periods. Recall that the 8-12 micron FLIR is an uncalibrated, AC-coupled sensor not intended for scientific measurements. This means that a qualitative IRTSS evaluation can be carried out with greatest confidence. An in-scene calibration target (placed near the test target) allows only limited quantitative analysis because the FLIR does not perform AC coupling over an entire image. AC coupling, for a given pixel, is based on an unspecified number of past scan lines (experimentally estimated to be 37 for a simple test image), and there is an unspecified (probably exponential) weighting of this past information. A calibrated FLIR sensor is required for accurate quantitative assessment of the end-to-end performance of IRTSS.

Qualitative results overall show good agreement between IRTSS and FLIR video, as shown in figure 3 by comparing relative brightnesses of test target plates in the IRTSS imagery with relative brightnesses of test target plates in the FLIR imagery. Some variations are visible in the second and fourth frames.

2.2 Cockpit Video Comparisons

Comparison of IRTSS imagery with cockpit video provides a bottom-line validation of the unique *predictive* scene visualization capability being developed for enhanced mission planning and situational awarness. Cockpit video for validation is being obtained from the Eglin AFB 46th Test Wing and from the Naval Strike and Air Warfare Center at NAS Fallon. This allows validation under varied climatic conditions.

Figure 4 shows a side-by-side comparison of IRTSS imagery with mission video obtained from Eglin AFB. The video was obtained from an 8-12 micron IR LANTIRN targeting pod for a mission flown over the Eglin AFB C-52 test range on 8 May. Mission time was 1300 local. Weather conditions included wind speed of 2 knots, wind direction of 190 degrees, no significant weather, 1/8 cloud coverage at 3500 feet, 7/8 cloud coverage at 25000 feet, a temperature of 71 degrees F, and a dewpoint of 64 degrees F. This is the first comparison of IRTSS with cockpit video.

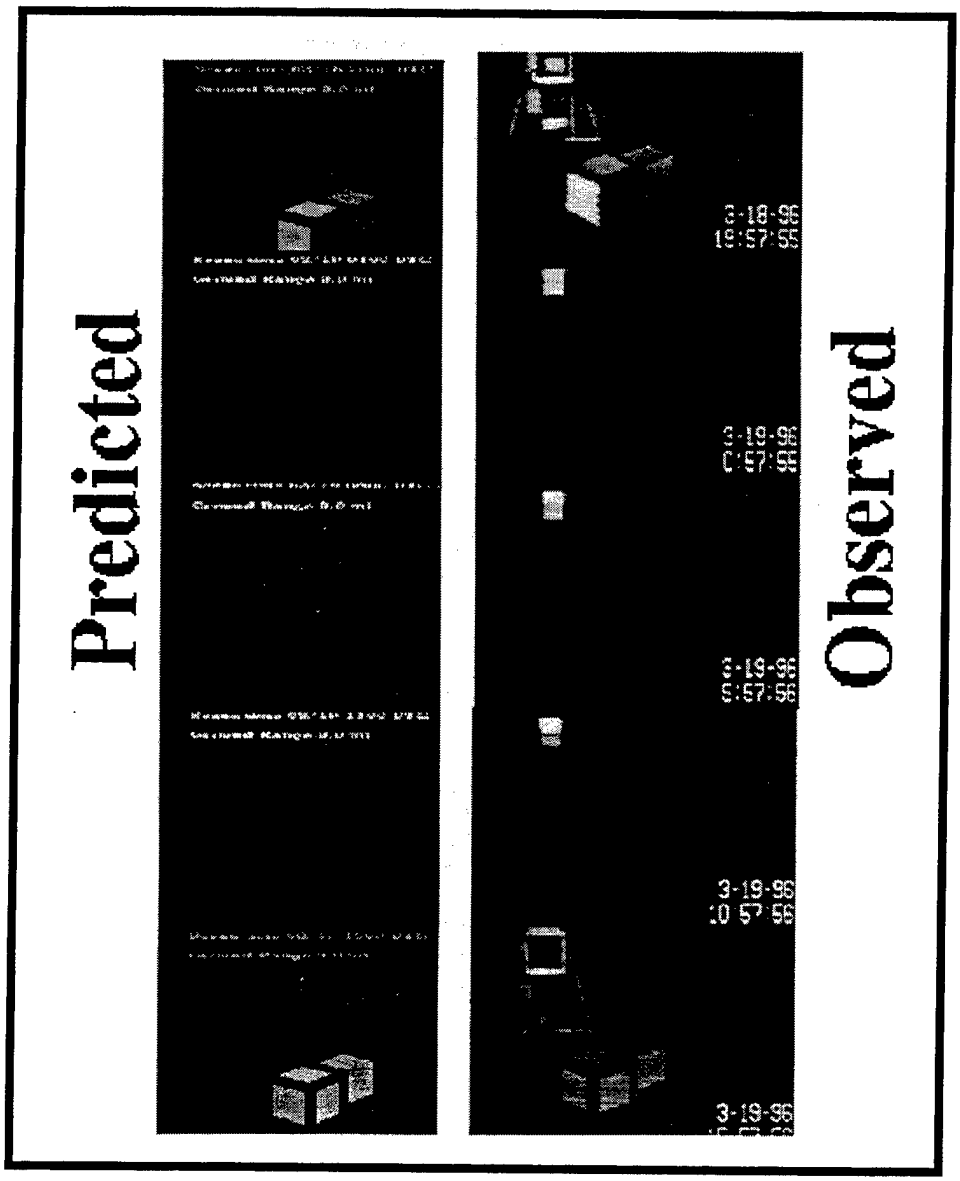

Figure 3: Time-lapse comparison of synthetic IRTSS imagery of simple test target with FLIR video.

In viewing the comparison, one first notices the lack of clouds in the IRTSS imagery. This omission is deliberate. IRTSS can render synthetic clouds corresponding to a predicted fractional cloud coverage, but there is no capability to predict the exact locations of clouds at mission time. Synthetic clouds would not contribute to visualization of the relative brightnesses of broad geographic features needed to find and identify a target. Although clouds are not rendered in a scene, the impact of clouds on inherent IR radiances is modeled.

Next observe that the relative brightnesses of geographic features in the IRTSS imagery are identical to those in the cockpit video. The runway is the brightest scene element. Clearings are brighter than the surrounding forest. The comparison does have minor errors, possibly caused by inaccuracies in the physics models or incorrect categorization of surface materials. Finally notice the significant geographic detail captured by IRTSS.

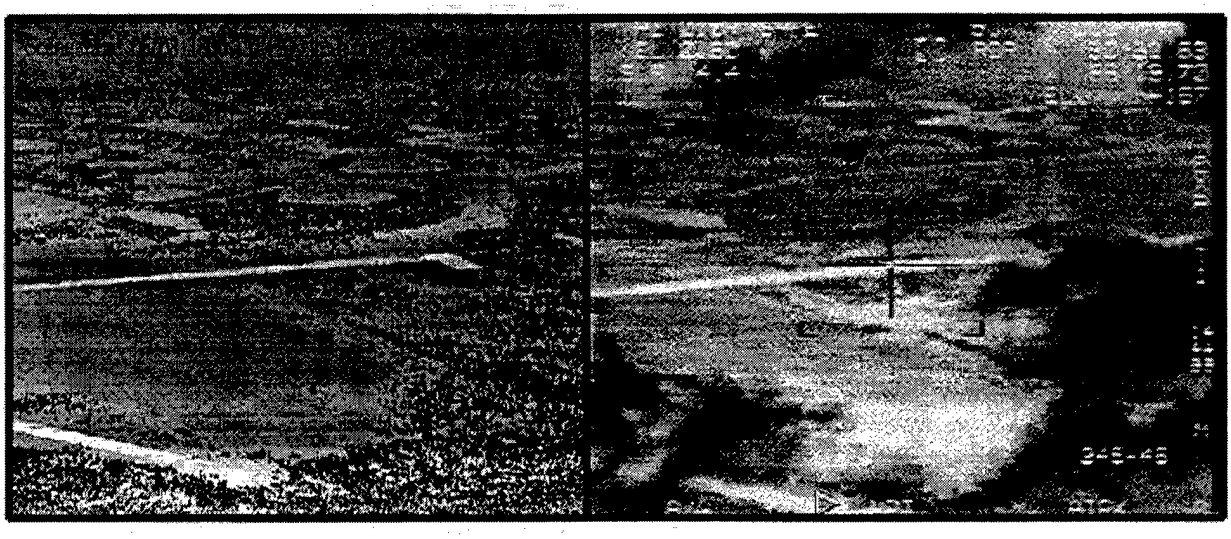

Figure 4: Comparison of IRTSS imagery (left) with cockpit video (right).

Synthetic clouds in IRTSS imagery can be useful in training and modeling and simulation contexts. IRTSS generates clouds using the AFRL Cloud-Scene Simulation Model (CSSM)[13] and the FastMap model.[14] Figure 5 shows IRTSS imagery with synthetic IR clouds.

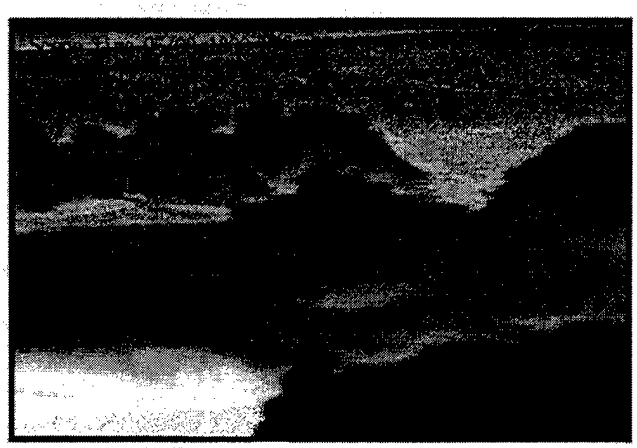

Figure 5: IRTSS imagery with radiometrically-realistic synthetic IR clouds.

3.0 NVG Model Validation Efforts

The WIDA NVG model validation effort is ensuring the accuracy of physics models in the NOWS software under varied weather and lunar conditions, eventually at multiple geographic locations. A validation plan has been developed by TASC Inc to provide measured input parameters to the NOWS physical models and measured values against which to validate model output

[13] M. Cianciolo, M. Raffensberger, E. Schmidt and J. Stearns. Atmospheric Scene Simulation Modeling and Visualization. Phillips Laboratory Geophysics Directorate Technical Report PL-TR-9602079, 1996.
[14] M. Cianciolo, M. Raffensberger, E. Schmidt and J. Stearns. Atmospheric Scene Simulation Modeling and Visualization. Phillips Laboratory Geophysics Directorate Technical Report PL-TR-9602079, 1996.

parameters. Experiments will focus on target contrast and atmospheric transmission modeling. If possible, an attempt will be made to validate illumination model parameters. No rigorous assessment of the sensor performance model is planned, but an attempt will be made to estimate detection range in a qualitative fashion. Throughout the experiments, simple test targets will be used to provide understandable scenarios for analysis. AFRL has developed a mobile validation trailer to support NOWS validation and has already deployed it for three experiment episodes. Data analysis from those episodes is ongoing at TASC.

3.1 Mobile Validation Trailer

Figure 6 shows the mobile trailer developed to support NOWS validation. The trailer allows measurement of natural night-time illumination levels concurrently with weather and atmospheric transmission for validation of NOWS target contrast models. Three spectroradiometers provide measurements of lunar radiance, target facet radiance, and total night sky irradiance. The basic systems are highly sensitive and are normally used in controlled laboratory conditions. They have been adapted for use under harsh field conditions. The suite of weather sensors is similar to those used in IR validation experiments. Mobility is a crucial, since night-time illumination measurements must be performed in remote areas with low light pollution. Trailer subsystems are described further below.

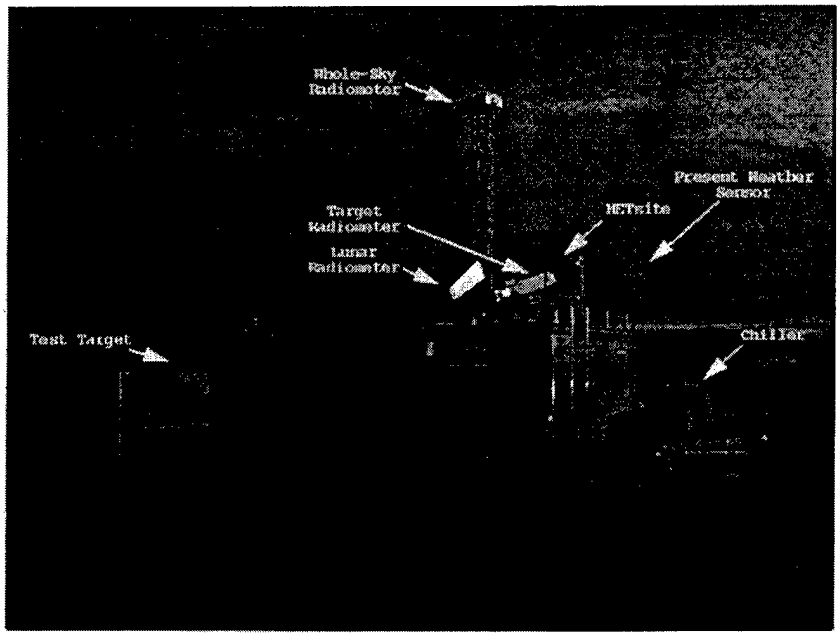

Figure 6: NOWS mobile validation trailer.

The spectroradiometer systems are manufactured by Gamma Scientific. Figure 7 shows how these systems have been adapted for field use. In the figure, whole sky spectroradiometer components have been packaged into an environmental enclosure and mounted on a tower. The enclosure provides temperature control, air circulation, and system monitoring, in addition to protection from the elements. The tower mount reduces ground illumination arriving at the entrance optics. The lunar and target spectroradiometers have similar enclosures. However, they are each mounted on a precision pointing system, allowing precise lunar tracking and target facet measurement. The three spectroradiometers each have controllers housed inside the trailer. Software has been developed for concurrent control and data logging.

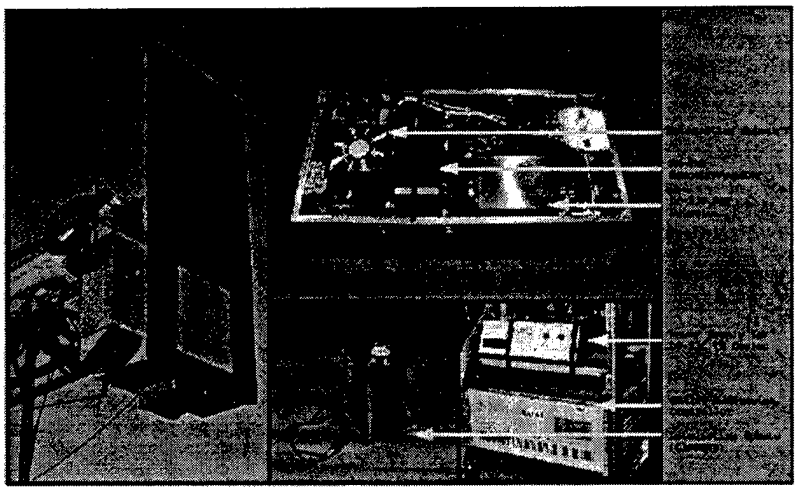

Figure 7: Whole-sky radiometer adapted for field use.

Instruments for atmospheric transmission and weather measurements, along with trailer support systems, are depicted in figure 8. An Optec transmissometer provides measurements at wavelengths of 550, 750, 800, and 900 nm. The transmitter and receiver components are housed in environmental enclosures and placed at a 3000-foot separation. The met site is implemented using a MILOS 500 weather station. The met site and the present weather sensor are identical to those used in the IR experiments described in section 2. A series of cameras, including the sky camera shown in figure 10, gather imagery in visible and NVG wavebands to facilitate data analysis. The chiller and data acquisition system support operation of trailer instruments.

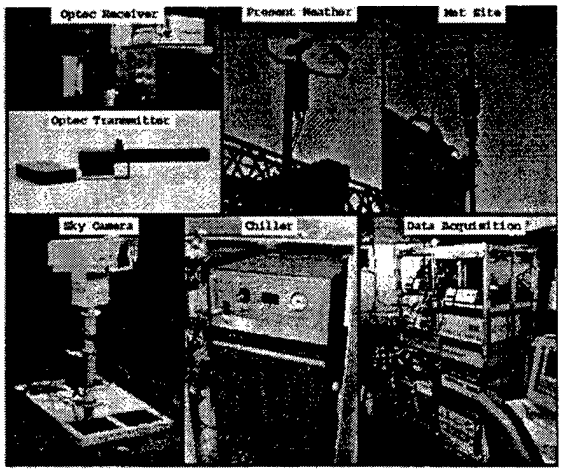

Figure 8: Weather and transmission instruments and trailer support systems.

3.2 First Experiment Episodes

The trailer has been deployed on three experiment episodes, with four data collection opportunities in each, both carried out at the KD test range at Camp Edwards on Cape Cod, MA. The episodes included evenings with a new, half, and full moon. Weather conditions varied from dry and clear to humid and clear to cloudy with light rain. Data analysis is just getting underway, and results will be reported as these efforts progress.

One of the key goals for the early data analysis efforts is to understand the data collection environment provided at the KD test range. Of particular interest is spectrally characterizing sources of light pollution. Light pollution is significantly lower than in metropolitan Boston, but it is still apparent, especially on humid or cloudy evenings. Two nearby sources include a Pave Paws radar site and the control tower for Otis ANGB. The latter is a revolving beacon with blue and white lamps. In addition, cultural illumination effects are visible to the west and east, especially on cloudy or humid evenings.

Data from 1 Oct 97 (a new moon), plotted in figure 9, indicates some of the spectral characteristics of light pollution on the test range. Weather conditions early in the evening included full cloud cover, and light pollution was visually apparent. As the evening progressed, cloud cover diminished to zero, and light pollution was no longer visually apparent. The plots show changes in the spectral content of the total night sky irradiance throughout the evening. The strong signal at 800 nm early in the evening appears to be caused by light pollution. At this point the source of that signal (Pave Paws, the beacon, or cultural lighting) is still being determined.

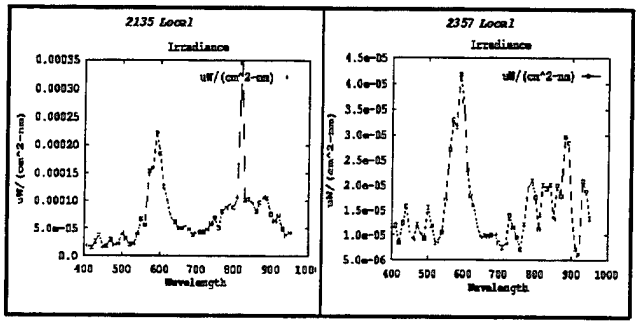

Figure 9: Night sky irradiance data under cloudy (left) and clear (right) new moon conditions.

4.0 Conclusion

The WIDA IR model validation effort is ongoing. The Hanscom test site will be augmented with calibrated 8-12 micron and 3-5 micron sensors on loan from the Army Cold Regions Research and Engineering Lab (CRREL). These sensors will allow a quantitative end-to-end evaluation of thermal, radiance, and sensor model accuracy. Additional cockpit video comparisons at various times of day and under various weather will be generated as video is received from Eglin AFB and NAS Fallon. Further comparison will be undertaken using a video archive maintained by the Joint Camoflauge, Concealment, and Deception (JCCD) program. Part of the work with the JCCD will include evaluating IRTSS as a tool for characterizing the effectiveness of CCD schemes applied to ground assets. Finally, as 3-5 physics are incorporated into IRTSS, validation will extend to cover that waveband as well.

NOWS experiments at the Camp Edwards KD test range will continue over at least the next year. Individual episodes will be focused on natural illumination, inherent and apparent target/background radiance, target shadow radiance, and sky and cloud backgrounds. The possibility exists of deploying the NOWS trailer to a remote national park for gathering data under minimal light pollution conditions. Finally, if time permits, the trailer will also be deployed to support IR model validation at Camp Edwards.[15]

[15] The trailer was previously deployed in July 1996 to Camp Edwards for IR background model validation. Data analysis is ongoing.

USE OF THE NAVY OCEANIC VERTICAL AEROSOL MODEL IN THE EOMDA

Dr. Robert E. Turner*
Science Applications International Corporation
550 Camino El Estero, Suite 205
Monterey, CA 93940-3231
Ph: 408-649-5242 Fax: 408-649-8048
E-Mail: turnerr@cpva.saic.com

Dr. Andreas K. Goroch
Naval Research Laboratory Monterey
7 Grace Hopper Avenue
Monterey, CA 93943-5506
Ph: 408-656-4889 Fax: 408-656-4769
E-mail: goroch@nrlmry.navy.mil

ABSTRACT

The development of the Navy Oceanic Vertical Aerosol Model (NOVAM) represents a major improvement over previous models which did not include realistic effects for the vertical profiles of the aerosol distribution. It is recognized that there are at least three oceanic aerosol distributions each of which is characterized by a different particle size distribution, composition, vertical scale height, and generation source. The NOVAM is now included in the Electro-Optical Meteorological Decision Aid (EOMDA) computer model as one of the options for an atmospheric condition. In addition, one can use this atmospheric state as well as other atmospheres such as those in the MODTRAN computer model for rural, urban, maritime, tropospheric, smoke, and fog states along with a realistic vertical profile of radiosonde data. Included in the radiosonde data are values for the relative humidity, pressure, temperature, and dewpoint as a function of the height of a particular level in the atmosphere. Besides being a more realistic representation of oceanic atmospheric conditions, the NOVAM allows one to make use of a greater number of values for the 24-hour average wind speed and the air-mass parameter than was possible with the older Navy Aerosol Model (NAM). A variety of actual radiosonde profile data have been used to illustrate the flexibility of the NOVAM for the analysis of the propagation of infrared radiation through a realistic aerosol atmosphere in the ocean environment.

1. INTRODUCTION

The Electro-Optical Meteorological Decision Aid (EOMDA) is a computer model that can use real-time or near real-time meteorological data to calculate the optical

properties of the atmosphere, the signal value at the target, and the detection and lock-on ranges for specified sensors. The emphasis in the current work is on the detailed optical properties of the atmosphere for the calculation of the line-of-sight (LOS) transmittance in the 8 to 12 micrometer spectral range. The operational computer program describing the original model for a two-layer atmosphere is given by DeBenedictus et al. [1]. The model had a horizontally and vertically homogeneous structure for the meteorological data for the lower boundary layer and also for the upper layer. A new, improved model has recently been developed by Hodges [2] for the thermal infrared model which allows for the detailed specification of the atmospheric data at many levels of the atmosphere. The user can input realistic radiosonde data and a subroutine in the program will produce the height (km) at the top of each level, the air temperature (degrees C), relative humidity (percent), pressure (hPa), and the dewpoint (degrees C) at the midpoint of each level.

2. AEROSOL MODEL STRUCTURE

The basic structure of the model atmosphere consists of a total of 34 homogeneous levels, each equally-spaced as depicted in Fig. 1. for the case of 23 levels in the lower layer and 11 levels in the upper layer. Note that the user can specify up to n levels in the boundary layer and the 34 - n in the upper layer, where n must be less than 30.

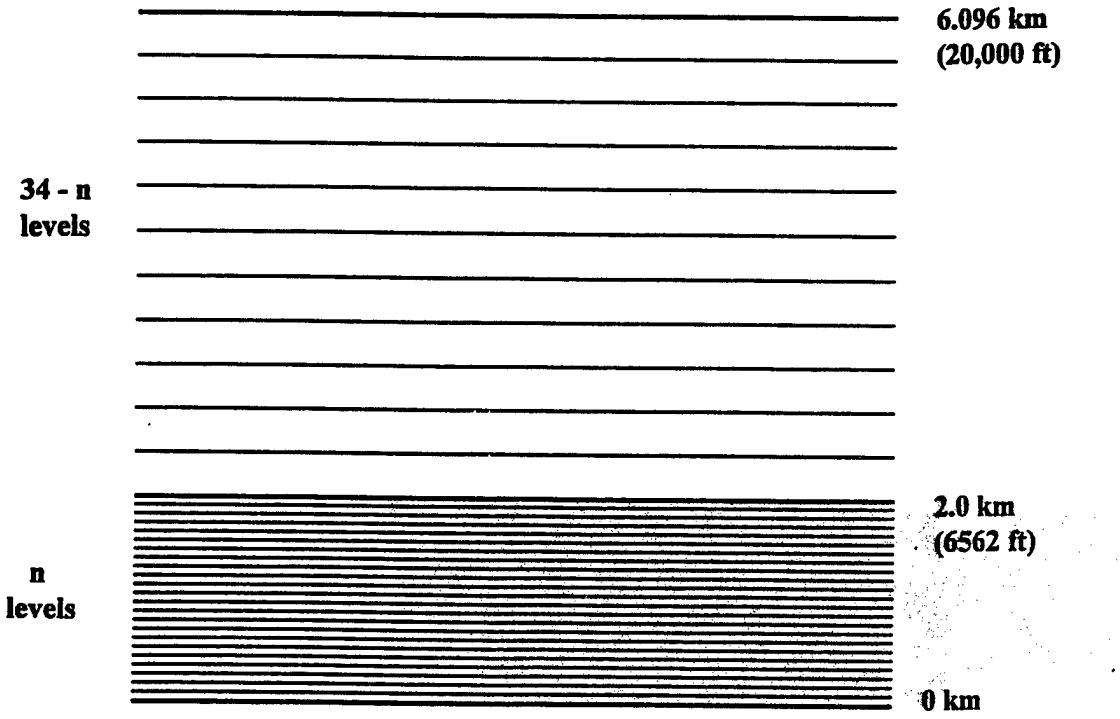

Fig.1. Multi-level EOMDA atmospheric structure for upper and lower layers.

In addition, one must input the cloud cover for each layer, the height of the boundary layer, the sensor height, the distance along the surface to the target, the horizontal visual range at the surface, the visibility in the upper layer, the precipitation rate, the current surface wind speed, the 24-hour average wind speed, the air-mass parameter, aerosol model type, and the specific radiosonde data file. The boundary-layer aerosol models are those used in the program LOWTRAN [3] , i.e., rural, urban, maritime, and tropospheric models which are functions of the visual range and relative humidity, the desert model which is a function of the visual range and the current wind speed, and the "old" Navy maritime model which is a continuous function of the current wind speed but which has discrete values for the average wind speed and the air-mass parameter. Also, there are three smokes, two fogs, and a battlefield-induced contaminant (BIC) model. All of these, with the exception of the BIC are functions of the specific radiosonde data.

The "new" model introduced here is the so-called Navy Oceanic Vertical Aerosol Model or NOVAM, as developed by Gathman and Davidson [4]. It has an advantage that there is a continuous range for the model parameters as well as having an inherent variation in the magnitude of the particulate components with altitude. The ranges are as follows:

$$50\ \% \leqslant \text{Relative Humidity} \leqslant 99\ \%$$
$$1\ \text{(open ocean)} \leqslant \text{AMP} \leqslant 10\ \text{(continental)}$$
$$0 \leqslant \text{Current wind speed} \leqslant 20\ \text{m/sec}$$
$$0 \leqslant \text{Average wind speed} \leqslant 20\ \text{m/sec}$$

where AMP is the air-mass parameter. The model is also a function of the quantities in the radiosonde data as stated in section 1.

3. VARIATION OF PARAMETERS

It is instructive to examine the variation in the NOVAM aerosol extinction coefficients in terms of the parameters on which the model depends. Given the values of the parameters in section 2. the visibility can be calculated. Figs. 2 and 3 illustrate the variation of the aerosol volume extinction coefficient K as a function of the visibility for three wind speeds for a region in the open ocean (AMP =1) and near the shore (AMP=10). In all of these examples it is assumed that the current wind speed is equal to the 24-hour average wind speed. It is interesting to note the large difference between the two regions that are represented. The open ocean condition has a smaller value of K than for the near-continent region and the atmosphere is much clearer as can be seen by the range in the visibility. Fig. 4 shows the variation in K in terms of wind speed for three values of the air-mass parameter for a high relative humidity situation of 99 percent and Fig. 5 illustrates the same variation as a function of the relative humidity for a fixed air-mass parameter of 1.0, i.e., for open ocean conditions. It is also true that there is essentially no difference for an air-mass parameter of 10.0, i.e., for near-continental conditions.

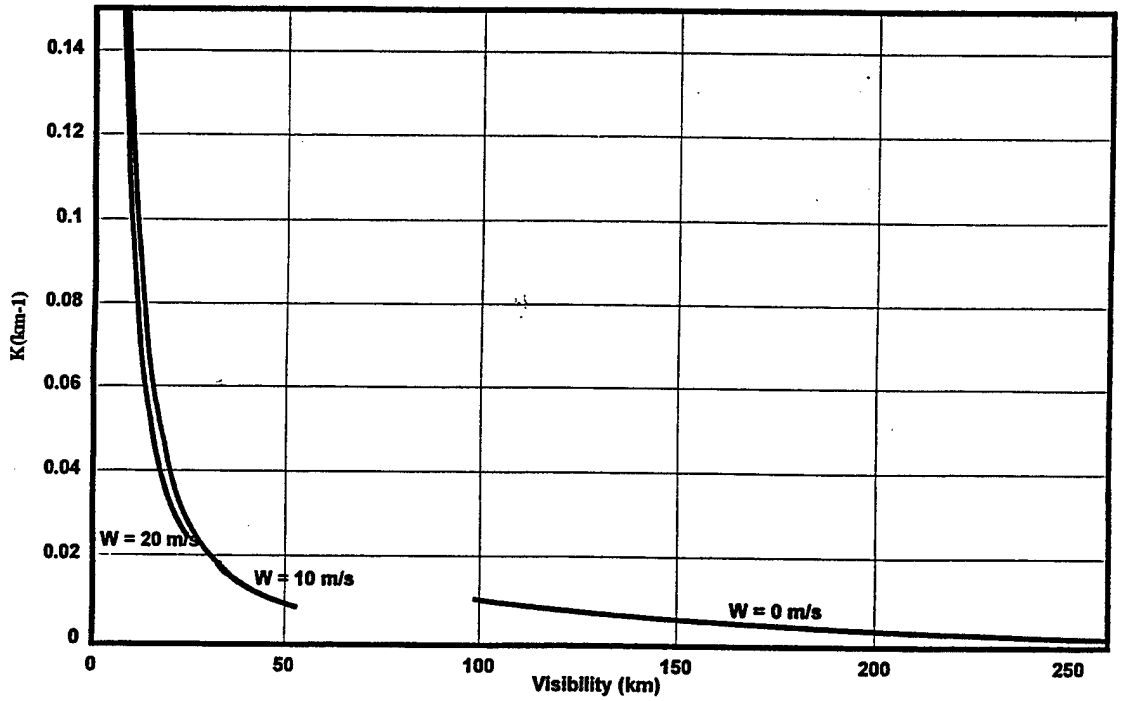

Fig.2. Aerosol extinction coefficient (8 -12 μm) vs. visibility for various wind speeds and open ocean conditions.

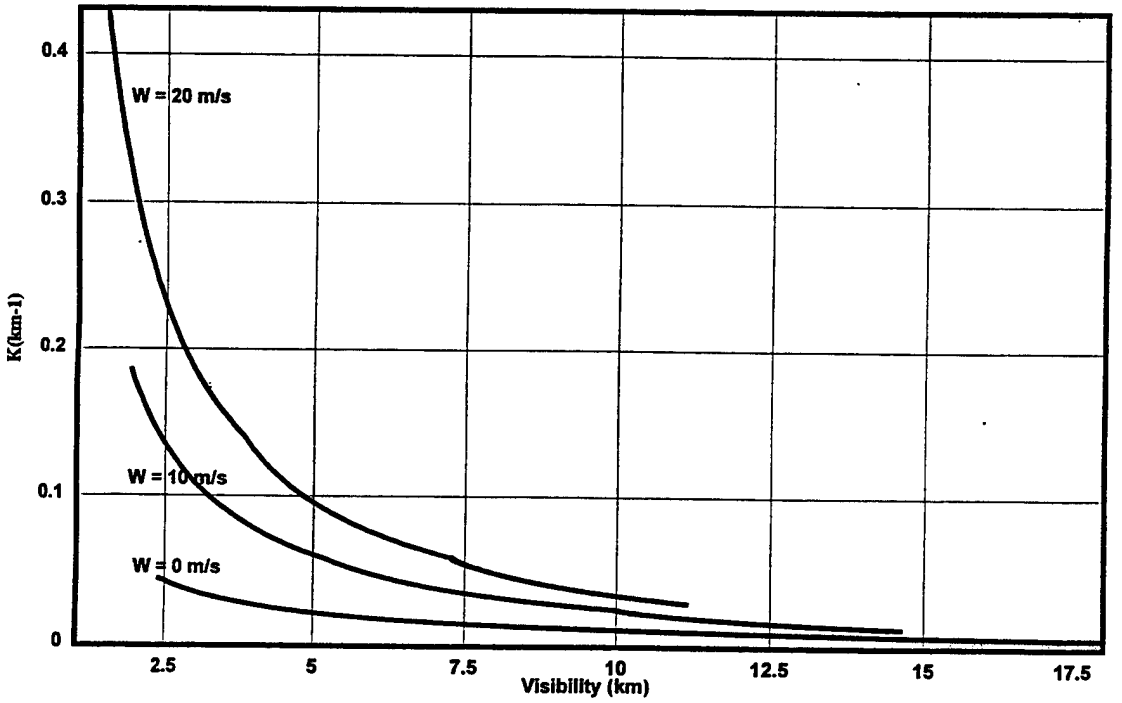

Fig.3. Aerosol extinction coefficient (8 -12 μm) vs. visibility for various wind speeds and near continental conditions.

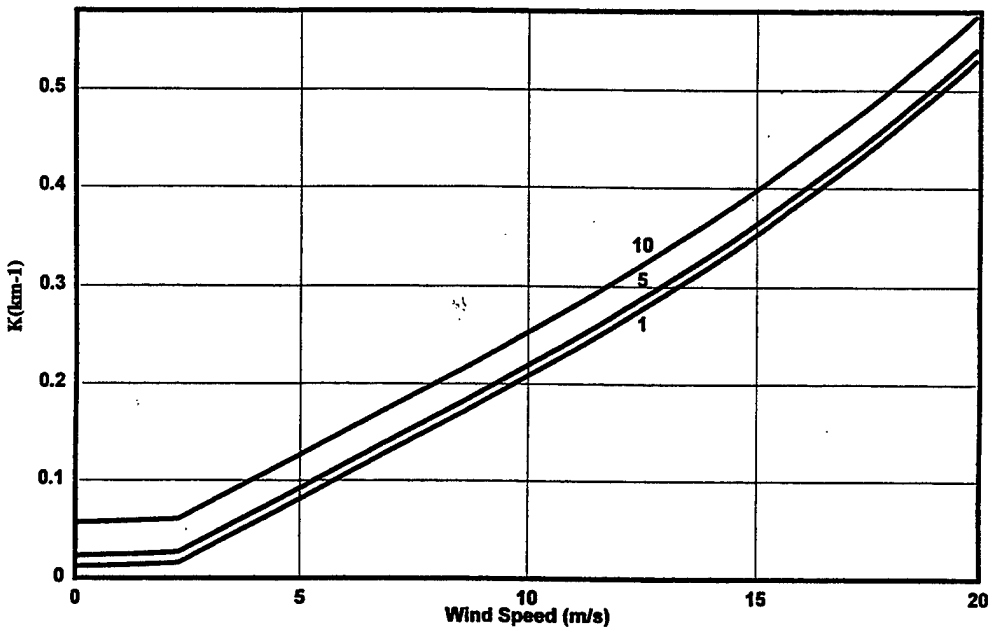

Fig.4. Aerosol extinction coefficient (8 -12 μm) vs. wind speed for various air-mass parameters and a relative humidity of 99 percent.

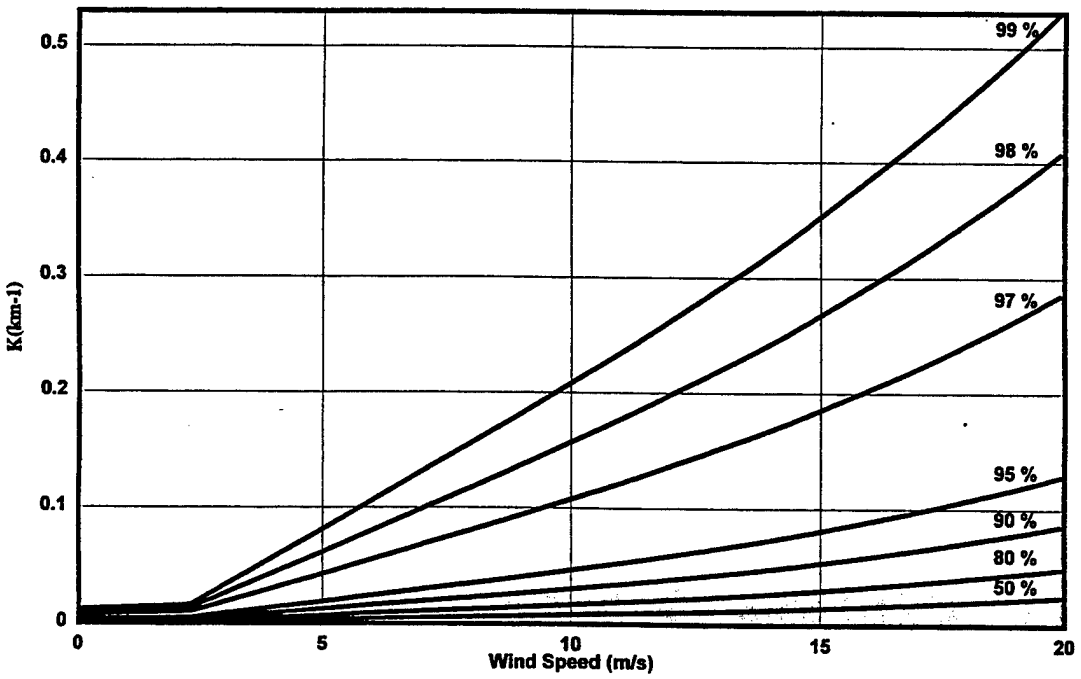

Fig.5. Aerosol extinction coefficient (8 -12 μm) vs. wind speed for various relative humidities for open ocean conditions.

4. VARIATION WITH RADIOSONDE DATA

We can now illustrate the variation in the LOS transmittance with radiosonde data obtained during SHAREM 120B over the sea of Japan off the coast of Korea for the period of April 3 - 8, 1997. Data were taken around a frontal passage with a moist pre-frontal air mass on the first and second radiosondes and on a dry post-frontal air mass on the last radiosonde. Fig. 6 depicts the temperature profiles and Fig. 7 shows the corresponding relative humidity profiles.

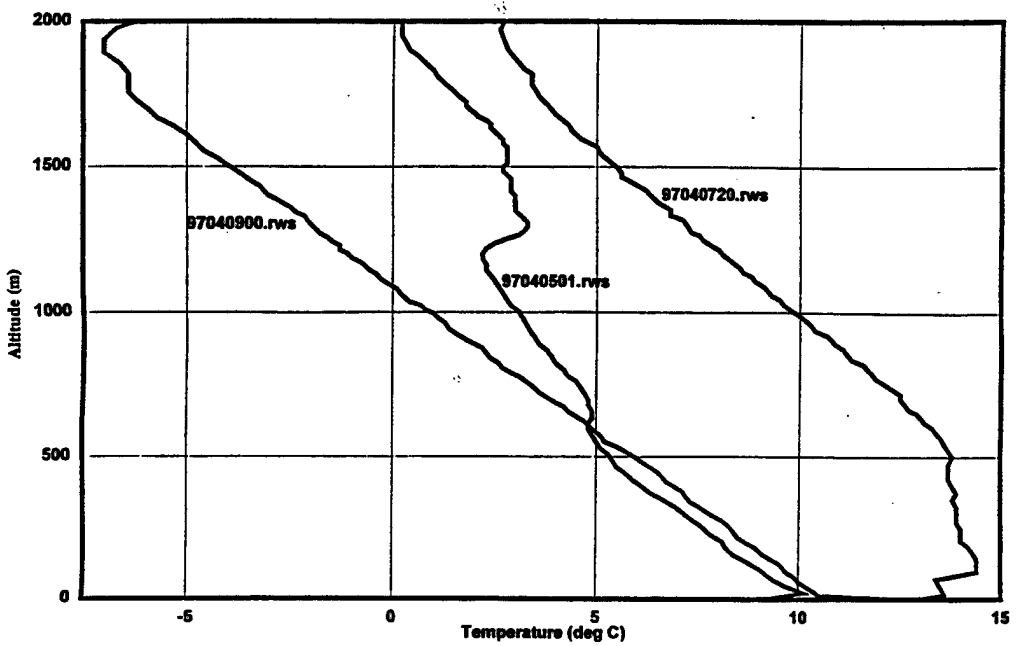

Fig. 6. Vertical temperature profiles for the period April, 1997 in the sea of Japan.

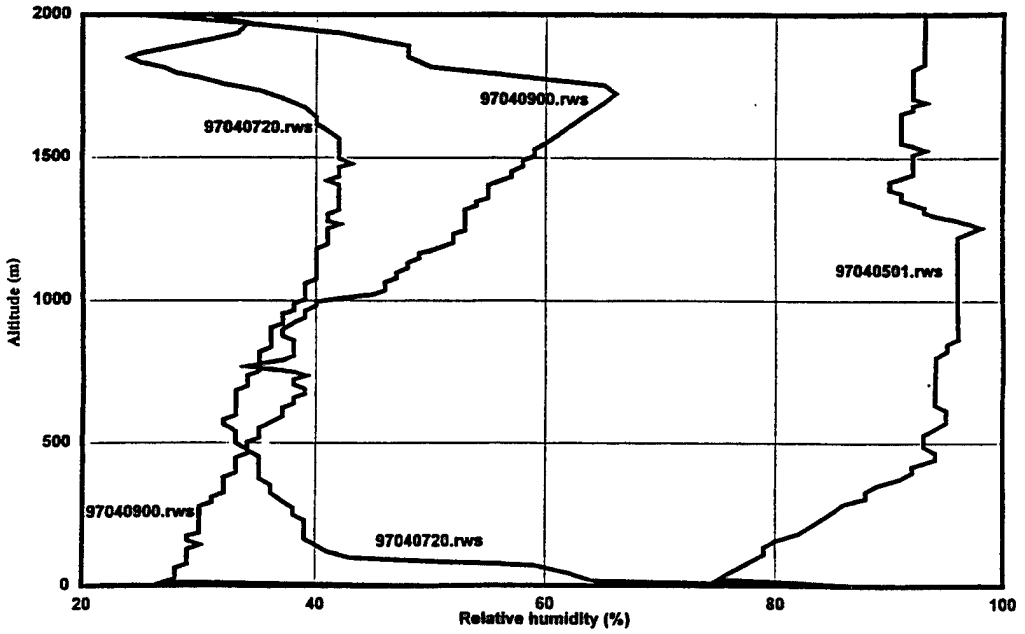

Fig. 7. Vertical relative humidity profiles for the period April, 1997 in the sea of Japan.

The corresponding extinction coefficients for the "moist" profile are presented in Fig.8. for two wind speeds and air-mass parameters. Also, included for comparison is the vertical profile for the gaseous component. Fig. 9 illustrates the LOS transmittance for a sensor at an altitude of 2.0 km looking at a target on the surface with a wind speed of 20 meters per second for open ocean conditions. There are 30 levels in the boundary layer.

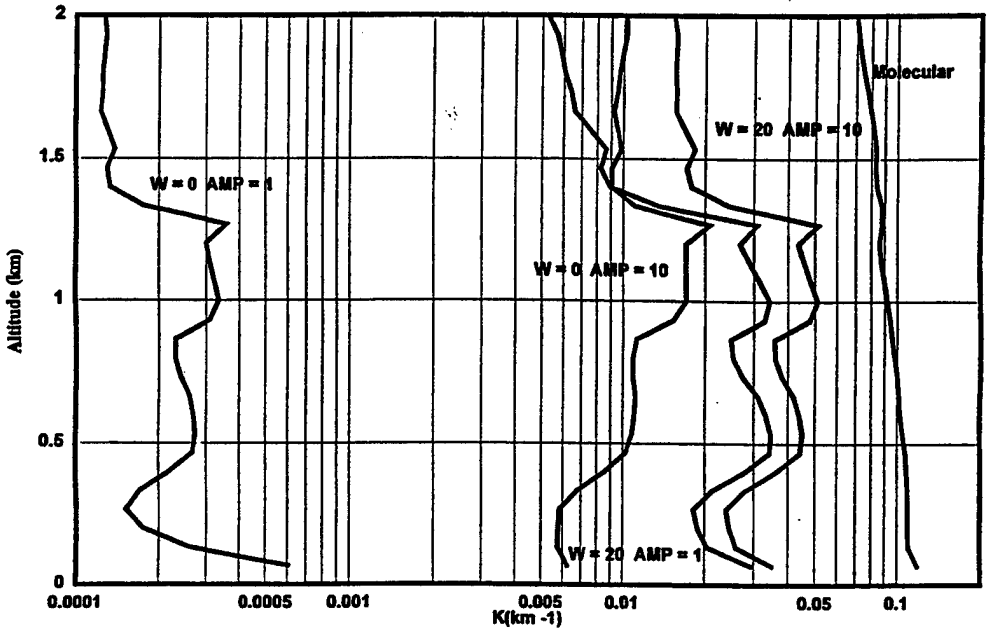

Fig. 8. Vertical extinction coefficient profile for two wind speeds and air masses for the "moist" profile 9704501.rws.

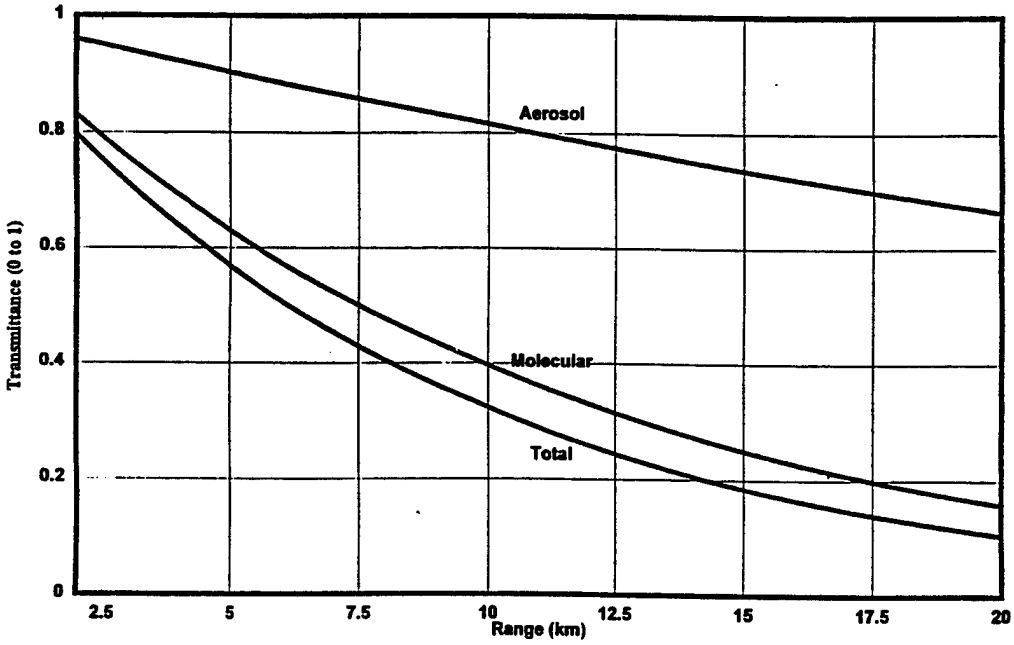

Fig. 9. Transmittance (8 - 12 μm) vs. slant range for radiosonde 97040501.rws. Sensor height = 2.0 km, wind speed = 20.0 m/s, AMP = 1.0, number of levels = 30.

Figure 10 shows the LOS transmittance for the same situation as in Fig. 9 except that the environment is near the continent and the wind speed is 0 meters per second. Figure 11 depicts the same case as for Fig. 10 except that the wind speed is 20.0 meters per second.

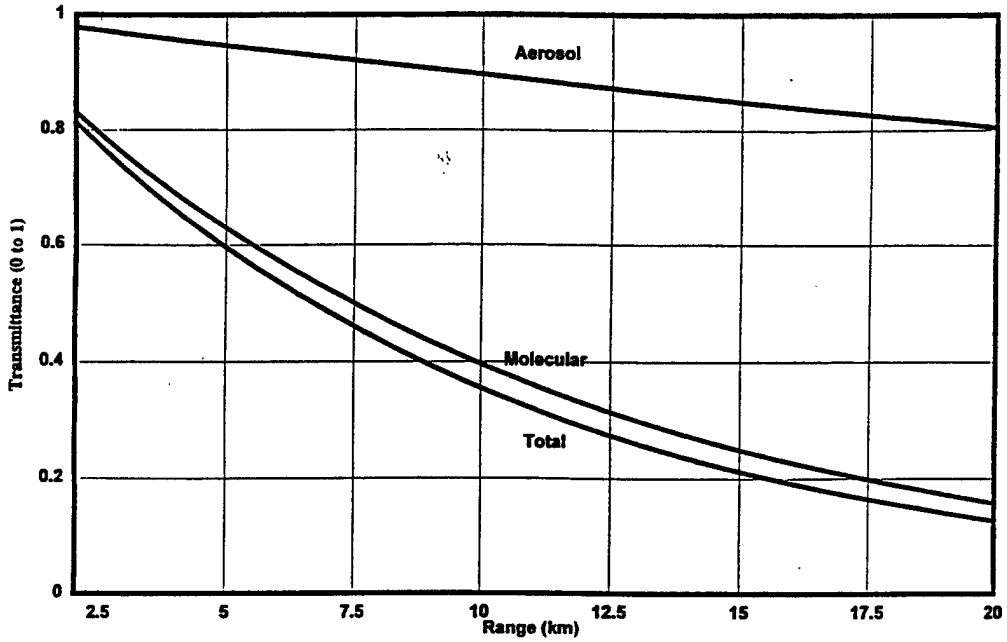

Fig. 10. Transmittance (8 - 12 μm) vs. slant range for radiosonde 97040501.rws. Sensor height = 2.0 km, wind speed = 0.0 m/s, AMP = 10.0, number of levels = 30.

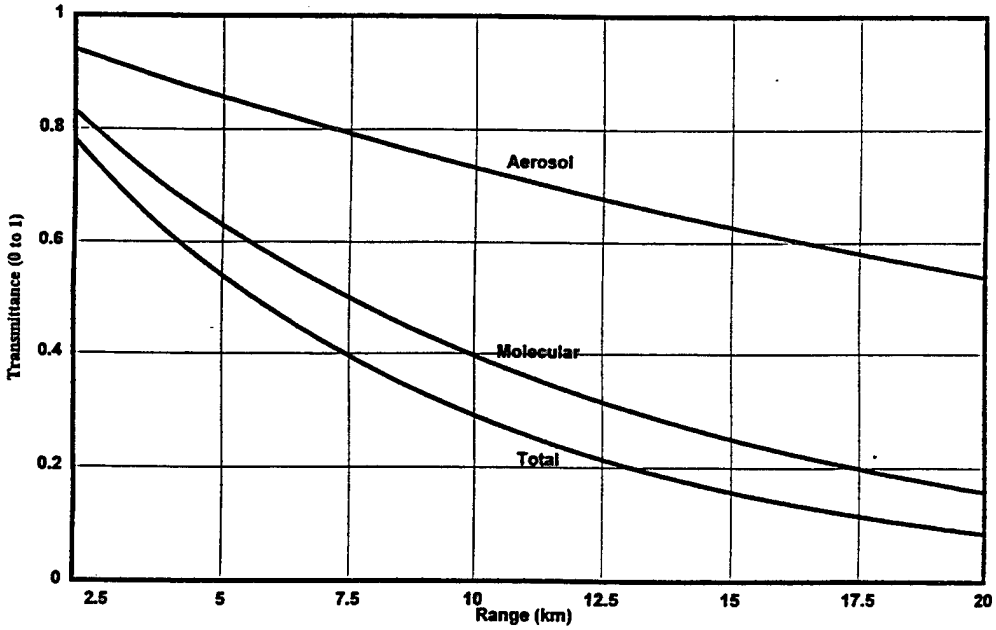

Fig. 11. Transmittance (8 - 12 μm) vs. slant range for radiosonde 97040501.rws. Sensor height = 2.0 km, wind speed = 20.0 m/s, AMP = 10.0, number of levels = 30.

Figure 12. Illustrates the LOS aerosol transmittance vs. slant range for the three radiosonde data for a near-continental environment and Fig. 13. shows the total (molecular + aerosol) transmittance for the same situation.

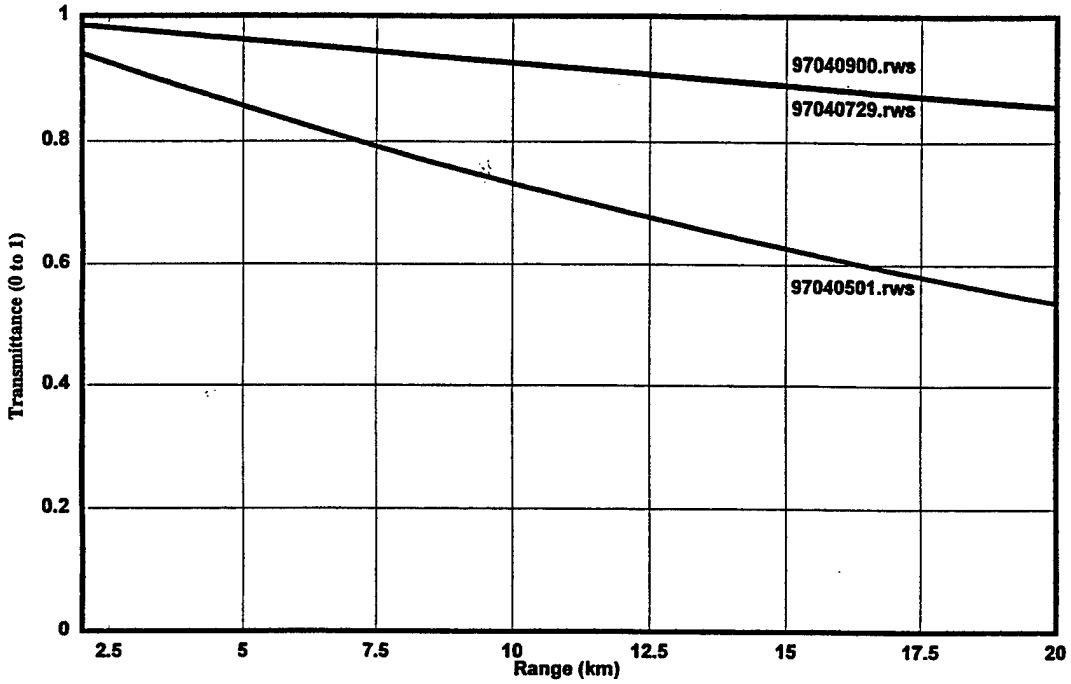

Fig. 12. Aerosol transmittance (8 - 12 μm) vs. slant range for three radiosonde profiles. Sensor height = 2.0 km, wind speed = 20.0 m/s, AMP = 10.0, number of levels = 30.

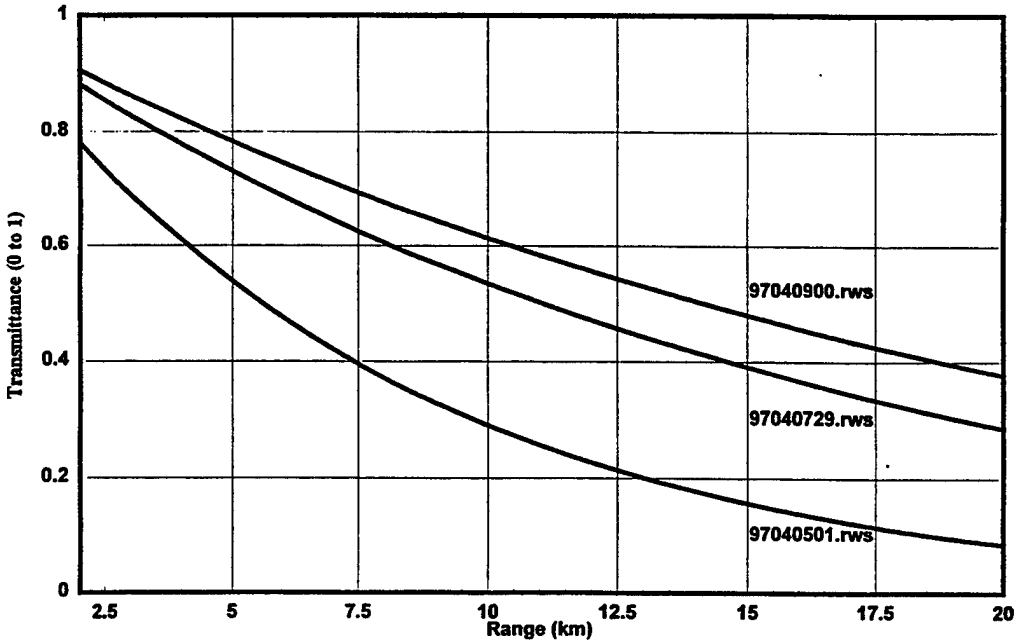

Fig. 13. Total transmittance (8 - 12 μm) vs. slant range for three radiosonde profiles. Sensor height = 2.0 km, wind speed = 20.0 m/s, AMP = 10.0, number of levels = 30.

5. CONCLUSIONS

From the analysis and the figures presented above several conclusions are apparent in the use of the NOVAM in the EOMDA. First, the aerosol volume extinction coefficient is quite sensitive to the wind speed, and, as can be seen from Figs. 2 and 3, this fact leads to a strong dependence on the surface visibility. Second, as is apparent from Fig. 4 that there is a weak dependence on the air-mass parameter, but from Fig. 5 we see a strong dependence on the relative humidity. Figures 6 and 7 show a large difference in the temperature and relative humidity profiles for the three radiosonde data and Fig. 8 clearly indicates the large dependence of the volume extinction coefficient for two wind speeds and two air-mass parameters. It should be noted that there is a much greater difference between K for the two wind speeds under the open ocean conditions than for the near-continental condition. The next three figures illustrate the variation in the LOS transmittance for the aerosol, the molecular, and the total components of the atmosphere. It is surprising that the attenuation is dominated by the molecular component. Finally, Fig. 12 shows the LOS transmittance due to the aerosols for all three data sets and Fig. 13 shows the corresponding total, i.e., the product of the aerosol and the molecular transmittances. It is suggested that the model be tested with other atmospheric profiles and for other aerosol scale heights. The exponential scale height for the intermediate size particle with a mode radius of 0.24 μm is 800 meters, whereas the scale height of the large particle component with a mode radius of 2.0 μm is 50 meters. Also, the model should be adapted to the 3 - 5 μm spectral band.

A model now exits that can be used to represent the variation in the vertical distribution of the atmospheric aerosols for many models, and in particular, for the NOVAM.

REFERENCES

1. D. A. DeBenedictus, J. M. L. Freni, M. J. Gouveia, I. M. Halberstam, P. F. Hilton, D. B. Hodges, D. M. Hoppes, M. J. Oberlatz, M. S. Odle, and C. N. Touart, "Electro-Optical Tactical Decision Aid (EOTDA), Maintenance Manual, Version 3, (Part I)", PL-TR-93-2119 (I), Scientific Report No. 49, Hughes STX Corporation, May 28, 1993.

2. D. B. Hodges, "Software Design Document for the Multiple-Level IR EOTDA", Hughes STX Corporation, April 26, 1995.

3. F. X. Kneizys, E. P. Shettle, L. W. Abreu, J. H. Chetwynd, G. P. Anderson, W. O. gallery, J. E. A. Selby, S. A. Clough, Users Guide to LOWTRAN 7, AFGL-TR-88-0177, Environmental Research Papers, No. 1010, August 16, 1988.

4. S. G. Gathman and K. L. Davidson, The Navy Oceanic Vertical Aerosol Model, Technical Report 1634, NRaD, San Diego, December, 1993.

A PROTOTYPE WEBPAGE FOR SATELLITE PRODUCTS IN THE TACTICAL ENVIRONMENT

Thomas F. Lee*, Jeffrey Hawkins, Roland Nagle, Kim Richardson, Joe Turk
Naval Research Laboratory
Marine Meteorology Division
Monterey CA 93943-5502

1. Introduction

NRL-Monterey specializes in multi-satellite/sensor data fusion. This is accomplished by accessing all four geostationary satellites (GOES-8,9, GMS-5 and Meteosat-6) via cooperative agreements with other R&D users. In addition, SSM/I data are acquired from the Fleet Numerical Meteorology and Oceanography Center (FNMOC) for all three operational SSM/I sensors. Our efforts are geared to near real-time processing, such that coincident data sets for specific purposes can be processed, extracted, viewed and saved for further study. This capability dramatically reduces the data set sizes to manageable sizes.

This paper explores the use of an internet web site for satellite products as a potential surrogate for the much powerful and expensive workstations traditionally used for this purpose. High-end workstations allow users to zoom and loop images, apply color, overlay metafiles, and use multispectral processing. However, since the cost has been high, this capability has been mostly restricted to workstations running in forecast offices and weather centrals. Our application, while not offering all the functionality of higher-end workstations, demonstrates that an internet browser can duplicate a surprising amount of this kind of capability. For this purpose we have created a page used by Navy 3rd Fleet users based in San Diego, California. While data processing is performed in Monterey California at NRL, the geographical focus of the web page is the marine region around San Diego, California.

The web page currently contains applications ranging from cloud and water vapor-tracked winds, aircraft icing aides, low cloud enhancements, cloud advection forecasts, and overlays of model output on satellite imagery. Multi-sensor capabilities are highlighted in our SSM/I section, where coincident passive microwave and Visible/Infrared products are created automatically for the southern California region. The reader is encouraged to connect to the homepage address listed below and view the applications described in each section: http://www.nrlmry.navy.mil/test_htdocs/images_homepage.html. The user name is newbeta; the password is wxatsea.

* Corresponding Author: Thomas F. Lee, Marine Meteorology Division, Naval Research Laboratory, 7 Grace Hopper Avenue, Monterey CA 93943-5502, lee@nrlmry.navy.mil.

2. Applications

2.1 GOES Images: Until recently geostationary images were commonly viewed in sensor coordinates. Now, however, modern computational power allows the routine remapping of geostationary images for optimal viewing, eliminating the spatial stretching or compression of image features introduced by satellite viewing geometry. The correction is especially important for data near the edge of the geostationary scan, transforming views which are nearly useless into viable images.

This section supports a number of high-resolution stills and corresponding loops (refresh every 15 min) of the West Coast of the United States, especially of California. This capability is made possible by the resolution of the GOES visible channel (1 km at subpoint). Thus, it is possible to view the evolution of small-scale phenomena that have been difficult to study by traditional satellite methods, such as fog banks or smoke plumes. The loops are updated every half-hour, demonstrating that realtime looping capability need not be confined to dedicated workstations, but can be made available inexpensively to remote users of web technology.

2.2 GOES Images with Model Overlays: Within some product delivery systems, this type of image is available only every six to twelve hours, corresponding to the valid time of model output. However, this approach often does not allow the user to follow the evolution of weather systems through time. Thus, our approach has been to time-interpolate output from the Navy

Operational Global Atmospheric Prediction System (NOGAPS) to perform overlay of the latest image every hour. To ensure that such a capability can be available in real time, we interpolate between the most recent analysis and a short-term forecast to arrive at data valid at image time. Loop buttons in this section demonstrate the capability to view a model/satellite combination over time. The loops are educational tools to show users the evolving interrelation between satellite cloud bands and model features.

2.3 Cloud Forecasts: These are produced by the Cloud Advection Model, a procedure for combining the high resolution observing capabilities of the GOES-8 and -9 satellite with the scales of atmospheric systems capable of accurate prediction with global weather prediction models. It is based on the ability of the earth/atmosphere/ocean complex to organize the atmospheric pressure systems into waves of different sizes, i.e., by wavelength and amplitude. The manner in which this is accomplished is as follows: NOGAPS analysis and forecasts at 12-hour intervals are processed to produce fields of the long wave component of the middle tropospheric pressure pattern; these fields are linearly interpolated to 2-hour intervals corresponding to the cloud forecast period. The long wave translation currents derived from these interpolated fields are used to displace the cloud patterns as observed at the initial time to later position (time). The initial cloud image and the forecasts, in image format, are output at 2-hour time intervals for the time period of the forecast; this allows the sequence of images to be displayed in animation.

It was found that the speed derived from the long waves provided a reasonably accurate translation velocity for displacement of the cloud patterns, but the clouds exhibited an additional rotational motion. Therefore, a component of the short wave motion was applied to the cloud patterns; this is effected in the translating frame of reference. You will also note in the animation that the terrain features in cloud-free areas remain stationary. This is accomplished through the use of cloud-free terrain brightness and temperature images. These images are produced by mosaicing the brightness and temperature of pixels which are pre-determined to be free of cloud. During the production of the forecast images, each land pixel is tested to determine if the corresponding cloud top height (temperature) is below 10,000 feet. When this condition occurs, the visible and infrared pixels are replaced with the corresponding pixels from the cloud- free mosaic images. This process eliminates clouds below 10,000 feet over land areas from the forecast images. A variation of the procedure is also used to prevent fog and coastal stratus clouds over the ocean from moving inappropriately over the land.

Limitations: This is a very simple kinematic approach to producing cloud forecasts which has certain limitations. The Model does not currently contain mechanisms for generating or dissipating cloud elements. Over the ocean areas and for the time periods of these forecasts, this is not a severe limitation. There is usually enough moisture over the oceans to support the formation of clouds with all but the weakest short wave systems. A more obvious attribute is the inability of the Model to dissipate middle and high clouds in areas of descending motions; the Model moves these types of clouds downstream and can be noted in the forecasts long after they have evaporated in the actual atmosphere. Over land areas, the Model does not attempt to predict the occurrence of clouds that occur or develop below 10,000 feet but only treats clouds associated with dynamic processes relevant to the middle of the troposphere. Therefore, clouds related to such phenomena as surface heating, and mountain effects, etc. are not forecast.

2.4 Cloud and Water Vapor Winds: These winds (overview of concept in Nieman et al. 1997) are produced several times a day for several regions, based on data from three different geostationary satellites, GOES-8, GOES-9, and GMS-5.

The Cloud Motion Vectors (CMV) at 6-h intervals are generated from image-pairs of the water vapor and infrared channels for GOES-8 and GMS-5 and at 3-hour intervals from GOES-9 data. The vectors cover the latitude band from 15N to 52N for the following geographical areas: U.S. East Coast and Atlantic Ocean, U.S. West Coast and Pacific Ocean, and Hawaii and Pacific Ocean. The images used in the CMV derivation are mapped from the original scanline format into Mercator projection at a nominal resolution of 5km. A preprocessing function is applied to the infrared images to remove cloud-free pixels to preclude the tracking algorithm from deriving vectors associated with the motion of terrain features due to uncertainties in the image navigation.

The tracking algorithm used is a modification of Wilson's Sequential Similarity Detection Algorithm (SSDA) (Wilson 1984). This algorithm computes the minimum difference between the initial cloud patterns in a template and cloud patterns in comparable templates in search

areas of the second image of each pair. The I,J location of the template which has the minimum difference from the initial template defines the displacement of the pattern over the time interval between images and is converted into a CMV direction and speed. The initial template is moved by 16 pixels (80km) across the image and 16 lines (80km) down the image until all possible positions in the 1024 x 1024 image arrays have been processed. The initial template is a 16 x 16 pixel array; the search area is a 48 x 48 pixel array centered on the initial template. The initial template is expanded, dynamically, to a 32 x 32 array if certain quality control thresholds are not met.

The CMV altitude is assigned as follows: the coldest and the mean brightness temperature, and the variance in the initial template is computed. The temperature profiles at the CMV location is derived from the FNMOC NOGAPS analyses and 12-hour forecast temperature fields by linear interpolation in time and space to the time of the satellite image. The temperature profile is searched upwards and the CMV is assigned to the pressure height corresponding to the level at which the brightness temperature matches the NOGAPS forecast temperature. If this height is at a pressure greater than 650hpa, the height assignment is repeated using the mean brightness temperature.

The reliability of the CMV is assessed with a compound algorithm. The first step makes use of the spatial-coherence inherent in the cloud motions. The angle between the current vector and the previous vector is computed. If this angle is less than a specified threshold, the vector is accepted; otherwise, the size of the initial template is expanded to a 32 x 32 array and the vector derivation is repeated. If the angle exceeds the threshold for the second pass, the variance of the scene is tested against a specified threshold and is flagged if it exceeds that threshold. A vertical consistency test is then made of the speed of the CMV in comparison the first-guess. If the CMV speed corresponds to the first-guess speed within an altitude-dependent threshold and within 50hpa of the assigned CMV altitude, the vector is accepted; otherwise the vector is flagged as "questionable". A "gross-error" check is then performed; CMVs with directions which deviate by more than 90 degrees from the first-guess are flagged. A final test is then made comparing the direction of the flagged vectors to the surrounding CMVs, and if the direction agrees within a specified angle, the vector is accepted.

The accuracy of the resulting vectors is compared to radiosonde observations and to the NOGAPS analyzed/forecast winds within 50km and one hour of the CMVs. Standard errors on the order of 5mps or less are being achieved.

2.5 Experimental Daytime Reflection Product and Aircraft Icing Products: The 3.9 micron channel aboard the GOES satellites gives the opportunity see a variety of cloud phenomena, which can not be viewed using visible or infrared images (Allen et al. 1990; Kleespies 1995; Lee et al., 1997). For examples, ship tracks composed of cloud drops smaller than ambient cloud drops can be detected in stratus cloud decks. The products shown here from this technique removes the emitted portion of the daytime radiance at 3.9 micron, leaving pure solar reflectance. Such a correction improves the quality of the output for subsequent quantitative applications and forecaster needs.

This section also shows a view of potential aircraft icing over the western United States. The algorithms used make extensive use of the 3.9 micron channel aboard the GOES-9 satellite. To a large degree this channel, in multispectral combination with the other GOES imaging channels, can distinguish supercooled liquid water regions (the cause of aircraft icing) from cloud-free regions or regions covered by ice crystal clouds (Thompson et al. 1997). The product colors potential icing regions in red with a visible image background; unlike some products it does not mid-identify ground snowcover as cloud (and a potential icing threat) because the algorithm correctly distinguishes between snowcover, however cold, and actual cloud.

2.6 Special Sensor Microwave Imager (SSM/I) Products: We include several products from the DMSP SSM/I to illustrate its usefulness in the tactical environment. Although the SSM/I data have been employed significantly for research applications for about a decade, its use in the operational environment has not kept pace. In the application here we remap realtime SSM/I data into convenient viewing regions. We apply color and scaling appropriate to the various parameters being displayed, which include wind speed, integrated water vapor, and 85 Ghz. We also the show the corresponding visible and infrared image from the GOES-9 imager. Since data from three SSM/I sensors are available, the refresh time between passes is relatively small. This means that forecasters can watch the evolution of weather systems over time.

3. Conclusions: Perhaps the greatest strength of the demonstration of satellite applications over the Internet is the possibility of interactive feedback between developers and users. Thus, we invite the reader to contact us at the email address at the bottom of the first page with your comments, suggestions, or questions.

4. Acknowledgments: The support of the research sponsor, the Oceanographer of the Navy through the program office Space and Naval Systems Command, under program element 0603207N is gratefully acknowledged.

5. References:

Allen, R.C., Jr., P.A. Durkee, C.H. Wash, 1990: Snow/cloud discrimination with multispectral satellite measurements. *J. Appl. Meteor.*, 29, 994-1004.

Kleespies, T.J., 1995: The retrieval of marine stratiform cloud properties from multiple observations in the 3.9-μm window under conditions of varying solar illumination. *J. Appl.. Meteor.*, 34, 1512-1524.

Lee, Thomas F., F. Joseph Turk, and K. Richardson, 1997: Stratus and Fog Products using GOES 8/9 data. *Wea. Forecasting.*, 12, 664-677.

Nieman, Steven J., W. Paul Menzel, Christopher M. Hayden, Donald Gray, Steven T. Wanzong, Christopher S. Velden, and Jaime Daniels, 1997: Fully Automated Cloud-Drift Winds in NESDIS Operations. *Bull. Amer. Meteor. Soc.*, 78, 1121-1133.

Thompson, G., T.F. Lee, and R. Bullock, 1997: Using Satellite Data to Reduce Spatial Extent of Diagnosed Icing. *Wea. Forecasting.*, 12, 185-190.

Wilson, Gregory S., 1984: Automated Mesoscale Wind Fields Derived from GOES Satellite Imagery. AMS *Conference On Satellite/Remote Sensing and Applications*, Clearwater, FL, 164-171.

TARGET SCENE SIMULATIONS USING A HIGH-RESOLUTION ATMOSPHERE

Gregory A. Vayda* and Steven J. Lowe
Science Applications International Corporation
550 Camino El Estero, Suite 205
Monterey, CA 93940
Ph: 408-649-5242 Fax:408-649-8048

1) Introduction

State-of-the-art environmentally based tactical decision aids (TDA's) are having an increasingly significant impact upon effective warfare planning/execution in the modern battle space. Whether it be satellites, aircraft, land based vehicles, or surface/subsurface vessels; the ability to assess the potential environmental impacts on weapon systems and sensors is critical in the modern warfare arena. The insights gained via the use of a TDA can enhance mission effectiveness, crew safety, and resource conservation (fuel, ordnance, etc.).

This paper addresses the analysis and forecasting of the infrared (8-12 micrometer) radiance field around a ground based target (Figure 1), as seen by an approaching aircraft or missile. The surface depicted in Figure 1 is a contoured radiance field for a perfectly homogeneous atmosphere. The Target Scene Generator (TSG) is a TDA that is being developed to forecast and depict the three dimensional IR radiance field around a target, while fully incorporating the effects of a three dimensional heterogeneous atmosphere. The model is based on the physics of the Electro Optical Meteorological Decision Aid (EOMDA) algorithms, which computes lock-on and detection ranges in the IR, visual, and laser regimes for a vertically varying, but horizontally homogeneous atmosphere. Clearly, the real atmosphere is anything but homogeneous. The TSG is designed to incorporate high resolution mesoscale atmospheric model output, so that a fine scale spatial/temporal resolution scene can be developed to represent the desired radiance field. The EOMDA predicts the performance of air-to-ground weapon systems and direct view optics based on environmental and tactical information. Performance is expressed primarily in terms of maximum detection or lock-on range. It supports systems in three spectral bands: IR (8 - 12 micrometers); visible (0.4 - 0.9 micrometers); and laser (1.06 micrometers). For purposes of this paper, the discussion will be limited to the IR case.

The EOMDA consists of three basic modules: the Target Signature Model (TSM), the Atmospheric Transmission Model (ATM), and the Sensor Performance Model (SPM). The TSM uses environmental parameters (air temperature, pressure, relative humidity, wind speed/direction, and short/long wave radiation) to determine the thermal environment of the target and background. The target to background temperature contrast generated by the TSM is the source of the radiance signal that is transmitted to the sensor. The ATM uses environmental parameters (air temperature, pressure, relative humidity, wind speed, and cloud type/height) to develop extinction coefficients to decay the radia-

tion signal between the target and the sensor. The SPM determines the threshold radiance value for the specified sensor.

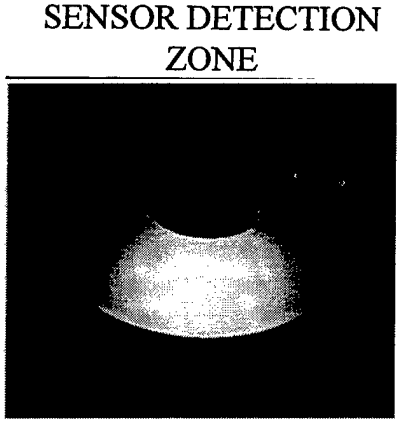

Figure 1

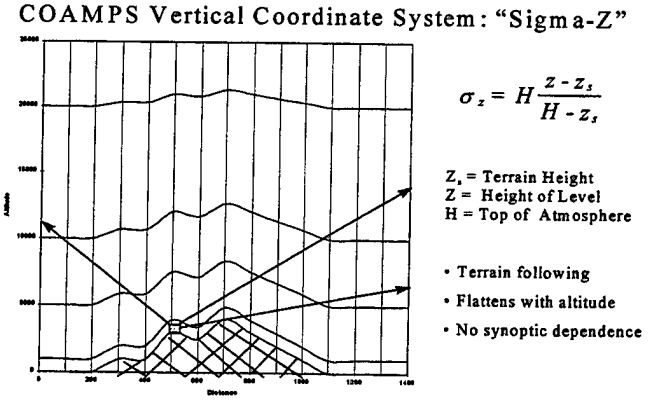

Figure 2

The EOMDA ATM module is a multilevel horizontally homogeneous model. Environmental data from a single upper-air sounding is used as the basis for computing ranges from the target. The EOMDA provides eight compass point values of range at the height of the approaching aircraft/missile. While the input sounding provides a realistic picture of the vertical structure of the atmosphere, it provides no information with regard to horizontal structure. The TSG improves on the ATM module by incorporating high resolution atmospheric data from the Coupled Oceanic and Atmospheric Predictions System (COAMPS), which is the navy's premiere mesoscale weather forecast model. Note that this allows the TSG to forecast sensor performance conditions, based on the COAMPS forecast.

2) Methodology

Due to the inherent resource requirements associated with three dimensional fields, the data integration was optimized by dividing COAMPS output into spatial and temporal components. The spatial data consists of all the geometry information for a specific region, (sigma-z levels, grid point spacing and terrain height) which is used to define the rectangular horizontal grid and sigma-z level vertical grid (Figure 2). The resultant matrix of dx/dy/dz volumes form the basis of the computational space. The slant path from the target to the sensor consists of a contiguous set of line-of-sight slant path vectors that slice through individual computational volumes. As long as the region and target location don't change, these parameters are computed only once and can be used for repeated simulations. The temporal data consists of standard meteorological parameters (pressure, temperature, humidity, mixing ratios, and wind vectors) that vary for each analysis/forecast of interest. This data is used to compute IR extinction coefficients (molecular, aerosol, precipitation, and cloud) which are stored at each COAMPS grid point (ie the vertices of each computational volume, Figure 3).

The extinction coefficient for a slant path vector is determined by doing a distance-weighted tri-linear interpolation of the extinction coefficients at the eight vertices of the volume to the mid-point of the slant path vector. The signal decay through each volume is governed by Lambert's (also known as Beer's) Law (equation 1), which attenuates the signal as an exponential decay function of the interpolated extinction coefficient and the slant path distance through the volume (Figure 4). Computing the signal decay through successive volumes, until the boundary of the study area or top of the atmosphere is reached, provides the signal strength as a function of radial distance from the target. However, since the radiance values are only computed where the vectors exit each volume, the resolution of the computed signal strength field is limited to the grid spacing.

The case studies presented in this paper use a horizontal grid spacing of 5 km. The COAMPS is capable of producing data at resolutions less than 1 km, however the exponential increase in computer resources for such a run would not be suitable for the operational environment.

$\chi = \chi_m + \chi_a + \chi_r + \chi_c$

$\chi_m = f(T,p,rh)$ $\chi_a = f(rh,W_s)$
$\chi_r = f(Q_r,T,p,rh)$ $\chi_c = f(Q_c, rh)$

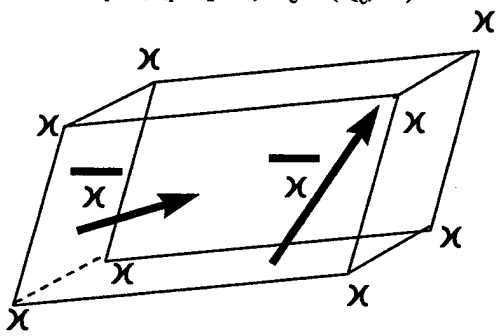

Figure 3

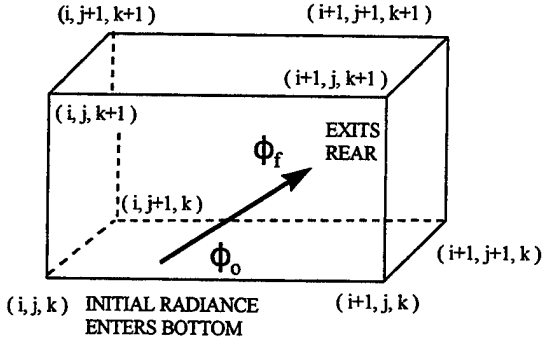

Figure 4

Equation (1) $\varphi_f = \varphi_o e^{-\chi r}$,

where:
φ_f - radiance value at the end of the slant path vector (w/m^2),
φ_o - radiance value at the beginning of the slant path vector (w/m^2),
χ - interpolated extinction coefficient (km^{-1}),
r - slant path distance (km).

Generation of a visual scene is the final product of the TSG. The resulting radiance field is used to render a 3-D visual image of the detection/lockon range around a target. The output from the main computation module, ir3, contains x, y, z position coordinates, relative to the target, and the radiance value at the end of each vector segment. A post processing program accesses the data output from ir3 and uses the positional and radiance data to do a logarithmic interpolation to the radiance value, required for lock-on for the specified sensor. The interpolation is required since the radiance values were only computed at the tips of each vector segment. The interpolation is logarithmic vice linear since

the radiance decays via an exponential decay function, Lambert's Law. The interpolated distances are put in a standard NURBS graphics format and rendered via the AVS graphics software. While AVS was used to render scenes for this report, other graphics software systems such as: VRML and VIS5D could also be used.

3) Extinction Coefficients

Four types of extinction coefficients are specific to the decay of a thermal IR signal: molecular, aerosol, precipitation, and cloud. The methodology employed for the computation of each type is described below.

3.1) Molecular

Molecular extinction is due to the state of the gas, which is a function of the temperature, pressure, and humidity. These variables are readily available from COAMPS. The specific waveband of interest is addressed via band models. The EOMDA develops coefficients for each vertical level, which are constant in the horizontal. Thus, the entire slant path, from the target to the sensor, is modeled with values that vary only in the vertical. The TSG takes advantage of the 3-D structure of the COAMPS fields to generate a matrix of extinction coefficients that vary in both the horizontal and vertical.

3.2) Aerosol

Aerosol extinction results from atmospheric particulates other than water, which are due to the distribution of ambient aerosol type, and are governed by wind speed and humidity. Aerosols are currently fixed for a variety of surface conditions: desert, urban, continental, maritime, etc.

3.3) Precipitation

Precipitation extinction is due to rain drops. The original EOTDA formulation provided a surface rain rate value at the target, from which extinction was computed. This value was applied to the entire slant path from the target to the sensor, allowing no variations in the horizontal or vertical. The TSG utilizes a formulation that uses the 3-D variables available from COAMPS. Marshall & Palmer (1948) provide a raindrop density distribution (equation 2), while Rutledge & Hobbs (1983) relate the slope of the distribution to the rain mixing ratio (equation 3). Due to the size range of the raindrop distribution (0.5mm to 5 mm) and the IR band (8 to 12 μm), the cross section for extinction can be approximated by the physical area of a raindrop (equation 4). Putting equation 2 into the differential form, combining with the cross section and integrating over the raindrop size range yields an expression (equation 5) for the extinction coefficient in terms of the parameters available from COAMPS.

Equation 2: $$N_D = N_o e^{-\lambda x},$$

where: N_D - raindrop number density per drop size (m^{-4}),
N_o - distribution coefficient (m^{-4}), 8×10^6
λ - slope of the density distribution (m^{-1}),
x - raindrop diameter (m).

Equation 3: $$\lambda = [(\Pi \varrho_l N_o)/(\varrho_a Q_r)]^{1/4},$$

where: ϱ_l - density of the raindrop (kg m^{-3}),
ϱ_a - density of the air (kg m^{-3}),
Q_r - rain mixing ratio (kg kg^{-1}).

Equation 4: $$\sigma = \Pi x^2/4$$

where: σ - cross-sectional area of raindrop (m^2)

Equation 5: $$\chi_p = \Pi/(2\lambda) N_o e^{-\lambda x}[-x^2/2 - x/\lambda - 1/\lambda^2]\Big\}_{x_1}^{x_2},$$

where: χ_p - extinction coefficient (m^{-1}),
x_2 - upper size limit of raindrop size, 0.005 m,
x_1 - lower size limit of raindrop size, 0.0005 m.

Note that equation 5 was obtained by integrating over the assumed raindrop size range of 0.5 mm to 5 mm.

3.4 Cloud

Cloud extinction results from condensed water around aerosol nuclei, which is not strictly an aerosol or water droplet case (as in the raindrop precipitation extinction). Clouds are highly attenuative and have a significant effect on the IR ranges. Comparisons between satellite clouds fields and the cloud mixing ratio fields from COAMPS indicate a mixing ratio of 10^{-4} kg/kg (Q_{ct}) (R. Wade, personal communication) as a realistic threshold value for indicating cloud presence. The EOMDA assumes that if a cloud field is present, the entire area is completely overcast, which is acceptable when no horizontal variation is permitted. However, by taking advantage of the discrete cloud data from COAMPS, a realistic cloud field can be modeled that allows discrete clouds. The army's Vertical Structure Algorithm (VSA) uses a geometrically based exponential function from the ground to the cloud base to approximate the extinction as a function of altitude, assuming a value of 7 km^{-1} as the extinction value at the cloud base. Then, using a relationship between extinction and relative humidity, they derive a relative humidity profile from the surface to the cloud base, which is an unrealistically smooth monotonic function. The VSA does not allow for non-monotonic variations in relative humidity or extinction coefficient from the ground to the cloud base. Reorganizing the VSA relationships yield an expression (equation 6) for the extinction coefficient as a function of relative humidity.

Equation 6: $$\chi_c = e^{[(RH-b)/a]},$$

where: χ_c - cloud extinction coefficient (km^{-1}),
RH - relative humidity (%),
a = $(100-RH_s)/\ln(7/d)$,
RH_s - surface relative humidity (%),
d = 3.912/vis - 0.012
vis - surface visibility (km)

$$b = 100 - a \ln(7).$$

Using Q_{ct} to establish cloud existence, the relative humidity is then used to compute the extinction coefficient. The uncertainty lies in the value of the surface visibility, which is currently user defined for various types of conditions.

4) Target Surface Parameters

Several of the parameters required by the TSM are the same as those used for the transmission computations: air temperature, pressure, and relative humidity. However, in conjunction with wind speed/direction and atmospheric long wave radiation, they are used to determine the temperature of the target by addressing the heat exchange with the environment. The added complication of solar heating of the target makes it necessary to consider the short wave energy. COAMPS provides all the needed parameters, with the exception of the direct (directional or beam) solar irradiance. The beam solar irradiance is determined by using the geometry module in reverse. Instead of extinction from the target outward, the signal gets attenuated from outside the atmosphere to the target. Since the visual part of the spectrum (0.55 micrometers) responds to Rayleigh scattering, a small module was developed to compute the visual extinction coefficients for the incoming radiation. Due to the highly attenuative nature of cloud fields, the incoming beam solar was attenuated with the same algorithm as the IR signal in the clouds. Computationally, computing the beam solar is much cheaper than computing the target decay for "n" radial line-of-sight vectors, since there is only one incoming line-of-sight for each analysis/forecast time. Comparison with the EOMDA beam solar values for a cloudless sky reveal that the EOMDA surface values are substantially higher (on the order of 100 to 200 w/m^2) than the TSG values. Due to the fine scale nature of the TSG computations and the absence of horizontal cloud structure in the EOMDA algorithm, the TSG predictions are favored over the EOMDA.

In conjunction with the parameters needed to determine the target temperature, the background temperature is also required to produce the required temperature contrast. COAMPS supplies a ground temperature value which is used for the background temperature. The original EOMDA has several background types available (concrete, asphalt, vegetation, soil, etc.) which used the same environmental parameters as the target to determine the background temperature. The TSG uses the COAMPS ground temperature for the background temperature.

5) Time Dependence

The TSG is currently a steady-state model. Thus, whatever parameters are applied, the model assumes those parameters are constant throughout time. This affects only the target, since the COAMPS ground temperature (fully time dependent) is being used for the background temperature. However, since the target/background contrast is the parameter of interest, the radiance values are affected. By comparison, the EOMDA is partially time dependent since it extrapolates backward in time to establish a thermal history for the target and background to account for the thermal impedance. Therefore, direct comparison between the EOMDA and TSG radiance fields are not possible at this time. It is

highly desired to improve the TSG by incorporating COAMPS data prior to the study date in order to establish the thermal history of the target. It should be noted that while EOMDA extrapolates the solar conditions backward in time, it does not vary the atmospheric parameters (temperature, pressure, humidity, etc) prior to the starting time of the run. Thus, by incorporating the solar and atmospheric time history into the TSG, it has the potential to become a superior tool.

6) Case Study

In order to demonstrate the lock-on-range (LOR) variability due to a non-homogeneous atmosphere, a case study east of the Mediterranean Sea is examined. The lower left corner of the study area is anchored at 38.86N 26.27E, extending north and east 150 kilometers, with the target placed slightly southeast of the center of the grid at 39.32N 27.31E. A 31 x 31 horizontal grid with 5-kilometer spacing was used for this study. Six COAMPS forecasts were made verifying at 04z, 08z, 12z, 16z, 20z, and 24z from an analysis at 1997080700. The forecast model predicts cloudless skies within the LOR of the target for 04z to 20z periods. However, at 24z a low cloud layer approaches from the east. We next examine how the radiance fields vary spatially and temporally.

The radiance fields output from the TSG are a composite of effects from both variations in the atmospheric state and the thermal state of the target and background. In order to isolate the atmospheric effects, the TSM is bypassed and the target/background contrast is set to a constant value of 10K° (CCT). Figure 5 depicts the LOR for a missile as a function of elevation angle for various forecast periods, for an approach from the east. The elevation angle was limited to 15 degrees so that the signal was confined to within the limits of the study area. The τ=24 case shows diminished ranges for low elevation angles due to the approach of the cloud field. Once the line-of-sight vector is raised above a few degrees the ranges are on the order of the other forecast periods. Note that the spread in ranges for the various forecast periods is attributable to diurnal heating effects. At τ=00 (~01L) the ranges are rather extended due to cool evening air. As time wears on, the atmosphere heats and the ranges decrease with increasing temperature. By τ=20, the sun has set and the cooling trend once again increases the range.

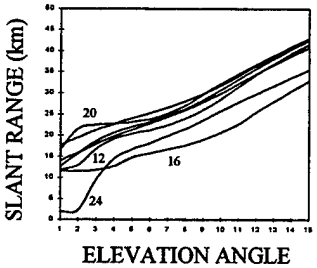

Figure 5

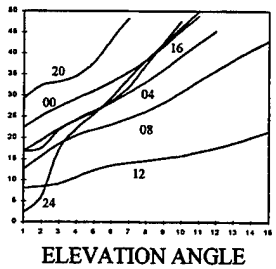

Figure 6

The same forecast periods and viewing angle is depicted in Figure 6, but with the TSM turned on, thereby showing the combined effects of varying the thermal signal and the atmospheric conditions. With the addition of the TSM response, the ranges extend significantly due to the increased target/temperature contrast for most of the forecast periods. However, the linear behavior as a function of increasing time is disrupted. Now τ=16 has the same influence as τ=04, which is contrary to the diurnal pattern.

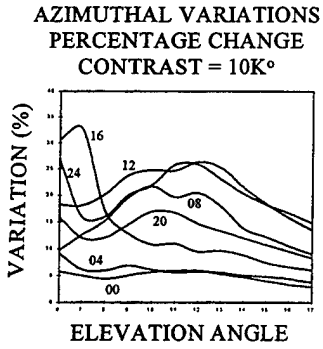

Figure 7

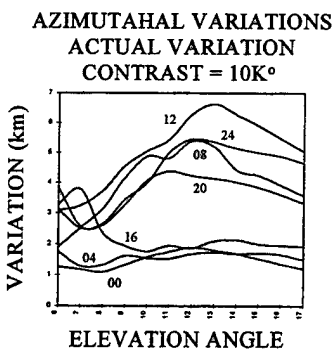

Figure 8

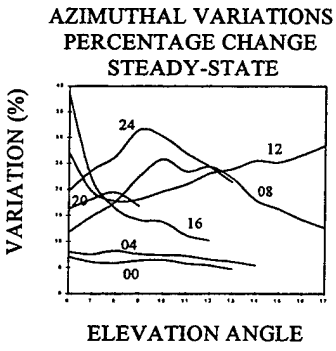

Figure 9

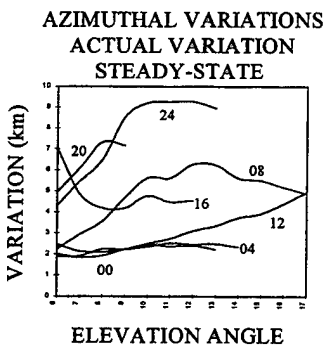

Figure 10

Thus, in some instances the solar influence may enhance the ranges associated with atmospheric conditions or it may make atmospheric influences retarded. Returning to the CCT, we now focus on the horizontal range variations as a function of elevation. Previously, Figures 5 and 6 showed the slant range variation as a function of elevation for a fixed azimuth. Figure 7 depicts the percentage difference of azimuthal range variations as a function of elevation for the CCT case. At each elevation all the azimuths are searched for the maximum and minimum ranges, which are used to compute percentage difference. Note that in Figure 7, the minimum elevation angle is set high enough to eliminate the cloud effects, so that the observed variations are due only to clear air variations in the meteorological parameters. The amount of range variation is extremely significant. The τ=16 and τ=20 forecast show marked asymmetry in the radiance field for low angles, while the τ=08, τ=12, and τ=20 forecasts show high levels of asymmetry between 8 and 13 degrees of elevation. Figure 8 shows the min/max slant range differences as a function of elevation angle for the various forecast periods. For periods τ=08, 12, 20, and 24, the difference in range exceeds 4 km, reaching as high as 6.5km at τ=12

and 13 degree elevation, which is tactically significant. It is apparent form Figure 9 that reintroducing thermal heating/cooling of the target alters the asymmetry profiles. In contrast to the CCT case (Figure 8), in certain instances, namely τ=16, the variation at low angle is highly enhanced, while at τ=24 the peak is shifted to a slightly lower angle, but loosing some variation at the 6 degree level. At τ=12 an inverse effect is noted, whereby a minimum is noted at approximately 8.5 degrees and continuing to increase thereafter. Figure 10 provides a comparison of the actual differences in range values vice the percentages (Figure 9). When compared with the CCT (Figure 8) it is apparent that the introduction of a varying target/background temperature contrast greatly enhances the azimuthal range variability. Forecast periods τ=08, 16, 20, and 24 show variability greater than 5km, reaching greater than 9 km. Figure 11 represents a time series of scenes for the indicated forecast periods. The orientation is such that the observer is standing to the south of the target looking north. The horizontal and vertical extent, as well as the curvature of the contoured surfaces, vary due to the varying source strength (target/background contrast) and the atmospheric conditions. At τ=24 hours the aforementioned low layer of clouds encroaches from the east and reduces the ranges at low elevation. While Figure 11 provides an excellent representation of the change in vertical profile of the surface, the top-view aspect represented by Figure 12 presents a good depiction of the horizontal evolution in range as a function of time.

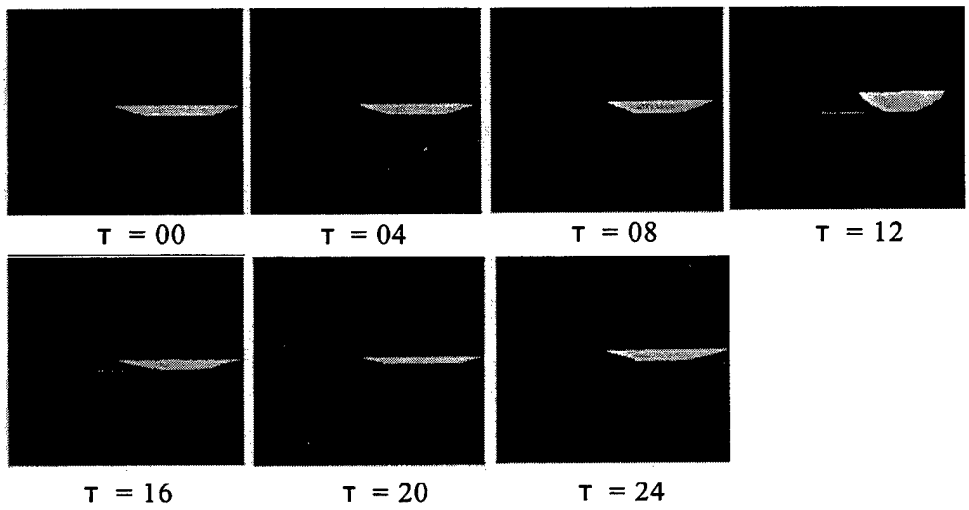

Figure 11

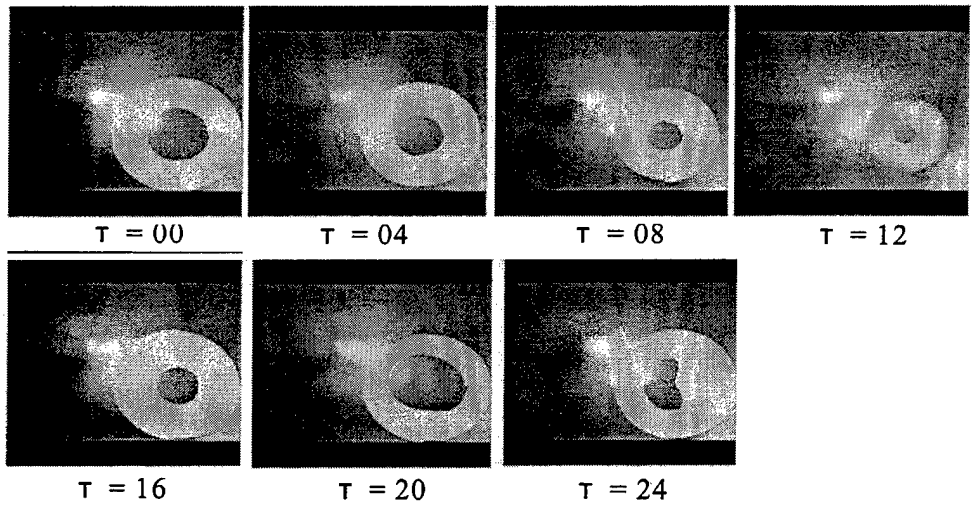

Figure 12

7) Summary and Conclusions

The TSG is a TDA being developed that combines the best aspects of the EOMDA with the fine-scale atmospheric structure provided by COAMPS. Techniques were developed to infuse large quantities of atmospheric model output data into the ATM portion of the EOMDA, which required the development of a sophisticated geometry software package, as well as robust methods of handling data conversion and derivation. A new physics model for IR extinction in precipitation was developed. Graphical techniques were employed to display contoured surfaces of radiance from a target, as seen by an approaching aircraft. The results confirm that horizontal variations in the state of the atmosphere dramatically affect the IR LOR that would be observed by an aircraft.

8) Future Work

While the TSG has shown excellent progress toward enhancing the arsenal of TDA's, future work will be required to make it an effective training and operational planning tool. In the short term, the TSG now contains a steady-state thermal model of the target, which needs to be made fully transient. An algorithm needs to be developed to incorporate variable visibility at the surface. A final graphics software tool needs to be selected. In the long term, multiple types of parameter surfaces should be displayed around a single target, as well as several targets being displayed in the scene. For instance, in addition to the IR LOR surface, currently done, a contoured RPO surface could be added so that the aircraft would not only be able to see where the maximum IR range would be, but also the areas where aircraft detection would occur. These combined offensive and defensive depictions would be a very effective tool for operational decision makers.

9) References

Marshall, J.S. and W.M. Palmer, 1948: "The distribution of raindrops with size", JOURNAL OF METEOROLOGY, Volume 5, August 1948, 165-166.

Rutledge, S.A. and P.V. Hobbs, 1983: "The Mesoscale and Microscale Structure and Organization of Clouds and Precipitation in Midlatitude Cyclones. VIII: A Model for the Seeder-Feeder Process in Warm Frontal Rainbands", JOURNAL OF THE ATMOSPHERIC SCIENCES, Volume 40, May 1983, 1185-1206.

AN ATMOSPHERIC PROPAGATION MODEL FOR THE 200 TO 700 NANOMETER SPECTRAL REGION

James B. Gillespie*
U.S. Army Research Laboratory
AMSRL-IS-EE
Adelphi, MD
Edward M. Patterson
Georgia Institute of Technology
Atlanta, GA

Abstract

UVTRAN is an atmospheric propagation and lidar model that has been developed by the Army Research Laboratory for transmission in the 200 to 700 nanometer spectral region. This model has recently been upgraded. These new upgrades consist of the addition of several of the Lowtran aerosol models, inclusion of multiple scattering, and the ability to change the field of view. The code is written in Fortran and a PC version that has a Visual Basic interface is available for use under Microsoft Windows. Computational comparisons are made with other models and examples of the graphical output are given. UVTRAN includes gaseous absorption from ozone and oxygen as well as several trace gases. A standard atmosphere is built in; however the user can override these values. Horizontal, vertical, and slant paths are available for path lengths up to 11 km. The model also includes user-changeable default parameters

Previous UVTRAN Capabilities

UVTRAN (UltraViolet atmospheric TRANsmission) was developed in 1988 as a simple to use program for calculating visible and ultraviolet (UV) transmission at low and high resolution, as well as the lidar return from both Mie and Fluorescent lidar systems. Attenuation in the model included atmospheric molecular scattering and absorption and aerosol scattering and absorption. Gaseous absorbers included SO_2, H_2O, NO_2, N_2O

The program was designed for use for wavelengths shorter than 700 nm. at relatively short ranges. Consequently, band models of gaseous absorption were not used and calculations of attenuation were done using a simple Beer-Lambert attenuation model. because of the requirement for short ranges, a plane parallel atmosphere was assumed. The model provided for calculations of atmospheric transmission between 200 and 700 nm., for multiple ranges and elevation angles. Atmospheric parameters in the model included a standard atmosphere density profile, the ability to input a full profile variation for ozone, the ability to input an overall concentration variation for the absorbing molecules.

Aerosol effects were parameterized in terms of visibility at the surface, an exponential variation of attenuation with height, and a wavelength variation given by the Koschmeider relation

$$\sigma_{aer}(\lambda) = \left[\frac{3.912}{V} - \sigma_{mol}(550)\right] * \left[\frac{\lambda}{550}\right]^{-q}$$

with σ_{aer} the aerosol attenuation at a wavelength λ, σ_{mol} the attenuation due to molecular scattering at 550 nm, and V the visual range at 550 nm. q is empirically related to the visual range by the equation

$q = .589 * V^{1/3}$ if $V < 24$ km

and

$q = 1.7$ if $V > 24$ km.

Low resolution transmission could be calculated for multiple wavelengths between 200 and 700 nm with linearly or logarithmically spaced intervals. High resolution transmissions could be made for one of several specific wavelengths. The wavelengths available were the Nd:YAG wavelengths of 266, 355, and 532, and the Excimer wavelengths of 248, 308, and 351. The gaseous attenuation was appropriate for the specific laser wavelength.

Lidar return calculations could be made for either an aerosol lidar or a fluorescence lidar at the same excimer or Nd:YAG laser wavelengths as the high resolution transmission calculations. The two way transmission from the lidar system to the scattering volume is calculated using the UVTRAN transmission module. The aerosol lidar module had the capability for the input of a scattering return profile as well as standard atmospheric profiles. The fluorescence lidar module had the capability of input of fluorescing material concentrations for aerosols or gases and fluorescence efficiencies as a function of wavelength shift with output as a function of the wavelength shift due to fluorescence.

Overall output included text file output and graphical output with user choice for all output options.

Limitations of previous UVTRAN model

There were several limitations to the earlier version of UVTRAN. Aerosol profiles could only be input using the exponential profile discussed above; wavelength effects could be incorporated only with the Koschmeider relation. In particular, there was no ability to tie the aerosol models to the standard LOWTRAN aerosol models incorporated into LOWTRAN and MODTRAN codes.

Additionally, for the transmission calculation mode, there was no capability for calculating any quantity except for the direct transmission. At UV wavelengths, light

scattered by the atmosphere can be a significant contributor to the total signal received by a wide field of view instrument; knowledge of these effects is important to the system designer.

A representation of the effect of increasing field of view (fov) on a received signal is shown in Figure 1.

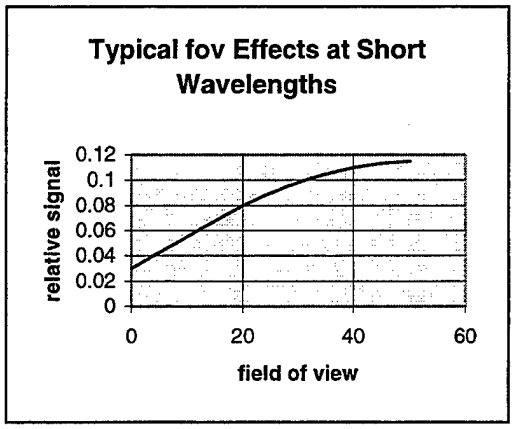

Figure 1. Effect of changing sensor field of view on received signal

The signal at 0° field of view is the directly transmitted signal, while the increase of signal with increasing field of view is due to the effects of atmospheric scattering. These effects were not included in the original UVTRAN.

Also for calculations that include the effects of increases in the field of view, the output of total irradiances onto the sensor are a natural and useful output, one that was not available to the original UVTRAN.

Modifications to UVTRAN

In order to address these limitations, an upgrade of UVTRAN was undertaken. This upgrade included

Modification to expand aerosol and atmospheric profile options and to add the capability to include LOWTRAN aerosol wavelength and profile models of aerosols

Addition of radiance calculation capability

Additional of an option, the full scattering calculation option, to include the effects of atmospheric scattering on received signal

Modification of the graphical user interface.

The major complexity lies in the addition of the code to include radiance and atmospheric scattering effects. There are many cases in which the scattering effects can not be described by a single scattering formalism, that is one in which each photon is scattered no more than once along the path from source to sensor; multiple scattering effects must be included. this need to include multiple scattering effects leads to increased complexity in the calculations.

Standard radiative transfer routines such as the multiple scattering routine in MODTRAN are not appropriate for the source sensor paths of interest in UVTRAN because the MODTRAN routine is designed to model the effects of solar scattering and so is not appropriate for source-sensor paths in which the source is near the sensor and the jpaths are near horizontal. Full Monte Carlo or successive orders of scattering routines are not appropriate because such codes are too time consuming for routine analysis.

In the modified UVTRAN currently being developed, we have adopted a formalism developed by SciTec (Princeton, NJ) for their off axis scattering intensity code (OSIC). This formalism is a single scattering formalism with modification of scattering parameters to mimic the effects of multiple scattering. The output of the module is the irradiance onto the sensor

The scattering geometry of the full scattering module is shown in Figure 2

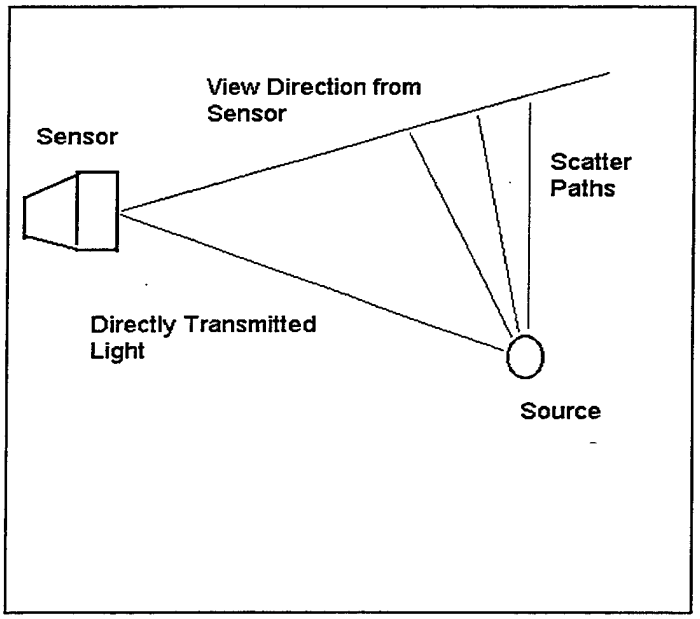

Figure 2. Scattering calculation geometry

The sensor is assumed to have a circular field of view and a view direction. The light reaching the sensor by direct transmission along the source-sensor path is calculated, and

the scattered light is calculated by a dual summation of scattering volumes along a view direction for a series of view directions that fill the space in the field of view of the sensor. For each of the scattering elements defined along each view direction, the contribution to the light received by the sensor from each scattering volume is calculated as the product of the light transmitted to the scattering volume from the source, the light scattered from within the scattering volume in the direction of the sensor, and the light transmitted from the scattering volume to the sensor.

The parameters in this single scattering formalism are modified to mimic the effects of multiple scattering. The specific changes are in the scattering attenuation terms affecting the transmission between source and scattering volume and between scattering volume and sensor and the scattering term in the scattering volume. Specifically the attenuation terms due to molecular and aerosol scattering are modified to account for the fact that some of light scattered from the path is returned to the path by second and higher orders of scattering and the phase function determining the angular scattering magnitudes is modified to approach a uniform phase function with increasing optical depth along the source to scattering volume path. The exponential attenuation term change can be written

$$\exp(-k_{scat} * r) \rightarrow \exp(-k'_{scat} * r) \text{ with } k' < k.$$

The parameterization of the modifications is based on empirical data.

In general, there is a significant expansion of the input requirements to specify the source and sensor characteristics and orientations for the full scattering radiance calculations.

Graphical User Interface Screens --Overview

The user interface has been designed to mimic the Wizard format of Windows 95 with a series of panels that are presented to perform the entry of parameters controlling the calculation. There are currently 10 panels shown by the list in Table I. The name of the active panel is darkened; the others are dimmed. The order of entry of the data is given by the order of the panels. Each panel has a series of default settings. Transition between panels is by means of a back or a next button , which is enabled or disabled, as appropriate. The calculate button is enabled when sufficient information has been entered to allow the calculation.

A list of the panels an a short description of each are shown in Table I

Table I

Panel Name	Description
Calculation type	Selects type of calculation
Wavelengths	Selects number and values of wavelengths
Atmosphere	Selects overall atmospheric model for calculation
Trace gas levels	Selects atmospheric concentrations of trace gases included in model
Aerosol characteristics	Selects wavelength characteristics of the aerosol based on LOWTRAN or other models
Aerosol profile	Selects aerosol altitude profile from LOWTRAN models
Aerosol phase functions	Selects appropriate phase function from LOWTRAN models or others
Geometry	Selects geometry for calculation
Sensor characteristics	Selects sensor characteristics
Source characteristics	Selects source characteristics

Panel Descriptions

The Calculation Type panel is shown in Figure 3. The user is given the option of six types of calculations: low resolution transmission, the standard calculation; high resolution transmission, for calculation laser wavelength transmission; irradiance due to direct transmission from a source; irradiance due to direct transmission and atmospheric scattered light; lidar return for a Mie lidar; and lidar return for a fluorescent lidar. Different versions of the succeeding panels will be enabled based on the choice of type of calculation.

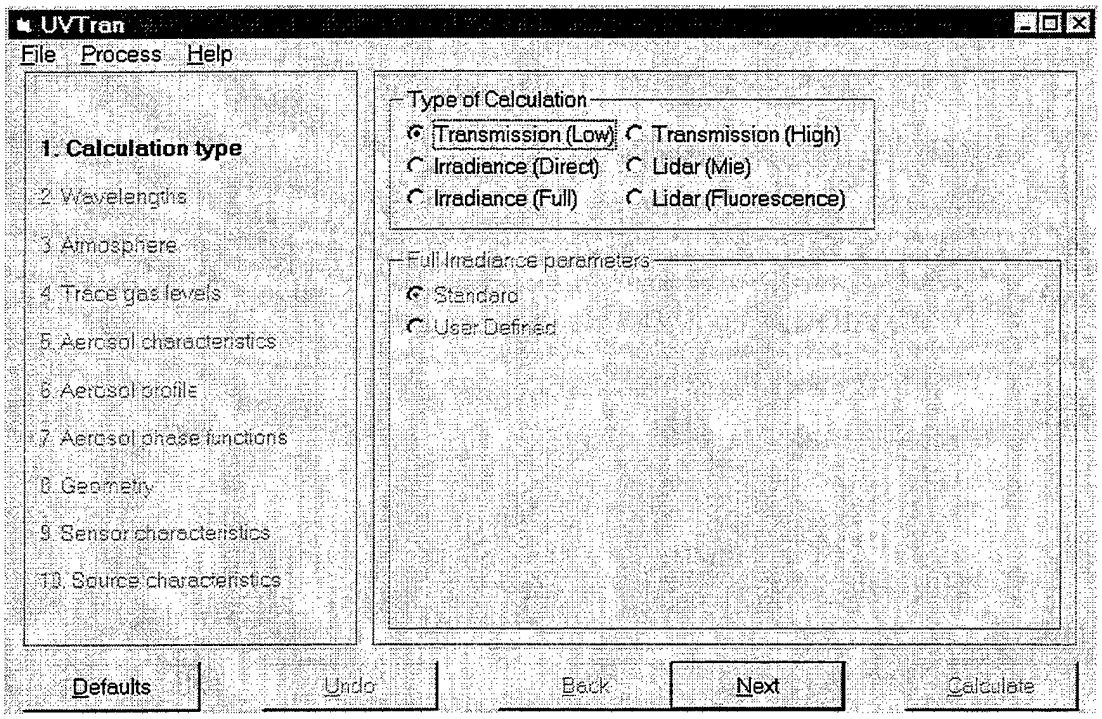

Figure 3. Calculation Type Panel

The Wavelengths panel for the low transmission and irradiance options is shown in Figure 3. There are three basic choices for the definition of wavelengths: wavelengths with equally spaced log intervals, wavelengths with equally spaced linear intervals, and a set of user defined wavelengths. The choice for wavelength definition is entered on the upper panel, and this choice determines the appearance of the lower panel. If either log or linear intervals are chosen, the user is asked to enter the number of wavelengths and the values for upper and lower limits. If the user defined option is chosen the user enters the number of wavelengths and panels for entering the wavelengths are presented. The Wavelengths panel for the high resolution transmission and the lidar options, shown in Figure 4 allow the user to choose one of a number of specific wavelengths associated with an individual laser type.

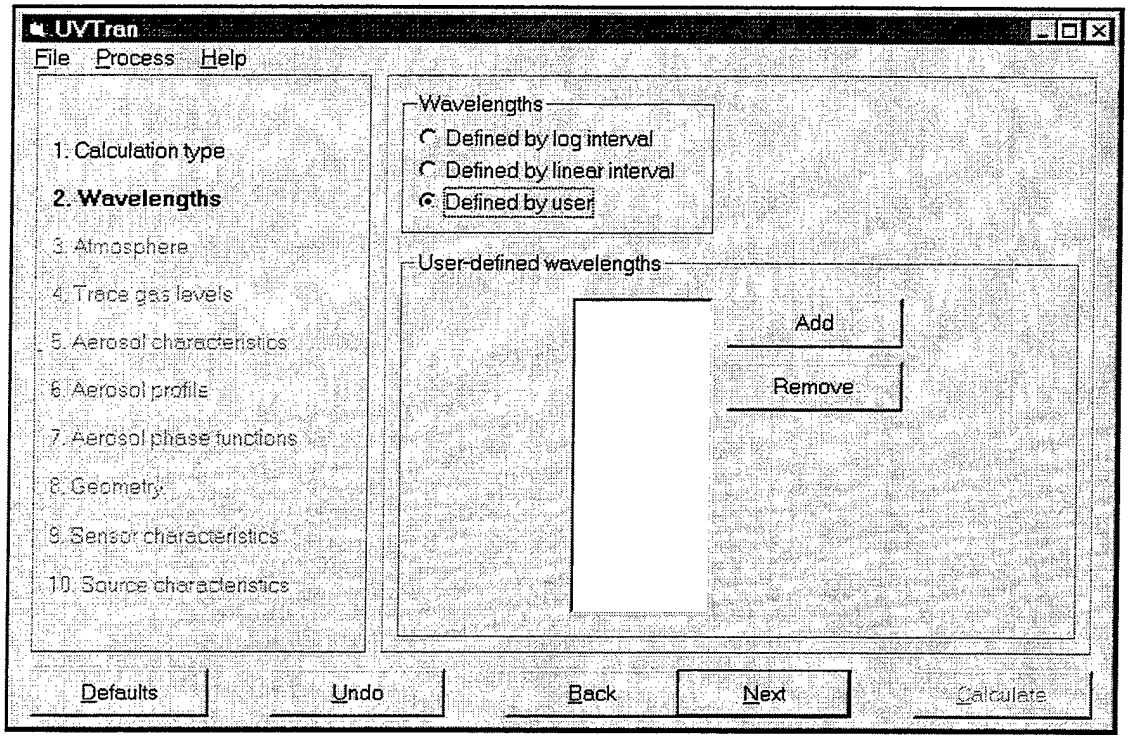

Figure 3. Wavelength Selection Panel for low resolution transmission

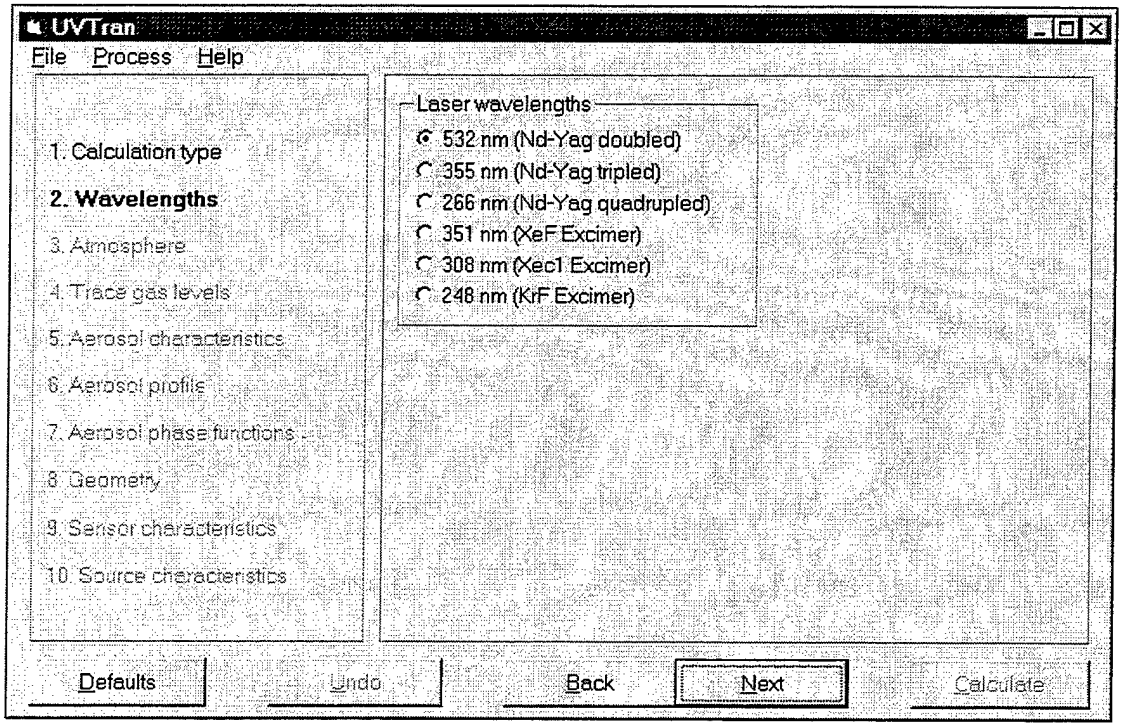

Figure 4. Wavelength Selection Panel for high resolution transmission

The Atmosphere panel, shown in Figure 5 allows the user to choose from four LOWTRAN atmospheric profiles and to enter a surface altitude and a surface temperature. Surface altitudes different from sea level or surface temperatures different from those of the standard atmosphere will modify the profiles. Altitudes different from sea level will result in a redefinition of the heights of the lowest levels of the atmosphere; temperatures different from the nominal will be blended into the profile over the lowest levels.

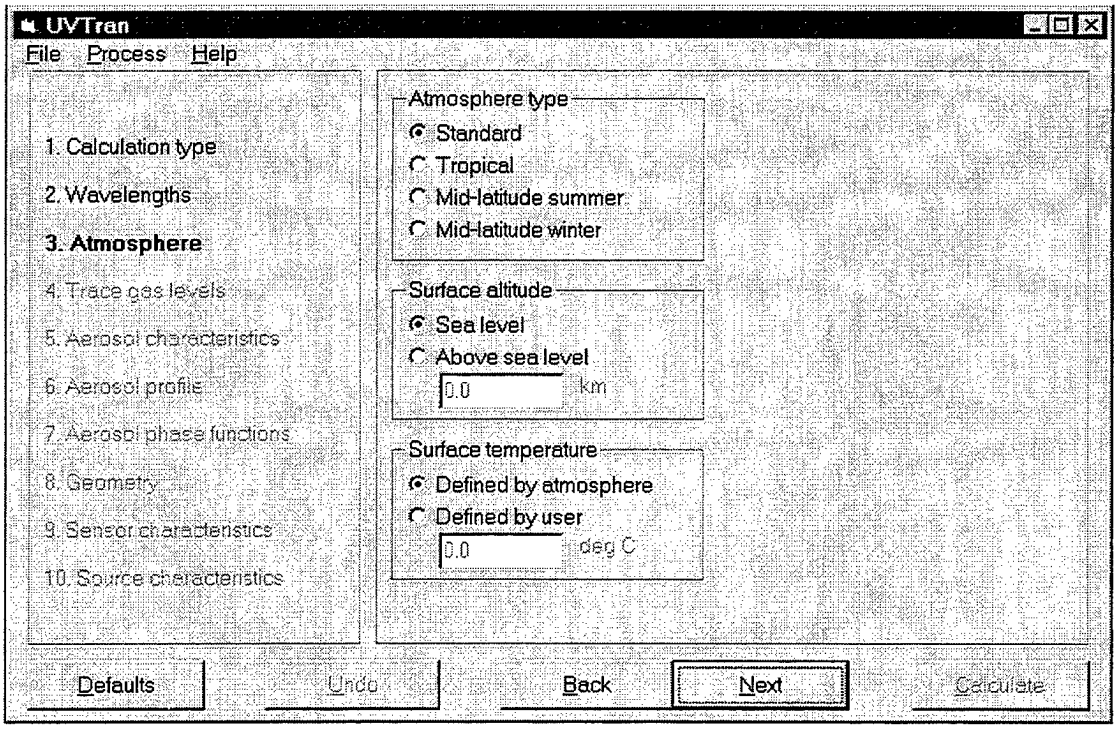

Figure 5. Atmosphere Panel

The Trace Gas Levels panel allows the user to accept default levels for the trace gases included in the model or to vary gas concentrations as desired. the water vapor concentration can be entered in terms of mixing ratio, relative humidity, or dew point.

The Aerosol Characteristics panel is shown in Figure 6. This panel is set up to input aerosol characteristics defining the wavelength behavior and the single scatter albedo both within the boundary layer and above the boundary layer. Additionally the surface visibility and the height of the boundary layer can be specified. Wavelength dependence can be specified as one of the standard LOWTRAN aerosol models, as the Koschmeider relation in UVTRAN 3.1, or as an aerosol that has a uniform extinction with wavelength. Visibility can be specified as one of a standard visibility or as a user defined visibility. It should be noted that the visibility should be input as meteorological ranges rather than observed visibility.

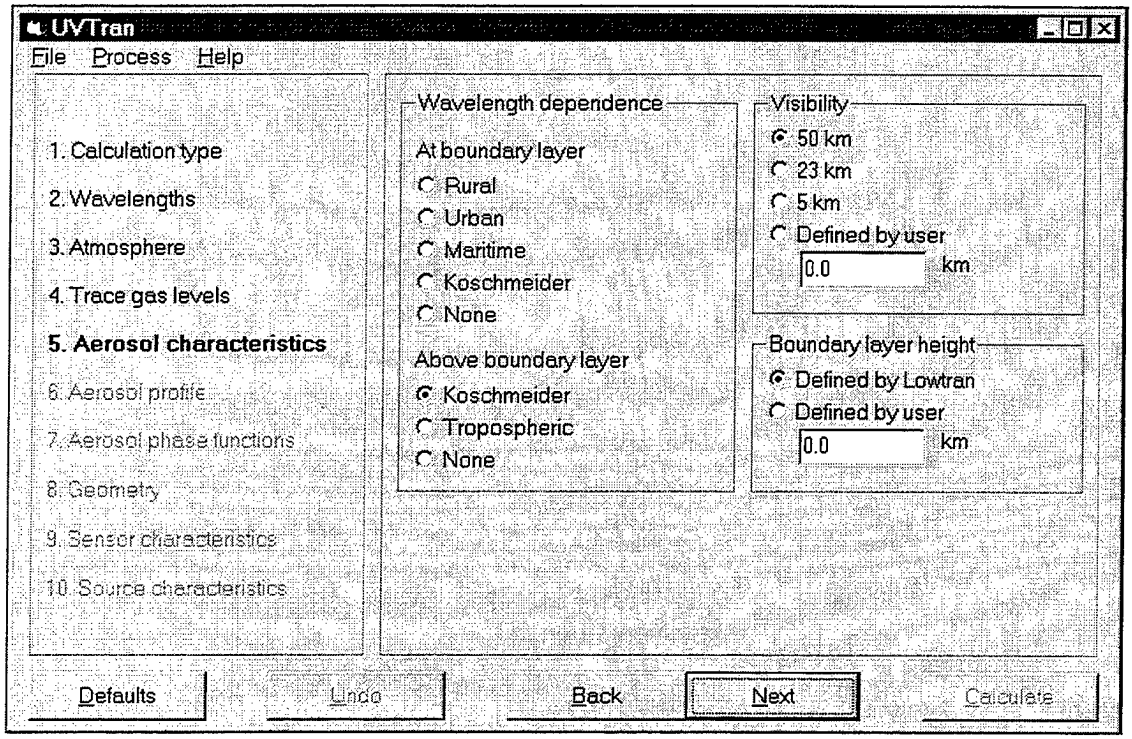

Figure 6. Aerosol Characteristics Panel

The aerosol profile in both boundary layer and above boundary layer can be described with the Aerosol Profile panel, shown in Figure 7. The user can select either of two LOWTRAN profiles, an aerosol that is constant with altitude or with an exponential increase or decrease. If the LOWTRAN profiles are chosen, the boundary layer behavior is determined by the aerosol characteristics determined on the preceding panel. The following aerosol panel, not shown, allows the user to choose default phase functions for the different levels.

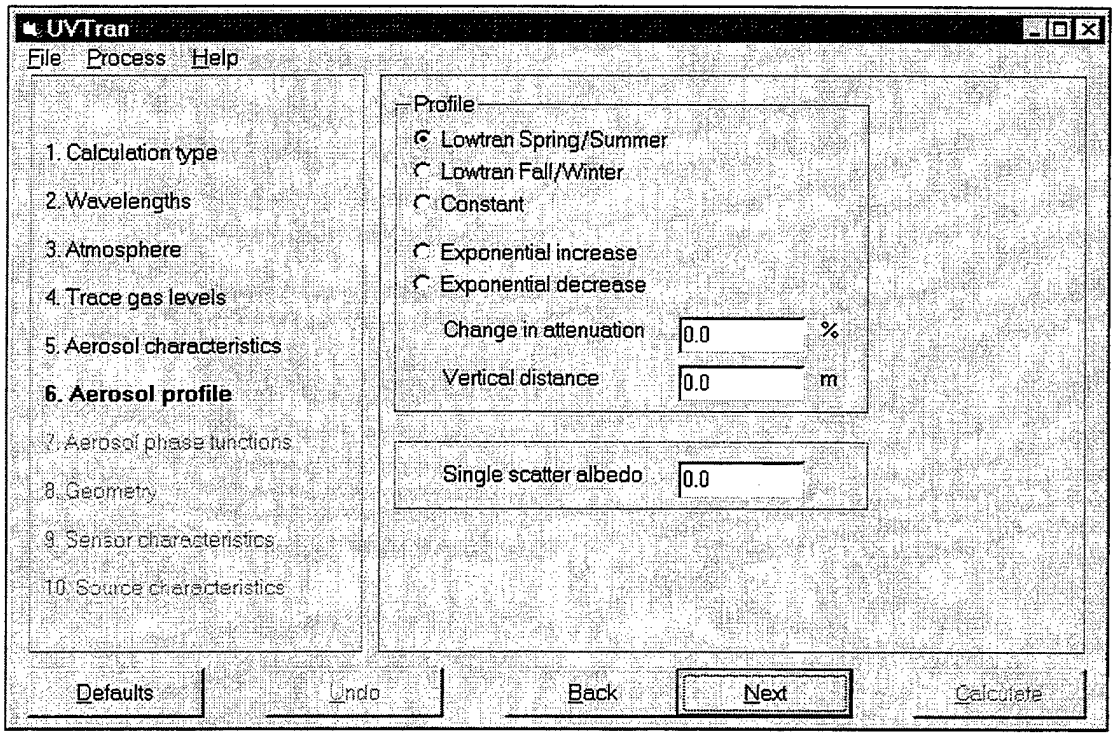

Figure 7. Aerosol Profile Panel

The geometry panel, Figure 8, offers options on choosing the position and orientation of sensor and source. The sensor is assigned a position at the origin of the x and y axes with an altitude determined by the user. Three options are available for path type, definition of range and elevation angle, definition of altitude and elevation angle, and definition of source position with path parameters calculated for source and sensor position. the path to source block for the range/elevation angle choice is shown in the figure. Additionally, the alignment of the source and sensor can be specified as aligned or with separate definitions for source and sensor.

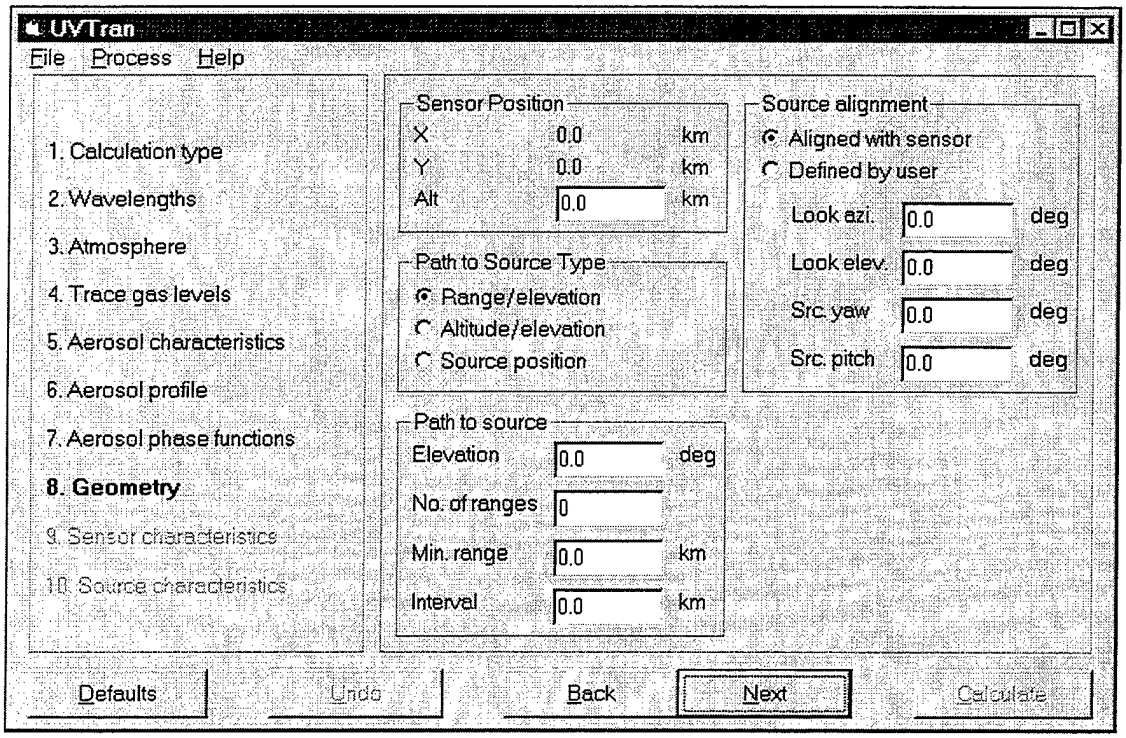

Figure 8. Geometry Panel

The Source Characteristic panel is shown in Figure 9. Each of the last two panels allows for the input of sensor or source characteristics needed for incorporation of specific characteristics. The source panel is the last in the sequence and the calculate button is enabled when this panel is completed so that calculations can be made.

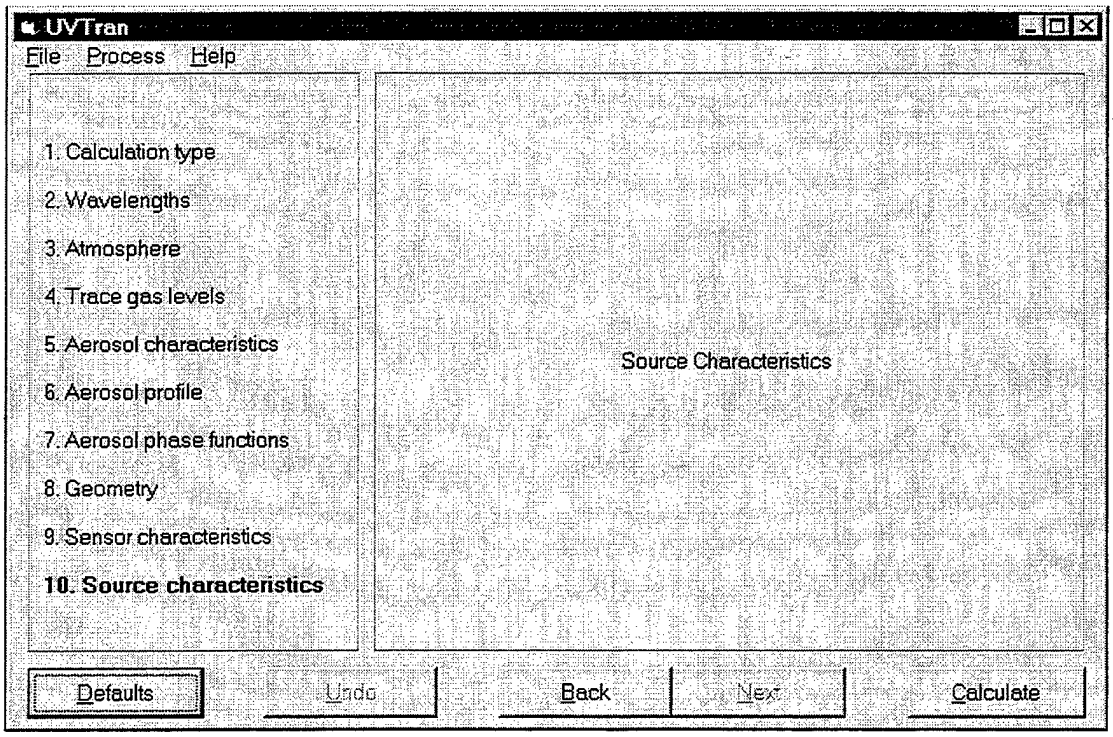

Figure 9. Source Characteristics Panel.

Measurements of scattering and propagation of solarblind ultraviolet radiation through the atmosphere

D. L. Hutt and C. Cully

Defence Research Establishment Valcartier
2459 Pie XI Blvd., North, Val-Belair, Quebec, G3J 1X5, CANADA
Tel: (902) 426 3100, FAX: (902) 426 9654, email: daniel.hutt@drea.dnd.ca

ABSTRACT

The "solarblind ultraviolet" (SBUV) waveband from 240 to 280 nm has been exploited for military surveillance and target detection. The SBUV is so called because solar radiation in this waveband is absorbed by stratospheric ozone resulting in a complete absence of solar background radiation at ground level. The absence of scene background allows relatively simple radiometer-type devices to provide useful information about local sources of UV radiation. We present measurements of various aspects of the propagation of radiation with a wavelength of 253.7 nm over ranges of 0.54 to 5.7 km with optical depths up to seven. The effect of receiver field of view and pointing direction on received irradiance is shown as well as the angular profile of the received irradiance and the angular profile of the degree of polarization.

1. INTRODUCTION

Recent interest in exploiting the solarblind ultraviolet (SBUV) waveband from 240 to 280 nm has led to development of EO systems for surveillance and target detection in both the military and civilian sectors. The SBUV is of interest because of the extremely low solar background levels that enable simple radiometer-type sensors to be used which require a minimum of signal processing. This translates into rapid detection, cost effectiveness and ease of use. Performance of these systems is directly linked to atmospheric propagation effects both in terms of UV power relayed to sensors through scattering and the loss of signal due to absorption by ambient ozone.

The modelling of SBUV propagation has proved difficult as a result of the substantial scattering optical depths encountered in practical situations and large average scattering angles. Problems of practical interest involve isotropic sources and wide field-of-view (FOV) receivers at ranges of the order of kilometers which have optical depths of the order of one. Therefore, the scattered contribution can be significant compared to the unscattered transmitted radiation. In fact, the low level of background radiation means that measurable scattered signals can be obtained from receivers pointing away from the source. Because of the large scattering angles and the large receiver FOVs, the scattered contribution is very sensitive to a variety of environmental parameters. Given the geometry of the source, receiver and ground plane and given the optical characteristics of the atmosphere, the determination of the scattered contribution to the received irradiance is the goal of UV propagation modelling.

In this paper we present a series of measurements of relevant UV propagation indices as a function of range, environmental conditions and source/receiver characteristics. The results provide a database of atmospheric effects that can be employed directly to estimate received power, detection range or other system performance parameters. But most importantly, the results provide a means to validate emerging models that deal with SBUV propagation such as those of Refs. 1 to 3.

2. ATMOSPHERIC PROPAGATION OF SOLARBLIND ULTRAVIOLET RADIATION

The irradiance I ($W/m^2/\mu m$) reaching a detector from an isotropic point source located at a range R (m) from the source is given by,

$$I = \frac{E}{R^2}\exp\left[\int_0^R -\alpha_t(z)dz\right] + I_s . \quad (1)$$

In Eq. 1, E is the radiant intensity of the source ($W/sr/\mu m$) and $\alpha_t(z)$ (km^{-1}) is the total atmospheric extinction coefficient. The first term on the right side of Eq. 1 is the unscattered or directly transmitted irradiance I_u and I_s is the contribution to the total irradiance due to scattering.

The effect of the atmosphere on propagation is often characterized by the transmittance T which is the ratio of irradiance received at the detector to the irradiance I_o that would be received if there were no intervening atmosphere:

$$T = (I_u + I_s)/I_o = \exp\left[\int_0^R -\alpha_t(z)dz\right] + I_s/I_o . \quad (2)$$

Neglecting variations in extinction along the propagation path T may be written

$$T = \exp(-\alpha_t R) + I_s/I_o , \quad (3)$$

where α_t is the path averaged total extinction coefficient and the product $\alpha_t R$ is the optical depth τ. Since α_t and T can be measured independently, information on I_s may be obtained.

The total atmospheric extinction coefficient is the sum of contributions due to Rayleigh scattering α_r, aerosol scattering and absorption, α_a and molecular absorption, α_m:

$$\alpha_t = \alpha_r + \alpha_a + \alpha_m . \quad (4)$$

All three extinction terms have important spectral dependencies over the solar blind band. However the measurements reported here were made at a narrow band centered at 253.7 nm.

The Rayleigh scattering coefficient is proportional to the concentration of air molecules and so depends on temperature, pressure and altitude. However, a simple expression for α_r, valid for the range of temperatures and altitudes of interest here is (Ref. 4)

$$\alpha_r = 0.315\left(\frac{254.0}{\lambda}\right)^4 . \quad (5)$$

where λ is the wavelength in nanometers and α_r is in km^{-1}. At $\lambda = 253.7$ nm, α_r equals $0.315\ km^{-1}$.

Extinction of UV radiation by aerosols is somewhat greater than it is for visible light. On the basis of standard models of the optical properties of aerosols, an approximate relationship between aerosol extinction at 253.7 nm and at 0.55 nm can be obtained. An analysis of the aerosol models of Ref. 5 shows that $\alpha_a(254\ nm) \cong 1.3\alpha_v$ where α_v is the visible extinction coefficient. Since α_v is due almost entirely to aerosols and is a readily available parameter derived from visibility V using (Ref. 6) $\alpha_v = 3.0/V$, the UV aerosol extinction coefficient can be estimated from the visibility using $\alpha_v(254\ nm) = 3.9/V$.

The absorption coefficient of ozone is proportional to the volume concentration of ozone and the air density. At standard temperature (20° C) and pressure (1013 mb) for $\lambda = 253.7$ nm, α_m is 0.0308 km^{-1}/ppb according to Hearn (Ref. 7). As an example of the relative sizes of the three coefficients, on a day with a visibility of 40 km and an ozone concentration of 20 ppb, $\alpha_r \cong 0.3\ km^{-1}$, $\alpha_a \cong 0.1\ km^{-1}$ and $\alpha_m \cong 0.6\ km^{-1}$.

3. INSTRUMENTATION FOR UV MEASUREMENTS

The UV propagation measurements were performed from July to August, 1997 at the Defence Research Establishment Valcartier (DREV), located 20 km northwest of Quebec City. The UV source was located at three different ranges; 538 m, 1080 m and 5700 m. For all measurements the receivers were located on top of a three-story building at a height of approximately 10 m above ground level. The ground altitude at the measurement site is 353 m above sea level.

The UV source was a model G4T4/1 U-shaped lamp available from The Second Source Inc., La Verne CA (see Fig. 1a). The UV source is a low pressure mercury vapor lamp with a peak spectral output at 253.7 nm. The quartz envelope which is 90 mm long by 30 mm wide absorbs the ozone-producing radiation at 185 nm. The output of the lamp is approximately 7.5 $\mu W/cm^2$ at 1 m. The lamp can be operated with a ballast available from Second Source. However, a custom power supply was developed to allow the lamp to be turned on and off every 10 seconds so that the background could be subtracted continuously from the received UV signal. The control circuit also measured the current flowing through the lamp and relayed the information by radio to the receiver station. The intensity of the lamp was found to vary linearly with current thus the radio signal enabled both synchronous detection of the UV signal and variations in UV lamp output to be corrected. A block diagram of the lamp control circuit is shown in Fig. 1b. Details of the lamp control circuit are available from the authors.

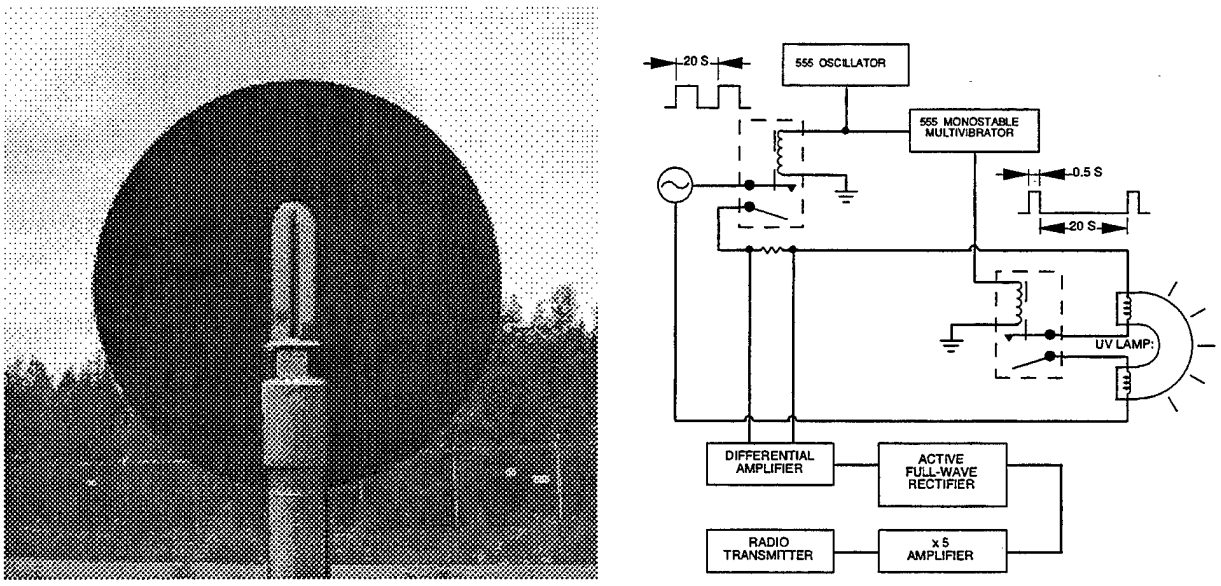

FIG. 1 UV lamp used for propagation measurements shown with a circular screen to restrict emission to one hemisphere (see Sect. 4.6) (a) and UV lamp control circuit (b).

The relationship between lamp current and UV output was established with the aid of a Goldilux Smart meter UV radiometer, model 70234-m manufactured by Oriel Instruments, Stratford, CT. A model 70239 sensor head designed for use in the UVC waveband (100 - 280 nm) was used with radiometer. The accuracy of the Goldilux radiometer is rated at better than 3%. It was factory calibrated at the same wavelength emitted by the UV source, 253.7 nm. During the measurements, the UV source was mounted at the top of a 4 m pole which was mounted on the roof of buildings located at ranges of 538 m, 1080 m and 5700 m. The source is shown in Fig. 2 at the 538 m location where its total height above ground level is approximately 7 m.

The receiver was a UV-sensitive photomultiplier tube with a multi-element absorption filter that limited the spectral response to the solar blind waveband (240 to 280 nm). The field of view (FOV) of the receiver is similar to a cosine angular response with a 1/e full angle width of 120°. The output of the sensor is a pulse train representing received photons. Output from up to four sensors was recorded simultaneously by a data logging computer. The sampling period used for all measurements was 10 mS. A fifth input of the computer monitored the status (on/off) of the source signal as received by the radio. A separate computer recorded the source current signal, also received by the radio. This second computer also recorded output from the ozone sensor and meteorological instruments. The accumulated data was then processed by subtracting background measurements (UV source off) from data with the UV source turned on and correcting the signal for any variation in source intensity.

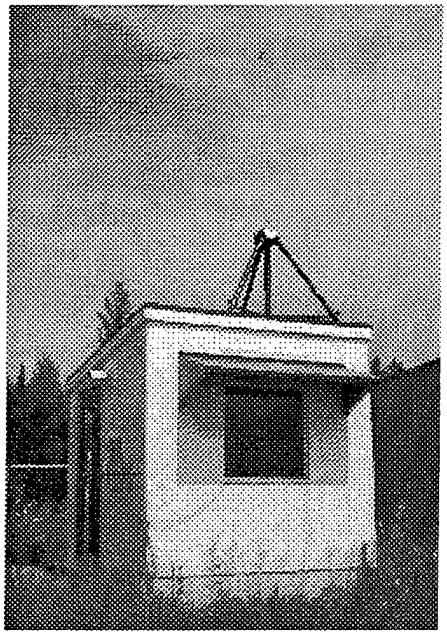

FIG. 2 UV lamp installed at top of a pole at 538 m location.

Ozone concentration was measured with a model 1008-AH UV photometric ozone analyzer from Dasibi Corp. The 1008-AH has a range of 0 to 1000 ppb with an accuracy and noise of 1.0 ppb. The time constant is 20 s and an analog output of 1 mV/ppb is provided which was recorded every 10 s. The ozone analyzer was located on the roof of a laboratory building near the UV receivers and inside a shelter with a 50 cm teflon intake tube. A teflon air filter was used at all times at the instrument intake and changed approximately once every week according to the manufacturers instructions. The calibration of the ozone analyzer was checked at the beginning and end of the measurement period by sampling known ozone concentrations produced by a Dasibi ozone calibrator. Other meteorological parameters were also measured: solar irradiation, air temperature and humidity, atmospheric pressure, rain rate, wind speed and direction and visible extinction coefficient. The visible extinction was measured with a model VR-301 visibility meter from HSS Inc. All meteorological sensors were located within 10 m of the UV receivers.

4. RESULTS

4.1. UV Transmittance

The atmospheric transmittance was found from experimental results using Eq. 2. Although I_o cannot be measured directly, it was deduced from the radiant intensity E of the source using $I_o = E/R^2$. In terms of measured quantities the transmittance is

$$T = IR^2/E \ . \tag{6}$$

Transmittance values from an open receiver pointing directly at the source are plotted in Fig. 3 as a function of optical depth τ both for a fixed source-receiver distance of 538 m for three different ranges of ranges 538 m, 1080 m and 5700 m (Fig. 3b). The optical depth is, assuming uniform extinction along the optical path,

$$\tau = R(\alpha_r + \alpha_a + \alpha_m) = R\alpha_t \ . \tag{7}$$

To evaluate τ, α_r was taken to be 0.315 km^{-1}, α_a was determined from the measured visible extinction coefficient using $\alpha_a(254\ nm) \cong 1.3\alpha_v$ and α_m was found from the ozone concentration using α_m is 0.0308 km^{-1}/ppb.

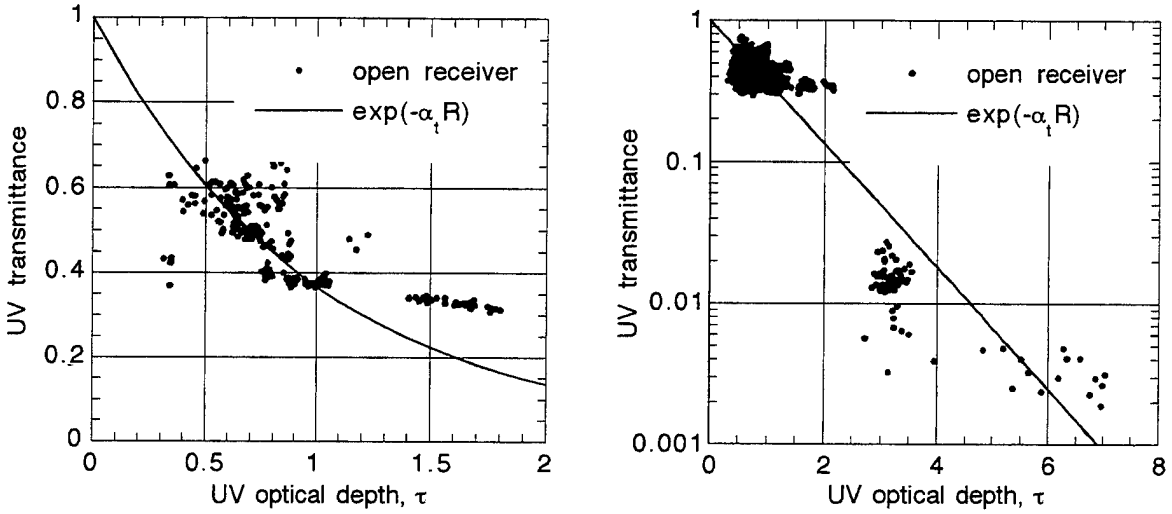

FIG. 3 UV transmittance as a function of optical depth for source-receiver distance 538 m (a) and ranges 538 m, 1080 m and 5700 m (b).

Also shown in Figs. 3a and b is the unscattered transmittance $T_u = e^{-\alpha_t R}$, which represents the transmittance due to absorption and single scattering losses. The measured transmittance should be greater than T_u due to the contributions of scattered power available to the wide field of view receiver used. In Fig. 3a the data points tend to be above the T_u curve particularly for optical depths greater than 1.5. Unfortunately the accumulated inaccuracies in both the measured transmittance and the extinction coefficients result in a considerable amount of scatter. In particular it was found that the measured ozone concentration was not representative of the entire path during conditions of low wind speed. Figure 3 shows data from several different sets of measurements. The data points at optical depths greater than four were obtained with the source at a range of 5700 m. The data gives an indication of the range of optical depths that can be encountered under conditions of good visibility and ranges up to 5 km.

4.2. Effect of receiver field of view

Better characterization of atmospheric effects may be obtained by measuring the ratios of received signals. To study the effect of field of view variations, measurements were made simultaneously with four receivers pointing at the source. Three of the receivers had fields of view limited by tubes extending in front of the receiver. The inside of the tubes were painted flat black to reduce scattering and the angular sensitivity profiles were measured in the laboratory. The field of view profiles were nearly rectangular with half-angle widths of 4, 10 and 40 degrees. During the measurements, one receiver was left completely open and its signal was used to normalize the others. Resultant ratios, expressed as percentages are shown in Fig. 4 as a function of ozone concentration with source-receiver distances of 538 and 1080 m.

All sensors receive the same unscattered irradiance but the scattered contribution is field-of-view dependent. The scattered contribution to a receiver is increased for a large field of view. For a given ozone concentration the ratios are smaller for the smaller fields of view because of the reduced scattered signal. The range of ozone concentrations common to both Figs. 4 a and b is 25 to 40 ppb. For these concentrations, the signal ratios are smaller at 1080 m than they are at 538 m, indicating that the scattered component diminishes with range more slowly than the unscattered component which falls off as $e^{-\alpha_t R}/R^2$. The fact that the ratios go down as ozone concentration increases shows that the scattered contribution to the limited receivers decrease more slowly than that of the open receiver since the unscattered components are equally affected by the ozone. This result is

surprising because the open receiver has highest scattered contribution. Scattered photons experience longer path lengths and thus should be attenuated more by a given increase in absorption than the unscattered component. This unexpected result may be related to the effect of the vertical profile of ozone which was not measured.

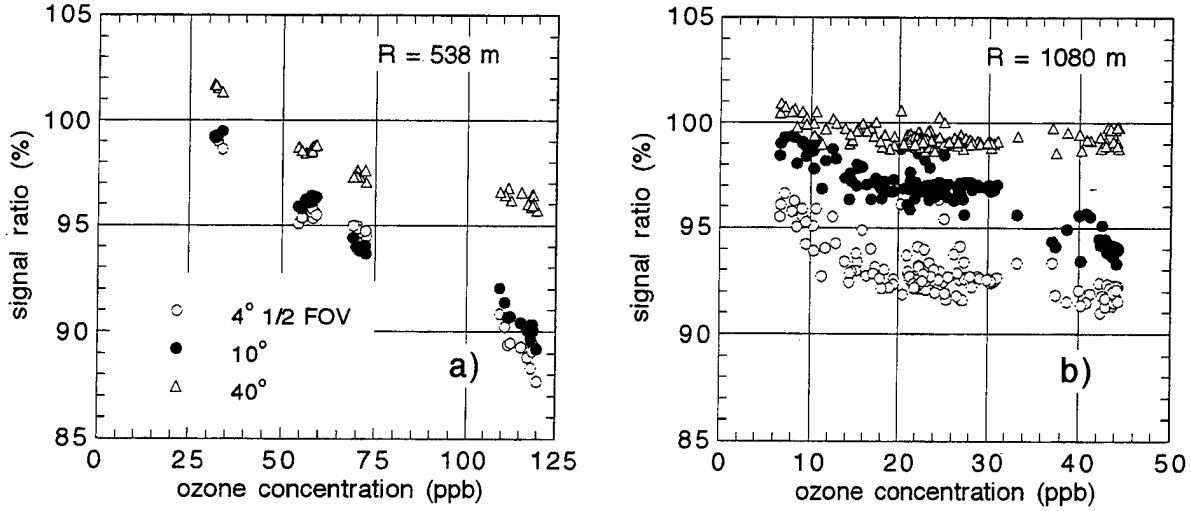

FIG. 4 Ratios of UV signal received with limited FOVs to an open receiver for R = 538 m (a) and R = 1080 m (b).

4.3. Effect of pointing angle on UV signals

As a result of the strong Rayleigh scattering, a source emitting in the SBUV is surrounded with a field of scattered radiation. A sensor pointing in any direction can receive multiply scattered irradiance, even a sensor pointing directly away from the source. Measurements were made with receivers pointing in four orthogonal directions with respect to the source: toward the source (0°), at 90° from the source in the horizontal plane, at 90° in the vertical plane (pointing straight up) and directly away from the source (180°) The signals from the receivers pointing away from the source were normalized by the signal from the receiver pointing at the source and are plotted in Fig. 5 as a function of ozone concentration.

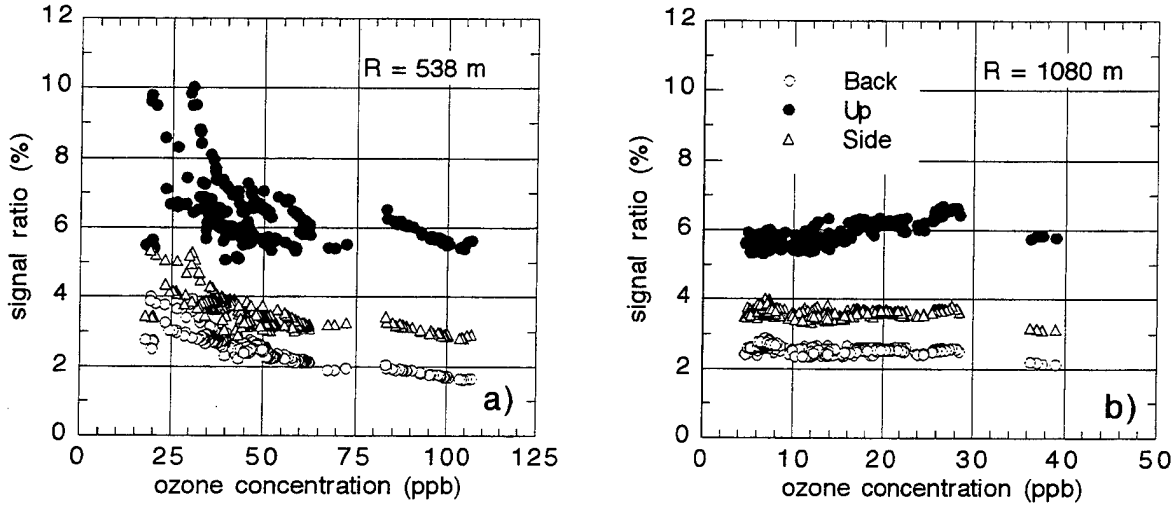

FIG. 5 Ratio of signals from open receivers pointing away from the source to signal from an open receiver pointing at the source for R = 538 m (a) and R = 1080 m (b).

Figure 5 shows that the signals of open receivers pointing away from the source are from 2 to 10% of the forward pointing receiver signal. The ratios do not change significantly between measurements made with R = 538 m and 1080 m. Figure 5a which shows a large variation in ozone concentration, indicates a reduction in all three ratios with increasing ozone level. Both figures show that the signal from the up-pointing sensor is approximately two times greater than the side-pointing receiver. Both of these receivers point at 90° with respect to the direction to the source but the field of view of the side-pointing receiver intersects the ground and thus sees approximately half of the scattering volume seen by the up-pointing receiver. Since the signal from the up-pointing sensor is approximately two times greater than that of the side-pointing receiver, it can be concluded that the ground plane acts as an effective absorber, eliminating half of the scattered signal.

4.4. Angular irradiance profile

The results presented in the previous two sections depend upon the angular profile of scattered irradiance at the receiver. Measurements of the profile were made with a receiver with the half-angle field of view limited to 4°. UV signals were recorded as a function of elevation and azimuth angle from 0 to 180° with respect to the source direction. Unfortunately, the signal for 0° includes the unscattered irradiance due to the limited angular resolution of the measurements and the shape of the irradiance profile cannot be determined for angles less than approximately 5°. The scattered signal increases rapidly for small angles due primarily to the proximity of the scattering volume to the source. The profile is modified by the absorption optical depth due to ozone, the scattering optical depth due to ambient aerosols and the shape of the aerosol angular scattering function which is related to the type of aerosols.

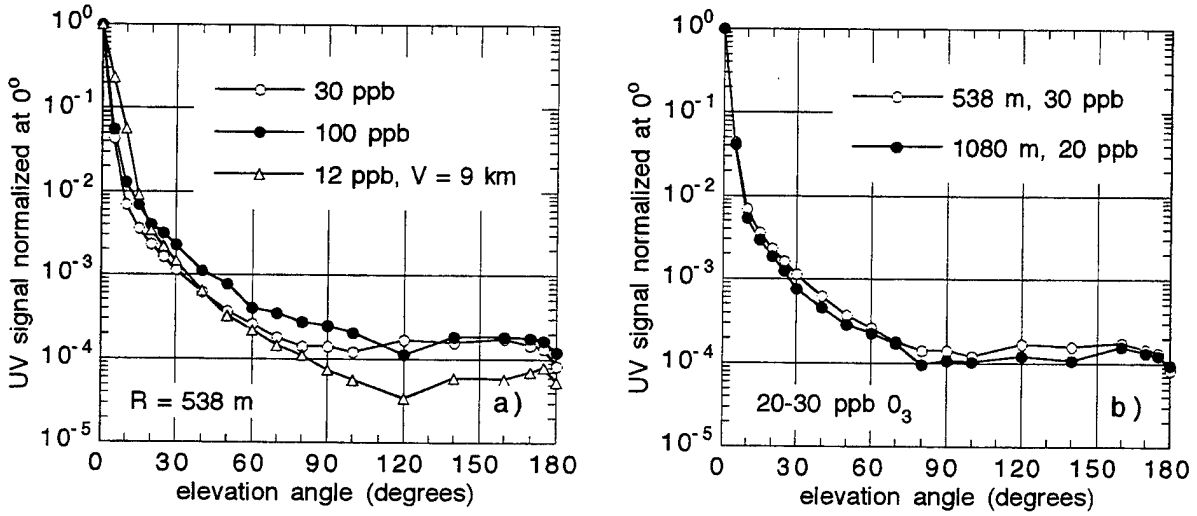

FIG. 6 Irradiance profiles measured with a resolution of 8° for various conditions.

Examples of scans normalized by the signal at 0° are shown in Fig. 6 for various conditions. It can be seen in Fig.6a that the profile made during reduced visibility conditions (high concentration of aerosols) is broader near 0° than the other two curves. This is believed to be due to forward scattering which is characteristic of high aerosol concentrations. It is akin to the bright halo seen around a street light on a foggy night. The other profiles made under clear conditions are very flat for angles greater than 80° and even increasing slightly for angles greater than 90°. This is believed to be due to the shape of the Rayleigh scattering function which is at a minimum at 90°. Figure 6a shows that there are only minor differences between the profiles made at 538 m for 30 and 100 ppb ozone concentrations although these conditions represent absorption optical depths of approximately 0.5 and 1.5 respectively. The two profiles made with similar ozone concentrations but ranges of 538 and 1080 m are similar.

4.5. Polarization of UV irradiance

Light scattered by the Rayleigh process may be strongly polarized. For isotropic Rayleigh scatters, the radiation scattered at 90° with respect to the direction to the source is completely polarized. This phenomenon is well known in visible sky light which is strongly polarized in a band across the sky at 90° from the sun. The polarization of light scattered from the UV source was measured using a linear polarizing filter placed on a UV sensor pointing in the vertical direction at 90° with respect to the source direction. The polarizer had an extinction ratio of 0.6% and transmittance of 15% at 253.7 nm. It was mounted in a rotation stage on the sensor aperture and rotated about the vertical axis. The rotation stage limited the field of view of the sensor to a half angle of approximately 30°. The relative intensity of the received signal is plotted in Fig. 7a as a function of rotation angle. It is clear that the downwelling radiation is strongly polarized. The degree of polarization P for the data in Fig. 7a is 0.62 where P is defined as

$$P(\theta) = \frac{I_{\parallel}(\theta) - I_{\perp}(\theta)}{I_{\parallel}(\theta) + I_{\perp}(\theta)}. \qquad (8)$$

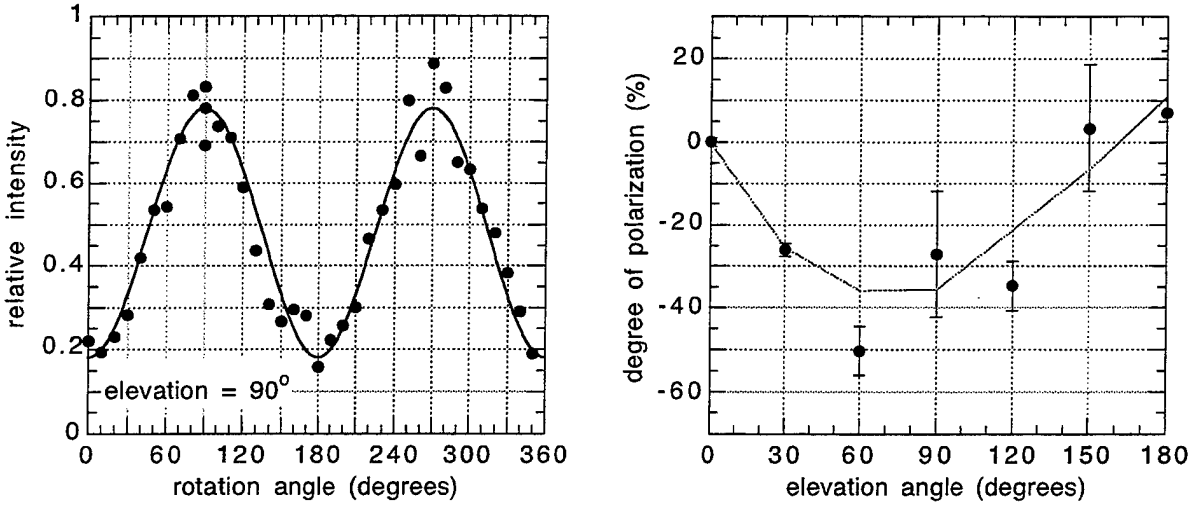

FIG. 7 Linear polarization of scattered UV radiation at 90° to source as a function of angle about the vertical axis (a) and degree of polarization as function of elevation angle (b).

In Eq. 8, $I_{\parallel}(\theta)$ and $I_{\perp}(\theta)$ are the intensity components parallel and perpendicular, respectively, to the plane of polarization and θ is the scattering angle. The high degree of polarization shown in Fig. 7a is remarkable because the field of view of the receiver was relatively wide and accepted light scattered at angles between 60 and 120°. The average value of P for angle 60 to 120° from ideal Rayleigh scatters is 0.85. The degree of polarization is reduced by multiple scattering which may be partly responsible for the difference between measured P and that of ideal scatterers. Also, the received signal has contributions from the entire upward-pointing field of view cone. Contributions from volume elements on the vertical axis located high above the receiver are not scattered at 90° and thus possess a reduced degree of polarization.

The elevation profile of P(θ) was measured using two sensors simultaneously, each with a linear polarizing filter. The axis of one filter was aligned parallel with the vertical scan plane and the other was aligned perpendicular. The fields of view of the two sensors were limited to 10° with tubes. The pair of sensors were scanned from 0 to 180 degrees and the degree of polarization was calculated from the simultaneously measured intensities. The result is shown in Fig. 7b, which indicates that the polarization profile is not symmetric about 90°.

4.6. Effect of source anisotropy on received irradiance

Real UV sources are rarely isotropic emitters (e.g. lightning) so the effect of the shape of the angular profile of the source intensity is of interest. A series of measurements were made with the source located at 538 m mounted with a 20 cm diameter black disk to constrain the source to radiate only in one hemisphere pointing in the horizontal plane. Measurements of the received UV signal were made with the source-disk assembly rotated in different directions as shown in Fig. 8. Comparing geometries 1 and 2 gives an indication of the contribution of the backward hemisphere to the total signal received by each UV receiver. In geometries 3 and 4 the disk is rotated so that no direct radiation reaches the receivers. The contribution of light scattered from the lateral hemisphere is thus determined. The measurements were made under clear conditions with an ozone concentration of approximately 30 ppb. Results are summarized in Table 1.

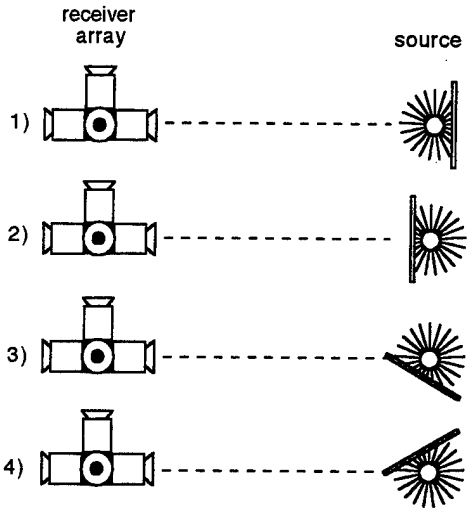

Fig. 8 Arrangements for source anisotropy experiments (top view).

Table 1

Source anisotropy results expressed as percentage of signal with no disk

geometry (Fig. 8)	receiver direction			
	back	up	side	forward
1	101	99	93	95
2	4.2	10	7.1	3.1
3	13	22	51	5.3
4	8.3	20	4.3	3.9

Comparison of results 1 and 2 in Table indicate that the hemisphere away from the receivers provides 3 to 5% of the signal received by the forward and back-looking sensors. A larger fraction between 5 and 10% is contributed to the up and side-looking receivers. Arrangements 3 and 4 give similar values from the laterally illuminated hemispheres of approximately 10, 20 and 4% for the back, up and forward-looking receivers. That the results be similar for these receivers is to be expected on the basis of symmetry. These results are only valid for the specific conditions of the experiment but provide an excellent means of testing predictions of models.

5. CONCLUSIONS

Results of experimental investigations into the propagation of solarblind ultraviolet radiation have been presented. The SBUV waveband extends from 240 to 280 nm and measurements were made with a nearly monochromatic UV source emitting near the center of the band at 253.7 nm. Measurements were made over horizontal ranges from 0.54 to 5.7 km with optical depths up to seven. Under clear air conditions most of the extinction is due to absorption by ambient ozone. In the SBUV Rayleigh scattering is approximately ten times stronger than it is in the visible. With a

scattering coefficient of approximately 0.3 km^{-1} and large scattering angles, Rayleigh scattering is responsible for strong signals at receivers pointing away from the source. Results showed signals with a 120° field of view receiver point directly away from the source were 2 to 4% of the signal from a receiver pointing at the source, depending on range and ozone concentration. By comparing signals received from sensors pointing up at 90° to the source direction to signals received from sensors pointing sideways at 90°, the effect of the ground was found to be that of an absorbing plane.

The angular profile of receiver UV irradiance was also measured in the vertical plane with a resolution of 8°. The effect of ozone concentration and aerosol loading on the profile was observed. One approach in propagation modelling is to calculated the shape of the angular irradiance profile and from that determine the power received by a receiver with a specific field of view and direction. Thus the measured curves presented here provide a test for proposed models.

Rayleigh scattering is characterized by strong polarization which was observed as a function of elevation angle. A degree of polarization of 0.62 was observed for an elevation angle of 90°. The polarization state of the received scattered irradiance contains information on the range (or optical depth) and direction to the source and thus may be of use in surveillance application. Comparison of results presented here with a Monte Carlo model (Ref. 1) and a finite element transport model (Ref. 2) are currently under way.

6. REFERENCES

1. Cully, C. and D. Hutt, "Monte Carlo modelling of the propagation of solarblind UV radiation in the lower atmosphere", Proc. of 1997 Battlespace Atmospherics Conf., Eds. K. Anderson and J. Richter, Space and Naval Warfare Systems Center Tech. Doc. 2989 (1997).
2. Crow, K., "OSIC: Model description and user's manual", SciTec Tech. Report, SciTec Inc., Princton, NJ (1995).
3. Patterson, E. and J. Gillespie, "Simplified ultraviolet and visible wavelength atmospheric propagation model", Appl. Opt. 28, 425-235 (1989).
4. Green, A. E. S., "Attenuation by ozone and the Earth's albedo in the middle ultraviolet", Appl. Opt. 3, 203-208 (1964)
5. E. P. Shettle and R. Fenn, "Models for the aerosols of the lower atmosphere and the effects of humidity variations on their optical properties", Air Force Geophysics Laboratory, AFGL-TR-79-0214 (1979).
6. Douglas, C. A. and Booker, R. L., "Visual Range: Concepts, Instrumental Determination, and Aviation Applications", National Bureau of Standards Monograph 159, U. S. Dept. of Commerce, Washington D. C. (1977).
7. Hearn, A. G., "The absorption of ozone in the ultraviolet and visible regions of the spectrum", Proc. Phys. Soc. London 78,932-935 (1961).

Effect of atmospheric optical turbulence on ultraviolet propagation

D.L. Hutt and C. Cully

Defence Research Establishment Valcartier
2459 Pie XI Blvd., North, Val-Belair, Quebec, G3J 1X5, CANADA
Tel: (902) 426 3100, FAX: (902) 426 9654, email: daniel.hutt@drea.dnd.ca

ABSTRACT

There has been increasing interest in exploiting the "solarblind ultraviolet" (SBUV) waveband from 240 to 280 nm for military surveillance and target detection. Solar radiation in this waveband is absorbed by stratospheric ozone resulting in a complete absence of solar background radiation at ground level. We investigate the effect of atmospheric optical turbulence on 253.7 nm radiation propagated over a range of 185 m. The UV scintillation index is measured as a function of the atmospheric turbulence structure parameter, which was measured independently with a laser scintillometer. The probability density of UV scintillations, power spectra and effect of aperture averaging on the scintillation index are also presented.

1. INTRODUCTION

When light propagates through turbulent air, it encounters inhomogeneities in the refractive index that transform its phase front. The inhomogeneities are caused by the mixing of air of different temperature by wind and convection. Near the ground, the intensity of temperature fluctuations depends on the type of ground cover, ambient temperature, solar irradiation and wind speed. Electro-optical (EO) systems depend on the propagation of light over large distances and are thus susceptible to the influence of optical turbulence. The turbulent atmosphere causes the intensity of a light beam to fluctuate or scintillate, causes beam wander and causes the distortion and random displacement of images. Turbulence can limit the angular resolution of an imaging system to values of hundreds of microradians, many times the diffraction limit of some imagers, thus resulting in significantly degraded performance. The effect of turbulence on EO systems is well known in the visible and IR wavebands but little consideration has been given to its effect in the UV even though new applications for UV radiation from 240 to 280 nm have been found for military surveillance and target detection. In this paper we report on a series of measurements of turbulence-induced phenomena at a wavelength of 253.7 nm. Results include UV scintillation index measured as a function of the atmospheric turbulence structure parameter, the probability density of UV scintillations, scintillation power spectra and the effect of aperture averaging on the scintillation index.

2. ATMOSPHERIC TURBULENCE

Turbulent structures have size-scales from millimeters to tens of meters and can induce optical effects with frequencies from fractions of Hz to thousands of Hz.Since turbulent fluctuations are random or unpredictable they must be described statistically. The intensity of atmospheric turbulence is characterized by the refractive index structure parameter C_n^2 . For homogeneous and isotropic turbulence C_n^2 is defined as (Ref. 1)

$$C_n^2 = \langle [n(\tilde{r}_1) - n(\tilde{r}_2)]^2 \rangle / |\tilde{r}_1 - \tilde{r}_2|^{2/3}, \quad (1)$$

where n is the index of refraction at points $\tilde{r}_1$ and $\tilde{r}_2$. C_n^2 has the dimensions of $m^{-2/3}$ and varies from about 10^{-16} to 10^{-12} $m^{-2/3}$ in the atmospheric boundary layer. Equation 1 is valid for distances $|\tilde{r}_1 - \tilde{r}_2|$ well within the inertial subrange or between approximately 10 and 100 cm.

3. UV SCINTILLATION MEASUREMENTS

The experiments were performed in Sept., 1997 at the Defence Research Establishment Valcartier (DREV), located 20 km northwest of Quebec City. The coordinates of DREV are approximately 46.9N, 71.5W. The site is a level grass covered field with sandy soil. It is about 300 m across, surrounded by spruce trees on the West and North sides and by low buildings on the East. The UV source and receiver were housed in small instrument sheds separated by a distance of 185 m. The propagation path was 1.8 m above the ground and oriented approximately North-South with prevailing winds coming from the West.

The source used for the UV scintillation measurements was a model 80-1057-01 Analamp manufactured by BHK Inc., Pomona CA (see Fig. 1a). The Analamp series are low pressure mercury vapor lamps with a peak spectral output at 253.7 nm. They have a quartz jacket that absorbs the ozone-producing radiation at 185 nm. The lamp has a 25 mm long bulb with a power output of 36 $\mu W/cm^2$ at a distance of 20 cm. The quartz jacket acts as an insulator to make the lamp less sensitive to ambient temperature changes. The lamp requires a special high frequency, 900 V power supply, also from BHK. The power supply output oscillates at 50 kHz with the result that the light output of the lamp has a 50% ripple at 50 kHz. The turbulence induced scintillation frequencies, on the order of 1 kHz and less, are sufficiently low that the 50 kHz ripple in the lamp output does not interfere with the measurements. The size of the emitting surface of the lamp was reduced to 6.4 mm diameter during the measurements to minimize spatial averaging effects at the source.

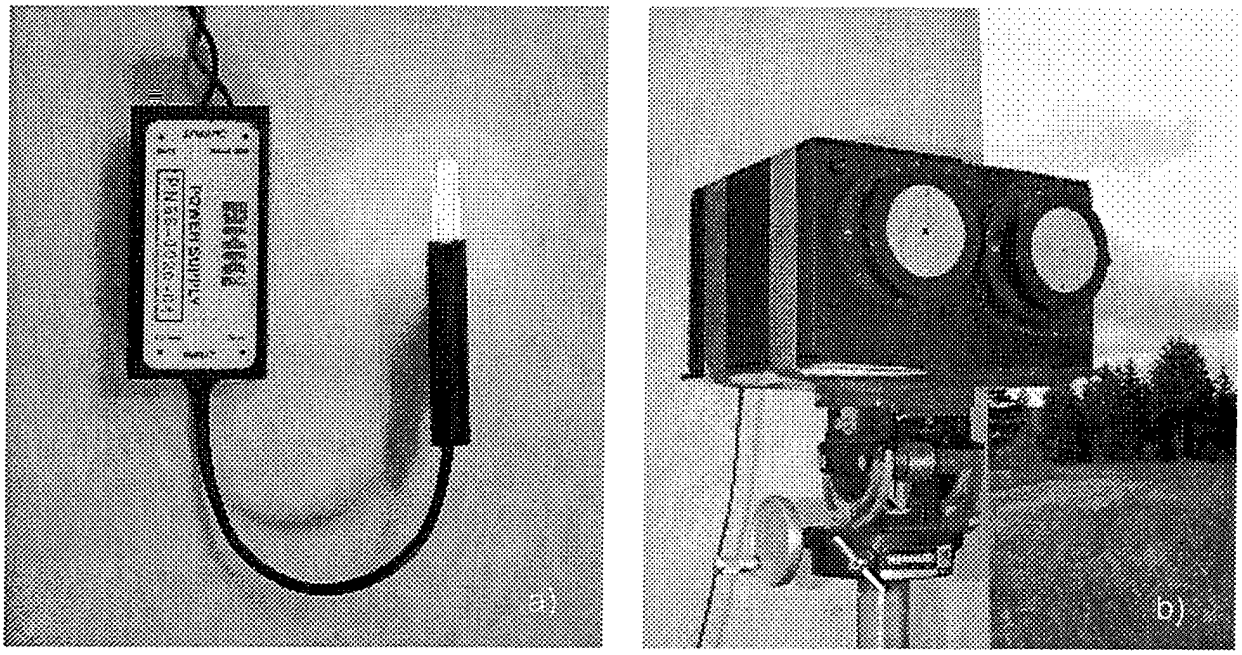

FIG. 1 UV source (a) and UV receivers (b) used for scintillation measurements.

The receiver used for the UV scintillation measurements was a UV-sensitive photomultiplier tube with a multi-element absorption filter that limited the spectral response to the solar blind waveband from 240 to 280 nm thus eliminating solar background signal. The output of the sensor is a pulse train representing received photons. The aperture of the receiver was limited to 3.2 mm for most of the measurements to minimize aperture averaging effects. The output of two sensors was recorded simultaneously by a data logging computer. The sampling period used for all measurements was 1 mS. The UV sensors are shown in Fig. 1b.

The measured scintillation is expressed as the scintillation index σ_I^2 which is the normalized variance of intensity fluctuations. σ_I^2 is defined as

$$\sigma_I^2 = \frac{\langle (I - \langle I \rangle)^2 \rangle}{\langle I \rangle^2}, \tag{2}$$

where I is the instantaneously measured intensity, and $\langle I \rangle$ is the time-averaged intensity. An example of UV intensity measurements is shown in Fig. 2. The intensity fluctuations are due to atmospheric turbulence which was moderately high during the measurement with $C_n^2 = 2.1 \times 10^{-13}$ $m^{-2/3}$. For the data of Fig. 2, $\sigma_I^2 = 0.21$.

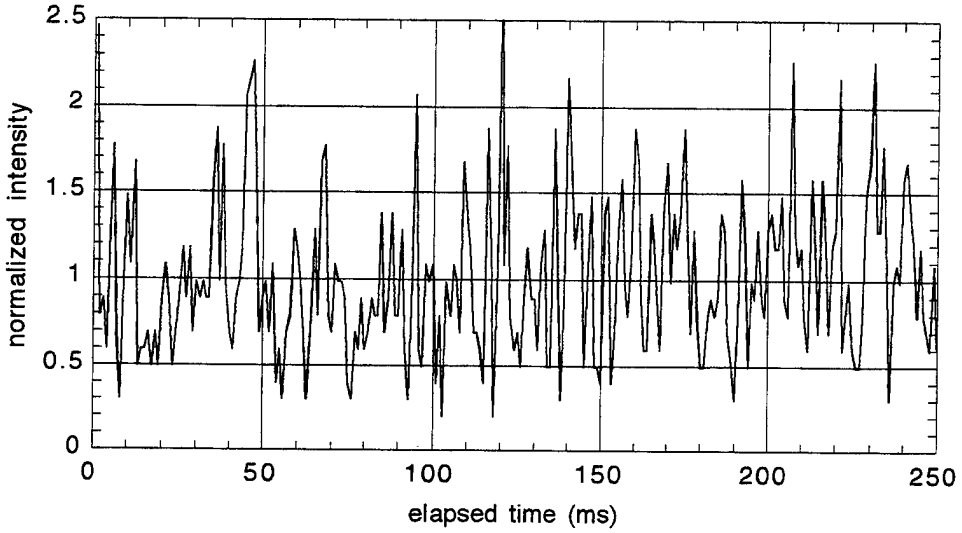

FIG. 2 UV intensity measurements for moderate-high turbulence ($C_n^2 = 2.1 \times 10^{-13}$ $m^{-2/3}$).

4. TURBULENCE MEASUREMENTS

The turbulence structure parameter C_n^2 was measured with a SLS-20 scintillometer manufactured by Scintec GmhB, Tübingen, Germany. The SLS-20 uses the independently measured scintillation of two displaced but parallel laser beams to derive C_n^2. The source is a 1 mW laser diode with a wavelength of 670 nm and divergence of approximately 5 mrad. The beam displacement of 2.7 mm is achieved by passing the beam through a birefringent calcite crystal which splits the beam into displaced but parallel components with crossed polarizations. At the receiver the two overlapping beams are resolved by a polarizing beam splitter, allowing the scintillation of each beam to be measured independently by two 2.5 mm diameter detectors. The transmitted laser beams are modulated at 20 kHz to allow AC coupling of the detector outputs which eliminates the background. The SLS-20 is described in detail in Refs. 2 and 3 and the receiver is shown in Fig. 3.

The calculations to derive C_n^2 are carried out in real time by the instruments laptop computer which also provides the turbulence spectrum inner scale ℓ_0, the temperature structure constant C_T^2 and other turbulence parameters. The SLS-20 scintillometer path was almost identical to the UV scintillation path with the SLS-20 source and receiver located in the same sheds as the UV source and receiver. A calibration of the SLS-20 was carried out for the 185 m path according to the manufacturer's instructions. The scintillometer provided a path-averaged value of C_n^2 (weighted toward the center of the path) every 60 S.

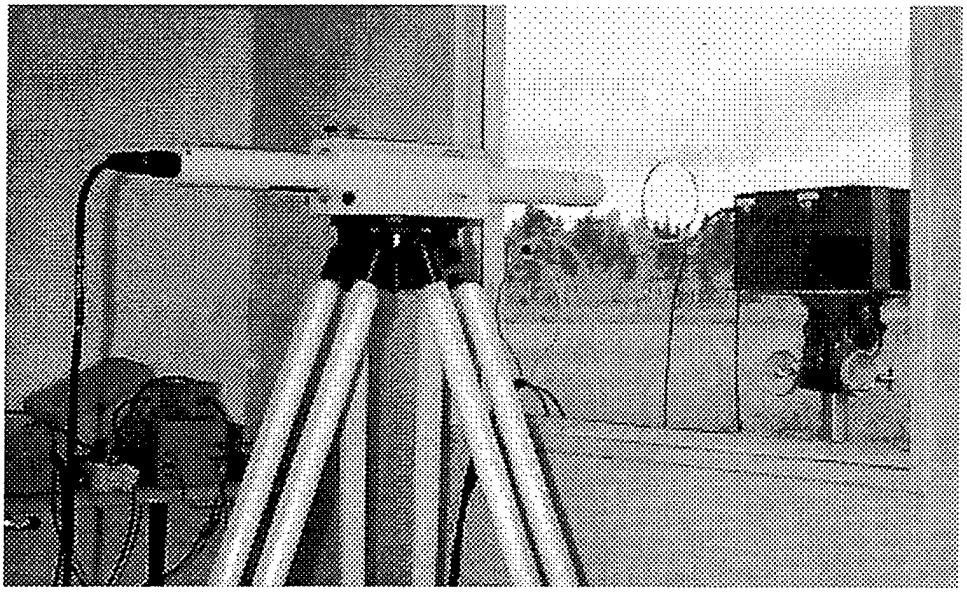

FIG. 3 Receiver of Scintec SLS-20 scintillometer installed for measurements.

The C_n^2 has a slight wavelength dependence from the infrared to visible wavebands, increasing more quickly as $1/\lambda^2$ toward the UV. The wavelength dependence of C_n^2 can be calculated from the spectral refractivity $N = 10^6(n-1)$. Edlén (Ref. 4) provides a function for the spectral refractivity of dry air. For a temperature of 20° C and atmospheric pressure of 1013 mb, Edlén's formula yields values of N(670 nm) = 271.6 and N(260 nm) = 294.1. However when the values of $n = 10^6N+1$ at 260 nm are used in Eq. 1 it is found that there is negligible difference between C_n^2 at 670 nm as measured by the scintillometer and at 260 nm, thus the SLS-20 C_n^2 measurements are used directly.

Meteorological conditions were also monitored simultaneously near the scintillometer path using standard sensors for wind speed, wind direction, barometric pressure, solar irradiation, air temperature and humidity.

5. SCINTILLATION INDEX AND TURBULENCE STRUCTURE

Assuming a point detector, a point source and constant turbulence along the propagation path, the scintillation index is related to C_n^2 by (Ref. 1)

$$\sigma_I^2 = \exp(4.24 C_n^2 \lambda^{-7/6} z^{11/6}) - 1 , \quad (3)$$

where λ is the wavelength (m) and z is the path length (m). Equation 3 is valid for as long as the following inequality is satisfied:

$$C_n^2 \lambda^{-7/6} z^{11/6} \leq 0.3 . \quad (4)$$

If the intensity of the turbulence or the path length are increased such that inequality 4 is not satisfied then the scintillation index maintains a nearly constant value of approximately 2.3 and becomes insensitive to changes in C_n^2 or path length. Under these conditions the scintillation is said to be "saturated". For our 185 m path and the UV wavelength of 254 nm, C_n^2 must be less than 4×10^{-13} $m^{-2/3}$ to satisfy inequality 4. Peak values of C_n^2 did occasionally exceed 4×10^{-13} $m^{-2/3}$ but most data was collected under nonsaturation conditions. Correct use of the Scintec scintillometer to measure C_n^2 also depends on measurements being made under nonsaturation conditions. For the scintillometer wavelength of 670 nm (and the 185 m path), C_n^2 would have to exceed 1×10^{-12} $m^{-2/3}$ which was never observed. Equation 4 shows that for a given path length, UV

radiation would saturate for a value of C_n^2 that is 42% of the value required to saturate visible light assuming $\lambda_{UV} = 260$ nm and $\lambda_{vis} = 550$ nm. Also, for a given C_n^2, UV radiation would saturate for a path length that is 62% of the value required to saturate visible light.

For small values of C_n^2, Eq. 3 can be approximated as

$$\sigma_I^2 \cong 4.24 C_n^2 \lambda^{-7/6} z^{11/6} \tag{5}$$

and σ_I^2 is proportional to C_n^2. An example of UV scintillation and C_n^2 measured over a period of eight hours is shown in Fig. 4 where the independent measurements of σ_I^2 and C_n^2 follow each other closely.

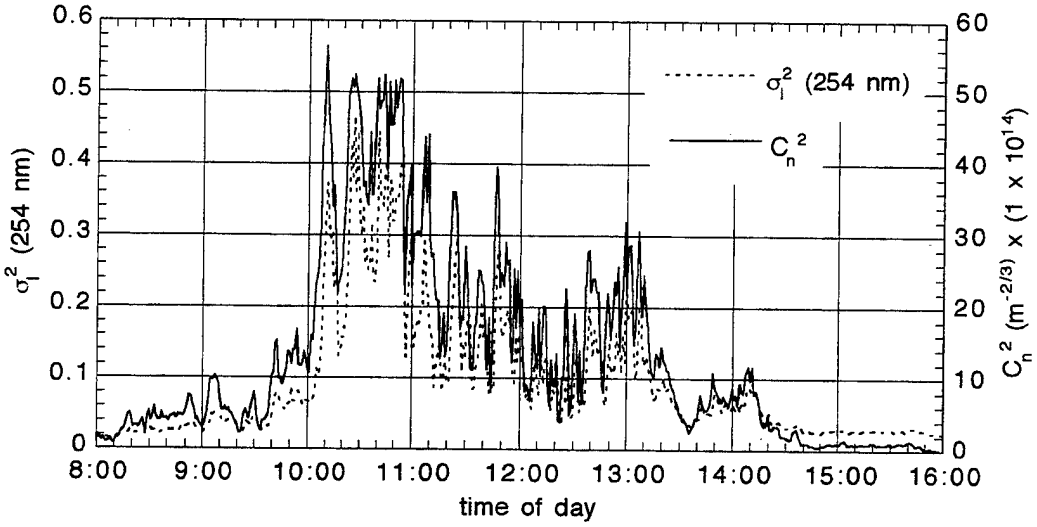

FIG. 4 Time plot of turbulence structure parameter C_n^2 and UV scintillation index σ_I^2.

Equation 5 allows the ratio of scintillation index in the UV to that in the visible for small C_n^2 to be calculated as,

$$\frac{\sigma_I^2(254 \text{ nm})}{\sigma_I^2(550 \text{ nm})} \cong 2.5 \ . \tag{6}$$

Thus scintillation in the SBUV can be expected to be more than twice as intense as in the visible under similar, nonsaturation conditions.

6. SCINTILLATION INDEX AND APERTURE AVERAGING

For weak turbulence, σ_I^2 is given as a function of C_n^2 by Eq. 3. Measurements of UV σ_I^2 are plotted as a function of C_n^2 in Fig. 5 along with the curve predicted by Eq. 3. It is clear from the figure that the measured σ_I^2 increases much more slowly with C_n^2 than predicted by the model. The reason for the disparity between the measurements and model is the effect of aperture averaging with a possible contribution from source averaging.

Atmospheric optical turbulence induces spatial variations or bright and dark regions in the intensity field at the receiver. These bright and dark regions are sometimes called speckles. The total power received by a real receiver with finite area is the integral of the spatially varying intensity across the surface of the receiver which has the effect of averaging out the signal variations. The speckles have a characteristic size, called the Fresnel scale given by $\sqrt{\lambda z}$. If the diameter of the receiver optics is much less than the Fresnel scale then the averaging effect is negligible. The receiver can

be considered to be a point receiver and the scintillation experienced by the receiver is adequately described by σ_I^2. If the receiver diameter is of the same order as the Fresnel scale or larger, then aperture averaging reduces the observed scintillation. For z = 185 m and $\lambda = 254$ nm, $\sqrt{\lambda z} = 7$ mm. Thus we can expect aperture averaging to affect the measured UV scintillation with aperture diameters of the order of millimeters. In order to ensure adequate signal, the smallest aperture used for the UV scintillation measurements was 1.6 mm in diameter.

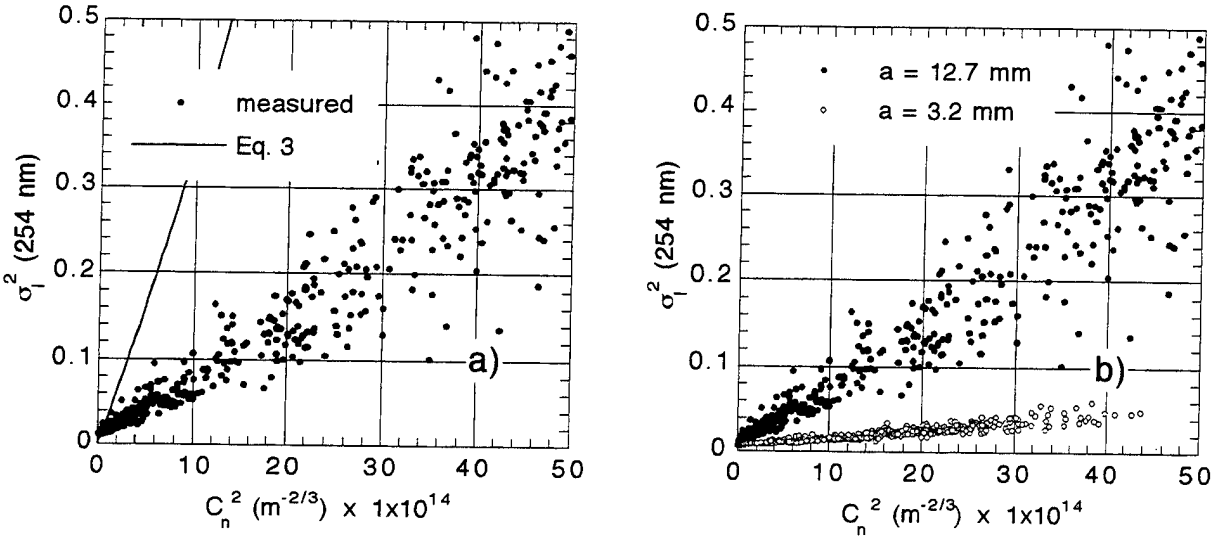

FIG. 5 Measured UV σ_I^2 versus C_n^2 and Eq. 3 prediction (a), UV σ_I^2 versus C_n^2 for simultaneously measured UV receivers with aperture radii 12.7 and 3.2 mm (b).

Fried (Ref. 5) provides an expression for a reduced scintillation index σ_s^2 caused by aperture averaging over an aperture s. The ratio $S = \sigma_s^2/\sigma_I^2$ is less than unity for a finite aperture and tends to 1 for a point receiver. From Ref. 5,

$$\sigma_s^2 = \frac{32\pi}{a^2}\int_0^\infty J_1^2(aK)\Phi_\chi(K)\,K^{-1}dK\ , \tag{7}$$

where a is the aperture radius, J_1 is the first order Bessel function of the first kind, $\Phi_\chi(K)$ is the Wiener spectrum for log-amplitude fluctuations χ as a function of the spatial frequency of the turbulent structure K.

Within the Rytov approximation and assuming that the inner scale of turbulence l_0 is negligibly small, the Wiener spectrum for spherical waves is given by (Ref.6),

$$\Phi_\chi(K) = 2\pi(0.033)k^2K^{-11/3}\int_0^z C_n^2(z')\left(\frac{z'}{z}\right)^{5/3}\sin^2\left[\frac{K^2z(z-z')}{2z'k}\right]dz' \tag{8}$$

where k is the wavenumber of the radiation equal to $2\pi/\lambda$ and z is the path length. The approximation $\sin(x) \cong x$ is used to evaluate the integral in Eq. 8, valid for sufficiently small K. The resulting expression for $\Phi_\chi(K)$ is then substituted in Eq. 7 yielding,

$$\sigma_s^2(a) = 2.32a^{-7/3}C_n^2\,z^3\ . \tag{9}$$

As a result of the approximations used, Eq. 9 is valid only for $a > \sqrt{\lambda z}$. Equation 9 is also independent of wavelength - a great cause for suspicion. For small C_n^2, σ_s^2/σ_I^2 is given by the ratio of Eq. 9 to 5:

$$\sigma_s^2/\sigma_I^2 = 0.55a^{-7/3}\lambda^{7/6}z^{7/6}. \tag{10}$$

We derived values of σ_s^2/σ_I^2 from scintillation measurements with seven different apertures ranging in size from 0.8 to 9.5 mm radius. Values of σ_s^2 were determined directly from the measured UV intensity using Eq. 2 and corresponding values of σ_I^2 were derived from Eq. 2 using the value of C_n^2 measured with the Scintec scintillometer and setting $\lambda = 260$ nm. The results are shown in Fig. 6 along with σ_s^2/σ_I^2 from Eq. 10.

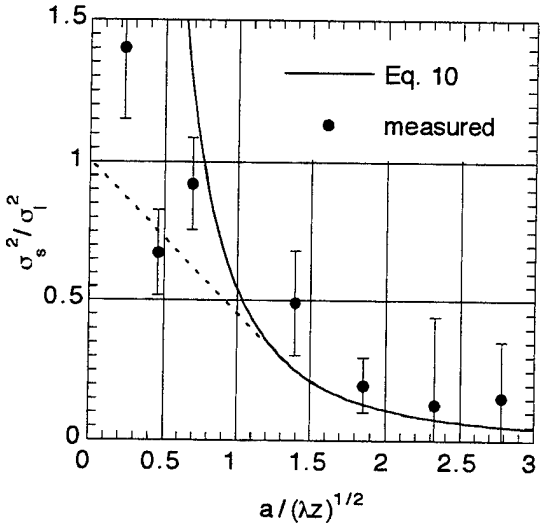

FIG. 6 Measurements of ratio σ_s^2/σ_I^2 and curve given by Eq. 10. Dashed line is expected behavior for $a/\sqrt{\lambda z} < 1$.

Since σ_s^2 approaches σ_I^2 as the aperture radius goes to zero, σ_s^2/σ_I^2 must tend to one for small a. Equation 10 is not valid for $a/\sqrt{\lambda z} < 1$, so a dashed line is plotted in Fig. 6 to indicated the expected behavior of the results for small a. As seen in the figure, Eq. 10 diverges for small a which is physically unrealistic. For $a/\sqrt{\lambda z} > 1$ the agreement between measurements and Eq. 10 is reasonably good. The main source of dispersion of the data points is caused by the fact that the measurement of σ_s^2 and C_n^2 is not simultaneous. Measurement periods for σ_s^2 were approximately 10 S while C_n^2 is based on 60 S of scintillation measurements. The error bars are based on the standard deviation of six separate C_n^2 measurements made by the scintillometer within each 60 S period. The UV source aperture had a radius of 3.2 mm during the measurements.

7. PROBABILITY DENSITY FUNCTION FOR INTENSITY

It is well known that the probability distribution p of intensity fluctuations caused by weak turbulence is described to good accuracy by a log-normal function. According to Ishimaru (Ref.7), turbulence may be considered weak if σ_I^2 is considerably smaller than 0.2 - 0.5. If I is the normalized intensity then p(I) may be written (Ref. 1)

$$p(I) = \frac{1}{2I\sigma_\chi\sqrt{2\pi}}\exp\left(-\frac{[\ln I + 2\sigma_\chi^2\ ]^2}{8\sigma_\chi^2}\right), \tag{11}$$

where σ_χ^2 is the variance of the log-amplitude of the transmitted wave front. σ_χ^2 is related to the measurable σ_I^2 by

$$\sigma_\chi^2 = \frac{1}{4}\ln(\sigma_I^2 + 1). \tag{12}$$

An example of a measured scintillation probability density is shown in Fig. 7a along with a best-fit curve from Eq. 11 obtained for $\sigma_\chi^2 = 0.06$. The data in Fig. 7a was collected with UV receiver and source aperture of 3.2 mm and C_n^2 approximately equal to 2×10^{-13} $m^{-2/3}$. For the path length and C_n^2 of this measurement ,the UV scintillation for a point source and receiver would have been approximately $\sigma_I^2 = 0.6$ which is within the strong turbulence regime. Thus the aperture averaging effect has restored the pdf to nearly a log-normal. Other distributions normally associated with strong turbulence and strong scintillation are the Rice-Nakagami and K class distributions (Ref. 8).

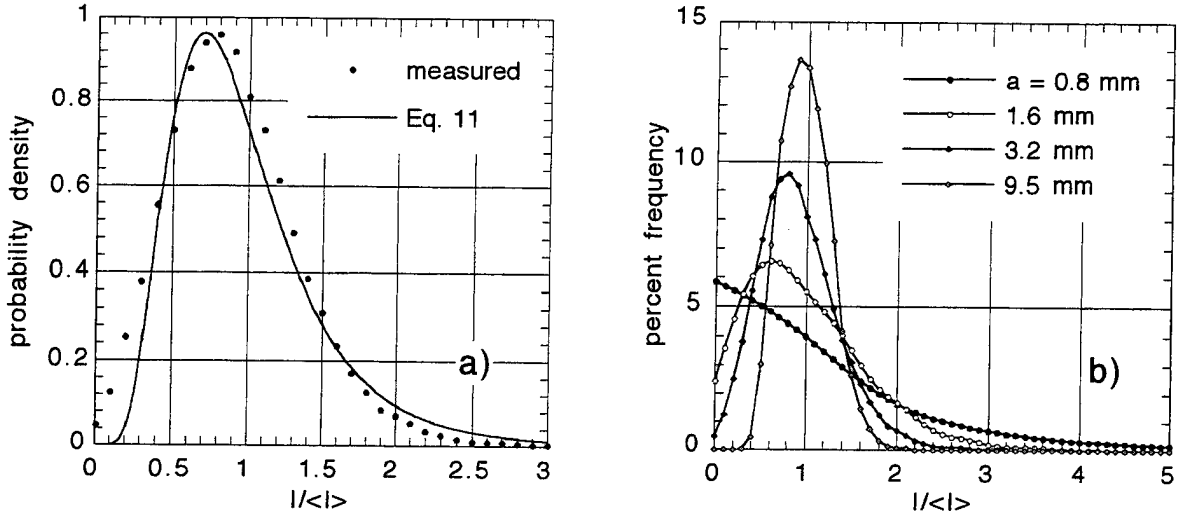

FIG. 7 Probability density function of UV scintillations compared to a best-fit log-normal function ($\sigma_\chi^2 = 0.06$) (a), pdf with different receiver apertures ($C_n^2 \cong 2.0 \times 10^{-13}$ $m^{-2/3}$).

Figure 7b shows pdfs measured with receiver apertures from 0.8 mm radius to 9.5 mm radius all under conditions with C_n^2 between 1×10^{-13} to 3×10^{-13} $m^{-2/3}$. For small apertures the probability density is spread out over a wide range of intensities and does not drop to zero for $I/\langle I \rangle = 0$. The skewing of scintillations to low intensity is characteristic of strong-turbulence pdfs. For larger apertures, the averaging effect causes the intensity probability to be restricted close to the average value, $I/\langle I \rangle = 1$.

8. POWER SPECTRUM OF SCINTILLATIONS

The temporal frequency distribution of scintillations depends on turbulence structure and the wind speed component v (m/s), perpendicular to the propagation path. A characteristic scintillation frequency is given by (Ref. 9)

$$f_o = \frac{v}{\sqrt{2\pi\lambda z}} \quad . \tag{13}$$

For our experiments $f_o \cong 59v$ Hz. the ratio of f_o in the UV to f_o at visible wavelengths is $\sqrt{\lambda_{vis}/\lambda_{UV}}$ or approximately 1.5 for $\lambda_{UV} = 260$ nm and $\lambda_{vis} = 550$ nm. According to Ref. 9, the temporal power spectrum amplitude for both spherical and plane waves is proportional to C_n^2 and varies as $\lambda^{-2/3}$ and $z^{7/3}$. Thus at a given frequency, and under identical conditions, the power spectrum components in the UV would be 1.7 times greater than in the visible for $\lambda_{UV} = 260$ nm and $\lambda_{vis} = 550$ nm.

Aperture averaging shifts the temporal power spectrum to lower frequencies as the smaller speckles which contribute the high frequencies are averaged out. This is illustrated in Fig. 8. The peak frequency for the 1.6 mm radius aperture is between 80 and 100 Hz while for the 9.5 mm radius aperture the peak frequency is between 25 and 50 Hz. For both measurements, the condi-

tions were similar (the measurements were made with 15 min of each other) with C_n^2 approximately equal to 2 x 10^{-13} $m^{-2/3}$ and the wind perpendicular to the path with v approximately 2 m/s. Thus aperture averaging has reduced the peak value from approximately 120 Hz, given by Eq. 13.

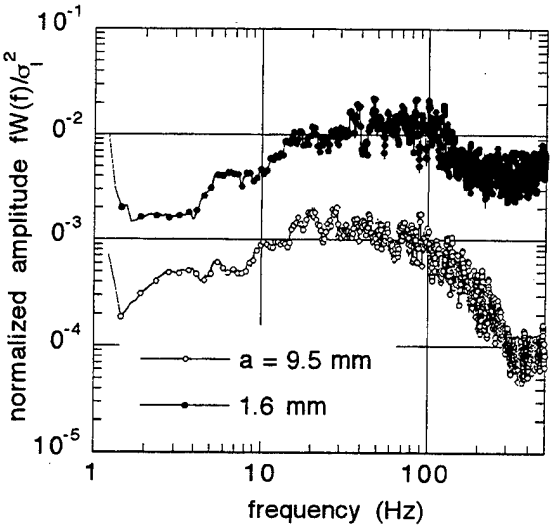

FIG. 8 Temporal power spectra normalized by σ_I^2 for apertures 1.6 mm and 9.5 mm radius. The data for 9.5 mm aperture is displaced down one decade for clarity.

9. CONCLUSIONS

The effect of atmospheric optical turbulence on EO systems is well known in the visible and IR wavebands but has not been studied in the UV even though new applications for the SBUV waveband from 240 to 280 nm have been found for military surveillance and target detection. The intensity of atmospheric optical turbulence is specified in terms of the refractive index structure parameter C_n^2. Although the spectral refractivity of air increases rapidly for wavelengths approaching the UV, C_n^2 is essentially the same in the SBUV as it in the visible.

Turbulence effects may be more pronounced in the UV than in the visible. For example, scintillation in the SBUV can be expected to be 2.5 times as intense as in the visible under similar, nonsaturation conditions. For a given path length, UV radiation would saturate or reach its maximum value of approximately 2.3 for a C_n^2 that is 42% of the C_n^2 required to saturate visible light, assuming λ_{UV} = 260 nm and λ_{vis} = 550 nm. Also, for a given C_n^2, UV radiation would saturate for a path length that is 62% of the value required to saturate visible light. In other words scintillation is more than twice as intense in the UV than it is in the visible and saturation conditions are encountered for turbulence intensities and path lengths that are about half those required to saturate visible light.

The characteristic size of turbulence induced speckles is $\sqrt{\lambda z}$. This parameter is approximately 30% smaller in the SBUV than in the visible thus making the UV scintillation measurements more susceptible to the effect of aperture averaging than measurements would be in the visible.Measurements of UV scintillation index as a function of C_n^2 showed the combined effect of aperture and source averaging was significant even for the smallest aperture used (0.8 mm radius). The reduction in scintillation caused by aperture averaging was found to be in reasonable agreement with a theoretical model for apertures larger than $\sqrt{\lambda z}$ or approximately 3 mm radius. It was also found that the probability density function for UV scintillations followed a log-normal distribution when the scintillation index was reduced below 0.1 as a result of aperture averaging. For high turbulence

conditions, apertures smaller than $\sqrt{\lambda z}$ yielded probability density functions skewed to small intensities as expected in the high turbulence regime. Aperture averaging also manifest itself in measurements of scintillation temporal power spectrum with the peak of spectral power shifted down by a factor of 2 for a 9.5 mm radius aperture compared to a 1.6 mm radius aperture. In general the peak power spectrum frequency is approximately 1.5 time higher in the SBUV than in the visible.

The implications of atmospheric optical turbulence on EO systems operating in the SBUV depend on the specific system and its use. Ground-based radiometer systems for target detection will frequently be in the saturation regime but aperture averaging provides a natural low pass filter that negates the turbulence induced scintillation to some extent.

10. ACKNOWLEDGMENTS

The authors would like to thank Mike Duffy, DREV for processing the raw UV scintillation data and Michèle Cardinal for assistance in setting up the experiment.

11. REFERENCES

1. Smith, F. G., Ed. 1993. The infrared & electro-optical systems handbook Vol. 2, Section 2.2.6, SPIE Optical Engineering Press, Bellingham.

2. Thiermann, V., 1992. "A displaced-beam scintillometer for line-averaged measurements of surface layer turbulence", 10th Symposium on Turbulence and Diffusion, Portland, Or.

3. Hutt, D. L. and F. Trépanier, 1995. "Surface layer turbulence measured with the Scintec SLS-20 scintillometer", Proc. SPIE 2471 Atmospheric Propagation and Remote Sensing IV, Orlando, FL, pp. 461-470.

4. Edlén, B., "The dispersion of standard air", J. Opt. Soc. Am., 43, 339-344 (1953)

5. Fried, D. L., "Aperture averaging of scintillation", JOSA 57, 169-175 (1967).

6. Wolfe, W. L. and G. J. Zissis, Eds., The Infrared Handbook Revised Edition, Chap. 6, Environmental Research Institute of Michigan (1989).

7. Ishimaru, A., "The beam wave case and remote sensing", Laser Beam Propagation in the Atmosphere, J. Strohbehn (Ed.), Springer-Verlag, New York (1978).

8. Mudge, D., A. Wedd, J. Craig and J. C. Thomas, "Statistical measurements of irradiance fluctuations produced by a reflective membrane optical scintillator", Optical & Laser Technology, 28 381-387 (1996).

9. Clifford, S. F., "Temporal-frequency spectra for a spherical wave propagating through atmospheric turbulence", J. Opt. Soc. Am. 61, 1285-1292 (1971).

Variability of ground-level ozone concentration and correlation with meteorological conditions and air mass origin

D.L. Hutt, M. Duffy and C. Cully

Defence Research Establishment Valcartier
2459 Pie XI Blvd., North, Val-Belair, Quebec, G3J 1X5, CANADA
Tel: (902) 426 3100, FAX: (902) 426 9654, email: daniel.hutt@drea.dnd.ca

ABSTRACT

Stratospheric ozone absorbs solar ultraviolet radiation from 240 to 280 nm thus eliminating solar irradiance at ground level. As a result, this waveband is called "solarblind ultraviolet" (SBUV). The absence of solar background means that local sources of UV radiation can be detected with simple radiometer-type sensors. Unfortunately, trace amounts of tropospheric ozone may have a significant impact on the intensity of the received signal. For example, typical ozone concentrations of 40 parts per billion (ppb) result in a transmittance of only 35% in the SBUV for a 1 km path. Furthermore, tropospheric ozone exhibits high variability which depends on local meteorology and geography. To investigate these variations, measurements of ozone concentration at a height of 10 m above ground level were made continuously from June to September, 1997 at Valcartier, Québec. The ozone concentration showed a pronounced diurnal cycle and showed some correlation with simultaneously measured meteorological parameters. Plots of air mass back-trajectories showed that local ozone concentration is linked to air mass origin.

1. INTRODUCTION

A standard altitude-profile of atmospheric ozone for mid-latitudes is shown in Fig. 1a. Although ozone concentrations are hundreds of times lower in the troposphere (altitudes less that 10 km) than in the stratospheric ozone layer, concentrations may be sufficiently high to limit the performance of missile approach warning systems (MAWS) operating in the solarblind ultraviolet (SBUV) waveband from 240 to 280 nm. The transmission over a 1 km horizontal path can vary by nearly an order of magnitude for the range of surface ozone values which are commonly observed as shown in Fig. 1b. As a result, the surface ozone concentration is the most significant unknown in modelling propagation in the SBUV waveband.

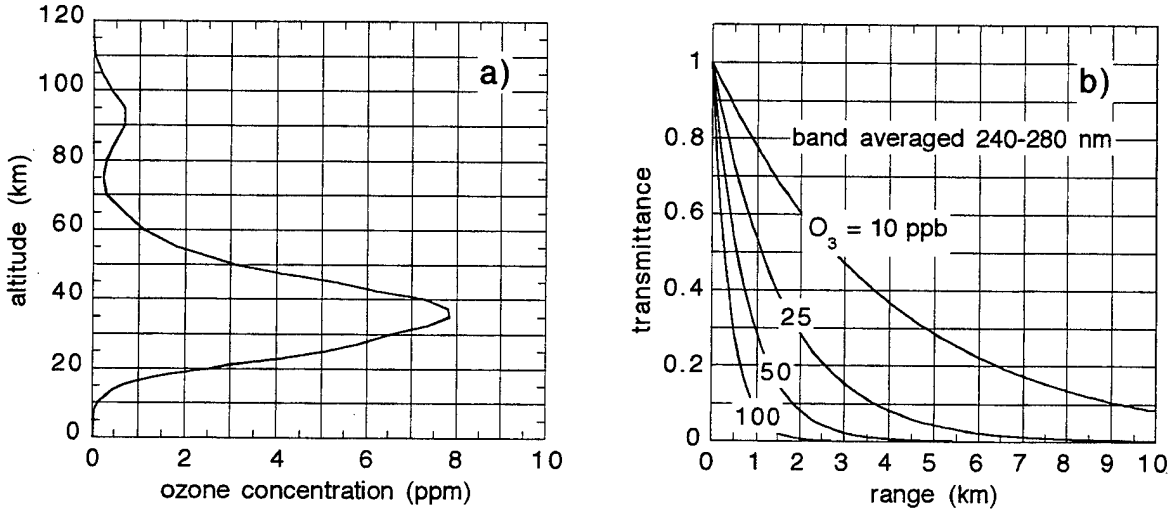

FIG. 1 Altitude-profile of atmospheric ozone (Ref. 1) (a) and band-average transmittance in the SBUV for different ozone concentrations (b).

Local ground-level ozone concentrations represent an equilibrium between a multitude of chemical production and destruction processes which are not entirely understood. Weather plays a role in determining tropospheric ozone concentration through the availability of solar radiation, turbulent mixing and the transport of ozone producing chemicals. As a result of the interaction of these disparate forces, ozone concentration is difficult to estimate and even more difficult to forecast. Ozone concentration varies with geographical location particularly with respect to distance from urban and industrial areas, thus information on ozone concentration is site-specific. Ozone concentration also exhibits fluctuations on time scales from minutes to years so information on the frequency distribution is useful only if based on a sufficiently long series of measurements.

2. SOURCES OF TROPOSPHERIC OZONE

Tropospheric ozone results from both tropospheric photochemical production and transport of ozone-laden air from the stratosphere. It has been estimated (Ref. 2) that the tropospheric photochemical production of ozone is about four times greater than the ozone originating in the stratosphere. Fabian and Pruchniewiez (Ref. 3) report that the mean annual flux of stratospheric ozone is greatest in mid-latitudes between 30° N and 60° N. According to Chung and Dann (Ref. 4), the seasons of maximum ozone concentration in the stratosphere (late winter and early spring) are expected to be the times of strongest transport to the troposphere. Thus the contribution of stratospheric ozone may be partly responsible for seasonal variations in tropospheric ozone. Some of the processes that lead to the exchange of ozone from the stratosphere and troposphere include large scale eddy transport and seasonal changes in the height of the tropopause as described by Reiter (Ref. 5).

The reaction responsible for ozone production is the combination of atomic oxygen (O) at ground state with molecular oxygen (O_2) in the presence of a third body (M), required for momentum and energy conservation:

$$O + O_2 + M \rightarrow O_3 + M \,. \qquad (1)$$

In the troposphere, the main source of atomic oxygen (Ref. 6) is the photodissociation of nitrogen dioxide NO_2:

$$NO_2 + h\nu \rightarrow NO + O \qquad (2)$$

which can take place with wavelengths of sunlight greater than 290 nm (in the stratosphere, atomic oxygen is created directly by the photodissociation of molecular oxygen O_2, which requires more energetic photons with wavelengths less than 240 nm). However, nitric oxide (NO) reacts rapidly with ozone to produce NO_2 and O_2. Thus NO_2 is required for the production of ozone but produces NO which destroys the ozone. The resulting equilibrium may be expressed as

$$[O_3] = K[NO_2]/[NO] \,, \qquad (3)$$

where K is a constant that depends on the intensity of solar radiation (Ref. 7). There are many sources of NO_2 including aircraft and automobile exhaust, and oxidation of methane, formaldehyde and carbon monoxide in the presence of NO (Ref. 8).

3. NEAR GROUND-LEVEL OZONE MEASUREMENTS

A series of measurements of ozone concentration near the ground were carried out from 28 June to 28 August, 1997 at the Defence Research Establishment Valcartier (DREV) located 20 km northwest of Quebec City. The coordinates of DREV are approximately 46.9N, 71.5W. The purpose of the measurements was to establish a database of ozone concentration at this location and to investigate the relationship between ozone levels and meteorological parameters and air mass origin. The local environment at DREV is rural. The measurements were made on top of a

three-story building at a height of approximately 10 m above ground level. The ground altitude at the measurement site is 353 m above sea level.

Ozone concentration was measured with a model 1008-AH UV photometric ozone analyzer manufactured by Dasibi Corp. The 1008-AH has a range of 0 to 1000 ppb ozone concentration with an accuracy and noise of 1.0 ppb. The time constant is 20 s and an analog output of 1 mV/ppb is provided. Ozone concentration was recorded every 10 s by a computerized data acquisition system which read the analog output. Ozone is highly reactive and care must be taken to ensure that intake tubes are very clean, made of a non-reactive material such as teflon or glass and kept as short as possible. For our measurements the ozone analyzer was located on the roof of a laboratory building inside a shelter with a 50 cm teflon intake tube. A teflon air filter was used at all times at the instrument intake and changed approximately once every week according to the manufacturers instructions. The calibration of the ozone analyzer was checked at the beginning and end of the measurement period by sampling known ozone concentrations produced by a Dasibi ozone calibrator.

Other standard meteorological parameters were also measured: solar irradiation (insolation), air temperature and humidity, atmospheric pressure, rain rate, wind speed and direction and visible extinction coefficient. All meteorological sensors were located within 5 m of the ozone sensor. Figure 2 shows the entire series of ozone concentration measurements displayed as five-minute averages. The wide range of ozone values encountered and the regular diurnal variation are apparent in the figure.

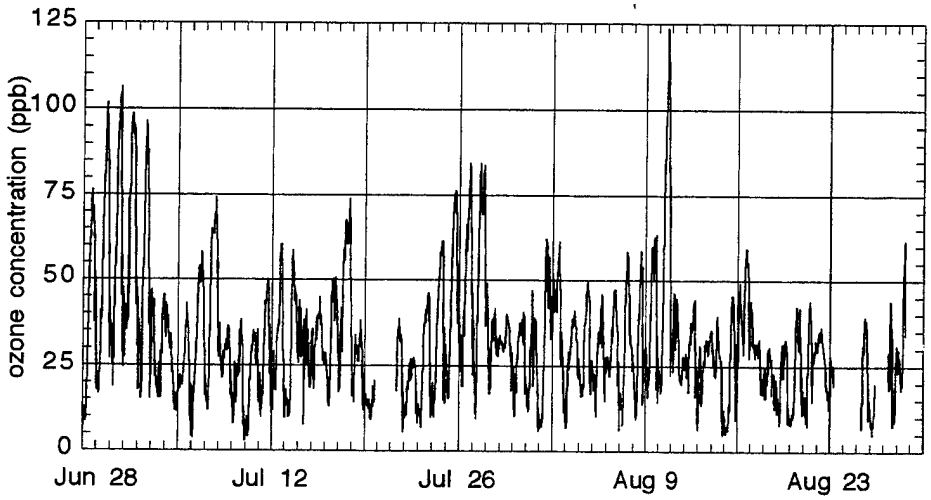

FIG. 2 Ozone concentration at DREV, 28 June to 28 August, 1997 (five-minute averages).

4. DIURNAL CYCLE OF GROUND-LEVEL OZONE

A time plot of ozone and insolation data for a single day (June 28) is shown in Fig. 3. The plot shows the gradual increase of ozone concentration beginning shortly after sunrise and reaching a maximum at approximately 16:00h. As the processes of ozone production depend on the intensity of solar radiation, the diurnal variations shown in Figs. 2 and 3 are to be expected and have been observed by many investigators (see for example Refs. 9 and 10). Photochemical production increases ozone levels during the day. At night, if a stable nocturnal boundary layer develops, ozone concentration is reduced near the ground by surface deposition (Ref. 10).

A plot of the diurnal variation of ozone concentration based on all recorded data is shown in Fig. 4. The minimum of the mean ozone occurs at 6:00h which is just before sunrise during the summer and this is also the time of maximum boundary layer stability. The daily ozone maximum occurs from 15:00h to 17:00h. Diurnal variations reported by Fehsenfeld and Liu (Ref. 10) recorded during a two-month period at Scotia, PA were similar to those reported here. However, studies made at mountain top locations showed a flatter diurnal cycle with the maximum occurring from 19:00h to 21:00h (Ref. 11) and measurements at American Samoa showed maximum ozone concentrations occurring from 6:00h to 10:00h (Ref. 12). Thus local effects can modify or shift the ozone diurnal cycle.

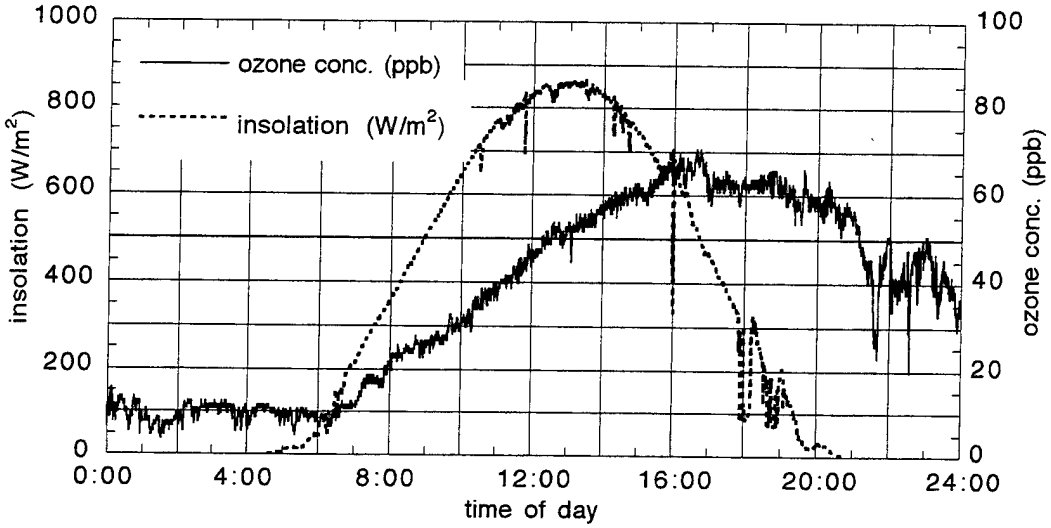

FIG. 3 Ozone concentration and insolation for 28 June, 1997 (10 s data points - no averaging).

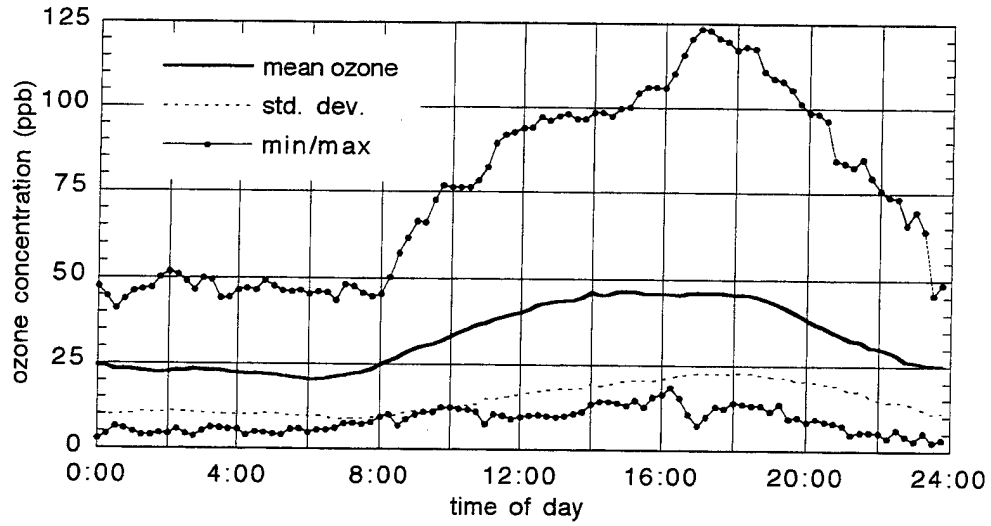

FIG. 4 Diurnal variation of ozone concentration based on 57 days of data.

The effect of weather conditions on ozone concentration is shown in Fig. 5 where the diurnal ozone pattern is plotted for days when the atmospheric pressure was greater than 997 mb or less than 991 mb (997 and 991 mb are the 75th and 25th percentile values of recorded pressure values). High pressure events are characterized by lower night time ozone levels and earlier occurrence of the midday ozone maximum. However, the maximum value of ozone is approximately the same for

both high and low pressure events. These results are similar to those found by Fehsenfeld and Liu (Ref. 10) who attributed the low ozone levels at night during high pressure events to greater boundary layer stability.

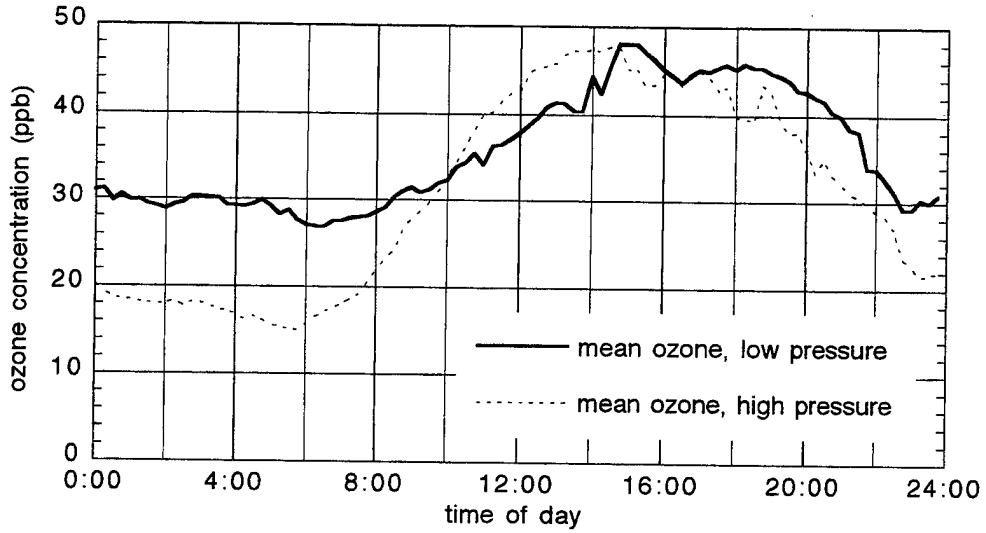

FIG. 5 Diurnal variation of ozone concentration for days of high and low pressure.

Measurements of ozone concentration by Bower et al. (Ref. 13) in the UK showed that in urban areas, maximum ozone concentrations were significantly higher on Sundays than on weekdays and that the ozone maximum occurred about two hours later on Sundays. Diurnal plots of our data for weekdays and weekends are shown in Fig. 6. Weekend ozone levels are significantly higher and occur later in the day, similar to the results reported in Ref. 13. It is believed that scavenging of ozone by locally produced NO_x is responsible for the lower weekday ozone concentrations in urban areas. The same phenomena was also observed to a lesser extent in rural areas.

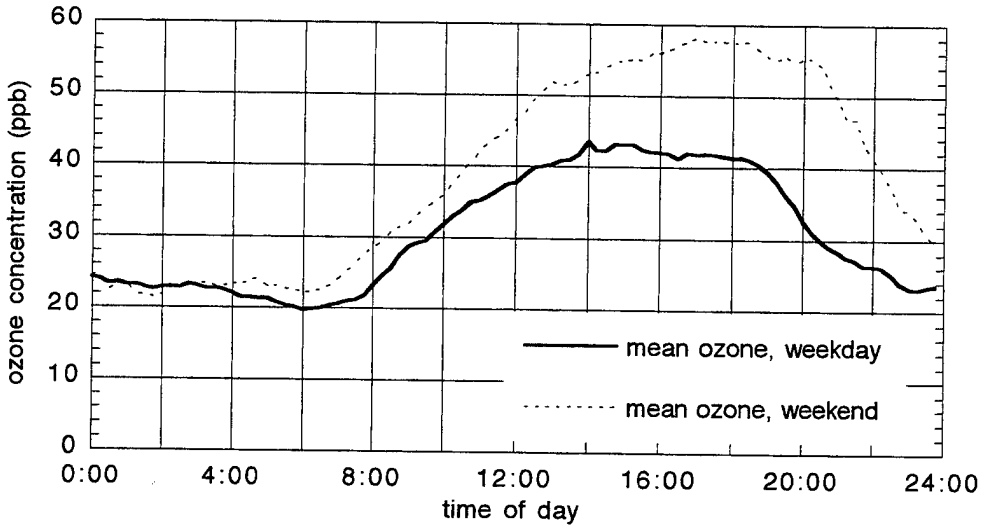

FIG. 6 Diurnal variation of ozone concentration for weekdays and weekends.

5. CORRELATION BETWEEN OZONE AND AIR TEMPERATURE

Scatter plots of ozone concentration versus temperature are shown in Fig. 7a for the data of June 28 and for all 57 days of measurements in Fig. 7b. The ozone concentration is well correlated with air temperature for June 28 which was a cloudless, sunny day. A linear regression on the June 28

data has a slope of 3.95 ppb/deg with a correlation coefficient of 0.97. However the correlation between ozone concentration and air temperature was found to be poor for cloudy days and during conditions of low wind speed. When the data for all 57 days is considered (Fig. 7b) the ozone-temperature correlation is considerably degraded with a linear correlation coefficient of 0.79. Thus air temperature alone is an unreliable predictor of ozone concentration.

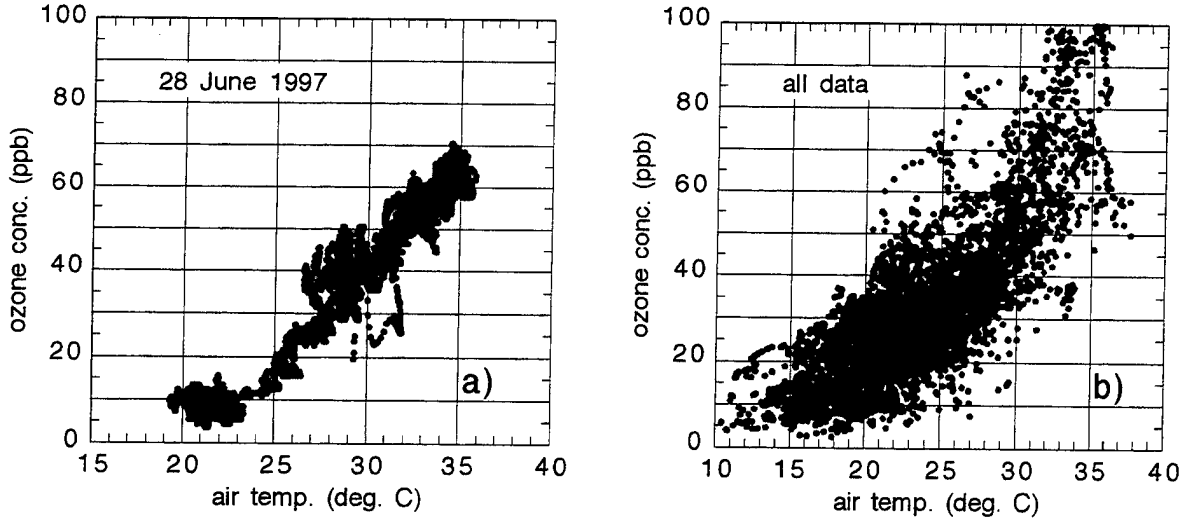

FIG. 7 Ozone level versus air temperature for a sunny day, June 28 (a) and for all 57 days (b).

6. EFFECT OF WIND AND PRECIPITATION ON OZONE

Guicherit (Ref. 14) reported a positive correlation between wind speed and ozone concentration based on eight years of measurements at Delft, NL. However a plot of our ozone measurements versus wind speed (Fig. 8a) shows no significant correlation. Peak and Fong (Ref. 15) showed that ozone concentration depends to some extent on wind direction as a result of transport of ozone precursors. Our data, expressed in Fig.8b as the product of ozone concentration and the unit vector of wind direction shows a tendency for high ozone to be associated with westerly winds. However this may merely be due to the fact that the prevailing winds are from the west and no particular significance has been attributed to the shape of the scatter plot in Fig.8b.

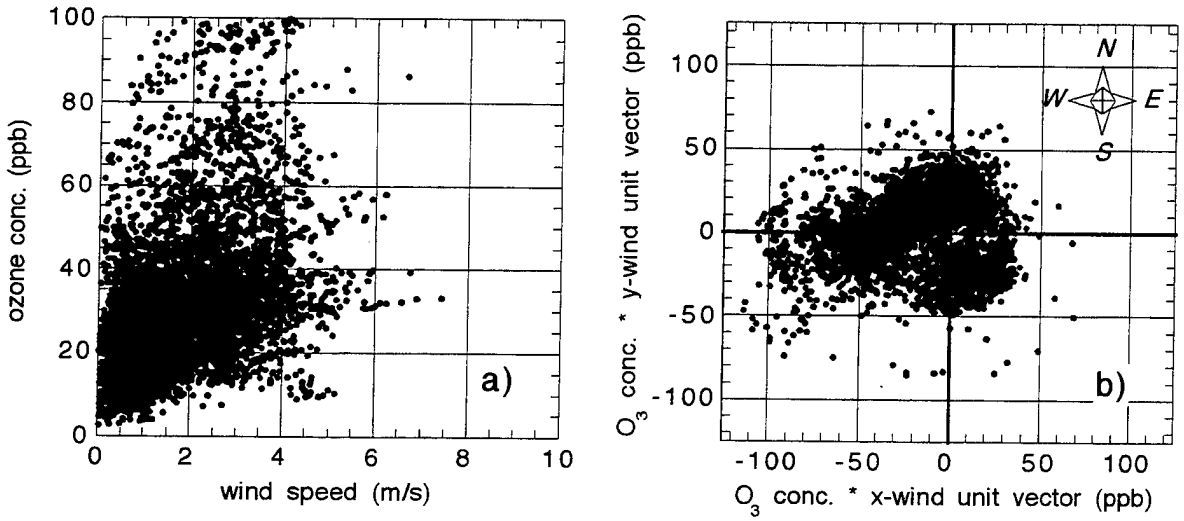

FIG. 8 Dependence of ozone concentration on wind speed (a) and wind direction (b).

It has been reported that lightning storms can cause strong ozone fluctuations due to the effect of down draft and the presence of lightning (Ref. 16). Although several lightning storms occurred during our measurements there were no noticeable fluctuations in ozone level. Neither was there any reduction in ozone concentration during periods of heavy precipitation.

7. EFFECT OF AIRMASS TRAJECTORY ON GROUND-LEVEL OZONE

As shown in the preceding sections, ground-level ozone concentration depends on many meteorological variables which in turn depend on synoptic-scale weather such as frontal passages, and high and low pressure systems. High pressure systems are characterized by clear skies, high temperatures, low wind speeds and reduced mixing depths that are favorable for ozone production. Vukovich et al. (Ref. 17) showed that in rural areas of the eastern United States, the highest ozone levels occurred close to the center of high pressure systems. Since weather systems are characterized by their trajectories and the path of air masses determines the loading of ozone precursors, there should be some connection between ozone concentrations and air mass origin.

Figure 9a shows tracks of air mass position for 48 hours preceding arrival at DREV for days when maximum ozone levels exceeded 36 ppb. These days represent relatively high ozone levels occurring for approximately 1/3 of the total number of days. Air mass trajectories for days when the maximum ozone concentration did not exceed 22.5 ppb are shown in Fig. 9b. A comparison of the two figures shows that the high ozone days are associated with westerly air flow while the low ozone days are often associated with northerly air. The westerly air passes over populated areas of the Great lakes while the northerly air comes from areas of very low population. One explanation for the differences between the high and low ozone air trajectories is that the westerly air contains higher concentrations of anthropogenic ozone precursors such as NO_x.

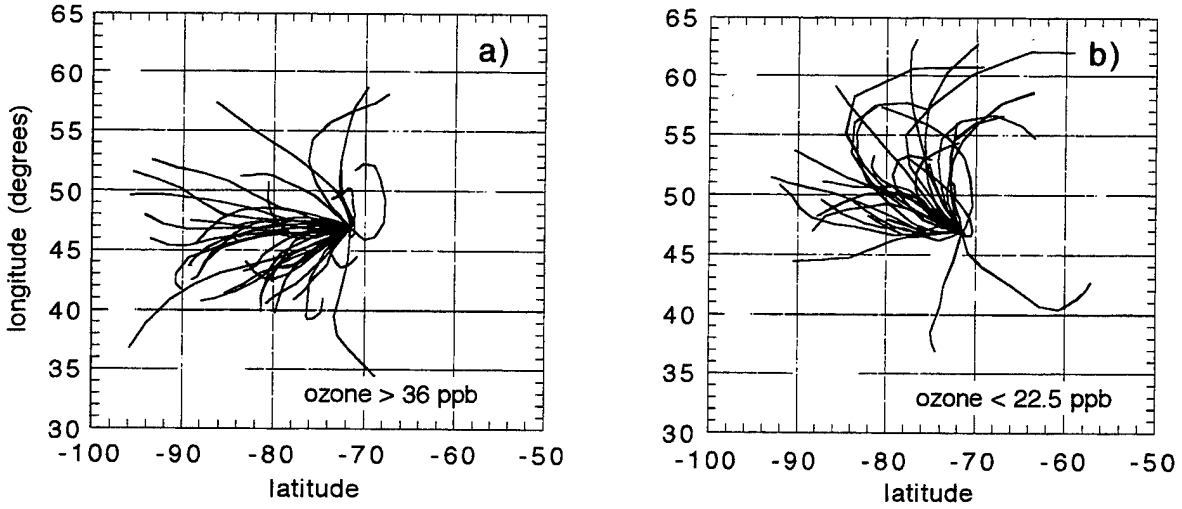

FIG. 9 Air mass trajectories for high-ozone days (a) and low-ozone days (b).

8. GROUND-LEVEL OZONE STATISTICS

The probability distribution of ground level ozone is an important element in the performance analysis of SBUV systems. The probability distribution of all measurements obtained at DREV is shown in Fig. 10a. As with many meteorological variables, the distribution of ozone concentration is well represented by a log-normal function of the form

$$p(R_n) = \frac{A}{2R_n\sigma_\ell\sqrt{2\pi}}\exp\left(-\frac{[\ln R_n + 2\sigma_\ell^2]^2}{8\sigma_\ell^2}\right) \quad (4)$$

where R_n represents ozone concentration normalized by the mean value, A is a scaling parameter and σ_ℓ^2 is the variance of the natural logarithm of R_n.

For the data presented here, the mean ozone concentration was 32.8 ppb. A least-squared best fit log-normal curve on the data is shown in Fig. 10b where $\sigma_\ell^2 = 0.071$ and A = 14.5. The fit between the log-normal curve and the measured frequency distribution is quite good. Thus Eq. 4 could be used to represent the distribution of ozone concentrations for our location in the summer. The data could be further analyzed to yield frequency distributions for day and night times and a longer series of measurements spanning a year or more would allow frequency distributions to be produced representing each season.

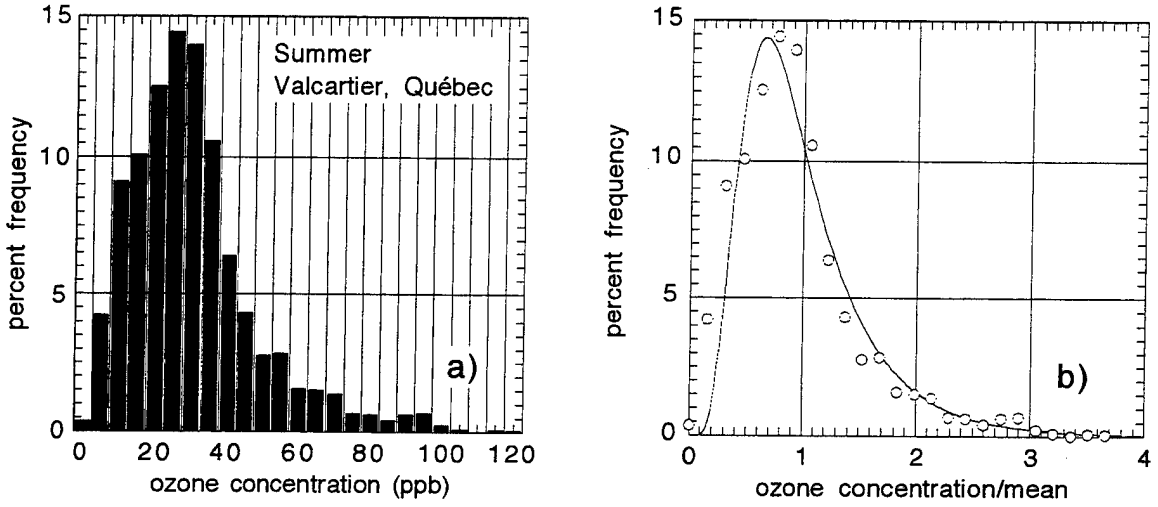

FIG. 10 Frequency of occurrence histogram of all ozone measurements (a) and log-normal curve fitted to the data (b).

9. CONCLUSIONS

We have measured ground-level ozone concentrations at Valcartier, Québec during the summer of 1997 and have attempted to find correlations between ozone level and other meteorological parameters. The diurnal pattern of ozone concentration was found to be similar to the diurnal pattern of air temperature and so ozone concentration and air temperature are positively correlated. For one cloudless day, the correlation coefficient for a linear fit was 0.97 but for all data measured the correlation coefficient falls to 0.79, thus air temperature alone is an unreliable predictor of ozone concentration. The ozone concentration is a function of many environmental variables such as amount of sunlight, concentration of NO_x and other ozone precursors and on atmospheric stability. Night time ozone concentrations were found to be significantly lower during high pressure events than for low pressure conditions possibly due to enhanced atmospheric stability during high pressure conditions. Also, daily maxima of ozone concentration were found to be significantly higher

on weekends compared to weekdays. This difference is believed to be due to scavenging of ozone by locally produced NO_x on weekdays. No significant dependence of ozone concentration on wind speed, wind direction or precipitation was observed.

Some evidence was found for dependence of daily maximum ozone concentration on air mass origin with the high ozone days associated with westerly air flow and low ozone days associated with northerly air. Since the westerly air passes over populated areas of the Great lakes and the northerly air comes from areas of low population density it is believed that the westerly air contains higher concentrations of anthropogenic ozone precursors which lead to higher ozone concentrations. Finally, the time series of ozone concentration measurements provide good characterization of local summer time ozone and can be used for performance prediction of SBUV-based systems. The frequency distribution of ozone concentrations was found to be well represented by a simple log-normal function.

10. ACKNOWLEDGMENTS

The authors would like to thank Dr. Vic Sells of Fanshawe College (London, Ontario) for carrying out the calibration of the Dasibi ozone analyzer and Dr. Robert Lowe and Ms. Hanna Krzeminska for many helpful discussions.

11. REFERENCES

1. Anderson, G. P., S. A. Clough, F. X. Kneizys, J. H. Chetwynd and E. P. Shettle, "AFGL Atmospheric constituent profiles (0-120 km)", Air Force Geophysical Laboratory TR-86-0110 Hanscom AFB (1986).
2. Murphy, D. M. and D. W. Fahey, "An estimate of the flux of stratospheric reactive nitrogen and ozone into the troposphere", J. Geophys. Res., 99, 5325-5332 (1994).
3. Fabian, P. and P. G. Pruchniewicz, Troposphaerisches ozon, Max-Planck-Institute fur Aeronomie, W. Germany (1976).
4. Chung, Y. S., and T. Dann , Observations of stratospheric ozone at the ground level in Regina, Canada, Atmospheric Environment, 19, 157-162 (1985).
5. Reiter, E. R., "Stratospheric-tropospheric exchange processes", Rev. Geophys. Space Phys., 13, 459-473 (1975).
6. Madronich, S., "Tropospheric photochemistry and its response to UV changes", in The role of the stratosphere in global change, edited by Chanin M. L., pp. 437-461, Springer-Verlag, Amsterdam (1993).
7. McKee, D.J., Tropospheric Ozone: Human Health and Agricultural Impacts, 333 pp., Lewis Publishers, London (1994).
8. Krzeminska, H. B. and R. P. Lowe, "Ozone variability assessment for UV sensors", Institute for Space and Terrestrial Science Report No. 3300-96-13, London Ontario (1997).
9. Finlayson-Pitts, B. J. and J. N. Pitts Jr., Atmospheric chemistry: Fundamentals and experimental techniques, 1098 pp., New York (1986).
10. Fehsenfeld, F. C. and S. C. Liu, Tropospheric ozone: Distribution and sources, in Global atmospheric chemical change, pp. 169 - 232, Chapman and Hall, New York (1995).
11. Aneja, V. P. and Z. Li, "Characterization of ozone at high elevation in the eastern United States: Trends, seasonal variations, and exposure", J. Geophys. Res., 97 (D9), 9873-9888 (1992).

12. Oltmans S. J., "Surface ozone measurements in clean air", J. Geophys. Res., 86, 1174-1180, 1981.

13. Bower J. S., Broughton G. F. J., Dando M. T., Stevenson K. J., Lampert J. E., Sweeney B. P., Parker V. J., Driver G. S., Clark A. G., Waddon C. J., Wood A. J., and Williams M.L., "Surface ozone concentrations in the U.K. in 1987-1988", Atmospheric Environment, 23 (9), 2003-2016, 1989.

14. Guicherit, R., "Ozone on an urban and regional scale", in Tropospheric ozone: Regional and global scale interactions, edited by I. S. A. Isaaksen, pp. 49-62, D. Reidel Publishing Company, Boston, 1987.

15. Peake, E. and D. Fong, "Ozone concentrations at a remote mountain site and at two regional locations in southwestern Alberta", Atmos. Environ., 24A (3), 475-480 (1990).

16. Sreedhara, C. R. and V. S.Tiwari, "Short-term ground ozone fluctuations at Poona", Pure and Applied Geophysics, 106-108 (V - VII), 1097-1105 (1973).

17. Vukovich, F. M., W. D. Bach, B. W. Crissman and W. J. King, "On the relationship between high ozone in the rural surface layer and high pressure systems", Atmos. Environ., 11, 967-983 (1977).

A Framework for Solarblind Ultraviolet Radiometry of Point-like Sources

R.M.J. Watson
DERA, St Andrews Rd, Malvern, Worcs, WR14 3PS, UK

Abstract.

An approach to the analysis of solarblind ultraviolet measurements that integrates spectroscopy, temporal signature, atmospheric measurements, radiation and sensor characteristics is presented. The objective is to predict the signal magnitude of an omnidirectional emitting point source such as a missile plume in a given atmosphere. Widely used atmospheric codes such as LOWTRAN and MODTRAN take into account only the contribution of radiation received along a direct path (the transmission) and not the contribution of scattered radiation collected over the sensor field-of-view. A new model, UVS (UltraViolet Sensor) which considers the important effect of multiple scattering is outlined. Radiometric measurements of a UV emitting source and UVS predictions for a wide field-of-view non-imaging solarblind sensor are presented.

1. Introduction

The solarblind ultraviolet (SBUV) is a relatively new waveband to be used in remote sensing applications and novel approaches need to be found for signature prediction and particularly to account for the effects of the atmosphere. Radiation emitted in the solarblind ultraviolet waveband (230-290 nm) tends to be due to highly energetic processes such as occur in flares, missile plumes, arc lamps and intense fires.

Detection in the lower atmosphere, below an altitude about 10 km, relies on the use of a good enough solarblind filter which exploits the abrupt cut-off in the solar spectrum between about 280 and 290 nm. The filter should ensure that virtually none of the background scene and solar radiation is detected while transmitting a significant proportion of inband radiation. Thus, the inherent clutter levels are very low and the signal to background ratio is very high, so reducing the false alarm probability and processing requirements. The type of applications include fire detection and missile warning systems.

In order to detect a small SBUV signal, typically a few hundred photons, the detector needs to have a high gain, e.g. a photomultiplier. A relatively small amount of scattered SBUV radiation can also be easily detected and this allows the possibility of non-line-of-sight detection, perhaps a unique feature in passive electro-optic sensing.

In the SBUV waveband there can be strong and variable absorption by ozone and also appreciable scattering by aerosol particles thus, in order to analyse sensor performance an understanding of the atmosphere is vitally important. Signature prediction is not as well established as in other detection wavebands due to a lack of adequate models, especially for multiple scattering. For example, the LOWTRAN code may be used to evaluate UV transmission only along a direct path and does not consider the contribution of off-axis scattered radiation collected over the sensor's field-of-view. For the case of a sensor and source aligned, the total off-axis scattered contribution to the signal can be the same order of magnitude as the direct contribution, especially for the following combination of factors:

-a wide field-of-view sensor (i.e. about 90° total field-of-view).
-optical thickness greater than about 3 (i.e. a range greater than about 1 km)
-an omnidirectional point source which emits in all directions.

Atmospheric conditions such as small ozone concentration and low visibility or a high number density of weakly absorbing 'large' scattering particles such as rain are also associated with a high degree of SBUV scattering.

The model UVS (UltraViolet Sensor) was developed at DERA Malvern as part of an applied research program. It was primarily designed to evaluate SBUV signal magnitude as a function of range, atmosphere, source and sensor characteristics and to take into account off-axis scattered radiation. Initial calculations indicated that the scattering process was multiple rather than a single scattering process for ranges greater than about 100 m. The current version of UVS may be used for signature prediction, source characterisation and to enable sensors to be calibrated. The aim of this paper is to outline an approach to solarblind ultraviolet radiometry of point sources, and, by way of an example, describe the measurement of a UV emitting flare.

2. Theory and Overview

In its present form UVS assumes an infinite homogenous atmosphere, and, a point-like source and a sensor to be aligned along the line-of-sight. The radiation source is referred to as point-like because the aureole due to scattering increases the apparent size of the source, i.e. when detected using a solarblind UV imager at a range of the order of 1 km or greater.

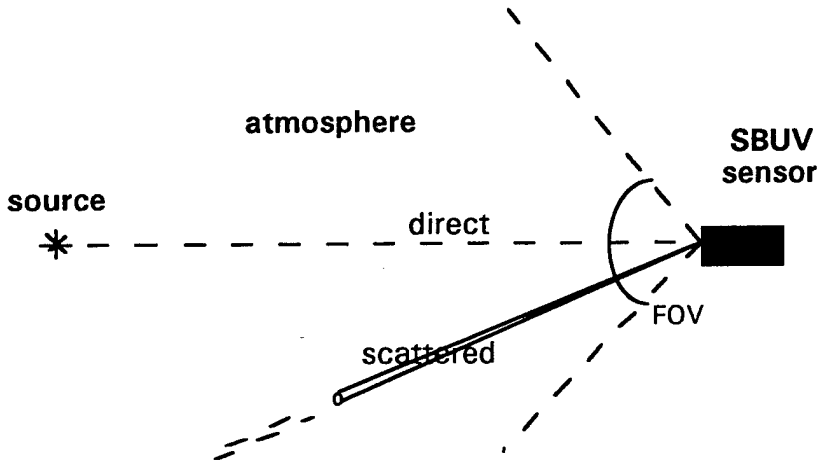

Fig. 1. Radiation geometry in UVS

The UVS model integrates the spatial radiance contributions of rays arriving off-axis at the sensor position (as indicated in figure 1) and it also integrates these rays spectrally. The atmosphere is parameterised in terms of a set of extinction coefficients for absorption and scattering by gas molecules and aerosols and also two scalar phase

functions for the angular distribution of radiation singly scattered by molecules and aerosol particles.

For the case of a radiometer, i.e. a non-imaging wide waveband sensor, the signal is proportional to the number of photons collected per unit area per unit time, referred to here as the photon flux and given the symbol q. The photon flux is a time average of the instantaneous photon arrival rates;

$$q = \frac{1}{\Delta t}\left[\int_{t}^{t+\Delta t} q(t')dt\right] \tag{1}$$

where Δt corresponds to the integration time of the detector.

The photon flux (photons cm^{-2} ms^{-1}) is divided into two contributions; the direct contribution and the scattering contribution,

$$q = q_d + q_s. \tag{2}$$

The background is assumed to be zero since the sensor is solarblind. Note that the irradiance (or power per unit area collected by the sensor) is not used here because the sensor is a photon counting device and that irradiance does not add up spectrally in the same way as photon flux. In the UVS model the radiance of the emitting region is approximated spatially as a delta function and the scattering aereole is considered to be an extended source. The direct contribution is given as

$$q_d = \frac{1}{hcr^2}\int_{\lambda} I_L(\lambda)\lambda R(\lambda)T(\lambda)d\lambda \tag{3}$$

where:-

λ is the wavelength (nm), $R(\lambda)$ is the relative spectral response, $I_L(\lambda)$ is the spectral radiant intensity ($mWsr^{-1}$ nm^{-1}) of the source, $T(\lambda)$ is the atmospheric transmission as a function of wavelength, r is the range (km), h is Planck's constant (6.626×10^{-34} Js) and c is the velocity of light (2.998×10^{8} ms^{-1}). The units used in UVS are indicated here in brackets.

The calculation of atmospheric transmission is well established in principle although further research is probably needed in UV absorption cross-sections of gases and aerosol extinction models in the SBUV. The UVS model evaluates molecular extinction coefficients as a function of wavelength given the absorption cross-sections for ozone, oxygen, NO_2 and SO_2. A correction is made for temperature and pressure. There are also three options for aerosol extinction; firstly the formula used in UVTRAN as a function of visibility [1], secondly tables of aerosol absorption and scattering extinction as a function of visibility and relative humidity for a given aerosol type, (i.e. rural and urban) [2] and thirdly a file of aerosol absorption and scattering extinction coefficient vs. wavelength.

The scattered photon flux is given by

$$q_s = \frac{1}{hc}\int_{\lambda}\int_{\Omega} L_s(\theta,\lambda)R(\theta)\lambda R(\lambda)\mathrm{Cos}\theta d\Omega d\lambda \tag{4}$$

where:-

$L_s(\theta, \lambda)$ is the spectral radiance of an off-axis ray at the sensor position. Because an infinite and homogenous atmosphere is assumed L_s is axisymmetric, $R(\theta)$ is the relative angular response of the sensor, assumed to be axisymmetric, and the cosine factor in Eq. 4 results from the definition of $R(\theta)$ and Ω indicates solid angle.

The scattered and direct contributions for the radiance which appear in Eqs. 3 and 4 may be evaluated by solving the time independent radiative transfer equation or some approximation based on it. A description of the radiative transfer equation is referred to in the textbook by Ishimaru [3]. The direct contribution corresponds to the Beer-Lambert law and relates to the transmission, $\exp(-k_e r)$ where r is the pathlength and k_e is the total extinction coefficient.

Methods to solve the radiative transfer equation for narrow beam geometries [4], infinite homogenous atmospheres and small arrival angles of the scattered rays [3] are to be found in the published literature. Solutions for the scattered contribution are more difficult to find for the general scenario envisaged in this work, i.e. a finite and inhomogenous atmosphere with ground plane and an omnidirectional source with some aspect dependence. Numerical methods or approximations must therefore be used. Monte Carlo is a suitable method to simulate the radiative transfer equation but the computation time and required accuracy are factors to consider. A phenomenological approach is used in UVS which is based on modification of the single scattering calculation according to the range, single scattering albedo, asymmetry parameter (degree of forward scattering) and arrival angle of rays. This method is chosen because it is potentially fast and fairly straightforward to implement. The recursive iteration method of Zachor [5] calculates each successive order of scattering and in the case of large angle off-axis rays for which $\theta > 90°$ and an optical depth of about 3, approximately 15 orders of scattering need to be calculated. The phenomenological method requires effectively one calculation for scattering and is inherently much quicker.

3. UVS Front End

The UVS (UltraViolet Sensor) code is based on the C source code and is compiled for a PC computer. Inputs may be parameters entered by the user or text format files. All outputs are in the form of a text file which can be easily imported into a spreadsheet program or a graphics utility. A wide variety of output quantities such as normalised radiance, transmission, extinction coefficients, irradiance and photon flux contributions should allow easy comparison with other models or to be integrated with data. From the initial conception of the UVS model, a flexible approach was needed so that SBUV radiometric characteristics could be investigated as a function of say, range,

wavelength, ozone concentration, visibility, aerosol phase function, sensor and source characteristics.

As illustrated in Figure 2 the front end of UVS is divided into input areas; source, sensor and atmosphere in which there are options to select various models.

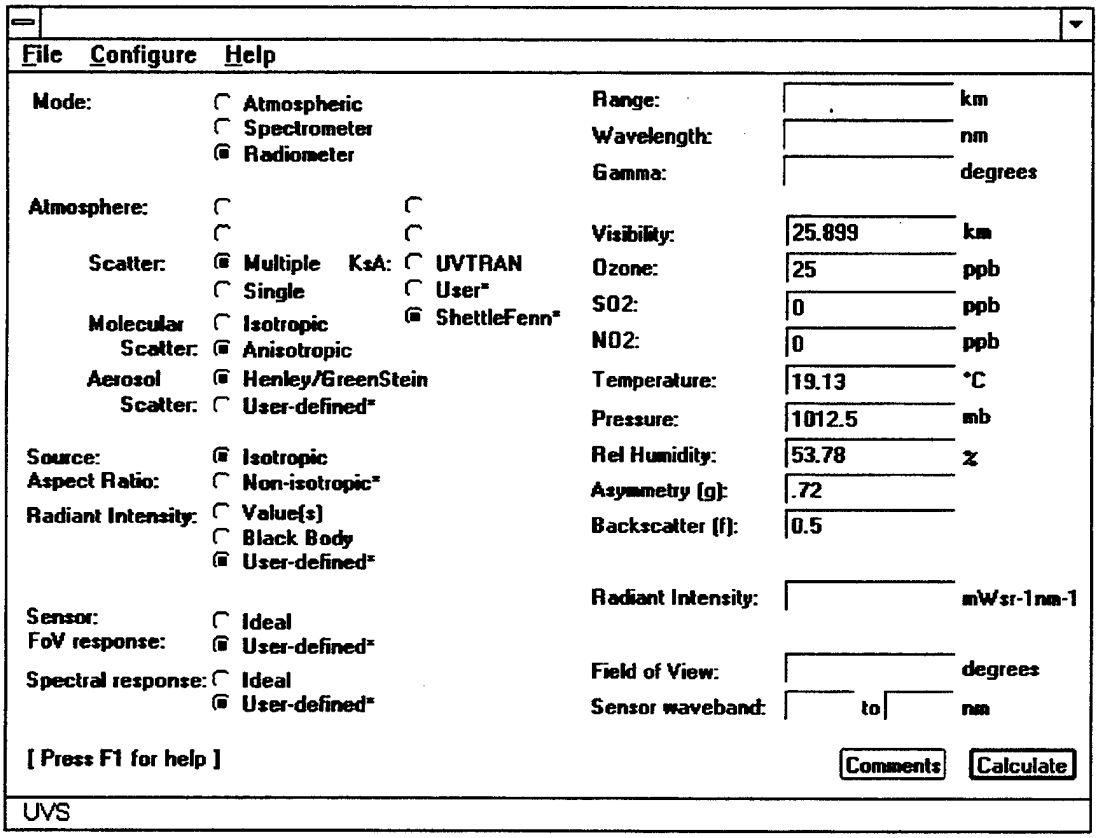

Fig. 2. Front end of UVS

There are also options to input text files of sensor relative angular response, relative spectral response, source spectral radiant intensity, aspect dependence or beam geometry, a time series of meteorological parameters and an aerosol scattering phase function. In this way the user can build up a library of source, sensor and atmospheric characteristics.

4. Example

Solarblind ultraviolet measurements were carried out of a flare (fired in a fixed vertical position near the ground) using two wide field-of-view non-imaging radiometer sensors and a spectrometer. Figure 3 indicates the positions of the radiometers, denoted by S_1 and S_2, at ranges of 87 m and 590 m respectively, and the spectrometer (Rees Instruments), positioned at a range of 87 m. The nearest radiometer S_1 was fitted with a variable aperture which was set to a fixed diameter to avoid saturation. Visibility, temperature, pressure and relative humidity were measured near to the

source position as was the ozone volume concentration (Enviro Technology plc ozone meter).

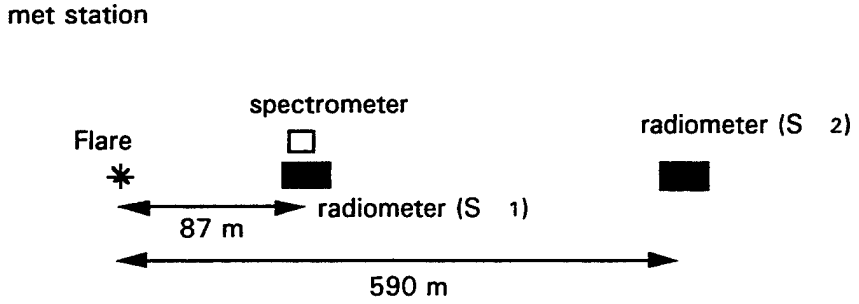

Fig. 3. Sensor and meteorological instrument positions for the measurement of a flare.

The two radiometers have been calibrated for responsivity and non-linear response using a primary standard, a deuterium lamp which was calibrated for spectral radiant intensity by the National Physical Laboratory (NPL).

Figure 4 shows the radiometer signal vs. time for the first 4 seconds after ignition of the flare. The total burn time was about 40 seconds. The signal corresponds to the number of counts registered for the given sample times of Δt =10 ms for S_1 and Δt = 1 ms for S_2.

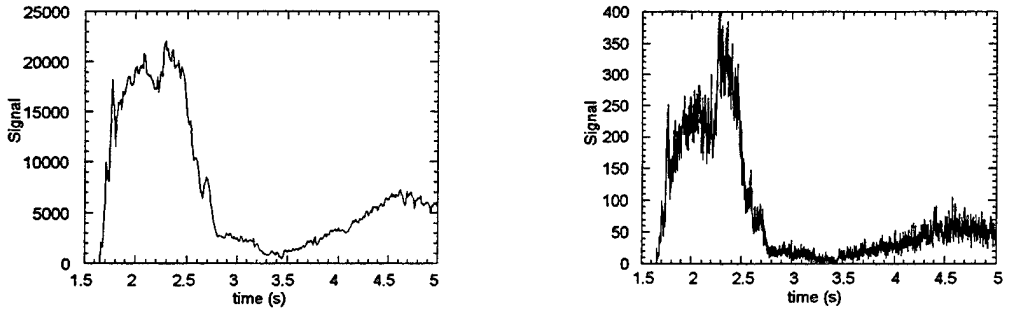

Fig. 4. Signal vs. time for (a) sensor 1 at a range of 87 m and (b) sensor 2 at a range of 590 m.

The spectrometer has been calibrated for relative spectral response. Figure 5 shows the spectral radiant intensity of the flare normalised to 290 nm. The spectrometer is not very sensitive, so a maximum monochromator slit width (0.89 mm) was used and the spectra averaged over a time interval of 5 seconds. At a finer spectral resolution the spectrum shown in Fig. 5 should consist of a continuum and superimposed emission lines.

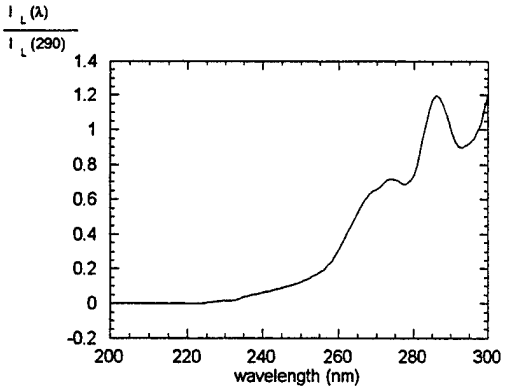

Fig. 5. Spectrum of a flare normalised to 1 $mWsr^{-1}$ nm^{-1} for $\lambda = 290$ nm.

Hence, given the source spectrum, atmospheric parameters and the sensor's relative spectral and spatial response the photon fluxes q_d and q_s for both radiometers could be evaluated using UVS. Table 3 shows the measured meteorological parameters. The photon fluxes evaluated using UVS and transmission (along the line-of-sight) are summarised in tables 4 and 5.

Table 3. Measured meteorological parameters during the flare firing.

Visibility (km)	25.9
O_3 (ppb)	25
Temperature (°C)	19.1
Pressure (mb)	1012.5
Relative humidity (%)	53.8

Table 4. Photon fluxes for a normalised spectrum evaluated using UVS.

Radiometer	Range (m)	q_d (q. cm^{-2} ms^{-1})	q_s (q. cm^{-2} ms^{-1})	q (q. cm^{-2} ms^{-1})
S_1	87	88719	3947	92666
S_2	550	1091.9	294.2	1386.1

Table 5. Transmission values evaluated using UVS and for comparison (in brackets) LOWTRAN 7 values.

Wavelength (nm)	Transmission (590 m)	Transmission (87m)
230	0.157 (0.145)	0.761 (0.696)
250	0.388 (0.387)	0.870 (0.869)
270	0.558 (0.555)	0.918 (0.917)
290	0.747 (0.745)	0.958 (0.958)

To account for the half-plane scattering volume and the presence of the ground the final values of q_s used to evaluate spectral radiant intensity were those in table 4 divided by 2. The calculated photon fluxes for the 'unit' radiation source were therefore, $q(1) = 90692$ q. cm^{-2} ms^{-1} for S_1 at 87 m and $q(1) = 1239$ q. cm^{-2} ms^{-1} for S_2 at 590 m.

The values of signal vs. time (as shown in fig.5) can be converted to experimental values of photon flux (or q_{expt}) vs. time by dividing the signal by the responsivity for each sensor. A correction was also made for the non-linear response to radiation of each sensor and for the aperture used with radiometer S_1. The spectral radiant intensity at 290 nm 'measured' by each radiometer is given by $q_{expt}/q(1)$ and is shown in figure 6.

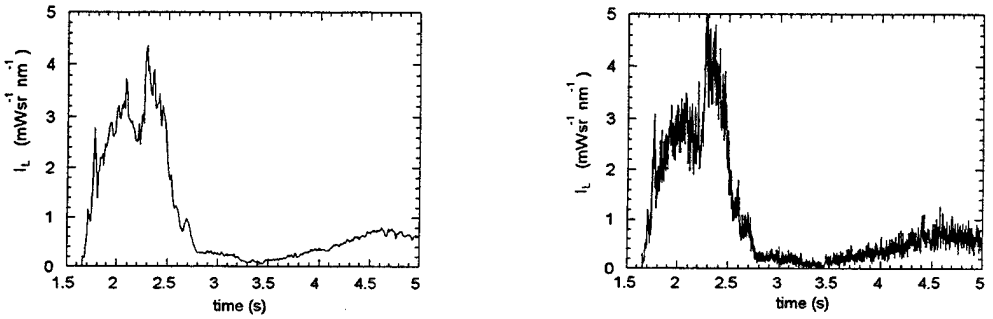

Fig. 6. Spectral radiant intensity (λ = 290 nm) of a flare corrected for atmosphere, scattering, and sensor calibration; (a) radiometer S_1 and (b) radiometer S_2.

5. Discussion

The analysis of the flare measurements show that it is possible using the UVS model to predict the SBUV signal given the spectral radiant intensity and atmosphere and sensor parameters with reasonable accuracy, at least for a range of 0.6 km. A flare was chosen as an example because it is an omnidirectional source and the scattering calculations in UVS are designed for this sort of beam geometry. Not all the parameters used in the model were measured. The aerosol scattering phase function was assumed to be a Henley Greenstein function with asymmetry parameter g = 0.72 which corresponds to an assumed moderate aerosol particle size and polydispersity. The concentrations of the minor absorbing gases SO_2 and NO_2 were assumed to be zero. The result might be slightly different if the spectrum had been measured to a better spectral resolution or that the aspect dependence of radiant intensity of the source was known rather than assumed to be isotropic. It may be argued that there are other factors which have been overlooked such as atmospheric inhomogenities (measurements of visibility and ozone were made at one location) and the nature of aerosol composition and size distribution. The significance of factors such as atmospheric inhomogenities is not known for certain but the initial results using UVS are encouraging.

The UVS values of transmission (for the direct signal contribution) are very similar to the LOWTRAN 7 derived transmission values because the same rural aerosol model and ozone cross-section values were used. The discrepancy at 230 nm in table 5 is due to a difference in the oxygen absorption cross-section values used. The magnitude of the calculated scattering contribution is more difficult to verify experimentally and theoretically. In the example given the contribution of scattering was calculated using UVS to be about 13 % of the direct contribution for a range of 0.6 km. Efforts are continuing to obtain similar data to that presented herein, but for longer ranges or for more optically dense atmospheres where scattering is more significant. More rigorous and accurate models would be needed to verify the scattering predictions of UVS and it is planned to update UVS to incorporate arbitrary sensor and source orientations and a ground plane. A layered inhomogenous atmosphere model might also be incorporated. Prediction of non-line-of-sight SBUV radiation should then be possible and this should allow further verification of the scattering model.

In summary, some of the methods outlined in this paper differ from more conventional approaches to radiometry used in wavebands other than the solarblind ultraviolet. Firstly, the sensor calibration parameters, namely the relative spectral and angular response are integrated with the atmospheric model, secondly, the use of photon flux rather than irradiance and thirdly, a model to account for off-axis multiply scattered radiation. It has been shown that the UVS model can be used to account quite well for atmospheric attenuation and scattering in the particular case of an aligned source and sensor examined here.

Acknowledgement

British Crown Copyright 1998/DERA. Published with the permission of Her Britannic Majesty's Stationary Office.

References

1. Simplified ultraviolet and visible wavelength atmospheric propagation model. E.M. Patterson and J.B. Gillespie. Appl. Opt. **28**, 425-429 (1989).

2. Models for aerosols of the lower atmosphere and the effects of relative humidity variations on their optical properties. E.P. Shettle and R.W. Fenn, AFGL Report AFGL-TR-79-0214 (1979).

3. Wave Propagation and Scattering in Random Media Vol. 1: Single Scattering and Transport Theory. A Ishimaru. Academic Press (1978).

4. Multiple scattering of narrow light beams in aerosols. L.R. Bissonnette. Appl. Phys. B. **60**, 315-323 (1995).

5. Aureole radiance field about a source in a scattering-absorbing medium. A.S. Zachor, Appl. Opt. **17**, 1911-1922 (1978).

Passive Sensing and Specification of Thunderstorms on the Battlefield

Kenneth E. Eis, Mel Nicholls, Al Bedard, and Roger Pielke
Cooperative Institute for Research in the Atmosphere
Colorado State University
Fort Collins CO 80523-1375
Phone: (970) 491-8397 Fax: (970) 491-8241
E-Mail: eis@cira.colostate.edu

Abstract

One of the major shortfalls on the battlefield and at sea is our inability to detect severe weather without the use of active emitting systems such as radar or Lidar. Although thunder has been detected, like lightening in spherics detectors, no passive sensor has ever been used to detect severe weather in non-audible acoustic wavelengths nor has a signal been "interpreted" to yield quantitative information from an acoustic signal. A new technique, which combines new acoustic transducer technology with high-resolution numerical diagnostic modeling has already yielded results. Unambiguous signals from thunderstorms, tornadoes, meteors, and the Space Shuttle have been measured. Thunderstorms have been modeled numerically and the observed pressure signature matches the modeled signal well. The coupling of diagnostic models with the acoustic waveform will allow the signal to be isolated (signal processing) and then the nature of the thunderstorm (hail, turbulence, and severity) calculated. We are not far from a demonstration system that can detect and classify acoustic signatures ~1000 km away - passively.

Introduction

The military has long been unhappy with active sensors on the battlefield. Radio silence has been actively practiced since WWI. Active radar and anti-radiation missiles mix for only a one-sided outcome. Convective weather, undetected and unforecast can also lead to unwanted outcomes. Despite the fact that the US forces can expect superiority on the battlefield and are less concerned about the use of battlefield radars, covert surveillance is still preferred. If the passive storm detection system has a range significantly greater then the active radar, the system is even more attractive.

Colorado State University researchers, in conjunction with Al Bedard of NOAA's Environmental Technical Laboratory (ETL) have been developing such a system over the last three years. The system is composed of three different acoustic sensor systems for the three propagation modes under review and a non-hydrostatic version of RAMS to model the waves. By beam steering, the acoustic array can locate the acoustic source to within approximately 0.1-degree. The waveform and intensity from the observed source can then be compared with the modeled output from the RAMS model. By iteration of the model's input, the two outputs can be made to converge. At convergence, the input parameters of the model represent a good guess for the intensity of the convective system.

Acoustic Propagation

There are three propagation modes of interest in this paper. Figure 1 shows the area of natural infrasound under consideration in a pressure amplitude vs frequency chart. Adiabatic heating processes in the atmosphere generate thermal-acoustic waves. A thunderstorm's latent

heat release acts as an opening piston, which displaces air. This displaced air creates three-dimensional compression waves that move away from the latent heat release site. These waves move at the speed of sound (~300 m/sec), but because of the boundary conditions, only dissipate as $1/(\text{Distance})^{0.5}$.

The second propagation mode is the gravity wave which propagates at about 30 m/sec and which dissipates as 1/(Distance). Since thunderstorms generate both gravity and thermal-acoustic waves, the difference in speeds and dissipation rates helps sort out the two waves but limits the ability of the system to completely separate the two modes at very short detection ranges (<25 km).

Both thermal-acoustic and gravity waves are detected at frequencies of less then one Hz.

The last propagation mode is infrasound that propagates at the speed of sound, dissipates as 1/D and is detected at 1 Hz and higher.

Description of the Sensor Array

Figure 2a shows the layout for one thermal-acoustic microphone. Figure 2b shows the infrasound microphone, and 2c shows the pressure zone microphone used for the gravity wave (mobile) observer platform. This devise is a very high signal to noise ration pressure transducer coupled to a octopus low frequency pass filter. The octopus is actually PVC piping with holes along its length. The reason for the pipe array is to filter out the high frequency turbulence and wind gusts that would add unwanted natural noise to the detected pressure signal.

Figure 3 shows the proposed pattern for the detection system. The gray circles each represent one of the thermal-acoustic sensors in Figure 2. The equilateral triangle geometry for the three adjacent microphones is called an acoustic observatory (AO). The internal AO microphone spacing is approximately 10 km. The AO signals are combined and the signals processed to allow beam steering. It takes two AO's to calculate the location of a signal source. To improve the beam steering location accuracy a third array in included, and the AOs are spaced approximately 200 km apart. Each AO can also detect gravity waves independent of the larger system.

Detected Acoustic Signatures

Figure 4 shows some of the possible sources of infrasound. Our array has successfully detected:

- Thunderstorms with and without hail – ranges varied from 10 of kilometers to well over a 1000 km (Boulder to the Mississippi River Valley).
- Avalanches – An avalanche warning system was the first funded task of an acoustical array system. The overpressures developed by the snow displacing air provide a very strong signal.
- Tornadoes – the infrasound array with much closer spacing (see figure 3) has detected several tornadoes. Tornado signatures are unique in that they represent the output of an acoustic dipole signal. The signature has been detected prior to a NEXRAD signal and verified by surface reports and subsequent vortex touchdown observations.
- Space debris and Shuttles – Bedard and Bloemker (1998) detail their recent detection of a Shuttle reentry and detection of meteor showers.

Modeling

A special non-hydrostatic version of CSU's RAMS model was used to create test thunderstorms and their resulting thermal-acoustic LAM waves and gravity waves. Figure 5 shows the pressure perturbation generated within the model 2702 seconds after a heat source was added to a test atmosphere with realistic vertical structure. Figures 6 and 7 show the thermal-acoustic and gravity waves generated several hundred kilometers distant. Thermal-acoustic waves have a large negative pressure on the leading edge whereas gravity waves have leading positive overpressures. When these waves match the observed patterns other parameters can be diagnosed about the thunderstorm in question. Figure 8 shows the rain condensate values within the modeled thunderstorm. Many other kinetic and thermodynamic features of the storm can be diagnosed from model output.

Current State of System

We have completed sensor selection, including an improved signal to noise ratio pressure transducer. These sensors have collected several storms, meteors, and a shuttle landing. One full three-sensor AO is available. Modeling activity is still improving with improved boundary and tropopause parameterizations. Interestingly, one of the problems currently being investigated by modelers is the larger then modeled thermal-acoustic waves observed in a thunderstorm from this Fall just north of Boulder.

Future Activities

We are planning on running a two AO system in the coming year for an extended period of time. This will allow other phenomena to be detected as well as our first attempts at isolation acoustic signals in more complicated source environments. Besides beam steering, we plan on using other signal processing techniques to isolate superimposed signals that are generated in squall lines and other multi-source episodes.

ACKNOWLEDGEMENTS

This work was sponsored by the DoD Center for Geosciences - Phase II at the Cooperative Institute for Research in the Atmosphere, Colorado State University, under grant DAAH04-94-G-0420.

REFERENCES

Bedard, A.J., Jr., and R. Bloemker, 1997: Detection of space debris and meteor impacts using atmospheric infrasound. (To be published in SPIE Proceedings.)

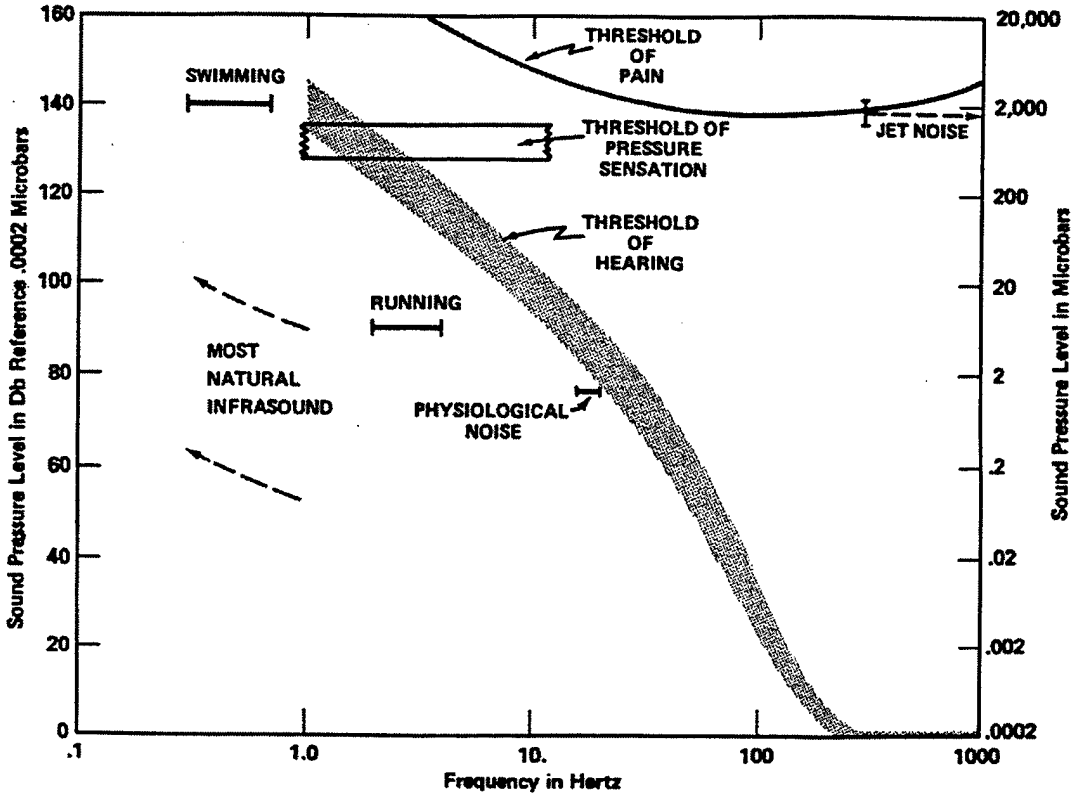

Figure 1

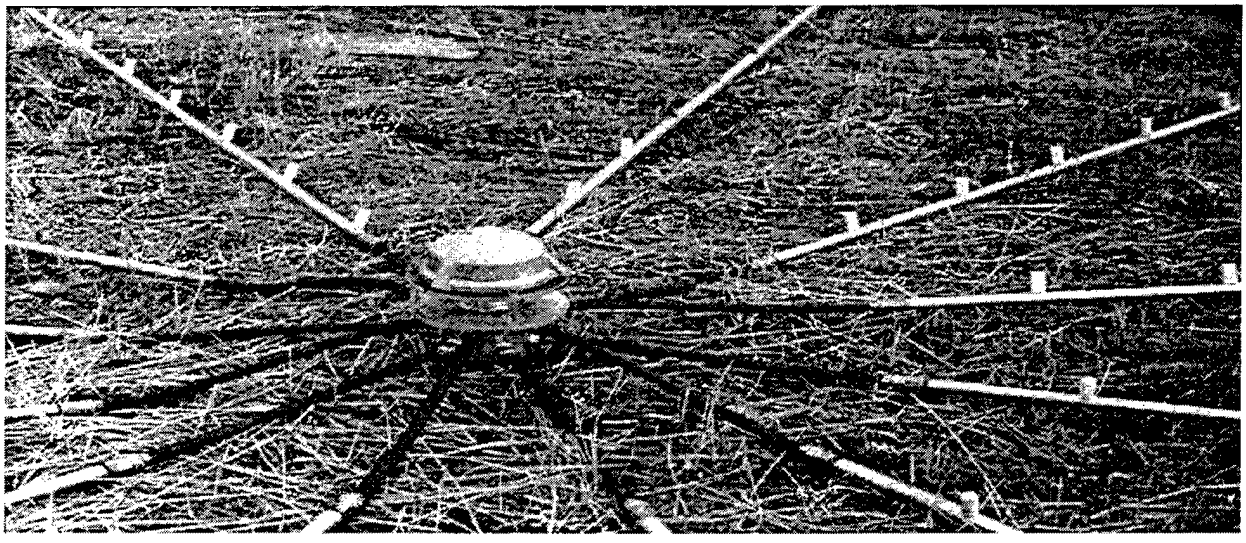

Figure 2a

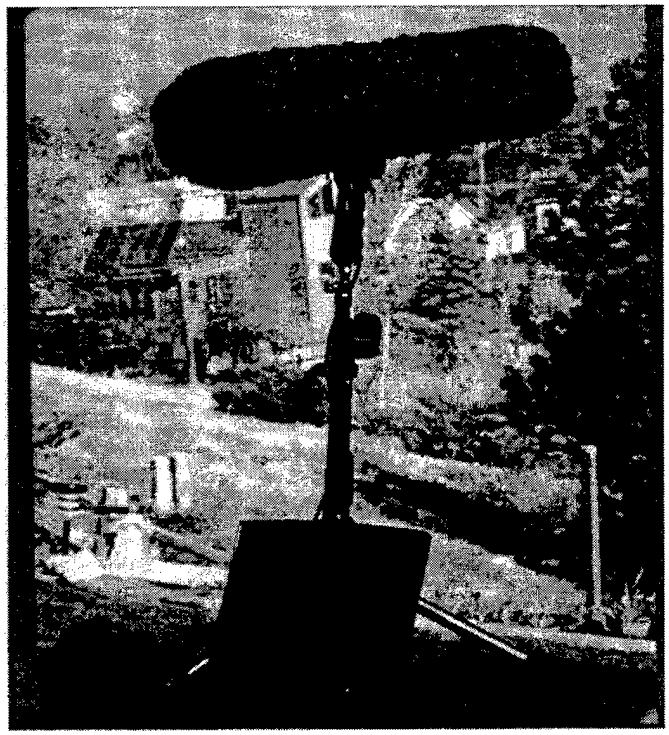

Figure 2b

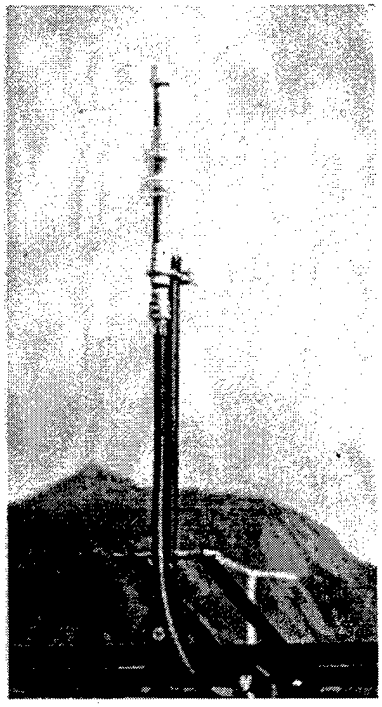

Figure 2c

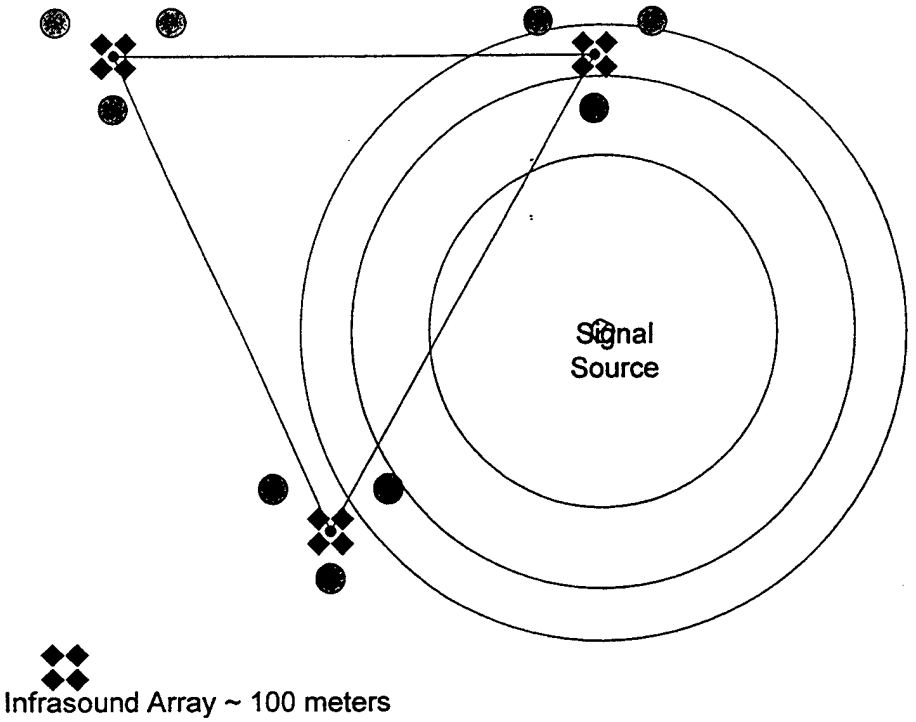

Figure 3

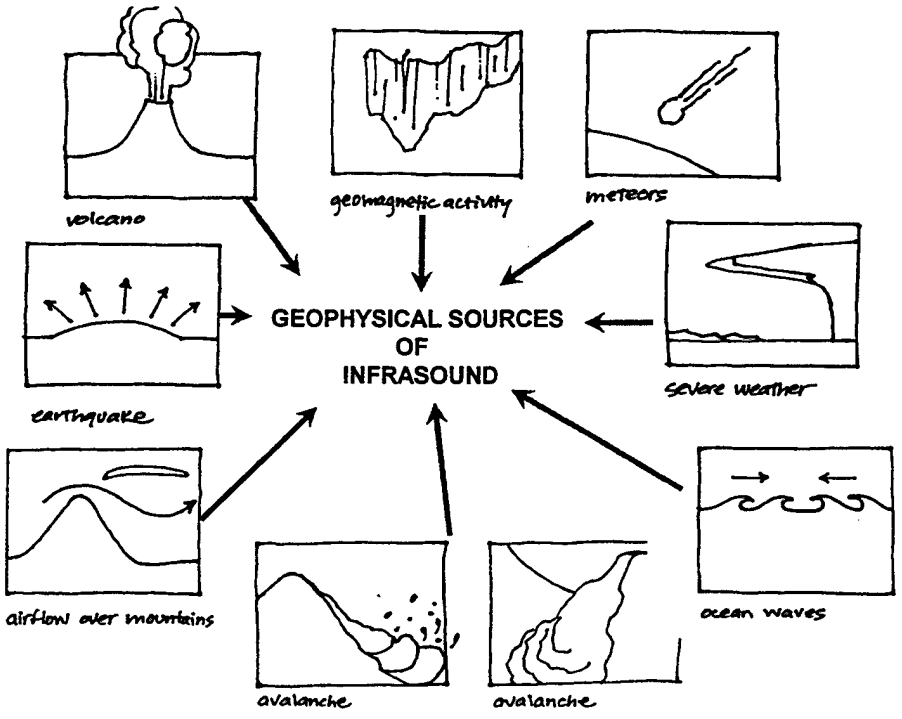

Figure 4

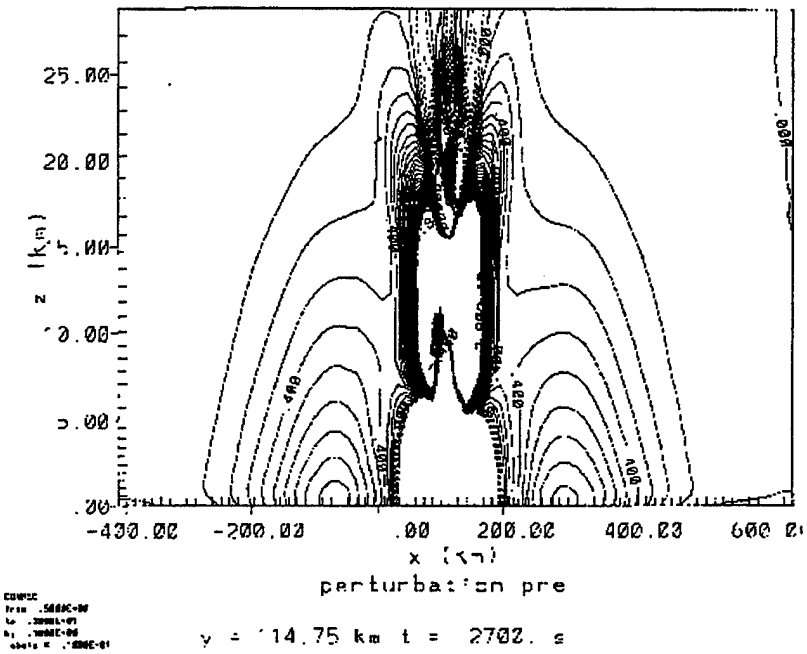

Figure 5

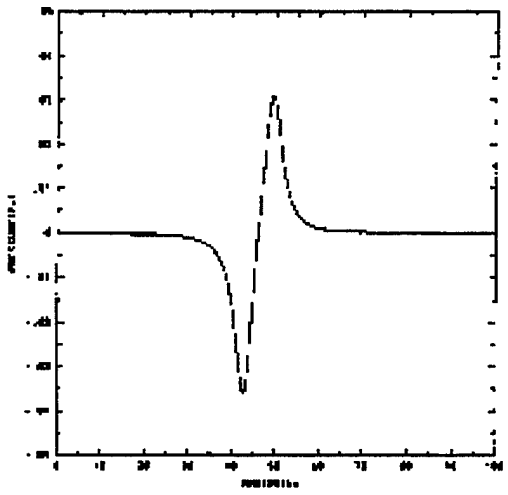

Figure 6

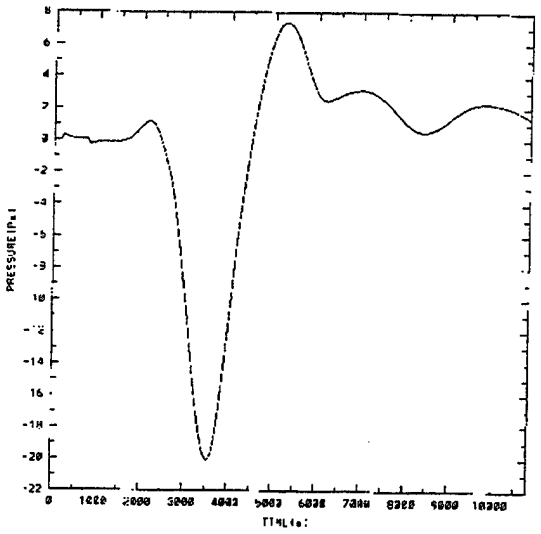

Figure 7

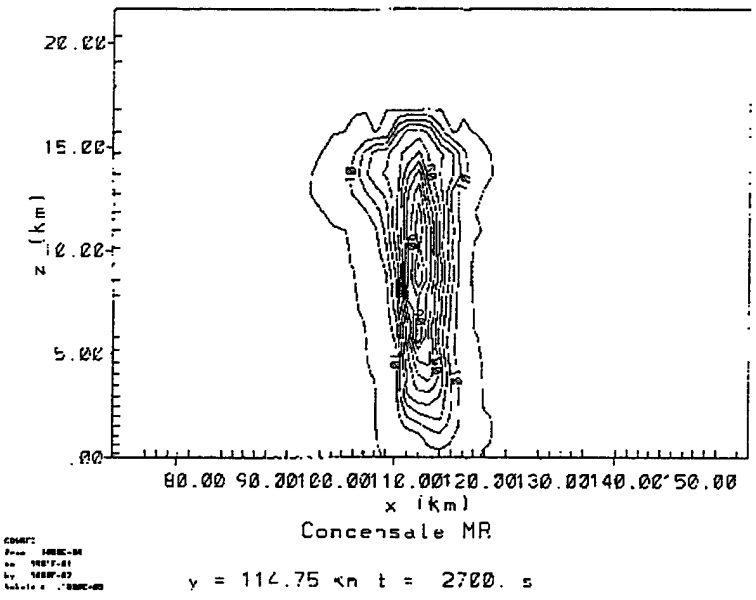

Figure 8

EFFECT OF TURBULENT ANISOTROPY ON DIRECTION-FINDING USING ACOUSTIC SENSOR ARRAYS

D. Keith Wilson
U. S. Army Research Laboratory
ATTN: AMSRL-IS-EE
Adelphi, MD 20783-1197

ABSTRACT

An important factor limiting the performance of acoustical systems used to estimate the direction (bearing) of a source is distortion of the propagating wavefronts caused by atmospheric turbulence. At the low frequencies typically used for detection and tracking applications, the role played by large-scale (energy-subrange) turbulence is especially important. As a result it is necessary to account for such features of energy subrange turbulence as anisotropy and inhomogeneity. The effect of anisotropy on acoustic wave coherence is analyzed in this paper using several rigorous spectral models for turbulent velocity fluctuations in a shear-driven, atmospheric surface layer: an anisotropic Gaussian model, an anisotropic von Kármán model, Kristensen et al.*'s model, and Mann's rapid-distortion model. It is found that turbulent anisotropy dramatically affects estimates of bearing accuracy, even when the spacing between the sensors is small. Bearing estimates are more accurate when the source is in the crosswind direction than when it is upwind or downwind.*

1. INTRODUCTION

An array of acoustical sensors can be used to determine the direction (bearing) of a source. The operational principle is simple: by using phase differences across the array, the orientation of the incident wavefronts can be determined. Provided there is little refraction, the wavefront normals correspond to the bearing of the source.

When acoustical arrays are deployed for the purpose of bearing estimation in the atmosphere, an important factor limiting the fidelity of the estimate is distortion of the propagating wavefronts caused by turbulence. The turbulence introduces random perturbations to the wavefronts, so that they are no longer perfectly spherical waves radiating outward from the source (Fig. 1). In situations where the signal-to-noise ratio (SNR) is high, the turbulence effect is often the dominant factor limiting performance of the array (Wilson, 1996).

The theory of wave coherence for propagation through inertial subrange (small-scale) turbulence was developed and verified in the 1960's and 1970's. It has been applied successfully to optical, ultrasonic, and other types of wave propagation. Treatment of the inertial subrange is made somewhat easier by the fact that the statistics of the small eddies are locally *isotropic* (independent of orientation) and *homogeneous* (independent of position).

In the case of low-frequency acoustical propagation, however, energy subrange (large-scale) turbulence plays an important role. This is due to the long wavelengths involved (about 0.1 to 10 m), the large sensor separations (a few m or less), the signal properties that are exploited (mostly phase), and other considerations. As a result, previous theories developed for the inertial subrange have limited applicability, and improved understanding of the wave coherence for propagation through energy-subrange turbulence is required.

Turbulence structure in the energy subrange is affected directly by the instability mechanisms, usually shear and buoyancy, producing the turbulence. Since shear and buoyancy are intrinsically directional forces, statistics of the energy subrange are intrinsically anisotropic and inhomogeneous. A well known example of anisotropy in a shear layer is that the variance for turbulent velocity fluctuations in the direction of the mean wind is several times larger than the variance for vertical velocity fluctuations. An example of inhomogeneity is the dependence of the variances on the height above the ground. Similar manifestations of anisotropy and inhomogeneity are also evident in the turbulence length scales.

The focus of this paper is on the effects of turbulence anisotropy. The specific case treated is a shear-driven, atmospheric surface layer. By focusing on the purely shear-driven case here, I do not intend to imply that buoyantly driven turbulence is unimportant for acoustic wave propagation: hopefully the effects of buoyantly driven turbulence can be considered in future research.

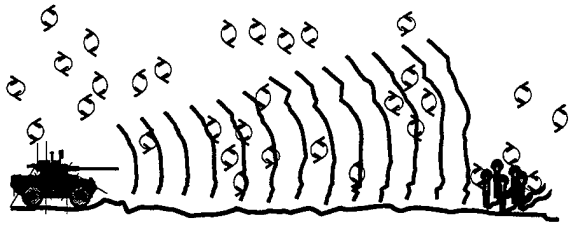

Figure 1: Random distortions in acoustic wavefronts caused by atmospheric turbulence.

Much of the turbulence modeling effort in this paper derives from the previous work of Kristensen *et al.* (1989). They developed an anisotropic spectral model for turbulence, and applied it to turbulence produced by various instability mechanisms, including the shear surface layer. In this paper Kristensen *et al.*'s model is applied to acoustic propagation. Two simplified versions of Kristensen *et al.*'s model are also considered: an anisotropic, von Kármán model, and an anisotropic, Gaussian model. The motivation for developing anisotropic versions of the von Kármán and Gaussian models is that these models are already very popular, in their isotropic forms, for wave propagation calculations, and it is interesting to see how they can be generalized.

A fourth model considered in this paper, due to Mann (1994), uses an entirely different approach than the one taken by Kristensen *et al.* It is based on rapid distortion theory, which hypothesizes that the shear distortions to an eddy can be calculated from linearized Navier-Stokes equations.

2. SIGNAL COHERENCE AND THE INCORPORATION OF ANISOTROPIC TURBULENCE

In a paper presented at the previous BAC (Wilson, 1996), it was shown how the accuracy of source bearing-estimations derived from a sensor array depends primarily on the mutual coherence function (MCF). The MCF describes the coherence between a pair of sensors as a function of their separation $\mathbf{r}_\perp$ normal to the direction of propagation. Usually the coherence of an acoustic wave propagating through the atmosphere depends mostly on the component of wind velocity fluctuations in the direction of propagation. In this case, the MCF is given by (Dashen, 1979; Ostashev, Mellert, Wandelt & Gerdes, 1997; Wilson, 1997)

$$\Gamma(\mathbf{r}_\perp) = \exp\left\{-\frac{2\pi}{c_0^2} X k_0^2 \left[b_\parallel(\mathbf{0}) - b_\parallel(\mathbf{r}_\perp)\right]\right\}, \quad (1)$$

where X is the propagation distance (range), $k_0 = 2\pi f/c_0$ the acoustic wavenumber, f the frequency, c_0 the sound speed, and $b_\parallel(\mathbf{r}_\perp)$ the *two-dimensional (2D) correlation function* of the velocity fluctuations parallel to the direction of propagation. Because the 2D correlation function is the statistical property of the turbulence that determines wave coherence, it is a focus of much of the following discussion in this paper. The 2D correlation equals a line integral of the usual, 3D correlation function $R_{\alpha\alpha}(\mathbf{r}) = \langle u_\alpha(\mathbf{r}+\mathbf{r}')\, u_\alpha(\mathbf{r}')\rangle$ along the propagation path. If the direction of propagation is the x_1-axis, for example, the 2D correlation function is

$$b_\parallel(\mathbf{r}_\perp) = b_{11}(r_2, r_3) = \frac{1}{2\pi}\int_{-\infty}^{\infty} R_{11}(r_1, r_2, r_3)\, dr_1. \quad (2)$$

The 2D correlation function also can be expressed in several alternative forms involving spectral density functions. For example, if the turbulence is homogeneous and isotropic, one has (Wilson, 1997)

$$b_\parallel(r_\perp) = \frac{1}{2}\int_0^\infty \frac{E(k_\perp)}{k_\perp} J_0(k_\perp r_\perp)\, dk_\perp, \quad (3)$$

in which $E(\kappa)$ is the specific kinetic energy spectrum of the turbulence,* and J_0 is the cylindrical Bessel function. Note that in isotropic turbulence, the 2D correlation function depends only on the magnitude of $\mathbf{r}_\perp$. Another important property of isotropic turbulence is that $b_\parallel(\mathbf{r}_\perp)$ can be calculated using any direction for the integration in (2). When the turbulence is anisotropic, however, $b_\parallel(\mathbf{r}_\perp)$ does depend on the direction of the integration. Furthermore, $b_\parallel(\mathbf{r}_\perp)$ may depend on the orientation of $\mathbf{r}_\perp$ in anisotropic turbulence.

Kristensen *et al.* (1989) have suggested partitioning the energy spectrum for anisotropic turbulence into three independent scalar functions, $A_1(k)$, $A_2(k)$, and $A_3(k)$. By their hypothesis the spectral density tensor of the turbulent velocity fluctuations has the form

$$\Phi_{ij}(\mathbf{k}) = \sum_{m=1}^{3} A_m(k)\left(\delta_{mi} - \frac{k_m k_i}{k^2}\right) \times \left(\delta_{mj} - \frac{k_m k_j}{k^2}\right). \quad (4)$$

It is beyond the scope of this paper to discuss the mathematical details and implementation of Kristensen *et al.*'s spectral density tensor. An important point that needs to be kept in mind, however, is

*The energy spectrum, when integrated from 0 to infinity, equals one-half the total variance of the velocity fluctuations.

that Kristensen *et al.*'s spectral tensor does *not* provide a fully general description of anisotropic turbulence. The tensor assumes certain symmetry properties that may be unrealistic. Application of the tensor is just a first (and useful) step toward incorporating fully general anisotropy. We will see later that even this first step leads to very significant complications.

When Kristensen *et al.*'s spectral tensor is employed, it can be shown that the 2D correlation function for propagation in the x_1-direction is determined from the equation (Wilson, 1998)

$$b_{11}(r_2, r_3) = 2\pi \int_0^\infty A_1(k_\perp) J_0(k_\perp r_\perp) k_\perp \, dk_\perp, \tag{5}$$

and similarly for the x_2- and x_3-directions. Note that as a result of Kristensen *et al.*'s hypothesis, $b_{\|}(\mathbf{r}_\perp)$ depends only on the magnitude of $\mathbf{r}_\perp$, as it did for isotropic turbulence. However, $b_{\|}(\mathbf{r}_\perp)$ *does* depend on the orientation of the propagation path.

3. VON KÁRMÁN MODEL

Derivation of an anisotropic model, that reduces to the popular von Kármán model in the isotropic limit, is outlined here. We start by considering the family of 1D turbulence velocity spectra whose wavenumber axes are parallel to the direction of the mean wind. (These spectra may be measured by recording time series with a stationary anemometer, and then converting the time series to approximate, spatial ones using Taylor's hypothesis. The Fourier transform of the approximate spatial series can then be used to determine the spectra.) The spectrum of the velocity fluctuations in the direction of the mean wind, called the longitudinal spectrum, is modeled by the equation

$$F_L(k) = \frac{1}{B(1/2, 1/3)} \frac{\sigma_1^2 \ell_1}{(1 + k^2 \ell_1^2)^{5/6}}, \tag{6}$$

where k is the wavenumber, $B(x, y) = \Gamma(x)\Gamma(y) / \Gamma(x + y)$ the beta function, σ_1^2 the variance of the longitudinal velocity, and ℓ_1 a length scale parameter. In isotropic turbulence, the transverse (horizontal component perpendicular to the mean wind) spectrum $F_T(k)$, and the vertical velocity spectrum $F_V(k)$, are equal to

$$F_T(k) = F_V(k) = \frac{1}{2}\left[F_L(k) - kF_L'(k)\right]. \tag{7}$$

Hence natural choices for $F_T(k)$ and $F_V(k)$ are $F_T(k)$ $= (1/2)\ F_0(\sigma_2, \ell_2, 5/3, 1/3; k)$, and $F_V(k) = (1/2)$ $F_0(\sigma_3, \ell_3, 5/3, 1/3; k)$, where

	von Kármán (isotropic)		von Kármán (anisotropic)	
i	σ_i^2/u_*^2	ℓ_i/z	σ_i^2/u_*^2	ℓ_i/z
1	2.97	1.60	4.77	3.64
2	2.97	1.60	2.68	1.53
3	2.97	1.60	1.46	0.617

Table 1: Values of the variances and length scales in the isotropic and anisotropic von Kármán models.

$$F_0(\sigma, \ell, h, \nu; k) = \frac{\sigma^2 \ell}{B(1/2, \nu)} \times \frac{1}{(1 + k^2\ell^2)^{\nu+1/2}} \left(1 + \frac{hk^2\ell^2}{1 + k^2\ell^2}\right), \tag{8}$$

Note that $F_L(k) = F_0(\sigma_1, \ell_1, 0, 1/3; k)$. When the variances σ_i^2 and length scales ℓ_i are all equal, the equations for $F_L(k)$, $F_T(k)$, and $F_V(k)$ reduce to the 1D spectral densities of the isotropic, von Kármán model.

The parameters in the anisotropic model can be selected to match the variances and inertial-subrange asymptotes in Kaimal *et al.*'s (1972) empirical equations for neutral, surface-layer turbulence. The method for doing so is described in Wilson (1998), with results given in Table 1.It should be pointed out that the requirement of isotropy in the inertial subrange ($k\ell_i >> 1$) implies that only four of the six parameters in the anisotropic von Kármán model are actually independent.

Kristensen *et al.*'s (1989) method for determining the three scalar energy functions from the 1D spectra is based on the following set of equations, which they derive:

$$A_1(k) = \frac{k}{4\pi}\frac{d}{dk}\frac{1}{k}\frac{dF_L(k)}{dk} + \frac{1}{2\pi}\left[-\beta\left(k^{-2}\right) - \zeta\left(k^{-2}\right)\right], \tag{9}$$

$$A_2(k) = \frac{k}{4\pi}\frac{d}{dk}\frac{1}{k}\frac{dF_L(k)}{dk} + \frac{1}{2\pi}\left[\alpha\left(k^{-2}\right) - 3\beta\left(k^{-2}\right) - \zeta\left(k^{-2}\right)\right], \tag{10}$$

and

$$A_3(k) = \frac{k}{4\pi}\frac{d}{dk}\frac{1}{k}\frac{dF_L(k)}{dk} + \frac{1}{2\pi}\left[-\alpha\left(k^{-2}\right) - 3\beta\left(k^{-2}\right) - \zeta\left(k^{-2}\right)\right]. \tag{11}$$

The first term in Eqs. (9)–(11) represents the isotropic contribution. By differentiation of Eq. (6), this

term is found to be

$$\frac{k}{4\pi}\frac{d}{dk}\frac{1}{k}\frac{dF_L(k)}{dk} = \frac{55\sigma_1^2}{36\pi B(1/2,1/3)}\frac{k^2\ell_1^5}{(1+k^2\ell_1^2)^{17/6}}. \quad (12)$$

The functions $\alpha(s)$, $\beta(s)$, and $\zeta(s)$ in Eqs. (9)–(11), which comprise the anisotropic contributions, are given by (Kristensen *et al.*, 1989; Wilson, 1998)

$$\alpha(s) = I\left(\sigma_2,\ell_2,1/\sqrt{2};s\right) - I\left(\sigma_3,\ell_3,1/\sqrt{2};s\right) + I\left(\sigma_2,\ell_2,-1/\sqrt{2};s\right) - I\left(\sigma_{33},\ell_3,-1/\sqrt{2};s\right), \quad (13)$$

$$\beta(s) = 2I(\sigma_1,\ell_1,1/3;s) - I(\sigma_2,\ell_2,1/3;s) - I(\sigma_{33},\ell_3,1/3;s), \quad (14)$$

and

$$\zeta(s) = 2I(\sigma_1,\ell_1,-1;s) - I(\sigma_2,\ell_2,-1;s) - I(\sigma_3,\ell_3,-1;s), \quad (15)$$

where

$$I(\sigma,\ell,q;s) = \frac{qs^q}{2}\int_0^s t^{1-q}\times \frac{d^3}{dt^3}\left[t^2F_0\left(\sigma,\ell,5/3,1/3;t^{-1/2}\right)\right]dt, \quad (16)$$

Calculating the necessary derivatives, and using the definition of the incomplete beta function $B_z(a,b)$, it can be shown that (Wilson, 1998)

$$I\left(\sigma,\ell,q;k^{-2}\right) = \frac{4675}{432}\frac{q\sigma^2\ell^3}{B(1/2,1/3)}(k\ell)^{-2q} \times\left[\frac{23}{15}B_{1/(1+k^2\ell^2)}\left(\frac{11}{6}-q,3+q\right) - B_{1/(1+k^2\ell^2)}\left(\frac{11}{6}-q,2+q\right)\right]. \quad (17)$$

Substitution of this result into Eqs. (13)–(15) yields the functions $\alpha(s)$, $\beta(s)$, and $\zeta(s)$, and hence the three scalar energy functions.

The 2D correlation functions now follow by substituting the scalar energy functions into Eq. (5). The isotropic contribution to the 2D correlation is found by integrating Eq. (12). This presents no great difficulties, and we find

$$b_{iso}(\sigma_1,\ell_1;r) = \frac{2\sigma_1^2\ell_1}{\sqrt{\pi}\Gamma(1/3)}\left(\frac{r}{2\ell_1}\right)^{5/6} \times\left[K_{5/6}\left(\frac{r}{\ell_1}\right) - \frac{r}{2\ell_1}K_{1/6}\left(\frac{r}{\ell_1}\right)\right]. \quad (18)$$

To calculate the anisotropic contributions, we need to solve integrals of the form

$$\overline{I}(\sigma,\ell,q;r) = \int_0^\infty I\left(\sigma,\ell,q;k^{-2}\right)J_0(kr)\,k\,dk, \quad (19)$$

in which $I(\sigma,\ell,q;s)$ contains incomplete beta functions. Not surprisingly, the integral has no solution in terms of common higher functions such as Bessel functions. One possible approach to solving the integral is to rewrite the incomplete beta functions as Meijer's G-functions [see, for example, Erdélyi *et al.* (1953)]. This approach leads to (Wilson, 1998)

$$\overline{I}(\sigma,\ell,q;r) = \frac{q\sigma^2\ell}{2\sqrt{\pi}\Gamma(1/3)}\left(\frac{r}{2\ell}\right)^{11/3}\times \left[G_{13}^{21}\left(\frac{r^2}{4\ell^2}\middle|\begin{matrix}q-11/6\\-11/6,\ -1,\ q-17/6\end{matrix}\right) - 8G_{13}^{21}\left(\frac{r^2}{4\ell^2}\middle|\begin{matrix}q-11/6\\-5/6,\ -1,\ q-17/6\end{matrix}\right) + \frac{13}{2}G_{13}^{21}\left(\frac{r^2}{4\ell^2}\middle|\begin{matrix}q-11/6\\1/6,\ -1,\ q-17/6\end{matrix}\right) - G_{13}^{21}\left(\frac{r^2}{4\ell^2}\middle|\begin{matrix}q-11/6\\7/6,\ -1,\ q-17/6\end{matrix}\right)\right]. \quad (20)$$

For the 2D correlation function in the along-wind direction, we now have from Eq. (9)

$$b_{11}(r) = b_{iso}(\sigma_1,\ell_1;r) - \overline{\beta}(r) - \overline{\zeta}(r), \quad (21)$$

where, from Eq. (14),

$$\overline{\beta}(r) = 2\overline{I}(\sigma_1,\ell_1,1/3;r) - \overline{I}(\sigma_2,\ell_2,1/3;r) - \overline{I}(\sigma_3,\ell_3,1/3;r). \quad (22)$$

Equations for $b_{22}(r)$, $b_{33}(r)$, $\overline{\alpha}(r)$, and $\overline{\zeta}(r)$ follow with obvious replacements.

Since routines for computing Meijer's G-functions are not widely available, it is often impractical to calculate the 2D correlations using Eq. (20). Rather, they must be calculated by performing the integration in Eq. (5) numerically.

4. GAUSSIAN MODEL

Although it is unrealistic for the inertial subrange, the isotropic Gaussian model has proven quite popular in wave propagation studies. The main advantage of the isotropic Gaussian model is that the equations for the correlation and spectral functions are easily obtainable. In this section we explore how the Gaussian model can be generalized to the anisotropic case.

	Gaussian (anisotropic)	Kristensen *et al.* (anisotropic)	
i	L_i/z	l_i/z	μ_i
1	6.21	5.50	0.52
2	3.59	1.59	0.49
3	0.774	0.343	0.68

Table 2: Values of the length scales and other parameters in the Gaussian and Kristensen *et al.* models.

For the Gaussian model it is assumed that the longitudinal correlation function has the form

$$R_L(r) = \sigma_1^2 \exp\left(-\frac{r^2}{L_1^2}\right). \tag{23}$$

By taking the Fourier transform of the correlation function, we find

$$F_L(k) = \frac{\sigma_1^2 L_1}{2\sqrt{\pi}} \exp\left(-\frac{k^2 L_1^2}{4}\right). \tag{24}$$

To obtain the proper reduction in the isotropic limit, we must set

$$F_T(k) = \frac{\sigma_2^2 L_2}{4\sqrt{\pi}} \left(1 + \frac{k^2 L_2^2}{2}\right) \exp\left(-\frac{k^2 L_2^2}{4}\right), \tag{25}$$

and similarly for $F_V(k)$.

Since the Gaussian model does not have a realistic inertial subrange, it is reasonable to select its parameters to obtain the best possible fit to spectral characteristics of the energy subrange, such as variances and integral length scales. The approach used here is to select the parameters to reproduce the variances and integral length scales of Kaimal *et al.*'s (1972) empirical equations. The resulting length scales (Wilson, 1998) are shown in Table 2. The variances are the same as the anisotropic von Kármán model, Table 1.

We will again determine the scalar energy functions A_i using Eqs. (9)–(11). The procedure is much the same as for the von Kármán model, except we find for the isotropic contribution

$$b_{iso}(\sigma_1, L_1; r) = \frac{\sigma_1^2 L_1}{2\sqrt{\pi}} \left(1 - \frac{r^2}{L_1^2}\right) \exp\left(-\frac{r^2}{L_1^2}\right). \tag{26}$$

The function $I()$ for the anisotropic contributions becomes

$$I(\sigma, L, q; s) = \frac{q\sigma^2 L^3}{8\sqrt{\pi}} \left(\frac{4s}{L^2}\right)^q \times \left[\Gamma\left(3+q, \frac{L^2}{4s}\right) - \frac{5}{2}\Gamma\left(2+q, \frac{L^2}{4s}\right)\right], \tag{27}$$

where $\Gamma(x, y)$ is the incomplete gamma function. The functions $\alpha(s)$, $\beta(s)$, and $\zeta(s)$ can now be determined using Eqs. (13)–(15). The result of performing the integration in Eq. (19) is (Wilson, 1998)

$$\overline{I}(\sigma, L, q; r) = \frac{3q\sigma^2 L}{2\sqrt{\pi}(1-q)} \times \left[{}_2F_2\left(4, 1-q; 1, 2-q; -\frac{r^2}{L^2}\right) - \frac{5}{4}\,{}_2F_2\left(3, 1-q; 1, 2-q; -\frac{r^2}{L^2}\right)\right], \tag{28}$$

where ${}_2F_2(\cdot)$ is a generalized hypergeometric function. As was the case for the von Kármán model, our result is not very helpful from a practical standpoint. Routines are not commonly available to calculate generalized hypergeometric functions. Hence the 2D structure function must be calculated numerically, by integrating Eq. (5). Even the simple Gaussian model, when generalized to the anisotropic case, eludes convenient solution for the 2D correlation function.

5. KRISTENSEN ET AL. MODEL

In this paper I distinguish between the Kristensen *et al. model*, and the Kristensen *et al. spectral tensor*. The Kristensen *et al.* model, like the anisotropic von Kármán and Gaussian models considered earlier, is based the form for the spectral tensor given by Eq. (4). However, a different equation is proposed for the 1D spectral densities. This equation is similar to the von Kármán model, except that it contains an additional parameter. Specifically, the definition for $F_0(\sigma, \ell, h, \nu; k)$ given by Eq. (8) is replaced by

$$H_0(\sigma, l, \mu, h; k) = \frac{l\sigma^2}{\pi} \frac{1}{\left\{1 + [kl/a(\mu)]^{2\mu}\right\}^{5/6\mu}} \times \left\{1 + \frac{h[kl/a(\mu)]^{2\mu}}{1 + [kl/a(\mu)]^{2\mu}}\right\}, \tag{29}$$

where $a(\mu) = \pi\mu/B(1/2\mu, 1/3\mu)$. The 1D spectra are $F_L(k) = H_0(\sigma_1, l_1, \mu_1, 0; k)$, $F_T(k) = (1/2)$ $H_0(\sigma_2, l_2, \mu_2, 5/3; k)$, and $F_V(k) = (1/2)\,H_0(\sigma_3,$ $l_3, \mu_3, 5/3; k$. The parameters l_i are integral length scales. The parameters μ_i control the sharpness of the spectral peak; larger values give a sharper peak. Setting the $l_i = a(\mu_i)\,\ell_i$ and $\mu_i = 1$ reproduces the anisotropic von Kármán model. Kristensen *et al.* chose the parameters in their model to approximate the empirical spectra of Kaimal *et al.* (1972), and

the resulting values for the l_i and μ_i are shown in Table 2. The variances are the same as the anisotropic von Kármán model, Table 1. Note that the μ_i's are significantly less than 1, indicating that the actual spectra have broader peaks than in the von Kármán model.

Derivation of the 2D correlations proceeds much as it did for the von Kármán model, except that the equations become more complicated due to the more complicated form for the 1D spectra. The resulting integrals cannot be solved, even in terms of Meijer's G-functions. The interested reader is referred to Wilson (1998) for details.

6. MANN MODEL

The Mann model (1994) is the result a first-principle theoretical treatment for turbulence in a constant shear layer. The main hypothesis upon which Mann's model is based is called *rapid distortion theory*. The idea is basically this: In a turbulent shear layer, new eddies are perpetually being created, subjected to the forces of shear, and then eventually broken down. Between the times when an eddy is "created" and when it is "destroyed" by the shear, there exists an interval for which the eddy exists in a state that is "typical" for eddies having its same spatial dimensions. This interval is called the *eddy lifetime*.

A full discussion of rapid distortion theory and Mann's model is beyond the scope of this paper. However, the relevant equations will be summarized here. Mann's equations for the 3D autospectra in a uniform (constant gradient) shear layer are

$$\Phi_{11}(\mathbf{k}) = \frac{E(k_0)}{4\pi k_0^4}\left[k_0^2 - k_1^2 - 2k_1 k_{30}\zeta_1 + \left(k_1^2+k_2^2\right)\zeta_1^2\right], \tag{30}$$

$$\Phi_{22}(\mathbf{k}) = \frac{E(k_0)}{4\pi k_0^4}\left[k_0^2 - k_2^2 - 2k_2 k_{30}\zeta_2 + \left(k_1^2+k_2^2\right)\zeta_2^2\right], \tag{31}$$

and

$$\Phi_{33}(\mathbf{k}) = \frac{E(k_0)}{4\pi k^4}\left(k_1^2+k_2^2\right). \tag{32}$$

In the equations above, $E(k_0)$ is the *initial* (before the onset of shear distortion) energy spectrum. The isotropic von Kármán energy spectrum is used. The initial wavenumber is $\mathbf{k_0} = (k_1, k_2, k_{30})$, where $k_{30} = k_3 - \beta k_1$, and β is the non-dimensional eddy lifetime, given by (Mann, 1994; Wilson, 1998)

$$\beta = \frac{\sqrt{3\Gamma}}{k\ell}\left[B_{1/(1+k^2\ell^2)}\left(\frac{1}{3},\frac{5}{2}\right)\right]^{-1/2}. \tag{33}$$

The ζ_i follow from the equations

$$\zeta_1 = C_1 - \frac{k_2}{k_1}C_2, \quad \zeta_2 = \frac{k_2}{k_1}C_1 + C_2, \tag{34}$$

where

$$C_1 = \frac{\beta k_1^2\left(k_0^2 - 2k_{30}^2 + \beta k_1 k_{30}\right)}{k^2\left(k_1^2+k_2^2\right)}, \tag{35}$$

and

$$C_2 = \frac{k_2 k_0^2}{\left(k_1^2+k_2^2\right)^{3/2}}\arctan\left[\frac{\beta k_1\left(k_1^2+k_2^2\right)^{1/2}}{k_0^2 - \beta k_{30}k_1}\right]. \tag{36}$$

For the purposes of this paper I select the parameter Γ such that the ratio σ_1^2/σ_3^2 (found by integrating the 3D spectra) matches the anisotropic models discussed earlier. The desired value of Γ, determined numerically, is $\Gamma_0 = 3.53$. Furthermore, to force σ_1^2 equal to $4.77u_*^2$ when $\Gamma = \Gamma_0$, we need to set (Wilson, 1998)

$$\sigma^2 = 1.88u_*^2 \tag{37}$$

in the initial energy spectrum. The proper inertial-subrange asymptote is obtained by setting (Wilson, 1998)

$$\ell = 0.805z. \tag{38}$$

The 2D correlations for the Mann model must be determined, in general, by calculating a 2D inverse Fourier transform of the 3D spectra. However, if we are interested in sensor separations along just one of the orthogonal coordinate axes, the integration can be simplified somewhat. For example,

$$b_{11}(r_2,0) = \int_{-\infty}^{\infty}\left[\int_{-\infty}^{\infty}\Phi_{11}(0,k_2,k_3)\,dk_3\right] \times \exp(ik_2 r_2)\,dk_2. \tag{39}$$

Note that the 2D structure functions in the Mann model depend on the direction of the displacement. This behavior distinguishes the Mann model from the ones considered earlier based on Kristensen *et al.*'s spectral tensor.

7. EXAMPLE CALCULATIONS

As discussed earlier, the 2D correlation function of the turbulence determines the spatial coherence of the acoustic wave. Specifically, the coherence depends on the difference $b_{\|}(\mathbf{0}) - b_{\|}(\mathbf{r}_\perp)$. Let us define a 2D structure function as

$$d_{\|}(\mathbf{r}_\perp) = 2\left[b_{\|}(\mathbf{0}) - b_{\|}(\mathbf{r}_\perp)\right]. \tag{40}$$

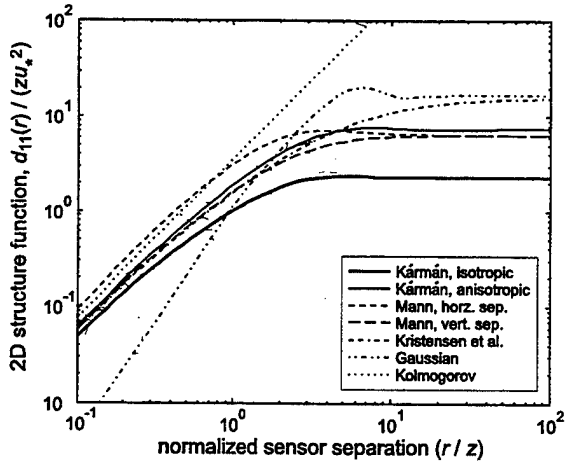

Figure 2: Two-dimensional structure functions for the various turbulence models. Propagation is along wind.

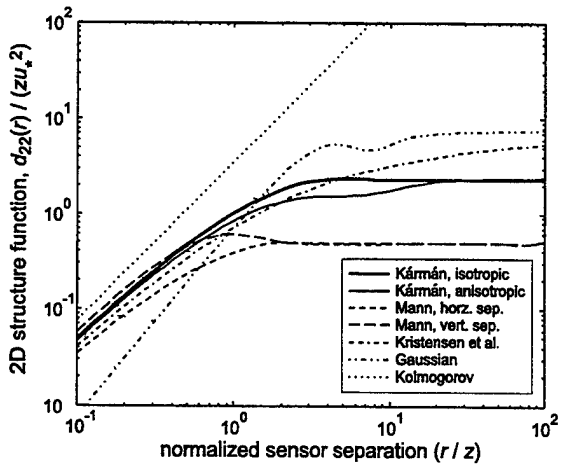

Figure 3: Two-dimensional structure functions for the various turbulence models. Propagation is crosswind.

Predictions of the 2D structure function for the various turbulence models discussed in this report are shown in Figs. 2–3. The structure functions are normalized by $u_*^2 z$, where u_* is the friction velocity and z the height. Also shown in the figures are predictions from the Kolmogorov (inertial subrange) model, computed using the equations in Wilson (1997). The plots clearly show that the Kolmogorov model only works well when the ratio of the sensor separation to the height (r/z) is much less than one. Convergence to the Kolmogorov prediction is very slow. Conversely, the Gaussian model is reasonable only in the energy subrange, where r/z is much greater than one. A peculiar (and probably unphysical) characteristic of the Gaussian model is the appearance of local peaks in the 2D structure function (at $r/z \approx 0.6$ in the along-wind direction and 0.3 in the cross-wind direction.)

In the along-wind (either upwind or downwind) direction, the energy-subrange 2D structure function is larger for all of the anisotropic models than for the isotropic von Kármán model. The main reason for this behavior is that the anisotropic models all use a longer length scale for the along-wind direction. In the cross-wind direction, the results are mixed. The 2D structure function is larger for the Kristensen *et al.* and Gaussian models than for the isotropic von Kármán model; for the Mann model it is considerably smaller, equal to about 1/10 the Kristensen *et al.* model predictions for large r/z. The essential reason is that the Mann model predicts a very small length scale for the cross-wind velocity fluctuations in the cross-wind direction. Symmetries inherent to the other anisotropic model based on Kristensen *et al.*'s spectral tensor lead to larger values for this length scale.

For the Mann model, note that the structure functions for both horizontal and vertical separations are nearly equal for small separations compared to the height (the inertial subrange), diverge for moderate separations, and then become equal for large separations. The reason for the close agreement in the inertial subrange is isotropy in that part of the spectrum. They become equal for large separations because $b_{\|}(r,0)$ and $b_{\|}(0,r)$ both approach zero for large r, so that the 2D structure function in the two cases is $d_{\|}(r,0) \simeq d_{\|}(0,r) \simeq 2b_{\|}(0,0)$.

An important application of the 2D structure functions is the prediction of source bearing estimation accuracy from acoustical arrays. A full discussion of this problem appeared in the previous BAC proceedings (Wilson, 1996). The procedure described in that report involved calculating the *Cramer-Rao lower bound* (CRLB) corresponding to a given array configuration, turbulence model, and noise environment. The CRLB is the standard deviation in the wavefront angle-of-arrival estimates about their actual value attained using an ideal estimation method.† Or, more simply put, when the CRLB is equal to α degrees, we can usually measure the direction of a source to an accuracy of α degrees, provided our equipment and processing algorithms are good.

†The CRLB is strictly the variance of the estimates, not their standard deviation (square root of the variance). Because the standard deviation has linear units and is therefore more natural to deal with, I have adopted the convention here of implying the square root of the CRLB whenever I refer to the CRLB throughout this report.

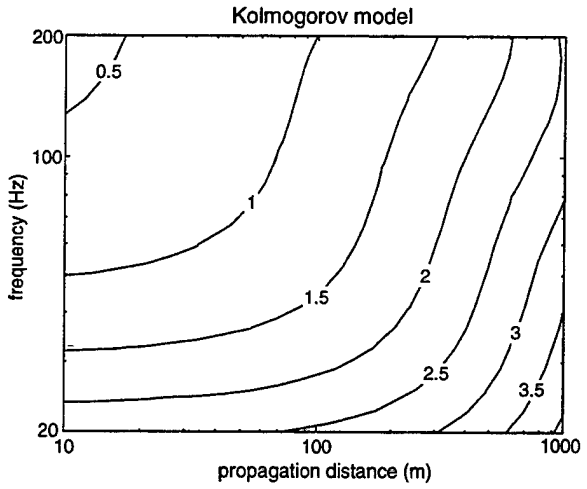

Figure 4: CRLB calculations for the Kolmogorov inertial-subrange model. Since the Kolmogorov model is isotropic, these calculations are valid in either the along-wind or crosswind directions.

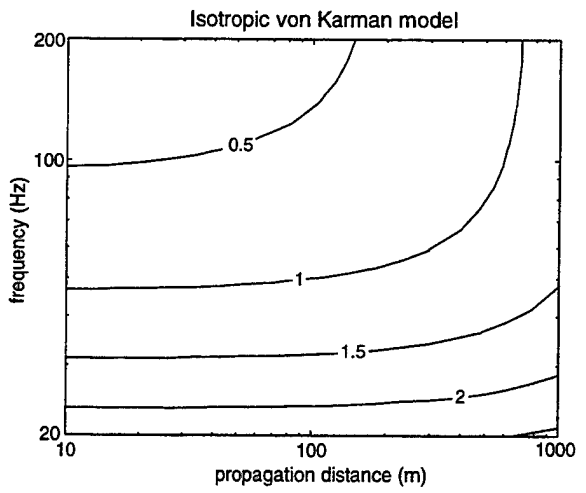

Figure 5: CRLB calculations for the isotropic, von Kármán model. Valid in either the along-wind or crosswind directions.

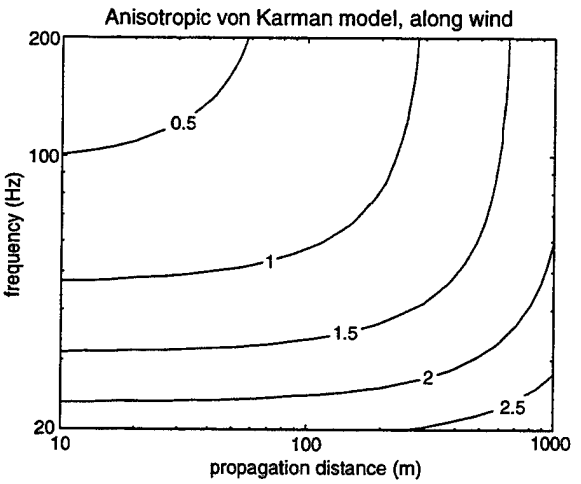

Figure 6: CRLB calculations for the anisotropic von Kármán model, for propagation in the along-wind direction.

Actual CRLB calculations, for many of the turbulence models discussed in this report, are shown in Figs. 4–11. The calculations were performed for a six-element array, with the sensors evenly spaced around a horizontal circle. The CRLB for such an array configuration is independent of the source direction. The source and array heights were both 1 m, the friction velocity was $u_* = 0.5$ m/s (windy conditions), the SNR was 20 dB, and it was assumed that 5 statistically independent measurements were used for each bearing estimate. The plots show the dependence of the CRLB for azimuthal bearings on source range (propagation distance) and acoustic frequency.

The general appearance of the CRLB plots, for all of the models, is similar. Near the source, and at low frequency, the CRLB is independent of range. This is because the main determinant of array performance near the source is the environmental noise. As the frequency and range are increased, however, the CRLB contours turn upward dramatically. It is in this region that distortion of the wavefronts by turbulence begins to be the most significant determinant of array performance.

The Kolmogorov model (Fig. 4) predicts higher values for the CRLB than the other models, particularly at lower frequencies and longer ranges. The reason is that the Kolmogorov model predicts too much energy at the large turbulence scales, which comprise the most important part of the spectrum for determining array performance. Therefore the Kolmogorov model should be avoided in this application. CRLB predictions for the isotropic von Kármán model (Fig. 5) agree qualitatively with calculations from the more complicated, anisotropic models (Figs. 6–11). Its predictions fall roughly midway between the along-wind and crosswind predictions of the Kristensen *et al.* (Figs. 8–9) and Mann (Figs. 10–11) models. Predictions from the anisotropic von Kármán model, in the along-wind direction (Fig. 6), are close to the corresponding predictions for the more complicated Kristensen *et al.* (Fig. 8) and Mann (Fig. 10) models. The anisotropic Gaussian model, in the along-wind direction (Fig. 7), also agrees well with the corresponding predictions from

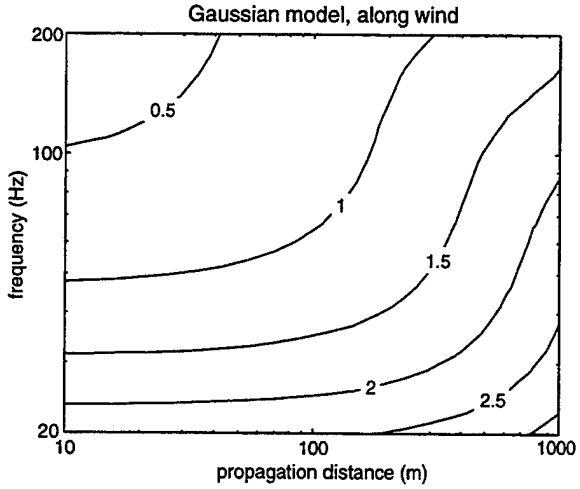

Figure 7: CRLB calculations for the anisotropic Gaussian model, for propagation in the along-wind direction.

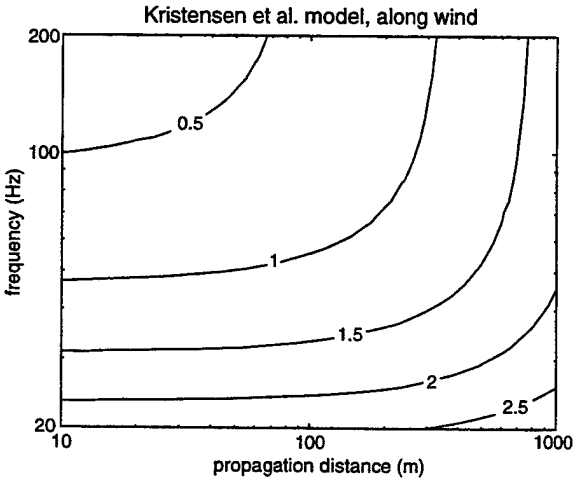

Figure 8: CRLB calculations for the Kristensen *et al.* model, for propagation in the along-wind direction.

the Kristensen *et al.* and Mann models, although the contours start to diverge for high frequencies and long propagation distances. This is due to the inability of the Gaussian model to realistically capture small-scale turbulence structure.

The Kristensen *et al.* and Mann models agree in most regards. One difference is that the anisotropic effect predicted by the Mann model is more pronounced than for the Kristensen *et al.* model. In the along-wind direction the Mann model (Fig. 10) predicts higher CRLB than the Kristensen *et al.* model (Fig. 8); in the crosswind direction it predicts lower CRLB (Figs. 9 and 11).

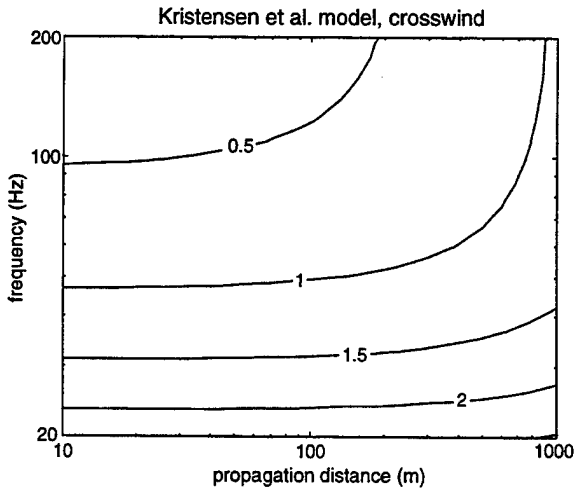

Figure 9: CRLB calculations for the Kristensen *et al.* model, for propagation in the crosswind direction.

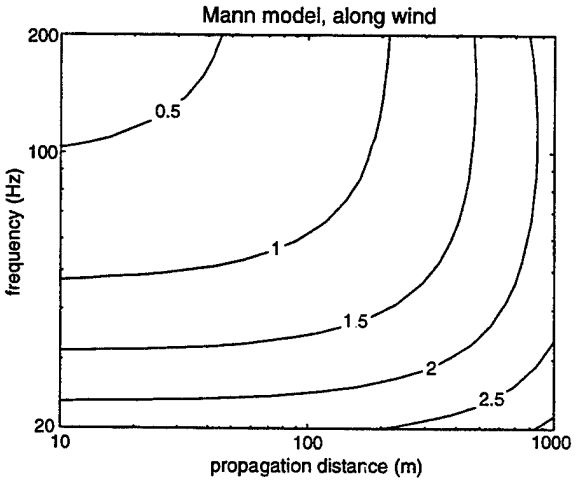

Figure 10: CRLB calculations for the Mann model, for propagation in the along-wind direction.

8. CONCLUDING REMARKS

The CRLB calculations clearly demonstrate that the Kolmogorov (inertial-subrange) is poor for assessing the accuracy of bearing estimates, and should therefore be avoided. The isotropic von Kármán model is much better, yielding fair results while retaining relative simplicity. But when accurate calculations are required, anisotropy effects must be accounted for.

One of the main purposes of this paper was to devise rigorous, anisotropic versions of the von Kármán and Gaussian models. Even though a simple, idealized form of anisotropy was assumed (Kristensen *et al.*'s spectral tensor), the mathematical

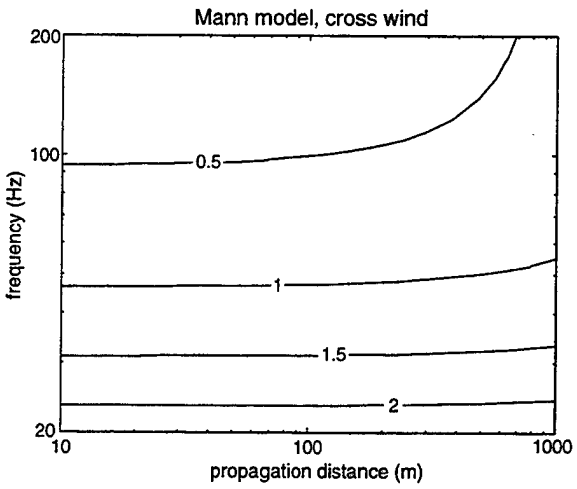

Figure 11: CRLB calculations for the Mann model, for propagation in the crosswind direction.

development of the anisotropic von Kármán and Gaussian models became quite complex. Convenient analytical results for the 2D correlation functions could not be derived, making numerical integrations necessary. Still, with modern computer technology, it is not difficult to implement the anisotropic von Kármán and Gaussian models.

Of the anisotropic models considered in this paper, the Mann model is likely the most realistic: it does not incorporate *ad hoc* assumptions regarding statistical symmetries of the turbulence field. Mann's model is also not much more difficult to apply than the ones based on Kristensen *et al.*'s spectral tensor.

This report has provided comparisons between several different statistical turbulence models, with and without anisotropy. Although such comparisons are a helpful first step towards understanding the effects of anisotropic turbulence on acoustic propagation, in the end experiments are needed to test how well the various anisotropic models actually work for predicting acoustic propagation characteristics. This will be an important topic for future research.

References

Dashen, R., 1979: Path integrals for waves in random media. *J. Math. Phys.*, **20**, 894–920.

Erdélyi, A., W. Magnus, F. Oberhettinger, and F. G. Tricomi, 1953: *Higher Transcendental Functions*, volume 1. McGraw-Hill, New York.

Kaimal, J. C., J. C. Wyngaard, Y. Izumi, and O. R. Coté, 1972: Spectral characteristics of surface layer turbulence. *Quart. J. Roy. Meteorol. Soc.*, **98**, 563–589.

Kristensen, L., D. H. Lenschow, P. Kirkegaard, and M. Courtney, 1989: The spectral velocity tensor for homogeneous boundary-layer turbulence. *Bound. Layer Meteor.*, **47**, 149–193.

Mann, J., 1994: The spatial structure of neutral atmospheric surface layer turbulence. *J. Fluid Mech.*, **273**, 141–168.

Ostashev, V. E., V. Mellert, R. Wandelt, and F. Gerdes, 1997: Propagation of sound in a turbulent medium. I. Plane waves. *J. Acoust. Soc. Am.*, **102**, 2561–2570.

Wilson, D. K., 1996: On the degradation of acoustic angle-of-arrival estimates due to atmospheric turbulence. In *Proceedings of the 1996 Battlespace Atmospherics Conference*, Richter, J. H. and Anderson, K. D., editors, NCCOSC, San Diego, CA, 243–252.

Wilson, D. K., 1997: Performance bounds for acoustic angle-of-arrival arrays operating in atmospheric turbulence. *J. Acoust. Soc. Am.* in press.

Wilson, D. K., 1998: Anisotropic turbulence models for acoustic propagation through the neutral, atmospheric surface layer. Technical Report ARL-TR-1519, U.S. Army Research Laboratory, 2800 Powder Mill Road, Adelphi, MD 20783.

SOUND SCATTERING CROSS SECTION FOR VON KARMAN SPECTRA OF TEMPERATURE AND WIND VELOCITY FLUCTUATIONS

V.E. Ostashev and G.H. Goedecke
Dept. of Physics, Box 30001/Dept. 3D,
NMSU, Las Cruces, NM 88003-8001

Abstract

The sound scattering cross-section per unit volume in locally homogeneous and isotropic turbulence with von Karman spectra of temperature and medium velocity fluctuations is calculated. It is shown that the temperature and medium velocity contributions to the sound scattering cross-section have dramatically different dependences on the scattering angle. It is also shown that, in the limiting cases of high and low frequencies, the sound scattering cross-section for the von Karman spectrum coincides with those for the Kolmogorov and Gaussian spectra, respectively.

1 Introduction

The knowledge of sound propagation and scattering in a turbulent atmosphere can significantly improve the performance of acoustical systems intended for source detection, ranging and recognition. The modern rigorous theory of sound propagation and scattering through locally homogeneous and isotropic turbulence has been developed towards accomplishment of the research grant [4] for the U.S. Army Research Office and presented in the book [9]. The main significance of the theory is that it distinguishes between the temperature, humidity and wind velocity contributions to the statistical moments of a sound field and provides a correct and complete set of equations for these moments. The modern theory of sound propagation and scattering through homogeneous and isotropic turbulence has been verified experimentally for the case of sound propagation through a turbulent jet [7]. This theory has already been adopted by scientists for calculations of statistical moments of a sound field [11, 12], and as a basis for development of new acoustic remote sensing techniques

in the atmosphere [6] and the ocean [3]. Note that the previous theories [2, 10] of sound propagation through a turbulent atmosphere contained several mistakes which have been corrected in the modern theory.

The modern theory of sound propagation and scattering in a turbulent medium will be developed further in the course of time. Here, we present a small 'step' towards such development: the derivation and detailed analysis of the sound scattering cross-section per unit volume, σ, for the von Karman spectra of temperature and medium velocity fluctuations. Although the emphasis is on sound scattering in a turbulent atmosphere, the results obtained are also valid for the case of sound scattering in a medium with arbitrary equation of state, for example, in a turbulent ocean.

2 Von Karman spectrum

The sound scattering cross section, σ, is one of the most important statistical characteristics of a sound field propagating in a turbulent medium. For the case of locally homogeneous and isotropic turbulence, the equation for σ is given by (see equation (7.16) of [9])

$$\sigma(\theta) = 2\pi k^4 \left[\beta^2(\theta) \frac{\Phi_T(K)}{4T_0^2} + \cos^2\theta \cos^2(\theta/2) \frac{F(K)}{c_0^2} \right] . \tag{1}$$

Here, θ is the scattering angle, $k = 2\pi/\lambda$ is the sound wavenumber, λ is the sound wavelength, Φ_T and F are the three-dimensional spectral densities of temperature and medium velocity fluctuations, $K = 2k\sin(\theta/2)$ is the magnitude of the scattering vector, and T_0 and c_0 are the mean values of the temperature and adiabatic sound speed. Furthermore, $\beta(\theta) = \beta_c + 2\beta_\varrho \sin^2(\theta/2)$, where β_c and β_ϱ are coefficients determined by formula (6.6) of [9]. These coefficients depend on the equation of state of a medium. In the atmosphere, $\beta_c = -\beta_\varrho = 1$ so that $\beta(\theta) = \cos\theta$.

For the von Karman spectra of temperature and medium velocity fluctuations, Φ_T and F are given by [5, 9, 10]

$$\Phi_T^{\mathrm{vK}}(K) = AC_T^2 (K^2 + K_0^2)^{-11/6} , \qquad F^{\mathrm{vK}}(K) = \frac{11}{6} AC_v^2 K^2 (K^2 + K_0^2)^{-17/6} . \tag{2}$$

Here, $A = \frac{5}{18\pi\Gamma(1/3)} \approx 0.0330$, Γ is the Gamma function, C_T^2 and C_v^2 are the structure function parameters for temperature and medium velocity fluctuations, the upper superscript vK

indicates that the function corresponds to that for the von Karman spectrum, and $K_0 = 2\pi/L_0$, where L_0 is the scale of largest inhomogeneities in a medium.

Substituting (2) into (1) and taking into account the values of K and A, one obtains the equation for the sound scattering cross section for the von Karman spectra of temperature and medium velocity fluctuations

$$\sigma^{\mathrm{vK}}(\theta) = \sigma_T^{\mathrm{vK}}(\theta) + \sigma_v^{\mathrm{vK}}(\theta) = \frac{5k^{1/3}}{2^{17/3}9\Gamma(1/3)\left(\sin^2(\theta/2) + (K_0/2k)^2\right)^{11/6}} \times \left[\beta^2(\theta)\frac{C_T^2}{T_0^2} + \frac{11\cos^2\theta\sin^2\theta}{6\left(\sin^2(\theta/2) + (K_0/2k)^2\right)}\frac{C_v^2}{c_0^2}\right] . \quad (3)$$

Here, $\sigma_T^{\mathrm{vK}}(\theta)$ and $\sigma_v^{\mathrm{vK}}(\theta)$ are the temperature and medium velocity contributions to the sound scattering cross-section. As far as we know, equation (3) is a new result. The density flux of acoustic energy scattered by wind velocity fluctuations with the von Karman spectrum, which is proportional to $\sigma_v^{\mathrm{vK}}(\theta)$, has also been considered in [1]. However, the results obtained in this reference differ from those in the present paper because an incorrect formula for F^{vK} has been used in [1]: $F^{\mathrm{vK}}(K) = (11/6)AC_v^2(K^2 + K_0^2)^{-11/6}$.

It follows from (3) that the contributions to the scattering cross-section due to temperature and medium velocity fluctuations are different. Let us study these contributions for the case of sound scattering in the turbulent atmosphere when $\beta(\theta) = \cos\theta$. In this case, $\sigma_T^{\mathrm{vK}}(\theta)$ and $\sigma_v^{\mathrm{vK}}(\theta)$, normalized to $5k^{1/3}/(2^{17/3}9\Gamma(1/3))$, are plotted in figure 1 as functions of the scattering angle θ. Also, it is assumed that $C_T^2/T_0^2 = 1$ and $C_v^2/c_0^2 = 2$, and that the parameter $K_0/2k = \lambda/2L_0$ is 1. It is clearly seen from the figure that the temperature and wind velocity contributions to $\sigma^{\mathrm{vK}}(\theta)$ have dramatically different radiation patterns. For example, $\sigma_T^{\mathrm{vK}}(\theta)$ has maximum at $\theta = 0$, while $\sigma_v^{\mathrm{vK}}(\theta)$ is zero at $\theta = 0$ and reaches its maximal value at $\theta \sim 40°$. Also note that $\sigma_T^{\mathrm{vK}} > \sigma_v^{\mathrm{vK}}$ for small values of θ (in figure 1, for $\theta < 30°$). This range of scattering angles is believed to be responsible for sound scattering into a refractive shadow zone. It follows from figure 1 that, even if C_v^2/c_0^2 is greater than C_T^2/T_0^2 (as it usually is in the atmosphere during daytime), insonification of a shadow zone can nevertheless be caused by sound scattering by temperature fluctuations since σ_v^{vK} vanishes at small θ.

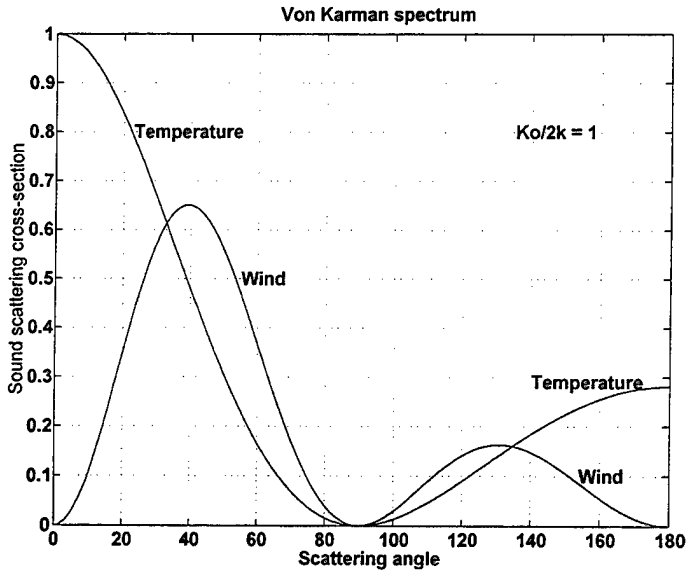

Figure 1: The normalized temperature (σ_T^{vK}) and wind velocity (σ_v^{vK}) contributions to the sound scattering cross-section for the von Karman spectrum of turbulence versus the scattering angle θ.

3 Kolmogorov and Gaussian spectra

It is worthwhile to compare (3) with equations for σ for Kolmogorov and Gaussian spectra of temperature and medium velocity fluctuations. Note that the von Karman, Kolmogorov and Gaussian spectra have been most often used in theories of waves in random media.

For the Kolmogorov spectrum, Φ_T and F are given by [5, 9, 10]

$$\Phi_T^{\mathrm{K}}(K) = AC_T^2 K^{-11/3}\,, \qquad F^{\mathrm{K}}(K) = \frac{11}{6} AC_v^2 K^{-11/3}\,. \tag{4}$$

Here, the upper superscript K indicates that the function corresponds to that for the Kolmogorov spectrum. As it should be, equations (2) coincide with equations (4) in the limiting case $K_0 \to 0$.

For the Gaussian spectrum, the three-dimensional spectral densities of temperature and medium velocity fluctuations are given by (see (6.40) and (6.43) of [9])

$$\Phi_T^{\mathrm{G}}(K) = \frac{\sigma_T^2 l^3}{8\pi^{3/2}} \exp(-K^2 l^2/4)\,, \quad F^{\mathrm{G}}(K) = \frac{\sigma_v^2 K^2 l^5}{32\pi^{3/2}} \exp(-K^2 l^2/4)\,. \tag{5}$$

Here, the upper superscript G indicates that the function corresponds to that for the Gaussian spectrum, σ_T^2 and σ_v^2 are the variances of temperature and medium velocity fluctuations, and l is the scale of inhomogeneities associated with the Gaussian spectrum.

In order to compare the sound scattering cross-sections σ for the Gaussian and von Karman spectra, we need to find a relationship between parameters σ_T^2, σ_v^2, l of the Gaussian spectrum and parameters C_T^2, C_v^2, K_0 of the von Karman spectrum. Of course, there is no 'general' rule for finding this relationship. Section 6.2.6 of the book [9] suggests that such a relationship can be obtained by equating the involved statistical moment of a sound field (in our case, σ) in the limiting case of small K. We will employ this suggestion, i.e. we will assume that $\sigma^{\mathrm{vK}}(\theta \approx 0) = \sigma^{\mathrm{G}}(\theta \approx 0)$. From this equality and equation (1) it can be shown that

$$\Phi_T^{\mathrm{G}}(K \approx 0) = \Phi_T^{\mathrm{vK}}(K \approx 0), \qquad F_T^{\mathrm{G}}(K \approx 0) = F_T^{\mathrm{vK}}(K \approx 0). \tag{6}$$

Substituting equations (2) and (5) into equation (6) yields the relationships between σ_T^2 and C_T^2, and between σ_v^2 and C_v^2:

$$\sigma_T^2 = \frac{20\sqrt{\pi}C_T^2}{9\Gamma(1/3)K_0^{2/3}(K_0 l)^3}, \qquad \sigma_v^2 = \frac{22}{3}\frac{20\sqrt{\pi}C_v^2}{9\Gamma(1/3)K_0^{2/3}(K_0 l)^5}. \tag{7}$$

Note that these relationships are different from those obtained in [9] (see (6.49) of [9]). The reason for this is that the latter relationships are obtained by equating the statistical moments of a sound field for Gaussian and von Karman spectra for line-of-sight propagation, while the relationships (6) are obtained by equating σ for these spectra.

As for the relationship between l and K_0, we shall assume that it is given by formula (6.51) of [9]

$$l = \frac{2\Gamma(5/6)}{\Gamma(1/3)}K_0^{-1} = 0.843K_0^{-1}. \tag{8}$$

This relationship is a consequence of the assumption that the integral lengths of the normalized correlation functions of temperature fluctuations for Gaussian and von Karman spectra are the same, and that the same is true for the integral lengths of the normalized longitudinal correlation functions of medium velocity fluctuations.

Replacing l in equation (7) by its value from (8) yields

$$\sigma_T^2 = \frac{5\sqrt{\pi}\Gamma^2(1/3)C_T^2}{18\Gamma^3(5/6)K_0^{2/3}} \approx 2.457\frac{C_T^2}{K_0^{2/3}}, \qquad \sigma_v^2 = \frac{55\sqrt{\pi}\Gamma^4(1/3)C_v^2}{108\Gamma^5(5/6)K_0^{2/3}} \approx 25.37\frac{C_v^2}{K_0^{2/3}}. \tag{9}$$

Equations (8) and (9) provide relationships between parameters σ_T^2, σ_v^2, l of the Gaussian spectrum and parameters C_T^2, C_v^2, K_0 of the von Karman spectrum.

4 Scattering cross-sections for different spectra

Substituting the values of $\Phi_T^{\mathrm{K}}(K)$ and $F^{\mathrm{K}}(K)$ from equation (4) into equation (1) yields the formula for the scattering cross-section for the Kolmogorov spectrum [9]:

$$\sigma^{\mathrm{K}}(\theta) = \frac{5k^{1/3}}{2^{17/3}9\Gamma(1/3)\left(\sin^2(\theta/2)\right)^{11/6}}\left[\beta^2(\theta)\frac{C_T^2}{T_0^2} + \frac{22\cos^2\theta\cos^2(\theta/2)}{3}\frac{C_v^2}{c_0^2}\right]. \tag{10}$$

This formula is well-known for the case of sound scattering in the atmosphere when $\beta(\theta) = \cos\theta$ (e.g. [2, 10]). As it should be, equation (3) coincides with (10) in the limiting case $K_0 \to 0$.

Substituting (5) into (1), one obtains the formula for σ for the Gaussian spectra of temperature and medium velocity fluctuations:

$$\sigma^{\mathrm{G}}(\theta) = \frac{k^4 l^3}{16\sqrt{\pi}}\left[\beta^2(\theta)\frac{\sigma_T^2}{T_0^2} + k^2 l^2\cos^2\theta\sin^2\theta\frac{\sigma_v^2}{c_0^2}\right]\exp\left(-k^2 l^2\sin^2(\theta/2)\right) : . \tag{11}$$

This equation has also been derived elsewhere [8]. Replacing σ_T^2, σ_v^2 and l in equation (11) by their values from equations (8) and (9) yields the formula for σ^{G} in terms of C_T^2, C_v^2 and K_0

$$\begin{aligned}\sigma^{\mathrm{G}}(\theta) &= \frac{5k^{1/3}}{2^{17/3}9\Gamma(1/3)(K_0/2k)^{11/3}}\left[\beta^2(\theta)\frac{C_T^2}{T_0^2} + \frac{11\cos^2\theta\sin^2\theta}{6(K_0/2k)^2}\frac{C_v^2}{c_0^2}\right] \\ &\times \exp\left(-\frac{\Gamma^2(5/6)\sin^2(\theta/2)}{\Gamma^2(1/3)(K_0/2k)^2}\right) .\end{aligned} \tag{12}$$

Let us now compare σ for different spectra. Figures 2 and 3 show the scattering cross-sections σ^{vK}, σ^{K} and σ^{G}, normalized to $5k^{1/3}/(2^{17/3}9\Gamma(1/3))$, as functions of the scattering angle θ for $C_T^2/T_0^2 = 0$ and $C_v^2/c_0^2 = 1/4$. Figure 2 corresponds to small values of the

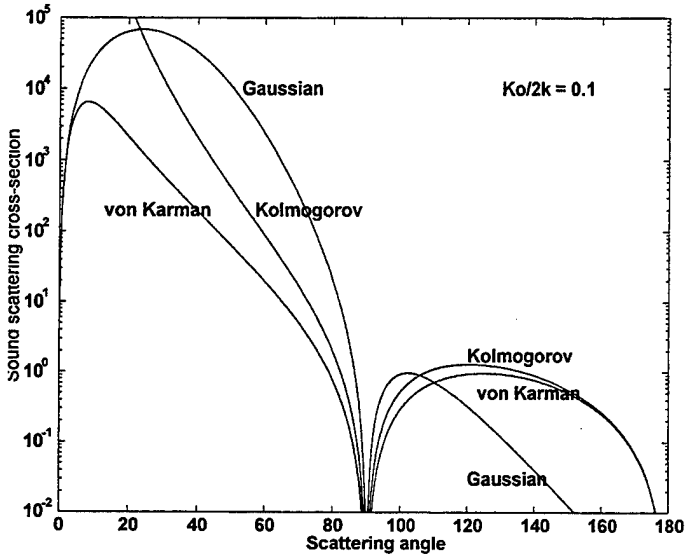

Figure 2: The normalized scattering cross-sections for the von Karman (σ^{vK}), Kolmogorov (σ^{K}) and Gaussian (σ^{G}) spectra of wind velocity fluctuations versus the scattering angle θ for small values of the parameter $K_0/2k$.

parameter $K_0/2k = 0.1$, i.e. to high sound frequencies and small values of K_0. As it should be for small K_0, $\sigma^{\mathrm{vK}}(\theta) \approx \sigma^{\mathrm{K}}(\theta)$ if the scattering angle θ is not small. On the other hand, $\sigma^{\mathrm{vK}}(\theta)$ significantly differs from $\sigma^{\mathrm{G}}(\theta)$ for almost all values of θ.

Figure 3 corresponds to relatively large values of the parameter $K_0/2k = 2$, i.e. to low sound frequencies and large values of K_0. In this case, $\sigma^{\mathrm{vK}}(\theta)$ differs significantly from $\sigma^{\mathrm{K}}(\theta)$. However, now $\sigma^{\mathrm{vK}}(\theta) \approx \sigma^{\mathrm{G}}(\theta)$ for almost all values of θ. Note that it can be rigorously shown from equations (3) and (12) that $\sigma^{\mathrm{vK}}(\theta) = \sigma^{\mathrm{G}}(\theta)$ if $K_0/2k \to \infty$.

5 Conclusions

The equation for the sound scattering cross-section per unit volume, $\sigma^{\mathrm{vK}}(\theta)$, for the von Karman spectra of temperature and medium velocity fluctuations has been obtained. Using this equation, the relative role of temperature and medium velocity contributions to $\sigma^{\mathrm{vK}}(\theta)$ has been studied in detail. It is shown that, for small scattering angles θ, the temperature

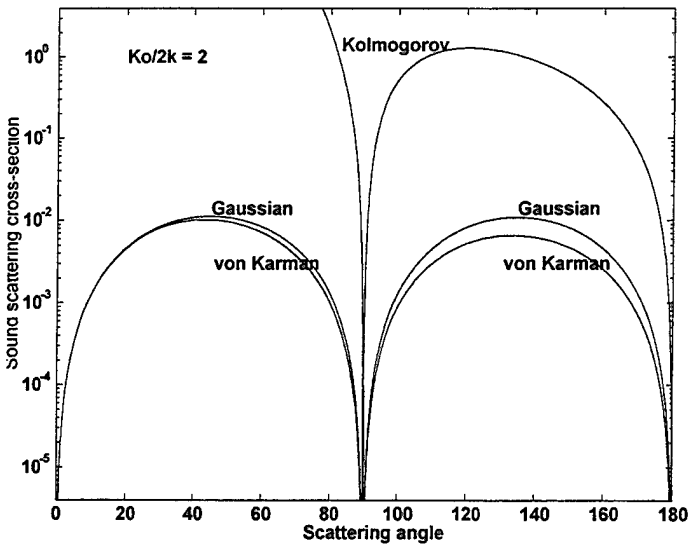

Figure 3: The normalized scattering cross-sections for the von Karman (σ^{vK}), Kolmogorov (σ^{K}) and Gaussian (σ^{G}) spectra of wind velocity fluctuations versus the scattering angle θ for relatively large values of the parameter $K_0/2k$.

contribution to $\sigma^{vK}(\theta)$ dominates over medium velocity contribution. This result is important for studies of sound scattering into refractive shadow zone since small scattering angles θ are believed to play the most important role in insonification of a shadow zone.

The sound scattering cross-section for the von Karman spectrum has also been compared with those for the Kolmogorov and Gaussian spectra. It is shown that in the limiting case of high frequencies (small values of the parameter $K_0/2k$) $\sigma^{\mathrm{vK}}(\theta)$ coincides with $\sigma^{\mathrm{K}}(\theta)$ and significantly differs from $\sigma^{\mathrm{G}}(\theta)$. On the other hand, for low frequencies (large values of the parameter $K_0/2k$) $\sigma^{\mathrm{vK}}(\theta)$ differs from $\sigma^{\mathrm{K}}(\theta)$ but coincides with $\sigma^{\mathrm{G}}(\theta)$.

Acknowledgments. This material is based upon work supported by the U.S. Army Research Office under contract number DAAH04-95-1-0593.

References

[1] Baikalova, R.A., Krekov, G.M. and Shamanaeva L.G. (1988) "Theoretical estimates of sound scattering by atmospheric turbulence", *J. Acoust. Soc. Am.*, **83** (4), 1332-1335.

[2] Brown, E.H. and Hall, F.F. (1978) "Advances in atmospheric acoustics", *Rev. Geophys. Space Phys.*, **16** (1), 47-110.

[3] Di Iorio, D. and Farmer, D.M. (1996) "Two-dimensional angle of arrival fluctuations", *J. Acoust. Soc. Am.*, **100** (2), (Part 1), 814-824.

[4] Goedecke, G. and Ostashev, V.E. (1995) "Development of the modern theory of sound propagation in the turbulent atmosphere", ARO Project No DAAH04-95-1-0593.

[5] Hinze, J. (1975) *Turbulence*, McGraw-Hill.

[6] Mellert, V. and Schwarz–Rohr, B. (1996) "Correlation and Coherence Measurements of a Spherical Wave Travelling in the Atmospheric Boundary Layer", *Proc. 7th Intern. Symp. on Long Range Sound Propagation*, Lyon, France, 391-405.

[7] Ostashev, V.E., Blanc-Benon, Ph. and Juvé, D. (1998) "Coherence function of a spherical acoustic wave after passing through a turbulent jet", *Comptes Rendus de l'Académie des Sciences* (accepted for publication).

[8] Ostashev, V.E., Mellert, V., Wandelt, R. and Gerdes, F. (1997) "Propagation of sound in a turbulent medium I. Plane waves", *J. Acoust. Soc. Am.*, **102** (5), 2561.

[9] Ostashev, V.E. (1997) *Acoustics in Moving Inhomogeneous Media*, E & FN SPON (An Imprint of Thompson Professional), London.

[10] Tatarskii, V.I. (1971) *The effects of the turbulent atmosphere on wave propagation*, Israel.

[11] Wilson, D.K. (1997) "Scattering of acoustic waves by intermittent temperature and velocity fluctuations", *J. Acoust. Soc. Am.*, **101** (5), 2980-2982.

[12] Wilson, D.K. "Performance bounds for acoustic angle-of-arrival arrays operating in atmospheric turbulence", *J. Acoust. Soc. Am.*, (in press).

A CONCEPT FOR THE APPLICATION OF RADAR ENVIRONMENTAL OBSERVATIONS TO NAVAL OPERATIONS

Nicholas J. Bucci, Henry S. Owen, Dr. James V. Melody, Dr. Harry Urkowitz
Lockheed Martin Government Electronic Systems, 199 Borton Landing Road, Moorestown, NJ, 08057

Dr. Dennis Thomson, Dr. George Young, Dr. Gregory Forbes
Pennsylvania State University, State College, PA

ABSTRACT

Sufficient and accurate knowledge of environmental conditions is essential to the efficiency and safety of all Naval operations. Consequently, knowledge of propagation conditions and the clutter environment can support the warfighter in a number of ways.

Lockheed Martin Government Electronic Systems and the Department of Meteorology at Penn State University have completed an experiment, under the sponsorship of the Office of Naval Research, in which diverse measurements of atmospheric conditions in the vicinity of a tactical radar, the AN/SPY-1 phased array radar, were made. Measurements were made of: precipitation, clear air turbulence, and clouds. This paper describes the potential use of the AN/SPY-1-based environmental observations in the conduct of Naval operations. Using data collected during our experiments we show examples of the types of data that are required to support battlegroup operations. In addition, a variety of products derived from these data, such as hazardous weather reports, wind profiles, and nowcasts, are presented.

1.0 Introduction

Sufficient and accurate knowledge of environmental conditions is essential to the efficiency and safety of all Naval operations. For example, local and regional refractive profiles and winds strongly influence the performance of diverse communications and defense systems over land as well as at sea. Consequently, knowledge of propagation conditions and the clutter environment can support the warfighter in a number of ways.

Lockheed Martin Government Electronic Systems and the Department of Meteorology at Penn State University have completed an experiment, under the sponsorship of the Office of Naval Research, in which diverse measurements of the atmospheric conditions in the vicinity of a tactical radar, the AN/SPY-1 phased array radar, were made. Measurements were made of: precipitation, clear air turbulence, and clouds. A description of the experimental methods and initial results was published first in a paper presented at the 1996 Battlespace Atmospherics Conference (BAC) [1]. Companion papers are also part of the present BAC [2] and [3]. This paper describes the potential use of the AN/SPY-1 based environmental observations in the conduct of Naval operations. Other radar sensors are also considered for the collection of environmental data. Using data collected during our experiments we show examples of the types of data that are required to support battlegroup operations. In addition, a variety of products derived from these data, such as hazardous weather reports, wind profiles, and nowcasts, are presented.

We show that the SPY-1 radar can assist in the collection of environmental data to support radar operations as well as other operations aboard ownship, within the battlegroup and in the theater.

Section 1.1 will describe the benefits to various Naval operations and the warfighter from the knowledge of the weather. Section 2.0 will present the concept of the collection and use of meteorological data for Naval Operations. Section 3.0 will provide examples of the products which can be generated from the meteorological data that is collected. Section 4.0 will provide some insight into the feedback to the ship, sensors, and theater operations. Such feedback is based on using the products described in section 3.0 with some additional data processing required.

1.1 Benefits to the Warfighter

The environmental data collected through a tactical radar such as the SPY-1 provides many benefits to the warfighter deployed throughout the theater. The weather data produced includes: high temporal and spatial resolution clutter map, hazardous weather condition detection and prediction, wind field mapping, cloud cover assessment, boundary layer detection, and short and long term forecasts. Figure 1 shows theater Naval Operations where weather observations could provide benefits.

Environmental data can be used aboard ownship to: 1) improve the radar's sensitivity, 2) aid / improve the prediction of propagation

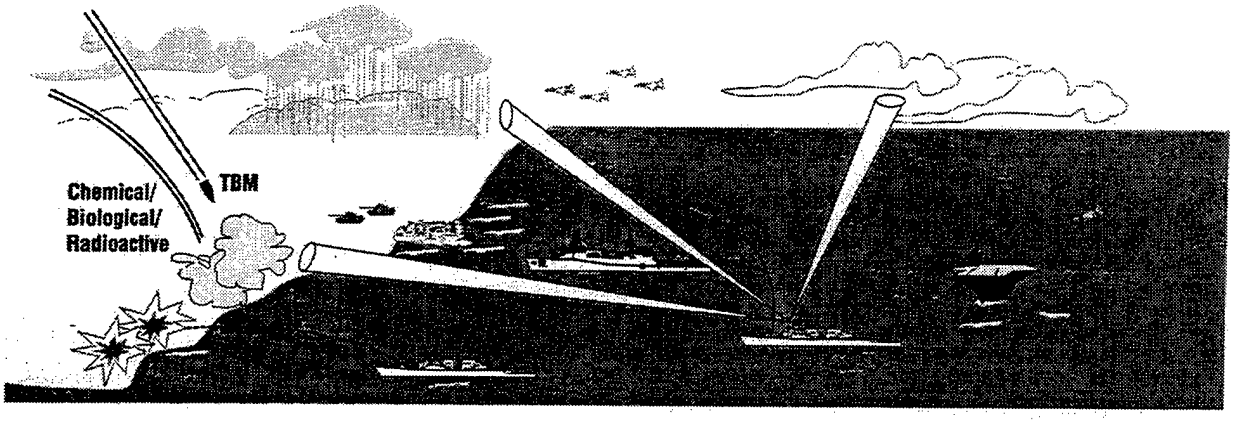

Figure 1: Environmental observations aid the warfighter in all aspects of theater operations

conditions for a variety of microwave and radio systems, and 3) improve the assessment of capabilities of other sensors, weapons, and the combat systems through real time tactical decision aids (TDAs). Overall battlegroup and theater operations are supported by: 1) improved safety of aircraft operations, 2) aiding in the efficient conduct of amphibious landing and expeditionary operations, 3) providing data to initialize onboard models (modified mesoscale or Large Eddy Scale, LES, models) for the production of in-situ nowcasts, 4) providing wind profiles to improve the accuracy of Naval Surface Fire Support, and 5) measuring winds to aid in the prediction of the dispersion and movement of Chemical, Biological, and Radioactive (CBR) fallout.

For forecasting / modeling weather phenomena and its movement, weather data from tactical sensors provides improved accuracy, resolution, and timeliness of weather forecasting to warfighters. Weather data collected locally (onboard ownship) is an enabling technology for in-situ forecasting models, allowing the warfighter to have direct access to forecasting and modeling data within the theater. This data allows rapid and accurate local nowcasts (short term forecasts). It provides high resolution local measurements to warfighters throughout the theater. Improved forecasting capabilities supports safer, more efficient littoral, amphibious and expeditionary operations, improved force mobility, and improved long term and global forecasts from Fleet Numerical Meteorological Oceanography Center (FNMOC) and other forecasting operations.

For aircraft operations, the nowcasts and forecasts generate weather information up to and over the target area which support safer, more effective air strikes, helo operations, and aircraft carrier operations. The nowcasts and detection of weather phenomena provide the warfighter with winds, wind shear, gust fronts, as well as cloud tops and bottoms, and storm extent and structure.

The weather data can improve force self defense and area anti-air warfare (AAW) for each sensor. The sensitivity of the sensors can be improved in two ways. First, the radar system can lower its detection thresholds (added sensitivity by detecting smaller targets) in the presence of clutter, which would inherently generate more clutter detections that can be screened by the detailed clutter map. Second, the waveform selection process uses the detailed clutter map to choose the proper waveform parameters (number of pulses, pulse repetition frequency, etc.) based in the reflectivity, mean velocity, and spectrum spread of the clutter in the region of the transmission to assure that clutter suppression is maximized and clutter detections minimized.

The radar system will have better radar resource management and improved awareness through the clutter map. Clutter tracks can be reduced, eliminating resources required to "track clutter". In addition, waveform selection can be made more efficiently eliminating the need to revisit beam positions with multiple dwells with varied parameters to achieve the necessary clutter visibility. The clutter map can also be used in conjunction with detection reports to infer propagation conditions. The detection results can confirm surface tracks appearing at longer ranges meaning that a surface duct exists. This can substantiate or refute the predicted propagation conditions and their homogeneity, particularly between time of propagation condition measurements. The improved situational awareness provided by the weather data can be useful in capability assessment through TDAs for a sensor / weapon system.

TDAs provide insight into the Weapons System's performance against a threat given the current environmental conditions and system status.

For Tactical Ballistic Missile (TBM) missions, weather data provides improved battlespace awareness through: assessment of cloud cover (by cloud layer detection), detection of three dimensional wind fields, and spectral characterization of the environment. The cloud cover assessment and storm structure supports the seeker selection for the defensive missile, to assure that IR seekers are not blind during an engagement in clouds or storms. Wind field maps aid in the prediction of the dispersion of the cloud produced by the warhead within the TBM. The winds fields and spectral characterization aid in the analysis of the environment within a TBM complex for kill assessment and perhaps debris discrimination. Wind fields and spectral characterization can aid in the engagement process if enough time is available and resources are limited, the engagement decision can be influenced by the predicted impact point and the anticipated dispersion cloud movement in relation to forces and civilians.

In CBR scenarios, wind fields can be used in much the same way it is used for TBM. Dispersion models can be driven with measured 3D winds rather than point measurements and modeled winds. Impact zones can be determined using the winds information. Also, wind data can improve: the engagement decisions, force mobility in the impact area, and evacuation of personnel from impact areas and areas of anticipated dispersion cloud contamination.

The winds information aids all types of fire support with improved accuracy of weapon delivery from measured accurate and timely 3D winds not point measurements or modeled winds, both at the gun and over the target area. Naval Surface Fire Support (NSFS) and ground based counterbattery fire will both be supported with accurate ballistic corrections. Also, clutter maps will aid fire support in identification of chaff for improved tracking.

2.0 Concept Description

The US Navy has published a roadmap for future surface combatants, the SC-21 family of ships. At the current time, the Navy vision calls is for the deployment of at least two ships in the SC-21 family. The first ship in the family has been given the designation, the DD-21. This ship is to be a multimission destroyer with an emphasis on a land attack mission. The second ship in the SC-21 family is the CG-21. This ship's missions are still evolving, but in general, this ship is anticipated to be a Air Dominance cruiser. Additional ships to be built in the LPD / LHD / LHA in the amphibious ship class, the CVN / CV(X) aircraft carrier class, and the DDG-51 class of guided missile destroyers.

The Navy has also developed a roadmap for future radar developments. The radar roadmap supports the anticipated surveillance requirements for the missions of each of the above ships. The radar roadmap consists of three radar developments: 1) the Volume Search Radar - a low cost radar for long range surveillance, situational awareness, 2) the Multifunction Radar - a horizon search and track radar, and 3) the SPY-2 radar - a long range search and track radar. In addition to these radars, additional sensors will be used aboard the Navy surface ships, these include the current SPY-1 phased array radar, the SPQ-9B, the Infrared Search and Track (IRST) system, future IR sensors, and MORIAH (which includes rocketsondes to measure lower atmospheric conditions).

Table 1 shows the various ship classes outlined above and the sensors that are to be deployed aboard these ships. An additional sensor included in the table is the support satellite, the DMSP. The concept presented herein is to utilize the data from this wide variety of sensors and ships to obtain vital meteorological information that can be used in almost all naval operations. The sensors described above will perform the measurements described in the third column of table 1, including: environment spectral characteristics; refractivity profiles; point measurements of temperature, wind, humidity, and barometric pressure; cloud tops and system movements. From these measurements a number of products can be generated, including: 3D clutter maps; volumetric refractivity profiles, tactical assessments (depth of fire of the weapon system); modified mesoscale model initialization data; nowcasts and forecasts; cloud maps; inputs to data assimilation; and ionospheric propagation.

Table 1: Environmental measurement platforms, sensors, and products generated

Platform	Sensors	Measurements	Processors Onboard	Products
DDG	SPY-1, SPQ-9B, IRST, MORIAH	Radar spectral moments; Refractivity profiles; Point - temperature, wind, humidity, barometric pressure	A) Spectral moment processor; B) Modified mesoscale / Large Eddy Scale (LES) model processors	1) 3D clutter maps; 2) Volumetric refractivity profiles; 3) tactical assessment capability (depth of fire)
CG-21	SPY-2, MFR, IR sensor, MORIAH			
DD-21	VSR, MFR, IR sensor, MORIAH			
LPD / LHD	VSR, MFR, IR sensor, MORIAH	Radar spectral moments; Refractivity profiles, Point - temp., wind, humidity, barometric pressure	A) Spectral moment processor; B) Mesoscale and Large Eddy Scale (LES) model processors	1) 3D clutter maps; 2) Volumetric refractivity profiles; 3) tactical assessment capability; 4) modified mesoscale model initialization data; 5) nowcasts / forecasts
CVN / CV(X)	VSR, MFR, IR sensor, MORIAH			
DMSP Satellites	Visual and IR	Cloud tops, systems movements, temperature and humidity profiles	N/A	1) Cloud maps; 2) inputs to data assimilation; 3) ionospheric propagation

Figure 2 shows the various platforms described above and the notional flow of information between them. The flow of information between the platforms is dictated by the processors and sensors that are aboard each ship. The fourth column of table 1 describes the processors that are aboard each ship. In general, all of the ships with radar measurements contain a processor to generate spectral moments and the products associated with them. The carriers and amphibious ships, the "big decks", it is assumed will have sufficient computing plant to perform in situ forecasting using Mesoscale and LES environmental models. The surface combatants are assumed to have limited computing plants aboard and therefore will not have the full capability to perform in situ forecasting. However, it is believed that a modified Mesoscale or modified LES model could be deployed aboard these ships such that some forecasting / nowcasting capability could be supplied to these ships. The modified models would require some initialization data from the next highest order model, this data would be provided on a periodic basis from the carrier and amphibious ships where these higher order models exist. These boundary conditions for the modified models could be used for successive runs of the modified models to

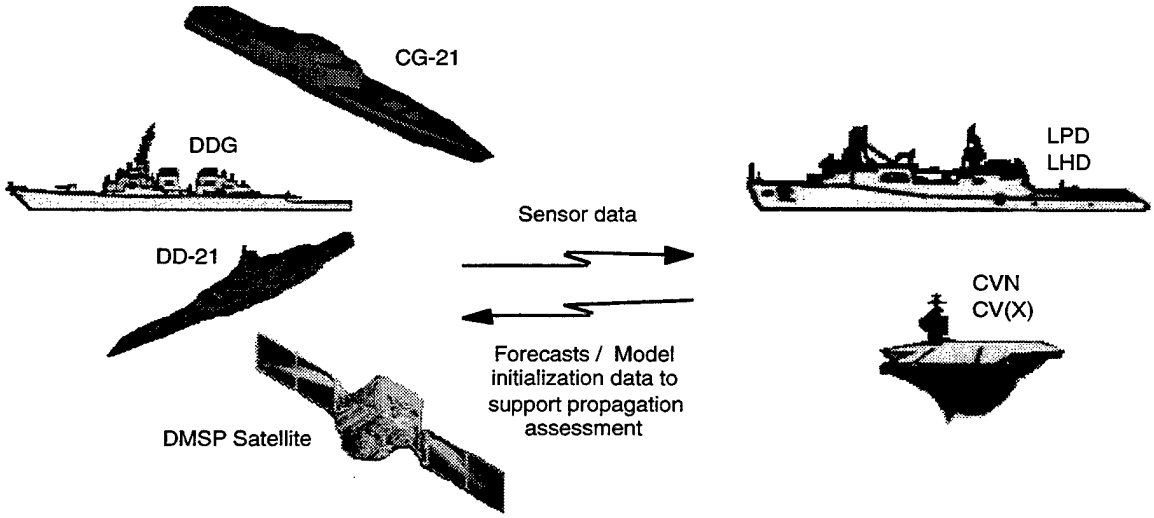

Figure 2: Platforms for environmental data collection and environmental data processing

generate updated forecasts until the next set of initialization data is available and required.

The capability will exist aboard all of the Navy's surface ships to generate sufficient meteorological data to drive onboard models. Each surface ship will collect weather information and disseminate it to the carrier and amphibious ships and to FNMOC for generation of forecasts.

3.0 Examples of Products

This section will present a number of the products that can be derived from the environmental data collected by the tactical sensors. These examples are data collected from the Tactical Weather Radar Experiment sponsored by ONR [2].

3.1 Battlespace Awareness

A significant benefit offered by observations of environmental conditions through tactical radars is improved situational awareness. The basic environmental measurements available through radars such as NEXRAD in CONUS are not available to deployed operational forces at sea. Providing the basic spectral moment measurements of conventional meteorological radars at sea would enable the generation of a number of products including:

- composite reflectivity 'quick-look' maps of storm extent
- 3-D, detailed clutter maps with spectral characterization to improve radar sensitivity and reduce clutter track generation through improved waveform selection
- provide up-to-the-minute detailed wind and precipitation maps for detailed nowcasts and to improve the accuracy of forecasts

Figure 3 shows a reflectivity plot from the SPY-1 radar. This map of precipitation extent was taken using a tactical, single-pulse waveform from the SPY-1 radar. It is presented in 'composite reflectivity' format, with the 3-D precipitation map collapsed to a geographical presentation for ease of interpretation. It provides an accurate map of precipitation as remnants of Hurricane Fran moved through New Jersey in September, 1996. This measurement capability, very similar to that provided by NEXRAD, would provide the basis for a number of valuable weather related products for improved weapon system performance and operational planning.

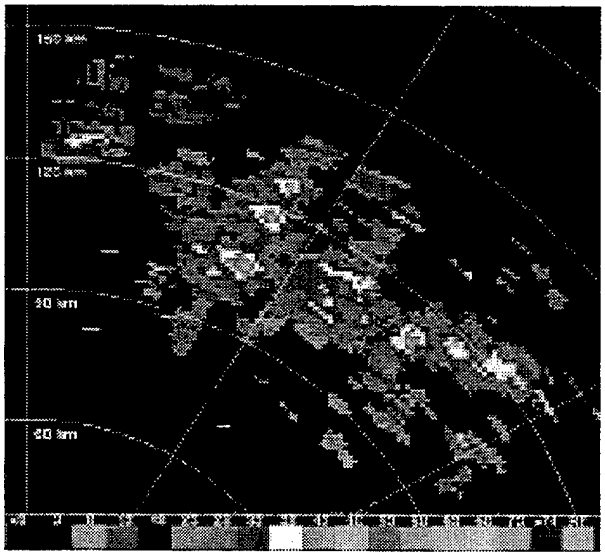

Figure 3: Reflectivity plot from Hurricane Fran

3.2 Assessment of Clutter Conditions

The spectral moment measurements conventionally used in meteorological sensing can also be used directly in weapon system operation. The same meteorological measurements which drive environmental algorithms and models can also be used to improve the operation of a radar in the clutter environment caused by a weather event. Even if no precipitation is present, these measurements can provide a 'spectral picture' of the surface clutter conditions that exist, so that the radar can be optimized more readily to reject the clutter that is present.

Figure 4 shows the types of spectral measurements performed in the SPY-1 experiment. This figure contains three plots. On the left hand side are two of the spectral moments measured in precipitation using SPY-1 tactical waveforms. The upper left hand plot shows a measurement of mean radial velocity versus range at a low elevation looking through a storm front. The lower left hand plot shows a measurement of spectrum width (an indicator of shear and turbulence) versus range for the same beam position. These measurements were made with a three pulse waveform.

The right hand plot shows the actual spectrum of the same conditions, taken after the three-pulse measurement using a NEXRAD pulse-doppler sequence transmitted from the SPY-1 radar. It provides a very clear picture of the precipitation spectrum (and therefore clutter spectrum) but requires the use of a radar resource intensive non-tactical waveform.

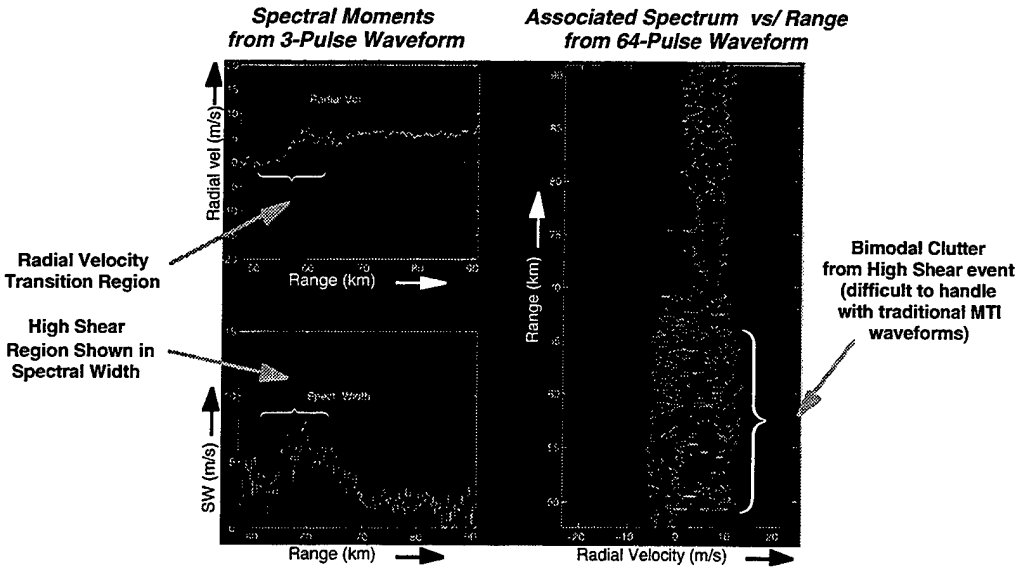

Figure 4: Clutter Assessment using spectral characteristics

Both the two left hand plots and the single right hand plot clearly show the presence of a dominant spectral component with a medium spectrum width at close ranges, followed by an increased in spectral width (in this case due to a vertical shear in the storm), followed again at 70 kilometers in range by a narrow spectral component showing outbound flow of precipitation. An important factor in these observations is that the plots on the left were generated using a short, tactical waveform normally transmitted by SPY-1. Also, the meteorological measurements which resulted provided critical information about an increase in spectrum width which occurs at ranges between 55 and 70 kilometers. At these ranges, the high shear level provides a clutter condition that may cause significant false alarms (resulting in an overall decrease in radar effectiveness) that could be counteracted by better waveform selection. These spectral moment measurements provide important information that is required for such a waveform selection improvement.

3.3 Wind Field Mapping

Another important piece of information for the warfighter is wind information. Wind information has long been recognized in the non-DOD community for forecasting and aircraft control. It also is critically important in such areas as CBR defense. Measurements made using the SPY-1 radar could be used to generate area maps of wind fields for all of these purposes. Figure 5 shows radial and dual doppler wind field data that would provide significant benefits to all naval operations.

The left hand side of this figure shows radial velocity maps from two separate radars located approximately 42 kilometers apart. The lower left plot shows radial velocity measurements taken by SPY-1 using tactical waveforms. The SPY-1 radar is located at the center of the range rings to the lower left of the plot. The upper left plot shows the same type of radial velocity measurement taken by the NEXRAD radar to the east of the SPY-1 (the NEXRAD is located at the lower right of the region presented in this plot). Dark regions show outflows from each radar, and white regions show zero radial velocity (tangential flows). This information alone can be difficult to interpret. If the two radial velocity maps are combined, however, a wind field map can be generated. The wind field map resulting from these scans is shown in the right hand plot. This wind field is easy to interpret, and provides data directly useful to meteorologists, aircraft controllers, and in CBR defense. Since it is common for two separate tactical radar systems to operate together in battle group operations, this type of product would be relatively easy to implement. Data bandwidth requirements to transmit the radial velocity estimates to a central site (one or both of the ships) are small compared to other communication bandwidth requirements in effect today.

Significant work is ongoing to allow for full Doppler wind retrieval, such as that shown in the right plot of Figure 5, through single radar systems. Data taken from SPY-1 during land-based experiments are being used for that purpose by Naval Research Laboratory investigators. Success in development of this

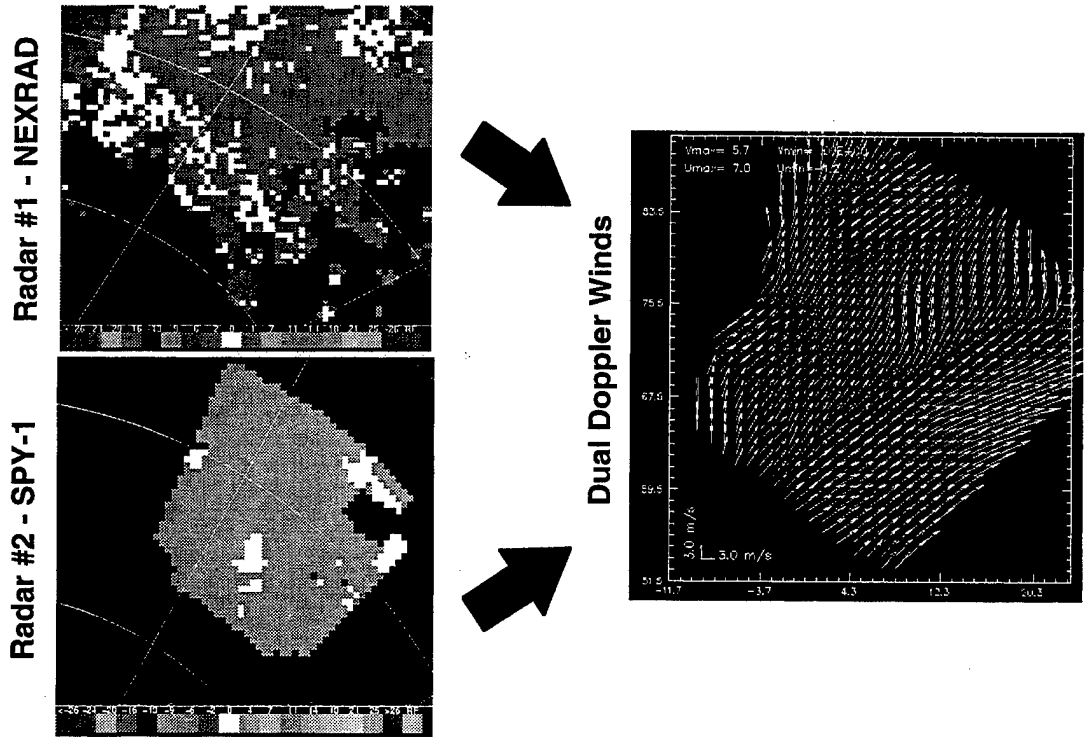

Figure 5: Radial and dual doppler wind field measurements capability would enable full wind field retrieval from radial wind measurements of one radar.

3.4 Cloud Cover Observations

Tactical radars often have sufficient sensitivity that would allow for observations of low reflectivity phenomena such as cloud layers. An example of cloud layer observations is shown in figure 6.

Figure 6 contains two plots. The one on the left is a range-altitude plot of a cloud snapshot taken by the SPY-1 radar during land based data collection. The plot on the left depicts a time-altitude plot of the same cloud conditions taken by Pennsylvania State University's 94 GHz (W-band) cloud profiling radar. For this data collection event, the cloud profile was positioned approximately 8 kilometers from the SPY-1 so that coordinated data collection events could be conducted. The cloud profiler looks directly upward (generating a profile of cloud conditions as clouds move overhead). The SPY-1 scans a vertical slice above the cloud profiler to provide snapshots of cloud conditions for a number of time intervals.

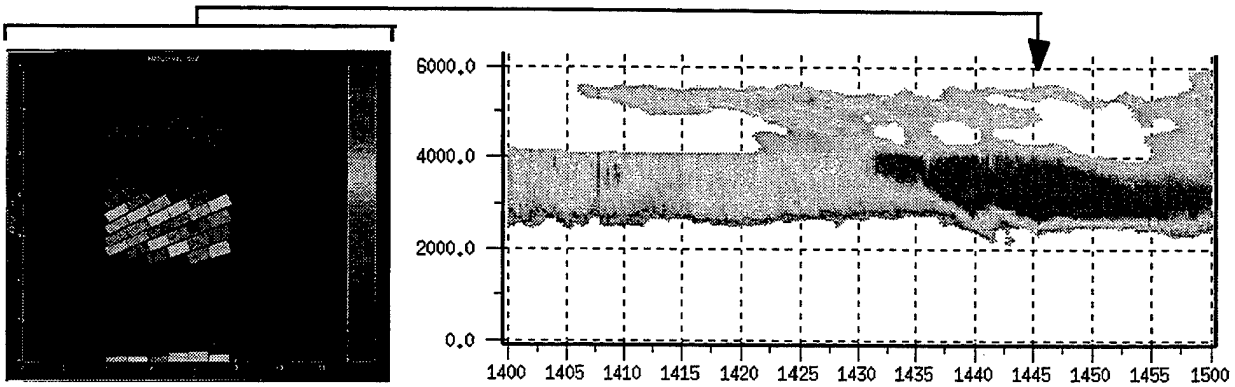

Single snapshot (Height versus Range)

High resolution data versus time

Figure 6: Cloud Observations

This figure depicts an overcast day (free from precipitation). The SPY-1 plots show a lower cloud band at an altitude of 2.5 kilometers to 4 kilometers. The plot is thresholded above the minimum sensitivity level of the SPY-1 radar. A higher cloud band is clearly shown at an altitude of approximately 5.5 kilometers. The snapshot was taken at 1446 UT (as depicted by the arrow leading to the W-band radar plot). The cloud profiling radar clearly shows the same higher altitude thin cloud layer also.

Knowledge of cloud cover conditions is becoming increasingly important with the emphasis that is being placed on electro-optical sensors. The performance of these sensors are significantly degraded by the presence of clouds. Knowledge of cloud extent would improve the ability of operators to plan engagements using real-time information about cloud layer extent. Optimization of sensor selection and exploitation of cloud cover to reduce counterdetection is an important benefit to the warfighter. Details of cloud observations by the SPY-1 radar can be found in [2].

3.5 Boundary Layer Observations

Another low reflectivity observation that is important to Naval operations is that of the marine boundary layer. The boundary layer plays an important role in forecasting as well as in the assessment of how tactical sensors and their associated weapon systems will perform against expected threats. S-band and L-band radars (typical frequency bands for many tactical sensors) are often capable of making observations of the boundary layer by observing backscatter from turbulence associated with the boundary layer. An example is presented in figure 7.

Figure 7 shows relative reflectivity levels from boundary layer turbulence observed by the SPY-1 radar. The Penn State W-Band radar used in conjunction with the SPY-1 clear air measurements cannot observe turbulence but it can observe other scatterer types such as clouds and insects. Simultaneous observations of the SPY-1 scan area by Penn State's W-band radar showed that the backscatter source shown in Figure 7 was not observable with the W-Band radar, therefore it confirmed that the backscatter source was turbulence. SPY-1 returns in this case show a strong horizontally distributed return at an altitude of approximately 750 meters, with decreasing signal levels above and below that altitude. This type of observation can provide important feature information about the boundary layer, such as general strength and depth of the layer. An important factor is that these observations can be made to observe boundary layer conditions accurately over an area and as temporal changes occur.

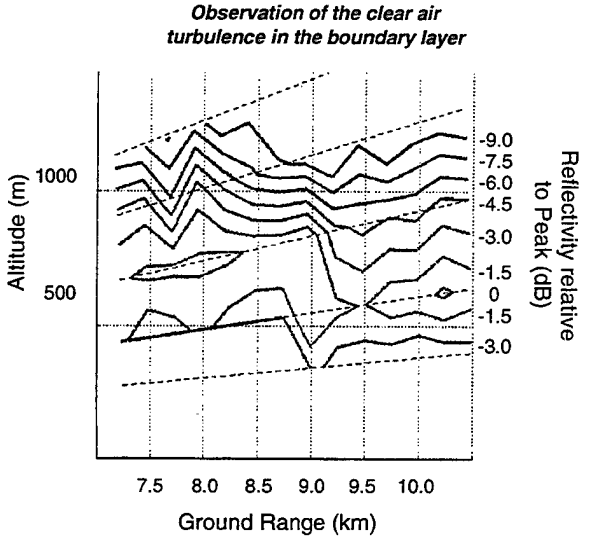

Figure 7: Observation of the boundary layer

4.0 System Performance Feedback

The general issue of radar and weapon system performance has long been an important one to the Navy. Environmental conditions change quickly and sometimes drastically (even more so in the littoral region than in the open ocean), and they have a profound impact on how radar signals propagate and at what ranges targets can be detected. With the movement by the Navy to more littoral missions, environmental measurements are even more critical for safe and efficient operations. Typical changes that occur may mean a reduction in detection range. While a weapon system operator can normally expect to see a given target at a range which provides adequate time for response, current conditions may preclude detection until it is too late to effectively engage an inbound threat. Real-time, volumetric assessment of these conditions remains a challenge that has not been fully addressed.

Current sounding techniques allow for accurate point measurements of refractivity conditions which govern propagation conditions. However, these measurements are made through rocketsondes that must be launched at close time intervals to maintain adequate sampling of the environment, and it is assumed that these point measurements can be

extrapolated to define refractivity conditions for the full volume of the tactical area surrounding a ship. Therefore, changes of the refractivity profile in time and distance from the tactical radar of interest naturally result in errors associated with the propagation assessment made. The bottom line is that a full volumetric, continuous update to propagation conditions is an important improvement that is needed in today's tactical environment.

Radar measurements can provide an important piece of information to solve this problem. No single sensing method currently exists to provide this volumetric picture. Other sensors which are currently being developed (such as LIDARS) will provide very important information, but will not be able to provide the necessary information in all weather conditions. A data fusion approach between multiple sensors is probably the most effective path to solve this challenging problem.

Radar measurements can provide a variety of information to be used for propagation assessment. Direct observations of boundary layer conditions will help define where ducting conditions exist and may provide insight into the general characteristics of those ducting conditions. Observations of surface reflections may be useful in the assessment of current propagation conditions by directly observing how much surface backscatter is resulting from ducting [4]. Also, meteorological radar measurements can provide basic initialization parameters for a set of large eddy scale (LES) models that are currently under development and may provide the link between various sensor inputs and full volumetric assessment and prediction of refractivity conditions.

This approach to propagation assessment will require the fusion of a number of sensors including (but not limited to) satellite sensors, rocketsondes, balloon sounding sensors, and shipboard sensors. Data fusion will include a cascade of model scales from global models, to nested mesoscale models, to large eddy scale models (with boundary initialization being supported by the larger scale models). The results will be a projection of high resolution refractivity profiles as they develop over time for various regions of interest. These types of range dependent refractivity profiles can then be readily assimilated into currently available propagation models and weapon system models to provide an operator key information on how a given weapon system is and will be performing.

Figure 8 shows a data flow diagram of the collection, fusion, processing, and use of meteorological data to generate products which are useful for the conduct of a number of Naval operations. The figure shows three columns: 1) the sensors which collect the data and the data that is collected, 2) the onboard environmental processing of the sensor data, and 3) the products generated by the processing and the uses of these products for Naval Operations.

Meteorological data is collected by a number of sensors, including satellites, rocketsondes, and balloons. Tactical radars, such as the SPY-1, SPS-48/49, SPN-43, SPQ-9B, MFR, VSR, and SPY-2, measure spectral information which is used along with the meteorological data above. Tactical radar data is processed by an onboard environmental signal processor [1] to generate spectral moment information which will be used to generate a high fidelity, 3D clutter map. This data is also used with other meteorological data in Mesoscale and high resolution, or LES, models. The meteorological data and the tactical radar spectral moment information are used in onboard processors (larger surface ships, CVN / CVX, LPD / LHD / LHA) and processors at the FNMOC in global models and mesoscale models to produce forecasts and nowcasts for the theater. The mesoscale models are also used to generate initialization data and boundary conditions for higher resolutions large eddy scale or modified LES models in onboard processors aboard the smaller surface ships (DDG, DD-21, CG-21). The initialization data / boundary conditions data is updated periodically, the tactical radar data is updated more often and the model outputs are generated with new tactical radar data. The output of the High resolution LES and modified LES models is used in electromagnetic propagation models.

The products generated by all of the models and processors are: forecasts and nowcasts, time varying volumetric propagation assessment, and improvements in radar sensitivity. The forecasts and nowcasts are generated from the global and mesoscale models. The volumetric propagation assessment maps are generated by the electromagnetic propagation models. The propagation assessment maps are used predict the performance the sensors and weapons in the weapon system. This capability assessment will enable an operator to understand the changes to weapon system performance as the environment changes in the theater. The

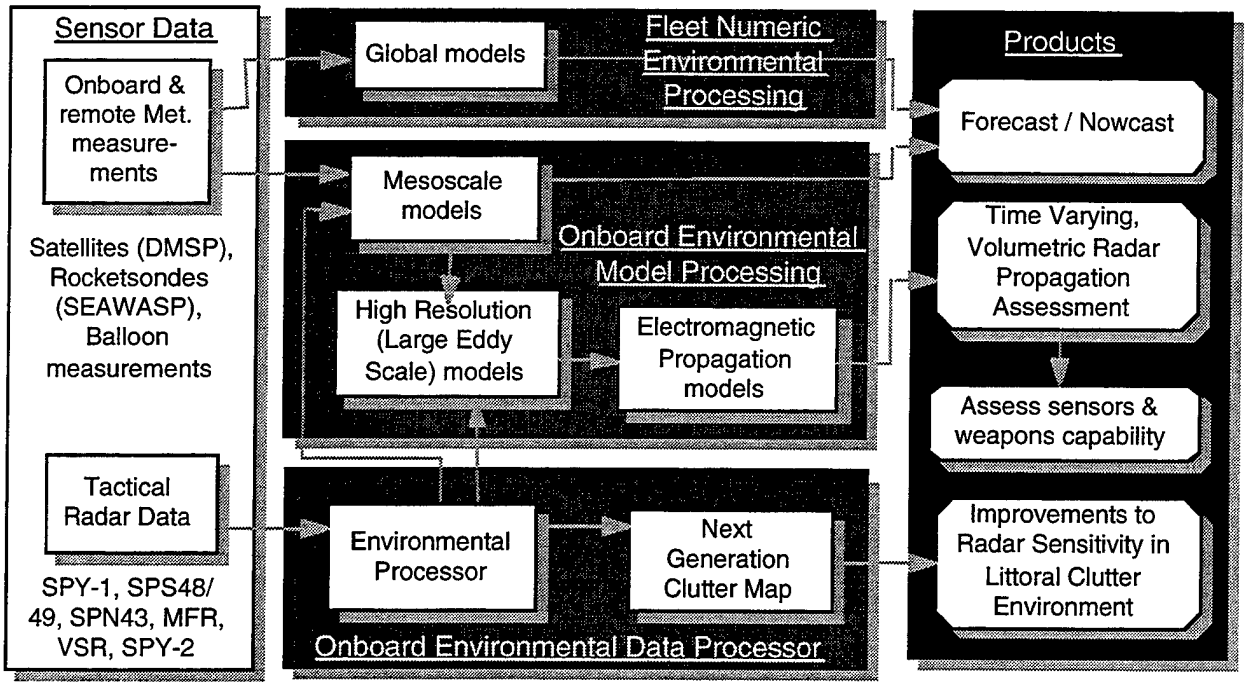

Figure 8: Environmental measurements and processing

operator will know when a ducting condition has changed the detection performance of his sensor such that the depth of fire for his weapons had gone from a level three to a level two. Finally, the high resolution, volumetric clutter map generated from the spectral moment data from the radar is used to improve the sensitivity of the radar by automating the selection of the waveform to be transmitted such that the degradation of performance from clutter is reduced and in some cases eliminated.

5.0 Summary

A concept for the collection, fusion, and processing of meteorological information from various current and future tactical sensors aboard current and future platforms throughout the theater has been presented. This concept has wide applicability for sensors deployed throughout the battlespace. The data collected from the various sensors can be fused to yield a picture of the propagation and clutter conditions within the theater. In addition, 3D wind fields, forecasts and nowcasts, and other advanced weather products, such as storm tracks and storm structure, can be generated and made available to the warfighter for the conduct of various operations.

Weather data have wide reaching benefits for the warfighter, beginning with improved performance of each sensor, as well as aiding in the capability assessment of each sensor. In addition, the data aid in more efficient, safer operations throughout the battlespace, from amphibious and landing operations, to expeditionary operations, force mobility, and air operations.

6.0 References

1. H. S. Owen, H. Urkowitz, N. J. Bucci, J. V. Melody, R. McLean, "Tactical Weather Radar Experiment For a Shipborne Radar", Proceedings of Battlespace Atmospherics Conference; Naval Command, Control and Ocean Surveillance Center, RDT&E Division; San Diego, CA; December 3-5, 1996
2. H. S. Owen, E.E. Clothiaux, G. S. Young, J. Kanefield, J. Melody, J. Verlinde, "Measurements of Cloud Layers and Clear Air Turbulence with a Tactical Shipboard S-Band Radar", Proceedings of Battlespace Atmospherics Conference; Space and Naval Warfare Systems Center; San Diego, CA; December 2-4,1997
3. J. Stephans, H. Urkowitz, G. Forbes, "Wind Field Measurements in Non-precipitation Conditions with a Tactical Shipboard S-Band Radar", Proceedings of Battlespace Atmospherics Conference; Space and Naval Warfare Systems Center; San Diego, CA; December 2-4, 1997
4. Personal Communication with Jeff Krolick of Duke University, Department of Electrical and Computer Engineering, Durham, NC, and Ted Rodgers of Space and Naval Warfare Systems Center, San Diego, CA.

MEASUREMENTS OF CLOUD LAYERS AND CLEAR AIR TURBULENCE WITH A TACTICAL SHIPBOARD S–BAND RADAR

H.S. Owen * , E.E. Clothiaux**, G.S. Young**, J. Kanefield*, J.V. Melody*, J. Verlinde**
* Lockheed Martin, Government Electronic Systems, Moorestown, New Jersey
** Department of Meteorology, Pennsylvania State University, University Park, PA

ABSTRACT

It has been demonstrated, in previous work, that NEXRAD–like meteorological measurements can be made by tactical radars without interrupting the tactical radar's primary mission. Data has been presented illustrating the accuracy of such measurements using the SPY–1 multifunction shipboard radar, at the Navy's Combat Systems Engineering Development (CSED) Site in Moorestown, NJ.

This work has continued, expanding to the measurement of non–precipitation phenomena, such as boundary layer turbulence and cloud layers. Comparisons were made between observations from SPY–1, the Pennsylvania State University's W–band (94 GHz) cloud profiling radar, and a NEXRAD located nearby.

These results indicate that the SPY–1 can accurately generate cloud profiles, using the W–band radar as truth. In addition, it has been demonstrated that the SPY–1 can make accurate measurements of boundary layer turbulence. Examples of both types of measurements are presented, using data from all three sensors present for the experiment.

The presence of cloud layers and the strength of refractivity gradients in the marine boundary layer affect the performance of a host of tactical EM/EO sensors. The ability to accurately determine cloud profiles and boundary layer characteristics will provide significant benefit to Naval operations. It will be an important step in aiding the warfighter to optimize sensor performance and operational tempo in a variety of environmental conditions.

OVERVIEW OF EXPERIMENT GOALS

The goal of this experiment was to determine the ability of tactical radars (namely the SPY–1) to provide useful measurements of cloud layer extent and boundary layer turbulence. These conditions are considered 'clear air' conditions for the purposes of this experiment.

These goals required collection of radar backscatter data from the SPY–1 radar for two basic sources: cloud layers and clear air turbulence. They also required corroboration of SPY–1 returns with other sensors suitable to verify measurement accuracy and verify that the scattering mechanisms of interest were actually observed.

Previous experiments under precipitation conditions have been accomplished using only SPY–1 tactical waveforms [1]. The goal of this experiment was to make more sensitive measurements with dedicated environmental measurement waveforms that could be implemented on tactical systems with very little impact on the radar's performance of its tactical mission.

SCATTERING IN 'CLEAR AIR'

For this experiment, 'clear air' was defined as non–precipitation conditions where the dominant backscatter is caused by turbulence, cloud droplets, and a variety of debris such as insects and other particles entrained into the lower atmosphere.

The strength of the backscatter is often defined in terms of radar reflectivity, denoted as η (in units of m^2/m^3). In cloud and precipitation conditions, when the dominant scatterer is water droplets, reflectivity is related to the meteorological parameter equivalent reflectivity factor (a measure of reflectivity which is related to drop size distribution). The relationship is given as [2]

$$\eta = (\pi^5 / \lambda^4)\ |K|^2\ Z_e \qquad (1)$$

where λ is the transmitted wavelength, $|K|$ is based on the index of refraction of the dominant scatterer (rain in this case), and Z_e is the equivalent reflectivity factor. Equivalent reflectivity factor is defined on the assumption that the wavelength of the transmitted signal is large enough compared to the scatterer diameter to result in a Rayleigh scattering condition. If this condition is not met, the actual radar reflectivity that is observed will be different than that defined by the previous equation.

When the dominant scatterer is not rain, but is instead fluctuations in the index of refraction of the air from turbulence, the definition of radar reflectivity becomes [3]

$$\eta = 0.38\ \lambda^{-1/3}\ C_n^2 \qquad (2)$$

where C_n^2 is the structure constant of the changes of refractivity due to turbulence, temperature gradients, and humidity gradients. This relationship is valid when the relationship between transmitted wavelength and the physical scale of the turbulent eddies support Bragg scattering. If no turbulence of the appropriate physical scale is present, no scattering will occur and the previous equation is not applicable.

The radar under investigation, the SPY–1 radar, is a S–band radar. If one assesses the system performance of typical tactical S–band radars, it will be observed that with the proper integration signals can be detected both from backscatter due to precipitation and from backscatter due to index of refraction irregularities alone. If one considers a higher wavelength radar, such as the Pennsylvania State University (PSU) W–band cloud profiling radar, it will be observed that droplets will be readily detected but that the Bragg scattering requirement for turbulent scattering will not be met since the very small turbulent scales required for such a high frequency radar do not exist. When making observations of reflectivity due to droplets with such a radar, one must also consider that when the drop size increases from typical cloud drop sizes to precipitation drop sizes, Rayleigh scattering is no longer present and the radar reflectivity described in equation (1) will be in error.

In summary, S–band radars (such as the SPY–1) can be expected to observe reflections both from water drops in clouds and precipitation and from clear air turbulence when the proper signal integration is provided. A radar such as PSU's W–band system will provide accurate measurements of cloud reflectivity factors when Rayleigh scattering occurs, will provide readily detectable returns when drop sizes are larger (heavy clouds and precipitation) which do not follow Rayleigh scattering, and will not be able to detect clear air turbulence. Both radars can be expected to detect the presence of debris such as insects, where the W–band radar may or may not be within the Rayleigh scattering regime.

Since SPY–1 has some ambiguity in determining scatterer types in 'clear air' conditions, the W–band radar can be very useful in helping determine whether clear air turbulence or clouds are being observed.

TECHNICAL APPROACH

Two corroborating sensors were chosen to collect data during SPY–1 operation to assess SPY–1's ability to make measurements of cloud layers and clear air turbulence. The first was the National Weather Service's (NWS) NEXRAD system located approximately 42 km from the Navy's Combat Systems Engineering Development (CSED) Site SPY–1 radar in Moorestown, NJ. Since both are S–band systems, the NEXRAD radar provides a valuable 'apples–to–apples' comparison in the measurement of some low reflectivity conditions. The second was PSU's 94 GHz cloud profiling radar. This radar provides accurate measurements of low reflectivity cloud conditions. Since it operates at 94 GHz, and therefore will most likely not observed clear air turbulence, it can also be a very useful tool in identifying scatterer mechanisms for the SPY–1 during optically clear air conditions.

The three radars involved in the clear air data collection events were located so that their coverage overlapped (figure1). The cloud profiling radar was located approximately 7.7 km from the CSEDS SPY–1 radar. It is a vertically pointing system, collecting data directly above the radar. The other two S–band radars, NEXRAD and SPY–1, had scan patterns which included the volume directly above the PSU W–band radar.

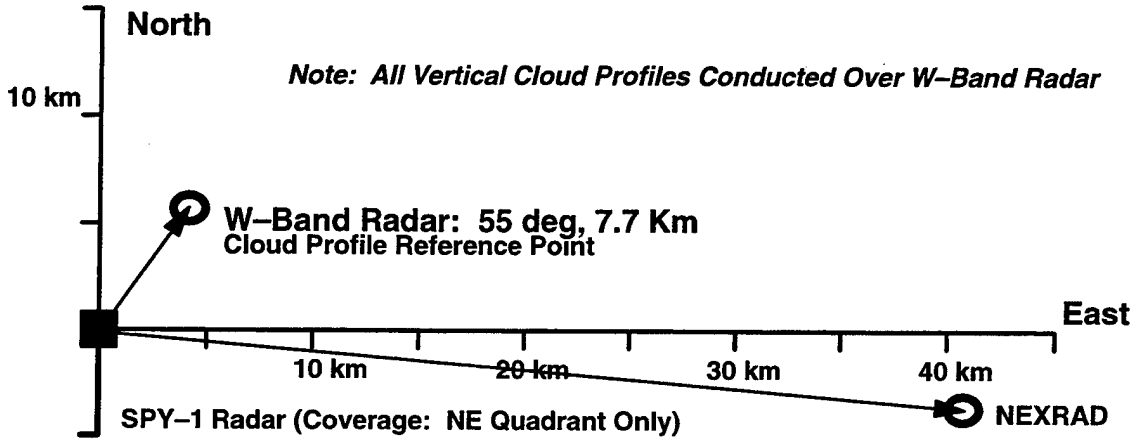

Figure 1: Radar Positions in Experiment (Top View)

Data was collected on a number of occasions from March 1997 through May 1997. A representative subset of the results is discussed in this report.

SIGNAL PROCESSING

During precipitation–related data collection session with the SPY–1 radar, only SPY–1 tactical waveforms with short pulse sequences were used to make meteorological measurements using pulse–pair processing techniques. In this phase of the experiment, however, longer pulse Doppler sequences were required. Additionally, a spectral processing framework was instituted. An overview of the signal processing techniques employed in clear air observations is presented here.

Typically, one may expect several components of signal when weather observations are made (figure 2). They include the actual signal due to environmental scattering (in this case clear air returns), surface clutter returns, receiver noise, and spectral 'artifacts' due to intermittent clutter, noise spikes, and interference from other RF sources. The upper left hand plot in figure 2 illustrates an idealized case where the clear air signal is large when compared to some of the other signals. Unfortunately, this is often not the case.

The first step in our processing scheme was to remove surface clutter using a filtering technique referred to as the Matrix Clutter Filter. This allows for the elimination of clutter and subsequent spectral interpolation across the filter notch to restore the full signal spectrum. Details of this filtering technique can be found in reference [4]. Removal of the surface clutter component and successful interpolation over the filter notch results in an idealized spectrum such as the upper right one in figure 2.

The next stage in processing includes a series of periodogram averaging and noise estimation and removal. Straightforward periodogram averaging, where a number of spectra are measured and averaged for each reporting range interval, is possible. But we also investigated the application of alternative averaging techniques such as median averaging components in each Doppler bin, application of statistical tests to remove components who are 'outliers' and probably result from an intermittent clutter source, and application of a version of the Statistical Averaging Method [5] which also addresses removal of intermittent clutter sources from the spectrum.

Also included in this stage was the application of a noise estimation and removal technique. We chose to use the Kolmogorov–Smirnov [6] technique which essentially estimates the signal level which contributes the flat portion of the signal spectrum and provides a method for removing it. This method has been shown to work with non–Gaussian noise sources.

The result is illustrated in the last plot of figure 2 where the resulting spectrum is cleaned and no significant interference signals remain. Of course this is an idealized case, but it is a good illustration of the processing techniques used in this experiment.

One major issue in the experiment was how to generate a sufficient number of periodograms so that reasonable periodogram averaging could be conducted. To this end, a 32–pulse sequence was used on transmission. As in many tactical radars, the SPY–1 provides range resolution that is much finer than most reporting range resolution requirements for meteorological processing. It also provides for multiple receiver channels which allow for an increase in the number of independent samples available for each pulse. SPY–1 parameters are not provided here, but consider the parameters of a fictitious radar as illustrated in table 1.

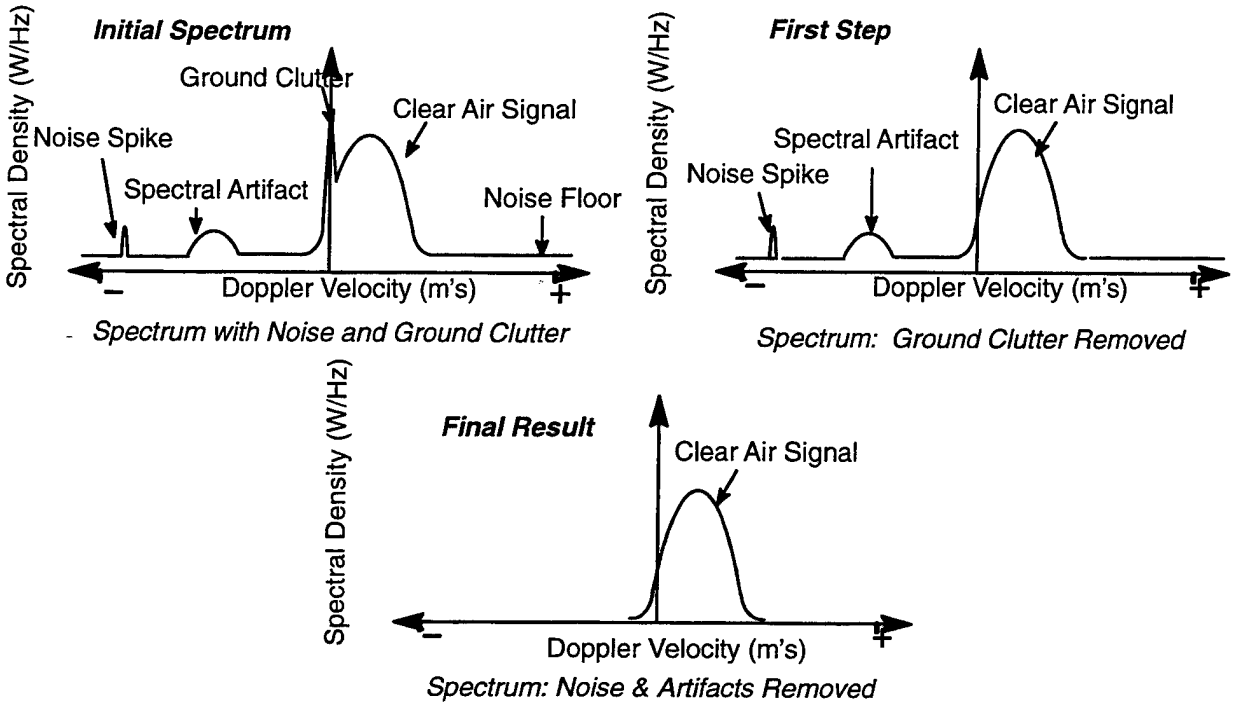

Figure 2: Idealized Ground Clutter and Noise Removal

This table illustrates a fictitious tactical radar which also is transmitting 32 pulses in a sequence. Assuming this radar has three independent receive channels and a 30 m range resolution, 960 samples can be applied to the generation of spectral moments over a 300 m reporting interval. If one uses only 16–point periodograms, this means that 60 periodograms are available for the averaging stage in the processing steps described previously. Of course more periodograms would be desired for a dedicated meteorological system, but this is a significant amount of averaging nonetheless. These parameters do not represent the actual averaging achieved from the SPY–1 system.

Waveform Type:	Pulse Doppler
Number of Pulses:	32
# Simultaneous Xmit/Rcv Channels:	3
Range Resolution:	30 m
Reporting Range Required:	300 m
Waveform Coding:	Yes
Total # Samples:	960

Table 1: Fictitious Tactical Radar Parameters

It should be noted that implementation of even a 32 pulse sequence for clear air measurements will have negligible impact on radar tactical performance if these scans are performed periodically, e.g. every 10 minutes or so.

It should be noted that processing this type of coded waveform is non–traditional in most meteorological radars. This is because of the smearing effect that results from the range sidelobes from coded waveforms. Doppler tolerant sidelobe suppression techniques developed by Lockheed Martin have been proven effective in reducing range sidelobe effects [7]. These techniques were used in processing the data from this experiment.

CLOUD MEASUREMENT RESULTS

Observations of cloud layers using SPY–1 are presented next. The SPY–1 radar returns were compared to those from the nearby NEXRAD and from the Pennsylvania State University's W–band cloud profiling radar. Due to fact that the NEXRAD was located 42 km away, its profiles were more coarsely reported in altitude. However, it provided a good comparison point for major features of heavier clouds, since both it and SPY–1 operate at S–band.

An example of the results of the cloud profiling events is shown in figure 3. On the left is the altitude –time profile generated by the vertically pointing W–band radar. On the right are two altitude–range pro–

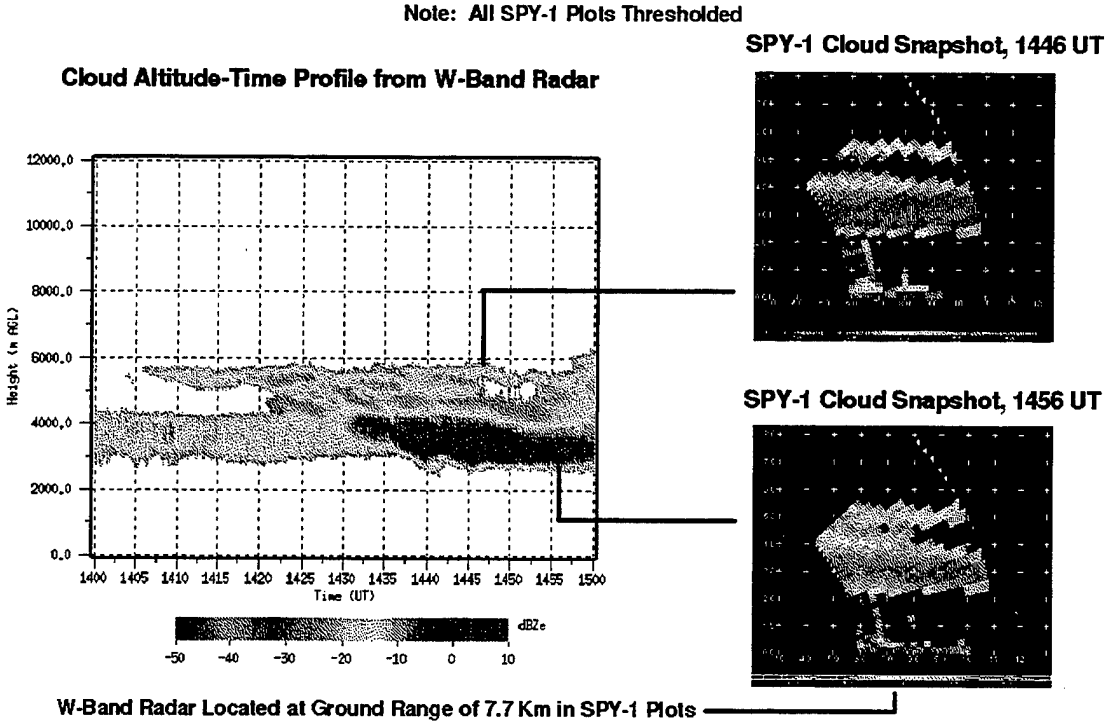

Figure 3: Cloud Profiles from PSU W–band Radar and SPY–1 Radar

files generated by SPY–1. The W–band radar provides a time varying view of what is occurring directly above that radar, while SPY–1 provides instantaneous snapshots of what is occurring over a volumetric region. The first SPY–1 profile corresponds to a time of 1446 UT on March 18, 1997, and the second SPY–1 profile was taken at 1456 UT. These snapshot times are marked on the W–band profile. The W–band radar is located at about the midpoint of the range interval in the SPY–1 plots.

At the first snapshot time, both radars show the same cloud levels. A large cloud layer extends from 2.5 to 4.5 km. A smaller cloud layer exists at about 5.5 km in altitude. The lower cloud layer has maximum reflectivity values of approximately 0 dBZ, and the higher cloud layer has maximum reflectivity values of approximately –15 dBZ. The SPY–1 profile is thresholded above its noise floor.

At the second snapshot both profiles show that the region between the two previous cloud layers is starting to be filled. The lower cloud layer is also decreasing in reflectivity level. The values reported along the ground are due primarily to ground clutter contamination. No effort was made in these plots to threshold this type of clutter return based on a clutter to noise ratio or some other similar measurement. All SPY–1 returns are thresholded at a certain signal–to–noise ratio. The threshold point of the plots is not related to the SPY–1 minimum sensitivity point.

A quantitative comparison was also made between the W–band radar reflectivity measurements, the SPY–1 measurements, and the NEXRAD reflectivity measurements. A vertical profile of reflectivity, for a series of points directly above the W–band radar, was generated for each radar. The results are presented here in a quad–chart format. For each snapshot time, four plots are presented (figure 4). In the upper right hand corner is a vertical profile of reflectivity, for the region directly above the W–band radar, from all three sensors (SPY–1, NEXRAD, and W–band radar). The SPY–1 data values are shown as stars, NEXRAD data are shown as an 'x', and W–band data are shown as dots. This plot shows the data as presented using the best available conversion constants for each sensor. In most cases, a bias appears to exist between the sensors (SPY–1 appears to be higher in reported reflectivity). In the upper left hand plot, the same profile is shown with the SPY–1 data shifted so that data from all three sensors is lined up (in all cases, a shift of 5 dB is applied). All SPY–1 data is again thresholded. For the lower right plot, the reflectivity values from SPY–1 are plotted against the W–band values to form a scattergram of their reflectivity measurements. In this plot, the SPY–1 data has the 5 dB shift applied.

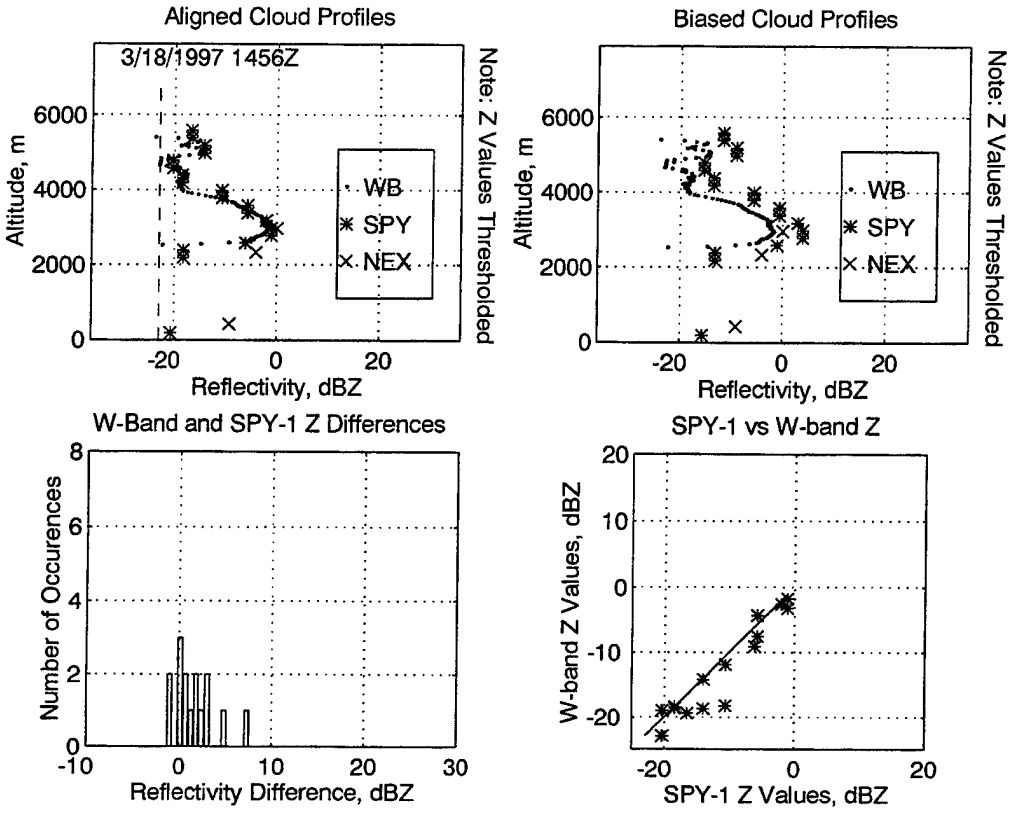

Figure 4: Comparison of Cloud Profile Measurements from Three Radars

In the lower left hand corner, a histogram is plotted of the difference between SPY–1 reflectivity and W–band reflectivity. This shows the distribution of the measurement differences between the two sensors. This plot also uses the shifted SPY–1 data.

For the data illustrated in figure 4, the NEXRAD was operating in clear air mode, so only four elevations are reported corresponding to altitudes of approximately 400 m, 1500 m, 2300 m, and 3000 m. The profiles from the three sensors follow each other well. The data at low elevations from the two S–band radars are suspect since they may include ground clutter return. A major cloud layer exists between 2 km and 4 km in altitude. A second layer comes back at about 5.5 km. All SPY–1 data that falls to the left of the dotted line is thresholded, and is not presented here.

The histogram shows a pretty good grouping, except for one data point which comes from the sharp gradient under the major cloud layer. The SPY–1 data values are generally slightly larger than the W–band values in the region above 0 dBZ. This is expected. At these reflectivity levels, it is possible that the W–band radar is past the Rayleigh scattering region, and the underlying assumptions assumed in the reflectivity conversion are no longer valid for that radar. It is also possible that the presence of turbulence in the cloud layer may contribute to increased received power levels for the two S–band radars.

DETECTION OF BOUNDARY LAYER TURBULENCE

The SPY–1 radar also demonstrated the ability to make measurements of clear air boundary layer turbulence. There is strong evidence supporting the detection of the planetary boundary layer from data collected on April 16, 1997. Inspection of SPY–1 signals indicates that significant returns were received below an altitude of 1.5 km. There were some wispy, high altitude clouds on that day, but there were no clouds below 8 km in altitude.

An investigation of W–band and SPY–1 data was undertaken to determine the source of the scattering. The NEXRAD radar was located too far away to provide any reasonable resolution at low altitudes. The W–band data was first analyzed using the general time–altitude plot.

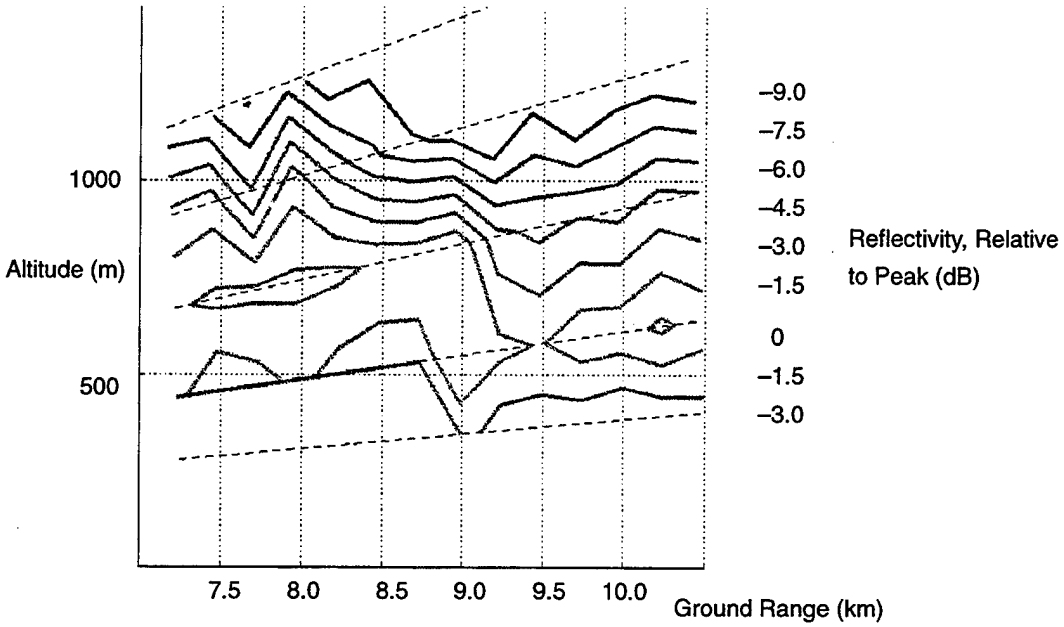

Figure 5: SPY–1 Boundary Layer Profile

Next, data was analyzed in detail on 1 second intervals from the W–band radar, for a period of a half an hour. The W–band radar showed a general absence of returns. Occasional returns were seen, but these reflectivity values were much below the level observed from SPY–1 on that day (the W–band radar observed values on the order of –40 to –50 dBZ) and were not restricted to the horizontal band observed by SPY–1. This indicates that no significant amount of cloud, insect, or general debris scattering occurred on that day.

The SPY–1 radar, however, showed a strong profile below 1.5 km, with a horizontally oriented layer with maximum reflectivity located at about 750 m in altitude (figure 5).

The dotted lines emanating from the lower left of the plot show the position of the beam positions used in the scan this day. The contours of reflectivity were developed by linearly interpolating between data points which are reported on the beam position centerlines every 250 m in range. The relative reflectivity values are shown in dB, relative to the peak. A difference of about 10 dB is shown on the plot. There were some degradations occurring on this day in the transmitted waveform. Occasional pulse to pulse frequency shifts made ground clutter rejection more difficult. As a result, all values below an altitude of 300 m are thresholded from this plot.

One of the major challenges which remains is to classify SPY–1 returns as cloud or turbulence (or give an indication of the mixture of the two) without corroboration of another radar such as Penn State's cloud profiler. This issue has not yet been resolved.

CONCLUSIONS

The SPY–1 radar can provide very useful measurements of cloud layer conditions and clear air turbulence as demonstrated in this experiment. These measurements can be made with dedicated waveforms of 32 pulses with very little impact on the radar's tactical operation. Measurements of boundary layer turbulence can provide critical information on boundary layer structure in real time. Measurements of cloud layers play an important role in a variety of Naval operations.

The SPY–1 measurements were shown to match well with the measurements of corroborating sensors such as a W–band cloud profiling radar and NEXRAD. Future work will extend this type of sensing to over–ocean operation. Calibration biases observed in this experiment will be resolved during the next stage of work.

ACKNOWLEDGEMENTS

The authors would like to thank Dr. Scott Sandgathe of the Office of Naval Research (ONR) for sponsoring this work, and the AEGIS Program Office for providing support and access to the CSEDS SPY–1 radar. The authors would like to thank the Mt. Holly, NJ National Weather Service office for their assistance in data collection, and the National Center for Atmospheric Research for providing their RDSS display package used in data analysis.

REFERENCES

[1] H. Owen, H. Urkowitz, N. Bucci, J. Melody, and R. McLean, "Tactical Weather Radar Experiment for a Shipborne Radar", *Proceedings of the 1996 Battlespace Atmospherics Conference*, San Diego, CA, December 3–5, 1996, pp. 541–549.

[2] Doviak, R.J., and Zrnic, D.S., 1993, *Doppler Radar and Weather Observations*, 2nd ed, San Diego, CA: Academic Press, Inc., 1993, sec. 4.4.5, p 82.

[3] Doviak, R.J., and Zrnic, D.S., 1993, *Doppler Radar and Weather Observations*, 2nd ed, San Diego, CA: Academic Press, Inc., 1993, sec 11.4, p 452.

[4] H. Urkowitz and H. Owen, "A Matrix Clutter Filter for Agile Beam Radars", *Proceedings of the 1998 IEEE Radar Conference*, Dallas, TX, 12–13 May, 1998.

[5] D. A. Merritt, "A Statistical Averaging Method for Wind Profiler Doppler Spectra", *Journal of Atmospheric and Oceanic Technology*, vol. 12, no. 5, October, 1995.

[6] H. Urkowitz, J. Nespor, and H. Owen, "Tests of Distribution Free Non–Gaussian Noise Removal in /Spectral Analysis of Meteorological Radar Echo," *Proceedings of the International Geoscience and Remote Sensing Symposium, 1994*, Pasadena, CA, August 1994, vol. 1, pp. 35–37.

[7] N.J. Bucci, H.S. Owen, K.A. Woodward, and C.M. Hawes, "Validation of Pulse Compression Techniques for Meteorological Functions," *IEEE Transactions on Geoscience and Remote Sensing*, Vol. 35, No. 3, May 1997, pp. 507–523.

WIND FIELD MEASUREMENTS IN NON–PRECIPITATION CONDITIONS WITH A TACTICAL SHIPBOARD S–BAND RADAR

James W. Stephans* and Harry Urkowitz

Lockheed Martin Government Electronic Systems
Moorestown, NJ

Gregory Forbes

Pennsylvania State University

State College, PA

* Address: Lockheed Martin GES
MS 108–210

P.O. Box 1027
Moorestown, NJ 08057–0927
jstephan@motown.lmco.com

Phone: 609–722–6115
Fax: 609–722–4074

1997 Battlespace Atmospherics Conference
San Diego, CA
Dec. 2–4, 1997

Abstract and Introduction

This paper describes wind field mapping experiments using a single face of an AN/SPY–1B radar at the Lockheed Martin Government Electronic Systems' Combat Systems Engineering Development Site (CSEDS) in Moorestown, N.J. The radar is an S–Band phased array with range resolution finer than NEXRAD because of pulse compression. This permits significant range averaging to get spectral moments in "reporting range intervals". Of particular interest is the mean radial velocity of clear air return estimated for each reporting volume of range, azimuth and elevation. Processing these values of mean radial velocity with Volume Velocity Processing (VVP), one may extract other kinematic parameters of the windfield in addition to the horizontal wind velocity. The other parameters include horizontal divergence, stretching deformation, shearing deformation and vertical fall velocity.

Processing the mean radial velocity values took the form of a weighted least squares analysis where the weighting accounts for the varying signal to noise ratio as affected by slant range and the antenna gain change with azimuth and elevation. To simplify our formulas, a flat earth approximation was made because the range coverage was not large. In our feasibility experiment, the azimuth coverage was limited to 65 degrees with 3 elevation angles of 21, 24 and 29 degrees.

The accuracy of our measurements and processing was judged by the rms residuals obtained from the least squares analysis. The residual is a check on both the model (e.g., flat earth, linear windfield) and on random errors from any cause. We found extremely small residuals (less than 0.1 meter/sec) at low altitudes with larger residuals at higher altitudes.

We show that the analysis provides a minimum variance unbiased set of measurements and, if the errors have a Gaussian distribution, the Cramer–Rao lower bound on the variance is achieved.

Wind Mapping Scan Strategies and Data Processing Algorithms

Wind mapping refers to the examination of a wind field in the vicinity of a Doppler radar. In the case of a single radar, the observations are of radial velocity and the estimation of wind field properties must be based on a sequence of Doppler frequency measurements made upon reflection from various points in the volume surrounding the radar. If the radar echo is truly to give information concerning the wind field, the echo must come from scatterers that move with the wind. In clear air, it is the fluctuations, in space and time, of refractive index that are the scatterers producing the echo and such scatterers move with the air mass in which they are embedded. Thus, for the wind field mapping, the volume of air surrounding the radar, or the particular volume of interest, should be free of extraneous scatterers, such as birds, aircraft, precipitation, and clouds. That is, the volume should be a clear air volume.

Various properties of the clear air wind field may be obtained from radial velocity measurements; these are described below. The essential difference between the wind mapping technique described in the literature (e.g., Doviak and Zrnic, 1993) and the techniques used in the experiment is that the other techniques were applied to mechanically scanning radars. Our experiments, on the other hand, were performed with an agile beam phased array radar. Although, we are limited as yet to a single spherical octant, the extension to any spherical sector is accomplished in the same way and the numerical algorithms are exactly the same.

The basic set of measurements for wind field mapping is the estimated mean radial velocity of the radar echo as a function of range, azimuth, and elevation. These values are the inputs to the wind mapping algorithms. These algorithms, in turn, depend on the scanning pattern used to get the radar echoes.

Velocity–Azimuth Display (VAD)

VAD is a technique for obtaining the horizontal wind at various altitudes above a scanning radar. The technique is particularly suitable for mechanically scanning radars that scan azimuthally at a fixed elevation angle. A uniform wind is assumed at a given height. The horizontal wind vector is V_h and the direction of the horizontal wind vector from north is b_o. The conventional wind direction is b_o+180 degrees. A uniform wind field is assumed at constant height, but the variation with height is arbitrary. No measurement perturbations are assumed and so, at a constant height, the radial component of the uniform horizontal wind will show a sinusoidal variation with angle from the wind direction. The vertical displacement of the sinusoid is equal to the actual vertical velocity of the wind, or whatever particulates are being carried by the wind. In general, the wind is considered horizontally laminar and so the vertical velocity is taken as "fall" velocity.

Actual measurements or estimates of radial velocity, will, of course, be subject to various errors and perturbations. It is clear that some sort of smoothing is necessary to extract the underlying sine wave. An effective form of smoothing is least squares fitting. In the case of the simple, or overhead, VAD scan, a simple least squares fit to the data, will yield the desired parameters. The principles and the formulas to be used are given in detail by [Urkowitz (1995)]. Under the assumption of a horizontally uniform wind field, the parameters extracted by the least squares algorithm are:

- the horizontal component V_h of the wind velocity,
- the wind direction, and
- the vertical fall velocity.

Offset Velocity–Azimuth Display (Offset VAD)

In some circumstances, a full VAD scan is not feasible, or even desirable. Then only a partial contour at a given height may be obtained. In our experiments, the available radar is a single face of a fixed phased array with an electronically agile beam. In addition to the contour being offset, we have determined that the wind field can be straightforwardly analyzed even if the contour is irregular. Of course, to be useful, the contour must still have a significant horizontal extent. We have analyzed the offset VAD technique and, in particular, applied a form of least squares estimate obtain wind parameters.

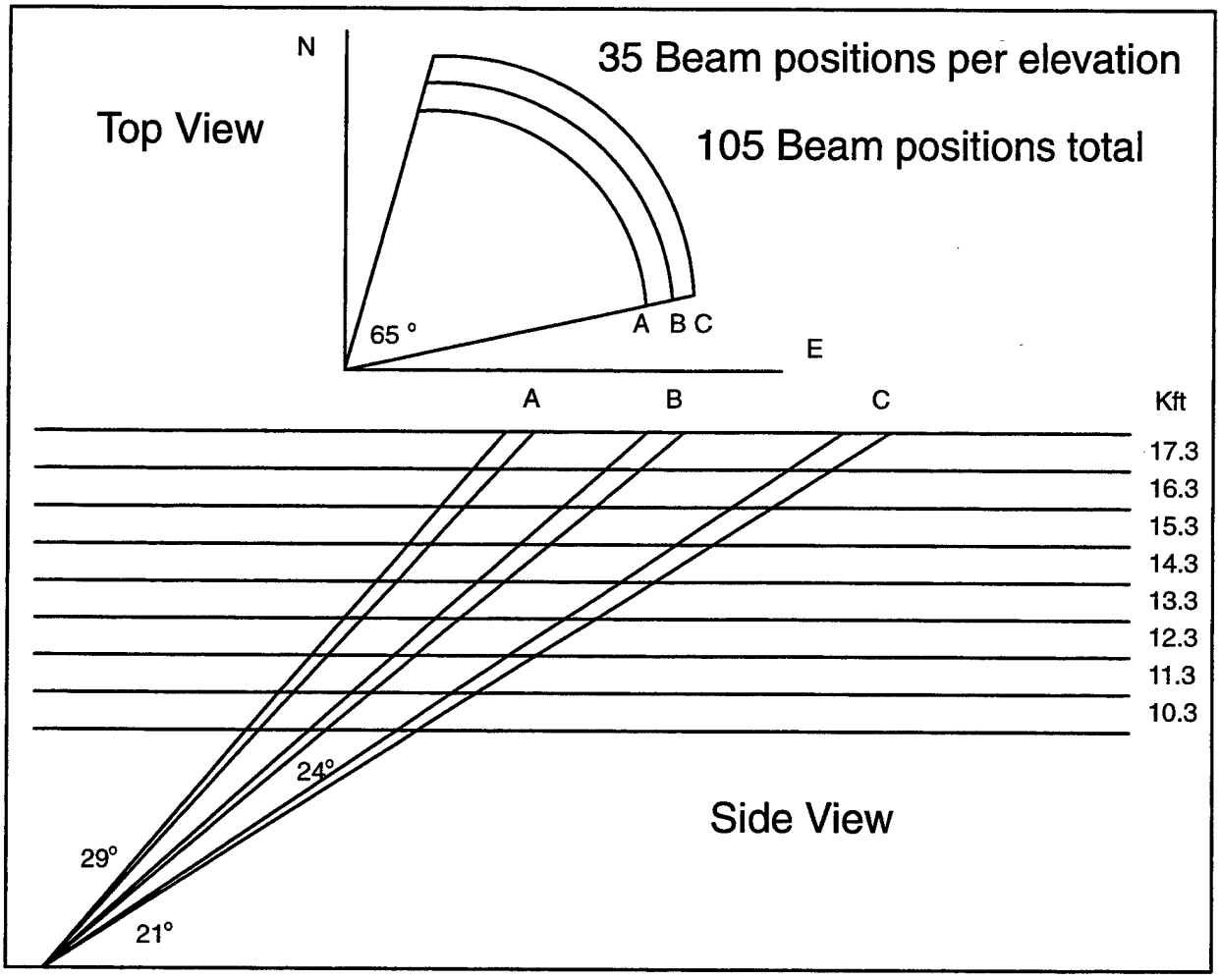

Figure 1: Wind Profiling Scan Strategy

Figure 1 illustrates the geometry of the offset VAD scan. A flat earth is assumed. The contour is at a constant height above the earth's surface making up the E–N plane. The radar is at the coordinate

origin. The figure shows the contour at one altitude viewed from above and as an elevation slice viewed from the side. Three elevations are used in the scan, with each elevation forming a contour of a portion of a circle in the NE quadrant from the radar. The antenna beam is moved through 105 beam positions as it scans around the contour. The contour need not be circular for a least squares estimation algorithm to be applied, but it should not be the simple least squares algorithm. The reason is that the errors (i.e., the noise errors) do not have a constant value at different locations around the contour. It is reasonable to expect that the measurement errors, as measured by the error variances, will be inversely proportional to the received signal to noise power ratio at each resolvable volume on the contour.

When the measurement error variances are not constant, it is appropriate to use a weighted least squares estimation algorithm. In this algorithm, each error is weighted inversely as its standard deviation. The square of the standard deviation is the variance and the variance is proportional to the reciprocal of the received signal to noise power ratio. For a "target" filling the resolvable volume, we have the following proportionality.

$SNR \sim G_i / (G_o r_i^2)$ where

SNR = signal to noise power ratio,
r_i = slant range to the measuring point, taken as the center of the resolvable volume,
G_i = two–way antenna power gain in the direction of that point,
G_o = maximum two–way antenna power gain, usually taken as the peak gain when the beam is steered to broadside.

The formulas and algorithm for the weighted least squares analysis for the offset VAD processing are given in [Urkowitz (1997)].

Volume Velocity Processing (VVP)

The VAD and offset VAD techniques are special cases of volume velocity processing (VVP). In this technique an entire volume is sampled and the estimated mean radial velocities are obtained from, in general, a large number of points in the surrounding hemisphere. However, in the experimental set–up with the radar at Lockheed Martin's Combat Systems Engineering Development Site (CSEDS), only one face of a four–faced phased array is available, so that only part of a hemisphere is capable of being sampled.

Figure 1 illustrates the sort of volume that was scanned during the experiment. For the CSEDS site, the full volume available for scanning is contained within the following dimensions;

Azimuth:	+ – 45 degrees
Elevation:	horizon to near zenith
Range Interval:	6 km to 20 km (approx.)

The upper limit on the range interval that was actually processed depended on the particular signal to noise ratio available.

In VAD or offset VAD processing, it is usually assumed that the wind is horizontally uniform at any altitude. In such a case, the parameters extracted from the VAD processing are:

- uniform wind speed and direction
- fall velocity.

These quantities are obtained at points directly above the radar. The least squares processing to produce these parameters is explained in detail in [Urkowitz (1995)].

Meteorologists are interested in more than the velocity of a uniform wind field. Certain kinematic wind parameters are also of interest, but many of these depend upon a more comprehensive model of wind motion than the assumption of a horizontally uniform wind. In our analyses, we have made the assumption of a horizontally linear wind field; that is, the wind is modeled, at a constant altitude, by vector field described by a constant vector plus a linear vector term giving the velocity gradients in both horizontal directions. The vertical component of velocity is assumed to be constant, at any altitude, over any horizontal extent of the scanned volume.

The weighted least squares analysis of the VVP scans is described fully in [Urkowitz (1996)]. Again, the variation in signal noise ratio over the volume is taken into account, as described in the previous section. Such an analysis can yield the following kinematic parameters of a wind field:

1. The horizontal wind magnitude and direction at any altitude above the radar.
2. The vertical component of velocity at any altitude above the radar. This vertical velocity, however, is usually attributed to the velocity of fall of small particulate matter.
3. The horizontal velocity divergence at any point in the analysis volume.
4. The stretching deformation of the velocity at any point in the analysis volume.
5. The shearing deformation of the velocity at any point in the analysis volume.
6. The vertical rate of change of the vertical velocity at any point in the analysis volume.
7. The variation, in the northward direction, of the northward component of the horizontal velocity at any point in the analysis volume.
8. The variation, in the eastward direction, of the eastward component of the horizontal velocity at any point in the analysis volume.

In addition to obtaining values for the kinematic factors described above, a weighted least squares analysis can provide a check on the suitability or value of the estimates made in two ways:

- the accuracy of the model used to describe a phenomenon and
- the fluctuation error of the measurements.

Both of these ways are measured by deviations of the measurements from the model. Our model for the VVP processing is a linear model. In such a model, it is assumed that the mean radial velocity, which is the measured quantity, is the result of the weighted linear combination of the kinematic parameters that describe a wind field. The difference between the measured radial velocities and the derived radial velocities comprise the deviations of measurement from model. These deviations arise from two sources:

- errors or fluctuations in measurements and
- departure from the linear model.

The first source is attributed to "noise," including both system noise and the "noisiness" of the phenomenon. The second source arises from departure from linearity of the actual kinematic properties of the wind field. The sum of the squared deviations divided by the number of measurements yields the estimated mean square deviation or residual. The square root of this number is the estimated root–mean–square (rms) residual and is used as the single number describing how good the set of measurements is, from both points of view: model error and random error.

Theoretical Properties of the VVP Least Squares Analysis

The small values of estimated standard deviation from the VVP least squares analysis led us to consider the theoretical properties of that analysis. The results of that consideration are presented by [Urkowitz (1997)]. There some scattered results from the literature are collected and new proofs are given. It is shown that:

1. The weighted least squares estimates are unbiased.
2. The estimates achieve minimum variance for linear estimates.
3. In addition, if the errors have a multivariate Gaussian distribution:
    a. The estimates are the maximum likelihood estimates.
    b. The estimates achieve the Cramér–Rao lower bound on the error variance.

The Cramér–Rao lower bound is the smallest value of variance that can be achieved by any estimation procedure, linear or not.

SPY–1 Wind Mapping Results

The following plots were generated from data collected on March 18, 1997 and April 27,1997 Non–precipitating clouds were present on both days. The plots show sample radial velocities versus azimuth and plots of RMS error versus altitude.

A single waveform type was used for wind profiling. A sequence of 32 coded pulses was used. Groups of 16 pulses were processed coherently. The entire scan took seconds (much less than one minute) to conduct.

The charts that follow are a comparison between the SPY–1 versus NEXRAD data taken on the same day and times. When differences occur, they may be due to the 65 degree sector of the SPY–1 Offset VAD scan as compared to the 360 degree scan of NEXRAD. Other contributing factors such as the 42 km distance between the sites, non–uniformity of the wind field, the higher SPY–1 beam elevation angle and Matrix Clutter Filter benefits.

The next plot from each day shows radial velocity measurements over a range of azimuths. These measurements are the ones used to generate the wind speed and direction information at each altitude.

Figure 2 shows a quantitative comparison of SPY–1 estimates of wind speed and direction (located directly above the SPY–1 radar) to NEXRAD estimates of wind speed and direction (located directly above the NEXRAD radar). In the upper left hand corner of each plot, the wind speed of SPY–1 (solid line) is compared to the wind speed estimated by NEXRAD. In the lower left plot, the difference between each radar's estimate is plotted as a function of altitude. In the upper right corner, the SPY–1 radar's estimate of wind direction (solid line) is compared to NEXRAD's estimate of wind direction. In the lower right corner, the difference between SPY–1 and NEXRAD measurements are plotted as a function of altitude.

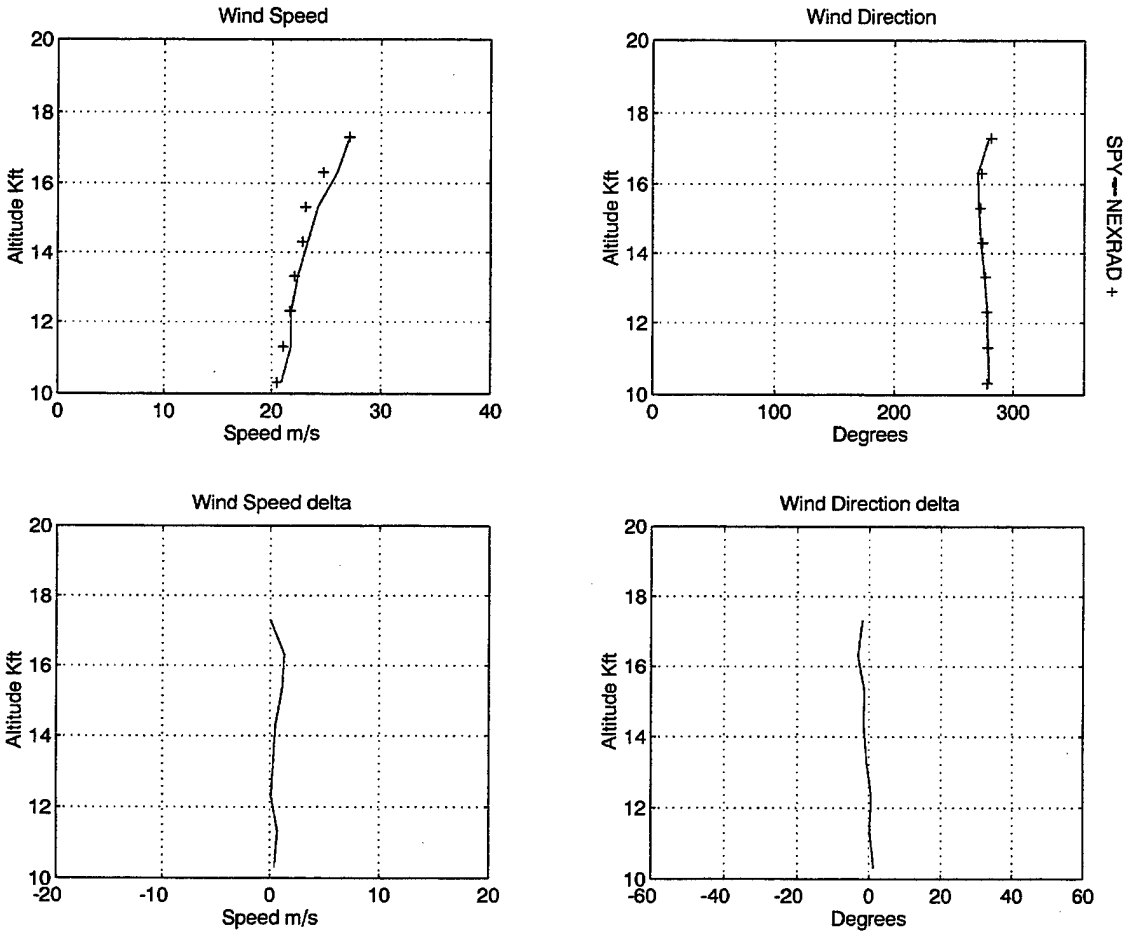

Figure 2: Wind Profile Difference Plots, Comparing SPY–1 to NEXRAD, 3/18/97, 1413 UT

The measurements from the two radars generally match very well on March 18. The primary scatterer, as mentioned previously, was cloud returns. Any errors between the two radars should probably be primarily associated with the fact that they are displaced from one another by a distance of 42 kilometers. Still, the profiles generated by the two radars match very well. One should keep in mind that the SPY–1 radar scan was limited to an azimuthal extent of 65 degrees for the experiment.

Figure 3 shows some characteristics of the data that was used to estimate the wind speed and direction on March 18. The upper plot shows the RMS error between the actual data taken at 1413 and the ideal curve that would result from a uniform wind field at each altitude. The very low RMS errors (on the order of 0.1 m/s) indicates that the assumption of uniform wind flow for this day is a reasonable one. The lower plot shows a sample of radial velocity estimates, taken from one elevation and slant range. The quarter sine wave appearance matches the expected radial velocity pattern from a uniform wind field at that altitude.

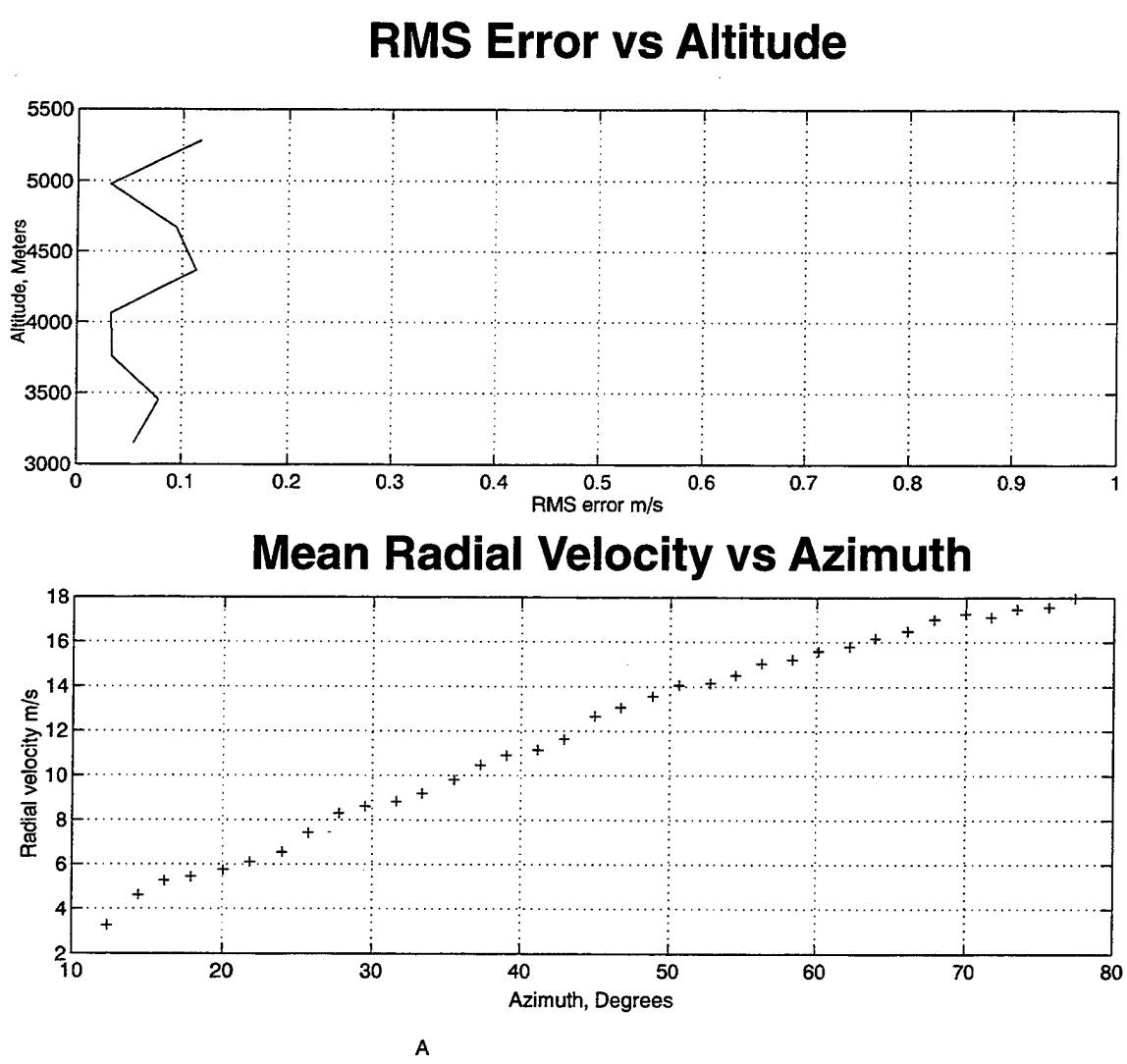

A

Figure 3: SPY–1 RMS Error and Azimuth Plots, 3/18/97, 1413 UT

The comparisons between SPY–1 and NEXRAD wind profiles are provided in figure 4. A review of figure 4 showing differences between the two radars, indicates that wind speed differences are less than 2 m/s, and wind direction differences are generally small.

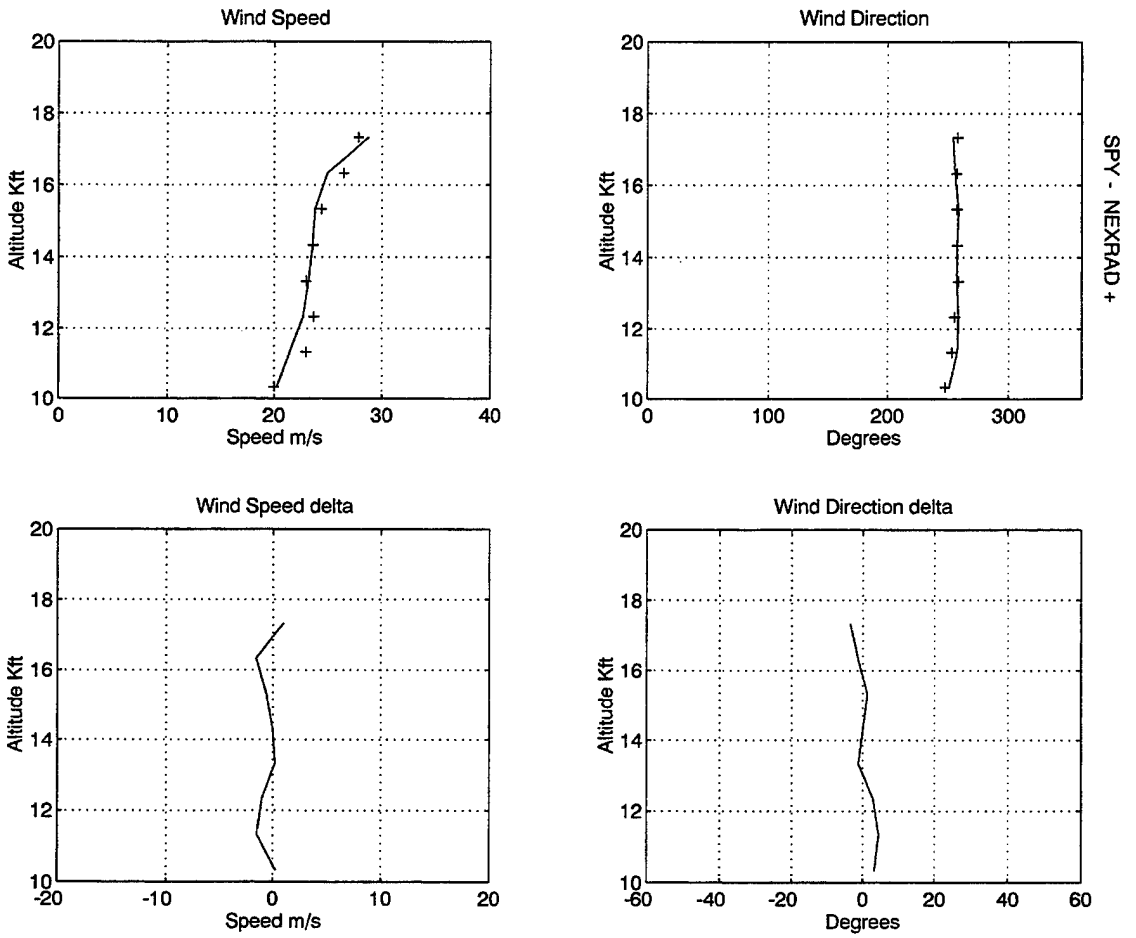

Figure 4: Wind Profile Difference Plots, Comparing SPY–1 to NEXRAD, 4/27/97, 2208 UT

A sample of the RMS error estimate to the least mean squared uniform wind flow is shown in figure 5 for snapshot time 2208 UT. The RMS error values are very low, with a maximum less than 0.2 m/s. The accompanying radial velocity curve over the full azimuth that is observed shows a well behaved section of a sinusoidal. In this case, the dominant scatterer is again clouds.

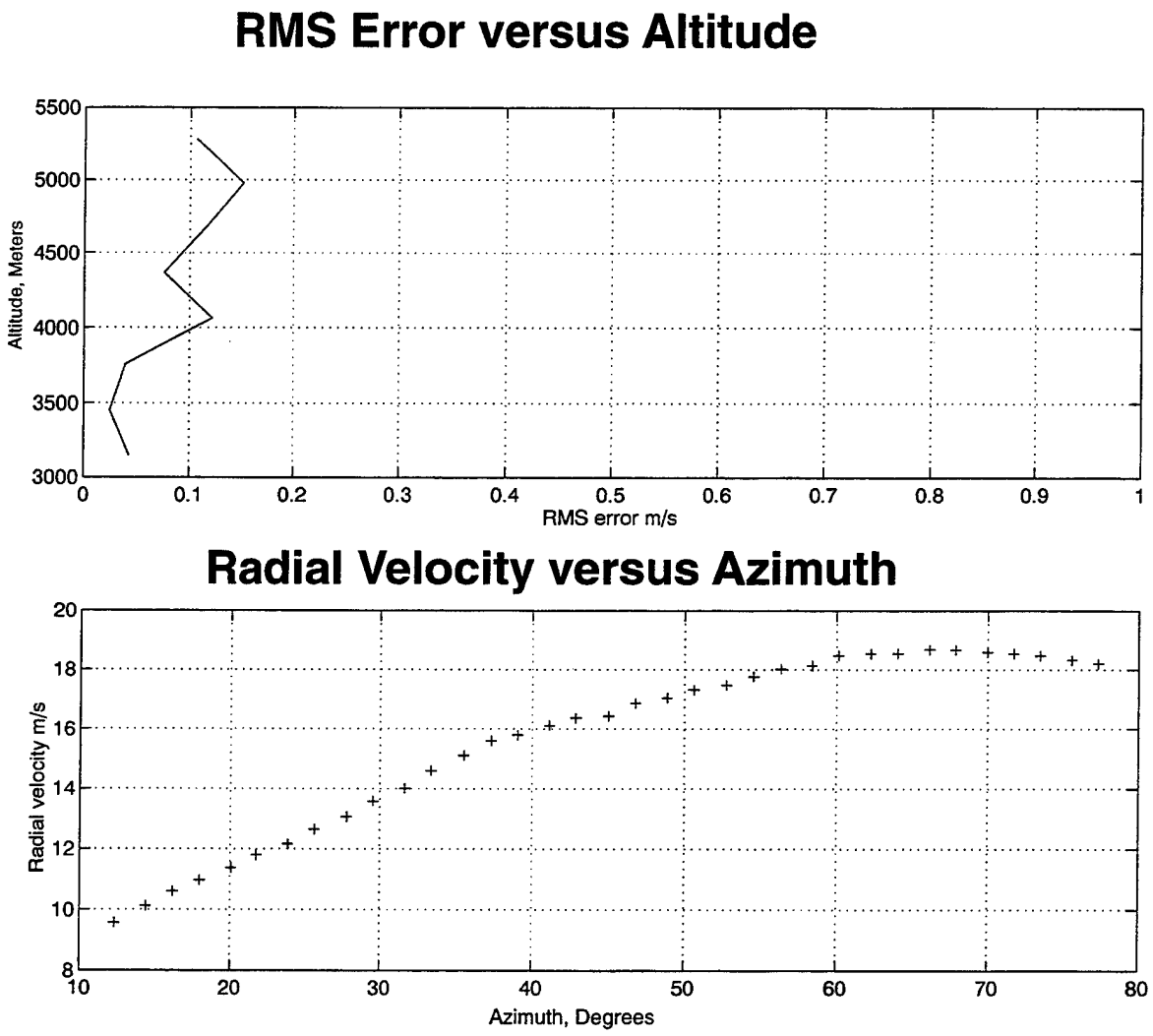

Figure 5: SPY–1 RMS Error and Azimuth Plots, 4/27/97, 2208 UT

INFERRING ATMOSPHERIC TURBULENCE USING SYNTHETIC APERTURE RADAR IMAGES OF THE OCEAN SURFACE

1997 Battlespace Atmospherics Conference, San Diego CA, December 1997

Pierre D. Mourad, Applied Physics Laboratory, University of Washington,
1013 NE 40th Street, Seattle, WA 98105
phone: (206) 543-6921 fax: (206)543-6785 email: pierre@apl.washington.edu

ABSTRACT: *The present work shows in a definitive manner that synthetic aperture radar (SAR) can image the signatures on the ocean surface of atmospheric turbulence of roll-vortex form. It also makes headway towards showing that SAR can image atmospheric surface-layer turbulence.*

Mourad and Walter (1996, JGR, V.101(C7)) presents the best published evidence to date that SAR imagery that contains "streaks" of enhanced radar backscatter is actually imaging the spatial modulation of the ocean's gravity-capillary waves caused by atmospheric roll vortices. They compared in detail contiguous and nearly simultaneous satellite-based cloud imagery and SAR imagery. The details of the structure agreed remarkably well. In a follow-up paper, Mourad (1996, JGR, V.101(C8)) noted that the SAR streaks were actually made up of a range of sub-structure that was strongly suggestive of atmospheric turbulence sub-structure that has been observed within atmospheric roll vortices, typically through in situ measurements. That sub-structure included boundary-layer scale thermals, and atmospheric surface-layer turbulence.

The present work shows, definitively, that SAR streaks can be caused by atmospheric roll vortices, thus validating a hypothesis first offered by Gerling (1986, V.91). (Note that Bernie Walter of NorthWest Research Associates in Bellevue, Washington is the first to do this, using this same data set, but with different analysis techniques.) It also offers steps towards testing the hypothesis of Mourad (1996) that SAR imagery can capture the foot prints of sub-roll atmospheric turbulence. Figure 1 shows the hypothetical signatures of atmospheric roll vortices in the radar backscatter patterns from the ocean surface. The top of Figure 2 shows roll vortex signatures in the time series that are of comparable scale to the hypothetical signatures in the SAR image. Taken together, this is a definitive correlation of in situ and SAR signatures of roll vortices. The bottom of Figure 2 shows the distribution of small-scale turbulence and its correlation with large-scale turbulence (that is, due to roll vortices). This shows for the first time in an unambiguous way the source and influence of large-scale turbulence (roll vortices, here) on the spatial distribution of gust microfronts – that is, on surface-layer momentum flux events. This is also an example of quadrant analysis, a way of identifying significant momentum-flux events in the atmospheric surface layer.

ACKNOWLEDGEMENTS: This work was funded by the Office of Naval Research, grant # N00014-97-1-0466.

Figure one: **A SAR image of the ocean surface during the ONR/MBL-ARI, on 3 May 1995, off of Monterey, CA.** The image measures 50 km to a side. The straight dark lines show the flight track of the NOAA LongEZ aircraft, whose turbulence data is shown in Fig. 2. The streaks from upper left to lower right are the signatures of atmospheric roll vortices in the oceanic surface-roughness patterns that are imaged by the SAR. Their spacing is on the order of 600 - 1000 m, about twice the height of the boundary layer at the time of the image, and they are oriented within five degrees of the surface-layer wind.

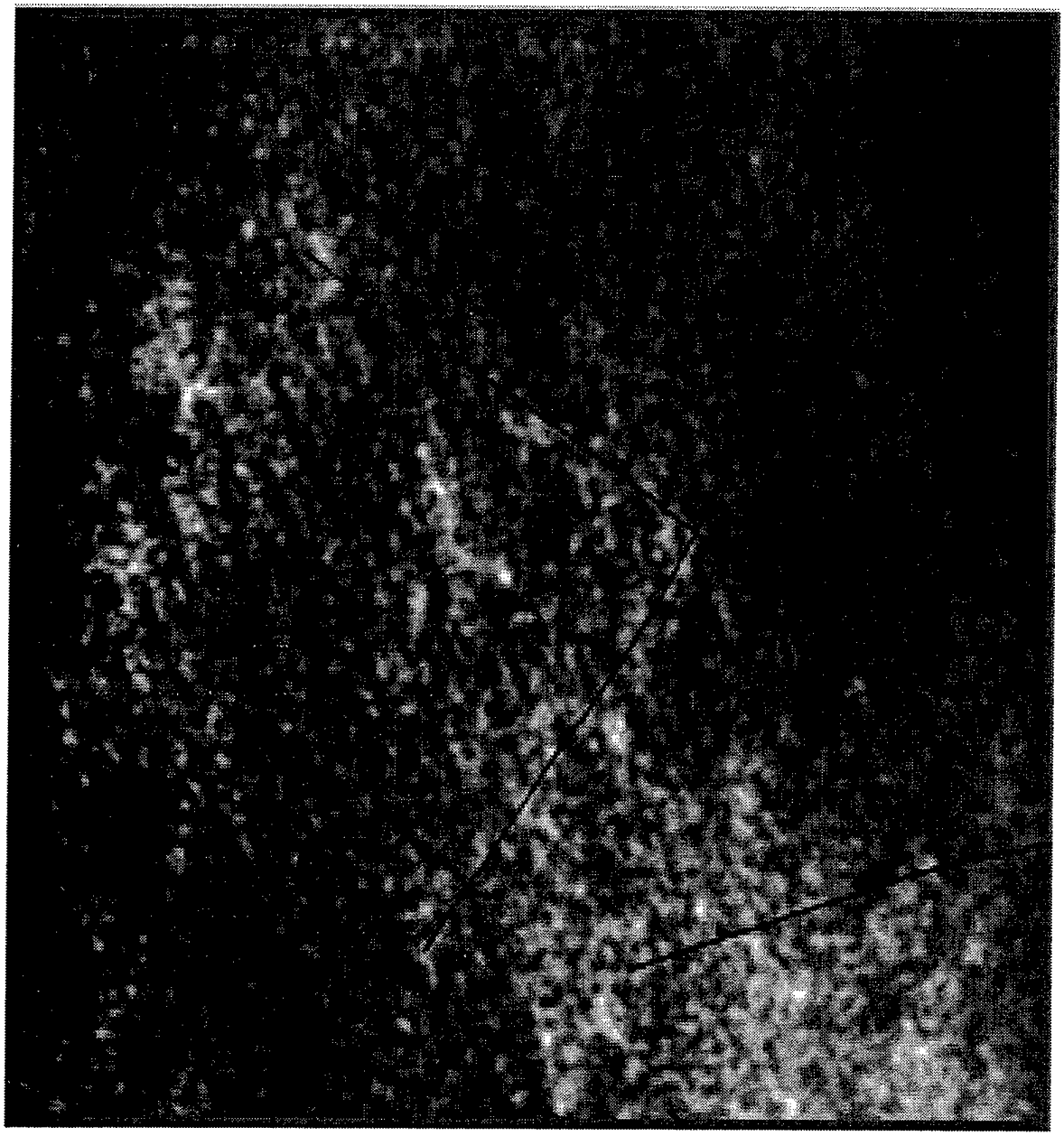

Figure two: **Signatures of roll vortices in in-situ time series of atmospheric turbulence.** The top line shows the perturbation to the mean flow (with a five-second running mean represented by the undulating solid line in this part of the figure) which contains the signature of roll vortices: negative values correspond to low-momentum air within roll-vortex updrafts; positive values correspond to high-momentum air within roll-vortex down drafts. The second line shows the five-second running mean of the cross-wind divergence. Positive values show areas of divergence (indicative of the bases of down drafts); negative values show areas of convergence (indicative of the bases of updrafts). Convergence/divergence regions are lag-correlated with low-/high- momentum regions. The third and fourth lines show the instantaneous vertical and cross-wind velocities, respectively, with their five-second running means. Note that the length scales of these roll-vortex signatures agree with the SAR streak spacing in Fig. 1.

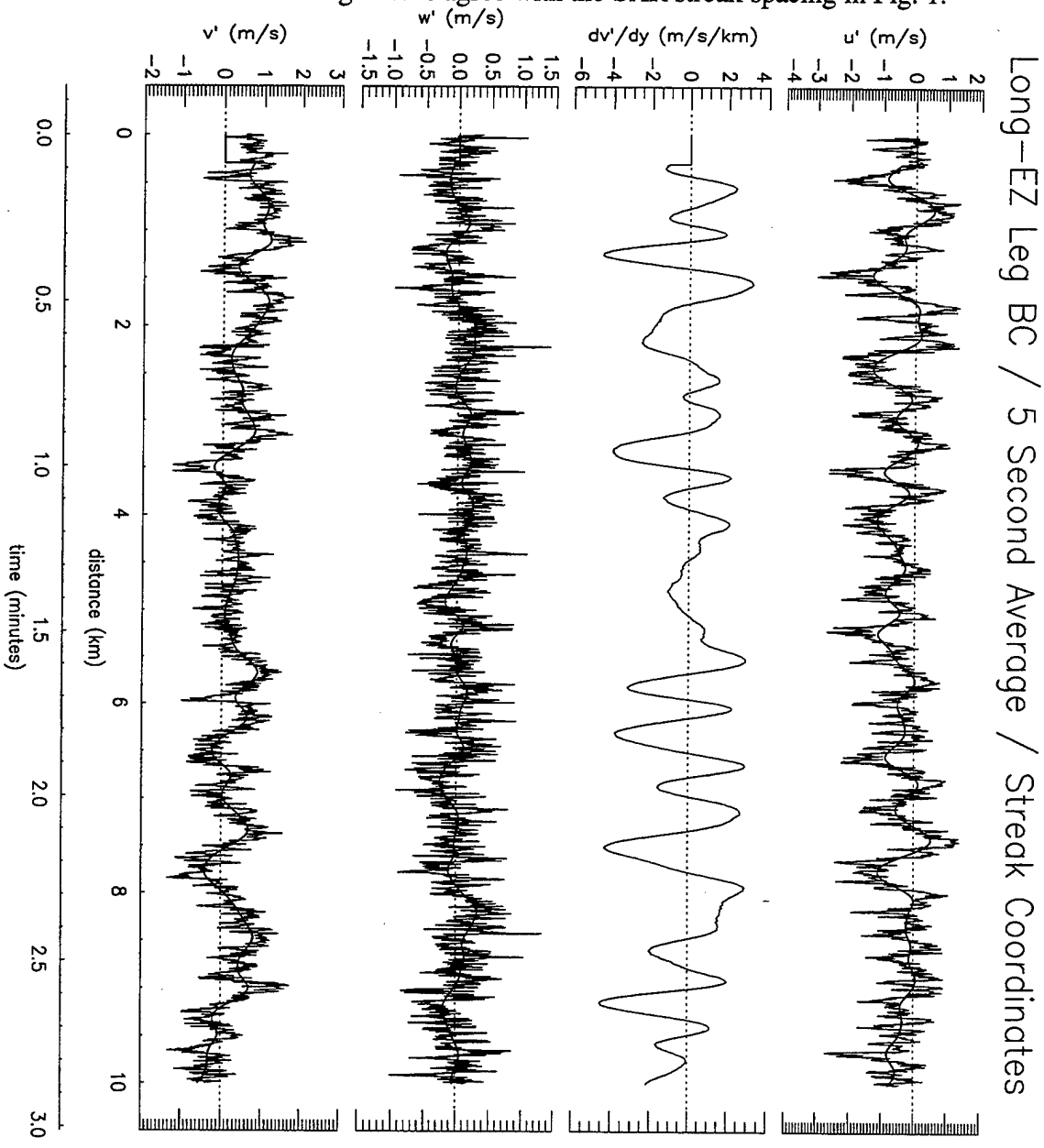

Figure three: **Preliminary quadrant analysis**. The first and second lines show the instantaneous wind components (along-wind and vertical wind components, respectively) relative to a twenty-second running mean. The third line shows their product: the instantaneous Reynolds stress or momentum flux caused by both roll vortices and smaller-scale turbulence known as gust microfronts. Using a "quadrant analysis" technique that identifies the significant momentum flux events, the bottom line shows a grouping of them within two categories: ejections (upward momentum-flux events) and sweeps (down ward momentum-flux events). The ejections are primarily within the roll-vortex updrafts and the sweeps are primarily within the roll-vortex down drafts. Indeed, the spacing between groups of ejections or groups of sweeps is the same as between roll updrafts and down drafts, respectively. This small-scale turbulence, modulated by the roll vortices, is what actually roughens the ocean surface in a way that can be imaged by SAR. Quantifying the spatial distribution of surface-layer turbulence in this or similar ways is a necessary step towards testing the hypothesis that fine-scale variability in SAR imagery can be caused by atmospheric surface-layer turbulence.

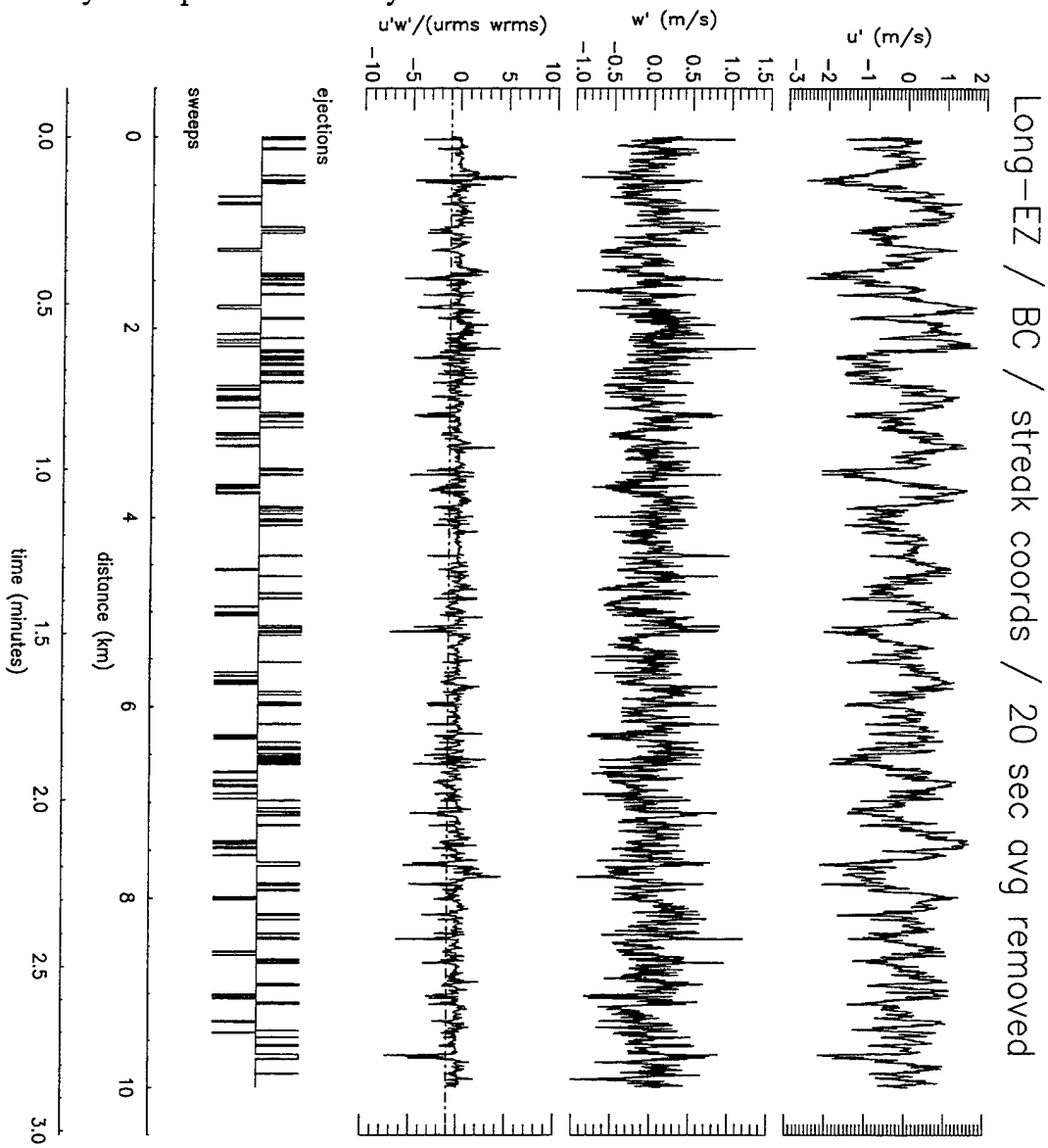

Neural network methods for extraction of temperature and wind velocity profiles from satellite sounder radiance data.

J. Cogan*, E. Measure, and G. Vaucher
Army Research Laboratory
Information Science and Technology Directorate
AMSRL-IS-EA
White Sands Missile Range, NM 88002-5501

W. Gutman and D. Bustamante
New Mexico State University
Physical Sciences Laboratory
Las Cruces, NM 88003

INTRODUCTION

Neural network methods can accurately retrieve temperature profiles from meteorological satellite sounder data. Preliminary results indicate some improvement over conventional retrieval methods, especially near the tropopause (Gutman et al, 1998; Bustamante et al, 1997; Butler et al, 1996), and when combined with data from a ground-based microwave radiometer (Measure et al, 1998). Early results also suggest that nearly the same accuracy may be obtained using data from a sounder with a reduced set of channels, thereby making the instrument itself less complex and reducing its cost.

Current methods of obtaining wind velocity profiles from satellite data are inadequate for many applications. Thermal, geostrophic, or gradient wind approximations may lead to very large errors under certain atmospheric situations. Cloud tracking and recently tracking of features found in satellite observed moisture fields (Velden et al, 1997) may provide useful wind velocities for some synoptic scale applications, and the latter for smaller horizontal scales if the application requires winds for only one or two relatively thick layers. To attempt to remedy these problems, a scheme has been developed for retrieval of wind velocity profiles from satellite sounder radiances using a neural network technique. Each wind velocity vector represents a mean value for a layer approximately centered at that standard height or pressure level. Input data consists of geo-located and calibrated radiances from the GOES sounder. A set of "co-incident" rawinsonde sounding provide the "truth" data set. Initial results indicate the feasibility of the method, although considerable further work is needed before we have an operationally capable technique.

TEMPERATURE

The methodology for retrieving temperature is the basis for the method developed for wind extraction described below, and the latter work started much more recently. Consequently we describe the methodology for temperature in greater detail.

Data Manipulation

Using MCIDAS we extracted files of sounder radiances for channels 1-18 from GOES Area files. "Truth" data came from files of corresponding rawinsonde temperatures. The several files output from MCIDAS (e.g., one file for each channel) were assembled into a single file where each record has all relevant information about a single pixel. GOES pixels within 0.5° latitude and longitude of a rawinsonde launch site were matched with the values from that rawinsonde. Time differences were mostly within 0.5 hr. The result was a file for each rawinsonde and set of pixels within the matching criteria. Each record contained the latitude, longitude, and elevation of the rawinsonde launch site, radiances, and the rawinsonde temperatures for the surface and standard levels from 850 through 100 hPa. The files were combined randomly by record into a training and a testing file. Figure 1 shows a top level "view" of the methodology for temperature retrievals.

Temperature profile retrieval is performed with feed-forward, back propagation, neural networks. A typical network consists of up to 21 input nodes, one hidden layer with 10 nodes, and 10 output nodes. The input values consist of the radiance values of the 18 infrared sounder channels along with the latitude, longitude, and surface elevation. The outputs consist of the temperatures at 10 levels in the atmosphere corresponding to the surface and the 850, 700, 500, 400, 300, 250, 200, 150, and 100 millibar significant levels. The networks are trained with temperature profiles taken from co-located rawinsonde flights. GOES sounder data for training were selected to correspond in time with the 0000 GMT and 1200 GMT rawinsonde launches.

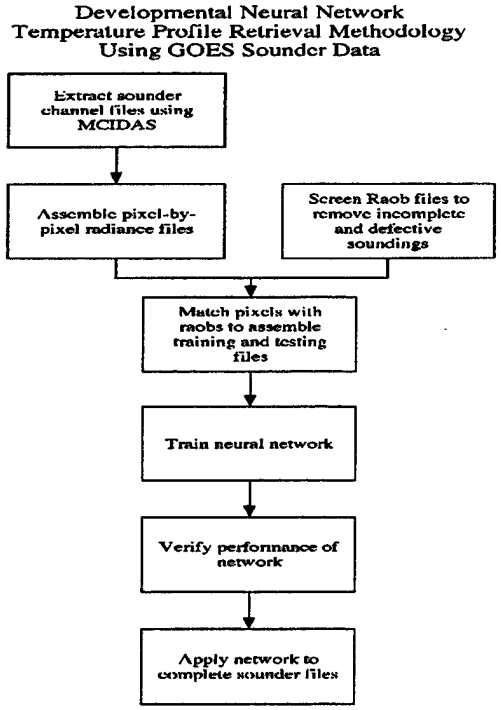

Figure 1. Top level description of temperature retrieval methodology.

Launch times did not vary by more than 40 minutes from the start of the GOES sounder scans, but the duration of balloon flights is variable.

Results

Networks initially were trained using over 7,000 matched pairs of satellite sounder and rawinsonde profiles (exemplars) over North America, concentrating on the 48 conterminous states of the U.S. using data collected twice per day over a 5-day period in November 1994. Figure 2 is a graphic representation of the RMS error (RMSE) by pressure height associated with a comparison between rawinsonde-measured temperatures and neural network-retrieved temperatures over the data set that consisted of more than 7,000 records on which the network had never been trained. With the exception of the surface and tropopause, RMS errors are approximately 2 K. Measure et al (1998) combined simulated radiances from a surface based microwave sounder with actual radiances from GOES. The results gave the expected improvement at lower levels (pressures > 400 hPa), but also noticeable decreases in RMSE at higher levels (pressures ≤ 400 hPa), even near the tropopause.

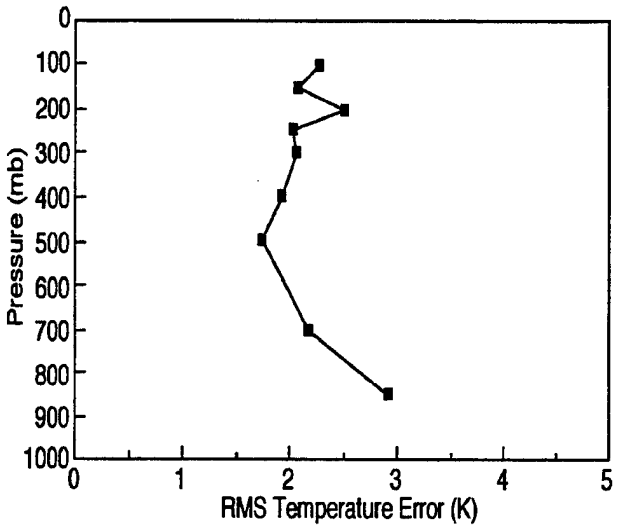

Figure 2. RMSE (K) of the retrieval as a function of pressure level relative to rawinsonde "truth" data.

The above RMS errors are similar to those reported for polar orbiting satellites. Examples include those from Butler et al (1996) who used a network based on work by Bustamante et al (1994) to obtain temperature retrievals from microwave radiances from the DMSP temperature sounder, and Bustamante et al (1996) who retrieved temperature soundings from infrared radiances gathered by the TOVS sounder on NOAA satellites.

Weighting of channels in neural network

In some sense, neural network profile retrieval is a "black box." The physical significance of the network parameters with respect to the underlying radiative transfer process is not obvious. It is not even necessary for the user to have more than superficial knowledge of the physics of

radiative transfer. In this paper, the connection between neural network retrieval and the radiative transfer process is examined through an analysis of the sensitivity of the retrieved temperature profiles to the sounder channel inputs.

Sensitivity analysis

Sensitivity analysis was performed using prepared input records. From the full set of over 7,000 records in the testing set, 25 were selected at random. Each of these was used in a channel–by–channel analysis procedure. For each of the 25, the 18 sounder channel values were dithered successively by 5%, The dithered and undithered records were assembled into a file. The dithered and undithered records were presented to the previously trained network for temperature retrieval.

Retrievals based on the modified records were compared with the unmodified retrievals. The fractional changes in the retrieved values were computed for the temperatures at all ten atmospheric heights. For each height, the fractional change was plotted as a function of channel number. All 25 test sets were analyzed.

For 11 of the 18 GOES sounder channels, the behavior of the sensitivity is very similar for all of the test cases analyzed. For channels 2, 6, 7, 8, 10, 11, and 12, differences are seen from one data set to another, and based on that behavior, the plots can be delineated into two categories. Figure 3 is a typical plot showing the sensitivity for the 11 channels that exhibit similar sensitivity for all data sets. Two distinct types of sensitivity for the remaining 7 channels are discussed in

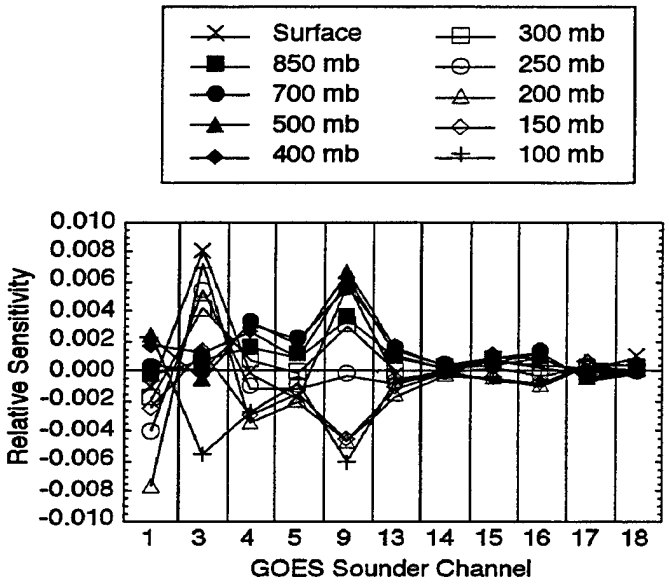

Figure 3. Sensitivity plot for the 11 GOES channels that exhibit similar behavior for all retrievals.

Gutman et al (1998). All 10 atmospheric levels for which temperatures have been retrieved are shown in the plots. For the most part, the sensitivity plots show altitude dependence for the various channels that is qualitatively similar to the weighting functions. For example, high

sensitivity to GOES channels 1 and 2 occurs for 100, 150, and 200 hPa pressure levels. The weighting functions for these channels peak at about 90 and 280 hPa, respectively. High sensitivity to channels 4 and 5 occurs at middle and lower atmospheric levels. The weighting functions for these latter channels reach their maximum at about 840 and 1000 hPa, respectively. The sensitivities to channels 17 and 18 are among the lowest, but they peak at the surface where the weighting functions reach their maximum.

Although the dependence of the sensitivity on channel number is similar to the weighting functions, there are a number of unexpected results. For example, there is strong sensitivity to channel 9, which is intended to indicate total ozone, for almost all atmospheric heights. This may be a result of diurnal variation in ozone concentration. At first examination, it is surprising that the sensitivity to channels 13–18 is relatively low. These channels are intended to provide temperature information at a succession of atmospheric heights. Examination of the weighting functions, however, shows that all but one of these channels actually reach their peaks at or near the surface.

These results are consistent with previously reported results pertaining to retrieval of temperature profiles from TIROS Operational Vertical Sounder (TOVS) data. The TIROS series consists of polar-orbiting satellites, and the sounders are similar to the GOES sounders in the number and characteristics of the channels (Bustamante, *et al.* 1997).

Analysis of reduced network

One of the results of the sensitivity analysis is insight into which of the GOES channels potentially may be excluded from neural network retrieval with minimal loss of accuracy. Neural network retrieval is fast, but network training and data preprocessing are time-consuming. Reduced networks would increase processing speed and reduce storage requirements. By examining the data presented in the previous section, it is clear that the retrieval overall is least sensitive to channel 14, and relatively low for all channels from 14-18. Although some levels exhibit low sensitivity to certain channels, the goal is to exclude only channels to which the sensitivity is low at all atmospheric heights.

A series of reduced networks was tested and the RMS errors computed. As expected, excluding channel 14 from the retrieval resulted in only a very small increase in the RMS error. Using the full network, the average RMS error was 2.23 K. The average RMS error of the reduced network that excluded channel 14 was 2.39 K. On the other hand, when channel 9 was excluded, the RMS error increased to 9.84 K. Additional reduced networks were tested, and the results of that testing are shown in Table 1. One somewhat surprising result is that excluding channels 14, 17, and 18 results in better performance than excluding only channels 17 and 18. This analysis clearly demonstrates that is possible to exclude a number of the 18 GOES sounder channels from the neural network retrieval with minimal effect on accuracy, but the channels to be excluded must be carefully selected. A similar analysis of temperature retrieval using TOVS data also demonstrated that reduced networks can be developed that largely preserve the accuracy of the retrievals.

Table 1. Mean RMSE for all atmospheric heights for the full network and listed reduced networks.	
Test condition	**Mean RMSE (K)**
Full network	2.23
Channel 14 excluded	2.39
Channels 14 and 17-18 excluded	2.71
Channels 17 and 18 excluded	2.94
Channels 14-18 excluded	4.02
Channels 13-18 excluded	6.41
Channel 9 excluded	9.84

WIND

The methodology for retrieving wind velocity is based in large part on that developed for temperature retrievals. In the following sections we omit much of the detail where it applies to both temperature and wind.

Data manipulation

Using MCIDAS we extracted files of sounder radiances for channels 1-18 from GOES Area files. "Truth" data came from files of corresponding rawinsonde wind velocities. Radiance gradient components (x, y directions corresponding to the u, v wind components) were computed for all channels using a 3 x 3 running sub-grid. For example, the x-component is taken as the mean of the six "east-west" gradients over the sub-grid and applied at the central grid point. The program generalizes easily to other sub-grid sizes. The several files output from MCIDAS (e.g., one file for each channel) were assembled into a single file where each record has all relevant information about a single pixel. Rawinsonde wind speeds and directions were converted to their u, v components. The result was a file for each rawinsonde and set of pixels within the matching criteria. Each record contained the latitude, longitude, and elevation of the rawinsonde launch site, radiances and respective gradient components for the sounder channels, and the rawinsonde u, v components for the surface and standard levels from 850 through 100 hPa. The files were combined randomly by record into a training and a testing file. Figure 4 presents the top level "view" of the wind retrieval methodology.

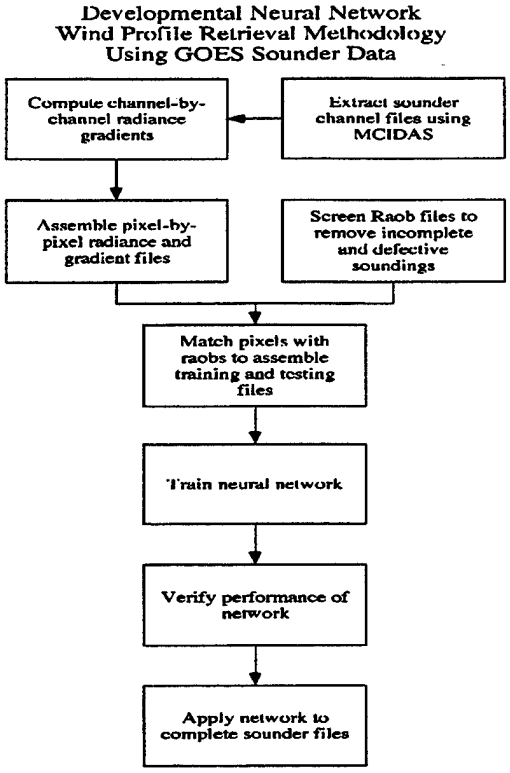

Figure 4. Top level description for wind retrieval methodology.

Network Architecture

The initial network was a feed-forward, back-propagation neural network containing one hidden layer. Other characteristics of the network include the following: norm-cum-delta learning rule, hyperbolic tangent transfer function, 57 input nodes, 20 nodes in the hidden layer, and 20 output nodes. A single net computed both the u and v components. Later the network was "split" into two, one network for the u-component and another for the v-component (10 output nodes each). Other characteristics remained the same. Wind speed and direction can be computed from the fields of u and v components for each standard height where each wind velocity vector represents a mean value for a layer approximately centered at that standard height or pressure level. For this preliminary effort we only computed the fields of u and v.

Preliminary Results

Preliminary results suggest that a neural network approach may indeed be a viable way to retrieve wind profiles from satellite sounder radiance fields. These results were computed to check the feasibility of the neural network method, and no attempt was made to optimize the technique (e.g., elimination of cloud "contaminated" pixels). Figure 5 shows the means and RMS errors of the u-component of the retrieved winds relative to rawinsonde values, and figure 6 shows the same for the v-component. Figures 5 and 6 also show results for networks where the u and v components were computed separately (vs. together in one net).

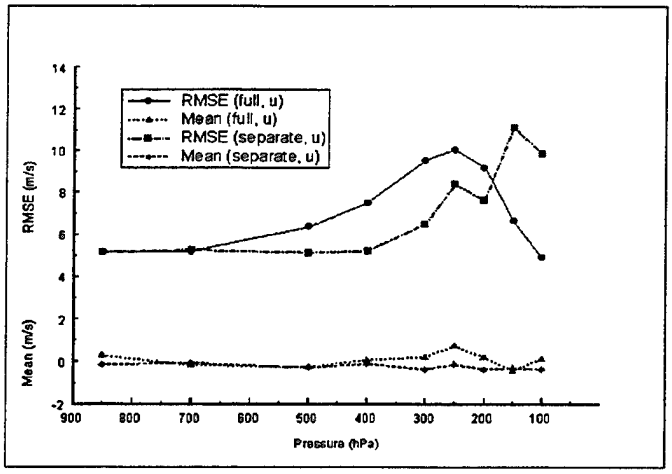

Figure 5. Mean and RMSE of the retrieved u-component of the wind relative to rawinsonde values.

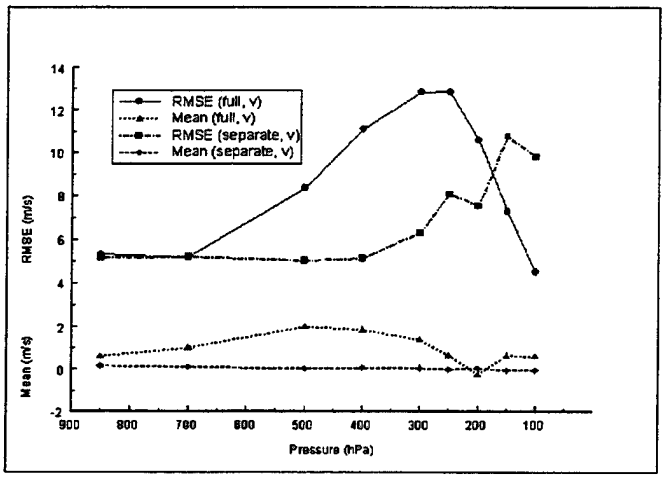

Figure 6. Same as figure 5, but for the v-component.

For the u-component there is a slight reduction in magnitude of the mean error near 250 hPa. The RMSE decreased noticeably from 500 through 200 hPa, and increased at 150 and 100 hPa. The mean error for the v-component decreased everywhere except at 200 hPa. The RMSE of the v-component dropped even more than that for the u-component over the same interval. As before, the RMSE increased at 150 and 100 hPa, though by a slightly lesser amount.

Work planned for the near term includes development of a readily applied method to minimize the effect of cloud, and evaluating variations in the network itself such as the type of learning rule and number of input or hidden nodes. Eventually, we plan to use output from the wind retrieval in conjunction with wind profiles from ground-based sensors (Cogan et al 1998). A

network that uses information from both the satellite and the ground-based sensors may produce better overall profiles, from the surface to the uppermost satellite data level. That type of method would in part build on the techniques described in Measure et al (1998) for temperature profiles.

CONCLUSION

Work to date suggests that retrieval of temperature soundings through the use of neural network methods may produce accuracies equal to, and possibly better than, those from conventional retrieval methods. For each atmospheric height, the network inherently weights channels in a manner analogous to the weighting functions of a conventional retrieval. Reduced networks can be developed that result in only a small loss of accuracy. Retrieval of profiles of wind from radiances measured by met satellite sounders using a neural network technique appears promising based on initial results. Ongoing work to optimize the network and preprocessing of input files (e.g., changing network parameters, removal of cloud contaminated pixels) should lead to a definitive evaluation of the value of this method for operational wind retrieval. Combining the method of this paper with output from ground-based wind profilers, or development of a neural network using data from both satellite and ground-based sensors, may lead to an algorithm for extracting accurate wind profiles from the surface to the highest data level of a satellite sounder.

REFERENCES

Bustamante, D., J. Cogan, and A. Duddenhoeffer, 1997. Neural network retrieval of atmospheric temperature profiles from TOVS data, *Meteorological Appl*, accepted.

_____, _____, _____, 1996. Analysis of neural network derived atmospheric thermal profiles, *Proc. IASTED Modeling, Simulation, and Optimization Conf. '96*, Gold Coast, Australia, 6-9 May 1996.

_____, _____, _____, 1994: "Comparison of Neural Network Derived Atmospheric Thermal Profiles with Rawinsonde Data," *Proc. 7th Conference on Satellite Meteorology and Oceanography*, 509–511.

_____, _____, W. Gutman, E. Measure, and G. Vaucher, 1996. Results and implications of neural network retrievals of satellite temperature soundings, *Proc. 1996 Battlespace Atmos. Conf.*, 3-5 Dec 1996, San Diego, CA.

Butler, C., R. Meredith, and A. Stogryn, 1996. Retrieving atmospheric temperature parameters from DMSP SSM/T-1 data with a neural network, *J. Geophys. Res.*, 101(D3), 7075-7083.

Cogan, J., E. Measure, E. Vidal, E. Creegan, B. Weber, and D. Wolfe, 1998. A mobile system for near-real time atmospheric soundings, *Second Symp. on Integrated Observing Sys.*, Phoenix, AZ, 11-16 Jan 1998, in press.

Gutman, W., D. Bustamante, J. Cogan, E. Measure, and G. Vaucher, 1998. Neural network temperature profile retrieval sensitivity analysis, *First Conf. On Artificial Intelligence*, Phoenix, AZ, 11-16 Jan 1998, in press.

Measure, E., J. Cogan, G. Vaucher, W. Gutman, R. Okrasinski, and D. Bustamante, 1998. Neural network retrieval of atmospheric temperature profiles from satellite and surface based radiometry, *First Conf. On Artificial Intelligence*, Phoenix, AZ, 11-16 Jan 1998, in press.

Velden, C., C. Hayden, S. Nieman, W. P. Menzel, S. Wanzong, and J. Goerss, 1997. Upper-tropospheric winds derived from geostationary satellite water vapor observations, *Bull. Amer. Meteor. Soc.*, 173-195.

A HMMWV based system for near real-time atmospheric soundings using combined satellite and ground-based remote sensing.

J. Cogan*, E. Measure, E. Vidal, G. Vaucher, and E. Creegan
Information Science and Technology Directorate
Army Research Laboratory
AMSRL-IS-EA
White Sands Missile Range, NM 88002-5501

B. Weber and D. Wolfe
Environmental Technology Laboratory
Environmental Research Laboratories
National Atmospheric and Oceanic Administration
325 Broadway
Boulder, CO 80303

INTRODUCTION

The Army Research Laboratory, Information Science and Technology Directorate, with assistance from the National Oceanic and Atmospheric Administration, Environmental Research Laboratories, Environmental Technology Laboratory, has developed a mobile system for measurement and analysis of atmospheric profiles in close to real-time (Cogan et al, 1997; Wolfe et al, 1995). This "Profiler" system initially combined a small receiver and processor for satellite data with a suite of ground based sensors that included a separate wind radar and Radio Acoustic Sounding System (RASS), two microwave radiometers, and other instruments in a towed shelter and an antenna trailer. This early system was modified by combining the wind radar and RASS into one unit on a new trailer, combining the radiometers into a single smaller instrument, and installing the processors and some other equipment into a somewhat smaller and more rugged towed trailer. Currently, the Profiler hardware and software are undergoing major upgrades that are leading to a smaller prototype carried in a shelter on a HMMWV towing a wind radar on a standard High Mobility Trailer (HMT), while increasing capability and user "friendliness." The radiometer with upgraded software will take over the function of temperature sounding from the ground, thereby eliminating the need for a RASS. A series of field tests with the earlier proof of concept (POC) system have demonstrated its capability to produce rapid refresh soundings that can lead to a significant improvement in a variety of military and civilian applications, including input profiles that significantly improve analysis and prediction capability of dispersion models over mesoscale areas (Cox et al, 1998). This paper briefly describes the Profiler in its earlier form and the expected upgraded version, and summarizes results from a variety of field tests in different meteorological conditions. Emphasis is placed on recent and ongoing upgrades to system hardware and software.

SYSTEM DESCRIPTION

Figure 1 shows the several component "sensors" of the Profiler after the series of upgrades presented in Table 1. Some of these upgrades have been completed (e.g., improved

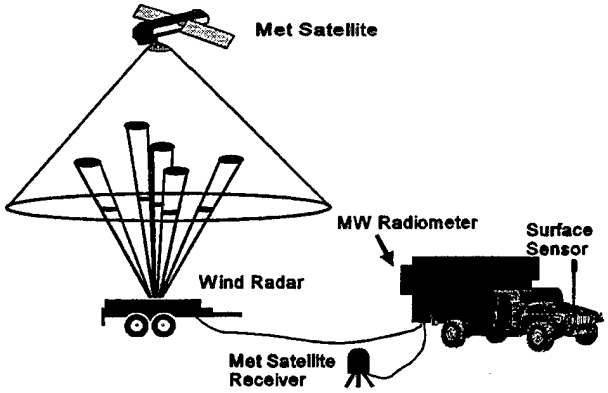

Figure 1. Sketch of the planned configuration showing principal components. Processors located inside shelter.

radiometer). Others such as the new 924 MHZ radar antenna will be completed during the next few months. The processors will fit inside the HMMWV shelter shown in figure 1. New software will contain the algorithms noted in Cogan et al (1997) and Wolfe et al (1995). Processing of moment information will be replaced by spectral processing for better quality control and more accurate met output. These algorithms will run on a modified version of the LAP-XM (Radian International) or equivalent processing system. Use of the on-board Battlescale forecast Model (BFM) will allow analysis and short term prediction over mesoscale areas (Knapp and Haines, 1997). The entire upgraded system should be ready for use in field tests before the end of 1998.

FIELD TEST RESULTS

A series of field tests demonstrated the ability of the original Profiler to produce accurate and timely data. Table 2 presents results from the Los Angeles Free Radical Experiment (LAFRE) as discussed in Wolfe et al (1995) and Cogan et al (1997), and tables 3-4 the results from a test at Wallops Island (Cogan et al, 1997), in summary form. Those references contain further details. The main difficulty lies in the extraction of wind velocity from met satellite data. The routines developed to adjust the met satellite data using the ground-based soundings help, but only slightly. Work is currently underway to improve the situation with satellite winds (Cogan et al, 1998).

The results from the wind profiling radar appear well within expected ranges, especially for wind speed. At Wallops Island a pair of radar tracked pibals were released about once every 15 minutes from the same location, with the second one of the pair launched three minutes after the first. The Profiler radar gathered data continuously over each 1-2 hour experimental period (usually one each morning and afternoon), with 3 min average soundings generated during the period of each pibal pair. The consecutive launches of pibals three min apart permitted an estimate of the variation of the wind velocity over the averaging period of the radar. The wind profiles from the radar were compared with the second pibal of each pair. In some cases differences between pibals exceeded those between pibal and wind radar.

TABLE 1. Profiler sensors, selected software packages, and characteristics. Initial configuration compared with recent and ongoing upgrades.

System	Initial Profiler as during LAFRE	Profiler with new/ongoing upgrades
Radar wind profiler	924 MHZ, phased array.	924 MHZ phased array, signal tapering.
RASS	~ 2000 Hz, 4 external sources.	No RASS (T from newer radiometer).
MW Radiometer	T: 50-60 GHz (O_2), PW, LW: 22.7, 31.4 GHz, 2 radiometers (T, PW/LW).	One radiometer operating in same frequency bands for same variables, smaller than either of older radiometers.
Satellite receiver and processor	HRPT from NOAA satellites (soundings and imagery).	Upgraded, smaller system: HRPT from NOAA and direct read-out DMSP.
Portable surface station	Standard meteorological variables, on mast mounted on trailer.	More rugged and portable version of earlier sensor suite. AN/TMQ-50 by middle of FY98.
Weather map receiver	Receive maps and other data via GOES.	Eliminated GOES link, maps and other weather data via Internet. Data for initialization of BFM from AFWA.
GPS receiver	Provides site location.	No significant change.
Radar wind processing software	Wind velocity computed from moment data.	Initially moment processing, with upgrade to spectral data processing during development cycle.
Mesoscale Model	None	BFM for analysis and short term forecasts.

TABLE 2. Means and averages of 0.1 km standard deviations of wind speed differences (ms^{-1}) for 0.3 km layers (indicated sensor vs. rawinsonde). Radar = radar wind profiler, Sat = Satellite. Days in September 1993.

Dates	Mean		Std Deviation		Layers	
	Radar	Sat	Radar	Sat	Radar	Sat
7-11	0.75	10.84	1.88	8.60	14	6
17, 20-23	1.53	8.61	2.75	2.88	11	6

TABLE 3. Means and standard deviations of differences of wind speed between Profiler (3 min. averages) and pibal, and between pibals 3 min apart. Averages of 100 m layer values shown, for the surface to 1.9 km. Days in July 1995. Number of comparisons (No.) also shown.

Day	No.	Mean (ms^{-1})		Std Deviation (ms^{-1})	
		Profiler vs. Pibal	Pibal vs. Pibal	Profiler vs. Pibal	Pibal vs. Pibal
18	8	-0.70	0.00	0.91	0.63
20	9	-0.31	-0.01	0.69	0.84
21	5	-0.36	-0.09	0.92	0.65

TABLE 4. Same as Table 3 except for wind direction. Values in parentheses are for $z \geq 300$ m.

Day	No.	Mean (deg)		Std Deviation (deg)	
		Profiler vs. Pibal	Pibal vs. Pibal	Profiler vs. Pibal	Pibal vs. Pibal
18	8	19.14 (18.92)	-0.31 (1.25)	13.00 (9.72)	9.53 (5.67)
20	9	7.13 (4.46)	-0.66 (-1.08)	8.56 (8.55)	8.13 (8.30)
21	5	11.71 (9.00)	0.64 (0.65)	3.96 (3.86)	4.21 (3.01)

Means and standard deviations of virtual temperature (T_v) differences generally averaged about $\pm$ 0.5 and 1.5 K, respectively. Based on limited data from Wallops Island, and somewhat more extensive data obtained at White Sands Missile Range, NM, the "new" microwave radiometer appears capable of retrieving sensible temperatures (T) up to an altitude of 3 km within about 1.5 K of that measured by nearly co-incident rawinsondes (to $\leq$ 1 K at heights < 1 km).

When comparing any instrument to rawinsonde measurements one should note that rawinsondes are not "standards." Cogan et al (1997) present data from one sonde sending data to two processing systems (Marwin and CLASS) that suggest errors of about 1 ms^{-1} in wind speed and $\pm$ 0.2 to $\pm$ 0.4 K in temperature. Wind direction differences were generally < 10°, but in one case exceeded 90°.

The experiment described in Cox et al (1998) illustrated the usefulness of rapid refresh data from the Profiler. In this experiment wind profiles for the lowest 4 km were sent via a wireless LAN to a separate shelter containing the processors that hosted the models used for near real time analysis and prediction. A diagnostic mesoscale wind model was run every half hour, with the resultant wind field feeding a Gaussian puff diffusion model. Cox et al (1998) reported that using the Profiler in place of 1 to 3 rawinsondes reduced the error in the location of the centroid of the predicted vs. the measured plume from about 50 % to 10 % after about 4 hours. The azimuth error decreased from 26° to 9° at a distance of 32 km, and the distance error dropped from 10 km too long to 4 km too short.

CONCLUSION

The early version of the profiler has demonstrated its ability to obtain useful data for a variety of applications from airfield operations to transport and diffusion experiments. The upgraded version should prove even more useful by allowing rapid deployment to locations where fixed site systems are too costly or impractical. The upgraded sensors (table 1) should lead to greater accuracy and reliability of the MMS-P prototype relative to earlier versions of the Profiler.

REFERENCES

Cogan, J., W. Gutman, E. Measure, G. Vaucher, and D. Bustamante, 1998. A preliminary method for "direct" extraction of wind velocity profiles from satellite sounder radiance data. *First Conf. On Artificial Intelligence*, Amer. Meteor. Soc., in press.

Cogan, J., E. Measure, and D. Wolfe, 1997. Atmospheric soundings in near-real time from combined satellite and ground based remotely sensed data. *J. Atmos. Oceanic. Technol.*, **14**, 1127-1138.

Cox, R., J. Cogan, J. Sontowski, C. Dougherty, R. Fry, and T. Smith, 1998. Comparison of atmospheric transport calculations over complex terrain using a mobile profiling system and rawinsondes. *Wea. Forcast.*, submitted.

Knapp, D., and P. Haines, 1997. Improving field artillery meteorological data for the U.S.Army

using a PC-based mesoscale model. *Proc. 1997 Battlespace Atmos. Conf.*, 2-4 Dec 1997, San Diego, CA, in press.

Wolfe, D., and Coauthors, 1995. An overview of the mobile profiler system: Preliminary results from field tests during the Los Angeles free-radical study, *Bull. Amer. Meteor. Soc.*, **76**, 523-534.

Atmospheric Temperature Profiles from GOES SATELLITE AND SURFACE-BASED RADIOMETRY

Edward M. Measure*, James Cogan, and Gail Vaucher
AMSRL-IS-EA
White Sands Missile Range, NM 88002
Ph: 505-678-3307 Fax: 505-678-3385
E-mail: emeasure@arl.mil

William Gutman, Richard Okrasinski, and Don Bustamante
Physical Science Laboratory, New Mexico State University
Las Cruces, NM 88003

Abstract

The Army Research Laboratory is developing a prototype profiler system for measuring vertical profiles of atmospheric winds, temperatures and densities needed by Army artillery. Atmospheric temperature soundings are expected to be provided by a combination of surface-based microwave radiometry and infrared satellite radiometry. The present work is an exploration of the performance of temperature retrieval from combined satellite and surface-based measurements using artificial neural networks.

A Neural Network has been constructed to retrieve atmospheric temperature profiles from GOES sounder radiance data and ground-based microwave radiometer measurements. The resulting network was trained on measured satellite radiances and simulated surface-based microwave radiances, using a set of simultaneous, co-located radiosonde observations as the truth set for the training sequences. A second set of satellite radiances and simultaneous co-located radiosonde observations was used to test the neural network performance. The second set of radiosonde observations was also used to generate simulated surface-based microwave radiances. The test and training data sets were generated by using all GOES sounder pixels near to United States radiosonde observation sites, and hence represent most climate regions of the contiguous United States.

Results show a significant improvement over methods using only satellite or surface based radiometric data. As expected, upper levels were retrieved better by the combined technique than the surface-based technique, and lower levels better than by satellite-based techniques.

1. Introduction

Accurate first round fire-for-effect cannon fire requires that account be taken of the variation of atmospheric drag with the wind, temperature, density and moisture content of the atmosphere. The natural range of

variability of the atmosphere is sufficient to cause errors of 10% or even more of the range if no correction for the meteorology is made. Consequently, the artillery has long put up with the difficult logistical burden of transporting and maintaining the facilities to launch radiosonde probes of the atmosphere and process their measurements.

In order to reduce this logistical burden, the Army Research Laboratory is developing a prototype of a compact, remote sensing atmospheric profiler system for measuring vertical profiles of atmospheric winds, temperatures and densities needed by Army artillery. Atmospheric temperature soundings by this system are provided by a combination of surface-based microwave radiometry and infrared satellite radiometry.

The present article concerns the exploration of a strategy for the performance of temperature retrieval from combined satellite and surface-based measurements using artificial neural networks.

2. Principles of Atmospheric Radiometry

Atmospheric radiometry exploits the natural thermal radiation of the atmosphere to determine its temperature, composition, and other physical parameters. Most of the radiation received by the radiometers in question can be classified either as *scattered radiation,* for example, sunlight scattered from cloud droplets, or as *thermal radiation*; that is radiation emitted by the volume under consideration and governed by the radiation law:

$$I_\nu = \alpha_\nu B_\nu[T] \quad \textbf{(1)}$$

where I_ν is the specific intensity of the radiation at frequency ν, α_ν is the absorption coefficient, T is the temperature, and B_ν is the Planck function, given by:

$$B_\nu = \frac{2h\nu^3}{c^2}\frac{1}{e^{h\nu/kT}-1} \quad \textbf{(2)}$$

where c is the speed of light, h is Planck's constant, and k is Boltzmann's constant. If we can neglect non-thermal radiation, then local thermodynamic equilibrium (LTE) applies, and the radiation received by the radiometer is given by:

$$I_\nu = I_\nu^{sc}\exp[-\tau(0,sc)] + \int_0^{sc}\alpha_\nu(s)B_\nu[T(s)]\exp[-\tau(0,s)]ds \quad \textbf{(3)}$$

where s is the distance from the radiometer, I_ν^{sc} is the specific intensity at a bounding surface at distance sc, and : $\tau(0,s) = \int_0^s \alpha_\nu(s')ds'$ is the opacity of the atmosphere between the radiometer and the volume at s.

Radiometric retrieval is the process of inferring temperature, composition and other parameters of the atmosphere from measured values of I_ν.

3. Neural Network Retrieval

Many techniques for retrieval of atmospheric temperature have been used, as reviewed, e.g., in Deepak (1988). Our technique is a variant of the neural network technique developed in Measure (1988, 1991), for surface based radiometry and subsequently applied to satellite based radiometry by Butler (1992) and Bustamante (1992).

The idea behind neural network retrieval methods is to train the network on situations where both a truth value and the measured parameters are known. For the temperature profile retrieval problem the truth values are supplied by radiosondes and the measured values are the radiances actually measured by the satellite radiometer, or, for surface based radiometry, simulated radiances calculated from the radiosonde observations.

The neural networks we have designed for this project each have 10 output nodes, corresponding to pressure levels from the surface to 100 mb., and 33 input nodes, corresponding to latitude, longitude, surface height, the 18 channels of GOES-8 sounder thermal infrared, and 12 channels of simulated surface based microwave radiometer data. Our experiments have included one or two intermediate layers with a variety of numbers of processing elements in each layers.

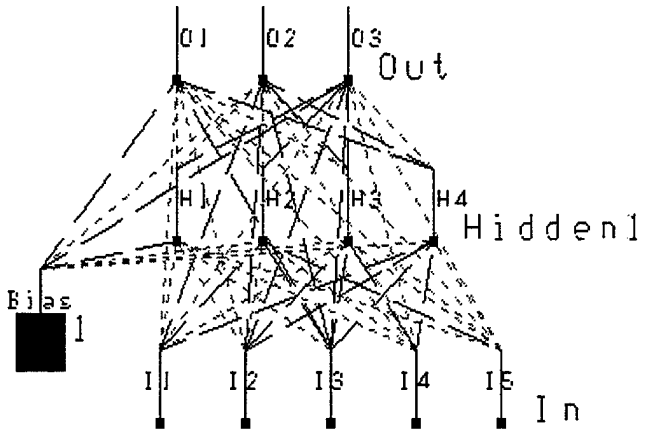

Figure 1. A small example neural network.

Figure 1 shows an example neural network, similar to those used in our studies except for having many fewer processing elements. The processing elements are represented by the labeled rectangular boxes. The input (In) layer is comprised of the 5 input elements I1-I5 plus the constant bias input. Similarly, the hidden layer is composed of the elements H1-H4 and the output (Out) layer has elements O1-O3. The various elements are connected by dashed or dotted lines, each of which has associated with it an associated weight. Signals propagate through the network from the input layer to the output layer, weighted by each of the connection weights and summed and otherwise processed at the processing elements. The process of training the network consists of the (automatic) adjustment of the connection weights in response to the transmission of signals through the network.

The neural networks were built using Neural Works Professional II/PLUS. All our experiments used a back-

propagation training scheme (see, e.g., Neuralware, 1993 or Rumelhart, 1986).

The data set used for training and testing consisted of 5 days radiosonde observations for the continental US and the corresponding GOES-8 sounder infrared data. The sounder data was randomly partitioned into a training set and a test set. After editing to remove soundings with missing data, the training set consisted of 9643 soundings and the test set of 7316 soundings. The radiosonde observations were also used to generate simulated surface based microwave radiometric soundings, using a code implementing a version of equation (3). Corresponding satellite and surface-based radiances were grouped to form 33 element measurement vectors, or *exemplars*.

Training the net consisted of repeated presentations of the satellite and simulated surface-based radiances to the network in conjunction with the radiosonde observations, which served as truth values. After each presentation, the difference between the network output and the desired (corresponding raob) value was computed, and an error term was generated for each output node. These error terms were then used (i.e. back-propagated) to adjust the initially random weights of each network connection. For most of the networks we trained, 50000 or so presentations of exemplars were required to reliably achieve minimization of the output error, so that each exemplar was presented to the network about seven times.

After the training process was complete, the network weights were frozen, and network was tested on the test set of radiances. The outputs of the testing process (temperatures at each of the ten levels) were then compared to the radiosonde observations.

4. Results

For each network we saved the results of the test in a spreadsheet of retrieved output and radiosonde "truth" temperatures. Each vector of the test set (exemplar) corresponded to a row of the spreadsheet, and the columns were associated with the ten pressure levels (actually 30 data columns in all: 10 for the raob "truth" values, 10 for the retrieved values, and 10 for the corresponding differences.

For each pressure height, we then computed the mean and root mean square error and the largest positive and negative error.

Table one summarizes these results for one neural network experiment, in this case a network with 20 nodes in a single intermediate layer.

	mean	rms	max error(+)	max error(-)
Surface	0.03	0.94	6.56	-5.13
850mb	0.05	1.53	8.69	-5.18
700mb	0.00	1.43	15.71	-11.95
500mb	-0.02	1.54	8.86	-13.14
400mb	-0.05	1.75	12.21	-10.10
300mb	-0.03	1.81	10.46	-11.30
250mb	-0.03	1.79	8.40	-10.70
200mb	-0.03	2.31	14.21	-19.46
150mb	0.01	1.86	8.24	-9.73
100mb	-0.02	1.91	13.56	-10.70

Table 1. Temperature errors (in Kelvins) as a function of pressure level.

It is notable that the mean errors displayed in Table 1 are very small, and that the rms errors are all less than 2 K except at 200 millibars. The largest positive and negative errors are many standard deviations, however. It is possible, but we have not yet checked, that the largest errors are associated with cloud contamination of the satellite radiances.

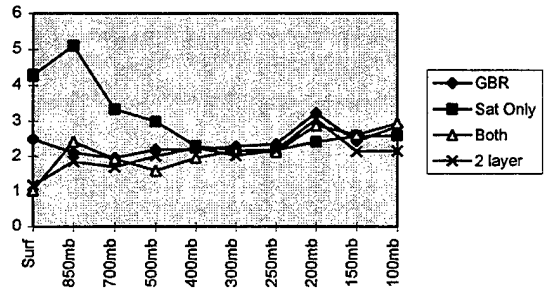

Figure 2. Error vs. Height for three different retrievals.

Figure 2 shows the results of different retrieval schemes. The retrieval labeled GBR uses only the simulated ground-based radiometric results, that labeled Sat uses only the satellite measured radiances, and that labeled Both uses both the above, in each case in a three layer network. The retrieval labeled 2-layer uses a two layer network to retrieve from the combined data.

The surprisingly good performance of the retrieval using only ground based radiances is probably due in part the advantages of using simulated data.

5. Discussion

The results achieved by the neural network look very good compared to results using satellite only except at 200 millibars. The presence of a small proportion of rather large errors deserves further study. We plan in future work to investigate the relationship of the large error cases to the meteorology of the measured pixels.

The present study had the following serious limitations, which we intend to remedy in ongoing work: First, the data used was all from a single period of just 5 days length, so it cannot be considered to represent the range of conditions likely to be encountered. Second, the visible channel data of the GOES-8 sounder was not used, hence cloud discrimination was intrinsically poor. Finally, we made no attempt to explicitly discriminate data vectors contaminated with clouds, which may account for some of the poorer temperature estimates.

References

Butler, Charles T., R. v. Z. Meredith, and A. P. Stogryn, 1992: Retrieving atmospheric parameters with neural networks, *AIRES 92*, Monterey, CA, Oct. 27-29.

Bustamante, Donald D., Arthur W. Duddenhoeffer, and James L. Cogan, 1992: Neural network retrievals of atmospheric profiles from TOVS radiances, *AIRES 92.*

Deepak, A., H. E. Fleming, and I. S. Theon, eds., 1988: *RSMR'87: Advances in Remote Sensing Retrieval Methods*, Deepak Publishing, Hampton, VA.

Measure, Edward M., and Jeff M. Balding, 1988: Application of neural network techniques to radiometric temperature profile retrieval, *Proceedings of the Ninth EOSAEL/TWI Conference,* Las Cruces, NM, November.

Measure, Edward M., Young P. Yee, Jeff M. Balding, and Wendell R. Watkins, 1991: Inverting radiometric measurements with a neural network, *AGARD Conf. Proc. 502, Remote Sensing of the Propagation Environment,* Cesme, Turkey, 30-1 to 30-6.

Neuralware, 1996: Software reference for Professional II/PLUS and Neuralworks Explorer, Neuralware, Pittsburgh, PA.

Rumelhart, David E., James L. McClelland and the PDP research group, 1986*: Parallel distributed processing: Explorations in the microstructure of cognition*, (2 vols.), MIT Press, Cambridge, MA.

Detection of PBL Forcing of Ground-Level Winds in a Desert using Wavelet Analysis Methods

David R. Miller[1], Yanshuo Wang[1], and Ronald M. Cionco[2]

[1]University of Connecticut, Storrs, CT

[2] US Army Research Laboratory, Adelphi, MD

ABSTRACT

Wind, turbulence, and boundary layer structure time series data collected at the Atmospheric Profiler Research Facility (APRF) located at BED's White Sands Missile Range site are analyzed. Wind and turbulence data are collected with a three dimensional sonic anemometer-thermometer mounted at the 3 meter level. The structure of the boundary layer is measured with BED's FM-CW radar at APRF. Data sets are obtained for hot, dry conditions in a desert landscape of moderately-spaced chaparral and mesquite bushes (~ 10m clumps spaced 15m apart), and undulating terrain. A time series of the boundary layer structure is compared to the wavelet decomposition of a simultaneous time series of turbulence near the ground in the surface layer. The large scale phenomena of the boundary layer growth and the thermal passage are detected as dominant forcing mechanisms in the surface layer's turbulence data.

1. INTRODUCTION

Knowledge of the mechanisms by which periodic surface layer structures near the roughness elements are ordered by Planetary Boundary Layer (PBL) scale thermals or large eddys is critical to current efforts to model surface and roughness layers and account for forcing from the larger boundary layer. It appears that the vertical dimensions of these surface layer structures are stability dependent, being on the order of Monin-Obukhov length

$$L = \frac{-u^{*3}\overline{\theta}}{kg(\overline{w'\theta'})} \qquad (1)$$

where U^* is the friction velocity, θ is virtual potential temperature, k is the von karman constant and g is gravity.

The streamwise extent of the surface layer structures are an order of magnitude larger than L in the convective boundary layer (Antonia et al. 1979) and on the order of the roughness element height , H, in the neutral boundary (Raupach et al. 1986). Thus they are not generally thermally induced. But they do not appear to be completely decoupled from the mixed layer structures. Observations in the surface convective boundary layer show characteristics at much lower frequencies. These have been called "superbursts" (Falco, 1977) and might be induced by intermediate scale thermal walls (Webb, 1984).

The purpose of the work presented here was to define the scale characteristics of the coherent wind and temperature structures near the ground surface, and to estimate the effects of the large eddy structures of a convective planetary boundary layer on these coherent structures.

2. METHODS

The general approach in this project was to compare simultaneous measurements of the large eddy structure of a convective PBL to time series measurements of wind and temperature fluctuations at the top of the surface roughness elements.

2.1 Measurements

The U.S Army Research Laboratory's, Boundary Layer Research team conducted the field measurements used in this study on 3 June, 1994. The site was a mesquite covered desert, 500 m North of the Atmospheric Profiler site at the White Sands Missile Range, NM. The desert vegetation was about 3m tall (h), sparse with less than half the ground covered and arranged in clumps spaced about 15m apart.

Measurements of the ground level wind dynamics were made with a 3-D sonic anemometer-thermometer (Applied Technologies Inc. Boulder, Colorado) at z = 3m. Simultaneous measurements of the PBL structures were made with the FM-CW radar described by Eaton et al. (1995). The radar image by the FM-CW radar shows relative intensities of values of the turbulence structure reflection parameter, Cn^2, calculated from the radar backscatter (McLaughhlin and Eaton, 1993).

$$Cn^2 = \frac{4.061 P_r R^2}{P_t R_g \frac{D}{R}} \qquad (2)$$

P_r is the received power, P_t is the transmitted power, R is the radar range and $R_G(D/R)$ is the antenna autocorrelation.

The data sets used in this analysis were acquired from 9:55 am to 11:45 am. In what follows, prime notations *U'*, *w'* and *T'* stand for the fluctuations of horizontal wind speed, vertical wind speed and temperature around their mean values, $\overline{U}$, $\overline{w}$ and $\overline{T}$, calculated for the period 9:55 am-11:45 am.

2.2 Wavelet Transformation of the Surface Wind Time Series

Analyses of atmospheric turbulent structures with wavelets is discussed in detail by a number of authors. For further detail the readers are referred to Morlet (1982), Kumar and Foufoula-Georgiou,(1994), Collineau and Brunet (1993), Meyers (1993); Weng and lau (1994), Katul and Parlange (1995), Katul and Vidakovic (1996), Yee et al (1996), Mahrt and Howell (1994), Cionco and Ohmstede, (1992), and Turner et al (1994). In this study the time series, T'(t), U'(t), and w'(t) were compared to a Daubechies Symmlet wavelet function, ψ (Daubechies, 1992). The wavelets were translated in time by a lag τ and scaled by an amplitude parameter α:

$$\psi(\tau,\alpha) = \frac{1}{\sqrt{\alpha}} \psi\left(\frac{t-\tau}{\alpha}\right) \qquad (3)$$

The wavelet transform is

$$WT_\chi(\tau,\alpha) = \int_{-\infty}^{+\infty} \chi(t) \psi\left(\frac{t-\tau}{\alpha}\right) dt \qquad (4)$$

where the variation in α is the dilation and τ is translation or location parameter.

The wavelet scale dependent variance is:

$$S(\alpha) = \int_{-\infty}^{\infty} \left| WT_{\chi}(\tau, \alpha) \right|^2 d\tau \tag{5}$$

and the wavelet power spectrum is

$$C_{\chi}(\alpha) = \int_{0}^{\infty} \int_{-\infty}^{\infty} \left| WT_{\chi}(\tau, \alpha) \right|^2 \frac{d\alpha d\tau}{\alpha^2} \tag{6}$$

3. RESULTS

The radar image measured by the FM-CW radar during the 1.75 hour period is shown in figure 1. Figure 2 plots the simulataneous surface wind speed measured with sonic anemometer.

The boundary layer growth from $z_i \sim$ 1600m to about $z_i \sim$ 2700m is clearly shown in this image. Between 8:46 am and 10:28 am (local time), surface heating was suppressed by a thin cloud cover and z_i was about 1600m. After 10:28 am, strong surface heating resulted in the formation of large PBL scale thermals and the boundary layer grew to 2400m by the end of the measurement period. The frequency of the thermals passing was ~4/hr in the period 10:28 to 11:50. Also from the image, we can clearly see the plume structure. The rising air from the ground surface to the top of the PBL is more turbulent than the subsiding air between the plumes. The most intense turbulence is shown at the tops of the plumes where the plumes are penetrating the overlying inversion.

The radar images in figure 1 show the large scale thermals organized from ground level to the top of the boundary layer. Therefore it is reasonable to expect some discrete effects of the thermals in the ground level wind field at the times these structures move by the ground sensor. A trace of the height of the top of the turbulent region in figure 1 shows the continuous time history of the dynamics in the maximum height of boundary layer due to alternating thermal passing and air subsidence.

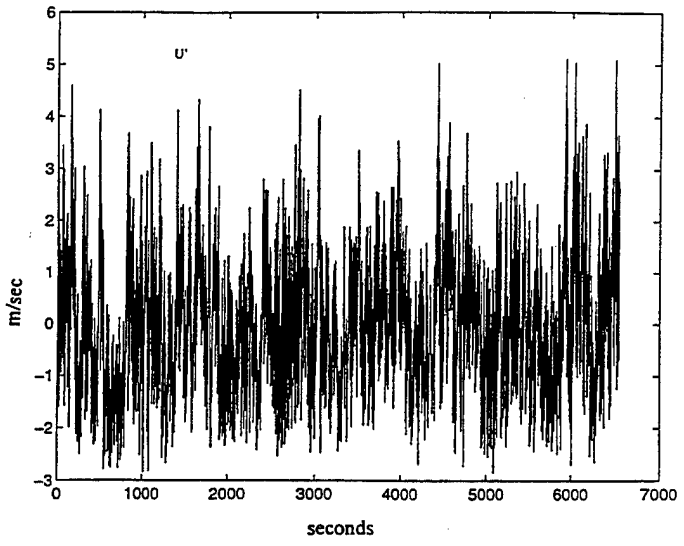

Figure 2. Time series of wind speed z = 3m simulations with the period in figure 1.

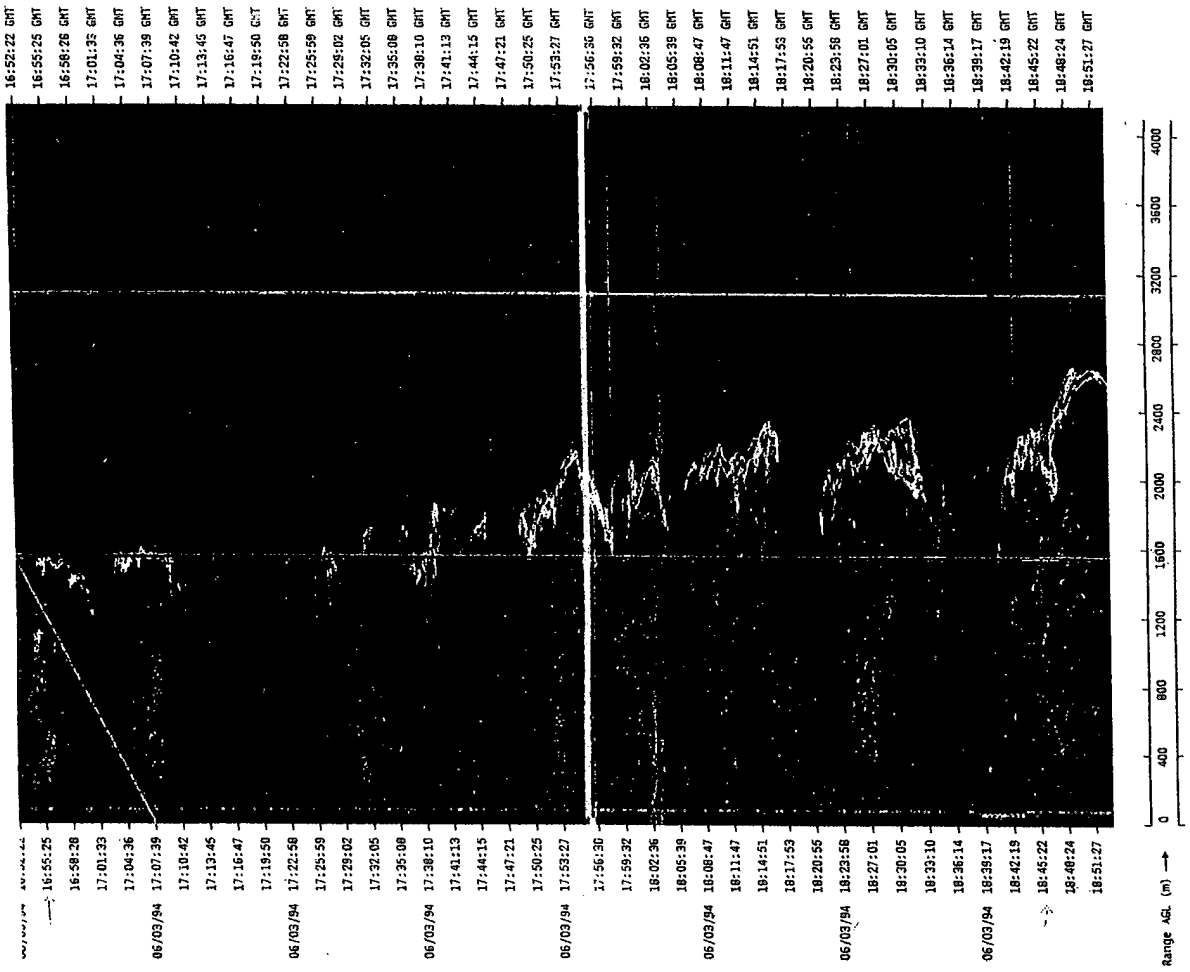

Figure 1. Two-dimensional (z,t) graph of relative C_N^2 in the Desert PBL measured with the FM-CW radar. The boundary layer grew from 1600 to 2400 m during the two hour period. Updraft thermals and cold downward moving air between the thermals are clearly visible.

Figures 3 display the wavelet variances for *T'*, *U'* and *w'* at 3m above the ground during the period (9:55am-11:45am) as calculated from the sonic anemometer-thermometer measurements. The spectra were calculated from 10 Hz data, where N=65536 points. In these log-log plots of wavelet variance (Var) vs. frequency (f), an inertial subrange is apparent in the *T'* and *U'* spectra at frequency *f^1Hz* where the slopes of the spectra were close to -5/3. Spectra peaks of *T'* and *w'* occur around $6.1*10^{-4}$(Hz), and $2.4*10^{-3}$(Hz), respectively. The horizontal velocity, U', spectra is less definitive but appears to have a broader peak about the same frequency as w'. Thus dominant scales of temperature and horizontal wind fluctuations occur around 1639s, and 416s, respectively.

Wavelet decomposition of *U', w'* and *T'* into different scales during the period (9:55am-11:45am) are shown in figures 4a, 4b and 4c as a function of time and scale. Wavelet coefficients were computed for the horizontal and vertical wind components and the temperature. Mallat's multiresolution pyramidal algorithm (Mallat, 1989) was used to decompose the original signal into different time scales. This decomposition allows the isolation of that portion of the variance contributed at the scales which approximate the dominant spectral peaks of 1639s for temperature and 416s for wind. The decomposed time series in figure 4 at scale 1638s for T' and at scale 409s are the comparable plots for w' and u'. The 1638 T' series shows two waves which approximately coincide with the two periods of rapid growth of the mean boundary layer height. The adjacent largest scale 3276s shows a single wave.

As noted earlier, there are two general periods shown, one before 10:50am with no general growth in the BL and one after 10:50am where the boundary layer was growing rapidly due to strong thermals penetrating the overlying inversion. The largest scale shown in figure 4(a) (3276.8s) reflects this boundary layer growth cycle with a single wave. This PBL growth cycle and its inflections are interpreted as the dominant forcing in the T' signals since these scales approximate the dominate spectra scales of T'. On the other hand the periods of the fluctuations in the 409s and adjacent w' and U' scales closely match the periods of the boundary layer height fluctuations caused by individual thermals penetrating the overlying inversion shown in figure 1.

4. DISCUSSION

The horizontal wind and temperature peak length scale in the convective surface sublayer was about 18 times the Monin-Obukhov length, *L = 91m*), while the vertical wind component scale was about 4.5 times the Monin-Obukhov length. Therefore the dominant scales are an order of magnitude too large to have been induced by the roughness elements.

Table 1. Average Turbulent Statistics during the period 9:55am-11:45am.

	mean	variance	std. dev.	skewness	kurtosis
U(m/s)	2.9378	1.3834	1.1762	0.4526	3.0333
w/(m/s)	0.4196	0.1087	0.3297	1.2270	5.0428
t (C)	32.0966	1.4541	1.2059	0.1501	2.4873
w't' bar	-0.02298	U'w' bar	0.0916	w*	1.1385
Heat flux	-23.21	MO length	-91(m)		

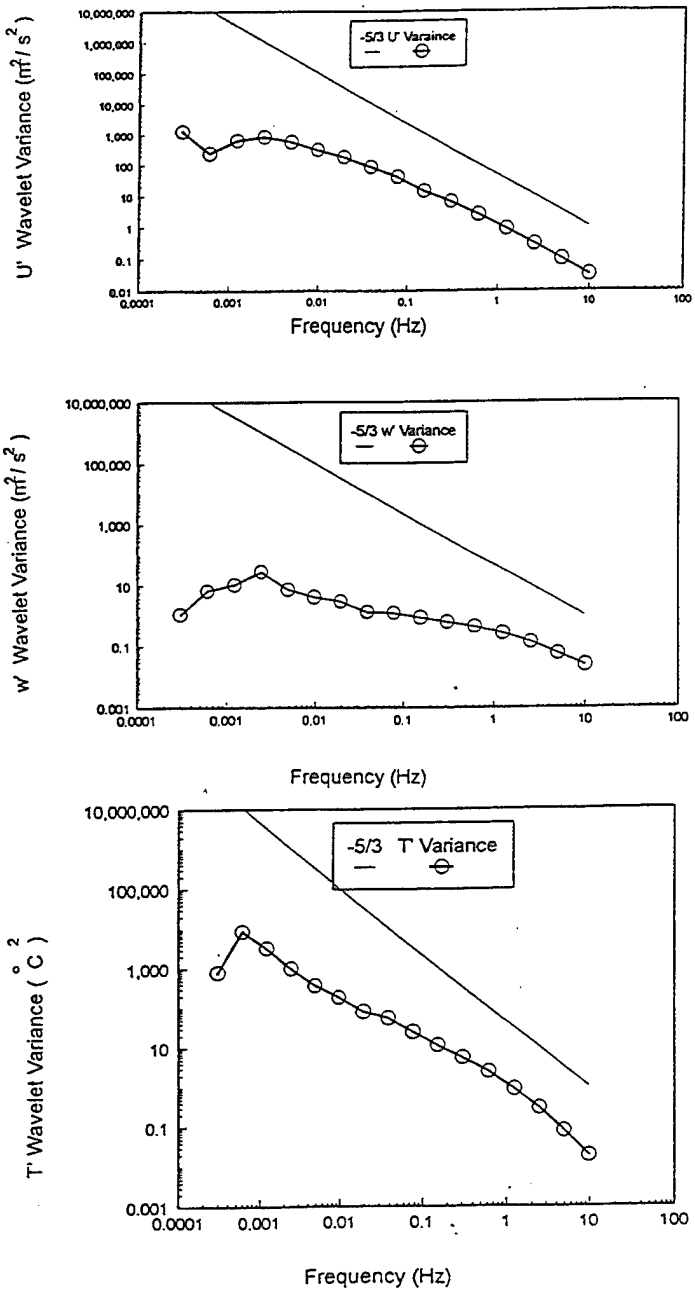

Figure 3. Wavelet variances spectra of T', U', and W'.

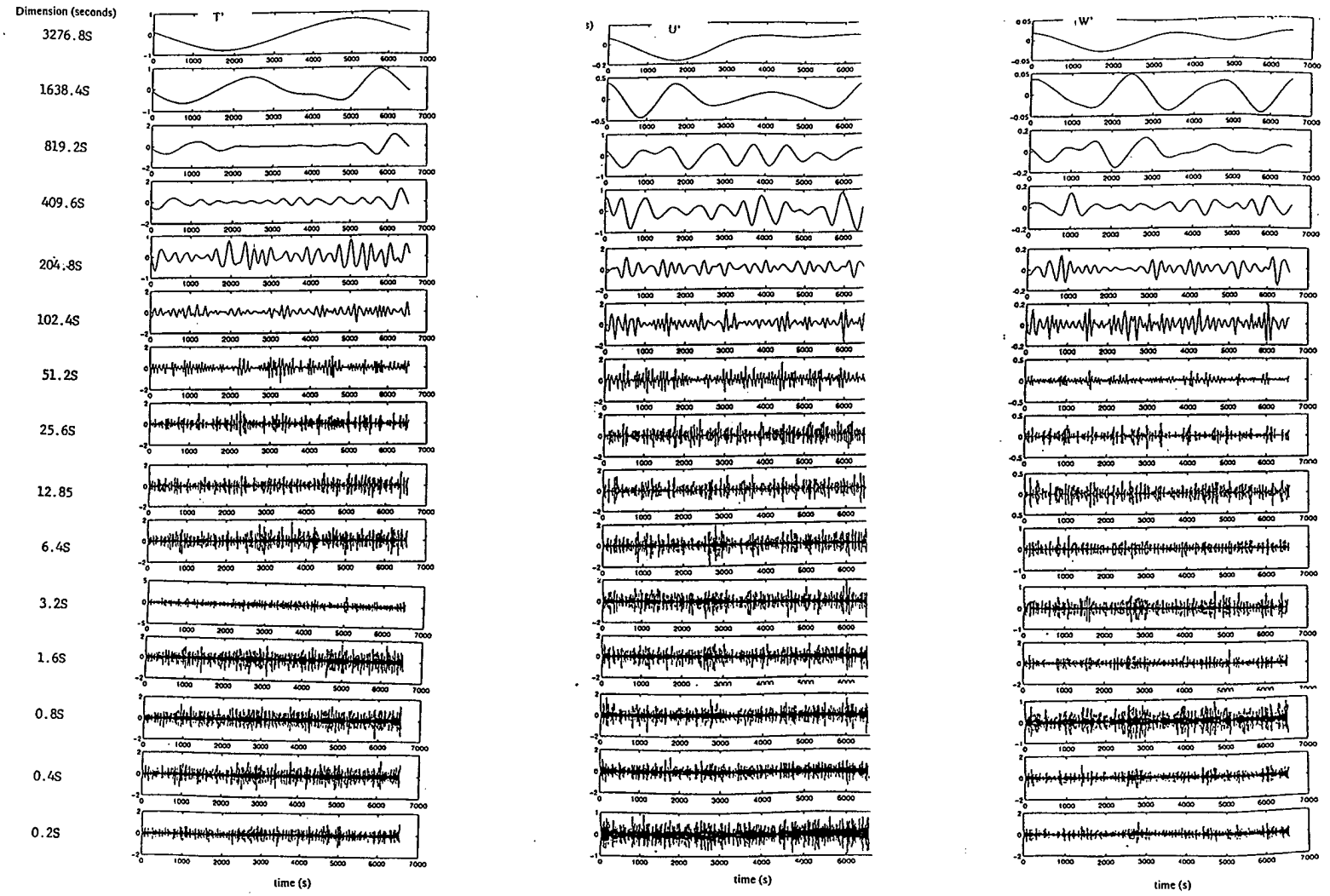

Figure 4. Time signals for T', U', and W' during the measurement period decomposed to show the contribution at each scale.

The w' wavelet scalogram in figure 5 shows periodic structures, designated by the dashed line, at the 25s (8th dyad on the graph) gradating into the 51s (9th) scale. The signals in figure 4 at these scales show a series of sudden increases in amplitude followed by a dampened oscillation. Close inspection of figure 1 reveals a series of wall like structures trailing to the ground below each thermal. Some of these occurs when the well-organized thermals are preceded by an updraft at ground level a few minutes prior to their passing at the top of the PBL. Several more occur as each thermal passes. A count of these as discrete events results in ~36 per hour during the measurement period, which is approximately the period of events in the 51s and 102s scale time series in the w' signal. Thus it appears that the trailing "thermal walls" trigger bursts of wind gusts at the surface that are detectable in the w' signal. Not only do the thermals force the large scale fluctuations in the surface wind, but the surface layer extensions of the boundary layer thermals trigger changes in the gust frequency and contribute to forcing the surface fluxes. These relationships were not apparent at these scales in the *T'* or *U'* signals.

5. CONCLUSIONS

Ground-level gust frequency is coupled to the boundary layer scale thermals in the convective PBL. Comparison of PBL thermal structures to the surface wind and temperature fluctuations, decomposed to individual scales, reflects the coupling of these large scale structures to specific signals in the ground level wind and temperature measurements.

The dominant time scale in the ground level U and T signals is forced by the total period trends in the height of the boundary layer. Whereas the dominant time scale in the w' signal is forced by the 4 to 8 minute frequency of the thermals passing. Wall-like structures in the surface layer trailing the PBL thermals trigger increases in gust frequencies and contribute to the surface flux forcing.

REFERENCES

Antonia, R. A., Chambers, A. J., Friehe,C.A.,and VanAtta,C.W. 1979, Temperature Ramps in the Atmospheric Surface Layer', *J. of the Atmosphere Sciences* **36**, 99-108.

Cionco, R. M. and Ohmstede, W. D. 1992, 'Intemittence, Events and Coherent Structures in Vegetative Canopies' Proceedings of the 1992 Battlefield Atmospheries Conference USARL, White Sands Missile Range, NM.

Daubechies, I., 1988. Orthonormal Bases of Compactly Supported Wavelets. *Commun, Pure Appl. Math.,* 41:909-996.

Eaton, F.D., McLaughlin, S.A. and Hines, J.R.: 1995b, 'A new FM-CW Radar for Studying the Morphology of the Planetary Boundary Layer', *Radio Science.*

Falco, R. E.:1977, 'Coherent Motions in the Outter Regions of Turbulent Boundary Layers'. *Phys. Fluids,* **20,** s124-s132.

Kumar, Praveen and Foufoula-Georgiou, Efi, 1994. Wavelet Analysis in Geophysics: An Introduction. *Wavelets in Geophysics,* Academic Press, pp 107-128.

Katul, G. and M. B. Parlange, 1995. The spatial Structure of Turbulence at production Wavenumbers Using Orthonormal Wavelets. *Boundary layer Meteor. 75:81-108.*

Katul, G. and B. Vidakovic. 1996. The Partitioning of Attached and Detached Eddy Motion in the Atmospheric

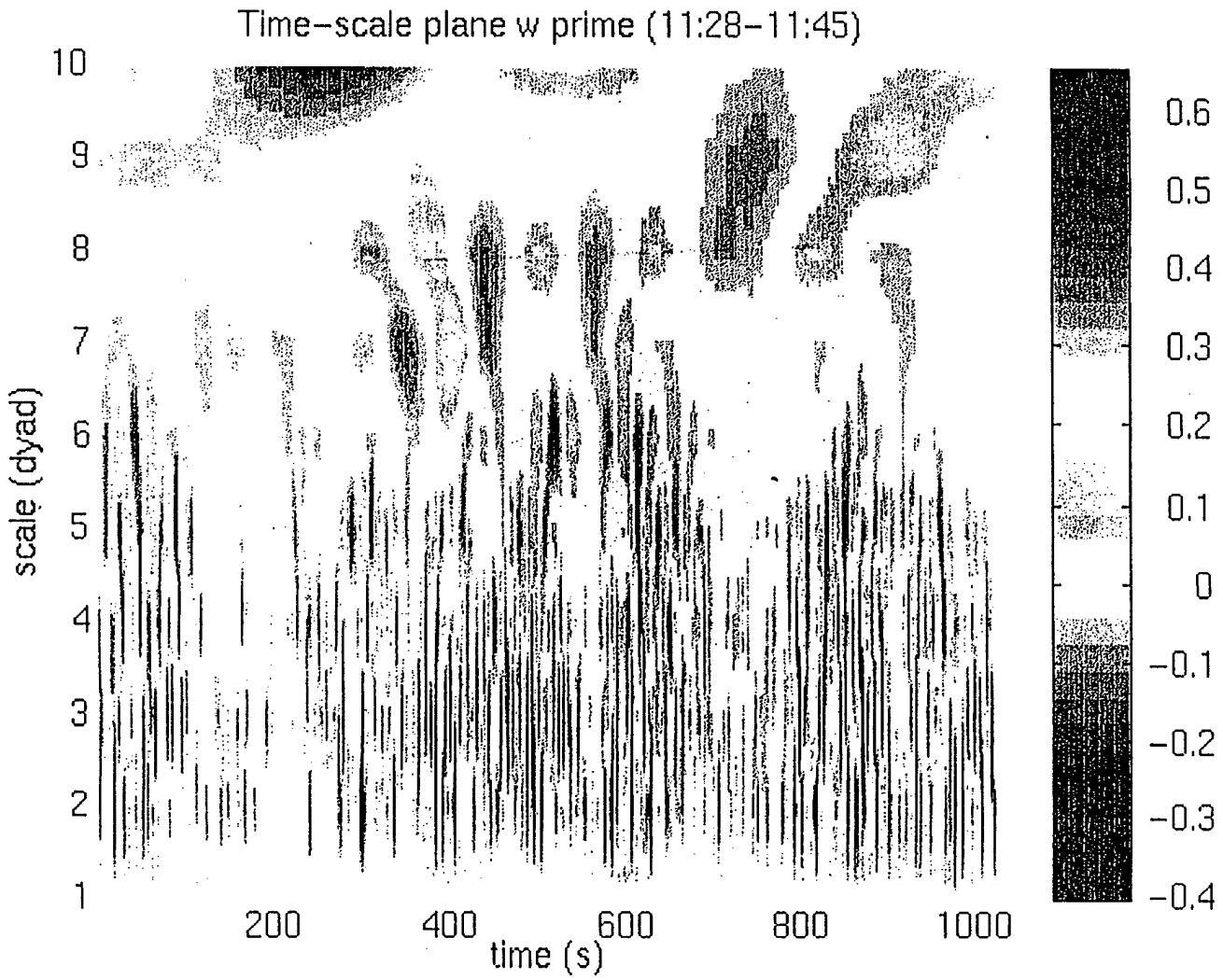

Figure 5. Wavelet scalogram of the surface W' signal. This plot shows a series of organized structures (marked by dotted line) at the 7 to 9 dyad. Dyads in this plot correspond to the first 10 time scales in figure 4.

Surface layer Using lorentz Wavelet Filtering. *Boundary Layer Meteor.* 77:153-172.

Mallat, Stephane: 1989, ' Multifrequency Channel Decomposition of Images and Wavelet Models', *IEEE Transactions on Acoustics, Speech, and Signal Processing,* **37**, 2091-2110.

Mahrt, L. and J. F. Howell. 1994. The Influence of coherent Structures and Microfronts on Scaling laws Using global and Local Transforms. *J. Fluid Mech.* 260:247-270.

McLaughlin, S. A. and Eaton, F.D.: 1993, ' Preliminary Results of the U.S Army Research Laboratory's New Boundary-Layer Profiling FM-CW Radar', Eighth Symposium on Meteorological Observations and Instrumentation, Anaheim, California Published by the American Meteorological Society, Boston, Massachusetts.

Raupach, M. R., Coppin, P. A. and Legg, B. J.: 1986, 'Experiments on Scale Dispersion within a Model Plant Canopy. Part I : the Turbulence Structure'. *Boundary-Layer Meteo.,* **35,** 21-52.

Turner, B. J., M. Y. Leclerc, M. Gauthier, K. E. Moore, and D. R. Fitzjarrald. 1994. Identification of Turbulence Structures Above a Forest Canopy Using A Wavelet Transform. *J. Geophysical Res. 99(D1):1919-1926.*

Webb, E. K.: 1984, 'Temperature and Humidity Structures in the Lower Atmosphere'. In. Brunner, F. K. (ed) Geodetic Refraction : Effects of Electromagnetic Wave Propagation through the Atmosphere. Springer, NY., 85-141.

Yee, E., R. Chan, P. R. Kosteniuk, C. A. Biltoft and J. F. Bowers. 1996. Multiscaling Properties of Concentration Fluctuations in dispersing Plumes Revealed Using an Orthonormal Wavelet Decomposition. *Boundary Layer Meteor.* 77: 173-207.

EOSAEL and PcEosael©

Dr. Alan Wetmore, Dr. Patti Gillespie, Army Research Laboratory, Adelphi MD

Mr. Andrew McCann, Dr. John Schroeder, Ontar Corporation

This work is implementing a Microsoft Windows™ interface for the Army Research Laboratory's (ARL) family of EOSAEL modules under a Phase II SBIR Contract (DAAL01-96-C-2007). The work is sponsored by the Army Research Laboratory, Adelphi, MD and is being directed by Dr. Alan Wetmore of ARL. He can be contacted via e-mail at Awetmore@arl.mil, or via the World Wide Web at www.EOSAEL.com. This paper briefly described EOSAEL, PcEosael, current and future software development directions, and distribution of EOSAEL products. User can keep up to data on EOSAEL development through the web page www.EOSAEL.com.

The **EOSAEL** is a state-of-the-art computer library comprised of fast-running, theoretical, semiempirical, and empirical computer programs that mathematically describe aspects of electromagnetic propagation in a battlefield environments. The 25 modules are connected through an executive routine, but often are exercised individually. They may be categorized into eight generic atmospheric effects areas: atmospheric gases, laser propagation, tactical decision aids, battlefield aerosols, natural aerosols, target acquisition, support modules, and radiative transfer.

The EOSAEL modules and documentation are currently distributed to approved users through TECNET. Approval to access the system is obtained by contacting Dr. Wetmore at the addresses given above. The user may obtain, upon approval: The FORTRAN source code of the module, PC executable code for the module, the module manual in a PostScript™ format, and several test cases to insure the proper compiling and running of the module. Data input is accomplished by using a text editor to produce the appropriately formatted ASCII file, and output are given in ASCII tables. Several of the modules have limited graphical output files in an ASCII format.

There are eight general categories of atmospheric effects covered in EOSAEL: atmospheric transmission and radiance, laser propagation, tactical decision aids, battlefield aerosols, natural aerosols, target acquisition, support modules, and radiative transfer. The modules currently in the EOSAEL library are: **AGAUS** a Mie scattering code, **BITS** a broad-band integrated transmittances, **CLIMAT** a climatology module, **COMBIC** an obscuration model for multiple battlefield-induced contaminants, **COPTER** obscuration due to helicopter-lofted snow and dust, FASCAT an algorithm for atmospheric scattering calculations, **FITTE** fire-induced transmission and turbulence effects, **GRNADE** smoke munitions self-screening applications, **ILUMA** natural illumination under realistic weather conditions, **KWIK** transmission threshold smoke munitions expenditures model, **LASS** large area screening systems application, **MODTRAN** atmospheric transmittance and radiance for broadband applications

LZTRAN laser transmittance and gaseous absorption algorithm, **MPLUME** missile smoke plume obscuration, **NBSCAT** narrow beam multiple scattering, **NMMW** near millimeter wave gaseous absorption, **NOVAE** nonlinear aerosol vaporization and breakdown effects, **OVRCST** contrast transmission, **PFNDAT** aerosol phase function database, **RADAR** millimeter wave system performance, **REFRAC** optical path bending code for near earth paths, **TARGAC** target acquisition, **UVTRAN** ultraviolet transmission and LIDAR simulation, and **XSCALE** natural aerosol extinction

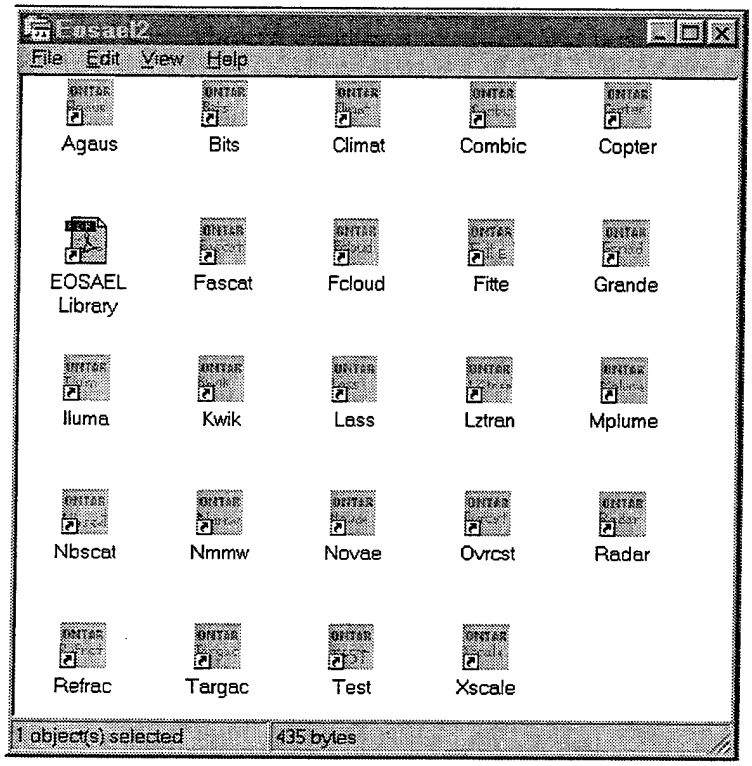

PcEosael is Ontar's implementation of a user-friendly, Microsoft Windows based interface for the for each of the EOSAEL modules together with and overall executive to link them into a unified package as shown by the figure to the left. The work will be completed by the Spring of 1998.

The interface allows the user to set parameters by an intuitive, visual point and click method, output plots of computed results, and generate images that are easily viewed. The interface is independent of the internal workings of the individual EOSAEL modules, and has on-line documentation for each of the modules and its suite of input parameters. It significantly simplifies setting scenario parameters common to all the modules (e.g. spectral band, range, etc.), and provides tools to easily compare the results from the different EOSAEL modules.

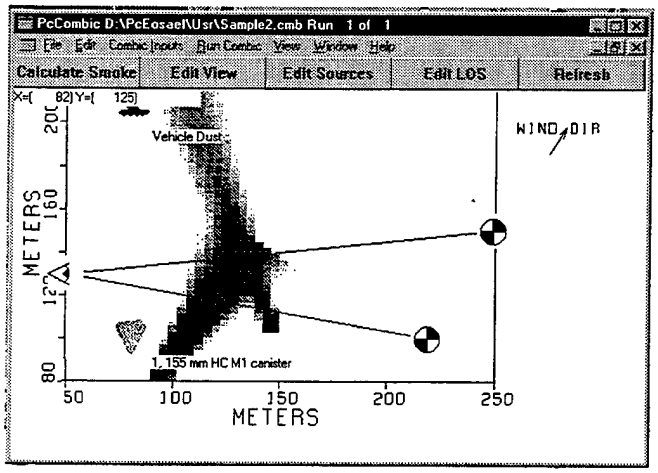

An example of the GUI is shown in the figure to the left which is produced by the COMBIC module. COMBIC compute the transmission through dust clouds, smoke, fire and other man made obstructions. The figure shows an observer (the eyeball), two paths (the end point are designated by the circles), and two obscurant sources. The first is the dust generated by a moving

vehicle which is designated by the tank symbol in the upper left corner of the screen. The second source is a smoke canister designated by the symbol at the bottom of the plot toward the left hand side. This visual representation is used to two purposes.

First, it allows the user to specify the location of the sources, and the end points of the paths for the calculation. The user can either click on the object, e.g. the eyeball, and bring up an input screen were he can input the numeric x-y values for the location, or he can click and drag the object on the screen to the desired location. Similarly he can add (or subtract) sources and other paths.

The second use of this GUI is to view the output from the COMBIC calculation. In this case we are showing the dissipation of the smoke cloud from the 155 mm canister at 43 seconds after the beginning of the scenario. The user does this by clicking on the horizontal bar near the top of the screen labeled "**Calculate Smoke**" which brings up the dialog box shown at the right of the figure. The user first specifies the time from the beginning of the scenario at which he wishes to view the cloud and the spectral band in which he wishes to see the results (in this example the 8 to 12 μm band). The result are shown, in this case, by the vertical strip running from the smoke canister at the bottom of the display area (near the 160 meter grid point) to the top of the screen. The dust from the moving vehicle has moved out of the viewing screen by 43 seconds. At an earlier both the smoke and dust clouds will be in the field of view.

The strip is a visual representation, projected onto a 2d plane, of the spatial extent and transmission of the smoke cloud at the time and in the spectral band specified by the user. In this case the display is at 43 seconds after the release for the . 8 to 12 μm spectral region. The spatial extent is indicated by the x-y spread in the data. The transmission is depicted as a gray scale going from black (0% transmission) to white (100% transmission). Another display allows the user to generate a transmission plot (0 to 100%) as a function of time along each of the paths shown in the display.

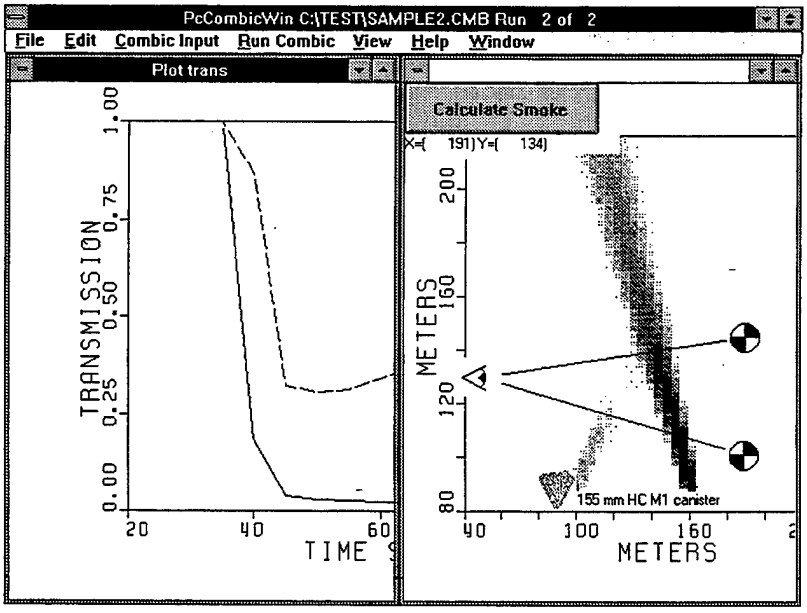

Similar GUI are available for the other EOSAEL module where it is appropriate to display the inputs and outputs in a graphical format.

Another significant feature of the PcEosael software is the online documents. This falls into three general categories: technical reports and conference proceedings, technical manual for each of the EOSAEL modules, and the help documentation for each modules.

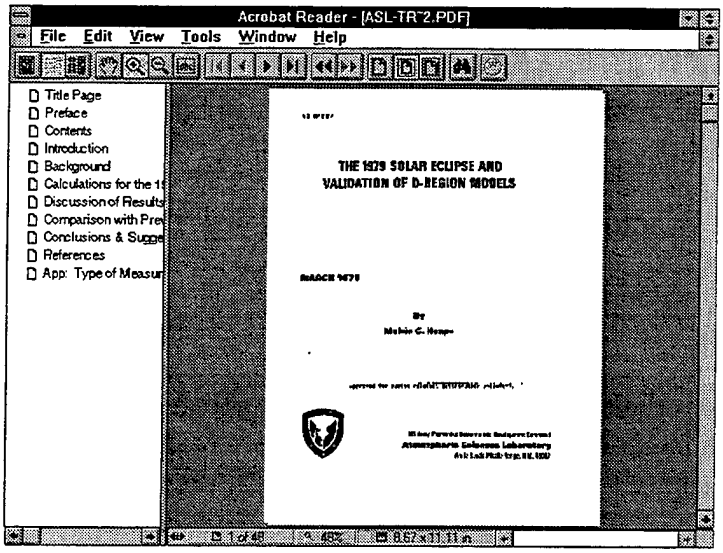

The Atmospheric Sciences Laboratory (ASL), now part of ARL, produced an important technical library of report and manuals related to their mission of characterizing atmospheric propagation under battlefield conditions. There are approximately 1300 of these documents which have been scanned and converted into the Adobe Portable Document Format (PDF) ™. These along with the manual and help files are available to the user on-line from each of the modules. A roadmap guides the user through the various options for selecting the appropriate document. The combination of these three sources makes the software one of the best documented packages of it type.

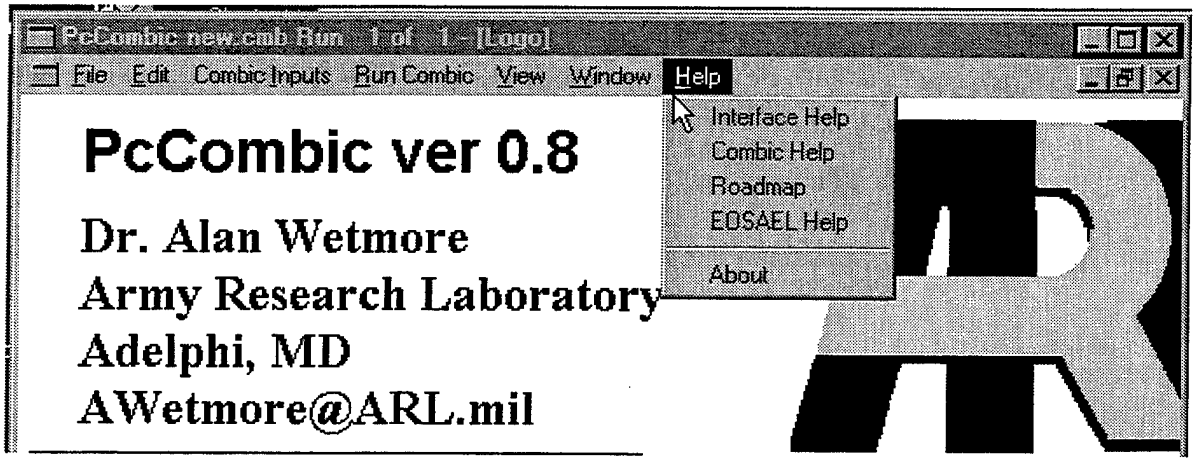

The software is designed for cross platform use, and the Windows software will be followed by corresponding UNIX versions. All documentation, including the ARL/ASL scientific reports, ARL technical manual for each module, associated software manuals, and on-line help is in the Adobe Acrobat Portable Document Format™ (PDF). The documentation is used as either a stand along product to be read at your leisure, or in conjunction with operation the software via hyperlinks.

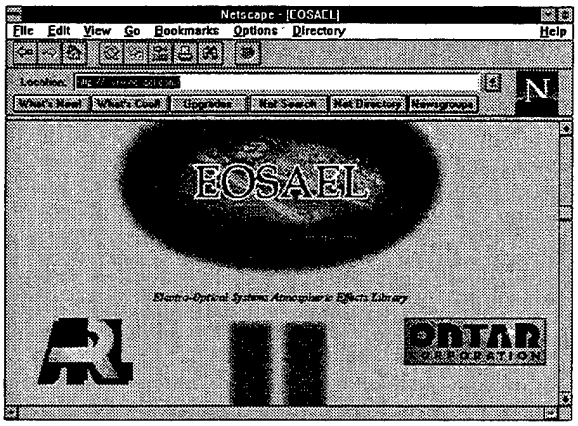

A second major objective of the work is to better keep user informed EOSAEL developments. The is being accomplished via the URL site www.EOSAEL.com. Requests for the access to TECNET can be sent via the web site which also contains a descriptions of each module and the interactions between the modules.

The complete PcEosael interface will be completed by the Spring of 1998. In the interim, beta versions of selected modules are available for testing. These can be obtained by contacting Dr. Wetmore.

Battlefield Environment Data Sets for the Master Environmental Library (MEL)

David Tofsted, Richard Shirkey, Donald Hoock
Max Bleiweiss, Jon Martin, and Chatt Williamson
Army Research Laboratory
Information Science and Technology Directorate
Battlefield Environment Division

Abstract

For the Defense Modeling and Simulation Office (DMSO) sponsored Master Environmental Library (MEL) program to ensure accurate transmission of data, programs must be tested. The Army Research Laboratory (ARL) has implemented a number of battlefield effects models and data bases. Specifically the following have been implemented through the ARL/Adelphi MEL resource site: 1) a radiative transfer model, database and visualization, for prediction of atmospheric illumination, radiance, and propagation information; 2) the XSCALE model, which calculates extinction coefficients and transmittance through naturally occurring aerosols of haze, fog, rain, snow, and ice fog; 3) obscurant field measurements of transmission and meteorological conditions, including videos taken from an extensive smoke/obscurants database of clouds and transmissometer measurements; and 4) simulation of battlefield smoke and dust cloud production, transport and diffusion. A discussion of these models and their method of implementation will be presented.

1.0 Introduction

The Master Environmental Library (MEL) is a Defense Modeling and Simulation Office (DMSO) sponsored project with the charter of providing internet access to authoritative databases and model outputs for the representation of the natural environment. MEL features on-line data discovery and retrieval of oceanographic, meteorological, terrain, and near space databases through geographically distributed "resource" sites. The MEL is entered through a single "access" site (http://www-mel.nrlmry.navy.mil) which guides the user through the selection of the different data bases available in MEL, the viewing of related metadata records describing those data bases, and the ordering of data through MEL via the custom order process. Although *access* to the data in MEL is centralized via the conduit of the access site, the data is actually stored at, and controlled by, the distributed resource sites.

At a high level the MEL is based on a library paradigm. Users query an interface which functions much like the standard card catalogue of an ordinary library. This interface resides at the access site and consists of an Internet HTTP server with supporting HTML and Java interfaces. The cards in the card catalogue are the common denominator among all datasets in the library. These cards are formatted metadata records compliant with the U.S. Federal Geographic Data Committee's (FGDC) Content Standards for Digital Geospatial Metadata[1]. Using either the HTML or Java interface, users with a WWW browser interactively create a query made up of region of interest, time range, category, keyword, and data center elements. A WAIS search engine is then used to compare the user's request information against metadata records for all the data centers specified in the query. Query results are presented to the user who can then examine the full text of any of the resulting metadata records. From each metadata page one can select to generate an order form customized for the chosen dataset. The Java query results interface provides a unique interactive information visualization and comparison capability that helps the user navigate to the datasets of interest from a potentially large result set. But currently the Java interface has not been written to handle data from test sites, and for historical reasons the Army Research Laboratory (ARL) site is still considered a test site. This condition should soon change.

MEL has several different levels of resource site compliance. An initial level includes sites which merely have the MRSS (MEL Resource Site Software) in place. This software includes several codes which link a given resource site into the rest of the MEL network. Components include PGP encryption, a PERL language interpreter, a job tracking mechanism, data extractors for each listed data set, and standard data

format creation algorithms such as produce GRIB and BUFR type formatted data. The use of the publicly available PGP encryption software enables the system to provide moderate security to ensure that data requests are not intercepted, that inter-MEL communications are secure and that a user can be assured that data is arriving from an approved and reliable source.

Orders for data sets are produced by filling out the custom order form. This form is generated by the access site software. Following user selection of the data criteria from the order form, the access site parses the order form data and produces an e-mail message which is then sent to the server at the appropriate resource site. This is the function of the access and resource site e-mail handlers. On the resource site side, the incoming e-mail message is parsed to determine the appropriate extractor to call to interpret the message. Each e-mail message consists of a series of parameters which were specified by the custom order form for the particular metadata record. A user has several delivery options, among which are FTP, e-mail, physical media, or via anonymous FTP pickup at the resource site.

A custom order form consists of a sequence of choice selections which determines parameters which divide a data base into logical pieces or which permits a data generator model to perform its calculation functions. Typical choice fields might include time and location information, variables to include in the returned data set, and parameters controlling the data generation technique. There are primarily 6 selection mechanisms for specifying choices: integer, float, and text data values, region of interest, single choice, and multiple choice. Integer, float, and text entries require the input of the specified type of data. Such fields might include time or spatial information or some specific name. Region of interest data selections generally apply to data sets of some spatial extent like would apply to fields of temperature data. Single choice usually allows the user to select from only a finite number of data values, like month, year, etc. Multiple choice is normally used to allow multiple data sets to be returned as a result of the inquiry.

2.0 The MEL Architecture

The three components of the MEL distributed architecture are the user site, the central access site and the distributed resource sites as shown in Figure 1. The user site, of course, is the interface the user accesses to communicate with the MEL main web site. This requires the availability of web access software, which the user must provide.

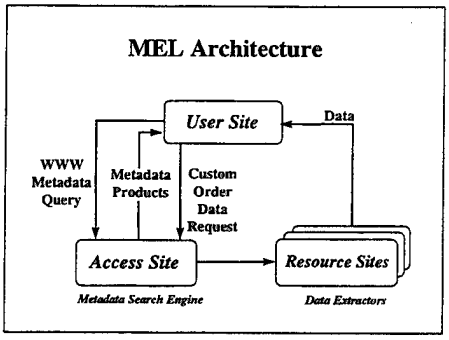

Figure 1. The three components of the MEL distributed architecture: the user; the central Access Site; and the distributed Resource Sites

2.1 The Access Site

The MEL Access Site provides a single, uniform interface for all users. It consists of a Hypertext Transfer Protocol server, HTML forms and Java applets, and supporting Common Gateway Interface scripts and programs. The user fills out a query form to specify the spatial and time range, keywords and data sites of interest. The MEL Access Site Software (MASS) is updated periodically to better reflect interactivity with the main WAIS metadata server. This is currently located at Naval Research Laboratory, Monterey, CA, (NRL-MRY).

In addition to the query capabilities the access site maintains a metadata validation service. Any metadata record that a developer wants to add to the MEL system must be validated using this service. Only validated records are searchable and the availability of registered sets has some bearing on the level of compliance of a given resource site.

2.2 The Resource Site

Orders for data are transferred to the resource site via electronic mail and processed by the MEL resource site software. This software is customizable and performs the functions of order parsing, access control, scheduling, data extraction, formatting, compression, encryption, delivery and notification. Resource sites specify in their metadata descriptions if the data is subsettable and how.

MEL, however, does not have specific resource site policies. Except for the program requirements associated with the MEL resource site software (MRSS) there is currently only a distinction between a "fully compliant" and a "level 1 compliant" site. The distinction is made in terms of the ability to order data using the custom order forms. Each data type is expected to have a registered and searchable metadata record at the access site. Sites with available metadata which can be accessed from the main access site are considered fully compliant. Sites which only provide data via custom runs or using means other than the custom order process are considered merely level 1 compliant.

3.0 MEL model-based and distributed computing capabilities

While the MEL was primarily developed to allow the distribution of precomputed archived data sets, the capability of producing data sets which may require input data to run a model or retrieve data from multiple sites was also inherent within this flexible paradigm. These on-demand data retrieval metadata allow users to produce specific data sets interactively based on the custom order information. In many ways this process also alleviates the complications associated with storing these data bases, since the data are describable using the model input more simply than archiving a large parameter space associated with the results of large numbers of model runs. The characteristics of large numbers of input parameters and on-demand computation characterize a large number of Army-related environmental models. ARL implementations of these models within MEL as part of the FY97 program thus affords MEL a unique opportunity for testing the flexibility of its library paradigm. The data bases implemented in MEL under the FY97 ARL effort included the XSCALE line-of-sight transmission effects calculations and the Atmospheric Illumination Module (AIM) radiance and illumination data sets. Other data base examples available from ARL include output from the Combined Obscuration Model for Battlefield Induced Contaminants model (COMBIC), the Battlescale Forecast Model (BFM), and sets of Smoke and Obscurants data derived from various battlefield obscuration field tests. In describing the implementation mechanisms selected for these models we begin with the simplest (level 1 compliant) implementation for the Smoke and Obscurants data sets.

3.1 Smoke and Obscurants Data Sets

This first example is simple primarily because we discovered that the data mining necessary to extract examples of data from smoke trials is a very tedious and difficult task. The smoke week tests from which this data was extracted involved numerous trials consisting of releases of smoke obscurants and simultaneous measurements of various meteorological parameters for describing the wind, temperature, humidity and turbulence conditions during the time of the test. Unfortunately this data was not archived fully at the time of the experiment and thus resurrection of the data and formatting of the information in forms that would be useful to a current user were manpower intensive. This archiving project was also made difficult by the multiple participants in the experimental process. Nevertheless, several trials were archived. In the level 1 implementation this information was simply provided in a form which can be directly downloaded from a web page at the ARL Adelphi MEL site. Obviously, given more data mined from the trials, the task of browsing the available data would be better served by the availability of a metadata record custom order form. However, due to minimal funding for the effort, insufficient variability in the data was available to warrant the initiation of a metadata record.

3.2 XSCALE Aerosol Extinction Vertical Scaling Model

As an example of the next level of complexity we consider the implementation of the XSCALE model[2] within MEL. Weather has a profound effect on the performance of all electro-optical devices that depend on the propagation of electromagnetic energy through the atmosphere. The XSCALE model[2], part of the Electro-Optical Systems Atmospheric Effects Library[3] (EOSAEL) determines the transmittance through various naturally occurring aerosols within the near-surface atmosphere. These aerosols include both horizontally homogeneous aerosols such as hazes, fogs, and ice fog, various intensities of rain, and snow, for both individual wavelengths and broadband averages in the ranges 0.2μm to 12.5μm for line-of-sight paths within 2 km of the Earth's surface. The models for the various aerosols are based on applications of

Mie theory to theoretical particle size distributions which are modeled as horizontally homogeneous, and an empirical vertical scaling algorithm to permit slant path computations. The haze results from XSCALE are consistent with those used in LOWTRAN[4] and agree with the mean values obtained in the Meppen 80[5] and Cardington[6] experiments. The algorithms used for generating extinction predictions for fog, rain, and snow are based on empirical and semiempirical models.

The aerosols are assumed to be horizontally homogeneous. Beer's law is then used under a monochromatic propagation assumption to calculate horizontal transmittance:

$$T_\lambda(R) = e^{-K_\lambda R}$$

Where $T_\lambda(R)$ is the transmittance at range R and wavelength λ, and K_λ is the extinction coefficient at λ. The model was developed by numerous researchers of the U. S. Army Atmospheric Sciences Laboratory in the 1980's. The input for XSCALE consists of easily obtainable meteorological parameters such as meteorological visibility, aerosol type, rain rate, relative humidity, temperature and wind velocity. In addition information is required about the transmission path: its length and whether or not the path is horizontal or slanted. The output information consists of the transmission and extinction coefficient at the requested infrared wavelength. (Since XSCALE requires a visible waveband visibility measure, it is primarily used to scale values between visibility experienced by a human observer and that experienced by IR sensors.) Finally the output is delivered, as mentioned above, either by e-mail or ftp.

The XSCALE module is fully MEL compliant. A metadata file for this code has been registered at the NRL-MRY access site and an extractor is available at the ARL-Adelphi site for data computation.

3.2 COMBIC Battlefield Environment Characterization

The Combined Obscuration Model for Battlefield-Induced Contaminants (COMBIC)[7] is also part of EOSAEL. It predicts time and spatial variations in line-of-sight transmission through multiple battlefield smoke and dust clouds. Inventory screening smoke sources, high-explosive sources creating dust and debris, and moving vehicle dust production can be specified by user input menus. Other obscurants can be specified by detailed user inputs. Time and space-dependent clouds are modeled as having components with gaussian concentration distributions which transport, diffuse and buoyantly rise with time. The input for COMBIC is comprised of meteorological, site and munition information as detailed in table 1; Table 2 details the output of phase I, to be provided at the Web site.

Table 1: COMBIC input

Meteorological parameters (a) Relative humidity (percent) (b) Windspeed at reference height (m/sec) (c) Pasquill stability category. (d) Air temperature at reference height (°C) (e) Air pressure at reference height (f) Reference height for input wind speed, temperature and pressure (m) (g) Height of the limiting inversion (if any) (m)
Site parameters (a) Latitude (degrees) (b) Longitude (degrees) (c)Julian date
Optional soil and surface parameters
Source Records (a) Munition definitions and type selection
Vehicle inputs (primarily for dust but also for any moving source)

Computations are performed in two phases. First, a cloud history file is preprocessed "off-line" for one or more obscurant source types selected from a menu or defined through user inputs. Except for wind

direction, all meteorological influences are included in these "Phase I" calculations of transport, rise and diffusion of the obscurant clouds. These effects are simulated through use of transport and diffusion parameterizations based on surface layer similarity theory characterization of the near surface environment. Additional effects of the atmosphere on aerosol properties are also included. In separate, "Phase II" calculations COMBIC builds a user-defined scenario of smoke and dust sources. By table look-up and scaling of Phase I histories, cloud concentrations at any given time are computed. Path integrated concentration is determined for each target-observer pair and transmittance is computed at each of seven wavelength bands for (in principle) any scenario defined by multiple sources and active lines of sight. The final outputs are computed using Beer's Law for transmittance.

Table 2: COMBIC Phase I Output

METEOROLOGICAL CONDITIONS
- (a) Reference Height (m)
- (b) Wind Speed (m/s)
- (c) Temperature (°C)
- (d) Surface Roughness (m)
- (e) Wind Direction (degrees east of north)
- (f) Inversion Height (m)
- (g) Pasquill Category
- (h) Relative Humidity (percent)

BOUNDARY LAYER PARAMETERS
- (a) Friction Velocity (m/sec)
- (b) Pasquill Class
- (c) Air Density (g/m^3)
- (d) Monin-Obukhov Length (m^{-1})
- (e) Kazanski-Monin
- (f) Sensible Heat Flux ($watt/m^{-2}$)
- (g) Cold Region Flag
- (h) Surface Buoyancy Flux (m^2/s^3)

DIFFUSION COEFFICIENTS

SURFACE CONDITIONS
- (a) Snow Cover Flag
- (b) Silt Content (percent)
- (c) Sod Depth (m)

VERTICAL PROFILE MODEL (the following parameters are vs height)
- (a) Windspeed
- (b) Atmospheric Temperature
- (c) Static Stability Parameter
- (d) Eddy Dissipation Rate

MASS EXTINCTION COEFFICIENTS (M^2 /GRAM)
- (a) Obscurant Code
- (b) Extinction .4-.7 um
- (c) Extinction .7-1.2 um
- d) Extinction 1.06 um
- (e) Extinction 3.-5. um
- (f) Extinction 8.-12. um
- g) Extinction 10.6 um
- (h) Extinction 94 ghz

CLOUD HISTORY *repeated for each cloud*
- (a) Munition Characteristics
  - i. XN No. of Sources
  - ii. Fill Weight
  - iii. Menu Selection Type
  - iv. Obscurant Type
  - v. Efficiency
  - vi. Yield Factor
  - vii. Number of Submunitions
  - viii. Burn Duration
  - ix. Burn Coefficients B_1,...B_7
  - x. Smoldering Time
  - xi. Smoldering Coefficient
- (b) Subcloud Structure repeated for each subcloud
  - i. subcloud characteristics
  - ii. subcloud trajectory (vs. height)

3.3 AIM Volumetric Radiance Calculations

The Atmospheric Illumination Module (AIM) is a more recent member of the family of ARL atmospheric characterization algorithms. The goal of AIM is to produce three-dimensional data sets of spectral radiance data which can be used in various applications. The method of computation of these 3-D radiance fields utilizes an extension of the discrete ordinates radiative transfer approach.[8] To initialize the model boundaries the Air Force MODTRAN code is used to determine incident direct (solar/lunar) and diffuse radiation at the top of the modeled volume. The inputs for running MODTRAN are determined based on user selected parameters input to the custom order form.

In addition, the AIM implementation within MEL features the results of a special MEL program termed "Distributed Computation". Within this program MEL developers were attempting to determine the possibility of running several interrelated models and use the outputs of some to provide input data to

others. In relation to the AIM modeling system the issues to be addressed related to whether it was possible to provide input data concerning weather conditions which would provide data for an AIM run. Specifically, AIM requires information about the state of the cloud geometry within its modeling volume in order to simulate the atmosphere. In its standalone mode AIM requires user input to assign cloud fractions, cloud layer positions (base and height), and cloud type information to be able to run. These data are input to AIM through a user interface. But in its MEL implementation the object was to provide AIM with the necessary information via a route consistent with the modeled weather in a particular region. This region was selected as the southwest United States, as is currently modeled within by the COAMPS data sets provided under MEL. But the COAMPS data sets do not include cloud information. To translate the COAMPS data into cloud prediction information that data was routed to a MEL site at Hanscom AFB, MA, where a second processing stage was performed on demand. Once an order for MEL data was received at the ARL-Adelphi MEL resource site a secondary call for data would be automatically produced and sent to Hanscom from Adelphi requesting a CSSM input data pack. CSSM (the Air Force's Cloud Scene Simulation Model) is the program run within AIM to generate the 3-D cloud geometry of liquid water content which can then be ingested by the remaining AIM codes. The call to Hanscom for data produces a packet of data suitable for input to CSSM. This data packet is then picked up and used by the AIM code to provide input for the remainder of the computations.

The outputs of the AIM product include 3 files. In the first, a radiance map of the model volume is produced on a cell-by-cell basis. For each cell directionally and spectrally dependent limiting path radiance and aerosol extinction information is provided. In the second, a higher density map of the model volume's extinction coefficient information is provided. In visualization experiments to determine the appearance of these cloud fields[9] it was determined that the standard ¼ km resolution of the radiative transfer model extinction output fields was insufficient, producing cloud shapes which appeared to rectangular. To attempt to solve this problem the second file provides information about the cloud extinction properties at 1/16 km resolution. At this resolution the clouds appear more natural during the rendering process. In the last file is contained information concerning the surface illumination in each region of the RT model volume. This information is then used in rendering the lighting conditions present on a surface to be placed beneath the clouds. With these 3 components a complete characterization of the modeled volume for propagation through aerosols is provided.

The mechanisms internal to the running of this distributed system bear some remark. First, we wanted to remain within the MEL paradigm of the order form process and operate through calls across the internet. However, to fully implement the distributed computing concept we did have to expand somewhat on the basic MEL approach. First, we extended the MEL order form's choice classes to include the possibility of inputting floating point and integer values. Since MEL had originally been designed primarily for the extraction of archived data sets it was not prepared for requirements for selecting parameters used as input to models. Second, the standard mechanism for ordering data within MEL only permitted the acceptance of orders originating at the MEL Access Site at Monterey. We had to extend this approach such that the ARL-Adelphi site could 'reorder' data from the Hanscom site. That is, we had to extend the MEL approach such as to allow resource site-to-resource site calls for data. In addition, the Hanscom site had to have in place a mechanism for receiving and analyzing the incoming COAMPS data sets in order to provide the data we would be requesting.

4.0 **Summary**

MEL provides a methodology for accessing data and products for the representation of the natural environment in Modeling and Simulation through an on-line Web site. Products currently available include the EOSAEL models XSCALE, for determination of transmission at infrared wavelengths, and COMBIC, for predicting time and spatial variations in line of sight transmission through multiple battlefield smoke and dust clouds. Other on-line products in MEL include forecasts from the University of Wisconsin's non-hydrostatic model[10], a meteorological forecasting model used to provide time dependent 3-D meteorological parameters over complex terrain. Prediction of atmospheric illumination, radiance, and propagation information, which are critical to accurate target acquisition and scene generation, are available for a 3-D variable atmosphere as a function of natural cloud type and amount, including partly cloudy skies at visual

wavelengths[11]. Also available are sample data from an extensive smoke/obscurant database in the form of short video clips. The database consists of videotapes of smoke/obscurants clouds and transmissometer measurements in the visible through far-IR as well as the corresponding meteorological measurements. Cloud growth dynamics are also presented. The database covers virtually all U.S. Army smoke field tests during the last 20 years.

The MEL implementation of ARL codes provides a useful benchmark upon which to evaluate the usefulness of MEL as an environmental library. Since MEL provides a basis for implementing and/or linking various models via a standard series of interface paradigms, including coded e-mail messages, standard mail handlers, PGP encryption, ftp delivery, etc. it can permit a wide range of models to communicate and interoperate. One particularly interesting feature of this paradigm is the relative independence between the developer and the user, in that the user community can have access to a product and yet developers can continue to improve these same products.

Overall the usefulness and availability of models to a user community can only be increased by the further development of the Master Environmental Library.

Acknowledgments

The authors would like to express their appreciation to Steve Lowe, et. al. for allowing usage of material in previously published proceedings[12].

REFERENCES

1. http://geochange.er.usgs.gov/pub/tools/
metadata/

2. Fiegel, R.P., 1994, Natural Aerosol Extinction Module, XSCALE, ARL-TR-273-1, U.S. Army Research Laboratory, Adelphi, MD.

3. Shirkey, R.C., L.D. Duncan, F.E. Niles, 1987, EOSAEL 87, Volume 1, Executive Summary, ASL-TR-0221-1, U.S. Atmospheric Sciences Laboratory, White Sands Missile Range, NM.

4. Kneizys, F.X., E.P. Shettle, L.W. Abreu, J.H. Chetwynd, Jr., G.P. Anderson, W.O. Gallery, J.E.A. Selby, S.A. Clough, 1988, Users Guide to LOWTRAN 7, AFGL-TR-88-0177, AFGL, Hanscom AFB, MA.

5. Lindberg, J. D., 1982, Early Wintertime Fog and Haze Report on Project Meppen 80, ASL-TR-0108, U.S. Army Atmospheric Sciences Laboratory, White Sands Missile Range, NM.

6. Lindberg, J. D., 1984, Final Report on the European Vertical Structure Experiment at Cardington, England, ASL-TR-0153, U.S. Army Atmospheric Sciences Laboratory, White Sands Missile Range, NM.

7. Ayres, S. D. and S. DeSutter, 1994, Combined Obscuration Model for Battlefield Induced Contaminants, COMBIC 92, ARL-TR-273-11, U.S. Army Research Laboratory, Adelphi, MD.

8. Tofsted, D.H and S.G. O'Brien, 1997, Characterizing the Effects of Natural Clouds on Scene Simulations, Proceedings of Targets and Backgrounds: Characterization and Representation III, 21-24 April 1997, Orlando, FL, SPIE, 3062, pp. 188-198.

9. O'Brien, S.G., and D.H. Tofsted, 1997, Visualization of Dense Cloud Cloud Radiation Data in Modeling and Simulations, Proceedings of Modeling, Simulation, and Visualization of Sensory Response for Defense Applications, 21-24 April 1997, Orlando, FL, SPIE, 3085, pp. 82-93.

10. Tripoli, G. J., 1992, A Nonhydrostatic Numerical Model Designed to Simulate Scale Interaction, Mon. Wea. Rev., **120**, 1342-1359.

11. Tofsted, D.H and S.G. O'Brien, 1997, Dense Cloud Radiative Transfer Scenarios and Model Validation, Proceedings of Cloud Impacts on DoD Operations and Systems, PL-TR-97-2112, Air Force Philips Laboratory, Hanscom AFB, MA.

12. Lowe, S., N. Alper, C. Stein, R. Siquig, J. Boyd, J. Corbin, V. Anantharaj, 1997, Product Generation within the Master Environmental Library (MEL), Spring Simulation Interoperability Workshop, 97S-SIW-160, http://siso.sc.ist.ucf.edu/siw/97spring/index.htm.

ARMY WEATHER EFFECTS CRITICAL VALUES DATABASE

Richard J. Szymber
U.S. Army Research Laboratory
Information Science and Technology Directorate
Battlefield Environment Division

U.S. Army Intelligence Center and Fort Huachuca
Directorate of Combat Developments (ATZS-CDS-W)
Fort Huachuca, AZ 85613
Ph: 520-538-0723
Fax: 520-538-0708
E-mail: szymberr@huachuca-emh1.army.mil

1. INTRODUCTION

Meteorological critical values are those values of weather factors (i.e., the critical thresholds) which can significantly reduce the effectiveness of or prevent execution of tactical operations and/or weapon systems. Significant variations above or below the critical values can prevent the successful accomplishment of a mission. Critical values define the operational limits beyond which it is not feasible to operate because of safety considerations or decreasing effectiveness. These operational limits are usually based on tests conducted during weapon system development and/or on the experience of weapon system users.

The United States Army Intelligence Center and Fort Huachuca (USAIC&FH), Army Weather Proponency Office has collected and established weather effects critical threshold values for Army operations, equipment, weapons, and personnel over the past 10 years. Meteorological critical values have also been obtained for certain Threat military systems, as well as for U.S. Air Force, Navy, and Special Operations Forces (SOF) systems and operations. In 1992, the critical values compiled to date were published in FM 34-81-1, *Battlefield Weather Effects* (Headquarters Department of the Army, 1992). Recently, the database of critical values has been updated and expanded, and is being validated and approved. This paper discusses the current and future status of the Army weather critical values database, with respect to it's expansion, validation, and utilization.

2. CRITICAL THRESHOLD VALUES

Mission planners must be aware of weather factors that will affect their operations, ensuring the greatest chance of mission success. They must be familiar with meteorological critical thresholds to effectively use weapon systems and other assets, and

to provide maximum safety for friendly personnel. The critical threshold is that value or point, or range of values, where the occurrence of a meteorological element causes a significant (i.e., moderate or severe) degradation/impact on a military operation, system, subsystem, or on personnel.

Many of the critical values in the Army database are based on limits imposed by peacetime constraints and safety considerations (e.g., safety of flight regulations for aviation). These limits are generally higher than the actual operational limits of the system. During war many of these peacetime constraints may be waived to less stringent wartime criteria, with the critical meteorological thresholds determined by operational commanders. Only commanders decide which thresholds are critical for their operation, weighing safety and efficiency factors of operations with the tactical situation and criticality of the mission.

3. DATABASE OF CRITICAL VALUES

The systematic collection of data required for establishing an Army-wide critical values database is a long, resource intensive process involving both literature research and field survey of subject matter experts. There is no central repository where all applicable Army publications (e.g., technical and field manuals) can be obtained for review. The many Army centers, schools, operational units, and other organizations must be contacted to obtain and certify the critical values that they are the responsible authority for. The Army-wide database should not be viewed as being all-inclusive; furthermore, it does not provide absolute values for every possible operation or piece of equipment/weapon on the battlefield.

Many potential sources of meteorological critical values are available. Some general sources include: military publications (e.g., technical manuals, field manuals, and training instructions); US Army Training and Doctrine Command (TRADOC) proponent centers/schools (survey of subject matter experts); Army tactical units (survey of operational users); research, development and acquisition, and testing and evaluation communities (e.g., Army Labs, Program/Project Managers, Research Development and Engineering Centers, and US Army Test and Evaluation Command); National intelligence centers (e.g., National Ground Intelligence Center (NGIC), National Air Intelligence Center (NAIC), and Defense Intelligence Agency); and miscellaneous publications (e.g., Janes Defense).

Some of the primary sources of data used in this project include: FM 34-81-1 (Headquarters Department of the Army, 1992); FM 34-81/AFM 105-4 (Departments of the Army and Air Force, 1989); FM 34-130 (Headquarters Department of the Army, 1994); FM 90-22 (US Army TRADOC, 1991); M 525-6 (US Special Operations Command, 1996); the Army Research Laboratory's Integrated Weather Effects Decision Aid (IWEDA) database (Chesley and Grocki, 1997); the Topographic Engineering Center's Environmental Thresholds and Impacts (ETI) database (1997 version); the 1997 draft of the *Joint Meteorology and Oceanography (METOC) Training Handbook*; the

Electronic Systems Center's 1997 draft technical report *Air and Space Natural Environment Modeling and Simulation Technical Requirements Analysis*; the 1990 USAIC&FH Intelligence and Electronic Warfare (IEW) Mission Area Analysis (MAA) weather survey; the 1980 Army Combined Arms Center (CAC) weather study; and production requests (in 1995 and 1997) to NGIC and NAIC for threat data.

The database structure has seven fields of information for each critical value entry (for example, see figure 1). These seven data fields are: 1.) Object/Name (tactical operation, equipment, weapon, system, subsystem, component, tactic, or personnel); 2.) Meteorological Element/Factor (condensed impact); 3.) Critical Value with Operator; 4.) Impact Statement/Explanation (full impact); 5.) Impact Magnitude/Degradation (color code); 6.) Original Source/Reference; and 7.) Validation Status (proponent and date). The magnitude of the weather impact is color coded in the "stoplight" format: Red, Amber, and Green. Red is unfavorable: operations prohibited (i.e., total or severe degradation/impact; exceeds operational limits or safety criteria). Amber is marginal: operational capability degraded (i.e., moderate degradation/impact). Green is favorable: no operational restrictions (i.e., no or low degradation/impact).

The critical values database project began in the summer of 1997 with about 500 friendly values and 50 threat values. The project will be completed in the summer of 1998 with a validated database of over 5,000 friendly and 500 threat values. All collected database objects/names (i.e., weapons systems, operations, etc.) and associated critical values were compiled and organized by the appropriate branch of the Army they came under, and then sent to that branch proponent for their review/evaluation and validation. Once all the results from all TRADOC proponents are received, they will be combined into the completed database and officially accredited by the USAIC&FH. The TRADOC Centers and Schools, and associated Army branch and operations involved are:

- Aviation Center, Fort Rucker, AL: Aviation (attack, assault, general support aviation).
- JFK Special Warfare Center and School, Fort Bragg, NC: Special Forces [SOF] (Special Forces, Special Forces aviation, Special Operations Forces, psychological operations, amphibious operations, civil affairs).
- Field Artillery School, Fort Sill, OK: Field Artillery (cannon artillery, rocket and missile artillery, target acquisition).
- Air Defense Artillery School, Fort Bliss, TX: Air Defense (short range air defense, theater air defense, theater ballistic missile defense).
- Chemical School, Fort McClellan, AL: Chemical [NBC] (NBC reconnaissance, smoke, decontamination).
- Ordnance Center and School, Aberdeen Proving Ground, MD: Ordnance (ammunition supply and maintenance, mechanical/electronic/missile maintenance, explosive ordnance disposal).
- Armor School, Fort Knox, KY: Armor (armor, armored cavalry, light cavalry).
- Infantry School, Fort Benning, GA: Infantry (light, mechanized, airborne, air assault, ranger).

- Intelligence Center, Fort Huachuca, AZ: Military Intelligence [IEW] (electronic warfare, counterintelligence, IPB, fusion and analysis).
- Signal Center, Fort Gordon, GA: Signal (signal support/communications, combat camera).
- Engineer School, Fort Leonard Wood, MO: Engineer (general engineering, topographic support, mobility and countermobility, survivability).
- Transportation School, Fort Eustis, VA: Transportation (highway transportation, rail transportation, water transportation, logistics-over-the-shore operations, movement control, terminal operations).
- Quartermaster School and Logistics Center, Fort Lee, VA: Quartermaster (supply/logistics, field services).
- Military Police School, Fort McClellan, AL: Military Police (military police combat support, enemy prisoner of war support).
- Soldier Support Institute and Center, Fort Benjamin Harrison, IN: Medical (medical support, medical evacuation, medical surveillance, combat and environmental stress).

Name	Value Operator	Condensed Impact	Impact	Original Source	Color Impac
!AGS-17!	800 meters <	Very Low Visibility	Visibility less than 800 meters makes it difficult to acquire/identify targets.	FM 34-81-1, pg. N-4, Dec 1992	Ambe
!AT-3!	3000 meters <	Low Visibility	Visibility less than 3000 meters makes it difficult to acquire/identify targets.	FM 34-81-1, pg. N-5, Dec 1992	Ambe
!AT-3!	800 meters <	Very Low Visibility	Visibility less than 800 meters makes it difficult to acquire/identify targets.	FM 34-81-1, Pg. N-4, Dec 1992	Re
!ERYX!	600 meters <	Very Low Visibility	Visibility less than 600 meters makes it difficult to acquire/identify targets.	FM 34-81-1, pg. N-4, Dec 1992	Ambe
!LOWBLOW!	light >=	Moderate Precipitation	Rain of intensity of light or greater degrades the effectiveness of the radar.	FM 34-81-1, pg. N-8, Dec 1992	Ambe
25MMGUN	2000 meters <	visibility	Visibility < 1.2 miles (2000 m) reduces the maximum effective range	FM 23-1, Para 1-8, Mar 1996	Ambe
30MMMACHINEGUN	4000 <	Reduced Visibility	Visibility < 2.5 miles (4000 m) reduces the operating capability.	(1st Cavalry Division, 1992);	Ambe
30MMMACHINEGUN	17 >=	surfacewindspeed	Surface wind speed >= 17 kts makes accurate firing of the weapon difficult.	(1st Cavalry Division, 1992);	Ambe
30MMMACHINEGUN	4000 <	visibility	Visibility < 2.5 miles (4000 m) reduces the operating capability.	(1st Cavalry Division, 1992);	Ambe
7.62MMCOAXMACHINEGUN	800 meters <	visibility	Visibility < 0.5 mile (800 m) reduces the maximum effective range.	FM 23-1, Para 1-4, Mar 1996	Ambe
A-10	CB	cloudtype	Thunderstorms affects control of aircraft, avoid all thunderstorms	55-1/Janes	Rec

Figure 1. Example of critical values and the database structure. The fields of information (columns) shown, from left to right, are: name/object, critical value and operator, condensed impact/weather element, full impact/explanation, original source/reference, and color impact or magnitude of degradation (not shown is the column for validation status). The top five entries (rows) are for threat weapons and the bottom six are friendly weapons/systems.

4. DATABASE MAINTENANCE AND UTILIZATION

The Army-wide database of critical values being prepared must be viewed as a continuing, ongoing program. Army (as well as threats, U.S. Air Force and Navy) materiel and systems are constantly being upgraded and replaced, resulting in a changing set of critical values. An institutionalized maintenance plan must be established that routinely identifies, collects, validates, and maintains all critical value data. An established system that maintains the evolving Army database would ensure that all users of the data always have current and accurate critical values. To facilitate this process, the Army Weather Proponency Office plans to conduct a periodic review/survey and re-validation of the critical values database every 2-3 years in order to expand the size of the database and to keep it current/updated. Secure storage of the database and secure, easy access to it by appropriate users is also necessary. The database should be archived at a central facility (e.g., the Air Force Combat Climatology Center) that would facilitate the accumulation of data and assist making the data available for digital dissemination over the Secret Internet Protocol Router Network (SIPRNET).

Meteorological critical values are the lowest common denominator in assessing weather support requirements; specific effects of weather on any system, subsystem, operation, tactic, and personnel; and who has the tactical advantage in adverse weather – friendly or threat forces. They are the basis upon which weather effects and warnings/advisories are established, and are the bridge or connection between the battlefield weather and it's warfighting operational impact. An accurate, complete database of critical threshold values for both friendly and threat capabilities is a key ingredient for "Owning the Weather" (Seagraves and Szymber, 1995).

Meteorological critical values have important applications in the Intelligence Preparation of the Battlefield (IPB), weather effects tactical decision aids (e.g., IWEDA), modeling and simulation, and testing and evaluation. This information is vital for the battlefield visualization of environmental effects. In mission planning, weapon system operators and planners can use the critical threshold values to familiarize themselves with factors that can affect their missions. Conversely, weather support personnel can use the critical values to familiarize themselves with the weather elements that require extra close examination while preparing forecasts.

5. SUMMARY

The Army Weather Proponency Office, USAIC&FH, is conducting an extensive survey of weather effects/impacts on Army equipment, systems, weapons, personnel, operations, and tactics. Analogous information is also being collected on various Threat, U.S. Air Force, Navy, and SOF systems/weapons and operations. The survey is structured by Army Branch/Operations, with the associated TRADOC School and Center serving as the proponent, subject matter expert, and responsible validating authority for the weather effects critical values pertaining to their materiel and operations. Our office is collecting and assembling all known documented meteorological critical values for submission to the appropriate TRADOC proponent, that will review and approve the data set provided.

After the results have been received from all the TRADOC Centers/Schools, the USAIC&FH will officially validate the complete database. A validated critical values database with approximately 5,500 values (i.e., 5,000 friendly and 500 threat values) will be established by the summer of 1998.

REFERENCES

Chesley, C.H. and V.P. Grocki, 1997: "Verification and Validation of Current IWEDA Rules." STC Technical Report 3157, Science and Technology Corporation, Hampton, VA, 12 December 1997.

Departments of the Army and the Air Force, 1989: FM 34-81/AFM 105-4, Weather Support for Army Tactical Operations. Washington, DC, 31 August 1989.

Headquarters, Department of the Army, 1992: FM 34-81-1, Battlefield Weather Effects. Washington, DC, 23 December 1992.

Headquarters, Department of the Army, 1994: FM 34-130, Intelligence Preparation of the Battlefield. Washington, DC, 8 July 1994.

Seagraves, M.A. and R.J. Szymber, 1995: "Weather: A Force Multiplier." Military Review, Vol. LXXV, No. 6, pp. 69-76, November-December 1995. US Army Command and General Staff College, Fort Leavenworth, KS.

United States Army Training and Doctrine Command, 1991: FM 90-22, Multi-Service Night and Adverse Weather Combat Operations. Fort Monroe, VA, January 1991.

United States Special Operations Command, 1996: M 525-6, Military Operations Critical Meteorological and Oceanographic Thresholds for SOF Operations. MacDill AFB, FL, 4 October 1996.

Joint Simulated Total Obscuration Results Model (J-STORM)

Ms. Jan Breeden and Mr. Frank Poleski
National Ground Intelligence Center
220 7th Street, NE
Charlottesville, Virginia 22902-5396

ABSTRACT

The Joint Simulated Total Obscuration Results Model (J-STORM) is a system of models and databases designed to calculate the total effects of the atmosphere and foreign obscurants in spectral regions ranging from ultra-violet (UV) through centimeter wavelengths (CMW). J-STORM is designed to be easy to use and to provide consistent results. This is accomplished by using built in databases from which meteorological conditions, equipment, and scenarios can be chosen by using an interactive WEB interface.

1. INTRODUCTION

The National Ground Intelligence Center (NGIC) is developing a dynamic user-friendly model called the Joint Simulated Total Obscuration Results Model (J-STORM). J-STORM is a suite of models and databases designed to calculate the total effects of the atmosphere and foreign obscurants on various parts of the electromagnetic spectrum, ranging from ultraviolet through centimeter wavelengths, including the radiance problem.

These calculations can be performed for any foreign country selected by the user. This will include the effects of the natural environment and that country's obscurant disseminating systems to produce a total effectiveness computation. Input parameters for J-STORM are extracted from the NGIC foreign obscurants disseminating systems database and a worldwide climatology database whose source is yet to be determined.

The motivation for J-STORM was the need to address several common problems often encountered by analysts and tacticians. The first problem is that many obscurant models, both natural and battlefield induced, often require expert knowledge of the model and the physical input parameters to be run reliably. The second problem is that results quoted by different users for the same scenario often do not agree. Different results are caused by the fact that most model users do not know the technical characteristics of foreign obscurant disseminating systems and therefore use U.S. data points. J-STORM seeks to solve these problems by providing the user with a standard set of models and input parameter databases, as well as a choice of geographic locations. The architecture also allows the user the option to select only the systems database and/or the climatology database without running any models.

Compounding the problem of modeling foreign disseminating systems is the fact that no single model is all-inclusive in its ability to handle both natural atmospheric and battlefield-induced obscurants. And, while some existing models do cover fairly wide spectral ranges, no model satisfactorily covers the entire 200 nanometer to 1 gigahertz range of interest. Likewise, physical phenomena such as scattering, absorption, and radiance are now recognized as very important factors that affect system performance, particularly in the infrared spectral regions.

2. J-STORM CONCEPT AND STRUCTURE

NGIC has the quad-service mission of determining the technical characteristics of foreign obscuring agents and disseminating systems as well as the total obscuration effect on the different parts of the electromagnetic spectrum. These data are essential for input to many models used by the R&D community and the commander in the field. A problem the R&D community faces with current models is the fact that engineers do not always know the defeat mechanism for the system. In addition to total effectiveness, J-STORM will identify the most significant defeat mech-

anism. The data retrieved from J-STORM will allow the R&D community and project/program managers to evaluate the robustness of their systems in a realistic obscurants environment during all phases of development,; thus there should be no surprises when the system goes to the field for engineering and operational testing.

J-STORM will allow the combat commands, to know the enemy's obscurants capability and what wavelengths they are effective against. This knowledge will allow commanders to evaluate their entire suite of munitions against the suspected obscurants environment. Before deployment all of their weapon systems can be evaluated against the suspected environment as well as the country's inventory of disseminating systems. thus allowing them to take only the more robust weapon systems as well as evaluate the best method to tactically employ them.

3. GENERAL DESIGN CONSIDERATIONS

A large part of the J-STORM concept is the inclusion of models capable of treating foreign dissemination systems. It is expected that to realize this goal, some existing models, such as the Electro-Optical Systems Atmospheric Effects Library (EOSAEL) module Combined Obscuration Model for Battlefield-Induced Contaminants (COMBIC), will be acceptable if modified. It is expected that new models will also need to be developed to cover spectral ranges, conditions, and systems not currently treated by existing models. The concept of J-STORM requires three distinct types of program applications: (1) database programs, (2) atmospheric and obscurants model programs, and (3) a graphical user interface program. Thus, J-STORM requires the assembly of a large, complex software application package. A primary goal of J-STORM is to allow users to perform analysis tasks unencumbered by the need to learn specialized language command or to be saddled with the frustration of not having the right data for model input. The J-STORM application will access databases and retrieve information for the user, it will apply user-defined scenario information to extract model input parameters, and it will provide a variety of output formats. The package will transfer user-defined input parameters to the selected library of models, activate the appropriate model codes, and retrieve the results. The construction of such software application requires careful planning and design. A complete understanding of user applications and requirements must be brought to bear during the design phase.

For the user, the operation of J-STORM will be straightforward, even through the underlying application program structures will be quite complex. The following description of J-STORM operation is to illustrate the intended power and versatility of the application from the user's perspective. The completed J-STORM application will be very complex, and this description does not fully represent the envisioned final product.

4. PHASES

Development of the fully comprehensive J-STORM application is estimated to take five to seven years. It is designed, however, to provide useful and valuable operational tools throughout the period of development. Completion of each successive phase will provide a new, fully functional application. Phase I, the architecture design, has been completed. The major focus of Phase II is to provide access to the foreign smoke/obscurants system and climate databases. During Phase II, models review will intensify and the initial set of J-STORM models will be selected. The fully operational J-STORM interface will be implemented and made accessible to users. This phase will draw on the design architecture built during Phase I. The most significant change in terms of J-STORM architecture will be implementation of user operations to review and extract information from the foreign systems database and/or the climatology database with activating J-STORM models.

The major focus during Phase II will be to provide full access to both the NGIC foreign smoke/obscurants disseminating systems, and agent databases, and a corresponding climatology database through the J-STORM interface. To accomplish this objective, these three databases must be built. Database design and the communication code between the databases and the user interface pages designed in Phase I will be developed and implemented. The most time-intensive portion of the Phase II work will be the actual collection and organization of the database information. Both the systems database and the climatology database data will require significant preprocessing and development before being archived. Under Phase II, the model identification and review process will intensify. The model literature search and review begun under Phase I will be extended. The selection of models for J-STORM will be influenced by the following guidelines: (1) fidelity of "real" world. (2) minimal user input requirements (3) computation speed, and (4) interface capabilities with other models. A major effort in following Phases will be the verification, validation and

accreditation of selected models.

Phase II will draw on the design architecture built during Phase I to populate the foreign obscurants system and agent databases and decide on the best climate database. Model versatility, model strengths and weaknesses, model capabilities, spectral regions considered aerosol physics, cloud transport and diffusion, types of scenario supported, and computational parameters such as transmittance and radiance will be reviewed. Selected models will be added to the J-STORM library during later phases.

REFERENCES

Davis, R.E., B.R. Bullard, and A.R. S pillane, 1995: Simulated Total Obscuration Results Model (STORM): Phase I, Architecture, STC Technical Report 2946, Science and Technology Corporation, 101 Research Drive, Hampton, Virginia

Progress in the Development of the Environmental Models and Algorithms Catalog (EMAC)

Edwin Núñez, John Medeiros, Beverly Burns
COLSA Corporation, Huntsville, Alabama 35806

and

Gary McWilliams
Executive Agent for Air and Space Natural Environment
Air Force Combat Climatology Center
Scott AFB, Illinois 62225

Introduction

This paper describes the tasks accomplished during the second phase of a project to build an electronic catalog of models and algorithms characterizing the natural atmospheric and space environment. It is part of a larger effort by the Defense Modeling and Simulation Office (DMSO) to compile information on environmental phenomenology from the modeling and simulation community. This information has been systematically collected and maintained in a database accessible to users and developers on the World Wide Web (WWW).

DMSO[1] is in charge of increasing the cooperation among different elements of DoD involved with the development and maintenance of models and simulations. As part of its objectives, DMSO wants to ensure timely, authoritative, and more accurate representations of the atmosphere, space, ocean and terrain components of the natural environment. Users and developers need the capability to access detailed information on existing natural environment models and algorithms. This initiative, will lead to more realistic and consistent representations of the environment in future versions of DoD models and simulations.

DMSO has delegated the supervision and management of this work to the Modeling and Simulation Executive Agents (MSEA). The Air and Space Natural Environment Modeling and Simulation Executive Agent[2] (ASNE MSEA) is concerned with the air and space environment, including anthropogenic effects, from "the troposphere, stratosphere, upper atmosphere, radiation belts, and interplanetary medium, to the surface of the sun." It is located at the Air Force Combat Climatology Center (AFCCC), Scott AFB, IL.

EMAC Characteristics

The ASNE MSEA decided to develop a catalog of models and algorithms related to the air and space natural environment known as the Environmental Models and Simulations Catalog / Air and Space (EMAC/A&S). The EMAC project captures key information on currently-existing environmental models and algorithms in a manner useful at two levels:

[1] http://www.dmso.mil

[2] http://thunder.safb.af.mil/msea

- general information helpful to interested users, and
- specific information for in-depth evaluation to support potential *re-use* by model developers.

EMAC is readily accessible on the WWW and easily used by all interested parties.

The current effort has met the needs of the ASNE MSEA through a three-part effort:

- acquisition of the model and algorithm information,
- analysis of the model and algorithm information, and
- database and web application development to make the information accessible to users.

Initially, ASNE MSEA envisioned EMAC as an integral part of Modeling and Simulation (M&S) Directories of DMSO's Modeling and Simulation Resource Repository (MSRR). Current plans, however, call for its direct integration into the Master Environmental Library (MEL)[3]. These integration efforts are still under development.

EMAC Development

The project is being conducted in three phases. The first phase was described in the proceedings of last year's Battlespace Atmospherics Conference (Núñez, *et al*, 1996). EMAC's Phase II was a continuation of Phase I efforts into 1998. Phase III is also planned and will continue development through 1998.

Phase I began in September 1996 and was completed in April 1997. Phase II, which is the subject of this paper, began in April 1997 and will be completed by February 27, 1998. Phase III will terminate the development efforts and support the transition to the maintenance phase. It will consist of maintaining the server, database, and web application. Duties will also require registering models and algorithms, . and populating of the database with additional resources.

EMAC Specifications

The primary objective of EMAC was to develop a catalog of models and algorithms describing the physical phenomenology of the atmospheric and space natural environmental. This catalog was designed with following specifications:

- include the key models and algorithms representing the physics of the air and space natural environment,
- provide sufficient detail to support in-depth evaluation of models and algorithms which will best apply to a given problem,
- have sufficient depth and utility to be acceptable within the air and space community,
- have a structure which is an integral part of M&S directories of the MSRR,
- integration with MEL,
- be readily accessible to users and developers on the WWW.

Phase I of this effort developed suitable criteria for model selection, provided a survey to elicit appropriate model information, and started the acquisition of information on candidate models. A preliminary version of the required database, known as the Database of Environmental Models and Simulations / Air and Space (DEMS/A&S), was also developed.

Phase II consisted of the extension of initial efforts to include additional models, and the development of a Web application based on a more mature data model. This data model was used within the Oracle data base to link the interrelationships between various aspects of the information about a given model or algorithm, as well as between various models and algorithms. The hardware and software to support the on-line Web application were installed, assembled, or built as necessary.

Structure and Organization of EMAC

The data supporting the EMAC application are stored in an Oracle Version 7.3.3 database. This database was developed by using the data model specifically designed to support EMAC. The data model is a physical and conceptual representation of the data needed to fully describe the resources in EMAC. The data model was designed and implemented in ERWiN

[3] http://www-mel.nrlmry.navy.mil

Version 2.6. This tool allowed the designer to capture all data requirements and the interrelationships between the data elements, permitting a full representation of the model, algorithm, and document resources. The data model also specified valid input data for certain data elements. Those validation rules were implemented in the physical representation of the Oracle database.

EMAC can be accessed on the World Wide Web via an Internet browser. The EMAC interface allows users to register new resources for inclusion into the EMAC system and to search the approved entries already cataloged. The interface for input of the new resources collects the data elements needed to fully describe the resource. Some data elements (such at the title of the resource, the submitter's name and the sponsoring organization) are required fields and must be input during the nomination process. The interface will not let a user continue the nomination until all required fields have been completed. The interface then processes the data elements entered, stores that information in the Oracle database in the correct format and location, and validates the data using the design specified by the data model. Following the nomination of a resource by an EMAC user, the resource information is reviewed and processed. If the resource satisfies the selection criteria, it is then approved and available in the system for viewing by approved users.

The information contained within the EMAC database is periodically reviewed and updated as needed to ensure it is accurate and current. Maintenance of the information is performed by the COLSA EMAC data analysts. They work with the resource owners to determine changes that must be made to the information. Database updates are made through a windows application that directly accesses the information in the Oracle database. This procedure provides a fast, convenient and easy method for data maintenance.

Searching Through EMAC

EMAC model and algorithm information is maintained on a dedicated server which houses the database and site home page[4]. While the primary purpose of the web site is to provide ready access to the catalog information, additional resource information, including links to other environmental resources on web, are also maintained on the home page.

Within the catalog itself, access to the model and algorithm information is provided through powerful browse and search capabilities. The application features the use of frames and left-side lists. One can elect to either view (*browse*) a list of all the models, algorithms, and documentation maintained in the database, or initiate a search through the catalog. In the *browse* mode, all the items in the catalog appear in a scrollable left side list. Selecting a resource in the list displays detailed information about it within the main application window. The displayed information appears as tabbed cards. Selecting a tab displays the pertinent model information. Selectable tabs include: model, version, point of contact (POC), key words, and related resources.

The *search* function includes the capability to search the catalog database through either specific keywords or text searches. The text search in the catalog can be within specific fields of the stored information, or in all fields.

Information Submission

There are two primary mechanisms by which resource information has been entered into EMAC. In the initial phases, the environmental modeling and simulation community was actively solicited for the specific information on their key models. This process entailed site visits to solicit resource owners to furnish information on their models. While some of this direct solicitation may continue, the primary mechanism for input will be through direct on-line submission by resource owners.

On first accessing the EMAC web application, a choice is offered to enter resource information. A set of forms appear where the submitter can enter resource-specific information, as well as submitter-specific contact information. The information is then reviewed for consistency by a Resource Coordinator. Afterwards, it is reviewed for acceptability by the EMAC Registrar. The Registrar is a government resource expert within the Executive Agent office. At present, all

[4] http://www.emac.colsa.com

resources are approved through the ASNE MSEA. If EMAC is expanded to include model and algorithm information within the areas of Oceans and Terrains, the associated Executive Agents will assign a registrar for the review and approval process in these domains.

Content of EMAC

A list of selection criteria were elaborated to accept models into EMAC. These were:

- frequency of use
- model acceptance within the air and space communities
- plans for model maintenance
- use during crisis or combat
- use for educational purposes and training
- availability of information on model

More information on these criteria is available in Núñez, *et al* (1996).

Algorithms present special problems for integration into a database like EMAC. All models are comprised of multiple algorithms of different levels of generality. More general algorithms are, in turn, composed of more elementary ones. Adding complexity to the problem is the fact that some models and simulations function as integrators of other fully-capable models. What is the appropriate or ideal level of generality for inclusion in the database? The answer to this difficult question is obviously subjective. EMAC will use as its working definition for algorithms the one appearing the Glossary of M&S Terms in DoD 5000.59-M, namely "A prescribed set of well defined and unambiguous rules or processes for the solution of a problem". Organizations responsible for model development and maintenance will each answer, to the best of their judgment, how many algorithms should be included and the level of detail desired.

Other criteria, resembling those used for models, can be elaborated to guide and support the decision.

- *Reusability* - Algorithms should be included only if they have the quality, stability and level of maturity necessary to be reused by other model developers.
- *Level of demand within air and space community* - Only algorithms supporting widely used techniques or processes should be included in EMAC.
- *Acceptance within the air and space community* - EMAC should only include algorithms on processes and techniques which have a high level of acceptance within the community of experts.
- *Relevance* - Only algorithms dealing with the most important phenomena or techniques in a model should be included in EMAC.
- *Information and documentation* - Sufficient information and documentation should be available to enable algorithm utilization by developers without an undue amount of labor or trouble.

Status and Future Plans

At present, EMAC is operational and available on the WWW through a server specifically dedicated to this task. The site address is http://www.emac.colsa.com. Any user will have the capability to search or browse. Data input or modification is strictly limited and controlled. Only users approved for supplying information will have the capability of making data input or modification. To have this privilege, users must undergo the registration, review and approval process described earlier in this paper.

Future expansion of EMAC will include the extension of its mission area from its current emphasis on Air and Space resources to the Oceans and Terrains natural elements. An obvious area for future efforts will be the compilation of additional information on existing models and algorithms and the expansion of EMAC to include other resources.

In addition, work is currently under way to integrate EMAC with MEL. In the future, the primary access to EMAC will occur from the MEL site. Thus, users and developers will have both vital model and algorithm information, as well as data, available from the MEL homepage.

Summary

EMAC has become a useful and easily accessible resource for information on environmentally-

related models and algorithms. To be successful, EMAC will require the active participation of developers and users of the key algorithmic and modeling resources currently in use in the environmental modeling and simulation community.

References

Núñez, Edwin, John Medeiros, Beverly Burns, and Gary McWilliams, 1996. *Proceedings of the 1996 Battlespace Atmospherics Conference 3-5 December 1996*, pp. 387-391. Technical Document 2938, Naval Command, Control and Ocean Surveillance Center, San Diego, CA.

The U.S. Navy
METOC Systems Program

Meteorology & Oceanography Systems
Program Office PMW 185

Steve Payne, SPAWARSYSCOM
Edward J. Harrison, Jr., CSC

Paynes@spawar.navy.mil
Harrisoe@spawar.navy.mil
Phone 619-524-7921
Fax 619-524-3034

Introduction

The Oceanographer of the Navy is responsible to the Chief of Naval Operations for managing the Navy's Meteorology and Oceanography (METOC) programs. Under the policy guidance and resource sponsorship of the Oceanographer, the METOC Systems Program Office (PMW 185) of the Space and Naval Warfare Systems Command (SPAWAR), oversees the development, acquisition and life cycle support of all METOC systems and associated applications software, and also serves as his METOC systems architect. The METOC systems under the purview of PMW 185 directly support the Commander, Naval METOC Command concept of operations. The system that will serve as the cornerstone of METOC support for the future is the Tactical Environmental Support System (Next Century) - TESS (NC). TESS (NC) will be a computer-based, interactive environmental data receiving, storing, processing and display system to be installed on major Navy ships and shore stations. TESS (NC) will dramatically upgrade and expand current capabilities and will be fully compliant with evolving Joint Command, Control, Communications and Computers and Intelligence architectures. The status of TESS (NC) as well as other systems being developed under the management of the METOC Systems Program Office will be described. In addition, software applications, which are being developed for atmospheric and oceanographic models, satellite data processing, and METOC decision aids to support the tactical commander at sea, will be discussed.

The PMW 185 METOC Program consists of the following systems:

- TESS (NC) - (NITES I through V)
- GEOSAT Follow-On
- Automated Surface Observing System
- USMC Meteorological Mobile Facility Replacement
- WSR-88D Next Generation Weather Radar (NEXRAD)
- Shipboard Meteorological and Oceanographic Observing System
- SMQ-11 Satellite Receiver-Recorder Upgrades
- Mini-Rawin System
- Supplemental Weather Radar
- METOC Air, Surface, Undersea Reporting Equipment (MEASURE)
- Software Development

TESS (NC) – NITES I

The TESS (NC) is a modular, interactive and computer-based METOC data processing and display system that collects, processes, analyzes, displays and disseminates oceanographic and meteorological data and products. It has been installed afloat on several major combatant ships such as aircraft carriers and ashore at oceanography centers and facilities such as Underwater Surveillance Warfare Operations Centers. Depending on the location, TESS (NC) interfaces digitally with a variety of Navy Command and Control, Communications and Computers, and Intelligence (C4I) systems via the Joint Maritime command Information System (JMCIS). In addition to the basic functions of producing METOC analysis and forecasting graphical and text products, TESS (NC) has a suite of software applications for generating products such as acoustic and electromagnetic propagation, tide data, SAR support predictions, and ship response. The TESS (NC) processes and displays the satellite imagery and provides satellite-tracking information. The METOC data and products provided by TESS (NC) are used to make assessments and predictions of environmental effects on Battle Group (BG), friendly, and enemy units, sensors, weapons, and communications systems.

On 29 October 1996, the Chief of Naval Operations (N096), Oceanographer of the Navy, issued a TESS (NC) Program Policy statement modifying the TESS (NC) program by calling for five Navy Integrated Tactical Environmental Support Systems (NITES) versions (I-V).

The Navy Integrated Tactical Environmental Subsystem has evolved from the TESS to take advantage of the latest industry-based Commercial-Off-the-Shelf (COTS) and Government-Off-the-Shelf (GOTS) technology in support of the warfighter in the twenty first century.

NITES I is our forecasting system for oceanography divisions afloat and major shore activities. The purpose of NITES I is to provide the METOC community (Users) with the tools necessary to support the warfighter (Customers). NITES I contains the hardware/software tools and databases of specific interest to environmental forecasters and provides data to widely distributed users via NITES II. NITES I replaces TESS (NC) and is scheduled for operation evaluation in September 1998. Follow On Test & Evaluation (FOT&E) is currently ongoing on the USS Wasp. SSC-SD Code D642 is In-Service Engineering Agent (ISEA) for TESS (NC) Transition and will be for NITES I. We have a rapid prototype build team and a production build team working in parallel to integrate COTS and GOTS as NITES I. OPEVAL will be completed on an East Coast CVN in October '98, with installs beginning as early as January 1999.

TESS (NC) – NITES II

NITES II, which used to be NITES, is a suite of software segments residing on a JMCIS or GCCS workstation providing customer access to the distributed METOC databases. It will include a wide range of UNIX segments including a METOC data broker, JMS, a cloud advection segment and elements of TDAs such as SIIP (SPPEDS ICAPS Integrated Product), EOTDA and MEDAL. These segments can be loaded on JMCIS and can access environmental databases as needed. NITES II contains highly visual tactical decision aids and tools of interest for both forecasters and non-forecasters to analyze the impact of weather and oceanography conditions on both weapons and systems.

TESS (NC) – NITES III

NITES III is the aviation support, MIDDS replacements system. It has simultaneous data ingest (satellite, radar, facsimile, alphanumeric, lightning, ASOS) with a Windows NT client server architecture and a User-friendly interface. It is the aviation forecast desk version and will be installed at about 60 METOC detachments at our Naval Air Stations. MIDDS 2.0 build in Beta Testing is scheduled for release in December 1998.

TESS (NC) - NITES IV

NITES IV is a portable version for Mobile environmental Teams, which will be replacing an interim system, Interim Mobile Oceanography Support system (IMOSS) via NAVO. It has a three-module configuration (Main, Comm and Sat) with live APT reception from polar orbiters and WEFAX geostationary satellites. It is LAN compatible and works in a Windows environment. Commercial utility programs include; Office 97, ProCom Plus, and others. It is packaged in ruggedized shipping containers. The upgrade to laptops began FY 96, with great reception and requests for more. PMW 185 procured 42 completed systems with SPAWAR FY 97 funds. These systems had the WxTrac software upgraded to NT version and added WEFAX capability for shore deployments in OCT 97.

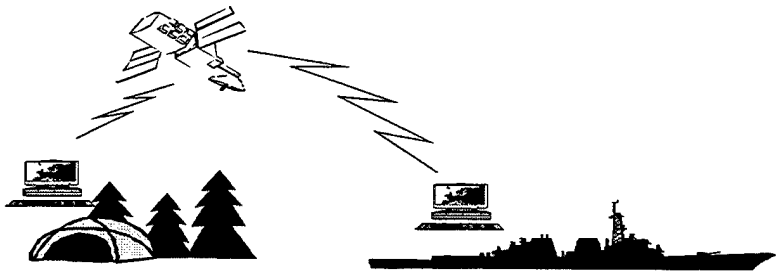

TESS (NC) - NITES V

NITES V is a Foreign Military sales version. It has currently been sold to Canada, Korea, Taiwan and multiple NATO sites. Some possible future sales are Argentina, Australia, Italy, Norway, Spain, and the United Kingdom. NITES V was used during Rapid Response/Dynamic Mix 97 and is scheduled for use in Rapid Response/Strong Resolve 98.

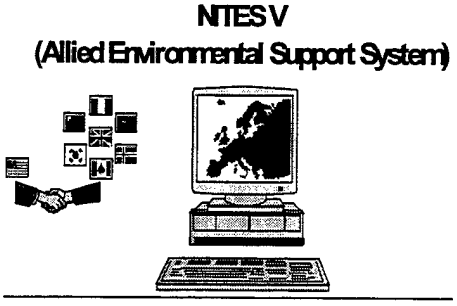

GEOSAT Follow-on

The GEOSAT Follow-on project is a near Polar-orbiting satellite used to measure ocean topography and other significant ocean features. It provides near real-time altimetry information support for ASW, AMW and Special Warfare areas until the year 2007 when NPOESS assumes this duty. The current launch date is scheduled for a 26 January 1998.

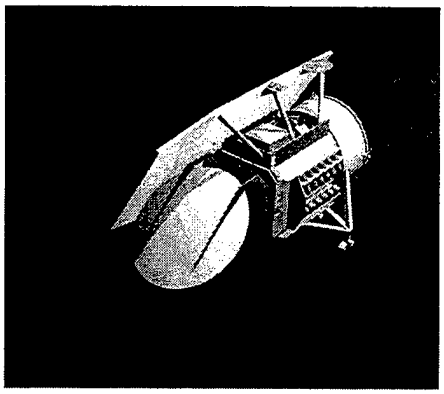

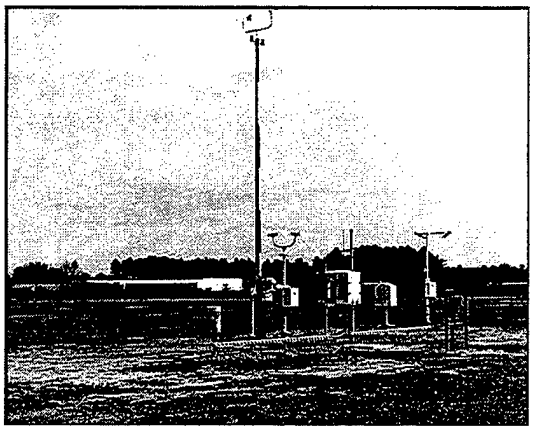

ASOS

Automated sensor suite, which measures, records and transmits METOC information. Installed at Naval and Marine Corps Air Stations. An interagency program under the lead of DoC.

METMF Replacement

(USMC Meteorological Satellite Program) A deployable system which provides full range of weather support to the Marine Corp. METMF (R) is a single van unit, which will replace the current four-van system. It has a central processing subsystem, which interfaces with MAGTF C4I and is enhanced with GOTS/COTS.

WSR-88D NEXRAD PUPs

The Next Generation Radar Principal User Processors is a wide area surveillance Doppler weather radar. The Navy is procuring Principal User Processors only as replacements for the aging FPS-106. It is installed at selected Naval and Marine Corps Air Stations.

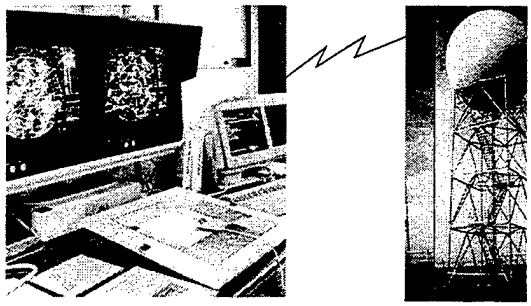

SMOOS/MORIAH

The Shipboard Meteorological & Observing Oceanographic System is a highly automated sensing system aboard major ships to provide METOC data to end users/customers. The follow-on program MORIAH is a collaborative effort with PMA-251's digital wind measurement system upgrade that is to be installed on most platforms. The COTS sensors that MORIAH is to measure include: Air Temperature, Humidity, Sea Surface Temperature, and Lower Atmospheric P/T/H Profiles, wind Direction and Speed and Barometric Pressure.

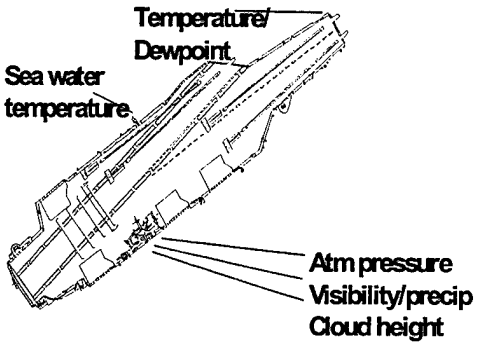

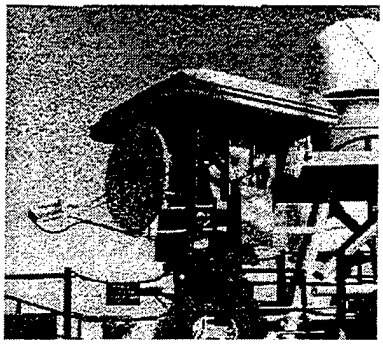

AN/SMQ-11

The AN/SMQ-11 environmental Satellite Receiver Recorder is a Next generation METOC satellite receiver-recorder. It receives remotely sensed data from DMSP, NOAA TIROS, GOES Wefax and GEOSAT Follow-on. It also is digitally interfaced to TESS.

Mini-Rawin System

With the addition of GPS capable sondes the Mini-Rawin system provides accurate wind profiles in addition to temperature, pressure and humidity. It is currently installed aboard 17 ships and 99% of the shore site installations are complete.

Supplemental Weather Radar (SWR)

The SWR is a lightweight Doppler radar system for sites outside NEXRAD coverage. It provides real-time surveillance and advanced warning of severe weather phenomena near or moving toward USN and USMC airfields and operation bases, including Meteorological Mobile Facilities.

Planned Installations

Naval Air Station Fallon, Nevada
Naval Base, Guantanamo Bay, Cuba
Naval Support Activity Naples, Italy
Naval Support Facility Diego Garcia
Marine Corps Air Station Iwakuni, Japan
Naval Station Rota, Spain
Naval Support Activity Souda Bay, Greece
Naval Air Station Sigonella, Italy
Fleet Activities Yokosuka, Japan
METMF Replacement

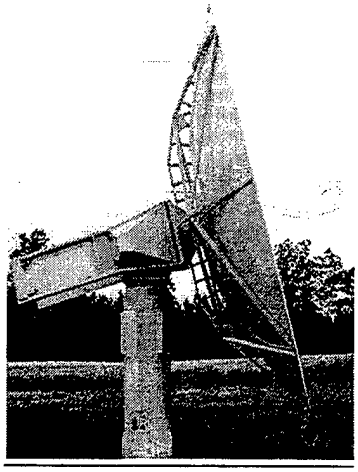

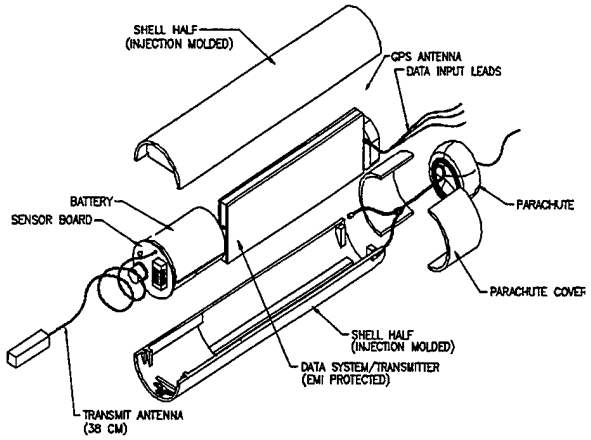

MEASURE

The METOC Air, Surface and Undersea Reporting Equipment (MEASURE) is a suite of expendable sensors, such as the tactical dropsonde, to measure pressure, temperature, humidity and wind profiles. It is deployable from standard DoD countermeasure dispensers ALE-39/40/47. It uses standard VHF communication links available on tactical aircraft and has been integrated into the Predator and Pioneer UAV platforms.

Research and Development Programs and Projects under PMW 185:

Program Element 0603207N - Air/Ocean Tactical Applications
- Project R0118 Ocean Measurement Sensors (newly acquired)
- Project X0513 Air/Ocean Prediction
- Project X0514 Air/Ocean Shipboard Measurement
- Project X0523 Air/Ocean Data Assimilation
- Project X0948 Precise Timing and Astrometry
- Project X1596 Satellite Ocean Tactical Applications
- Project R1987 Mapping Charting & Geodesy Techniques
- Project X2008 Tactical Ocean Data Assimilation and Prediction

Program Element 063785N - Combat Systems Oceano. Performance Assessment
- Project R0120 Advanced Environmental Acoustic Support
- Project R2017 Advanced U/Water Acoustic Modeling Project
- Project V0823 Sensor Performance Prediction

Program Element 0604218N - Air/Ocean Equipment Engineering
- Project X0532 Fleet Air/Ocean Equipment
- Project R1740 Air/Ocean Survey Engineering
- Project X1752 Tactical Environmental Support System

Program Element 0305160N - DMSP
- Project X1452 GEOSAT Follow-On (GFO)

THE ON-SCENE TACTICAL ATMOSPHERIC FORECAST CAPABILITY (STAFC)

John Cook, Jerome Schmidt, Rich Hodur, Pedro Tsai, Sue Chen, and Larry Phegley
Naval Research Laboratory
Marine Meteorology Division
7 Grace Hopper Ave.
Monterey, CA 93943-5502

1. Introduction

The Naval Research Laboratory (NRL), under the sponsorship of the Office of Naval Research (ONR 322 AM) and the Space and Naval Warfare Systems Command (SPAWAR PMW 185) with support from the Naval Meteorology and Oceanography Command (COMNAVMETOCCOM), is developing the On-Scene Tactical Atmospheric Forecast Capability (STAFC). STAFC is a fully functional automated portable data assimilation system. As a component of the strategy designed to meet the Oceanographer of the Navy's (N096) Rapid Environmental Assessment (REA) requirement (Whitman 1997), it will allow forward deployed forces to make use of the growing volume of perishable atmospheric data available on-scene. The core of STAFC is the atmospheric component of the nonhydrostatic NRL Coupled Ocean/Atmosphere Mesoscale Prediction System (COAMPS) (Hodur 1997). The STAFC graphical user interface built around COAMPS allows one to both easily tailor numerical weather nowcasts and forecasts for areas of tactical interest and to set up customized output data sets, for example surface wind forecasts every 30 min. By using STAFC as a "front end" to decision aid applications, this capability has the potential to help address several Command Technology Issues (CTI) such as Theater Missile Defense, Ship Self Defense, Improved EM/EO Sensor Prediction System, and Simulation/Stimulation Embedded in Exercises.

The current prototype STAFC system is composed of three UNIX workstations connected to either the classified (SIPRNET) or unclassified (NIPRNET) internet network. The network is used primarily to transfer fields from the Navy Operational Global Atmospheric Prediction System (NOGAPS), run at Fleet Numerical Meteorology and Oceanography Center (FNMOC), that provide lateral boundary conditions and initial background fields for COAMPS. STAFC can also automatically decode, store, and quality control observational data from both serial and network data feeds. The output data products from STAFC are designed to support operational interests, for example range-dependent refractivity, and can be transmitted by the system to any node on the network. In addition to COAMPS, the STAFC software suite consists of: a) the Tactical Environmental Data Subsystem (TEDS) relational data base; b) a user-friendly graphical user interface; and c) a world wide web-based product visualization program. An early analysis-only prototype of STAFC was field tested at the Naval Central Meteorology and Oceanography Facility, Bahrain during SHAREM 110a and at the Naval European Meteorology and Oceanography Center, Rota during SHAREM 117. The full data assimilation capability, including both on-scene analyses and forecasts, was successfully tested at sea on board the USS NIMITZ (CVN-68) during a transit down the U.S. west coast during June 1997. This paper describes the STAFC system, its operation, and the USS NIMITZ field test.

2. Description of STAFC

STAFC is a UNIX workstation-based automated portable data assimilation system that is built around the same COAMPS kernel that is installed operationally at FNMOC. STAFC includes three computer systems: 1) the COAMPS computational server, a multiprocessor workstation with the COAMPS software installed, including world-wide data bases of static parameters, such as 400 m resolution coastlines, 1 km resolution terrain height, 1 deg resolution albedo, land use, etc.; 2) the TEDS data base server, a workstation with the TEDS relational data base management system installed; and 3) a graphics console/workstation that provides the capability to extract gridded fields, satellite derived winds, and conventional observational data from TEDS, and visualize the data for evaluation and diagnostic purposes. In addition, this workstation hosts a web server which provides the graphical products over the network. This workstation also hosts the graphical user interface (GUI) for COAMPS that allows an operator to easily set up, modify, and automatically execute a forecast.

2.1 Core Capability

As shown schematically in Figure 1, the core capability of STAFC allows a site to independently ingest local observations, satellite-derived observations, and boundary conditions from a central or regional site and maintain an organic data assimilation capability including automated quality control (QC) software, a multivariate optimum interpolation (MVOI) analysis, and the COAMPS

nonhydrostatic forecast model. These components are controlled by the user through the GUI. Both the COAMPS model and the TEDS data base application programming interface (API) have the ability to calculate derived sensible weather parameters from the basic atmospheric state variables. STAFC provides these "hooks" in order to support the further processing of environmental data for visualization, decision making, and as input to other codes such as Meteorology and Oceanography (METOC) Decision Aids (MDA) and Tactical Decision Aids (TDA). The "bridge" between the environmental and tactical communities is provided by the Navy Integrated Tactical Environmental Subsystem (NITES) which has its interface through the TEDS data base. Thus, STAFC installations at a forward field location provides the ability to organically perform high resolution nonhydrostatic (less than 10 km) atmospheric analyses and forecasts (out to 24 - 48 hr) in support of decision aids and tactical models that require high fidelity, high resolution atmospheric data not currently available. Examples of the types of models that can be supported include electromagnetic and electro-optical (EM/EO) propagation models, and chemical, biological, and radioactive dispersion (CBRD) models.

2.2 Why STAFC?

Since COAMPS runs at FNMOC, a legitimate question is why does the Navy need a workstation version that can run at forward-deployed locations? There are three reasons that led us to develop STAFC: 1) to exploit local data sources that may not be available in a timely manner at FNMOC, including water vapor and infrared (IR) cloud-tracked winds derived from the geostationary satellites and, in the future, ship board radar weather observations; 2) the flexibility to quickly place a COAMPS domain anywhere it is needed, to tailor the output data products to exactly meet the user's requirements, to access results every model time step if appropriate, and to control dissemination of the products over the network; and 3) to produce a more timely product by automatically maintaining a physically consistent atmospheric data base based on a continuous hourly nowcast procedure and multiple 24 – 48 hr forecast runs per day. An additional benefit of having an easy to use data assimilation system available forward-deployed locations is the ability to use the system in research mode to study phenomena of local interest to forecasters.

2.3 COAMPS

The COAMPS kernel that STAFC workstation is built around is the same code that runs on the Cray supercomputers. COAMPS is written as a single source code for both vector and symmetric multiprocessing (SMP) computer architectures, and is maintained at NRL using the Concurrent Version System (CVS). COAMPS is a state-of-the-art atmospheric mesoscale data assimilation system that utilizes a unique nested nonhydrostatic atmospheric model and sophisticated precipitation microphysics which are appropriate for numerical predictions using horizontal grid spacing of less than 10 km. COAMPS is currently comprised of modules for atmospheric data quality control; analysis of wind, temperature, mass, and moisture; initialization; and the nonhydrostatic forecast model. COAMPS allows for the explicit prediction of water vapor, cloud droplets, ice crystals, raindrops, snowflakes, and subgrid-scale mixing, and it includes a cloud-interactive radiation parameterization (Hodur 1997). COAMPS is very well suited to perform in littoral regions where there is a significant mesoscale forcing from the surface. Surface irregularities such as topography and coastlines can force circulations in COAMPS even though they may not be well represented in the initial data.

2.4 TEDS Data Base

TEDS is currently built around the commercial Informix relational data base product. TEDS decodes and stores both the large-scale gridded fields received over the network that COAMPS uses for lateral boundary conditions and analysis background, and observations, including satellite derived winds, from local serial and network connections. TEDS provides interfaces for data acquisition and APIs for application programs while storing, managing, and making COAMPS results available to other applications over a network interface using a stand-alone data dissemination program.

2.5 Operating Procedure Time Line

STAFC has progressed from a local atmospheric analysis system to a fully integrated data assimilation system that typically makes two 36 hr forecasts a day, at operator selected times, and automatically maintains an hourly updated nowcast based on the most recent forecast fields. The methodology chosen for the forecast procedure is similar to the early Mediterranean regional model run at FNMOC. As shown in the top half of Figure 2, the Mediterranean regional model at FNMOC begins with a data cutoff about 2.5 hr after the synoptic time (00 UTC or 12 UTC) and uses lateral boundary conditions from the NOGAPS global fields produced from the previous synoptic time (-12 hr). In other words, instead of waiting for NOGAPS to complete (at about +5 hr) before running the regional model, the Mediterranean regional model uses the global forecasts generated at

the previous analysis time for the lateral boundary conditions. As the models run at FNMOC, data products are created and distributed over the network. This procedure is repeated twice a day at the 00 UTC and 12 UTC synoptic times.

The bottom portion of Figure 2 contrasts the local STAFC procedure for running the COAMPS forecast model. TEDS receives the gridded global forecast fields used by COAMPS for the lateral boundary conditions transmitted from FNMOC. Typically, we also wait about 2.5 hr after the initial time for the data cutoff (for the observational data to be processed and transmitted), however, we are not constrained to this delay nor to running only at a synoptic time. If desired, a STAFC user can initiate an analysis or forecast at any time through the simple GUI. Although most of the synoptic upper air data is only available shortly after the synoptic times, there may be instances where a user needs a forecast immediately for a tactical purpose or in support of a local data collection exercise and feels that the trade-off between forecast accuracy and waiting for more initial data is worth the risk. STAFC can also use satellite-derived wind data that is available hourly about 45 min late. This satellite data can be provided locally by the enhanced Navy Satellite Display System – Enhanced geostationary (NSDS-E), or over the network by a remote NSDS-E with access to the appropriate data sets. In the future, we envision upgrades to the capability of STAFC to utilize other unique sources of local data, such as those developed for the Navy MEASURE program which consists of many off-board sensors (tactical dropsondes, buoys, Unmanned Aerial Vehicle (UAV) environmental package, etc.), and ship board meteorological radar observations from the SPY-1 system.

On the current generation of multiprocessing UNIX workstation (STAFC currently uses a Silicon Graphics Inc. (SGI) four-processor Origin 2000 Deskside model), COAMPS takes approximately 3 hr for a 36 hr forecast to complete for a triple nest, 43 X 40 - 81 km, 61 X 61 - 27 km, 52 X 52 - 9 km grid, with 30 vertical levels, running with full physics enabled. Thus, the first 3 hr of the forecast cycle are used by COAMPS as it executes. Because the workstation has multiple processors, while the forecast is being produced the nowcast is continuously run every hour, using the newly produced forecast fields as background conditions and updating them with more recent observations and satellite-derived winds (Fig. 2).

The output data product from STAFC is typically a series of hourly "nowcasts" or analyses of current conditions and a 36 hr forecast product. Intermediate forecast products are also available at operator selected intervals as they are computed, for example the 12 hr forecast is available after 1 hr of computation time. Since the TEDS data base manages both the input and output data, all the products are available for dissemination over the network as data or graphical products, to both local users and tactical customers. As the nowcast and forecast products are created, the visualization scripts run to create the graphical output products. These graphics are then automatically placed on web pages where they can be viewed directly by the operator and served over the network to remote customers.

The forecast process is set up once using the GUI and placed on the computer clock for automatic execution. No operator intervention is required unless the domain or output needs to be changed. After a "cold start" using the global NOGAPS fields as background conditions for the initial analysis, COAMPS uses its own forecasts for background fields during subsequent analyses and forecast initialization. Global forecast fields from FNMOC are still required for updating the lateral boundary conditions during the COAMPS forecast period. Typically, the NOGAPS forecast fields from the 12 – 48 hr forecast period are distributed to STAFC to support the COAMPS 36 hr forecasts, however, the ending time of the NOGAPS forecasts transmitted may be increased if longer COAMPS forecasts are desired out in the field. The trade-off is that the larger global data set takes longer to transmit and has a larger impact on the wide area network throughput. To minimize the network impact, NRL has developed and demonstrated a technique to subset the global fields before transmission, decreasing the amount of data transmitted over the network by about a factor of 17 (6 MB versus 100 MB) for reasonable size areas (half ocean basin). A preprocessing step is then required by STAFC in order to utilize the subset fields instead of the global fields. The dimensions of the subset area are picked up by the GUI and displayed to the operator who is not allowed to place a COAMPS grid outside of the subset area.

STAFC can be operated and maintained by operational personnel with a reasonable amount of on-site training. The computer systems are high-end but "vanilla" UNIX workstations and can be maintained with support and training procured from standard government contracts. Much of this type of computer hardware already resides in the Fleet. Operators can be trained to use the GUI, COAMPS, visualization tools, and web interface as part of their collateral duties (a full time operator is not required).

NRL is currently developing a remote monitoring capability for STAFC so installed systems can be monitored via the classified or unclassified internet from a central location. This remote monitoring capability will allow support personnel to determine the status and help debug data, system, and model problems on installed systems, as well as providing a centralized graphical display for the nowcast and forecast products. Software and non-routine data base maintenance may also be performed by support personnel either on site or via the network.

3. STAFC Field Tests

The STAFC prototype atmospheric analysis capability has been field tested during two Ship Antisubmarine Warfare Readiness/Effectiveness Measuring exercises (SHAREM 110 and 117), and tested at the Battle Management Interoperability Center (BMIC) at the Naval Air Warfare Center Weapons Division (NAWCWPNS), Pt. Mugu. The complete data assimilation capability has been run for multiple areas at NRL nearly continuously since December 1995. COAMPS has also been ported to Sun and Digital Equipment Corp. (DEC) workstations and recently, TEDS and COAMPS have been ported to the Hewlett-Packard (HP) TAC-4 workstation.

3.1 USS NIMITZ At-Sea Test

During the 18 - 22 June 1997 underway period on board the USS NIMITZ, NRL, FNMOC, and NAWCWPNS teamed to complete the processing of the world's first three-dimensional numerical weather predictions at sea. The R&D effort was sponsored by ONR 322 AM and SPAWAR PMW 185, and supported by COMNAVMETOCCOM. The STAFC hardware and software suite, consisting of two networked HP TAC-4 computers and software, was installed by NRL on the USS NIMITZ prior to getting underway and tested during the transit south along the U.S. west coast (Fig 3). Two NRL researchers, assisted by a USNR METOC Officer, generated six 36 hr high resolution weather forecasts for four different forecast areas coordinated with the ship's projected and intended movement report.

As shown schematically in Figure 4, NOGAPS global grid fields were transmitted in GRIB format via SIPRNET from FNMOC to an unmanned Tactical Environmental Support System (TESS) database hub located at the NAWCWPNS Battle Management Interoperability Center (BMIC), which was simulating a regional center. Twice daily, subset areas of the global fields, which included a large portion of the eastern north Pacific, were automatically extracted from the simulated regional center database and transferred, again in GRIB format via SIPRNET, to the USS NIMITZ. Surface and upper-air observational data for the same area were also collected at the simulated regional center in BMIC and transmitted to the USS NIMITZ in BUFR format. During the test phase, SIPRNET communications connectivity was sporadic in port and for the first 48 hr at sea, and required operator intervention to ensure data transfers. Later, communications reliability improved, but interruptions still occurred during maneuvers.

In cooperation with the USS NIMITZ OA Division, several geometries for a COAMPS double nest forecast grid (45 km and 15 km horizontal resolution, 25 vertical levels) were developed for the ship's area of operation (see Figure 5). COAMPS was configured to run automatically in the data assimilation mode, using the previous forecast as the background condition for the second and each subsequent forecast in a series. As previously mentioned, whenever the grid geometry is changed or the grid moved, a cold start from NOGAPS background conditions is required to initiate the data assimilation cycle. COAMPS forecasts were produced out to 36 hr for both nests during each 12 hr cycle. Products were provided to the USS NIMITZ OA Division for forecast support and were also automatically updated on the web home page at NAWCWPNS BMIC. Limited verification at-sea showed good skill with detailed surface wind forecasts, particularly with eddies in the SOCAL bight; up to 2 mb differences were noted comparing sea level pressure forecasts to ship observations.

Each 36 hr forecast made on the single PA-7200 processor of the HP TAC-4 model J210 required 12 hr of computer time to complete. We have already demonstrated an improvement by a factor of four (to 3 hr) for a much more computationally demanding triple nest grid on the four-processor SGI Origin 2000. We expect that processing time lines will continue to improve with better computer hardware, improved software to take better advantage of multiple processors, and faster, more reliable communications.

4. Summary

NRL is developing a fully functional automated portable data assimilation system for forward deployed forces called STAFC. Designed to meet the requirements for Rapid Environmental Assessment (REA) levied by N096, STAFC allows forward deployed forces to make use of the growing volume of perishable atmospheric data available on-scene. Although the core of STAFC is the nonhydrostatic

NRL COAMPS atmospheric model, STAFC includes the TEDS relational data base, automated QC, the MVOI analysis, a GUI, and a web-based product visualization program. STAFC has been successfully field tested during two SHAREM exercises, at the NAWCWPNS BMIC facility, and on board the USS NIMITZ. The next step for the STAFC program will be trial installations at Navy METOC Regional Centers and development of the concept of operations.

Acknowledgements. The support of the sponsors, the Office of Naval Research (322 AM) through program PE-0602435N, and the Space and Naval Warfare Systems Command (PMW 185) through program PE-0603207N, and the support of the Naval Meteorology and Oceanography Command (COMNAVMETOCCOM) and the Oceanographer of the Navy (N096), is gratefully acknowledged.

References

Hodur, R.M., 1997: The Naval Research Laboratory's Coupled Ocean/Atmosphere Mesoscale Prediction System (COAMPS). *Mon. Wea. Rev.*, **125**, 1414-1430.

Whitman, E.C., 1997: EM/EO performance prediction in the Navy's METOC CONOPS. Proc., *Electromagnetic/Electro-Optics Prediction Requirements and Products Symposium*, Monterey, CA, E-L.

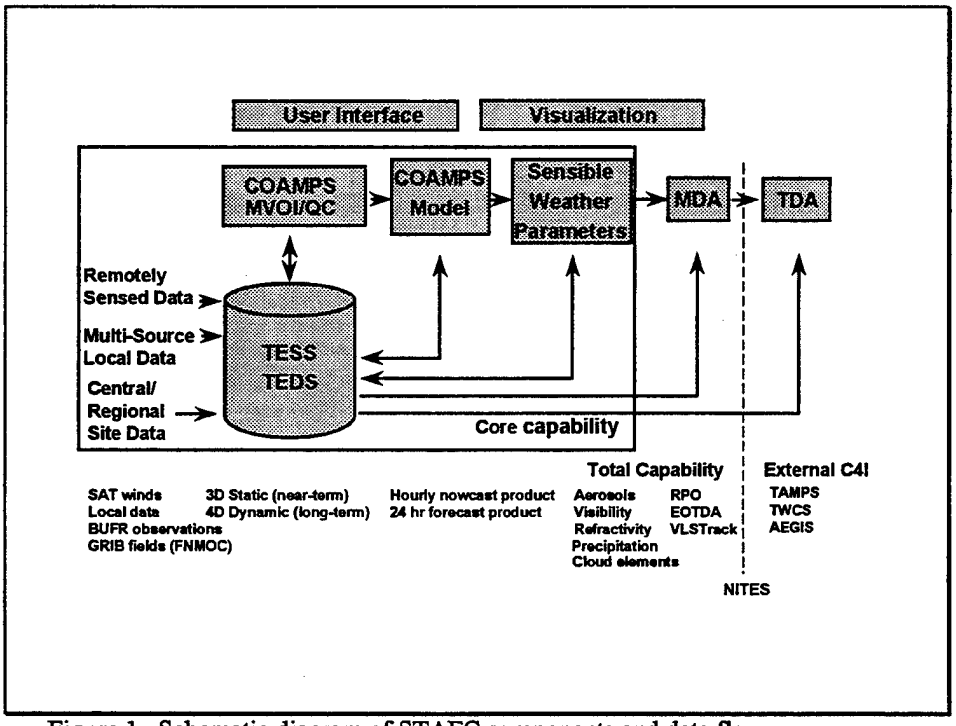

Figure 1. Schematic diagram of STAFC components and data flow.

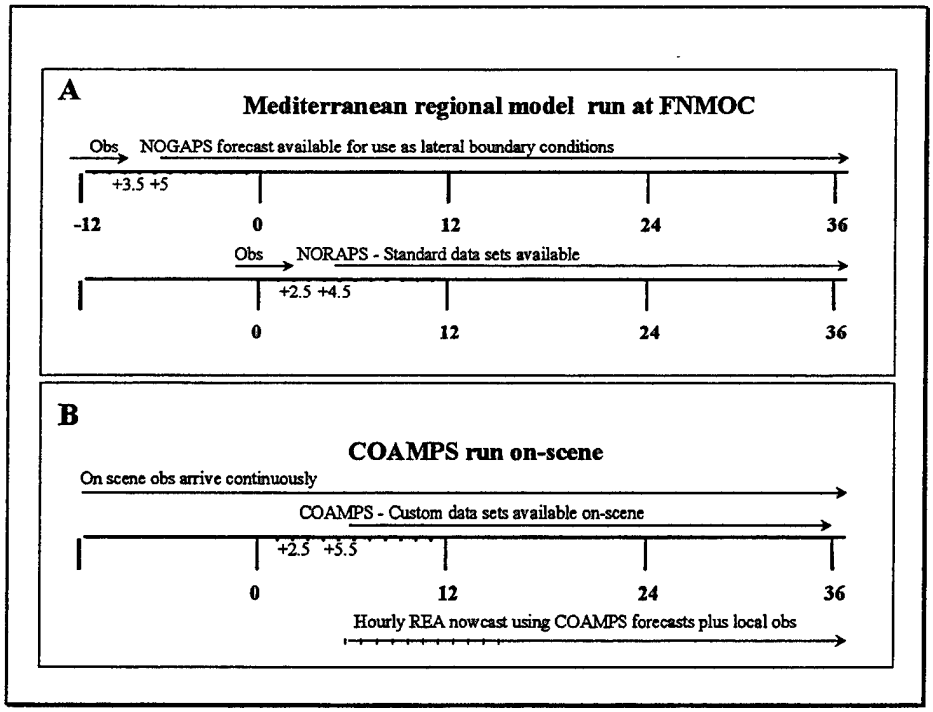

Figure 2. Example STAFC timeline for forecasts and nowcasts. a) FNMOC early Mediterranean regional model run. b) On-scene COAMPS model runs.

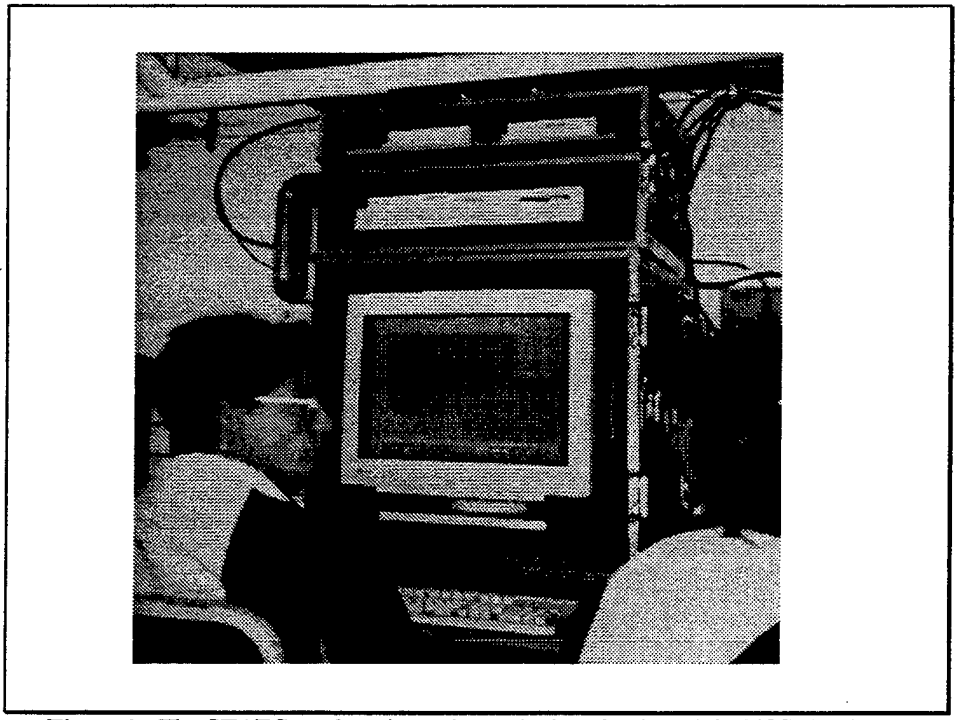

Figure 3. The STAFC workstation suite as deployed onboard the USS NIMITZ. Research personnel Mr. Mike Frost (left) and Ms. Linda Frost (right).

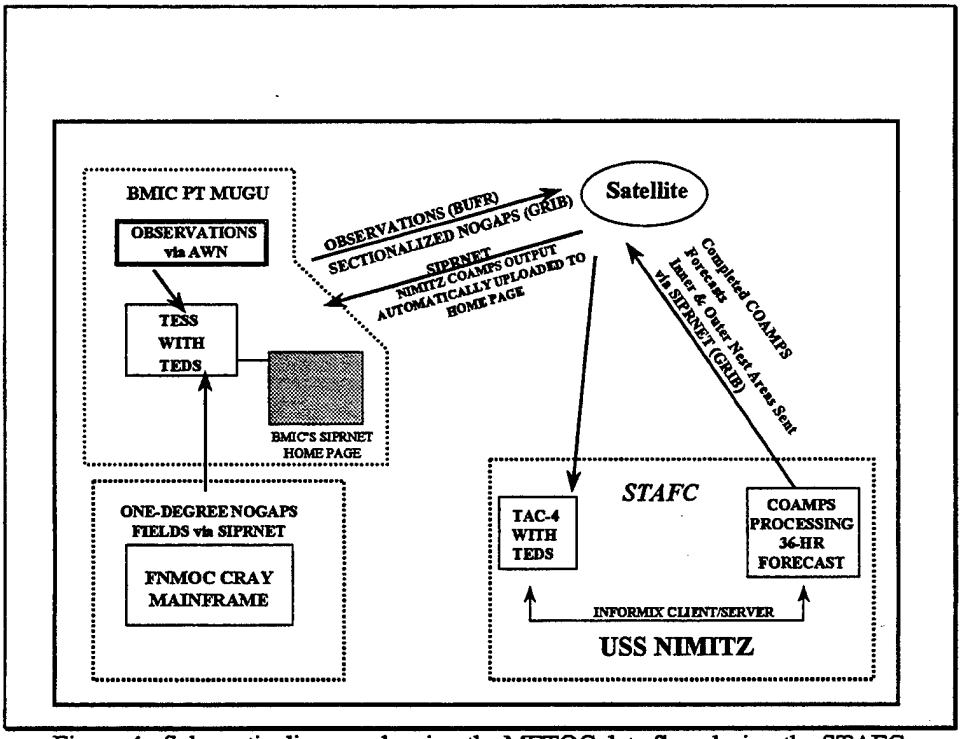

Figure 4. Schematic diagram showing the METOC data flow during the STAFC experiment onboard the USS NIMITZ.

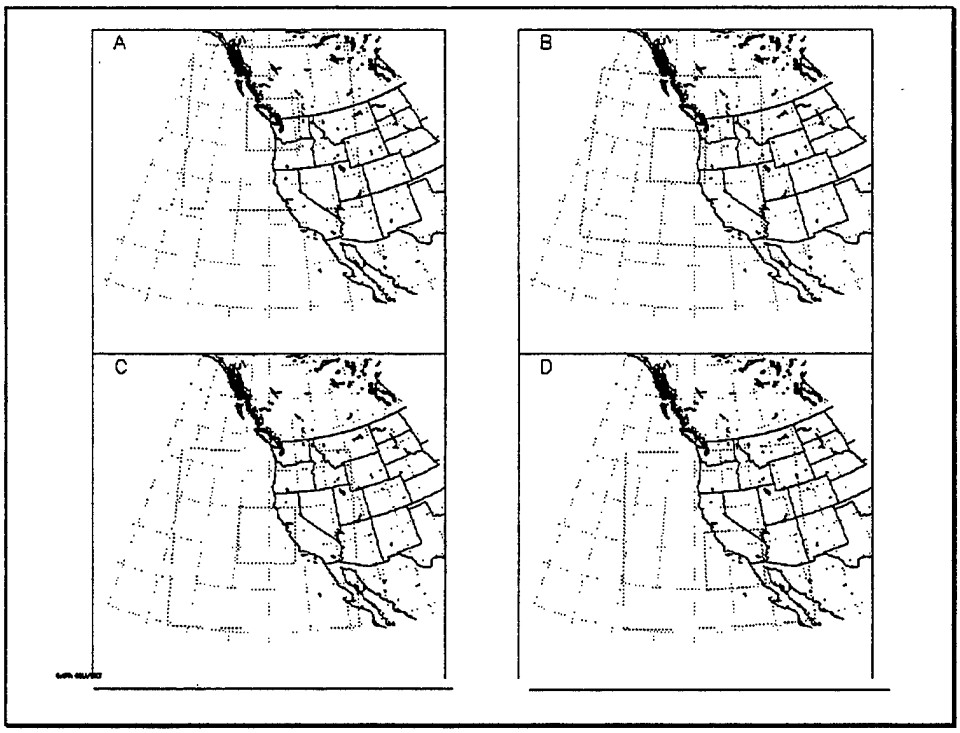

Figure 5. Map boundaries showing the COAMPS double nest forecast areas during the USS NIMITZ transit. The outer nest represents a 55 X 55 grid with 45 km spacing and the inner nest represents a 52 X 52 grid with 15 km spacing. a) Seattle area - two 36 hr forecasts; b) Oregon area - one 36 hr forecast; c) San Francisco area - one 36 hr forecast; and d) San Diego area - two 36 hr forecasts. Note the capability of COAMPS to offset the inner computational nest from the center of the outer, coarse grid.

COASTAL ATMOSPHERIC BOUNDARY LAYER FLOWS

Stephen D. Burk and Tracy Haack
Naval Research Laboratory
Marine Meteorology Division
Monterey, CA 93943-5502
Ph: 408-656-4797 Fax: 408-656-4769
E-mail: burk@nrlmry.navy.mil

Abstract

The nested, nonhydrostatic NRL COAMPS mesoscale model is used to investigate marine boundary layer (MBL) structure in complex coastal regimes. The observed scales of MBL variability within the coastal zone place strong demands for high mesoscale model resolution. Presented here are two detailed studies of coastal MBL dynamics. The first involves a basic research investigation of unusual wave clouds that occasionally are observed along coastal California. The second study uses the VOCAR data set to evaluate the fidelity of COAMPS refractivity forecasts. Anomalous refractive effects tend to be most pronounced in boundary layer controlled flows, rather than in large-scale, synoptically active conditions. Thus, the model's physical parameterizations, particularly its boundary layer package, is of paramount importance.

1. Introduction

Hodur (1997) describes the Naval Research Laboratory's Coupled Ocean/Atmosphere Mesoscale Prediction System (COAMPS). In this paper use is made of the atmospheric portion of COAMPS. We present several separate studies designed to show the power and utility of COAMPS in producing very high resolution mesoscale forecasts for time scales on the order of a day and domains spanning several hundred kilometers on a side. First we use COAMPS in a basic research investigation of enigmatic wave cloud formations occasionally observed along the California coast. Then we study the ability of COAMPS to produce high fidelity microwave refractivity forecasts.

COAMPS is a complete mesoscale numerical weather prediction system, using a terrain-following sigma coordinate, having a full suite of physical parameterization packages and an intermittent data assimilation procedure. COAMPS may be run either as a single grid model, or with a set of nested grids. In the nested grid configuration, each smaller grid has a factor of three better resolution than does its immediate predecessor.

2. Coastal wave clouds

An unusual set of wave clouds occurs infrequently along the California coast, primarily during summer months. These wave clouds, generally most prominent just to the west of the Monterey peninsula, typically appear near midday and are absent by the next morning. They give a rather stationary appearance in GOES 9 satellite imagery

because their general form does not change appreciably over several hours; however, this aspect may need more careful examination. They are not typical boundary layer roll vortices as they are aligned more nearly perpendicular than parallel to the prevailing upstream wind. Further, they are not lee waves as they occur upstream of the orography of the Monterey peninsula. Figure 1 shows a GOES-9 image of these wave clouds off of the Monterey/ Big Sur coastline at 2324 UTC June 23, 1996. The wave clouds first occur off of Monterey around 2100 UTC. We use COAMPS to forecast the mesoscale structure and dynamics in the MBL on this day.

A twelve-hour COAMPS forecast was conducted using 5 nested grids having grid spacings of 81, 27, 9, 3, and 1 km. There are 30 vertical levels, compressed so as to give high MBL resolution. The model forecast is initialized at 1200 UTC 23 June 96 using fields from the Navy's global model. Throughout the period of the forecast the wind is from the NNW. The MBL offshore and upwind of Monterey is very shallow (~100 m) and capped by a strong inversion. Early in the forecast period there is nothing unusual in the forecast fields; the flow impacts the Monterey peninsula, is blocked, splits into a branch moving southward along the coast and another branch which enters the Salinas valley. Near 2100 UTC (1400 LT), however, the COAMPS forecast MBL winds strengthen and a remarkable feature appears in the boundary layer wind field off of the coast. Figure 2 shows the 10-m forecast wind field from the innermost mesh ($\Delta X = 1$ km) at 2200 UTC (every third vector is plotted for clarity). The flow approaching the coast undergoes an abrupt directional and speed change along an arc extending either side of the Monterey peninsula. This flow structure resembles a detached bow shock wave that forms ahead of a blunt object within supersonic flow. The analog to supersonic flow in this situation is supercritical flow, in which the MBL wind speed, U, exceeds the phase speed of internal gravity waves, C. Here $C = (g' h)^{1/2}$, where g' is the reduced gravity and h the MBL depth. A Froude number, $F_r = U/C$, equal to 1 is indicative of the transition point between subcritical flow and supercritical flow, and is analogous to the Mach number in supersonic flow. The shock-like feature in Fig.2 actually is a manifestation of a hydraulic jump. The blocking of the Monterey peninsula forces the approaching, high Froude number MBL flow to decelerate such that F_r decreases to less than 1. (This actually is an *oblique* hydraulic jump and, therefore, the important wind speed entering the computation of F_r is the flow component *normal* to the jump, rather than total wind speed.)

The Froude number computed from COAMPS at 2200 UTC is displayed in Fig. 3. Along an arc extending either side of the peninsula, the Froude number drops abruptly to less than 1. Vertical cross sections of potential temperature and wind speed (not shown) taken normal to the shock show an abrupt increase in MBL depth and decrease in wind speed that is indicative of a hydraulic jump. Such hydraulic jump features have been observed previously in transcritical MBL flow (e.g., the CODE experiment; Winant *et al.*, 1988). Although COAMPS has resolved the oblique hydraulic jump feature that apparently is associated with the wave clouds, as yet, the wave clouds themselves do not appear in the model solution. The observed spacing between cloud lines is 2-3 km; our 1 km mesh is inadequate to resolve such a feature. Figure 4 shows a schematic depiction of

our hypothesized relationship between the hydraulic jump and the wave clouds. Downwind of the leading edge of the hydraulic jump, we postulate the presence of an undulations in the MBL top, such as occur with an undular bore, that are cloud-topped at their crests. The undulations (shown in cross section A-B) may be generated locally by shear instability. However, it also is possible that waves from upstream propagate into the shock front zone and are amplified.

Support for this speculation concerning the nature of the wave clouds is provided by data collected during the Coastal Observation and Simulation with Topography (COAST) experiment conducted along the U.S. West Coast during the summer of 1996. The NCAR EC130Q aircraft was flown during this field experiment (P.I.: Dave Rogers, Scripps). The aircraft carried a full complement of meteorological measuring systems: lidar, radiometric, turbulence, aerosol, and other standard probes. On 23 and 24 June 1996, the day of our wave cloud study, this aircraft made extensive measurements off of the central California coast. In particular, several flight legs were flown along the track indicated by line C-D in Fig.2. These flight legs covered the time period from 0047 to 0138 UTC on 24 June 1996, and they cross several of the wave clouds. Further, the southern end of this flight track covers the supercritical expansion fan region in the flow rounding Pt. Sur. Much of the data from the COAST aircraft flights, as well as satellite images, may be found on the Scripps webpage at http://penarth.ucsd.edu/. For example, run 24 reproduces the lidar results along flight track C-D and covers a ten minute flight period that corresponds to ~60 km in distance. The MBL is very shallow in the first ~25 km of this track and then abruptly deepens in the region where the MBL waves are encountered. Three prominent waves, about 400 m deep, appear to be cloud topped. The MBL upstream of the wave clouds is quite shallow. The spacing between waves is estimated to be about 4 km from these lidar observations. The satellite images near this time show, in agreement with the lidar, that the cloud wavelength has broadened from its earlier 2-3 km value.

Thus, COAMPS apparently has done a remarkable job of forecasting the features and associated dynamics of the wave cloud environment. Forecasts on the innermost mesh ($\Delta X = 1$ km) reveal the presence of a hydraulic jump feature at the leading edge of the wave cloud field. This grid, however, does not resolve the wave clouds. As of this writing, we have added a 6th grid ($\Delta X = 1/3$ km) in an effort to forecast the MBL undulations themselves; results are yet to be analyzed.

3. Forecasting refractivity during VOCAR

We turn now to a separate use of COAMPS in the study of mesoscale coastal meteorology. An intensive field program, termed the Variability of Coastal Atmospheric Refractivity (VOCAR) experiment, was conducted in the Southern California Bight during the period 23 August to 3 September 1993. Special high-resolution radiosondes were launched every four hours (except local midnight) at eight sites in this region. There also were three profiler sites, aircraft flights, a research ship, numerous surface stations, and two radio transmitter-receiver links. Figure 6 (from Paulus, 1995) shows the location of

the radiosonde sites and the transmission links from San Clemente Island to Pt. Mugu and to San Diego. The broad goal of VOCAR was to observe the mesoscale variability of the microwave refractivity field in a coastal environment, while collecting transmission data along several lengthy over water paths. These dense observations in a mesoscale coastal environment provide an excellent data set for mesoscale model evaluation. Here we discuss COAMPS refractivity forecasts during VOCAR, using the special data set for model validation. Further description of the VOCAR experiment itself appears in Paulus, 1995.

While we could have used the special VOCAR data set as part of the COAMPS data assimilation cycle, our goal is not simply to produce the best COAMPS forecasts possible. We recognize that such special data generally will be unavailable for operational forecasting. Our goal, instead, is to determine how the current COAMPS model can be expected to *routinely* perform when forecasting coastal refractivity conditions. Thus, we use the special VOCAR data for model validation only. In a similar vein, for time-dependent outer boundary conditions we use fields formed from a sequence of global model *forecast* fields. Since this model integration is conducted long after the fact, we could instead use a sequence of global model *analysis* fields to provide the time-dependent boundary conditions. This would eliminate some of the boundary errors due to inaccurate global model forecasts. However, this could not be done operationally, and clearly would tend to yield an overly optimistic assessment of COAMPS operational forecast skill. Finally, we do not nudge COAMPS results towards analyzed conditions because such a procedure is not feasible operationally -- the analyzed state being known only after the fact.

Burk and Thompson (1997; hereafter, BT97) presented an evaluation of refractive conditions during VOCAR using the Naval Operational Regional Operational Prediction System (NORAPS) with 20 km grid spacing. Our intention here is to extend that study to higher horizontal resolution and to the new COAMPS model. BT97 compares NORAPS forecast modified refractivity (M) profiles with M-profiles computed from verifying radiosondes at each of the special VOCAR observational sites. They note the impact of several specific mesoscale and synoptic events (e.g., sea/land breeze; a migrating low) upon the character of the refractivity field within the Southern California Bight. BT97 find that NORAPS is capable of providing reasonable forecasts of the *general trends* to be expected in the refractivity field (e.g., will a given duct strengthen in the next 24 h? will it deepen? change from surface-based to elevated? etc.). However, much less skill is evidenced when attempting to provide *quantitative* forecasts of propagation loss along specific propagation paths. BT97 also noted several other shortcomings of the NORAPS forecasts during VOCAR. They found a bias towards underforecasting marine boundary layer depth. And, during the middle portion of VOCAR, NORAPS did not properly represent moisture advection aloft associated with the breakdown of a tropical system south of the Baja peninsula. This negatively impacted NORAPS forecasts of refractivity during that time period.

For this study, COAMPS was run in a triply nested format, the nested meshes having grid spacings of 63, 21, and 7 km and 30 vertical levels with a highly resolved MBL. A data assimilation cycle, beginning 0000 UTC 23 Aug 1993 was run throughout the VOCAR period. This cycle consists of a sequence of 24-hour forecasts, each of which is initialized from data assimilation using a 12h forecast first guess field. As of this writing, our results are only very preliminary and much analysis remains to be done. Early results, however, indicate some significant areas of improvement as compared with the NORAPS forecasts presented in BT97. First, COAMPS seems to contain a significantly smaller bias in its boundary layer depth forecasts. Greater vertical resolution may account for part of this improvement. Secondly, COAMPS does a much better job of capturing the advection of a moist layer above the boundary layer that occurs during the mid-period of VOCAR. Improvements to the global model (NOGAPS) since the time of the BT97 forecasts, and hence better time-dependent boundary conditions, may contribute to these better COAMPS results.

Here, due to space limitations, we present only a very small sample of the model and observational results. Figure 5 displays NORAPS refractivity forecasts at San Nicolas Island taken from the BT97 study. Four separate 24h refractivity forecasts --spaced 12h apart -- are shown in Fig.5, along with the verifying refractivity profiles computed from the San Nicolas Island radiosondes. NORAPS successfully forecasts the existence of an elevated-trapping region in each of these four forecasts. However, the improper representation of moisture advection above the marine layer during this time period clearly results in a poor representation of refractive structure above the boundary layer. Figure 6 shows our new COAMPS results at San Nicolas Island during this same time period. COAMPS has not only correctly forecast the existence of the elevated trapping layer throughout this period, but done a remarkably accurate job of depicting the strength and structural features of the trapping layer. It correctly captures the temporal trends evident, as the duct lowers and strengthens. Furthermore, the greatly improved representation of moisture advection above the MBL yields excellent agreement with the refractivity field aloft.

Acknowledgments. This work was supported by the Office of Naval research, Program Element 0601153N.

References

Burk, S.D., and W.T. Thompson, 1997: Mesoscale modeling of summertime refractive conditions in the Southern California Bight. *J. Appl. Meteor.*, **36**, 22-31.

Hodur, R.M., 1997: The Naval Research Laboratory's coupled ocean/atmosphere mesoscale prediction system (COAMPS), *Mon. Wea. Rev.*, **125**, 1414-1430.

Paulus, R.A., 1995: An overview of an intensive observation period on variability of coastal atmospheric refractivity. *AGARD/NATO Conf. On Propagation Assessment in Coastal Environments,* Bremerhaven, Germany, NATO, 30:1-6.

Winant, C.D., C.E. Dorman, C.A. Friehe, and R.C. Beardsley, 1988: The marine layer off Northern California: an example of supercritical channel flow, *J. Atmos. Sci.*, **45**,3588-3605.

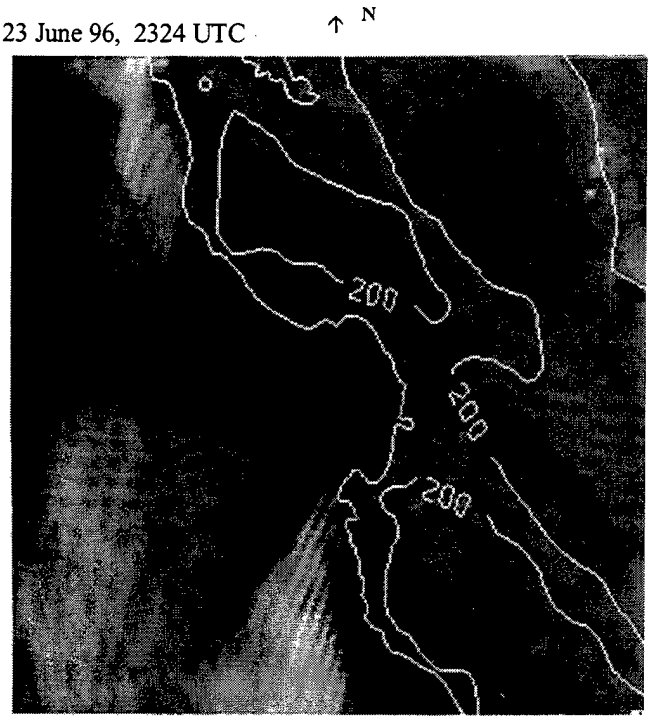

Fig.1 GOES visible image
2324 UTC 23 June 96

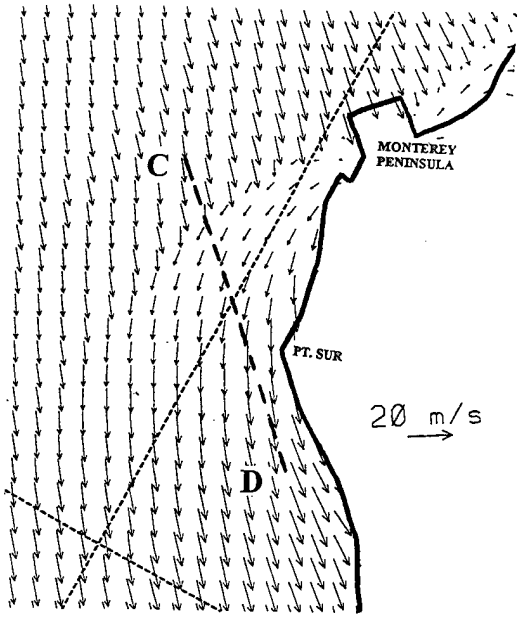

Fig.2 10-m wind (m/s)
at 2200 UTC 23 June 96

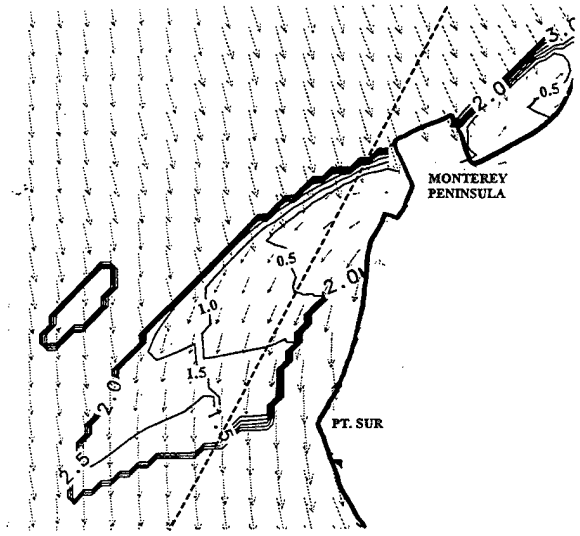

Fig. 3 Froude number
at 2200 UTC 23 June 96

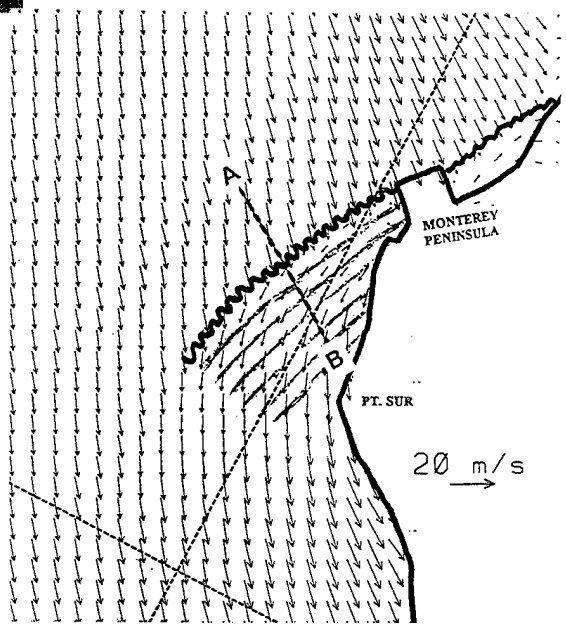

$F_o = V_{no}/[g' h_o]^{1/2} > 1$ $F_1 = V_{n1}/[g' h_1]^{1/2} < 1$

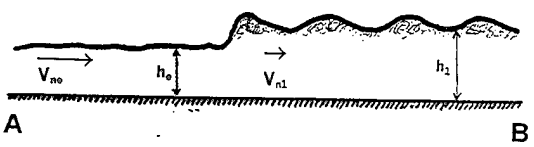

Fig.4 Schematic of hydraulic
jump and undular cloud waves

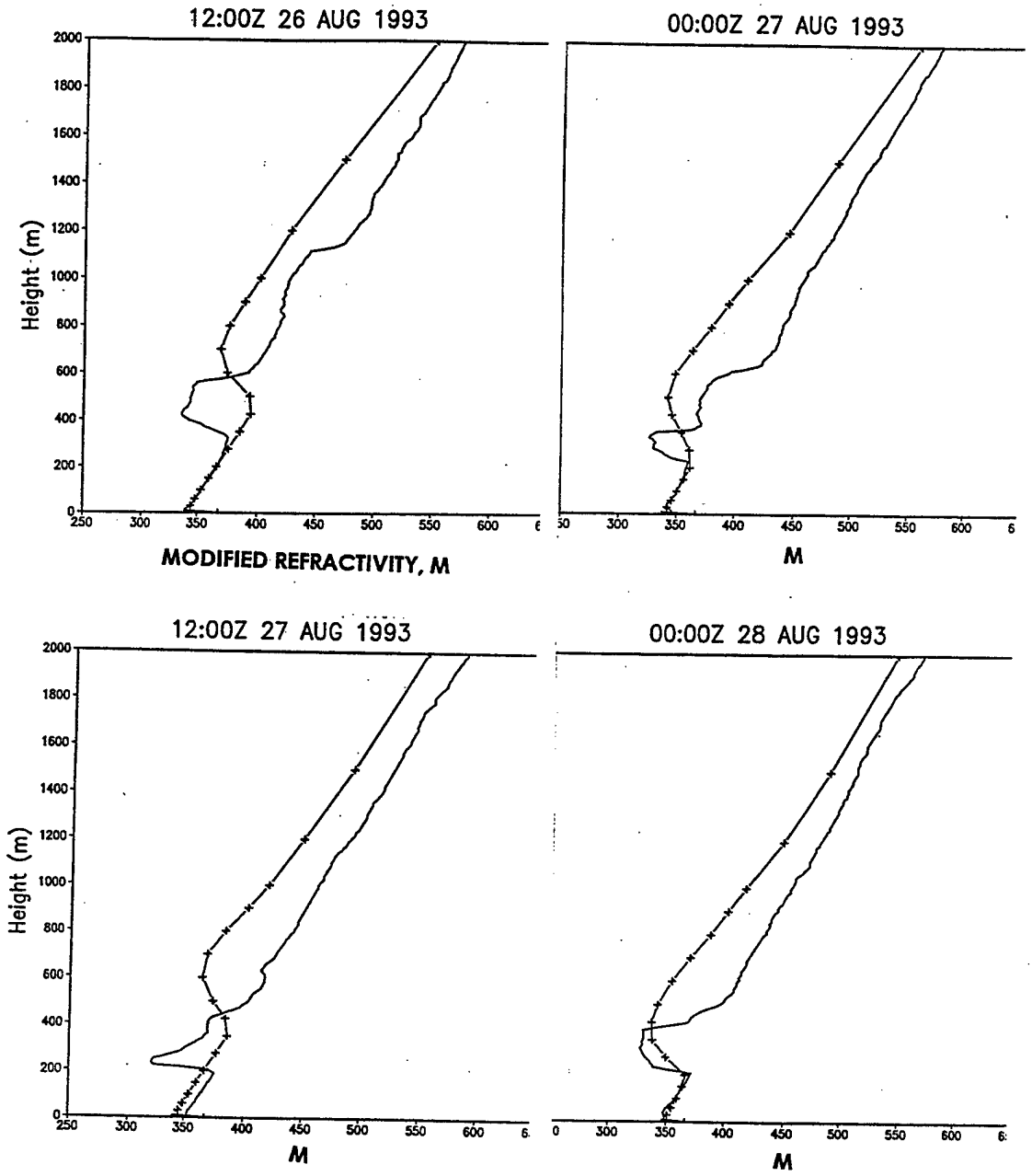

Fig.5 Four separate NORAPS 24-h forecasts of modified refractivity at San Nicolas Island (lines with crosses) and verifying radiosonde profiles (solid lines).

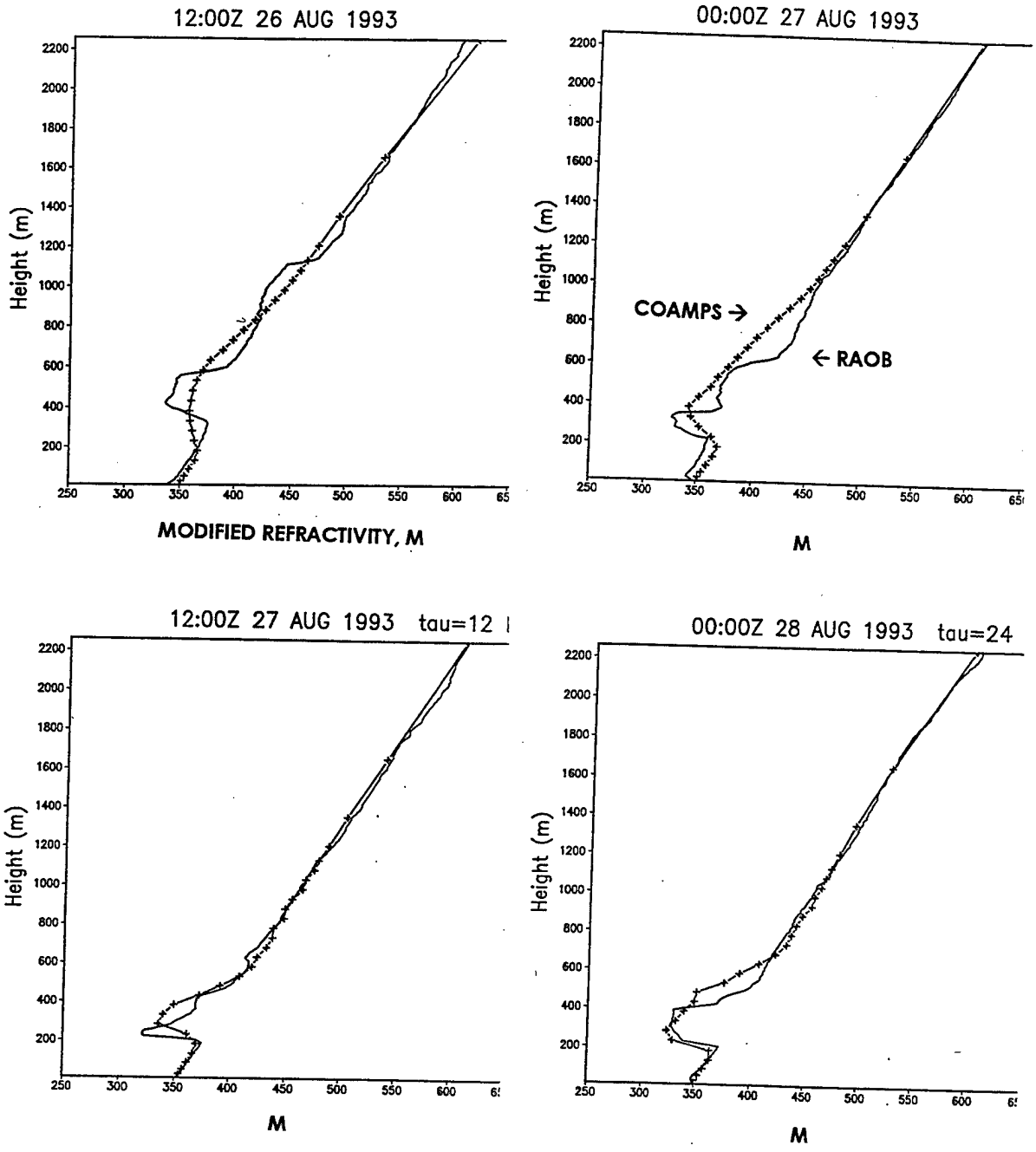

Fig.6 Four separate COAMPS forecasts of modified refractivity at San Nicolas Island (lines with crosses) and verifying radiosonde profiles (solid lines).

EOPACE Satellite and In Situ Optical Depth Studies

Carlyle H. Wash, Mary S. Jordan and Phillip A. Durkee
Department of Meteorology
Naval Postgraduate School
589 Dyer Rd., Room 254
Monterey, CA 93943-5114, USA
Phone: 408-656-2516 Fax: 408-656-3061
wash@nps.navy.mil

Pepijn Veefkind and Gerrit de Leeuw
TNO Physics and Electronics Laboratory
The Hague, The Netherlands

1. INTRODUCTION

Knowledge of the coastal Marine Atmospheric Boundary Layer (MABL) for the entire battlespace is critical for modern Navy operations. To support modern weapon and sensor systems, quantitative assessment of a number of MABL properties are needed. They include: optical depth, boundary layer depth, sea surface temperature, and surface layer temperature and moisture. These needs are even more critical in the coastal zone with the sparse surface observations away from the coast and the high temporal and spatial variability of littoral circulation systems. Remote sensing is the only data source that can measure MABL properties in the coastal zone with the needed high spatial resolution. However, many of the uses of satellite data are qualitative. Quantitative remote sensing methods need to be tested to provide these needed littoral data.

The EO Propagation Assessment in Coastal Environments (EOPACE) program is focused on the characterization of aerosol and boundary layer properties in the coastal zone and the determination if air mass parameters in various coastal locations can be derived, to a practical degree, from satellite imagery. In support of this project, several Intense Observing Periods (IOPs) have been conducted. The combination of satellite data with several in situ surface and aircraft data sets offers an excellent opportunity to monitor significant optical depth and aerosol changes and in the coastal zone. In addition, quantitative comparisons can be made. The objective of this paper is to evaluate satellite-derived aerosol optical depths estimates using aircraft and ship-based aerosol measurements, a ship-based lidar and rawinsonde profiles of the MABL.

2. SATELLITE OPTICAL DEPTH RETRIEVALS

Radiative transfer theory provides the basis for methods used to characterize aerosol properties from satellite remote measurements. In a cloud-free, marine environment, the shortwave, solar radiation measured by a satellite radiometer is primarily the result of scattering by both molecular constituents of the atmosphere (Rayleigh scattering) and larger suspended aerosol (Mie scattering). Corrections to solar irradiance of less than 5% for ozone absorption are applied and aerosols are assumed to be non-absorbing. In the absence of sun glint, reflectance from the ocean surface is also small and contributions to the satellite-measured radiance due to surface foam and subsurface reflection are accounted by empirical measurements.

For atmospheres with small optical depths such as the clear, marine atmosphere, contributions by multiple scattering can be neglected. After accounting for Rayleigh scatter, the satellite-measured radiance can be related to optical depth, as illustrated in Equation 1.

$$L_a = \frac{\omega_o F_o}{4\mu} p(\psi_s)\delta_a \qquad (1)$$

where L_a is the measured radiance at the satellite due to aerosol scattering at a given wavelength, ω_o is the single scattering albedo, F_o is the incoming solar radiance at the top of the atmosphere, P is the scattering phase function, ψ_s is the scattering angle, δ_a is aerosol optical depth, and μ is the satellite zenith angle (Durkee et al, 1991).

Durkee et al (1991) and Rouault and Durkee (1992) proposed a method of parameterizing the scattering phase function, P, based on the ratio of the aerosol radiance measured in channel 1 (visible) and channel 2 (near-IR) of the NOAA AVHRR satellite sensor. Because scattering efficiency of an aerosol distribution is wavelength dependent, scattering for a specific

aerosol population peaks when the radius of the aerosol is nearly equal to the radiation wavelength. Subsequently, radiance counts measured by the AVHRR visible and near-IR channels will change with aerosol size distribution changes such that the ratio of channel radiances will be larger for smaller size particle distributions and smaller for larger size particle distributions. Durkee et al (1991) called the ratio of the channel aerosol radiances the particle size parameter, S12. Since S12 varies pixel by pixel over the entire image, the scattering phase functions can be parameterized pixel-by-pixel allowing variations in aerosol distributions to be properly factored into the optical depth retrieval. In addition, the S12 permits characterization of the aerosol size properties for the clear air in the image.

3. EOPACE IOPs

This paper will study the EOPACE IOP that was conducted from 2-12 April 1996 off the Southern California coast. During this IOP the R/V Point Sur traversed the coastal zone with a vertical pointing 1.06 micrometer LIDAR (provided by TNO), frequent rawinsonde temperature and moisture measurements (provided by NPS) and surface layer aerosol measurements. In addition, an instrumented aircraft measured aerosols and basic meteorological parameters in the region. Polar orbiting NOAA satellite data was received and processed at NPS for the period. This IOP was of particular interest in that significant changes in MABL properties and aerosols occurred during the measurement period.

4. RESULTS

After leaving port on 2 April, the R/V Point Sur moved southward along the coast on 3 April. During this day, low and mid tropospheric flow was from the northwest and maritime aerosols spectra dominated the MABL. The MABL was very deep with a thickness of approximately 1100 m. NOAA satellite pass (not shown) from 2227 GMT 3 April showed clear conditions along the coast. The retrieved optical depth in this region was .25 associated with the larger-size marine aerosol size distribution and deep MABL. The S12 ratio for this area shows small values ranging between 1.7 and 1.9. These values indicate the larger, maritime aerosols dominate the MABL. This is consistent with ship-based data and air trajectories for this day.

Significant changes occurred in the low-level flow during the next 24 hours. Strong offshore northeasterly flow developed as illustrated in the 1000 mb streamline analysis for 0000 GMT 5 April in Figure 1. Doppler wind profilers in the region also show the development of a Santa Ana wind regime. The profiler at the Ontario airport measured NE winds in excess of 30 knots during the afternoon of 4 April while the coastal profiler at Los Angeles (LAX) airport measured north and NE winds of 10-20 knots above 700 m.

Associated with this flow, an elevated layer of continental aerosols was observed by ship, aircraft and satellite sensors. Figure 2 presents an aircraft profile at 1853 GMT 4 April showing a distinct layer of aerosol extinction at 600-800 meters. Rawinsonde temperature, moisture, and wind data, collocated with the aircraft extinction data, are also included in this figure. These winds show NE winds in this layer of 15 to 20 knots. Figure 3 presents a timesection of backscatter from the TNO mini lidar aboard the R/V Point Sur. The emitter is a 60 mJoule Nd/YAG laser. and lidar returns are averaged over 10 minute periods. Data from 4 April, left side of the figure, shows strong backscatter return in a layer from 400 to 700 m. The layer of strong backscatter is in agreement with the high extinction values from the aircraft.

The NOAA satellite data from 2216 GMT 4 April is presented in Figure 4. High values of optical depth are estimated over the entire Southern California coastal area. Values range from .17 to .38. There is a distinct plume of aerosols leaving the coast between Los Angeles and San Diego. The S12 ratio from this pass indicates a much higher ratio than 24 hours earlier. Values range from 2.9 to 3.1 indicating small aerosol sizes, typical of continental sources, are dominating the region. This is consistent with the lidar and aircraft data discussed earlier.

On April 5 the R/V Point Sur moved southeastward toward the plume observed by the NOAA satellite on 4 April. Subsidence associated with the offshore flow was quite intense this day and the MABL depths were very shallow, less than 100 m. Aircraft profiles and ship-based lidar (Fig. 3) continue to show aerosols in the lowest 1000 km. The aircraft data does not show a distinct layer of elevated extinction, but small values of aerosol extinction are present throughout the lowest 1 km. Satellite data for 2205 GMT 5 April (not shown) indicated lower values of optical depth (.15 to .25) but the remnant of the plume is still detectable.

The ship steamed though the plume location between 15 and 24 GMT 5 April. The stronger lidar backscatter values at that time (Figure 3) are consistent with the satellite data. The S12 ratio continues to be

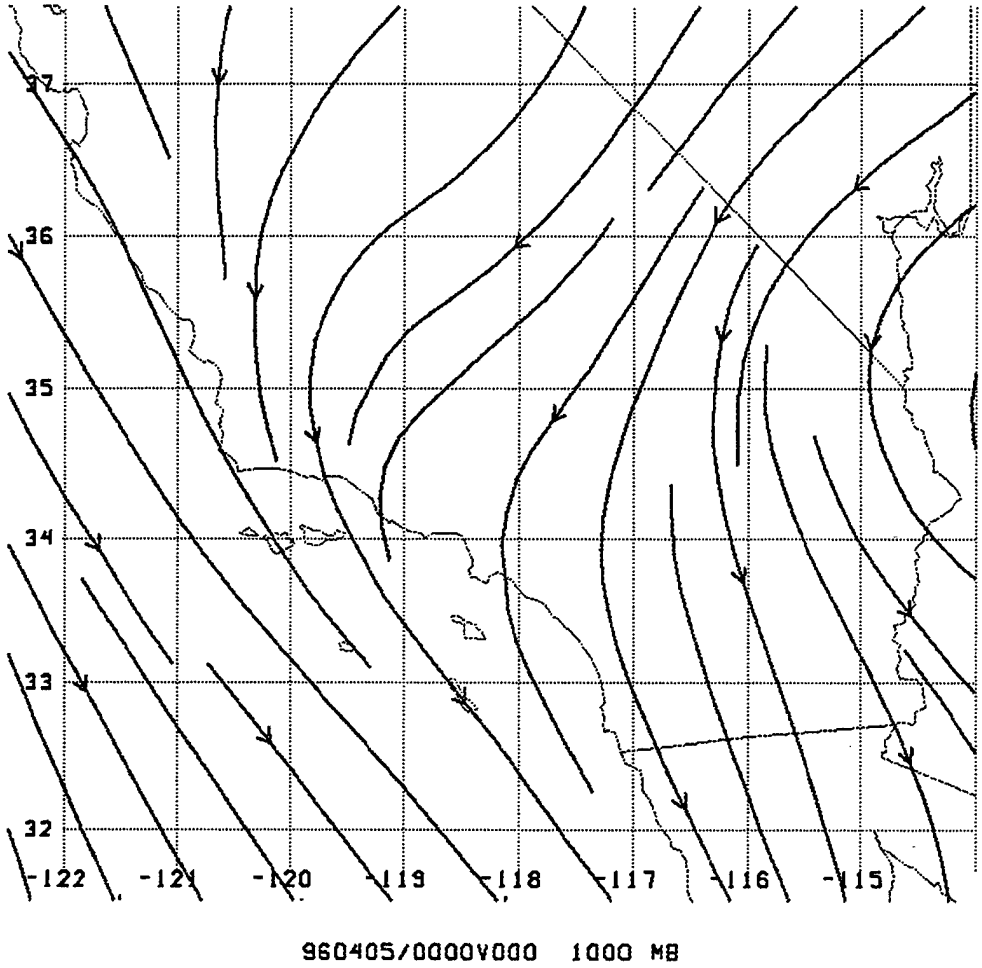

Fig. 1. 1000 mb streamlines for 0000 GMT 5 April 1996. Wind flow in the coastal region of the Southern California bight is offshore, bringing continental aerosols over the water.

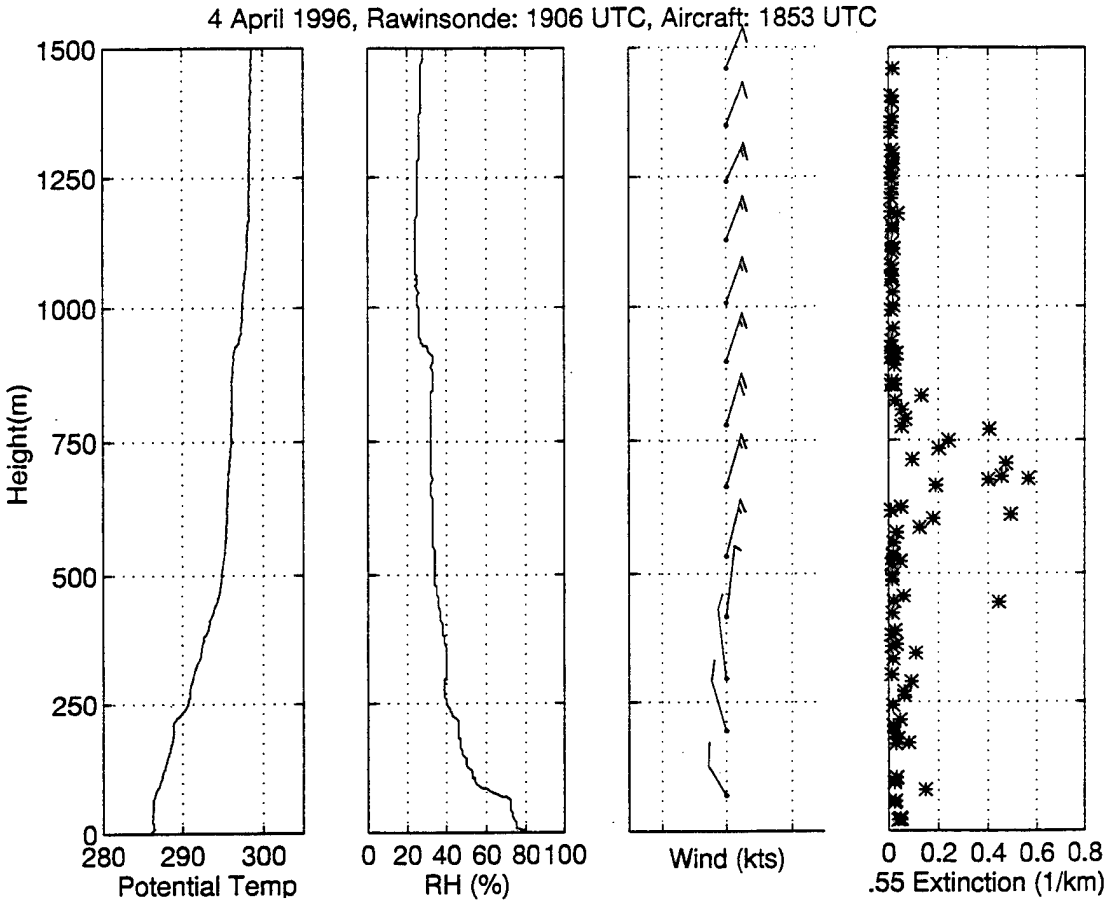

Fig. 2. Rawinsonde for 1906 GMT and aircraft aerosol extinction data for 1853 GMT 4 April 1996. Rawinsonde was launched from the R/V Pt. Sur and the aircraft concurrently flew a spiral vertical profile over the Pt. Sur. From the left is plotted rawinsonde measured potential temperature (C), relative humidity (%), winds (kts), and aircraft measured aerosol extinction at 0.55 microns.

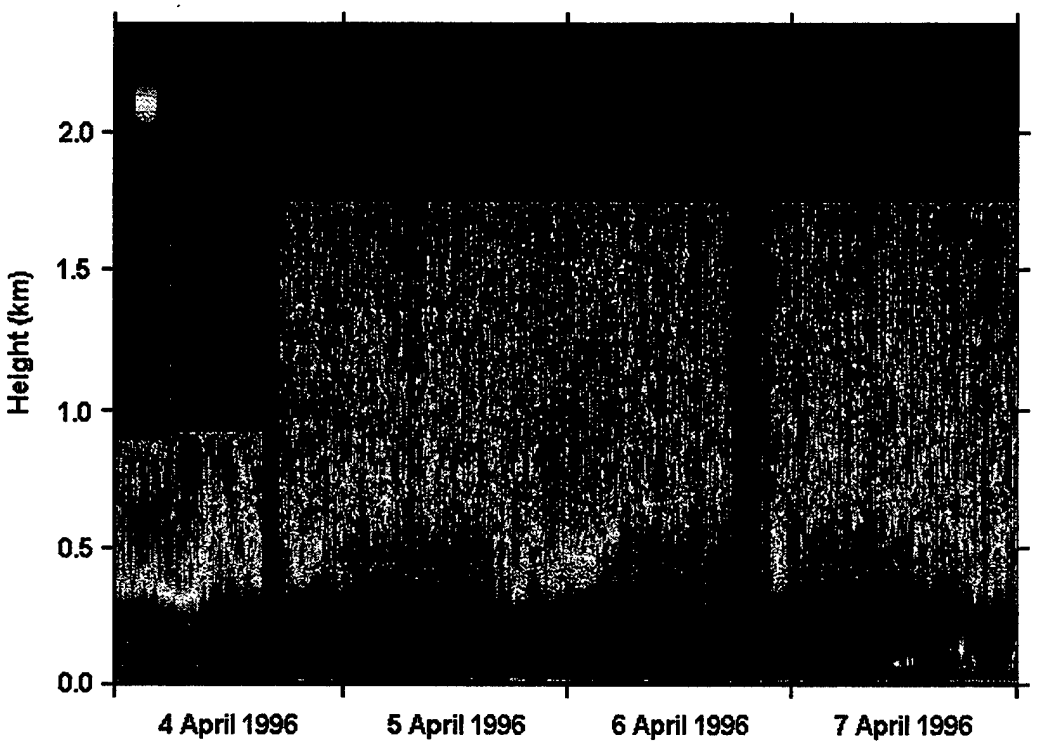

Fig. 3. Backscatter from the TNO mini lidar aboard the R/V Point Sur for 00 GMT 4 April - 00 GMT 8 April 1996. The emitter is a 60 mJoule Nd/YAG laser and returns are averaged over 10 min periods.

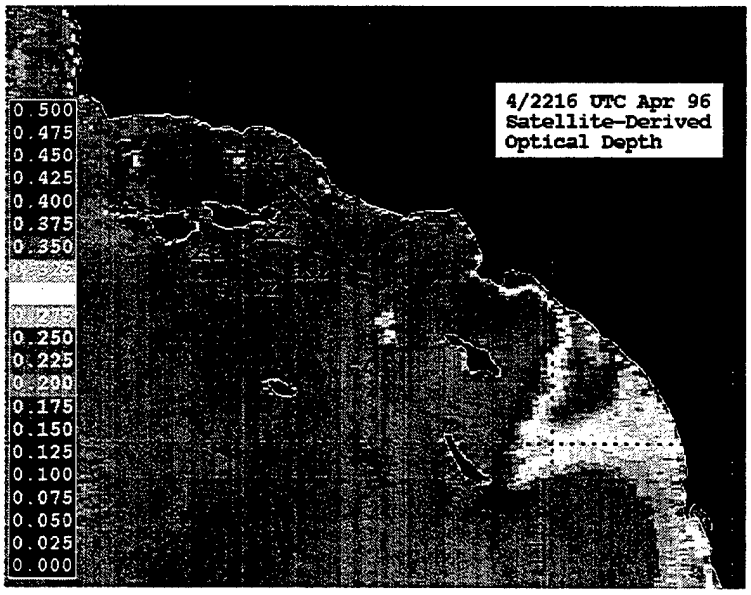

Fig. 4. Optical depth estimated from NOAA AVHRR data for 2216 GMT 4 April 1996. The R/V Point Sur ship track is indicated by the blue line. Rawinsonde launch locations are denoted by the red dots.

high indicating smaller, continental aerosols over the coastal zone. In addition, Doppler wind profilers in the region also show the strengthening of this Santa Ana regime. The profiler at Ontario airport showed NE winds between 25 and 40 knots in the lowest 500 m during the afternoon of the 5 April while the coastal profiler at LAX airport showed N wind of 20 knots below 700 m.

On 6 April, the Point Sur traversed along the coast, 20 miles offshore, between Oceanside and Long Beach, which was the area of the plume on 4-5 April. The MABL continued to be quite shallow, less than 100m, due to subsidence and strong offshore flow. By 2100 GMT, rawinsonde data indicates that 10-15 knot westerly flow was reestablished below 1200m, and the strong NE winds continued above that level. The lidar (Fig. 3) for 6 April measured strong backscatter off the aerosol early in the day, but the significant decrease in backscatter at the end of the day is consistent with the return of westerly flow and a marine air mass.

On 7-8 April, the Point Sur traversed around San Clemente and Santa Catalina Islands and then returned near the coast, south of Long Beach, on its way to San Diego. During this period the offshore flow ceased, the MABL deepened to 300 m, with NW low-level winds. This was accompanied by more low-level cloudiness in the MABL. In the clear areas, optical depth values decreased to .10 to .15 and the S12 ratio decreased indicating the return of maritime aerosols in the MABL. This was confirmed by in situ measurements aboard the R/V Point Sur.

5. CONCLUSIONS

During this IOP satellite retrievals of aerosol optical depth and the ship and aircraft measurements were in good qualitative agreement. The NOAA satellite S12 ratio successfully depicted regions of maritime aerosol during the beginning and later parts of the IOP and the period of continental aerosol associated with the strong offshore flow of the Santa Ana event.

At the time of the conference, quantitative data from the lidar and aircraft of aerosol extinction are not available. Therefore, a more quantitative assessment of satellite versus in situ data is not available. This will be a major priority in future studies with this and other IOP data sets.

The new generation of geostationary satellite, GOES-9, was operating over the West Coast at this time. The higher radiometric resolution from the sensors on this satellite provide the opportunity to retrieve aerosol depth. GOES-9 data from this period will be used to add to the temporal resolution of the satellite data for this period. In particular, GOES data should be able to monitor the development of the aerosol plume on 4 April.

6. ACKNOWLEDGMENTS

The NPS work is supported by SPAWAR Systems Center, San Diego through Office of Naval Research funding. The Netherlands Ministry of Defense, assignment A95KM729, and the US Office of Naval Research, Grant N00014-96-1-0581, support the participation of TNO-FEL in EOPACE. Aerosol retrieval work at TNO-FEL is supported by SRON EO/008. The authors would be to thank Kenneth Davidson, NPS, Michael H. Smith and Martin K. Hill, Centre for Marine Atmospheric Sciences, University of Sunderland, Sunderland, United Kingdom, and Kathleen Littfin, SPAWAR Systems Center, San Diego, CA, for sharing data and their expertise. EOPACE coordination and direction is provided by Dr. D. R. Jensen for the SPAWAR Systems Center, San Diego, CA.

7. REFERENCES

Durkee, P. A., F. Pfeil, E. Frost, and R. Shema, 1991. Global analysis of aerosol particle characteristics. *Atmos. Env.*, **25A**, 2457-2471.

Rouault, M. and P. A. Durkee, 1992. Characterization of aerosols from satellite remote sensing. In Nucleation and Atmospheric Aerosols, 357-360, N. Fukuta and P. E. Wagoner (Eds), A. Deepak Publishing.

A Quantitative Basis for Evaluating Multiple-Wavelength Lidar Inversion for Aerosol Size Distributions

Dale P. Winebrenner, John Sylvester, and William E. Asher
University of Washington

Abstract

The accuracy of atmospheric extinction modeling in the 3-5 and 8-12 micrometer bands using, for example, MODTRAN depends strongly on knowledge of the atmospheric aerosol size distribution. Because aerosol distributions are highly dynamic in space and time, observations that cover regions several kilometers on a side with resolution of 10-100 meters are of high value. Lidar has proven to be a valuable tool, but conventional (single-wavelength) lidar inversions rely on a 'constitutive' relation (i.e., assumption) between backscattering and attenuation which forces inferences about aerosol size distributions to be qualitative. Technological progress has recently cleared the way for independent, multi-spectral observations of attenuation and backscattering as functions of range. The problem is now that neither the information content of observations at the various (usually technologically constrained) wavelengths, nor the best way to extract the size distribution information in those observations, are clear. Using analytic linear inverse theory, we can derive quantitative measures of the utility of given wavelength combinations for estimating marine atmospheric boundary layer aerosol size distributions. The analysis is based on the calculation of eigenvalues of a matrix derived from Mie scattering extinction and backscattering kernels, and shows which observations are informative and which contribute more noise than information. We present some initial examples at commonly used wavelengths, assuming a standard marine aerosol size distribution.

1 Introduction

The ability to predict operational infrared sensor performance is valuable in many situations, not least in the tactical selection of sensors for defense against low-level missile threats and for littoral operations. Such an ability depends on accurate modeling of extinction and scattering in the atmosphere, which in turn are strongly influenced by aerosols. Aerosol populations are highly variable in space and time, and their dynamics are not well understood. Improved understanding requires knowledge, and thus the ability to observe, spatial and temporal evolution of aerosol size distributions over regions of several kilometers on a side, yet with spatial resolutions of tens to hundreds of meters.

Lidar has long seemed a promising tool to provide such information, but conventional (single-scattering) lidar provides only a single measurement, returned power, as a function of range. Returned power is a function of both backscattering and extinction cross sections (per unit volume) for both molecular (Rayleigh) and aerosol scattering; it therefore cannot be inverted for either backscattering or extinction alone without the addition of further information or assumptions. The now-classical 'solution' to this problem is to assume a functional relation between total (Rayleigh plus aerosol) backscattering and total

extinction, i.e., a so-called 'constitutive law' [Klett, 1981; Klett, 1985]. The assumption of any particular constitutive law, however, amounts to a strong, a priori assumption as to the aerosol size distribution [Ansmann et al., 1992; Mitev et al., 1992]; it is therefore not possible to make more than qualitative inferences about aerosol scattering on the basis of conventional conventional (single-scattering) lidar data.

Recent lidar methods using Raman scattering from atmospheric molecular species [e.g., Ansmann et al., 1992] or very high spectral resolution and sharp line filters [Krueger et al., 1993; Piironen and Eloranta, 1994] can provide profiles of true aerosol extinction and backscattering at a few (typically 1 to 5), irregularly-spaced visible and near-infrared wavelengths. The available wavelengths are strongly determined by laser technology and the resonances of available atomic and molecular species. This fact motivates the question: How much information on the aerosol size distribution is contained in a given set of spectral extinction and backscattering observations? Moreover, because technological development leading to observations at any new wavelength is typically expensive, an understanding of which new wavelength(s) would provide the most new information would also be valuable. Analytic linear inverse theory for optical particle sizing [Twomey, 1977; Capps et al., 1982; Ben-David et al., 1988; Curry, 1989] now provides the means to address precisely these questions in the case of spherical (Mie-scattering) aerosols and single-scattering observations.

In the following section, we provide a brief, limited review of analytic inverse theory as applied to lidar wavelength selection. We then examine quantitatively the information content in backscattering and extinction observations at the wavelengths used in one currently operational Raman lidar system in section 3. Finally, we conclude with brief discussion of immediate research directions suggested by this work.

2 Background

Lidars using Raman scattering [Ansmann et al., 1992] and high spectral resolution methods [Krueger et al., 1993; Piironen and Eloranta, 1994] can, in principle, now provide independent observations of aerosol extinction and backscattering at a few, selected visible and near-infrared wavelengths. Such observations at present remain technologically challenging, but the trend is toward more, and more accurate, measurements of this kind.

We will therefore assume, for purposes of this discussion, that we are given a set of such observations that include both the geophysical signal and some noise and calibration errors. Then, in the single-scattering regime, the data at wavelengths λ_1, $lambda_2$, ... ,λ_n are related to the scatterer size distribution according to:

$$\beta_a(\lambda_1, r) + E_B(\lambda_1) = \int f_V(R) K_B(R, \lambda_1) dR$$

$$\sigma_a(\lambda_1, r) + E_E(\lambda_1) = \int f_V(R) K_E(R, \lambda_1) dR \qquad (1)$$

$$\beta_a(\lambda_2, r) + E_B(\lambda_2) = \int f_V(R) K_B(R, \lambda_2) dR$$

and so on

where $\beta_a(\lambda_i, r)$ is the aerosol backscattering cross section per unit volume of air at wavelength λ_i and range r; $E_B(\lambda_i)$ is the error in the backscattering observation at that wavelength; $\sigma_a(\lambda_i, r)$ and $E_E(\lambda_i)$ are the corresponding aerosol extinction cross section per unit volume and measurement error, respectively; $f_V(R)$ is the volume size distribution (i.e., the fractional volume of particles in the lidar resolution cell with radii between R and $R + dR$ – we consider this distribution rather than the number size distribution because the resulting inversions are somewhat better conditioned); and the kernels K_B and K_E are related to the conventional Mie backscattering and extinction efficiencies, Q_B and Q_E, respectively [Bohren and Huffman, 1983], by the relation:

$$K(R, \lambda) = \frac{3}{4CR} Q(R, \lambda) \tag{2}$$

Representative examples of the kernel functions are shown in Figure 1.

From a physical standpoint, there are essentially two main things that can go wrong when trying to invert equations 1 to obtain an estimate of f_V. First, there may be very little overlap between any of the available scattering kernels (i.e., the kernels corresponding to the available spectral backscattering or extinction observations) and the size distribution of the aerosols, as illustrated in figure 2a. Mathematically, the size distribution is nearly orthogonal to all of the measurement kernels, the observations contain nearly no information about the size distribution, and the size distribution can therefore obviously not be estimated accurately.

The second potential problem, illustrated in figure 2b, is the possibility that the available measurement kernels are in fact all highly similar to each other. Mathematically, this problem is one of nearly linearly-dependent kernels – that is, although there may be n observations, there are fewer than n independent pieces of information in the observations. Blindly proceeding to estimate f_V using the full set of such observations adds more noise than additional information to the estimate, as will be shown more precisely momentarily.

These problems can be addressed mathematically as follows. (For a detailed but accessible explanation of the material in the remainder of this section, consult first Twomey [1977], and then the other references on analytic linear inverse theory cited above.) Let us write the problem schematically as

$$g_i = D_i + E_i = \int K_i(R) f(R) dR \tag{3}$$

or, in operator notation,

$$g = Kf \; . \tag{4}$$

The data g_i are discrete and small in number – they form a vector g – yet we are seeking to estimate a function, f. The problem is (very significantly) underdetermined – there are in general many functions f_2 such that $Kf_2 = 0$, and for any putative solution f_1 of equation 4, $f_1 + f_2$ is also a solution.

Heuristically, this is the first of the problems mentioned above. Mathematically, the problem is that the operator $\mathcal{K}$ generally has a nontrivial nullspace.

We therefore agree to seek only those solutions f_1 not in the nullspace of $\mathcal{K}$, that is, we seek as an intermediate step some vector w defined by $f_1 = \mathcal{K}^\dagger w$, where $\mathcal{K}^\dagger$ is the adjoint of the operator $\mathcal{K}$ (defined, as usual, by reference to the inner product of functions like f). The problem of solving for w is that of inverting a square matrix:

$$f_1 = \mathcal{K}^\dagger w \;\Rightarrow\; g = (\mathcal{K}\mathcal{K}^\dagger)w = \mathcal{M}w \tag{5}$$

where

$$\mathcal{M}_{ij} = \int K_i(R)K_j(R)dR \tag{6}$$

Note that the matrix elements depends in general on the range of particle sizes over which the integral is carried out.

Such an inversion is formally possible provided only that $\mathcal{M}$ is not singular. In practice, cases in which $\mathcal{M}$ is ill-conditioned (i.e., cases where some kernels are almost linearly dependent) lead to a fatal amplification of noise and errors in the observations. The factor by which errors are amplified is

$$\frac{\gamma_{max}}{\gamma_{min}} = \text{Amplification of Errors} \tag{7}$$

where the γ's are the eigenvalues of matrix $\mathcal{M}$. This is the second problem illustrated heuristically above. It can be addressed by limiting the choice of kernels to yield a well-conditioned matrix $\mathcal{M}$, by imposing constraints on the estimate of f_1, or by some combination of these actions. For purposes of assessing potential data sets in the presence of the given noise level, we choose the first approach. Then the estimate of f_1 is given by

$$f_1 = \mathcal{K}^\dagger \mathcal{M}^{-1} g \tag{8}$$

3 Information in Prospective Lidar Data

A multi-wavelength Raman lidar for the study of coastal aerosols has recently become operational at the University of Hawaii [Sharma et al., 1997]. This lidar will provide true aerosol extinction profiles at 532 nm, 355 nm, and 266 nm, and may in addition provide aerosol backscattering profiles profiles at 532 nm and extinction profiles 1500 nm and 1064 nm.

Consider the case in which all prospective observations would be used, i.e., in which we compute a 6x6 matrix $\mathcal{M}$ and consider its eigenvalues. Figure 3 shows normalized eigenvalues computed on the basis of Mie-scattering from particles with a wavelength-independent index of refraction 1.48+i0.02. The normalization is division of all eigenvalues by the largest – this makes apparent the number of independent pieces of information in the prospective data set for a given level of observational noise and error. Although there are nominally 6 observations, there are evidently only 4 usable pieces of independent information unless noise and errors are less than 3%. For 10% errors, there are only two useful pieces of information. An examination of elements of $\mathcal{M}$ indicates that the 266 nm and 355 nm extinction channels are least independent, as

might be expected. The next most nearly dependent channels are extinctions at 1500 nm and 1064 nm. Backscattering observations at 532 nm add significant information to the extinction observations at the lower noise level.

Figure 4a shows a trial inversion of data from a log-normal size distribution with mean particle radius 1 micron and geometric standard deviation of 1.2, using all of the prospective data (but computing in double-precision without noise). Figure 4b shows the analogous results in the case of a mean particle radius of 0.5 micron and geometric standard deviation 1.2. These results suggest that estimation of size distributions using 4 or 6 of the channels considered will be approximate at best, but that useful constraints on the size distribution are eminently possible.

4 Discussion

This study is too limited to support strong conclusions, but it does suggest that significant aerosol size distribution information may be obtained from new multi-wavelength lidar systems. Theoretical work to strengthen and refine this result is initially straightforward. First, it is necessary to relax the (somewhat unrealistic) assumption that aerosol refractive indices are independent of particle size and laser wavelength. Second, the robust estimation of size distributions from actual data will require consideration of various constraints to determine those most useful for lidar data, as well as comparison of trial inversion methods with data from field and perhaps laboratory experiments. Finally, the work presented here is limited to spherical scatterers, whereas dust and other scatterers of significant interest are most certainly not spherical. Extension of the methods here to treat data from nonspherical scatterers

5 References

Ansmann, A., U. Wandinger, M. Riebesell, C. Weitkamp, and W. Michaelis, "Independent measurement of extinction and backscatter profiles in cirrus clouds by using a combined Raman elastic-backscatter lidar", *Applied Optics* **31**(33), pp. 7113-7131, 1992.

Ben-David, A., B.M. Herman, and J.A. Reagan, "Inverse problem and pseudoempirical orthogonal function method of solution. 1: Theory", *Applied Optics* **27**(7), pp. 1235-1242, 1988.

Bohren, C.F., and D.R. Huffman, *Absorption and Scattering of Light by Small Particles*, John Wiley and Sons, New York, 1983.

Capps, C.D., R.L. Henning, and G.M. Hess, "Analytic inversion of remote-sensing data", *Applied Optics* **21**(19), pp. 3581-3587, 1982.

Curry, B.P., "Constrained eigenfunction method for the inversion of remote sensing data: application to particle size determination from light scattering measurements", *Applied Optics* **28**(7), pp. 1345-1355, 1989.

Klett, J.D., "Stable analytical inversion solution for processing lidar returns", *Applied Optics* **20**(2), pp. 211-220, 1981.

Klett, J.D., "Lidar inversion with variable backscatter/extinction ratios", *Applied Optics* **24**(11), pp. 1638-1643, 1985.

Krueger, D.A., L.M. Caldwell, R.J. Alvarez II, and C.Y. She, "Self-consistent method for determining vertical profiles of aerosol and atmospheric properties using a high spectral resolution Rayleigh-Mie lidar", *Journal of Atmospheric and Oceanic Technology* **10**, pp. 533-544, 1993.

Mitev, V.M., I.V. Grigorov, and V.B. Simeonov, "Lidar measurement of atmospheric aerosol extinction profiles: a comparison between two techniques – Klett inversion and pure rotational Raman scattering methods", *Applied Optics* **31**(30), pp. 6469-6474, 1992.

Piironen, P., and E.W. Eloranta, "Demonstration of a high-spectral-resolution lidar based on an iodine absorption filter", *Optics Letters* **19**(3), pp. 234-236, 1994.

Sharma, S.K., B.R. Lienert, T.F. Cooney, J.N. Porter, D. O'Conner, A.D. Clarke, J.M. Howell, W.I. Rose, "A multi-wavelength Mie-Rayleigh scanning lidar for measurement of marine aerosols in coastal areas", *Eos* **78**(46), pg. F119, 1997.

Twomey, S., *Introduction to the Mathematics of Inversion in Remote Sensing and Indirect Measurements*, Elsevier, Amsterdam, 1977.

6 Figure Captions

Figure 1. Representative normalized extinction and backscattering kernels, as functions of (spherical) particle radius, assuming a wavelength-independent index of refraction of 1.48 + i0.02 for the particles.

Figure 2. Heuristic illustration of the two main ways in which inversion of spectral extinction and backscattering data can fail. (a) There is little or no overlap between kernels and the size distribution to be estimated. (b) The available measurement kernels are almost linearly dependent on each other, so that few pieces of independent information are actually resident in the data.

Figure 3. Normalized eigenvalues (in descending order) of the $\mathcal{M}$ matrix for the six prospective channels of the University of Hawaii lidar system.

Figure 4. Trial inversions of backscattering and extinction data from log-normal size distributions using all 6 of the prospective channels of the University of Hawaii system. (a) Mean particle radius 1.0 micron, geometric standard deviation 1.2, particle index of refraction 1.48 + i0.02, independent of wavelength. (b) Mean particle radius 0.5 microns, other parameters identical to case a.

Figure 1.

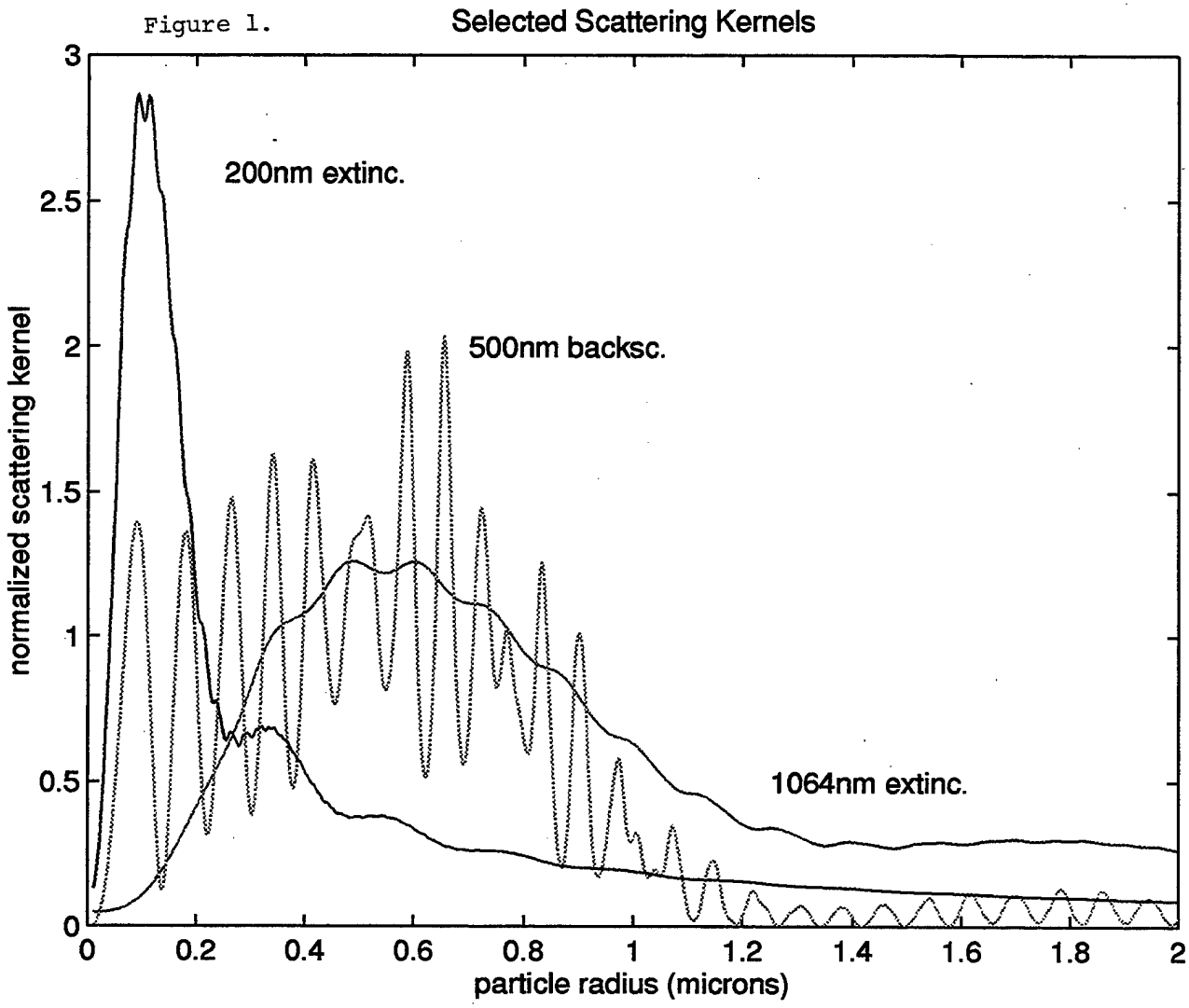
Selected Scattering Kernels
200nm extinc.
500nm backsc.
1064nm extinc.
normalized scattering kernel
particle radius (microns)
0
0.5
1
1.5
2
2.5
3
0.2
0.4
0.6
0.8
1.2
1.4
1.6
1.8

Figure 2a.

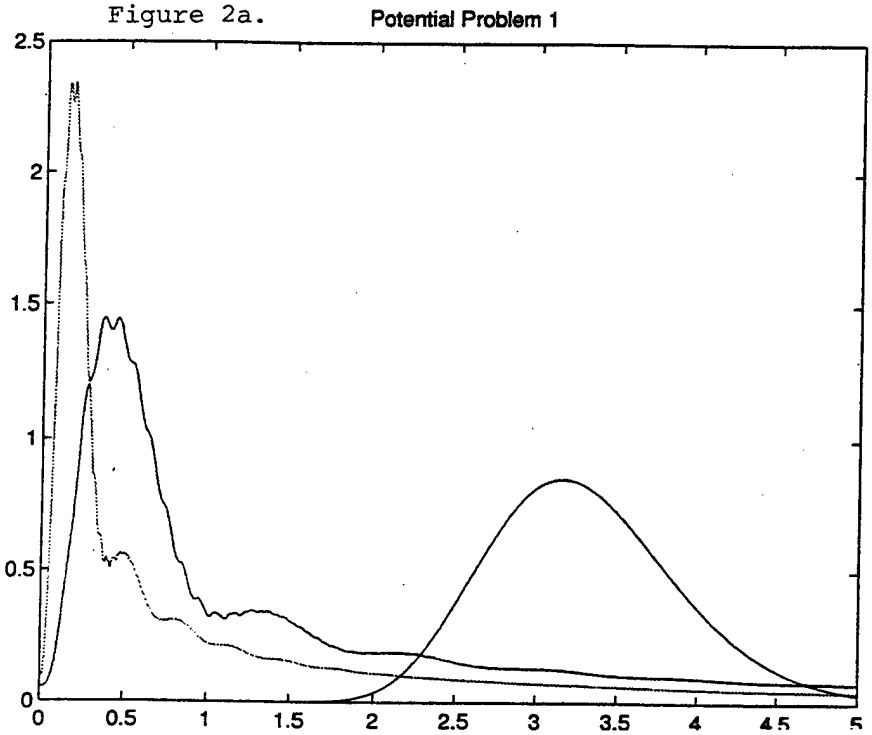

Figure 2b.

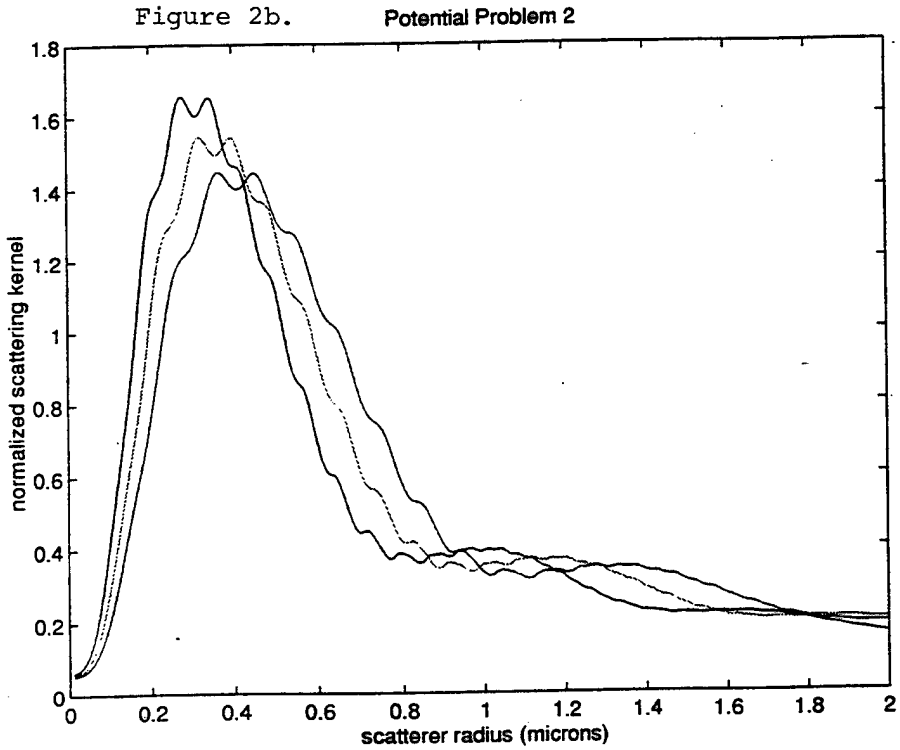

Figure 3.

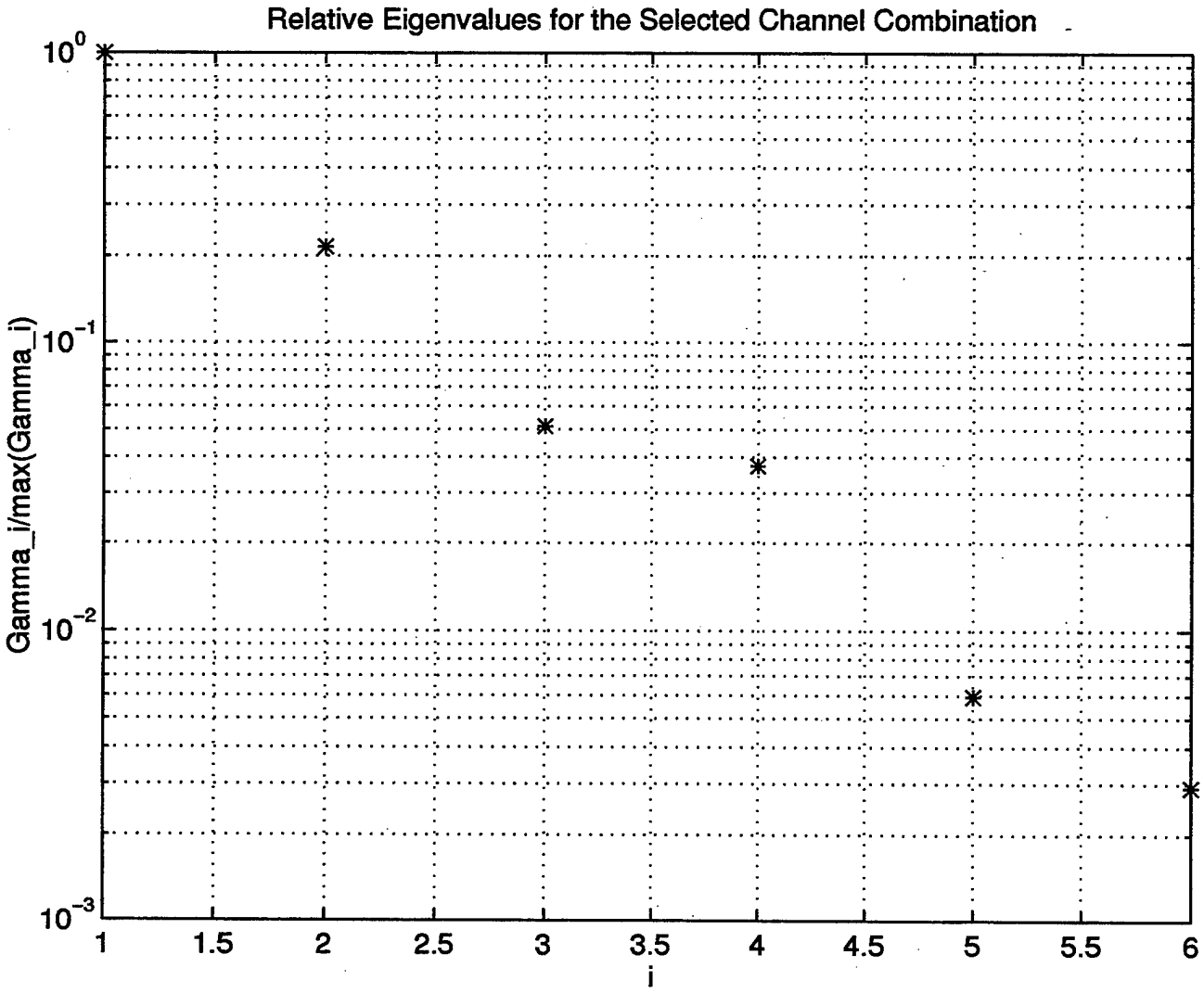
Relative Eigenvalues for the Selected Channel Combination
Gamma_i/max(Gamma_i)
10^0
10^{-1}
10^{-2}
10^{-3}
1
1.5
2
2.5
3
3.5
4
4.5
5
5.5
6
i

Figure 4a.

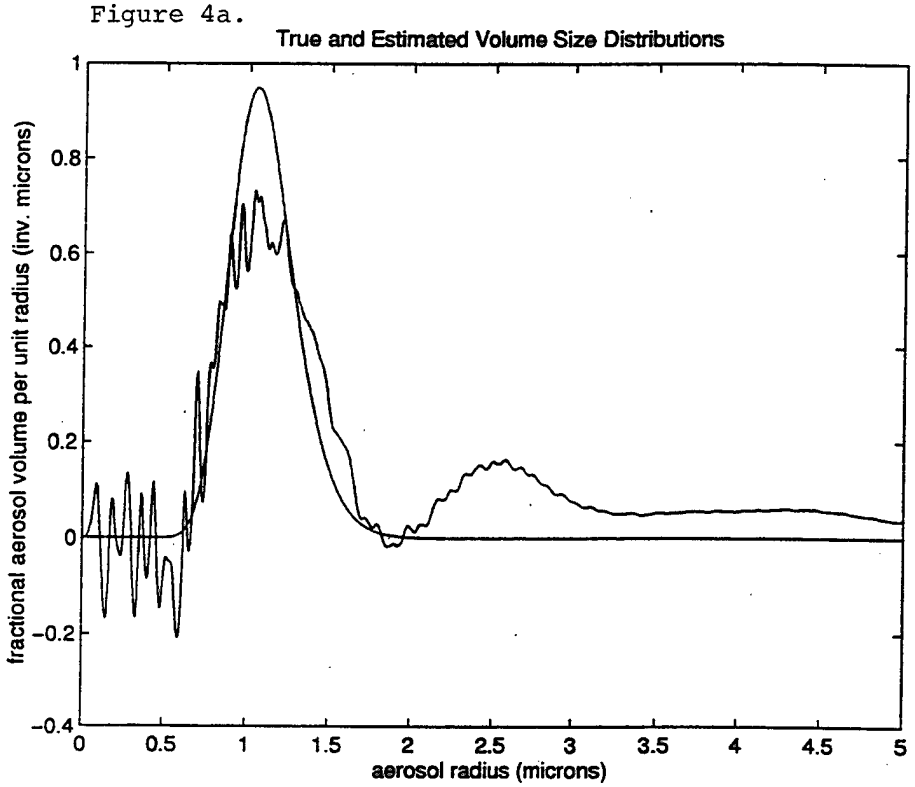

Figure 4b.

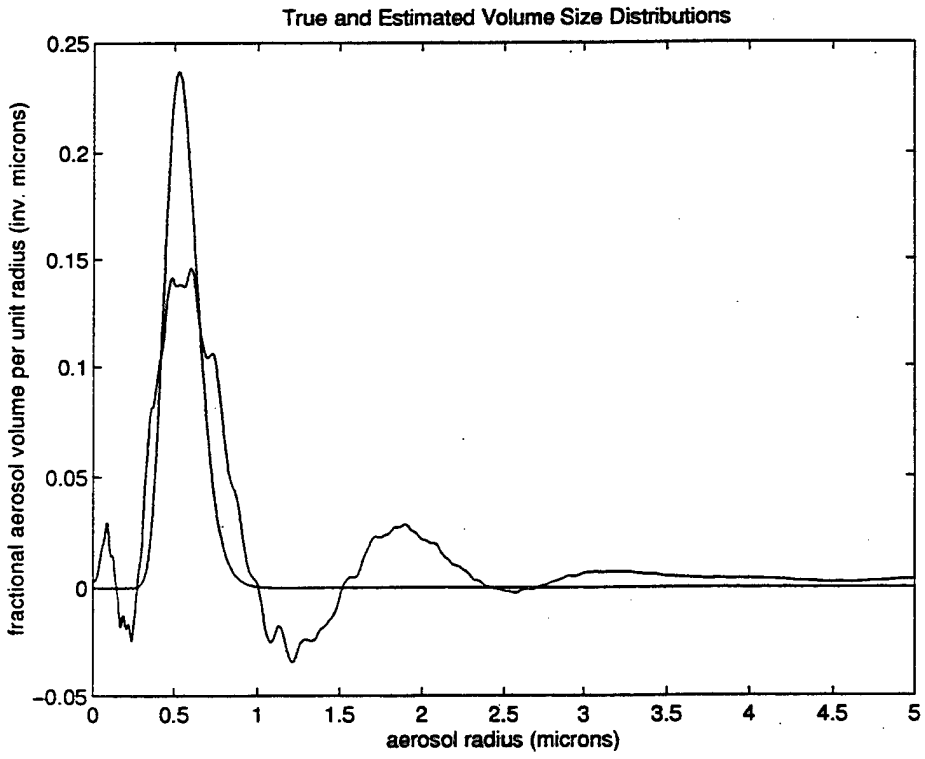

High Spectral Resolution Lidar for Measuring Atmospheric State Parameters and Aerosol Properties.

Authors: Johnathan Hair, David A. Krueger, and C.Y. She
Physics Department of Colorado State University
Center for Geosciences

ABSTRACT

High spectral resolution lidar (HSRL) can be used to determine vertical profiles of atmospheric state variables and aerosol properties if the molecular and aerosol components of the received Rayleigh-Mie signal can be separated spectrally. Such a system was proposed in 1983[3]. Atmospheric measurements, with the use of an barium atomic vapor filter, of temperature and extinction coefficients profiles have been reported[4] . In this paper we present current measurements with the HSRL operated at the popular doubled YAG wavelength of 532 nm with an iodine vapor filter. The system is capable of measuring simultaneously both the state parameters and the aerosol properties with only a pressure input at one altitude range and does not require any other independent calibrations. The lidar system, using all solid state lasers and implementing a relatively small telescope, could be made portable and automated.

HSRL INVERSION METHOD

The outgoing laser beam is a single frequency Fourier transform limited beam that is tuned to an absorption line of molecular iodine. The collected backscattered is composed of several components: Rayleigh scattering, rotational and vibrational Raman scattering, and aerosol (Mie) scattering. Since the aerosols are much more massive than the molecules, the spectral broadening of the Mie scattering (~ 10 MHz) is much smaller than the Rayleigh scattering (width ~ 2 GHz). The Raman scattering is separated from the laser frequency by more than 150 GHz and is filtered using a narrow bandpass filter (130 GHz FWHM) and therefore not considered in equations below. The total scattering return, both the aerosol and molecular scattering, can be expressed as equation 1 where $\beta_{m,\alpha}$ denotes the molecular and aerosol volume backscatter coefficients respectively. ξ, E, A, α, are the channel efficiency (including telescope overlap), total outgoing energy, telescope area, and the total extinction coefficient, respectively.

$$(1) \qquad N_t = \xi_t \frac{E}{h\nu}\frac{A}{z^2}\Delta z \left[\beta_m^{\pi} + \beta_a^{\pi}\right] e^{-2\int_0^z \alpha\, dz}$$

To obtain atmospheric state parameters, we use the iodine vapor filters as band stop filters to remove the aerosol scattering signal which is centered at the laser frequency. Equation 2 shows the lidar equation with the aerosol scattering signal removed using the iodine filter transmission, $F_i(\nu)$. Only Rayleigh transmission is passed through the iodine filters and is determined by $f_{m,i}$ in equation 3, where i represents two independent filters at different temperatures and m denotes molecular scattering. The Rayleigh scattering function center at the laser frequency ν_0, $R(T,P,\nu-\nu_0)$, can be determined from the model of Tenti[10] where T and P are the air temperature and pressure, respectively. After filtering the aerosol signal and knowing the transmission of the iodine filters one can invert for the temperature and pressure profiles using the ratio of $N_{m,1}/N_{m,2}$ from two independent iodine filters. Equation 4 gives the temperature from the measured ratio and an input pressure at one

altitude. Then assuming hydrostatic equilibrium and the ideal gas law allows one to obtain temperatures and pressures at other altitudes. In addition, once the temperature and pressure profiles are determined from the ratio, the total extinction can be deduced from equation 2 from one of the filtered channels using the definition in equation 3 for β_m where n(T,P) is the air density and $d\sigma/d\Omega$ is the differential scattering cross section. The total scattering and one molecular channels form a ratio giving the backscatter ratio as shown in equation 5 once the temperature and pressure have been determined. This forms a self consistent inversion method to calculate the state parameters, backscatter ratio, and extinction coefficients.

$$(2) \qquad N_{m,i} = \xi_{m,i} \frac{E}{h\nu} \frac{A}{z^2} \Delta z \left[\beta_m^{\pi} \, f_{m,i}(T,P)\right] e^{-2\int_0^z \alpha(z')dz}$$

$$(3) \qquad \beta^{\pi} = n(T,P) \left.\frac{d\sigma}{d\Omega}\right|^{\pi} \qquad f_{m,i}(T,P) = \int_{-\infty}^{\infty} R(\nu - \nu_o, T, P)\, F_i(\nu) d\nu$$

$$(4) \qquad \frac{N_{m,1}}{N_{m,2}} = \frac{\xi_{m,1}}{\xi_{m,2}} \frac{f_{m,1}(T,P)}{f_{m,2}(T,P)}$$

$$(5) \qquad \frac{N_t}{N_{m,i}} = \frac{\xi_t}{\xi_{m,i}} \left[\frac{\beta_m^{\pi} + \beta_a^{\pi}}{\beta_m^{\pi}}\right] \frac{1}{f_{m,i}(T,P)}$$

The iodine filters have been measured, frequency scaled, and characterized for the inversion method discussed. Measured transmission curves for iodine filters are shown in figure 1. The two filters operated at 85^0 C and 60^0 C have different absorption as a function of frequency allowing for the two independent molecular scattering signals. Even though the filters have complicated spectra, the extinction at line center is greater than 34 dB and the width is ~2 GHz which is on the same order as the Rayleigh scattering width. The Doppler free saturated absorption spectrum which is used to lock the laser to an absolute frequency centered in the iodine absorption line 1108 is shown in figure 2.

LIDAR DESCRIPTION AT 532 nm

Since the lidar system uses the spectral information from the scattered returns and must be capable of tuning to the center of an absorption line of iodine, the laser transmitter must have high spectral resolution (~100 MHz) and be tunable over ~10 GHz. Our current lidar setup which is shown in figure 3 and consists of a Lightwave model 142 cw dual wavelength laser having 50 mW of both 1064 nm and 532 nm light. The 1064 nm light is used to seed a pulsed doubled YAG laser from Spectra Physics model DCR-3D producing the transmitted laser beam, which is tunable and Fourier transform limited. The cw seed laser is frequency locked using iodine Doppler-free saturated absorption spectroscopy, with an active feedback control loop to provide an absolute frequency reference. The laser transmitter properties are summarized in Table 1.

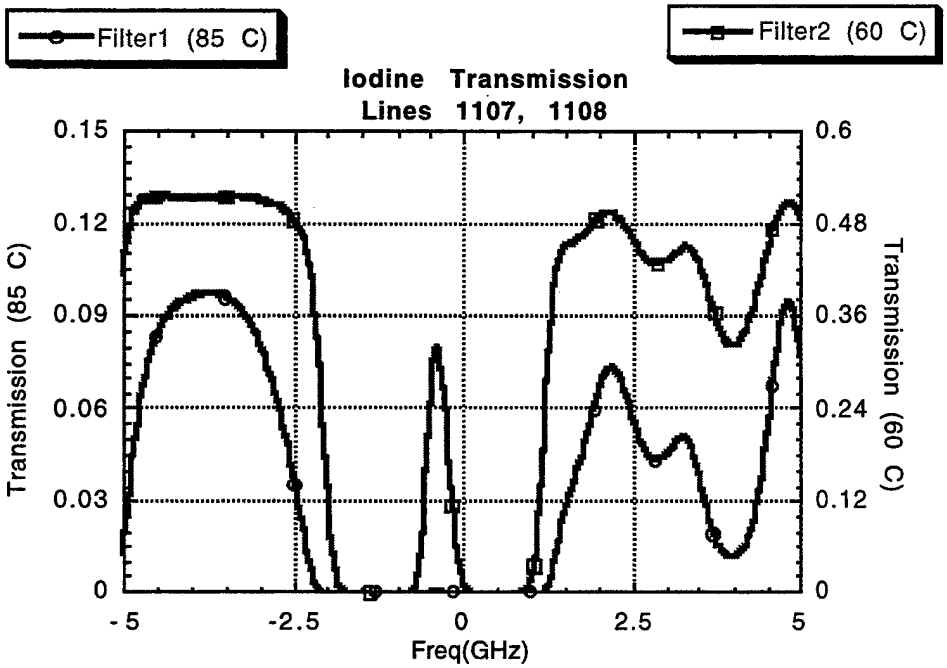

Figure 1. Measured iodine transmission near the lines 1107, and 1108 of iodine at 532.29 nm. There are two transmission curves for the two filters expressed in equation 2. The filters are temperature controlled at 85° C and 60° C, respectively, giving the two independent signals needed to form the ratio in equation 4. The hotter filter has a broader absorption line than the cooler cell thus sampling different portions of the Rayleigh scattering spectrum.

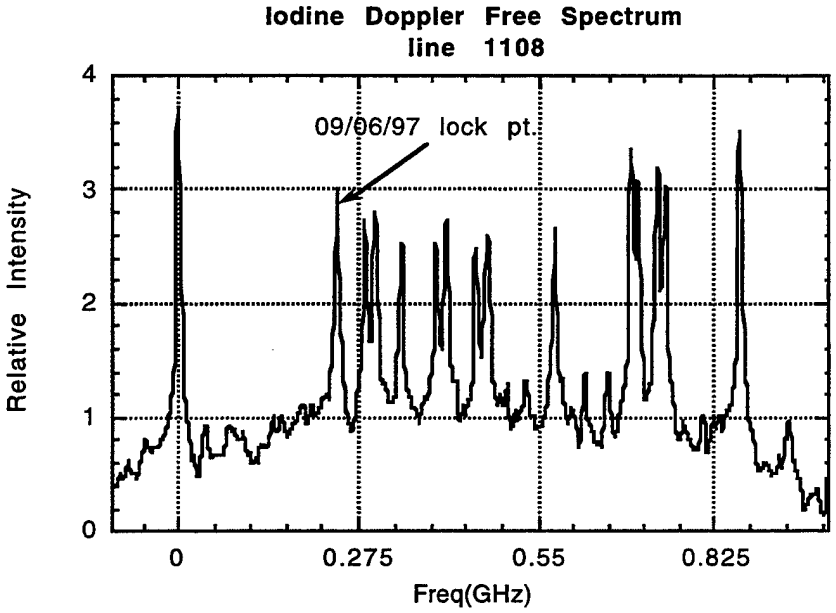

Figure 2 . Doppler broadened absorption spectra of Iodine at line 1108. Data was taken simultaneously with figure 1 transmission curves.

PULSED DCR-3D	
Average Power	5 Watts at 532 nm
Pulse Duration	5 ns
Divergence	0.5 mrad full angle
Pulse Repetition Rate	20 Hz
Linewidth	60 MHz

CW LIGHTWAVE MODEL 142	
Average Power	50 mW at 532 nm 50 mW at 1064 mW
Linewidth	< 10 kHz
Tuning Range	> 10 GHz
Locking Accuracy	2 MHz

DETECTION SYSTEM	
Telescope	8 inch diameter Cassegrain
PMT's	H5783P Hamamatsu
Daystar Filter	1.3 angstrom FWHM
Counting Board Interface	Optech 700 MHz Multichannel Scalar Ave.

TABLE 1 System parameters for transmitter and receiver.

The detection system uses a relatively small 8-inch Cassegrain telescope. A Daystar filter with a FWHM of 130 GHz has been added to the system to eliminate rotational and vibrational Raman scattered light from the return signal, eliminating the need to include them in data analysis. In addition, this also allows measurements to be made at dusk and dawn . The signal is then split into three channels. The molecular scattering channels have iodine vapor filters, while an unfiltered channel measures the total Rayleigh-Mie scattering and is shown in figure 3.

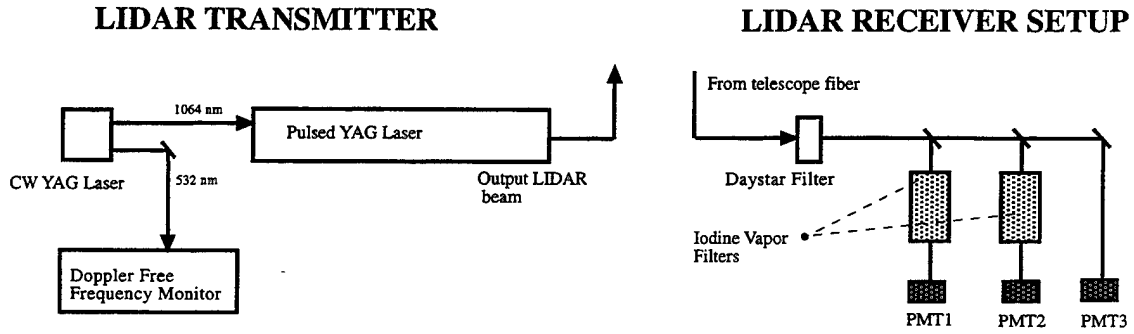

Figure 3. Schematic of HSRL transmitter and receiver. The transmitter system consists of the cw YAG laser to seed the pulsed YAG laser allowing a single longitudinal mode 60 MHz linewidth. The receiver setup consists of the collected light being split into three channels two with iodine filters measuring Rayleigh scattering only and one channel that measures the sum of Rayleigh and Mie scattering.

4

ESTIMATED ERRORS FOR CURRENT SYSTEM

Working with the current lidar system near 532 nm, considerable progress has been made allowing us to characterize the lidar system and proceed to obtain initial field measurements. There are two very significant improvements made to the HSRL lidar system; installation of a stabilization algorithm which permits real-time monitoring of laser frequency to within 0.5 MHz, and installation of separate temperature controls on the cell and finger of the iodine filter which has achieved stability within 0.05K and 0.01K respectively in a 10 hour run. The table below shows the lidar measurements using the iodine filters at 589 nm has achieved atmospheric temperature measurements of 3.4 K at 1 Km. Most of this uncertainty is attributed to photon noise in the counting statistics. The photon noise has been reduced by a factor of 3 using new PMT's and faster multichannel scaling averagers to record the data.

	Estimated Error	Estimated Error	Estimated Error
Error Source	Barium Setup	Iodine at 589 nm	Iodine at 532 nm
Oven temperature fluctuations	7.0 K	< 0.1 K	<0.1 K
Frequency lock fluctuations	(40 MHz) < 1 K	(0.5 MHz) 1.5 K	(2.0 MHz) 1 K
Photon noise at 1 Km	1 K	3 K	1 K
Total Error due to above estimates	7.1 K	3.4 K	1.4 K
Total Error without Photon noise	1 K	1.5 K	1 K

Table 2. Air temperature error sources for the current lidar system.

FIELD MEASUREMENTS at 589 nm

The first system that was incorporated using the iodine filters was done at 589 nm and data is shown to demonstrate that the extinction of the filters are sufficient to suppress the aerosol scattering. The laser system was readily available and the transmitter was already tested for high spectral resolution operation. Figure 3 shows that temperature measurements were made in the presence of a relatively large aerosol layer at 4 km as seen in the backscatter ratio. Field measurements were conducted on several night in January and February of 1995 and additional nights have been measured January, March, and June of 1996. Profiles of both atmospheric temperature, density, extinction, and backscatter ratios have been measured on these nights. The estimated uncertainty due to photon noise for a measurement time of 82 min. is 3 K, 6 K, and 11 K at 1 Km, 2 Km, and 4 Km respectively. The major error is photon noise due to small count rates that were available with the photomultipliers used in this interim lidar system, which can detect only 4 photons in 0.5 μs without significant photon piling-up. For this reason, the transmitter laser power was reduced to 15 mW average power for the 8-inch diameter receiving telescope. The simulated data in figure 3(a) was created to give lidar profiles that would match the balloon data. The lidar data created had similar count rates from the measured data to compare the statistics. Photon noise was then added to the simulated lidar data and then analyzed with the same method as the measured data. The simulated data shows the same wave like structures as the experimental data resulting from the photon noise.

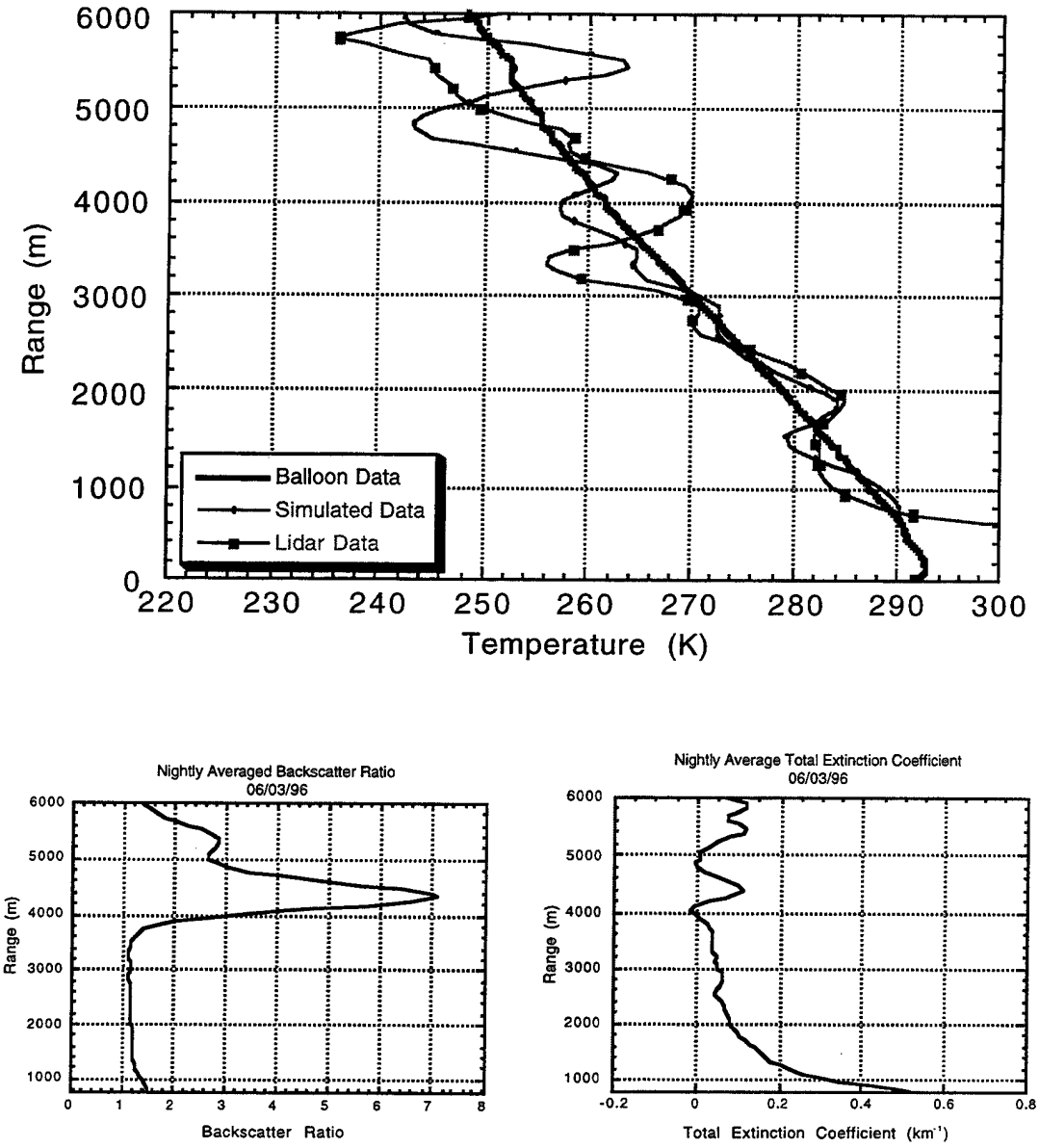

Figure 3. (a) Nightly averaged Temperature lidar profile and balloon data taken at Ft. Collins, CO on June 3, 1996 compared to a simulated profile using the balloon data and adding photon noise to show signal error was dominated by photon noise. (b), (c) total extinction, and backscatter ratio profiles taken at Ft. Collins, CO on same night.

FIELD MEASUREMENTS at 532 nm

Using higher count rate PMT's which were available at 532 nm, initial field measurements were made using the seed pulsed YAG laser. The state parameters and the aerosol properties were both measured on several nights. The first night of May 5, 1997 only two molecular channels were taken so only the temperature profile is shown. It should be noted that temperature is the most demanding of the measurements for the lidar system. It requires accuracy of 0.25%/Kelvin while the backscatter ratio is acceptable within 1-2% accuracy.

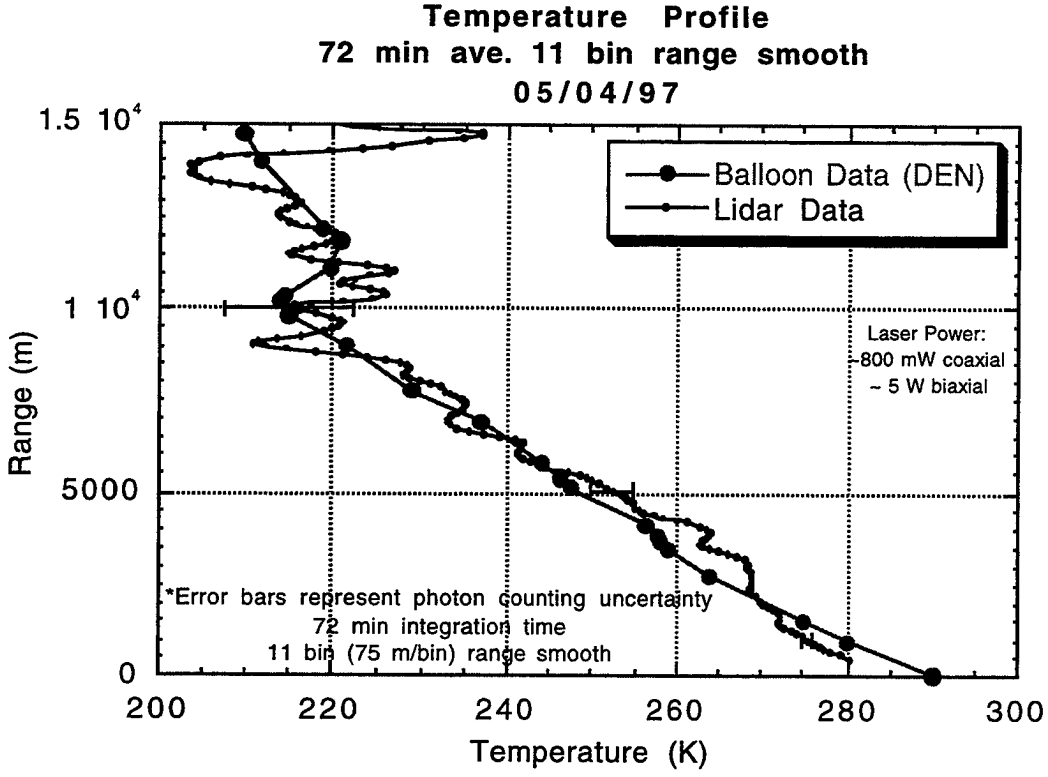

Figure 4. Temperature profiles for May 05, 1997 taken with HSRL in Ft. Collins, CO averaged over 72 minutes. For comparison, balloon data taken in Denver, CO is also shown.

The data in figure 4 shows the uncertainties in photon noise at several altitude ranges. The uncertainty at 1 Km is less than 1 K for the 72 min. integration time. This demonstrated that the system at 532 nm has improved the integration times and counting statistics. This was mostly due to higher count rates using faster electronics and new PMT's. In addition, a dual beam was used to put more light at higher altitudes with a biaxial beam and the lower altitudes were covered with a coaxial beam at lower laser power. This allowed one to use all the available laser power without saturating the detectors. There was some small aerosol leakage in this initial field run taken on May 5, 1997 and probably is the reason for the small inversion at 3 and 4 km.. This has been improved by changing the optics of the pulsed YAG laser system. Field data on September 6, 1997 is shown in figures 5-7. This night all three channels were taken to measure both the state parameters and backscatter ratio.

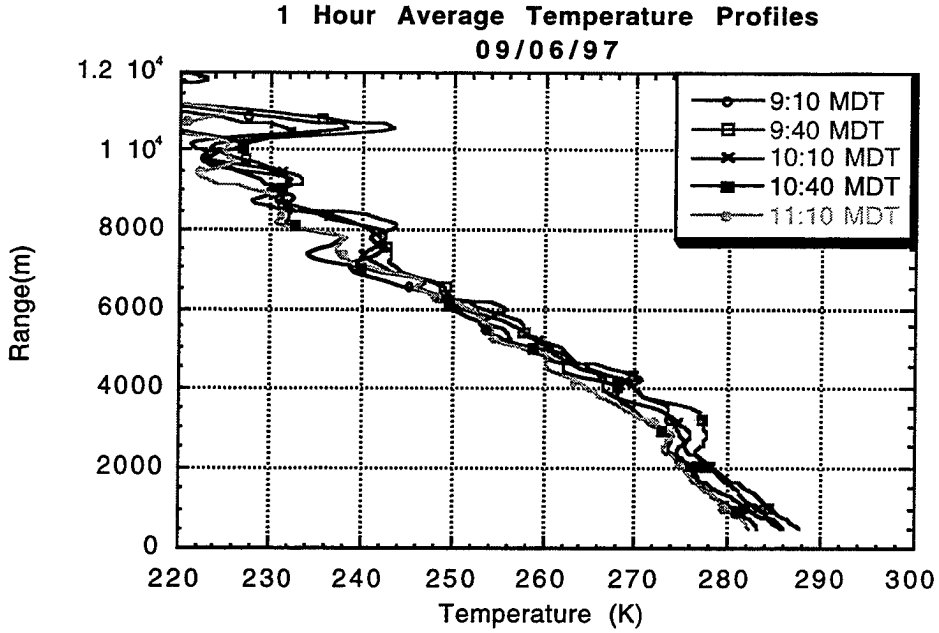

Figure 5. Temperature profiles for September 6, 1997 in Ft. Collins, CO, with running time average of 1 hr. separated by 0.5 hr. Data shown shows a small 5K drop in temperature over the night. Even though this may be an actual trend, there may be some correlation between the stability of iodine cell temperature and this temperature offsets. Photon counting noise error is not shown, but temperature precision at 1 km (5 km) is less than 1 K (5 K).

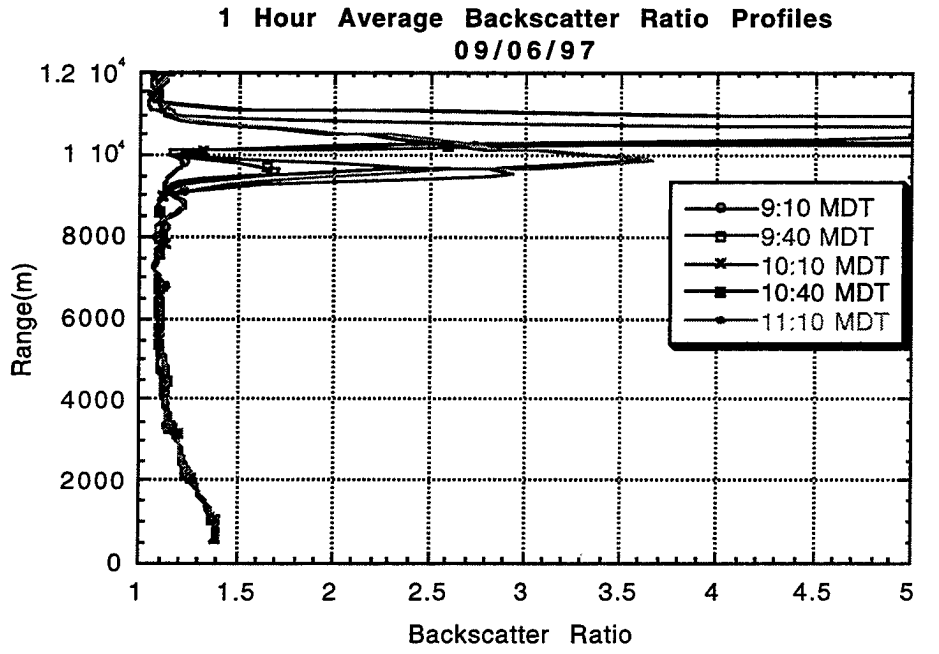

Figure 6. The backscatter ratio ($1+ \beta_a/\beta_m$) for September 9, 1997 in Ft. Collins, CO. The data shows a decrease in aerosol back scattering from 2 km to 7 km and a high clouds at 10 km. The cloud was relatively large with backscatter ratios larger than 20.

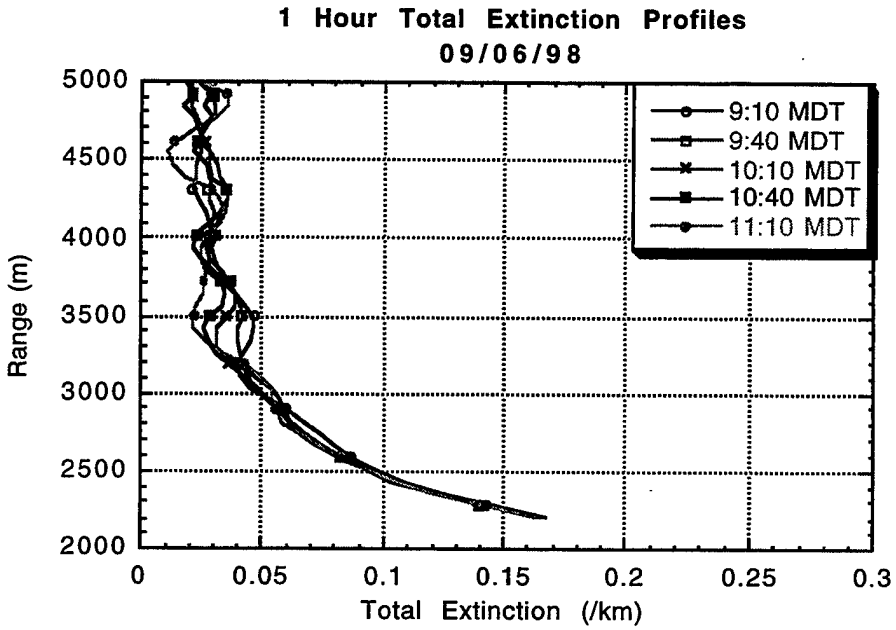

Figure 7. Total extinction profiles for September 6, 1997 in Ft. Collins, CO. The extinction coefficient is dependent on the overlap function of the telescope and transmitter laser beam and was not included at this time but will be included with future measurements.

The backscatter ratio for September 6, 1997 has a large cloud at 10 km with backscatter ratios over 20. The time evolution of the measured backscatter ratio suggests the capability of using our HSRL for the study of cirrus cloud dynamics. With aerosol scattering collected by the lidar system 20 times more than the Rayleigh scattering and the purity of the laser being 1 part in 1000, there is small Mie scattering leakage in the molecular channels. This is apparent in the temperature profile in figure 5. It is expected that, with backscatter ratios of < 5, the system is able to determine temperature profiles within 1K.

Summary

The HSRL system provides a robust system to measure atmospheric profiles of temperature, density, pressure, aerosol extinction, and aerosol backscatter ratios. As such, it offers unique lidar measurement capability to date. Ongoing field measurements and comparisons to balloon sondes and others available instruments will help access and characterize the lidar accuracy. The system uses a relatively small telescope, 8 inch diameter, and a typical 5 W pulsed doubled YAG laser and can provide continual high resolution vertical profiles of temperature and aerosol optical properties. This lidar system is capable of measuring atmospheric temperatures with < 1 K accuracy at 1 km in a 60 minute average and backscatter ratios with uncertainties of < 1%. This HSRL system operated at 532 nm could be incorporated into other lidar systems and possibly automated for routine measurement of atmospheric temperature and aerosol properties.

Acknowledgment

This work is supported in part by DOD Center for Geoscience, Phase II (DAAH04-94-G-0420) at Colorado State University.

References

1. Measures, R. M., *Laser Remote Sensing: Fundamentals and Applications.* John Wiley & Sons, 510 pp., 1984.

2. She, C.Y. "Remote measurement of atmospheric parameters: new applications of physics with lasers", Contemp. Phys., 31, pp. 247-260,1990.

3. Shimizu, H. S., Lee, S. A., and She, C. Y., "High spectral resolution lidar system with atomic blocking filters for measuring atmospheric parameters", Appl. Opt., 22, pp. 1373-1381, 1983.

4. Alvarez II, R. J., Caldwell, L. M., Wolyn, P. G., Krueger, D. A., McKee, T. B., and She, C. Y., "Profiling Temperature, Pressure, and Aerosol Properties Using a High Spectral Resolution Lidar Employing Atomic Blocking Filters", J. Atm. Oceanic Tech., 10, pp. 546-556, 1993.

5. Caldwell, L. M., *A High Spectral Resolution Lidar using an Iodine Vapor Filter at 589 nm,* Ph.D. thesis, Dept. of Physics, Colorado State University, Ft. Collins, Co., 1995.

6. Piironen, P., Eloranta, E. W., "Demonstration of a high-spectral-resolution lidar based on an iodine absorption filter", Opt. Lett., 19, pp. 234-236, 1994.

7. Harms, J., "Lidar return signals for coaxial and noncoaxial systems with central obstruction", Appl. Opt., 18, pp. 1559-1566, 1979.

8. Zhao, Y., Hardesty, R. M., Post, M. J., Appl. Opt., 36, pp. 7623-7632, 1992.

9. Liu, Z. S., Chen, W. B., Hair, J. W., and She, C.Y., "Proposed Ground-based Incoherent Doppler Lidar with Iodine Filter Discriminator for Atmospheric Wind Profiling", this volume.

10. Tenti, G., Boley, C. D., Desai, R. C., "On the kinetic model description of Rayleigh-Brillouin scattering from molecular gases", Can. J. Phys., 52, pp. 285-290, 1974.

Atmospheric Measurements with Doppler Lidar and Instrumented Kite-Platforms

Rod Frehlich, Ben Balsley and Mike Jensen
Cooperative Institute for Research in the Environmental Sciences (CIRES)
University of Colorado, Campus Box 216, Boulder, CO 80309
Phone:303-492-6776 FAX:303-492-1149 Email:rgf@cires.colorado.edu

Stephen Hannon, Sammy Henderson, and Phil Gatt
Coherent Technologies, Inc., 655 Aspen Ridge Drive
Lafayette, Colorado 80026 USA
Phone:303-604-2000 FAX:303-604-2500 Email:steveh@csn.org

Introduction

Coherent Doppler lidar [1]-[13] has become a promising technique for the measurement of atmospheric winds and has been used for mapping hazardous wind fields from airplanes, for shuttle launches, and around airports. One of the most promising methods for real-time measurements of wind hazard is to profile the radial velocity along the glide path of landing airplanes using an eye-safe coherent Doppler lidar. The major advantages of this method are high sensitivity, high spatial and temporal resolution measurements, high accuracy and low bias.

The experimental investigation of the atmosphere is difficult because of the rapid three-dimensional variations of basic variables like wind and temperature. The parameterization of boundary layer processes requires knowledge of the wind speed profile, fluxes, and spectra from near the surface to the height of the boundary layer. The Doppler lidar is a very promising technique for measurements of wind satistics.

Three-dimensional in situ measurements of the atmosphere are difficult. Remote sensing techniques like radar, lidar, and sodar have provided new measurement capabilities. Instrumented kite-platforms [14, 15, 16] have become a promising new method for in situ measurements because of new developments in kite construction (parafoil designs), Kevlar kite lines, light-weight and low power atmospheric sensors, and new data storage devices. The use of multiple sensors provides unique three-dimensional information about atmospheric processes.

Doppler Lidar Measurements

The first lidar measurements of winds used 10-μm coherent Doppler lidars [1]. The more recent work emphasizes the improved performance of the 2-μm lidar [7, 10, 11]. Coherent or heterodyne detection is a sensitive method for the detection of weak signals and is immune to the effects of background light which is essential for daytime operation. A short laser pulse is transmitted and the photons scattered by aerosol targets are collected by a telescope, focused onto a detector, and mixed with a frequency-stable laser beam called the Local Oscillator (LO). The radial velocity v of the scatterers produce a Doppler frequency shift f given by $v = \lambda f/2$ where λ is the wavelength of the laser. For a 2-μm laser pulse, 1 m/s of radial velocity corresponds to a 1 MHz Doppler frequency shift, which can be estimated as the pulse travels through the atmosphere. Because the velocity is determined from a frequency measurement, the velocity bias is mainly due to the frequency drift of the reference laser and is not a function of the velocity or the magnitude of the return signal. This permits accurate corrections for velocity bias using the estimated Doppler frequency from non-moving targets [10, 11].

The improved velocity accuracy and range resolution of solid state Doppler lidar produces accurate remote measurements of many atmospheric processes. These short wavelength Doppler lidars will have [7, 10, 11] a range resolution of 50 meters and the ability to produce 10,000 estimates of the radial velocity every second along a line of sight from a range of 100 m to several kilometers. The potential for

rapid measurements of real, three dimensional, wind fields is enormous. In addition, the small transverse dimensions of the lidar beam (typically less than 0.5 m) samples the radial velocity along the propagation axis, which greatly simplifies the interpretation of data when the velocity fluctuations over the range gate become important because only the one-dimensional statistics are required. By contrast, for Doppler radar, the transverse dimensions of the beam are comparable or greater than the radial dimension of the beam and the three dimensional statistics of the wind field are required to fully interpret the data.

The spatial extent of the lidar pulse Δr is determined by the temporal power profile $P_L(t)$ of the transmitted pulse where t denotes time. For a solid-state lidar, the transmitted pulse is well approximated as [10, 11]

$$P_L(t) = P_0 \exp(-t^2/\sigma^2) \tag{1}$$

where P_0 is the maximum power and σ [s] is the pulse 1/e width. The sensing volume of the illuminated aerosol targets is defined by

$$I_n(r) = W(r) / \int_{-\infty}^{\infty} W(x)dx \,, \tag{2}$$

where

$$W(r) = P_L(2r/c) \tag{3}$$

is the range weighting function of the Gaussian lidar pulse as a function of the distance r along the lidar transmit axis and c [m/s] is the speed of light. For a Gaussian transmitted pulse [see Eqs. (1)-(3)],

$$I_n(r) = \frac{2}{\sqrt{\pi}\sigma c} \exp[-4r^2/(\sigma^2 c^2)] \,. \tag{4}$$

and the Full-Width at Half Maximum (FWHM) of $W(r)$ is

$$\Delta r = \sqrt{\ln 2} c\sigma \tag{5}$$

which defines the spatial extent of the lidar pulse along the transmit axis which is typically 30 meters.

As the pulse propagates through the atmosphere, the Doppler lidar data is digitized and converted to a complex data sequence with a sampling interval $T_S = 0.02\ \mu s$. The range gate length Δp is defined as the distance the laser-illuminated aerosol volume moves during the observation time per estimate $T = MT_S$ where M is the number of complex data samples per estimate, i.e.,

$$\Delta p = MT_S c/2 \,. \tag{6}$$

For all the data presented here, $\sigma = 0.115\ \mu$s, $\Delta r =$ 30 m, M=16, and $\Delta p = 48$ m.

The radial velocity can be estimated over a maximum possible velocity search space

$$v_{search} = \frac{\lambda}{2T_S} \tag{7}$$

which would be 52.25 m/s, however, for all the data presented here, $v_{search} = 26.125$ m/s was sufficient. The maximum possible velocity search space determines the sampling interval T_S and the range-gate length Δp determines M, the number of samples per velocity estimate.

The estimated velocity is a spatial average of the instantaneous radial velocity $v(r,t)$ over the sensing volume of the pulse where r is the distance along the transmitted beam axis and t denotes the time of the measurement. Various estimators for the radial velocity have been investigated [10, 11, 17, 19, 20, 21]. The Maximum Likelihood (ML) estimate is the velocity that maximizes the log-likelihood function of the data assuming that the radial velocity and the aerosol distribution over the range-gate are constant [17]. The ML estimator has the best performance, i.e., the smallest estimation error. If the signal statistics from multiple pulses are accumulated [10, 11, 17, 19, 20, 21], the quality of the estimates improves and the maximum measurement range increases. The performance of velocity estimators with high-order pulse accumulation for typical surface-layer measurements have also been determined with computer simulations [19] and verified with 2-μm coherent Doppler lidar data [11]. We use the ML estimator with pulse accumulation for all the data considered here.

Velocity estimates $\hat{v}(z,t)$ for $v(z,t)$ are generated for range-gates centered on $z = k\Delta p$ and for a time interval centered on time $t = l\Delta t$ where Δt is the time interval between velocity estimates. For all the data presented here $\Delta t = 1.02$ s. Examples of ML velocity estimates for a vertical-pointing lidar are shown in Fig. 1 and are characteristic of a convective boundary layer.

If the average vertical velocity is zero, the average radial velocity for the non-vertically pointing beams is given by

$$< \hat{v}(r) >= \sin(\theta) < v_x(r) > \tag{8}$$

where $< \cdot >$ denotes ensemble average over the random velocity field and random lidar signal, $< v_x(r) >$ is the component of the average horizontal velocity in the direction of the lidar beam and θ is the angle between zenith and the lidar transmit axis. Profiles of

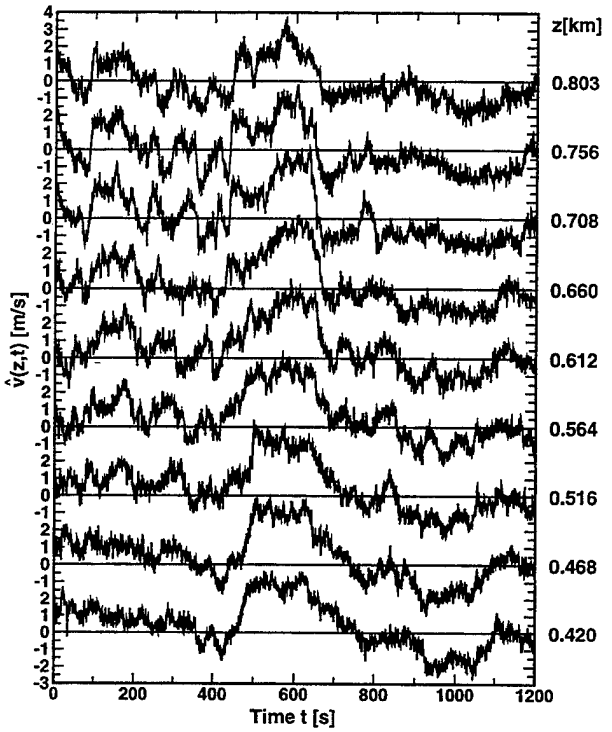

Figure 1: Doppler lidar velocity estimates $\hat{v}(z,t)$ as a function of height z and time t for a vertically-pointing lidar.

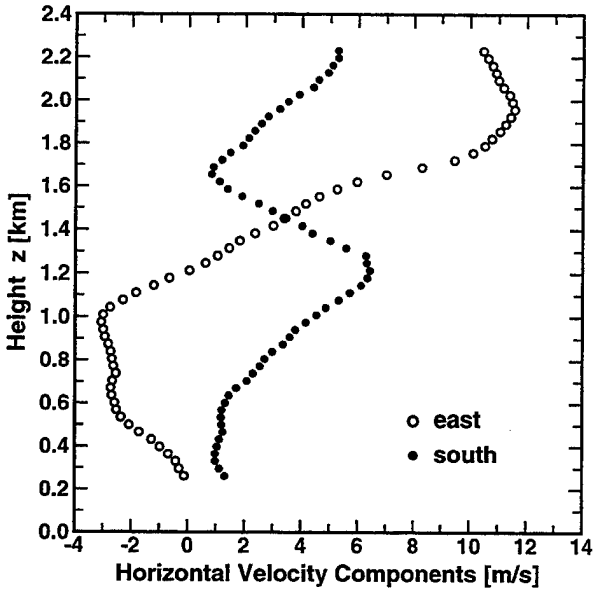

Figure 2: Profiles of average east component and south component of the horizontal velocity.

the east and south component of the horizontal velocity as a function of height $z = r\cos\theta$ are shown in Fig. 2. There is a well defined mixed layer with an inversion height $z_i \approx 1.0$ km. The horizontal wind in the mixed layer is approx 2 m/s which results in few independent samples of the convective structures (see Fig. 1) and a larger sampling error in the turbulent statistics [22].

The statistical description of the Doppler lidar velocity estimates $\hat{v}(R,t)$ is a function of the lidar parameters and the radial velocity $v(z,t)$ along the lidar beam axis. The Doppler frequency shift produced by the moving aerosol particles produce random fluctuations of the lidar signal which is well described as a zero-mean Gaussian random process or "speckle" process [23, 24] because the total optical field collected by the lidar is the superposition of many randomly-phased scattered fields from the aerosol targets in the measurement volume. In addition, the lidar signal from shot to shot is uncorrelated [23, 24]. The lowest level conditional statistic of $\hat{v}(R,t)$ is produced by taking an ensemble average over the random location (random phases of the backscattered laser field) of the illuminated aerosol particles in the range-gate for a given $v(r,t)$, lidar design, aerosol distribution, and atmospheric extinction [18, 24]. This ensemble average is denoted $< \cdot >_a$. The ensemble average $< \hat{v}(R,t) >_a$ is a function of the lidar parameters, the random radial velocity $v(r,t)$, and the atmospheric backscatter.

When the Doppler lidar signal power is high (see Fig. 1), the velocity estimates can be represented as

$$\hat{v}(R,t) =< \hat{v}(R,t) >_a + e(R,t) \qquad (9)$$

where $e(R,t)$ is the estimation error due to the random fluctuations of the lidar signal [17, 18]. The estimation error $e(R,t)$ is clearly visible in Fig. 1 as the rapid fluctuations in the velocity time series. The statistical properties of some common velocity estimators were investigated using computer simulations [18] and assuming a Kolmogorov model for the spatial spectrum of $v(r,t)$. The Probability Density Function (PDF) of the velocity estimates is well described by a two-component Gaussian PDF [18]. For typical atmospheric velocity fields, an excellent approximation for $< \hat{v}(R,t) >_a$ is the pulse-weighted velocity [18]

$$< \hat{v}(R,t) >_a = v_{wgt}(R,t)$$
$$= \frac{1}{\Delta p}\int_{R-\Delta p/2}^{R+\Delta p/2} v_{pulse}(r,t)dr \qquad (10)$$

where

$$v_{pulse}(r,t) = \int_{-\infty}^{\infty} v(x,t)I_n(r-x)dx\ . \qquad (11)$$

The random function $v_{wgt}(R,t)$ is a convolution of the radial velocity $v(R,t)$ with respect to the range R for each fixed time t. The kernel of the convolution is the convolution of the normalized pulse profile $I_n(r)$ with a normalized rectangle of width equal to the range-gate dimensions Δp [18]. The pulse-weighted approximation to Eq. (9) is

$$\hat{v}(R,t) = v_{wgt}(R,t) + e(R,t)\ . \tag{12}$$

Because of the high spatial and temporal resolution of coherent Doppler lidar velocity measurements, they are ideally suited for estimation of the spatial statistics of the atmospheric wind field. For locally stationary atmospheric turbulence, it is standard practice to decompose the velocity components into a mean velocity and a fluctuating or turbulent component [2, 25, 26]. For the radial velocity along the lidar beam axis, the fluctuating component is

$$v'(r,t) = v(r,t) - < v(r) > \tag{13}$$

where the mean velocity $< v(r) >$ is the total ensemble average over a locally stationary time interval.

An important description of the turbulent velocity is the covariance defined by

$$B_v(s,r) =< v'(r-s/2)v'(r+s/2) > \tag{14}$$

where $< \cdot >$ denotes ensemble average over the locally stationary velocity fluctuations, s is the separation of the two observation points, and r is the centroid of the observation points. The variance of the turbulent velocity $v'(r)$ is then

$$\sigma_v^2(r) = B_v(0,r) =< v'(r)^2 >\ . \tag{15}$$

Another important description of the turbulent velocity is the structure function defined by

$$D_v(s,r) =< [v'(r-s/2) - v'(r+s/2)]^2 >\ . \tag{16}$$

For high Reynold's number locally homogeneous and isotropic turbulence [26]

$$D_v(s,r) = C_v \epsilon^{2/3}(r) s^{2/3} \tag{17}$$

for s in the inertial range where $C_v \approx 2$ is the Kolmogorov constant and $\epsilon(\mathrm{r})[\mathrm{m}^2/\mathrm{s}^3]$ is the local energy dissipation rate centered at r. A useful empirical model for the structure function is

$$D_v(s,r) = 2\sigma_v^2(r)\Lambda[s/L_0(r)] \tag{18}$$

where $L_0(r)$ is a measure of the outer scale of turbulence,

$$\Lambda(x) = (\alpha x)^{2/3}\left[1 + (\alpha x)^{\rho}\right]^{-\frac{2}{3\rho}} \tag{19}$$

and

$$\epsilon(r) = \left[2\sigma_v^2(r)/C_v\right]^{3/2} \alpha / L_0(r) \tag{20}$$

is required for equivalence of Eqs. (17) and (18) when $s << L_0$.

The Doppler lidar estimates $\hat{v}'(R,t)$ of the velocity fluctuations are given by

$$\hat{v}'(R,t) = \hat{v}(R,t) - \bar{v}(R) \tag{21}$$

where

$$\bar{v}(R) = N^{-1}\sum_{l=1}^{N} \hat{v}(R, l\Delta t) \tag{22}$$

is an estimate for the mean velocity $< v(R) >$.

The frequency distribution of the power of the velocity fluctuations at range R is described by the temporal spectral density $\Phi_v(f,R)$ where the frequency f is in Hz. An estimate $\hat{\Phi}_v(f,R)$ for $\Phi_v(f,R)$ is given by

$$\hat{\Phi}_v(f,R) = \frac{\Delta t}{N}|P(f/\Delta f, R)|^2 \tag{23}$$

where

$$P(j,R) = \sum_{l=0}^{N-1} \hat{v}'(R, l\Delta t)\exp(-2\pi i j l/N) \tag{24}$$

is the Discrete Fourier Transform (DFT) of $\hat{v}'(R, l\Delta t)$, N is the number of velocity estimates for a range-gate centered at range R, $|\cdot|$ denotes absolute value or modulus, $i = \sqrt{-1}$, $\Delta f = 1/(N\Delta t)$ [Hz] is the frequency resolution, and the maximum frequency or Nyquist frequency $F_N = 0.5/\Delta t$. The integral of the spectrum is equal to the variance of $\hat{v}'(R,t)$, i.e.,

$$\int_{-F_N}^{F_N} \hat{\Phi}_v(f,R)df = \sigma_{\hat{v}'}^2(R)\ . \tag{25}$$

If the estimation error $e(R,t)$ and $v_{wgt}(R,t)$ are statistically independent [see Eq. (12)]

$$\sigma_{\hat{v}'}^2(R) = \sigma_{v_{wgt}}^2(R) + \sigma_e^2(R)\ . \tag{26}$$

For locally isotropic atmospheric turbulence, the temporal spectral density for a point measurement of any component v' of the velocity fluctuations satisfies the Kolmogorov scaling in the inertial range [26], i.e.,

$$\Phi_v(f,R) \propto [\epsilon(R)U(R)]^{2/3} f^{-5/3} \tag{27}$$

where $U(R)$ is the average horizontal wind speed at range R along the transmit axis.

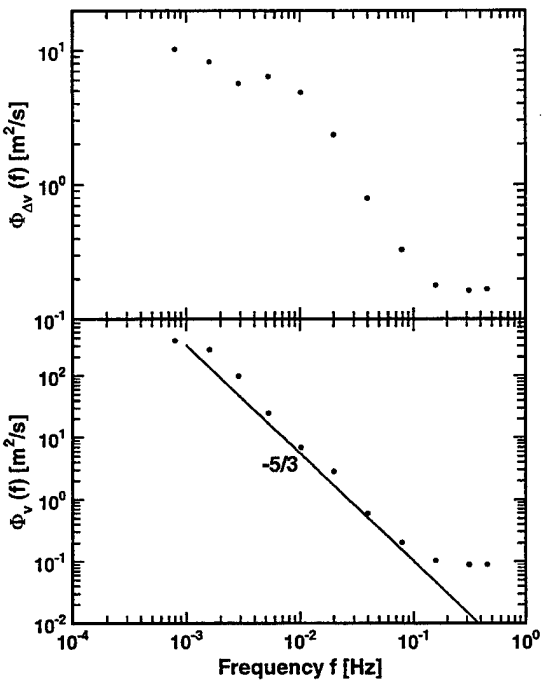

Figure 3: Temporal spectrum $\Phi_v(f)$ of radial velocity and temporal spectrum $\Phi_{\Delta v}(f)$ of the difference of velocity estimates for range gates with a separation of 48 m using the vertically-pointed lidar data in Fig. 1. The Kolmogorov -5/3 slope is shown as a solid line.

An example of a velocity spectrum is shown in the bottom panel of Fig. 3 [the spectral estimates Eq. (23) were averaged over the range-gates and also over frequency to reduce the statistical variability]. The velocity spectrum agrees with Eq. (27) for the Kolmogorov scaling of $f^{-5/3}$. The vertical velocity spectrum of Fig. 3 is typical of a convective boundary layer and indicates an outer scale at low frequency. The constant level at high frequency describes the uncorrelated estimation error $e(R,t)$ of the Doppler lidar velocity estimates [10]. An unbiased estimate $\hat{\sigma}_e^2(R)$ for the variance of the estimation error $e(R,t)$ [see Eq. (12)] is

$$\hat{\sigma}_e^2(R) = \frac{1}{(N/2 - j_T + 1)\Delta t} \sum_{j=j_T}^{N/2} \hat{\Phi}_v(j\Delta f, R) \quad (28)$$

where j_T is the threshold index that separates the wind field spectral component at low frequency from the constant estimation error component. The threshold frequency was chosen as 0.2 Hz for all the data analysis presented here.

The statistics of the difference of velocity fluctuations for two different range-gates

$$\Delta\hat{v}'(R_1, R_2, t) = \hat{v}'(R_1, t) - \hat{v}'(R_2, t) \quad (29)$$

is important for understanding the estimates of the velocity structure function. If Eq. (12) is valid

$$\Delta\hat{v}'(R_1, R_2, t) = \Delta v'_{wgt}(R_1, R_2, t) + \Delta e(R_1, R_2, t)\,, \quad (30)$$

$$\Delta v'_{wgt}(R_1, R_2, t) = v'_{wgt}(R_1, t) - v'_{wgt}(R_2, t)\,, \quad (31)$$

$$v'_{wgt}(R, t) = v_{wgt}(R, t) - \bar{v}(R, t)\,, \quad (32)$$

and

$$\Delta e(R_1, R_2, t) = e(R_1, t) - e(R_2, t)\,. \quad (33)$$

The variance $\sigma^2_{\Delta v}(R_1, R_2)$ is given by

$$\sigma^2_{\Delta v}(R_1, R_2) = D_{wgt}(R_1 - R_2, R_0) + \sigma^2_{\Delta e}(R_1, R_2) \quad (34)$$

where $R_0 = (R_1 + R_2)/2$,

$$D_{wgt}(R_1 - R_2, R_0) = < [v'_{wgt}(R_1, t) - v'_{wgt}(R_2, t)]^2 > \quad (35)$$

and $\sigma^2_{\Delta e}(R_1, R_2)$ is the variance of $\Delta e(R_1, R_2, t)$. If the two components $\Delta e(R_1, t)$ and $\Delta e(R_2, t)$ were statistically independent, then $\sigma^2_{\Delta e}(R_1, R_2) = \sigma^2_e(R_1) + \sigma^2_e(R_1)$ and the unbiased estimate $\hat{\sigma}^2_e(R)$ Eq. (28) could be used to estimate $\sigma^2_{\Delta e}(R_1, R_2)$. However, for adjacent range-gates, the two components $\Delta e(R_1, t)$ and $\Delta e(R_2, t)$ are correlated and an unbiased estimate for $\sigma^2_{\Delta e}(R_1, R_2)$ is produced from the spectrum of the difference of velocity estimates. The estimate $\hat{\Phi}_{\Delta v}(f, R_1, R_2)$ for the temporal spectral density of the difference of velocity fluctuations $\Delta\hat{v}'(R_1, R_2, t)$ is given by Eqs. (23) and (24) with $\hat{v}'(R, t)$ replaced with $\Delta\hat{v}'(R_1, R_2, t)$. An example of the spectrum of the difference of velocity fluctuations is shown in the top panel of Fig. 3 (the spectral estimates were averaged over the range bins and also over frequency to reduce the statistical variability). The constant level at high frequency is consistent with the assumption of temporal statistical independence of the estimation error difference $\Delta e(R_1, R_2, t)$ and the velocity fluctuation difference $v'_{wgt}(R_1, t) - v'_{wgt}(R_2, t)$. An unbiased estimate $\hat{\sigma}^2_{\Delta e}(R_1, R_2)$ is given by

$$\hat{\sigma}^2_{\Delta e}(R_1, R_2) = \frac{1}{(N/2 - j_T + 1)\Delta t} \sum_{j=j_T}^{N/2} \hat{\Phi}_{\Delta v}(j\Delta f, R_1, R_2) \quad (36)$$

where j_T is the threshold index that separates the wind field spectral component at low frequency from the constant component at high frequency. The threshold frequency was chosen as 0.2 Hz for all the data analysis presented here.

An estimate for the velocity structure function of Doppler lidar velocity estimates is given by

$$\hat{D}_{v_{wgt}}(R_1 - R_2, R_0) = N^{-1} \sum_{l=1}^{N-1} [\hat{v}'(R_1, l\Delta t) - \hat{v}'(R_2, l\Delta t)]^2 - \hat{\sigma}^2_{\Delta e}(R_1, R_2) \,. \quad (37)$$

This estimate is a true spatial estimate and does not require Taylor's frozen hypothesis to map a temporal statistic to a spatial statistic. In practice, these estimates are averaged over a few range-gates.

When Eq. (10) is valid for the average Doppler lidar velocity, the ensemble average of $\hat{D}_{v_{wgt}}(R_1 - R_2, R_0)$ is $D_{wgt}(R_1 - R_2, R_0)$ and because $v_{wgt}(R,t)$ is given in terms of the convolution of $v(R,t)$, the structure function $D_{wgt}(s,R)$ can be written in terms of the structure function for in situ point measurements $D_v(s,R)$ [18], i.e.,

$$D_{wgt}(s,R) = 2\sigma_v^2(R) G(s/\Delta p, \mu, \chi) = C_v[\epsilon(R) L_0(R)/\alpha]^{2/3} G(s/\Delta p, \mu, \chi) \quad (38)$$

where

$$G(m,\mu,\chi) = \int_{-\infty}^{\infty} F(x,\mu) \Big[\Lambda(\chi|m-x|) - \Lambda(\chi|x|)\Big] dx \,, \quad (39)$$

$$F(x,\mu) = \frac{1}{2\sqrt{\pi}\mu}\Big\{\exp[-\mu^2(x+1)^2] + \exp[-\mu^2(x-1)^2]\Big\} + \frac{x}{2}\Big\{\mathrm{erf}[\mu(x+1)] + \mathrm{erf}[\mu(x-1)] - 2\,\mathrm{erf}(\mu x)\Big\} + \mathrm{erf}[\mu(x+1)]/2 - \mathrm{erf}[\mu(x-1)]/2 - \frac{1}{\sqrt{\pi}\mu}\exp[-\mu^2 x^2] \quad (40)$$

$\mu = \sqrt{2\ln 2}\Delta p/\Delta r$, $\chi = \Delta p/L_0(R)$, and

$$\mathrm{erf}(z) = \frac{2}{\sqrt{\pi}} \int_0^z \exp(-t^2) dt \quad (41)$$

is the error function.

An estimate for the point velocity structure function is produced by minimizing the mean-square-error between $D_{wgt}(s,R)$ and $\hat{D}_{v_{wgt}}(s,R)$ with respect to the parameters $(\epsilon, L_0, \alpha, \rho)$ in Eq. (38).

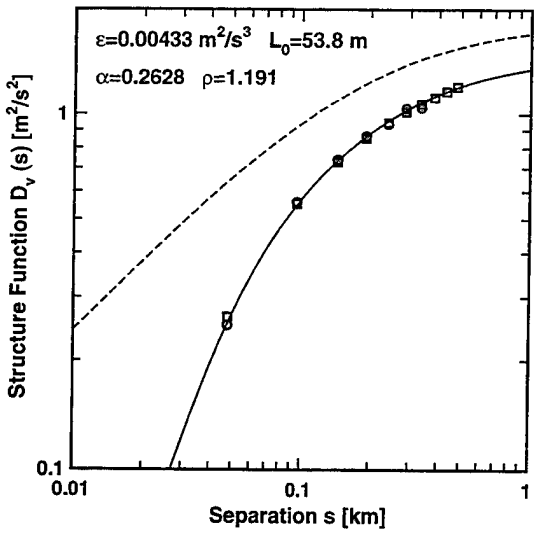

Figure 4: Doppler lidar estimates for the velocity structure function (o) Eq. (37) using the vertically-pointing lidar data in Fig. 1, the best-fit model (____) Eq. (38), the velocity structure function $D_v(s,R)$ for point measurements (- - -) Eq. (18) based on the best-fit parameters $(\epsilon, L_0, \alpha, \rho)$, and the results from computer simulation (□).

The structure function estimate $\hat{D}_{wgt}(s,R)$ Eq. (37) using all the data in Fig. 1 is shown in Fig. 4 as well as the best fit $D_{wgt}(s,R)$ Eq. (38), the corresponding structure function $D_v(s,R)$ from Eq. (18), and the results from ideal computer simulation assuming the velocity statistics are given by $D_v(s,R)$. The computer simulations are described in Appendix C of Ref. [18] where coherent Doppler lidar data is generated with velocity fluctuations $v'(z,t)$ that have a Gaussian PDF described by $D_v(s,R)$ and with the signal statistics from the data in Fig. 1. The simulated data is then processed with the same algorithms that were applied to the data. The best fit model $D_{wgt}(s,R)$ and the results of the simulation agree very well with the estimated structure function. The true structure function $D_v(s,R)$ that would result from ideal in situ measurements is more than a factor of two higher at small separations s. This illustrates the impact of the spatial filtering of the random velocity $v(z,t)$ by the finite extent of the lidar pulse.

The structure function analysis for the high-shear region of Fig. 3 is shown in Fig. 5. Here, the random velocity $v(z,t)$ for the simulation of the Doppler lidar data is generated as a zero mean Gaussian random process for the turbulent fluctuations $v'(z,t)$ plus a linear shear in the radial velocity of 20.0 m/s/km which corresponds to a shear of the horizontal veloc-

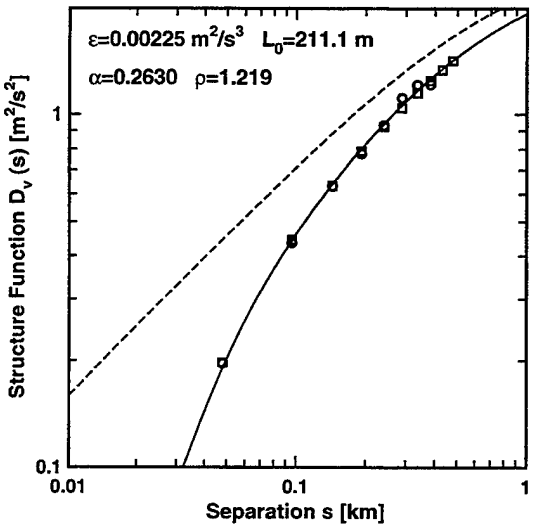

Figure 5: Doppler lidar estimates for the velocity structure function (o) Eq. (37) for the high-shear region (see Fig. 3, range between 1.62 and 2.10 km or altitude between 1.14 and 1.48 km), the best-fit model (____) Eq. (38), the velocity structure function $D_v(s,R)$ for point measurements (- - -) Eq. (18) based on the best-fit parameters $(\epsilon, L_0, \alpha, \rho)$, and the results from computer simulation (□).

ity component of 28.3 m/s/km. In this high-shear regions, the velocity structure function is well described by Eq. (18).

An unbiased estimate $\hat{\sigma}^2_{v_{wgt}}(R)$ for the variance of the Doppler lidar velocity fluctuations $\hat{v}'(R)$ is given by

$$\hat{\sigma}^2_{v_{wgt}}(R) = N^{-1} \sum_{l=1}^{N-1} [\hat{v}'(R, l\Delta t)^2 - \hat{\sigma}^2_e(R)] \qquad (42)$$

where $\hat{\sigma}^2_e(R)$ [see Eq. (28)] is the unbiased estimate for the variance of $e(R,t)$. If the pulse-weighted approximation $v_{wgt}(r,t)$ is valid, $< \hat{\sigma}^2_{v_{wgt}}(R) > = \sigma^2_{v_{wgt}}(R) = B_{wgt}(0,R)$ and [18]

$$B_{wgt}(0,R) = \sigma^2_v(R) K(\mu, \chi) \qquad (43)$$

where

$$K(\mu,\chi) = 2 \int_0^\infty F(x,\mu)[1 - \Lambda(\chi x)]dx \qquad (44)$$

and $\chi = \Delta p / L_0$. An unbiased estimate for the variance $\sigma^2_v(R)$ of the velocity fluctuations $v'(R)$ is given by

$$\hat{\sigma}^2_v(R) = \hat{\sigma}^2_{v_{wgt}}(R) / K(\mu, \chi) \, . \qquad (45)$$

The scaling factor $K(\mu,\chi)$ has a weak dependence on the parameter $\chi = \Delta p / L_0$ when $\chi < 1$. The estimate $\hat{\sigma}^2_v(R)$ is equivalent to an in situ point estimate of $\sigma^2_v(R)$ whenever $\Delta p < L_0(R)$ or when accurate estimates of L_0 can be extracted from the data.

Profiles of energy dissipation rate $\epsilon(R)$ can be produced from Doppler lidar estimates $\hat{D}_v(s,R)$ Eq. (37) provided that the pulse-weighted approximation $v_{wgt}(r,t)$ is valid [see Eq. (10)], or equivalently, that the theoretical calculation Eq. (38) for the measured structure function is valid. For a typical convective boundary layer, $\epsilon(R)$ has a weak dependence on the range R. Estimates $\hat{\epsilon}(R)$ for $\epsilon(R)$ are produced by minimizing the mean-square-error between the structure function estimates $\hat{D}_v(s,R)$ Eq. (37) and the pulse-weighted approximation $\hat{D}_{wgt}(s,R)$ Eq. (38) over a sliding range window, which was chosen as 340 m for the results presented here.

The mixed-layer parameters have been estimated from profiles of vertical velocity variance [25, 27]. The profiles of vertical velocity variance have been modeled as [28]

$$\sigma^2_w(z) = 1.44 w_*^2 \times \left[(z/z_i)^{2/3} (1 - 0.7 z/z_i)^2 + \frac{10}{9} \frac{u_*^2}{w_*^2} \right] \qquad (46)$$

where w_* is the convective velocity scale (related to the surface heat-flux), z_i is the inversion height, and u_* is the friction velocity which is related to momentum flux. The profiles of energy-dissipation rate have been approximated by [28]

$$\epsilon(z) = \frac{w_*^3}{z_i} \left[0.75 + 1.84 (z/z_i)^{-2/3} (1.0 - z/z_i)^2 \frac{u_*^2}{w_*^2} \right]^{3/2} . \qquad (47)$$

In Fig. 6, profiles of vertical velocity variance σ^2_w for a convective boundary layer with a vertically-pointing lidar beam are compared with the best-fit model Eq. (46). The parameters of this best-fit model are used to predict the profile of energy-dissipation rate ϵ using Eq. (47). The inversion height z_i from the best fit agrees with the location of the beginning of the shear layer (see Fig. 3). The error bars for the vertical velocity variance are large which reflects the skewness of the vertical velocity and a low number of independent samples [22] (see Fig. 1). A longer data set is required to produce more independent samples of the vertical velocity. The agreement of the data and model for $\epsilon(z)$ is poor. This may be due to the high-shear layer at the top of the mixed layer or the

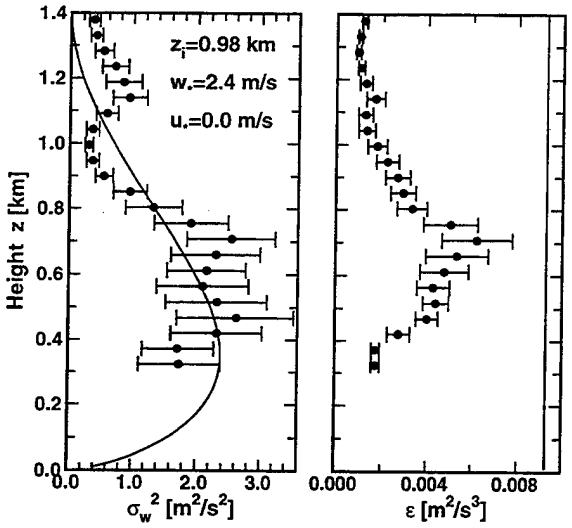

Figure 6: Profiles of vertical velocity variance σ_w^2 and energy dissipation rate ϵ with 1-σ error bars for data from a vertically-pointed lidar (see Fig. 1), the best-fit model (____) Eq. (46), and the resulting predictions of Eq. (47) (____).

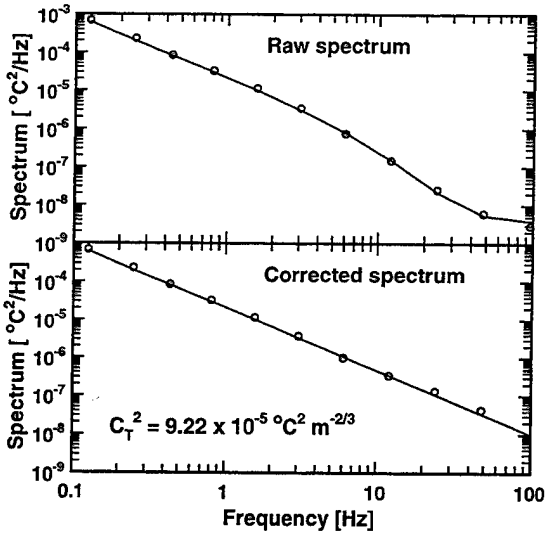

Figure 7: Spectrum of temperature fluctuations from an instrumented kite platform at a height of 300 m for 128 s of data, the best-fit theoretical model (___), and the spectra with corrections for the probe instrument response.

anisotropy of the wind field statistics, i.e., the magnitude of the structure function in the vertical beam is smaller than the structure function for the horizontal wind components. Since the outer scale L_0 is larger than the measurement volume (Δr and Δp), the estimates for the parameters of the structure functions should be accurate.

Instrumented Kite Platforms

The use of kites for atmospheric research dates back well over two hundred years. Atmospheric research using kites peaked sharply around the turn of the twentieth century, with near-daily observations being made at many observatories throughout the world. Kite-borne technology continues to have a well-defined niche in meteorological research [14, 15, 16]. There are definite advantages provided by having an instrumented kite flying for extended periods a few kilometers above the earth's surface that cannot be provided by any other means. This statement can be made even stronger if one considers that the kite can be used as a "sky hook" and the kite tether as a means of guiding a wind-driven, instrumented platform rapidly up and down the tether under radio control. Such a platform, or WindTRAM, provides a means of profiling a wide variety of atmospheric quantities simultaneously, rapidly, quasi-continuously, and at relatively low cost. Moreover, such systems gather data from ground level up to many kilometers, i.e., well into the free atmosphere. The totality of this region is difficult to access more-or-less continuously by any other technique. Tethered balloons have difficulty reaching altitudes above a kilometer or two and aircraft have obvious difficulties in covering the lowest heights. The only other possibility is to use a series of non-tethered balloonsondes that pass once through the region but are then typically unrecovered and the sensors lost. Quasi-continuous sampling using balloonsondes would, therefore, be exceedingly expensive.

The ability of kite-borne or TRAM-borne instruments [14, 15, 16] to continuously obtain data at one altitude for extended periods is important for studying the dynamic properties of the atmosphere. It is also feasible to use multiple sensors suspended below the kite or KiteTRAM to measure the three-dimensional properties of dynamic processes such as atmospheric turbulence.

High-speed measurement of turbulent temperature fluctuations were produced using an inexpensive thermo-couple probe and recorded on a small onboard storage device. Temperature samples were obtained every 2.5 milliseconds for a period of approximately two minutes at an altitude of 300 m. A power spectrum of 128 seconds of data is shown in Fig. 7 along with a best-fit theoretical turbu-

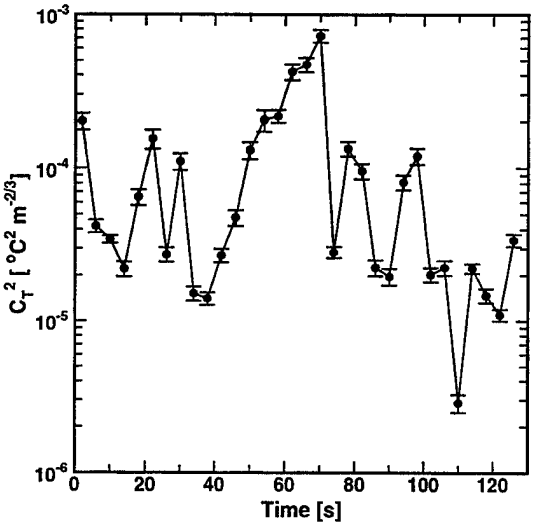

Figure 8: The intermittency of C_T^2 using 4 sec of data for each estimate. The 1-σ error bars calculated from the mean-square-error of the best-fit model spectrum are also shown.

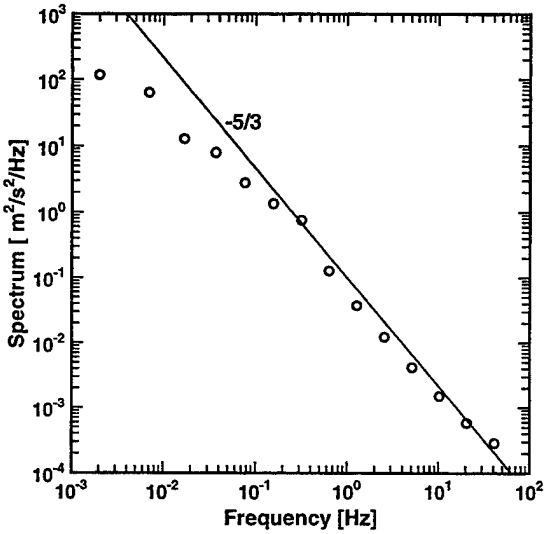

Figure 9: The velocity spectrum from measurements using a pitot-tube at a height of 50 m. The -5/3 Kolmogorov slope is also shown.

lence spectrum modeled as a Kolmogorov power law $Kf^{-5/3}$ multiplied by the frequency response of the probe $(1+f^2/f_0^2)^{-1}$ with $f_0 \approx 10$ Hz. The spectrum with the correction for the probe response is shown in the bottom panel of Fig. 7. Note the close correspondence between the actual data points and the theoretical curve. The level of the spectrum K (estimated for frequencies less than 16 Hz.) and the average flow velocity of 5 m/s produce an estimate for the average C_T^2 which is shown in the bottom panel of Fig. 7. Applying the same spectral analysis to consecutive 4-second sections of data produce the high temporal resolution estimates of C_T^2 shown in Fig. 8. The 1-σ error bars are produced from the mean-square error of the fit assuming that these short sections of data are locally stationary with statistically independent spectral estimates. These large random variations in C_T^2 have been called "global intermittency" [29] and are typical of boundary-layer turbulence.

Turbulent velocity fluctuations can also be measured with a pitot-tube oriented into the direction of the wind using a vane. A velocity spectrum is shown in Fig. 9. The level of the velocity spectrum defines the energy dissipation rate ϵ which can be used to estimate the inner scale of turbulence. The temperature and velocity spectrum provide important information about the atmosphere that is crucial for such problems as imaging, electromagnetic propagation, communications, target tracking, and understanding atmospheric processes.

This work was supported by the National Science Foundation, the Army Research Office, and the National Aeronautics and Space Administration.

References

[1] M. J. Post and R. E. Cupp, "Optimizing a pulsed Doppler lidar," Appl. Opt., **29**, 4145-4158, (1990).

[2] T. Gal-chen, M. Xu, and W. L. Eberhard, "Estimations of atmospheric boundary layer fluxes and other turbulence parameters from Doppler lidar data," J. Geophys. Res., **97**, 409-418, (1992).

[3] R. M. Huffaker and R. M. Hardesty, "Remote sensing of atmospheric wind velocities using solid-state and CO_2 coherent laser systems," Proc. IEEE, **84**, 181-204, (1996).

[4] S. D. Mayor, D. H. Lenschow, R. L. Schwiesow, J. Mann, C. L. Frush, and M. K. Simon, "Validation of NCAR 10.6-μm CO_2 Doppler lidar radial velocity measurements and comparison with a 915-MHz profiler," J. Atmos. Oceanic Technol., **14**, 1110-1126, (1997).

[5] M. J. Kavaya, S. W. Henderson, J. R. Magee, C. P. Hale, and R. M. Huffaker, "Remote wind profiling with a solid-state Nd:YAG coherent lidar system," Opt. Let., **14**, 776-778, (1989).

[6] S. W. Henderson, C. P. Hale, J. R. Magee, M. J. Kavaya, and A. V. Huffaker, "Eye-safe coherent laser radar system at 2.1-μm using Tm,Ho:YAG lasers," Opt. Lett., **16**, 773-775, (1991).

[7] S. W. Henderson, P. J. M. Suni, C. P. Hale, S. M. Hannon, J. R. Magee, D. L. Bruns, and E. H. Yuen, "Coherent laser radar at 2-μm using solid-state lasers," IEEE Trans. Geo. Remote Sensing **31**, 4-15, (1993).

[8] J. G. Hawley, R. Targ, S. W. Henderson, C. P. Hale, M. J. Kavaya, and D. Moerder, "Coherent launch-site atmospheric wind sounder: theory and experiment," Appl. Opt., **32**, 4557-4568, (1993).

[9] S. M. Hannon and J. A. Thomson, "Aircraft wake vortex detection and measurement with pulsed solid-state coherent laser radar," J. Mod Opt., **41**, 2175-2196, (1994).

[10] R. Frehlich, S. Hannon, and S. Henderson, "Performance of a 2-μm coherent Doppler lidar for wind measurements," J. Atmos. Oceanic Technol., **11**, 1517-1528, (1994).

[11] R. Frehlich, S. Hannon, and S. Henderson, "Coherent Doppler lidar measurements of winds in the weak signal regime," Appl. Opt., **36**, 3491-3499, (1997).

[12] S. M. Hannon and S. W. Henderson, "Wind measurement applications of coherent lidar," Rev. Laser Eng., **23**, 124-130, (1995).

[13] R. Frehlich, S. Hannon, and S. Henderson, "Coherent Doppler lidar measurements of wind field statistics," Boundary-Layer Meteorol., in press.

[14] B. B. Balsley, J. B. Williams, G. W. Tyrrell, and C. L. Balsley, "Atmospheric research using kites: Here we go again!," Amer. Meteor. Soc., **73**, 17-29, (1992).

[15] B. B. Balsley, J. W. Birks, M. L. Jensen, K. G. Knapp, J. B. Williams, and G. W. Tyrrell, "Vertical profiling of the atmosphere using high-tech kites," Environmental Science and Technology, **28**, 422A-426A, (1994).

[16] B. B. Balsley, M. L. Jensen, and R. G. Frehlich, "The use of state-of-the-art kites for profiling the lower atmosphere," Boundary-Layer Meteorol., in press.

[17] R. G. Frehlich and M. J. Yadlowsky, "Performance of mean frequency estimators for Doppler radar and lidar," J. Atm. Ocean. Tech., **11**, 1217-1230, (1994).

[18] R. G. Frehlich, "Effects of wind turbulence on coherent Doppler lidar performance," J. Atmos. Oceanic Technol., **14**, 54-75, (1997).

[19] R. G. Frehlich, "Simulation of coherent Doppler lidar performance in the weak signal regime," J. Atmos. Oceanic Technol., **13**, 646-658, (1996).

[20] B. J. Rye and R. M. Hardesty, " Discrete spectral peak estimation in incoherent backscatter heterodyne lidar. I. Spectral accumulation and the Cramer-Rao lower bound," IEEE Trans. Geo. Sci. Remote Sensing, **31**, 16-27, (1993).

[21] B. J. Rye and R. M. Hardesty, "Discrete spectral peak estimation in incoherent backscatter heterodyne lidar. II. Correlogram accumulation," IEEE Trans. Geo. Sci. Remote Sensing, **31**, 28-35, (1993).

[22] D. H. Lenschow, J. Mann, and L. Kristensen, "How long is long enough when measuring fluxes and other turbulent statistics?", J. Atmos. Oceanic Technol., **11**, 661-673, (1993).

[23] J. H. Churnside and H.T. Yura, "Speckle statistics of atmospherically backscattered laser light," Appl. Opt., **22**, 2559-2565, (1983).

[24] R. G. Frehlich, "Coherent Doppler lidar signal covariance including wind shear and wind turbulence," Appl. Opt., **33**, 6472-6481, (1994).

[25] R. B. Stull, *An Introduction to Boundary Layer Meteorology* Kluwer Academic Publishers, (1988).

[26] A. S. Monin and A. M. Yaglom, *Statistical Fluid Mechanics: Mechanics of Turbulence*, Volume 2, MIT Press, (1975).

[27] W. M. Angevine, R. J. Doviak, and Z. Sorbjan, "Remote sensing of vertical velocity variance and surface heat flux in a convective boundary layer", J. Appl. Meteorol., **33**, 977-983, (1994).

[28] L. Kristensen, D. H. Lenschow, P. Kirkegaard, and M. Courtney, "The spectral velocity tensor for homogeneous boundary-layer turbulence," Boundary-Layer Meteorol., **47**, 149-193, (1989).

[29] L. Mahrt, "Intermittency of atmospheric turbulence," J. Atmos. Sci. **46**, 79-95 (1989).

Functional Description of a "Closed-Loop", "Environmentally-Adaptive", Electromagnetic/Electro-optical Sensor System

Commander David G. Markham, USN
Naval Research Laboratory, 4555 Overlook Avenue, S.W.
Washington, DC 20375-5320

Abstract

This paper describes the functional components of a hypothetical, "closed-loop", "environmentally-adaptive", electromagnetic/electro-optical (EM/EO) sensor system. Those components include: a meteorological data module for the input/ingest, assimilation, and analysis of atmospheric measurements; terrain, EM refractivity, EO background, EM propagation/EO transmission, and climatological data bases; a propagation/-transmission assessment module for the modeling and characterization of EM/EO conditions; a system performance prediction module, which includes sensor and target characteristics, for evaluating the dynamic performance of EM/EO sensors against potential target plat-forms; a performance monitoring module for real-time system assessment and "clutter/noise" measurement; and, a decision aids module for the display and output of knowledge-based products to be used in operational planning, tactical decision making, and system employment optimization. In the "environmentally-adaptive" mode, realtime measurements of background "clutter/noise" and "through-the-sensor" propagation/transmission conditions will be compared to predicted system performance characteristics, and "corrections" automatically applied in order to optimize system operating parameters. The goal is, with sufficient compute power, to be able to update and optimize the EM/EO sensor system's performance automatically "sweep-to-sweep" or "scan-to-scan".

1. INTRODUCTION

The modern battlespace is a very complex environment, where high technology weapons and increasingly sophisticated delivery platforms (both manned and unmanned) are capable of significant destructive power with greatly improved precision. While these new weapons/platforms may offer warfighters considerable advantages, like their predecessors they are all still limited, or affected, by the environment in which they operate. For many, the single biggest technical challenge of new weapon/platform programs is the development of an "all weather" capability (i.e., the ability to carry out the mission in all conditions, or minimize the effects, of the environment on system performance).

Many of these new weapons/platforms employ electromagnetic (EM) and/or electro-optical (EO) sensors. Because EM/EO sensors "look" through the atmosphere, they are impacted by variability (in both space and time) of atmospheric conditions, such as refractivity and extinction. Existing (or so-called "legacy") sensor systems are often designed based on empirical or statistical averages (e.g., the "standard atmosphere") rather than using *in-situ* or on-scene characterizations and/or assessments of the "real" atmosphere. In dynamic environments where conditions are in a state of flux, real-time measurements can provide the difference between success and failure.

In most cases, legacy capabilities are also built as stand-alone or "stovepiped" systems; they are not fully integrated with the supported weapons system and/or host platform. There are some notable exceptions to this pattern, however; for example, the Aegis Combat System on board the U.S. Navy's *Ticonderoga*-class cruisers and *Arleigh Burke* destroyers has a powerful radar, the AN/SPY-1, closely integrated with its weapons control system. On the other hand, the AN/SPY-1 suffers from anomalous propagation conditions and other atmospheric effects like all radars, but has no built-in or "integrated" means of assessing the impact of those conditions on its performance in real-time.

Current EM/EO sensor systems were developed with a particular weapon system and/or platform type in mind. The data these sensors collect are not easily transmitted to, and assimilated by, other weapons/platforms. Yet, data fusion (i.e., the combining of different types of data such that the "sum of the parts" is greater than any single type of data alone) remains a key objective of battlespace management and situational awareness. In order to fuse data from different sensors, those data must

be brought together into a single processor or data management system and have compatible formats. This remains an elusive goal due to technical and programmatic restrictions which constrain legacy capabilities to be sensor/system/platform specific.

Finally, most EM/EO sensor systems are not fully integrated with other important capabilities required for real-time system performance optimization and tactical decision making. As a result, accomplishing such tasks often requires a great deal of "human-machine interfacing" (HMI). In general, the entire process requires several hours and the use of numerous hardware/software systems external to the sensor.

Future sensors and weapon systems, as well as related systems such as the information-intensive Cooperative Engagement Capability (CEC), will require the ability to characterize the environment on-scene; a high degree of system integration; near-continuous data fusion; and, automation in order to reduce HMI. In addition, concepts like the ability of the system to "adapt" interactively to its physical and operational environments will be possible in the near future with improvements in measurement, modeling, and data processing systems. These improvements will be facilitated and enhanced by the development of data inversion (or "through-the-sensor") techniques.

2. NEED AND POTENTIAL BENEFITS

It is clear from a review of key U.S. Defense Department requirements documents, such as the Joint Warfighting Science and Technology Plan (JWSTP) and Defense Technology Area Plan (DTAP), that several critical Defense Technology Objectives (DTOs) specify capabilities like those described herein. A number of those same DTOs are supported by funded Advanced Technology Demonstrations (ATDs) or Advanced Concept Technology Demonstrations (ACTDs). One such DTO/ATD proposes to develop and demonstrate passive infrared systems capable of "autonomous and continuous wide-area volume search, detection, tracking, and identification of low-flying threat aircraft." Another DTO, which does not have ATD or ACTD support, would "develop and validate the models which translate the measured or forecasted state of the atmosphere into terms that define the impact of the atmosphere on specific combat systems and operations." Not only DTOs, but high priority Service S&T requirements (e.g., from the Navy's S&T Requirements Guidance or STRG), as well as some Operational Requirements Documents (ORDs) and Mission Needs Statements (MNS), reinforce the need for an "end-to-end" capability to improve warfighting effectiveness by incorporating the environment.

The autonomous operation of EM/EO sensors, or truly integrating atmospheric effects on those sensors, will require a total "system" approach. Potential benefits of such an approach may include the ability in real-time to characterize or assess system performance in both the physical and operational environments; to take the results of that assessment and rapidly or continuously optimize the performance of the system; and, using either real-time assessments or predicted system performance characteristics, for operational planning or to make system/platform employment decisions.

3. "END-TO-END" SENSOR SYSTEM

The hypothetical EM/EO sensor system described in this paper has six key modules. Each module has "inputs" and "outputs" that connect it to other modules. Taken together, all six modules with the various "inputs" and "outputs" comprise an "end-to-end" system.

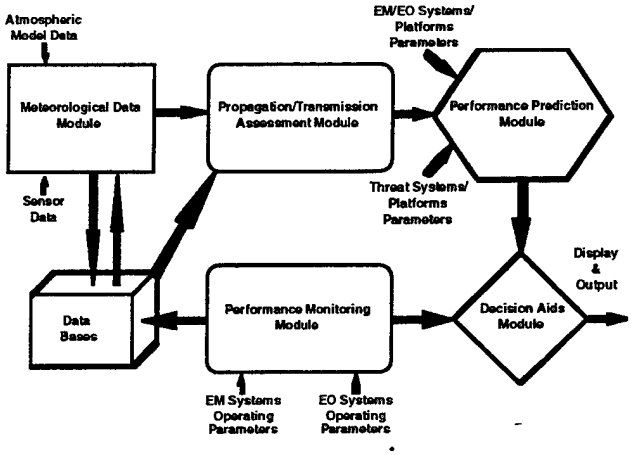

Figure 1. Functional Diagram of an "End-to-End" EM/EO Sensor System

A. Meteorological Data Module

The Meteorological Data Module enables the input/ingest of data from atmospheric forecast models and meteorological sensors into the system. Gridded output from high resolution mesoscale atmospheric forecast models, whether on-scene or remote, could be ingested and used to generate

"synthetic" profiles or cross-sections of EM/EO conditions. Point, single or multiple profiles, or volumetric measurements could be input from *in-situ* and remote sensors, such as sondes (balloon-borne, dropped, or rocket launched), radiometers, lidars, aerosol spectrometers, or nephelometers. Those data are then assimilated or fused to provide a real-time, three-dimensional (3-D), dynamically consistent characterization of the physical environment. The primary output products of this module, local 3-D analyses and forecasts of EM refractivity and EO extinction, would be available for input into the Propagation/Transmission Assessment Module. In addition, appended or fused profiles of EM/EO parameters of tactical interest (e.g., air temperature, humidity, particle size distribution, etc.) would be merged with climatological data and stored in a data base for potential re-use later by the system.

B. Data Bases

The Data Bases module performs the function of both a central repository for climatological data and for the storage of data collected on-scene by the host platform. The types of data, which the system requires in order to support the other modules, may include digitized terrain; climatological or observed tactical atmospheric parameters; climatological EM refractivity and EO background conditions; and, climatological or observed EM propagation and EO transmission loss. Appended real or "synthetic" observations of tactical atmospheric parameters are obtained from the Meteorological Data Module. Measured EM propagation and EO transmission loss are input from the Performance Monitoring Module (derived from EM/EO sensor data using "through-the-sensor" inversion techniques). Potential outputs from this module include: atmospheric climatology (gridded fields, profiles, or point data) for use by the Meteorological Data Module in the absence of direct measurements; and, digitized terrain, EM refractivity/EO background conditions, and EM propagation/EO transmission loss for use by the Propagation-/Transmission Assessment Module.

C. Propagation/Transmission Assessment Module

The Propagation/Transmission Assessment Module is comprised of algorithms for modeling and characterizing EM/EO conditions. It takes the output of the Meteorological Data Module (i.e., 3-D analyses and forecasts of EM refractivity and EO extinction), extracts "missing" information from the Data Bases module, and then calculates either EM propagation or EO transmission loss. In addition to EM refractivity and EO extinction conditions, propagation/transmission algorithms require information on the terrain within the model domain (when modeling over land). In the absence of "real" EM refractivity and EO extinction, climatological data can be used. If "derived" propagation/transmission loss data are available, they could be compared to the analyzed/predicted loss. The main output from this module, analyses or forecasts of 3-D propagation/transmission conditions, is provided to the Performance Prediction Module.

D. Performance Prediction Module

The Performance Prediction Module's purpose is, as the name implies, to evaluate or predict the performance of EM/EO sensors. The module has two primary inputs: (1) analyses/forecasts of 3-D propagation/transmission conditions from the Propagation/Transmission Assessment Module; and, (2) operating parameters for EM/EO sensors and potential threat systems/platforms. Integral to this module are friendly and threat systems data bases or "models." These data, along with the estimated or measured operating parameters (e.g., frequency or wavelength, radar cross-section or target contrast, etc.), are used to compute the "figure of merit" corresponding to a specified probability of detection for a particular sensor system. Output from the Performance Prediction Module, either an evaluation (i.e., "nowcast") or a prediction (i.e., forecast) of EM/EO sensor system performance, is provided to the Decision Aids Module.

E. Performance Monitoring Module

The Performance Monitoring Module performs an essential, although often overlooked, function by monitoring the performance, and reporting the status, of EM/EO sensors. In addition to reporting the usual system performance parameters, such as detection range, this module would collect "clutter/noise" data for use in the "environmentally-adaptive" mode of system operation (see paragraph 4 below). Collectively, data from this module represents a characterization of the operational environment and can be exploited in real-time using "through-the-sensor" techniques to derive actual (or "observed") EM propagation/EO transmission

conditions for archiving in the Data Bases module, as well as observed EM/EO sensor system performance. The latter data are output to the Decision Aids Module for display, manipulation, and output, as well as for comparison with predicted system performance data.

F. Decision Aids Module

The Decision Aids Module is comprised of algorithms and graphical tools for the display and output of knowledge-based products, which can be used to make system optimization and/or platform employment decisions. Predicted EM/EO sensor system performance data from the Performance Prediction Module would support tactical planning (i.e., "what if" scenarios), while observed system performance data from the Performance Monitoring Module could be particularly useful for conveying a "snapshot" of how well that system is performing in real-time. Additionally, insight into the "end-to-end" performance of the entire EM/EO sensor system can be gained by comparing the predicted to the observed performance data.

4. ENVIRONMENTAL "ADAPTIVITY"

The expression, "environmentally-adaptive," as it is used here, refers to the capability of the system to respond to changing conditions of the physical environment by automatically adjusting/modifying the system's operational parameters (i.e., optimizing the performance of the system with no "man-in-the-loop"). This automated feedback process would create a "closed loop" between the EM/EO sensor systems, Performance Monitoring Module, and the Decision Aids Module.

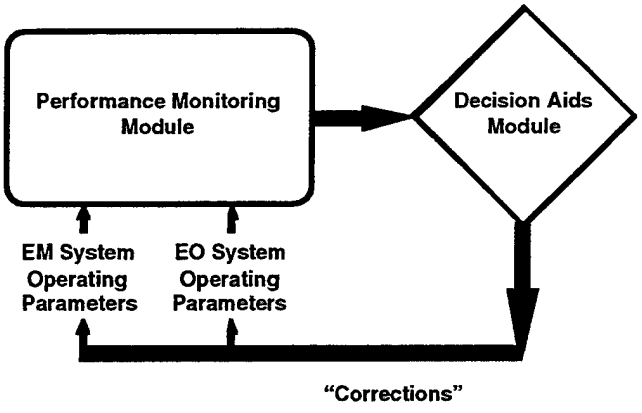

Figure 2. A "Closed Loop" EM/EO Sensor System

Performance data collected by the Performance Monitoring Module, as well as "clutter/noise" data, would be provided to the Decision Aids Module, where those data could be compared to predicted performance data. In addition to its normal display and output capabilities, in the "environmentally-adaptive" mode of operation, the Decision Aids Module would also output system set-up parameters (or recommended "corrections") based on a validated set of rules, or potentially an expert system (i.e., neural network). The goal of such a capability would be to perform system optimization on a "sweep-to-sweep" or "scan-to-scan" basis.

5. CONCLUSION

This paper described the functional components of a hypothetical, "closed-loop", "environmentally-adaptive" EM/EO sensor system. While such a system may not exist today, many of the components have been developed and need only be integrated to provide a robust, "end-to-end" capability that would significantly enhance warfighting using future EM/EO sensors and weapon systems.

ACKNOWLEDGEMENTS

I would like to acknowledge the following individuals for their assistance and advice in developing this concept: Mr. Rich Paulus (SPAWARSYSCEN); Dr. Andreas Goroch and Mr. John Cook (NRL); Mr. Dan Dockery and Mr. Pete Econ (JHU/APL); and, Mr. David Lewis (DREA).

A Multi-scale Approach for EM Propagation Assessment within the Marine Boundary Layer

Kenneth E. Gilbert and Xiao Di
Applied Research Laboratory and The Graduate Program in Acoustics

Martin J. Otte, Samir Khanna, John C. Wyngaard, and Nelson L. Seaman
Department of Meteorology

The Pennsylvania State University
University Park, Pennsylvania

Abstract

Mesoscale meteorological models are being increasingly used to study the refractive conditions of the marine boundary layer. However, researchers have reported poor agreement between observed propagation measurements and propagation models using mesoscale refractivity fields. Presumably, some of the poor results can be explained by the omission of scales smaller than the mesoscale grid. To alleviate this deficiency in the mesoscale fields, we add subgrid structure to the mesoscale refractivity fields using large-eddy simulation (LES) datasets. LES is a powerful tool that can compute refractivity fields on scales of 50 m up to 5 km. For scales smaller than 50 m, Khanna and Wyngaard developed a technique to extend the LES fields down to scales of about a meter, which can be important for Bragg scattering of EM waves by atmospheric turbulence. We demonstrate this method by computing two-dimensional high-resolution refractivity fields from 128^3 LES fields and using them in a parabolic-equation wave-propagation model. The inclusion of small-scale information dramatically changes the propagation calculations due to the effect of turbulent small-angle scattering.

1. Introduction

Meteorological processes within the marine boundary layer play on important role in determining electromagnetic (EM) wave propagation. The temperature and humidity fields in the atmosphere determine the refractivity conditions. These fields vary on scales from the synoptic ($\approx$ 1000 km) down to the smallest turbulent scales ($\approx$ 1 mm). A proper characterization of the refractivity field for EM propagation computations should include information on all these scales.

Advances in numerical weather prediction, coupled with increased computing power, are allowing for improved forecasts of refractivity by mesoscale meteorological models. These models can provide three-dimensional forecasts of refractivity on horizontal scales ranging from the synoptic scale down to about 10 km. Burk and Thompson (1995) found that the Navy Operational Regional Atmospheric Prediction system (NORAPS) performed well in describing the general refractivity conditions observed during the Variability of Coastal Atmospheric Refractivity (VOCAR) experiment. However, they reported poor agreement between observed propagation measurements and propagation models using the mesoscale refractivity fields.

Corresponding author address: Martin J. Otte, 503 Walker Bldg., Department of Meteorology, University Park, PA 16802-5013

Presumably, some of the poor results can be explained by the omission of scales smaller than those resolved by a mesoscale model. This deficiency can be alleviated by adding subgrid structure to the mesoscale refractivity fields using large-eddy simulation (LES) datasets. LES is a powerful technique that provides three-dimensional, time-dependent fields of the turbulent scales of motion that can not be resolved by mesoscale models. Such detailed information on atmospheric turbulence cannot currently be obtained in any other way. On today's supercomputers LES can typically resolve turbulence on a 256^3 numerical grid, which typically gives spatial resolutions from a few kilometers down to tens of meters.

LES has not been fully explored for studying the effect of atmospheric turbulence on wave propagation, in part because of the insufficient spatial resolution of LES data. For propagation calculations, Gilbert *et al.* (1996) show that refractivity fields must be resolved on scales down to the Bragg wavelength in order to model turbulent scattering of waves. For turbulent scattering of radar at GHz frequencies within the marine boundary layer, the Bragg wavelength is about a few meters. A method to extend the LES fields down to the Bragg wavelength scales has been developed by Khanna and Wyngaard (1996), and is described in Khanna *et al.* (1998). We combine an extended LES refractivity field with a typical mesoscale refractivity profile and use them in a parabolic-equation wave-propagation model. The inclusion of small-scale information dramatically changes the results, showing the importance of these scales to the propagation calculation.

2. The refractive-index fields

To use EM propagation algorithms such as a two-dimensional parabolic equation (PE), one needs the index of refraction n as a function of horizontal range and height. We consider the index of refraction at any given instant of time to be composed of a sum of two components: a mean part $\overline{n}$, which is deterministic and can be provided by a mesoscale model; and a fluctuating part n' which varies with both height and horizontal range, and is regarded as stochastic. The fluctuating refractivity field is provided from LES.

Since the variations of the quantity $\overline{n}$ - 1 are of the order 10^{-5} , and the fluctuations n' are of order 10^{-6}, it is customary in the EM propagation community to define a scaled index of refraction, called "refractivity," that is given by

$$N = (n-1) \times 10^6. \tag{1}$$

The mean refractivity $\overline{N} \equiv (\overline{n}-1) \times 10^6$ is computed from the mean temperature $\overline{T}$, pressure $\overline{P}$, and vapor pressure $\overline{e}$ fields using the relationship of Bean and Dutton (1968):

$$\overline{N} = \frac{77.6}{\overline{T}} \left(\overline{P} + \frac{3610\overline{e}}{\overline{T}} \right). \tag{2}$$

To account for the curvature of the earth, a modified mean refractivity $\overline{M}$ is defined as $\overline{M} = \overline{N} + (z/a_e) \times 10^6$, where z and a_e are, respectively, the altitude above sea level and the radius of the earth. For this study we use a prescribed mean field which is a function of height only and is typical of mesoscale conditions from the marine boundary layer. Figure 1 shows this range-independent mean refractivity field. The profile is of an upward-refracting atmosphere, with a kink in the refractivity profile at a height of 800 m at the level of the inversion capping the marine boundary layer. No ducting levels exist in this profile.

The fluctuating refractivity $N' \equiv n' \times 10^6$ is computed from the LES fluctuating potential temperature θ and specific humidity q fields (Wesley, 1976):

$$N' = C(\theta + \alpha q), \tag{3}$$

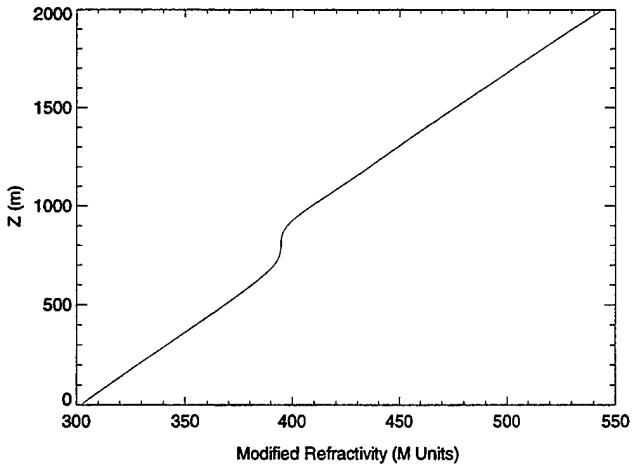

FIG. 1. The mean modified refractivity profile used in the EM wave propagation calculations. The refractivity fluctuations for standard LES and extended LES, respectively, were added to this mean profile to produce the complete refractivity profile.

where C and α are dimensional constants that depend on the frequency of the propagating EM wave. For microwave frequencies, with the potential temperature given in degrees Kelvin and the specific humidity given in grams of water per kilogram of air, the values of C and α are, respectively, 0.862 (K^{-1}), and -7.8 (kg/gK).

In the analysis below, we are concerned with computing the fluctuations in the index of refraction, n', using large-eddy simulation. To test our approach, we generated 128^3 LES fields of a highly convective, cloud-free boundary layer over a 5 km $\times$ 5 km $\times$ 2 km domain using Moeng's (1984) LES code. The resolution of the simulated fields was 40 m in x and y and 15 m in z. The simulated fields included potential temperature along with two conservative scalars, from which we can obtain a "bottom-up" scalar b, which has a surface flux with no entrainment flux, and a "top-down" scalar c, which has an entrainment flux but zero surface flux (Moeng and Wyngaard, 1984). The specific humidity field was computed as a linear combination of b and c:

$$q(x,y,z,t) = b(x,y,z,t)\frac{\overline{wq}_0}{\overline{wb}_0} + c(x,y,z,t)\frac{\overline{wq}_1}{\overline{wc}_1}, \tag{4}$$

where subscripts 0 and 1 imply the surface value and the value at the top of the mixed layer (i.e., the entrainment value), respectively. The surface and entrainment moisture fluxes used in (4) were each set to 0.05 g·m/(kg·s) to represent typical conditions in a convective marine boundary layer as reported by Wyngaard *et al.* (1978).

Figure 2 shows isocontours of the perturbation refractivity N' along an arbitrary $x-z$ plane of the LES. The figure shows that the largest N' values occur at a height of about 800 m, which again corresponds to the level of the inversion that caps the turbulent boundary layer. This is the region where the moist, potentially cooler air from within the boundary layer mixes with the drier, potentially warmer air from aloft. This creates large perturbations of refractivity which are an order of magnitude larger than in the rest of the LES domain.

Vertical profiles of N' at four x locations within the arbitrary $x-z$ plane are shown in Figure 3. The figure shows perturbation refractivity profiles directly from the LES (top), and after the fine-scale extension of Khanna and Wyngaard (1996) were applied (bottom). The profiles are noticeably altered near the surface and the capping inversion, with a distinct fine structure that was lacking in the original LES data. The fine-scale enhancement is especially striking in the entrainment region which is poorly resolved by LES.

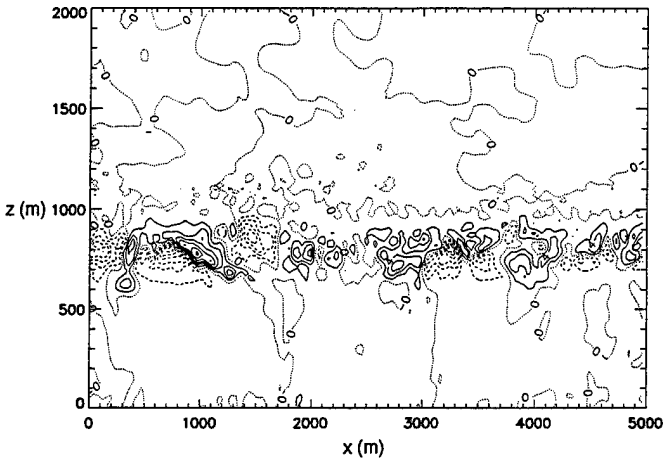

FIG. 2. Isocontours of refractivity perturbation N obtained from LES. Dashed lines denote negative values, solid denote positive values, and dotted lines are the zero contour. The contour interval is 2 M-units.

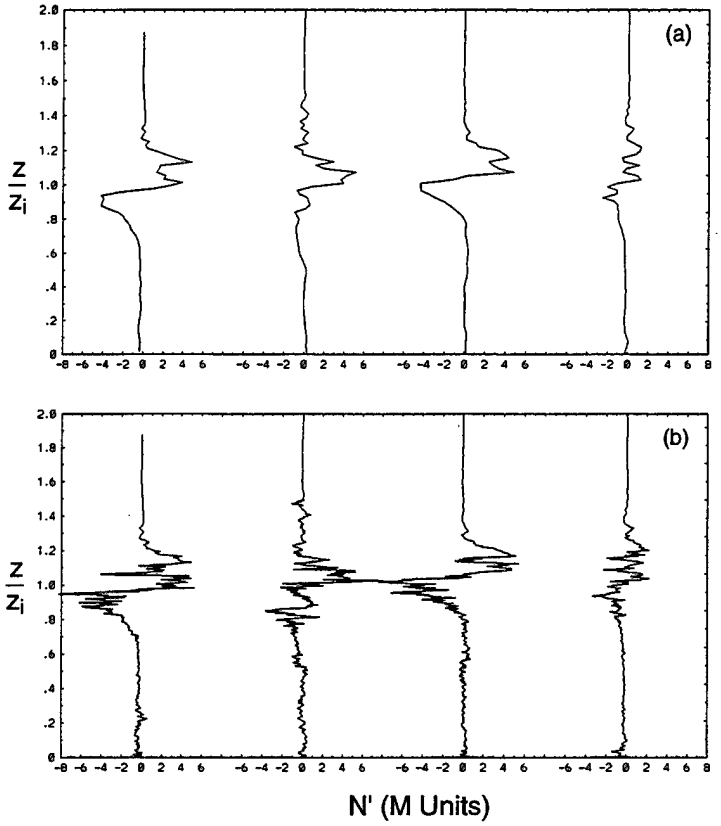

FIG. 3. Vertical profiles of instantaneous refractivity fluctuations at four arbitrary x-y locations for (a) LES and (b) extended LES.

3. Propagation through high-resolution refractivity fields

Parabolic-equation (PE) calculations done with a generalized form of the split-step Fourier PE called the "Green's Function Parabolic Equation" (GF-PE) (Gilbert and Di, 1994) were performed with the refractivity fields described in the previous section. The purpose of the calculations given

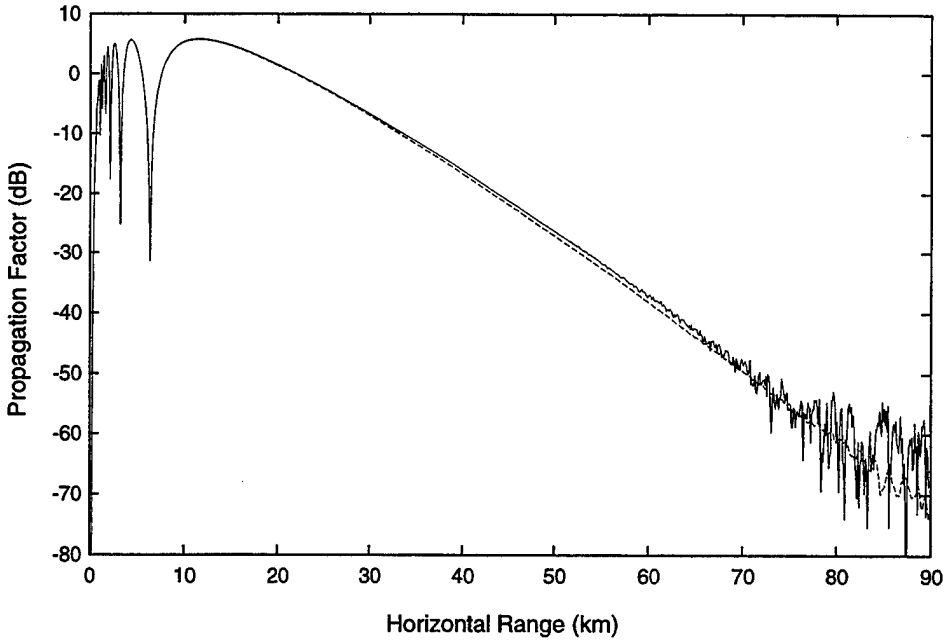

FIG. 4. Propagation factor versus horizontal range for the mean refractivity profile (dashed line) and for the mean profile plus the 2D standard LES refractivity field (solid line). Note that for both cases, a deep shadow is created for near-ground receivers downrange. Hence it can be seen that the refractivity fluctuations from standard LES do not significantly affect levels in the shadow.

here is to show in a particular example the effect of LES-scale and extended LES-scale turbulent structure on EM propagation. In section 3a we give a purely numerical demonstration of the effect, and in section 3b we interpret physically the numerical calculations.

a. Parabolic equation calculations for EM propagation through refractivity fields computed with standard and extended LES

Figure 4 shows the propagation factor computed for the mean refractivity profile only (dashed line) and for the mean profile plus the 2D standard LES fluctuation field (solid line). Since the mean profile is upward refracting, a deep shadow is created for near-ground receivers down range. The addition of the LES fluctuations to the mean profile raises the levels 5–10 dB starting at about 75 km. Even with the inclusion of the LES fluctuations, the level at 90 km is still at least 10 dB below the level (−50 dB) computed by Rogers (1996) using a standard atmosphere and the troposcatter model of Hitney (1993). It is apparent that in this case refractivity fluctuations from standard LES fields do not significantly affect EM intensity levels in a refractive shadow.

Figure 5 shows the propagation factor for the mean refractivity profile (dotted line) and for the mean profile plus the extended LES fluctuations (dashed lines). Realizations for the extended LES fluctuations were computed every 2.5 m in range, and, accordingly, the horizontal range steps in the parabolic (PE) calculations were also 2.5 m. At ranges exceeding 60 km, the intensity levels due to scattering from small-scale refractivity structure are significantly larger than the intensity levels due solely to deterministic upward refraction. As a result, from 60 km to 90 km the average propagation factor is totally dominated by scattering from small-scale structure. At 90 km the propagation factor has been raised on average by approximately 30 dB above the mean profile level and is 8-10 dB above the −50 dB level reported by Rogers (1996). Thus we can see that the added small-scale structure in extended LES refractivity fields dramatically affects the intensity levels in a shadow zone.

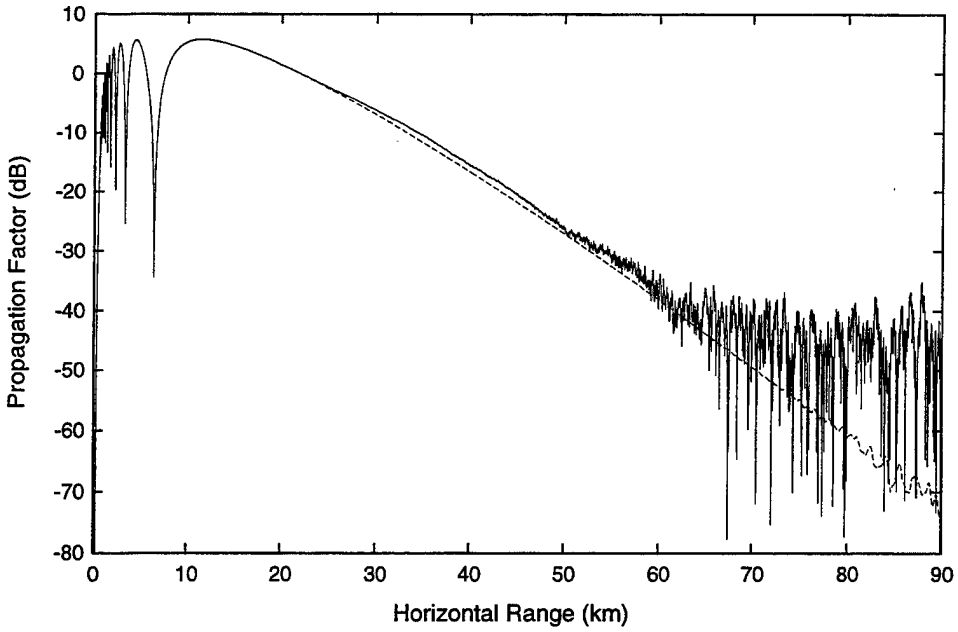

FIG. 5. Propagation factor versus horizontal range computed for the mean profile (dotted line) and for the mean plus the extended LES fluctuations (solid line). Note that by 60-90 km, scattered energy from the small-scale structure given by extended LES has, on average, raised the propagation factor by approximately 30 dB relative to the level with just the mean profile. Hence the small-scale structure in extended LES refractivity fields dramatically increases the levels in a refractive shadow zone.

b. Physical interpretation of EM propagation calculations

The key to relating the EM intensity in a refractive shadow zone to the small-scale structure in the refractivity field is the Born approximation for scattering from a random medium (Tatarskii, 1961). For example, for a plane EM wave incident on a finite volume of the atmosphere that has a fluctuating index of refraction, the ensemble mean scattered intensity $\langle|\Psi|^2\rangle$ for a scattering angle θ_{scat} is given by Tatarskii (1961),

$$\langle|\Psi|^2\rangle = C\left[k_o^4\,\Phi(\mathbf{k_B})\,V\right], \tag{5}$$

where k_0 is the wavenumber, $\Phi(\mathbf{k_B})$ is the power spectral density of the index of refraction fluctuations, $\mathbf{k_B}$ is the vector Bragg wavenumber, V is the volume of the scattering region, and C is a constant. The Bragg wavenumber $\mathbf{k_B}$ is given by $\mathbf{k_B} = \mathbf{k_{scat}} - \mathbf{k_{inc}}$, where $\mathbf{k_{inc}}$ and $\mathbf{k_{scat}}$ are the vector wavenumbers for the incident and scattered waves respectively. When $|\mathbf{k_{scat}}| = |\mathbf{k_{inc}}| = k_0$, the magnitude of the Bragg wavenumber is given by $|\mathbf{k_B}| = 2k_0\sin(\theta_{scat}/2)$, where θ_{scat} is the scattering angle between $\mathbf{k_{inc}}$ and $\mathbf{k_{scat}}$, i.e., $(\mathbf{k_{inc}}\cdot\mathbf{k_{scat}})/k_0^2 = \cos(\theta_{scat})$.

It is shown in Gilbert *et al.* (1996) that Eq. (5) also applies to propagation from a point source in an upward-refracting, turbulent atmosphere if one interprets V as the volume sampled by the EM wave, and θ_{scat} as the average scattering angle in the sampling volume between the source and receiver. With these replacements in Eq. (5), the ratio of the scattered intensity with extended LES (XLES) and standard LES can be written,

$$\frac{\langle|\Psi_{scat}(\mathrm{XLES})|^2\rangle}{\langle|\Psi_{scat}(\mathrm{LES})|^2\rangle} = \frac{\Phi_{\mathrm{XLES}}(\mathbf{k_B})}{\Phi_{\mathrm{LES}}(\mathbf{k_B})} \tag{6}$$

where in Eq. (6) the symbol $\langle\ \rangle$ denotes the ensemble average for a fixed sampling volume between source and receiver. In Eq. (6) we have assumed that the sampling volume is the same whether

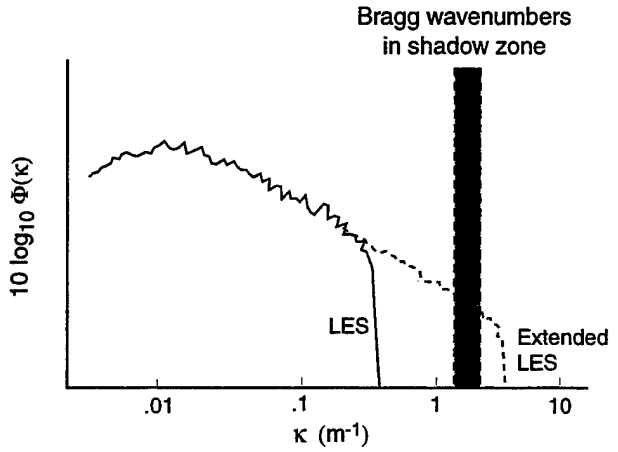

FIG. 6. The spectra for standard LES (dashed line) and extended LES (solid line) along with the Bragg wavenumbers of the EM waves scattered into the refractive shadow zone (shaded region). The wavenumber spectrum for standard LES does not go beyond about .4 m^{-1} (vertical resolution of 15 m), while the spectrum for extended LES reaches 6 m^{-1} (vertical resolution of 1 m). Hence the extended LES spectrum easily includes the region of the Bragg wavenumbers while the standard LES spectrum does not. As a result, scattering of energy into the refractive shadow is much higher with extended LES than with standard LES.

the refractivity field is computed by LES or extended LES. Since the scattering is weak in either case, such an assumption is reasonable.

For ground-to-ground propagation in a shadow zone, the x and y components of the wavenumber $\mathbf{q} \equiv \mathbf{k_{scat}} - \mathbf{k_{inc}}$ are small compared to the z-component, so that $\mathbf{k_B} \cong (0, 0, q_z)$. Hence we can compute the decibel measure of scattered levels in shadow zones, $10\log_{10}[|\Psi_{scat}(\mathrm{XLES})|^2/|\Psi_{scat}(\mathrm{LES})|^2]$, by computing $10\log_{10}\Phi_{\mathrm{XLES}}(q_z) - 10\log_{10}\Phi_{\mathrm{LES}}(q_z)$, where Ψ and Φ refer to the 2D EM fields and 2D refractivity fields used for the numerical calculations in Figs. 4 and 5. Figure 6 shows $10\log_{10}[\Phi_{\mathrm{XLES}}(q_z)]$ (solid line) and $10\log_{10}[\Phi_{\mathrm{LES}}(q_z)]$ (dashed line) as functions of $10\log_{10}(q_z)$. The difference between the solid and dashed lines gives the decibel measure of the ratio in Eq. (6).

To use Fig. 6 to understand how the propagation factors shown in Figs. 4 and 5 are connected with the structure of the refractivity fields computed by LES and extended LES, we need to estimate $|\mathbf{k_B}| = q_z$ as a function of range. Since the scattering occurs in the capping inversion region, the volume- plus ensemble-averaged scattering angle $\langle\theta_{scat}\rangle$ can be estimated by assuming straight-line propagation to the capping inversion at a horizontal range mid-way between source and receiver, i.e., $\tan(\langle\theta_{scat}\rangle/2) \cong H/(R/2)$, where H is the height of the capping inversion and R is the horizontal distance between the source and receiver. For $R \gg H$, $\langle\theta_{scat}\rangle \cong 4H/R$, and the volume- plus ensemble-averaged value for $|\mathbf{k_B}|$ is $\langle|\mathbf{k_B}|\rangle \cong \mathbf{k_0}\langle\theta_{\mathbf{scat}}\rangle$. For the frequency used, 2 GHz, the wavelength is 0.15 m so that $k_0 = 42$ m^{-1} and $\langle|\mathbf{k_B}|\rangle \cong 168(H/R)$ m^{-1}. For $H = 800$ m, $\langle|\mathbf{k_B}|\rangle \cong 1.3 \times 10^5/R$). To determine the relevant values for R, we note that the scattered EM energy dominates the total EM field only in the shadow region where the upward-refracted field is much less than the scattered field. From Fig. 5, we can see that scattering dominance starts at about 60 km and continues to 90 km, the longest range computed. For a range of 60–90 km, the approximate values for the Bragg wavenumber are $\langle|\mathbf{k_B}|\rangle \cong 2.2$ to 1.5 m^{-1}.

Figure 6 shows that the extended LES spectrum goes out to $\kappa \approx 6$ m^{-1} (the vertical resolution = 1 m), while for standard LES the spectrum extends only to $\kappa \approx 0.4$ m^{-1} (vertical resolution = 15 m). Consequently the maximum vertical wavenumber in the extended LES refractivity field easily includes the Bragg wavenumbers associated with scattering into the shadow zone, but standard

LES does not.

As a result of the above analysis, we can conclude that for ground-to-ground propagation into a shadow zone, at any given range, the scattered EM field samples a relatively narrow band of wavenumbers in the spectrum of refractivity fluctuations. Consequently, to predict intensity levels at a particular range in a refractive shadow, it is essential that the power spectrum for the refractivity fluctuations be correct for the Bragg wavenumbers associated with the scattered waves at that range. We saw, for example, that the standard LES refractivity fields were essentially zero beyond a wavenumber of about 0.4 m^{-1}, and as a consequence, the shadow zone intensity levels were only about 5−10 dB above the levels computed with the mean (non-fluctuating) refractivity profile. Extended LES refractivity fields, on the other hand, contained wavenumbers as large as 6 m^{-1}. As a result, with extended LES refractivity fields, the intensity levels in the refractive shadow were raised by as much as as 30 dB above the levels computed with the mean refractivity profile. Thus it is clear that for GHz-range EM propagation, higher wavenumber components (smaller structure) in the refractivity field must be represented accurately in order to have accurate levels in a refractive shadow zone.

4. Summary

Large-eddy simulation is a powerful technique for studying the instantaneous local structure of the atmospheric boundary layer. However, LES has not been fully explored for studying the effects of atmospheric turbulence on wave propagation, in part because of its insufficient spatial resolution. The spatial resolution required in the numerical solution of the parabolic equation for one-way wave propagation, for example, is much finer than that of typical LES.

The technique developed by Khanna and Wyngaard (1996) allows for the extension of the LES fields down to resolutions suitable for capturing the turbulent scattering of EM waves. An explanation of this technique, along with the propagation results show here, is presented in Khanna *et al.* (1998). The combination of the extended LES fields and a deterministic mean mesoscale field resulted in more realistic propagation computations than when using just the mean field or when using the mean and standard LES fields. It is expected that applying this methodology to actual mesocale model fields may result in refractivity forecasts suitable for propagation models.

Acknowledgments. This work was supported by Army Research Office Grant DAAL03-92-G-0117 and Office of Naval Research Grant N00014-92-J-1688. We are grateful to Ted Rogers and Dennis W. Thomson for helpful discussion.

References

Bean B. R. and E. J. Dutton, 1968: *Radio Meteorology.* Dover Publications, New York, 423 pp.

Burk S. D. and W. T. Thompson, 1995: Mesoscale modeling of refractive conditions in a complex coastal environment. *Propagation Assessment in Coastal Environment*, AGARD Conf. Proc. 567, 40-1–40-6.

Gilbert K. E., and X. Di, 1994: A fast Green's function method for one-way sound propagation in the atmosphere. *J. Accoust. Soc. Am.*, **94**, 2343–2352.

Gilbert K. E., X. Di, and R. R. Korte, 1996: Distorted-wave born approximation analysis of sound levels in a refractive shadow zone. In *Proceedings of the 7th Long Range Sound Propagation Symposium*, Ecole Centrale de Lyon, France.

Hitney, H. V., 1993: A practical tropospheric scatter model using the parabolic equation. *IEEE Trans. Antennas and Propagation*, **41**, 7, 905–909.

Khanna S., and J. C. Wyngaard, 1996: Local refractive index structure-function parameter and its application to wave propagation. In *Proceedings of the 1996 Battlespace Atmospherics Conference*, ed. Richter, J. H. and Anderson, K. D., NRAD Tech. Doc. 2938, San Diego, CA., 433-440.

Khanna S., M. J. Otte, J. C. Wyngaard, K. E. Gilbert, and X. Di, 1998: Electromagnetic wave propagation through simulated atmospheric refractivity fields. Submitted, *Radio Sci.*

Moeng C.-H., 1984: A large-eddy simulation model for the study of planetary boundary-layer turbulence. *J. Atmos. Sci.*, **41**, 2052–2062.

Moeng C.-H. and J. C. Wyngaard, 1984: Statistics of conservative scalars in the convective boundary layer. *J. Atmos. Sci.*, **41**, 3161–3169.

Rogers, L. T., 1996: Effects of the variability of atmospheric refractivity on propagation estimates. *IEEE Antennas and Propagation*, **44**, 460–465.

Tatarskii, V. I., 1961: *Wave Propagation in a Turbulent Medium*, R. A. Silverman, Translator. McGraw-Hill, New York, 285 pp.

Wesley M. L., 1976: The combined effect of temperature and humidity fluctuations on refractive index. *J. App. Meteorol.*, **15**, 43–49.

Wyngaard J. C., W. T. Pennell, D. H. Lenschow, and M. A. LeMone, 1978: The temperature-humidity covariance budget in the convective boundary layer. *J. Atmos. Sci.*, **35**, 47–58.

Convective Boundary Layer Features from a Volume-imaging Radar and Large-eddy Simulations

Brian D. Pollard[1], Samir Khanna[2], Stephen J. Frasier[1],
John C. Wyngaard[3], Dennis W. Thomson[3], Robert E. McIntosh[1]

[1] Department of Electrical and Computer Engineering
University of Massachusetts
Amherst, MA

[2] was with Department of Meteorology
Pennsylvania State University
University Park, PA
now with Telecommunications Products Division
Corning Incorporated
Corning, NY

[3] Department of Meteorology
Pennsylvania State University
University Park, PA

Abstract

In this paper we study the structure and evolution of the convective boundary layer (CBL) through measurements obtained with a volume-imaging radar, the Turbulent Eddy Profiler (TEP). TEP has the unique ability to image the temporal and spatial evolution of the boundary layer velocity field and local index of refraction structure-function parameter, $\tilde{C}_n^2$. TEP images consist of several thousand pixels with spatial resolutions on the order of 30 m by 30 m by 30 m. A typical image formation time is on the order of 1 s.

We apply a TEP CBL data set to comparisons with large-eddy simulation (LES) data. We compare $\tilde{C}_n^2$ and velocity vector features from TEP and LES, and find similar features in the two data sets. Our comparisons suggest that recent LES results may be correctly predicting $\tilde{C}_n^2$ behavior in the CBL.

1. Introduction

Studies of electromagnetic propagation in atmospheric boundary layer (ABL) often use the refractive-index structure-function parameter C_n^2 defined in [Tatarskii 1971] as a measure of the influence of refractive index gradients. The relationship in [Ottersten 1969],

$$\eta = 0.38\ C_n^2\ \lambda^{-1/3}\ , \tag{1}$$

where η is the volume backscattered power coefficient and λ is the radar wavelength, suggests that radars can measure the structure of C_n^2 in the ABL. Wind profilers [Ecklund et al. 1988], FM-CW systems [Richter 1969; Eaton et al. 1995] and other clear-air radars successfully measure vertical profiles of η in the ABL, but are limited in their horizontal profiling capability. The TEP system introduced in [Mead et al. 1998] uses digital beamforming techniques to form three-dimensional images of η in the boundary layer with pixel resolutions on the order of 30 m, and with image formation times on the order of 1 s. Such images are necessary to study the three-dimensional structure and variability of η in the ABL.

The ABL modelling community has also moved away from the analysis of one- or two-dimensional time series data toward the three-dimensional fields of large-eddy simulations (LES). LES was first applied to studies of the convective boundary layer (CBL) by [Moeng 1984], and since that time has been applied to several studies of the velocity field structure [Mason 1989; Schmidt and Schumann 1989; Khanna and Brasseur 1998]. Recent work in [Peltier and Wyngaard 1995; Khanna and Wyngaard 1997] suggests that LES could also contribute to the study of electromagnetic propagation in the ABL.

Peltier and Wyngaard [1995] define local structure-function parameters that differ from the traditional structure-function parameters of [Tatarskii 1971]; the local parameters are three-dimensional, time-varying quantities as opposed to the traditional, deterministic quantities defined through an ensemble average. Khanna and Wyngaard [1997] relate the local refractive-index structure-function parameter $\tilde{C}_n^2$ to the scattered intensity of an incident electromagnetic wave. They suggest that the time-varying η measured by a sensor should be proportional to the time-varying, local parameter $\tilde{C}_n^2$.

Application of LES to wave propagation would be a very useful addition to wave propagation studies. To our knowledge, however, the LES $\tilde{C}_n^2$ predictions have yet to be

compared with measured data. This paper presents a comparison of LES $\tilde{C}_n^2$ features from a CBL with data measured with the TEP system at an August 1996 deployment. Features of TEP measured $\tilde{C}_n^2$ and velocity vectors are shown from a convective boundary layer, and similar features are seen in LES data set. The next section of this paper reviews the two data sets, and section 3 shows the TEP and LES CBL features. A summary of the results appears in section 4.

2. Descriptions of the Data Sets

This paper presents data from an August 1996 TEP deployment at Rock Springs, PA. The data shown here are from approximately 15:30 EDT of 22 August, with a ground temperature of 26.2 °C, ground winds of 1.7 ms^{-1}, and clear skies. The geostrophic wind is measured with the TEP system by estimating the wind speed above the capping inversion layer, and is shown in table 1 to be 0.9 ms^{-1}. The inversion layer height z_i is measured from the height of the maximum power return as suggested by [Wyngaard and LeMone 1980], and is also shown in table 1.

An array of sonic anemometers is intalled at the Rock Springs site, and was run at approximately 13:00 EDT on 22 August 1996. The anemometers measure the surface temperature flux and friction velocity u_* from which the Monin-Obuhkov length scale L is calculated [Stull 1988]. The surface temperature flux combined with z_i also allows the convective velocity scale w_* to be calculated. Table 1 summarizes the TEP and anemometer parameters discussed here.

Table 1 also shows the parameters from the LES data set. These data are originally from [Khanna and Brasseur 1998] and were not generated especially for this study. The stability, $-z_i/L$, of the LES data is 506, higher than the value of 46 for the TEP data, but both should be characteristic of a convective boundary layer.

3. CBL Features

Typical features discussed in boundary layer structure studies have scales of order z_i [Khanna and Brasseur 1998]. The 25° TEP field of view makes it difficult to study structures of that size; 25° corresponds to an approximate area of 650 m by 650 m at the

Table 1: LES parameters and TEP measured meteorological conditions for 22 August 1996.

Parameter	LES	TEP
geostrophic wind U_g (ms^{-1})	1.0	0.9
surface temperature flux $<w\theta>_s$ (K ms^{-1})	0.24	0.047
surface moisture flux (ms^{-1} g of vapor/kg of air)	0.05	
mean boundary layer depth z_i (m)	810	1140
Monin-Obukhov length scale L (m)	-1.6	-25
velocity scale w_* (ms^{-1})	1.85	1.20

maximum TEP altitude of 1500 m. TEP is better suited to the study of smaller, 100 m-scale structures, as figures 1 and 2 illustrate. Figure 1 shows a series of images of TEP $\tilde{C}_n^2$ from a constant height of 930 m, or $z = 0.87z_i$, from a local time of 15:38:11 EDT. A region of high intensity propagates through the image from left to right, with the mean wind. The time difference between frames is 10.24 s, and each frame represents 1.28 s of data. Measured horizontal velocity vectors are overlaid on each image, and show a convergence on the area of high intensity. Figure 2 shows the vertical velocity frames corresponding to the intensity frames in figure 1, with the same horizontal velocity vectors overlaid. The region of high intensity corresponds to a downdraft feature in vertical velocity.

LES shows similar correspondence between converging horizontal winds, coherent downdrafts in vertical velocity, and locally high $\tilde{C}_n^2$ values. The top frame in figure 3 shows the $\tilde{C}_n^2$ LES predictions at $z = 0.95z_i$ plotted on a logarithmic scale, with LES horizontal velocity vectors overlaid; the bottom frame in figure 3 shows the corresponding LES vertical velocity image. The global mean wind of 1 ms^{-1} is subtracted from the horizontal vectors in those two images. The remaining fluctuating wind components are seen to converge on a small feature of locally high $\tilde{C}_n^2$, and a downward motion in the vertical velocity.

The actual values of the locally high $\tilde{C}_n^2$ differ for the TEP and LES cases, but the

contrast with the surrounding values is quite similar, on the order of 4-5 dB. The values of the vertical velocities are also similar for TEP and LES.

The character of the feature for the above comparisons is chosen because the vertical downdraft surrounded by a larger updraft feature, with converging horizontal winds and a locally high $\tilde{C}_n^2$, makes it easy to identify. The qualitative similarity that we show between the measured and predicted CBL structures suggest that LES may correctly predict the local behavior $\tilde{C}_n^2$. Such predictions could be extrememly valuable to wave propagation studies of the turbulent ABL.

4. Summary

This paper shows CBL features from TEP measured data and LES data. Similar features of locally high $\tilde{C}_n^2$, converging horizontal velocity vectors, and a downdraft in vertical velocity are seen in both TEP and LES. We believe that these are the first such comparisons of measured, volume-imaged $\tilde{C}_n^2$ structures with LES.

The comparisons shown here are a preliminary but encouraging step toward the validation of LES as a tool in ABL propagation studies. We are in the process of preparing a more detailed manuscript with both statistical and morphological comparisons of TEP measurements and LES predictions of CBL behavior.

Acknowledgments

This work is supported at UMass by the US Army Research Office under grant DAAL03-92-G-0110, and by ARO (DAAL03-92-G-0117) and the Office of Naval Research (N00014-92-J-1668) at PSU. The authors would like to thank Chenning Tong for collecting and analyzing the anemometer data, and Dick Thompson and Minfei Leng for their assistance in the TEP deployment.

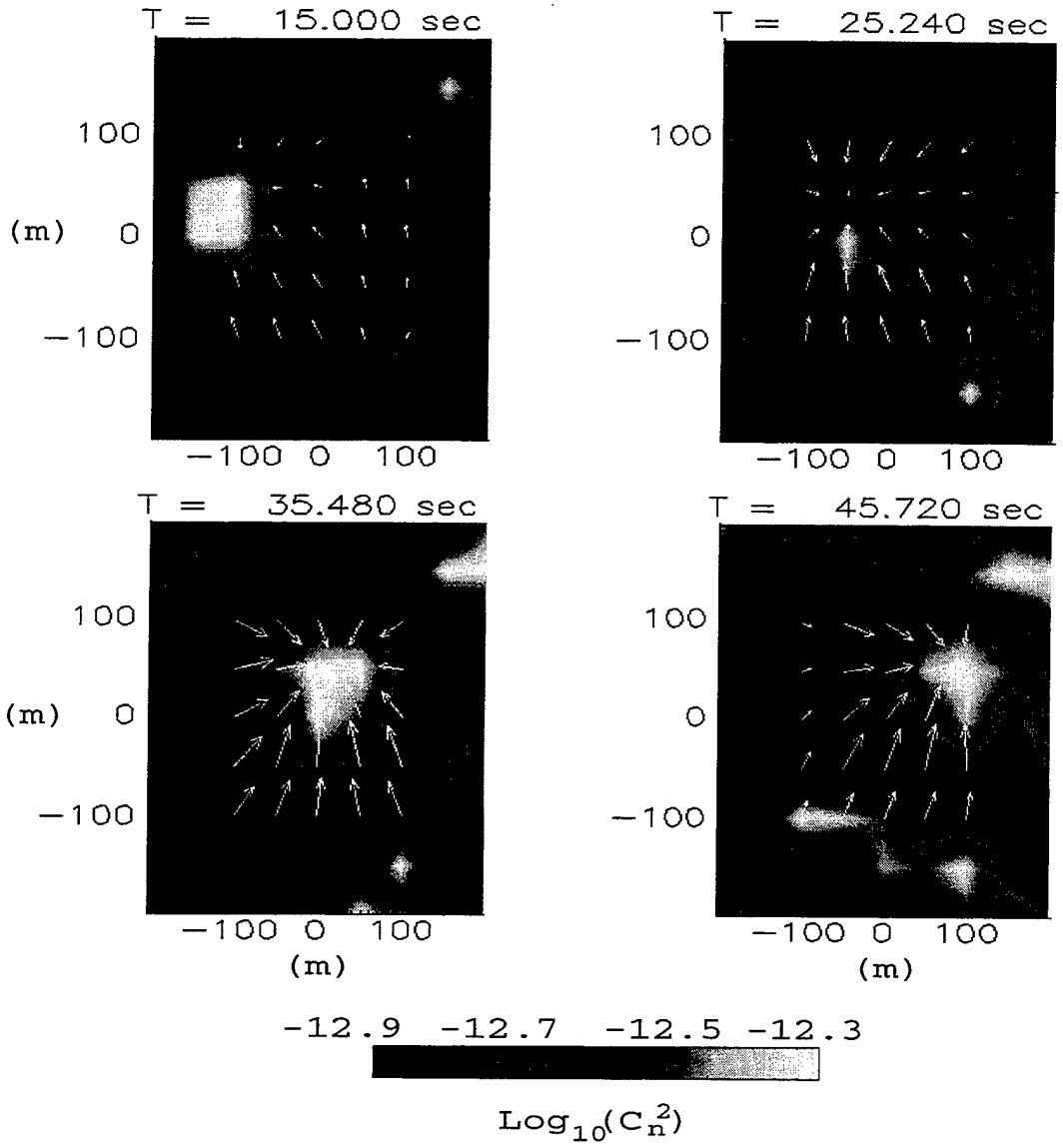

Figure 1: TEP intensity images from $z = 0.87z_i$ with horizontal velocity vectors overlaid.

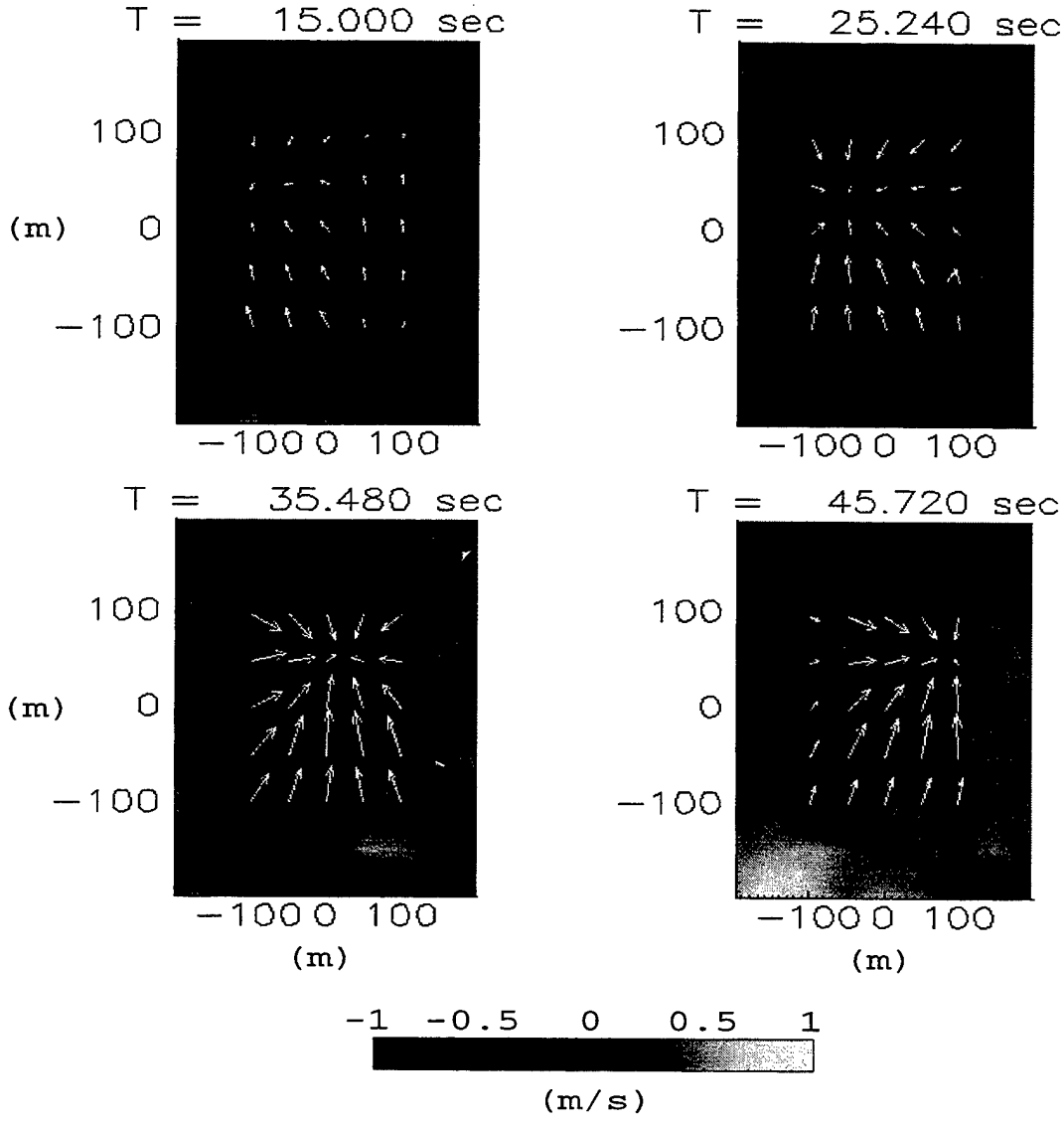

Figure 2: TEP vertical velocity images from $z = 0.87z_i$ with horizontal velocity vectors overlaid.

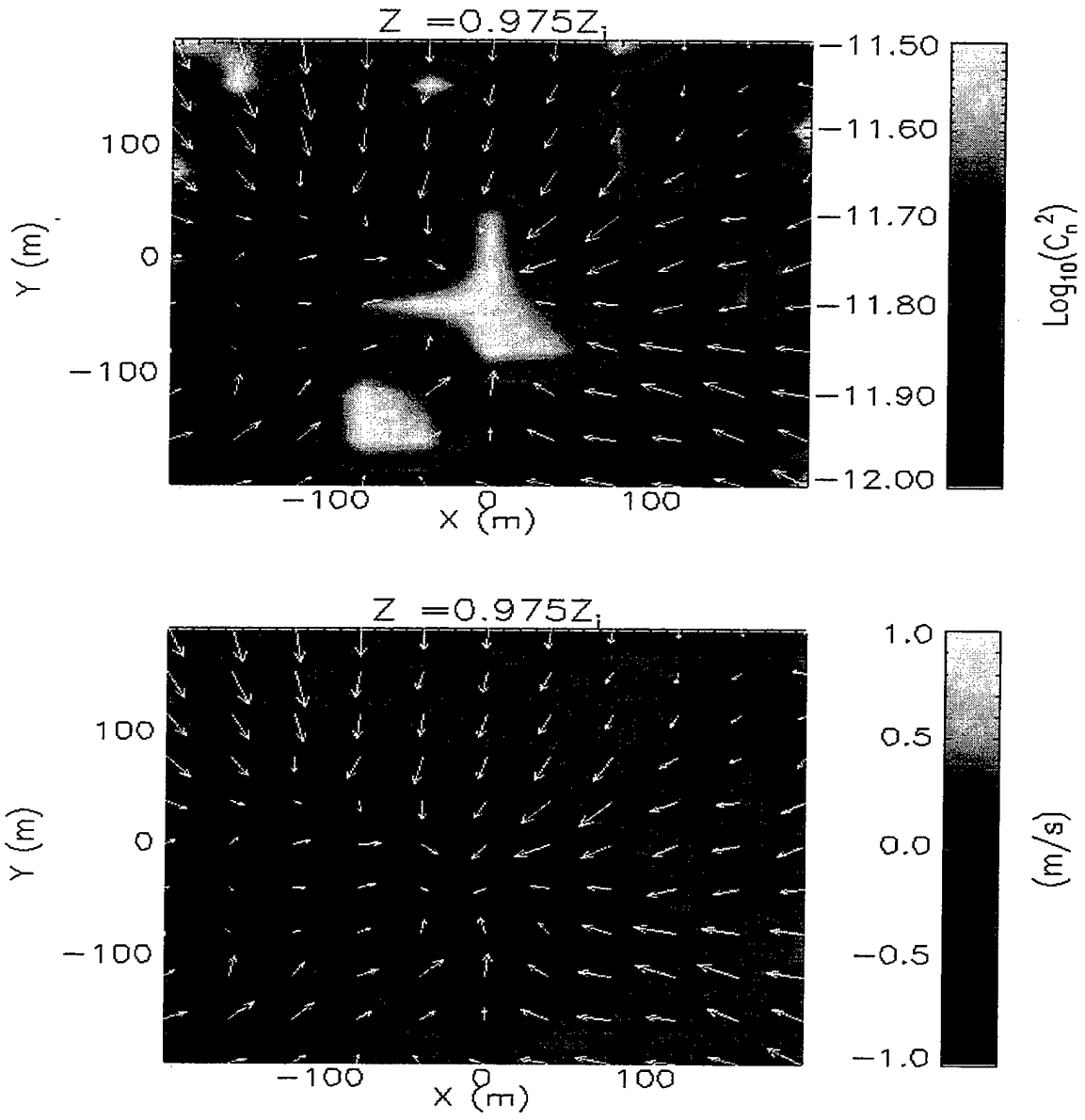

Figure 3: LES intensity and vertical velocity horizontal images from $z = 0.95z_i$ with horizontal velocity vectors overlaid.

References

Eaton, F. D., McLaughlin, S. A., and Hines, J. R., 1995. A new frequency-modulated continuous wave radar for studying planetary boundary layer morphology. *Radio Sci.*, **30**, 75–88.

Ecklund, W. L., Carter, D. A., and Balsley, B. B., 1988. A UHF wind profiler for the boundary layer: brief description and initial results. *J. Atmos. Oceanic Tech.*, **5**, 432–441.

Khanna, S. and Brasseur, J. G., 1998. Three dimensional buoyancy- and shear-induced local structure of the atmospheric boundary layer. *J. Atmos. Sci.* in press.

Khanna, S. and Wyngaard, J. C., 1997. Local refractive index structure-function parameter and its application to wave propagation. In *Proceedings of the 1996 Battlespace Atmospherics Conference.*

Mason, P. J., 1989. Large-eddy simulation of the convective atmospheric boundary layer. *J. Atmos. Sci.*, **46**, 1492–1516.

Mead, J. B., Hopcraft, G., Frasier, S. J., Pollard, B. D., Cherry, C. D., Schaubert, D. H., and McIntosh, R. E., 1998. A Volume-Imaging Radar Wind Profiler for Atmopsheric Boundary-Layer Turbulence Studies. *J. Atmos. Oceanic Tech.*, **15**. to appear in No. 3.

Moeng, C. H., 1984. A large eddy simulation model for the study of planetary boundary-layer turbulence. *J. Atmos. Sci.*, **41**, 2052–2062.

Ottersten, H., 1969. Atmospheric structure and radar backscattering in clear air. *Radio Sci.*, **4**, 1179–1193.

Peltier, L. J. and Wyngaard, J. C., 1995. Structure-function parameters in the convective boundary layer from large eddy simulation. *J. Atmos. Sci.*, **52**, 3641–3660.

Richter, J. H., 1969. High resolution tropospheric radar sounding. *Radio Sci.*, **4**, 1261–1268.

Schmidt, H. and Schumann, U., 1989. Coherent structure of the convective boundary layer derived from large-eddy simulations. *J. Fluid Mech.*, **200**, 511–562.

Stull, R. B., 1988. *An Introduction to Boundary Layer Meteorology.* Klewer Academic Publishers.

Tatarskii, V. I., 1971. *The Effects of the Turbulent Atmosphere on Wave Propagation.* Kefer Press [NTIS TT 68-50464].

Wyngaard, J. C. and LeMone, M. A., 1980. Behavior of the refractive index structure parameter in the entraining convective boundary layer. *J. Atmos. Sci.*, **37**, 1573–1585.

HIGH RESOLUTION METEOROLOGICAL TRANSPORT AND DIFFUSION SIMULATIONS IN A COMPLEX RIVER VALLEY

Ronald M. Cionco
US Army Research Laboratory, Adelphi, MD 20783

and

Harald Weber and Welfhart aufm Kampe
German Military Geophysical Office, Traben-Trarbach, GE

ABSTRACT

Micrometeorological wind and diffusion fields are simulated for a winding river valley cutting through a complex terrain domain. The simulation site is the Mosel River Valley in the vicinity of Traben-Trarbach, Germany. The meteorological simulation code calculates the mean wind field and several turbulence parameters for input into a gaussian puff diffusion code so that aerosol plumes can travel with the deformed wind field. Cases are prepared to investigate flow regimes (a) along the river's main axis (about 225 degrees) and (b) cross valley (about 315 degrees). Each case is run for both moderate (about 5 m/s) and light (about 2 m/s) wind speed conditions and unstable and stable atmospheric conditions. Directional influences are also imposed for down slope and down valley drainage flow during stable conditions and up slope and up valley flow during unstable conditions. High resolution calculations are made for a grid size of 100 m within a computational domain of 10 km x 10 km. The wind fields clearly respond to a variety of terrain and meteorological conditions as did the behavior of the aerosol plumes.

1. INTRODUCTION

To date, numerous terrain scenarios have been addressed and simulated for study and evaluation using high resolution micrometeorological and diffusion models from our inventory. Terrain configurations, such as those listed in Table 1, were also exercised with morphological features added to these simulation scenarios. One terrain configuration not attempted is the case where a meandering river makes a deep, serpentine cut into moderately complex surrounding terrain. The site selected for simulation is the Mosel River Valley in the vicinity of Traben-Trarbach, Germany. Figure 1 presents the course of the Mosel River for some 70 km downstream to the Rhein River. Figure 2 is the more limited area that defines the simulation domain of 10 km x 10 km. The "loop' of land where Traben-Trarbach and Mount Royal are located dominates the computational area as the river cuts a complex pattern. Micrometeorological wind and diffusion fields are simulated in this study for such a complex river valley.

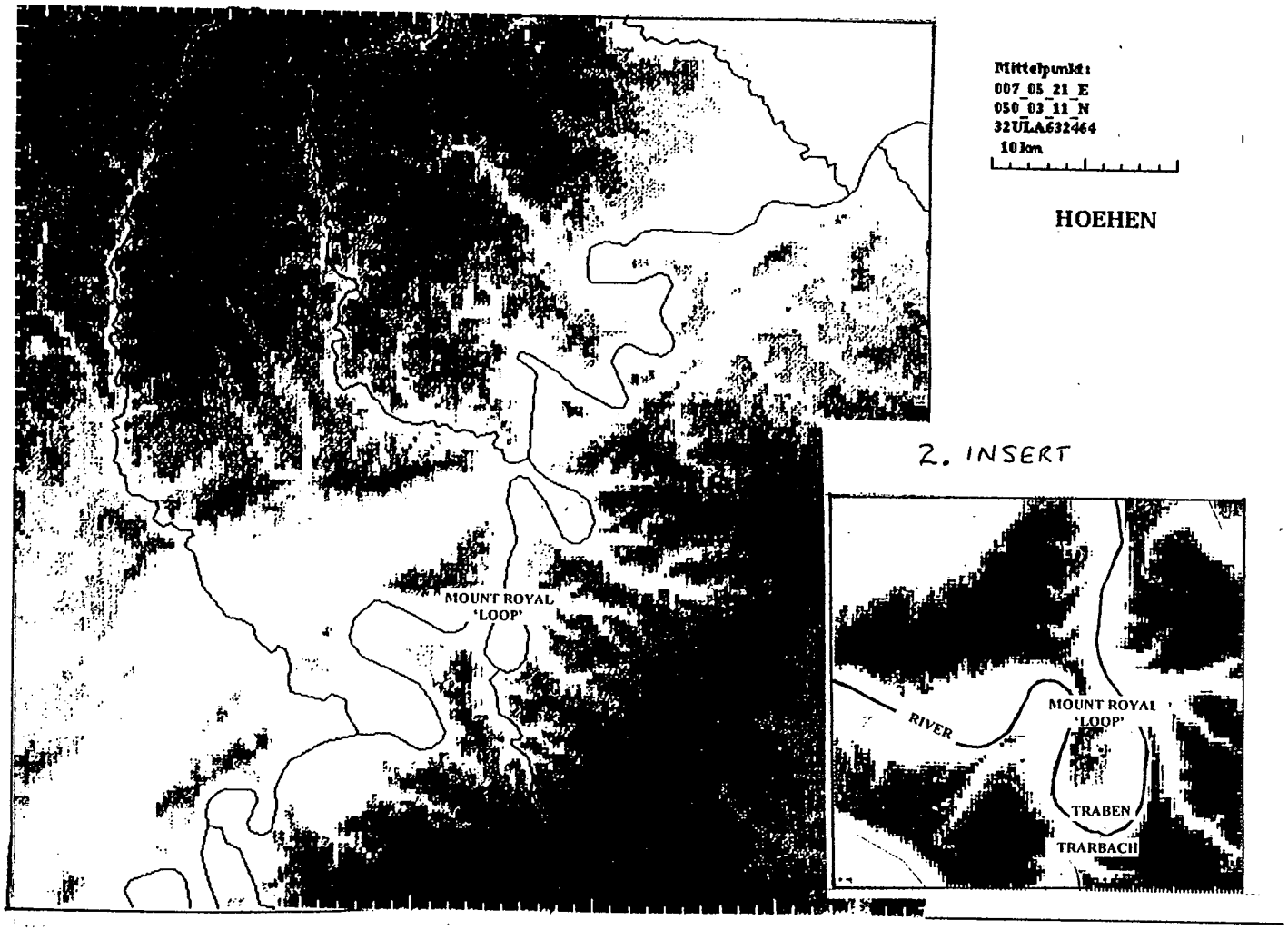

Figure 1. Map of general area of the Mosel River Valley, Germany.

Figure 2 Insert. Local area of simulation study in the vicinity of Traben-Trarbach as a 10Km x 10Km domain centered on the Mount Royal "loop".

Table 1. High resolution terrain scenarios addressed in previous simulations and additional simulation cases that also incorporated surface morphology features

TERRAIN DOMAIN	PLUS MORPHOLOGY
Near flat with slight slope	+ several orchards in domain
Rolling hills	+ forests, grass, & buildings
Rolling hills - close set	+ heavily forested
Rolling hills w main drainage	+ fully forested w clearings
Hills and plains	+ villages and forested hills
Plains adjacent to mountains	(no morphology data)
Plateau on mountain slope	+ forested w large clearing
Shallow valley on mtn slope	(no morphology data)
Wide valley flanked by mtns	+ airfield buildings
Low elevation peninsula in bay	+ forest, grass,& buildings
High elevation mtn slopes	+ forests, grass, & water

2. SIMULATION CODES

The meteorological simulation code calculates the mean wind field and several turbulence parameters with high resolution for input into a gaussian puff diffusion code so that aerosol plumes can travel with the terrain-deformed wind field. Both codes were used previously during the conduct of the MADONA Field Study (Cionco et al, 1995) and follow-on studies. The simulated fields are readily viewable with existing graphics programs (Weber et al, 1995) for both the meteorological solutions and the diffusion concentration fields (as contour plots) and dosage amounts.

The high resolution wind field simulation code (Cionco, 1985; Ball and Johnson, 1978) simulates wind flow over complex terrain with high resolution in the lower part of the boundary layer. Both mechanical and thermal forcing produce buoyancy- and terrain-influenced wind fields with computational grids of some 100 meters. Grid size can vary from 40 m to 400 m. For the proposed 10 Km x 10 Km domain with 100 meter grid spacing, calculations will be made for a 101 by 101 computational array.

Figure 2 defines the more limited area of the 10 km x 10 km simulation domain. The "loop' of land where Traben-Trarbach and Mount Royal are located dominates the computational area as the river cuts a complex pattern. Because the study area is heavily vegetated and reasonably populated, the local morphological features as shown in figure 3 are digitized and incorporated into the surface boundary condition (same domain as in Figure 2). Features such

as forests, buildings, farming-vineyards, built-up areas and the river's water are digitized and located with the same 100 m resolution. A terrain-following coordinate system is imposed and computations are performed at a level equal to 1/10th the grid size -therefore at 10 meters.

The diffusion code (Thykier-Neilsen et al, 1993) computes the gaussian downwind and lateral dispersion of aerosol puff parcels as they are transported downwind in a deformed wind field. Analyses can include meandering for periods of more than an hour. The diffusion code produces concentration and dosage values to quantify the plume's downwind behavior with the same high resolution.

3. SIMULATION CONDITIONS

Cases are prepared to investigate flow regimes (a) along the river's main axis (about 225 degrees) and (b) cross valley (about 315 degrees). Each case is run for both moderate (about 5 m/s) and light (about 2 m/s) wind speed conditions and unstable and stable atmospheric conditions. A stronger speed case of 10 m/s is also included to show an analysis of terrain effects in near neutral atmospheric conditions. Directional influences are also imposed for down valley and cross valley flow during stable and unstable conditions. Table 2 defines the input conditions for these cases.

Table 2. List of meteorological input conditions for the wind field simulations

CASES	WIND SPEED,M/S	DIRECTION (^{0})	STABILITY
10/225NN	10.0	225	NEAR NEUTRAL
5/225U	5.0	225	UNSTABLE
5/225S	5.0	225	STABLE
2/225U	2.0	225	UNSTABLE
2/225S	2.0	225	STABLE
2/315U	2.0	315	UNSTABLE
2/315S	2.0	315	STABLE

Terrain elevation and morphology features are also digitized for input information with a grid resolution of 100 m for the 10 km x 10 km simulation domain.

4. METEOROLOGICAL SIMULATION RESULTS

Several examples solutions of the cases defined by the conditions in Table 2 are shown to exhibit the behavior of the flow fields as wind speed, direction, and atmospheric stability interact with and change over the complex features of this river valley.

Case 10/225NN: The imposed initial conditions of 10 m/s for an unstable/near neutral atmosphere is sufficiently strong to produce minimal deformation and speed changes as shown in figure 4. The model simulated good mixing with only minor terrain effects such as what would be expected for near neutral conditions.

Retaining the along valley direction and slowing the initialization speed to 5 m/s, the resultant wind field exhibits notable terrain interactions with additional upward lifting in the unstable case and downward suppression in the stable case. Results are given for:

Case 5/225U: Figure 5 shows considerable flow deformation over the terrain features with some enhanced channeling in 'canyons' that outlet to the northeast (along flow).

Case 5/225S: This simulation generates airflow off of the higher terrain with extensive down slope accelerations for east and north facing slopes as well as considerable 'canyon' flow especially at Trarbach out onto to river's surface shown in figure 6.

Slowing the initialization speed to 2 m/s for along and cross valley flow, the resultant wind fields exhibit strong contrasting conditions as stability and the wind's angle of attack change.

Case 2/225U: The imposed slow wind field flows smoothly as it follows the terrain with minor variations occurring downwind from two isolated 'finger' ridges as well as along the downwind slope of the Mount Royal 'Loop' as depicted in figure 7.

Case 2/225S: Changing the bulk stability of the domain but not speed and direction, the simulated wind field shows significant down slope accelerations and channeling especially at the river level and over the 'neck' of the 'Loop' shown in figure 8.

Case 2/315U: Changing the wind direction to cross valley flow but not the speed, this change in the wind's angle of attack produces notable deformation and acceleration s enhanced by the orientation of the 'Loop' and some 'finger' ridges as well as increased channeling up several canyons which are basically oriented some 315°. The resultant field shown in figure 9 exhibits more terrain interactions than is apparent in figure 7.

Case 2/315S: Retaining speed and direction but changing the bulk stability generates more areas of down slope acceleration as well as greatly enhanced up-canyon flow and more areas of along-river-valley flow alignment depicted in figure 10.

5 DIFFUSION SIMULATION RESULTS

Calculations of the downwind diffusion of plumes (smoke plumes) driven by the simulated high resolution wind fields of figures 7 through 10 are shown in figures 11 through 14 for conditions of 2 m/s from 225° and 315° for unstable and stable atmospheric conditions. Note that only every other vector is plotted in these figures and that only about 50% of the domain is displayed to focus on the behavior of the plumes.

For wind field Case 2/225U, figure 11 shows the release of plumes at two locations in the bottom of the river valley in a wind field of light to moderate deformation. The two plumes are transported in a parallel manner with moderate lateral diffusion and minor steering and the highest concentrations have difficulty leaving the main valley (about 1200 m downwind). Conversely for Case 2/225S (figure 12), the two plumes are released at exactly the same points now in the more stable atmosphere, but now converge while still in the river valley within a

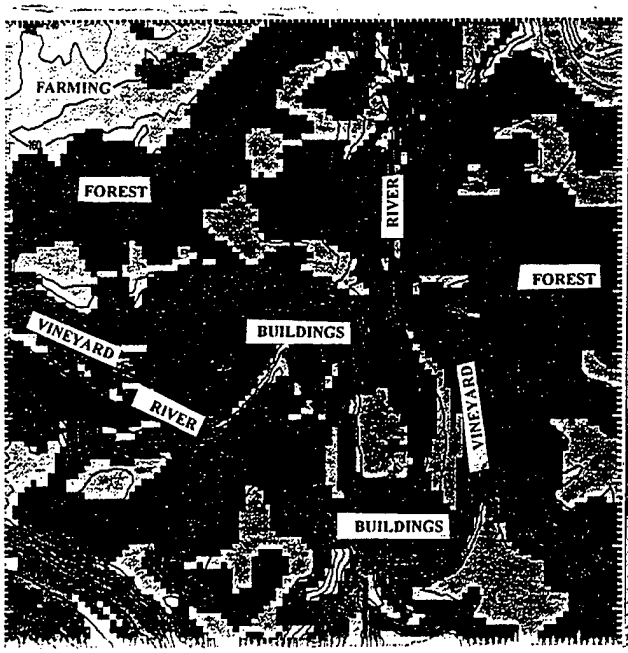

Figure 3. Map of morphology features for the simulation area

Figure 4. Wind field simulation for 10m/s wind from 225° and near neutral stability

Figure 5. Wind field simulation for 5 m/s wind from 225° and an unstable condition

Figure 6. Wind field simulation for 5 m/s wind from 225° and a stable condition

Figure 7. Wind field simulation for 2 m/s wind from 225° and an unstable condition

Figure 8. Wind field simulation for 2 m/s wind from 225° and a stable condition

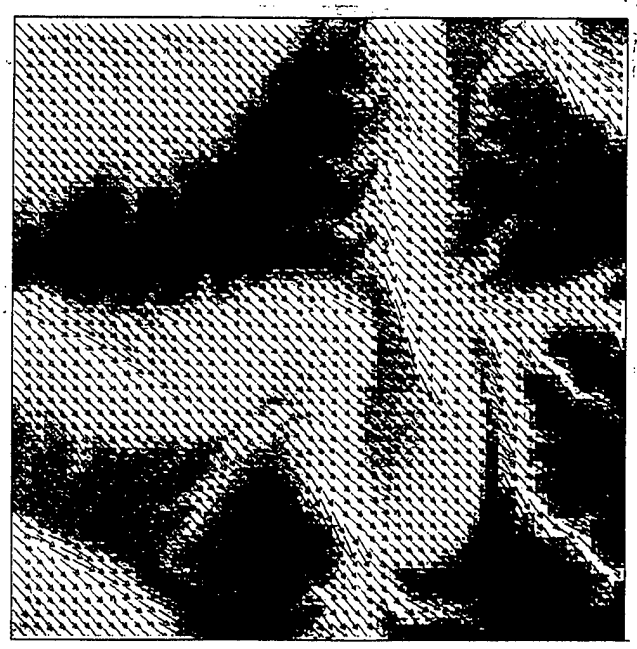

Figure 9. Wind field simulation for 2 m/s wind from 315° and an unstable condition

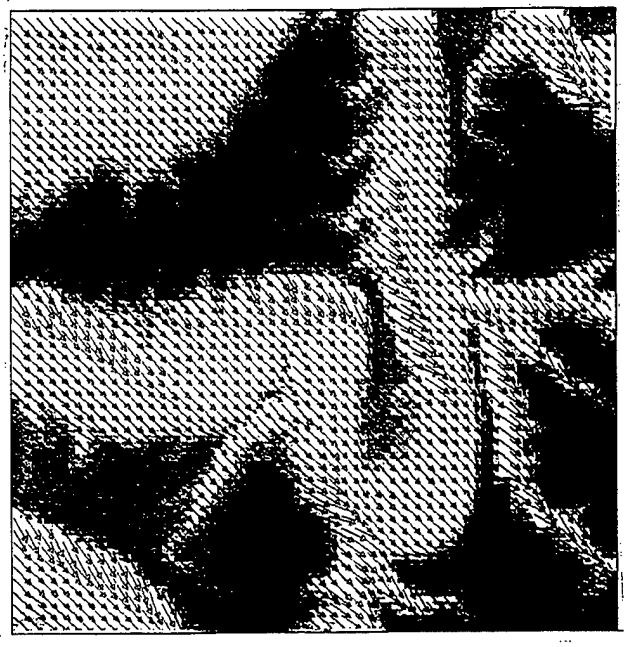

Figure 10. Wind field simulation for 2 m/s wind from 315° and a stable condition

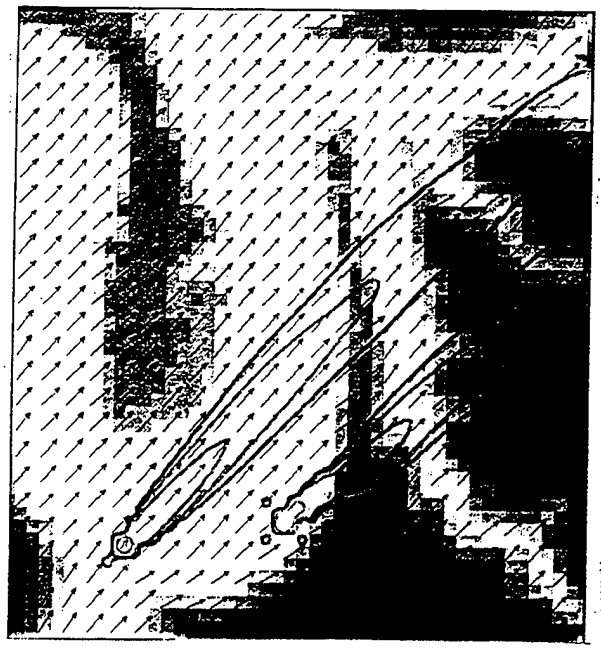

Figure 11. Simulations of puff behavior in the along valley simulated wind field Case 2/225U

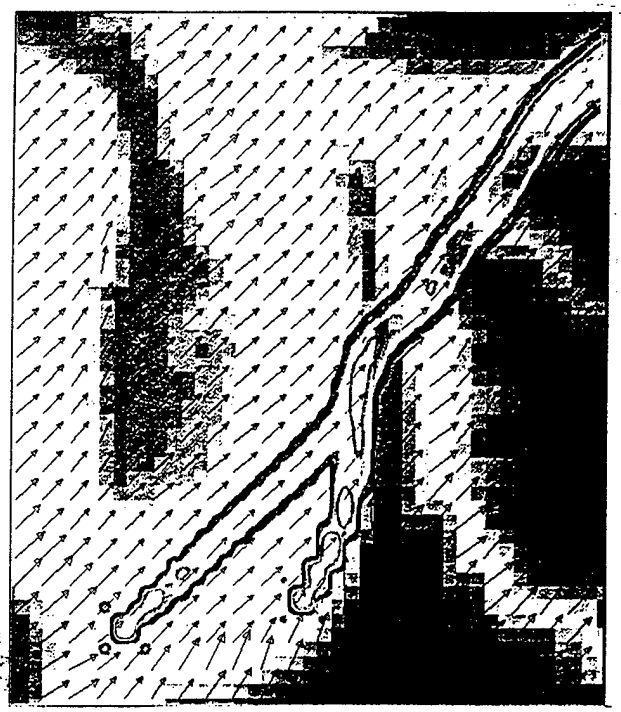

Figure 12. Simulation of puff behavior in the along valley simulated wind field Case 2/225S

Figure 13. Simulation of puff behavior in the cross valley simulated wind field Case 2/315U

Figure 14. Simulation of puff behavior in the cross valley simulated wind field Case 2/315S

field of greater deformation and higher concentrations notably at the east wall (some 1600-1800 m) of the valley (near center of the domain) and even farther downwind (more than 3600 m) into the hills than had occurred in the unstable case.

As the wind direction is rotated to be cross valley, the unstable Case 2/315U shown in figure 13 exhibits a long broad plume with higher concentrations not reaching (about 1200 m) the Mount Royal "loop" in a wind field of moderate deformation. For the stable flow condition of Case 2/315S, the plume's higher concentrations in figure 14 travel farther beyond the "loop" to the next hill (about 3800 m) with less lateral diffusion even though the wind field has greater deformation into and out of the river valley.

6. CONCLUSIONS

The wind fields clearly respond to the variety of meteorological conditions for this complex terrain and morphology scenario. They exhibit greater deformation and speed changes in the stable atmospheric condition than they do for the unstable condition with its additional buoyancy contribution. The angle of attack of the flow field upon the terrain orientation also produces markedly different wind fields.

The diffusion code is easily driven by these simulated wind fields. For stable conditions, the resultant plumes exhibit less lateral diffusion and higher concentrations farther downwind than in unstable conditions.

REFERENCES

Cionco, R. M. et al, 1995: 'An Overview of MADONA: A Multi-Nation Field Study of High Resolution Meteorology and Diffusion Over Complex Terrain', Proceedings of the 11th Symposium on Boundary Layers and Turbulence, Charlotte, NC, AMS, Boston, MA.

Cionco, R. M., 1985: 'Modeling Wind Fields and Surface Layer Wind Profiles Over Complex Terrain and Within Vegetative Canopies', The Forest-Atmosphere Interaction, Ed: B. A. Hutchison and B. B. Hicks, D. Reidel Publishing Co, The Netherlands.

Ball, J. A. and S. Johnson, 1974: 'Physically-based High-Resolution Surface Wind and Temperature Analysis for EPAMS', ASL-CR-78-0043-1, US Army Atmospheric Sciences Laboratory, White Sands Missile Range, NM.

Thykier-Neilsen, S. and T. Mikkelsen, 1993: 'Rimpuff User Guide, Version 33 (PC)', Meteorology and Wind Energy Department, Risoe National Laboratory, Roskilde, Denmark.

Weber, H., W. aufm Kampe, and R. M. Cionco, 1995: 'Visualization of the MADONA Data Base and Use of Selected Sequences in a Wind Flow and Diffusion Simulation System', Proceedings of the 11th Symposium on Boundary Layers and Turbulence, Charlotte, NC, AMS, Boston, MA

Battlescale Forecast Model at Ft. Irwin, Ca
and
Statistical Evaluation of 24 Hour Forecast Fields

Teizi Henmi
Battlefiled Environmental Division
Information Sciences and Technology Directorate
Army Research Laboratory
White Sands Missile Range, New Mexico 88002-5501

The US Army's Battlescale Forecast Model (BFM) was operationally used for forecasting surface meteorological parameters during the Department of Defence (DOD) Task Force XXI exercise which was held at the National Training Center (NTC), Ft. Irwin, Ca, in March, 1997.

The results of the BFM forecast calculations were unsatisfactory, primarily due to the following physical and numerical shortcomings in the model operation:

i) Scarcity of input meteorological data.
ii) Poor selections of surface albedo and soil heat conductivity values.
iii) Nudging method used to assimilate large scale meteorological data dominating the solutions of the equations of motion.

After the exercise, in an attempt to improve the model's performance, forecast data obtained by using different input and boundary condition data and an improved model numerical scheme were statistically compared with surface automated sensor data collected at the NTC during March, 1997.

Based on the study, it was concluded that that the updated numerics used in addition to an upgraded grid distribution of the NOGAPS forecast data from 2.5 to 1 degree resolution (used to provide the large scale forcing for the BFM) resulted in substantial improvement in the model's forecast skill.

I. Introduction

The Battlescale Forecast Model (BFM), which was developed at the US Army Research Laboratory (ARL) (Henmi and Dumais, 1997), was used operationally to forecast boundary layer weather during the Task Force XXI Exercise (TFXXI). TFXXI was held in March, 1997 at the National Training Center (NTC), Fort Irwin, California.

During TFXXI, the BFM was used in various configurations with different grid spacings and model domain sizes. However, the BFM did not perform as well as expected. Notable shortcomings were:

i) Amplitudes of the diurnal variation of surface temperature were not as large as observed.

ii) Terrain effects on diurnal variation of wind direction were supressed beyond the 12 hour forecast time.
iii) Surface wind speed during high wind conditions was lighter than observed.

The purposes of this paper are to describe physical and meteorological causes for the sub-par performances of the BFM at NTC including recent corrections made to improve the BFM performance, along with showing statistical comparisons of the BFM performances at NTC both before and after the corrections. In TFXXI, the BFM was most frequently used with the model configuration of horizontal grid numbers of 21 X 21 with grid spacing of 2.5 km (model domain of 50 km x 50 km) . In this study, all of the BFM calculations are done by using this particular configuration. Thus, the feasibility of the BFM application to a model domain with 2.5 km grid spacing will be also learned. The model had very rarely been used in this model configuration until this time. Figure 1 shows the location of the NTC model domain.

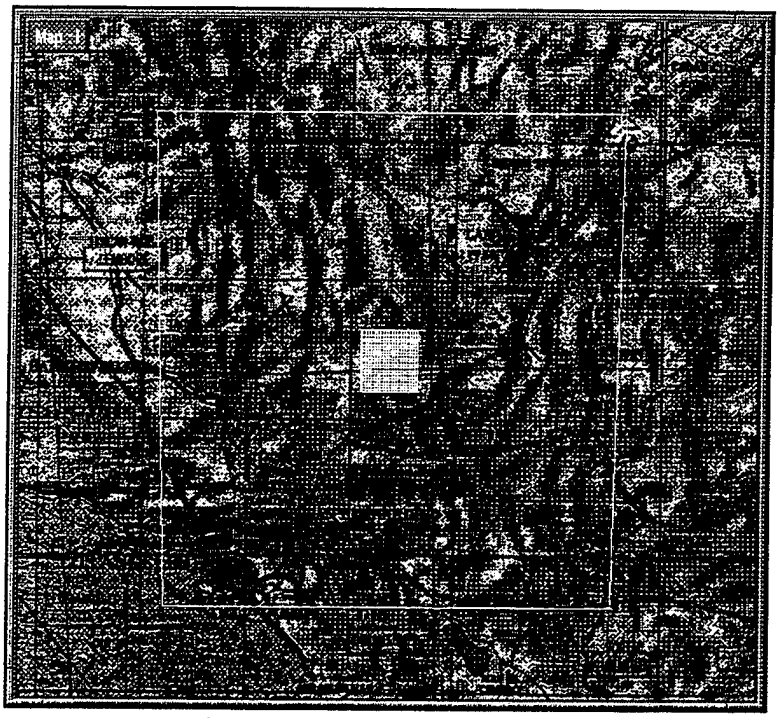

Figure 1 BFM model domain, where the large square used for upper air data collection covers an area of 400 km X 400 km, and the gridded square (the BFM domain) covers an area of 50 km X 50 km. The center of the model domain is located at 35.417 ° N and 116.625 ° W.

II. Causes of unexpected performances of BFM and improvements made

1. Scarcity of input meteorological data for initialization and time dependent boundary conditions

Currently, the US Air Force Global Weather Center (AFGWC) receives the NOGAPS (Navy Operational Global Atmospheric Prediction System) analysis and forecast data generated by the US Navy Fleet Numerical Meteorological and Oceanographical Center (FNMOC). NOGAPS data are originally calculated horizontally, over the entire globe gridded with every 1 degree, and vertically at every mandatory level (1000, 925, 850, 700, 500, 400, 300, 250, 200, 150, 100, 70, 50, 30, and 10 mb) and selected heights above ground level. In order to utilize old software developed for the US Air Force Global Spectral Model (GSM), AFGWC reduces NOGAPS data horizontally to 2.5 degree grid spacing and vertically to the following levels: 1000, 850, 700, 500, 300, and 200 mb.

For the BFM operation at NTC, upper air and NOGAPS data available in the outer square in Fig. 1 are used to produce three-dimensional data fields for initialization and time-dependent boundary values. For this model configuration, input data were scarce with only two NOGAPS data and one upper air sounding data available.

The 1 degree resolution NOGAPS data obtained from the Master Environmental Library (http://www-mel.nrlmry.navy.mil/homepage.html) and surface meteorological data obtained in NTC are used in this study as input data to the BFM, and the results are compared with those of the BFM operated at NTC.

2. Improper selections of the values of surface albedo and specific heat capacity of soil

Surface air temperature obtained by the BFM at NTC showed smaller diurnal variations than observed, and, in particular, diurnal maximum temperatures were lower than observed. Default values for surface albedo and specific heat capacity of soil were set to the constant values of 0.30 and 1100 ($Jkg^{-1}K^{-1}$), respectively. Following Pielke (1984), in order to take the soil characteristics into account, these two soil parameters are now expressed as a function of both geographical locations and time of the year in BFM's initialization routines. For the NTC area, the albedo value is chosen as 0.175 and the specific heat capacity of soil as 800 ($J\ kg^{-1}K^{-1}$). As can be seen in the following section, these modifications improved BFM's forecast skill of the surface temperature field.

3. Improper nudging method of meteorological parameters in the boundary layer

The BFM at NTC did not produce diurnal variations of the wind field over complex terrain as expected. In BFM, the equation of motion for the zonal component of wind is written as:

$$\frac{DU}{Dt} = f(V-V_g) + g\frac{\overline{H}-z^*}{\overline{H}}\left(1-\frac{\langle\theta_v\rangle}{\theta_v}\right)\frac{\partial z_g}{\partial x} + \frac{\partial}{\partial x}\left(K_x\frac{\partial U}{\partial x}\right) + \frac{\partial}{\partial y}\left(K_{xy}\frac{\partial U}{\partial y}\right) + \frac{\overline{H}}{H-z_g}\frac{\partial}{\partial z^*}\left(-\overline{uw}\right) + C_n(U_t-U) \qquad (1)$$

The symbols in equation (1) are:

C_n nudging coefficient

f Coriolis parameter

H material surface top of the model in z coordinate ,
$\overline{H}$ material surface top of z^* coordinate
K_x horizontal eddy diffusivity in x direction
K_{xy} horizontal eddy diffusivity in xy direction
U east-west component of horizontal wind vector
U_t east-west component of target wind vector
u fluctuation of east-west wind component
w fluctuation of vertical wind component
z_g ground elevation
and
θ_v fluctuation of vvirtual potential temperature.

In the above expression, $<\theta_v>$ is the base state virtual potential temperature, which we are defining as the initial virtual potential temperature obtained by the three dimensional objective analysis of input data. Details of BFM equations can be found in Henmi and Dumais (1997). In the BFM, version used at NTC, because of the large magnitude of the assigned nudging coefficient, the nudging term became dominant so that the terrain effect expressed by the second term of the right hand side of equation (1) was supressed. Therefore, the wind field within the boundary layer, became numerically stagnant due to the damping effect of the nudging term, and the diurnal variation of the boundary layer wind was not produced. In order to remove the above problem, the nudging term was removed from all numerical calculations in the vertical layers below 150 meters above the ground when the large scale flow was weak (judged by whereever NOGAPS forecast wind speeds below 1000 meters above sea level do not exceed 10 m/sec at any level). This is not applied to the intialization process in which the BFM fields are dynamically nudged toward the three dimentional data fields generated from NOGAPS and upper air data, and the surface observed data. The assumption behind this approach is that meteorological fields in the boundary layer are mainly dominated by surface exchanges of temperature, moisture and momentum under weak large-scale flow.

In order to solve the problem of the BFM surface forecast of wind speeds being smaller than observed during the periods of strong wind speed, the following scheme is incorporated: Horizontal wind vector components of the model in the layers between the surface to 1000 m level are nudged to the wind vector components at the 1000 m level of the input data, (1) if the maximum wind speeds of NOGAPS data in the layers between the surface to 1000 meters above is greater than 10 m/sec, (2) if the difference of wind direction between the 10 m and 1000 m levels is smaller than 35 degrees, and (3) if the solar radiation intensity is greater than 300 watts/m^2. This approach is based on the assumption that during daytime under strong wind conditions, wind vectors in the boundary layer tend to become uniform due to mixing.

III. Statistical evaluation of model performance

In the following sections, "old" BFM is defined as the BFM used at NTC for TFXXI, and "new" BFM as the one improved as described in the previous section. The present BFM domain does not include any model grid point, but the number of grid points over the 400 km x 400 km area are more numerous than the one for old BFM.

In this report, surface temperature, wind speed, and horizontal wind vector components, u and v, are used for the comparison study. The moisture data archived were in the form of relative humidity at the sea surface level. They were not suitable for the present study.
Surface observed data covering the period from March 16 through 25, 1997 were used to compare with forecast data. Unfortunately, there was no high surface wind case during this period. Therefore, the model improvement designed to incooperate with high surface-wind speed conditions was not tested in this study.
The 24 hour forecast data sets of the following are statistically compared with surface data observed at 11 sites located in the model domain of 50 km x 50 km :

A. Simulation Data Sets in the study

(1) Archived data of old BFM operated at NTC

During the TFXXI exercise, output files of the BFM forecast calculations were archived. The BFM's initialization data were provided by two NOGAPS grid points from AFGWC, one conventional upper air sounding site, and one surface observation site. Time-dependent boundary condition data were supplied by two NOGAPS grid points spatially and temporally interpolated onto the BFM domain. The NOGAPS 12-hour forecast fields were used for the BFM initialization, while the NOGAPS 24-hour and 36-hour forecast fields were used to provide the BFM's 12-hour and 24-hour boundary conditions respectively.

(2) 1 degree NOGAPS data interpolated spatially and temporally to the model domain

The 1 degree NOGAPS data valid for forecast times of 0, 12 and 24 hours were spatially and temporally interpolated to the BFM model domain, and compared with the surface observation data.

(3) Old BFM data obtained by using 1 degree NOGAPS data and surface data for initialization

The 1 degree NOGAPS data , and surface observation data shown in Figure 3, are used to initialize the old BFM. The time-dependent boundary values were supplied by nudging to the NOGAPS data. The upper air sounding data was not used.

(4) New BFM data obtained by using only 1 degree NOGAPS data for initialization

The new BFM was initialized only by 1 degree NOGAPS data, and time-dependent boundary values were given by nudging towards the NOGAPS fields as in (1) and (3). Raw surface and upper air observations were not used in the initialization.

(5) New BFM data obtained by using NOGAPS data plus surface observation data for initialization

The new BFM was initialized by using 1 degree NOGAPS data plus surface observation data,

while NOGAPS data provided time-dependent boundary values by way of nudging (as in (1), (3) and (4)). Upper air sounding data is not used in the initialization.

From the comparison between (4) and (5), the effects of utilization of surface observation data for initialization can be seen. From the comparison between (3) and (5), the skills of old and new BFM can be distinguished. Comparisons between (2) , and (4) or (5) make it possible to examine the influence of the BFM over the NOGAPS. In the following, these five sets are represented by (1), (2), etc.

B. Statistical Parameters

The following statistical parameters between forecast data and surface observed data are calculated by using the data obtained for the period from March 16 through 25, 1997.

1. Mean Difference

$$MD = \frac{\sum_{i=1}^{n} (x_{o,i} - x_{p,i})}{n} \tag{2}$$

Here the subscripts o and p represent observation and prediction, respectively. The subscript i represents the i-th data.

2. Mean Absolute Difference

$$AD = \frac{\sum_{i=1}^{n} |x_{o,i} - x_{p,i}|}{n} \tag{3}$$

3. Root Mean Square Error

$$\sigma = \sqrt{\frac{\sum_{i=1}^{n} (x_{o,i} - x_{p,i})^2}{n}} \tag{4}$$

4. Correlation Coefficient

$$R = \frac{\sum_{i=1}^{n} [(x_{o,i} - \overline{x_o})(x_{p,i} - \overline{x_p})]}{\sqrt{\sum_{i=1}^{n} (x_{o,i} - \overline{x_o})^2 \sum_{i=1}^{n} (x_{p,i} - \overline{x_p})^2}} \tag{5}$$

Among these four parameters, better agreements between observation and forecast are recognized, in general, in smaller values of AD and σ, and larger values of correlation coefficient, R. If MD is positive, model calculated values are smaller than observed values.

C. Statistical comparisons for each surface observation site

The statistical parameters described above were calculated for each site. Forecast data at 0, 3, 6, 9, 12, 18, and 24 hours were combined together without discriminating forecast time. Table 1 and 2 show the statistics, respectively, for temperature and wind speed.

Table 1 Statistics for Temperature

Data Sets	(1)	(2)	(3)	(4)	(5)
Mean abs. diff.	5.4	5.4	4.9	4.9	4.9
Corr. coeff.	0.26	0.43	0.52	0.55	0.56
Mean diff	-1.86	3.5	1.9	1.3	1.3

Table 2 Statistics for Wind speed

Data Sets	(1)	(2)	(3)	(4)	(5)
Mean abs. diff.	2.7	2.7	2.2	2.3	2.0
Corr. coeff.	0.07	0.03	0.23	0.19	0.32
Mean diff.	2.1	0.3	0.8	0.5	0.2

D. Time dependencies of the statistical parameters

Figure 2 shows the time dependencies of the four statistical parameters for surface temperature calculated by using the data of all sites combined (for each data set). In Figure 2, (2) and (5) represent the different data sets defined in the section A. Similar figures are obtained for ther other data sets, but are not shown in the present paper due to space limitation.

The following can be inferred :

1) Data sets (4) and (5) produced very similar temporal variations in all the parameters. The nudging of observed surface temperature did not produce noticeable improvement in the forecast of surface temperature.

2) Data sets (4) and (5) produced better statistical results than (1) and (2) through 18 hours, but at the 24 hour forecast period, the statistics for (4) and (5) became worse than those of (1) and (2). The combined effects of model physics and nudging of NOGAPS data apparently produced larger values of AD and RMSE and smaller values of R for the 24 hour

forecast. Note how the statistics at 24 hours for the data set (2) show similar tendencies with those for (4) and (5).

3) The old BFM operated at NTC produced surface temperature fields that were not well correlated with observation during the first 12 hours of the forecast period, due to the shortcoming of the old BFM that were unable to produce diurnal variation of the surface temperature field.

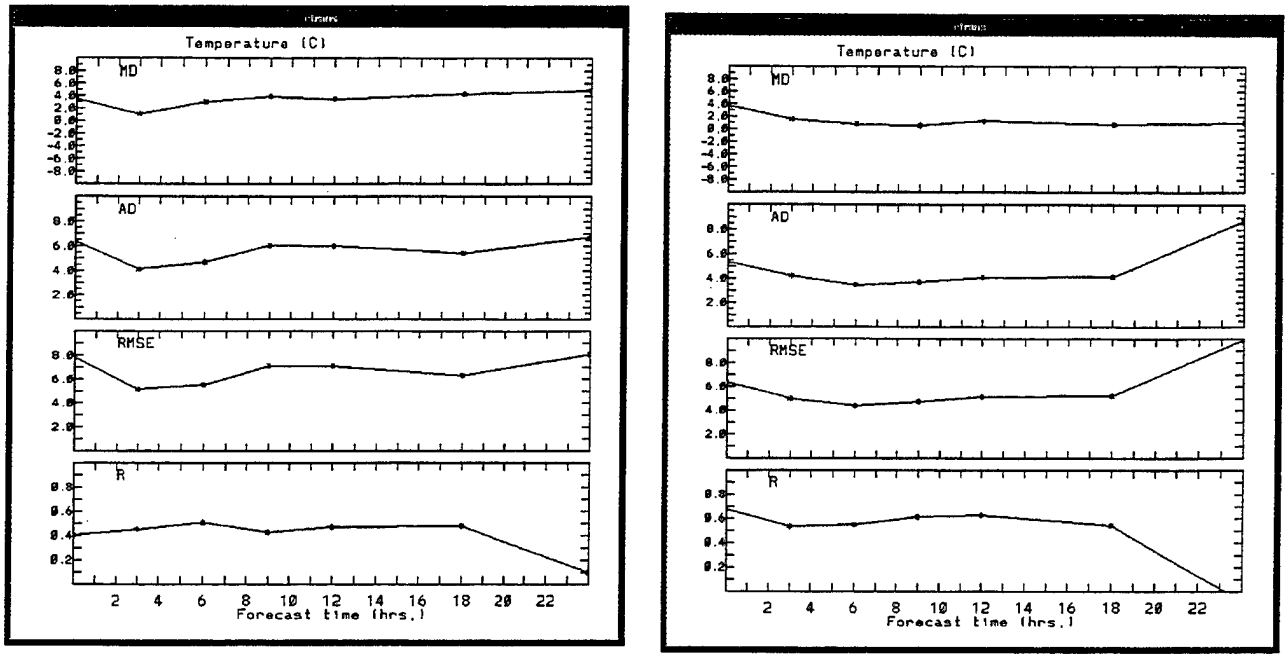

(2) (5)

Figure 2 Time changes of statistical parameters for temperature for data sets (2) and (5).

Time dependencies of the statistical parameters for wind speed for the data sets (2) and (5) are shown in Figure 3. For wind speed, the data set (5), produced by the new BFM resulted in the best statistics among the four data sets. The differences between the data sets (4) and (5) were noticed in the first 6 hours of forecast. Nudging of surface wind data improved surface wind fields in the early hours of forecast, but after six hours of forecast, the influences of surface wind data nudging seemed to disappear. In the BFM model, the nudging effects of surface data are dumped by multiplying exp(- kt) to the nudging terms in the surface layers after initialization time (Henmi and Dumais, 1997). Here, k is an empirical coefficient, and t is the time after the completion of initialization. In effect, the initial value of nudging coefficient and empirical damping coefficient k are such that the value of the nudging coefficient damp to an inconsequential value after 6-hours.

Data sets (4) and (5) showed substantial improvements in the value of statistical parameters for wind speed over data sets (1) and (2). Again, the influences of nudging of surface wind

data were seen for wind speed in the first several hours of forecast run, by comparing time variations of the four statistical parameters for data sets (4) with those of (5).

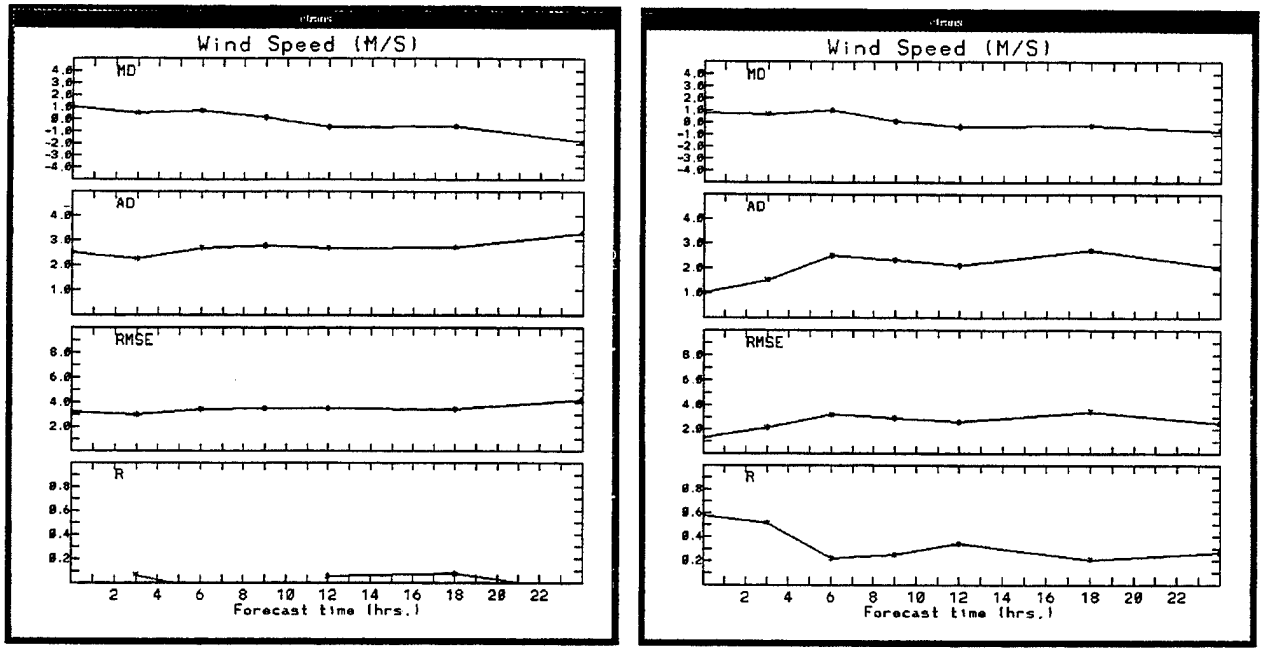

(2) (5)

Figure 3 Time changes of statistical parameters for wind speed, for different data sets (2), and (5).

From these statistical studies, it can be concluded that the new BFM has produced statistically better surface forecast fields in temperature and wind, and that NOGAPS data with one degree grid spacing have substantially contributed to produce these improved fields of temperature and wind.

V. Summary

The BFM, used operationally for 24 hour weather forecasting at NTC during the TFXXI exercise (March, 1997), produced several unsatisfactory results. Diurnal variations of surface temperature and wind direction were not as large as the observed variations, and the surface wind speeds during high wind cases were lighter than observation. It was found that the following three items were the major causes of the degraded forecasting results:

(1) Scarcity of input data for initialization and time dependent boundary conditions.
(2) Improper choices of the values of ground surface albedo, and of specific heat conductivity of soil.
(3) Too large a value for nudging coefficients of wind, temperature, and moisture in the boundary layers.

In order to examine the effects of data density, NOGAPS data with 1° grid spacing were used as input data for initialization and for time-dependent boundary conditions. The values of surface albedo and specific conductivity were adjusted for NTC (dry and warm desert area). In order to eliminate the damping effects of nudging terms, which tend to create numerical stagnation effects on meteorological fields in the boundary layer, nudging terms in the equations of motion, temperature, and mixing ratio were eliminated after three hours of initializing calculation when the large scale flow was weak.

The following five different 24 hour forecast data sets, obtained for the periods between March 16 and 25, 1997, over the model domain (21 x 21, 2.5 km grid spacing) covering the National Training Center, were compared with surface observation data , and statistically analyzed:

(1) Archived data of new old BFM operated at NTC.
(2) NOGAPS forecast data interpolated spatially and temporally to the BFM model domain.
(3) Data from the old BFM obtained by using 1 degree NOGAPS and surface data for initialization and time-dependent boundary conditions.
(4) Data from the new BFM, obtained by using 1 degree NOGAPS data only for both initialization and time-dependent boundary conditions.
(5) Data from the new BFM, obtained by using 1 degree NOGAPS and surface data for initialization and time-dependent boundary conditions.

Data set (2) has produced statistically compatible results to (1), indicating that good input data for initialization and boundary condition are essential for good forecasting results. It was shown that the old BFM initialized with NOGAPS data (1 ° grid spacing) produced better forecast fields for both surface temperature and wind speed than the old BFM initialized with NOGAPS (2.5 ° grid spacing).

The new BFM showed substantially superior performances to the "old" BFM in surface temperature and wind speed forecasts. The combination of model improvement made in the present study, and denser data points of NOGAPS with 1° grid spacing are likely the reasons for superior performance.

The utilization of surface data for initialization improved the forecasts of surface wind fields for the first several hours of calculation, but did little to improve surface temperature fields. There were some questionable observation sites for temperature, so that the above conclusion should be treated as tentative.

The present study also showed that the BFM on a model domain with 2.5 km grid spacing is capable of producing reliable forecast results.

References

[1] Henmi, T. and R. Dumais, Jr, " Description of the Battlescale Forecast Model", ARL Technical Report, in print, 1977.

AN APPROACH TO USING METEOROLOGICAL SATELLITE ANALYSIS TO SUPPORT BATTLESCALE FORECAST AND DECISION AID APPLICATIONS

Donald W. Hoock, Max P. Bleiweiss
and Robert Dumais

Battlefield Environment Division
Information Sciences and Technology Directorate
U.S. Army Research Laboratory
White Sands Missile Range, NM 88002-5501

ABSTRACT

Boundary layer energy budget and radiative transfer processes are critical to forecasting and quantifying many significant battlefield terrain conditions and atmospheric effects. Meteorological satellite data, when combined with terrain information databases, scattered surface met observations and high resolution weather forecasts, have the potential to provide more accurate and valuable information on surface energy balance and atmospheric EM propagation over widespread and otherwise data-denied areas. In this paper we identify some of the ways that the surface energy budget parameters (e.g., evapo-transpiration) and propagation parameters (e.g., scattering and emission at visual and infrared wavelengths) impact on the Battlescale Forecast Model (BFM) and Weather Effects Decision Aids (WEDA). Besides being inter-dependent themselves, the surface energy balance and propagation parameters also affect the interaction of battlescale weather with the state of the terrain; the modeling of surface illumination; target/scene contrast; the estimation of target acquisition range; surveillance image quality; and the quantitative thresholds for weather-impact decision aids. Therefore, we outline an approach to exploit met-sat analysis methods, terrain characterization and radiative transfer models that could ultimately enhance the capabilities currently provided in systems such as the Army's battlefield Integrated Meteorological System (IMETS). As examples, we discuss the accuracy of parameters derived from satellite data. We also demonstrate the sensitivity of BFM forecast winds and temperatures to input surface albedos which are key to accurate knowledge of surface energy balance parameters.

INTRODUCTION

The Integrated Meteorological System (IMETS) provides detailed meteorological data and impacts to the battlefield Tactical Operations Center (TOC) Army Battle Command Systems (ABCS). At this time, IMETS assets include synoptic scale weather forecast data downloaded from Air Force Weather, the Battlescale Forecast Model (BFM; Henmi 1997, Dumais, 1997) run locally on the battlefield Army Common Hardware/Software (ACHS II), and the commander's Integrated Weather Effects Decision Aids (IWEDA; Sauter, 1997). In addition, basic meteorological satellite (met-sat) image loops help to identify synoptic and mesoscale weather features. Significant improvements to IMETS are possible for the future in the form of new battlefield visualization and weather effects products tailored for the individual ABCS C4I systems. Decision aid improvements will focus on developing more quantitative interaction of the weather impact rules with both physics-based weather effects and system performance parameters for critical values.

We are also looking at exploiting met-sat MMW sensor data and multi-band image channels. Combining met-sat analysis with forecasts can improve the initializing data for both the met-sat data extraction algorithms and for the BFM terrain, illumination and surface energy balance inputs. Among the products that these data could support are EO and acoustic propagation forecasts, estimates of terrain-state, soil moisture and meteorological visibility from remote sensing, and improved estimates of diurnal target area illumination and scene radiance. Met-sat data can help validate BFM forecasts for data-denied areas. Derived atmospheric effects on line of sight and target acquisition ranges for situation maps and mission rehearsal will be integrated with other new weather and effects visualization tools and into the ABCS common map-overlay tool kits.

To help prioritize improvements, this paper and others at the conference (Shirkey, 1997) seek to identify sensitivities and to assess the significance of model and algorithm interactions. In the next sections of this paper we look at sensitivity of BFM to input surface albedo, a parameter that is shared in common between the EO effects, met-sat analysis and forecast models. We also review some of the currently available met-sat algorithm products.

COMMON SURFACE ENERGY BALANCE FACTORS

Met-sat analysis, meteorological forecasts and atmospheric propagation models share many atmospheric parameters and processes in common. One of the most fundamental processes in the atmospheric boundary layer is the surface energy balance between the terrain and air. This is driven by solar illumination, surface reflectance (albedo), surface thermal emissivity, upwelling and down-welling infrared radiation, soil temperature and thermal conduction. Exchanges in momentum and thermal energy are strongly coupled to winds at the top of the boundary layer, atmospheric convection and buoyancy, and the evaporation and condensation of liquid water and water vapor in both the soil and atmosphere. Other terrain-atmosphere interactions include boundary layer turbulence and surface friction. These are influenced by terrain surface roughness and by dynamic changes in surface state such as seasonal vegetation, local rainfall and snow cover. Incident solar radiation and thermal emission are also affected by the generation of surface layer aerosols and particulates and by the formation and effects of natural clouds and fog.

The net radiation balance at the terrain-air interface can be written as

$$R = \lambda \cdot E + H - G = (1-a) \cdot S \downarrow + \varepsilon \cdot (B_{sky} \downarrow - B_{sfc} \uparrow) \qquad (1)$$

R is the net thermal energy flux, equal to the difference between the radiant energy absorbed by the surface and that emitted by the surface. It also equals the sum of the upward sensible heat flux to the air H minus the downward thermal energy flux into the ground G plus the latent heat flux λE (where E is the water evaporation rate and λ is the latent heat of vaporization). The incoming radiative thermal energy is partly the difference in the incident short-wave solar energy S minus the fraction sunlight αS (where α is the surface albedo) that is reflected. Similarly, the absorbed incoming long-wave infrared thermal flux εB_{sky} from sky and clouds is reduced by the emitted thermal radiant flux εB_{sfc} from the surface (where ε is the thermal emissivity and equals the thermal absorption coefficient). When solved for in terms of λE, Eq. 1 is called the "evapo-transpiration" equation.

Apparent surface radiances, both reflected sunlight αS and emitted infrared radiance εB_{sfc}, are observed through the atmosphere by the visible and IR waveband sensors of the meteorological satellites. In addition, the satellites also receive passive millimeter wave radiance emitted from the surface and at various depths of the atmosphere (Kidder, 1995). These same quantities are essential to physically accurate scene generation and to determining contrast of objects against terrain for sensor and target acquisition models.

They also appear in the surface energy balance model of the BFM to couple soil and atmosphere properties. Latent and sensible heat fluxes are coupled to wind speed and to the difference in soil and air temperatures. BFM accounts for the forecast cloud cover in estimating the incoming radiance from sun and sky. Terrain albedo and emissivity are thus potentially important input data variables to the accuracy of BFM forecasts.

One goal in our development of improved weather applications to support the war fighter will be to investigate whether forecasts can be combined with met satellite data extraction algorithms to improve both. Knowledge of estimated air temperatures, water vapor, cloud cover, surface state and other forecast parameters should help improve application of physics-based extraction algorithms for remote sensing satellites. The satellites, in turn, can help provide the surface state and albedo information needed to initialize the forecasts, and to confirm the BFM forecasts in data-denied areas. More quantitative information on radiances, surface albedo, thermal emissivity, soil moisture, and optical depths through the atmosphere will support a new generation of quantitative propagation and target acquisition decision aids that require gridded meteorological and effects parameters.

First, however, we need to determine how sensitive the models and algorithms are to uncertainties in these input data. This will support analysis to determine how accurate the model inputs and outputs need to be.

IMPACT OF ALBEDO ON THE BFM FORECAST

To examine the impact of surface albedo on BFM forecast winds and temperatures, we ran the BFM for three cases with identical initializing conditions except for different input terrain albedo maps. In two cases the surface albedo was assumed to be uniform across the entire domain. To represent the range of values we chose these uniform albedos to be 0.1 and 0.8 respectively. Then we ran a map of actual surface albedo averaged over 10 km squares across the region, resulting in a mean albedo of 0.3. Two-thirds of all values fall between 0.25 and 0.35.

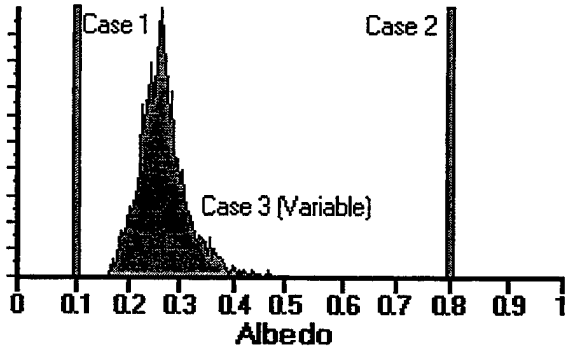

Figure 1. Albedo Histogram

Figure 1 is histograms of albedo for the three cases. In Fig. 2 a domain-sized county map of New Mexico is laid over an image proportional to the terrain albedo used for Case 3. The White Sands Monument area with albedo close to one represents less than one-half of one percent of the total domain area. Somewhat larger desert regions in Mexico SSW of El Paso also have relatively high albedo. The Sacramento Mountains 40 km east of the monument and those in the Gila wilderness along the west-central border of the domain have albedos somewhat less than the average. Two objectives of model comparisons are to see when the Case 3 albedos are most significant and whether albedo gradients across the domain have added effects.

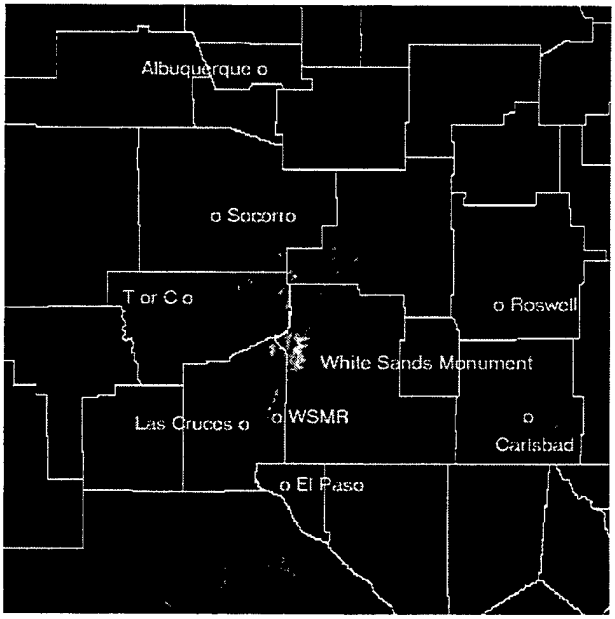

Figure 2. NM County Map and Albedo Image.

The output forecast domain is 500 x 500 km on a uniformly spaced horizontal grid of 10 km spatial resolution centered on 106.216 deg west longitude and 33.174 deg north latitude. For Case 1 with 0.1 albedo we expect high surface absorption of incident solar radiation during the day and correspondingly high air temperature near the surface. For the high reflectance Case 2 of 0.8 albedo we expect less terrain heating and smaller surface temperatures during daylight. These effects were easily observed in the model outputs.

Figures 3 and 4 show the forecast temperature contours in deg F at 2 m above the local terrain surface for 1100 local time, 20 November 1997. The separation between contours of the same color is 2 deg F, with warming as one moves south. In each figure the white contours are for Case 3 (variable albedo). Black contours are for Case 1 with 0.1 uniform albedo (dense vegetation) and Case 2 with 0.8 uniform albedo (snow or light desert soil) in Figs. 3 and 4 respectively. The background image shows Case 3 albedos, contrast-reduced to allow the contours to be better seen, for the 51 x 51 grid of 10 x 10 km elements. Temperatures across the region are 41.2 - 71.8, 29.7 - 56.1, and 41.4 - 71.4 deg F for the three cases.

Figure 3 shows 0.2 to 0.5 deg F differences in forecasts. The shift of contours to the south in Case 3 is consistent with a dynamic process of solar heating, where terrain temperatures in regions of higher albedo lag those of lower albedo. It is not clear, however, if there is any significant effect from spatial gradients in albedo in Case 3. Such effects may be masked by the more dominant effect of terrain elevation (see later figures for wind speed vectors). In Fig. 4, the temperatures for Case 2 with high albedo are significantly less than Case 3 by about 16 deg F. Except for small pockets of cool air and warm air in the NE quadrant, the contours in Case 2 mostly parallel those of Cases 1 and 3.

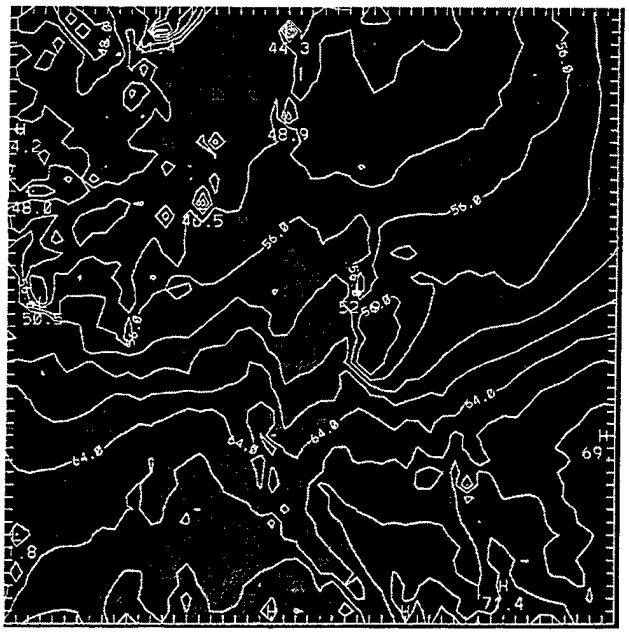

Figure 3. Temperature forecast for 1100 local time (white: α=var; black: α=0.1)

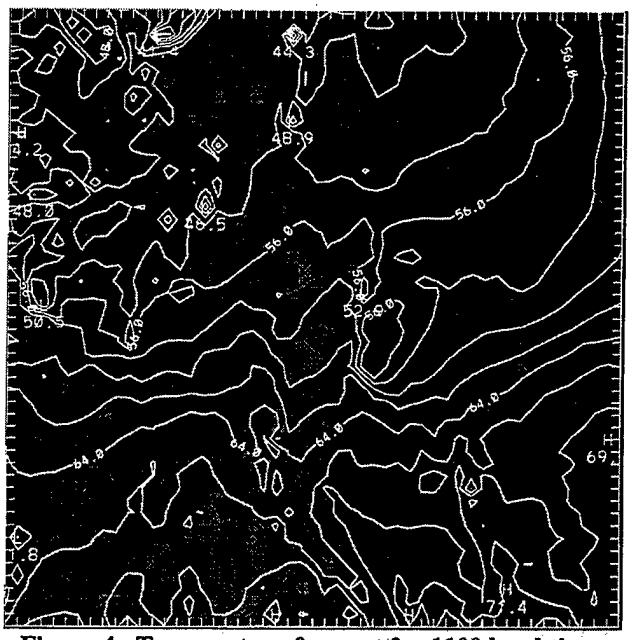

Figure 4. Temperature forecast for 1100 local time (white: α=var; black: α=0.8)

Figures 5 and 6 show 2m forecast temperatures at 1700 local time. Solar heating of terrain reached a maximum in early afternoon (not shown). The 2m air temperatures have now dropped over the region by about 4-5 deg F from that maximum, resulting in almost identical temperatures for Cases 1 and 3. In electro-optics and thermal scene modeling this is called "thermal cross-over time", where scene elements of very different emissivity radiate with essentially the same thermal contrast. Thus, it is not surprising that there is no evidence in Fig. 5 of any sensitivity to albedo (or spatial gradients in albedo) for Case 3.

In Fig. 6 the temperature differences between Case 2 and Case 3 are 7 to 10 degrees. The Case 2 contours significantly cross those of Case 3, but this is mainly because the terrain never heated as much during the day for Case 2. Temperatures across the region are 33.9 - 68.5, 27.0 - 57.5, and 33.9 - 68.5 deg F for cases 1 through 3.

Figures 7 and 8 show the forecast at 2300 local time when the process of radiative cooling is very active. The Case 3 contours have significantly separated by 10 to 70 km to the north of those for Case 1 since lower albedo areas radiate heat more efficiently, although actual temperature differences at each point are at most about 1-2 deg F. These differences indicate the importance of terrain albedo at these times. Albedo gradient effects may also be indicated by the significant differences in Case 1 and Case 3 contour directions and by their crossings.

Figure 5. Temperature forecast for 1700 local time (white: α=var; black: α=0.1)

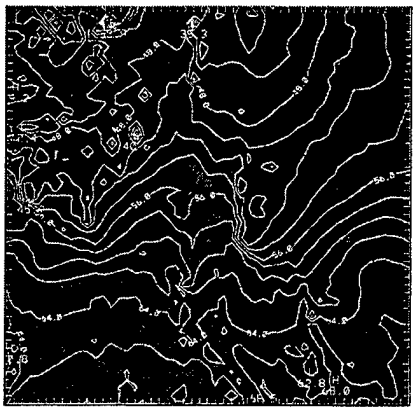

Figure 6. Temperature forecast for 1700 local time (white: α=var; black: α=0.8)

Figure 7. Temperature forecast for 2300 local time (white: α=var; black: α=0.1)

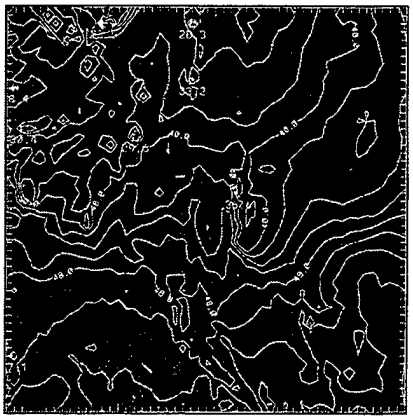

Figure 8. Temperature forecast for 2300 local time (white: α=var; black: α=0.8)

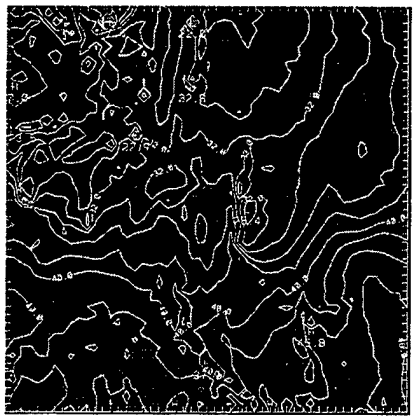

Figure 9. Temperature forecast for 0500 local time (white: α=var; black: α=0.1)

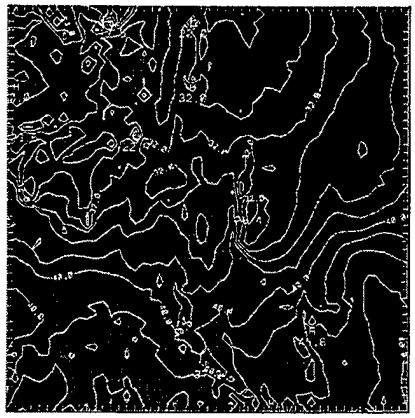

Figure 10. Temperature forecast for 0500 local time (white: α=var; black α=0.8)

Figure 8 shows that at 2300 local time the radiative cooling for Case 3 is "catching up" to the lower temperatures but smaller cooling rate of the high uniform albedo of Case 2. Temperatures in Case 2 are now only about 4-6 deg F cooler than for Case 3. The minimum to maximum ranges over the entire region for cases 1 through 3 are 22.7 - 54.6, 19.7 - 51.5, and 23.5 - 55.1 deg F respectively.

Figures 9 and 10 show the results for 0500 local time the next morning (21 November 1997). Radiative cooling has slowed, and the differences between Case 1 and Case 3 are only about 0.2-0.5 deg F over most of the region. The contours for Case 1 are now slightly south of those for Case 3 (within 10-20 km for most regions), just the opposite of those at 1100 local time. These are consistent with the lower albedo and more rapid cooling for Case 2. For Case 1 versus Case 3 the differences are only about 2-4 deg F. Temperature ranges over the region are 16.7 - 46.5, 15.4 - 44.1, and 17.5 - 48.0 for cases 1 through 3.

Figure 11 shows the wind vectors at 1100 local time for Cases 1 and 3. The upper (white) vectors in each terrain element are for Case 3. The lower (gray) vectors are for Case 1. The contours are elevation data used in the BFM forecast. They range from a low of 1000 m in the SE corner to 1250 m at the White sands monument, 2847 m in the Sacramento Mountains 40 km east of the monument, and 3118 m in the Gila wilderness on the west-central border. Maximum wind speeds are 13.6 kts for Case 3 and 11.4 kts for Case 1.

The forecast wind vectors are mostly in the same direction and have comparable speed at this time of day, regardless of albedo differences.

Figure 12 shows the wind vectors at 1100 local time for Cases 2 and 3. Again, Case 3 winds are the upper (white) vectors, Case 2 the lower (gray) vectors.

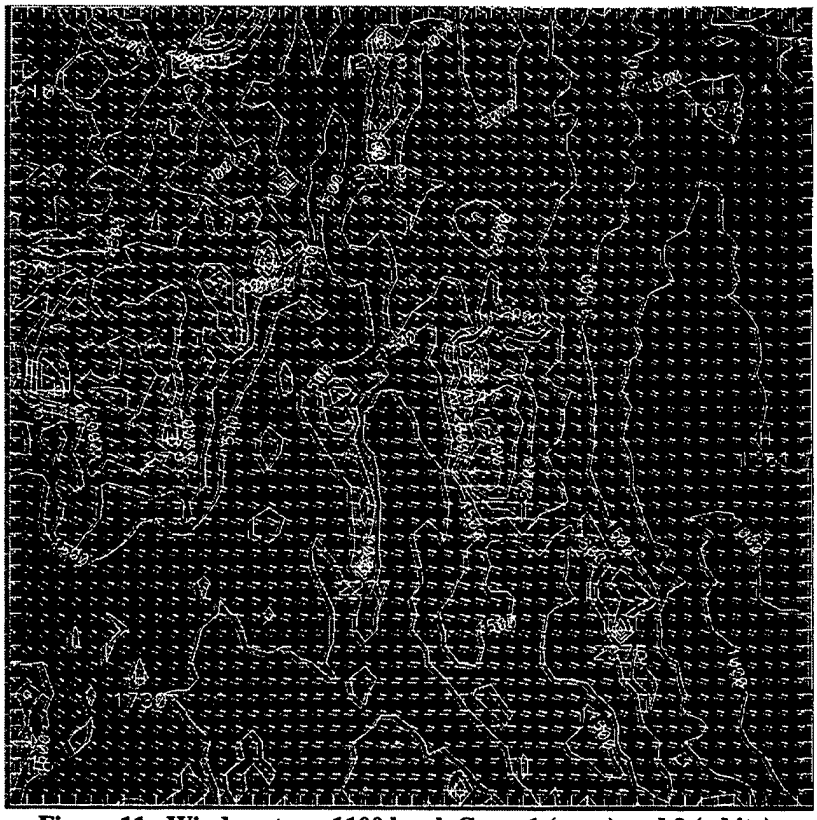

Figure 11. Wind vectors, 1100 local, Cases 1 (gray) and 3 (white)

The maximum wind speed for Case 2 is 9.0 kts. The directions and speeds are comparable, although the wind directions are more from the west in the NE and SE corners of the map. As with the comparison between Case 1 and Case 3, it is difficult to identify any striking effects of albedo on wind direction and wind speed.

Since it is difficult to see features on a map at this scale, the following figures have been extracted from the larger domains. Figures 13 and 14 show the wind vectors for 1700 local time in the vicinity of White Sands. Figure 13 compares Case 3 (upper, white vectors) to Case 1 (lower, gray vectors). Figure 14 compares Case 3 (upper, white vectors) to Case 2 (lower, gray vectors). The maximum forecast wind speeds at 1700 local over the entire NM domain are 12.4, 10.8 and 14.4 kts for Cases 1 through 3. Figures 15 and 16 are the corresponding forecasts for 2300 local time. The maximum wind speeds over the NM domain are 8.8, 7.0 and 12.6 kts for Cases 1 through 3. Figures 17 and 18 are for 0500 local time the next morning. The maximum wind speeds are 14.6, 12.5 and 16.6 kts for Cases 1 through 3.

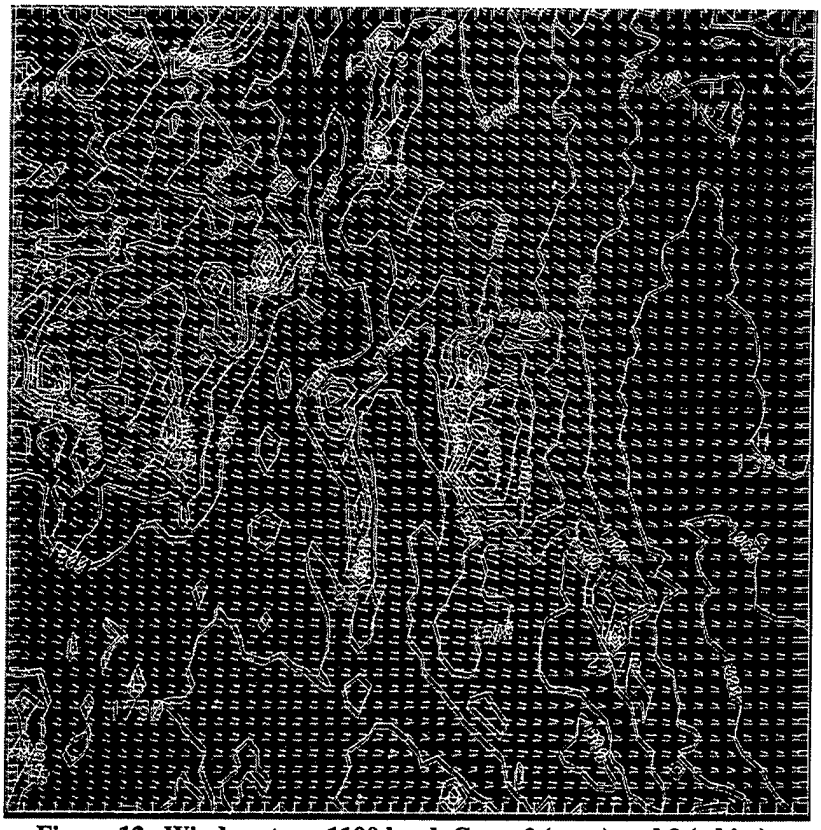

Figure 12. Wind vectors, 1100 local, Cases 2 (gray) and 3 (white)

From these figures it is evident that there is some sensitivity to albedo in forecast wind speeds (maxima of about 2-4 kts) and directions (about 5-30 deg) for the cases that we ran through BFM. However, the average differences appear to be small except for only a few areas on the map. It is perhaps significant that the greatest wind speeds are all for Case 3, indicative of some influence of the albedo gradients. The larger albedo of Case2 results in a consistently lower maximum wind speed, although there are areas in Figs. 12 and 16 where Case 2 wind speeds are larger. In addition the nocturnal flow east to west off the Sacramento Mountains into the White Sands area (center of Figs. 15 through 18) show significant differences in direction and speed, especially during cooling at 2300.

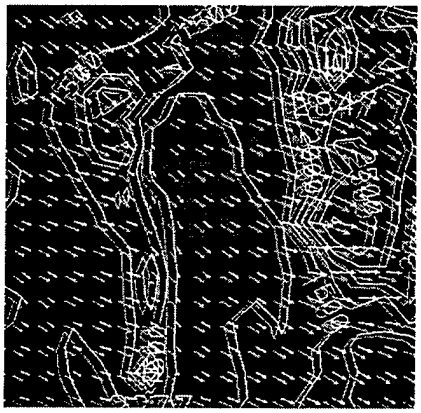

Figure 13. Wind Vectors, 1700 local, Cases 3 (white) and 1 (gray)

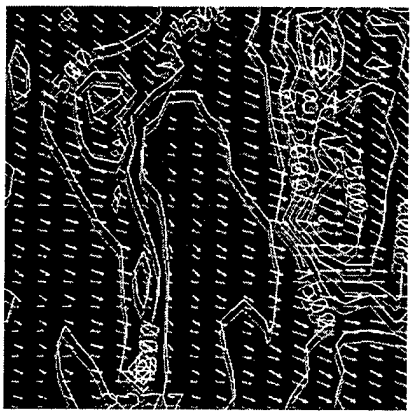

Figure 14. Wind Vectors, 1700 local, Cases 3 (white) and 2 (gray)

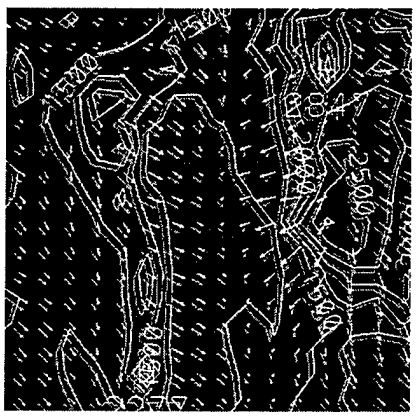

Figure 15. Wind Vectors, 2300 local, Cases 3 (white) and 1 (gray)

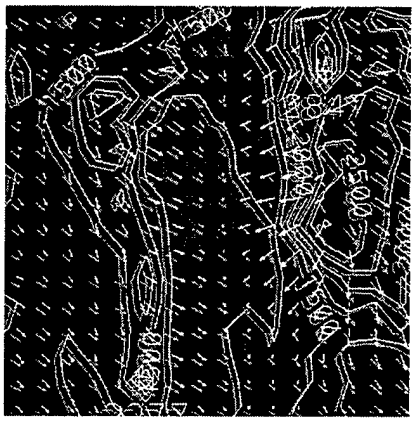

Figure 16. Wind Vectors, 2300 local, Cases 3 (white) and 2 (gray)

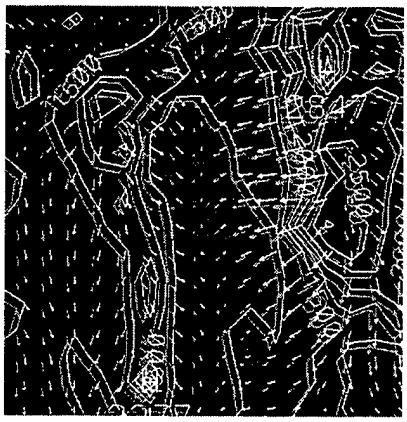

Figure 17. Wind vectors, 0500 local, Cases 3 (white) and 1 (gray)

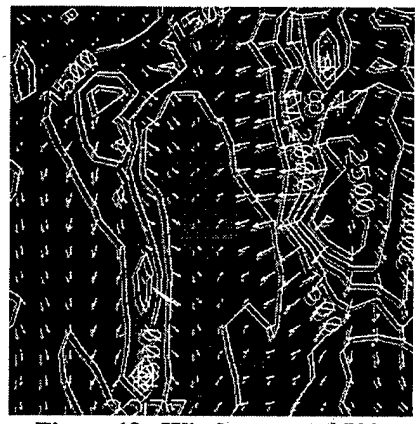

Figure 18. Wind vectors, 0500 local, Cases 3 (white) and 2 (gray)

Of course the actual effects on winds and temperatures of gradients in terrain albedo could be larger than those forecast. We have not yet examined the effects of varying other soil and vegetation thermal characteristics on the forecast. Furthermore, the BFM is a hydrostatic model and thus does not capture all the convective (vertical) dynamics. Finally, for each run we used the same initializing large spatial-scale forecast wind and temperature inputs. These vertical profile data are at wide latitude and longitude spacing (1 deg, corresponding to 111 km north-south data spacing). They also span the forecast time period, and BFM "nudges" its solutions well above the surface layer to agree with these forecasts. We did not test what the effects of different albedos would also be on the larger scale initializing forecast.

METEOROLOGICAL SATELLITE DATA

Satellite receivers were recently used by the IMETS in the Advanced Warfighter Experiments to provide image products for posting on the C4I weather homepages. Visible and infrared image data are available from polar orbiting satellites (Defense Meteorological Satellite Program Optical Line Scanner, DMSP/OLS; NOAA Advanced Very High Resolution Radiometer, NOAA/AVHRR) and geostationary satellites (NOAA Geostationary Operational Environmental Satellite NOAA/GOES). In future we would like to make qualitative and, if possible, quantitative use of the microwave DMSP channels for their derived quantities, discussed below.

Figures 19 and 20 show output from the DMSP OLS in the visible and infrared (11 μm) bands. The regions covered are New Mexico, west Texas, parts of surrounding states of Arizona and Colorado, and Mexico. Because

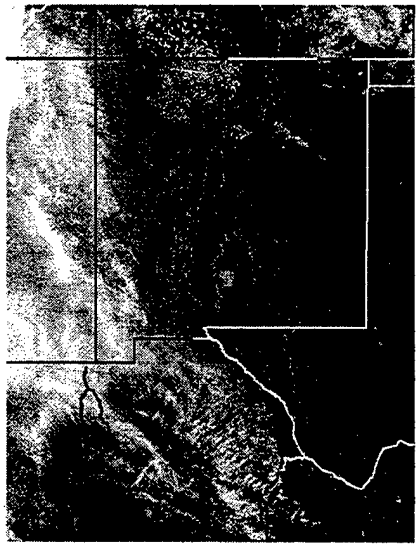

Figure 19. DMSP OLS Visible (09/02/97)

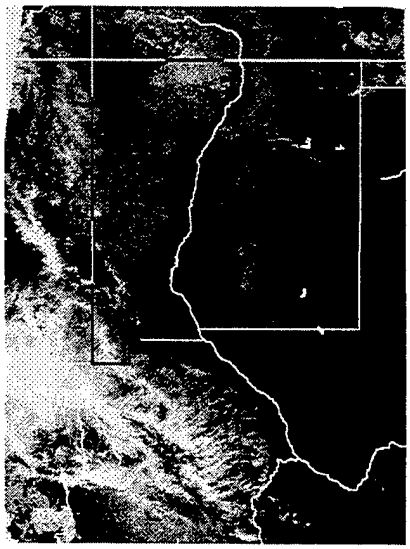

Figure 20. DMSP OLS IR (black hot) (09/02/97)

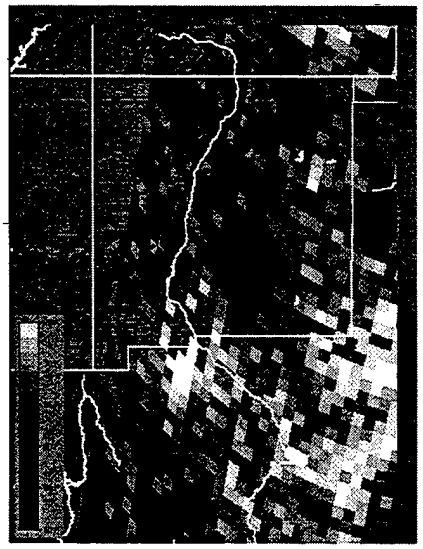

Figure 21. DMSP SSM/I Surface Temperature (deg F) (09/02/97)

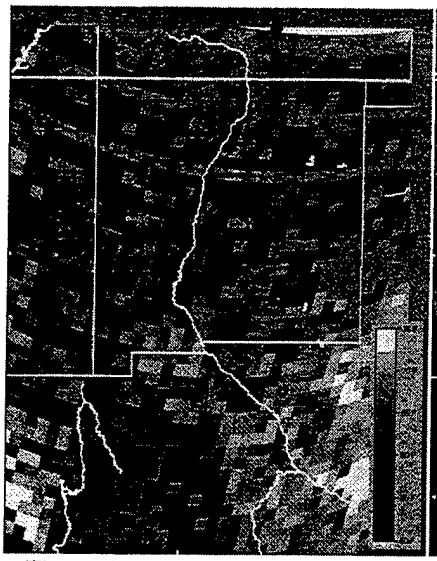

Figure 22. DMSP SSM/I Surface Temperature (deg F) (08/14/97)

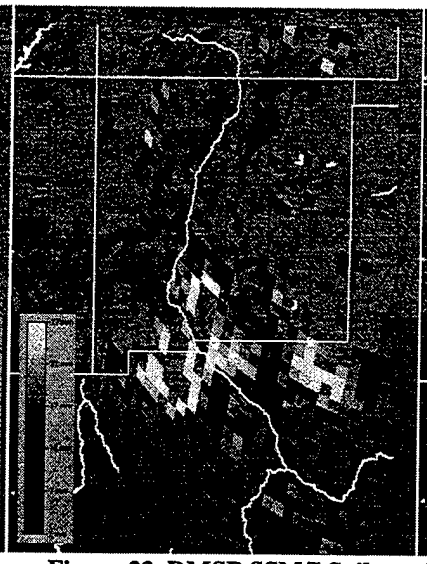

Figure 23. DMSP SSM/I Soil Moisture (mm) (09/02/97)

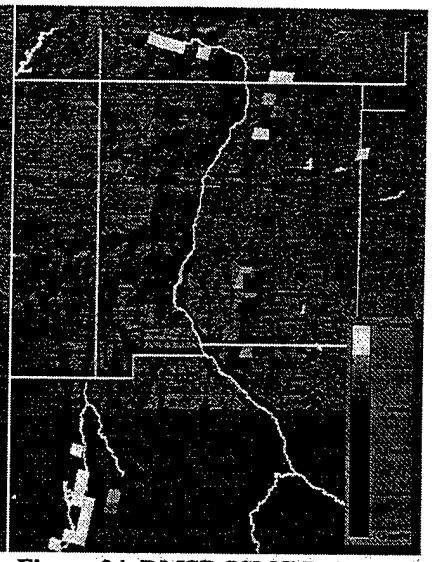

Figure 24. DMSP SSM/I Rain rate (mm/hr) (08/14/97)

the main DMSP pass of interest occurs primarily just after dawn (0600-0700 local time), one can see the terrain relief clearly, including the White Sands Monument and the Sacramento Mountains east of the monument. Looked at closely, the visible image shows the long shadows cast by these and other mountains along the Rio Grande River. Note the infrared image shows relatively cool areas around White Sands and the much colder Sacramento Mountains as bright areas of the image. The dark band along the Rio Grande and the Texas-Mexico border is moist, warm air.

The DMSP Special Sensor Microwave/Imager (SSM/I) is a seven-channel, four-frequency linearly polarized passive microwave radiometric system that measures brightness temperatures at 19.3 (V/H), 22.2 (V), 37.0 (V/H) and 85.5 GHz (V/H). It has been in operation on DMSP satellites for slightly more than ten years. It was designed to provide a number of parameters of great interest, including: land surface temperature, soil moisture, precipitation over land, cloud liquid water content, integrated columnar water vapor, surface type classification and other information on cloud cover, winds over the ocean, and on ice and snow cover (Hollinger, 1990). Designed resolutions are 50 km, 30 km and 15 km for the 19-22, 37 and 85 GHz bands, respectively.

Figures 21 and 22 show derived surface temperatures in deg F. Compare temperatures along the Rio Grande and west Texas with the warm (black hot) parts of Fig. 20. The extraction algorithm used was the "AFGWC D-matrix" coefficient method. This method was first developed in 1987 (Hollinger, 1987) as linear, four-channel regression fits to polarized brightness temperature data and simulations. The "D-matrix" refers to separate sets of coefficients developed for 11 different climate codes for each hemisphere. The significant channels are 85 and 22 GHz. Data from the initial flights of the sensors were compared to ground truth in studies published in 1990, and the coefficients were modified where appropriate. For example, McFarland, et al. (McFarland, 1990) derived coefficients for surface temperatures and compared results to ground truth. The rms errors were on the order of 2.0 - 2.6 deg C (3.5-4.7 deg F) for crops, moist soils and dry soils. Their revised algorithms use land classification to select the best sets of coefficients. It should not be used where precipitation is occurring, over dense vegetation, lakes, standing water, snow or frozen surfaces due to their effect on polarization differences between channels.

Figure 23 shows extracted soil moisture in mm H2O. These are based on extraction using AFGWC D-matrix coefficients. Soil moisture is one of the more important environmental quantities because of its obvious impact on maneuver and trafficability. The 37 GHz and 85 GHz brightness temperature differences are the indicators of soil moisture, at least for surface water and soil depths to a few millimeters (Neale, 1990). Values shown in this figure indicate high soil moisture near the surface, corresponding to about 1 inch of rainfall.

Figure 24 shows high rain rate regions extracted from the SSM/I using the D-matrix algorithms. The small regions are rain rates on the order of 16-17 mm/hr. Figure 25 shows the areas of potentially lighter rain rates of 2.6-

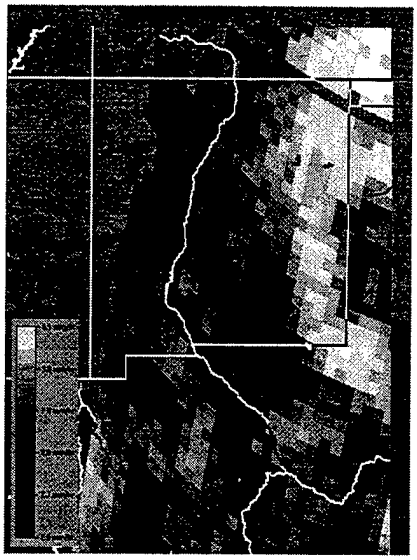

Figure 25. DMSP SSM/I Potential Rain Rates (mm/hr) (09/02/97)

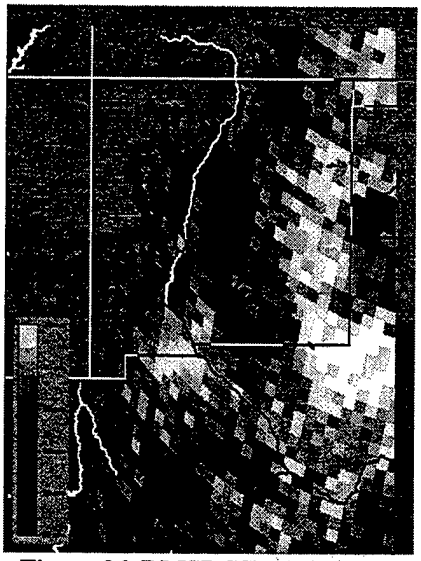

Figure 26. DMSP SSM/I Column Water Vapor (kg/m^2) (09/02/97)

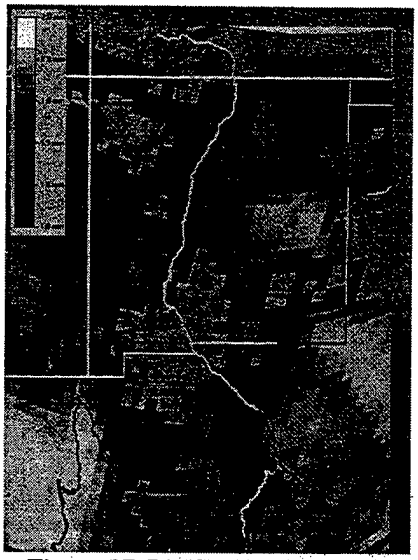

Figure 27. DMSP SSM/I Liquid Water Content (kg/m^2) (08/14/97)

3.1 mm/hr. The extraction algorithm is that of Wentz (Wentz, 1987). (The regions of potentially low rain rates generally correlate closely to total liquid water content and columnar liquid water.)

Figure 26 shows extracted values for columnar water vapor (in kg/m^2 or mm H2O) in the range of 58-73 Kg/m^2 using the revised extraction coefficients of Alishouse (Alishouse, 1990). Figure 27 shows total liquid water content (in kg/m^2 or mm H2O) in the range of 1.52-1.96 Kg/m^2 also using the method of Alishouse (Alishouse, 1990) for a different date. The extraction coefficients had been substantially revised from the D-matrix coefficients in their 1990 studies. Allihouse, et al. determined that the algorithm was much more accurate over the ocean than over land. Over the ocean the cloud liquid water data showed rms differences from ground truth of 0.035 Kg/m^2 for a mean of 0.136 Kg/m^2. They also determined that the algorithm had very low correlation, however, when applied over land. Thus, these values may be suspect. Other algorithms in the literature are being investigated.

Other methods for extracting quantitative data from met-satellite sensors exist in the literature. A very useful quantity that can be applied in computing meteorological corrections to line-of-sight visibility is remotely sensed optical depth. Figure 28 shows the logic applied to a physics-based extraction method for analysis of AVHRR polar orbiter data. The data include 5 EO channel images from 0.62 to 12 μm. The method requires that the satellite be within 50 deg of overhead and that the sun be within 50 deg of the horizon. Tests of the 10.8 μm channels are made for high clouds and at 0.91 μm for low clouds. If the radiance ratio at 0.62 μm to that at 0.91 μm is larger than 1.5, then the observed point on the surface is declared cloud free. The channel radiances are then analyzed using angular scattering functions for aerosols and by applying standard radiative transfer equations. Cloud-free optical depths can be estimated up to optical depths of 5 and to a resolution of 0.2 in optical depth.

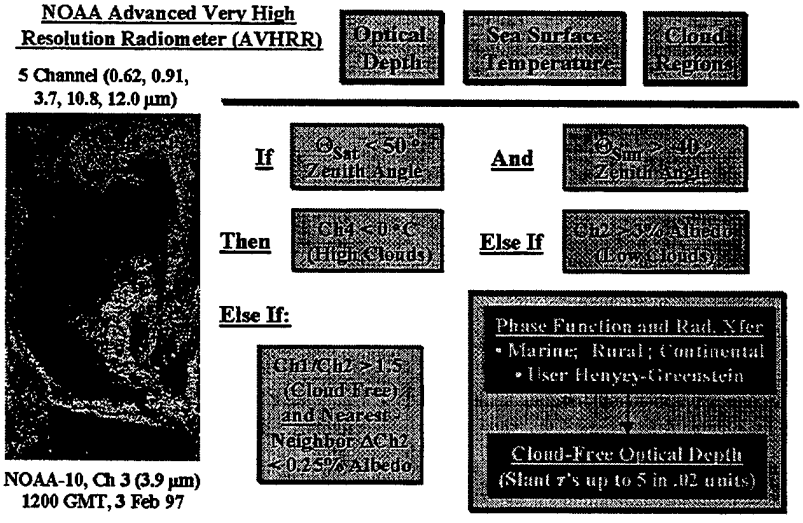

Figure 28. Cloud Cover and Optical Depth Algorithm

CONCLUSIONS

We believe that the fusion of information from forecasts, energy balance models, surface state data and meteorological satellite exploitation will benefit all four areas. Greater exploitation of meteorological satellite-based and surface databases of terrain characteristics are fruitful areas for supporting the next generation of quantitative weather effects parameters and model products for battlefield weather support to C4I systems. The investigation of the particular effects of surface albedo data on BFM forecasts in this paper show that albedo has a significant effect, particularly on the dynamic periods of temperature changes at night and during mid-day. Their impact on forecast wind speeds and directions are much less evident, whereas effects of terrain elevation are much more significant. Based on this study it appears that accuracy in surface albedo of 0.1 is probably sufficient for BFM.

The millimeter wave radiometer channels of the DMSP satellites can provide important environmental data that can be used to validate the BFM forecasts and perhaps provide inputs for otherwise data-denied areas. We will need to establish whether satellite data are sufficiently accurate for use in quantitative decision aids. Nonetheless, they can still provide valuable qualitative information on regions of high soil moisture, rain rates and surface temperature. We will also look at the existing algorithms for extracting data from the visible and infrared channels of the NOAA AVHRR and GOES satellites. The GOES stationary satellites are, of course, potentially more versatile than the polar orbiters since they will allow continuous monitoring of the changes in weather and surface state.

REFERENCES

Alishouse, J., J. Snider, E. Westwater, C. Swift, C. Ruf, S. nyder, J. Vongsathorn and R. Ferraro, 1990; "Determination of Cloud Liquid Water Content using the SSM/I", IEEE Transactions on Geosciences and Remote Sensing, 28, Sep 1990, 817-845

Dumais, R., 1997; "The US Army Battlescale Forecast Model Over the Southern California Dessert: case Study of 16 April 1997", Proceedings of the 1997 Battlespace Atmospherics Conference, Dec 1997, San Diego, CA

Henmi, T., 1997; "Battlescale Forecast Model at Ft. Irwin, CA and Statistical Evaluation of 24 Hour Forecast Fields", Proceedings of the 1997 Battlespace Atmospherics Conference, Dec 1997, San Diego, CA

Hollinger, J., J. Peirce and G. Poe, 1987; "Special Sensor Microwave/Imager Users Guide", Naval Research Lab, Washington DC, 120 pp.

Hollinger, J., 1990; "Introduction, Guest Editor to the IEEE Transactions on the SSM/I", IEEE Transactions on Geosciences and Remote Sensing, 28, Sep 1990, 779-780.

Kidder, S. and T. Vonder Haar, 1995; Satellite Meteorology: An Introduction, Academic Press, New York.

McFarland, M., R. Miller and C. Neale, 1990; "Land surface Temperature Derived from the SSM/I Passive Microwave Brightness Temperatures", IEEE Transactions on Geosciences and Remote Sensing, 28, Sep 1990, 839-845.

Neale, C., M. McFarland and K. Chang, 1990; "Land Surface-Type Classification using Microwave Brightness Temperatures from the Special Sensor Microwave/Imager", IEEE Transactions on Geosciences and Remote Sensing, 28, Sep 1990, 829-838.

Sauter, D., 1997; "IWEDA for Brigade Task Force XXI: Assessment and Lessons Learned", Proceedings of the 1997 Battlespace Atmospherics Conference, Dec 1997, San Diego, CA

Shirkey, R., 1997; "Quantitative vs. Qualitative Tactical Decision Aids: Is There a Difference?", Proceedings of the 1997 Battlespace Atmospherics Conference, Dec 1997, San Diego, CA.

Wentz, F., 1987; "Derived Precipitation from DMSP SSM/I", Journal of Geophysical Research, V91, C2, 2289.

IMPROVING FIELD ARTILLERY METEOROLOGICAL DATA FOR THE U.S.ARMY USING A PC-BASED MESOSCALE MODEL

David I. Knapp (dknapp@arl.mil)
Patrick Haines
U.S. Army Research Laboratory
Battlefield Environment Division
Information Sciences and Technology Directorate
White Sands Missile Range, NM 88002-5501

1. INTRODUCTION

Meteorological conditions along the trajectory of a projectile or rocket directly impact its route of flight. Additionally, other factors affecting trajectory include muzzle velocity and temperature, aiming, and numerous other variables associated with firing the munition towards the target. However, variations in atmospheric density, temperature, wind speed and wind direction are the most sensitive and critical factors which may cause the munition to miss its intended target, assuming the muzzle was properly aimed. Ignoring weather impacts in artillery aiming calculations can account for close to 50% of the bias error for projectile targeting and nearly 95% of the bias error for rocket targeting (Lillard, 1990). Clearly, providing accurate meteorological data for artillery targeting algorithms can dramatically improve the chances for first-round success.

2. CURRENT ARTILLERY METEOROLOGY CAPABILITIES AND NEAR-TERM IMPROVEMENTS

Deployed artillery units rely on meteorological data supplied by weather balloons launched within a few kilometers of the gun location. Upper-air data supplied by these balloons are converted into an alpha-numeric Fire Control Computer Met Message which covers 26 "lines" or vertical zones of meteorological data from the surface to 20 km AGL. Each line contains an average zone wind direction, wind speed, virtual temperature, and pressure data used by the fire control computers in artillery aiming algorithms. The upper-air data is assumed to accurately depict the vertical profile of meteorological parameters over the apogee point of the projectile's trajectory. Problems with this assumption include the following:

- For a launch site at least 20-30 km away from the target, the apogee location may actually be located in a completely different microclimate such as on the opposite side of a hill or mountain. Data collected by the balloon may not accurately reflect true data at the apogee location, or at the target location.

-The balloon data could be "time stale," or more than an hour old. This is an important concern when temperature inversions are present (dawn/dusk, high pressure regimes, etc.) or frontal boundaries, jet streaks, and other phenomena are causing significant changes in the local wind and temperature patterns.

-Artillery Meteorology (ArtyMet) units do not exchange meteorological data, thus a more recent balloon launch a short distance away from an artillery battery may be ignored and stale data used instead.

-In the complete absence of balloon data, "default met" or standard atmosphere curves of temperature and dew point are used, and wind speed/direction is assumed to be zero everywhere. This is the worst case scenario and is the cause for the most serious artillery aiming errors.

Improvements to the current ArtyMet capabilities are being implemented in 1998. The Time Space Weighted model (TSW) (D'Arcy, 1997) will be included as part of a hardware/software upgrade for ArtyMet equipment. Artillery units will be able to exchange local balloon data with other ArtyMet units deployed in their immediate area. Thus, data from up to three recent weather balloons from different

locations will be used to generate the Computer Met Message (MET-CM). TSW addresses the time staleness and lack of data exchange problems of current limited capabilities. The model utilizes all recent available ArtyMet balloon data, weights the data temporally and spatially in an objective analysis to produce a vertical profile, and allows for "stale" data up to four hours old to be included with more recent and current data. The main problem with TSW is that even though more current and accurate data may be collected for generating the MET-CM, the data is still only collected from a few localized ArtyMet locations, with data again "assumed" to be valid far away at the apogee of the trajectory. Additionally, TSW does not consider terrain and local diurnal heating/cooling effects on the objectively analyzed meteorological parameters.

Though TSW does indeed provide significant improvement over single-station data, and dramatic improvement over default standard atmosphere data, there is still a very important need for improving meteorological data for aiming algorithms at the apogee location, over the target area, and along the entire trajectory of the shell. Future weapon systems will also require data for trajectories and targets up to hundreds of kilometers away from the launch location. In addition to wind speed/direction, virtual temperature, and density/pressure calculations along the trajectory, advances in projectile munition and submunition sensitivities and target acquisition needs lead to the requirement for forecasting such parameters as clouds, precipitation, visibility, icing, turbulence, and severe weather over the target area. To meet these long-range targeting sensitivity needs, four dimensional gridded mesoscale model output can supply ArtyMet units and Fire Control algorithms with on-site and real-time launch site, trajectory, and target area weather data. The Battlescale Forecast Model (BFM) is the first model being tested to meet these needs.

3. MESOSCALE MODELING ON A PERSONAL COMPUTER: THE PC-BFM

To meet the near-term needs of the Army's ArtyMet soldiers, the mesoscale model of choice has to run on Army Common Hardware. For ArtyMet hardware, this will be the Pentium personal computer platform. The goal is to be able to host a mesoscale model which can produce real-time nowcasts over horizontal areas as large as 250 km x 250 km. The first version of the BFM is driven by the Higher Order Turbulence Model for Atmospheric Circulations (HOTMAC), a hydrostatic model which meets the initial needs of the ArtyMet mission (Henmi and Dumais, 1996). As PC hardware and software evolve in the future, a major goal is to transition to a more sophisticated hydrostatic or non-hydrostatic model.

The HOTMAC-driven BFM is a boundary layer model which has been tailored to meet the Army's specialized battlefield needs. Model physics include latitudinal, seasonal, and diurnal radiation effects, a dynamic boundary layer, and land/water contrasts. It is run on the PC with 32 vertical levels from the surface to 12 km MSL. Horizontal resolution is normally 8 km across the domain, but can be changed as the user desires. PC hardware requirements for running the BFM include a Pentium 200MHz system with 128 meg of RAM and one 2-Gigabyte hard drive. The SCO UNIX operating system is currently used, with plans to transition to Windows NT in the future. For research purposes (not necessary for operational use by ArtyMet personnel), output is analyzed using the VIS 5D program. The BFM takes an average of five minutes per hour of model output to run, with the same time ratio applied to the fifteen minutes of model spinup time (three model hours) necessary to start producing forecast data.

The BFM can be run in two modes of operation. The full mode includes initializing the model with all available raw data recently received from the model domain area of coverage, plus supplemental upper air data from the domain's boundary area. Additionally, the full mode includes regional model initialization grids for BFM "steering" towards the desired forecast hour solution, allowing the BFM to produce forecasts out to twelve hours and beyond. In degraded mode, the BFM can be run without the benefit of regional model steering grids, but model output is restricted to a maximum of six hours.

When fielded, the BFM will receive data from two sources. Regional model initialization grids and raw data from the BFM domain and surrounding boundary areas will be shipped from DoD communications channels down to the artillery units. Additionally, local ArtyMet data consisting of recent surface and upper-air observations not in the regional database will be available to each system running the BFM.

4. INITIAL PC-BFM VERIFICATION

PC-BFM verification is ongoing and addressing a wide range of topographical and climatological scenarios. One such project involves using the BFM in a degraded mode with archived surface and upper-air data from the Prototype (Meteorological) Artillery Subsystem (PASS) database from 1974 (Barrett, 1976). For this experiment, nine upper air data locations were set up in and around the White Sands Missile Range (WSMR), NM area. These data sets were collected at varying hours from dawn to dusk on each test day and provide an excellent source of information for evaluating the BFM in degraded mode.

Figure 1 depicts the area of interest and the upper air stations used in the study. The two northernmost stations (Apache and Holloman) were treated as the "targets" or BFM forecast locations.

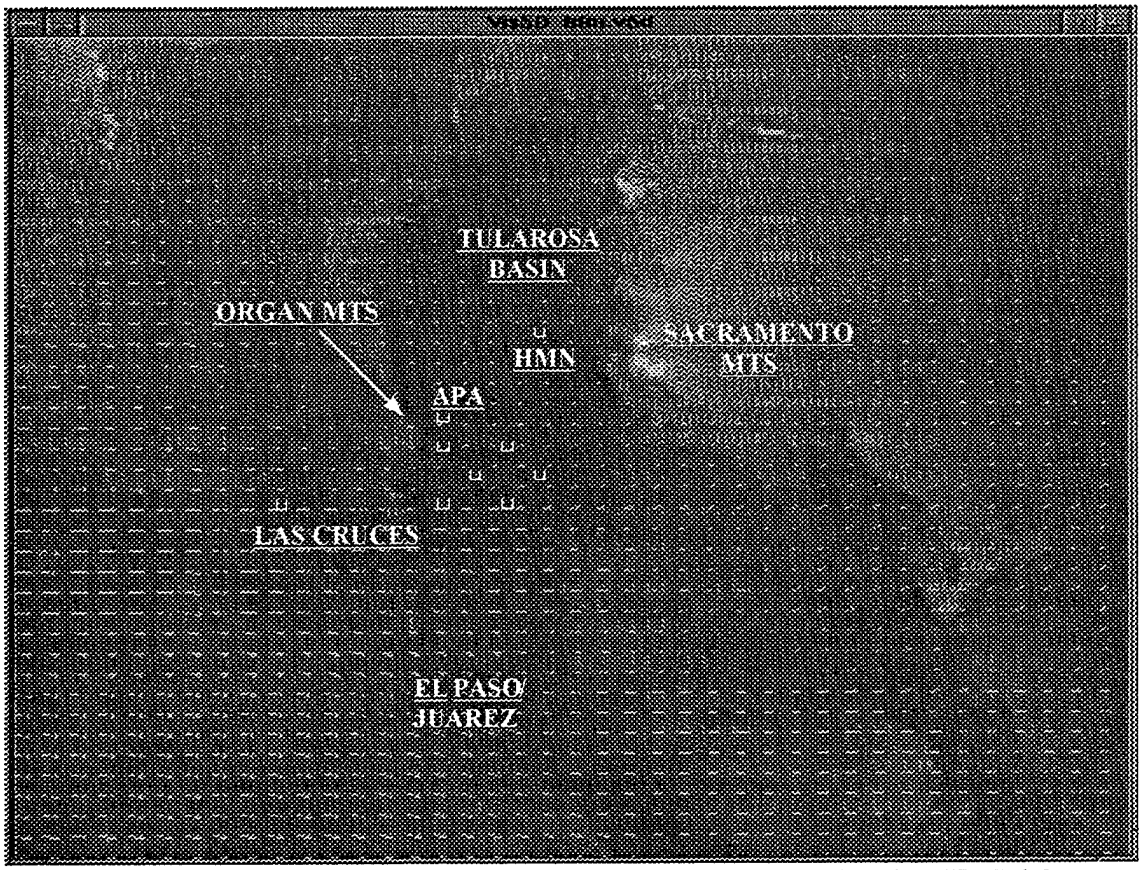

Figure 1. PASS Database topographical depiction with locations of upper air data sites (U). Brighter terrain depiction corresponds to higher elevations. BFM 0-hr output at 1700 UTC, 2 Dec 1974 is presented. Wind vectors shown are at 3 km MSL at each model grid point (8 km horizontal resolution). APA (Apache Site) and HMN (Holloman Air Force Base) are the target locations used to verify BFM output. Distance from Las Cruces (U) to HMN (U) is 100 km.

Verification has been completed for wind speeds at the lowest ten MET-CM levels from the surface to 3500 m AGL using different combinations of southern WSMR stations to initialize the BFM for 0-hour model output verification at APA and HMN. Comparisons of BFM results against TSW calculations have also been accomplished. Results of all comparisons are shown in Table 1. Data shown represent 52 cases for the BFM runs using all seven stations and for the Default Met cases. For the TSW and BFM runs using TSW stations, 32 cases were studied. Statistics show the significant improvement of TSW over default met. More importantly, comparisons of TSW against the BFM (run using the same three southern

WSMR stations as comparable TSW calculations) show the BFM improving upon TSW by 8-10%. When including all seven southern WSMR stations in the model runs, BFM improvements range from 20-22% better than TSW.

	Default Met	TSW	BFM 0-hr (TSW stations)	BFM 0-hr (All 7 stations)
RMSE (kts)	17.71	4.99	4.58	4.00
MAE (kts)	13.82	3.70	3.33	2.88

Table 1. Root Mean Square Error (RMSE) and Mean Absolute Error (MAE) verification statistics for PASS cases. Data shown include verification calculations for all 10 MET-CM levels.

More detailed comparisons of Mean Absolute Errors between TSW and BFM output by MET-CM level are shown in Table 2, broken out by verification location. Some of the more interesting results show that the combined statistics for the BFM outperform TSW except at the surface and at the highest verified level. Since this study has been completed, modifications to the BFM's use of raw surface data have been implemented which should eliminate these low-level problems. Breaking out the low-level statistics by location, TSW was better at the Apache site, yet the BFM was better at Holloman AFB, further away from the initializing stations used. This comparison shows the utility of using a mesoscale model for depicting boundary layer conditions far from the areas where raw initializing data was collected. Aloft, the BFM was the better model at the Apache site, but TSW was better at Holloman AFB at levels 2250, 3250, and 3750 m AGL. These errors aloft would be reduced or eliminated if the BFM is run in full mode using regional model initialization gridded data. Also, the longer range uses of the BFM for target area conditions more than 50km away from the raw data input locations would be expected to show the BFM outperforming the TSW.

Level	Apache		Holloman AFB		Combined	
(m AGL)	TSW	BFM	TSW	BFM	TSW	BFM
Surface	3.86	4.07	3.03	2.87	3.43	3.45
100	3.00	3.48	4.65	3.16	3.85	3.32
350	3.35	2.83	3.55	3.29	3.45	3.07
750	3.48	2.62	3.39	3.32	3.43	2.98
1250	3.83	2.93	5.29	4.16	4.58	3.57
1750	4.00	3.10	4.68	4.00	4.35	3.57
2250	3.55	3.28	2.74	2.94	3.13	3.10
2750	4.17	3.38	3.87	3.23	4.02	3.30
3250	3.59	3.21	2.52	2.87	3.03	3.03
3750	3.86	3.79	3.55	4.06	3.70	3.93
All Levels	3.67	3.27	3.73	3.39	3.70	3.33

Table 2. Mean Absolute Error (kts) verification statistics by vertical levels comparing Time Space Weighted model with Battlescale Forecast Model output at each verification location and combined.

5. SUMMARY

A mesoscale model for battlefield artillery meteorology applications has been successfully hosted on a personal computer for the U.S. Army. The Battlescale Forecast Model provides improved artillery firing calculation accuracy over the Time Space Weighted objective analysis output as shown in initial verification of wind speed calculations. Verification continues for the wind speed cases in an effort to show statistics for virtual temperature, pressure/height, and wind direction accuracy from the surface to 4 km AGL. The BFM will provide ArtyMet soldiers with much needed accuracy and timeliness for future implementation of precision guided munitions requiring meteorological data forecast along the proposed trajectory, as well as over the target area.

The PC-BFM can be transitioned for use by any local area forecasting application. It's use at local forecast offices (DoD and civilian) and by researchers can provide fine-scale mesoscale model forecasts at low cost. In the future, two primary improvements to test will be increasing the resolution of the BFM output (down to 1 km) as initialization model grid resolution improves, as well as transitioning to a more sophisticated hydrostatic or non-hydrostatic model.

REFERENCES:

Barrett, Kenneth M., 1976: Technical Report*: A Description of the Artillery Meteorological Comparisons at White Sands Missile Range, October 1974-December 1974 ("PASS" - Prototype Artillery [Meteorological] Subsystem)*, Atmospheric Sciences Laboratory, White Sands Missile Range, NM.

D'Arcy, Edward M., 1997: The Effects of a Time-Space Weighted Model on the MLRS. *ARL-TR-1043*, Army Research Laboratory, Battlefield Environment Division, White Sands Missile Range, NM.

Henmi, Teizi and R.E. Dumais, 1996: Description of the Battlescale Forecast Model, *ARL-TR-1032*, Army Research Laboratory, Battlefield Environment Division, White Sands Missile Range, NM.

Lillard, Robert L., 1990: Technical Report: *Field Artillery Accuracy Improvement Analysis.* U.S. Army Field Artillery School, Ft. Sill, OK.

Experimental Evaluation of the Integrated WAVES - CSSM Models

Dr. Alan Wetmore (awetmore@arl.mil, DSN 290-2249)
Dr. David Ligon (dligon@arl.mil, DSN 290-1799)
Dr. Patti Gillespie (pgillesp@arl.mil, DSN 290-1374)
Army Research Laboratory - Adelphi Lab Center, MD

Michael Seablom
TASC, Inc.

Dr. Guy Seely
Radex, Inc.

Dr. Joel Mozer (mozer@hurricane.phl.af.mil)
Air Force Research Laboratory - Hanscom AFB, MA

January 16, 1998

Abstract

WAVES (Weather and Atmospheric Effects for Simulation) comprises a suite of models designed to calculate illumination and propagation effects in realistic near earth partly cloudy conditions. The component models include the discrete ordinates radiative transfer model BLIRB (Boundary Layer Illumination and Radiative Balance), optical turbulence parameter model ATMOS, geometric radiance interpreter VIEW, and the scene modifier PIXELMOD. VIEW and PIXELMOD are examples of a general class of utility models, whereas BLIRB and ATMOS are models of physical processes. These models are integrated together to provide either modifications to existing scenes or parameters for real time computer image generation or radiances values for a defined scenario. WAVES does not attempt to impose any particular rendering method, but does provide data to support a wide range of possible user implementations.

Current research projects include an integration and end to end evaluation with the AF CSSM (Cloud Scene Simulation Model). This project includes developing the appropriate hooks with the WAVES suite to include all cloud types modeled by CSSM, and use that input to appropriately modify the radiative transfer. The results of this integration is then being evaluated over a two year program funded the EA for Space and Atmosphere.

The CSSM–WAVES end-to-end evaluation includes a field test, held in August 1997, at Hanscom AFB. This test will compare surface illumination magnitudes and variability at several wavelengths with computed values based on: surface and rawinsonde observations; used to initialize CSSM; liquid water content fields from CSSM used to initialize BLIRB; and surface illumination output from the BLIRB component of WAVES. The evaluation will include statistical evaluation of the measured time series illuminations with both advected cloud field calculations and time-evolved CSSM cloud fields.

Our currently plan for WAVES is to develop a suite of simulation models for the US Army that have broad application in wargames & simulation, information & planning, test & evaluation, training, and engineering & development that have either integrated or connections to models providing other environmental effects. In the past the EOSAEL was this solution. Tomorrow's solution will be WAVES.

1 Introduction

There are many Defense Department systems that are affected by the presence of clouds in the battlespace. The effects can be on entire systems or limited to degradation of individual sensors; adapting to these effects can change either the tempo of operations or call for modifications to tactics or doctrine. Some effects are as simple as total obscuration of line-of-sight by a cloud. Blocking of line-of-sight can affect both air-to-air engagements, air-to-ground, and potentially ground-to-ground engagements. Sometimes the effect is complete and long lasting, such as when low level clouds prevent detection of ground targets or carrying out

battle damage assessments. At other times, the optical and infrared radiative properties of clouds reduce the lock-on-range for a sensor and change mission profiles and force pilots to approach closer to an enemy target. Another major effect of clouds on battlespace endeavors is the variation of illumination they create. Combined with the secondary effects of induced variation of thermal signatures, clouds and their variability can change the scenes to be observed in addition to their role in interposing themselves between observer and observed.

In the first, blocking case, knowledge of the exact location of clouds either through observations or modeling would allow the theoretical exploitation by avoiding clouds that interfere with target detection or approaching clouds to use them as concealment. In the latter case a more detailed analysis of the radiative effects must be undertaken. False positive triggering of space based surveillance systems by sun glint off of cloud tops must be accounted for when developing those systems. In air-to-air scenarios the complex radiative patterns of the clouds serve as clutter in the field of view of sensors. In ground based targeting, the rapid changes in solar flux on surfaces increase the variability in surface clutter that makes targets difficult to detect. One solution to this problem has been ongoing development of both cloud simulation models CSSM[1] and Radiative Transfer models WAVES.

These radiative effects are the subject of our present validation effort. The dynamic nature and variability of clouds have made validation of accurate predictive models difficult. We are developing the a system to accurately generate synthetic atmospheric scenarios that will simulate the radiometric conditions in a battlespace containing natural clouds. The combination of the Air Force's Cloud Scene Simulation Model (CSSM) and the Army's Boundary Layer Illumination and Radiation Balance (BLIRB) model are the basis for these capabilities. Validation of the extent that our synthetic radiative scenarios match real-world conditions is necessary before allowing the decision makers to depend on our models. Section 2 gives a short description of the models we are integrating and validating. Our plans for and preliminary results of this validation effort are described in section 3.

2 Overview

The CSSM was developed by The Analytic Sciences Corporation (TASC) for the US Air Force Phillips Laboratory. It's purpose is generate high resolution synthetic cloud fields for use in DoD modeling and simulation activities. The representation of clouds by the CSSM is Liquid Water Content (LWC). The CSSM takes as input, atmospheric wind, temperature, and moisture data, such as from radiosonde or numerical weather prediction, along with cloud descriptive parameters (cloud type, amount coverage, etc.) for a given region. The output of the CSSM is a four-dimensional (time and space) field of cloud LWC which is statistically consistent with the input values, but at a much higher spatial and temporal resolution.

The CSSM uses a fractal algorithm to generate the variable structure which is characteristic of clouds. The free parameters of this fractal algorithm were determined via an analysis of aircraft measurements of liquid water content in real clouds. This empirical process is augmented within the CSSM with simple physics-based algorithms to add realism to the structure, development, and motion of the cloud fields. The current (CSSM version 2.0) is capable of generating complex cloud scenarios consisting of multiple layers of up to 12 different cloud types, including structures such as cloud streets and lee wave clouds. An example of a cloud field from the CSSM model is shown in figure 1.

BLIRB is a component of the Weather and Atmospheric Visualization Effects for Simulation (WAVES) suite of tools. One purpose of WAVES is to give the user the ability to modify images to include the effects of weather and the atmosphere. BLIRB is the 3-D spectral radiative transfer code used within WAVES. Other components include VIEW, which evaluates line-of-sight radiance and transmittances; ATMOS, an optical turbulence model; and PixelMod, for image spectral estimation and modification of images.

WAVES performs range-dependent calculations using line-of-sight radiative transfer methodology for the actual image modifications. These line-of-sight calculations require a description of the radiative fluxes and extinction throughout the local environment. Radiative fluxes, turbulence parameters, and extinctions are calculated by the first phase of the WAVES models. Image modification is done by the PixelMod program using line-of-sight data created by the VIEW program using the 3-D databases created by the BLIRB program.

The foundation of the WAVES suite of algorithms is an 8-stream, or 24-stream, radiative transfer model,

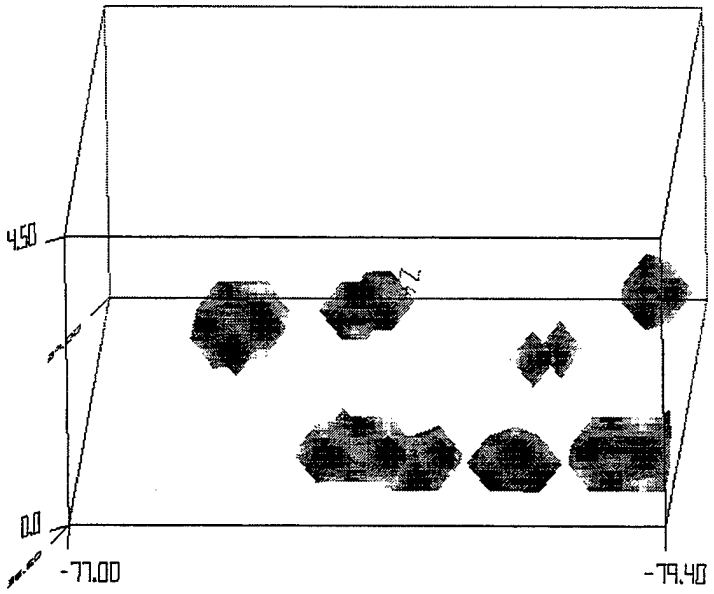

Figure 1: Cloud Liquid Water Content Distribution.

BLIRB[2]. BLIRB accounts for the scattering and aerosol extinction in the atmosphere and uses MODTRAN molecular extinction profiles. BLIRB was designed for near-earth scenarios, and deals with a region up to 10 kilometers in length and width, and a height of either 5 or 12 kilometers above ground level (AGL). This allows most cloud related effects to be explored. BLIRB uses an iterative discrete-ordinates approach to calculate the direct and diffuse solar (or lunar) flux, the directional radiances, and the total extinction and scattering for all points on a grid with typical spacing of 250 meters. It performs these calculations for spectral bands as defined in MODTRAN. The calculations allow complex inhomogenious cloud fields to be used as input. This extension beyond the one dimensional vertical profiles available in MODTRAN is essential to realistic modeling of the battlefield. The directional effects allow for realistic changes in the scenes as the observer turns,; the inhomogeneity allows for clouds to engulf the observer or target, or pass between them; all in a self-consistent, radiometrically correct manner. Figure 2 shows an example of a BLIRB calculation of the direct solar component at the surface.

The result of the BLIRB model is a database of extinction, scattering, and directional radiances, that depend upon the wavelength and position in 3-D space. These values are used by viewing and imaging tools as they project lines-of-sight through space from the observing sensor to the elements that make up the scene[3].

Evaluation of BLIRB for simple cloud geometries has been reported in [3, 4, 5]. These evaluations have shown reasonable agreement off the BLIRB model with standard models, but have also exposed weaknesses. These areas are current research areas for BLIRB.

The ultimate goal is to validate the entire chain from weather to CSSM to WAVES and surface illumination and cloud scene radiances. The overall chain of models must work together as well as operate as individual models.

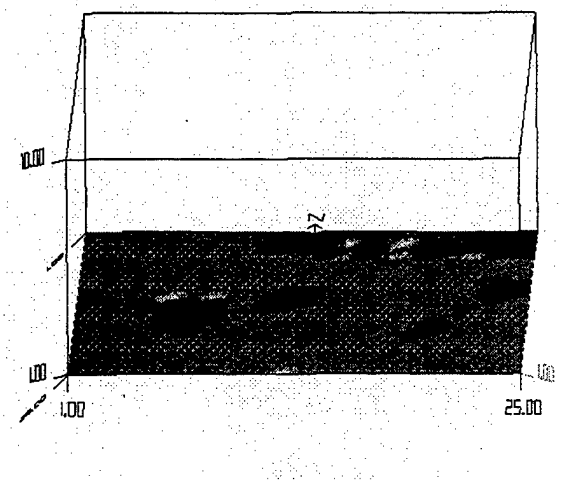

Figure 2: The surface illumination showing the shadows from the clouds.

3 Approach

The principle focus of the radiometric validation effort is to assess and improve the physical realism of 2-D synthetically generated cloud scenes. Our approach to this goal is to start with the simple, gross characteristics of synthetic images as compared to images of real clouds and progressively work towards more subtle and complex comparisons. The basic idea is to select a set of representative metrics for cloud containing images and compare the statistics of these metrics for a large sample of real and synthetic images of similar cloud fields. The results of these comparisons will then be used to evaluate and adjust, if necessary, the simulation methodology.

Because we never generate the actual cloud field experienced during the experiment we need to generate sufficient synthetic cloud fields to yield statistically valid comparisons. The agreement of these multiple synthetic fields should ever be any better than the agreement of multiple different "equivalent" cloud fields themselves.

The first step of this process is to determine the appropriate metrics. The first category of these metrics emphasize the bulk statistical properties of the rendered image at the expense of spatial information. "Classical" statistical measurements such as mean, variance, skewness, and kurtosis fall into this category. These measures are often difficult to use in interpreting complex imagery. One promising approach we have investigated is the Chi-Squared testing of histogram distributions as detailed in [6]. It is also important to remember that sensors and target acquisition systems can be sensitive to extreme values and the shapes of the tails of the distributions, so that matching central metrics is not an adequate test.

Another category of metrics emphasizes spatial properties of the synthetic imagery. These types of metrics are largely independent of the details of the radiative transfer scheme and depend strongly on the shape of the generated cloud fields. Examples of these types of measures are spatial image spectra in Fourier or wavelet bases and spatial correlation functions[7]. Some results on spectra of spatial effects compared with ground-based instrumentation are shown in figure 3. The time series of both pyranometer data and TPQ-11 radar data is shown. The power spectra seem to exhibit significant agreement to the universal -5/3 power law.

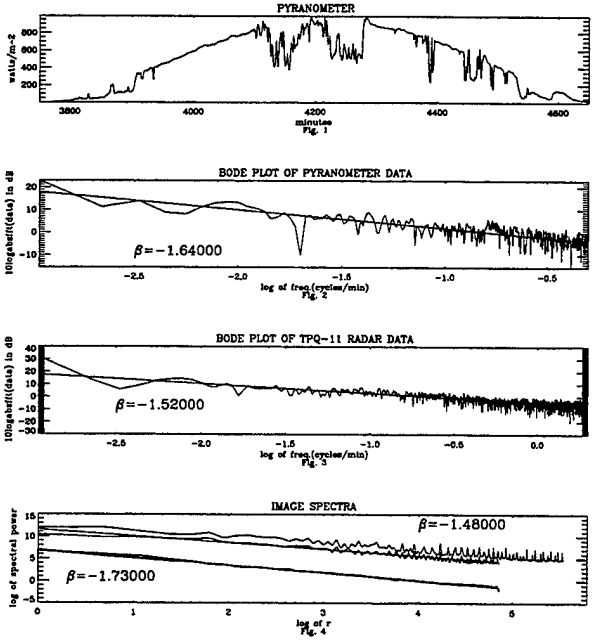

Figure 3: Preliminary analysis of the pyranometer data.

Both spatial and bulk metrics need to be examined for a variety of wavebands to verify proper spectral behavior. An overall figure of merit can be constructed by determining the distance between a representative

set of real and synthetic scenes in metric space. Determining the weight of each specific metric is a difficult problem. We believe metrics that have a clear physical interpretation and thus have quantifiable effect on the generated imagery should be weighted most heavily in any overall figure of merit.

The concept of the experiment is to monitor and instrumented target area on the ground next the Phillips Laboratory building from the building roof. On the roof will be the RTISR, and 3–5 μm and 8–12 μm imaging sensors. Figure 4 shows the RTISR; this instrument can sample at 30Hz over 20 wavebands in the visible and has internal absolute calibration. The 8–12 μm FLIR is shown in figure 5. There is an additional television camera shown in figure 6 for monitoring sky and cloud conditions. The imaging sensors are all focused on a nearby test site containing blackbody targets and cubical targets with measured surface temperatures.

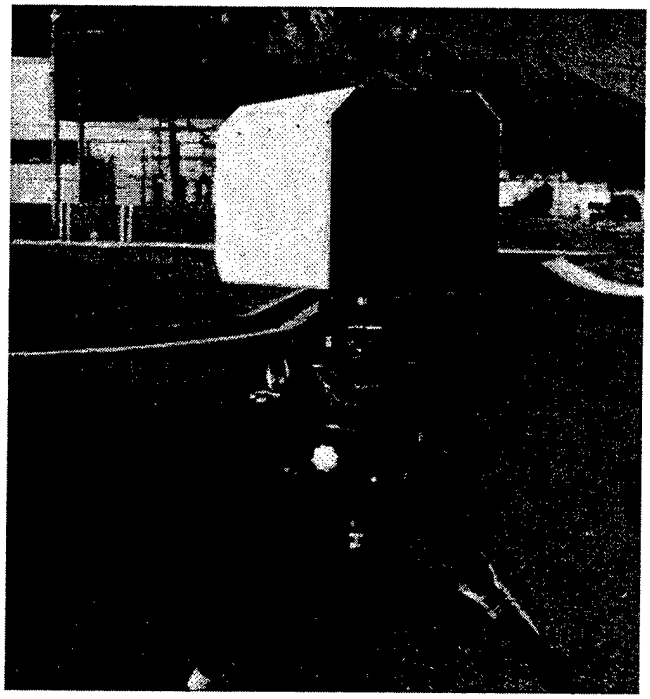

Figure 4: Real Time Imaging Spectral Radiometer (RTISR)

The original experiment was planned for execution in August 1997. In July 1997 however, the real-time spectral imaging radiometer (RTISR) failed. Loss of this piece of equipment has caused a delay in the field experiment. The RTISR is now undergoing repairs and the field experiment has been rescheduled for March 1998. A short data gathering experiment was held during the original August 1997 experiment period. The remainder of the instrumentation functioned and some preliminary data was obtained and analyzed.

Also at the target site are pyranometers and radiometers as well as standard meteorological measurements of temperature, pressure, wind speed and direction and relative humidity. 200 meters away is a TPQ-11 radar shown in figure 7 and the balloon launch site for obtaining profile data. All measurement and data

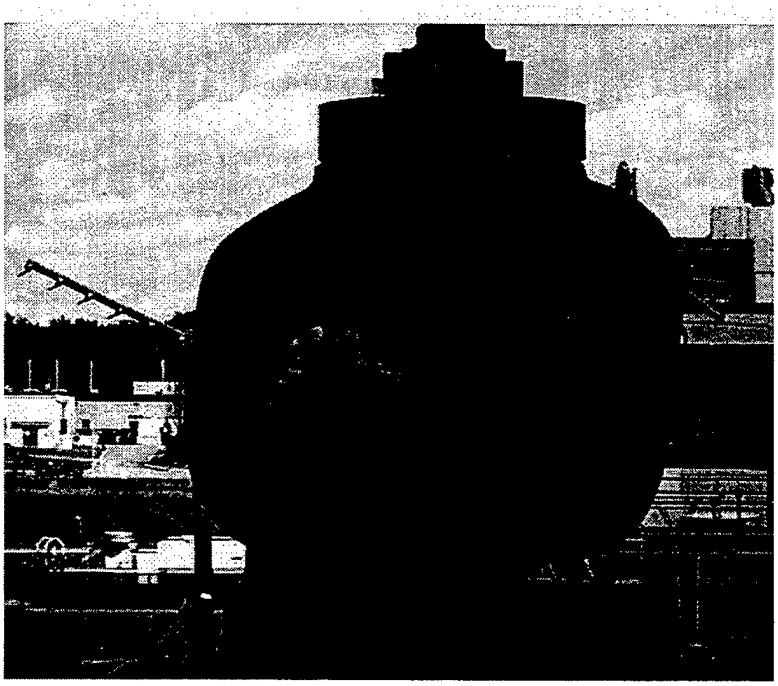

Figure 5: The FLIR camera.

collection are computerized and recorded at a central indoor site.

There are really only two additional things that we would like to be able to measure. The first is the actual 3-D cloud density function, though we do have the TPQ-11 radar data to reassure us that our synthetic cloud distributions are reasonable. The second is a large scale (100's of meters) high resolution measurement of surface illumination values instead of the approximately 10 to 20 meter images that we can record.

As mentioned earlier we are only expecting statistical correlations with our measurements because the cloud fields we are generating with CSSM are not exactly the same as those we are measuring in, only "like" them. We also are dealing with approximately point measurements to validate both area measurements of surface illumination and the scenes presented by 3-D cloud distributions. One thing we can do is use the time series at our measurement site of measurements caused by the advection of slowly changing cloud fields across our measurement area as a surrogate for the wide area measurements that we would like to make.

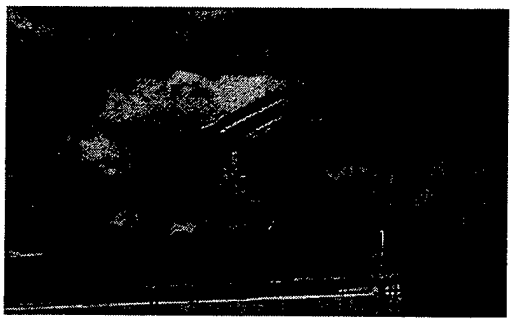

Figure 6: The rooftop camera used for cloud awareness.

Figure 7: The TPQ-11 cloud radar.

4 Conclusions

We have described the CSSM and BLIRB models that are being integrated to calculate synthetic cloud scenes and our preliminary approach to a validation methodology. The principal motivation for this effort is to demonstrate the feasibility for using synthetic cloud scene imagery in a quantitative for design, evaluation, training, and planning applications. This evaluation work is continuing and so we present this preliminary review of approach at this time.

References

[1] M. E. Cianciola, M. E. Raffensberger, E. O. Schmidt, and J. R. Stearns. Atmospheric scene simulation modeling and visualization. Technical Report PL-TR-96-2079, Air Force Phillips Laboratory, Hanscom Air Force Base, MA, 1996.

[2] A. E. Wetmore and A. Zardecki. The boundary layer illumination and radiation balance model (BLIRB). In *Proceedings of the Cloud Impacts on DoD Operations and Systems 1993 Conference*, Fort Belvoir, VA, November 1993.

[3] David Tofsted, Patti Gillespie, and Alan Wetmore. The WAVES modeling suite: Extensions and evaluation update. Ground Target Modeling and Vehicle Target Conference, August 1995.

[4] Michael. B. Wells. Monte Carlo code for evaluating the boundary layer illumination and radiation balance model (BLIRB). Technical Report ARL-CR-193, January 1995.

[5] Michael. B. Wells. Monte Carlo code for evaluating the boundary layer illumination and radiation balance model (BLIRB). Technical Report ARL-CR-205, November 1995.

[6] J. P. Welch. Smart weapons operability enhancement (SWOE) joint test and evaluation (JT&E) program. Technical Report SWOE Report 94-10, August 1994.

[7] G. Seeley, J. B. Mozer, and E. Emre. Time series cloud forcing study of cloud scene model. In *Proceedings of the Cloud Impacts on DoD Operations and Systems 1997 Conference*, Newport, RI, September 1997.

THE U.S. ARMY BATTLESCALE FORECAST MODEL OVER THE SOUTHERN CALIFORNIA DESERT: CASE STUDY OF 16 APRIL, 1997

Robert E. Dumais, Jr. *
United States Army Research Laboratory
Battlefield Environment Division
White Sands Missile Range, NM, 88002-5501
Ph: 505-678-4650
E-mail: rdumais@army.arl.mil

The U.S. Army Battlescale Forecast Model (BFM) is a meteorological mesoscale modeling code that can simulate radiationally driven boundary layer flow patterns such as valley daytime upslope and nighttime downslope winds, along with coastal land/sea breeze circulations. Large scale meteorological temporal and spatial boundary conditions are supplied to the BFM from the U.S. Navy Operational Global Atmospheric Prediction System (NOGAPS). Additionally, available local upper air radiosonde and surface sensor observations are used in the BFM initialization. For this study, the model is run using a ten kilometer horizontal terrain resolution on a 51x51x16 grid configuration, with the model top at 7000 meters above the maximum terrain gridpoint. The day of April 16, 1997, over the Ft. Irwin area of southern California provided a good opportunity to test the model, since the synoptic scale meteorological forcing was weak and the solar insolation was strong. Additionally, the terrain is very rugged and complex, including some coastline, which should generate some fairly complex boundary layer wind and temperature fields under such a synoptic regime. A number of different model initializations are used to generate a set of 24-hour simulations, in order to test the model's sensitivity to initial data input. Using available surface and upper air observation sites, model data is verified both every hour (surface) and every twelve hours (upper air).

1.0 INTRODUCTION

The U.S. Army Battlescale Forecast Model (BFM) is a mesoscale meteorological forecast model that was designed primarily to forecast boundary layer meteorology over complex terrain, at high terrain resolution. The model typically runs over small areal domains (<= 500 km X 500 km) at a horizontal grid space resolution of 10 km (although spacing as fine as 2.5 km are possible). Terrain elevation for the model is derived by using the Defense Mapping Agency Level 1 Digital Terrain Elevation Data of the World (DTED). The model uses 16 vertical levels, log-linearly placed so that maximum resolution is near the surface, with a rigid top 7000 meters above the surface (at the model grid point of maximum terrain elevation). The model is hydrostatic and quasi-Boussinesq, which means that vertical accelerations are assumed to be insignificant and that horizontal temperature gradients must not become extremely large. In addition, the model does not incorporate sophisticated parameterization schemes for precipitation microphysical processes, nor for subgrid- scale convection. The model does use a terrain-following vertical coordinate system, and it incorporates sophisticated parameterizations for calculating surface radiation fluxes. In addition, an order 2.5 turbulence closure scheme is used by the model. Although not capable of forecasting large-scale meteorological processes or mesoscale processes driven by convection, it is on the other hand very capable of forecasting boundary layer circulations driven by diurnal radiation variations (such as land/sea breezes and mountain upslope/downslope winds). For the model to perform well, it is necessary for the larger- scale meteorological variations to be incorporated into the BFM by way of a second model, either regional or global. For the current version of the BFM, the time-dependent large-scale meteorological forcing is supplied by the Naval Operational Global Atmospheric Prediction System (NOGAPS) model (Van Tuyl (1996) or Hogan and Brody, (1993)) and assimilated by using a Newtonian nudging method described in Henmi and Dumais (1997). The full set of model equations, along with assumptions and parameterizations, can be found in either Henmi and Dumais (1997) , Yamada and Bunker (1989), or Yamada (1981).

This study examines how the BFM forecast fields of winds, temperature and moisture vary over a 24-hour period, given 9 different configurations of input data. The area selected was a 500 km x 500 km area centered on Ft. Irwin, California, due to its desert locale and the relatively rugged terrain features found within. The model was run at a horizontal grid spacing (terrain resolution) of 10 km. The day studied was April 16, 1997, with the model run starting at 1200 UTC (0400 LST) on the 16th and ending at 1200 UTC (0400 LST) on the 17th. This day was considered suitable due to the fact that the large- scale meteorological forcing was weak and that the radiational heating and cooling over the complex terrain could be expected to have a substantial influence on the boundary layer flow structure.

2.0 BFM INITIALIZATION FIELDS

The BFM used in this study is initialized using objectively analyzed meteorological fields

derived from using the Navy's NOGAPS model forecast fields and/or all the available upper level radiosonde observations within a 1600 km x 1600 km area around the model's center grid point. For some of the model runs, surface observation data were also used and were assimilated (nudged) dynamically during the model's 3-hour spinup cycle. However, unlike the upper air data, the surface data were only collected within the model's 500 km by 500 km forecast grid area.

Currently, the BFM receives the NOGAPS data from the Air Force Global Weather Center (AFGWC) through the Automated Weather Distribution System (AWDS). The full NOGAPS forecast fields can be obtained from the Fleet Naval Numerical Oceanographic Center (FNNOC) at 1 degree spatial resolution and at the following vertical pressure levels: 1000, 975, 925, 900, 850, 700, 500, 400, 300, 250, 200, 150, 100, 70, 50, 30, 20, 19, and 10 mb (including both the 2 and 10 magl levels). In addition, the forecast grids are produced at 6-hour intervals during the forecast cycle. However, the AWDS grid system is still configured for the US Air Force Global Spectral Model (GSM) resolution, which was the predecessor to the NOGAPS at AFGWC. The horizontal resolution of the GSM that was transmitted through the AWDS was nearly 380 km, while in the vertical mandatory pressure levels were supplied (not including the 975, 925, or 900 mb levels). Forecast grids were produced at 12-hour intervals. Therefore, in order for the AWDS system to transmit the NOGAPS fields on the old GSM grids, the NOGAPS data must be interpolated (and thus degraded) to the coarser resolution. This is currently the biggest deficiency within the framework of the current BFM data collection process, and its effects can be expected to be negative on the overall model performance out to 24 hours. In this paper, to be consistent with the current operational mode of the BFM, the degraded NOGAPS obtained via the AWDS is used.

It should be made clear that although the actual BFM forecast area in the study is a square grid of 500 km x 500 km (51x51 grid points at 10 km horizontal spacing), the upper air data (radisonde and NOGAPS) collection area used for the objective analysis is considerably larger in size: 1600 km by 1600 km. The horizontal resolution interpolated to in this larger area remains at 10 km, so that the objectively analyzed meteorological fields within the 500 km by 500 km BFM subregion are simply "cut out" of the larger domain. The reason for this is to ensure that a larger quantity of radiosondes and NOGAPS forecast grid points are used by the interpolation schemes that produce the 3-dimensional analysis fields. The data are first interpolated horizontally onto the BFM gridpoints, either at constant pressure levels (NOGAPS) or predefined height levels (radiosonde). Once completed, both the radiosonde and the NOGAPS data are then interpolated separately to the model terrain following vertical levels, with a compositing technique used to finally merge/blend the NOGAPS and radiosonde data. Since the surface observation data are not objectively analyzed, but are instead dynamically assimilated by the model during its 3-hour spinup cycle, they are collected only within the BFM 500 km by 500 km domain.

For this study, seven different variations of initial data used for model initialization were experimented with. The purpose of doing this was to examine both qualitatively and quantitatively the effects of initial data on subsequent 24-hour BFM forecast fields. In addition, two additional simulations were run with i.) less model smoothing of prognostic fields and ii.) nudging to the initial moisture profile through the entire simulation. Model smoothing is discussed in Yamada and Bunker (1989), and it is done in such a way using the terrain following coordinates that it is possible for some undesired vertical diffusion to be introduced. These extra simulations were run to see how much of an effect the model smoothing has on the forecast

fields, in addition to seeing how useful it might be to retain the initial moisture profile structure in short term forecasts within very weak synoptic regimes. That is, will nudging to the NOGAPS moisture fields possibly degrade the BFM moisture forecast when the large scale forcing is negligible? Table 1.0 lists the various combinations of initial data used in the model simulations studied.

TABLE 1.0 24-HOUR BFM SIMULATIONS COMPARED IN STUDY

USING APRIL 16, 1200 UTC INITIAL DATA

	MODEL	**INITIAL DATA**	
SIMULATION	NOGAPS	RAOBS	SURFACE OBS
A	Y	Y	Y
B	Y	Y	N
C	Y	N	Y
D	Y	N	N
E	N	Y	Y
F	N	Y	N
G *$_1$	Y	Y	Y
H *$_2$	Y	Y	Y
I *$_3$	N	Y	Y

*$_1$ model smoothing factor set to 0.15 for winds and 0.075 for temperature and dewpoint (for all other runs, the factor is set 0.5 for winds and 0.25 for temperature and dewpoint)

*$_2$ same as simulation A except that the Vandebergh raob is removed.

*$_3$ same as simulation E except that the Vandebergh raob is removed and the model is nudged to the initial moisture profile throughout the entire simulation.

3.0 Observation Sites used for Model Comparison Study

A total of 28 surface observation sites were originally selected for use in the model statistical study. However, only 17 of these sites had more then 20 out of the 25 possible observation hours during the forecast cycle reported. These sites are listed in Table 2.0, along with the number of hours of reports available and the associated mean surface wind speed recorded for these hours. In addition, the radiosonde site located at Desert/Mercury, Nevada

Table 2.0 Surface Observation Sites used for Model Statistical Study

Site No.	Site Location	Station ID	Lat (Deg N)	Long (Deg W)	Site Elevation	No. Obs.	Avg. Sfc. Wind Speed
1	Las Vegas, NV	KLAS	36.08	115.17	664.0 m	25	4.16 kts.
2	Nellis AFB, NV	KLSV	36.23	115.03	570.0 m	25	4.40 kts.
3	29-Palms, CA	KNXP	34.30	116.17	626.0 m	22	1.45 kts.
4	Ontario, CA	KONT	34.05	117.60	287.0 m	22	3.68 kts.
5	Edwards AFB, CA	KEDW	34.90	117.88	702.0 m	24	6.71 kts.
6	Riverside, CA	KRIV	33.88	117.27	469.0 m	24	4.58 kts.
7	Dagget-Barstow, CA	KDAG	34.85	116.78	587.0 m	21	9.14 kts.
8	Mercury Site, NV	KDRA	36.62	116.02	1009.0 m	24	3.92 kts.
9	Blythe, CA	KBLH	33.62	114.72	121.0 m	22	5.00 kts.
10	Kingman, AZ	KIGM	35.27	113.95	1033.0 m	24	5.75 kts.
11	Camp Pendleton, CA	KNFG	33.30	117.35	24.0 m	24	4.83 kts.
12	San Berna., CA	KSMF	34.10	117.23	353.0 m	23	5.48 kts.
13	Long Bch., CA	KLGB	33.82	118.15	12.0 m	24	4.21 kts.
14	Los Ang., CA	KLAX	33.93	118.40	32.0 m	24	7.13 kts.
15	San Diego, CA	KSDM	32.57	116.98	160.0 m	25	4.12 kts.
16	San Diego, CA	KSAN	32.73	117.17	9.0 m	25	5.40 kts.
17	Thermal, CA	KTRM	33.63	116.17	36.0 m	23	6.09 kts.

(DRA), was used to statistically examine the model's performance at the following heights above ground level: 250 m, 500 m, 1000 m, and 1500 m. In addition, the mandatory pressure levels of 700 mb and 500 mb were also examined. Statistics for meteorological parameters above the surface were generated every twelve hours, at the 0, 12, and 24 hour model forecast times. Parameters examined are temperature, dewpoint temperature, u and v wind components, and wind speed magnitude. In this paper, only the mean absolute error statistic is discussed.

4.0 Results of Model Simulations

A. Synoptic Weather Situation for April 16, 1997

The large-scale synoptic weather pattern over the forecast area during the day of April 16, 1997, was extremely tranquil and uneventful. At the surface, the region was located in a relative col between strong high pressure over the Northern Plains (~ 1030 mb), a weaker 1022 mb high center well of the California coast, a weak 1015 mb high over the Baja of Mexico, and a 995 low pressure center approaching British Columbia, Canada. At 850 mb a similar flow pattern existed, with a tongue of 16-20° C temperatures running from Yuma, Arizona to Death Valley, California. In the upper levels, a ridge of high pressure existed in the northern Rockies, with strong shortwave troughs over both the Great Lakes and off the Pacific Northwest/British Columbia coast. Additionally, a very weak cutoff low pressure circulation was present well southwest of San Diego and west of the Baja Peninsula. The flow over southern California was very weak at both the 500 mb and 300 mb levels and somewhat anticyclonic. Within such a regime, the boundary layer flow patterns over southern California can be expected to be strongly influenced by the mesoscale diurnal temperature gradients generated over the complex terrain and near the water/land coastal interface. Thus, this day was selected for the present study.

B. Summary of Model Simulations

1. General Observations

In each of the simulations, the model was able to reproduce very similar flow patterns near the surface over the forecast domain. These patterns were mostly diurnally driven upslope/downslope and sea breeze/land breeze circulations. During the early morning hours of the simulation, surface wind vector plots depicted drainage flow off the higher terrain into the valley floors, along with an offshore landbreeze flow along the coastline. The afternoon surface wind field vector plots are characterized by upslope flow along the higher terrain and offshore seabreeze flow along the shoreline. This is consistent to what is typically observed over complex terrain within weak synoptic flow regimes, particulary when strong solar heating at the surface is present. Upper level model winds indicate a weak anticyclonic circulation over the forecast area, in line with what was observed.

Forecast temperature fields appear consistent among all nine simulations, with the exception that the surface temperatures in simulation 7 (reduced model numerical smoothing) verified somewhat better on the whole. Each simulation exhibited a strong diurnal range of temperature over the deserts (~ 30 F) although at some sites the model cooled down at the

surface much too quickly after sundown. This seems to be a phenomena that is common over desert urban/residential locales where nighttime temperatures tend to remain very high well after dark, while temperatures well away from the urban center plummet after the solar input is removed. Low clouds were not a factor in this particular simulation.

2. Analysis of Mean Absolute Differences

In general, the model mean absolute differences over the 24-hr period for winds and temperature compared quite well to observations at all model levels. Wind speed errors were in the neighborhood of 1.5 to 2 m/s near the surface, and less then 1.5 m/s in the upper levels, for nearly all of the simulations. Simulation G, which used a very weak numerical smoothing, produced some of the larger wind speed errors just above the surface. The low values of mean absolute error were anticipated, since the mean observed wind speeds over the 24-hr period ranged from a high of 5.15 m/s at the surface to a low of 3.00 m/s at 250 meters above ground. Temperature errors were generally 3.3 deg C or less at all levels and simulations, with the exception of C which did not use radiosondes, but did use surface observations for initialization. Dewpoint temperature errors were quite large (particularly just above the surface), with the exception of simulation I which produced pretty reasonable results. These large errors in dewpoint temperature were largely due to a poor resolution of the area (particularly the coastline) by the 2.5 degree NOGAPS data. Tables 3.0, 4.0 and 5.0 show mean absolute errors for each of the parameters at the surface, 250 magl, and 500 mb levels. Surface means were taken from the 24 hourly reported surface observations, while upper air means were taken using the 3 radiosonde times concurrent with the 24-hr period studied.

Table 3.0 Mean Absolute Model Errors at Surface

Simulation	u (m/s)	v (m/s)	speed (m/s)	temp (c)	dpt temp (c)
A	2.09	2.00	1.76	3.21	3.40
B	2.13	2.00	1.76	3.30	3.54
C	2.20	2.06	1.75	3.25	4.52
D	2.36	1.67	1.63	2.90	4.63
E	2.15	1.65	1.61	3.17	3.28
F	2.20	1.69	1.60	3.15	3.37
G	2.25	1.71	1.83	2.89	3.53
H	2.05	1.63	1.65	3.37	3.37
I	2.07	1.63	1.67	3.34	2.81

Table 4.0 Mean Absolute Model Errors at 250 magl

Simulation	u (m/s)	v (m/s)	speed (m/s)	temp (c)	dpt temp (c)
A	2.26	1.75	0.97	2.71	4.69
B	2.29	1.73	0.93	2.71	5.21
C	1.88	2.07	0.55	4.88	6.96
D	1.56	2.27	1.45	2.83	8.02
E	2.11	1.87	1.79	1.83	4.32
F	2.20	1.84	1.71	1.86	4.33
G	2.93	2.68	3.17	3.03	5.56
H	2.31	1.75	1.56	2.29	4.93
I	2.28	1.79	1.54	2.35	3.20

Table 5.0 Mean Absolute Model Errors at 500 mb

Simulation	u (m/s)	v (m/s)	speed (m/s)	temp (c)	dpt temp (c)
A	0.95	0.52	0.68	1.42	1.68
B	0.94	0.51	0.68	1.42	1.68
C	1.19	0.92	0.74	1.70	3.08
D	1.26	0.90	0.80	1.64	3.08
E	1.31	0.51	0.73	1.33	2.54
F	1.32	0.55	0.73	1.33	2.54
G	1.09	0.75	0.80	1.10	1.63
H	1.31	0.58	0.74	1.31	2.51
I	1.46	0.64	0.86	1.29	0.94

The most glaring observation that can be made from these tables is that the moisture forecasts were substantially improved by simply ignoring the NOGAPS guidance, and nudging continously to the initially observed moisture field throughout the 24-hr simulation. As noted earlier , the poor 2.5 degree resolution NOGAPS fields are most likely the cause of these moisture problems (see Table 6.0). This finding lends some support to the idea of nudging back to the initial moisture fields whenever large-scale moisture advection is weak, particularly for short duration forecasts. Although not shown here , the effects of incorporating surface

observations were found to be greatly diminished by 3 hours into the forecast , and essentially non-existent beyond 6 hours. By the time the model is twelve hours into its cycle, the forcing of the NOGAPS forecast fields dominates whatever initial conditions were present.

Table 6.0 Mean Absolute Error of NOGAPS Model at 700 mb

u (m/s)	v (m/s)	speed (m/s)	temp (c)	dpt temp (c)
1.16	1.42	0.84	3.66	8.67

C. Summary

Comparison of different combinations of initial data and their effects on the BFM's 24-hr model forecast fields in complex terrain (in a weak synoptic regime) was done for the day of April 16, 1997 over the Ft. Irwin area of California. The BFM was run at 10 km terrain resolution, and time-dependent large-scale forcing was supplied by the 2.5 degree NOGAPS forecast data fields supplied by the AWDS from the US Air Force. In general, each of the nine different simulations produced similar results beyond 6 hours, with daytime upvalley/seabreeze and nighttime drainage/landbreeze circulations prevalent. However, distinct differences were discovered. Specifically, since the 2.5 degree NOGAPS fields poorly resolved the moisture gradient along the coastline, assimilating the NOGAPS moisture degraded the BFM forecast of that variable near the surface. In this case, since there was weak flow and thus weak moisture advection, nudging back to the initial moisture analysis during the entire simulation produced a superior result. Likewise, the simulations that used the available raw upper air and surface observations forecasted temperature and moisture, in particular, much better. The effects of surface observations in influencing the BFM forecasts appeared to be strong in the first 3 hours, and minimal thereafter. After 6 hours of forecast, no apparent effect of the initial surface observations was present in the simulations that used them. Beyond twelve hours of forecast time, the forcing supplied by the NOGAPS fields (via nudging) seems to completely dominate whatever initial data conditions were present. Finally, it is pretty apparent that to improve the short-range forecasts of all the fields, use of the full 1 degree NOGAPS data with greater detailed vertical resolution will be required.

References

Henmi, T. and R. E. Dumais, Jr., 1997, *Description of the Battlescale Forecast Model*, accepted as an U.S. Army Research Laboratory Technical Report, November, 1997.

Hogan, T. and L.Brody, 1993, *Sensitivitiy studies of the Navy's global forecast model parameterizations and evaluation of improvements to NOGAPS*, Mon. Wea. Rev., 121, 8, 2374-2395.

Van Tuyl, A., 1996, *Physical initialization with the Arakawa-Shubert scheme in the Navy's*

operational global forecast model, Meteor. & Atmos. Phys., 60, 47-55.

Yamada, T., 1981, *A numerical simulation of nocturnal drainage flow*, J. Meteor. Soc. Japan, 59, 108-122.

Yamada, T. and S. Bunker, 1989, *A numerical model study of nocturnal drainage flows with strong winds and temperature gradients*, J. Appl. Meteor., 28, 545-554.

A Preview of the Advanced Navy Aerosol Model

Stuart G. Gathman
Propagation Division
SPAWAR SYSTEMS CENTER D883
49170 Propagation Path
San Diego CA 92152-7385
USA

Alexander M. J. van Eijk
TNO-FEL, P.O. Box 96864
2509 JG The Hague, The Netherlands

ABSTRACT:

This paper will discuss concepts of an Advanced Navy Aerosol Model, ANAM that describes the aerosol and the electro optical properties of the marine atmosphere from above the inversion down to the tops of the highest wave. The largest of these aerosols are the result of white caps produced by wind wave interactions. This work borrows heavily from the rotorod measurements obtained from towers, boats and ships over the past decade. Rotorod devices, while time consuming to analyze, nevertheless allow large undisturbed samples of giant droplets to be obtained. Data from these devices are used to empirically determine profiles of large aerosol from just above the water surface to 15 meters or more above the water. These data are fitted to a log normal function that is in turn related statistically to parameters such as wind speed and stability. Furthermore, under unstable conditions, profiles of parameters describing these lognormal aerosol size distributions are fitted to profile functions related to a stability parameter. Thus, an aerosol size distribution can be constructed at any level from wave tops to 15 meters and the electro optical parameters from these droplets calculated from Mie theory.

Introduction:

The topic of this report is the construction of an Advanced Navy Aerosol Model, ANAM, which attempts to describe the large aerosol size distribution found in the atmosphere from above shipboard level down to the tops of the highest waves. Mie theory then allows the calculation of electrooptical properties of the atmosphere to be determined with the assumption that these aerosols are sea salt solution aerosol. A problem exists in that the physical processes involved in the formation of a whitecap and its relation to the wave structure and the influence of the wave structure on the injection of aerosol into the marine boundary layer have not been

measured directly in nature. Only complex numerical models can address detailed pieces of this problem but these in turn are difficult to simplify for applications. In addition there are not many measurements available on which to statistically base an empirical model. The lack of data becomes most prominent for high wind speeds and rough seas that produce effects of a serious nature on propagation.

EMPIRICAL BASIS FOR ANAM

Methods for obtaining giant aerosol size spectra

There are only a few ways to obtain in situ measurements in the region below 15 meters in extreme weather conditions and they require some form of platform at sea on which to support the aerosol instrumentation. Preferably, the measurements should not disturb the air flow and the device should be cheap and/or waterproof (since it may get submerged by a wave or be sprayed by water). The small concentration of large sea salt particles require large samples of air in order to get statistically significant results. In addition the inertia of these large droplets makes the sampling of these droplets difficult in that because of their mass, they simply will not follow an air stream around sharp turns in sampling tubes. The simple rotorod device (see de Leeuw, 1986) turns out to be the best method developed up to this point of obtaining the required data in this region but it is very labor intensive in its operation.

An example of Aerosol data: MAPTIP

During the fall of 1993, a field experiment called MAPTIP (Marine Aerosol Properties and Thermal Imager Performance trial) (Jensen *et.al.*, 1993) was planned and carried out by NATO AC/243 (Panel 04 / RSG.8), with the collaboration from AC/243 (Panel 04 / RSG.5). A major objective of this field experiment was to assess marine boundary layer effects on thermal imaging systems. The data collected from this experiment is used here to create a model for the evaluation of the infrared propagation near the ocean surface related to marine-generated aerosols, turbulence and meteorological factors.

The key facility used in MAPTIP was the "Meetpost Noordwijk" (MPN), an oceanographic research tower (owned by the Dutch Department of Harbors and Public Works "Rijkswaterstaat") situated at approximately 9 km from the Dutch coast near the village of Katwijk (52° 11' 51.6" N, 04° 22' 57.6" E). On this tower were situated many types of instruments for the MAPTIP experiment and the data from these measurements are coordinated with other mobile platforms (aircraft, ship and buoys) and a shore location. The location of a stable platform situated in the North Sea where the high probability of strong northerly winds and their associated waves makes this an ideal experiment location.

The portion of the aerosol spectrum from 0.3 to 50.0 micrometers radius were measured using both rotorod samplers and optical counters such as Particle Measurement Systems (PMS) instruments during MAPTIP. These devices were either mounted on movable platforms which could be raised and lowered to the water surface, fixed on the tower, or mounted on a small wave rider buoy floating on the water.

An example of a combined MAPTIP data set is shown in figure 1. On this plot are shown the data from an experiment on 25 October 1993 in which simultaneous profiles were obtained at approximately the same time (07:10 UTC) at the tower. The data shown in the figure were taken at an approximate altitude of 12 meters. It is obvious from placement of points in figure 1 that although the ranges of the devices differ from each other that there is sufficient overlap to allow for a much broader composite spectrum of the aerosol size distribution to be constructed than could be done with individual instruments. Of particular interest in the figure is the "hump" of the aerosol size spectrum that was seen by the two rotorod devices but was beyond the useful range of the PMS probe.

The MAPTIP 1993 data set was chosen since it contains wide spectra profiles utilizing the combined data from the PMS and rotorod devices from close to the surface to 12 meters in height as well as a broad range of wind speed conditions. There is one flaw in the data set recorded at the MPN tower and that is caused by the nearby land. For some of the profiles, the wind direction was such that the nearby land induces fetch effects on the waves which must eventually be taken into account. Nevertheless it is the best data set available at this time and will be used for the first construction of the model.

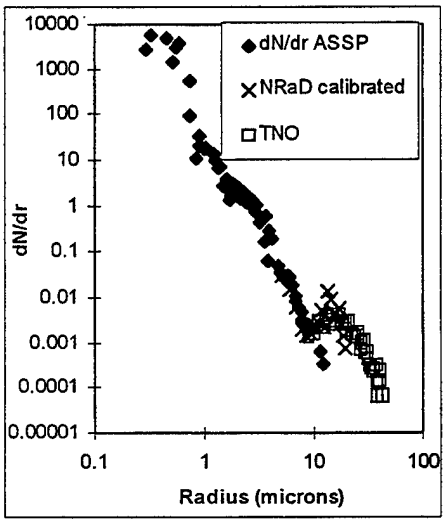

Figure 1: MAPTIP measurements of aerosol size distribution.

The aerosol size distributions from MAPTIP were fitted by an analytical curve for parameterization purposes. These curves were analyzed for a maximum in dN/dr values and associated mode radii in the region between 5 and 20 microns in order to find the mode radius and mode amplitude represented by the large aerosol group (shown as the "hump" in figure 1).

It is now possible to look for relationships between the aerosol size distribution mode descriptors and some of the measured meteorological (e.g., wind speed) and geometrical (e.g., height) data that are available from the MAPTIP data set. The individual observations taken at different altitudes

but close to each other in time were combined into profiles so that the average meteorological parameters during the period of the profile would show the effect on the profiles themselves.

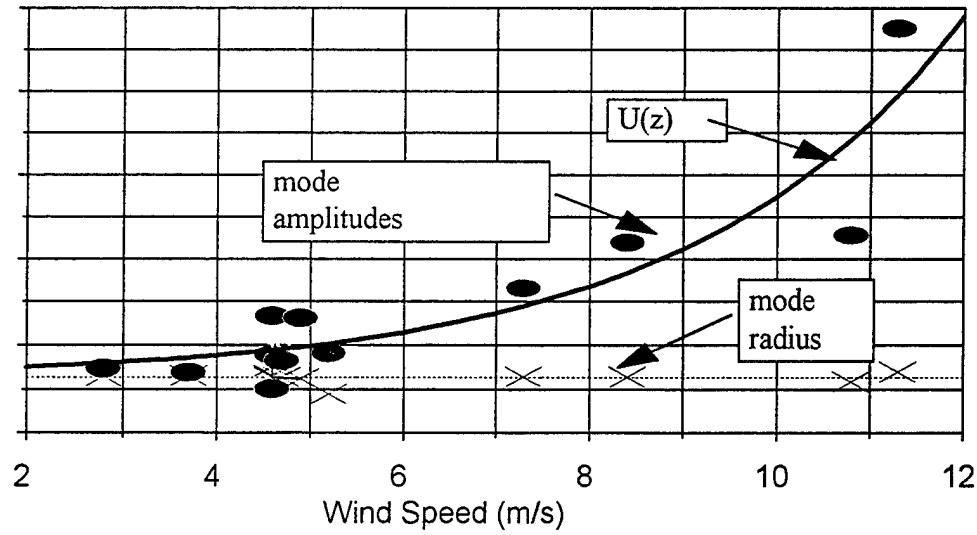

Figure 2: Windspeed dependence of the mode amplitude and the mode radius.

A useful feature of the MAPTIP experiment is the existence of a consensus meteorological data set which statistically combines and filters up to nine simultaneous measurements of the key meteorological parameters made by the various MAPTIP participants. Figure 2 shows an empirical relationship of the mode amplitude A_4 on the consensus wind speed at 10 meter height. The data show an exponential increase in the amplitude with wind speed for the range of wind speeds encountered during MAPTIP.

The same type of analysis was then applied to the mode radius, r_{o4} which was obtained from the set of observation analysis similar to that described above. These mode diameters when plotted against wind speed in figure 2 (at 10 meter height) and show no relationship with wind speed over the range of wind speeds encountered in MAPTIP. Thus the mode radius of the A_4 term is constant and has a value of about 15 micrometers.

Finally, some additional statistical information can be gleaned from the experiment as to vertical altitude variation to be expected for the A_4 term. Figure 3 shows a major feature of the large aerosol structure in the surface layer (below about 15 meters) obtained with the SSC SD rotorod system at MAPTIP. In this figure the data from a single profile are used to compute the correlation coefficient between the altitude of the observation and the amplitude of the A_4 term. This coefficient is plotted against wind speed. In this analysis, a value of zero correlation indicates that there is no observed vertical variation in the large aerosol concentration within the spatial limits of the experiment. On the other hand, a negative correlation indicates that there is a decrease in large aerosol concentration as one gets higher above the

wave tops. The figure definitely shows that the A_4 amplitude decreases with altitude at lower wind speeds but at high wind speed these aerosol are mixed to much higher levels before they drop off. It shows that the low altitude structure is lost in high wind and turbulence.

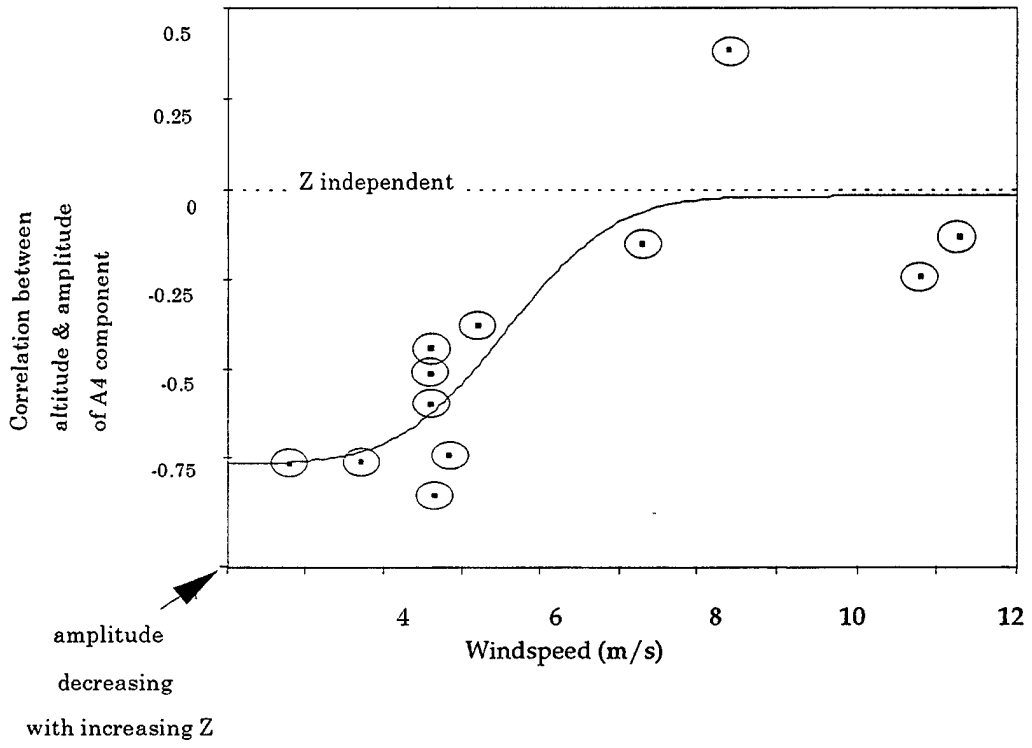

Figure 3: Profile structure with respect to wind speed.

The conclusions from this analysis can be stated as:

1) There is indeed a large size aerosol population produced by the white water process over the ocean and its concentration at 10 meters is related to wind speed.
2) The mode radius of this population seems to be independent of wind speed over the wind speeds and directions encountered in MAPTIP.
3) The amplitude of the large aerosol mode is a function of wind speed, altitude and atmospheric stability.

The functional form of the mode amplitude parameter

An effort was made to obtain an empirical expression for the variation of the A_4 amplitude with altitude in the surface layer below 10 meters. The MAPTIP (SSC SD) rotorod profiles exhibited a certain structure with respect to height which seemed to depend on the stability of the atmosphere as well as the surface aerosol production which is of course related to wind speed. This phenomenon is hinted at in figure 3 where by correlation of the peak of

the fourth mode aerosol component seemed to depend on mechanical turbulence and/or thermal instability.

Because the instability of the atmosphere has been described by both mechanical mixing due to surface shear on the wind and on the heat flux through the air sea interface, similarity theory has used a parameter which combines both and is expressed here as L, the Monin-Obhukov length, which is defined by:

$$L = - \frac{u_*^3 T_v}{g \kappa \overline{w' T_v'}}$$

where T_v is the mean virtual temperature, and $w'T_v'$ the virtual heat flux. In practice, the values of u_* and L are inferred from standard shipboard meteorological observations such as wind speed, air and sea temperatures and relative humidity using a micrometeorological bulk model, such as the LKB model (Liu *et.al.*, 1979). This parameter L will be incorporated into an empirically developed profile function. The mode amplitude of this aerosol component, A_4 will be a function of the wind speed, the altitude above the water and the atmospheric stability reflected in the parameter L.

THE INITIAL STRUCTURE OF ANAM:

The construction of version 1.0 of ANAM is based on an endeavor to empirically duplicate the aerosol size distribution at various altitudes just above the wave tops as measured in MAPTIP. This is accomplished by constructing formulas based on the log normal parameters derived from the MAPTIP data set. ANAM will be a multi-component model which includes an element to describe the very large aerosol in the region from about 15 meters down to the top of the highest wave. The description of this aerosol will be a log normal component which we will call the ANAM component. The aerosol size description will then be the superposition of four log normals. From this size distribution, the electrooptical properties can be calculated by either the direct integration of the aerosol size distribution with Mie theory over the sizes of interest or with the use of a pre-calculated set of table values such as was done with the Navy Oceanic Vertical Aerosol Model, NOVAM (Gathman and Davidson, 1993) and the Navy Aerosol Model, NAM (Gathman, 1983).

ANAM version 1.0 is a simple model with inputs consisting of the regularly available meteorological parameters such as: air mass parameter (visibility, radon, or nephelometer data), sea surface temperature, air temperature (at 10 m), relative humidity (at 10m), current wind speed (at 10 m) and 24 hour average wind speed (at 10 m).

The final form of ANAM is the superposition of four lognormal terms, the first three are identical with those of NAM/NOVAM, while the fourth term has a height dependence feature that is related to the atmospheric mixing and stability. These largest aerosols are represented by a single lognormal size distribution, which is parameterized with wind speed at 10

meters. The size distribution of this component is described as the following lognormal:

$$\frac{dN_4}{dr} = A_4(w,z,L)\cdot\exp(-C_4(\sigma_4)\cdot\log^2\left[\frac{r}{r_{04}f(z,rh)}\right])$$

where σ_4 is the standard deviation of these large particles, r_{04} is the mode radius of the fourth term, and $A_4(w,z,L)$ is the amplitude of this term. In this simple model, the humidity effects of the droplet sizes is represented by the swelling factor, f (Fitzgerald, 1978). The swelling factor is a strong function of relative humidity that is modeled in this region using the LKB model. The A_4 is related to wind speed, the height above the mean water level and the stability factor, L. At this stage of development, there is not enough data to determine any fetch effects on the function.

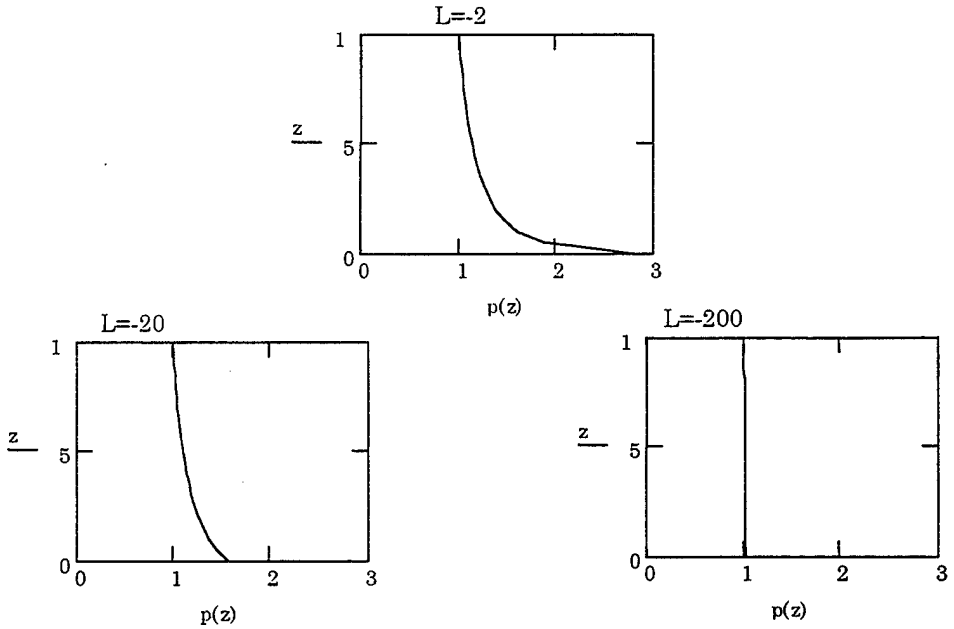

Figure 4: The profile function of ANAM for various values of L.

From figure 2, the mode radius of the fourth term was found to be independent of wind speed at least for the MAPTIP experiment. The value of this parameter was determined by the use of the calibrated rotorod measurements to be 15 micrometers radius. The C_4 (σ_4) term when parameterized with respect to the calibrated data set has a value of –5, whereas the C parameters for the other modes in NAM and NOVAM require the value of –1.

The most complicated term for the fourth component is that of the mode amplitude parameter. ANAM version 1.0 represents it by first setting the wind dependence of the term at the height of 10 meters using the data shown in figure 2. The construction of the profile function used here must have several features so that it can mimic the features, which are observed in

the MAPTIP profiles. It must first of all have the value of 1 at 10 meters altitude so that the profile function can scale the whole range of altitudes to the empirical wind controlled value which was observed at MAPTIP as shown in figure 2. Secondly, there are no adequate measurements of these large aerosol at altitudes higher than the tower so that the actual function above 10 meters is not critical for the problem at hand but it is known that the function is zero at the inversion height which serves as a practical limit to this term.

Below the reference height where the function has a value of 1, the value increases with lower altitudes as is indicated in figure 3. Furthermore its behavior in this lower region is a function of instability which is represented here as the parameter L and must have no vertical structure at large negative L values. The plot of the profile function between the wave tops and 10 meters is shown in figure 4 where p(z) is plotted as a function of z for three different values of L. The function p(z) is based in part on the classic non dimensional profile function $\varphi(\psi)$ of Businger and Dyer. The mode amplitude of the fourth component at 10 meters at a wind speed of w is obtained from figure 2 as U(w) and is assumed independent of L. The scaling with respect to height above the water is done by multiplying the profile function, p(z) mentioned above as:

$$A_4(w, z, L) = U(w) \cdot p(z, L)$$

Only cases in which L is negative are allowed in this preliminary empirical model, as all of the data from MAPTIP were done under unstable conditions. The total aerosol size distribution then is related to the superposition of all of the sub components that make up the aerosol. In this case, NAM is assumed to describe the smaller three modes of the size distribution and the A_4 term described above is added to finish the model.

Testing the consistency of the model with MAPTIP data

It was the intended objective of this work to represent the measured results of the MAPTIP aerosol experiments by a model that should extend the existing applicability ranges of NAM/NOVAM. The empirical model was developed from MAPTIP data but it should be constructive to see how well the model represents the actual set of noisy real world measurements from MAPTIP.

The total ANAM aerosol size distribution represented by the four component ANAM model is shown as a line in figure 5 where it is plotted on top of all of the measured points of real data shown in figure 1. This figure shows that the four component model should be adequate to represent the type of aerosol seen during MAPTIP.

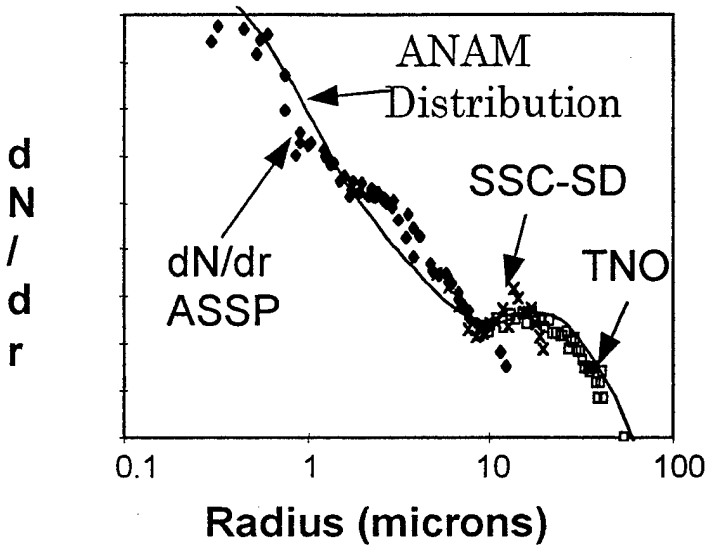

Figure 5: Model and measured aerosol size distribution from MAPTIP

Profile measurements from a typical MAPTIP experiment are shown in figure 6 where the 15-micrometer rotorod counts of 22 October 1993 of the TNO experiment are plotted with respect to altitude. The oval symbols

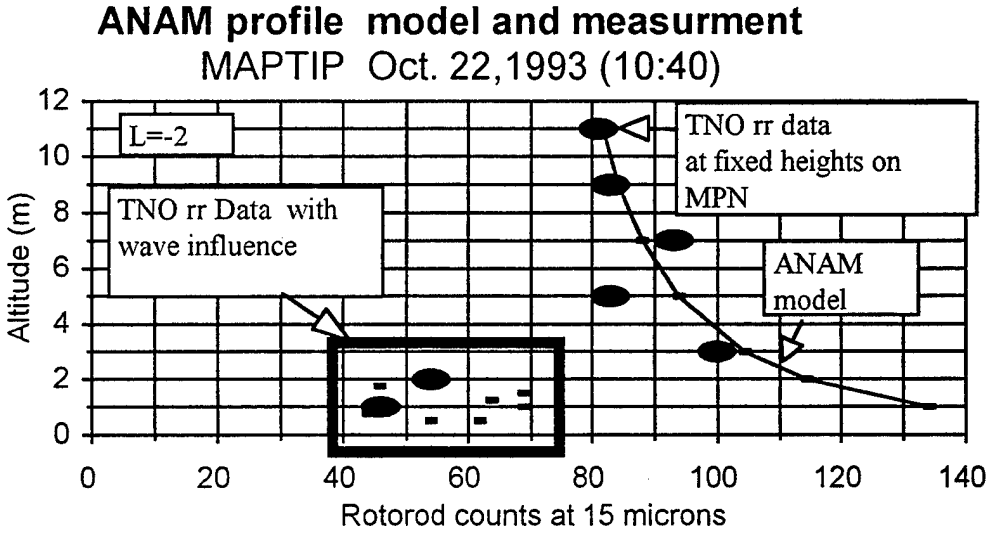

Figure 6: Typical aerosol concentration profile seen during MAPTIP together with the ANAM profile function.

represent the TNO values from fixed height rotorods whereas the solid square symbols represent the values from the wave rider buoy.

A strong discontinuity seems to exist between the upper fixed height counts and the counts measured from the buoy. The buoy data seem to be significantly less than the measurements made above. We hypothesize that this is the result of the non-uniform production of aerosols from whitecaps in the moving waves. Such a non-uniform concentration would of course greatly affect the accuracy of sampling over a period of time and causing the measurements near the wave to give an inaccurate average measurement. Hence we suggest that the profile be extrapolated down from above to the top of the wave.

CONCLUSIONS

The model matches the aerosol size distributions observed during the MAPTIP experiment within acceptable limits. The question is whether or not it will describe other sets of observations. This testing with other data sets will be the first round verification of the model. The addition of the electrooptical outputs that will eventually be needed by the program can be added at any time. They are left out at this stage as the verification of the correctness of the aerosol distribution predicted by the model can more easily be made by comparing model and measured aerosol size distributions.

ACKNOWLEDGEMENTS

The authors wish to acknowledge the support given this project by Dr. Scott Sandgathe and Dr. Ron Ferek of ONR and of Dr. Juergen Richter of SSC SD The authors acknowledge G. de Leeuw for making available the TNO-FEL rotorod data, and the dedication of the TNO-FEL personnel when making the rotorod measurements. The TNO participation in the development of ANAM is sponsored by the Royal Netherlands Navy (assignments A95KM729 and A96KM795).

REFERENCES

De Leeuw, G. "Size Distributions of Giant Aerosol Particles Close Above Sea Level", J. Aerosol Sci. Vol 17, pp293-296, 1986.

D.R. Jensen, G. de Leeuw, and A. M. J. van Eijk,"Work Plan for the Marine Aerosol Properties and Thermal Imager Performance Trial (MAPTIP)", TD2573, NCCOSC, RDT&E Div, San Diego, CA 92152-5001, Sept. 1993.

Fitzgerald, J. "On the growth of aerosol particles with relative humidity", NRL (Naval Research Laboratory) memorandum report #3847, 1978.

Gathman, S.G., Opt Engi., 22(1) p57, 1983.

Gathman, S.G. and K.L. Davidson, "The Navy Oceanic Vertical Aerosol Model", TR1634, NCCOSC RDT&E DIV, San Diego, CA 92152-5001. Dec 1993.

Liu, W.T., Katsaros, K.B. and Businger, J.A.. "Bulk parameterization of air-sea exchanges of heat and water vapor including the molecular constraints at the interface", J. Atmos. Sci. 36, p1722, 1979.

MEASURING AND MODELLING THE INFLUENCE OF ATMOSPHERIC EFFECTS ON THE CONCENTRATION DISTRIBUTIONS WITHIN TRANSIENT AEROSOL PLUMES

William S. Andrews and Johnathan R. Costa
Department of Chemistry and Chemical Engineering
Royal Military College of Canada
Kingston, Ontario, Canada K7K 7B4
Phone: (613) 541 6000 ext 6052, Fax: (613) 542 9489
Email: andrews_w@rmc.ca

Gilles Roy
Defence Research Establishment Valcartier
Val-Belair, Quebec, Canada G3J 1X5

A series of field trials has been conducted in order to determine the aerosol concentration distributions within plumes resulting from releases under atmospheric conditions falling within Pasquill stability criteria for categories A, B and A-B. The aerosols released included kaolin, fog oil, red phosphorus (from standard L8A1 military screening grenades) and hexachlorethane (from L5 screening grenades). Concentration measurements were made using the Defence Research Establishment Valcartier laser cloud mapper, which is based on a scanning LIDAR operating at 1.06 μm.

Inversion of the backscattered laser signals permitted the determination of the spacial and temporal volumetric extinction coefficient distributions, which are directly proportional to the corresponding aerosol concentration distributions. The analysis of a limited number of test releases of kaolin under atmospheric conditions falling within the same Pasquill stability category (A) and scaled to a common wind speed (2.8 m/s) is reported upon. Among the products of this analysis are individual and averaged cloud concentration distributions, which are compared to distributions predicted by physically based (Gaussian plume) models. Indications to date are that the Gaussian modelling approach using currently-accepted fitting parameters does not provide particularly good predictions of measured distributions. An outline of future work is included.

Introduction

For a number of years, the Defence Research Establishment Valcartier (DREV) has been using a Laser Cloud Mapper (LCM)[1] to support research and development work on obscurant aerosols.[2,3,4] Data collected using the LCM has been investigated for the feasability of providing information on the concentration distributions of aerosols released from transient point sources. Unfortunately, the data reported were incomplete (amounts and compositions of aerosol released, and a number of meteorological parameters were not available)[5] As a result, attempts at training an artificial neural network (ANN) had only limited success, although the ANN model of a very limited data set provided better predictions than the physically-based (transport and diffusion theory) Gaussian plume model.[6]

One conclusion of this previous work was that values for more

parameters were needed to enhance the effectiveness of ANN models, i.e., more system variables were required as separate inputs into ANN models. Consequently, it was decided that a greater number of controlled releases would be measured, with special attention paid to conducting a number of releases under as near identical atmospheric conditions as possible, as well as trying to cover as broad a range of conditions as possible.

The classical modelling approach for aerosol dispersion in the atmosphere is to apply a Gaussian distribution to either a puff (instantaneous) or a plume (continuous) type of release. As much more work has been conducted on characterizing plumes, the Gaussian plume fitting parameters are felt to be more valid than comparable values used for puff fitting. This paper will concentrate on reporting the adequacy of Gaussian plume models to predict the measured concentration distributions.

Gaussian Modelling

The two Gaussian models, the plume and the puff, are based on diffusion theory, with the concentration decreasing exponentially from the centreline or centre.[7] The general Gaussian plume equation describing aerosol concentration, C (g/m^3), from a continuous source, is

$$C = \frac{Q}{2\pi\sigma_y\sigma_z u}\left(e^{-\left(y^2/2\sigma_y^2\right)}\right) \times \left[e^{-(z+h)^2/2\sigma_z^2} + e^{-(z-h)^2/2\sigma_z^2}\right], \quad (1)$$

where Q is the source/production rate (g/s), σ_y and σ_z are dispersion coefficients or standard deviations in azimuth and elevation respectively (m), y and z are respective azimuthal and vertical distances from the centreline (m), h is the distance of the plume centreline above ground (m) and u is the wind speed (m/s) taken as being along the x axis.

A Gaussian distribution, by definition, has two fitting parameters, a mean (in this case the centreline concentration provided by the first term on the RHS of Eq.1) and a standard deviation (here contained in the σ_y and σ_z terms). It is noteworthy that for the aerosol dispersion application, these standard deviations are determined from the appropriate Pasquill stability categories,[8] which in turn are functions of distance from the source (x), cloud cover, time of day, etc. The basic assumptions inherent in the Gaussian plume model are constant emission, conservation of mass, (no ground deposition), steady wind and that the results are time averaged. Such parameters as ambient temperature, relative humidity, surface roughness as well as ground deposition, any chemical kinetics or aerosol/atmosphere reactions are not explicitly or even implicitly included in the basic model, although additional terms can be added. Two further limitations are that the Gaussian plume model predicts rather poorly less than 100 m from the source and that the quality of predictions varies inversely with distance from the centreline.[9]

Although some of the limitations mentioned above could be addressed by physically-based or semi-empirical fittings (notwithstanding that the σ_y and σ_z values are themselves semi-empirical in nature), it was decided to use the

general Gaussian plume model as the basis of comparison for ANN models.

The instantaneous Gaussian puff model, which intuitively should provide a better prediction of aerosol dispersion from screening grenades than the continuous plume model, was found to perform not nearly as well. This is probably due to the fact that the wider use of the plume model has led to much better characterizations of the standard deviation (σ_y and σ_z) values used for predictions.[10]

Data Collection and Handling

The field trials for the aerosol concentration distribution measurements were held at Canadian Forces Base Valcartier, just adjacent to DREV, on a level plain abutted by a steep, tall hill. The trials were conducted during the periods 26-29 May and 4-12 August 1997, and comprised in all 206 separate releases of kaolin, fog oil, red phosphorus (from L8A1 service screening grenades) and hexachlorethane (from L5 screening grenades). The releases were effected at or near (within 1 m of) the ground surface. The range layout can be seen in Fig 1.

The aerosol reported on in this paper was kaolin, a fine ground ceramic ($H_2Al_2Si_2O_8.H_2O$) with a particle diameter of less than 3 μm and a measured mass extinction coefficient of 1.2±0.2 m^2/g. The kaolin was released in 50 g lots from a generator, i.e., with both horizontal and vertical momentum. The small size and weight of the particles, however, were felt to minimize the influence of this initial momentum on concentration distributions for cloud areas increasingly removed in time and space from the point of release. The main influences on distributions, then, were felt to be diffusion and advection.

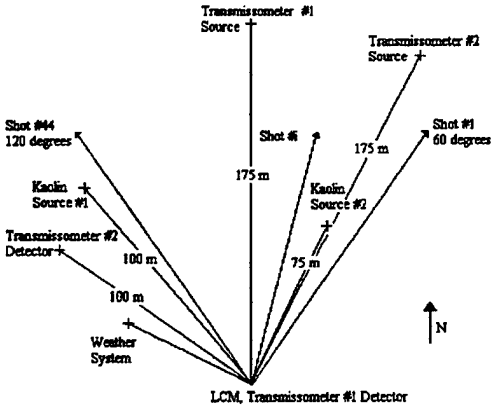

Fig 1. Range layout at CFB Valcartier for kaolin releases in August 1997.

The laser cloud mapper was based on a scanning light detection and ranging (LIDAR) device, using a NdYAG laser operating at 1.06 μm. The LCM was adjusted to scan a 10° vertical arc and a 60° horizontal arc. This was accomplished by firing 44 shots in each of 6 to 8 successively elevated horizontal sweeps. An average of 6 scans (complete sweeps through both horizontal and vertical arcs) were conducted per individual test (separate release). The LCM raster scanning pattern can be seen in Fig. 2. The sampling frequency was set at 10 ns for the backscattered signals. Resolution of the measured signals was felt to be 1.5 m in range, with a beam divergence of 4 mrad or about 0.4 m within the aerosol cloud. This would provide potentially 316,800 data points per test. The useful number of data points (actual cloud reflections as opposed to background backscatter), was about 70,000 per test.

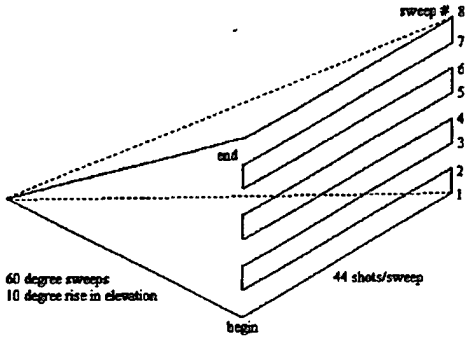

Fig 2. Raster scanning pattern used with DREV laser cloud mapper during kaolin aerosol release tests.

The software supporting the LCM employed an inversion algorithm of the LIDAR equation to convert the backscattered signal reflections to volumetric extinction coefficients (σ in m^{-1}).[11] This value is effectively the αC or mass extinction coefficient-concentration product of the aerosol applied to the electromagnetic signal. Its relationship with the mass extinction coefficient (α in $g.cm^{-2}$) can be seen in the Beer-Lambert Law:

$$\frac{I}{I_0} = e^{-\alpha CL}, \qquad (2)$$

where I/I_0 is the transmittance through the path length L (m). The mass extinction coefficient α (m^2/g) can be considered the removal (scattering and absorption) cross section per unit mass and must be determined empirically. It is a function of aerosol particle size distribution, particle shape, and electromagnetic wavelength.[12] The product αC (m^{-1}) can be considered as the volumetric extinction coefficient, σ, and is the value that is generated by the LCM support software. The volumetric extinction coefficient values can be converted to concentrations by dividing by the mass extinction coefficient value, which for kaolin has been measured as being 1.2 ± 0.2 m^2/g, a value consistent with other sources.[13,14]

Concentration Distributions

The process of determining concentration distributions involved initially determining the cloud centroid, which was considered the origin of the Cartesian coordinate system applied to the analysis. The x axis was aligned with the downwind direction at the beginning of the trial, with the y and z axes being orthogonal and in the azimuthal (horizontal) and elevational (vertical) directions, respectively. Specific volumetric extinction coefficient values corresponding to backscattered signals were then mapped into the new coordinate system. This permitted the search through the LCM-generated files for values in the same sweep (z values) and the same downwind distance (x value). Examples for specific tests can be seen in Figs 3 to 6, which were chosen for having the same wind speed (but not necessarily the same direction), Pasquill stability category (A) and same scan, i.e., the data were all from the second scan of the test.

The data points in Figs 3 to 6 are joined by straight lines only to make the general trend more apparent and not to indicate a continuous distribution. All four appear to indicate a general Gaussian distribution. Shifts in wind direction are quite apparent, however, as shown by the shifting of the cloud mean from the initial centreline determined

from the preceeding (first) scan. This is particularly marked in Fig 6, where the cloud seems to have shifted 11 m off the initial centreline.

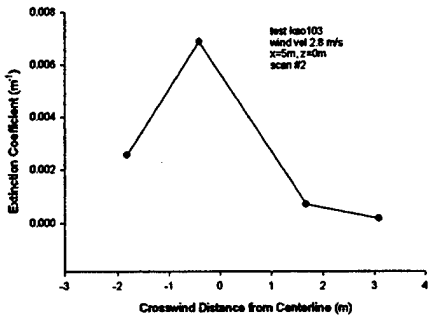

Fig.3. Extinction coefficient (concentration) distribution of points 5m downwind from initial cloud centroid near ground level for kaolin release at 1138 hrs 12 Aug 97.

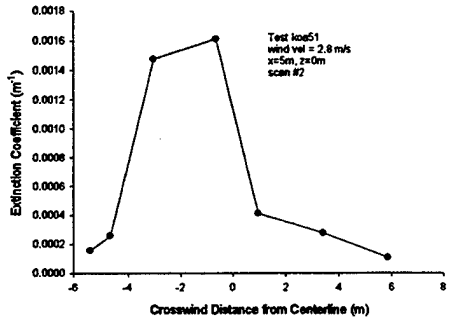

Fig.4. Extinction coefficient (concentration) distribution of points 5m downwind from initial cloud centroid near ground level for kaolin release at 0948 hrs 5 Aug 97.

In order to obtain the profile of an average cloud under uniform atmospheric conditions, the points from the four distributions were combined, σ values were averaged and then the averaged distribution was cubic-spline fit and sampled every 10 cm. The resultant average cloud extinction coefficient (σ) or concentration distribution is depicted in Fig 7. Here the contributions of the individual tests can be seen clearly.

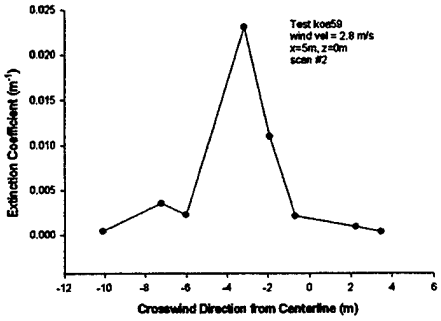

Fig.5. Extinction coefficient (concentration) distribution of points 5m downwind from initial cloud centroid near ground level for kaolin release at 1018 hrs 5 Aug 97.

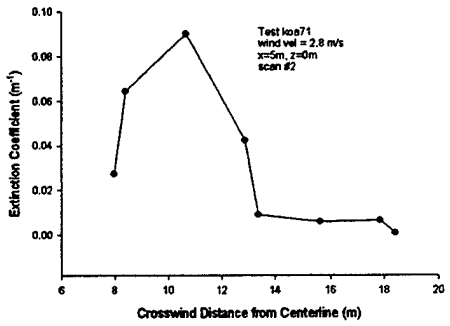

Fig. 6. Extinction coefficient (concentration) distribution of points 5 m downwind from initial cloud centroid near ground level for kaolin release at 1536 hrs 6 Aug 97.

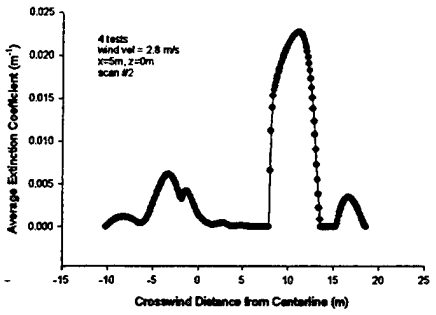

Fig. 7. Average extinction coefficient (concentration) distribution of 4 kaolin releases along a section near ground level 5 m downwind of initial cloud centroid.

In order to determine the average from a broader statistical sample, data were taken from tests conducted under atmospheric conditions characterized by Pasquill categories A, B and A-B, with the distributions normalized to that corresponding an initial downwind (advection) of 2.8 m/s by a linear correction. Averaged concentration distributions are shown in Figs 8 to 12 at varying downwind and vertical distances. The number of tests considered depended on the availability of appropriate concentration data within the test files. All data were taken from the second scan, so were roughly at the same time after release (10 s), although some tests under consideration were data poor at distances farther removed from the origin (initial centroid location). The averages were determined in the same manner as discussed for the 4-test example.

Superimposed on each of these distributions is a Gaussian distribution confining an area identical to that under the corresponding averaged distribution (determined by the trapezoidal rule). The dispersion coefficients σ (corresponding to the standard deviations of the Gaussian distribution in Eq 1), were applied and the mean was adjusted to confine the appropriate area. It is of interest to note the inadequacy of the Gaussian in describing either the shape of the averaged distribution or the location of the mean. It is aknowledged that the traditional Gaussian model uses fitting values (σ and μ) which are for time averaging over a period of 10 minutes. The kaolin tests reported on above were conducted over a period of some two weeks. There was some normalizing, however, as all the initial wind direction vectors were treated as being coincident. These distributions, then, may well illustrate the weakness of the Gaussian model near the source. Unfortunately, in the case of small releases (including those from screening grenades), concentration distributions beyond about 100 m are of little practical interest, as the plume becomes optically transparent. Increasing advection effects would transport the cloud (plume /puff) farther downwind but would, in turn, enhance dispersion through turbulence. In any event, the variability in the distributions from test to test underscores the randomness of dispersion due to atmospheric turbulence. Further analysis will attempt to determine more appropriate fitting parameters for a mono-modal Gaussian distribution and perhaps even for the multimodal distributions observed.

Work has also been conducted on developing and training an artificial neural network model, which has the advantage of considering system variables explicitely (temperature, time of day, relative humidity, atmospheric pressure, etc.) rather than having these implicitely contained in the dispersion

coefficients of the Gaussian model. Efforts to date have not yet been fruitful.

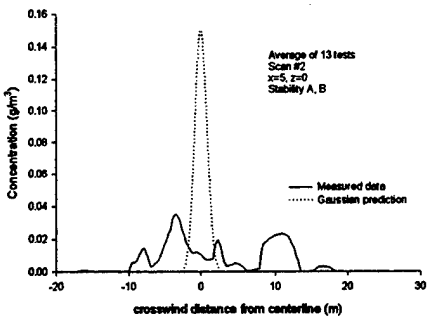

Fig. 8. Average concentration distribution of kaolin along a cross-sectional path near ground level and 5 m downwind from the initial cloud centroid. Data were averaged over 13 tests and are from the second scan of each test.

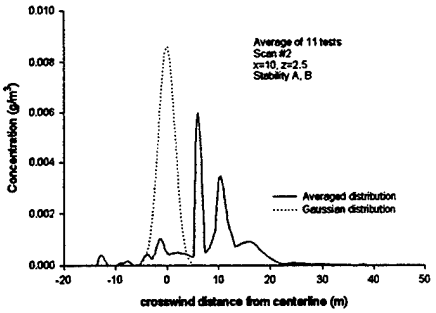

Fig. 10. Average concentration distribution of kaolin along a cross-sectional path 2.5 m above ground level and 10 m downwind from the initial cloud centroid. Data were averaged over 11 tests and are from the second scan of each test.

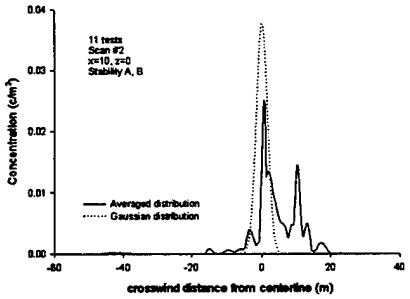

Fig. 9. Average concentration distribution of kaolin along a cross-sectional path near ground level and 10 m downwind from the initial cloud centroid. Data were averaged over 11 tests and are from the second scan of each test.

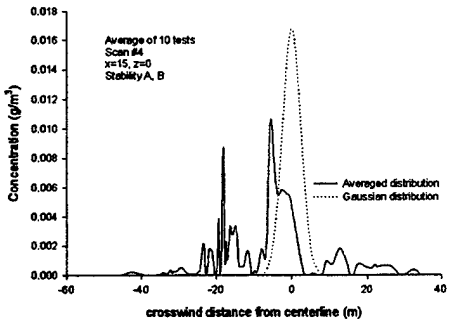

Fig. 11. Average concentration distribution of kaolin along a cross-sectional path near ground level and 15 m downwind from the initial cloud centroid. Data were averaged over 10 tests and are from the second scan of each test.

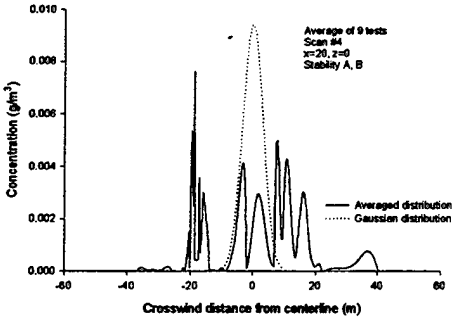

Fig. 12. Average concentration distribution of kaolin along a cross-sectional path near ground level and 20 m downwind from the initial cloud centroid. Data were averaged over 9 tests and are from the second scan of each test.

Conclusion

Examination of the dispersion distributions from a small (albeit statistically significant) subset of the overall data set have demonstrated the highly random nature of aerosol dispersion in the atmosphere. It has also highlighted the weakness of current Gaussian models in predicting this dispersion. Attempts will continue to refine fitting parameters for Gaussian models, to develop effective artificial neural network models and to examine the remainder of the data set. Further work will also include continued physical measurements of aerosol distributions to broaden the database.

Acknowledgement

The data reported on were collected by personnel of the Defence Research Establishment Valcartier. This work was supported, in part, by the Academic Research Program of the Department of National Defence of Canada.

References

1. Evans, A.J., "A Preliminary Assessment of the DREV Laser Cloud Mapper," CDE Porton Down, UK (1982).
2. Evans, B.T.N., Kluchert, R.E. and Levesque, R.J., "Field Evaluation of a Canadian Laser Cloud Mapper and Canadian IR Screening Aerosols," DREV 4271/82, Valcartier, Quebec (1983).
3. Evans, B.T.N., Roy, G. and Ho, J., "The Detection and Mapping of Biological Simulants: Preliminary Biological Results," DREV 4480/89, Valcartier, Quebec (1989).
4. Twardawa, P., Roy, G., Evans, B.T.N. and Vallee, G. "Cold Weather Evaluation of Visual and Infrared Screening Grenades for the Self-Protection of Armoured Fighting Vehicles," DREV R-4632/91, Quebec (1991).
5. Andrews, W.S., Roney, S.D. and Roy, G., "An Examination of Modelling Approaches for Predicting the Dispersion of Aerosols from Obscurant Grenades," Proceedings of the 1996 Battlespace Atmospherics Conference, Naval Command Control and Ocean Surveillance Center, RDT&E Division, San Diego, CA, 3-5 December (1996).
6. Andrews, W.S., Roney, S.D. and Roy, G., "Comparison of Modelling Approaches for Predicting Dispersion of Aerosols from Screening Grenades," submitted to *Propellants, Explosives, Pyrotechnics.*
7. Csanady, G.T., *Turbulent Diffusion in the Environment*, D. Reidel Publishing Co., Dordrecht Holland. (1973).

8. Pasquill, F and Smith, F.B., *Atmospheric Diffusion, 3rd Ed.*, Ellis Horwood Ltd., Chichester UK (1983).
9. Turner, D.B., *Workbook of Atmospheric Dispersion Estimates, 2nd Ed.*, Lewis, Boca Raton (1994).
10. Hanna, S.R., Briggs, G.A. and Hosker, R.P., "Handbook on Atmospheric Diffusion," DOE/TIC-11223, Springfield VA (1982).
11. Roy, G., Valée, G. and Marcelin, J., Lidar-Inversion Technique Based on Total Integrated Backscatter Calibrated Curves," *Applied Optics*,**32**, 33, 20 November (1993).
12. Evans, B.T.N., "An Interactive Program for Estimating Extinction and Scattering Properties of Most Particulate Clouds," MRL-R-1123, Materials Research Laboratory, Ascot Vale, Victoria, Australia (1988).
13. Hoock, D.W. and Sutherland, R.A., "Obscuration Countermeasures," *The Infrared & Electro-Optical Systems Handbook, Vol 7. Countermeasure Systems*, Infrared Information Analysis Center, Ann Arbor MI, (1993).
14. Ayres, S.D. and DeSutter, S., *Combined Obscuration Model for Battlefield Induced Contaminants (COMBIC92) Model Documentation*, U.S. Army Research Laboratory, White Sands Missile Range NM (1995).

Proceedings, Battlespace Atmospheric Conference, San Diego, CA, Dec 1997

AEROSOL VERTICAL STRUCTURE IN THE ARABIAN GULF

Andreas K. Goroch
Marine Meteorology Division
Naval Research Laboratory
408-656-4889
goroch@nrlmry.navy.mil

David P. Rogers and Ian M. Brooks
Scripps Institution of Oceanography
San Diego, CA
619-534-6412
drogers@ucsd.edu

Introduction

The aerosol particle concentration in the Arabian Gulf is responsible for reduction of visibility in the region, as well as being an important phenomenon in the radiative energy transfer affecting both meteorological dynamics and climate. The origin of the aerosol particles is attributed to a number of sources: locally generated from a combination of pollution, desert and marine aerosol sources which can be mediated by the mesoscale dynamics of the local meteorological regime. The moisture environment of the aerosol particles can vary widely, from very moist near the sea surface, to very dry in air parcels originating in nearby continental areas.

Aerosol particle generally are affected by the humidity environment in two ways: evaporation and growth due to the condensation of vapor on the curved particle surface, generally occurring at humidity greater than 70%, and deliquescence and efflorescence at humidity less than 50% [*Hanel*, 1976; *Hanel and Zankl*, 1979; *Tang and Munkelwitz*, 1994]. At low humidities, the latter phenomenon is responsible for the observed hysteresis in the growth behavior: the equilibrium size of the aerosol particle at a given relative humidity depends on whether the particle had previously been in a lower or higher humidity environment. [*Pruppacher and Klett*, 1980]. As small particles grow to equilibrium with the local relative humidity, they grow along a particular growth curve. As large particles shrink to equilibrium they follow a different curve so that the size is greater than for growing particles. At a particular humidity, the particles suddenly deliquesce and join the curve of the growing particles. The value of humidity at this deliquescence point depends on composition of the dry aerosol [*Tang and Munkelwitz*, 1994].

This report describes observations of the distribution of aerosol particles in the central Arabian Gulf. Aerosol concentrations and meteorological parameters were measured aboard the UK Meteorological Research Facility C-130 [*Rogers et al.*, 1995].

Measurements

The measurements described here were conducted in the Arabian Gulf on 23 April, 1996. The measurements were obtained aboard the UK Meteorological Research Facility C-130, instrumented with a standard meteorological suite including temperature, moisture, and wind, and aerosol measurements using a PCASP aerosol spectrometer. Instrumentation and data collection procedures have been described elsewhere[*Rogers et al.*, 1995]

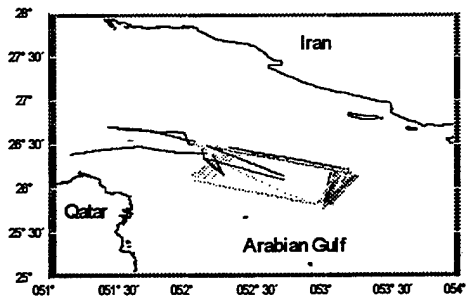

Figure 1. Aircraft ground track on 23 April 1997. Aircraft flights consisted of crosswind ladders (SW-NE runs) and profiles (SE-NW runs)

The aircraft tracks consisted of a series of slant runs and ladder runs (Figure 1). Slant runs uniform ascents or descents parallel to the mean wind flow for a distance of approximately 50 n mi.

Table 1 . Altitude (m) of level runs flown during ladder profiles

Series	East - 1	West - 1	East -2
1	32	30	31
2	67	64	61
3	148	149	
4	247	249	250
5	311	301	314
6	480	482	477

Ladder runs were flown for a distance of 20 n mi perpendicular to the mean wind direction for a range of altitudes starting from about 30 m to 400 m. Ladder runs were flown twice in the eastern region and once in the western region (53°E, 26°N, West 1 from 12:57 to 13:47 UTC).

The altitudes of each ladder component are shown in TABLE 1. The altitude at each point in the run was maintained within 10 m of the average altitude.

Atmospheric conditions

A high pressure region dominated the general atmospheric flow over Saudi Arabia and low Pressure in Iran. The surface winds were from the Northwest at a speed of 12 to 15 knots.

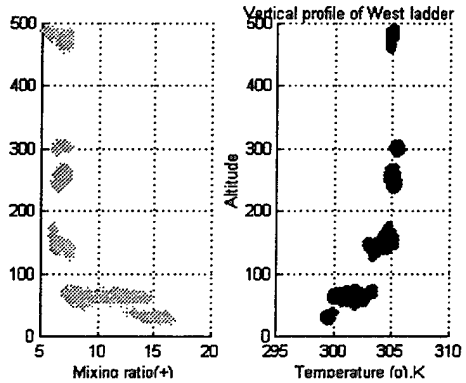

Figure 2 . Mixing ratio and temperature profiles during west ladder profile.

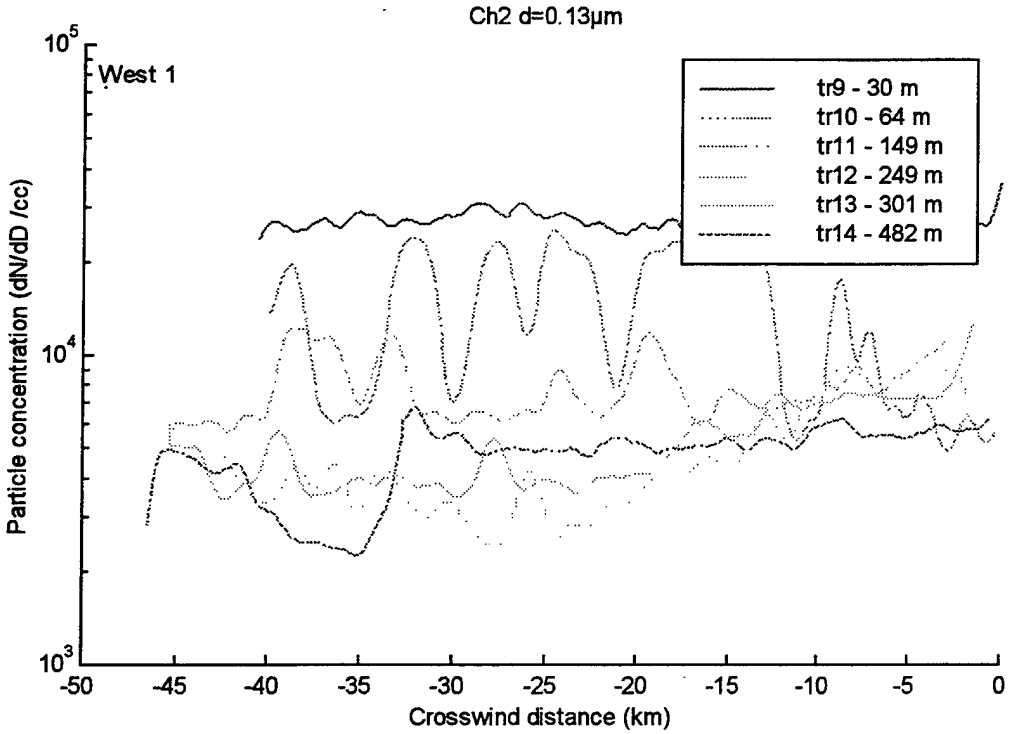

Figure 3. Aerosol concentration in channel 5 during the west ladder profile.

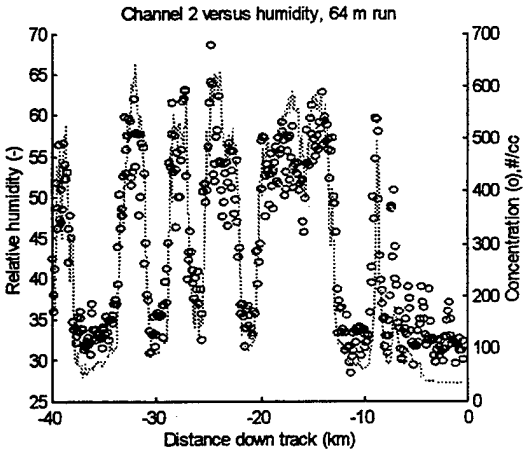

Figure 4 .Channel 2 concentration versus humidity during 64 m run.

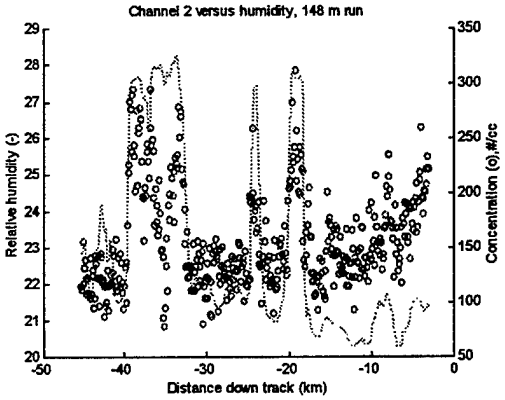

Figure 5. Channel 2 concentration versus humidity during 149 m run.

Temperature and humidity profiles

The atmosphere was characterized by a moist layer from the surface to 50 m above the ocean, with mixing ratio of about 18 g/kg. Above 50 m, the atmosphere was approximately 5°C warmer and much drier with a mixing ratio of 6 g/kg. The vertical structure was slightly stable. The temperature and virtual potential temperature profiles for the ladder are shown in Figure 2.

The aerosol concentrations in the different channels exhibited a strong dependence on altitude, with higher concentrations at the surface and lower concentrations aloft. During most of the level runs, the aerosol concentrations remained relatively constant. However, within each size channel there was at least one altitude which was evidently a mixture of the surface and aloft aerosols. Figure 3 shows an example of the varying concentrations in channel 2, corresponding to a particle diameter of

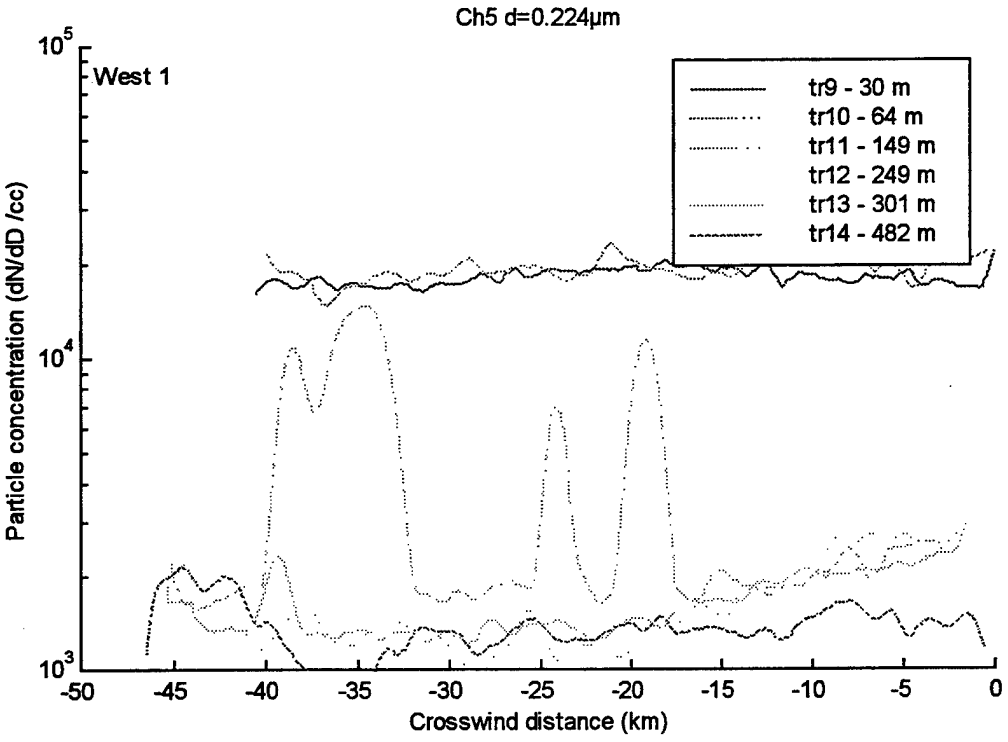

Figure 6. Aerosol concentration in channel 5 during west ladder profile.

0.11 micrometers.

The altitude at which the concentration varied and the extent of variation within each run were different for different channels. It was expected that the main variation would be in the crosswind rather than the down-wind direction. The horizontal distance dimension was changed to the projection of the horizontal distance to the average wind direction at the lowest level. The origin of the coordinate system was at the start of the lowest level run .

Channel 2 particles (d = .11 μm)

Small particles showed most change at lower elevations. Aerosols measured in Channel 2 (d = .11 μm) were observed with two concentrations; the surface with a concentration of approximately $3 \cdot 10^4$ cm^{-3} near the surface (30 m), and aloft with a concentration of $5 \cdot 10^3$ cm^{-3} at the 148 m altitude and higher. The concentration varies between the two values during the 61 m run. The concentrations are shown in Figure 3.

Table 2 . Correlation of channel 2 aerosol concentration at 64 m with moisture, temperature, wind, and aircraft parameters.

RH	0.9630
Qt	0.9575
T	-0.9513
u	0.4122
v	-0.7039
w	0.2703
Wind speed	0.5483
Altitude	-0.3187
heading	0.1098
pitch	-0.2381

The particles observed at the 64 m level seemed to be most closely related to ambient humidity. Correlation coefficients of particle concentration and temperature, relative humidity, mixing ratio, wind, and aircraft parameters were calculated and found to be highest for the two moisture variables. The relative humidity showed a slightly higher correlation than mixing ratio (.963 versus .958) , but this difference is not significant. An example set of correlations is shown in Table 2.

The simultaneous aerosol concentrations and relative humidity for the 64 m level run are shown in Figure 4. The aerosol concentration follows the relative humidity quite closely for the entire humidity range of 30 to 65%. Figure 5 is the corresponding plot at the 149 m level. Here, the concentration still follows the relative humidity, although spatial variations when humidity is below 24 % do not seem to be present in the aerosol data.

Channel 5 particles (d = .224 μm)

The altitude dependence of the larger sizes was dramatically different. For example channel 5, with a median bin diameter of 0.224 showed that the higher concentrations were observed at the two lowest levels, 30 and 64 m. Mixing between the low level and high level concentration did not occur until the 148-m level. The relative concentrations are shown in Figure 6.

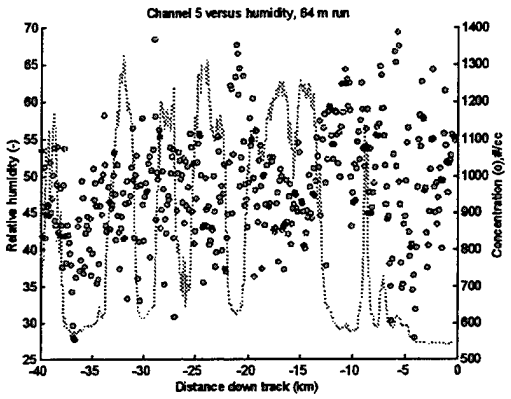

Figure 7. Channel 5 concentration versus humidity during 60 m run

The simultaneous aerosol concentrations and relative humidity for the 64 m level run are shown in Figure 7. These particles, do not seem to have any relation to humidity at the lower altitude. Although the humidity varies from 30 to 70%, the aerosol concentration varies between 600 and 1400 particles per cm^3 independently of humidity. The correlation coefficient between the concentration and relative humidity is only 0.244.

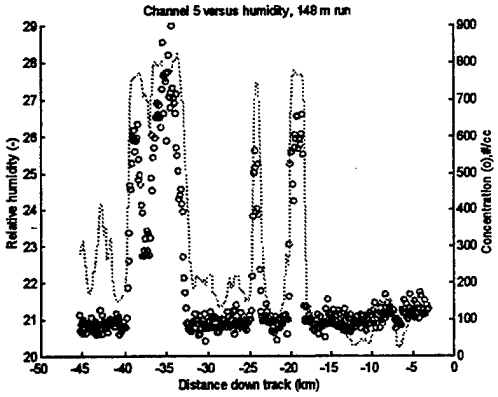

Figure 8. Channel 5 concentration versus humidity during 149 m run

At the 149 m altitude, the relationship of concentration and relative humidity is immediately evident. The humidity is quite low ranging from 23 to 30%, but the concentration responds immediately to humidity changes. The concentration and humidity have a correlation of 0.93. Figure 8 shows the aerosol concentration and the humidity during this run

Relation of size to relative humidity

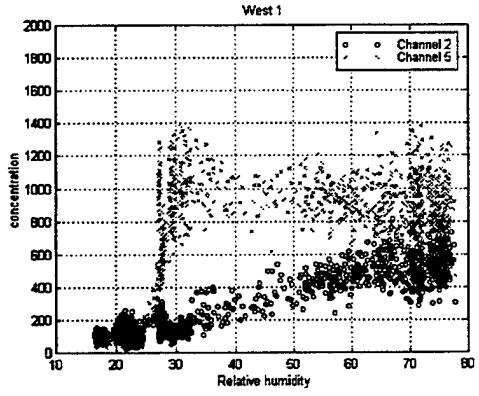

Figure 9. Concentration dependence on relative humidity in west ladder profile

The correlation of moisture and aerosol concentration showed some interesting relationships between aerosol size and relative humidity. The particle concentrations collected during the entire series of constant altitude segments of the ladders were plotted against the local ambient relative humidity (Figure 9). Channel 2 particles increased in size linearly with increasing relative humidity. Channel 5 particles abruptly increased in concentration at 28% relative humidity, with concentration seemingly independent of humidity at higher humidities. This implies that the larger particles are being activated, while the smaller particles increase in concentration consistently with monotonically relative humidity.

Air parcel characterization

To determine whether the differences in aerosol characteristics were characteristic of the common distribution or the sampling occurred in a region of two separate air parcels we examined mixing behaviour of the sampled region. . The air mass can be characterized by plots of two conservative variables, equivalent potential temperature (EPT) and mixing ratio [*Paluch*, 1979]. Figure 10 shows plots of mixing ratio versus EPT for the entire ladder, with the several level runs labeled by average altitude. Essentially, the plots demonstrate similarity of different parcels comprising a vertical profile. Since the variables mix linearly, a line joining two regions indicates mixing between the two segments of the vertical

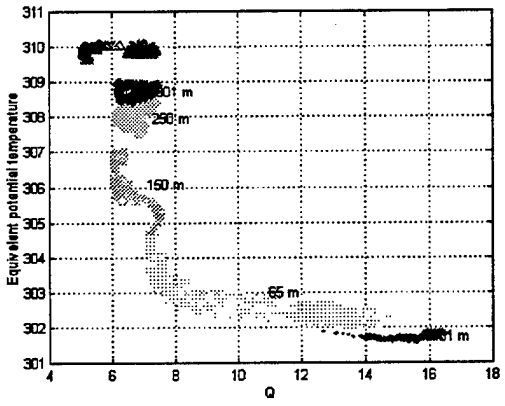

Figure 10. Equivalent potential temperature versus mixing ratio for west profile.

profile. We infer then that the aerosol distribution is uniform in the sampling region, with variation due to the characteristics of the particular aerosol mixture rather than the variation resulting from measurement in two different air masses.

Conclusions

The observations of aerosol concentrations showed a unique mixing of boundary layer and aloft aerosols. Although relative humidity was below 30% above 50 m, the aerosols were closely correlated to the changes in humidity, in contrast to the growth predicted by models in common use [*Gathman and Davidson*, 1993], [*Hanel and Zankl*, 1979]. This correlation is consistent with the hysteresis associated with deliquescence of salts [*Tang and Munkelwitz*, 1994] where particles have different sizes depending on their previous history. The resulting metastable particles have been previously reported in desert regions [*Rood et al.*, 1989], but have not been documented over marine regions. The existence of these metastable states implies that modeling of aerosol concentrations in tropical marine regions should include these deliquescence phenomena.

ACKNOWLEDGMENTS

The authors would like to acknowledge the continued enthusiasm and support by the Surface Warfare Development Group in the planning, conduct, and analysis of the SHAREM exercises, and the UK Meteorological Research Facility for support of the C-130 measurement program. This work is sponsored by the Oceanographer of the Navy (OP-096) through the Space and Naval Warfare Systems Command, PMW-185, program element 0603207N for the development of electro-optical tactical decision aids.

References

Gathman, S.G., and K.L. Davidson, The Navy Oceanic Vertical Aerosol Model, Naval Command, Control, and Ocean Surveillance Center, RDT&E Div., San Diego, 1993.

Hanel, G., The properties of atmospheric aerosol particles as functions of the relative humidity at thermodynamically equilibrium with the surrounding moist air, in *Advances in Geophysics*, edited by H.E. Landsberg, and J. VanMieghem, pp. 73-188, Academic Press, New York, 1976.

Hanel, G., and B. Zankl, Aerosol sizes and relative humidity: Water uptake by mixtures of salts, *Tellus, 31*, 478-486, 1979.

Paluch, I.R., The entrainment mechanism in Colorado cumuli., *Journal of Atmospheric Science, 36*, 2467-2478, 1979.

Pruppacher, H.R., and J.D. Klett, *Microphysics of Clouds and Precipitation*, Reidel, London, 1980.

Rogers, D.B., D.W. Johnson, and C.A. Friehe, The stable internal boundary layer over a coastal sea. I: Airborne measurements of the mean and turbulence structure, *Journal of Atmospheric Science, 52*, 667-683, 1995.

Rood, M.J., M.A. Shaw, T.V. Larson, and D.S. Covert, Ubiquitous nature of ambient metastable aerosol, *Nature, 337*, 537-539, 1989.

Tang, I.N., and H.R. Munkelwitz, Aerosol phase transformation and growth in the atmosphere, *Journal of Applied Meteorology, 33*, 791-796, 1994.

COMPARISON OF THREE METHODS OF CHARACTERIZING AN AIR MASS

Kathleen Littfin*
Propagation Division
Space and Naval Warfare Systems Center San Diego D883
49170 Propagation Path
San Diego, CA 92152-7385
Ph: 619-553-6939 Fax: 619-553-1417
E-mail: littfin@spawar.navy.mil

Andreas Goroch
Naval Research Laboratory
Marine Meteorology Department
Monterey, CA 93943

Terry Battalino
Naval Air Warfare Center Weapons Division
Point Mugu, CA 93042-5001

ABSTRACT

The origin of an air mass is an important factor in predicting performance of electrooptical systems. The aerosol content varies significantly depending upon whether the air mass is anthropogenic or natural, marine or continental, rural or urban. Most areas of military interest today are in coastal environments, where there can be a wide variety and rapid changes of atmospheric conditions. Atmospheric models need a reliable and easily obtainable indication of air mass because the ability to characterize an air mass is essential to accurately predict aerosol extinction and detection ranges. This paper explores and compares three methods of air mass retrieval: radon concentration, condensation nuclei concentration, and scattering from aerosol. These measurements, along with a full complement of meteorological and aerosol data, were obtained during two EOPACE (Electrooptical Propagation Assessment in Coastal Environments) experiments conducted in San Diego, California, in November 1996 and August/September 1997.

INTRODUCTION

When trying to predict the behavior of electrooptical systems, a major unknown is aerosol extinction. And in determining aerosol extinction, a primary unknown is the composition of the air mass through which the electrooptical system is sensing. In the Navy Aerosol Model (NAM), Gathman[2] introduced a quantity called the air mass parameter (AMP)

which quantifies this composition of an air mass as a number between 1 (entirely marine in origin) and 10 (entirely continental in origin). NAM is included in the present version of MODTRAN.

Aerosol extinction can vary significantly depending on whether the origin of the air mass is marine or continental, anthropogenic or natural, rural or urban. Most areas of military interest today are in coastal environments, where there can be a wide variety and rapid changes of atmospheric conditions. Characterizing the air mass is essential to accurately predicting EO systems behavior, but AMP is a difficult parameter to measure. This paper explores three methods of determining the air mass parameter: measuring radon concentration, measuring scattering with a nephelometer, and measuring condensation nuclei concentration. Other methods that have been explored with limited success are air trajectories, which have proven to be time consuming and complicated, and observed visibility which is too subjective.

THE RADON METHOD

A traditional and reliable method of determining the marine or coastal air mass parameter is to measure the beta radioactivity of radon daughter products.[3, 4] This method has the advantage that its measurements are not affected by contaminants such as smoke, smog, or exhaust. It is not dependent on the aerosol content itself or on visibility but is actually a tracer reflecting how long the air mass has been at sea, since various natural processes clear out small aerosol over time. Radon, which is produced over land but not over water, is in a much higher concentration when the air mass has just traveled over land.

Radon devices used to test communities for the presence of radon are not sufficient; the sensors we use are three orders of magnitude more sensitive. Instrumentation used to measure radon is not readily available for shipboard or aircraft use. So, although measuring radon may be the most accurate method known for tracing an air mass, a more practical and readily available method has been sought.

THE NEPHELOMETER METHOD

In a method recently developed, Goroch[5] uses scattering measurements obtained from a three wavelength integrating nephelometer. In this method the air mass parameter is calculated by using nephelometer data and aerosol size distribution equations of the Navy Aerosol Model[1, 2]. As shown in figure 1, the coefficients of the three lognormal components of the aerosol size distribution depend directly on air mass, 24-hour average wind, and current wind, as described by Gathman[2].

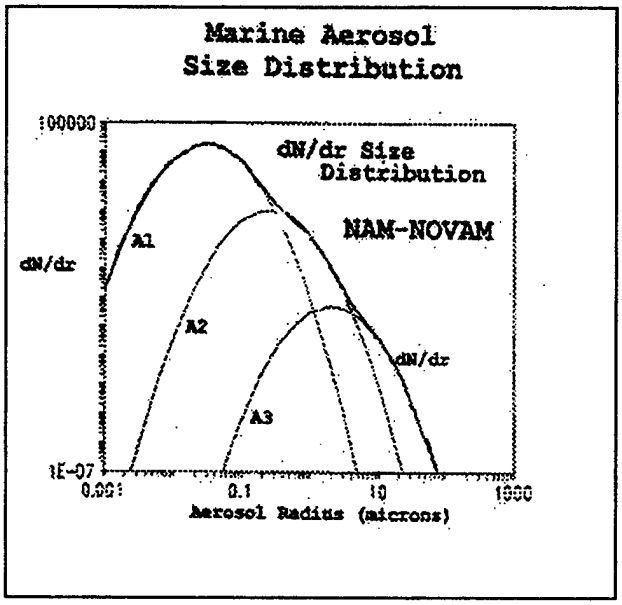

$$\frac{dN}{dr} = A_i \frac{\exp\{-1[\log(r/C_i f)]^2}{f}$$

(i=1,2,3)
where r = radius
f = particle swelling factor (based on RH)
$A_1 = 2000 * AMP^2$
$A_2 = \max[(5.866 * \text{avg wind} - 2.2), 0.5]$
$A_3 = 10^{(0.06 * \text{(instantaneous wind)} - 2.8}$
$C_i = 0.03, 0.24, 2.0$, respectively

Figure 1. Note that the A_1 component (the largest curve) is dependent of the square of the air mass parameter. The AMP has significant effect on the aerosol size distribution.

In the nephelometer method[6], the extinction resulting from the presence of the aerosol distribution in an air parcel is proportional to the Mie scattering efficiency integrated over the particle concentration:

$$\sigma \propto \int Q(m,r) \frac{dN}{dr} \pi r^2 dr \qquad (1)$$

where Q is the Mie Scattering Efficiency, m is the complex index of refraction and r is the particle radius. The integral is dependent on the relative humidity and the aerosol size distribution, along with the other meteorological information included in the coefficients as shown in figure 1. In the NAM model, the size distribution is represented by three lognormal functions. The largest component represents the smallest particles, the background aerosols which are usually advected to the area rather than being locally generated. This largest component is a function of the air mass parameter; in fact, the A_1 coefficient is proportional to the square of the AMP. The air mass parameter has a most significant effect on the aerosol extinction in the shorter wavelengths.

The NAM model extinction can be evaluated at the measured nephelometer wavelengths: blue (450 nm), green (550 nm), and red (700 nm). From that, the air mass parameter needed to satisfy the model is calculated[5].

CONDENSATION NUCLEI METHOD

A method of determining the air mass parameter from condensation nuclei (CN) measurements was developed by Battalino[7]. CN monitors measure submicron sized particles present in a specific volume of air. They count the total number of particles only; there is no size distribution.

Since the measurement depends directly on the number of particles present in the sample, contamination of the sample by smoke or exhaust from local sources such as generators, smokestacks, or car exhaust is a problem. The air in the vicinity of the CN monitor may indicate a very high number of particles, whereas the general large-scale air mass in the area may be relatively low in particles. Thus it is very important to locate the CN monitor away from particle-producing sources to obtain accurate background aerosol information.

In the CN method of determining the air mass parameter, Battalino[7] also uses the Navy Aerosol Model[2]. The CN method equates the measured CN count to the CN count obtained by integration of the NAM size distribution spectrum over radius limits specified by the particle size measurement range of the CN monitor. This leads to determination of the A_1 component which is proportional to the square of the air mass parameter (see figure 1). Battalino developed a table with fixed ranges of CN particles per cubic meter corresponding to the 1-10 range of the air mass parameter in the NAM. His method is independent of relative humidity and almost completely independent of wind speed. CN is an intrinsic property of the air mass; however, the monitor must carefully placed away from sources of aerosol contamination.

MEASUREMENTS

Characterization of the coastal air mass is one of the major objectives of the international effort called Electrooptical Propagation Assessment in Coastal Environments[8] (EOPACE). Two intensive operational periods were conducted in San Diego from 4-22 November 1996, and from 25 August - 5 September 1997. Figure 2 shows the location of equipment. A radon monitor, a three-wavelength nephelometer, and a condensation nuclei monitor were co-located at the receiver end of two infrared transmission paths (labeled "IR receiver" in figure 2) at the Naval Submarine Base San Diego. In the November experiment, the nephelometer was also located at the receiver end of the paths. In the August/September experiment, the nephelometer was located on an instrumented boat which traveled along both transmissions paths and was equipped with meteorological and aerosol sensors. Supporting meteorological instrumentation for both experiments included a shadowband sun photometer, a visiòmeter, a particulate volume monitor, air temperature and relative humidity probes, an anemometer, and an aerosol spectrometer. Similar meteorological equipment was located at the transmitter ends of both paths, and on midpoint buoys along both paths.

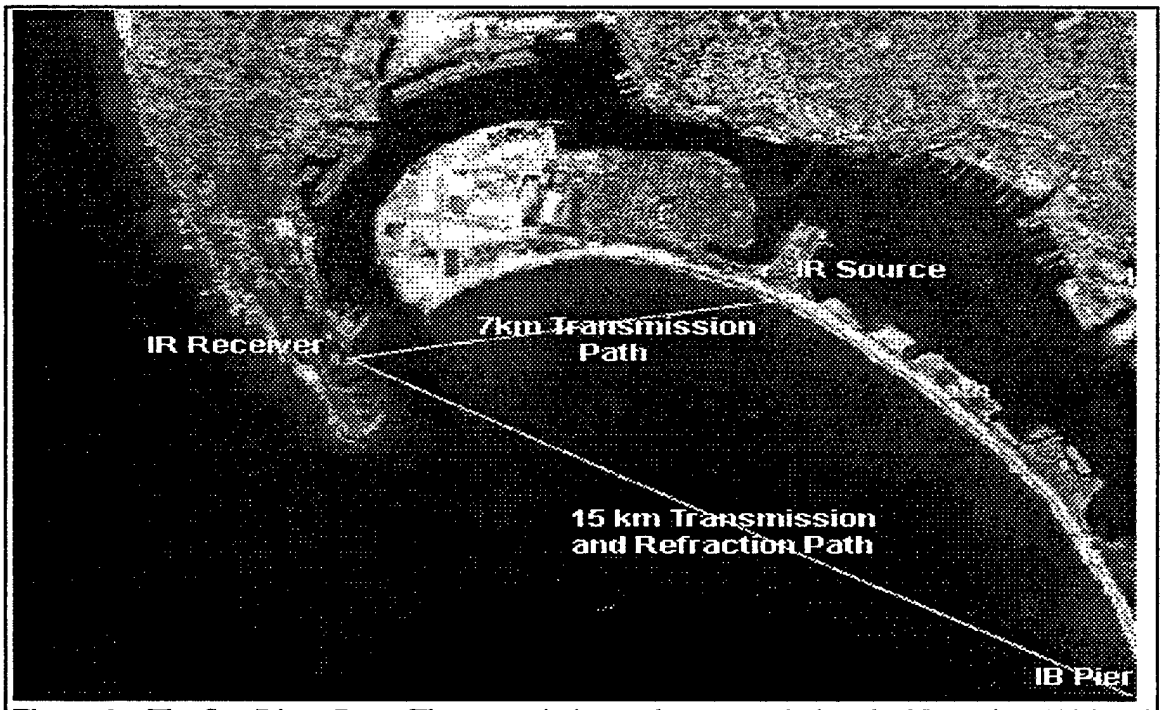

Figure 2. The San Diego Bay. The transmission paths set up during the November 1996 and Aug/Sept 1997 EOPACE experiments were instrumented at each end, and at midpoint buoys. The end marked "IR Receiver" shows the location of the nephelometer, radon monitor, condensation nuclei monitor, and supporting meteorological equipment. An instrumented boat also traveled along both paths.

COMPARISON

Air mass parameters were calculated using each of the three methods: radon, nephelometer and condensation nuclei. In the Navy Aerosol model, the air mass parameter was chosen to be a unitless value from 1 to 10, with 1 being an entirely marine origin and 10 being a completely continental origin.

Figure 3 shows the calculated AMPs for all three methods for a four day period from 1-4 September 1997. The nephelometer was located on a boat which traveled along both transmission paths (shown in figure 2). The radon monitor and CN monitor were located at the receiver end of the transmission path. The agreement is good, especially considering that the three methods are comparing independent parameters: the radon method acts as a timer indicating how long an air mass has been out to sea, the nephelometer measures light

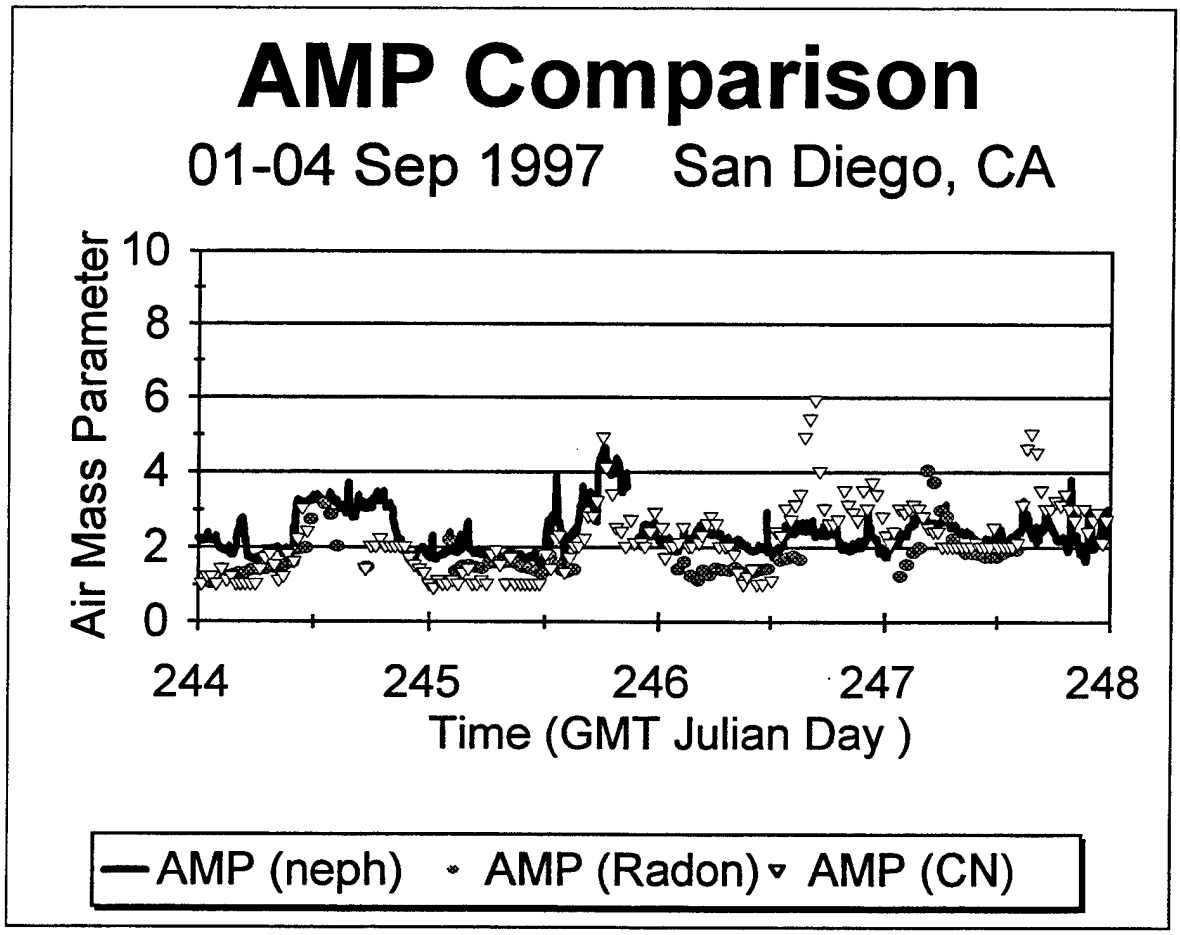

Figure 3. Graph shows air mass parameter comparison for a four day period 01-04 September 1997, during an EOPACE experiment. The three methods of AMP retrieval are nephelometer scattering measurements (solid line), radon decay measurements (circles), and condensation nuclei counts (triangles).

scattering due to the aerosol, and the CN method counts total number of small aerosol. The graph in figure 3 indicates a mostly marine air mass. Because this is a coastal environment, there will almost certainly be some continental influence, but an AMP under 4 can be considered marine. During this particular experiment, there was not the usual diurnal shift from onshore to offshore winds normally seen in San Diego. The wind direction stayed mostly westerly (onshore).

Figure 4 shows the same information for an earlier experiment from 15-18 November 1996. The agreement between the nephelometer method and the radon method is quite good, and the CN method follows the same trends, but is somewhat higher than the

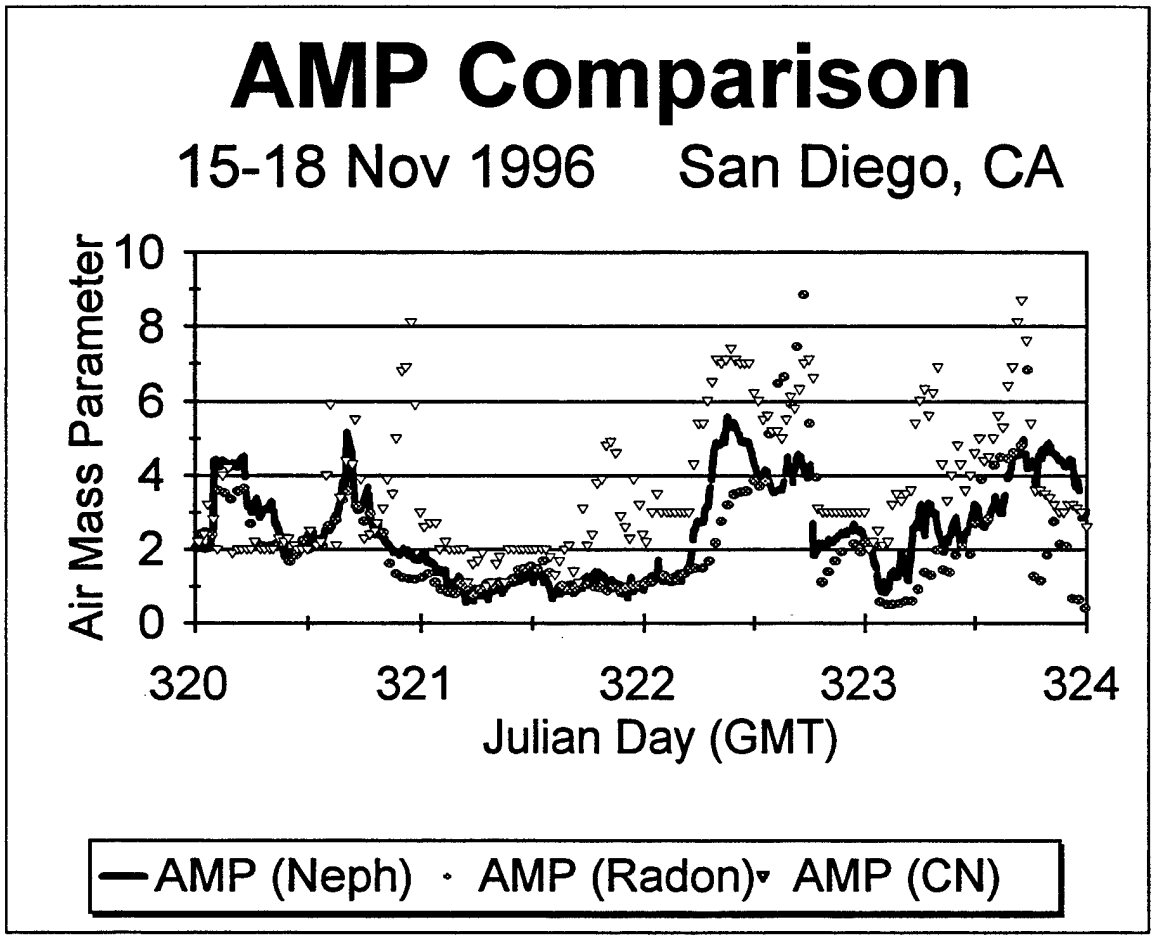

Figure 4. Graph shows air mass parameter comparison for three methods of AMP retrieval for a four day period 15-18 November 1996, during an EOPACE experiment. The three methods of AMP retrieval are nephelometer scattering measurements (solid line), radon decay measurements (circles), and condensation nuclei counts (triangles).

others. This could be due the presence of a larger quantity of smaller particles than the nephelometer responds to, since the nephelometer measures at three discrete wavelengths. The graph shows this difference is significant in only a couple places. At the end of day 320 and the end of day 321, the CN AMPs spike up, apparently influenced by a local aerosol source, while the nephelometer and radon AMPs indicate a definite marine air mass. In the other places where the CN AMP was higher (Julian day 321 through 323.7), it did track the other two methods, changing from marine to more continental in nature as the winds shifted from onshore to offshore.

At Julian day 322.3, the supporting meteorological measurements indicate that the visibility dropped significantly due to haze, causing more scattering and higher calculated nephelometer and CN AMPs. At Julian time 322.6, as the wind direction shifted from westerly (onshore) to easterly (offshore), the radon AMP went very high. At Julian day

322.7, the wind shifted again suddenly to an offshore flow, and is clearly indicated on the graph by the large increase in AMP.

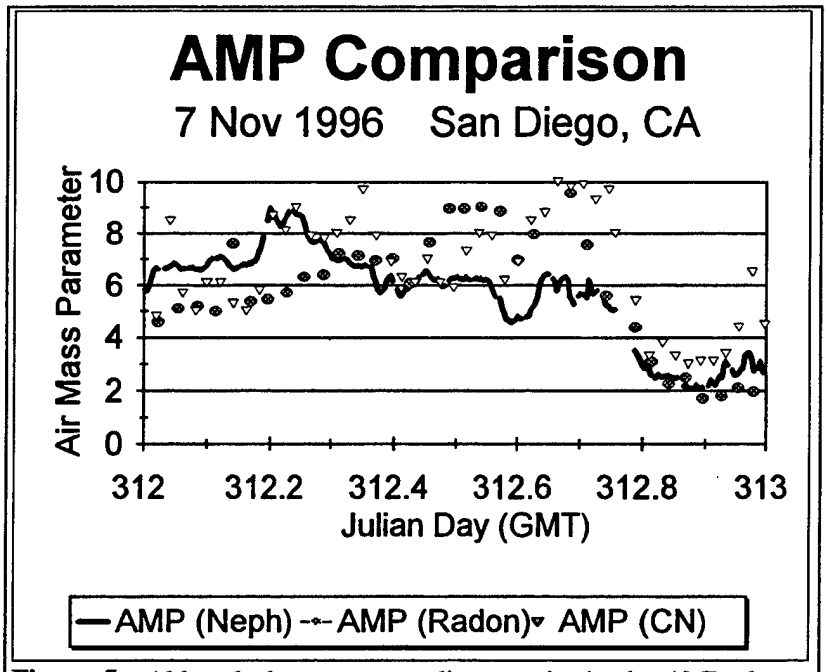

Figure 5. Although there are some discrepancies in the AMPs due to differences in what is actually being measured by the three methods, each accurately indicated this continental air mass, and each tracked the transition to a marine air mass.

Figure 5 shows an air mass transitioning from continental to marine. All three AMP methods accurately tracked the process. This example shows that using an AMP is an accurate indicator; while the three methods varied some due to differences in what each actually measured, the AMP in each case clearly indicated the continental or marine nature of the air masses and the transition between them. That knowledge aids in an accurate prediction of aerosol extinction.

The nephelometer method for determining an air mass parameter is as valid as the traditional radon method. It is easier to measure, more readily available, and is a function of the aerosol itself.

The CN method is also valid if the instrument is properly located. Figures 6 and 7 show a vast difference in the CN AMP. In figure 6, the CN monitor was located at the Naval Submarine Base, while in figure 7 the CN monitor was located on the boat that was transversing the transmission paths. By looking at wind direction data, it is obvious that the generator exhaust influenced the boat CN readings. For this reason, a relative wind direction indicator was located on the boat, and the only readings used for analysis were those where the wind direction blew exhaust away from the CN monitor intake. (Evidently the nephelometer ranges do not include the extremely small particles detected by the CN monitor.) Figure 8 shows the same CN data as figure 7, but the boat CN readings are selected as a function of wind direction, and data is purged where helicopters or ships passed by our boat.

CONCLUSION

The air mass origin is an important factor in predicting performance of electrooptical systems. The traditional method of measuring the beta radioactivity of radon daughter products has been a reliable method, but is not available for widespread use, and not directly a function of the aerosol. Two new methods of determining the air mass parameter use scattering measurements obtained from a three-wavelength nephelometer, and total aerosol loading from condensation nuclei measurements. The three methods were compared and results show that all are able to accurately identify a continental air mass, a marine air mass, and the transitions in between.

The nephelometer AMP method is more closely correlated to the traditional radon AMP method. The condensation nuclei AMP method gives valid information if the monitor is carefully located away from other aerosol sources; if near an aerosol source, wind direction must be taken into account.

An air mass parameter gives quick, valid information on whether an air mass is continental or marine in origin, and that aids researchers and modelers in determining the aerosol extinction. Real-time models depend upon speed and a valid estimation may prove more useful than an exact answer which takes hours of computing time.

ACKNOWLEDGEMENTS

This work was sponsored by the Office of Naval Research, ONR-322.

REFERENCES

1. Gathman, S. G., and K. L. Davidson, "The Navy Oceanic Vertical Aerosol Model," Technical Report 1634, Naval Command, Control and Ocean Surveillance Center, 1993.
2. Gathman, S. G. "Optical properties of the marine aerosol as predicted by the Navy aerosol model," *Optical Engineering,* 22 (1) p. 57, 1983.
3. Larson, R. E., and D. J. Bressan, "Automatic radon counter for continual unattended operation," *Rev. Sci. Instrumen.,* 49(7), pp. 965-969, 1978.
4. Larson, R. E., and W. Kasemir, "Measurements of Atmospheric ^{222}Rn at San Nicolas Island and Over Nearby California Coastal Areas During CEWCOM-78," Naval Research Lab Memorandum Report 3941, 1979.
5. Goroch, Andreas K., "Retrieval of size distribution information from nephelometer measurements," Naval Research Laboratory report, currently in publication.
6. Littfin, K., and A. Goroch., "Determination of an air mass using nephelometer measurements and the Navy Aerosol Model," *SPIE Conf. Proceedings* July 1997, Vol 3125, pp. 59-65.
7. Battalino, T. E., "Numerical and Analytical Solutions of the Small Particle Amplitude in the Navy Aerosol Model," Naval Air Warfare Center Weapons Division Geophysics Technical Note No. 199, June, 1996.
8. Littfin, K. M. and D. R. Jensen, "An Overview of EOPACE (Electrooptical Propagation Assessment in Coastal Environments), Including In Situ and Remote Sensing Techniques, *AGARD Conference Proceedings 582*, paper #10, 1996.

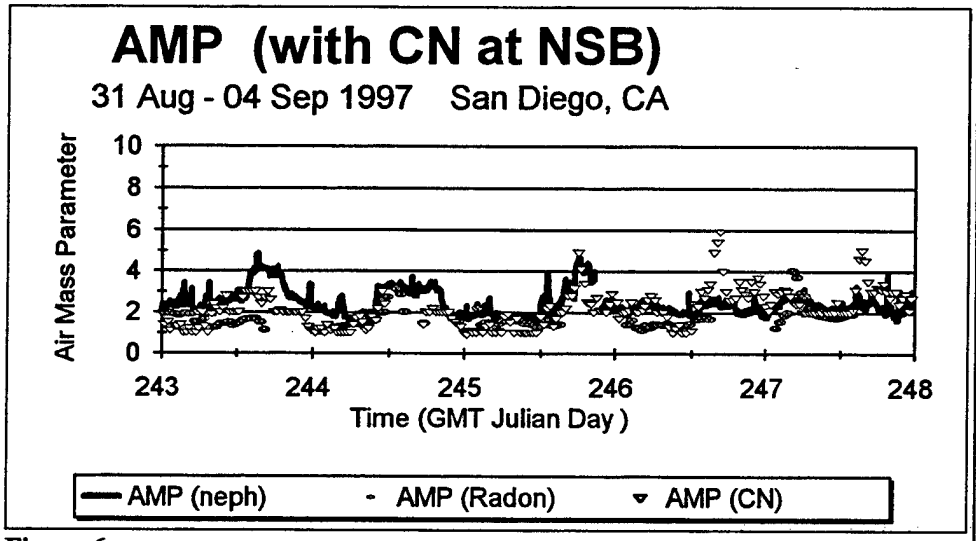

Figure 6.

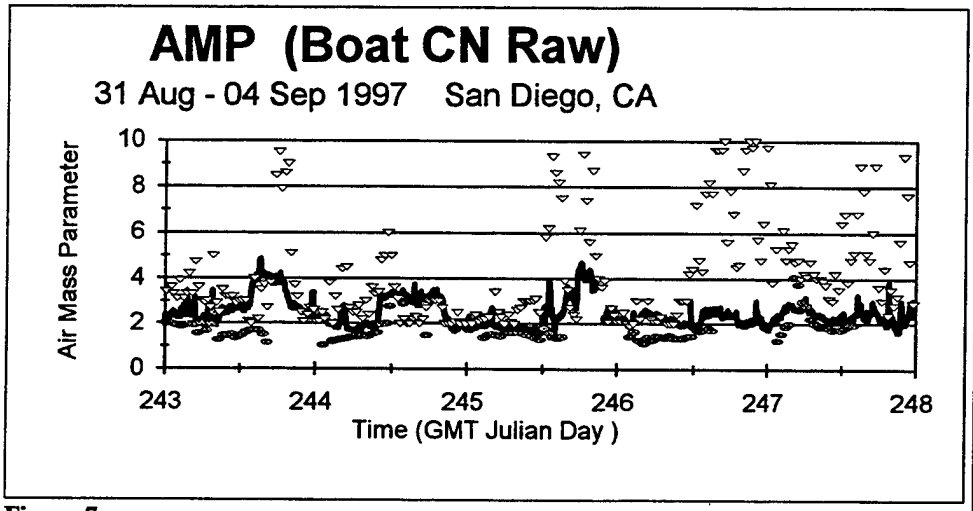

Figure 7.

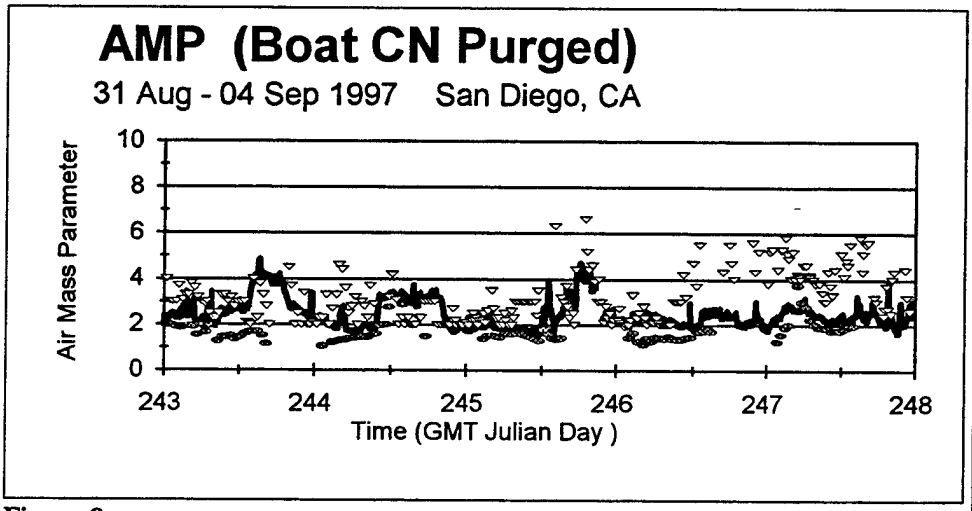

Figure 8.

Figures 6, 7, & 8. The CN method of AMP retrieval requires caution in the placement of the CN monitor and attention to wind direction if an aerosol-producing source is near. In figure 6, the CN AMP proves to be an accurate indicator when the CN monitor is located at the Naval Submarine Base at the receiver end of the transmission path away from aerosol producers. In figure 7, the raw CN AMP is obviously not an accurate indicator when the CN monitor is located on the boat, unless relative wind direction is recorded. Otherwise the generator-produced aerosols contaminate the sample at times when the exhaust is blowing into the CN monitor intake. Figure 8 shows the same data as figure 7, after purging those readings taken when there was an unfavorable wind direction, and purging readings taken when aerosol sources such as ships and helicopters were passing .

Proceedings, Battlespace Atmospherics Conference, San Diego, CA, Dec 1997.

Air mass parameter retrieval from nephelometer data in the Sea of Japan

Andreas K. Goroch
Marine Meteorology Division
Naval Research Laboratory
VOX:408-656-4889
FAX: (408)656-4769
E-MAIL: goroch@nrlmry.navy.mil

Abstract

Aerosol scattering data were collected using a TSI 3 wavelength nephelometer during a SHAREM exercise near the Korean coast. The nephelometer measures the total integrated scattering and the backward integrated scattering coefficients at three visible wavelengths. The exercise period included the passage of a cold front, with a distinct change of air mass from pre-frontal moist air with some precipitation to very dry, cool conditions. The nephelometer data are used to calculate the air mass parameter that describes the relative concentration of background aerosols in the Navy Aerosol Model (NAM). The air mass parameters shows the variation of visible and infrared aerosol extinction at the ocean surface during a rapid atmospheric change. The operation also demonstrates successful operation of an aerosol measurement device on operational Navy vessels.

Introduction

The environment affects the performance of an electro-optical system by causing molecular and aerosol extinction. Molecular extinction is well understood and accurately described with measurements of pressure, temperature and moisture. Aerosol extinction is more difficult and currently remains as on of the most important uncertainties in the prediction of electro-optical system. Direct measurement of aerosol concentrations requires complex instrumentation. The usual technique is to relate conventional measurements to an aerosol model that is then related to aerosol extinction at the appropriate wavelength.

Marine aerosol models

The marine aerosol distribution model consists of a sum of three log normal distributions. Each distribution is characterized with an identical width parameter and a mode size parameter. The aerosol radius in each distribution is affected by humidity, which accounts for condensation and evaporation of water from the aerosol surface. The coefficients of the component distributions are related to wind, average wind, and air mass parameter. The number concentration of particles per unit radius, per unit volume is given as

$$\frac{dN}{dr} = n(r) = \sum_{i=1}^{3}\left[\frac{10^{-3}}{f_i} A_i \exp-\left\{\ln\left(\frac{r}{r_i f_i}\right)\right\}^2\right], \quad (1)$$

where i refers to the constituent, A_i is the environment dependent coefficient, r_i is the constituent mode radius, and r is radius. Note that observed data suggest the width parameter for each component distribution is unity. The size distribution and its components are shown in Figure 1.

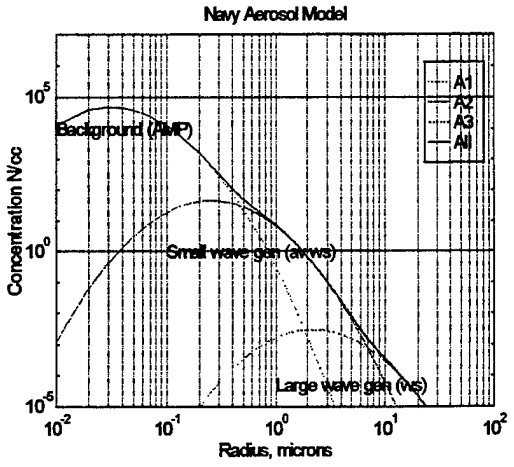

Figure 1. Size distribution of components of Navy Aerosol Model.

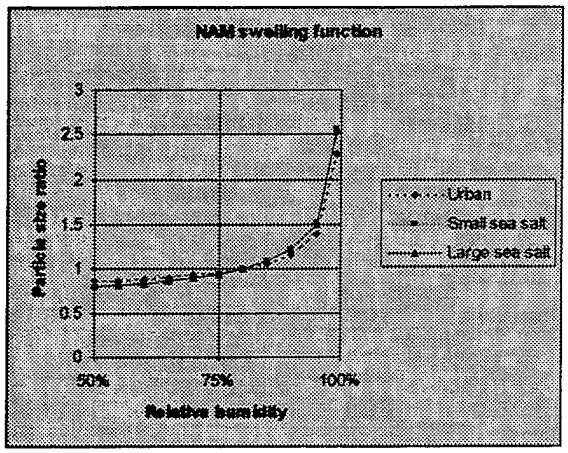

Figure 2. Swelling function used in NAM.

The particle swelling coefficient f_i, describes the equilibrium radius of the particle as a function of the relative humidity[*Gerber*, 1985]. The swelling coefficients for each of the distributions are shown in Figure 2 as a function of relative humidity.

The three environment dependent coefficients are conceptually related to the characteristics of the ambient air mass, the average wind, and the current wind. The physical model assumes the two larger modes are related to wave breaking and particle generation at the sea surface. The coefficient of the largest mode is parameterized with current wind and the coefficient of the middle mode is parameterized with the 24 hour average wind, within the observed air parcel. This Lagrangian property requires some knowledge of the trajectory of the air parcel. The coefficient of the smallest component is related to the history of the aerosol, that is, whether the air parcel source has been a continental or maritime region.

The air mass parameter has been determined by correlation with a number of observed and predicted variables. Originally the parameter was strictly subjective [*Barnhardt and Streete*, 1970], simply being the relative weight assigned to modified Gamma functions with marine or continental parameters. This model was modified to include three log normal distributions [*Gathman*, 1983] in which the marine or continental influence was assigned to the background aerosol component, with other components determined by an averaged wind and a current wind speed observation, respectively. The air mass parameter (AMP) was first related to a radon concentration based on a series of Naval Research Laboratory ocean cruises[*Gathman*, 1983; *Larsen and Bressan*, 1978; *Larsen and Kasemir*, 1979]. The parameter has lately been related to visibility [*Gathman and Davidson*, 1993]. Since visibility is commonly a subjective measurement, it would be appropriate to relate the AMP to an objective observed variable, with the attendant advantages of stability and reproducibility of the measurement.

The extinction resulting from the presence of the aerosol distribution in an air parcel is primarily due to scattering, with little absorption in the visible wavelengths. The is given by the total scattering, which is the integral of the scattering

$$\sigma = \int_0^\infty Q(m,r,\lambda)\frac{dN}{dr}\pi r^2 dr \quad , \quad (2)$$

efficiency factor $Q(m,r,\lambda)$, over the total particle population,

where m is the complex index of refraction and r is particle radius. Since the total scattering is

$$\sigma = \int_0^\infty Q(m,r,\lambda)\sum_{i=1}^{3}\left[\frac{1}{f_i}A_i \exp-\left\{\ln\left(\frac{r}{r_i f_i}\right)\right\}^2\right]\pi r^2 dr$$

$$= \sum_{i=1}^{3}\frac{\pi A_i}{f_i}\int_0^\infty Q(m,r,\lambda) r^2 \exp-\left\{\ln\left(\frac{r}{r_i f_i}\right)\right\}^2 dr \quad . \quad (3)$$

linear in the three components, the distribution components can be separated.

Using the NAM model with known mode radii and indices of refraction, the integrals are dependent only on the relative humidity and the mode radius, with the other meteorological information completely included in the coefficients. These integrals have been evaluated numerically [*Gathman and Davidson*, 1993].

Retrieving the aerosol model coefficients

The aerosol model extinction parameterization can be evaluated using Eq. 3 at the three nephelometer wavelengths as

$$\sigma_{blue} = \frac{A_1(AMP)}{f_1}\left[B_1(RH)\right] + \frac{A_2(w_{avg})}{f_2}\left[B_2(RH)\right] + \frac{A_3(w)}{f_3}\left[B_3(RH)\right] \quad (4)$$

$$\sigma_{green} = \frac{A_1(AMP)}{f_1}\left[G_1(RH)\right] + \frac{A_2(w_{avg})}{f_2}\left[G_2(RH)\right] + \frac{A_3(w)}{f_3}\left[G_3(RH)\right]$$

$$\sigma_{red} = \frac{A_1(AMP)}{f_1}\left[R_1(RH)\right] + \frac{A_2(w_{avg})}{f_2}\left[R_2(RH)\right] + \frac{A_3(w)}{f_3}\left[R_3(RH)\right]$$

where B, G, and R are the scattering coefficient integrals (Eq. 3) in the blue, green, and red wavelengths of the three component aerosol distributions. The system can be expressed in a more compact fashion if we consider the column vector of NAM coefficients, $A = \begin{pmatrix} A_1 \\ A_2 \\ A_3 \end{pmatrix}$ and the matrix of humidity modified scattering

$$E = \begin{pmatrix} B_1/f_1 & B_2/f_2 & B_3/f_3 \\ G_1/f_1 & G_2/f_2 & G_3/f_3 \\ R_1/f_1 & R_2/f_2 & R_3/f_3 \end{pmatrix} \quad (5)$$

contributions for each color and mode,

$$\sigma = E \cdot A, \quad (6)$$

This equation has the solution,

$$A = E^{-1} \cdot \sigma \quad (7)$$

This system consists of three linear equations with three unknowns. It is possible to solve the three equations for the three unknowns. However the third coefficient, A_3, relates to large particles, which do not contribute greatly to scattering in the visible wavelengths [*Heintzenberg and Quenzel*, 1973]. Since the large particles are parameterized by the most directly measured atmospheric variable, wind speed, the parameterization can be used to independently calculate A_3. The E matrix is separated into segments for the two small modes and the larger mode.

$$E_{12} = \begin{pmatrix} B_1/f_1 & B_2/f_2 \\ G_1/f_1 & G_2/f_2 \\ R_1/f_1 & R_2/f_2 \end{pmatrix}, E_3 = \begin{pmatrix} B_3/f_3 \\ G_3/f_3 \\ R_3/f_3 \end{pmatrix}. \quad (8)$$

The equation for the scattering coefficients can

$$\sigma - A_3 \cdot E_3 = E_{12} \cdot \begin{pmatrix} A_1 \\ A_2 \end{pmatrix}, \quad (9)$$

be rewritten in the form
This is an overspecified equation which can be solved in a least squares sense by factoring A using Householder orthogonalization with column pivoting [*Mathworks*, 1992].

Exercise measurements

Aerosol measurements

The aerosol measurements were collected during the US Navy SHAREM 120B during April 3-7, 1997. The nephelometer samples were collected 10 m above sea level at the bow of the ship. The sample was led through a 2.5 cm inside diameter 6 m length plastic tube to the nephelometer located below deck. The data were averaged over a 5-minute period and stored on a laptop computer. The stored data are shown in included total integrated scattering coefficients at the three wavelengths, backward integrated scattering a the three wavelengths, pressure, temperature at the sample inlet and in the sample chamber and sample relative humidity.

Meteorological conditions

Meteorological measurements were obtained from the standard ship deck weather logs. Wind was obtained from the anemometer mounted on the second yardarm approximately 40 m above the surface. Temperature was measured with a hand held thermometer in an unobstructed location on the bridge, approximately 25 m above the surface. Wind, temperature, and dew

point were subjectively quality controlled, and found to be reasonable for the time interval used in this analysis.

The exercise began with a low pressure area to the east of the region and gradually traversing easterly. The surface conditions were generally cloudy with intermittent rain showers until 5 April. Wind was 5-15 knots from the southeast. A frontal passage occurred on 5 April, with

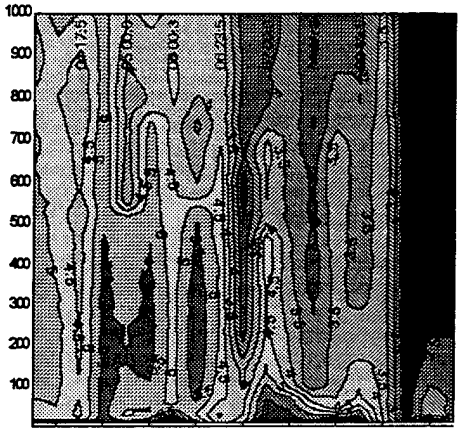

Figure 3. Mixing ratio cross section from soundings collected during the SHAREM 120B exercise. Day in April 1997 and UTC time are annotated.

generally dry air advecting from the east. A cross section of moisture profiles for the time period is shown in Figure 3.

Air mass parameter observations

The air mass parameter during the exercise was obtained from the nephelometer total integrated

scattering measurements. The relative humidity within the sampling chamber was used to determine the scattering kernels in Eq. 4. The current wind observed on the bridge was used to determine the A_3 parameter. The air mass parameter observations are shown in Figures 4 and 5. The data illustrate the change of the AMP during the first and second parts of the exercise.

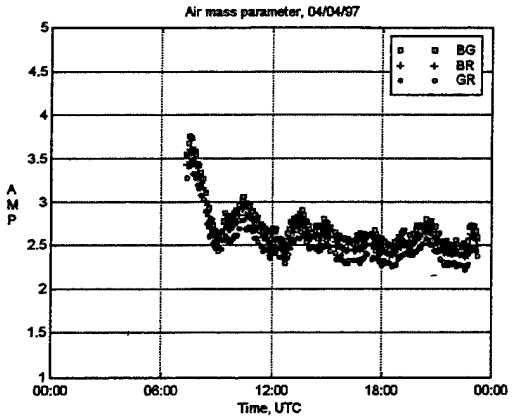

Figure 4. . Air mass parameter using pairs of nephelometer total scattering measurements on 4 April 1997.

During the first period, the AMP was low, indicative of a reduced fraction of background particles. This is consistent with the general southwesterly flow with a mainly maritime trajectory, as well as possible concentration reduction by washout.

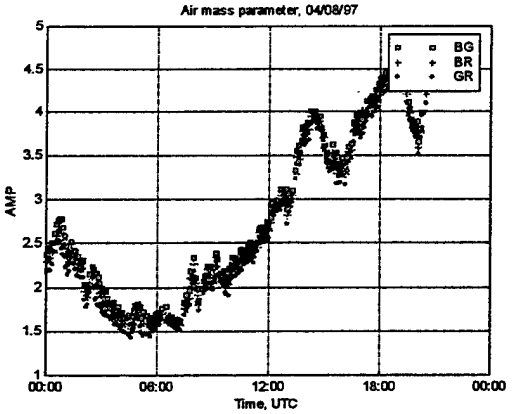

Figure 5 . AMP retrievals on 8 April 1997.

During the second period, with warmer drier air, the AMP steadily increased consistent with the advection of desert dust from the Chinese continent.

The aerosol characteristics during this period were also obtained from the Angstrom coefficient, which is related to the slope of the size distribution. The Angstrom coefficient is obtained from the scattering coefficient values using the standard relation of equation 10.

$$\sigma = \sigma_0 \lambda^{-\alpha} \qquad (10)$$

The Angstrom coefficients for 8 April 97 are shown in Figure 6 and 7.
The Angstrom coefficient is seen to be more variable than the air mass parameter. Since the

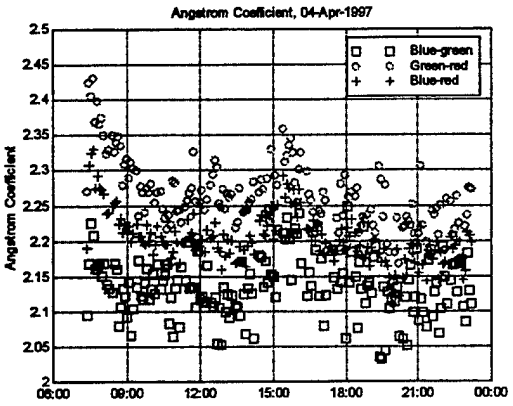

Figure 4 . Angstrom coefficients for the nephelometer measurements on 4 April 1997.

visibility and presumably aerosol extinction was observed to be similar from hour to hour, this result points out that the air mass parameter is probably a more appropriate parameter than the Angstrom coefficient .

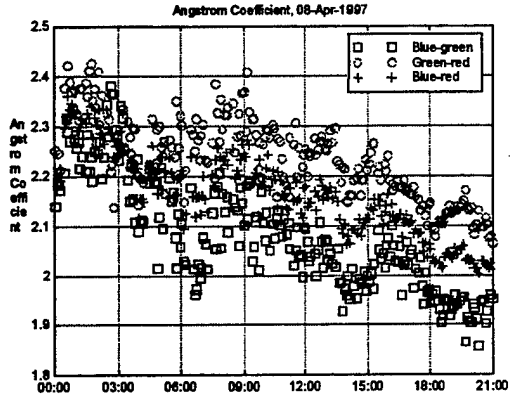

Figure 5 . Angstrom coefficient calculated from observations taken during 8 April 1997.

Conclusions

A technique for retrieving size distribution information from measurements of multispectral aerosol scattering has been developed. The method is based on the assumption that the marine aerosol concentration can be modeled with the Navy Aerosol Model, which parameterizes the particle concentrations by wind, average wind, and air mass parameter. The retrieval is based on the fact that scattering is most sensitive to the smallest size particles, which are empirically related to parameters which are difficult to measure. The scattering is almost insensitive to the largest particles; these are inferred with the NAM parameterization, which relates current wind speed to the concentration of large particles. The resulting inferences of aerosol distribution parameters are quite consistent with expectation of the empirical model.
The retrieval is applied to observations taken aboard ship South Korean coastal regions during SHAREM 120B. The results indicate that the nephelometer is a useful and practical instrument for support of EO performance predictions. The calculations of parameters from the observed scattering are quite similar to expectations where model calculations are not available and to calculated values where data are available. The nephelometer provides greatly increased time resolution, since the models use average wind in the data derivation.
The similarity of calculations from the model and from observations builds confidence in the use of the model for scattering in the near and far infrared windows. Previous studies have shown an important dependence on extinction by smaller particles[*Rozenberg et al.*, 1977]. With the addition of nephelometer measurements to characterize the background part of the aerosol size distribution an objective measure of aerosol extinction can be obtained to support optical performance calculations.

Acknowledgments

I would like to acknowledge the continued enthusiasm and support by the surface Warfare Development Group in the planning, conduct, and analysis of the SHAREM exercises. This work is sponsored by the Oceanographer of the Navy (OP-096) through the Space and Naval Warfare Systems Command, PMW-185, program element 0603207N. for the development of electro-optical tactical decision aids.

References

Barnhardt, E.A., and J.L. Streete, A method of predicting atmospheric aerosol scattering in the infrared, *Applied Optics, 9*, 1997-1344, 1970.

Gathman, S.G., Optical properties of the marine aerosol as predicted by the Navy aerosol model, *Optical Engineering, 22* (1), 57-63, 1983.

Gathman, S.G., and K.L. Davidson, The Navy Oceanic Vertical Aerosol Model, Naval Command, Control, and Ocean Surveillance Center, RDT&E Div., San Diego, 1993.

Gerber, H.E., Relative humidity parametrization of the Navy Aerosol Model (NAM), Naval Research Laboratory, Washington, D.C., 1985.

Heintzenberg, J., and H. Quenzel, Calculations on the determination of the scattering coefficient of turbid air with integrating nephelometers, *Atmospheric Environment, 7*, 509-519, 1973.

Larsen, R.E., and D.J. Bressan, Automatic radon counter for continual unattended operation, *Review of Scientific Instruments, 49* (7), 965-969, 1978.

Larsen, R.E., and W. Kasemir, Measurements of Rn222 at San Nicholas Island and over nearby California Coastal areas during CEWCOM-78, Naval Research Laboratory, Washington, D. C., 1979.

Mathworks, I., *MATLAB V 4.0 User's Guide*, 209 pp., Mathworks, Inc., Natick, MA, 1992.

Rozenberg, G.V., Y. Georgiyevskiy, V.N. Kapustin, Y.S. Lyubovtseva, A.P. Orlov, S.M. Pirogov, A.I. Chavro, and A.K. Shukurov, Submicron aerosol fraction and light absorption in the 8-12 mm transparency window, *Bulletin(Izvestia), Academy USSR, Atmospheric and Oceanic Physics, 13* (11), 815-820, 1977.

AEROSOL CONTRIBUTION TO MARINE ATMOSPHERIC SURFACE LAYER REFRACTIVITY

Philip Walker
Physics Department, Code PH
Naval Postgraduate School
Monterey, CA 93943
Ph: 408-656-2674 Fax: 408-656-2834
E-mail: walker@physics.nps.navy.mil

Shipboard infrared search-and-track (IRST) systems serve as passive sensors for the detection of sea-skimming cruise missile threats. The missiles fly in the marine surface layer (MSL) where marine optics is distorted by large refractivity gradients caused by large vertical changes in temperature and humidity in the first 50 meters above the sea surface. Computer models used to predict sensor performance must accurately calculate ray bending between the missile target and an IRST aboard ship. Mermelstein[1] observed that refractive index profiles based on the LKB method yield excessive ray bending near the sea surface inconsistent with experimental observations, but aerosol contribution to atmospheric refractivity was not taken into account. Although aerosols are primarily thought of as scatterers, they must also contribute to the average volumetric atmospheric refractivity and if there is a vertical gradient of liquid water content, they must also contribute to ray bending. Refractivity and scattering due to the smallest possible droplets ought to approach that of an equivalent amount of water vapor. With increasing droplet size refractivity ought to decrease smoothly; whereas, scattering ought to increase. Thus, an upper limit to aerosol refractivity effects can be established by comparing liquid water content and water vapor in the MSL. Aerosol size distributions in the first few meters above the sea surface are not so easy to find. Toba[2,3] has been suggested as a place to start for vertical profiles of water droplet size.

INTRODUCTION

Of current interest to the Navy is the use of Infrared Search and Track (IRST) systems to detect and track in-coming, sea-skimming anti-ship missiles. The performance of IRST systems is degraded by atmospheric turbulence and refractivity effects, causing blurring, scintillation, and miraging. The seriousness of the refraction problem can be seen in Figure 1. Figure 1a is a visible light photograph of the Dutch Meetpost Noordwijk (MPN) tower that was used as a light source platform for the Marine Aerosol Properties and Thermal Imager Performance Trial (MAPTIP). Visible lamps were mounted by the Canadian Defense Research Establishment Valcartier (DREV) at differing heights above mean sea level (msl) from about 3.5 to 20 meters for the study of refractivity effects. [4] Figure 1b is a photograph of the same scene taken in the infrared (IR) after off-shore winds advected a cold air mass over the relatively warm sea-surface between the Katwijk Beach Station and the MPN tower. The two lowest lights are clearly a mirage because they are seen to be an inverted image of the pair above them. If one of these lights were an in-coming missile it would not be possible to ascertain its altitude because both, upper and lower, images are heavily refracted.

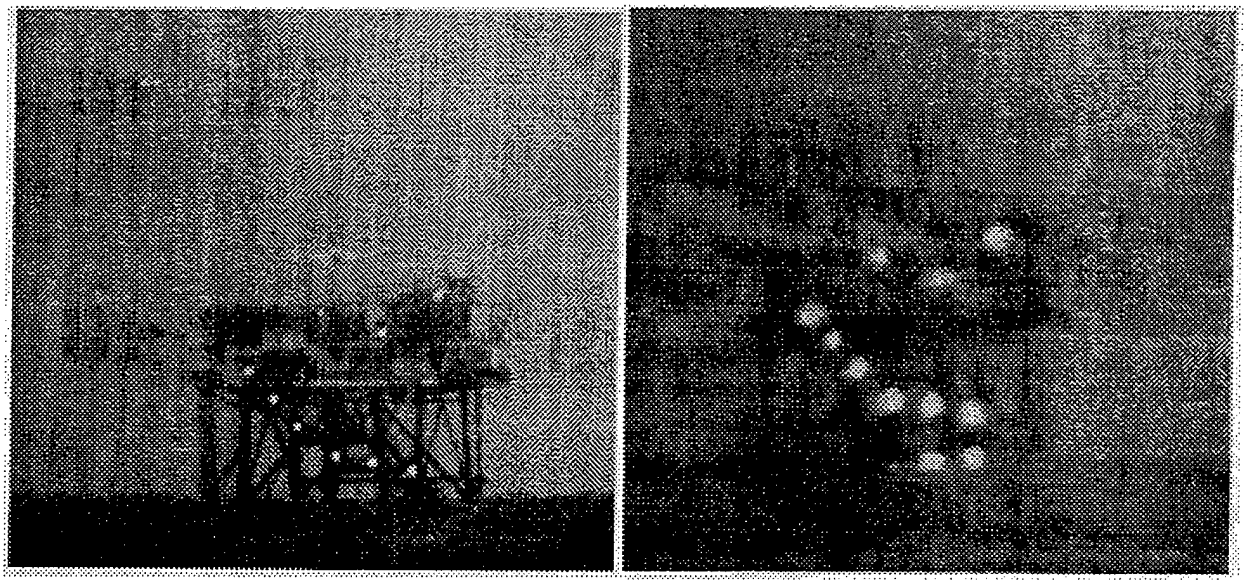

Figure 2. Visible and Infrared Images of the MPN Oceanographic Tower. These pictures were scanned from Reference 4.

The topics covered in this article will be, in order, a review of the background of near-sea-surface optical phenomenology, the modeling algorithms that have been developed, the experimental validation of these models and, finally, a discussion of whether an aerosol contribution to atmospheric refractivity could account for some discrepancies between measurement and prediction.

REFRACTION PHENOMENOLOGY

Atmospheric refraction is caused by vertical, and to a lesser extent, horizontal gradients of the index of refraction of the atmosphere. Refractive gradients are created by gradients of atmospheric density which are in turn created by temperature and pressure gradients and by partial pressure gradients of the non-uniformly mixed gases; water vapor and CO_2. Electro-magnetic waves, including light, bend toward the direction of increasing refractivity. In the presence of a refractive gradient the radius of curvature of refracted rays is given by

$$r^{-1} = -\frac{dn}{dz}$$

where n denotes the atmospheric index of refraction and z the vertical coordinate. The gradient is usually a negative quantity in that it decreases with increasing altitude; thus, a positive radius of curvature denotes a downward facing arc.

The index of refraction of air is a number very close to one. Hence, the index of refraction

is expressed in terms of refractivity which is proportional to the difference between n and 1 and is defined as

$$N=(n-1)x10^{6}$$

and so in terms of refractivity the index of refraction gradient is given by

$$\frac{dn}{dz}=\frac{dN}{dz}x10^{-6}$$

The refractivity of humid air is given by the sum of the refractivity of dry air plus refractivity due to water vapor

$$N=N_{dryair}+N_{H_2O}$$

which is

$$N=[77.6\frac{K}{mb}\frac{P}{T}]_{dryair}-[5.6\frac{K}{mb}\frac{e}{T}-3.73x10^{5}\frac{K^2}{mb}\frac{e}{T^2}]_{H_2O}$$

where e is the partial pressure of water vapor. Typical values are P = 1000 mb, T = 300 K, and e = 20 mb yielding N = 330.

Ray bending in the vertical plane depends upon the vertical gradient, given by

$$\frac{dN}{dz}=\frac{\partial N}{\partial P}\frac{dP}{dz}+\frac{\partial N}{\partial T}\frac{dT}{dz}+\frac{\partial N}{\partial e}\frac{de}{dz}$$

yielding

$$\frac{dN}{dz}=-49km^{-1}-1.4\frac{1}{K^{-1}}\frac{dT}{dz}+4.5\frac{1}{mb^{-1}}\frac{de}{dz}$$

Notice that there will be refraction even without the humidity gradients due to the temperature and pressure gradients. These gradients are incorporated in the ray bending subroutine in MODTRAN[5]. For the U.S. Standard Atmosphere model dT/dz = -6.5 °K/km and de/dT=0 (no humidity gradient). These assumptions yield an over-the-horizon ray bending of 15^{0}.

MARINE BOUNDARY LAYER REFRACTIVITY MODELS

Several analytical models have been developed to describe refractivity profiles in the marine surface layer. Among these are the constant flux model, the LKB[6] model as modified by Fairall[7], the L(W)WKD[8] model from DREV and the PIRAM[9] model from CELAR. The constant-flux model of the near-surface marine boundary layer was formerly used in Irtool[10]. This model depends upon turbulent transport driven by dry convection under conditions where the sea is warmer than the air and/or by mechanical turbulence due to the shearing instability of the near-surface wind. Typically, the depth of the surface layer is 50 meter or so. The applicability of the constant-flux model to extend low-altitude IR imaging over the ocean depends mostly upon the degree of horizontal homogeneity. Offshore-wind conditions in coastal regions represents one regime where such a model may not be adequate. Another regime of inapplicability might be a highly stratified surface layer (large positive air-sea temperature difference) with such low winds that turbulent transfer is too intermittent horizontally. The constant flux model has been replaced by the LKB model in IRtool and is the model that was used in the Mermelstein experiment to be discussed. (A specific requirement for IRtool input is that the 10 meter wind speed be at least 3 m/s.)

OPTICAL RAY TRACING MODELS

The spherical shell atmospheric model used in MODTRAN incorporates a ray tracing model that uses the step-wise variable refractivity of an onion-layer-like model of the Earth's atmosphere. Temperature, pressure, density, relative humidity, aerosols and non-uniformly gas amounts are assigned to each atmospheric layer from either radiosonde data or one of the Phillips Laboratory's atmospheric models, then are used to calculate optical refractivity and extinction for each layer. Snell's Law refraction is assumed to take place at layer boundaries with linear ray propagation within layers. Unfortunately, MODTRAN is limited to 33 layers, which means that the large refractivity gradients that exist near the sea surface cannot be accommodated by this code. It would be possible, of course, to extract the ray tracing algorithm from MODTRAN and increase the number of its layers enough to accommodate large MSL refractivity gradients. MODTRAN is most appropriate for large scale, space to earth and earth to space, simulations because of the coarseness of its atmospheric model.

The Parabolic Arc Model[11] is well suited for tactical simulations, unlike MODTRAN, because the number of shells can be infinite and their thicknesses infinitesimal. This model assumes the Earth's surface is flat with flat atmospheric layers stacked above it. Un-refracted light rays are parabolas in this model. Rays that are bent toward the surface are flatter parabolas. Rays that are bent away from the Earth's surface have a more narrow parabolic shape. The parabolic approximation is valid for ranges over a few tens of kilometers.

A TEST OF THE OPTICAL AND REFRACTIVITY MODELS USED IN IRTOOL

A principle difficulty in evaluating the ray tracing and refractivity algorithms is that they are coupled together into single optical propagation codes. Separate optical propagation and refractivity profile measurements, or even separate temperature and water vapor profile measurements, are not made. A validation of the coupled parabolic arc ray tracing / LKB refractivity profile model was performed by Mermelstein, et al. in 1996[1]. A description of that experiment follows.

Transmission measurements were conducted over Monterey Bay in June of 1996. Monterey Bay provides a very favorable location for evaluation of mirage and looming effects due to positive and negative air-to-sea surface temperature gradients that produce sub-refractive and super-refractive conditions in the MSL producing in turn serious effects in target imaging, detection and tracking of sea skimming missiles. A laser transmitter was placed at Pt. Pinos and an optical receiver was stationed at Marina Beach 12.8 km away across the bay. The elevations of the source and receiver were varied causing the apparent position of the source to be lowered below the horizon. The primary environmental data taken for model input were wind speed at 4 meters, air-sea temperature difference and the relative humidity in the bay at the mid-point of the ray path. The photo detector was lowered from a higher elevation until the transmitter disappeared. The air-sea temperature difference varied from approximately -2.6 to -0.2 °C and the wind speed ranged from 3.1 to 7.5 m/s.

The problem for optical propagation modeling in the marine surface layer is illustrated in Figure 2. These are plots of ray height elevation above the mean sea level based on the LKB model. The vertical axis on the right hand side of the plot shows receiver height corresponding to observed probability of detection (PoD) points. The dashed line corresponds to a non-refracting atmosphere.

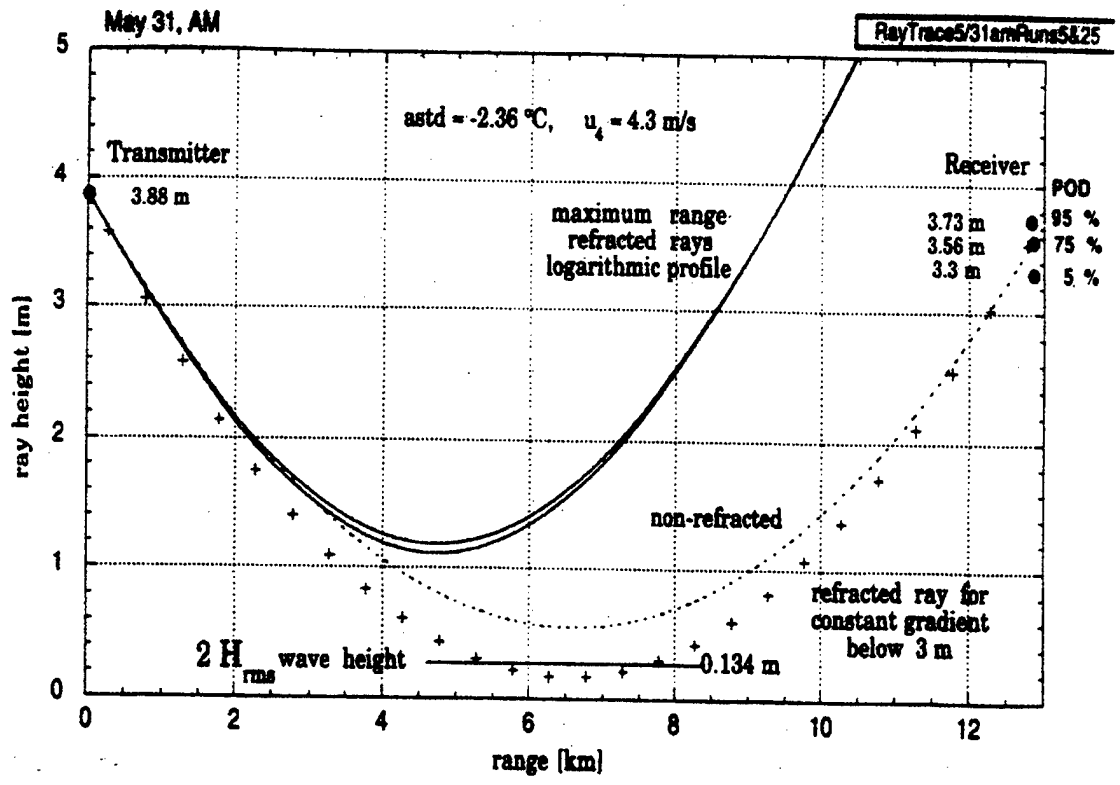

Figure 2. Cross-Bay Parabolic Arc-Style Ray Height Plots. The dashed curve is a non-refracted ray. It could be seen on the detector side of the bay, but not be tangent to the ocean at mid-point at the same time. The solid lines are rays refracted according to LKB. The refraction gradient, which yields an upward bending arc, is too strong. Only the ray bent by the artificially damped refractivity gradient (+) can both been detected across the bay and be tangent to the sea surface at mid-bay. (This figure was scanned from Figure 16, Reference 1.)

The solid line corresponds to the ray trace for the refractive atmosphere as modeled by the LKB model. It is seen that model allows no depression angle such that viewing of the laser by the optical receiver is possible, when in fact the laser was viewed with unity probability. This is attributed to the excessive ray bending associated with the LKB model. Theory could be made to match observation if the gradients below 3 m were reduced to 25% the gradient value at the 3 m height. The resultant ray trace is indicated by crosses. One physical effect that could cause this and is being over-looked is a modification of the refractivity profile caused be the presence of large marine aerosols.

AEROSOL CONTRIBUTION TO ATMOSPHERIC REFRACTIVITY

Aerosols do contribute to atmospheric refractivity. [12,13] The question is, how much and whether the aerosol refractivity gradient ameliorates the refractivity gradient predicted by LKB. Three things need to be known in order to analyze their effect: There must be an expression for the refractivity of a volume of space containing aerosols. This information is available in the literature. The refractivity can be approximated by an expression that is proportional to the liquid water content of the atmosphere. The liquid water content, in turn, must to be extracted from the literature or from current experiments intended to determine droplet size distributions just above the sea surface. The gradient of liquid water content can then be used to calculate the refractivity gradient. Since this article uses a model from a 30 year old paper discussions of gradients are not appropriate at this time.

REFRACTIVITY

Atmospheric refractivity caused by aerosol particles has been worked out before. There is no new theory needed for this problem. The far field solution for single particle plane wave extinction is a result of interference of the incident plane wave and the scattered spherical wave at the position of the observer. In addition, there is a phase lag associated with that wave interference. The accumulation of these phase lags effectively slows down the propagation speed of the plane wave. This is equivalent to a plane wave passing through a medium of some index of refraction n. Both van de Hulst[12] and Ishimaru[13] have explicit expressions for this induced index of refraction. Now if there is a transverse gradient in the index of refraction the wave front will tilt. Van de Hulst (page 38) has an approximate expression for the index of refraction, actually refractivity, that does not depend on knowledge of particle size distribution. Since size distribution information is not available in Toba's papers[2,3] van de Hulst's approximation will be used. Van de Hulst's approximation for refractivity of an aerosol medium is given by

$$N = (n-1)x10^6 \times LWC$$

where LWC is the liquid water content of the atmosphere just above the sea surface. The liquid water content of the atmosphere is the fractional volume of atmosphere occupied by the net volume of the water droplets. The units are cc/cc.

LIQUID WATER CONTENT OF THE MSL

Toba has estimated the size dependent aerosol concentration just above the sea surface by extrapolating from measurements made at the stratus cloud layer a few hundred meters above the sea surface. His estimates are plotted in Figure 9 of his second paper, which cannot be reproduced here

because the article is copyrighted. For wind speeds of about 5 m/s the estimated aerosol mass density is 1.54×10^{-7} gm/cc, which is the same as a LWC = 1.54×10^{-7} cc/cc. Assuming index of refraction of pure water is 1.33 this gives a refractivity of

$N = 5.1 \times 10^{-2}$

Typical figures for refractivity are $N_{dry\ air} = 259$ for dry air and for water vapor $N_{water\ vapor} = 82.5$

So, the aerosol refractivity is 0.062% of that due to water vapor. Laboratory work on bursting bubbles[14] indicates that droplets of 400 micrometers diameter might exist. These are 5 times the size of the droplets considered above. Enough of these or slightly larger droplets could yield an aerosol refractivity comparable to that of water vapor.

CONCLUSIONS

A first cut estimate of aerosol induced atmospheric refractivity in the MSL has been made with some confidence. The refractivity is miniscule compared to that of dry air and water vapor for typical values of these quantities. However, laboratory data indicate that Toba's 30 year old estimates may be low. Particles up to 400 micrometers diameter may exist in swell troughs where Mermelstein's laser beams must have passed. In addition, water vapor pressure less than the 20 mb typical value might exist at the same time that large particles do. The conclusion is that aerosol refractivity as an influence on ray bending in the MSL is not very promising, but still somewhat tantalizing.

FUTURE WORK

Toba's work is a good place to start for determining the properties of MSL aerosols; however, a thorough review of the current literature is most needed at this point. Vertical aerosol gradients must also be obtained. Toba's model is too crude for that, too. There may be circumstances where even a small amount of aerosol induced refractivity would be important. Those cases, if they exit, can be found by running simulations that include all sources of refractivity plus the parabolic arc ray tracing model for all plausible meteorological conditions.

REFERENCES

1. M.D. Mermelstein, E. H. Taken, R. G. Priest, E.J. Stone and T.P. Thorpe, "Target Detection and Wave Obscuration at the Ocean Horizon". Proceedings of the 1997 Meeting of the IRIS Specialty Group on Targets, Backgrounds and Discrimination, Monterey, CA 1997.

2. Yoshiaki Toba, "On the Giant Sea-Salt Particles in the Atmosphere I", Tellus XVII (1965) 131.

3. Yoshiaki Toba, "On the Giant Sea-Salt Particles in the Atmosphere II. Theory of the Vertical Distribution in the 10-m Layer Over the Ocean", Tellus (1965) 365.

4. Jensen, de Leuw and van Eijk, "Summary of the Marine Aerosol Properties and thermal Imager Performance Trial (MAPTIP)" in AGARD-CP-567.

5. F.X. Keizys, E.P. Shettle, L.W. Abreu, J.H. Chetwynd, G.P. Anderson, W.O. Gallery, J.E.A. Selby, and S.A. Clough. MODTRAN: A Moderate Resolution Model LOWTRAN 7. AFGL-TR-89-0122. 30 April, 1989

6. W.T. Liu, K.B. Katsaros and J.A. Businger, "Bulk Parameterization of Air-Sea Exchanges of Heat and Water Vapor Including Molecular Constraints at the Interface", J. Atmos Sci **36** 1722-1735 (1979).

7. C. W. Fairall, E.F. Bradley, D.P. Rogers, J. B. Edson and G. S. Young, "Bulk parameterization of air-sea fluxes for Tropical Ocean-Global Atmosphere Coupled-Ocean Atmosphere Response Experiment". JGR **101** C2 (February 15, 1996) 3747-3764.

8. D. Dion and B. Leclerc, "Investigation of the air Refractivity Effects on IR Sensors in the Marine Boundary Layer", DREV-R-4570/90, August 1990.

9. J. Claverie and Y. Fromont, "Le Modele PIRAM (Profils d'Indice de Refraction en Atmosphere Marine)", Fiche Technique no. GEOS/189/GEOS.SOP 10548, CELAR, August 1995.

10. IRTool Algorithm Description Documents, Arete Associates, irtool@arete.com.

11. W. H. Lehn, "A simple parabolic model for the optics of the atmospheric surface layer". Appl. Math. Modeling **9** (December, 1985) 447.

12. H.C. van de Hulst, Light Scattering by Small Particles. Dover, New York. 1981.

13. Akira Ishimaru, Wave Propagation and Scattering in Random Media, Volume 2. Academic Press, New York. 1978.

14. Francois Resch and George Afeti, "Film Drop Distributions from Bubbles bursting in Seawater", JGR 10,681 (June 15, 1991).

Proceedings, Battlespace Atmospherics Conference, San Diego, CA, Dec 1997.

Current capabilities of environmental characterization during SHAREM exercises

Andreas K. Goroch
Marine Meteorology Division,
Naval Research Laboratory
7 Grace Hopper Ave.
Monterey CA 93943
408-656-4889,
e-mail: goroch@nrlmry.navy.mil

Patrick Jackson
COMSURFWARDEVGRU,
2200 Amphibious Dr.,
NAB Little Creek,
Norfolk, VA 23521-5160
804-464-7965
e-mail: pjj@navo.hpc.mil

Introduction

The program of SHAREM exercises is being conducted to develop and evaluate tactics for surface ships engaged in under sea warfare. The program is designed to be site-specific, addressing particular threat issues that are affected by uniquely local conditions. Characterization of the combat environment plays a critical role in the conduct of SHAREM exercises, both below the sea surface and in the atmosphere above. This paper will discuss the current state of environmental characterization of the operational environment. This includes the utilization of dedicated environmental measurement systems, as well as the extraction of relevant environmental information from combat systems. We will also contrast the current capability of above surface and below surface environmental characterization in an operational environment.

SHAREM exercise objectives

The Ship ASW Readiness Effectiveness Measurement (SHAREM) program is designed to develop and evaluate new tactics for surface vessels, and to evaluate ambient environmental conditions is particular threat areas recognized by the several fleet commanders. The exercises are a combination of scripted objective events of warfighting system performance and freeplay within the context of a combat scenario. The participants generally include submarines, ASW surface vessels, helicopters attached to the surface ships, and surface and airborne survey assets. A general description of exercise events has been documented earlier (Nissen et al., 1997). The purpose of this report is to provide details of some of the environmental characterization conducted within SHAREM exercises.

Prior and during the exercise, an airborne survey is conducted to evaluate oceanographic conditions, with a regular grid of expendable bathythermographs (XBT) providing surface temperature, temperature profile, and salinity profiles. These are used to determine mixed layer depth, currents, and sound speed profiles.

During scripted events, participants act as targets or sensors or both depending on the particular exercise objectives. During the events submarine targets are proceeding along a course designed to optimize the variety of environmental (surface and underwater) conditions. System performance is evaluated both objectively with calibrated sources and receivers and in actual operations with operators providing real-world documentation of target detection. Observers are assigned to sonar, radar and EO sensor systems to aid in documentation and to describe system performance.

Environmental characterization

Acoustic

Survey and ship measurements

Surface search sonar requirements generally require characterization of the sound propagation vertical profile, the bottom scattering properties, and ambient noise sources. The sound propagation should

be available within the operating area of the ship, generally operating at a speed of 25 knots or less, and with an sonar radius of about 10 n mi. The sound propagation profiles are first generated from the aircraft survey. These are supplemented with expendable bathythermographs (XBT) drops provided when observations indicate the potential changes from the survey conditions. The bottom reflection conditions are determined by analysis of surveys and bottom measurement. The sonar propagation conditions are then continually updated with loss curves observed by the sonar and displayed to the tactical user. The entire picture is updated with a new P-3 survey over the regions if the acoustic conditions have suffered a large change, or if the operating region is changed.

Helicopter sonar

Sonar conditions are also obtained from the surface ship with a real time data link. The helicopter provides XBT drops as required. These are sent back to the ship via the same data link. They are then integrated with the ship acoustic database and distributed to the participating surface combatants.

Non-acoustic

Ship radar

Ship radar is used for detection of surface and airborne targets. SHAREM programs have been primarily concerned with surface targets, with limited aircraft operations. With the increasing threat of low flying cruise missiles, there has been an increasing evaluation of radar use against surface targets.

Surface clutter, propagation conditions, and clutter from non-target scattering affect ship radar. The main atmospheric effect generally evaluated is the vertical atmospheric profile on the radar propagation. The vertical profile has usually been measured in the vicinity of one or several nearby ships using standard rawinsonde soundings, or to a lesser extent, rocketsonde soundings. The measurements provide the description of trapping layers that are responsible for extended ranges, or radar 'holes' where targets are expected to be detectable under normal conditions, but are not in fact detected. The vertical profiles are supported by surface measurements which describe the surface evaporation duct caused by the near surface cooling and evaporation of the sea surface.

Helicopter radar

Helicopter radar is also supported by shipborne measurements. While the helicopter is often beyond the range of the ship measurement capability, it has no organic assets to measure temperature, moisture and wind profiles*. The helicopter generally remains within 100 n mi of a potential heliport.

Case study - SHAREM 120B

SHAREM 120B was conducted in the Sea of Japan along the coast of South Korea from 3 April to 9 April 1997. The primary purpose of the exercise was to evaluate ASW performance, but the exercise included a helicopter FLIR performance event in which FLIR was used during

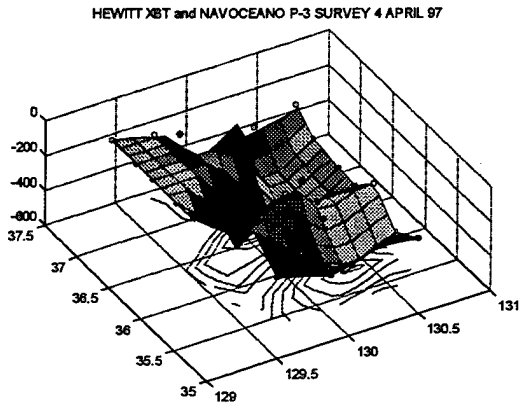

Figure 1. Mixed layer depth surface from P-3 survey, indicating flight track (o) and USS Hewitt XBT soundings (*), 4April 1997.

structured runs with a Spruance class destroyer as target. The available measurements included a P-3 survey flight

* Helicopters do measure outside air temperature (OAT), but the data are seldom archived and the validity has not been documented.

before the exercise, a survey flight during the exercise, continuing XBT measurements aboard the ship, surface measurement aboard a surface combatant, and rawinsonde launches every 6 hours during the exercise. An example of the integrated measurements is shown in Figure 1. The combined aircraft and ship soundings provide a valuable visualization of the acoustic environment suitable to the tactical situation of surface and airborne assets.

Oceanographic profiling

The underwater thermal profiles were obtained from the P-3 surveys and from the XBT's dropped from the USS Hewitt. These measurements were integrated as available, although communication did not permit integrating XBT information from the other participants in the exercise. The main parameters analyzed here were the mixed layer depth from the thermal profiles, and the sea surface temperature measured from the XBT and from the surface vessel.

Time change of oceanographic conditions

The time change of the area distribution of the mixed layer depth and SST can be observed by analyzing the two surveys conducted 31 Mar 97 and 4 April 1997. The contours were calculated from XBT observations from the P-3 and the USS Hewitt. The data were interpolated onto a fixed geographic grid with nearest neighbor

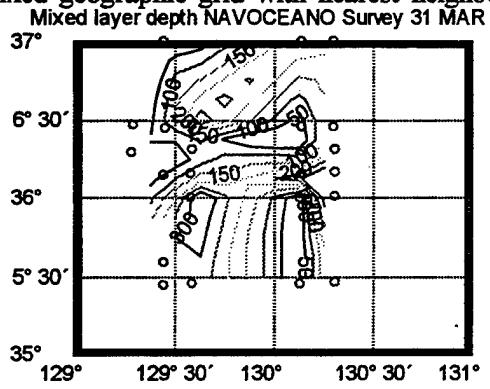

Figure 2. Mixed layer depth contours from P-3 flight ([o] XBT sounding) 31 March 97.

polynomial interpolation. The range of the interpolation was limited to the observed range by setting interpolated values outside the limits to the minimum or maximum observed value as appropriate.

The earlier MLD contour shows two deep regions separated by a shallower region

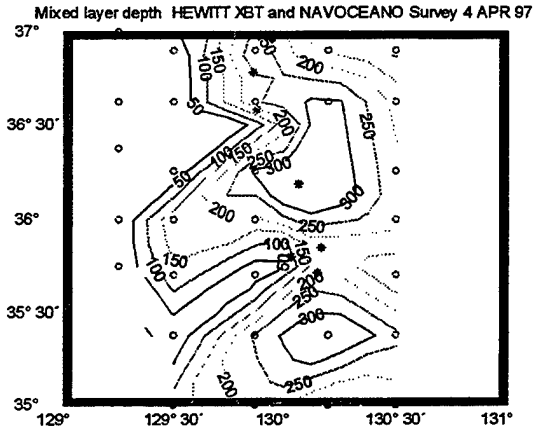

Figure 3. Mixed layer depth contours from P-3 flight ([o] XBT sounding) and USS Hewitt ([x] - XBT sounding) survey, 4 April 97.

on a north-south axis at 129°40' E. The more southerly region is about 300 ft deep, approximately 100 ft deeper than the northerly region. (Figure 2). The second contour shows that the general characteristics of the region are similar but translated 50 km east to 130°15'E. The northerly region is now deeper and larger in extent than the southerly region. (Figure 3).

The sea surface temperature contours suggest the physical mechanisms that may cause the changes. The early

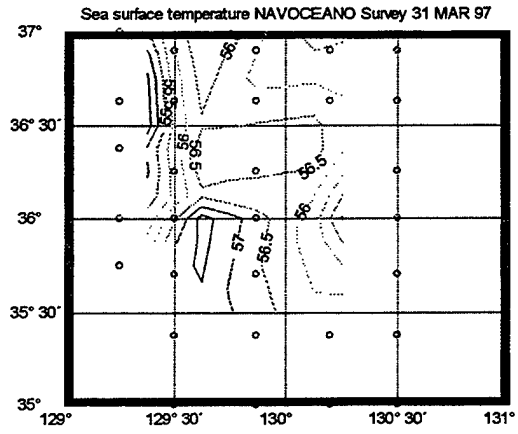

Figure 4. Sea surface temperature contours from P-3 flight ([o] XBT sounding) and USS Hewitt ([x] - XBT sounding) survey, 3 April 97.

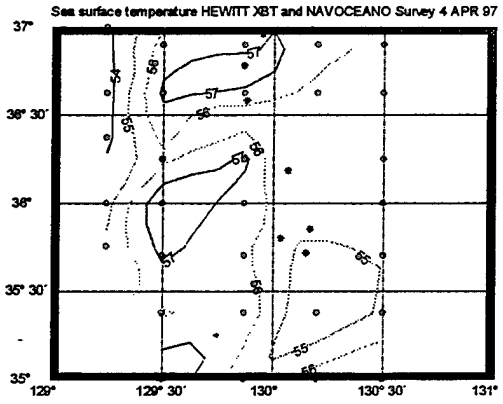

Figure 5. SST contours from P-3 flight [o] and USS Hewitt [x] survey, 4 April 97.

contour shows a warm water region in the southern part of the survey area (Figure 4). The later contour shows the intrusion of a pool of warm water from the north (Figure 5). This warm water is evidently responsible for the development of a deeper mixed layer, resulting in a moderately different acoustic environment in the operating area

Importance of data integration

It is instructive to examine the effects of added data to the analysis of mixed layer depth during this exercise. On 4 April 1997, the oceanographic data obtained by the P-3 was supplemented by the XBT profiles obtained by the USS Hewitt. The analysis obtained using only the P-3 survey shows a

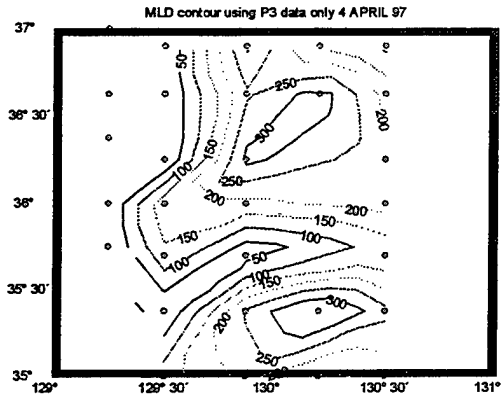

Figure 6. Mixed layer depth contours from P-3 flight [o] XBT soundings only, 4 April 97.

general characteristic of two deep mixed layer zones separated by a region of approximately 100 ft depth (Figure 6). The Hewitt observations were obtained in the

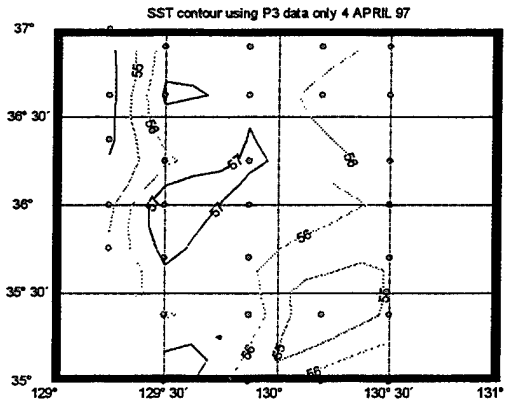

Figure 7. Mixed layer depth contours from P-3 flight [o] XBT and USS Hewitt [x] survey, 3 April 97.

regions missed by the P-3 and identify that the trough between the deep zones is actually 100 foot deeper the inferred (Figure 7). The effect of the integration of the additional surface data is to provide greater detail than originally seen. While it is often assumed the MLD variation is on a larger scale than 50 km, this instance demonstrates that in fact smaller scales are observed. These small scales can be critical to acoustic operations in a coastal zone.

Atmospheric measurement

EM support

Continuous meteorological measurements and six hourly atmospheric profiles provided EM support. The continuous measurements were a combination of ship deck log records and measurements taken at the bow with an atmospheric measurement system (Davidson et al., 1997).

EO support

Enhanced aerosol measurements using a nephelometer provide a new capability to measure extinction due to scattering. The nephelometer was fixed on the ship and sampled air by the bow. Since the information is basically a point measurement with no information on the vertical profiles. This precluded the ability to forecast vertical profiles of extinction in support of LAMPS FLIR employment.

Needed Capability

Measurements

The data show the need for advanced environmental instrumentation and techniques to support operations in Navy relevant regions. The acoustic measurements provide a versatile capability of inferring underwater propagation conditions. Atmospheric capability is not as advanced. There is no radar evaluation corresponding to the real time assessment of sonar system performance and the use of this information to update the environmental characterization.

Modeling

The physical modeling of underwater conditions demonstrates the utility of a preliminary guess of the profile, prior to the integration with local measurements. The addition of the USS Hewitt observations to the P-3 data provided enhanced detail of the local sonar propagation conditions. Similar atmospheric soundings are seldom available, although numerical weather forecasts could be used to provide an initial guess field. The addition of aircraft profiles and surface ship soundings would provide relevant tactical information on a finer spatial scale than currently available.

References

Davidson, K.L., Goroch, A.K., Pastore, M.J., Rowland, J. and Wash, C.H., 1997. Development of the Surface Combatant In Situ METOC Sensors (SCIMS) Suite, EM/EO Symposium, Monterey, CA.

Nissen, J., Goroch, A.K. and Pastore, M.J., 1997. Tactical Observations of Environmental Impact on EM/EO Sensor Performance during SHAREM Exercises., EM/EO Symposium, Monterey, CA.

Overview and Objectives of the DoD Center for Geosciences Sponsored "Complex Layered Cloud Experiment" (CLEX)

Thomas H. Vonder Haar, Stephen K. Cox, Graeme L. Stephens, John M. Davis,
Timothy L. Schneider, Walter A. Petersen, Arlie C. Huffman, Kenneth E. Eis,*
Donald L. Reinke, and John M. Forsythe
Colorado State University
Fort Collins CO 80523
Phone: (970) 491-8397 Fax: (970) 491-8241
E-Mail: reinke@cira.colostate.edu
Fuk K. Li
NASA Jet Propulsion Laboratory
Pasadena CA
Gregory A. Sadowy
University of Massachusetts
Boston MA

The DoD Center for Geosciences at the Cooperative Institute for Research in the Atmosphere (CIRA), Colorado State University, CO is sponsoring an ongoing field experiment called the Complex Layered Cloud Experiment (CLEX). The CLEX addresses a better physical understanding of the morphology of extensive layers of non-precipitating clouds in the middle and upper troposphere. A coordinated land, air, and space-based data collection produced a unique research data set during June, 1996. Data were collected from the NASA DC-8 airborne 95-GHz cloud radar, the U. Wyoming King Air in-situ microphysical collection systems, GOES, DMSP, and AVHRR meteorological satellites, Penn State Univ. 94-GHz cloud radar, and the Desert Research Inst. Mobile Microwave Radiometer, and a wide range of ground based systems at the Oklahoma ARM-CART site.
In the last five years several realizations have caused us to elevate the scientific priority of understanding the origin and duration of complex single and multi-layer cloud systems. Specifically, mid-level clouds had a significant effect on several key DoD operations during Desert Shield and Desert Storm. Various post-campaign reports and publications have documented the shortfalls and importance of understanding, forecasting, and simulating such cloud layers in the future.
An overview of the CLEX objectives and a summary of data collected and analyzed during CLEX-1 in June-July of 1996 are presented.
* This work is sponsored by the DoD Center for Geosciences - Phase II at the Cooperative Institute for Research in the Atmosphere, CSU under grant DAAH04-94-G-0420

1. INTRODUCTION

The CLEX experiment addresses a better physical understanding of the morphology of extensive layers of non-precipitating clouds in the middle and upper troposphere. These are in a sense the "forgotten" clouds on Earth. National weather services do not forecast these clouds and with a few exceptions, the civilian community generally ignores them.
Within the climate research community, only a subset of "CLEX clouds" – layers of "radiatively significant" cirrus – have been identified as a high-priority for study and understanding regarding their role in the climate system. However, in the last five years three realizations have caused us to greatly elevate the scientific priority of understanding the origin and duration of complex single and multi-layer cloud systems; Desert Storm, increased emphasis on the assimilation of satellite imagery into models, and new insights into the role of clouds in the radiation balance and atmospheric dynamics. Specifically:
1. Mid-level clouds had a significant effect on several key DoD operations during Desert Shield and Desert Storm. Various post-campaign reports and publications have documented the importance of understanding and forecasting such cloud layers and their details will not be repeated here.
2. The advent of new 3-D and 4-D variational assimilation of satellite radiance data into operational forecast models – and the improved forecast skill that resulted (Burridge, ECMWF, 1996) – focus special attention on proper model representation of these clouds (Tiedke, 1993) and forward radiances from them.

3. Third is a realization from the climate research community that the layer-to-layer and layer-to-surface radiative effects of extended cloud layers not only may play a key role in their morphology but may also strongly impact regional atmospheric dynamics. Additional details and background may be found in Vonder Haar et al. (1994) and (1996).

The first phase of CLEX, called CLEX-1, covered the period of 19 June - 3 July 1996 over the Central Great Plains of CONUS. Subsequent CLEX tests will be developed as needed. During CLEX the DoD Center of Geosciences will operate in collaboration with JPL and NASA as they concurrently test their new Airborne Cloud Radar for cloud layer profiling. Several other university and government groups are participating and assisting with CLEX. All data will be collected and organized into a central database for use by a wide group of scientists.

2. SCIENCE OBJECTIVES

CLEX will provide data to answer questions surrounding our understanding of "Complex Layered Clouds". These can generally be viewed as non-precipitating mid-level clouds that are of sub-tropical origin or not associated with large convective complexes. Preliminary results and a further discussion of these clouds are given in Vonder Haar et al. (1996). Specific questions that are being addressed are:

1. Can cloud bases and layers be estimated using satellite-only techniques?
2. Can existing layer cloud conditions be detected and serve as input to atmospheric models?
3. How does cloud layer-induced radiative heating/cooling impact the layer cloud lifetime?

3. FIELD MEASURMENT SYSTEMS

Satellite - Satellite data include *GOES-8* and *9* geostationary data (all channels, 1-minute rapid scan when possible), *DMSP* overpasses including *SSM/I* and *SSM/T2* data, and *AVHRR* data aboard the *NOAA 11* and *12*.

Aircraft Systems -

The *University of Wyoming King Air* was flown to collect *in-situ* cloud microphysical data measurements. Instrumentation on the King Air included: a) cloud-droplet spectra/particle imaging probes such as Particle Measurements Systems (PMS) FSSP (.5 - 45 μm), 1D-C (12.5-186 μm), and 2D-C (25-800 mm); b) for precipitation the PMS 2D-P (200-6000 μm) probe; and c) for liquid water content, both in-house and Johnson-Williams (J-W) hot-wire probes (accuracy 0.2 g m^{-3}). The King Air team also visually identified cloud layer tops and bases during the collection operation and captured the forward-looking view on video tape.

The *NASA DC-8 and JPL Airborne Cloud-Profiling Radar* (ACR) was flown above the cloud layers to provide measurements of cloud bases, tops, and structure including estimates of cloud liquid water and ice content. The ACR is a scanning, Doppler, cloud-radar that operates at a frequency of 95 GHz. The minimum detectable signal of the radar for cloud-heights of 200 m (approximately 11 km from aircraft cruising altitude) is ~-30 dBZ. The beamwidth of the radar is 0.56°, providing cross -track and along-track resolutions of approximately 120 m at aircraft cruising speeds. Vertical resolution (pulse length dependent) of ~ 90 m. (See example of cloud radar imagery in figure 1.)

Ground-Based Systems -

The *Desert Research Institute (DRI) Dual Freq. Mobile Microwave Radiometer* is a van-mounted, scanning, dual-frequency (20.6 and 31.65 GHz) passive microwave sensor that is used to estimate column integrated water vapor and cloud liquid water. The instrument was operated in both mobile and stationary mode. When in scanning mode the radiometer can scan a full 360 degrees (+/- 1° accuracy), at a fixed elevation angle (+/- 0.1° accuracy). Temporal resolution in the scanning mode is approximately 3 minutes. The beam sampling angle is 2.6°. The instrument has an accuracy of 5-10%, and will measure values of water vapor and liquid water over ranges of 0-5 cm for vapor and 0-5 mm for liquid water.

The *Pennsylvania State University Cloud Radar* provided measurements of cloud bases, tops and liquid water content. The Doppler radar operates at a frequency of 94 GHz. The radar was operated at the Oklahoma ARM site in vertically pointing mode only. Data were collected for altitudes between 200 m and 15 km at a temporal resolution of 2 seconds and a vertical resolution of 50 m at a Nyquist velocity of 1.2 m s^{-1}. The beamwidth of the radar is approximately 0.3° , providing a horizontal resolution of approximately 30m at 10 km altitude.

A full compliment of *Surface Observations* including *Automated Surface Observing System (ASOS) Data* and *Rawinsonde Soundings* were collected and archived. ASOS data at 5 minute temporal resolution were collected from locations in the general area of operations for CLEX-1. These data consist of all meteorological information collected by the ASOS suite of sensors including laser ceilometer measurement of cloud bases (to 12,000 ft AGL) and sky cover. Special soundings were released at the ARM CART site, combined with radio theodolite soundings.

Table 1 provides a breakdown by operations day of observational platform participation during CLEX-1. Ground-based instrumentation at the ARM-CART site are collectively grouped into a single category "CART-ARM" in Table 1.

Table 1. Dates of data collection by platform

PLATFORM	6/10-6/15	6/21	6/22	6/23	6/24	6/25	6/26	6/27	6/28	6/29	7/1-7/2
King Air	-	X	$	*	*	*	*	-	*	*	-
DC-8	X	-	$	-	*	X	*	X	-	-	X
DRI Radiometer	-	-	#	#	*	#	*	#	-	-	-
PSU Radar	-	#	#	#	#	#	#	#	*	#	-
CART-ARM	-	#	#	#	#	#	#	#	*	#	-
SSM/I	X	X	$	X	X	*	*	X	X	X	X
SSM/T2	X	X	X	*	*	*	*	X	X	*	X
GOES 1-min.	-	-	-	-	*	-	-	-	-	-	-
GOES 7.5-min.	-	-	$	-	*	-	-	-	-	-	-
GOES 15-min.	X	X	$	*	*	*	*	X	X	X	X
ASOS 5-min.	-	X	$	*	*	*	*	X	X	X	-

$ = Coordinated/collocated data collection between TWO aircraft and other platforms
* = Coordinated/collocated data collection between SINGLE aircraft and other platforms
# = Collocated data collection without aircraft;
X = Independent collection
- = Platform down or no data collected for CLEX

4. DATA ARCHIVE

CLEX data are archived at CIRA. For further information including case study examples, view the CLEX web site at: http://www.cira.colostate.edu/geosci/clex/overview.htm . For additional questions contact Mr. Don Reinke, e-mail: reinke@cira.colostate.edu phone: (970) 491-8465.

ACKNOWLEDGEMENTS

Many scientists and groups have contributed to CLEX discussions and planning. Dr. Fuk Li and colleagues at JPL developed the Airborne Cloud Radar (ACR) segment along with Professor Graeme Stephens of CSU. The ACR planning has paralleled and stimulated our CLEX science concepts. Dr. Bob Curran and Dr. Ramesh Kakar of NASA have been helpful with their discussions and questions as have

Dr. Walter Bach, Jr. and other members of the DoD Center for Geosciences, Phase II Advisory Panel. Mr.Greg Sadowy at UMASS provided pre-processing of radar imagery from the airborne radar.

REFERENCES

Burridge, D., 1996: (personal communication of 1994 forecast model operations and results at the ECMWF).

Tiedke, M., (1993): Representation of Clouds in Large-Scale Models. *Mon. Wea. Rev.*, **121**, 3040-3061.

Vonder Haar, T.H., et al., 1994: Technical Proposal and Briefings submitted to the DoD Advisory Panel for the Center for Geosciences Research at CSU.

Vonder Haar, T.H. et al., 1996: DoD Center for Geosciences - Phase II, Annual Report (1994-1995), 138 pp.

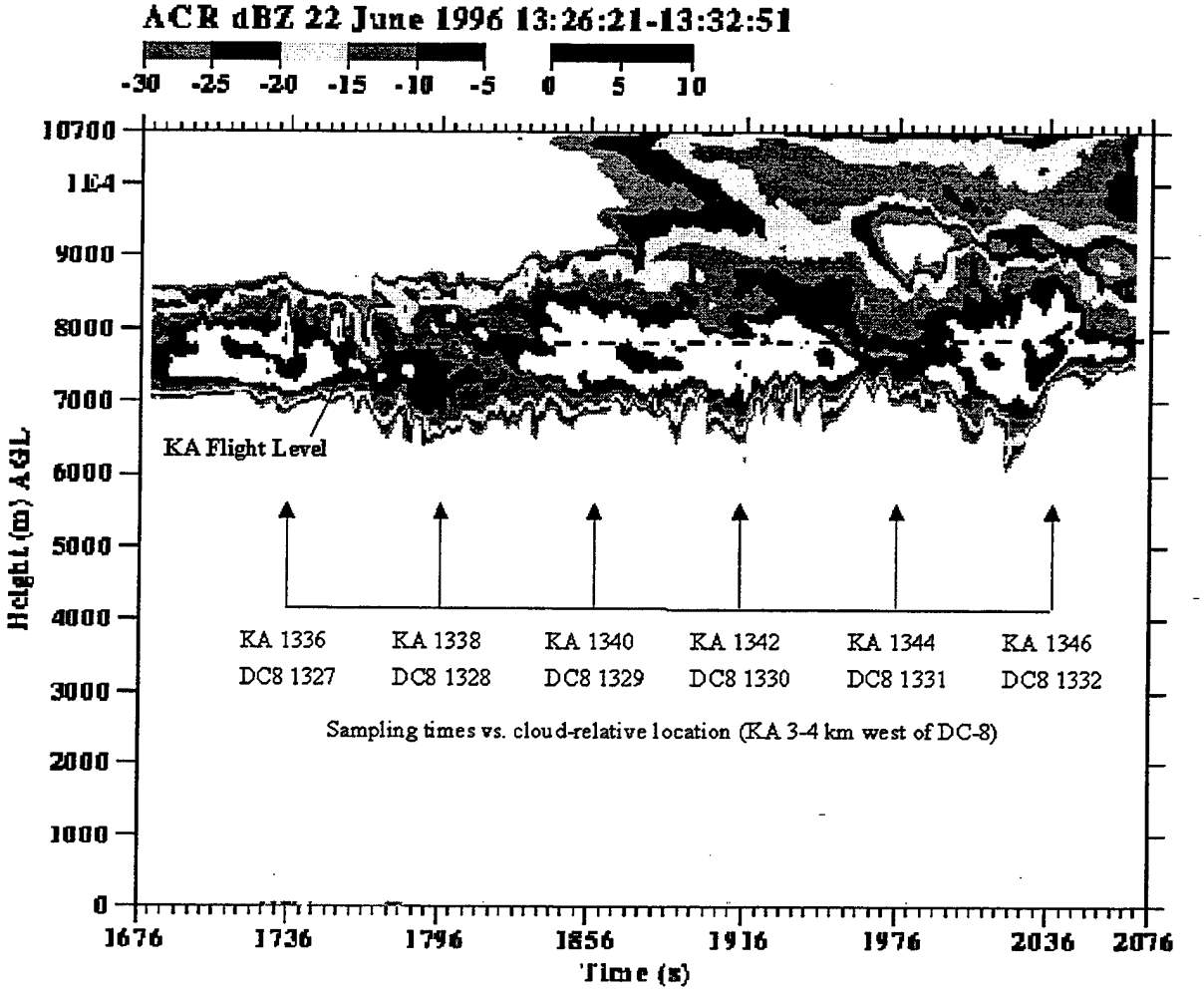

Figure 1. Sample of imagery from the 95GHz airborne cloud radar showing coincident sampling times of the King Air (flight level shown as dashed line at 7.3 km elevation) on 22 June, 1996 flight during CLEX-1.

A NOVEL TEMPORAL UPDATING SCHEME FOR CLOUD CLASSIFICATION[1]

Bin Tian, Mahmood R. Azimi-Sadjadi*, Ken Eis* Thomas H. Vonder Haar***

**Signal /Image Processing Laboratory, Department of Electrical Engineering*
*** Cooperative Institute for Research in the Atmosphere (CIRA)*
Colorado State University, Fort Collins, CO80523
Tel: (970)-491-7956 Fax: (970)-491-2249 E-mail: azimi@engr.colostate.edu

Abstract

Automatic cloud classification of satellite imagery is greatly needed in a lot of meteorological studies including accurate weather forecasting for battle field. . Temporal changes are one of the main factors that cause degradation in the classifier performance when a sequence of imagery is to be processed. A probability neural network (PNN)-based cloud classification system and its temporal updating scheme is proposed in this paper. This novel approach can track the temporal changes in the images by utilizing the temporal contextual information and adjust the neural network to adapt to such changes. . Whenever a new frame arrives, the old PNN provides an initial classification result. Due to the short time intervals between the two consecutive frames, the PNN fine tuned to the last frame can still correctly classify most part of the new image. At the same time, a predictor system using Markov chain models will also perform prediction based on the temporal context information and the classification results of the previous frame. The results of both the initial classification and the predictor will then be combined together and used to update the PNN classifier. The Maximum Likelihood (ML) criterion is adopted in the updating process while the Expectation-Maximization algorithm is used to estimate the new parameter set of the PNN. The input frame will be reclassified by the updated PNN and the result is sent out to display system. The proposed scheme is examined on Geostationary OperationalEnvironmental Satellite (GOES) 8 cloud imagery and very promising results have been achieved. The proposed scheme can also be applied to a lot of other temporal sensitive applications.

I. Introduction

Whether condition is always an important factor in the battlefield. Automatic cloud classification system for satellite imager is greatly needed in a lot of meteorology studies including accurate whether forecasting for battlefield. In recent years, considerable research has been focused on this area, and a good overview of the previous works is provided by Pankiewicz [1]. In [2], Welch also made a comparison of several widely used approaches. Despite these efforts, most of the current cloud classification schemes are still far from being practical. One of the important reasons is that the temporal variation in the data factor was not considered. The temporal factor is extremely important in the satellite cloud imagery classification and other remote sensing applications. Generally speaking, there are two kinds of the temporal factors. The first one is the temporal contextual information (short term). Since clouds and background are unlikely to move or change a lot in short time intervals (one hour), there is a strong correlation between two consecutive images. The second type of temporal factor that must be considered corresponds to longer term temporal changes. As time elapses, certain types of clouds may look different in the visible channel due to the changes of the sun angle. On the other hand, the ground and low level clouds will be heated up during the day time and cooled down at night thus look differently in the infrared (IR) channel. Although these variations may not be very prominent in short term, it will accumulate over longer time. Thus, a fixed neural network may not be able to deal with a sequence of

[1] This work is supported by DOD under the contract #DAAH04 94 G0420

images obtained at different time of the day. In order to solve this problem, a novel temporal adaptive neural network based cloud classification system is proposed in this paper. A simplified PNN is used as the classifier due to its good generalization ability and fast learning capability which are crucial for on-line updating [3]. Moreover, a novel temporal updating scheme for PNN was developed to accommodate the temporal changes. The idea behind this approach is to find these temporal changes by utilizing the temporal contextual information and then making suitable adjustments to the neural network classifier.

The organization of this paper is as follows. A brief review of the PNN is given in Section II. In Section III, the proposed temporal updating scheme for PNN is discussed. Experimental results of this new cloud classification system on GOES 8 satellite data are presented in Section IV.

II. Probability Neural Networks For Cloud Classification

PNN is a kind of supervised neural network which is widely used in the area of pattern recognition, non-linear mapping, and estimation of probability of class membership and likelihood ratios [3]. The original PNN structure, which was proposed by Specht in [4], is a direct neural network implementation of the Parzen non-parametric probability density function (PDF) estimation [5] and Bayes classification rule. Although its training scheme is very simple and fast, one major drawback is that potentially a very large network will be formed since every training pattern needs to be stored. This leads to increased storage and computational time requirements during the testing phase. One natural idea to simplify the PNN is to reduce the number of neurones , i.e., use fewer kernels but place them at optimal places. In [6],[7] Streit *et al* improved the PNN by using finite Gaussian mixture models. This neural network structure is adopted in this paper and briefly described below.

For any class c_i, i=1,..,K, suppose the class conditional distribution is modelled approximately by a Gaussian mixture, i.e,

$$p(\mathbf{x} \mid c_i) = \sum_{j=1}^{M_i} \pi_{ji} p_{ji}(\mathbf{x}; \mu_{ji}, \Sigma_{ji}) \qquad (1)$$

where $\mathbf{x}$ is the feature vector, M_i is the number of Gaussian components in class c_i and π_{ji}'s are the weights of the components which satisfy the constraint $\sum_{j=1}^{M_i} \pi_{ji} = 1$, $p_{ji}(\mathbf{x}; \mu_{ji}, \Sigma_{ji})$ denote the multivariate Gaussian density function of the j th component in class c_i and μ_{ji} and Σ_{ji} are its mean vector and covariance matrix, respectively. This Gaussian mixture model can be easily mapped to the PNN structure and the resultant PNN will need much less neurones. The price paid for this simplification is that non-iterative training procedure will no longer exist. Instead, the weights of the PNN i.e., the parameter sets of the mixture model for each class, need to be estimated from the training data set.

Let $\lambda_i = \{\pi_{ji}, \mu_{ji}, \Sigma_{ji}\}_{j=1}^{M_i}$ denote the parameter set used to describe the mixture model of class c_i and $\Lambda = \{\lambda_i\}_{i=1}^{K}$ denote the whole parameter space for the PNN. If we assume that the parameters Λ are unknown fixed quantities, the maximum likelihood (ML) estimation method is a suitable choice i.e.

$$\Lambda^* = \arg\max_{\Lambda} \sum_{i=1}^{K} \sum_{\mathbf{x} \in X_i} \log[p(\mathbf{x} \mid c_i; \Lambda)] \qquad (2)$$

where X_i is the set which includes all the training samples belong to class c_i . Direct analytical solution for Equation (2) is difficult to obtain. Instead, we will apply the well-known Expectation-Maximization (EM) approach [8]. The EM approach can help to achieve the maximum-likelihood estimation efficiently when the observations can be viewed as incomplete data. There are two major steps in this approach: the Estimation (E) step and Maximization (M) step. The E step extends the likelihood function to the unobserved variables, then computes an expectation with respect to them using the current estimate of the parameter set. In the M step, the new parameter set is obtained by maximizing the resultant expectation function. These two steps are iterated until the convergence is reached. The reader is referred to [8] for the detail information on EM algorithm and to [6],[7] for the training of PNN using EM.

There is one important property of the ML estimation: the estimation for parameter set of class c_i is only dependent on the training samples in this class, i.e, the optimization process can be solved separately for each class without considering the effect of the others. This is especially suitable for the cloud classification

application since a new cloud type can be easily added to the system without affecting the other classes. Moreover, in the updating process, we have the choice of only updating those classes which are affected by the temporal changes. Another benefit of this scheme is the reduced training time due to the fact that each class can be trained separately thus requiring a small number of neurones and training samples in each training process.

III. Temporal Updating of the PNN

Once the parameter set is estimated using EM, the PNN can be applied to the satellite cloud image classification problem. However, the temporal factor must be taker into account when processing a sequence of satellite images, since the temporal changes of feature space will accumulate and finally degrade the performance of the classifier significantly. In this section, a novel temporal adaptation scheme for the PNN is proposed the block diagram of which is shown in Figure 1.

Suppose that the cloud images at previous time frames up to frame n-1 have correctly been classified and the weights of the neural network have been updated to the frame n-1. Now, the new frame n arrives which involves both the visible (ch1) and IR(ch4) channels. These new images will go through the feature extraction stage and will then be applied to the PNN classifier. If the interval between the adjacent frames is short enough (½ or 1 hour for GOES 8 satellite data), the changes of these features won't be too much, thus the old PNN can still correctly classify most of the data. Due to the rich temporal class contextual information between adjacent frames, a prediction can also be made based on the classification results of the previous frame. The initial classification result of the PNN and the output of the predictor are then compared. For every block, if it is labelled to the same class by both of the PNN and predictor, then it is classified into that class with certain confidence. We refer to this kind of class information as "pseudo truth". All the blocks of this kind will form the set $\mathbf{X}^{(1)}$. On the other hand, all the blocks for which the old PNN and the predictor provide different class labels will form the data set $\mathbf{X}^{(2)}$. Both data sets, $\mathbf{X}^{(1)}$ and $\mathbf{X}^{(2)}$ will be used for the PNN updating though the learning schemes will be different. After the temporal adjustment, the new weights of the PNN will be used to classify the cloud data again and the resultant image is taken as the final result for this frame n. This process will be repeated whenever a new frame is arrived. In the following sub-section, both the prediction process and the PNN updating schemes will be described in details.

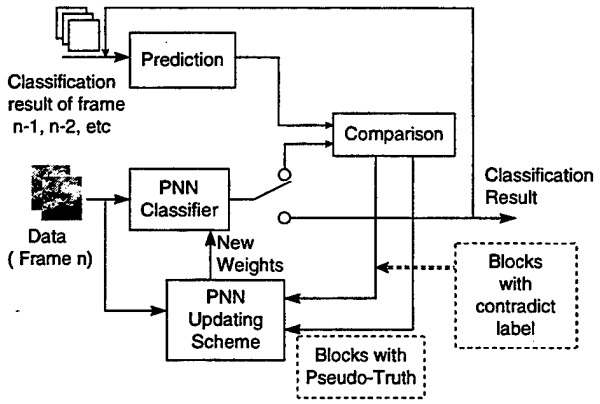

Figure 1. The block diagram of the proposed temporal updating scheme.

III.1 Prediction

The prediction block in Figure 1 is designed to make an initial "guess" of the class of the current data based on the previous classification results. Its feasibility lies in the fact that there is rich temporal contextual information between adjacent frames.

Assume $\mathbf{x}(\mathbf{r};n)$ denotes the feature vector of block $\mathbf{r}$ in frame n, where $\mathbf{r}=(k,l)$ is the location vector of that block in the image and $c(\mathbf{r};n)$ refers to its physical class. We define its spatial temporal neighborhood in frame n-1 as $H(\mathbf{r};n)=\{\mathbf{x}(\mathbf{r}+\mathbf{v};n-1)\,|\,\mathbf{v}\in\Psi\}$ where Ψ is the neighbor-hood set. One example of Ψ is shown in Figure 2.

We assume that all the temporal class contextual information for that block is conveyed by its spatial-temporal neighborhood in frame n-1. Furthermore, we use $C_H(\mathbf{r};n)=\{c(\mathbf{r}+\mathbf{v};n-1)\mid \mathbf{v}\in\Psi\}$ to represent the class label of H(**r**,n).

Now let us assume that the previous frames up to frame n-1 have correctly been classified, i.e., $C_H(\mathbf{r};n)$ is known for block **r**. For the current frame n, we want to predict the label of block **r** based on the *a posterior* conditional probability, i.e.,

$$\hat{c}(\mathbf{r};n)=\arg\max_{c_i} P(c(\mathbf{r};n)=c_i \mid C_H(\mathbf{r};n)) \qquad i=1,...,K \tag{3}$$

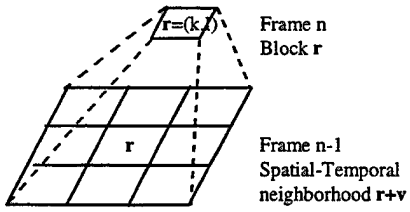

Figure 2. Example of a temporal neighborhood . In this case, $\mathbf{v}\in\Psi=\{(-1,-1),(-1,0),(-1,1),(0,-1),(0,0),(0,1),(1,-1),(1,0),(1,1)\}$

However, it is difficult to find this conditional probability which specifies the spatial-temporal class dependency context. To overcome this problem, we specify a model to describe the temporal changes. Assume that there are two underlying Markov chains. The first one describes the spatial movement of the object, such as cloud drifting. For the object of block **r** in the current frame, it may come from any block in its spatial-temporal neighborhood. A random vector ξ is defined to represent this spatial movement, i.e., the object in block $\mathbf{r}+\xi$, $\xi\in\Psi$ in frame n-1 will move into block **r** in frame n. On the other hand, the second Markov chain describes the possible class change of that object. For example, certain kind of cloud may be generated, terminated or evolved to other classes. Apply this model, we can rewrite the *a posterior* probability as

$$\begin{aligned} P(c(\mathbf{r};n)=c_i \mid C_H(\mathbf{r};n)) &= \sum_{\mathbf{v}\in\Psi} P(c(\mathbf{r};n)=c_i,\xi=\mathbf{v}\mid C_H(\mathbf{r};n)) \\ &= \sum_{\mathbf{v}\in\Psi} P(c(\mathbf{r};n)=c_i \mid \xi=\mathbf{v}, C_H(\mathbf{r};n))\, P(\xi=\mathbf{v}\mid C_H(\mathbf{r};n)) \end{aligned} \tag{4}$$

For the sake of simplification, two more assumptions are made as follows:

- For the spatial transition Markov chain, we assume that
  $$P(\xi=\mathbf{v}\mid C_H(\mathbf{r};n))=P(\xi=\mathbf{v}) \tag{5}$$
  i.e., the spatial transition probability is only decided by the relative position of that block in the spatial-temporal neighborhood and is independent of the class label in its spatial-temporal neighborhood.
- After the content of block $\mathbf{r}+\xi$ in frame n-1 moves to the block r of the current frame, its class may also change. It is reasonable to assume that such class transition is solely dependent on the class of that object in frame n-1, i.e, $c(\mathbf{r}+\xi;n-1)$ and not relate to the label of other blocks in the spatial-temporal neighborhood. So we can get
  $$P(c(\mathbf{r};n)\mid \xi, C_H(\mathbf{r};n))=P(c(\mathbf{r};n)\mid c(\mathbf{r}+\xi;n-1)) \tag{6}$$

Under these assumptions, the predictor in Equation (4) can be computed as

$$\hat{c}(\mathbf{r};n)=\arg\max_{c_i} \sum_{\mathbf{v}\in\Psi} P(c(\mathbf{r};n)=c_i \mid c(\mathbf{r}+\mathbf{v};n-1))P(\xi=\mathbf{v}) \tag{7}$$

where the value of both position and class transition probability can be obtained from the training data or decided based on the physical background of the problem [9].

It is very clear that accurate prediction can not be achieved only based on the temporal contextual information. However, if the output of the PNN achieved the same classification result for the same block, then much more confidence can be assured. All the blocks that have the same labels from both the predictor and the PNN updated to frame n-1 will form the data set $X^{(1)}$ while the others form the set $X^{(2)}$. In the following section, these two data sets will be used to update the PNN.

III.2 PNN Temporal Updating Scheme

The updating process of PNN is a kind of on-line training. There are basically two requirements for the updating process. First, the updating process must be stable, i.e, the updated PNN must maintain good classification capability for those previously established categories. Second, the updating must be plastic to accommodate temporal changes of the data and new class generation. Note that the only thing available in this updating process is the "pseudo truth" obtained by utilizing the temporal contextual information and the old classifiers results, however, this class information will be used as if they are the truth.

Assume that the training samples drawn independently from the current feature space form the training set X. This training set can be further separated into two sets: $X^{(1)}$ and $X^{(2)}$, where $X^{(1)}$ includes all the samples for which the class is assumed to be known, while all the samples of unknown types belong to $X^{(2)}$. Moreover, let $X_i^{(1)}$, i=1,..,K, denote a subset of $X^{(1)}$ in which all the samples are known to belong to c_i. The neural network structure is the same as that discussed in Section II and will not change in the updating process. The goal of updating is to re-estimate the parameter set for PNN so that it can more accurately represent the distribution of the temporal changed feature space. Maximum likelihood (ML) criterion is adopted in this PNN updating process, i.e.

$$\Lambda^{opt} = \arg\max_{\Lambda} F(X;\Lambda)$$

where

$$F(\mathbf{X};\Lambda) = \sum_{x\in X} \log(p(x;\Lambda))$$

$$= \sum_{i=1}^{K}\left[\sum_{x\in X_i^{(1)}} \log(p(\mathbf{x}\mid c_i;\lambda_i))\right] + \sum_{x\in X^{(2)}} \log(p(x;\Lambda)) \qquad (8)$$

There are two parts in this cost function. Maximizing the first part corresponds to the supervised learning process which can help to keep the stability of the training. On the other hand, updating the second part leads to unsupervised learning which can help to form more accurate representation of the distribution for the whole feature space hence providing the plasticity needed for this problem. Fortunately, we can use the EM approach to maximize this cost function as a whole. The detail derivation is given in [9]. It can be proven that the local maxima of this cost function can be achieved by iteratively using the following 2-steps till convergence. The parameter set of the old PNN can be used as the initial values.

- E step

$$E[z_{ji}(\mathbf{x})\mid X;\Lambda^{old}] = \frac{p_{ji}(\mathbf{x};\mu_{ji}^{old},\Sigma_{ji}^{old})\pi_{ji}^{old}}{\sum_{m=1}^{M_i} p_{ji}(\mathbf{x};\mu_{mi}^{old},\Sigma_{mi}^{old})\pi_{mi}^{old}} \quad \text{where} \mathbf{x}\in \mathbf{X}^{(1)} \qquad i=1,\ldots.K, \text{ and } j=1,..,M_i$$

(9a)~(9b)

Both $z_{jii}(\mathbf{x})$ and $z_{ji}(x)$ are the random variable indicating which Gaussian component generates the observation pattern, however, they are defined on different set. z_{jii} is defined on the $X^{(1)}$ set where the class label of the input is known, while z_{ji} is defined on the $X^{(2)}$ set and in this case neither the class nor Gaussian component information is known.

- M step

$$\pi_{ji} = \frac{\sum_{x\in X_i^{(1)}} E[z_{jii}(\mathbf{x})\mid X,\Lambda^{old}] + \sum_{x\in X^{(2)}} E[z_{ji}(\mathbf{x})\mid X,\Lambda^{old}]}{\sum_{m=1}^{M_i}\left\{\sum_{x\in X_i^{(1)}} E[z_{mii}(\mathbf{x})\mid X,\Lambda^{old}] + \sum_{x\in X^{(2)}} E[z_{mi}(\mathbf{x})\mid X,\Lambda^{old}]\right\}} \qquad \mu_{ji} = \frac{\sum_{x\in X_i^{(1)}} E[z_{jii}(\mathbf{x})\mid X,\Lambda^{old}]\mathbf{x} + \sum_{x\in X^{(2)}} E[z_{ji}(\mathbf{x})\mid X,\Lambda^{old}]\mathbf{x}}{\sum_{x\in X_i^{(1)}} E[z_{jii}(\mathbf{x})\mid X,\Lambda^{old}] + \sum_{x\in X^{(2)}} E[z_{ji}(\mathbf{x})\mid X,\Lambda^{old}]}$$

$$\Sigma_{ji} = \frac{\sum_{x\in X_i^{(1)}} E[z_{jii}(\mathbf{x})\mid X,\Lambda^{old}](x-\mu_{ji})(x-\mu_{ji})^t + \sum_{x\in X^{(2)}} E[z_{ji}(\mathbf{x})\mid X,\Lambda^{old}](x-\mu_{ji})(x-\mu_{ji})^t}{\sum_{x\in X_i^{(1)}} E[Z_{jii}(\mathbf{x})\mid X,\Lambda^{old}] + \sum_{x\in X^{(2)}} E[Z_{ji}(\mathbf{x})\mid X,\Lambda^{old}]}$$

(9c)~(9d)

There are some remarks for the application of the above equations in the temporal updating. Generally speaking, the final updating effect is decided by a lot of factors such as the set $X^{(1)}$,$X^{(2)}$, and the amount of temporal changes. Not all the neurones need adjustments. If there are too few samples in $X^{(1)}$ set for one certain

class, then the unsupervised training will dominant the final result, thus the neurones for this class will not be changed. Moreover, the cost function in Equation (8) can be modified as

$$F(\mathbf{X};\Lambda) = \beta \sum_{x \in X^{(1)}} \log(p(x;\Lambda)) + (1-\beta) \sum_{x \in X^{(2)}} \log(p(x;\Lambda)) \quad (10)$$

where β is the combination parameter which can be specified to balance between the unsupervised and supervised training. This is currently studied.

IV. Results

The proposed temporal adaptive cloud classification scheme was examined on a sequence of GOES 8 satellite imagery which were acquired on May 1, 1995 between 15:45-20:45 UTC* at one hour interval. Figures 3(a),(b) and 4(a),(b) show the images obtained at the beginning, 15:45 UTC and at the end, 20:45 UTC, of the sequence, respectively. Visually inspect this image sequence can find some temporal changes, but they are more clearly demonstrated when scatter plots are compared. Figures 3(c) and 4(c) give the corresponding scatter plots of the first and last images. The y axis is the pixel value in the IR channel which reflects the temperature. Generally land is the warmest class at day time in May which corresponds to the largest pixel value, followed by the water, low level clouds, middle level clouds, while the cirrus is the coolest one. On the other hand, the values on the x axis describe the reflectivity in the visible channel. Water has the lowest reflectivity which corresponds to the smallest value, followed by ground. Careful comparison of the two scatter plots can easily reveal the differences. The most obvious distinction is in the upper left corner which corresponds approximately to the land areas. Due to the heating up effects, this region has been expanded over a larger area only after five hours. In the mean time, due to sun angle changes, clouds are not as bright in the visible channel as they were before. There are a lot of pixels whose values exceed 0.5 at the visible channel in 15:45 UTC while very few of them exist at 20:45 UTC.

Two meteorologists were first asked to analyze this image series and identify all possible cloud types as well as the background areas. Approximately 30 percent of each image were identified and they were classified into totally eight cloud/background classes which are: Land, Water, Cumulus, Altostratus, Stratocumulus, Cirrus Over Land, Cirrus Over Water and CirroStratus .

Before these images were applied to the cloud classification system, they were first divided into small blocks of size 8x8 (32km x 32km) with overlapping 4 pixels in each direction. Then feature extraction operation was performed on these blocks. Based on the comparison study in [10], the Singular Value Decomposition (SVD) is adopted here due to its effectiveness and reduced computational cost. After feature extraction stage, the features from both the visible and IR channel images are combined together and fed to the PNN classifier.

The image pair of the first frame obtained at 15:45 UTC was used to initially train the PNN based upon the known classes identified by the meteorologists. Half of the labelled blocks made up the training set while the rest formed the test set. For each class, the initial number of Gaussian components in PNN and the initial values of the parameter set were decided experimentally. The classification result is shown in Figure 5. Visual inspection of this color coded image indicates that different cloud/background areas have been well-separated and the results agree very well with the meteorologist labelling. However, when this PNN was applied to the images obtained at 20:45 UTC, the results were very poor, as it is shown in Figure 6. The proposed temporal adaptation approach was then applied to this image series. The updating process happens every hour. Figure 7 shows the classification result of the same image pair using the updated PNN. Compared with the no updating result in Figure 6, significant improvements can be observed. For example, the clouds in the upper center area have been correctly classified to the Stratocumulus type, while the error made by the old PNN for the Cirrostratus cloud in the upper right part has also been corrected. The classification accuracy improvements of the updated PNN are not limited to the middle and high level clouds. The land area in Florida has also been correctly identified. On the other hand, for those regions that were not changed, the updated PNN made the same decisions as the non-updated PNN. This clearly demonstrates the stability of the updating approach. Although there are still some minor errors in the updated PNN result, e.g. some water areas have been mislabelled to land, overall the proposed updating-based PNN achieved much better and more consistent classification results than

* UTC : Universal Time Code.

that of the non-updated ones. These results conform very well with the meteorologist labelling and show the promise of our proposed temporal adaptive cloud classification approach.

References

[1] G. S. Pankiewicz, "Pattern recognition techniques for identification of cloud and cloud systems", Meteorol. Appl., pp257-271, 1995.

[2] R. M. Welch, et al., "Polar cloud and surface classification using AVHRR imagery: An intercomparison of methods", Journal of Applied Meteorology, Vol. 31, pp405-420, May 1992.

[3] D. F. Specht, P. D. Shapiro, "Generalization accuracy of probabilistic neural networks compared with back-propagation networks", Proc. of IJCNN'91, pp458-461, July, 1991.

[4] D. F. Specht, "Probabilistic Neural Network", Neural Networks, vol.3, pp109-118, 1990.

[5] E. Parzen , "On Estimation of a Probability Density function and mode", Annals of Mathematical Statistics, 33, 1065-1076, 1962.

[6] R. L. Streit and T. E. Luginbuhl, "Maximum Likelihood Training of Probabilistic Neural Networks", IEEE Trans. on Neural Networks, vol 5, No. 5, pp764-783, 1994.

[7] S. Lin, S. Y. Kung and L. Lin, "Face recognition/detection by probabilistic decision-based neural network", IEEE Trans. on neural networks, Vol. 8, No. 1, pp764-783, 1997.

[8] A. P. Dempster, N. M. Laird and D. B. Rubin, "Maximum likelihood from incomplete data via the EM algorithm", Journal of the Royal Statistical Society, series B, vol. 39, pp1-38, 1977

[9] B. Tian, M. R. Azimi-Sadjadi, et al., "Temporal Updating Scheme for Probability Neural Network with Application to Satellite Cloud Classification", submitted to IEEE Trans. on Neural Networks.

[10] M. A. Shaikh , "Neural Network-based Cloud Detection/Classification Using Various Textural Feature Extraction Schemes", M.S. thesis, Dept of EE, Colorado State Univ., 1996

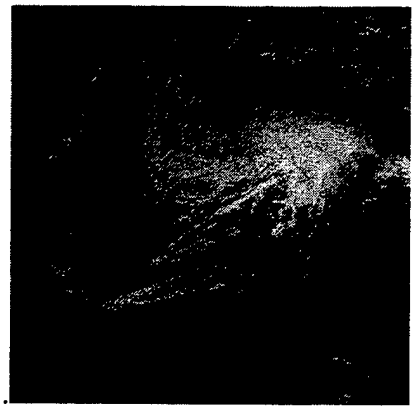

a) Visible channel

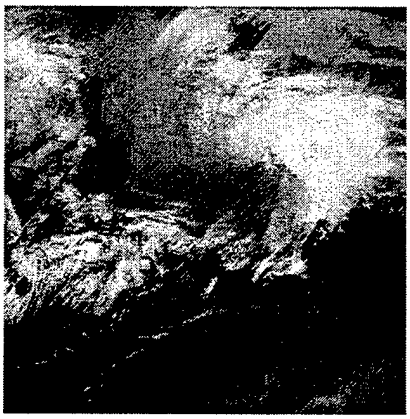

b) IR channel

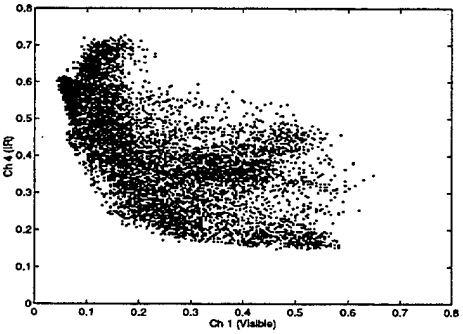

c) Scatter plot

Figure 3. GOES 8 satellite images obtained in May 1st, 1995 at time15:45 UTC and its scatter plot.

a) Visible channel

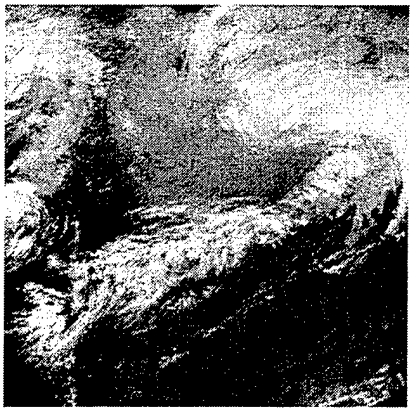

b) IR channel

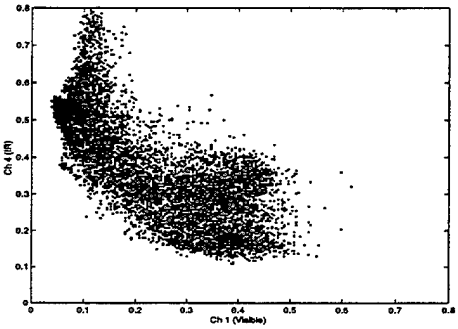

c) Scatter plot

Figure 4. GOES 8 satellite images obtained in May 1st, 1995 at 20:45 UTC and its scatter plot.

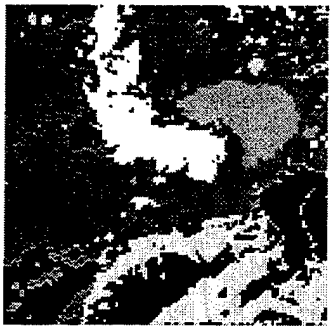

Figure 5. Classification result at time 15:45 UTC.

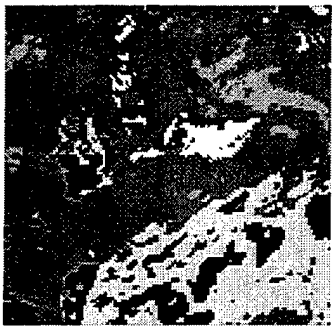

Figure 6 Classification result of the Non-updated PNN at time 20:45 UTC

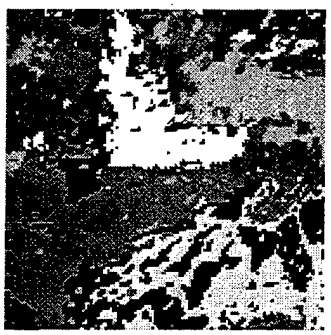

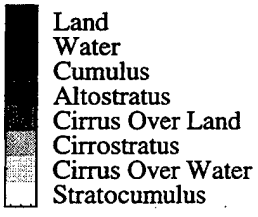

Figure 7. Classification result of the updated PNN at time 20:45 UTC.

Advanced Propagation Model

Amalia E. Barrios
Propagation Division
Space and Naval Warfare Systems Center San Diego D883
49170 Propagation Path
San Diego, CA 92152-7385
Ph: (619) 553-1429
Fax: (619) 553-1417
E-mail: barrios@spawar.navy.mil

ABSTRACT

Previous high-fidelity electromagnetic (EM) propagation models developed at the Naval Command, Control and Ocean Surveillance Center, Research Development Test and Evaluation Division (NCCOSC RDT&E DIV [NRaD], the predecessor to SPAWAR SYS CEN San Diego) include the Radio Physical Optics model (RPO) and the Terrain Parabolic Equation Model (TPEM). RPO is a hybrid ray optics and parabolic equation (PE) model and was designed for surfaced-based systems and over-water applications. TPEM is a pure split-step PE model and was designed for both over-water and over-land applications. Both models have, until recently, been developed in parallel. With the development of the Advanced Refractive Effects Prediction System (AREPS), the need to combine the capabilities of both RPO and TPEM into one model became apparent. The Advanced Propagation Model (APM) is the result. APM is a hybrid ray optics and PE model that incorporates some of the techniques used in both RPO and TPEM, along with newly developed techniques. APM has all of the capabilities of both RPO and TPEM, plus more. APM will be described, along with its capabilities and limitations.

1. BACKGROUND

In October 1992, the first version of RPO, developed at NRaD, was delivered to the Oceanographic and Atmospheric Master Library (OAML) and was subsequently approved for OAML in January 1996 [1]. RPO was the first electromagnetic propagation model to combine a high fidelity PE algorithm with simpler ray optics and flat earth models. The impetus behind this development was that a stand-alone PE model could not give loss predictions over extremely high angles at close ranges, and the numerically intensive calculations required for normal radar applications would be unsatisfactory for a real-time operational model. This "hybridization" resulted in a very efficient high fidelity model that has now been in use by the operational and scientific community (since its initial release in 1992) with overall excellent results and positive feedback from users.

TPEM, also developed at NRaD, was delivered to OAML in May 1997 [2] and is currently undergoing the test and evaluation process necessary to become OAML approved. TPEM is a pure split-step PE model that accounts for variable terrain effects along the path of propagation and has been available for use since mid FY95.

In FY95, the Commander, Sixth Fleet staff expressed a serious interest in having an EM assessment capability that would also account for terrain effects in support of Sixth Fleet ships and aircraft operating in the Adriatic [3]. In response to this, the Radio Propagation Over Terrain (RPOT) software assessment system was developed and delivered to the Sixth Fleet Flagship USS La Salle in June 1996. RPOT contains both RPO and TPEM as separate models surrounded by a Windows 95-based graphical user interface (GUI). With the development of RPOT it became apparent that maintaining two separate models for any kind of software system integration would be cumbersome, and because of the many parallels between RPO and TPEM, in the long run would have resulted in time and money wasted unnecessarily. Therefore, a new model, the Advanced Propagation Model (APM) was developed that combines the capabilities of both RPO and TPEM. With improvements and the development of a new internal model, a more user-friendly and capable GUI was also developed. The new GUI using APM exclusively will now be called the Advanced Refractive Effects Prediction System (AREPS).

2. HYBRID METHOD

Similar to RPO, APM consists of a hybrid of four sub-models: flat earth (FE), ray optics (RO), extended optics (XO), and split-step PE. Each sub-model will be briefly described in the following sections. Refer to Figure 1, where a general height vs. range coverage diagram shows where each sub-model is applied.

2.1 Flat Earth

This model is applied at all ranges and heights for the first 2.5 km from the source. Beyond 2.5 km, it is applied at ranges and heights corresponding to propagation angles greater than or equal to 5°, where there are virtually no refractive effects. The propagation factor is determined from the antenna pattern factors of the direct and reflected rays and the path length difference between both rays. The path length of each ray is found from straight line geometry, thereby, ignoring all refractive effects, although earth-curvature is still taken into account [1]. A cut-off angle of 5° was chosen because at propagation angles less than this, refractive effects come into play and must be taken into account. This is done in the RO model.

2.2 Ray Optics

This model is applied where the FE model ends, namely, the region corresponding to propagation angles less than 5°. It's lower angular limit corresponds to the maximum propagation angle determined for the PE sub-model. Briefly, the RO model consists of tracing a series of direct and reflected rays, determining both the magnitude and phase angle between them, to calculate the propagation factor, F. The full refractivity profile [specified by the user] is taken into account when performing the ray trace, however, the current version of APM assumes the refractivity profile is horizontally homogeneous throughout the region in which the RO model is applied. This portion of APM is described in detail in [1].

2.3 Extended Optics

The extended optics sub-model is normally applied at long ranges and high altitudes and is an approximation based on the parallel ray assumption. That is, in the region in which it is applied, the assumption is that both the direct and reflected rays are parallel, and constructive and destructive interference between the two rays no longer occurs. For this reason, the XO model is applied from the top of the PE region, below which all anomalous refractivity and terrain effects are accounted for, to the maximum height specified for the desired coverage diagram or the maximum PE propagation angle. At the top of the PE region, the propagation angle with which the field propagates outward at each range step is determined via spectral estimation. These angles are then used to trace the field in range and height, keeping F constant along each ray trajectory.

2.4 Parabolic Equation

The last sub-model is the split-step PE model. All refractivity and terrain information specified by the user is processed, and a maximum propagation angle and Fourier transform size are determined as follows. The maximum propagation angle is determined from the local maximum angle of a ray that, when traced, will clear terrain peaks along its trajectory. The initial ray angle must be greater than the critical angle (the angle above which no trapping occurs for ducting cases). The transform size is then calculated based on the maximum PE propagation angle and the height needed to encompass the greater of the highest trapping layer height, or 20% above the highest terrain peak along the path. For details of the PE algorithm in APM, refer to [2].

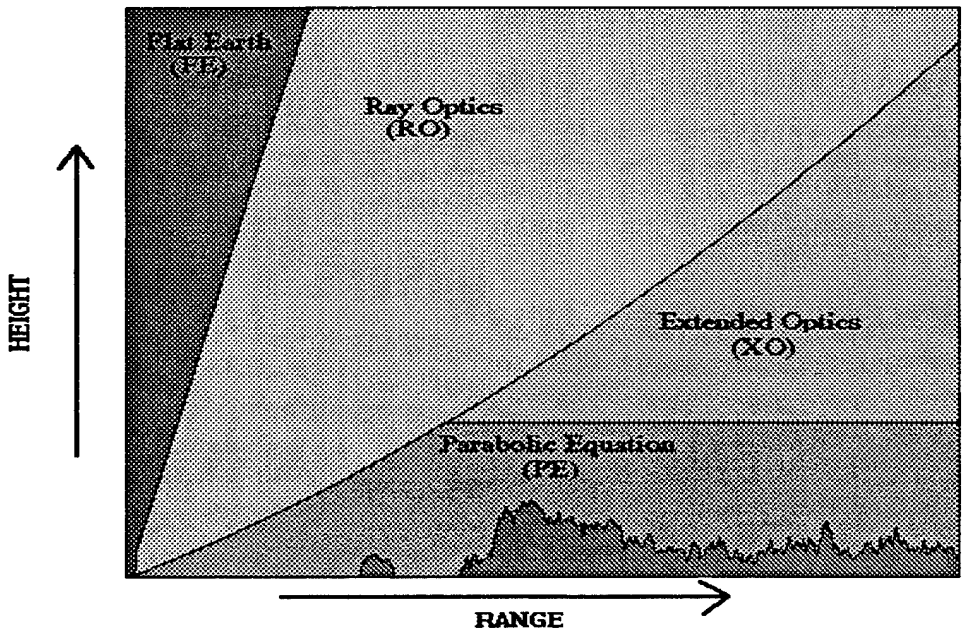

Figure 1. Coverage diagram displaying regions of APM sub-models.

3. EXAMPLES

Unlike RPO, APM is not restricted in antenna height, nor in the type of terrain profile it can accept. However, because of this, it will not always use all four sub-models for a given application. It runs in three "execution modes", determined automatically from within APM, depending on system and environmental inputs. These will be described below.

1) **Full Hybrid:** In this mode all four sub-models are used, producing a coverage diagram that gives propagation loss at all heights and ranges within a specified area. This mode is used only for surface-based platforms, i.e., antenna heights less than 100 m, and if the specified terrain profile is flat for the first 2.5 km from the source. The requirement that the terrain be initially flat is due to the FE and RO sub-models. Since both use ray theory to determine propagation loss, this can only be done easily if the field can be determined from 2-ray interference (direct and reflected rays only). Therefore, for surface-based platforms and over-water applications, this mode will always be used. An example of a coverage diagram produced from APM under this mode is shown in Figure 2.
2) **Partial Hybrid:** In this mode only the PE and XO sub-models are used. APM will use this mode for surfaced-based platforms and for specified terrain profiles which are not flat for the first 2.5 km from the source. In general, this mode will always be used for surface-based platforms and over-land applications. An example from APM for this mode is shown in Figure 3.

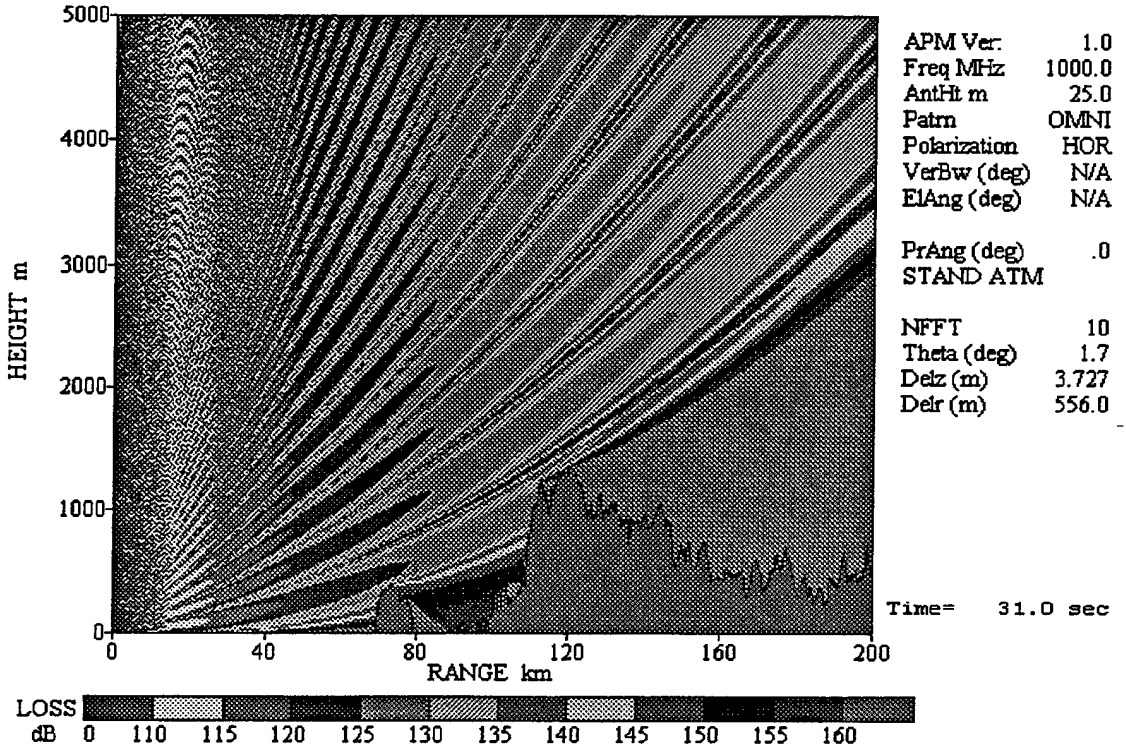

Figure 2. APM coverage diagram using full hybrid mode.

3) **Parabolic Equation:** Lastly, APM will use only the PE sub-model for all applications not falling into the above two categories. Primarily, this is used for all airborne applications, regardless of terrain profile. An example coverage diagram is shown in Figure 4.

4. CAPABILITIES

APM is designed to run in the frequency range from 100 MHz to 20 GHz. It allows for range-dependent refractivity profiles and also accommodates variable terrain profiles specified by height/range pairs. APM incorporates the discrete mixed transform impedance boundary algorithm [4], thereby modeling vertically polarized fields propagating over a finite conducting surface. Dielectric ground constants are specified by the user and are allowed to vary with range. Lacking any specific knowledge about the dielectric properties of the immediate area, general ground type descriptions can be specified according to [5], such as *wet ground*, *dry ground*, etc. Permittivity and conductivity are then calculated as functions of frequency from curve fits to the permittivity and conductivity graphs shown in [5]. For horizontal polarization, no ground types need be specified as APM models all horizontal polarization cases assuming the surface is a perfect conductor. This is typically done for over-water cases, but is also a suitable approximation for over-land applications.

APM allows the specification of several antenna pattern types, those being omni-directional, Gaussian, Sin(X)/X, Cosecant-squared, generic height-finder, and specific height-

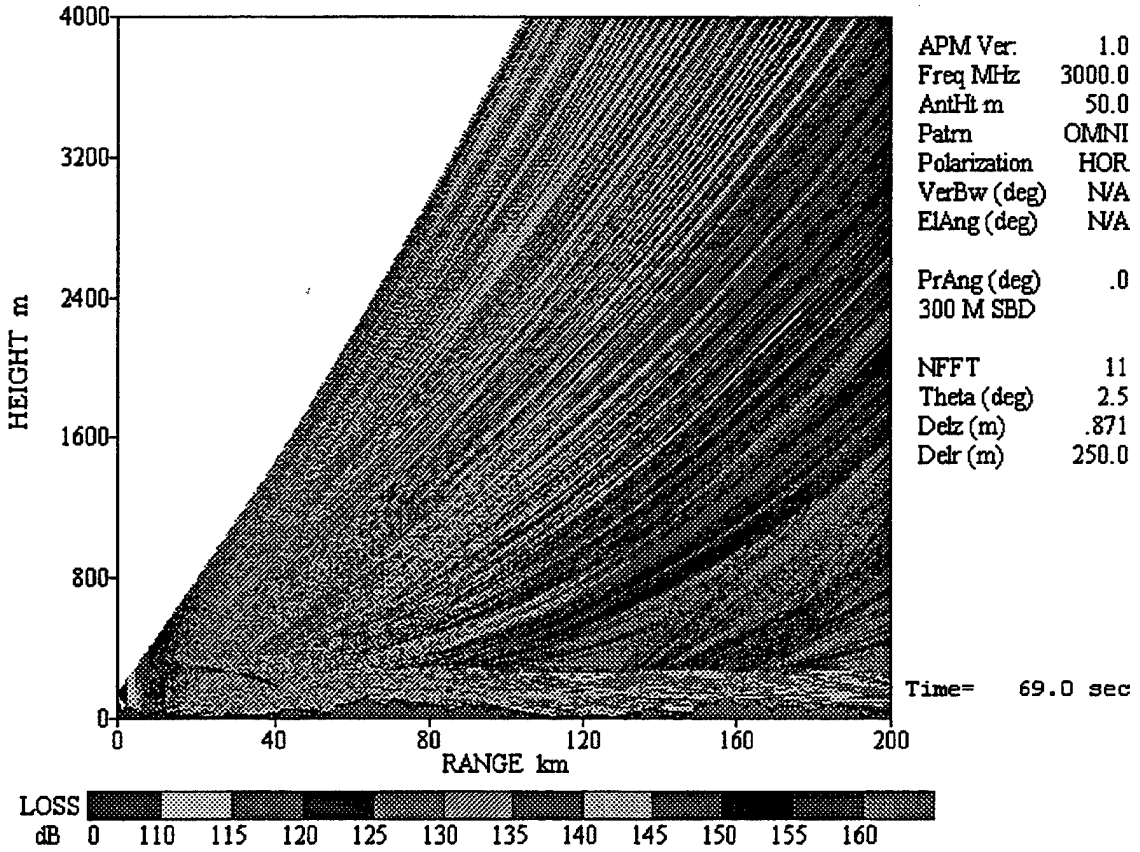

Figure 3. APM coverage diagram using partial hybrid mode.

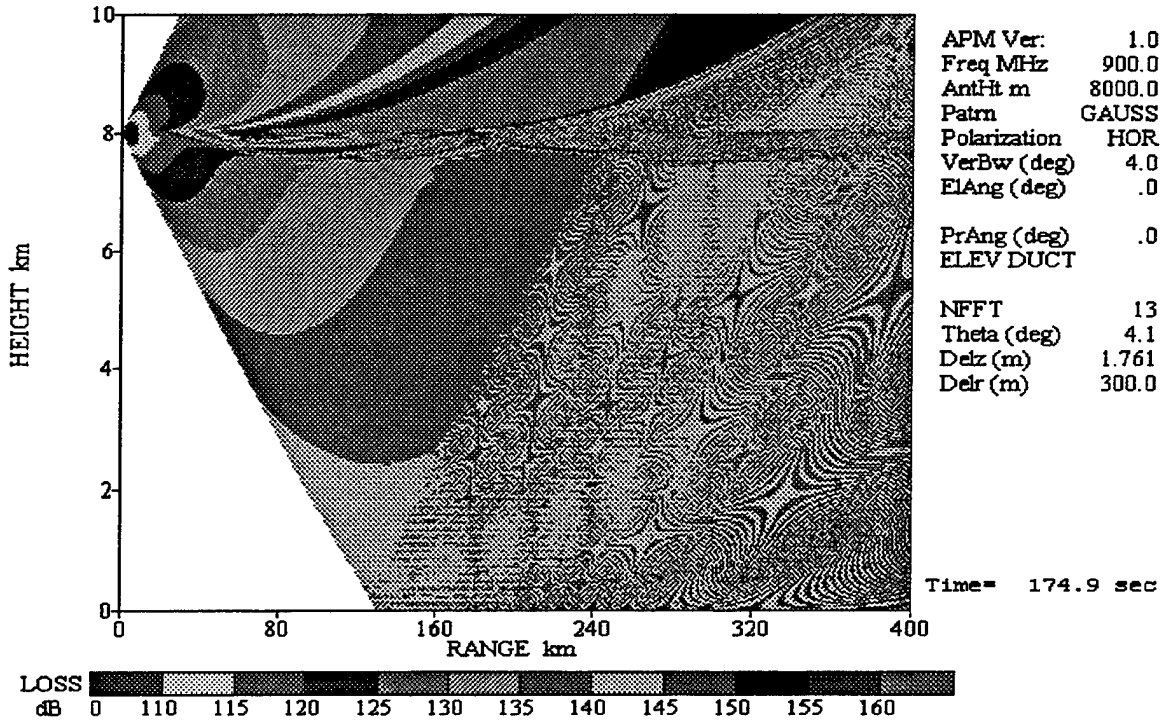

Figure 4. APM coverage diagram using PE mode.

finder in which you also specify cut-back angles and power factors. A troposcatter model is also included in APM that is based on [6].

Finally, a gaseous absorption model is also included [7] in which you are required to specify the absolute humidity and air temperature near the surface. APM will then calculate an attenuation rate which, when multiplied by the receiver range, is added to the final propagation loss. Alternately, lacking any humidity or temperature data, you can explicitly specify a numerical value for the attenuation rate.

5. LIMITATIONS

Although APM includes the mixed transform algorithm (as mentioned previously), in which effects due to a finite conducting, rough surface boundary can be accounted for, it currently does not calculate loss due to a rough sea surface. The reason is that there are still some unresolved questions as to how valid current models are, based on a rough surface reflection coefficient [8]. Once some of these questions are resolved, adding the capability to account for rough sea surface effects can be done with little difficulty.

In the region in which RO calculations are done, the refractivity is assumed to be horizontally homogenous. However, since the PE sub-model fully accounts for range-dependent refractivity and is run in a region where propagation angles are above the critical angle for ducting cases, discontinuities occur only for the most extremely varying refractive environments.

Finally, for applications in which APM does not use the full hybrid mode there will be limited field coverage due to the inherent angle limitations in the PE sub-model.

6. FUTURE WORK

One of the limitations we plan to address soon is the limited angle coverage problem for airborne applications. An airborne hybrid model will be included in APM by the end of FY98 which is based on very simple flat earth calculations. The calculations will be applied in the regions corresponding to angles below and above the PE sub-model angular limits, which (for airborne cases) will always be *at least* 5°. Propagation loss will be computed from the antenna height to the ground for angles less than the maximum PE limit, ignoring reflections from these high angles in the total field calculations. Normally, interference effects from these high angle reflections will occur at close range and neglecting these effects should not have a significant bearing on propagation effects far down range, where you are most likely to make an operational assessment.

7. SUMMARY

In merging both RPO and TPEM, along with adding new techniques and making improvements in the existing sub-models; a new, more capable model was developed. APM is now an "all-inclusive" model that can accommodate more applications than both RPO and TPEM.

REFERENCES

1) W.L. Patterson, H.V. Hitney, "Radio Physical Optics CSCI Software Documents", *NRaD TD 2403, Rev. 1 April 1997.*
2) D.B. Sailors, A.E. Barrios, "Terrain Parabolic Equation Model (TPEM) Computer Software Configuration Item (CSCI) Documents", *NRaD TD 2963, May 1997.*
3) H. Hitney, A. Barrios, W. Patterson, "Radio Propagation Over Terrain", *Proceedings of the 1996 Battlespace Atmospherics Conference 3-5 December 1996*, NRaD TD 2938, December 1996, pp. 103-111.
4) G.D. Dockery, J.R. Kuttler, "An Improved Impedance Boundary Algorithm For Fourier Split-Step Solutions Of The Parabolic Wave Equation", *IEEE Trans. On Ant. And Prop., Vol. 44, No. 12*, December 1996, pp. 1592-1599.
5) International Radio Consultative Committee (CCIR), "Propagation in Non-Ionized Media", *Recommendations and Reports of the CCIR*, Vol. V, 1986.
6) L.P. Yeh, "Simple Methods for Designing Troposcatter Circuits", *IRE Trans. CS-8*, pp 193-198, 1960.
7) International Radio Consultative Committee (CCIR), "Propagation in Non-Ionized Media", *Reports of the CCIR*, Vol. V, Report 719-3, 1990.
8) H.V. Hitney, "Evaporation Duct Propagation over a Rough Sea", *Proceedings of the 1997 Battlespace Atmospherics Conference 2-4 December 1997*, SSC SD TD, December 1997.

Advanced Refractive Effects Prediction System

W.L. Patterson
Propagation Division
Space and Naval Warfare Systems Center, San Diego, D883
49170 Propagation Path
San Diego, CA 92152-7385
Fax: (619) 553-1417; DSN 553-1423; wayne@spawar.navy.mil

Abstract

The Space and Naval Warfare System Center, San Diego (SSC SD) has a full spectrum research, development, test and evaluation program with a long and proud history of rapidly responding to critical fleet requirements and deploying systems to address these requirements.

One such system is the new Advanced Refractive Effects Prediction System (AREPS). AREPS grew out of a fleet requirement for EM assessment capability over varying terrain. The fleet requirement was initially met with the Radio Propagation Over Terrain (RPOT) program, provided to Commander, Sixth Fleet and subsequently to many other fleet units; Department of Defense (DoD) organizations; educational institutions; and domestic and foreign commercial companies. The internal propagation model is the Advanced Propagation Model (APM) a hybrid ray-optic and parabolic equation model which allows for range-dependent refractivity over various terrain or sea paths.

AREPS computes and displays radar probability of detection, Electronic Support Measures (ESM) vulnerability, and UHF/VHF communications capability versus range, height, and bearing from the transmitter. Refractivity data can be entered using several methods, including a fully automatic decoding of common World Meteorological Organization (WMO) codes already available on many local area networks and from Internet homepages of many meteorological organizations. In addition, a 921 station world-wide upper-air climatology database is included within AREPS for assessment using climatological refractivity data. For each bearing, terrain elevation data are automatically extracted from the National Imagery and Mapping Agency's (NIMA) Digital Terrain Elevation Data (DTED), supplied on CD-ROMs. For those without access to the NIMA DTED data, AREPS allows for their own terrain elevation data including bearing and range-dependent surface conditions, either selected from an array of surface type (i.e. sandy loam, concrete, etc.) or entered specifically with surface conductivity and permittivity values. AREPS allows for many antenna types including specific-system height-finding antennas and as an option, will allow for your own unique specification of antenna radiating pattern.

The power of AREPS derives not only from its improved propagation model but from its Windows 95/NT interface. As a Windows 95/NT application, it makes full use of drop-down and pop-up menus, object linking and embedding (OLE) features such as file drag and drop and graphics export, and an extensive on-line help with colorful graphic examples.

Organizational History

In 1945, the University of California Division of War Research combined with the Navy's Radio and Sound Laboratory in San Diego. The combination produced the Navy Electronics Laboratory (NEL). During the next 30 years, NEL developed a Navy-wide reputation for its work in radio, radar, sonar, tactical warfare simulations, and information display and data management systems. In 1967, the Navy reorganized its west coast laboratories and NEL became the Naval Electronics Laboratory Center (NELC). The center's work focus became more centered upon command, control, and communications. The work in radio propagation continued unbroken however. In 1977, NELC consolidated with the Naval Undersea Center into the Naval Ocean Systems Center (NOSC) to provide broad-spectrum systems capability and to facilitate the system's integration into major mission areas. In 1992, the Navy established 4 major warfare centers by consolidating 7 Navy research and development centers with 29 engineering and fleet support activities. One of the four, the Naval Command, Control and Ocean Surveillance Center (NCCOSC), was headquartered in San Diego. NOSC was reorganized as a division under NCCOSC. In 1997, NCCOSC was disestablished and its research and development division was reorganized as a division directly under the Commander, Space and Naval Warfare Systems Command (SPAWAR).

While our name has changed many times over the years, our work in radio propagation has continued unbroken and in more recent years, has increased even more dramatically with radio-meteorological experiments, EM propagation modeling efforts, and fielding EM system performance assessment systems.

Propagation assessment systems

The primary transition path for our modeling efforts is to the Oceanographic and Atmospheric Master Library (OAML). Our propagation models have been incorporated into such Navy systems as the Tactical Environmental Support System (TESS), the Navy Integrated Tactical Environmental Subsystem (NITES), the Geophysical Fleet Mission Program Library (GFMPL), the Mobile Oceanographic Support System (MOSS), the Joint Operational Tactical System (JOTS), and the Tactical Automated Mission Planning System (TAMPS). One of the missions for our command, however, is fleet support and over the years we have responded to critical fleet needs.

In 1978, we delivered directly to the fleet, the Navy's first operational EM propagation assessment system, Integrated Refractive Effects Prediction System (IREPS). The original system was hosted on Hewlett-Packard desktop computers and the programming language was HP-BASIC. In addition to the IREPS software, we provided the HP desktop computers to all CV and CVN platforms. The explosion of personal computer (PC) capability made possible the rehosting of IREPS to an IBM compatible PC using a combination of C and FORTRAN programming languages. Over the years, hundreds of copies of the IREPS program have been distributed world-wide.

Responding to a need within research and development organizations, we assembled a collection of individual programs designed to assist an engineer in properly assessing EM propagation effects of the lower atmosphere on proposed (or operational) radar, electronic warfare, or communications systems. This collection of programs is known as Engineer's

Refractive Effects Prediction System (EREPS) (Patterson, et al., 1994). While the propagation models of EREPS are similar to those of IREPS, the user interface is designed for maximum flexibility in EM parameter manipulation. EREPS has the additional capability of reading binary files of propagation loss versus range and height that may be generated by more sophisticated propagation models such as RPO and TPEM. EREPS may, therefore, be used for detailed comparative studies using interactive graphic displays. Like IREPS, EREPS has been met with great success, a success in no small part due to its hosting on personal computers.

With the Navy's involvement in the Bosnian situation, the Commander, Sixth Fleet identified a critical fleet need for an EM propagation assessment system that would consider terrain effects. Within the "Technologies for Rapid Response," a blue-book maintained by the Office of Naval Research (ONR), was an item identified as "Radar Propagation Over Terrain (RPOT)." This item consisted of our efforts in atmospheric and terrain range-dependent EM modeling efforts. It should be noted at this time that RPOT was not under development.

RPOT's objective was to provide an interim capability to compute and display radar and radio propagation effects over water, across coastlines, and over varying terrain, including range-dependent refractive effects, for land-based, sea-based, and airborne platforms. Our efforts began in November, 1996, and by August, 1997, a ten month period, an EM propagation assessment system was hosted and delivered on a PC using the Microsoft Windows 95 operating system. The propagation models used within RPOT are RPO and TPEM. Since the assessment system also included a UHF/VHF communications capability, the name of the system became "Radio Propagation Over Terrain." With the acceptance of RPOT by the Commander, Naval Meteorology and Oceanography Command (CNMOC) and SPAWAR, we began fleet-wide distribution of RPOT. To date, RPOT is being used by over 200 Department of Defense, U.S. and foreign government contractors, commercial organizations, foreign governments and their military organizations, and private individuals . RPOT has spread to over 28 countries.

Advanced Refractive Effects Prediction System (AREPS)

The success of RPOT, in addition to the Navy's move toward IT-21 technology, has prompted the development of AREPS which will replace the interim RPOT with an expanded operational capability.

The internal propagation model for AREPS is the Advanced Propagation Model (APM). This is a hybrid model that consists of four sub-models: flat earth, ray optics, extended optics, and split-step parabolic equation (PE). APM employs the techniques for both the Radio Physical Optics (RPO) model and the Terrain Parabolic Equation (TPEM). The result is a new and improved EM propagation model that has the following capabilities:

1. Range-dependent refractivity environments
2. Variable terrain
3. Range-varying dielectric ground constants for finite conductivity and vertical polarization calculations
4. Troposcatter
5. Gaseous absorption

Displays

The primary displays of AREPS are height-versus-range and bearing coverage, a propagation loss/signal-to-noise versus height/range and bearing, simultaneous radar probability of detection and ESM vulnerability, ESM vulnerability, and communications. Figure 1 illustrates such a coverage display for a sea-based air-search radar with its probability of detecting a "small" sized jet. For this case, the atmosphere is range-dependent, with a surface-based duct existing at the transmitter location, rising to become an elevated duct over the terrain features. To the lower right of the coverage display is a small map, in a simulated plan-position-indicator (ppi) picture format, showing the transmitter location, the current display's bearing, and the terrain heights.

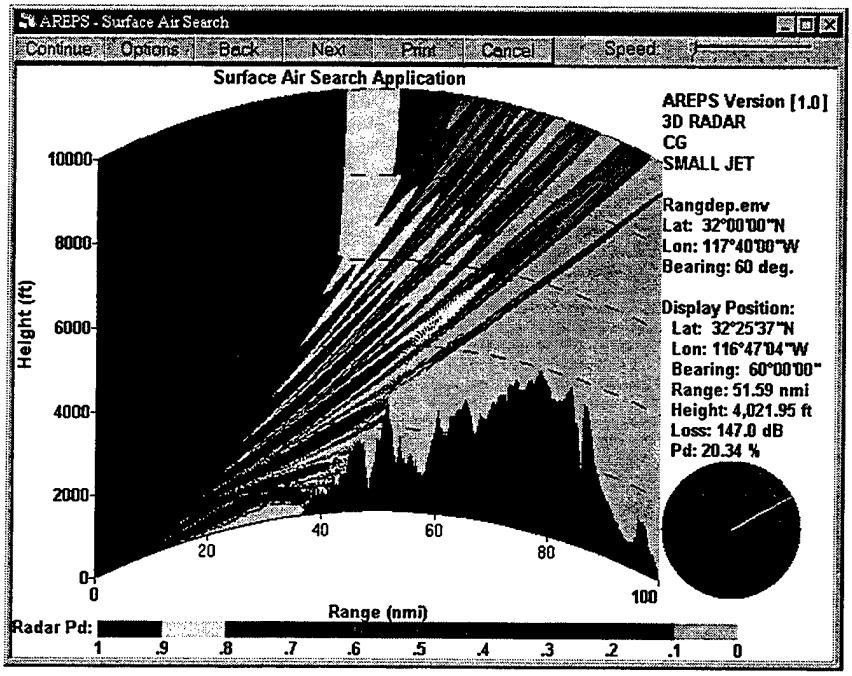

Figure 1: AREPS radar probability of detection coverage display

At the top of the display window is a series of buttons which allow you to animate the display in bearing, both forward and backward, to pause the animation, and obtain a printed copy of the display. Because AREPS is a Windows 95/NT program, the full capabilities of the operating system are available. For example, should you desire to brief the display, you may "copy" the display to the Windows 95/NT clipboard and "paste" it directly into a presentation package such as Microsoft PowerPoint. Because propagation loss values are computed for the coverage display, there is no need to execute the APM again to obtain propagation loss or signal-to-noise versus range and or height displays (figures 2 and 3). These displays are shown for a particular height or range simply by clicking the right mouse button on the coverage display. You are unlimited in the number of displays appearing on the screen.

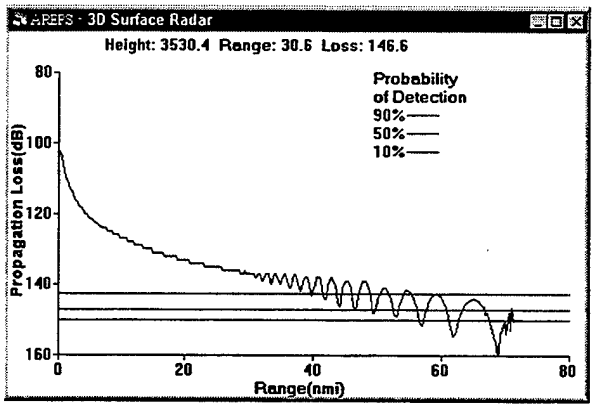

Figure 2: Propagation loss versus range display.

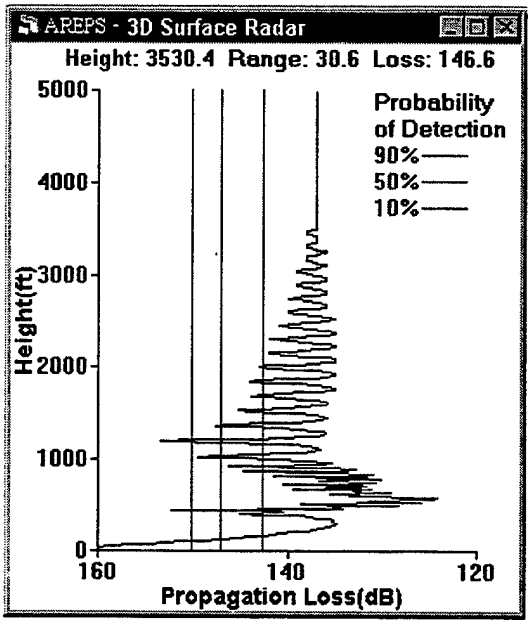

Figure 3: Propagation loss versus height display.

Figures 4, 5, and 6, illustrate the coverage for an airborne transmitter in the presence of an elevated duct, simultaneous surface-based radar coverage and ESM vulnerability, and UHF communication assessment respectively. Note also the three earth surface depictions of dual curved, curved, and flat.

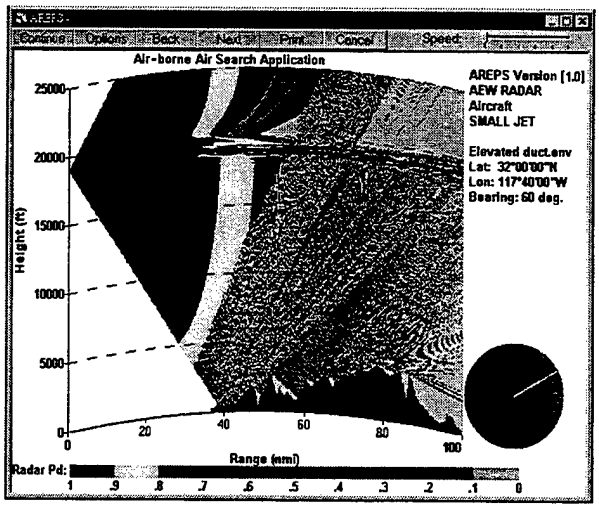

Figure 4: AREPS air-borne air search application.

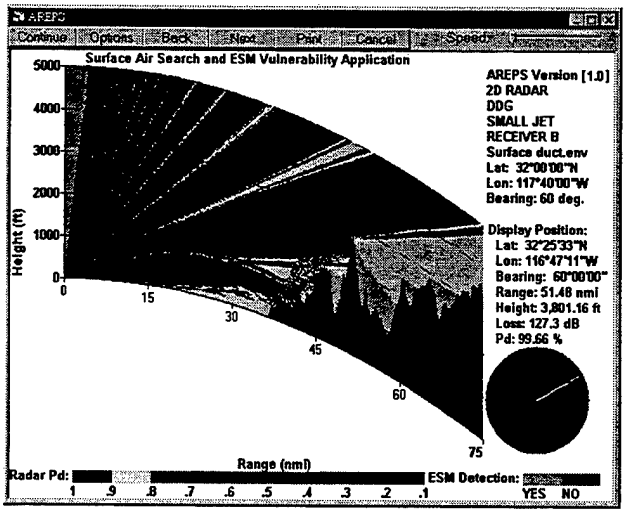

Figure 5: AREPS radar probability of detection and ESM vulnerability application.

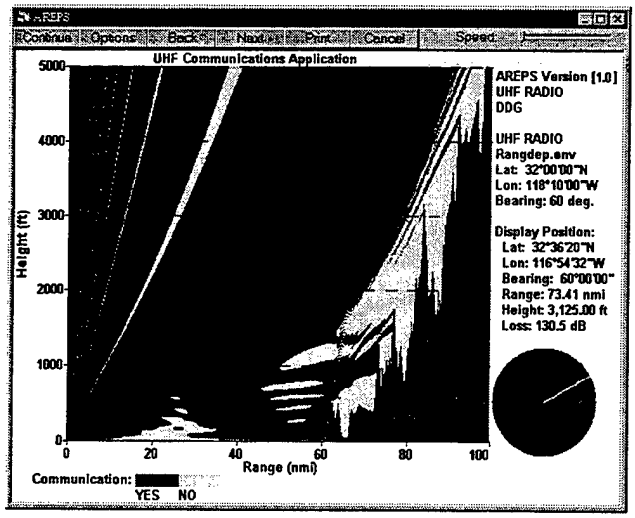

Figure 6: AREPS Communications application.

EM systems database

AREPS is a completely unclassified program and as such, does not include any pre-established EM system parameters database. You are solely responsible for creating a system parameter database appropriate to your situation. To assist you in this task, a database creation and maintenance capability is provided using fill-in-the-blank forms. Figure 7 is an example of such a form for a radar system. As you navigate about the form, input prompts, parameter limits, and other guidance are displayed in a status bar located at the bottom of the window.

AREPS capabilities not included in RPOT are the expanded antenna radiation patterns of specific system height finder antennas and a user defined antenna pattern. In addition, detection thresholding calculations now include radars using incoherent and coherent integration techniques.

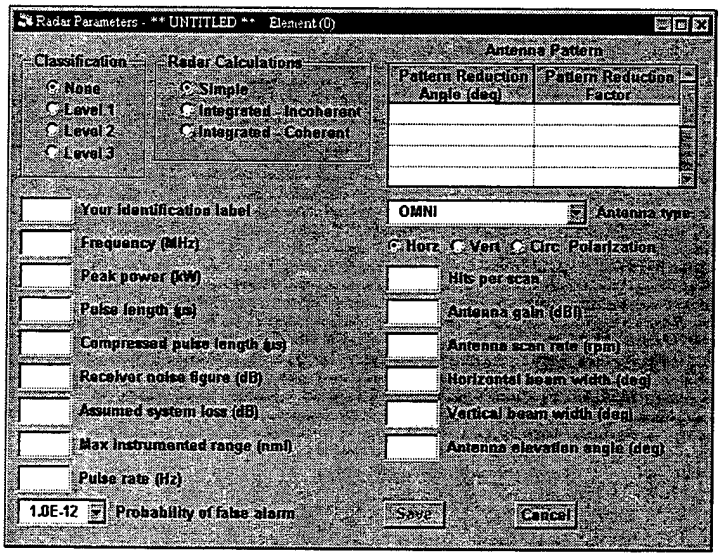

Figure 7: AREPS radar system input form

Terrain data

AREPS primarily derives its terrain height data from the Digital Terrain Elevation Data (DTED) provided by the National Imagery and Mapping Agency (NIMA). DTED data are provided in level 0, level 1, and level 2 formats. Level 0 post spacing is 30 arc seconds in horizontal resolution (approximately 1 kilometer). DTED level 0 data is unlimited distribution and may be obtained directly from NIMA's INTERNET homepage. DTED level 1 post spacing is 3 arc seconds in horizontal resolution (approximately 100 meters). Level 2 post spacing is 1 arc second in horizontal resolution (approximately 30 meters). Level 1 and 2 data are limited distribution. For this reason, DTED data are not and may not be distributed with AREPS. If you have a connection to the Secure Internet Protocal Router Network (SIPRNET), you may download the DTED level 1 and 2 data directly from NIMA's SIPRNET homepage. AREPS will accept DTED level 0, 1, and 2 coverage whereas RPOT accepts only level 1 data. For ease of input when using DTED CD-ROMs, you need only specify the latitude and longitude location of your transmitter. The

AREPS program will determine which CD-ROM is required, prompt you to insert the CD-ROM into the drive, and automatically extract the terrain data needed.

In addition to DTED terrain data, AREPS is capable of using terrain data you may specify yourself. A terrain window, figure 8, provides a convenient entry method. In addition, the terrain window may be used to edit terrain created from DTED data. The increased capability of the APM now allows for specification of range-dependent surface conditions should you be concerned about surface types for vertically polarized antennas. AREPS uses the surface conditions as defined by the International Telecommunication Union, International Radio Consultative Committee (CCIR). These conditions are broken into seven categories based upon surface characteristics and for convenience, AREPS provides plain language descriptors which fall within the seven categories. These surface descriptors may be selected from a drop down menu or the surface characteristics may be entered directly if they are known.

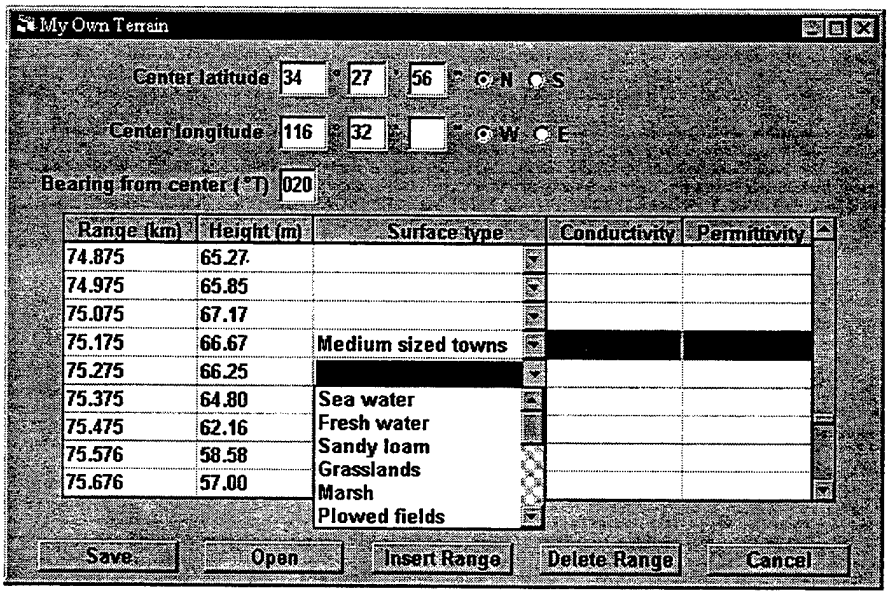

Figure 8: AREPS terrain input window with surface conditions dropdown menu.

Environmental Input

One of the limitations of IREPS and EREPS is their capability to ingest atmospheric data. While the data is derived from World Meteorological Organization (WMO) radiosondes, the data must be entered over the keyboard. This can, at times, be a tedious operation and may lead to errors because of typing skills, number transposition or inattention. The entry of environmental data into AREPS has been completely automated by using the capabilities of the Windows 95/NT operating system. Within normal naval message traffic, WMO coded radiosonde messages are routinely available. Figure 9 illustrates such a message.

You need only locate the message, (for a ship, the message is available on the ship's local area network), open the message file using any ASCII text editor such as Notepad that is provided with Windows 95/NT, "copy" the text to the Windows clipboard, and "paste" it into the Import WMO Code window of AREPS, figure 10. All extraneous text is filtered, the message is decoded, and a height versus M-unit profile is automatically created. Should the observation be from a sea-based platform, the surface temperature and humidity are used to calculate a neutral profile evaporation duct profile and this profile is appended to the upper-air portion of the observation. If you have surface observations available, you may override the neutral profile and include full stability dependency.

```
FM UPPERAIR OBSERVER
TO REGION METOC CENTER
USS SHIP ONE
USS SHIP TWO
USS SHIP THREE
USS SHIP FOUR
BT
SUBJ/UPPER AIR OBSERVATION//
UUAA  77003 99xxx xxxxx xxxxx
99018 17822 29023 00171 18258 31535 92838 16461 32022
85554 13464 31029 70169 05272 31032 50581 13764 29033
40747 25976 30041 30949 421// 30548 25069 /////
88999 77999
UUBB  77005 99xxx xxxxx xxxxx
00018 17822 11989 19063 22845 13466 33835 14268 44817
13069 55/// ///// 66771 10467 77754 09667 88/// /////
99731 08874 11730 08873 22/// ///// 33707 06073 44578
07359 55551 09757 66540 10158 77539 09558 88511 12369
99463 18546 11429 22563 22414 24760 33406 25373 44381
27780 55258 505// 41414 12345
21212 00018 29023 11012 31532 22002 31535 33934 32022
44826 31030 55/// ///// 66718 30528 77496 29034 88258
31049
UUCC  7700/ 99424 10053 18025 NIL
UUDD  7700/ 99424 10053 18025 NIL
2. PASS TO OA DIV/MET DET.
BT
#5557
NNNN
```

Figure 9: WMO radiosonde message.

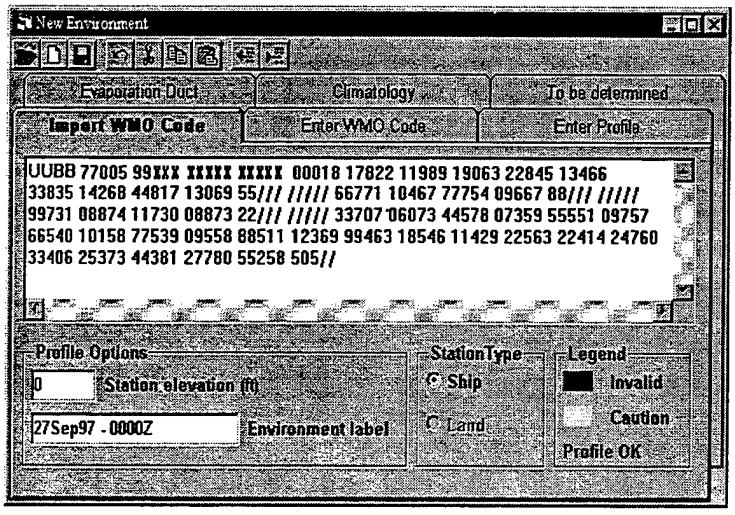

Figure 10: Import WMO code tab for new environmental input.

It is not always necessary to have access to a local area network for the WMO observation. Many organizations and ships post their local radiosonde observations on their Internet or SIPRNET homepage. Once such a homepage is found for the particular area of interest, the WMO report may be copied to the Windows 95/NT clipboard directly from the browser (such as Netscape or Microsoft Internet Explorer), and then pasted into the Import WMO Code window. For military users, WMO reports are also available from the Fleet Numerical Meteorology and Oceanography Center via the Joint METOC Viewer (JMV) and the Naval Oceanographic Data Distribution System (NODDS). For both military and civilian users, reports may be obtained from the Air Force Global Weather

Center's Dial-in Subsystem (AFDIS) and the National Oceanic and Atmospheric Administration (NOAA) Forecast Systems Laboratory's North American RAOB database homepage.

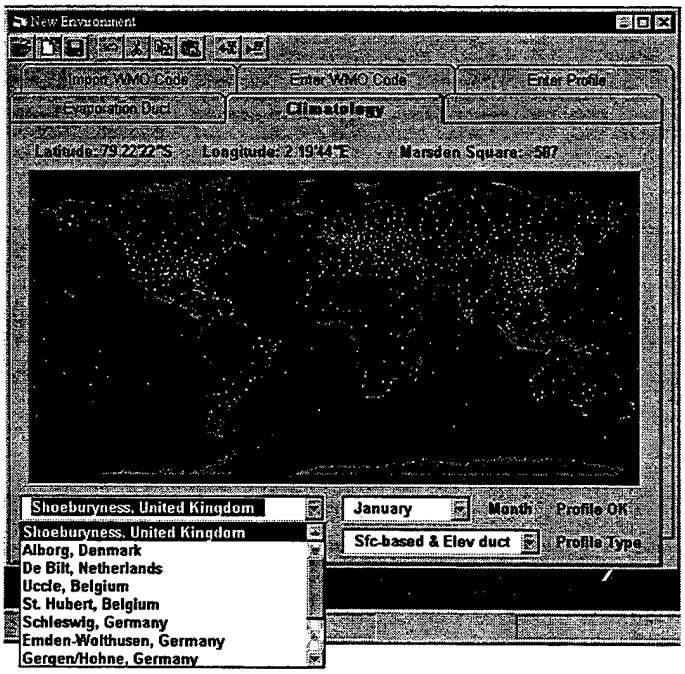

Figure 11: AREPS refractive conditions climatology.

In addition to WMO inputs, AREPS has included a refractive conditions climatology assembled by GTE Sylvania, under contract by the Department of Defense. 921 WMO observing stations world-wide are shown as dots on a world map, figure 11. Clicking on the map will fill the station name dropdown menu with the names of all the observing stations within the Marsden square. You may then select a station name from the name dropdown menu, a month of interest from the month dropdown menu, and a profile type (standard atmosphere, surface-based duct, elevated duct, and a combination of surface-based and elevated ducts) from the profile type dropdown menu.

Training

As with any new computer software, operator training is a major consideration. To leverage the training already amassed by using other Windows 95/NT programs, AREPS had been designed to "look like" and "behave like" other programs. For example, the task bar icons used for environmental input are identical in look and action to those used in Microsoft products such as Word or PowerPoint. AREPS also contains an extensive on-line help including index search features and graphics examples. Figure 12 illustrates just one such help topic window.

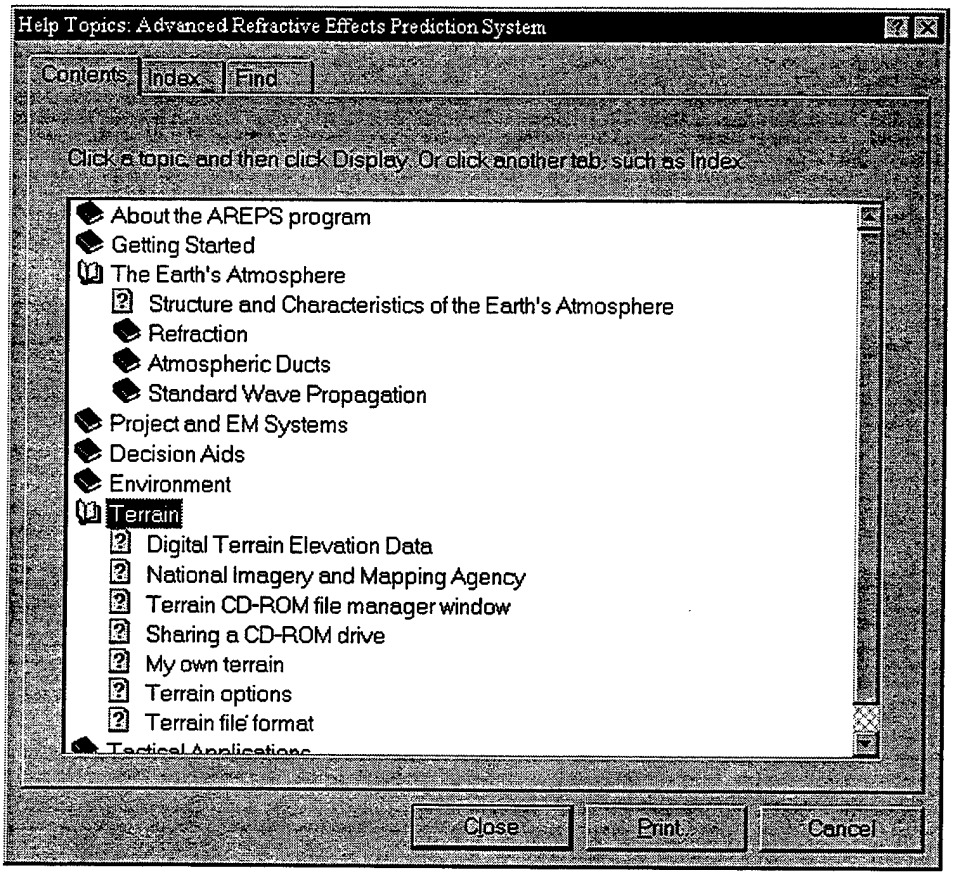

Figure 12: AREPS on-line help topics.

Distribution, support, and future plans

We are the sole distribution and technical support for the AREPS program. Distribution is provided on CD-ROM through the U.S. mail system or by direct download of the program from our Internet homepage (http://sunspot.spawar.navy.mil). In addition to the program software, our homepage includes help topics, frequently asked questions, and program service packages as necessary.

We plan to maintain a PC capability within our modeling efforts to serve as a testbed for APM and its follow-on improvements. In addition we will use AREPS for expanded visualization techniques, and other tactical applications such as battlegroup vulnerability and ECM effectiveness. AREPS is currently being modified for Defense Information Infrastructure (DII) compliancy and will be submitted as a Global Command and Control System (GCCS) segment. Simultaneously AREPS is being implemented into the Geophysical Fleet Mission Program Library (GFMPL-NT) suite of software for distribution to all mobile environmental support teams world-wide.

Bibliography

Barrios, A.E., "Terrain Parabolic Equation Model (TPEM) Version 1.5 User's Manual," NRaD Technical Document 2898, February 1996.

Hattan, C.P., "Specification for a Standard Electromagnetic Propagation Model," NOSC Technical Document 1772, June 1990.

Patterson, W.L., "Integrated Refractive Effects Prediction System (IREPS) User's Manual Revision PC-2.0," NOSC Technical Document 1874, August 1990.

Patterson, W.L. and H.V. Hitney, "Radio Physical Optics CSCI Software Documents RPO Version 1.16," NRaD Technical Document 2403 Revision 1, April 1997.

Patterson, W.L. and C.P. Hattan, G.E. Lindem, R.A. Paulus, H.V. Hitney, K.D. Anderson, A.E. Barrios, "Engineer's Refractive Effects Prediction System (EREPS) Version 3.0," NRaD Technical Document 2648, May 1994.

EVAPORATION DUCT PROPAGATION OVER A ROUGH SEA

Herbert V. Hitney
Propagation Division

Space and Naval Warfare Systems Center San Diego D883
49170 Propagation Path
San Diego, CA 92152-7385
Ph: 619-553-1428 Fax: 619-553-1417
E-mail: herb@spawar.navy.mil

ABSTRACT

The evaporation duct can substantially enhance signal levels for over-the-horizon over-sea paths at frequencies above several GHz. Waveguide and other propagation models and some limited experimental data indicate that wind-driven sea-surface roughness counteracts the effectiveness of the evaporation duct when both the duct height and the wind speed are high. Several methods have been proposed to model the effects of surface roughness under these ducting conditions, but these models have not been experimentally verified. A summary of existing waveguide and parabolic equation models will be presented along with results from two previous measurement programs. A new Rough Evaporation Duct (RED) propagation experiment will be described that is specifically designed to address these effects. The proposed propagation path for RED is a 45 km over-water link between the islands of Molokai and Oahu, Hawaii, which should be subject to both high wind speeds and high evaporation duct heights much of the time over a uniformly rough path. Low terminal heights of 2 to 5 meters and frequencies of 3, 10, and 18 GHz are planned for a 60 day period in the summer of 2000. Propagation loss will be measured versus time simultaneously for all three frequencies and compared to modeled propagation loss based on suitable meteorological measurements.

INTRODUCTION

The rapid decrease of humidity near the ocean surface creates a surface duct at radio frequencies commonly called the evaporation duct. It has been well established that this duct can substantially enhance radio signal levels on over-the-horizon paths at frequencies generally above about 3 GHz [1]. The strength of the evaporation duct is primarily determined by the evaporation duct height which is the height at which the modified refractivity profile reaches a minimum, which from a ray optics point of view is the height at which the radio ray curvature exactly equals the earth curvature. Evaporation duct heights vary from zero to about 40 meters, with a worldwide average of about 8 meters. The evaporation duct height can be determined from fairly simple meteorological measurements of sea surface temperature, and air temperature, humidity, and wind speed at a height a few meters above the sea surface. Distributions of duct height have been prepared from long term historical observations of these meteorological measurements and are readily available in data bases and personal computer (PC) programs [2]. When these duct height distributions are properly combined with appropriate radio propagation models, predicted distributions of propagation loss compare very well with measured distributions of propagation

loss for over-the-horizon paths, as the two following examples from [3] illustrate. The first example is a 2.3 GHz 77.2 km link from the north coast of Germany to Helgoland over the North Sea using a transmitter 28 m above mean sea level (msl) and a receiver 31 m above msl. The median duct height is 6 m and the median measured signal was enhanced 12 dB compared to diffraction, and the model showed a median enhancement of 13 dB. The second example is an 18 GHz 35.2 km path in the Agean Sea between Naxos and Mykonos Islands in Greece, with a transmitter 4.5 m above msl and a receiver 17.8 m above msl. The median duct height in the Agean Sea is 12.5 m and the median measured and modeled signal enhancements compared to diffraction are 29 and 28 dB, respectively. The higher duct height and frequency in this example compared to the first are responsible for the much greater enhancements, but in both cases the predicted and measured medians are within 1 dB. However, surface roughness is not an important factor in either of these examples, since the duct heights are not high enough at the given frequencies to make any difference at typical wind speeds.

For combinations of high frequencies, high duct heights, and high wind speeds, models indicate that surface roughness can reduce the effectiveness of the evaporation duct. Since there are no known radio-meteorological experimental data sets taken in areas where very high duct heights are common, this paper will examine the highest frequency of 37 GHz that was measured in two locations of moderate ducting to examine roughness effects. It is the objective of this paper to at least partially verify these propagation models.

PROPAGATION MODELS

This paper will use the MLAYER normal mode propagation model [4]. In MLAYER, the reflection coefficient from the lower boundary is an integral part of the modal equation. The Miller-Brown rough surface model [5] has been incorporated into this reflection coefficient as a function of grazing angle, and hence the modal solutions fully contain the rough surface effects of the Miller-Brown model. The applicability of the Miller-Brown model to ducted propagation is not clear, however, as it was developed for and verified by propagation paths within the horizon. Nevertheless this formulation in MLAYER is thought to be mathematically correct, since grazing angle is implicit in the model.

The model by Miller and Brown is given by

$$R = R_0 \exp\left[-2(2\pi g)^2\right] I_0\left[2(2\pi g)^2\right]$$

where R is the rough-surface coherent reflection coefficient, R_0 is the smooth-surface Fresnel reflection coefficient, I_0 is the modified Bessel function, and the "apparent ocean roughness" g is given by

$$g = (\sigma_h \sin\psi)/\lambda$$

where σ_h is the standard deviation of the sea-surface elevation, ψ is the grazing angle, and λ is the electromagnetic wavelength. The relationship of σ_h to wind speed is derived from the Phillips' saturation curve spectrum [6] and is given by

$$\sigma_h = 0.0051\, u^2$$

where u is wind speed in meters per second.

Parabolic equation (PE) models use several techniques for surface roughness. The most common technique employs the Miller-Brown model also, but in this case grazing angle must be estimated, since it is not an implicit quantity in the usual parabolic equation method. This is normally done with a spectral estimation technique or an independent geometric optics calculation [7]. An alternate technique also uses the Miller-Brown model, but casts the PE equations in terms of incident and reflected plane waves, so that grazing angle is implicit in the method [8]. However, this method has proven to be very computationally intensive and is not very practical. A recent PE method that shows good promise is the use of non-local boundary conditions [9]. These PE methods all have advantages over the waveguide method since they are usually robust and allow for range-varying refractive index profiles. It is the goal of our current work to eventually recommend a rough surface PE method, but for this paper only the MLAYER model is used since it is assumed to be more rigorous.

GREEK EXPERIMENT

A multi-frequency over water over-the-horizon propagation experiment was conducted in the Aegean Sea in 1972 [10]. Transmitters were installed on Naxos Island and receivers were installed on Mykonos Island for an unobstructed path of 35.2 km. Frequencies of 1.0, 3.0, 9.6, 18.0, and 37.44 GHz were used, but in this paper only the highest frequency is considered to maximize the influence of sea roughness. Only horizontal polarization was used. At 37.44 GHz, the transmitter height was 5.1 m above msl. Two receiver heights were used at heights of 3.6 and 8.6 m above msl. Signals were averaged for 5 minutes for each receiver height during each 15 minute period, and approximately 12 days of data were recorded in November 1972.

Figures 1 and 2 show the MLAYER model results for the 3.6 and 8.6 m receiver antennas, respectively, including 6.6 dB for average absorption by oxygen and water vapor on the path. Propagation loss in dB is shown plotted versus evaporation duct height, parametric in wind speed. Both figures show that a duct height of at least 4 meters and a wind speed of at least 4 m/s are required before there is any substantial difference in results compared to the smooth surface case. It is also apparent that the lower antenna height of Figure 1 is affected more than the higher antenna height of Figure 2. Figures 3 and 4 show propagation loss versus time calculated from MLAYER for both smooth and rough conditions and the corresponding observed data. The calculations are based on hourly meteorological measurements made at Mykonos at the receiver site. The sea temperature and air temperature, humidity, and wind speed were used to derive a stability-dependent refractivity profile in the manner described by Paulus [11]. MLAYER then used this profile and the local wind speed to compute propagation loss, which was then corrected for absorption by oxygen and water vapor using the methods of [12]. To maximize the influence of surface roughness, Figures 3 and 4 show results only for duct heights of at least 4 m and wind speeds of at least 4 m/s. Figures 3 and 4 also show reference lines for free space and standard-atmosphere troposcatter levels. The modeled results for a rough surface are closer to the observed data for both antenna heights, but the results are best at the lower height.

Figure 5 shows cumulative distributions of the same data as in Figures 3 and 4. At the low antenna, the median loss for the rough model was 3 dB lower than observed, while the smooth model was 18 dB less than observed. It appears the rough surface model in MLAYER is

accounting for 15 of the 18 dB that the smooth-surface model is under-predicting in the observations, and based on this low antenna height one might conclude the model is working fairly well. However, at the higher antenna height, the median rough surface model is 8 dB less than observed, while the smooth surface model is 14 dB less than observed. The reason for this poorer performance at the higher antenna height is not known. Since many of the meteorological observations indicated a wind flow across the land at Mykonos, a cross check of the distributions of Figure 5 was prepared from long-term meteorological data. One of the products available in [2] is an annual cross distribution of wind speed with duct height. Since the individual distributions of both wind speed and duct height for November are quite close to the annual distributions, it seemed reasonable to use the annual cross distribution to prepare a propagation loss distribution using MLAYER. However, in this case duct heights less than 4 m and wind speeds less than 4 m/s cannot be excluded when comparing to the observed data, since there is no way of knowing which observed loss points to exclude. Thus all duct heights and wind speeds were considered, and the results are presented in Figure 6. The results are very close to those obtained using the actual meteorological measurements in Figure 5, including the poorer performance of the rough surface model for the higher antenna.

CALIFORNIA EXPERIMENT

A propagation experiment was conducted in March 1973 in California using the same 37.44 GHz equipment from the Greek experiment. The transmitter was on Catalina Island with an antenna height 5.3 m above msl. The receiver was on San Clemente Island and the two receiver antenna heights were 9.1 and 13.6 m above msl. The path was an unobstructed over-water path 35.7 km long. Horizontal polarization was used in this experiment also. Data were collected for approximately 24 days in March 1973.

Figure 7 shows the cumulative distributions of modeled and observed propagation loss for the 2 antenna heights using the same methods as for the Greek experiment shown in Figure 6. It was again fortuitous that the individual distributions of both duct height and wind speed for March were very close to the annual distributions, which again seemed to justify the use of the annual cross distribution of duct height and wind speed used to prepare the modeled distributions of propagation loss. In California the lower antenna height was about equal to the higher height in Greece, and the corresponding distributions in Figures 6 and 7 are roughly comparable. For the 9.1 m antenna height in Figure 7, the median rough surface modeled loss was 6 dB less than the observed median loss, while the smooth model result was 12 dB less. For the higher antenna, the median rough and smooth results were 12 and 14 dB less than observed, respectively. Thus the trend observed in the Greek Island experiment of a worse match with increasing antenna height is also apparent in the California measurements.

DISCUSSION

Figure 8 shows the difference between the median observed loss and the median modeled loss for rough surface conditions versus receiver antenna height for both experiments. This error versus height follows an approximate linear relationship of 1 dB per meter. It is not clear what the source of this error is. The error may be in the use of the Miller-Brown model in MLAYER, which has never been verified for this over-the-horizon application. It may also be a result of some experimental error, such as misalignment of antennas. Both experiments used antennas with half-power beamwidths of only 42 minutes, but alignments were checked to within 3 minutes of arc by various methods. The error may also be due to non-representative meteorological conditions encountered during the experiments which were then not well matched by the long term historical meteorological data. The error may also be related to a variation of gaseous absorption with height in the first few meters, which was not accounted for in the models. For Greece an average total absorption of 6.6 dB was assumed for the path based on historical data and for California a similar total of 5.4 dB was assumed.

To resolve the above described error, a combination of more analysis and radio propagation experiments are apparently needed. This analysis will continue on other existing propagation data sets as practical. A new propagation experiment is planned for Spring 1998 at Wallops Island, Virginia that may help to explain the error noted in this paper. This experiment will include frequencies as high as 18 GHz, but the proper combination of high duct heights and high wind speeds may not occur during the experiment to fully resolve the rough surface modeling issues. An experiment more focused on the rough surface modeling issues would be desirable in an area of high duct heights and high wind speeds. Such an experiment called the Rough Evaporation Duct (RED) experiment is tentatively planned for Hawaii in summer 2000 which will use frequencies of 3, 10, and 18 GHz and collect continuous propagation data on a fixed 45 km path for 30 to 60 days.

CONCLUSION

Although the rough surface model in MLAYER seems to be working at the lowest receiver antenna heights, there is an apparent systematic error of about 1 dB per m of receiver antenna height. The model appears incomplete. At 37 GHz, errors of at least 12 dB (24 dB for radar applications) are possible for important shipboard applications.

REFERENCES

[1] Richter, J.H. and H.V. Hitney, "The Effect of the Evaporation Duct on Microwave Propagation," Naval Electronics Laboratory Center TR 1949, Apr. 1975.

[2] Patterson, W.L., "Historical Electromagnetic Propagation Condition Database Description," Naval Ocean Systems Center TD 1149, Sep. 1987.

[3] Hitney, H.V. and R. Vieth, "Statistical Assessment of Evaporation Duct Propagation," *IEEE Trans. Antennas & Propagat.*, Vol. 38, no. 6, June 1990.

[4] Baumgartner, G.B., "XWVG: A Waveguide Program for Trilinear Tropospheric Ducts," Naval Ocean Systems Center TD 610, June 1983

[5] Miller, A.R., R.M. Brown, and E. Vegh, "New derivation for the rough-surface reflection coefficient and for the distribution of sea-wave elevations," IEE Proc., Pt. H, 131, 2, April 1984, pp 114-116.

[6] Phillips, O.M., "Dynamics of the Upper Ocean," London, Cambridge Univ. Press, 1966.

[7] Dockery, G.D. and J.R. Kuttler, "An Improved Impedance-Boundary Algorithm for Fourier Split-Step Solutions of the Parabolic Wave Equation," *IEEE Trans. Antennas & Propagat.*, Vol. 44, no. 12, Dec. 1996.

[8] Janaswamy, R., "A Rigorous Way of Incorporating Sea Surface Roughness into the Parabolic Equation," Naval Postgraduate School Report NPS-EC-95-008, Sep. 1995.

[9] Levy, M., "Rough Sea Surface Effects on Ducting Propagation," Battlespace Atmospherics Conference, Space and Naval Warfare Systems Center, 2-4 Dec. 1997.

[10]Richter, J.H. and H.V. Hitney, "Antenna Heights for the Optimum Utilization of the Oceanic Evaporation Duct," Naval Ocean Systems Center TD 1209, vols. 1 and 2, Jan 1988.

[11]Paulus, R.A., "Propagation in the Evaporation Duct," Naval Command, Control and Ocean Surveillance Center, RDT&E Division TR 1644, Mar. 1994.

[12]International Radio Consultative Committee (CCIR), "Propagation in Non-Ionized Media," Recommendations and Reports of the CCIR, Vol. V, Report 719-3, 1990.

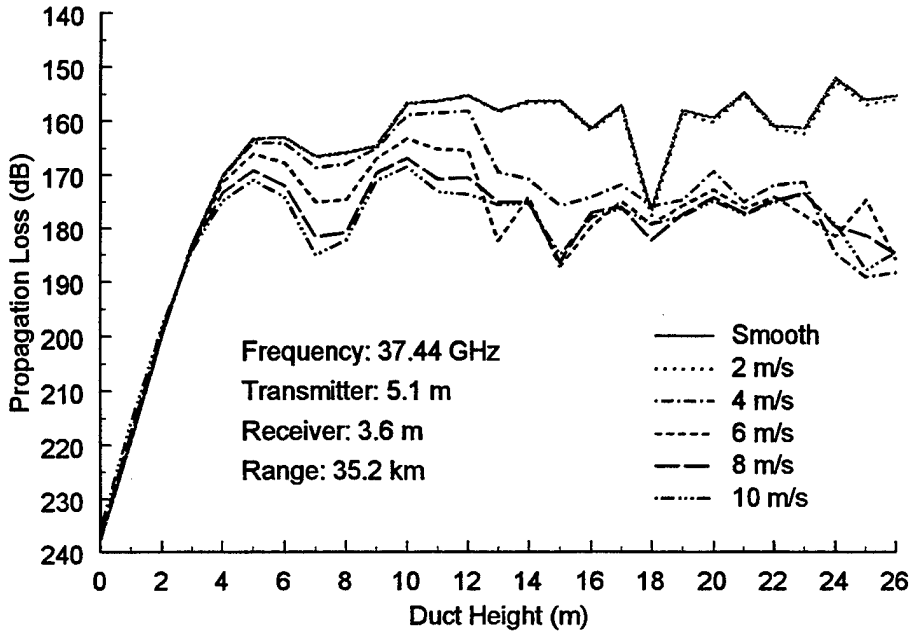

Figure 1. Propagation loss versus duct height from MLAYER for the Greek experiment 3.6 m antenna height, parametric in wind speed.

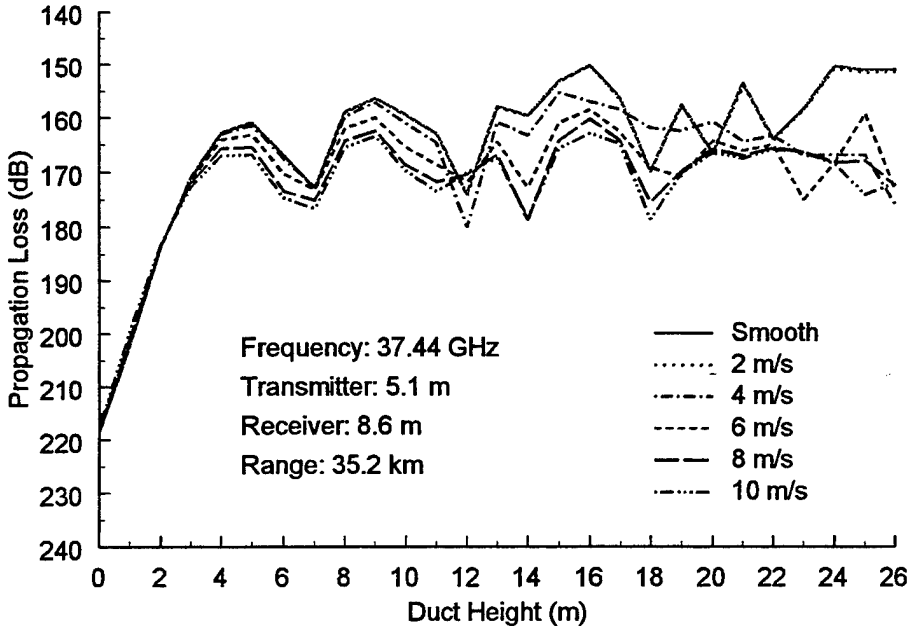

Figure 2. Propagation loss versus duct height from MLAYER for the Greek experiment 8.6 m antenna height, parametric in wind speed.

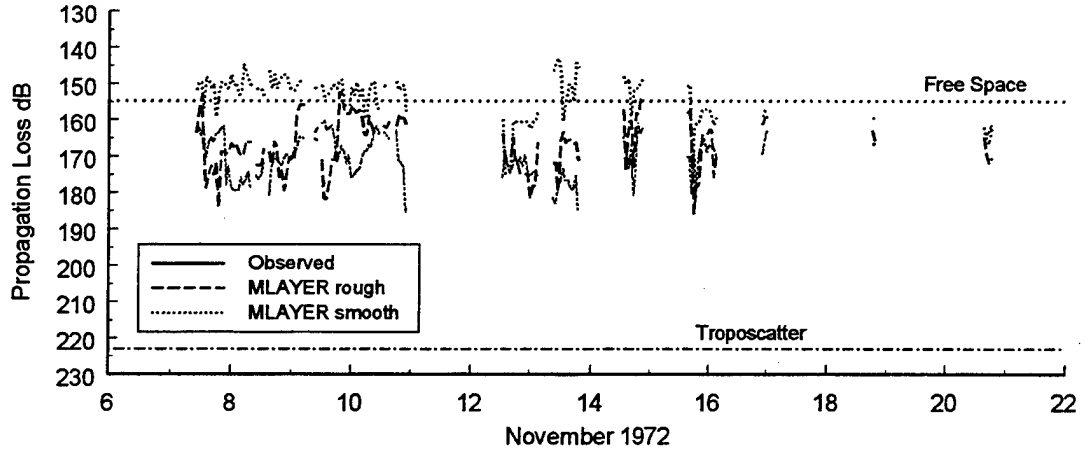

Figure 3. Propagation loss versus time for the Greek experiment for the 3.6 m receiver antenna and duct heights of at least 4 m and wind speeds of at least 4 m/s.

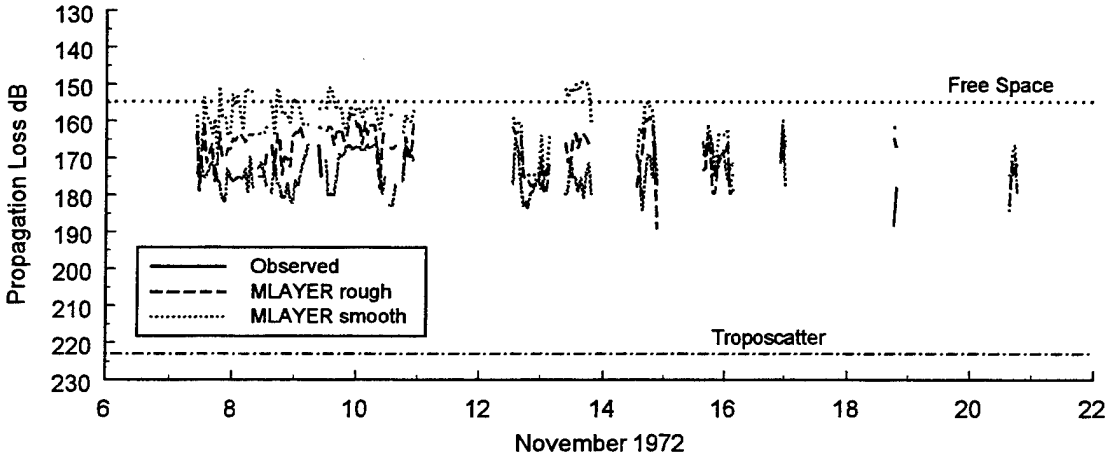

Figure 4. Propagation loss versus time for the Greek experiment for the 8.6 m receiver antenna and duct heights of at least 4 m and wind speeds of at least 4 m/s.

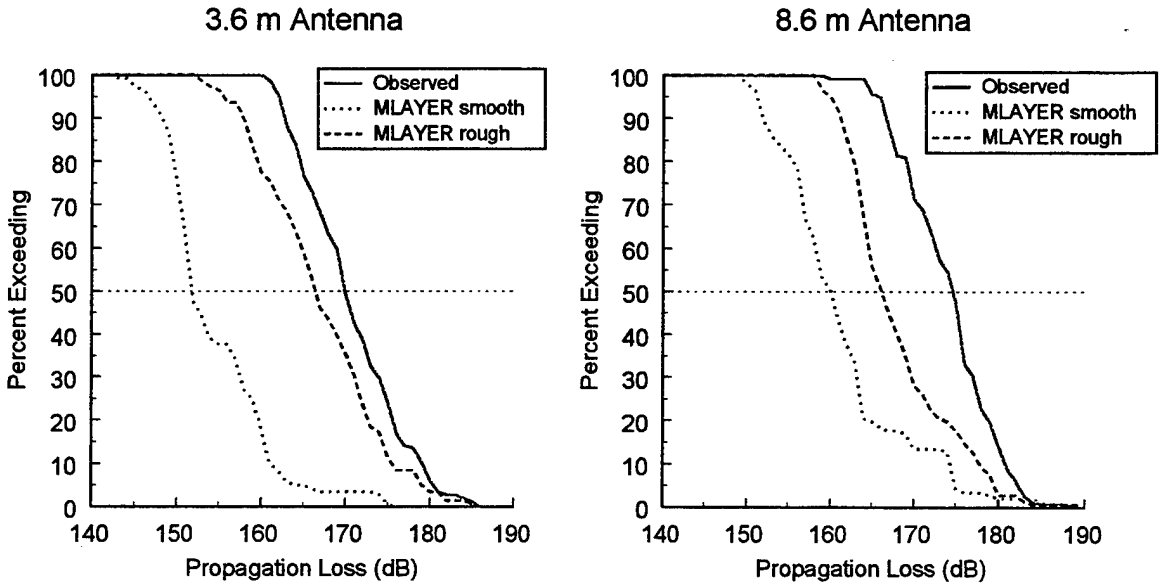

Figure 5. Cumulative propagation loss distributions for the Greek experiment for both receiver antenna heights for actual meteorological measurements. Only duct heights of at least 4 m and wind speeds of at least 4 m/s were used.

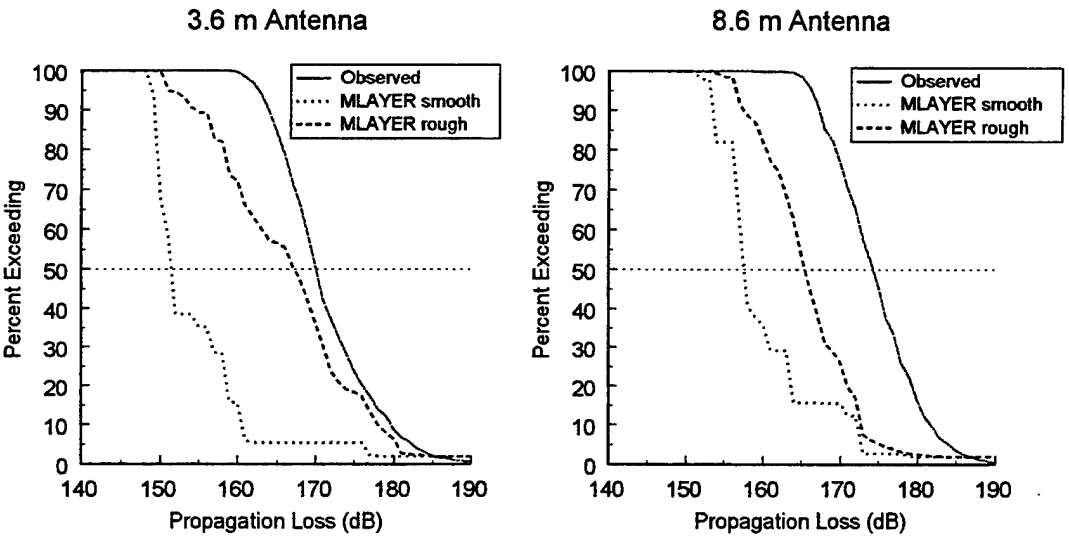

Figure 6. Cumulative propagation loss distributions for the Greek experiment for both receiver antenna heights based on historical meteorological measurements.

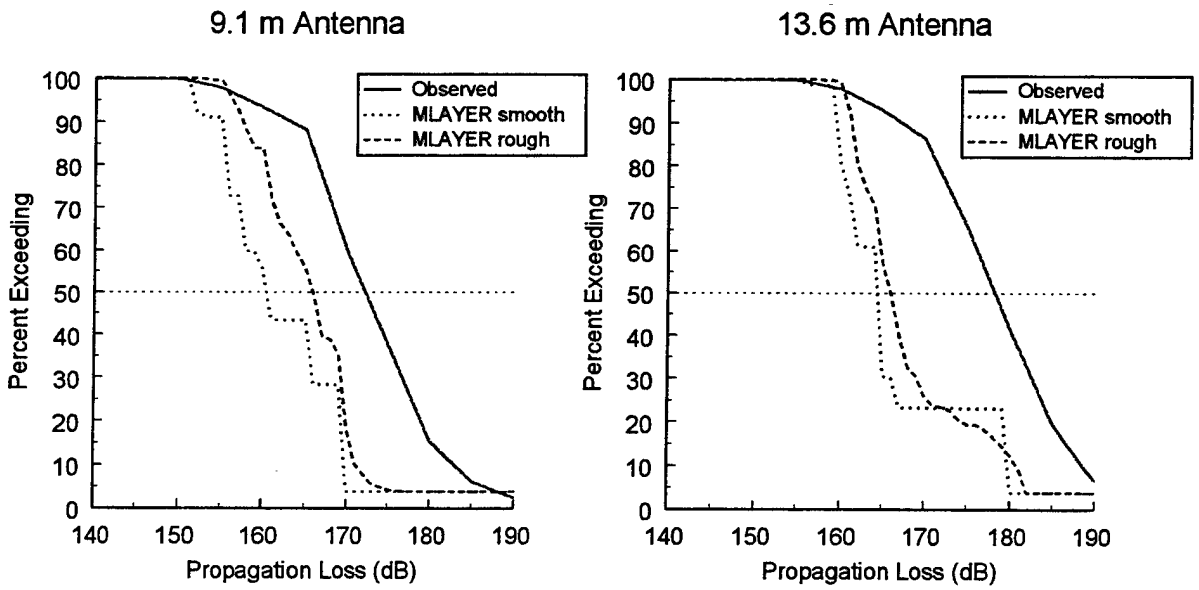

Figure 7. Cumulative propagation loss distributions for the California experiment for both receiver antenna heights based on historical meteorological measurements.

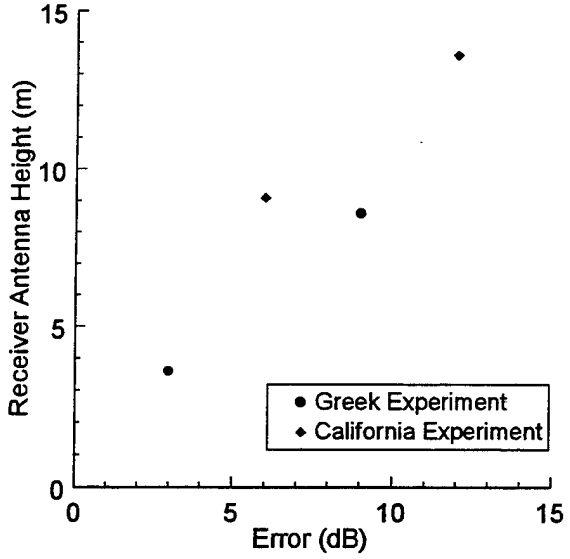

Figure 8. Error between observed and rough model median loss versus receiver antenna height.

ROUGH SEA SURFACE EFFECTS ON DUCTING PROPAGATION

Mireille F. Levy
Rutherford Appleton Laboratory
Chilton, Didcot, Oxon OX11 0QX, UK
E-mail: m.levy@rl.ac.uk

ABSTRACT

Propagation over the rough sea surface in a ducting environment can be treated by parabolic equation techniques. If the surface can be defined in terms of effective reflection coefficients for plane-wave incidence, efficient non-local parabolic equation algorithms are available. Since they do not require the determination of local incidence angles, these should work equally well in all ducting environments. However preliminary results indicate a problem for large surface refractivity gradients and very rough surfaces. This could be caused by the possible dependence of effective reflection coefficients on surface refractivity gradients.

1. INTRODUCTION

The performance of shipborne radar systems is greatly affected by the ducts which form in the air/sea boundary layer. Low altitude coverage can be extended substantially as electromagnetic energy becomes trapped in ducting conditions. At frequencies above 10 GHz or so, the propagation mechanism which allows the trapped energy to propagate at great distances becomes very sensitive to rough surface effects: basically the rougher the sea surface, the more energy will be scattered diffusely, leaving less and less coherent reflections to propagate along the duct. This effect is illustrated in Figure 1, which shows the coverage of a 10 GHz source in a surface duct. Figure 1a corresponds to propagation over a smooth surface, where the ducted energy is allowed to bounce up and down in the duct with negligible losses. In Figure 1b, the sea surface is rough, with r.m.s wave height of 1 m, corresponding to a wind speed of 14 m/s. After the first bounce on the rough surface, most of the energy has been scattered away and the benefits of ducting propagation have been lost. It is of course crucial for many operational applications to assess these effects as accurately as possible.

Parabolic equation (PE) models have the potential to model both the rough sea surface and the refractive index variations [1]. The most accurate method consists in representing the rough surface explicitly, using spectral models for wind-generated seas [2]. This is time-consuming since quite small range steps must be used to represent the sea surface accurately. Also each run of the model provides just one realization of the random propagation process, and Monte-Carlo simulations are needed to get average values of the field.

In order to speed-up parabolic equation calculations, one may try to replace the undulating sea surface by a flat surface with a reduced reflection coefficient. The most commonly used model is the Ament-Miller-Brown model, which gives the roughness reduction factor as a function of rms wave height of the rough surface and grazing angle of the incident electromagnetic plane wave [3,4].

One difficulty with ducting environments is that the field can non longer be described globally in terms of incident and reflected plane waves. One approach is to assume that one can still do this at least

This work was carried out with the support of the Radio Communications Agency of the DTI. Participation to BAC'97 was supported by Department of the Navy Grant N00014-98-1-4009 issued by the Office of Naval Research European Office.

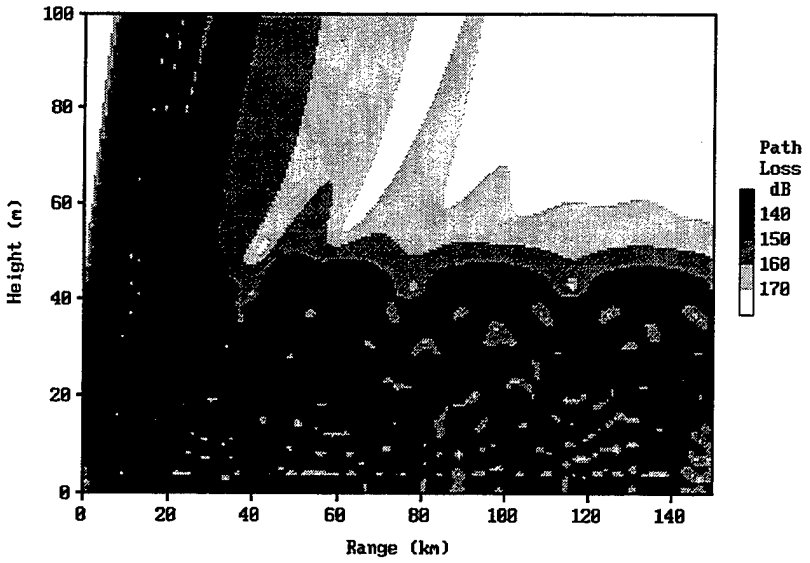

a) Smooth sea

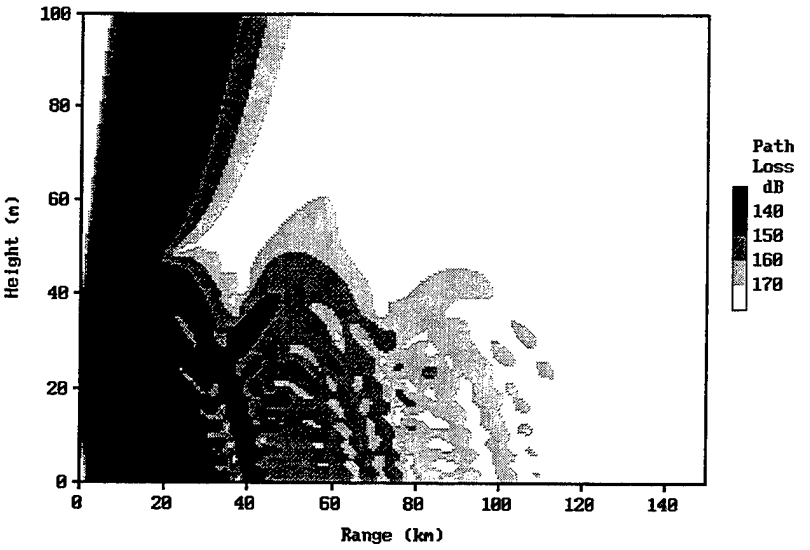

b) rough sea; rms wave height = 1 m.

Figure 1. Effects of rough sea surface on 10 GHz source in ducting environment.

at each range, a main grazing angle is computed either from a ray-trace or from a spectral algorithm like MUSIC, and this angle is used to define a local boundary condition for the PE model. The boundary condition is of the form

$$\frac{\partial u}{\partial z}(x,0) = ik\delta(\theta(x))u(x,0) \tag{1}$$

where k is the vacuum wave number, $\theta(x)$ is the grazing angle at range x and δ is the surface impedance modified by the roughness coefficient corresponding to the grazing angle. A very efficient split-step/Fourier algorithm, the discrete mixed Fourier transform (DMFT), may be used to implement this model [5].

2. NON-LOCAL METHODS

The local boundary condition approach has drawbacks: in some strong ducting cases, several families of rays may intersect at a given range, and the single incidence angle approximation may be inaccurate. Also, the strong surface gradients associated with evaporation ducts make it very difficult to define a dominant grazing angle beyond the optical horizon [5]. For these reasons it is worth looking at the non-local formulation of boundary conditions [6]. The idea here is to decompose the field into plane waves along the horizontal direction and to use the appropriate plane wave boundary condition for each plane wave component in the spectral domain. No approximations are made beyond the original parabolic approximation, which neglects backscatter. The resulting boundary condition is of the form

$$u(x,0) = \int_0^x \frac{\partial u}{\partial z}(t,0) w(x-t)\,dt \tag{2}$$

where the convolution kernel w is the inverse Fourier transform of the admittance function

$$W(s) = \frac{i}{\sqrt{4\pi k s}} \frac{1+R(s)}{1-R(s)}.$$

The spectral parameter s corresponds to a horizontal plane wave component with grazing angle

$$\theta = \sqrt{\frac{4\pi s}{k}}.$$

Equation (2) shows that the boundary condition at range x depends on the field at all previous ranges, hence the "non-local" terminology. Grazing angles are not required: the necessary information is implicitly present in the spectral domain corresponding to horizontal plane wave decomposition.

There is no difficulty implementing the non-local condition (2) with PE methods using a finite-difference scheme, but this has the usual drawback of requiring small range steps, so that integration times can become impractically long. A Fourier split-step implementation is much more desirable in terms of efficiency. A matched transform approach was presented in [7], replacing the field with a new function matched to the boundary condition (2) and then propagating this with a SINE transform. This technique is actually quite slow because it involves solving an integral equation at each step, and it can also run into stability problems.

Here we use a much more efficient approach, where we still define a matched function, but this time in terms of a discretized version of Equation (2). The split-step Fourier solution now involves a generalization of the Discrete Mixed Fourier Transform of [5]. The great advantage of the Generalized Discrete Mixed Fourier Transform (GDMFT) is that the integral equation is replaced by a straighforward tridiagonal matrix inversion, resulting in a fast and stable algorithm.

We first rewrite Equation (2) as

$$u(x,0) = \int_0^{x-\Delta x} \frac{\partial u}{\partial z}(t,0) w(x-t)\,dt + \int_0^{x-\Delta x} \frac{\partial u}{\partial z}(x-t,0) w(t)\,dt \tag{3}$$

This can be written in the form

$$\frac{\partial u}{\partial z}(x,0) + \alpha u(x,0) + \gamma(x) = 0 \tag{4}$$

The term $\gamma(x)$ represents the non-local part of the boundary condition, approximated by a constant between one grid range and the next. The GDMFT consists of the following sequence of operations:

- transform the field with the DMFT corresponding to α;
- propagate in transform space using non-homogeneous first-order differential equation in range;
- invert DMFT at forward range as usual.

Computational overheads depend on the shape of the convolution kernel w. A gentle roll-off, typical of very rough surfaces, gives relatively long memory, but in most cases the kernel drops very rapidly to zero and the non-local boundary condition has short memory. To illustrate this point, Figure 2 shows the kernels corresponding to the Ament-Miller-Brown roughness factor for a frequency of 10 GHz and various wind speeds.

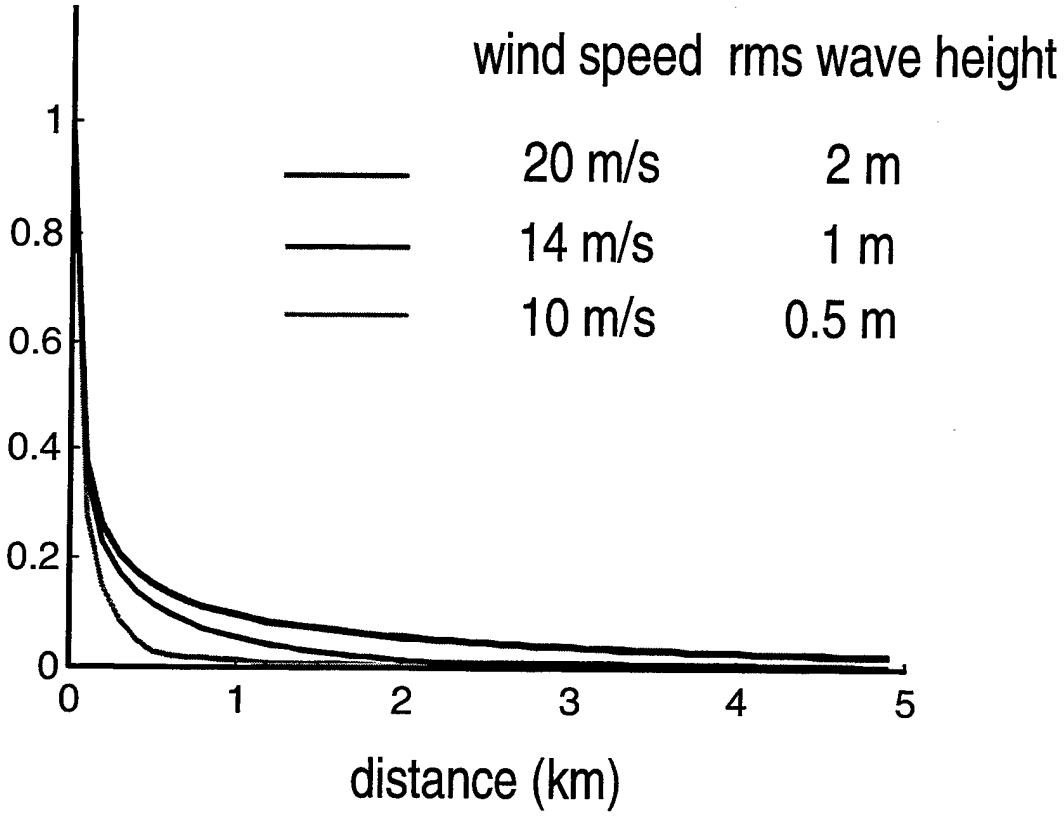

Figure 2. Ament-Miller-Brown rough sea kernel w at 10 GHz for several wind speeds.

For a wind speed of 10 m/s, the influence of ranges more than a kilometre or so before the current range is negligible, but this distance increases to 2 km for a wind speed of 14 m/s. For a wind speed of 20 m/s, the kernel rolls off quite slowly and ranges more than 5 km from the current range still play some role in the determination of the boundary condition.

3. RESULTS AND DISCUSSION

The GDMFT implementation of the non-local boundary condition (2) has been tested against local boundary conditions applied with a range-varying incidence angle calculated with a ray-trace. Results

are in good agreement for moderate wind speeds, as shown in Figure 3. The source here is a 10 GHz vertically polarized antenna located at 25 m above mean sea level. Wind speed is 10 m/s, and the refractive index environment is a bilinear surface duct (gradient -400 M-units/km between 0 and 50 m). Figure 3 shows path loss against range at 25 m amsl.

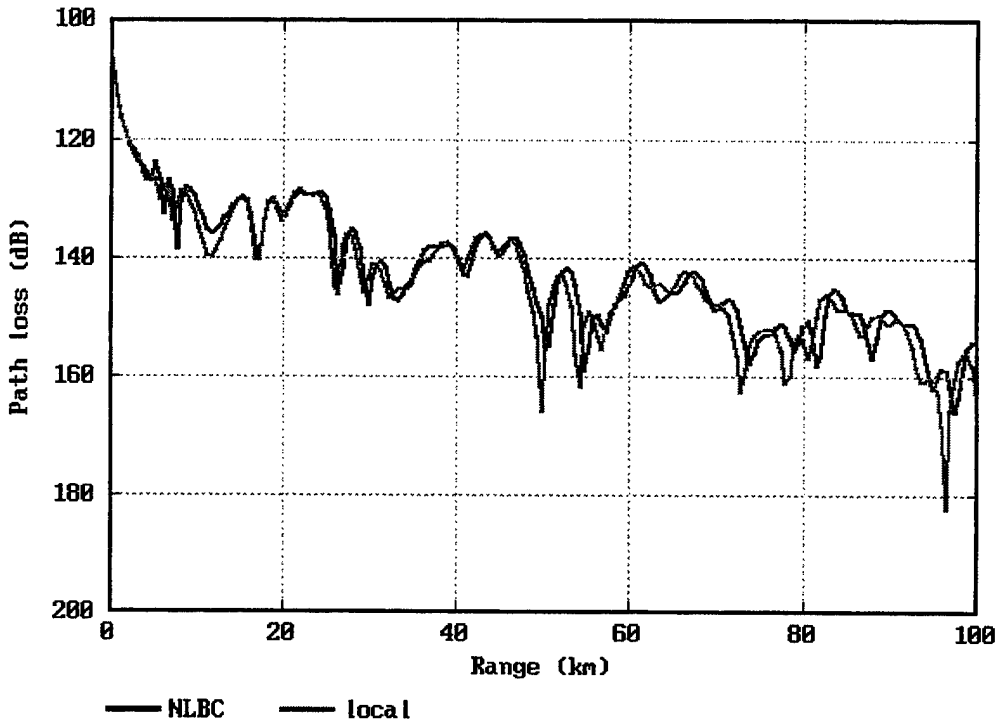

Figure 3. Comparison of local and non-local models for 10 GHz antenna in strong surface duct.

Comparisons for stronger wind speeds are underway. The GDMFT has also been applied to evaporation duct situations, where local methods run into the difficulty of defining a local grazing angle. There were no convergence problems, and results were satisfactory for moderate and strong wind speeds. However surprising results were obtained for very strong wind speeds, for which an increase in signal was found instead of the expected decrease. Figure 4 shows coverage diagrams for a 10 GHz source in a 24 m evaporation duct, for varying wind speeds. The field decreases as the wind speed increases up to 14 m/s, but increases again at 20 m/s. This anomaly is currently under investigation. One possible cause is the use of the Ament-Miller-Brown model, which was derived for a homogenous background medium. There is no reason to suppose that the reflection coefficients obtained from this model would be valid under ducting conditions, let alone with evaporation ducts where surface gradients are very large (typically -50000 M-units/km). Indeed the Ament-Miller-Brown derivation relies on the fact that rays are straight lines to compute the phase difference between the direct and reflected rays, and it is not clear how accurately this extends to curved rays.

4. CONCLUSIONS

Propagation over a rough surface described in terms of reflection coefficients for plane wave incidence can be treated rigorously with parabolic equation techniques using the non-local boundary condition formulation. Results based on the Ament-Miller-Brown roughness model are satisfactory for surface ducts and also for evaporation ducts at moderate to strong wind speeds. However with evaporation ducts they display an unexpected behaviour as wind speed increases. It would be useful to investigate the derivation of mean reflection coefficients for a rough surface in the presence of ducting. If rough surface

reflection coefficients depend on the surface refractivity gradient, very different results could be obtained for evaporation ducts in view of their extremely large surface gradients.

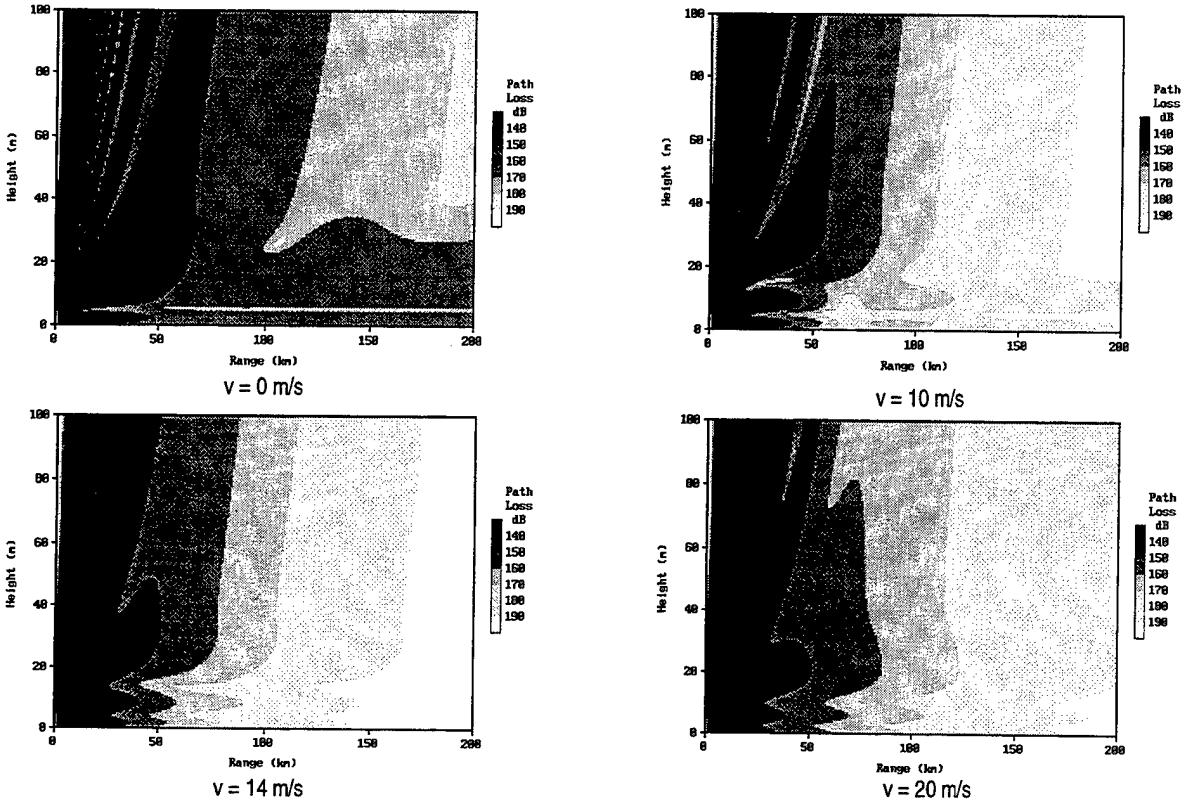

Figure 4. 10 GHz source in 24 m evaporation duct with several wind speeds.

5. REFERENCES

1. A .E. Barrios, "A terrain parabolic equation model for propagation in the troposphere", *IEEE Trans. Antennas Propagat.*, vol. 42, pp. 90-98, 1994.

2. M.F. Levy, "Parabolic equation modelling of backscatter from the rough sea surface", AGARD-CP-501, paper 7, 1991.

3. W.S. Ament, "Towards a thoery of reflection by a rough surface", *Proc. IRE*, vol. 41, pp. 142-146, 1953.

4. A.R. Miller, R.M. Brown and E. Vegh, "New derivation for the rough-surface reflection coefficient and for the distribution of sea-wave elevations", *IEE Proc.*, vol. 131, Pt H, pp. 114-116, 1984.

5. G.D. Dockery and J.R. Kuttler, "An improved impedance algorithm for Fourier split-step solutions of the parabolic wave equation", *IEEE Trans. Antennas Propagat.*, vol. 44, pp. 1592-1599, 1996.

6. J.S. Papadakis, "Exact, nonreflecting boundary conditions for parabolic-type approximations in underwater acoustics", *J. Comput. Acoust.*, vol. 2, pp. 83-98, 1994.

7. M.F. Levy, "Modelling of rough surface effects with the matched transform PE", AGARD-CP-582, paper 13, 1996.

Electromagnetic Wave Scattering from a Rough Surface in a Surface-Based Duct Created by a Linear-Square Refractive Index Profile

Ra'id S. Awadallah and Gary S. Brown
ElectroMagnetic Interactions Laboratory
Bradley Department of Electrical Engineering
Virginia Tech
Blacksburg, VA 24061

Abstract - It is evident that the most rigorous formalism of the rough surface scattering problem in either homogeneous or inhomogeneous media is the boundary integral equation formalism. In this approach, surface currents are determined by solving an integral equation. These currents are then used in the appropriate radiation integrals to determine the scattered field in the medium.

The problem of low grazing angle (LGA) electromagnetic wave scattering from a rough surface in a ducting environment created by the presence of a linear-square refractive index profile is formulated via an integral equation approach. The kernel (Green's function) that appears in the resulting integral equation is obtained in closed form using the method of steepest descents. The resulting integral equation is then solved using the Method of Ordered Multiple Interactions (MOMI) that was developed by D. Kapp and G. Brown to tackle the problem of LGA scattering. The proposed method incorporates the effects of surface roughness and medium inhomogeneity on the scattering problem in an exact and rigorous manner.

I. Introduction

The problem of wave propagation and scattering over rough terrain in a ducting environment has been receiving considerable attention in the literature. A very popular approach to modeling such a problem is the parabolic wave equation (PWE) approximation [1]. In this method, the Helmholtz equation is replaced by a PWE under the assumption of predominant forward propagation and scattering. The resulting PWE is an initial value problem that can be solved numerically by marching techniques such as the split-step Fourier algorithm. As is obvious from the assumptions on which it is based, the accuracy of the PWE approximation deteriorates in situations involving an appreciable backscattered field, i.e., when the terrain under consideration is rough. Furthermore, the PWE-based techniques crudely account for effects of surface roughness and medium inhomogeneity on the scattering problem. There is a number of formulations possible for the PWE [2].

An alternative approach, that became more promising after the development of the Method of Ordered Multiple Interactions (MOMI) by D. Kapp and G. Brown [3], is the integral equation approach. In this approach, surface currents are determined by solving the Magnetic Field Integral Equation (MFIE) using MOMI. These currents are then used in the appropriate radiation integrals to calculate the field scattered by the

surface. In a homogeneous medium, the implementation of MOMI is straightforward since the homogeneous-space Green's function (kernel) used in the integral equation is well known. This is not the case, however, in inhomogeneous media where the Green's function is not readily known. Spectral ($\vec{k}$ -space) representations of Green's functions in inhomogeneous media can be obtained in closed-form for some special refractive index profiles. One of these profiles being the linear-square refractive index profile ($n^2(z) = a - bz$, where a and b are constants). A space domain expression of the Green's function is obtained by taking the inverse Fourier transform of the spectral representation. The above procedure results in an integral that cannot be evaluated exactly and one needs to resort to either a numerical or asymptotic evaluation. Numerical integration of such integrals does not easily converge because of the oscillatory nature of the integrands, and the only choice left is the asymptotic evaluation which is accurate either in the high frequency limit or for observation points located in the far-field of the source point [4].

In this paper, an explicit expression for the Green's function in a medium with a linear-square refractive index profile is obtained using the method of steepest descents. This Green's function is then used in the MOMI approach to study wave scattering from a rough surface in a surface-based duct created by such a refractive index profile. The proposed method incorporates the effects of surface roughness and medium inhomogeneity in an exact and rigorous manner. The results are compared to those obtained using PWE approximation.

II. Problem Formulation

The Green's function for the scalar Helmholtz equation in a medium with a refractive index profile that varies only in the z direction is governed by

$$\frac{\partial^2 G}{\partial x^2} + \frac{\partial^2 G}{\partial z^2} + k_o^2 n^2(z) G = -\delta(x - x')\delta(z - z'), \tag{1}$$

where $k_o = 2\pi/\lambda_o$ is the free-space wavenumber. A time-harmonic dependence of $\exp(j\omega_o t)$ is suppressed in (1). The linear-square refractive index profile in our case is given by

$$n^2(z) = 1 - \varepsilon z, \tag{2}$$

where ε is a constant called the ducting parameter.

In order to solve (1) for the Green's function, we proceed as follows: First we Fourier transform the x variable in (1) into the k_x-space. The resulting ordinary differential equation, which governs $\tilde{G}(k_x, z)$ (the x-Fourier transform of $G(x,z)$) is the so-called Stokes equation. The solution $\tilde{G}(k_x, z)$ is constructed in the k_x space and then transformed back into the space domain to obtain $G(x,z)$. The transformation integral is very cumbersome to handle even numerically because of the oscillatory nature of the integrand. The preferred method was via a saddle-point technique.

The problem of low-grazing angle (LGA) electromagnetic wave scattering from a 1-D randomly rough perfectly conducting surface located in a surface-based duct created

by a linear-square refractive index profile is formulated in terms of the Magnetic Field Integral Equation (MFIE). The general idea by which the derivation of MFIE is conducted can be described as follows. An incident field illuminates a surface and excites surface currents on it. These surface currents radiate and give rise to a scattered field. By writing an expression for the total field as the sum of incident and scattered fields, bringing the observation point in this expression to the surface and applying the relevant boundary condition, one obtains MFIE. This is then solved for the surface currents. Once these currents are known, the scattered field off the surface can be calculated using the appropriate propagator. The MFIE solved in this work is given by:

$$J(x) = J^i(x) + \int_X P(x,x')J(x')dx' \tag{3}$$

where $J(x)$ is the unknown surface current, $P(x,x')$ is the propagator and $J^i(x)$ is the current induced on the surface due to the incident field only and it is usually referred to as the "Kirchhoff current". The domain of integration X in (3) is infinite in principle. However, it can be made finite by using an appropriately tapered incident field. For TE waves, i.e. when the incident electric field E^i is tangential to the surface, the quantities involved in (3) are defined as follows:

$$J^i(x) = 2\frac{\partial E^i(x,z)}{\partial n}\Big|_{z=\zeta(x)}, \tag{4}$$

$$J(x') = \frac{\partial E(x',z')}{\partial n'}\Big|_{z'=\zeta(x')}, \tag{5}$$

$$P(x,x') = -2\frac{\partial G(x,x')}{\partial n}\sqrt{1+\zeta_x^2(x')}, \tag{6}$$

For TM waves, i.e. when the incident magnetic field H^i is tangential to the surface, the above quantities are defined as follows:

$$J^i(x) = 2H^i(x,z)\Big|_{z=\zeta(x)}, \tag{7}$$

$$J(x') = H(x',z')\Big|_{z'=\zeta(x')}, \tag{8}$$

$$P(x,x') = 2\frac{\partial G(x,x')}{\partial n'}\sqrt{1+\zeta_x^2(x')}. \tag{9}$$

In (4)-(9), $G(x,x')$ is the Green's function propagator, $\partial/\partial n$ is the derivative along the surface normal at a given point, E and H are the total electric and magnetic fields evaluated on the surface. The factor $\sqrt{1+\zeta_x^2(x')}$ results from converting the integral along the rough surface into an integral along the mean surface plane.

For the rough surfaces under consideration, it is convenient to work with Cartesian coordinates where the $x-$axis extends along the mean plane of the surface and the surface height above the mean plane is given by the function $z=\zeta(x)$. The x-coordinate of all surfaces used in this work is centered at the origin.

IV. Results and Discussion

The geometry of the problem under consideration is shown in Fig. 1.

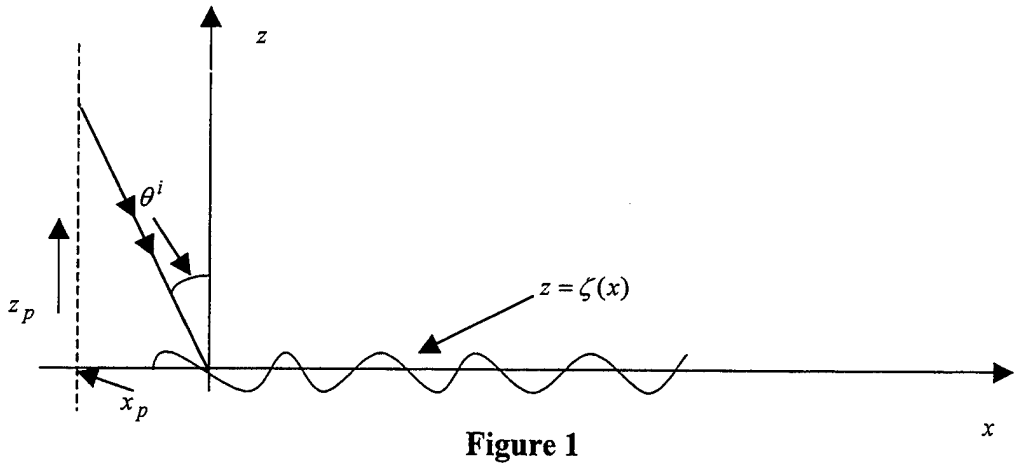

Figure 1

The field generated by the source antenna aperture located on the initial plane, (x_p, z_p), in Figure 1 is defined as follows:

$$E_a(x_p, z_p) = \frac{1}{\sqrt{\pi}\Delta\theta} \int_{-\pi/2}^{\pi/2} e^{\left[-(\theta-\theta^i)^2/(\Delta\theta)^2\right]} \exp\left[-jk_o\left(x_p \sin\theta - z_p \cos\theta\right)\right] d\theta \qquad (10)$$

where θ^i is the angle of incidence, $\Delta\theta = 2/k_o g \cos\theta^i$ and the parameter g has been called the half-beam waist by some authors. The integral in (10) is evaluated numerically to obtain the field $E_a(x_p, z_p)$ on the initial plane located at $x = x_p$; in this study, $x_p = -500\,\lambda_o$. Using equivalence theorem and given the knowledge of $E_a(x_p, z_p)$, one can calculate the field that exists everywhere inside the duct, specifically the field incident at the rough surface.

Numerical simulations of the TE and TM cases have been carried out for sinusoidal surfaces as well as random rough surfaces which were generated via the spectral method [6]. Figure 2 displays the magnitude (dB) of the field scattered by the smooth sinusoidal surface, $z = \zeta(x) = A + A\cos(k_s x)$; $A = 1.5/\pi\,\lambda_o$ and $k_s = 2\pi/50\,\lambda_o$, for TE polarization. In this example, $\theta^i = 85°$, $g = 200\,\lambda_o$, $\varepsilon = 0.0001$ and $SL = 1000\,\lambda_o$ (SL stands for illuminated surface length. In the case of two illuminated spots discussed below, SL refers to the total length of the two illuminated portions of the surface). Figure 3 shows the magnitude (dB) of the field scattered by a randomly rough surface having a Gaussian spectrum with a height variance of $0.25\,\lambda_o$ and a correlation length of $2\,\lambda_o$, for TM polarization. In this example, $\theta^i = 80^o$, $g = 40\lambda_o$, $\varepsilon = 0.0001$

and $SL = 300\ \lambda_o$. Figure 4 shows the magnitude (dB) of the TE polarized field scattered by a random rough surface having a Gaussian height distribution and a Pierson-Moskowitz (PM) power spectrum. The PM surface is characterized by specifying the wind speed v and the operating electromagnetic wavelength λ_o. In this example, the wind speed and wavelength are 5 m/s and 0.3m, respectively. Other parameters in this example are: $\theta^i = 85^o$, $g = 140\,\lambda_o$, $\varepsilon = 0.0001$ and $SL = 1000\ \lambda_o$. In Figures 5-a and 5-b, the magnitude (dB) of the scattered field as computed by the integral equation approach is compared to that computed by the split-step solution of the PWE, for TE and TM polarizations respectively. The surface used in this example is the sinusoidal surface as described above. The scattered field is computed at a plane located at $x_f = 2000\,\lambda_o$ and extends in the $z-$direction from the rough surface to a specific point. In this example, $\theta^i = 85^\circ$, $g = 200\,\lambda_o$ and $\varepsilon = 0.0001$. We note that the two methods' agreement is good in the forward direction where the PWE is expected to do well. However, as we expect, the agreement deteriorates as the height increases.

The integral equation approach can also be used to calculate the scattered field due to multiple illuminated spots on the surface. In Figure 6, the scattered field due to two illuminated spots on a flat PEC surface is calculated: $\theta^i = 80^o$, $g = 40\lambda_o$ and $\varepsilon = 0.0001$. Due to its narrow beamwidth localized around $\theta^i = 80^o$, the incident field on the first spot results in well-defined reflected field. The medium inhomogeneity causes this narrow beam to widen. As a result, the field that impinges on the second spot is not localized around the specular direction. This means that different parts of this field impinge on the surface at different angles which results in a wide variation of specular reflection angles; the interference between these reflected fields gives rise to the pattern shown in Figure 6. Figure 7 displays the surface currents induced on the two illuminated spots of the flat surface used in the current example. This same example is repeated for a slightly rough Gaussian surface with a height variance of $0.25\,\lambda_o$ and a correlation length of 50 λ_o. From Figure 8 it is obvious that the rough surface encountered at the second illuminated spot causes a diffuse scattered field. Figure 9 shows the surface currents induced on the two illuminated spots of the rough surface for the current example. Figure 10 exhibits a TE polarized field scattered in the near backscattering direction by a PM surface corresponding to $v = 5\,m/s$ and $\lambda_o = 0.23\,m$; here, $\theta^i = 85^o$, $g = 200\,\lambda_o$, $\varepsilon = 0.0001$ and $SL = 1000\,\lambda_o$.

V. Conclusion

The problem of electromagnetic scattering from rough surfaces in a ducting environment was formulated using an integral equation approach. The resulting integral equation was solved using MOMI. This formulation takes into account in a rigorous manner the combined effect of a rough surface and a surface-based evaporation duct on the scattering problem. Contrary to the PWE-based methods, the proposed method does not neglect backscatter and works well at both grazing and off-grazing scattering

directions. Numerical simulations for both sinusoidal and random rough surfaces were carried out. Some comparisons with the split-step solution of the PWE were provided which showed that the PWE-based techniques may give good results for smooth surfaces at low-grazing angle incidence and scattering. MOMI can be used to characterize multiple illuminated spots on the surface. This was illustrated for flat as well as rough PEC surfaces. The proposed method finds application in the area of radar targeting in a ducting environment at LGAs and in the area of wave propagation over the ocean. It provides a concrete check case for people working with the PWE.

References

[1] Charles L. Rino, "A propagation algorithm for grazing incidence," To appear in *IEEE Trans. Antennas & Propagat, 1997.*

[2] Finn B. Jensen, William A. Kuperman, Michael B. Porter, and Henrik Schmidt. *Computational Ocean Acoustics,* American Institute of Physics, New York, 1994.

[3] D. A. Kapp and G. S. Brown, "A new numerical method for rough surface scattering calculations," *IEEE Trans. Antennas Propagat,* vol. 44, no 5, pp. 711-721, May 1996.

[4] Leopold B. Felsen and Nathan Marcuvitz, *Radiation and Scattering of Waves,* IEEE press, New York, 1994.

Figure 2

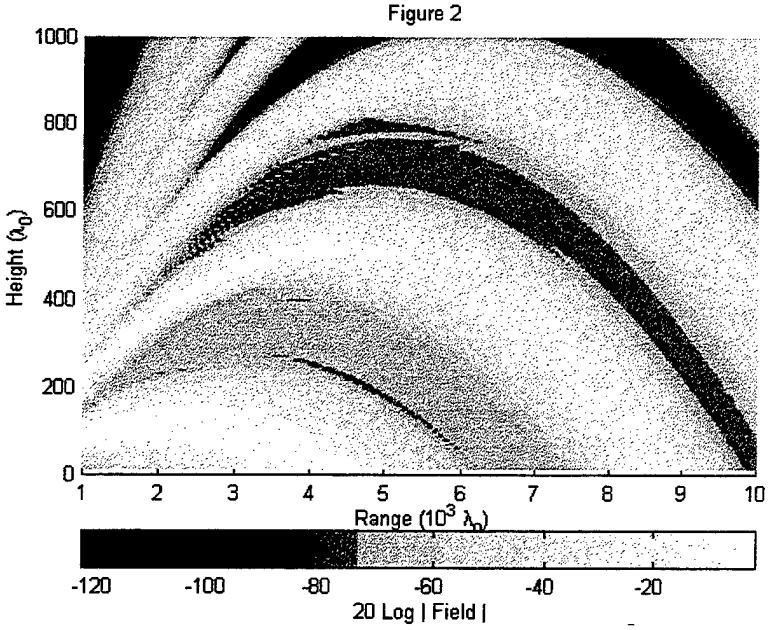

Figure 3

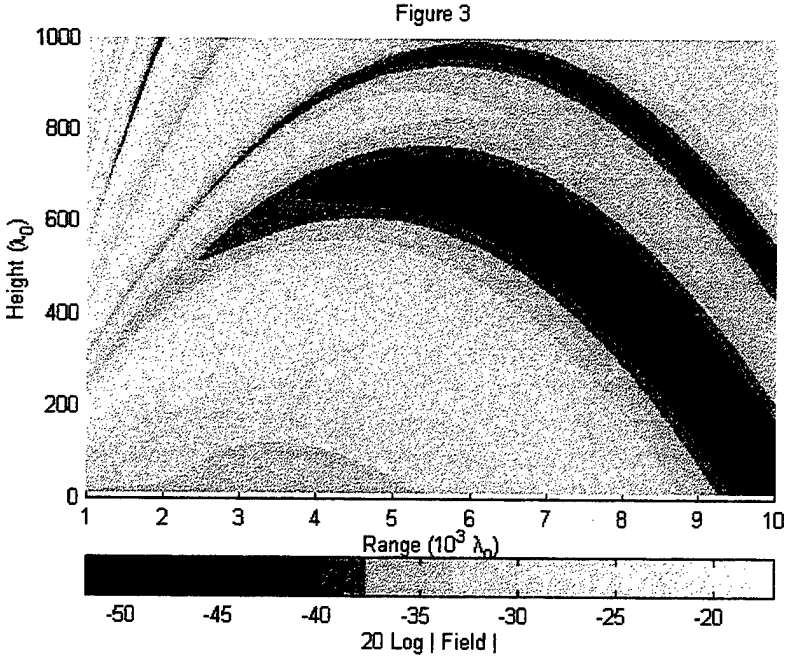

Figure 4

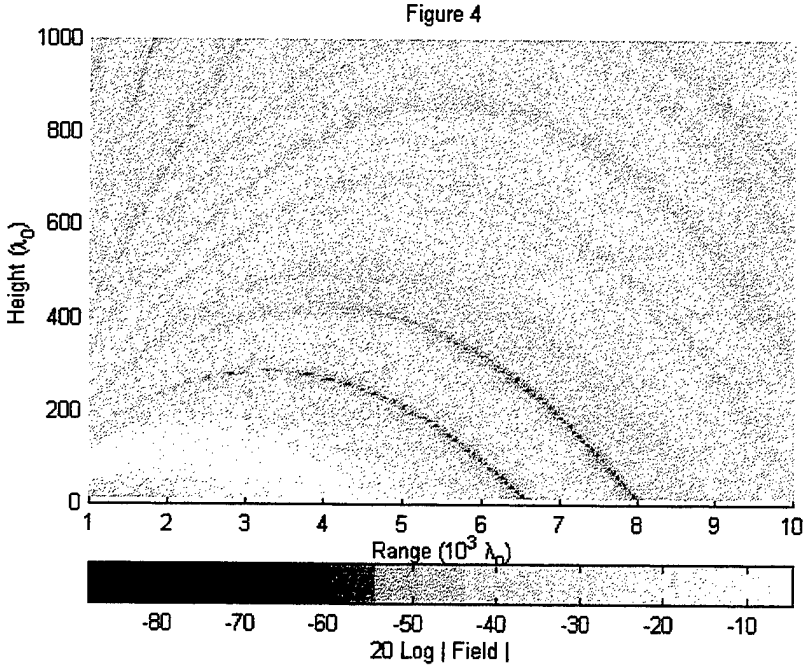

Figure 5-a

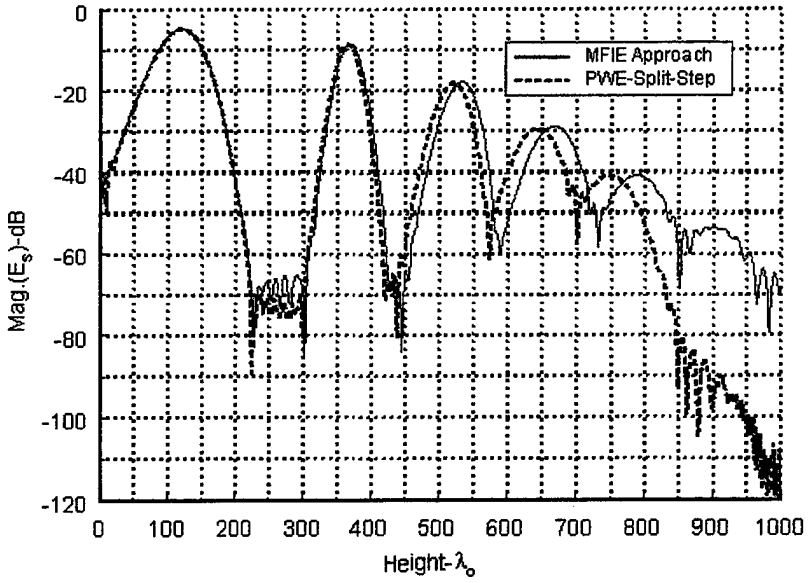

Figure 5-b

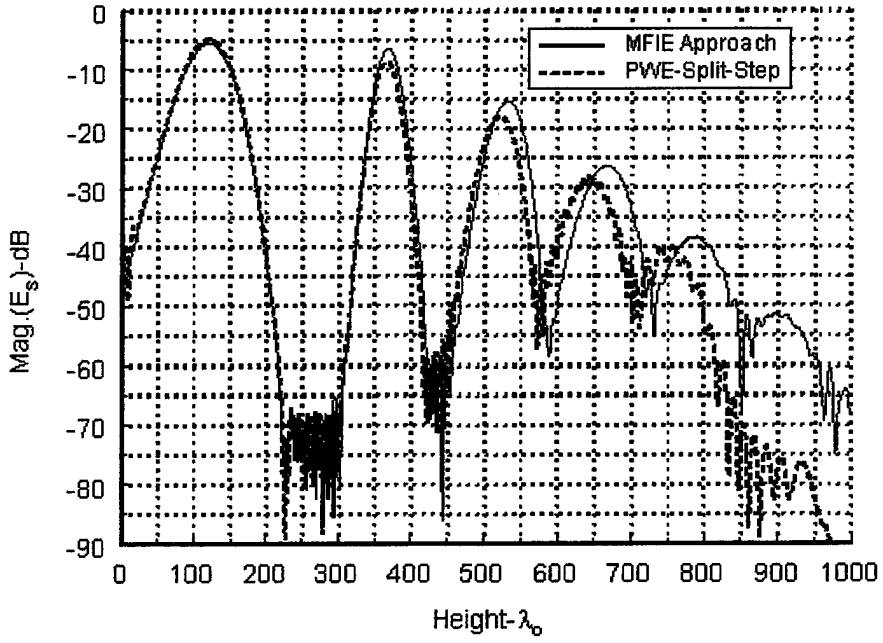

Figure 6

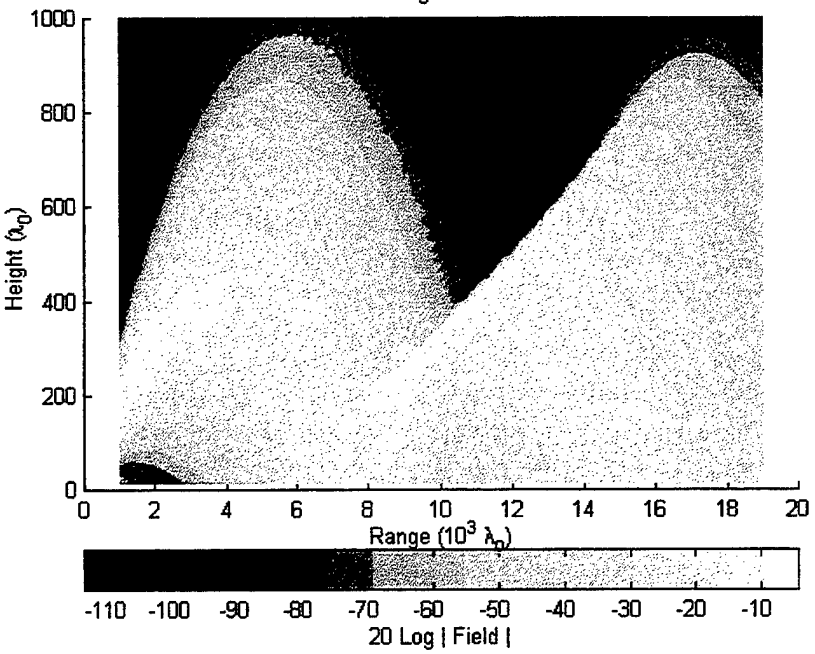

Figure 7

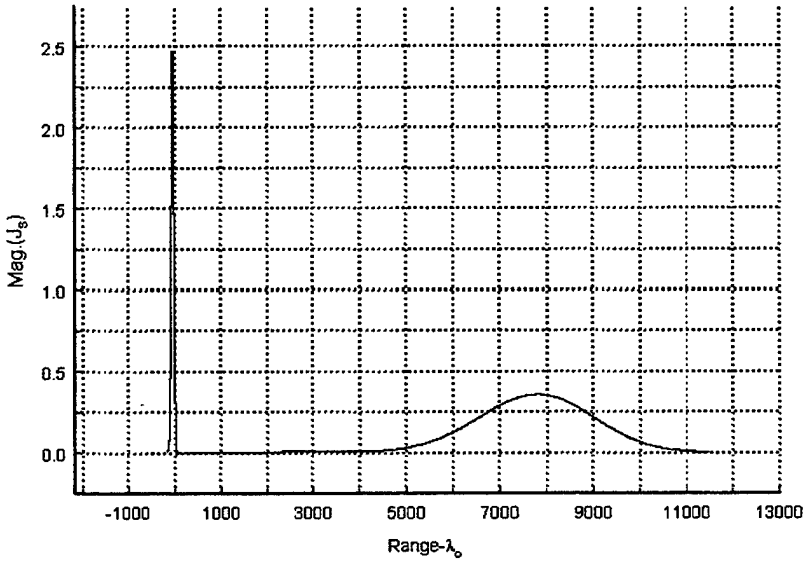

Figure 8

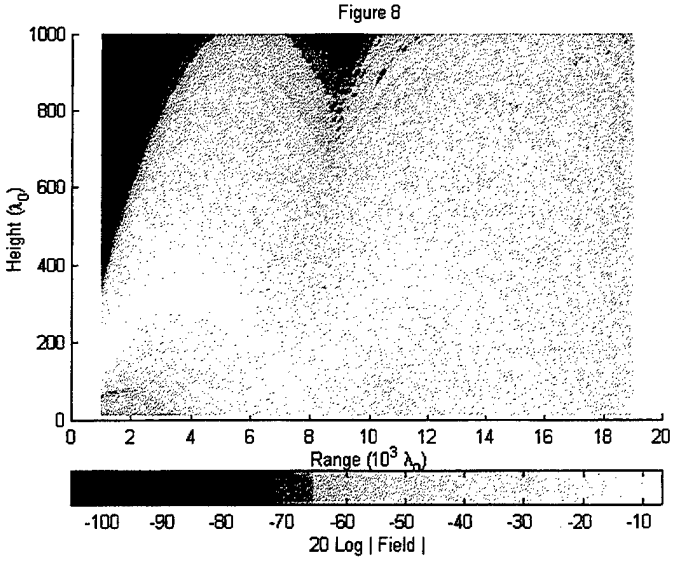

Figure 9

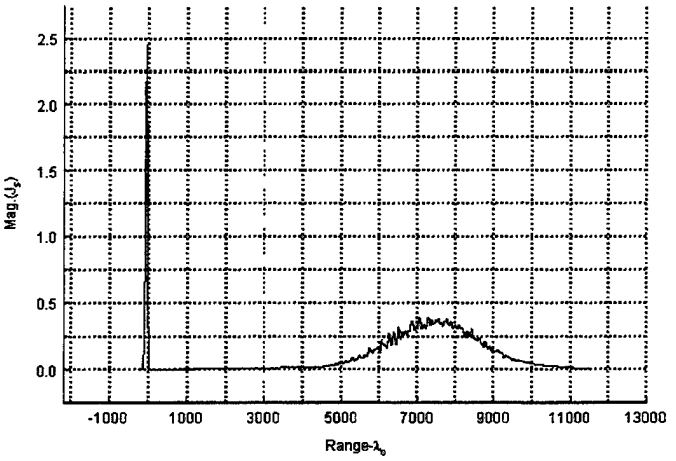

Figure 10

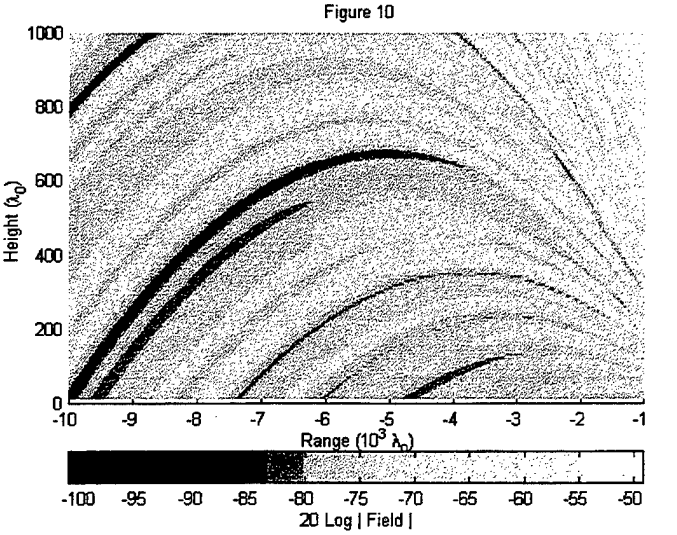

Electromagnetic Wave Scattering from a Rough Surface in a Ducting Environment.

RECENT ADVANCES IN THE TROPOSPHERIC ELECTROMAGNETIC PARABOLIC EQUATION ROUTINE (TEMPER) PROPAGATION MODEL

Michael H. Newkirk
The Johns Hopkins University Applied Physics Laboratory
Johns Hopkins Road
Laurel, MD 20723
(301) 953-6976 (Voice)
(301) 953-5494 (FAX)
Michael.Newkirk@jhuapl.edu

Abstract

The Tropospheric Electromagnetic Parabolic Equation Routine (TEMPER) propagation model is used to accurately model electromagnetic wave propagation in the forward direction over rough (small-scale) surfaces in the presence of anomalous atmospheric conditions. A few applications of this model include communication link and radar detection and tracking performance analysis. Recently, TEMPER has undergone a complete recoding for two major reasons: (a) to increase its overall efficiency; and (b) to facilitate the incorporation of several new features. A few of the new features that will be discussed include the incorporation of geometric optics (ray-tracing) and improved spectral estimation algorithms for grazing angle determination; the recently corrected implementation of the wide-angle propagator; and a terrain handling method based on the Beilis-Tappert mapping technique. The result of this effort is a propagation model that is more efficient and consequently faster than its previous version, and can model propagation over terrain with slopes as large as 15 degrees more accurately than before. Several examples of the variety of TEMPER output products will be given that illustrate its new capabilities. Finally, an outline of future TEMPER enhancements will be presented.

Introduction

The Tropospheric Electromagnetic Parabolic Equation Routine (TEMPER) is a propagation model based on the split-step solution technique for the parabolic equation [1]. TEMPER makes use of the discrete mixed Fourier transform method to account for the general impedance boundary [2]. This boundary can also be modified to incorporate small-scale roughness effects via the Miller-Brown roughness model [3]. Until now, TEMPER was limited in the size of problem it could handle, in terms of maximum altitude and terrain and refractive data. In addition, rough surface modeling was limited by the methods used to obtain grazing angles as a function of range, a key part of the Miller-Brown model. General terrain boundaries were accepted, but only for use by a simple terrain masking technique. Also, the parameters used to describe the surface, both electrical and physical, were constrained to be constant with respect to range.

Recently, TEMPER has undergone a major revision to include many new features, while improving its overall efficiency. The result of this effort is a more robust and capable parabolic equation (PE) propagation model. The new features allow for larger problem sizes, range-dependent surface parameters, more robust grazing angle estimation methods, and more accurate

modeling for general terrain boundaries. In this paper, these improvements will be briefly discussed and examples will be given that demonstrate this new capability in TEMPER.

Discussion of Improvements

When the task was started to add new features such as expanded grazing angle calculation capability, it was realized that the existing code and algorithmic design would not be adequate. TEMPER was completely rewritten in order to accommodate these new features.

Algorithm recoding

Previous TEMPER code was written such that the real and imaginary parts of the complex field were handled separately. This was necessary in order to use a discrete real sine transform algorithm for getting back and forth between real and transform (also called p-) space. This philosophy results in more overhead than necessary to manipulate the field at each range step. TEMPER 3 uses fully complex math in its algorithm. The same real sine transform routine is used, but a novel interface was created to trick the transform routine into separately operating on the real and imaginary parts, but returning the complex result to the PE algorithm. This change alone resulted in reducing the time required to run a finite conducting case by nearly 40%. Calculation times for perfect conducting cases were not reduced as much because there is proportionally less complex math to perform. Nevertheless, significant improvement in computation time was obtained.

The original TEMPER code was written to be Fortran-77 compliant. Array sizes were limited to allow TEMPER to run on the memory- and processor-limited computers of that time. TEMPER 3 has been written to take advantage of several Fortran-90 specific features; most notable of these is the concept of allocatable arrays. The sizes of nearly all arrays in the program are now defined at run-time rather than compile-time. In doing so, only as much memory is used as is needed to run the case at hand. Valuable system memory is not wasted to run relatively small problems while very large problems can still be accommodated. The other benefit is that the specified refractivity and terrain height profiles can have an unlimited number of data points, but the practical limit is effectively set by the computer platform used to run TEMPER. Finally, TEMPER still has a transform size limit of 2^{21}, which has been found to be sufficient for all but the most stressing cases. This limitation is imposed by the legacy sine transform routine; alternate methods are currently being investigated to circumvent this limitation.

In addition, output file information has been enhanced and reorganized. The header of the binary output file has been augmented with many more parameters to assist in automating the analysis of TEMPER output. Also, the binary file format was changed from sequential to direct access so that analysis software can open and read from the file when needed rather than reading the entire file into memory. This was deemed a critical change as some planned applications require simultaneous access to numerous files, each of which can be several megabytes in size.

Wide-Angle Propagator

Previous TEMPER versions have made use of the wide-angle propagator, which was introduced by Thompson and Chapman [4]. This was thought to be superior to the narrow angle

version originally used by Hardin and Tappert [5]. However, there was some concern with this propagator when small errors were seen at very large propagation angles for problems that had analytical solutions to which TEMPER could be compared. It became evident that the problem was not in the wide-angle propagator itself, but in how the source field was created for this method. As a result, the correct implementation of the source model was outlined by Kuttler and Dockery [6]. The result is that the source field must be modified to account for how it is propagated into the far field. The modification is

$$F(p) = S(p)\, k^{3/2} \left(k^2 - p^2\right)^{-3/4}, \tag{1}$$

where $S(p)$ is the source field specified as a function of p, the transform variable, k is the electromagnetic wavenumber and $F(p)$ is the correct field to start the PE solution. The result of using this method is summarized in Figure 1, which shows a dramatic difference in the field magnitude for wider angles (zero angle is effectively at 300 feet, while wide angles are away from 300 feet, both above and below). The error associated with the improper use of the wide-angle propagator is small for cases where wide-angle results are not needed, such as smooth earth problems. But as general terrain height capability is added to PE methods, it becomes more important to accurately model propagation for angles farther away from horizontal. Errors of more than 4 dB at $\pm 45°$, or equivalently at altitudes of 150 or 450 feet, are possible in these cases if the correction is not used.

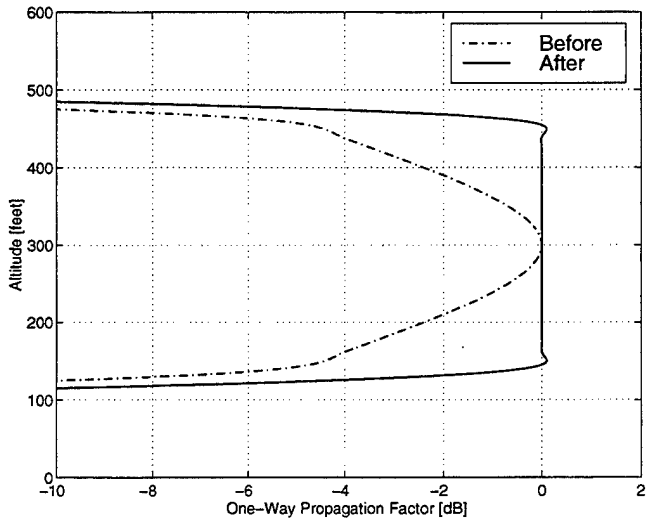

Figure 1. Comparison of the field resulting from using the wide-angle propagator before and after the correction outlined in equation (1). The 1 GHz, omnidirectional source at an altitude of 300 feet has been propagated in free space to a range of 150 feet using a 45° problem angle.

Grazing Angle Estimation

The previous version of TEMPER incorporated a small-scale rough surface scattering technique based on the Miller-Brown roughness model [3]. This method uses the local grazing angle to modify the reflection coefficient and consequently the effective surface impedance which is used in the Discrete Mixed Fourier Transform (DMFT) method employed by TEMPER

[2]. The key to using this method is in estimating the grazing angle at each range step. TEMPER's previous approach to obtaining these angles required the user to select one of three methods:

1. assume a standard atmosphere and use 4/3 earth spherical geometry; or,
2. propagate a separate field through the same environment but over a perfect conducting surface, then use the field near the surface in a spectral estimation (SE) method based on the MUSIC algorithm [7]; or,
3. use grazing angles calculated by some external program such as a geometric optics (GO) or ray-tracing program.

In all cases, TEMPER used 4/3 earth angles (option 1) for close-in ranges, until the grazing angle value was less than 1.5°.

The problems associated with this approach were numerous. First, an external program was required to generate grazing angles for cases where spectral estimation was not feasible. An example of this is the case where strong evaporative ducts are present. In such cases, grazing angles can be underestimated by as much as a factor of two [2]. Second, the external program would have to be able to estimate grazing angles in the presence of terrain. The SE method used in the previous TEMPER was unable to do this, and GO methods cannot easily determine these angles in shadowed regions. Third, the 4/3 earth option was only valid for large grazing angles and close-in ranges, and only for standard atmosphere at greater ranges. Finally, requiring the user to keep track of all this proved to be problematic, at best.

Two of the most significant improvements to TEMPER in Version 3 are the incorporation of a geometric optics algorithm and improved logic for automatically determining which grazing angle method should be used for a given problem. The GO algorithm is the grazing angle calculation portion of a ray-tracing algorithm has been used extensively at JHU/APL; all power calculations in the original code were removed. This method launches a spread of 500 rays from +1° to -1.5° in elevation and records the range and incidence angle each time a rays strikes the surface. Multiple "bounces" for each ray are possible in ducting environments. After all rays have been propagated, the resulting angles are sorted in range order and then interpolated onto the TEMPER range grid. The only significant limitation to the GO algorithm included in TEMPER is that it currently does not recognize terrain features. However, this limitation is not critical to the new logic used for grazing angle determination, as discussed below.

The spectral estimation method used by the previous version of TEMPER has been retained, but its capability has been significantly improved. The new version has been modified to provide better angle resolution, in addition to grazing angle estimates over terrain. The only drawbacks are that a separate PE solution must be run to get these angles and, as stated previously, the estimates obtained in evaporative ducting environments can be in error. To address these problems, new logic has been implemented that can automatically recognize when one or both of the GO or SE techniques should be used. The logic can be summarized as follows:

1. in all cases, use 4/3 earth-derived geometric angles for close-in ranges until the grazing angle is less than 1.5°;

2. if the refractivity data shows no signs of a strong evaporative duct, use SE over all remaining ranges;
3. if an evaporative duct is present and there is no terrain (i.e. flat surface), use GO over all remaining ranges;
4. if an evaporative duct is present and there is terrain present over some portion of the range extent, use GO over the smooth portion(s) and use SE over all the terrain and where the SE-derived angle is greater than the GO derived grazing angle.

This method removes the burden of choosing the proper grazing angle estimation method from the user.

A simple example of how this method works is shown in Figure 2. A 3° "island" is located about 20 nmi downrange, with a height of 1000 feet and base width of 6 nmi, as shown in the lower plot of Figure 2. A 1 GHz, 25-foot high sector source is radiating in the presence of a 20-meter evaporative duct on either side of the island. Since the refractivity profile is fixed with respect to mean sea level, the duct effectively goes away over the island as the terrain height quickly surpasses the duct height. The upper plot in Figure 2 shows how the individual angle estimate methods perform in this environment. In addition, the combination of the methods, indicated by the "auto" curve, is shown. We see that the SE method is underestimating the grazing angle before as well as far beyond the island; however, it immediately picks up the expected 3° grazing angle at the front of and just behind the island. The back side of the island should actually have a grazing angle of zero since the source is blocked by the island peak, but the SE method does give a small non-zero angle in the region. Figure 3 shows the resulting plot of propagation factor versus range and altitude for this case. Notice that the propagation factor values on the backside of the island are very low. This gives rise to the erroneous SE-derived grazing angle values in that region. This has little consequence since the power incident on the backside of the island is so small. For the GO method, we see that it behaves as if the island were not there at all. None of the rays actually reach behind the island, as they are blocked by the peak. For this reason, the GO-derived angles should be used behind the island only when they are larger than the SE-derived angles.

Linear Shift Mapping

A simple terrain handling method was introduced with the previous version of TEMPER. This method, referred to as terrain masking (or TM), modeled the effects of terrain by simply setting the normally-propagated field to zero at each range step for altitude grid points located below the local terrain height. It turns out that this method, which equivalent to using knife-edge theroy, is remarkably effective given its simplicity. Recognizing that this method was by no means rigorous, an alternate terrain handling method was developed that is based on the technique developed by Beilis and Tappert [8]. In this method, called linear shift mapping (LSM) method, the terrain boundary is effectively mapped onto a flat calculation boundary by adjusting the PE solution at each range step using the local terrain slope dependence to

1. modify the use of the refractivity profile in the z-space propagator;
2. multiply the field by a phase factor, essentially steering the field over the terrain; and

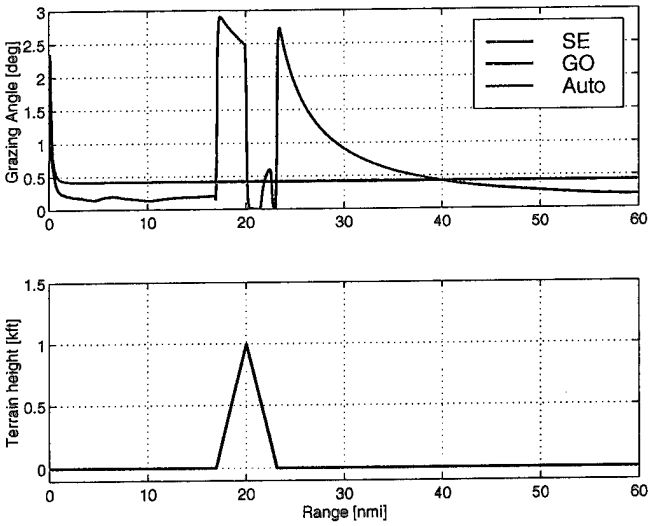

Figure 2. The "island" case. An example of obtaining grazing angle estimates in problems where both terrain and strong evaporative ducts are present. The upper plot shows the grazing angle values as a function of range for the SE, GO and automatic selection methods. The lower plot shows the terrain height profile. The blue portion represents the ocean and the green portion represents an island with slopes of 3° on both the front and back sides.

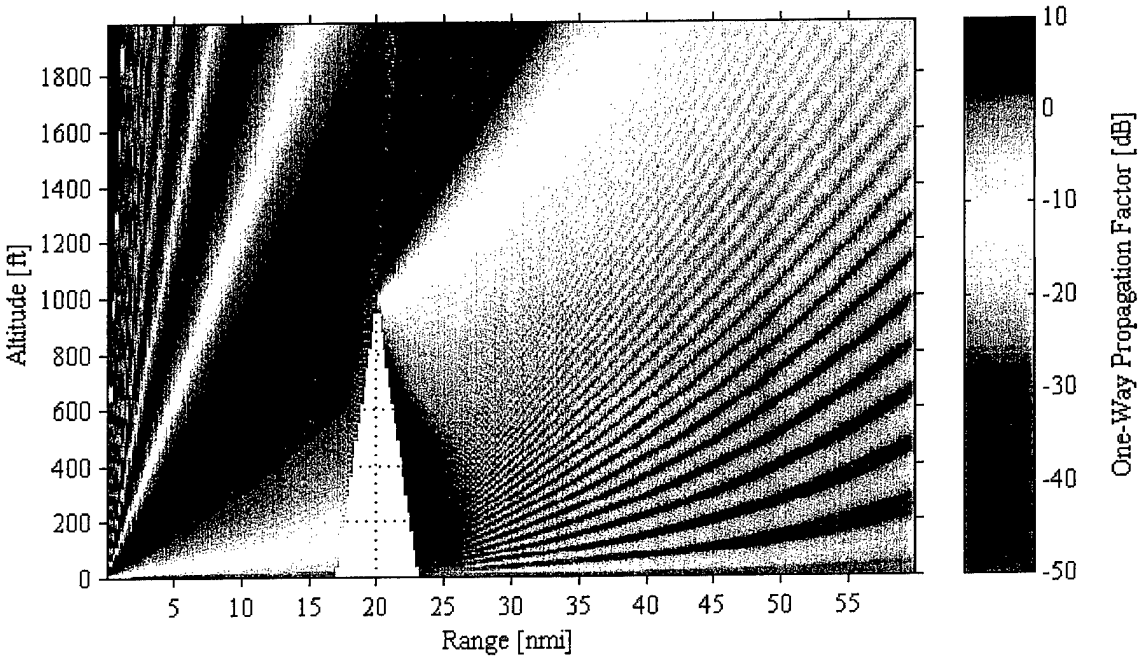

Figure 3. One-way propagation factor versus range and altitude for the island case of Figure 2. This example also illustrates the linear shift (LS) terrain handling method.

3. modify the effective surface impedance.

This method requires that the PE solution use a maximum problem angle of at least twice the maximum slope of the terrain profile. This effectively limits the maximum terrain slope that can be accommodated to roughly 15°. Higher sloped regions would begin to show distortions in the field due to the phase steering described in step 2. Figure 3 used this method to model the effects of the "fabricated" island. In that example, the strong reflection off the front face of the island is apparent. The terrain masking method would have missed this effect.

A comparison of these terrain methods is shown in Figures 4 and 5 for a terrain profile taken from the Persian Gulf region, looking due west into Saudi Arabia, having a 4.9° maximum slope. For both, a 3 GHz, 50-foot high, 1° beamwidth (– 40dB SLL Taylor pattern) was used. The problem angle used for this case was 17.6°, resulting in a 2^{13} transform size. We see very little difference between these two figures; however, near the surface TM has overestimated the propagation factor compared to the LSM method. This is somewhat expected, since the TM method is not correctly accounting for the impedance boundary, while the LS method does.

Figures 6 and 7 compare the two methods for a rougher terrain profile, again taken from the Persian Gulf; however, this profile looks eastward into Iran. The maximum terrain slope for this profile is 16.25°. In this case, the 1 GHz omnidirectional source is 2500 feet high (e.g. an airborne platform) and TEMPER's maximum problem angle is 45.7°, resulting in a 2^{14} transform size. In this case not only is the propagation factor on the surface different, but also the strength of the reflections off the terrain are lower for the TM method. This case also begins to show one of the limitations of the LS method; there is an abrupt terrain peak between 40 and 50 nmi that has caused a slight distortion in the field at all altitudes just above the peak, caused by the excessive phase steering required in step 2 above.

Range-Dependent Surface Parameters

Previous versions of TEMPER were only capable of using surface electrical and roughness parameters that were constant with respect to range. With TEMPER 3 the user can now specify the surface electrical parameters, either as a combination of relative permittivity and conductivity or as the real and imaginary parts of the complex permittivity, as well as the surface roughness as a function of range. To do this, the user specifies these parameters in the surface parameter input file, which is the same file used to provide terrain height profiles to TEMPER. It is not necessary that all parameters be range dependent; for example, one can specify constant electrical parameters with varying roughness. The example given in Figures 2 and 3 used default electrical parameters over the ocean combined with $\epsilon = 80$ and $\sigma = 4$ S/m over the terrain portion of the problem. In addition, the rms surface roughness was 0.1 ft over water and 0.5 ft over land. Also, one need not have a terrain profile to use range-dependent surface parameters. This provides a very flexible method for modeling the effects of various mixed paths.

Future Work

A few of the planned enhancements to TEMPER include (a) variable transform sizes as a function of range to allow the use of finer altitude sizes only where required rather than over the entire problem; (b) variable range increments to allow faster field propagation over relatively

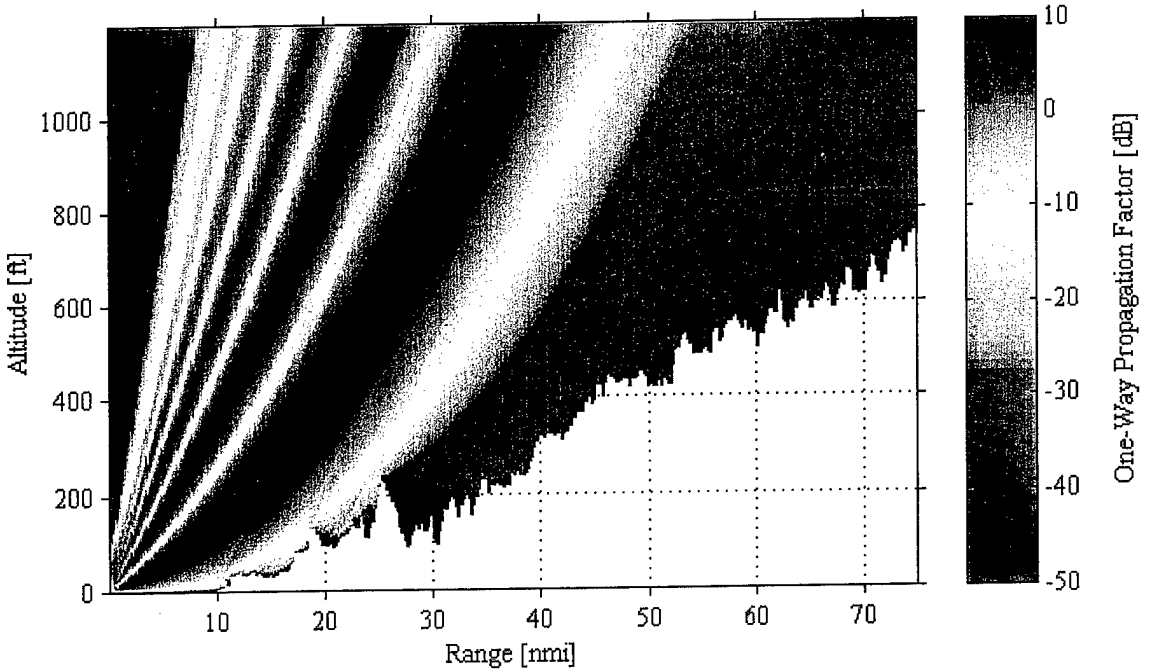

Figure 4. An example of the linear shift (LS) method for real terrain. The maximum terrain slope is 4.9°

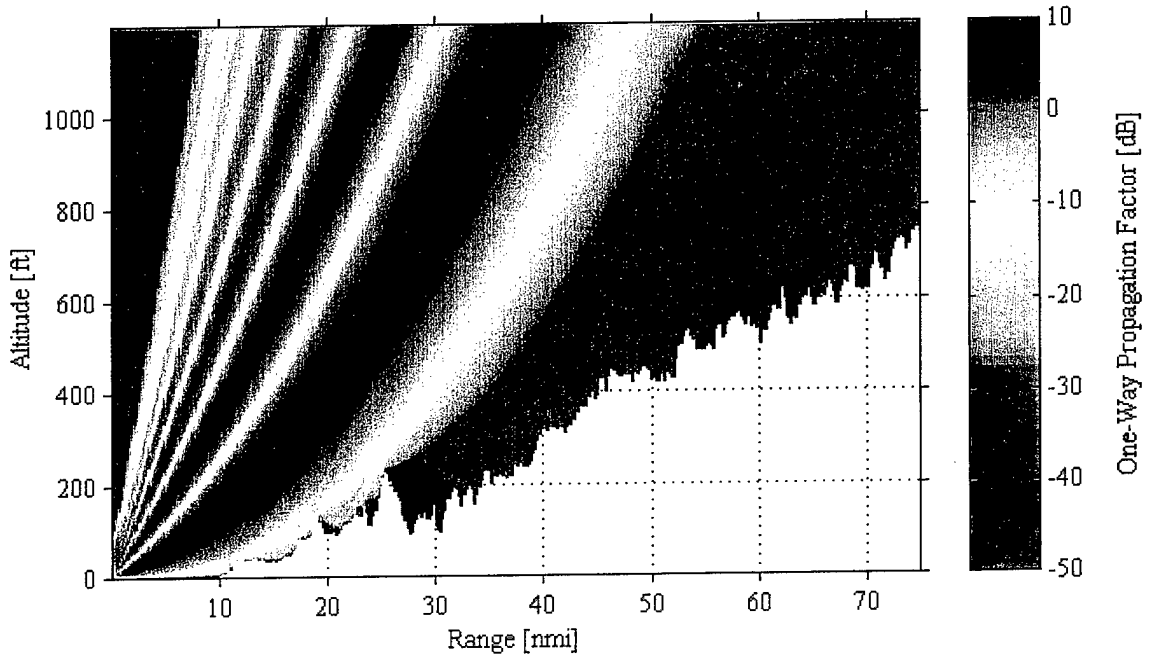

Figure 5. An example of the terrain masking (TM) method for the same terrain profile in Figure 4.

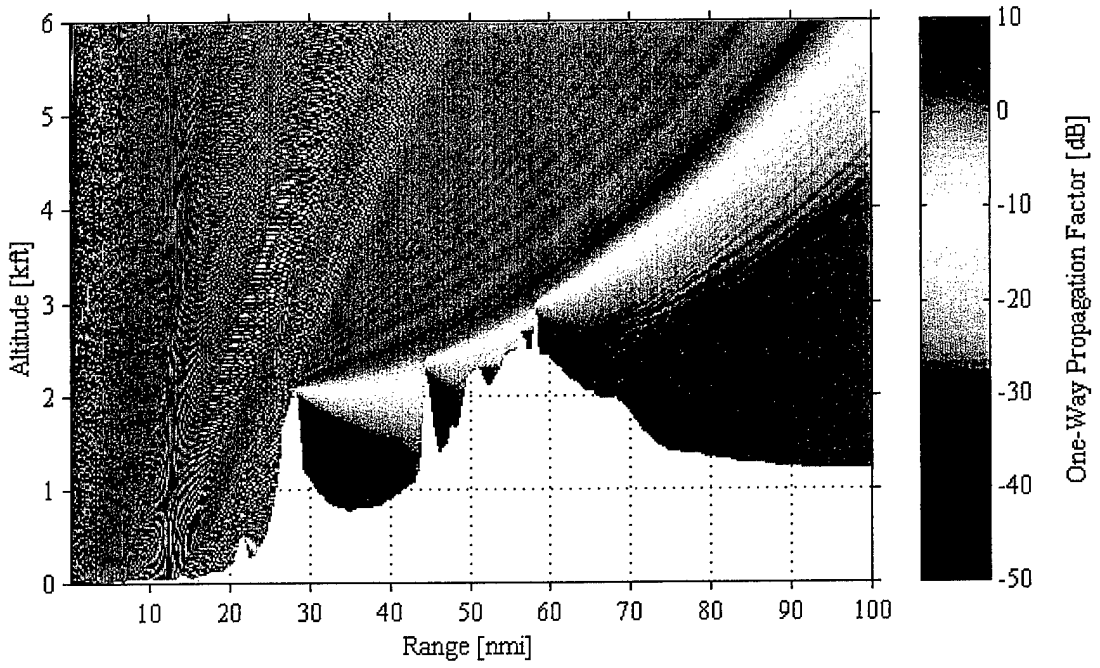

Figure 6. An example of the linear shift (LS) method for steeper terrain. The maximum terrain slope is 16.25°.

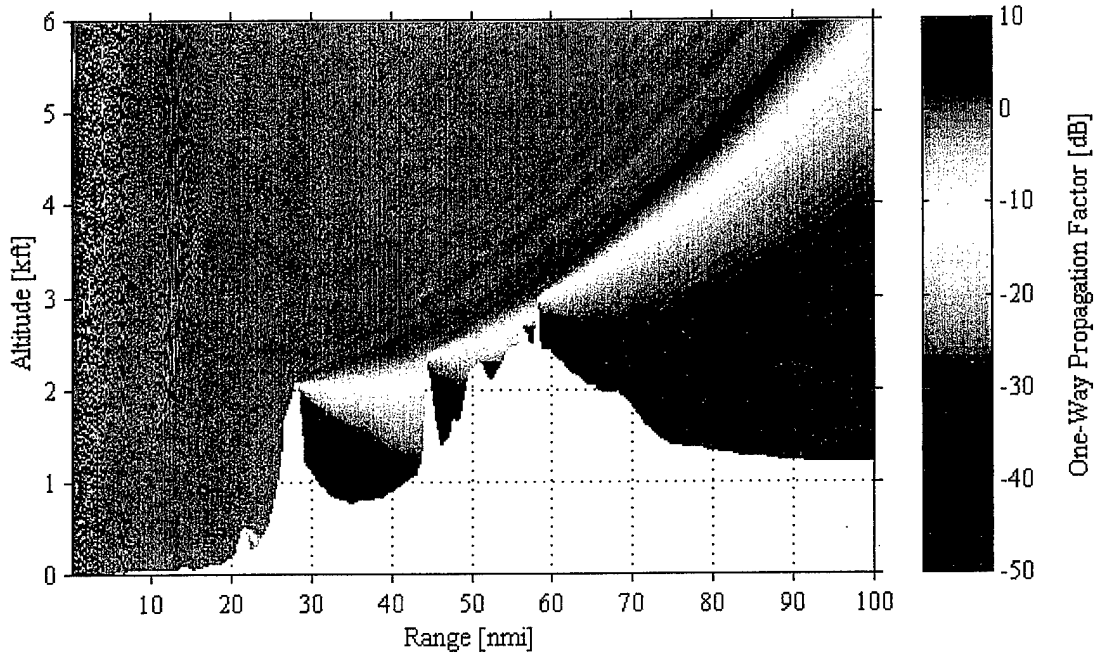

Figure 7. An example of the terrain masking (TM) method for steeper terrain.

benign portions of the problem; (c) a more robust linear shift terrain method to permit larger terrain slopes; and (d) incorporation of the DTED and/or DFAD database information through a new Windows 95/NT interface. Each of these future enhancements will help to speed up and expand the range of problems that TEMPER will encounter as modeling of more complex scenarios becomes important.

Summary

The TEMPER propagation model has undergone a complete reworking that has allowed the inclusion of several important, new features, while simultaneously improving its overall performance. This new version can now handle larger, more complex problems, but only uses as much computer memory as is needed. TEMPER can now more accurately model the effects of propagation over terrain and general surfaces with range-varying electrical and roughness parameters. An important new feature is the inclusion of a geometric optics algorithm that is used to obtain the correct grazing angle as a function of range, as required by the rough surface algorithm. In addition, advanced logic is now employed to automatically determine when either or both of the significantly improved grazing angle estimation methods are needed. The result is a more robust and capable propagation model for a wider variety of needs.

References

[1] J.R. Kuttler and G.D. Dockery, "Theoretical description of the parabolic approximation / Fourier split-step method of representing electromagnetic propagation in the troposphere," *Radio Science*, vol. 26, no. 2, pp. 381-393, 1991.

[2] G.D. Dockery and J.R. Kuttler, "An improved impedance-boundary algorithm for Fourier split-step solutions of the parabolic wave equation," *IEEE Trans. Antennas Propagat.*, vol. 44, no. 12, pp. 1592-1599, 1996.

[3] A.R. Miller, R.M. Brown and E. Vegh, "New derivation for the rough-surface reflection coefficient and the distribution of sea-wave elevations," *IEE Proceedings*, vol. 131, part H, no. 2, pp. 114-116, 1984.

[4] D.J. Thompson and N.R. Chapman, "A wide-angle split-step algorithm for the parabolic equation," *J. Acoust. Soc. Am.*, vol. 74, pp. 1848-1854, 1983.

[5] R.H. Hardin and F.D. Tappert, "Applications of the split-step Fourier method to the numerical solution of nonlinear and variable coefficient wave equations," *SIAM Review*, vol. 15, p.423, 1973.

[6] J.R. Kuttler and G.D. Dockery, "The wide-angle versus the narrow-angle propagator," manuscript in preparation for *IEEE Trans. Antennas Propagat.*

[7] R.O Schmidt, "Multiple emitter location and signal parameter estimation," vol. 34, pp. 276-280, 1986.

[8] A. Beilis and F.D. Tappert, "Coupled mode analysis of multiple rough surface scattering," *J. Acout. Soc. Am.*, vol. 66, no. 3, pp. 811-826, 1979.

TROPOSCATTER CALCULATIONS WITH A PARABOLIC EQUATION MODEL

Richard A. Paulus
Propagation Division

Space and Naval Warfare Systems Center San Diego D883
49170 Propagation Path
San Diego, CA 92152-7385

Ph: 619-553-1424 Fax: 619-553-1417
E-mail: paulus@nosc.mil

Abstract. *The capability of a parabolic equation propagation model to predict the statistics of troposcatter signals in the upper VHF and UHF is examined. A method to account for tropospheric scatter in parabolic equation (PE) modeling of radio and microwave propagation was proposed by Hitney [1993]. The atmospheric refractivity profile is represented in the PE model at equally spaced vertical points separated by a height interval, δz, which varies between approximately 0.5 and 18 m depending upon frequency and the refractivity profile. The troposcatter model adds a random fluctuation to the mean refractivity at each vertical point in the refractivity profile sampled from the one-dimensional spectrum of refractive index fluctuations. An effective refractive index structure parameter profile described by Doviak et al. [1983] is utilized to account for variation with height. This model was shown by Hitney to yield single realization results comparable to the EREPS empirical model and measured data.*

Using Hitney's model, the statistics of the output of the model generated from numerous model runs are compared with signal distributions measured in the southern California Bight. Signal levels were measured at 143.09, 262.85, and 374.95 MHz on a 127.2 km path between San Clemente Island and Point Loma in San Diego.

INTRODUCTION

In fulfilling requirements for electromagnetic propagation models that can accommodate range-varying refractive structure, the parabolic equation technique has come to the fore. A hybrid ray optics/parabolic equation model (Radio Physical Optics - RPO) was developed by *Hitney* [1992] that utilized the strengths of each of these techniques to optimize the ability to display radar coverage of typical radars and targets throughout the full extent of altitudes and ranges of interest on commonly available PCs. However, application of the RPO model to communications or intercept problems suffered because the model contained no means of accounting for tropospheric scatter. Subsequently, a method to account for this mechanism was proposed by *Hitney* [1993]. By this method, the atmospheric refractivity profile is represented in the PE model at

equally spaced vertical points separated by a height interval, δz,

$$\delta z = \frac{\lambda}{2} \frac{1}{\sin(\theta_{max})} \quad (1)$$

which varies between approximately 0.5 and 18 m depending upon the radio wavelength (λ) and the refractivity profile (which determines an elevation angle, θ_{max}, which is the boundary between the PE and ray optics models). The troposcatter model adds a random fluctuation, n_f, to the mean refractivity at each vertical point in the refractivity profile sampled from the one-dimensional wave number spectrum of refractive index fluctuations $S_n(k)$. This random fluctuation is given by

$$n_f = \frac{r - 0.5}{0.408} \sqrt{S_n(k)} \quad (2)$$

where r is a uniformly distributed random number between 0 and 1 and

$$S_n(k) = 0.249 C_n^2 k^{-5/3} \quad (3)$$

An effective refractive index structure parameter, C_n^2, profile described by *Doviak et al.* [1983] is utilized to account for variation with height:

$$C_{ne}^2 \cong 3.9 \times 10^{-15} e^{-z/2000} \quad (4)$$

This model was shown by Hitney to yield single realization results comparable to the empirical model contained in EREPS [*Patterson et al.*, 1994] and measured data.

This paper extends the single realization results to examine the capability of the RPO troposcatter model to predict both the median and distribution of VHF/UHF signals.

TROPOSCATTER SIMULATIONS

Figure 1 shows the effects of including troposcatter into a vertical coverage diagram for a 130 km overwater propagation path at a frequency of 374.95 MHz with a transmitter at 16.6 m msl. The top frame shows propagation loss versus range and altitude for a standard atmosphere refractivity profile (118 *M*-units/km) considering only diffraction beyond the horizon. The first propagation loss contour has been set to 126 dB (the free space propagation loss for 374.95 MHz and a range of 130 km) and the contour interval is 10 dB. The resulting propagation loss for the link geometry is in the range of 196-206 dB (-70 to -80 dB propagation factor). Also noticeable at these high propagation loss levels are irregularities in the contours which result from the use of single precision variables in the numerical implementation of RPO. This is not really of concern since practical propagation problems in the real atmosphere do not reach great loss values because of troposcatter. The lower frame shows propagation loss for a standard atmosphere refractivity profile now also considering troposcatter beyond the horizon. Fluctuations in propagation loss begin to be apparent at 156 dB propagation loss (-30 dB propagation factor). The resulting propagation loss for the link geometry is now in the range 166 to 186 dB (-40 to -60 dB propagation factor) for this realization. (It is also useful to note here that these troposcatter effects are generally important only for one-way propagation problems and have little or no effect for two-way radar assessment problems.)

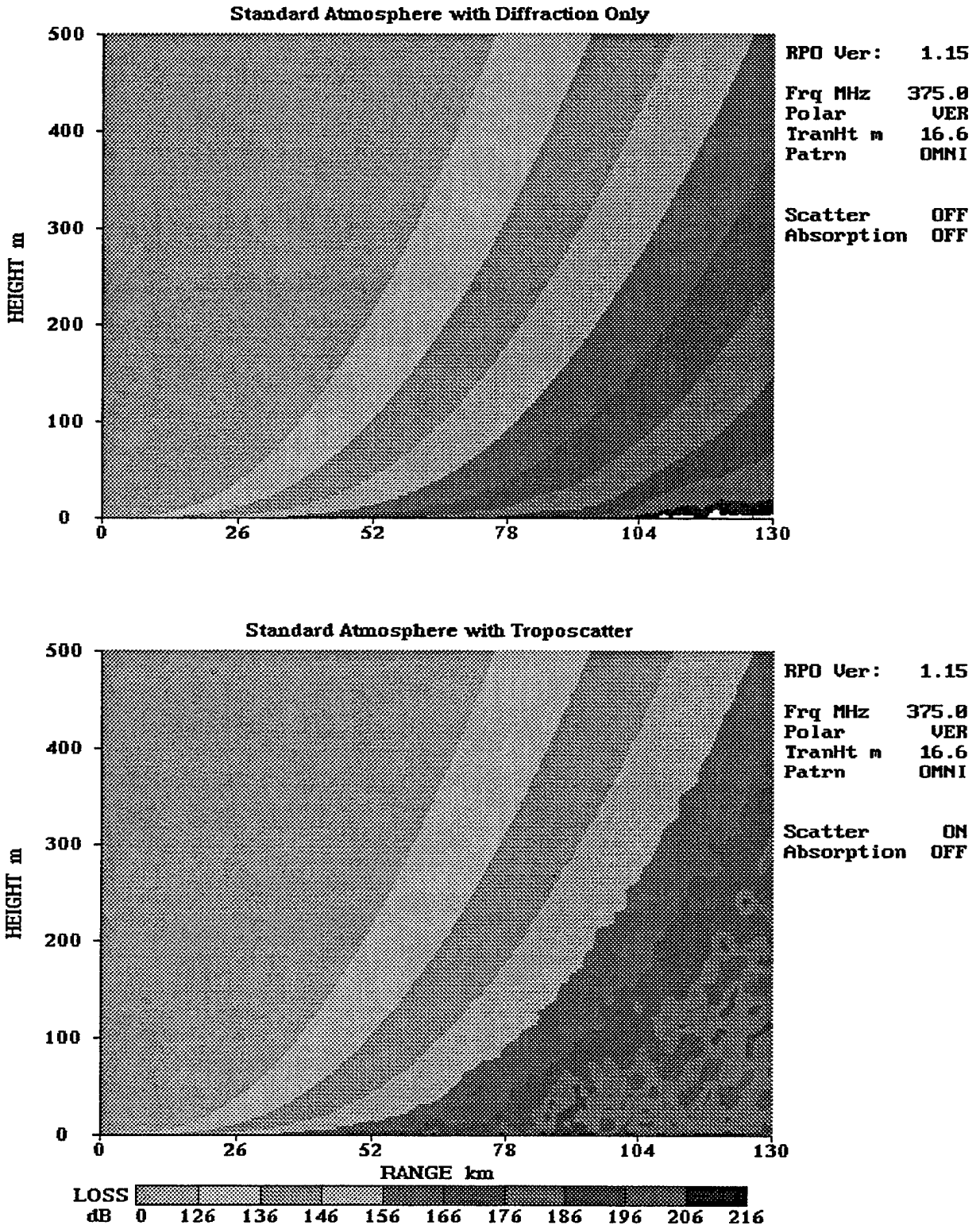

Figure 1. Top frame shows the propagation loss increase with range for a standard atmosphere accounting only for diffraction beyond the horizon. Bottom frame shows a single realization of the effects of the troposcatter model in causing lower values of loss and fluctuations in loss beyond the horizon.

RPO was set up to run 1000 realizations for each of three frequencies: 143.09, 262.85, and 374.95 MHz with a transmitter height of 16.6 m msl; these are the transmitters used for the VOCAR experiment [*Rogers*, 1996]. The propagation link geometry selected was a 127.2 km path and a receiver height of 47.9 m msl and the propagation factor was extracted for this range and altitude from each RPO realization. The resulting distribution of propagation factor for each of the frequencies is shown graphically in Figure 2. The simulated distributions have a Rayleigh shape that *Hall* [1979] indicates is typical of troposcatter.

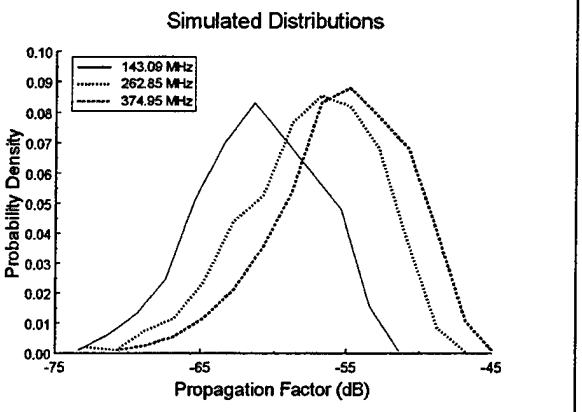

Figure 2. Probability density distributions for simulated troposcatter signals.

TROPOSCATTER DATA

A propagation link with frequencies of 143.09, 262.85, and 374.95 MHz is currently being tested between San Clemente Island and Point Loma in San Diego (L. T. Rogers and W. K. Moision, private communication). Based upon inspection of the received signal levels and National Weather Service (NWS) soundings taken in San Diego, 22 October 1997 was subjectively selected as representing troposcatter data. A time series of the data at 262.85 MHz is shown in Figure 3 for 22 October 1997 from approximately 0448 to 0936 PDT. The signal is not steady but rather fluctuates about 5 dB about its short term mean level with occasional deeper fades.

Figure 4 shows modified refractivity profiles derived from soundings taken at 0500 and 1700 PDT at the NWS site about 20 km

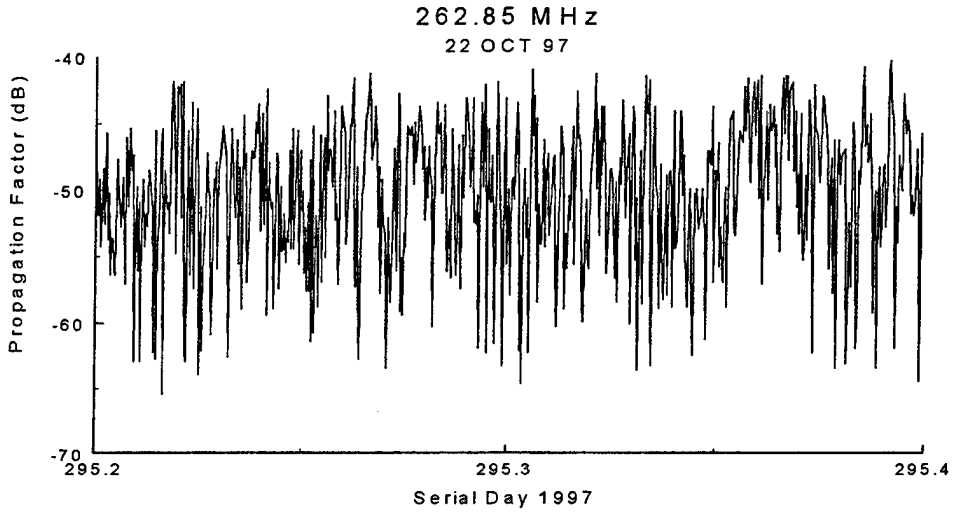

Figure 3. Time series of propagation factor received at Point Loma for approximately 5 hours during the morning of 22 OCT 97.

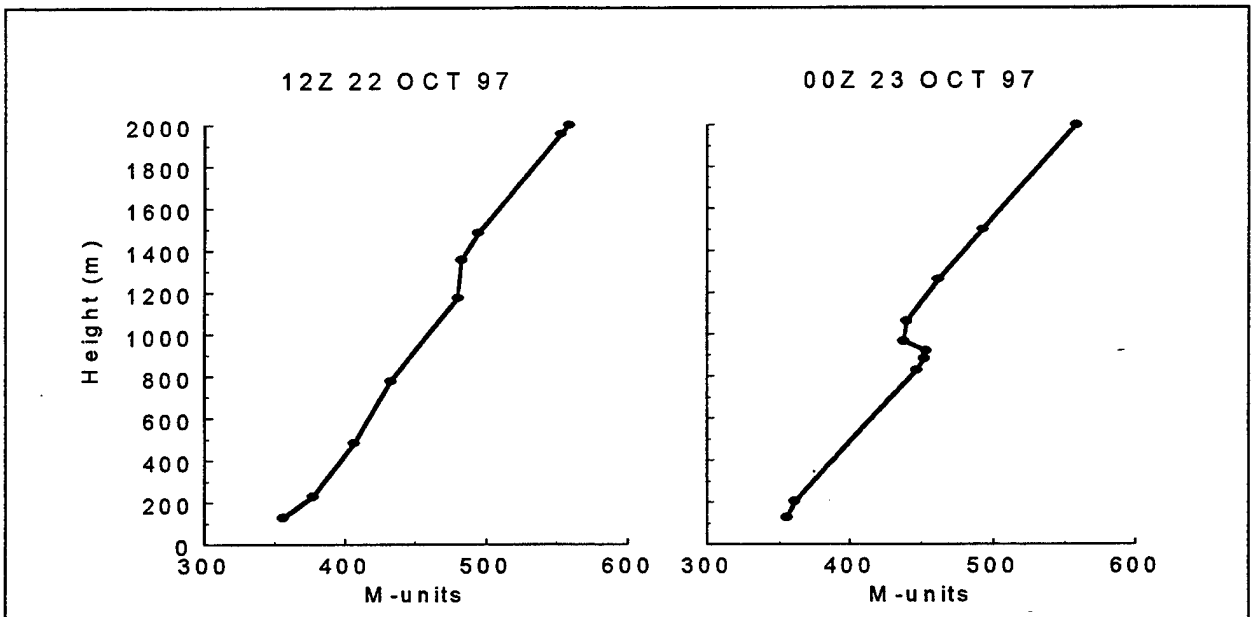

Figure 4. Modified refractivity profiles derived from routine National Weather Service upper air observations in San Diego.

Table I. Numerical values for the profiles of Figure 4.

22/12Z Oct 97	
Height (m)	M-units
128	356.1
230	377.6
483	406.5
778	432.2
1176	480.1
1357	482.8
1484	494.5
1958	553.3
3077	700.0

23/00Z Oct 97	
Height (m)	M-units
128	352.2
206	360.8
830	446.9
885	452.0
922	453.4
968	437.9
1063	439.9
1265	461.7
1501	492.5
3108	702.0

northeast of Point Loma with a balloon launch altitude of 128 m and Table I lists the numerical values. The 12Z sounding (0500 PDT) shows a mean gradient of 118 *M*/km between 128 and 1176 m and then the modified refractivity gradient decreases through the inversion at the top of the marine boundary layer. The 23/00Z sounding (1700 PDT on the 22nd) shows a mean gradient of 132 *M*/km between 128 and 885 m with the inversion now strong enough to show a trapping layer with a base at 922 m. The signal level data of Figure 3 begin about the time of the 12Z sounding and end about four and one-half hours later; the 12Z refractive conditions should be representative of conditions over the propagation path. However, the effects of the differing mean gradients and variations of C_n^2 associated with these gradients on the measured propagation loss data have not been modeled and could impact the level of the measured signals.

Figure 5 shows the comparison between the distributions of the data in Figure 3 and the simulated 262.85 MHz data. The shape of the distributions are very similar but the median of the observed data is higher. Similar comparisons at the other two frequencies provided similar results. Table II shows the comparison of the medians at each of the frequencies where the column headed RPO represents the median of the simulated

distributions and the column headed EREPS is the median value predicted by the troposcatter model utilized in EREPS. At 143.09 MHz, the median for the data is closer to the RPO-simulated median. At the other two frequencies, the medians for the data are much

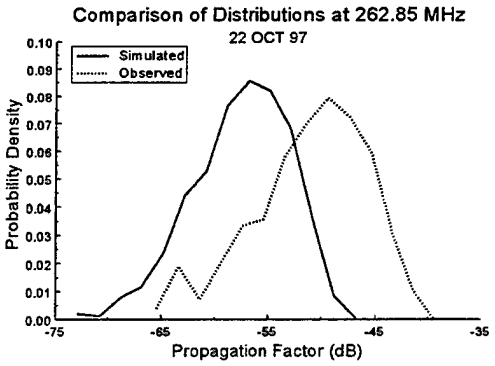

Figure 5. Simulated and observed distributions of propagation factor for the 262.85 MHz frequency.

closer to the medians predicted by the empirical model in EREPS.

Table II. Median propagation loss for measured data, RPO simulations, and the EREPS semi-empirical model.

Freq. (MHz)	Median Propagation Loss (dB)		
	22 Oct 97 Data	RPO	EREPS
143.09	-55.7	-59.4	-49.6
262.85	-49.4	-56.5	-48.8
374.95	-49.9	-54.1	-48.9

DISCUSSION

The bias between the simulated and observed distributions could arise from several sources. First, the scattering model in RPO may suffer from the use of a uniform distribution to represent the refractive index fluctuations or the assumption that the dominant scale of scattering is represented by the vertical PE mesh size, δz. The latter seems to be a justifiable assumption as δz as defined in Equation (1) is related to the Bragg-scatter wavelength for forward scattering [*Gossard and Strauch*, 1983] and numerical experiments conducted by Hitney in developing his troposcatter model did not show any significant differences between using the uniform distribution and a gaussian distribution for refractive index fluctuations. Second, the use of an effective median refractive index structure function, C_{ne}^2, may be underestimating the scattering of the maritime tropical air mass that typically is off the west coast of southern California; *Doviak et al.* [1983] show a range of about an order of magnitude of C_n^2 in their Figure 1 for maritime air as taken from *Gossard* [1977]. Third, even though the mean gradient in the boundary layer of the 22/12Z sounding is 118 *M*/km, the same as used in the RPO simulations, the actual profile has 4 gradients slightly different from this value that may cause higher signal levels in the data.

If the use of a linear gradient of refractivity and an effective median structure parameter profile are the larger contributors to the bias in simulated and observed medians, then the remaining task is to more properly characterize the profile inputs to the propagation model. This would entail a means to calculate profiles of C_n^2 from gradients of temperature and humidity as measured by a radiosonde or output by numerical weather prediction models. This will be pursued as this work continues.

ACKNOWLEDGEMENTS

The VHF/UHF radio data used in this report were collected and reduced by Ted Rogers and Bill Moision, SPAWARSYSCEN San Diego. This work was supported by the Office of Naval Research, ONR-322.

REFERENCES

Doviak R.J., R.M. Rabin, and A.J. Koscielny, "Doppler Weather Radar for Profiling and Mapping Winds in the Prestorm Environment," *IEEE Trans. Geosci. Remote Sens.*, vol. GE-21, no. 1, pp. 25-33, 1983.

Gossard, E.E., "Refractive Index Variance and Its Height Distribution in Different Air Masses," *Radio Sci., 12*(1), pp 889-105, 1977.

Gossard, E.E. and R.G. Strauch, *Radar Observations of Clear Air and Clouds*, 280 pp., Elsevier, NY, 1983.

Hall, M.P.N., *Effects of the Troposphere on Radio Communication*, 206 pp., Peter Peregrinus Ltd, New York, 1979.

Hitney, H.V., "Hybrid Ray Optics and Parabolic Equation Methods for Radar Propagation Modeling," *Radar 92*, IEE Conference Publication No. 365, pp. 58-61, Brighton, UK, 12-13 Oct 1992.

Hitney, H.V., "A Practical Tropospheric Scatter Model Using the Parabolic Equation," *IEEE Trans. Antennas Propagat., 41*(7), pp. 905-909, 1993.

Patterson, W.L., C.P. Hattan, G.E. Lindem, R.A. Paulus, H.V. Hitney, K.D. Anderson, and A.E. Barrios, "Engineer's Refractive Effects Prediction System (EREPS)," NRaD TD 2648, May 1994.

Rogers, L.T., "Effects of the Variability of Atmospheric Refractivity on Propagation Estimates," *IEEE Trans. Antennas Propagat., 44*(4), pp. 460-465, 1966.

DETECTABILITY OF MILLIMETER WAVE RADIATION SCATTERED BY AIRBORNE FIBERS

Robert A. Sutherland
U.S. Army Research Laboratory
Survivability Lethality and Analysis Directorate
White Sands Missile Range, NM 88002
Ph:505-678-4520 Fax:505-678-8822
E-mail:rsutherl@arl.mil

Roger E. Davis
Science and Technology Corporation
555 Telshor Blvd, Suit 200
Las Cruces, NM 88011

ABSTRACT

As a consequence of operating at (relatively) short wavelengths, modern millimeter wave (MMW) radars have become more sensitive to scattering of the main beam (by atmospheric constituents) than their longer wavelength counterparts. This causes problems in two ways: (a) increased backscatter giving rise to the possibility of false targets, and (2) increased susceptibility to remote detection via off-axis scattering in all directions. In this paper we present methods for calculating how much radiation may be scattered in both cases for a realistic battlefield scenario including modern MMW obscurants (i.e., carbon fibers). The calculations include effects of both extinction and scattering and employ realistic concentrations of battlefield obscurants which are modeled as thin cylindrical shaped carbon fibers approximating those used in modern smoke munitions such as the M81 self screening smoke grenade. Results are presented in the form of differential scattering cross-sections for obscurants that are analogous to bistatic and backscatter cross-sections of hard targets used by the radar community. We then show how these results can be used in the (slightly modified) standard radar range equation to produce estimates of the detectability of such radiation by real instruments. Polarization effects and particle orientation are also included in the study. Results are reported in terms of obscurant equivalent radar cross-sections, look up tables, and scaling equations which can be used with the radar equation for further analysis. Preliminary results show that the radar scattering cross-sections of realistic clouds can be on the same order as some military targets (1-10 m^2) which supports our supposition on the possibility of obscurant induced false targets and of remote beam detection.

1. INTRODUCTION

In going to the shorter wavelengths, modern radar systems have gained certain advantages over their longer wavelength counterparts, such as component size and improved optical resolution. On the other hand there are some accompanying disadvantages, especially in the millimeter wave (MMW) regime where scattering and extinction by airborne particles is generally increased. In this paper we present results of our study utilizing MMW propagation algorithms to simulate attenuation and scattering by battlefield aerosols. Of particular interest to this study is off-axis scattering (including backscatter) by cylindrical shaped fibers sometimes used as an electromagnetic countermeasure (i.e. obscurant) on the modern battlefield. The strength and detectability of such scattered radiation by airborne particles in realistic battlefield scenarios is addressed. An idealized scenario is shown in the sketch of Fig. 1.

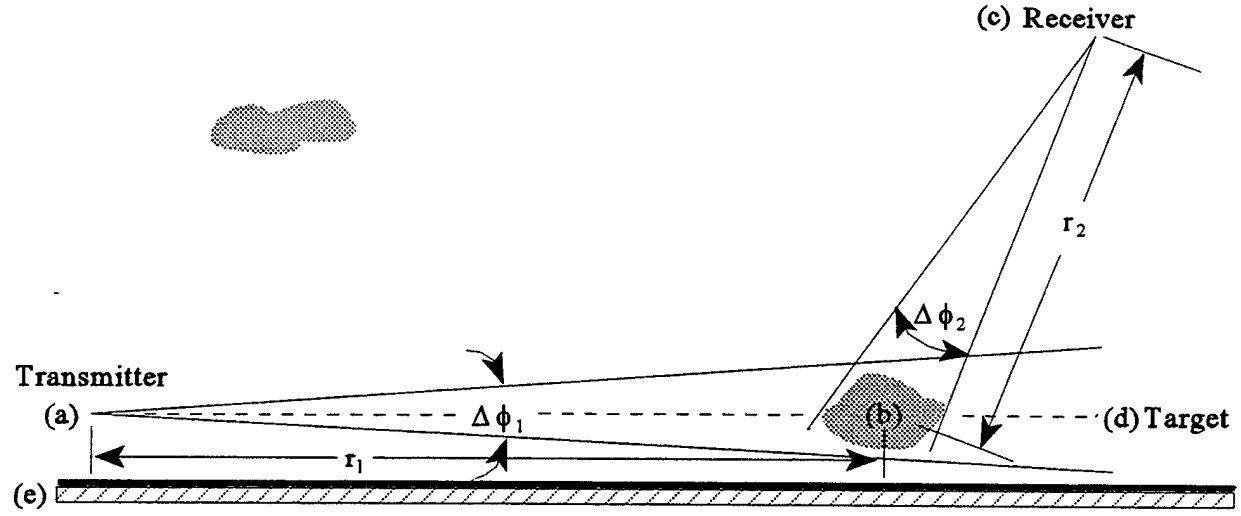

Figure 1: Idealized scenario used for the calculations (side view).

The basic scenario illustrated in Fig. 1 includes (a) a distant scanning radar transmitter, (b) a localized obscurant cloud, © a remote airborne surveillance sensor, (d) a reflective Lambertian target and, (e) a Lambertian emitting surface. The idea is to calculate how much radiation reaches the sensor via off-axis scattering of the radar beam. For the baseline calculations we assume that both the radar and sensor are sufficiently far away so that all rays, either entering or exiting the cloud, can be treated as parallel and unidirectional (this is not at all necessary except that it helps in the interpretation of the radar equation). We also assume that the beam is always horizontal to the earth and wide enough to encompass the entire obscurant cloud within the field of view (the far field approximation). Under these conditions the radar range equation can be written in the following general form (Ref. 1):

$$P_{rec} = [\eta_1 P_1 \frac{G_1}{4\pi\Delta\phi_1^2 r_1^2}] T_1 [\rho A_g] T_2 [\frac{G_2}{4\pi r_2^2} \eta_2 \frac{D_2^2 \pi}{4}] \qquad (1)$$

The factors T_1 and T_2 represent the atmospheric transmittance along the respective distances r_1 and r_2 (Fig. 1). The factor $\eta_1 P_1$ on the left represents the total power of a single pulse averaged over the transmitter angular beam width $\Delta\phi_1$. Defined as such, the product of the terms in the first set of brackets with T_1 represents the total power density (watt/m^2) incident at the facing edge of the obscurant cloud. The factor inside the middle brackets represents the radar cross-section of a hard target of Lambertian reflectivity, ρ, and geometric cross-section, A_g. Thus the product of all of the factors up to and including the middle brackets represents the total scattered power (watts) exiting the target surface in the direction of the sensor. The factors in the rightmost bracket include the receiver efficiency, η_2, and aperture size, D_2 and, written as such, represent the receiver response to an apparent point source (which we will later have cause to modify). The factors, G_1 and G_2 are the antenna gain functions defining the systems' directional response over the respective transmitter and receiver fields of view ($\Delta\phi_1$,$\Delta\phi_2$). There are several forms available for the antenna functions serving various specific applications. For our calculations we choose both to be unit step functions. We have neglected various details

of real systems that we feel are not particularly germane to the task at hand but may be of interest to the reader. Further details of real systems can be found in any of several texts (cf. Refs. 1,2)

The above expression as defined here applies to a single pulse and as such ignores both the receiver sampling time, ΔT_{rec}, and the effect of the radar beam sweep rate, ω_o (radians sec-1). Taking these factors into account the total energy collected by the receiver over the finite sampling time is approximated as:

$$E_{rec} = E_{\max}\frac{\Delta T_{rec}}{\Delta T_{\max}}$$

$$\text{where } E_{\max} = f_t \Delta\tau P_{rec}\frac{\Delta\phi}{\omega_o} \qquad (2)$$

where, from simple geometry , $T_{max}=(\Delta\phi_1/\omega_o)$. Other factors are the pulse repetition rate, f_t (sec^{-1}), and the pulse width, $\Delta\tau$(sec). Equations (1) and (2) will form the basis for the systems. In the remainder of this paper we will work on the development of the center term of Eq. (1) to include the effect of a localized obscurant.

2. METHODS

There are four basic steps in the calculations: (a) calculate realistic obscurant concentration levels, (b) given the concentration levels, calculate the underlying electromagnetic scattering and extinction properties of the obscurant, © given the concentration levels and electromagnetic properties, calculate the total extinction and scattering over all source to sensor paths (i.e. the scattering cross-section), and (d) use the results from above to estimate real (sensor) systems' performance in the radar equation.

a. Concentration levels and optical properties.

Steps (a) and (b) are accomplished using the existing models COMBIC to determine typical obscurant concentration levels (Ref. 3) and DRI-97 to determine the optical properties of the (non spherical) obscurant particles (Ref. 4). Together, the models supply the following three quantities which we define as the obscurant mass extinction coefficient, α_i , the single scattering albedo, ω_i , and the differential scattering efficiency, $q_{i,j}$ as:

$$\alpha_i = \frac{1}{m_p}\sigma_{i,ext} = \alpha_{i,sca}+\alpha_{i,abs}$$

$$w_i = \frac{\sigma_{i,sca}}{\sigma_{i,sca}+\sigma_{i,abs}} \qquad (3)$$

$$q_{i,j} = \frac{1}{a_g} n(r)\,\sigma_{i,j}(\theta,\phi;\theta',\phi')$$

where n(r) is the obscurant particle number density at any point (r), a_g is the orientation averaged single particle geometric cross-section, m_p is the volume averaged single particle mass, $\sigma_{i,sca}$ and $\sigma_{i,abs}$ are the total scattering and absorption cross-sections (m^2) and $\sigma_{i,ext}$ is the total extinction cross-section ($\sigma_{ext} = \sigma_{sca} + \sigma_{abs}$). The quantity, $\sigma_{i,j}$ $(\theta,\phi\ ;\theta',\phi')$ is the differential scattering cross-section ($m^2\ Sr^{-1}$) and is essentially a measure of how much radiation from a particular direction (θ,ϕ) is scattered into the direction (θ',ϕ'). In all cases, the subscripts i,j refer to the incoming and scattered polarimetric components, respectively, of the radiation field (cf. Ref. 4).

b. Obscurant cloud cross-sections.

We next focus on the middle term in Eq. (1) which represents the effect of the obscurant and proceed to determine an obscurant radar cross-section analogous to the hard target definition in Eq. (1). We do this by separating the radar beam into an ensemble of parallel rays as demonstrated in the sketch of Fig.2.

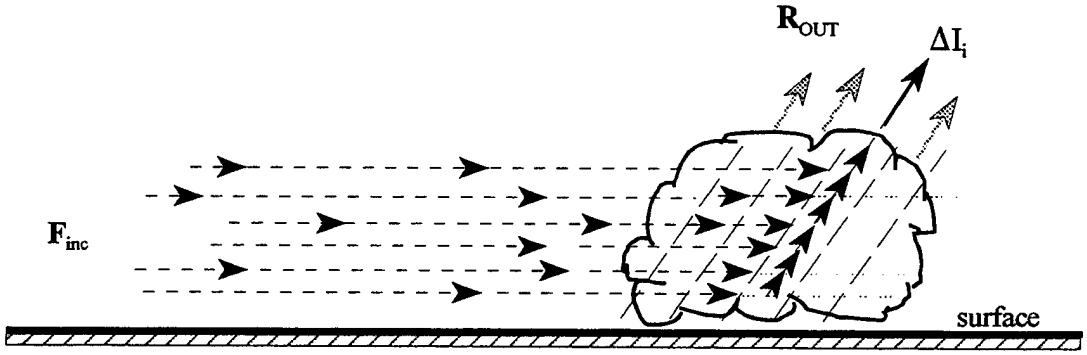

Figure 2. Sketch demonstrating method for computing obscurant total cross-section.

The idea is to compute the radiance emanating from each ray and then sum over all rays to obtain the total radiance exiting the cloud in the direction of the (distant) receiver. The starting point is the well known radiative transfer equation, written here in a form suitable for the problem at hand :

$$\Delta I_i = I_{dir} + \int_o^{r_2} \omega_o\, n(r)\, J_{scat}(r)\, e^{-\tau(r)} dr$$
$$\text{where} \quad \tau(r) = \int_r^{r_2} \alpha\, C(r)\, dr \qquad (4)$$

In Eq. 4 ΔI_i represents the contribution to the total scattered radiance (watt $m^{-2}\ Sr^{-1}$) over some suitable elemental surface area. The first term, I_{dir}, represents the direct contribution from any hard targets (including the surface) in the line of sight and is added for completeness but will be dropped later. Our main interest here is in the second term which represents all contributions arising via in-scattering from the surroundings into the line of sight, sometimes called the diffuse, or non-coherent component. The remaining factor in Eq. (3) is the obscurant mass concentration, C(r), which is related to the particle number density as $[n(r)=C(r)/m_p]$.

The quantity, $J_{scat}(r)$, in Eq. (4) is the so-named optical source function that accounts for all in-scattering from the surroundings and is written formally (dropping the polarimetric notation for the time being) as:

$$J_{scat}(r,\theta,\phi) = \frac{1}{4\pi}\int\int_{4\pi} I'(r;\theta',\phi')\,\sigma(\theta,\phi;\theta',\phi')\,d\theta'\,d\phi' \qquad (5)$$

The angular integration covers all angles (θ',ϕ') over the full 4π upper and lower hemispheres. For our case the integration in Eq. (5) is particularly simple owing to the fact that the (distant) radar beam can be approximated by a single point parallel source, which means that the radiance is treated as a delta function, i.e. $I'(\theta',\phi') = F_{inc}\,\delta(\theta'-0)\,\delta(\phi'-0)$. With this substitution the integration is trivial and yields the following simple expression for the source function:

$$J_{scat}(r;\theta,\phi) = \frac{F_{inc}}{4\pi}\,\sigma(\theta,\phi)\;\; e^{-\tau_o(x)} \qquad (6)$$

We have simplified the notation such that the differential scattering cross-section, $\sigma(\theta,\phi)$, assumes the input beam to always be horizontal (θ,ϕ still refer to the direction of the receiver). The term, F_{inc}, represents the radar beam power density incident on the cloud surface, i.e. identical to first bracketed term of Eq. (1). The factor $\exp[-\tau_o(x)]$ represents the transmittance along the horizontal straight line path between the radar position and the scattering point, r, analogous to the transmittance factor, T_1 of Eq. (1). Substitution of Eq. (6) into Eq. (4), and dropping the direct term, I_{dir}, yields:

$$\Delta I_i^* = \frac{F_{inc}}{4\pi}\, e^{-\tau_o(x)} \int_o^{r_2} n(r)\,\sigma(\theta,\phi)\, e^{-\tau(r)}\,dr \qquad (7)$$

where we have used the (*) notation to indicate diffuse radiation only (a consequence of dropping the direct term). The total diffuse radiance exiting the cloud in the direction of the receiver is then found by appropriate integration over all transmitter-to-receiver paths which we represent here in finite form as:

$$R_{out} = \frac{\Sigma_i \Delta I_i\; dA_i}{\Sigma\, dA} \qquad (8)$$

where dA_i is the incremental area of integration (actually summation). We next define the total cloud cross-section, Σ_n, and efficiency Q_g as follows:

$$\Sigma_n = \frac{R_{out}}{F_{inc}} A_g = Q_n A_g \qquad (9)$$

where, as indicated, $Q_n = R_{out}/F_{inc}$. Note that the units of Σ_n are m^2 per steradian, the same as $\sigma_{i,j}$, the differential cross-section.

c. Polarimetric formulation and final form of the radar equation.

It is a straightforward matter to extend the concept to include linear polarization by breaking up the input and output beams into their respective orthogonal components and defining the polarization matrix as follows:

$$\begin{vmatrix} R_v^{out} \\ R_h^{out} \end{vmatrix} = \begin{bmatrix} Q_{vv} & Q_{vh} \\ Q_{hv} & Q_{hh} \end{bmatrix} \begin{vmatrix} F_v^{inc} \\ F_h^{inc} \end{vmatrix} \qquad (10)$$

The subscripts "v" and "h" refer to vertical and horizontal polarization, respectively. The definition of the scattering elements are then found by appropriate substitution of the polarimetric differential scattering cross-sections in to Eqs. 7, 8, and 9, that is:

$$Q_{i,j}(\theta,\phi) = \frac{1}{A_n} \Sigma_k \left[\int_0^{r_2} [n(r)\ \sigma_{i,j}(\theta,\phi)\ e^{-(t-t_o)}\, dr] \right] dA_k \qquad (11)$$

where all terms remain as defined in previous sections. With the differential scattering cross-sections so defined and making other substitutions suggested in the text, the final form of the expression for the power collected by the receiver is:

$$P_{rec} = \left[\frac{\eta_1 P_1}{4\pi\, \Delta\phi_1^{\,2}} \frac{G_1}{r_1^2}\right] T_1 \left[Q_n A_g\right]_{i,j} T_2 \left[\frac{G_2}{r_2^2} \frac{\eta_2 D_2^2}{16}\right] \qquad (12)$$

We have rearranged such that the middle term represents the total obscurant contribution. Note that the product of the first two bracketed terms represents the total power reaching the receiver per unit solid angle. Because $A_g/(r_2)^2 = \Delta\phi_o$ is the solid angle subtended by the cloud at the receiver, the product of this angle with the first two bracketed terms (with the transmittances T_1, T_2) represents the total power density reaching the receiver and all of it is collected as long as the receiver field of view ($\Delta\phi_2$) is larger than this angle. Otherwise, only that amount within the receiver field of view is collected.

3. RESULTS

In this section we present results of calculations to produce a digital array of the obscurant cloud cross-sections given by Eqs. (10) and (11) using methods similar to those of the FORTRAN program PILOT-81 (Ref. 5). These results are then presented in the form of digital arrays, or "maps" overlaying some particular area of interest as viewed from an overhead receiver. The results can be scaled for the four polarimetric modes of Eq. (10) using the look-up table described in subsection 3b. The data from these maps can be input directly into the radar equation (Eq. 12) to determine power levels sensed by the receiver. Inputs to the model include obscurant concentration (or number density) as a function of spatial coordinates and optical properties which are obtained from appropriate models (Refs. 3, 4). The scenario is basically the far field scenario of Fig. 1 with the radar at

10 meters above the surface. The receiver in our example was placed 5000 m downrange at an altitude of 100 m. The method can accommodate localized obscurant distributions or large area hazes (not addressed here).

a. Obscurant concentrations, COMBIC model.

Obscurant concentration levels were determined using the ARL COMBIC model employing an 8 round volley of self screening M81 grenades detonated at a burst height of 20 meters. As shown in Fig 3, this resulted in a composite toroidal shaped cloud approximately 35 meters in diameter with a mass concentration on the order of 0.50 g/m^3, corresponding to a particle number density of about 2.4 X 10^6 m^3 (for fibers 3 mm in length). This particular slice was generated shorted after launch (9 seconds) at a height of 17 meters and still

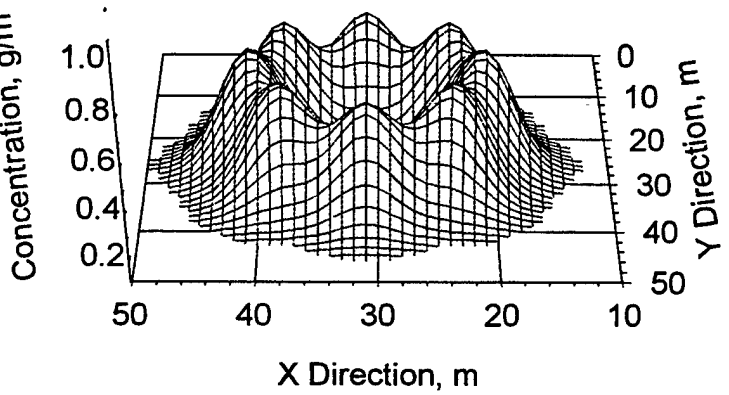

Figure 3. Mass density slice map of COMBIC generated obscurant cloud.

shows details of the source origin. Note for example the 8 distinctive maxima marking the location of the individual munitions. Based upon the mass extinction coefficient value of 2.54 m^2/gm (next section) this resulted in vertical and horizontal maximum optical depths of about 15 and 25 respectively. Atmospheric conditions were modeled as stable (Pasquill Category C) with a wind speed of 2.5 m/sec.

b. Obscurant optical properties, DRI97 model.

The volume averaged differential scattering efficiencies as calculated with the DRI97 model for the four polarization modes assuming a uniform random orientation distribution are shown in Table 1. The particular results presented here have been averaged over the azimuth and are thus a function of the scattering zenith angle (θ) only and were generated assuming the incident beam in the horizontal plane (θ_{inc} =0). The second column represents the unpolarized result and the remaining columns represent the various polarimetric components as labeled. As one may expect there is some symmetry in that, for all angles, the pairs (vv, hv) and (hh, vh) are identical and that the sums (vv + vh) and (hh+hv) sum to a constant (0.50). Therefore we really have only two cases to consider. For this example the mass extinction coefficient was found to be 2.54 m^2/g with a polarization ratio of 0.50. The volume averaged total scattering and absorption efficiencies were found to be 14.9 and 47.2, respectively. Thus, from Eq. (3), q_{ext} = 62.1 and ω = 0.24.

TABLE 1
Differential Scattering Efficiencies for Polarimetric Scaling Factors

THSCAT	PNOT	V V	V H	VV+HH	H H	H V	HH+VV
0.0	1.00	.250	.250	.500	.250	.250	.500
10.0	0.99	.248	..252	.500	..252	.248	.500
20.0	0..97	.242	.258	.500	.258	.242	.500
30.0	0.94	.233	.267	.500	.267	.233	.500
40.0	0.89	.221	.279	.500	.279	.221	.500
50.0	0.85	.206	.294	.500	.294	.206	.500
60.0	0.81	.191	.309	.500	.309	.191	.500
70.0	0.77	.177	.323	.500	.323	.177	.500
80.0	0.76	.168	.332	.500	.332	.168	.500
90.0	0.75	.165	.335	.500	.335	.165	.500
100.0	0.76	.168	.332	.500	.332	.168	.500
110.0	0.77	.177	.323	.500	.323	.177	.500
120.0	0.81	.191	.309	.500	.309	.191	.500
130.0	0.85	.206	.294	.500	.294	.206	.500
140.0	0.89	.221	.279	.500	.279	.221	.500
150.0	0.94	.233	.267	.500	.267	.233	.500
160.0	0.97	.242	.258	.500	.258	.242	.500
170.0	0.99	.248	.252	.500	.252	.248	.500
180.0	1.00	.250	.250	.500	.250	.250	.500

c. Obscurant cross-sections.

The results of the obscurant cross-section calculations are presented in Fig. 4 in the form of a pseudo radar scan format. The resultant pie shaped area is marked off in equal distant sectors in range and azimuth. The number in each sector indicates an obscurant cloud differential scattering cross-section that results from an obscurant cloud located in the center of the sector and viewed 100 m above the location marked X (radar receiver position) in Fig 4. The radar transmitter is located at the origin and is assumed to scan a 90 degree full field of view. No shadowing of any cloud by any other cloud is allowed for these calculations. That is, each cloud is fully irradiated by the transmitter. Thus the quantities displayed in Fig. 4 are equivalent to the factor $[Q_n A_g]$ in Eq. (12) and can be substituted directly into the radar equation.

The values in Fig. 4 represent the vertically polarized case for both the transmitter and receiver (VV) but can be used as the baseline to find other combinations using the results of Table 1. Note, however, that this does require knowing the scattering angle, which can be found from simple geometry defined in Fig. 4, and the fact that the sensor height for the calculations was 100 m.

This scaling approach eliminates the need for a set of new calculations to determine different polarization scenarios. Because the scattering efficiencies are scattering angle dependent, the user must use the calculated cross-sections only at the angles specified. However, any transmitter power and distance and any receiver distance along the scattering angle can be considered.

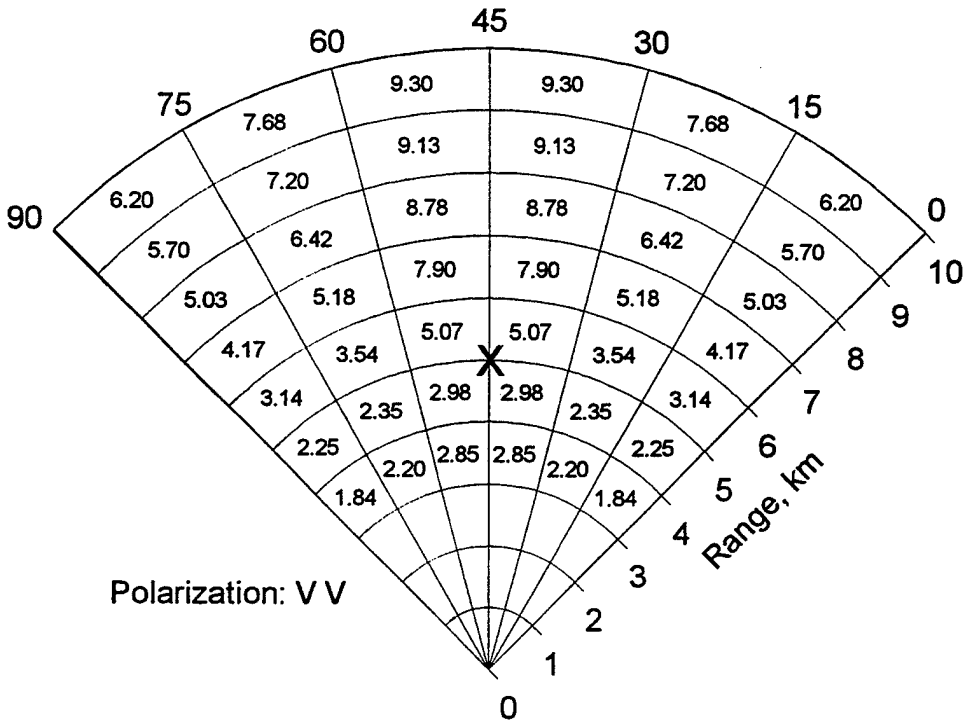

Figure 4. Obscurant cloud radar cross-sections values for various locations

4. SUMMARY & CONCLUSIONS

In this paper we have reported results of our efforts to calculate (bistatic) radar cross-sections of obscurant clouds that are equivalent to the 'hard target' descriptions used by engineers in the radar range equation. Our preliminary results give values of the obscurant cloud radar cross-sections on the order of 1 to 10 square meters. These values vary depending upon the transmitter-cloud-receiver geometry and the polarization of incident and scattered radiation. These values are significantly large, being roughly on the same order as many of the "hard" targets on the modern battlefield. The results here are based upon an 8 round volley of vehicle self-screening grenades dispensing MMW countermeasure materials (which we assume probable on the battlefield).

The obscurant concentrations and optical properties were obtained with the ARL COMBIC and DRI97 models and are based upon the specifications of the M81 grenade and thin dielectric carbon fibers recently developed as a MMW obscurant. Model results yield a value of 0.30 for the obscurant scattering-to-absorption ratio. While these results indicate a dominance for absorption, scattering is still significant enough to make scattered radar beams detectable. For a horizontal scanning radar beam the (hh) and (vv) polarization ratio is a function of bistatic viewing angle and, based upon our calculations, varies for a value of 1.0 for both forward and backscatter directions (0 and 180 degrees) to a value of 2.0 in the 90 and 270 degree directions. For a uniform random fiber orientation distribution, the composite (hh + hv and vv + vh) components are equal, giving a polarization ratio of unity.

Based on our results our main conclusion is that MMW radar beams are certainly more susceptible to remote detection (via the scattering mechanism) than their longer wavelength counter parts. Also, based upon the magnitude of the calculated cross-sections, which are comparable to 'real' target values, there is a strong possibility that such obscurants can appear as 'false targets' to some modern radars. We furthermore estimate that our results may be somewhat low because we have neglected higher order scattering terms which would tend to increase the scattered signal. However, whether or not this will actually happen depends on several other factors, the most significant being the radar signal processing algorithms, which are the subject of further analysis

ACKNOWLEDGMENTS

We would like to acknowledge Mr. Bernie Farran and Mr. Steve Lacy who helped with the figures and graphs and Ms Scarlett Ayres who helped with the COMBIC results.

REFERENCES

1. The Infrared and Electro-Optics Handbook, Vol 6: Active Electro-optical Systems, Executive Editors: Accetta and Shumaker, Infrared Information Analysis Center and SPIE Optical Engineering Press, 1994.

2. Skolnik, Merrill, 1990, Radar Handbook (2nd Edition), McGraw-Hill Publishing Company.

3. Hoock, et.al., 1987, "Combined Obscuration Model for Battlefield Induced Contaminants (COMBIC)" US Army Atmospheric Sciences Laboratory Technical Report, EOSAEL 87, Vol. 11, ASL-TR-0221-11.

4. Sutherland, R.A., 1997, "Methods for Calculating the EM Properties of Cylindrical Shaped Thin Dielectric Fibers", US Army Research Laboratory Technical report, in preparation.

5. Howerton, R.H. and R.A. Sutherland, 1997, "Atmospheric Transfer Functions for the SLAD Pilot Program", US Army Research Laboratory Technical Report, in review.

Using the Global Positioning System To Detect Surface-Based Ducts

Kenneth D. Anderson
Propagation Division
Space and Naval Warfare Systems Center San Diego D883
49170 Propagation Path
San Diego CA, 92152-7385
1 619 553 1420, 1 619 553 1417 (Fax)
kenn@nosc.mil

Abstract

Terrestrial propagation of radio waves at frequencies somewhere above 30 MHz is often significantly affected by the composition of the troposphere (*Hitney, et al., 1985*), especially when both terminals are near a coastline. A famous example of anomalous propagation effects occurred in India during World War II when a 200 MHz radar (with an expected detection range of several hundred miles) detected Arabia some 1700 miles away (*Freehafer, 1951*). Similar effects have been observed near the southern California coast by cell phone users in Los Angles and San Diego who, instead of connecting with their local cell, are sometimes connected with a remote cell, perhaps 100 miles away. Such anomalous effects are usually measured indirectly by sensing atmospheric properties with an instrumented weather balloon, a process that is both time-consuming and expensive. However, recent work with the Global Positioning System (GPS) demonstrates that earth-based measurement of GPS satellite signals can detect these anomalous propagation conditions. Therefore, by capitalizing on the existing technology of GPS, an affordable, all-weather, anomalous effects measurement capability is readily available.

1. Introduction

In the mid-1970s a flurry of activity arose regarding the development of computer-based refractive effects assessment systems designed to calculate and display propagation effects. One such system for radio frequency propagation analysis over sea, known as the Integrated Refractive Effects Prediction System (*Hitney and Richter, 1976; Baumgartner et al. 1983*), was installed onboard all U.S. Navy aircraft carriers to support mission planning for radar, communication, and aircraft operations. Of crucial importance to the accuracy in predicting radar detection ranges or maximum microwave communication ranges is a thorough knowledge of the refractive environment. In many situations, one can indirectly sense the local vertical refractive environment using radiosondes (which measure pressure, temperature, and relative humidity and telemeter these data to a ground station as the balloon ascends) and apply the results to modeling signal propagation as if the refractive environment were homogeneous in both range and time. However, near the coast, it is likely that the refractive environment looking seaward is different from the refractive environment looking towards land. Local or in-situ observations of the

environment using radiosondes are inadequate for reasonably accurate predictions of refractive effects on radio frequency system performance in coastal areas.

The mechanisms that control radio wave propagation in the troposphere are either normal (standard) or anomalous (nonstandard). Normal propagation mechanisms are those associated with the so-called standard atmosphere, where the radio refractive index, n, defined as the ratio of the speed of light to the speed of the radio wave, decreases exponentially with increasing height. Close to the surface, the speed of the radio wave is slightly less than the speed of light, and n is typically a number like 1.0003. The term *refractivity* is related to the radio refractive index as $N=(n-1)10^6$ and defines a convenient set of numbers (e.g., 300 versus 1.0003); it is also related to atmospheric parameters (pressure, P; temperature, T; and water vapor pressure, e) as $N=77.6/T(P+4810e/T)$, where the units are hPa and K. For a normal troposphere, the refractivity gradient with respect to height falls between -79 and 0 N units per kilometer of height and represents long-term averages for a particular area. For the continental United States, the normal refractivity gradient near the surface is -39 N units per kilometer (*Bean and Dutton, 1968*); a ray launched horizontally into this channel will be refracted downward but at a rate less than the curvature of the earth, so the radio wave will bend away from the earth with increasing range from the transmitter.

Anomalous propagation effects are divided into three categories: subrefractive, superrefractive, and trapping. If the refractivity gradient exceeds 0 N km^{-1}, a ray will bend upwards, shortening the horizon, and the channel is said to be subrefractive. A gradient between -157 and -79 N km^{-1} refracts a ray downward at a rate greater than normal but less than the earth's curvature, extending the horizon, and the channel is said to be superrefractive. The most dramatic nonstandard effect on terrestrial systems occurs when the refractivity gradient is less than -157 N km^{-1}, which is called a trapping gradient. In this case, a ray is refracted downward at a rate exceeding the earth's curvature, leading to a condition called ducting, where a ray propagates to ranges well beyond the normal radio horizon. A surface-based duct is said to exist if there is a trapping layer such that a ray is *refracted* downward and eventually *reflects* off the surface. If the surface is a good reflector of radio frequency energy (like the ocean's surface), the reflected ray rises in height with increasing range until it is refracted downward by the trapping layer, eventually striking the surface again, but at a greater range, and propagating with a low attenuation rate. Modified refractivity, M, defined as $M = N + 0.157z$, where z is the height (m) above the surface, is a useful term in propagation analysis because a trapping gradient is readily identified as a negative M unit gradient. Table 1 lists the four refractive conditions and their relation to N and M gradients, and Fig. 1 graphically illustrates the curvatures.

Table 1. The four refractive conditions described by the gradients of N and M.

Condition	N-Gradient (N/km)	M-Gradient (M/km)
Trapping	$dN/dz \leq -157$	$dM/dz \leq 0$
Superrefractive	$-157 < dN/dz \leq -79$	$0 < dM/dz \leq 78$
Normal	$-79 < dN/dz \leq 0$	$78 < dM/dz \leq 157$
Subrefractive	$dN/dz > 0$	$dM/dz > 157$

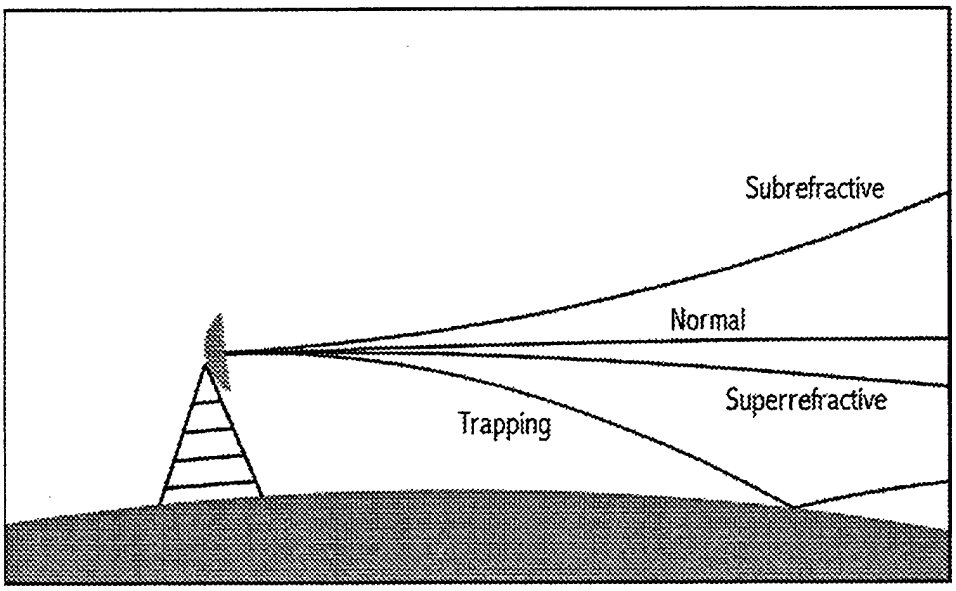

FIG. 1 Refractive bending for each of the four refractive conditions.

These refractive effects can be measured using known radio frequency transmitters. One set of well-known radio frequency transmitters is the GPS satellite constellation. These 24 satellites, which are in 12-hour orbits, provide coverage so that anyone, anywhere on the earth, can see at least four satellites at one time. Signals from these satellites are used to establish a near-earth coordinate: Three satellites are needed to determine the position by geometric triangulation, and a fourth satellite is needed to minimize position error due to offsets between the clocks on each satellite (*Leick, 1990*). However, the signals do not travel in a straight line from the satellite to a receiver on the earth.

In the ionosphere, the straight-line path is distorted by the distribution of electrons trapped in the earth's magnetic field. (The manner in which the electrons are distributed is primarily due to solar activity and the concentration of electrons is greater in that portion of the ionosphere facing the sun.) These electrons refract the signal and make the satellite appear to be several meters farther away than it is, causing a triangulation error. The designers of GPS provide a correction for this ionospheric error by broadcasting signals at two frequencies so that the receiver can apply a position correction based on the differential propagation delay between transmitted signals (*Flock, 1986*).

In the troposphere, path distortion is primarily due to the distribution of water vapor, which refracts the signal path and makes the satellite seem farther away. Errors caused by tropospheric refraction can be minimized by selecting satellites that are at least 10 degrees above the horizon—the higher the angle, the less tropospheric refraction affects positioning. However, even though tropospheric-induced errors can be significantly reduced by selecting high-elevation-angle satellites, in tropic and temperate climes, especially near the coast, tropospheric-induced errors for low-elevation-angle satellites are significant.

2. Experimental Measurements

An example of tropospheric-induced errors was obtained during a series of measurements made in early February 1997. Data representing both a normal refractive atmosphere and a surface-based duct are compared in Fig. 2 as *M-z* plots. These data were measured in the southern California coastal region as part of a test involving low-elevation-angle GPS observations. On 10 February the *M* gradient is 128.5 *M*/km (solid curve), which is close to normal (and closer to the rate of 130 *M*/km that is expected in a normal maritime environment). However, on 13 February the *M-z* plot (dashed line) clearly indicates a 160 m thick surface-based duct. During the week of tests, local radiosondes were planned for 2000 UTC (1200 noon local), and additional radiosondes were independently taken at 0000 and 1200 UTC from a National Weather Service site approximately 10 miles to the north and several miles inland.

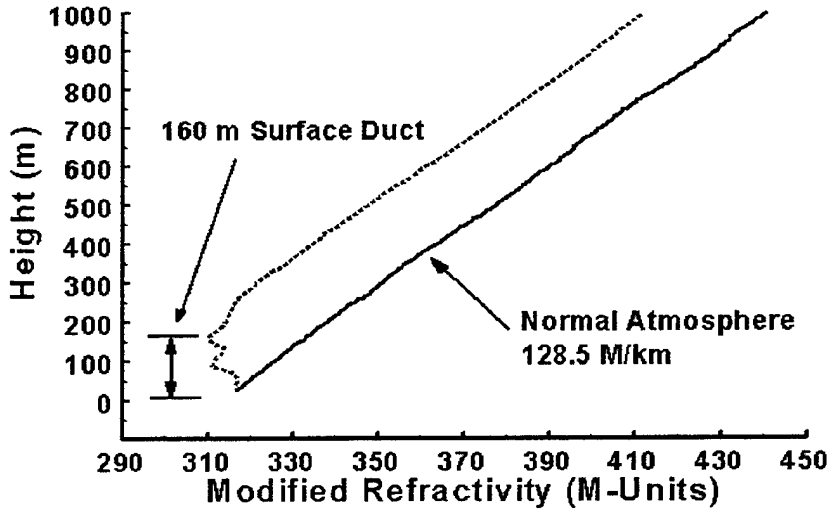

FIG. 2 Two refractive environments measured on the southern California coast during low-elevation angle GPS signal measurements. A normal refractive condition was observed on 10 February 1997 (solid line) and a strong surface-based duct was observed three days later on 13 February (dashed line).

The GPS signals received from the same satellite on these two days differ dramatically (see Fig. 3). On 10 February the satellite signal (solid curve) is lost as the satellite descends below a geometric elevation angle of -0.81 degrees. (The rise and fall of the signal prior to this time is due to multipath effects, which are the constructive and destructive summation of two rays transmitted from the satellite; one ray traverses space directly from the satellite to the receiver antenna, whereas the second ray arrives at the antenna after reflecting off the ocean's surface—also known as Lloyd's mirror effect). On 13 February the signals (indicated in Fig. 3 as the dashed line) were tracked until the satellite was at a geometric elevation angle of -1.95

degrees. The only way this extended tracking could happen is if a strong surface-based duct trapped the signals and allowed them to propagate when the satellite was well over the horizon. This event occurred about 1½ hours before the scheduled radiosonde, so to confirm the suspected refractive condition, the radiosonde was rescheduled for immediate launch. The data in Fig. 2 (dashed line) confirm the environmental condition. These measurements represent the first instance where a suspected surface-based duct, detected using radio frequency signals, has been confirmed by meteorological observations.

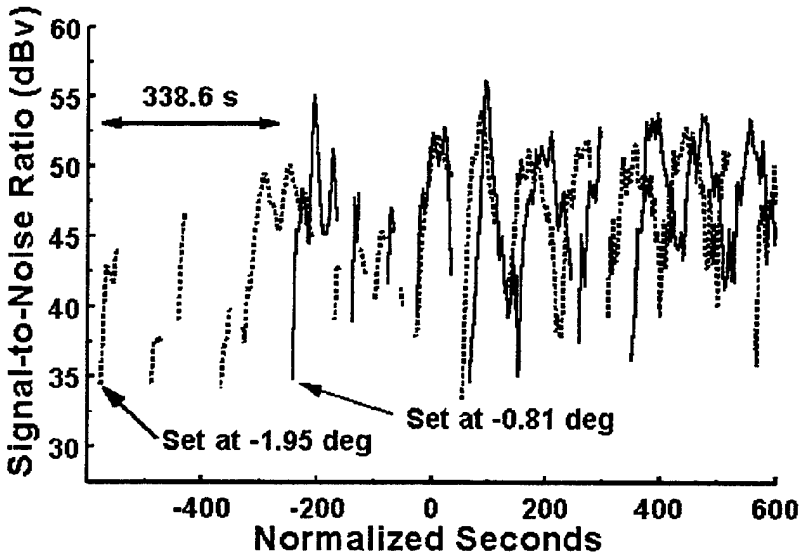

FIG. 3 The abscissa is normalized seconds, where zero is defined as the epoch when the satellite (PRN 4) is at exactly zero degrees elevation (geometric) with respect to the receiver antenna (which was located on a pier approximately 23 m above the ocean surface). The ordinate is signal-to-noise ratio for one of the receiver's channels (specifically, the Coarse Acquisition control loop monitoring the 1 MHz bit rate GPS code transmitted on the 1,575.42 MHz carrier) and is a measure of received signal strength. Data taken during normal refractive conditions (10 Feb. 1997) are shown as the solid line. Data taken during a surface-based ducting condition (13 Feb. 1997) are shown as the dashed line.

3. Conclusions

Recent experimental measurements demonstrate the ease with which observations of low-elevation angle satellite RF signals can be used to declare *normal* and *surface-based ducting* refractive conditions. Even though the measurements indicate only two refractive conditions, future measurements will clearly demonstrate that this method can readily detect all four refractive conditions.

References

Baumgartner, G.B., Jr., Hitney, H.V., Pappert, R.A., *Proc. Inst. Elec. Eng.*, **130**, 630-642 (1983).

Bean, B.R., Dutton, E.J., *Radio Meteorology*, (Dover, New York, 1968).

Flock, W.L., *Propagation Effects on Satellite Systems at Frequencies Below 10 GHz*, (NASA Ref. Pub. 1108, 1987).

Freehafer, J.E., in *Propagation of Short Radio Waves*, Ed. Kerr, D.E., 9-22, (McGraw-Hill, New York, 1951).

Hitney, H.V., Richter, J.H., *Nav. Eng. J.*, **88**, 257-262, (1976)

Hitney, H.V., Richter, J.H., Pappert, R.A., Anderson, K.D., Baumgartner, G.B., Jr., *Proc. IEEE*, **73**, 265-283 (1985).

Leick, A., *GPS Satellite Surveying*, (John Wiley & Sons, New York, 1990).

Acknowledgement

This work is sponsored by the Office of Naval Research, Dr. Scott Sandgathe, Code 322MM.

MODELLING THE INFLUENCE OF ATMOSPHERIC EFFECTS ON THE PERFORMANCE OF ELECTRO-OPTICAL SYSTEMS IN A MARINE ENVIRONMENT UNDER UNSTABLE CONDITIONS

William S. Andrews and Capt S. Craig Jorgenson
Department of Chemistry and Chemical Engineering
Royal Military College of Canada
Kingston, Ontario, CANADA K7K 7B4
Phone: (613) 541 6000 ext 6052, Fax: (613) 542 9489
Email: andrews_w@rmc.ca

J. Luc Forand and Daniel L. Hutt
Defence Research Establishment Valcartier
Val-Belair, Quebec, CANADA G3J 1X5

The limiting factor in electro-optical system performance is often the degradation caused by atmospheric turbulence. This is especially true in the marine environment, where engagements close to the water surface are typically made over distances of tens of kilometers. The long pathlengths and proximity to the water surface maximize the impact of the atmosphere. In fact, atmospheric effects on visible and infrared imagery, such as blurring, distortion, scintillation and random image displacement, can be predicted reasonably well by conventional theory for unstable and neutral conditions. This notwithstanding, current models are complex and computationally intensive.

This paper reports on the analysis of data extracted from video images from a visible CCD camera showing an array of light sources at a distance of 10.4 km to a stationary platform and 28 km to a moving ship over the North Sea (albeit under primarily unstable conditions). The data were obtained during the Marine Aerosol Properties and Thermal Imager Performance (MAPTIP) experiment sponsored by NATO and conducted off the Dutch coast in 1993. Analysis has been conducted primarily using artificial neural network (ANN) technology to establish correlations between various atmospheric input parameters and image characteristics, particularly mirages. ANN predictions of maximum intervisibility range and minimum mirage range were within 2% out to 28 km and mirages were correctly predicted for 96% of the cases using a ship target. For the platform target, image and mirage detection was correctly predicted 96% and 97% of the time respectively and image and mirage separation angles were predicted within 5% and 18% of measured values, respectively.

Introduction

Most military sensors and imaging devices operate using electromagnetic (em) radiation. Consequently, the em propagation properties of the atmosphere must be understood and able to be predicted in order to maximize the effectiveness of these devices. Straight-line propagation of em radiation is only possible, however, in non-refractive atmospheres. Unfortunately, the atmosphere's refractive index varies with

pressure,temperature and water vapour content, causing radiation to follow a curved path. This condition is exacerbated in a marine environment by the presence of aerosols. Consequently, in general, the apparent elevation angle from an observer to a target is not that given by a straight line between the two. This would have an obvious impact on the chances of a successful engagement of the target by a weapon system relying on em targetting.

North Atlantic Treaty Organization (NATO) maritime countries have been interested in the concentrations and properties of marine aerosols and the impact of these aerosols on the performance of imaging systems within the marine boundary layer (MBL). To this end, a joint international trial was conducted off the Dutch coast from 18 October to 3 November 1993 called the Marine Aerosol Properties and thermal imaging Performance (MAPTIP) trial.[1] A portion of the trial involved measuring the performance of imaging systems sited on shore under a variety of atmospheric and sea conditions, with the targets being a static platform and a moving ship, both mounting patterns of lights. Imaging data collected by Canadian, French and German teams has been analyzed by the Refractive Effects in the Visible and Infrared working group, with a report of the analysis having been drafted.[2]

Refractive Effects

The consequence of em refraction in the MBL leads to two important phenomena. One, known as sub-refraction (which may result in a mirage), occurs when radiation from the target appears to be coming from two distinct sources at different elevations. The other phenomenon is known as super-refraction or ducting and occurs when em radiation is observed from a source that would not be observable under non-refractive (straight line-of-sight) conditions. For both these phenomena, the amount of deviation from non-refractive conditions is highly dependent on atmospheric conditions and the em wavelength.

The MBL extends from the water surface to a height which may vary from 20 to 100 m. If the air and sea surfaces are at different temperatures (a common occurrence) the vertical temperature and humidity gradients will be significant. This, in turn, will affect systems relying on em propagation through the MBL.

The refractivity is a function of dry atmospheric prerssure, air temperature and water vapour pressure, with the vertical refractivity gradient being a function of the vertical gradients of these three quantities, as well as air temperature and refractivity.

Monin-Obukhov similarity theory can be used to determine the refractivity at any height above the mean water level (MWL). One model based on this theory is the L(W)WKD,[3] which solves a series of coupled differential equations. This program uses a ray-tracing algorithm to predict image effects of sources/targets transmitting em radiation in the MBL. The program, although predicting well under unstable and neutral conditions, i.e., when the sea water temperature is greater than or equal to the air temperature, the model is computationally intensive and requires a trained operator. It was decided, then, to investigate another modelling approach which might produce comparable or better predictions with fewer computations. The modelling technique

chosen for investigation was the artificial neural network (ANN).

Artificial Neural Network Models

Artificial neural networks are considered a branch of artificial intelligence and found their origins in psychologists attempts at modelling the brain's functions. The seminal work on the back propagation paradigm, the most widely used of ANN models, was only published in 1986.[4]

Basically, an artificial neural network takes raw input data, maps it into an input space, and then introduces it into the network. The network itself is an interconnection of nodes or processing elements (also sometimes called artificial neurons) which are arranged in layers (Fig. 1). The input layer contains a node for each variable, with each complete set of variables describing a specific input vector. For example, each measured value of volumetric extinction coefficient has a corresponding vector of measured experimental variables and parameters. In addition to the input variables, the input layer also contains a bias node which is permanently assigned a value of 1 and is analogous to an electrical ground. Its presence was found to aid convergence during training.

Each node in the input layer is connected to each node in the next layer, which is usually called the hidden layer. The scaled (mapped) input values each have a weight applied to them before the values are introduced into the hidden layer. At each hidden node, the weighted inputs are summed and then mapped back into the range -1 to +1 by the application of a hyperbolic tangent transfer function before being passed to the output layer. Conventionally, there are one or two hidden layers, with the interconnections between nodes in the two hidden layers being analogous to those between the input and first hidden layer.

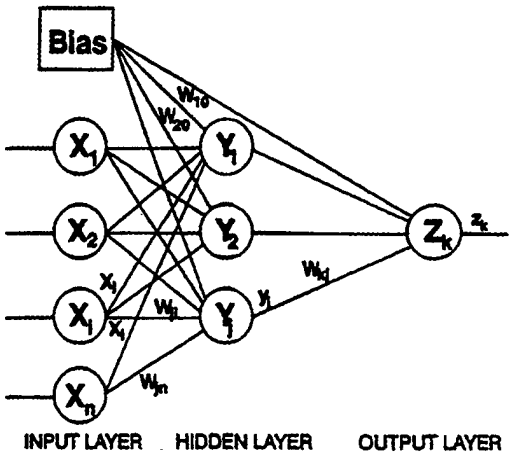

Fig. 1. Typical architecture of a back propagation neural network.

Again, each hidden node in the final hidden layer, as well as the bias node, is connected to each output node, with the process of applying weights to each connection, the weighted inputs being summed and then having a transfer function applied being repeated. The output of the output node(s) must then be mapped back into real-world value(s).

To initial scaling of input variables, is effected by:

$$x_i = 2V_i\left(\frac{M_i + m_i}{M_i - m_i}\right), \qquad (2)$$

where V_i is the unscaled i^{th} input value, M_i is the maximum value of the range of the i^{th} input, m_i is the minimum value of the range of the i^{th} input and x_i is the scaled i^{th} input value.

The scaled inputs (which can also be considered as the outputs of the input layer) have the appropriate connecting weights, w_{ji} applied. These weighted outputs become the inputs for the nodes of the first hidden layer, where

they are summed and then transformed using a transfer function, as outlined by the following equations:

$$I_j = \sum_{i=0}^{n} w_{ji} x_i \,, \qquad (3)$$

where w_{ji} is the connection weight between the j^{th} hidden node and the i^{th} input node, and I_j is the sum of the weighted inputs to the j^{th} hidden node, and

$$y_j = \tanh\left(I_j\right) = \frac{e^{I_j} - e^{-I_j}}{e^{I_j} + e^{-I_j}}, \qquad (4)$$

where y_j is the output of the j^{th} hidden node.

This process is repeated for the second hidden layer and the output layer. The output value from the output layer must then be mapped back to provide a real value for the logarithm of the volumetric extinction coefficient. In fact, this process is essentially the reverse of the initial scaling described in Eq.2, although it is simplified by only having to consider the mapping of one variable. This is accomplished by

$$C = \frac{(M - m)z + (Rm - rM)}{R - r} \qquad (5)$$

where C is the predicted value desired (presence of image or mirage, range or angular separation) corresponding to the specific input vector defined by $x_1, x_2 \ldots x_9$, M and m are the real (measured) maximum and minimum of the output variable, z is the network output value, whose range falls between the maximum and minimum values R and r (for the tanh function, these values are taken as 0.8 and -0.8 respectively).

At the start of the training process, the connecting weights throughout the network are given random values. When the output value is generated, it is compared to the corresponding actual measured value. The difference between these two values is considered the global error and is propagated backwards through the network. An iterative process is carried out of adjusting the connecting weights to minimize the global error. A gradient descent optimization is used to adjust each of the connecting weights locally. Once the global error has been minimized over the whole training set, the weights can be fixed and the network can be used to make blind predictions.

A trained ANN lends itself particularly well to incorporation into a spreadsheet which can be driven by a macro. It can also be incorporated into computer codes to provide real-time determination of the atmospheric parameters, as required.

The basic characteristics of ANN models which seemed appropriate for the application reported in this paper were that they could provide n-dimensional non-linear correlations, they are capable of reproducing synergistic effects among system variables, the input variables need not be linearly independent, they are particularly good at handling noisy and incomplete data, they provide a smoothing function and they can provide (through examination of the weight space or by sensitivity analysis) the relative significance or importance of the input variables.

Data Collection

A shore installation, centred on the Katwijk Beach House (Fig. 2) was established for the various video

cameras used, with imaging in the visible and infrared wave bands.

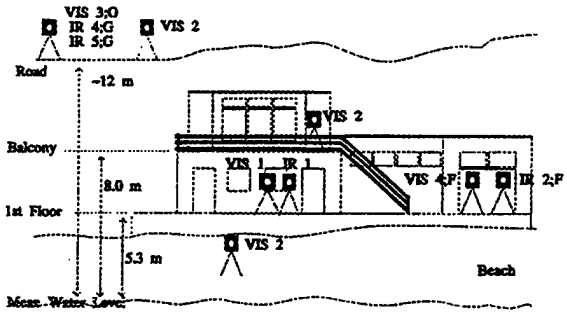

Fig. 2. Diagrammatic representation of the shore installation at Katwijk Beach House used for data collection during MAPTIP trials. Image from Reference 2.

The static target was the Meetpost Nordwijk platform (fig. 3), which mounted 500 W halogen lamps at heights varying from just above the mean water lever (MWL) to 20 m above MWL.

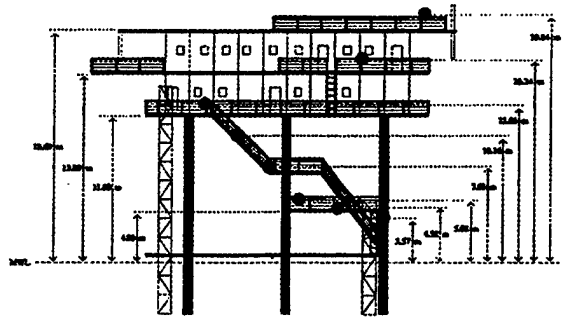

Fig. 3. Diagrammatic representation of the fixed target installation, Meetpost Nordwijk, showing the location of the halogen lamps. Image from Reference 2.

The moving target was the Hr. Ms. Tydeman (Fig. 4), a research vessel of the Royal Netherlands Navy. It mounted six 500 W halogen lamps in the pattern indicated in Fig. 4.

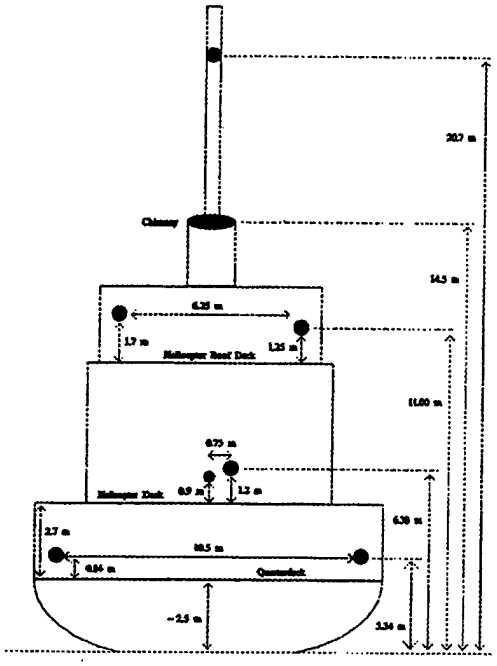

Fig. 4. Diagrammatic representation of the moving target Hr. Ms. Tydeman, showing the locationof the halogen lamps. Image from Reference 2.

The data consisted initially of video recordings of the Hr. Ms. Tydeman sailing along a planned path or the Meetpost Noordvijk under varying atmospheric conditions. A number of different environmental measurements were also taken during the video recording, including water and air temperatures, air pressure, relative humidity, wind speed and direction, water level with respect to MWL, wave height, solar radiation, rain rate and air-sea temperature difference (ASTD). The ASTD values were all found to be negative (-0.30°C to -9.5°C), indicating that the MBL was always unstable and sub-refractive (suggesting potential mirage phenomena). The video images were then studied and analyzed to provide data, such as, for the ship, the maximum intervisibility range (MIVR), whether or not a mirage was detected

and the minimum range at which the mirage was detected (MMR). The platform videos were analyzed to determine whether or not an image or mirage was detected and, if so, the vertical angular separation between the image and the reference (topmost) source.

Data Handling and ANN Training

From the raw and measured data collected, a number of separate events were identified for each parameter to be predicted. These were then subdivided into training and test sets on roughly a 4:1 ratio, with the test set data being completely separate and distinct from the training set values, although both sets fall within the same ranges of values. Each target value for ship data (MIVR, mirage prediction or MMR) had associated with it 38 values for input or independent variables, while each platform value had 31 variable values associated with it. These input variables included source and receiver heights, air and sea temperatures, imaging wavelength, relative humidities, air pressure, solar radiation, wave height and wind speed and direction. The number of individual data points used for training and testing ANN models is shown in Table 1.

A separate ANN model was trained for each prediction or estimation, with the number of hidden nodes varying between 5 and 8 in a single hidden layer.The percentage of successful predictions in the test sets for whether or not images/mirages would be detected, along with the average relative errors in range or angular separation predictions are shown in Table 2.

Table 1. Number of separate cases or data points used in training and testing ANN models.

	Training Set	Test Set
Ship Data		
MIVR	116	29
Mirage	92	24
MMR	69	18
Platform		
Image	312	78
Separation	596	149
Mirage	132	32
Separation	66	16

Table 2. Quantitative measures of ANN model predictions of MAPTIP measured results.

	Correct Predictions %	Relative Error in Predictions %
Ship Data		
MIVR		1.9
Mirage	95.8	
MMR		2.0
Platform		
Image	97.4	
Separation		4.9
Mirage	100	
Separation		18.0

The effectiveness of the range predictions can be seen quite clearly in Figs 5 to 8 in the form of scatter plots depicting measured values vs those predicted by ANN models. The values quoted for errors on the figures are the normalized error (E_n), the average absolute or root-mean-square error (E_{rms}) and the average relative error (E_{rel}). It is these latter values which have been quoted in Table 2.

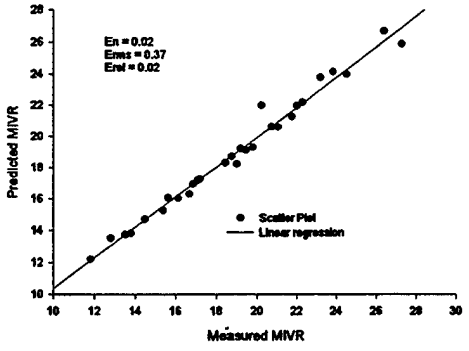

Fig 5. Scatter plot of measured vs predicted ranges in km for the maximum intervisibility ranges (MIVR) for sources on board the ship target.

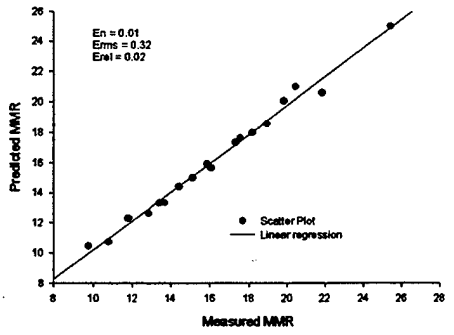

Fig. 6. Scatter plot of measured vs predicted ranges in km for minimum range at which mirages were detected (MMR) for sources on ship target.

The accuracy of the ANN models is clearly indicated. These models also have the advantage of being easy to use and providing unequivocal predictions. A quantitative comparison with L(W)WKD predictions of comparable data has not yet been made, but qualitatively the ANN predictions are felt to be at least as good as those of L(W)WKD. One of the reasons for the good performance of the ANN models is probably that they are able to use all the physical data available rather than the more limited data inputs allowed in the physical model.

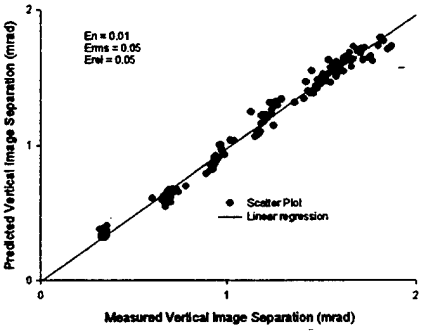

Fig. 7. Scatter plot of measured vs predicted angles of separation between images and reference source on platform.

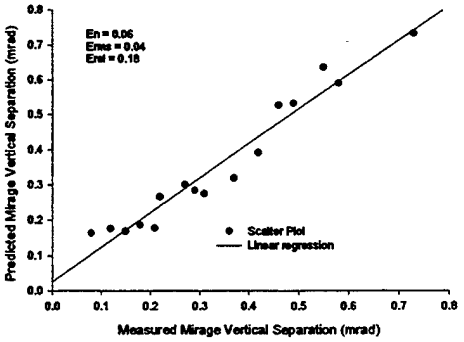

Fig. 8. Scatter plot of measured vs predicted angles of separation between mirages and reference source on platform.

The ANN models have also yet to be examined to determine the hierarchy or relative importance of the input variables. This would be accomplished through an analysis of the distribution of the interconnecting

weights within the weight space and by a sensitivity analysis. Such information should, in turn, lead to a pruning of the input space to the minimum number of variables required to give good predictions while being available for a deployed model. Also, any significant inputs identified for the ANN but not utilized by the physical model should be considered seriously for inclusion in the latter.

It is also noteworthy that the ANN models are limited in usefulness to interpolating or predicting within the range of the input space. The input space itself is composed of data collected over a 17 day period in 1993. More data should be collected to expand the range of the input space and thus the applicability of the models.

Conclusion

The ANN modelling approach has been used to generate models capable of predicting image or mirage detectioncorrectly for between 96% and 100% of the predictions. Other ANN models were trained to predict separation angles for images and mirages to within between 2% and 5%, except for one model where the relative error was 18%. This excellent agreement with measured values has yet to be compared to the accuracy of comparable predictions made by the physical model L(W)WKD.

Also yet to be addressed are a pruning of the models' input spaces to more useful and deployable sizes from the current 30+ variables.

Finally, the ANN modelling approach would be enhanced in value if the input space could be expanded, by acquiring more data over a broader range of conditions.

Acknowledgement

The data analyzed in this report were collected and processed by defence scientists and technicians from the Defence Research Establishment Valcartier of the Department of National Defence of Canada, as well as from France and Germany.

References

1. Jensen, D.R. and de Leeuw, G., *Work Plan for the Marine Aerosol Properties and Thermal Imager Performance Trial (MAPTIP)*, NCCOSC RDT&E Division Technical Document 2573, September 1993.
2. Forand, J.L., Dion, D., Hurtaud, Y. and Stein, K., *MAPTIP Work Group Report – Refractive Effects in the Visible and the Infrared,* DREV-R-9621, Valcartier, Quebec, March 1997 (Draft).
3. Forand, J.L., *The L(W)WKD Marine Boundary Layer Model,* DREV R-9618, Valcartier, Quebec, 1996.
4. Rumelhart, D.E. and McClelland, J.L., *"Parallel Distributed Processing – Explorationsin the Microstructure of Cognition Vol I: Foundations,* MIT Press, Cambridge MA, 1996.

Estimating the Refractive Index Structure Parameter (C_n^2) Over the Ocean Using Bulk Methods

Paul Frederickson and Kenneth Davidson

Department of Meteorology, Naval Postgraduate School, Monterey, CA 93943-5114

Carl Zeisse and Ike Bendall

Space and Naval Warfare Systems Center, San Diego, CA 92152-7385

ABSTRACT

During the Electro-Optical Propagation Assessment in a Coastal Environment (EOPACE) experiment of August-September 1997, infrared transmission measurements were obtained along a 7 km path over San Diego Bay. Simultaneous meteorological measurements were obtained from a buoy located at the midpoint of the transmission path. In this study transmission-derived values of the refractive index structure parameter, C_n^2, are compared with bulk model-derived estimates obtained from the mean buoy data. The bulk C_n^2 estimates agreed very well with the transmission measurements in unstable conditions. The bulk estimates were very poor in near-neutral conditions because of the great difficulty in accurately measuring the small air-sea temperature differences (ΔT) encountered, upon which C_n^2 is highly dependent. The bulk C_n^2 estimates agreed less well with the transmission measurements in stable conditions than unstable conditions. A theoretical error analysis shows that the bulk C_n^2 estimates become extremely sensitive upon the measured value of ΔT over a narrow Bowen ratio range and under such conditions it is virtually impossible to accurately estimate C_n^2 using bulk methods.

1. Introduction

Electro-optical (EO) sensors are a means of detecting and tracking low flying threats to naval assets. However, optical imagery through the atmosphere near the ocean surface can be strongly affected by refraction, molecular and aerosol absorption and scattering, and scintillation. Scintillation is the phenomenon occurring when EO images exhibit rapid intensity fluctuations due to atmospheric turbulence. Scintillation is closely related to the refractive index structure parameter, C_n^2. In an operational environment it would be useful to be able to evaluate the effects of scintillation on EO imagery by estimating C_n^2 from routinely measured air-sea parameters. Bulk models have been developed to estimate near-surface atmospheric turbulence properties from mean meteorological measurements. The relations between these atmospheric turbulence properties and C_n^2 have also been established, thereby allowing C_n^2 to be estimated from mean air-sea measurements. The purpose of this study is to determine how accurately C_n^2 can be estimated from bulk models under various conditions. This study is base on data obtained during the EOPACE (Electro-Optical Propagation Assessment in a Coastal Environment)

intensive observing period (IOP) of August-September 1997. Bulk C_n^2 estimates computed from mean measurements obtained on a buoy are compared with concurrent optical transmission-derived C_n^2 measurements along an over-water propagation path to determine how closely the two methods agree under various air-sea conditions. In addition, a theoretical error analysis of the bulk C_n^2 estimates is conducted.

2. Theory

The structure parameter for a quantity y is given by

$$C_y^2 = \frac{\overline{[y(x) - y(x+r)]^2}}{r^{2/3}}, \tag{1}$$

where $y(x)$ and $y(x + r)$ are the values of parameter y at two points separated by a distance r along the mean wind direction and the over-bar indicates an ensemble average. The refractive-index structure parameter, C_n^2, can be expressed according to the structure parameters for temperature, C_T^2, humidity, C_q^2 and the temperature-humidity fluctuation correlation, C_{Tq}, as follows (e.g. Andreas 1988):

$$C_n^2 = A^2 C_T^2 + 2ABC_{Tq} + B^2 C_q^2, \tag{2}$$

where the coefficients A and B are known functions of the wavelength (λ) and the mean atmospheric pressure (P), temperature (T), and specific humidity (q). The first term on the right hand side of Eq. (2) represents temperature fluctuations and is always positive, the second term represents the correlation of temperature and humidity fluctuations and can be positive or negative, while the third term represents humidity fluctuations and is always positive. For optical and infrared wavelengths the first term in Eq. (2) generally dominates, however, when the air-sea temperature difference is small the last two humidity-dependent terms can dominate.

3. The Bulk Surface-Layer Model

Monin-Obukhov similarity (MOS) theory is used to relate the structure parameters to the mean properties of the atmospheric surface layer. According to MOS theory, the fluxes of momentum, sensible heat and latent heat are assumed to be constant with height in the surface layer. In practice, the surface layer is regarded as the region near the surface where the fluxes vary by less than 10%, generally extending to a height of roughly 20 to 200 m. All dynamical properties in the surface layer are assumed to depend only upon the height above the surface, z, and upon certain scaling parameters, which are defined in terms of the assumed-constant fluxes, as follows:

$$u_* = (-\overline{w'u'})^{1/2}, \qquad T_* = -\frac{\overline{w'T'}}{u_*}, \qquad q_* = -\frac{\overline{w'q'}}{u_*}, \tag{3}$$

where u_*, T_* and q_* are the surface layer scaling parameters for wind speed, temperature and humidity, respectively, defined in terms of the kinematic fluxes of momentum ($-\overline{w'u'}$), sensible heat ($-\overline{w'T'}$), and latent heat ($-\overline{w'q'}$), respectively. When a dynamical property is properly scaled by these parameters, it can be expressed as a universal function of ξ, defined as:

$$\xi = \frac{z}{L} = \frac{zkg(T_* + 0.61Tq_*)}{T_v u_*^2}. \tag{4}$$

Here L is the Monin-Obukhov length scale, k is the von Karman constant (= 0.4), g is the acceleration due to gravity and T_v is the virtual temperature. ξ is often referred to simply as the 'stability', and is negative in unstable conditions, zero in neutral conditions, and positive in stable conditions.

According to MOS theory, the surface layer scaling parameters T_*, q_* and u_* can also be expressed in terms of the mean surface layer properties by the expression:

$$x_* = (\Delta x)k[\ln(z/z_{ox}) - \psi_x(\xi)]^{-1}, \tag{5}$$

where x represents wind speed (u), temperature (T) or specific humidity (q) and the symbol Δ denotes the mean air-sea difference. The ψ functions are the integrated dimensionless profile functions, defined by Andreas (1988). The parameters z_{ox} are known as the 'roughness lengths,' and were determined by the bulk surfaced-layer model formulated by Fairall et al. (1996). The reader is referred to this paper for further details on the bulk model employed.

When the structure parameters for temperature (C_T^2), the temperature-humidity correlation (C_{Tq}) and humidity (C_q^2) are properly scaled according to MOS theory, they can be expressed as:

$$C_T^2 = T_*^2 z^{-2/3} g_T(\xi), \qquad C_{Tq} = T_* q_* z^{-2/3} g_{Tq}(\xi), \qquad C_q^2 = q_*^2 z^{-2/3} g_q(\xi), \tag{6}$$

where g_T, g_{Tq}, and g_q are dimensionless functions of ξ which must be determined empirically. Observations have not demonstrated that these functions are different from each other and MOS theory implies they should be similar (Hill 1989). Therefore, we have assumed that $g_T = g_{Tq} = g_q \equiv g$. Measurements of g for highly stable conditions ($\xi > \sim 1$) are rare and exhibit much scatter. In this study we have used the function for g_T given by Andreas (1988):

$$g_T(\xi) = \frac{C_T^2 z^{2/3}}{T_*^2} = \begin{cases} 4.9(1 - 6.1\xi)^{-2/3}, & \xi \le 0 \\ 4.9(1 + 2.2\xi^{2/3}), & \xi \ge 0 \end{cases}. \tag{7}$$

Substituting Eq. (6) into (2) results in:

$$C_n^2 = g(\xi) z^{-2/3} \left[A^2 T_*^2 + 2ABT_* q_* + B^2 q_*^2 \right]. \tag{8}$$

C_n^2 can now be estimated from mean air-sea measurements by solving equations (4), (5), (7) and (8) by an iterative process.

4. Experimental Setup

The EOPACE experiment of August-September 1997 took place in San Diego Bay. Infrared (IR) transmission measurements were obtained by SPAWAR System Center, San Diego (SSC-SD). The transmission path was 7 km in length over San Diego Bay, with the IR source (transmitter) located at the Naval Amphibious Base and the IR receiver located near the Bachelor Officers Quarters at the Naval Submarine Base (see Figure 1). Meteorological data were obtained concurrently with the transmission data from an instrumented buoy deployed by the Naval Postgraduate School (NPS) at the mid-point of the transmission path.

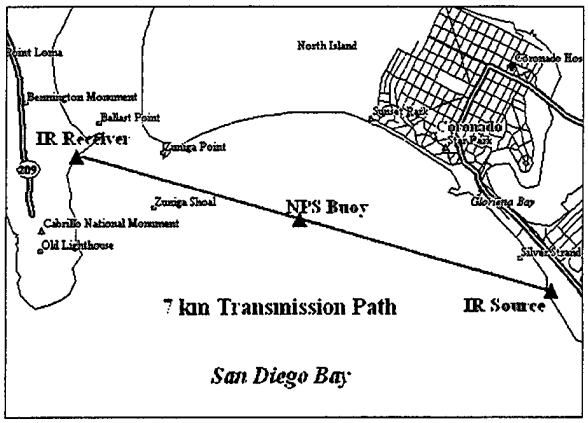

Figure 1. The EOPACE experimental setup during the August-September 1997 IOP.

5. Buoy Meteorological Measurements

The NPS buoy was deployed in San Diego Bay from 22 August to 8 September 1997. The following measurements were obtained on the NPS buoy: wind speed at a 4.9 m height above the surface, air temperature and humidity at 3.1 m, atmospheric pressure at 0.4 m, and sea temperature measured by a thermistor imbedded in the buoy hull 0.8 m below the surface. Only data obtained at night is included in this study, because it was discovered that solar radiation could penetrate the radiation shield and heat the temperature sensor, especially at low solar angles shortly after sunrise and before sunset. A fully enclosed, forced aspiration radiation shield could not be used on the buoy due to power constraints. The buoy measurements were averaged over 10 minute intervals and bulk estimates of C_n^2 were then computed from these mean values. Since C_n^2 is height dependent (Eq. 8), the bulk C_n^2 estimates were corrected for tidal sea level variations using tide data computed by the model 'Tides and Currents for Windows 95' by Nautical Software, Beaverton, OR.

6. Infrared Transmission Measurements

The SSC-SD transmission measurements were obtained from 23 August to 9 September 1997, using a setup similar to that described by Zeisse et al. (1997). The transmitter at the Amphibious Base was 6.2 m above mean sea level (MSL) and the receiver at the Submarine Base was 4.9 m above MSL. High-frequency mid-wave (3.5 to 4.1 μm) IR transmission measurements were obtained hourly over a 41 second interval with a sampling frequency of 200

Hz. The lock-in time constant was 1 ms with a roll-off of 1 dB per octave (wait time 5 ms, equivalent noise bandwidth 0.025 Hz). The measured detector noise was 0.03% of the free space signal, as compared to turbulent fluctuations between samples of about 50% of free space. C_n^2 values were obtained by fitting the normalized variance of the transmission data to the model formulated by Churnside et al. (1992).

7. Bulk versus Transmission C_n^2 Comparison Results

A scatter plot of the NPS bulk and SSC-SD transmission C_n^2 values is presented in Figure 2. A summary of the comparison statistics is presented in Table 1. The data have been separated into air-sea temperature difference (ΔT) intervals, as measured on the NPS buoy. The standard linear correlation coefficient between the two populations is presented in the second column. The '% difference' is the average value of $(C_n^2{}_{(\text{trans})} - C_n^2{}_{(\text{bulk})})/C_n^2{}_{(\text{trans})}$. The 'root-mean-squared % difference' is the value of $[(C_n^2{}_{(\text{trans})} - C_n^2{}_{(\text{bulk})})^2]^{1/2}$, where the brackets denote an average, divided by the mean value of $C_n^2{}_{(\text{trans})}$.

Table 1. Bulk versus transmission C_n^2 comparison.

ΔT Range	Corr. Coeff.	% Diff.	rms % Diff.
$\Delta T < -0.5$ °C	0.93	−16	35
−0.5 °C $< \Delta T <$ 0.5 °C	−0.05	33	358
0.5 °C $< \Delta T <$ 1.5 °C	−0.02	−45	86
1.5 °C $< \Delta T$	0.16	−260	224

The agreement between the bulk and transmission C_n^2 data is very good for unstable conditions, defined as ΔT less than −0.5 °C. For these conditions the percentage difference between the two methods is −16% and the correlation coefficient is 0.93. The agreement between the two methods is very poor for near-neutral conditions, defined as ΔT being greater than −0.5 and less than 0.5 °C. Under these conditions the scatter is very great (rms % difference of 358%), with the bulk C_n^2 estimates being much lower than the transmission measurements in most cases. In weakly stable conditions, defined as ΔT being greater than 0.5 and less than 1.5 °C, the comparison between the two methods exhibits much more scatter than for unstable cases (rms % difference of 86% as compared to a rms % difference of 35% for unstable conditions). For strongly stable conditions, defined as ΔT being greater than 1.5 °C, the transmission C_n^2 measurements are systematically lower than the bulk estimates, by 260% on average. It is possible that the optical transmission data were 'saturated' for these very stable conditions, thereby causing the transmission values to be much lower than the bulk estimates.

8. Error Analysis

A theoretical error analysis was conducted for the bulk C_n^2 estimates, using methods similar to those of Andreas (1988). The sensitivity coefficient for C_n^2 upon ΔT, $S_{\Delta T}$, was computed, defined as:

$$S_{\Delta T} = \frac{\Delta T}{C_n^2}\left[\frac{\partial C_n^2}{\partial \Delta T} + \frac{\partial C_n^2}{\partial \xi}\frac{\partial \xi}{\partial \Delta T}\right]. \tag{9}$$

A large value of $S_{\Delta T}$ indicates that the bulk C_n^2 estimates are highly sensitive to the measured value of ΔT, while a small value of $S_{\Delta T}$ indicates that the bulk C_n^2 estimates are virtually independent of ΔT. The relative error in the bulk C_n^2 estimates is given by multiplying $S_{\Delta T}$ by the assumed relative error in the ΔT measurement, as follows:

$$\frac{\delta C_n^2}{C_n^2} = S_{\Delta T} \frac{\delta \Delta T}{\Delta T}. \tag{10}$$

$S_{\Delta T}$ turns out to be highly dependent upon the Bowen ratio, Bo, which is the ratio of the sensible heat flux over the latent heat flux, or $Bo = c_p T_* / L_v q_*$, where c_p is the specific heat of air at

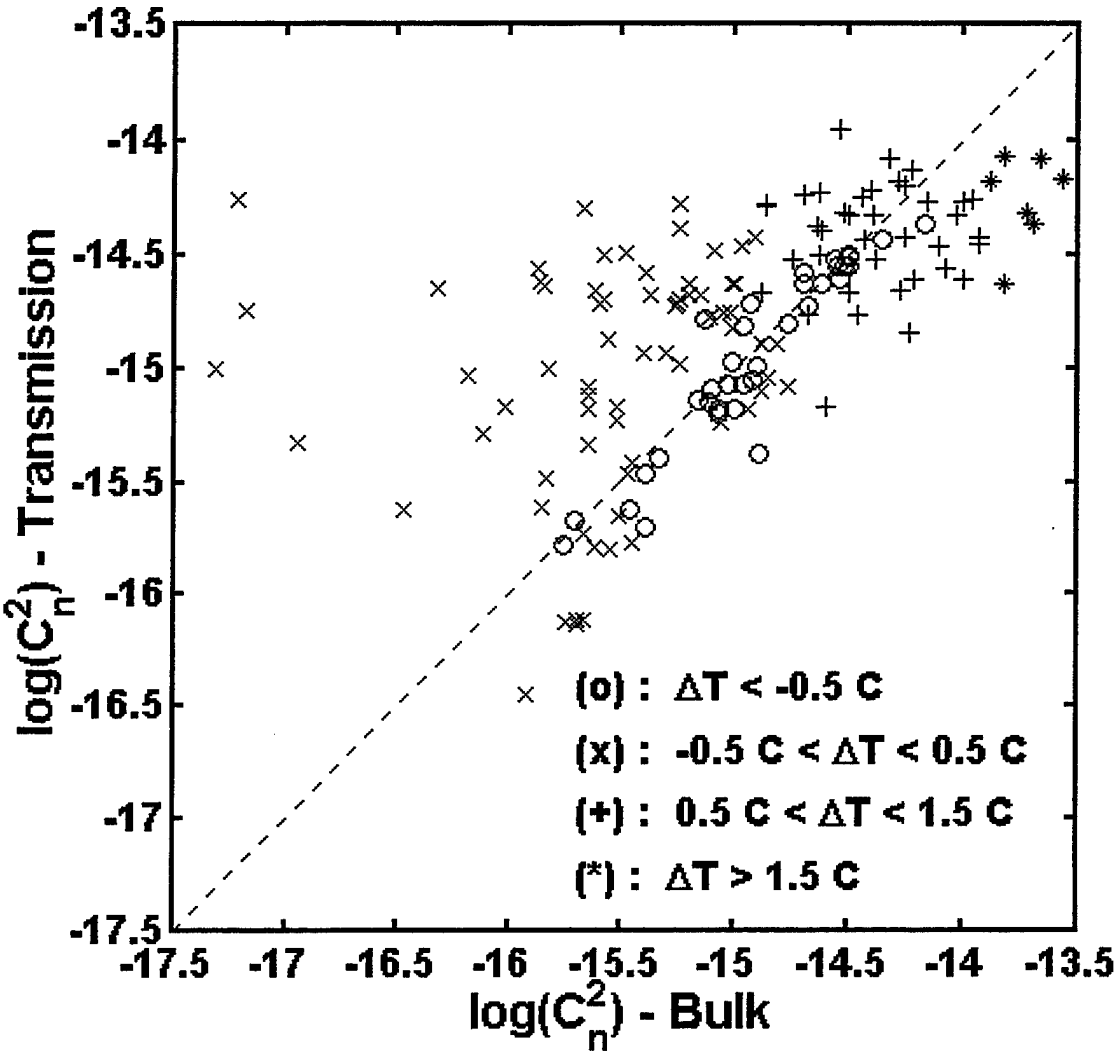

Figure 2. Scatter plot of transmission $\log(C_n^2)$ measurements versus bulk $\log(C_n^2)$ estimates, separated into different air-sea temperature difference (ΔT) intervals: $\Delta T < -0.5$ °C indicated by o's; -0.5 °C $< \Delta T < 0.5$ °C indicated by x's; 0.5 °C $< \Delta T < 1.5$ °C indicated by +'s; $\Delta T > 1.5$ °C indicated by *'s.

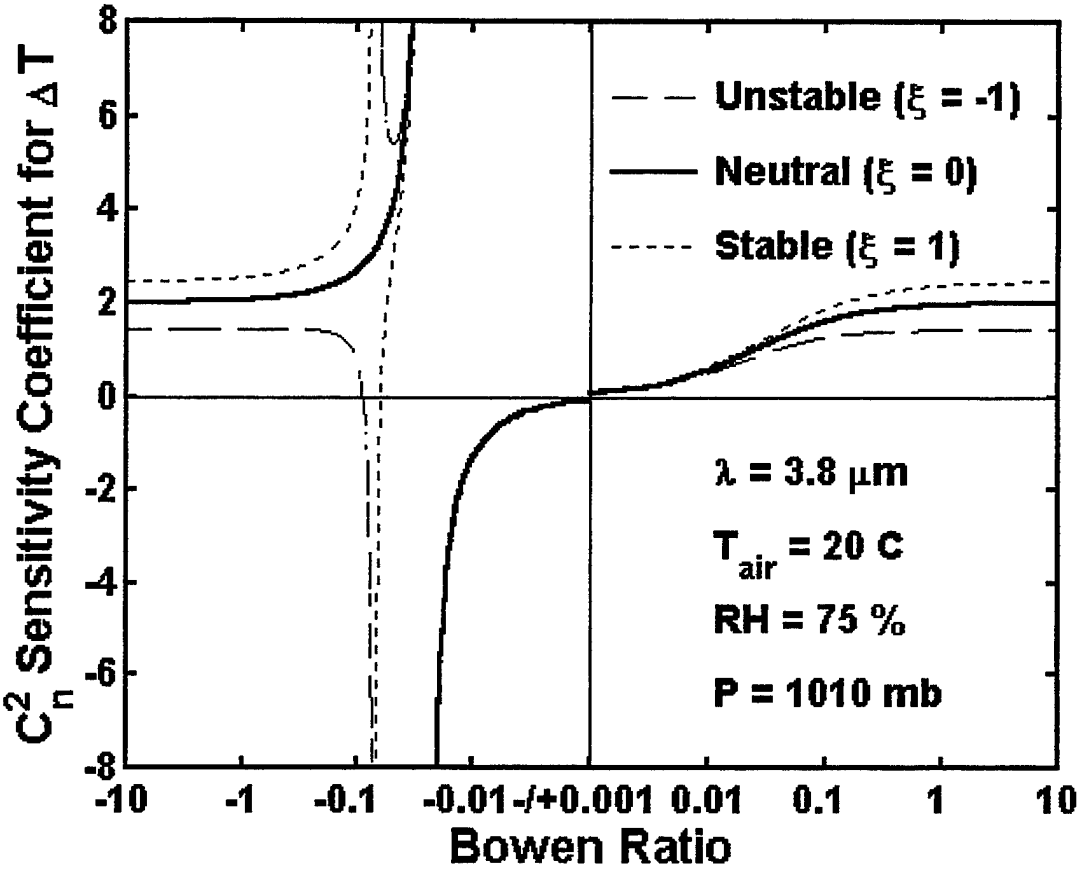

Figure 3. C_n^2 sensitivity coefficient for ΔT, $S_{\Delta T}$, plotted versus the Bowen ratio for unstable conditions with $\xi = -1$ (dashed line), neutral conditions with $\xi = 0$ (solid line) and stable conditions with $\xi = 1$ (dotted line).

constant pressure and L_v is the latent heat of vaporization. $S_{\Delta T}$, as computed for representative conditions encountered during the experiment, is plotted versus Bo for different values of the stability, ξ, in Figure 3. It can be seen that over a narrow Bowen ratio range (roughly $-0.1 < Bo < -0.015$) the bulk C_n^2 estimates become extremely sensitive upon the measured value of ΔT, making it virtually impossible to accurately estimate C_n^2 by bulk methods in these conditions. These small negative values of Bo generally only occur under near-neutral conditions (small T_* and, therefore, ΔT values) and when the sensible and latent heat fluxes have opposite signs. From Figure 3 it can also be seen that the relative errors in bulk C_n^2 estimates due to measurement uncertainties in ΔT are smallest for unstable conditions and largest for stable conditions, for a given value of ΔT. This is in agreement with the observations presented in Figure 2, with the bulk versus transmission C_n^2 comparison exhibiting less scatter in unstable conditions (rms % difference of 35%) than in stable conditions (rms % difference of 86%). In near-neutral conditions the relative measurement uncertainties in ΔT will tend to be large because it is very difficult to accurately measure the small $|\Delta T|$ values encountered, leading to large relative errors in C_n^2. This is indicated in Figure 2 by the very large scatter in the bulk versus transmission C_n^2 comparison for near-neutral conditions (rms % difference of 358%).

9. Conclusions

This study has demonstrated that C_n^2 can be accurately estimated in unstable conditions from routinely obtained meteorological measurements using bulk surface-layer methods. Under neutral and stable stratification the use of bulk methods to estimate C_n^2 was less successful. The poor accuracy observed in bulk C_n^2 estimates in neutral conditions arises from the difficulty in accurately measuring the small ΔT values encountered with neutral stratification, upon which the bulk C_n^2 values are highly dependent. In addition, over a narrow Bowen ratio range ($-0.1 < Bo < -0.015$) which occurs only in near-neutral conditions, the bulk C_n^2 values become extremely sensitive upon the measured value of ΔT, making it impossible to accurately estimate C_n^2. There are several reasons for the poor accuracy observed in bulk C_n^2 estimates in stable conditions. First, the error analysis demonstrated that the bulk C_n^2 estimates are the most sensitive upon the meteorological measurements in stable conditions. Second, the dimensionless structure function parameter, $g(\xi)$, upon which C_n^2 is directly related, is poorly known in stable conditions and the function in use may be greatly in error. Third, in very stable conditions turbulence is suppressed by the atmospheric stratification, which can allow the atmosphere to become de-coupled from the surface, thereby invalidating MOS theory and the bulk C_n^2 model used in this study.

Acknowledgments

This work was funded by the U. S. Office of Naval Research, program managers Dr. Scott Sandgathe and Dr. Ronald Ferek. The authors thank Mr. Keith Jones and Mr. Doug McKinney (McKinney Technology) for their efforts in deploying the NPS buoy and Mr. Bill Moision and Dr. Brett Nener for their assistance in acquiring the transmission data. A special thanks is due to Dr. Douglas Jensen for his able organizational skills during EOPACE and for providing the tide data used in this study.

References

Andreas, E. L.: 1988. Estimating C_n^2 over snow and ice from meteorological data. *J. Opt. Soc. Am.* A, **5**, 481-495.

Churnside, J. H., R. J. Lataitis and J. J. Wilson, 1992. Two-color correlation of atmospheric scintillation. *Appl. Optics*, **31**, 4285-4290.

Fairall, C. W., E. F. Bradley, D. P. Rogers, J. B. Edson and G. S. Young: 1996. Bulk parameterization of air-sea fluxes for Tropical Ocean-Global Atmosphere Coupled-Ocean Atmosphere Response Experiment. *J. Geophys. Res.*, **101**, 3747-3764.

Hill, R. J., 1989: Implications of Monin-Obukhov similarity theory for scalar quantities. *J. Atmos. Sci.*, **46**, 2236-2244.

Zeisse, C., and others, 1997: Low altitude infrared transmission. *Proceedings, Battlespace Atmospherics Conference*, San Diego, CA, December 1997 (these proceedings).

Low-Level IR Transmission Measurements over a 15 km Littoral Path

J. Luc Forand, Denis Dion, and Mike Duffy
Defence Research Establishment Valcartier
2459 Pie XI Blvd., Val-Belair, QC, Canada G3J 1X5
Ph: 418-844-4503 Fax: 418-844-4511
E-mail: luc.forand@drev.dnd.ca
Arie de Jong and Gerrit de Leeuw
TNO Physics and Electronics Laboratory
P.O. Box 96864, 2509 JG The Hague, The Netherlands
Ph: +31-70-3740456 Fax: +31-70-3740654
E-mail: deJong@fel.tno.nl
Stuart Gathman and Kathleen Littfin
Space and Naval Warfare Systems Center (SPAWAR)
Propagation Division
49170 Propagation Path, San Diego, CA, USA 92152-7385
Ph: 619-553-1418 Fax: 619-553-1417
E-mail: gathman@nosc.mil
Paul Frederickson and Ken Davidson
Naval Postgraduate School (NPS), Code 63/DS
589 Dyer Road, Room 252, Monterey, CA, USA 93493-5000
Ph: 408-656-2309 Fax: 408-656-3061
E-mail: davidson@osprey.nps.navy.mil

ABSTRACT

Results of far IR and mid IR transmission measurements taken over a 15 km transmission low-level path across San Diego Bay are presented along with an analysis illustrating the effects that refraction, aerosol extinction and molecular extinction can have on EO systems. The measurements were taken as part of the EO Propagation Assessment in Coastal Environments (EOPACE) campaign during November 1996 (IOP 4) by TNO-FEL. Simultaneous meteorological measurements were taken by various groups at both ends of the path, and by a NPS meteorological buoy at the mid-path. SPAWAR operated a small boat to investigate the homogeneity along the path, and to make in-situ measurements of the aerosol size distribution for a determination of the aerosol extinction coefficients in the two bands. The IRBLEM computer models developed by DREV and TNO-FEL used the meteorological measurements to predict the effects of refraction, aerosol extinction, and molecular extinction on the transmission for both bands over a wide variety of conditions. For the mid IR, the predictions show that the molecular transmittance is generally quite constant compared to the greater variability found for the far IR, the high variability of the aerosol transmittance, and the sometimes dramatic effects produced by refraction. Comparison with the measured transmissions are reasonably good and show that the total transmission depends critically on all three effects, where the molecular transmittance depends upon the absolute humidity, the aerosol transmittance on the aerosol loading, and the refractive effects on the stability of the marine boundary layer or air-sea temperature difference.

1. INTRODUCTION

The intensive operational period (IOP 4) of the EO Propagation Assessment in Coastal Environments (EOPACE) campaign that was conducted in San Diego during November 1996, was a good opportunity to obtain excellent transmission data within the marine boundary layer (MBL) and to compare it to predictions made by the IR Boundary Layer Effects Model (IRBLEM). This was made possible due to the good quality of the mid-infrared (MIR) and far-infrared (FIR) transmission data obtained by Arie de Jong over the 15 km transmission path, the basic meteorological data obtained at both ends and in the middle of each transmission path, and the measurement of the aerosol size distributions obtained over the transmission path by Stuart Gathman.

To better understand how the data was obtained and how the analysis was performed using IRBLEM[1], the following section presents a brief discussion of the effects which can affect the transmission of IR radiation in the MBL and the modules that IRBLEM uses to model them. The subsequent section gives a short description of the various meteorological and transmission equipment that was used and its location around San Diego Bay, and the last three sections present the results of the study, a discussion of the results, and finally some conclusions.

2. IR TRANSMISSION IN THE MARINE BOUNDARY LAYER

The marine boundary layer (MBL) is a region of the atmosphere which extends from the marine surface to a height which may vary from 20 to several 100 meters. As the air and marine surface can often be at different temperatures, this region of the atmosphere, through convection and air transport, can possess strong vertical gradients of temperature, humidity, and aerosol concentration. The MBL is also a region that is a source of maritime aerosols and a sink, particularly in coastal regions, for terrestrial aerosols (particulates). The various gradients, the concentrations, type and particle distribution of the aerosols, and the amount of water vapour in the MBL all have important consequences on the transmission of IR radiation. The gradients can cause significant refractive effects (mirage formation, focussing and defocussing), while the composition of the MBL determines the amount of IR radiation that is scattered or absorbed.

Following[2], for a spherical wavefront of frequency, ν, the intensity, $I(\mathbf{r},\nu)$, at some vector position, $\mathbf{r}$, from a point source can be expressed by:

$$I(\mathbf{r},\nu) = \frac{I_0(\nu)}{r^2}\sum_{j=1}^{m}\rho_j(\mathbf{r},\nu)\,\tau_{jM}(\mathbf{r},\nu)\,\tau_{jA}(\mathbf{r},\nu) = \frac{I_0(\nu)}{r^2}\sum_{j=1}^{m}T_j(\mathbf{r},\nu) = \frac{I_0(\nu)}{r^2}T(\mathbf{r},\nu), \tag{1}$$

where m is the number of images (m is greater than 1 when there are secondary images or mirages), j is an image index,

$$T(\mathbf{r},\nu) = \sum_{j=1}^{m}T_j(\mathbf{r},\nu) = \sum_{j=1}^{m}\rho_j(\mathbf{r},\nu)\,\tau_{jM}(\mathbf{r},\nu)\,\tau_{jA}(\mathbf{r},\nu) \tag{2}$$

is the total transmission, and

$$\tau_{jx}(\mathbf{r},\nu) = e^{-\int_0^r \alpha_x(r(s_j),\nu)\,ds_j}\quad ;\ for\ x = M,\ A \tag{3}$$

is either the molecular transmittance, $\tau_{jM}(\mathbf{r},\nu)$, or the aerosol transmittance, $\tau_{jA}(\mathbf{r},\nu)$, and the integral is taken over the path followed by the ray creating the image and the respective extinction coefficient, $\alpha_x(\mathbf{r},\nu)$. $I_0(\nu)$ is the total emitted intensity, and $\rho(\mathbf{r},\nu)$ is the refractance at the vector position, $\mathbf{r}$ for frequency, ν. For straight rays (i.e., no refraction) the refractance equals 1; however, if the rays are focussed, the refractance becomes greater than 1, and if they are defocussed, the refractance becomes less than 1. Thus, the refractance can be thought of as an optical amplifier with a gain of ρ.

The IR Boundary Layer Effects Model (IRBLEM)[1] has been designed to calculate each of the above terms for rays which propagate within the MBL. Figure 1 shows IRBLEM's internal modular structure with the meteorological inputs situated at the top and the various outputs at the bottom. The required meteorological data is passed to each of the four subsequent routines which calculate the molecular extinction ($\tau_M(\nu)$), the vertical refractivity profile (N(h)), the vertical refractivity structure parameter profile ($C_n^2(h)$; turbulence), and the vertical aerosol extinction profile ($\alpha_A(h)$). The molecular extinction is spectrally calculated using a call to MODTRAN[3] in the horizon mode for the height at which the air temperature was measured, the desired wavelength band, and for a nominal resolution of 5 cm^{-1}. The molecular extinction is not height dependent. The vertical structure parameter profile, which was not required for this study, is calculated using SRS_BULK[4] and will not be discussed any further. For the calculation of the vertical aerosol extinction coefficient profile, a module was provided by TNO[1], that allows the user to select one of three models to estimate the aerosol extinction at 10 meters above the surface for a wavelength of either 4 μm (center of the 3-5 μm waveband) or 10 μm (center of the 8-12 μm waveband). The model choices are the Navy Aerosol Model (NAM)[5], the Open Ocean[6] model, and the TNO MPN[7] model. The vertical variation is computed after de Leeuw [8] using LKB[9] for estimating the characteristic MBL parameters and assuming that the vertical distribution for all particle sizes follows that of the 1 micron particles. Calculation of the vertical refractivity profile is carried out using subroutines taken from DREV's LWWKD[10] model that makes calculations for the mid IR and far IR bands. It is an MBL model that is based upon the similarity theory work of Monin and Obukhov[11]. The results of these calculations are then passed to a DREV developed ray-tracing program[1] that is capable of calculating the change in the intensity along any ray due to lensing effects (the refractance) using a technique developed by Blanchard[12], and calculates the molecular transmittance and aerosol

transmittance by performing the integral in Eq. 3 over each ray.

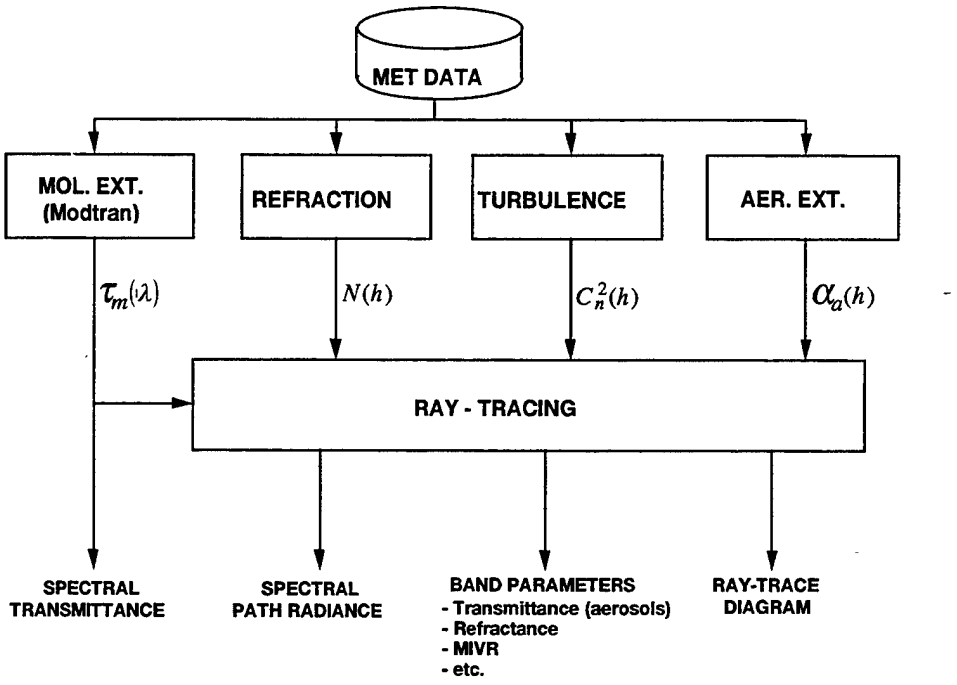

Figure 1 - Schematic diagram showing the modular structure of IRBLEM.

3. EXPERIMENTAL DETAILS

Figure 2 shows a map of Southern California and San Diego Bay which indicates the sites where the various equipment was used during EOPACE's intensive operational period (IOP 4) of November, 1996. The Naval Postgraduate School in Monterey had positioned a "MEAN" weather buoy at the midpoint of the 7 km transmission path (between the Subbase and Coronado), and a "FLUX" weather buoy at the midpoint of the 15 km transmission path (between the Subbase and the pier at Imperial Beach). Both buoys made continuous measurements of the air temperature, water temperature, relative humidity, atmospheric pressure, wind speed and direction during most of the IOP. The FLUX buoy also made measurements of the wave spectra and their amplitudes. TNO had meteorological stations placed at both ends of the 15 km path where they measured the irradiance, relative humidity, air temperature, atmospheric pressure, wind speed and direction. Similarly, SPAWAR had meteorological stations placed at both ends of the 7 km path where they measured the air temperature, relative humidity, wind speed and direction. The visibility, condensation nuclei (CN), and radon were measured continuously at the Subbase by SPAWAR. The air temperature, water temperature and relative humidity were also obtained, about once each day, over each of the transmission paths by a small boat operated by SPAWAR. They also measured the aerosol size distribution from the boat and calculated the aerosol extinction coefficients at 3.5 μm and 10.6 μm using Mie theory.

To properly compare the waveband transmission measurements, over the different paths, with the spectrally dependent (every $\Delta\nu = 5\ cm^{-1}$) predictions from IRBLEM, the predictions must be weighted using a weighting function, $w(\nu)$, over the appropriate waveband (weighted average). Following[2], the frequency dependent weighting function, $w(\nu)$, can be expressed as a function of the emission, $I_0(\nu,T)$, of the transmissometer's source, the temperature of the source, T, and the response, ϵ, of its detector by:

$$w(\nu) = \frac{I_0(\nu,T)\epsilon(\nu)}{\int_{\nu_{min}}^{\nu_{max}} I_0(\nu,T)\epsilon(\nu)\,d\nu}; \quad w_i = \frac{I_{0i}(T)\epsilon_i}{\sum_{i=0}^{n} I_{0i}(T)\epsilon_i \Delta\nu}. \tag{4}$$

For the TNO transmissometer[13,14,15] used over the 15 km path, Fig. 3 shows the response of both detector components and the calculated weights ($w\Delta\nu$) for the system. The transmissometer is a dual band system which could be alternately operated in either the mid-infrared or the far-infrared wavelength band and whose source has a blackbody temperature of 900 °C.

Using Eq. 4, the total waveband transmission, $T(\nu_{min},\nu_{max})$, between the frequencies ν_{min} and ν_{max},, can be expressed by;

$$T(\nu_{min},\nu_{max}) = \int_{\nu_{min}}^{\nu_{max}} w(\nu)T(\nu)d\nu \approx \sum_{j=1}^{m}\sum_{i=0}^{n} w(\nu_i)\Delta\nu\,\tau_{jM}(\nu_i)\rho_j(\nu_i)\tau_{jA}(\nu_i)$$
$$\approx \sum_{j=1}^{m}\rho_j(\nu_b)\tau_{jA}(\nu_b)\sum_{i=0}^{n} w(\nu_i)\Delta\nu\,\tau_{jM}(\nu_i) \approx [\sum_{j=1}^{m}\rho_j(\nu_b)]\tau_A(\nu_b)T_M \approx \rho(\nu_b)\tau_A(\nu_b)T_M, \quad (5)$$

where

$$T_M = \sum_{i=0}^{n} w(\nu_i)\Delta\nu\,\tau_{jM}(\nu_i), \quad (6)$$

$T(\nu)$ is the total transmission given by Eq. 2, and $\rho(\nu_b)$ and $\tau_A(\nu_b)$ are the refractance and aerosol transmittance for the waveband as produced by IRBLEM. Furthermore, we have assumed that the refractance and the aerosol transmittance are wavelength independent over the band, and that the molecular and aerosol transmittance are path independent. (Note: the vector position, **r**, has been suppressed for clarity.)

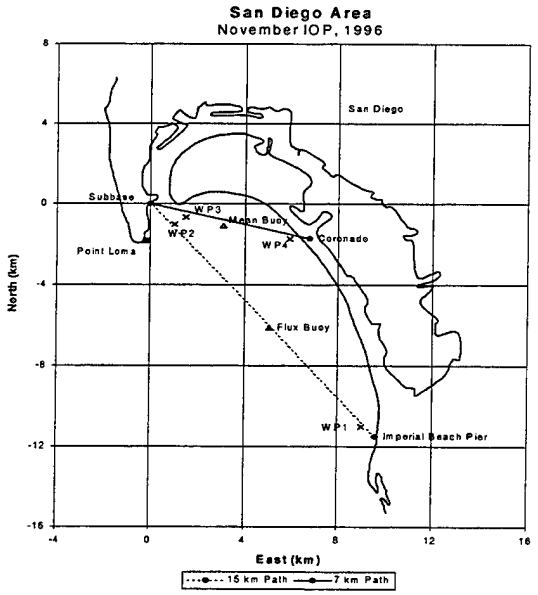

Figure 2 - Schematic map of San Diego Bay showing the placement of the two transmission paths, the two met buoys and the various waypoints.

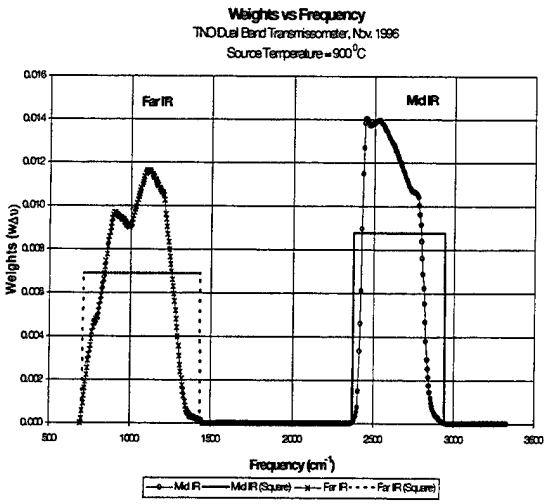

Figure 3 - Calculated instrument and square weights for the mid-IR and far-IR bands.

4. RESULTS

The first eight graphs (Figs. 4a,b,c,d and Figs. 5a,b,c,d) are meant to give the reader an idea of the range of boundary layer conditions that were measured by the flux buoy and a visibility meter situated at the Subbase on Nov. 6th and Nov. 11th. Figures 4a and 5a show the daily variation of the air and sea temperatures, and that of the air-sea temperature difference (ASTD), Figs. 4b and 5b show the daily variation in the absolute humidity and the visibility, Figs. 4c and 5c show the daily variation in the wind velocity, and Figs. 4d and 5d show the daily variation of the

significant wave height ($H_{1/3}$) and the height of the tide. As the measured wave height was not yet available, the formula[16]

$$H_{1/3} = 0.022 * v_w^2 \quad (7)$$

with v_w being the wind speed, was used. Ten data points were obtained over each day, with as many as possible corresponding to periods during which aerosol measurements were obtained by the small boat, to periods during the early morning when the air temperature was near its daily minimum, and to periods during the late afternoon when the air temperature was near its daily maximum.

On Nov. 6th, the ASTD started out near 0 °C, then dropped to approximately -2.7 °C near 0600h, climbed to +2.0 °C during the afternoon before returning to 0 °C near midnight. The visibility varied from 6 to 14 km with minima measured at 0900h and 2100h, and the absolute humidity between 4.0 and 5.5 g/m^3 with a minima near 0900h. The wind was light (< 3 m/s) and from the land until 0900h before strengthening to 7 m/s and coming from the northwest (Pt. Loma). After 1800h the wind veered and again came from the land at 2-4 m/s. The wave heights varied with the wind speed from 0.1 to 0.8 meters. The tide was low near 0100h and 1400h and high near 0700h and 1900h. On Nov. 11th, the ASTD started out near 1 °C, climbed to +3.7 °C during the afternoon before dropping back to near 1 °C by 1900h. The visibility was extremely good (> 40 km) during the entire day. The absolute humidity was 4.0 g/m^3 until 1100h before climbing to a maximum of 7 g/m^3 at 1600h and then dropping to about 5 g/m^3 near midnight. The wind was relatively light (< 3 m/s) for most of the day. It came from the land until 0900h before strengthening to 4 m/s and coming from the west (sea). After 1800h the wind lightened and veered to come from the land. The wave heights were less than 0.2 m throughout the day while the tide was low near 0300h and 1700h and high near 1000h and 2400h. The meteorological data for these two days is quite typical for San Diego where a light wind comes from the land during the early morning, strengthens and comes from the west, northwest during the day before lightening and coming from the land again in the evening. At the same time the air temperature and ASTD increase during the day and then drop during the night to reach their minima just before sunrise.

Figures 6a-j show the results of our study of the IR transmission measurements taken on Nov. 6th. Figure 6a shows the calculated molecular transmittances for both the MIR and FIR using the weighting function show in Fig. 3 (o's and x's) and using a uniform (square or average) weighting function. As can be seen, the two different weighting functions can produce differences of close to 0.05 in both bands; thus, it is very important to properly determine the response of the transmissometer. Figure 6b shows the linear variation of these same molecular transmittances with respect to the absolute humidity for both bands and weighting functions, and shows that a difference of 0.05 is possible for a 1 g/m^3 change in specific humidity. Figures 6c-d illustrate the total refractance (◇'s) and those for both the primary (□'s) and secondary (△'s) images calculated by IRBLEM for both bands. Zero-values for the total refractance indicate that the source is below the horizon. Looking at the predictions for 0130h in particular, we note that the refractive power in the FIR is expected to be slightly stronger than that in the MIR. Figures 6e-f show the variation of these refractances with respect to the ASTD for both the total (◇'s) and secondary (△'s) images. A second order fit to the total refractance is also shown on each graph. What one notices from both graphs is the prediction of a secondary image near an ASTD of -0.3 °C for the FIR while for the MIR this is not observed until an ASTD near -1 °C. Also, one notices that both the secondary refractance and the total refractance increase quite significantly, in both bands, as the ASTD drops to -2.0 °C, and then very quickly drop to zero when the source disappears below the horizon. Figures 6g-h show the aerosol transmittances calculated by IRBLEM (◇'s) and the measured aerosol transmittances (■'s) for both bands. The labels next to the measured values indicate at which waypoint or between which waypoints the measurements were obtained. As can be seen, while the differences between the IRBLEM calculated values and the Mie theory calculated values are within 0.10 for the measurements at 1400h and 1600h, the differences are more than 0.20 to 0.40 at 0900h and 1200h. Figures 6i-j show TNO-FEL's measured total transmittances (■'s), the transmittances calculated for the primary image (◇'s), secondary image (△'s), and the total (○'s) using IRBLEM, and those obtained using the measured aerosol transmittances at 1400h (x's) instead of those calculated by IRBLEM. As can be seen, the agreement is quite good in the FIR; however, there are only three measurements (0130h, 1800h, and 2100h). In the MIR, there are eight measurements; however, the agreement is not quite as good.

Figures 7a-d show the results of our study for the IR transmission measurements taken on Nov. 11th. The calculated molecular transmittances for both the MIR and FIR are not shown as they can be obtained from the absolute humidity given by Fig. 5b and the linear functions given by Fig. 6b. Figure 7a illustrates the total refractance for the MIR (◇'s) and for the FIR (□'s) as calculated by IRBLEM. No secondary images are predicted for either band. Again,

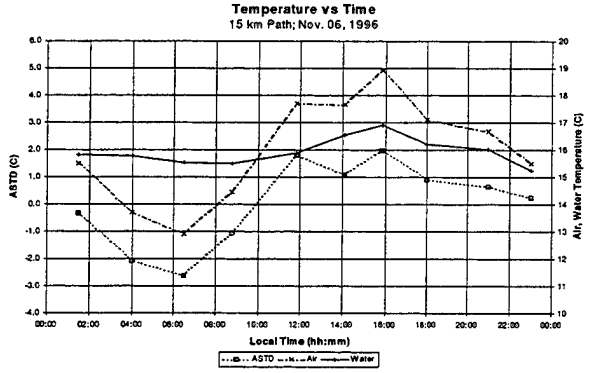

Figure 4a - Measurements of the air and sea temperatures on Nov. 6th, 1996.

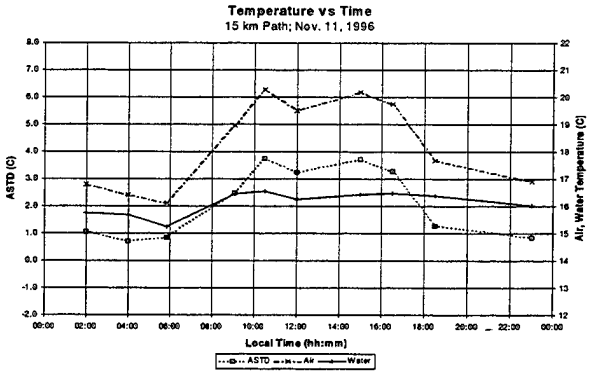

Figure 5b - Measurements of the air and sea temperatures on Nov. 11th, 1996.

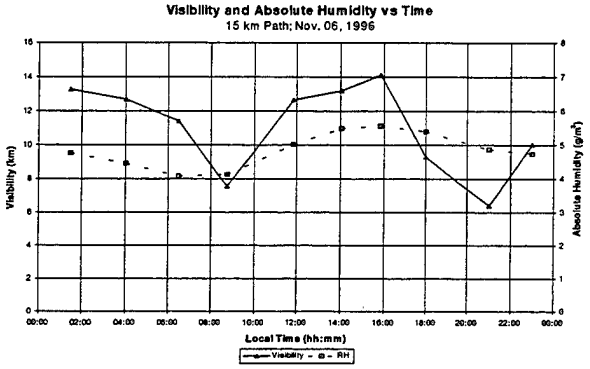

Figure 4b - Measurements of the visibility and absolute humidity on Nov. 6th, 1996.

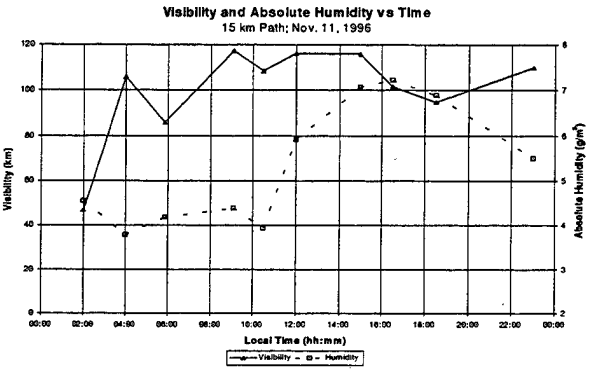

Figure 5b - Measurements of the visibility and absolute humidity on Nov. 11th, 1996.

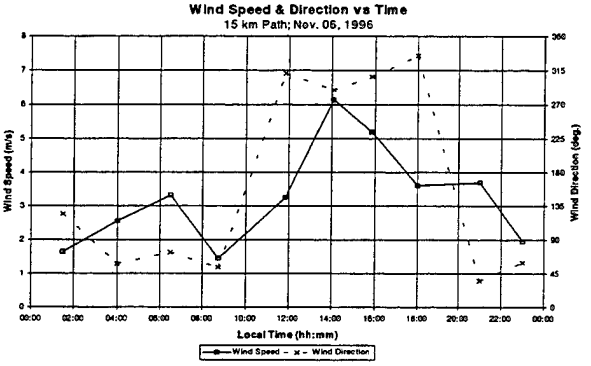

Figure 4c - Measurement of the wind velocity on Nov. 6th, 1996.

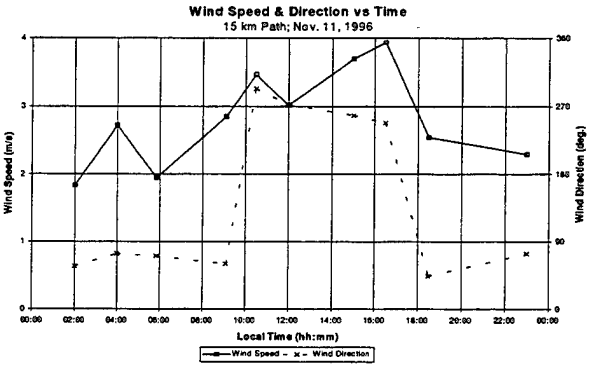

Figure 5c - Measurement of the wind velocity on Nov. 11th, 1996.

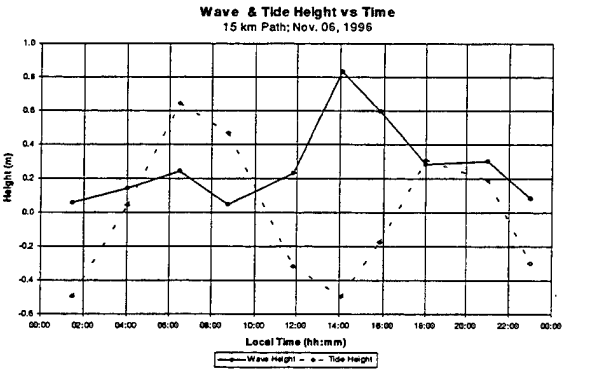

Figure 4d - Measurement of the significant wave height and tide height on Nov. 6th, 1996.

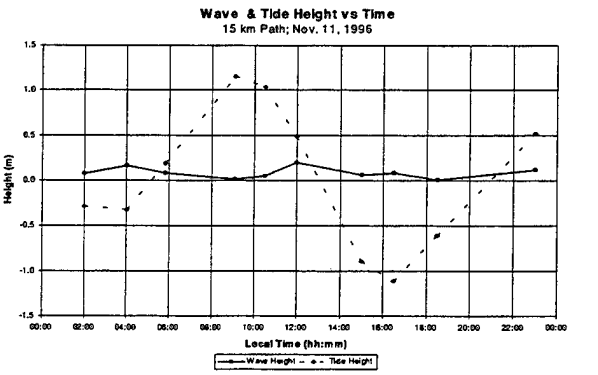

Figure 5d - Measurement of the significant wave height and the tide height on Nov. 11th, 1996.

we note that the refractive power in the FIR is generally expected to be slightly stronger than that in the MIR. Figure 7b shows the aerosol transmittances calculated by IRBLEM (◇'s: MIR & □'s: FIR) and the measured aerosol transmittances (♦'s:MIR & ■'s: FIR). The labels next to the measured values indicate at which waypoint or between which waypoints the measurements were obtained. As can be seen, while the differences between the IRBLEM calculated FIR values and the Mie theory calculated values are very good for the measurements at 1030h and 1200h , it is poor at 0900h and extremely poor at 0600h. In the MIR the situation is even worse, as even those measured at 1030h and 1200h have differences of 0.20. Figures 7c-d show TNO-FEL's six measured total transmittances (■'s), the total transmittances (○'s) calculated using IRBLEM (there are no secondary images), and those obtained using the measured aerosol transmittances at 1030h (x's) instead of those calculated by IRBLEM. As can be seen, the agreement is quite good in the FIR as the differences do not exceed much more than 0.05. However, in the MIR, the five measurements only give reasonable agreement at 0900h and 1030h.

5. DISCUSSION

Looking at Figs. 6i and 7c, one notices that the MIR measured transmissions (■'s) vary from 0.11 to 0.70 and that the model predicts total transmissions for the waveband ranging from 0.00 to 0.88. The model predicts two cases where secondary images are expected and one case (0600h) when the source is expected to be below the horizon. Comparing these three cases with the three measurements leads one to believe that the effect of refraction is too strong. This could be due either to the LWWKD component within IRBLEM or to a problem with the measurement of the ASTD (a less negative ASTD would produce better agreement with the data). Lower tide heights and wave heights could also help produce better agreement with the data.

From Figs. 6i and 7c, one notices that the FIR measured transmissions (■'s) vary from 0.06 to 0.24 and that the model predicts total transmissions for the waveband ranging from 0.00 to 0.50. The model predicts three cases where secondary images are expected and one case (0600h) when the source is expected to be below the horizon. However, due to the scheduling of the transmissometer, no data was obtained during these time periods.

For the other cases, and for both bands, we believe that much of the difference may be due to problems in calculating the aerosol transmittance. As we noticed earlier, very significant differences were observed between the aerosol calculations obtained using IRBLEM and those measured in situ. We don't believe there is necessarily a problem with the molecular transmittance calculations as one would expect any such differences to be fairly uniform over all the measurements unless their are significant differences in the absolute humidity along the path.

6. CONCLUSIONS

An analysis is presented showing the effects of refraction, aerosol extinction, and molecular extinction on transmission measurements obtained during the EO Propagation Assessment in Coastal Environments (EOPACE) campaign carried out in San Diego during November 1996 (IOP 4). Infrared transmission measurements were made over a 15 km path using a dual band transmissometer (mid IR and far IR) at heights below 10 m above sea level (i.e., within the marine boundary layer). In the FIR, the differences between the measured total transmittances with results obtained using the IR Boundary Layer Effects Model (IRBLEM) were found to be relatively small and may mostly be due to uncertainties in the aerosol transmittance. However, as the only measurements were taken during periods of positive ASTD, the effect of refraction is more difficult to determine. In the MIR, the differences between the measured total transmittances with results obtained using IRBLEM were found to be much more significant. However, here again, while the refractance calculated by IRBLEM appears to be too strong, much of the differences are probably also due to uncertainties in the contribution of the aerosol transmittance.

The effect of molecular transmittance is found to reduce the transmission by about 48% for the MIR and between 80 and 90 %, depending upon the specific humidity, for the FIR. The effect of aerosol transmittance, as calculated using a variation of the Navy Aerosol Model (NAM), is found to reduce the transmission from 20% to70% for the MIR, and from 15% to 60% for the FIR. The effect of refractance, the focussing and defocussing of radiation due to atmospheric refraction, on the predicted transmissions is found to predict gains of more than 100% and losses of 100% (source below the horizon). Due to the importance of these effects and their dependence on different, though not necessarily completely independent, meteorological parameters, IR transmission models for the marine boundary layer (MBL) must properly take the effects of molecular extinction, aerosol extinction, and refractance into account. Furthermore, due to the relative constant behaviour of the molecular transmittance in the MIR, compared to the high variability of the aerosol transmittance, and the sometimes dramatic effects produced by refractance, the total transmission can be thought of as fluctuating about the molecular transmittance with the fluctuations being controlled by the amount of aerosol in the MBL, and then being further refined by the air-sea temperature difference, while in the

FIR, where the molecular transmittance is much smaller and its variation more significant, the effects of both the molecular and aerosol transmittances on the total transmittance can be of equal importance.

ACKNOWLEDGEMENTS

Special mention must be made to acknowledge the efforts of Petr Fritz and Marcel Moerman of TNO, and to Douglas Jensen of NRaD, whose tireless efforts brought the EOPACE campaign to life.

REFERENCES

1. D. Dion and P. Schwering, "On the Analysis of Atmospheric Effects on Electro-Optical Sensors in the Marine Surface Layer", IRIS Conference, UK, June 1996.
2. J.L. Forand, M. Duffy, C. Zeisse, S. Gathman, A. de Jong, and D. Dion, "Atmospheric Effects on Low Elevation Transmission Measurements at EOPACE", Proc. SPIE, Vol. 3125, Propagation and Imaging throug the Atmosphere, pp. 123-134, 1997.
3. A. Beck, L. S. Bernstein, D. C. Robertson, "MODTRAN: A Moderate Resolution Model for LOWTRAN 7", Final Report, Spectral Sciences, Inc., Burlington, MA, 1989.
4. P. Schwering and G. Kunz, "Infrared scintillation effects over sea", SPIE Proc., Vol. 2471, pp. 204-215, 1995.
5. S. G. Gathman, "Optical properties of the marine aerosol as predicted by the Navy Aerosol Model", Opt. Eng., Vol. 22(1), pp. 57-62, 1983.
6. G. de Leeuw, A.M.J. van Eijk, and G. R. Noordhuis, "Modeling aerosols and extinction in the marine atmospheric boundary layer", Proc. SPIE., Vol. 1968, pp. 70-80, 1993.
7. A.M.J. van Eijk and G. de Leeuw, "Modeling aerosol particle size distributions over the North Sea", Journal of Geophysical Research, Vol. 97C, pp. 14417-14429, 1992.
8. G. de Leeuw, "Modeling of extinction and aerosol backscatter profiles in the marine mixed layer", Applied Optics, Vol. 28, pp. 1356-1359, 1989.
9. W. T. Liu, K.B. Katsaros, and J.A. Businger, "Bulk Parametrization of Air-Sea Exchanges of Heat and Water Vapor Including the Molecular Constraints at the Interface", Journal of Atmospheric Sciences, Vol. 36, pp. 1722-1735, 1979.
10. J. L. Forand, "The L(W)WKD Marine Boundary Layer Model", DREV R-9618, March, 1997, UNCLASSIFIED.
11. A. S. Monin and A. M. Obukhov, "Basic Regularity in Turbulent Mixing in the Surface Layer of the Atmosphere", Trad. Geophys. Inst. ANSSSR, No. 24, p. 163, 1954.
12. A. Blanchard, "Phase and intensity ray tracing to study the propagation of coherent radiation in the atmosphere and other media", DREV R-4699, 1993, UNCLASSIFIED.
13. C.R. Zeisse, S.G. Gathman, A.N. de Jong, G. de Leeuw, J.L. Forand, D. Dion and K.L. Davidson, "Low Elevation transmission measurements at EOPACE part 1: molecular and aerosol effects", SPIE Proc., Vol. 3125, 1997.
14. A.N. de Jong, G. de Leeuw and K.L. Davidson, "Low elevation transmission measurements at EOPACE part III: scintillation effects", SPIE Proc., Vol. 3125, 1997.
15. A.N. de Jong and P.J. Fritz, "EOPACE Transmission Experiments Spring 1996; Preliminary Results", TNO Report, FEL-96-A090, March 1997.
16. L. Gardenal, "Étude de l'interaction des ondes électromagnétiques sur une surface maritime pour l'amélioration d'un algorithme de pistage à basse altitude de cibles", p. 17, M.Sc. Thesis, Laval University, November 1994.

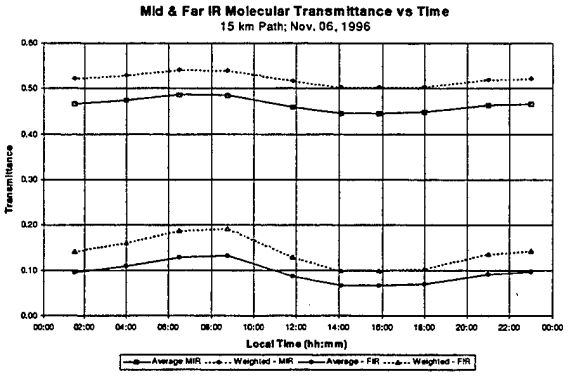

Figure 6a - Molecular transmittance calculations for Nov. 6 using IRBLEM.

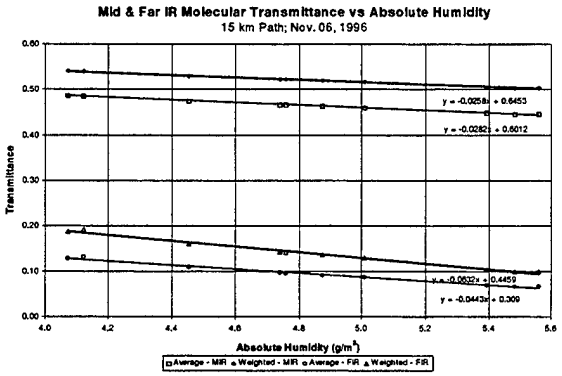

Figure 6b - Molecular transmittance calculations using IRBLEM versus the measured spec. humidity for Nov. 6.

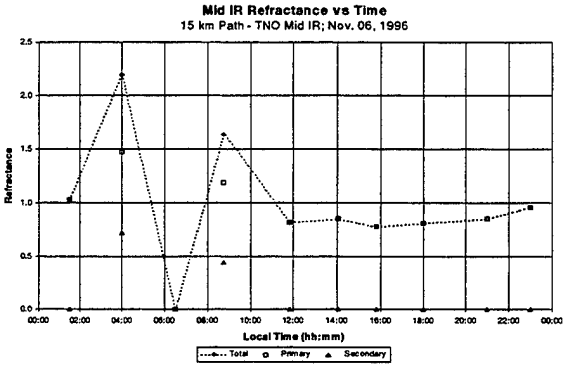

Figure 6c - MIR refractance calculations for Nov. 6 using IRBLEM.

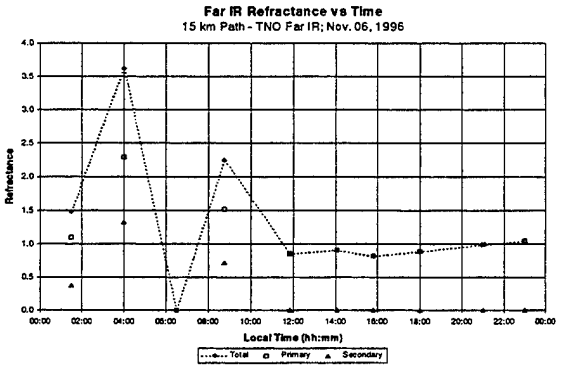

Figure 6e - FIR refractance calculations for Nov. 6 using IRBLEM.

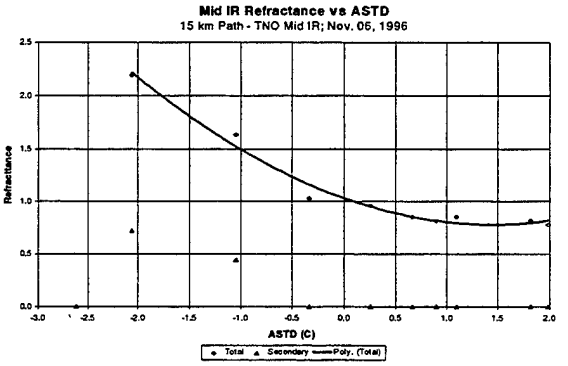

Figure 6d - MIR refractance calculations versus ASTD for Nov. 6 using IRBLEM.

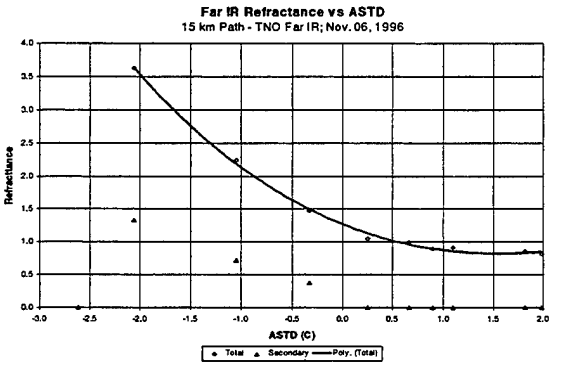

Figure 6f - FIR refractance calculations versus ASTD for Nov. 6 using IRBLEM.

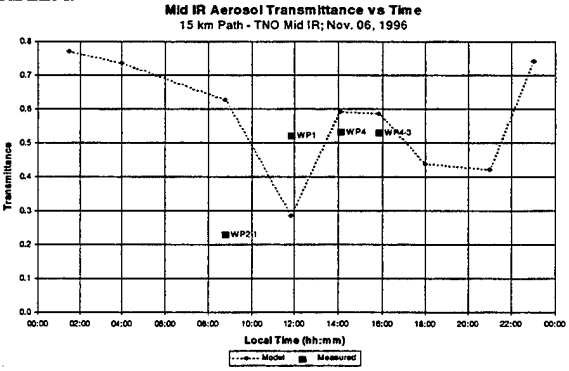

Figure 6g - MIR aerosol transmittance measurements and IRBLEM calculations for Nov. 6.

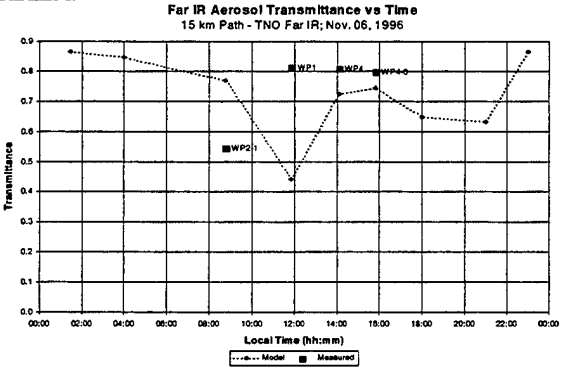

Figure 6h - FIR aerosol transmittance measurements and IRBLEM calculations for Nov. 6.

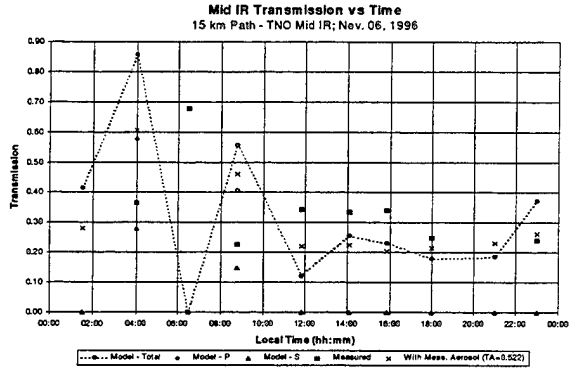

Figure 6i - MIR transmittance measurements and IRBLEM calculations for Nov. 6.

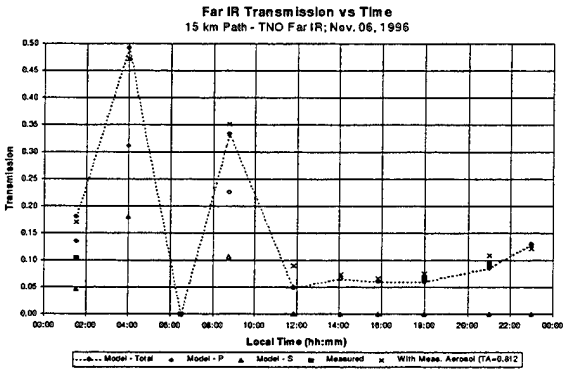

Figure 6j - FIR transmittance measurements and IRBLEM calculations for Nov. 6.

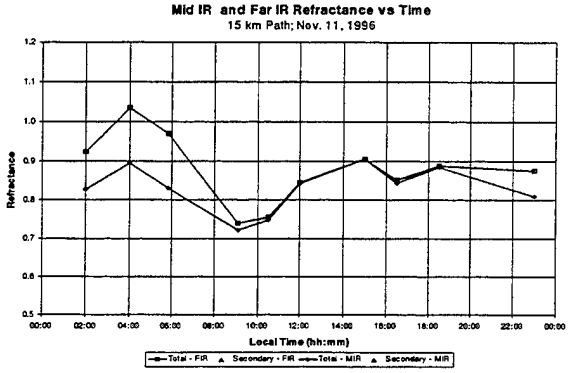

Figure 7a - MIR and FIR molecular transmittances calculated using IRBLEM for Nov. 11.

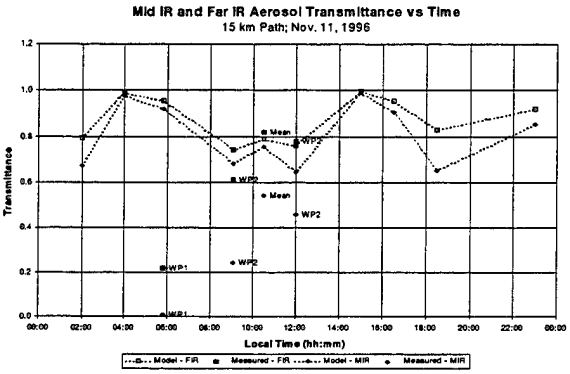

Figure 7b - Measure MIR and FIR aerosol transmittances and those calculated using IRBLEM for Nov. 11.

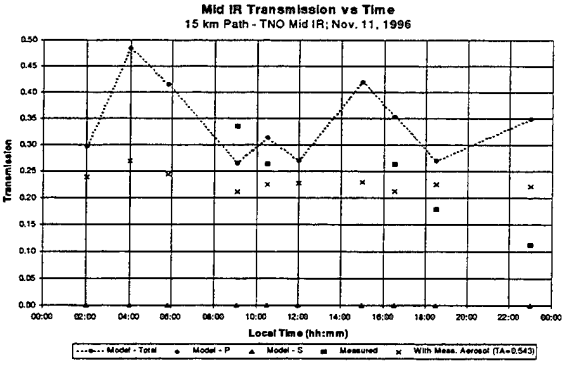

Figure 7c - MIR transmittance measurements and IRBLEM calculations for Nov. 11.

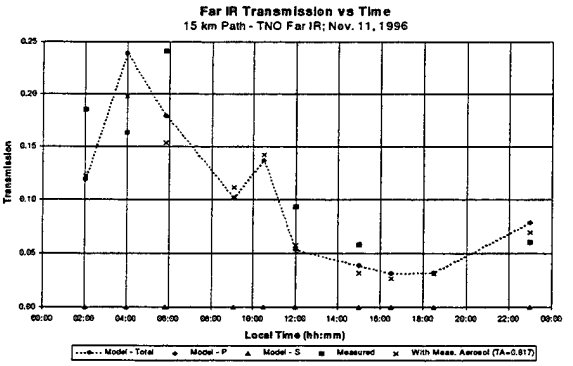

Figure 7d - FIR transmittance measurements and IRBLEM calculations for Nov. 11.

LOW ALTITUDE INFRARED TRANSMISSION

Carl Zeisse, Stuart Gathman, Amalia Barrios, and Bill Moision
Space and Naval Warfare Systems Center D883
49170 Propagation Path
San Diego, CA 92152-7385,
Ph: 619-553-3602
Fax: 619-553-1417
E-mail: zeisse@spawar.navy.mil

Ken Davidson and Paul Frederickson
Naval Postgraduate School, Code 63DS
589 Dyer Road, Room 252
Monterey, CA 93493-5000

Brett Nener
Department of Electrical and Electronic Engineering
The University of Western Australia
Nedlands, Western Australia
Australia 6907

ABSTRACT

Broad band infrared transmission has been measured over San Diego Bay along a 7 km path at heights from 4 to 7 meters above sea level. Data in the mid and long wave infrared bands were collected during a field experiment in November 1996. Simultaneous meteorological measurements were obtained from a buoy placed at the mid-point of the path. An aerosol spectrometer was used to measure the aerosol size distribution over the path.

Transmission data have been analyzed for aerosol effects with Mie theory, for molecular effects with MODTRAN, and for refractive effects with refractivity profiles obtained from the LKB evaporation duct model using the Monin-Obukhov similarity theory.

In general, aerosols cause the infrared transmission to vary between a lower limit of 0% (when fog is present, for example) and an upper limit given by the clear air molecular value. Occasionally, transmission values exceeding the free space value have been observed; these are attributed to refractive effects.

BACKGROUND

The high-speed sea skimming missile is a serious threat to Navy ships. Infrared systems such as the infrared search and track system (IRST) are being considered as a supplement to radar for detecting and responding to these missiles. The optical path involved in this scenario constitutes a difficult geometry for infrared systems. First of all, the path is always low, and low

constitutes a difficult geometry for infrared systems. First of all, the path is always low, and low altitude aerosols will absorb and scatter the radiation, causing the received intensity to vary on a daily basis between zero (in foggy conditions, for example) and an upper limit set by molecular absorption and scattering. Next, the path is also long when the missile is first detected. For long, low paths refractive effects will be important. For example, there may be more than one image of the target: one will be real and one will be a mirage. Or, the intensity of the image may increase or decrease because the refractive atmosphere can act as a positive or negative lens. Finally, the image intensity will scintillate: there will be large, rapid intensity fluctuations due to turbulence in the atmosphere. It will be difficult enough to account for these effects in the open ocean, and further complications will arise in waters near the coast because of the strong influence of the nearby land mass on aerosol composition and refractive index gradient.

During the middle two weeks of November 1996, a field experiment in the San Diego area was held as part of an experimental program called Electro-Optical Propagation Assessment in Coastal Environments (EOPACE). The overall purpose of the experiment was to obtain information pertinent to the coastal operation of shipboard infrared systems such as the IRST. Analysis of these data shows that refractive effects are occasionally present, but for most of the time the predominant atmospheric effect is extinction of the signal by aerosols and molecules.

THE TRANSMISSION EXPERIMENT

Transmission data were collected across San Diego Bay between November 7 and November 19, 1996 (days 311 to 323 inclusive). An overhead satellite photograph of San Diego Bay is shown in figure 1. Transmission data were recorded along both of the paths shown in figure 1, but only the data collected on the shorter 7 km path will be discussed in this paper. The 7 km path stretched between an infrared transmitter at the Naval Amphibious Base, Coronado, and an infrared receiver at the Naval Submarine Base, Point Loma. Meteorological data were taken at these two locations and at a buoy moored in the bay. The optical path necessarily passed over small sections of land and several tens of meters of surf at Coronado, and it also passed over a jetty and sheltered water at the entrance to San Diego Harbor. The optical beam was often obscured by passage of Navy ships and small boats sailing in and out of the harbor. The prevailing winds in the San Diego region come from the northwest, and as a result the Point Loma receiver location is generally sheltered from the wind whereas the transmitter location at Coronado was exposed to the wind.

Figure 1. A satellite view of San Diego Bay.

32° 40' 03.9" and longitude W 117° 09' 54.0". From these data the range from the receiver to the transmitter was 6996.8 m at a bearing of 104.1° True.

The height of the optical path at the transmitter, 6.2 ± 0.2 m above mean sea level, was obtained by comparing it to the receiver height with a GPS survey. The height of the optical path at the receiver, 4.9 ± 0.2 m above mean sea level, was measured by using a transit to compare it to local sea level and assuming that this sea level was identical to that measured by a tide gauge at Broadway pier in San Diego.

The transmitter consisted of a black body source at 1200K located in the focal plane of a Newtonian reflecting telescope. The black body aperture was 6.4 mm in diameter. The primary mirror was a gold-coated 200 mm diameter paraboloid with a focal length of 1229 mm (F/6). The secondary mirror obstruction was about 8% of the primary aperture. The receiver consisted of two identical Newtonian reflecting telescopes, one with a mid wave infrared detector at its focus, and one with a long wave infrared detector at its focus. The receiver telescopes were off-the-shelf Celestron "Star Hopper" amateur astronomy telescopes [1]. The primaries were nominally 200 mm diameter aluminum coated paraboloids with a nominal focal length of 1220 mm (also F/6). The secondary mirror obstruction was nominally 4% of the primary area. The angular field of view of each receiver was 0.8 mrad.

The infrared detectors were manufactured by Belov Technology [2]. The mid wave detector was InSb 1 mm square and was covered with a cold optical filter with a nominally square pass band between 2416 cm^{-1} (4.14 μm) and 2810 cm^{-1} (3.56 μm). The long wave detector was HgCdTe 1 mm square and was covered with a cold optical filter with a nominally square pass band between 877 cm^{-1} (11.4 μm) and 1020 cm^{-1} (9.80 μm). Each detector was liquid nitrogen cooled, and Dewar hold time was approximately 12 hours. Each detector was followed by a pre-amplifier with nominal gain of 1000X, after which the signal was fed into a lock-in amplifier. The black body was chopped at a frequency of 750 Hz and a chopper reference signal was transmitted to the lock-in by means of a radio signal at 160.1 MHz. The lock-in time constant was set to 10 s with a roll-off of 6 dB per octave (wait time 50 s, equivalent noise bandwidth 0.025 Hz). The output of the lock-in was recorded every minute and stored on disk. The measured detector noise to free space signal[1] ratio was 0.003 % in the long wave band and less than 0.001 % in the mid wave band.

The transmissometer was calibrated in the laboratory to an absolute accuracy of ± 30 % by a procedure that essentially amounts to "chopping the distance". That is, the signal when the path is several m long (in the laboratory) is used to predict the free space signal when the path is 7 km long (in the field). The calibration procedure used conservation of radiance, assumed that laboratory transmission was 100%, and assumed that nothing changed between laboratory and field except the length of the path.

[1] The free space signal, loosely described as "100% transmission," is the signal that would be expected when there is no atmosphere: namely, no molecules, no aerosols, and no ray bending.

Aerosols were measured by transporting a classical scattering aerosol spectrometer probe [3] in a small boat outbound (from receiver to transmitter) and inbound (from transmitter to receiver) along the over-water portion of the path. A one-way run took about ½ hour. Although the intake to the aerosol spectrometer faced toward the bow of the boat, there were occasions when the prevailing wind blew diesel exhaust from the stern past the bow, suggesting that exhaust particles might contaminate the aerosol data. Therefore, we only accepted runs for which the prevailing wind direction was within ± 30° of the path blowing from bow to stern. Aerosol data were acquired at 1 s intervals and later summed over longer time intervals, typically 10 minutes, in order to attain sufficient statistical significance, a precaution that is especially important at larger radii where particle counts are very low. By the end of the experiment 64 aerosol measurements had been made on the short path for which there was no diesel contamination and transmission data were simultaneously available.

DATA ANALYSIS

In order to analyze the transmission data, τ, we combined the effects of refraction, aerosols, and molecules according to the formula

$$\tau = F^2 \cdot e^{-\beta L} \cdot \tau_m \qquad (1)$$

In this equation, F, the propagation factor, accounts for refractive effects. F is the dimensionless ratio of the electric field received under prevailing refractive conditions to the electric field that would have been received in free space, normalized to unity gain antennas. The second factor accounts for aerosol effects and is determined by the product of aerosol extinction β (km^{-1}) and range L (km). The third factor, τ_m, is the dimensionless molecular transmission predicting the effects of molecular extinction (scattering plus absorption). The form chosen for the second and third factors in (1) reflect the fact that broad band aerosol transmission obeys Beer's Law (exponential decay of transmission with range) whereas broad band molecular transmission does not. Predictions according to (1) are only possible when β is known. Hence transmission predictions are only available when aerosol data have been measured, which was for 64 separate occasions during the experiment. Transmission data, on the other hand, were recorded almost continually every minute throughout the entire experiment.

Each of the three infrared effects entering into the transmission analysis will now be described in slightly more detail.

Refraction

Bulk meteorological measurements made from the buoy mid-way along the path were used to determine evaporation duct profiles based on the LKB evaporation duct model [4]. Refractivity profiles were determined from bulk measurements made at times corresponding to the aerosol data measurements. These refractivity profiles were then fed into two different propagation models to compute the propagation factor, F, at the detector/receiver end. One propagation model is based on ray optics techniques (RO), and the other uses the split-step

parabolic equation (PE) algorithm. Both models were created from modifications made to the radio-wave propagation models called Radio Physical Optics (RPO) [5] and Terrain Parabolic Equation Model (TPEM) [6].

Radio-wave transmissions are coherent in nature and are easily modeled as such in RPO and TPEM. Therefore, in modeling IR transmission, some thought had to be given in how to model propagation effects due to an incoherent source using these two techniques. The approach was to determine all possible ray paths from the IR source to the detector (i.e., direct, reflected, mirage) and determine the propagation factor for each ray path separately. A ray trace was used to determine the initial launch angles of ray paths reaching the sensor for a given refractivity profile. These pre-determined ray angles were then used to start the RO and PE calculations. Both techniques are briefly described below.

RO model. Within the ray optics calculations each ray reaching the sensor is traced, keeping track of the amount of spreading the ray is undergoing at each range step. Following [5], F is determined from

$$F_{RO}^2 = \left| \frac{r}{\theta_d \dfrac{\partial r}{\partial \theta_s}} \right| \tag{2}$$

where r is the distance between source and detector, θ_d is the local ray angle at the detector, and $\dfrac{\partial r}{\partial \theta_s}$ is the change of r with respect to the initial launch angle at the source, θ_s.

PE model. The source field within TPEM is inherently modeled and propagated as a coherent source, therefore, a "brute force" method was used to determine F for each ray path. The source was modeled using a Gaussian antenna pattern with a very narrow vertical beam width. Each initial ray angle then corresponded to the pointing angle of the main beam. This effectively models the ray as a "thick beam" and minimizes interference effects from other ray paths within the beam width of the antenna. The split-step PE algorithm is given by $F_{PE} = |u|\sqrt{r}$, where $|u|$ is defined as

$$u(r + \Delta r, z) = e^{ik_0 \Delta r M'(\lambda, z)} F^{-1}\left\{ P_{fs}(\lambda, \Delta r, \theta) F\left\{ u(r, z) \right\} \right\} \tag{3}$$

Here, Δr is the PE range step, $M'(\lambda, z)$ is a function of wavelength, λ, and the modified refractivity profile; P_{fs} is the free-space propagator and is a function of propagation angle, θ; and F^{-1} and F represent the inverse and forward Fourier transform, respectively. For details on the split-step algorithm, refer to [7].

While it is not the intent in this paper to delve into the pros and cons of the two methods of determining F for this particular application, we used both methods as a simple cross-check and to determine the feasibility of applying a more sophisticated model like the PE method to EO applications. The RO technique does behave poorly near caustics, and for this reason the values for F were numerically limited. Also, the propagation factor determined from the RO method is essentially a measure of *intensity* relative to free space and not a measure of field strength as strictly defined by Kerr [8]. For this reason, F_{RO} is independent of wavelength and will give the same values for F regardless of wave band when applied to IR applications. The PE method is generally superior to the RO method; however, there are certain restrictions in using this method that also make it less desirable for IR applications. A more detailed look at these two methods for this particular application will be dealt with in a future paper.

Aerosols

A representative aerosol spectrum collected over a 10 minute interval is shown in figure 2. The figure shows dN/dr (cm^{-3} μm^{-1}), the number of aerosol particles per unit volume whose radii lie between r and $r + dr$ μm, as a function of particle radius. The data, shown as solid circles in figure 2, were fit with a fifth order polynomial, truncated abruptly at the minimum and maximum observed radii, and integrated according to Mie theory using

$$\beta(\nu) = \int_0^\infty \pi r^2 Q(\nu) \frac{dN}{dr} dr \tag{4}$$

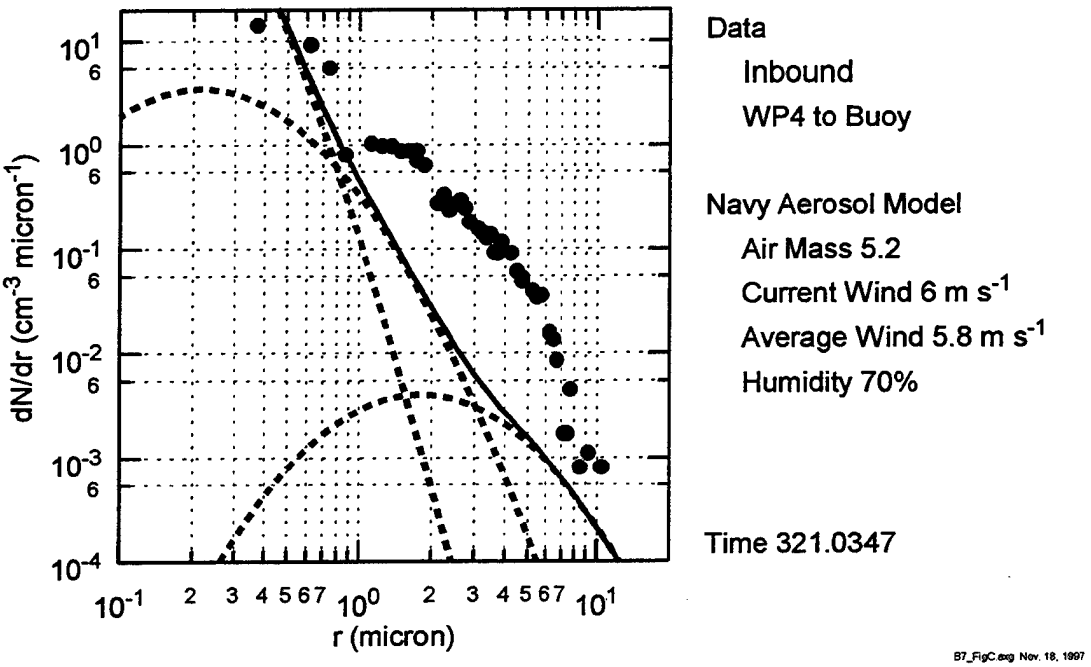

Figure 2. Aerosol size distribution measured (solid circles) and predicted by the Navy Aerosol Model (solid line). Dashed lines show the three independent log-normal components of the Navy Aerosol Model.

Here $Q(\nu)$ is the dimensionless Mie efficiency factor for extinction, provided in our calculations by the Dave code [9]. During the integration we always chose a wave number, ν, of 2858 cm^{-1} (3.5 μm) for the mid wave region and 943 cm^{-1} (10.6 μm) for the long wave region. We have implicitly made the assumption, generally valid for aerosols, that Mie extinction does not vary rapidly with wave number. For the data of figure 2 this procedure resulted in an aerosol extinction of 0.0724 km^{-1} in the mid wave band and 0.0217 km^{-1} in the long wave band.

Molecules

To analyze the effect of molecules we relied on the predictions of MODTRAN 3.5 [10]. We neglected the role of pressure and temperature and assumed the transmission to be uniquely determined by absolute humidity for the wave numbers to which our detectors were sensitive. We also assumed that the relative spectral responsivity of our detectors had the shape of a "top hat," that it was unity inside the pass band and zero outside. With these assumptions, the transmission predicted by MODTRAN 3.5 is shown in figure 3. Then, using the meteorological data from the mid path buoy, we calculated the absolute humidity and predicted the transmission in each band from the data shown in the figure. We note that, because absolute humidity is always available,

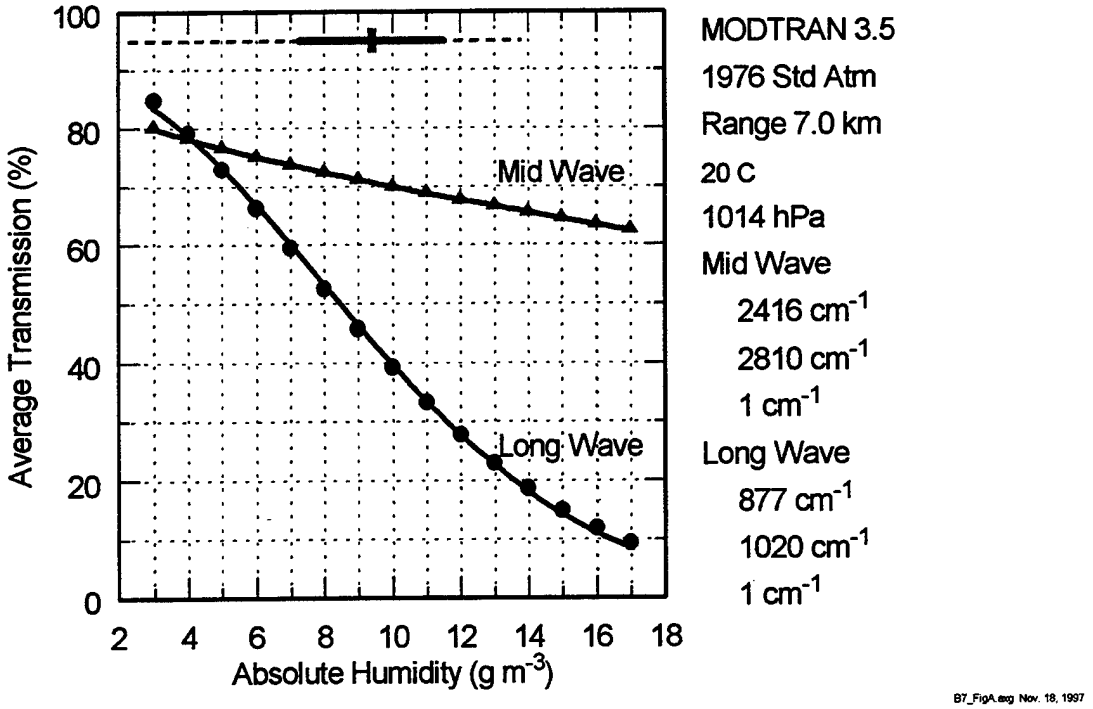

Figure 3. Broad band transmission versus absolute humidity as predicted by MODTRAN 3.5. The lines at 95% transmission indicate the absolute humidity encountered during the experiment as follows: the vertical line is the mean, the solid horizontal line spans one standard deviation either side of the mean, and the dashed horizontal line spans minimum to maximum.

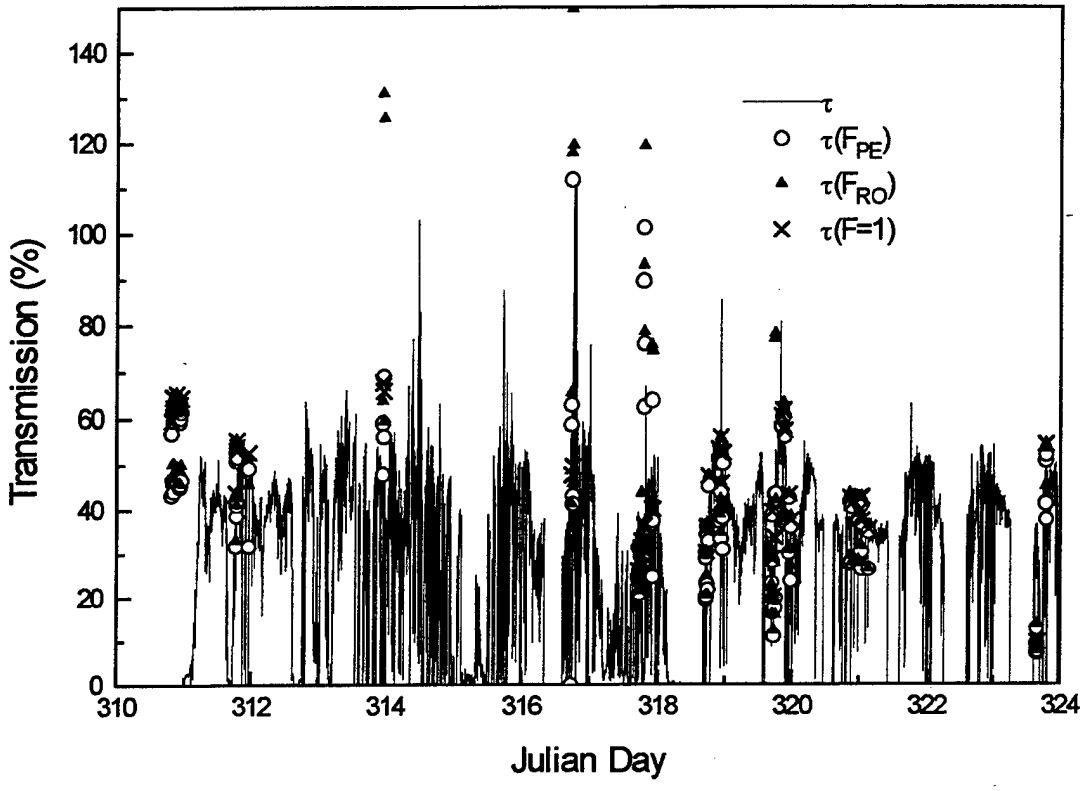

Figure 4. Infrared transmission measured (solid line) and predicted (symbols) for the mid wave band. The predictions differ only in the method used to arrive at the propagation factor: via the parabolic equation (open circles), ray optics (solid triangles), or free space (crosses).

molecular predictions are always available.

DATA

The transmission data measured in November 1996 are shown by the solid line in figures 4 for the mid wave band and 5 for the long wave band. The solid symbols in each figure represent the transmission that would be predicted from equation (1) under various methods for calculating the propagation factor.

DISCUSSION

A striking feature of figure 5 is the existence of isolated data larger than 100%; these occur, for example, near the middle of day 314 and the end of day 317. When it is further realized, as shown in figure 3, that molecules provide an upper limit to clear air (aerosol free) transmission of 80% in either band, it is apparent that refractive focusing events were observed even more often than these two isolated examples indicate. Although there is no rigorous way to rule out

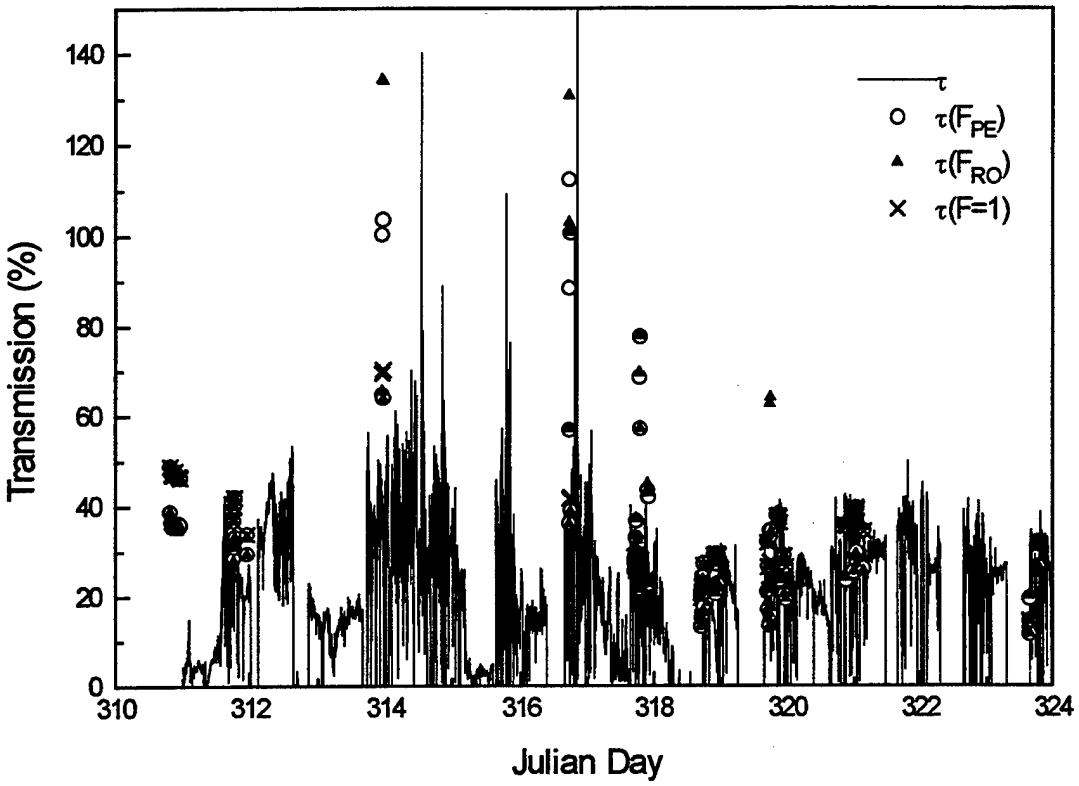

Figure 5. The same as figure 4 for the long wave band.

scintillation as the cause of these particular events, the rather long time constant (a time of 50 s to respond to within 99% of an arbitrarily applied step input) makes refractive focusing a more palatable cause.

On the other hand, given the fact that about fifteen thousand transmission observations at one minute intervals were recorded in each band throughout the course of this experiment, it must be conceded that refractive events remained rare. So it is not surprising that, on the 64 occasions when we were able to directly compare measurements with predictions, only a few show any major refractive effects. Refractive effects are strongly dependent on the path length and altitude and apparently, at a 7 km length and a 4 to 7 m altitude such as we have used for this experiment, refractive effects are only beginning to come into play.

This line of reasoning suggests that a useful first approximation to infrared transmission can be obtained by considering molecules and aerosols alone; that is, by ignoring refraction entirely and equating the propagation factor to unity. If this is done, then the rms error[2] between

[2] Since rms error takes both bias and correlation into account, it is a more meaningful statistic than bias or correlation alone.

prediction and measurement, for the 64 occasions when a comparison could be made during this experiment, was 12.5% in the mid wave band and 9.5 % in the long wave band. Since these errors are less than the 30% error in the calibration of the transmissometer, we may conclude that combined effects of aerosols and molecules on infrared transmission successfully explain our data. This suggests further that, continuing to assume a propagation factor of unity, we may divide our data (always available) by the molecular prediction (always available) and arrive at a reasonable approximation to the aerosol transmission (seldom available). In equation form,

$$\beta \approx \frac{-\ln(\tau/\tau_m)}{L} \tag{3}$$

Thus we argue that our data may stand in for aerosol extinction, and that the goodness of this substitution will depend, first of all, on the extent to which the effect of refraction can be neglected, and, second of all, on the extent to which the prediction from MODTRAN can be accepted.

The obvious next step is to compare aerosol extinction derived this way from transmission with aerosol extinction as it might be predicted with our best model. As a first attempt in this direction, let us use the Navy Aerosol Model (NAM) an empirical aerosol model developed for the open ocean. The solid line in figure 2 represents the aerosol spectrum predicted, according to NAM, from the following meteorological parameters observed simultaneously with the aerosol data: air mass parameter (determined in our case from a radon count), current wind speed, average wind speed, and relative humidity. If the NAM curve is integrated according to equation (2) then the result is an aerosol extinction of 0.0255 km^{-1} (mid wave) and 0.00769 km^{-1} (long wave). These values are significantly lower than the values of 0.0724 km^{-1} (mid wave) and 0.0217 km^{-1} (long wave) inferred from the actual data.

The lower NAM extinction is a straightforward consequence of fact that, as shown in figure 2, NAM under-predicts the number of particles per unit volume. In order to force NAM into better agreement with the data, the current wind speed has to be increased from 6 to 20 m s^{-1} and the average wind speed has to be increased from 5.8 to 10 m s^{-1} (without changing the air mass parameter or relative humidity). Therefore, at least in this particular case, forcing NAM to match the data requires unreasonable meteorological values. This result is not very surprising; on the contrary it is just what we would expect. That is because NAM was developed for clean conditions in the open ocean. But our data were taken in San Diego Bay where there is every reason to expect additional aerosols in the air arising from city smog, nearby ship wakes, surf, and diesel exhaust, to name just a few possible sources. Hence, we expect that further comparisons will confirm what has just been described for figure 2, that NAM will not serve to model coastal aerosols, and that a new model will have to be developed.

CONCLUSION

We have measured infrared transmission along a 7 km path over San Diego Bay at heights from 4 to 7 meters above sea level. Data in the mid and long wave bands were recorded at one minute intervals during 13 consecutive days in November 1996.

Isolated examples of transmission in excess of the 80% clear air maximum were observed in both bands; the maximum observed transmission was 150% in the long wave band.

The data were compared with the predictions of a model combining the effects of aerosols, molecules, and refractivity. The refractivity model provided an explanation of the excess transmission; namely, the simultaneous reception of direct and mirage ray bundles. Model predictions were available on 64 occasions when aerosol size distributions had been measured along the path. Neglecting refractive effects (i.e., setting $F = 1$), the rms error between prediction and measurement was 13% in the mid wave band and 10% in the long wave band. Since this is well within the experimental transmission error we conclude that, for this particular location and path, the total transmission is well described by the product of aerosol and molecular transmissions.

ACKNOWLDEGEMENTS

Special thanks to Herb and Linda Hitney for their efforts in obtaining a ray optics model for our particular application.

Dr. Scott Sandgathe and Dr. Ronald Ferek of the United States Office of Naval Research sponsored this work.

REFERENCES

1. Celestron International, 3825 Columbia Street, Torrance, CA 90503.
2. Belov Technology Co. Inc., 345 Sandford Street, New Brunswick, NJ 08901.
3. Model CSASP-100-HV, Particle Measuring Systems Incorporated, 5475 Airport Boulevard, Boulder, CO 80301-2339.
4. W. T. Liu, K. B. Katsaros, J. A. Businger, "Bulk Parameterization of Air-Sea Exchanges of Heat and Water Vapor Including the Molecular Constraints at the Interface", *JAS, Vol. 36, 1979*, pp. 1722-1735.
5. W.L. Patterson, H.V. Hitney, "Radio Physical Optics CSCI Software Documents", *NRaD TD 2403, Rev. 1 April 1997.*
6. D.B. Sailors, A.E. Barrios, "Terrain Parabolic Equation Model (TPEM) Computer Software Configuration Item (CSCI) Documents", *NRaD TD 2963, May 1997.*
7. J.R. Kuttler, G.D. Dockery, "Theoretical Description of the Parabolic Approximation/Fourier Split-Step Method of Representing Electromagnetic Propagation in the Troposphere", *Radio Science, Vol. 26, 1991*, pp. 384-393.
8. D.E. Kerr, *Propagation of Short Radio Waves*, New York: McGraw Hill, 1951.
9. V. Dave, "Subroutines for Computing the Parameters of the Electromagnetic Radiation Scattered by a Sphere," *IBM Palo Alto Report 320-3237*, pp. 1-65, 1968.
10. Berk, L. S. Bernstein, and D. C. Robertson, "MODTRAN: A Moderate Resolution Model for LOWTRAN 7," *Air Force Geophysics Laboratory Report GL-TR-89-0122*, pp. 1-42, 1989.

Sensitivity Analysis for Infrared Propagation

Stephen Hammel
SPAWAR Systems Center, D883
San Diego CA 92040
hammel@nosc.mil

Abstract

Infrared Search and Track (IRST) systems are important to the Navy for detection of low-flying missile threats. However, the atmospheric refractive index within the marine atmospheric surface layer is strongly dependent on the air-sea temperature difference, and the near sea surface propagation environment can distort infrared images. These distortions include dramatic changes in the location of the optical horizon and the appearance of multiple mirage images.

A negative air-sea temperature difference is the necessary condition for inferior mirages. I will describe work to exploit sub-refractive mirage conditions for range-finding applications. The primary analytical tool is a refractive ray-bending simulator I built to study the effects of refractive index variations in the atmosphere. The existence of two images of a single source or target can be utilized to provide both range and height information.

I present results from experimental observation of inferior mirages and compare the experimental data with simulator predictions.

1 Introduction

Infrared Search and Track systems are currently in development by the Navy to be used as shipboard defense systems against sea-skimming missile threats. The near sea surface environment is difficult for radar systems, and a reliable passive IR (infrared) system has the potential to provide useful target detection data.

However, the near sea surface environment can also distort images in the infrared. In particular, refraction effects have a strong effect on IR systems, and the occurrence of mirages is not uncommon. I will describe work to exploit one type of mirage, the inferior mirage, to determine range and height of the source creating the mirage image.

The first two sections describe the analysis tool utilized for the studies described in this paper. Following that is a brief overview of the field test facility, and the type of data collected. Finally I outline the technique to extract range and height information from a source given the appearance of an inferior mirage of that source.

2 Refractive Propagation

The primary computational tool for analysis of refractive effects is a simulation tool called *IRWarp* which I developed to predict refractive effects [1]. This tool is a widget-based application which utilizes meteorological conditions as input data for a ray-trace module [2]. The ray-trace data is utilized to generate detailed information about geometrical transformations induced by the propagation environment. The ultimate goal is to utilize IRWarp to generate a corrected detection scene with the corresponding probabilities of detection accurately predicted.

The ray-tracing method utilized within IRWarp is from a model by Lehn [3]. However, the formulation in Lehn's model does not express refractive index as a function of wavelength, and utilizes a refractive index for visible wavelengths. I have modified the method to incorporate a variable wavelength using an expression from Hill [4]. The refractive index n is defined in terms of refractivity $N = (n-1) \times 10^6$. Although the full expression includes refractivity contributions from anomalous dispersion due to resonances, and the presence of water vapor, these factors do not make significant contributions for the problem considered here. Thus, I use $N = N_d$, the refractivity of dry air:

$$N_d = N_0(\lambda)\frac{T_0 P}{P_0 T},$$

where P is total atmospheric pressure and T is absolute temperature. The reference refractivity $N_0(\lambda)$ for wavelength λ in μm is given by

$$N_0 = 64.328 + \frac{29498.1}{(146. - \lambda^{-2})} + \frac{255.4}{(41. - \lambda^{-2})}$$

for a standard temperature $T_0 = 288K$, and pressure $P_0 = 101325$ Pa.

A ray propagating through a medium with a gradient in refractive index will define a curved path. The refractive index n is:

$$n = 1 + N_0(\lambda)\frac{T_0 P}{P_0 T} \times 10^{-6} = 1 + \alpha(\lambda)\frac{P}{T},$$

where $\alpha(\lambda) = N_0(\lambda)T_0 \times 10^{-6}/P_0$. Hence the refractive gradient is:

$$\frac{dn}{dz} = \frac{\alpha(\lambda)}{T^2}\left(T\frac{dP}{dz} - P\frac{dT}{dz}\right) \tag{1}$$

To find dP/dz, note that the hydrostatic equation gives

$$\frac{dP}{dz} = -g\rho \tag{2}$$

for density ρ and gravitational acceleration g. The equation of state of a perfect gas

$$\rho = \frac{M_r P}{RT} = \beta\frac{P}{T} \tag{3}$$

where $\beta = 3.485 \times 10^{-3}$, and the molecular weight of the dry atmosphere is $M_r = 28.98 \times 10^{-3}$ kg mol^{-1} and gas constant $R = 8.3145$ J mol^{-1} K^{-1}. Substitution of equations (2) and (3) into (1) gives

$$\frac{dn}{dz} = -\frac{\alpha(\lambda)P}{T^2}\left(g\beta + \frac{dT}{dz}\right) \tag{4}$$

The radius of curvature of a ray can be found as in Lehn's formulation [3], since curvature is defined:

$$\kappa = -\frac{\sin(\theta)}{n}\frac{dn}{dz}.$$

θ is the angle between the ray and the normal to the local surface tangent plane, and since the rays considered here have very small slopes with respect to that plane, $\sin(\theta)$ is taken to be 1. The radius of curvature is $r = 1/\kappa$, and this yields

$$r = \frac{nT^2}{\alpha(\lambda)\ P\ (g\beta + dT/dz)} \tag{5}$$

The ray-trace algorithm first defines the vertical profile as a set of discrete layers, each with a characteristic temperature and refractivity gradient. A characteristic radius of curvature is then assigned to each layer using eqn. (5) above.

3 Temperature Profile

The vertical temperature profile is based upon a surface layer similarity theory developed by Monin and Obukhov. I follow an approach and formulation based upon bulk methods for calculating turbulence parameters described by Davidson et al. [5] Measurements are taken at the sea surface, and at a reference height. In particular, the sea surface temperature is T_0, and the temperature $T(z)$ at a height z above the water surface is given by:

$$T = T_0 + T_*\left[\frac{\ln(z/Z_{0T}) - \Psi_T(z/L))}{\alpha_T k}\right]$$

where Z_{0T} is the roughness length for the temperature profile, T_* is the potential temperature scaling parameter, and α_T is the ratio of heat transfer to momentum transfer at the surface. L is the Monin-Obukhov length, and $\Psi_T(z/L)$ is a stability correction function.

A ray-trace can be generated from the temperature profile by determining a characteristic radius of curvature for each horizontal layer using eqn.(5). Fig. 1 displays the traced rays from the ray-trace algorithm for a coordinate system transformed so that the sea surface is the flat x-axis. The figure shows a ray-trace generated from a temperature profile from field data for a test on September 19 at Dahlgren Virginia. The air-sea temperature difference ≈ -3.5 K. The number of rays has been reduced to make the graphic more legible. The apparent kinks in some of the more sharply bent rays are an artifact: the actual path for the ray is a carefully determined smooth curve, but points on the path are saved only intermittently as needed.

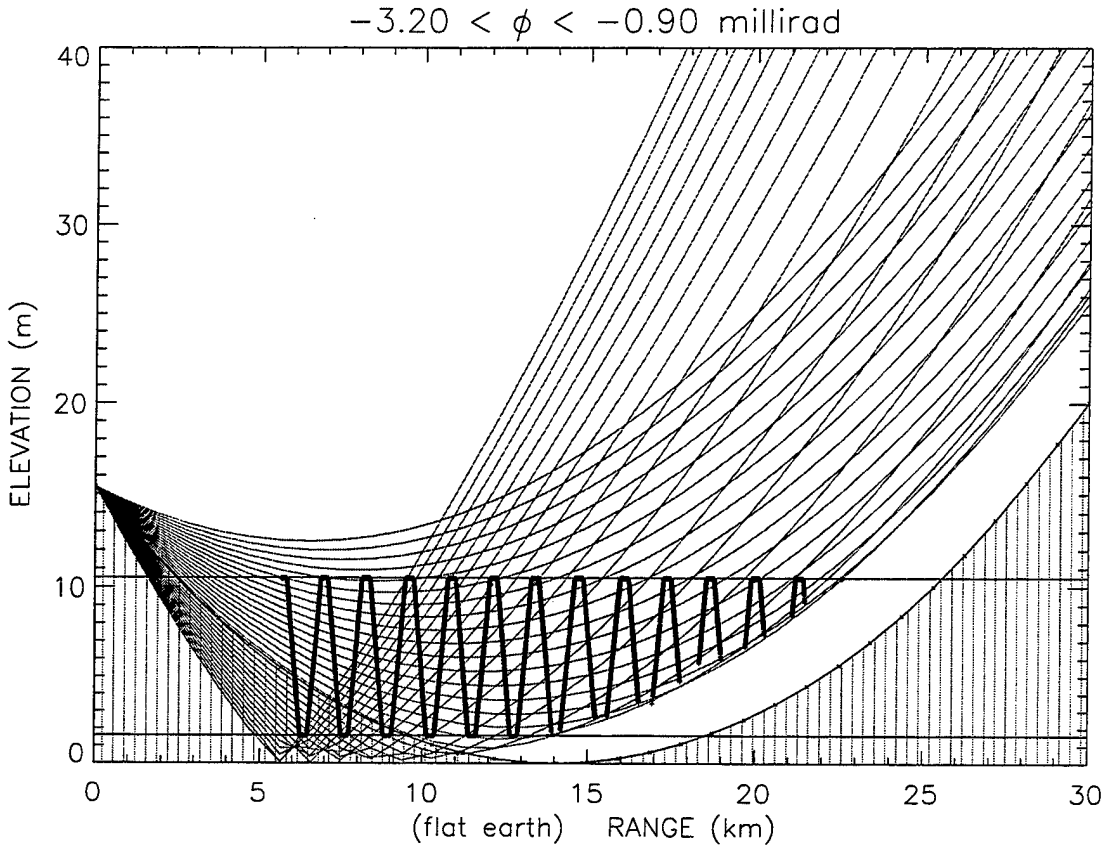

Figure 1: The vertical scale is in meters above the surface, while the horizontal scale is in kilometers downrange from the IRP sensor which is shown at a height of 15.4 meters. The curve bounding the vertically-hatched region indicates the path of a horizon-grazing ray *in the absence of a refractive medium.* The heavy zig-zag path is the set of height and range data returned from the field test IR source on the boat's tower for an outbound run.

An atmospheric surface layer for which the air-sea temperature difference is negative exhibits a crucial feature: the rays form a local coordinate system starting at some point downrange. The logarithmic temperature profile ensures that lower elevation rays are deflected to intersect upper elevation rays. The existence of a locally non-degenerate coordinate system implies that in some region of range-height space there exists a one-to-one correspondence with an upper elevation-lower elevation pair that is unique to that point.

4 Field Test Configuration

The Infrared Propagation (IRP) field test facility which generated the data utilized in this paper is located on the lower Potomac River at the Naval Surface Warface Center (NSWC) in Dahlgren, Virgina. The test configuration and results are described in an NSWC technical

report [6]. I am grateful to both authors of the report (Bill Trahan and Homar Rivera) for access to the test data, and for assistance in many other aspects of the field test work.

The IRP sensor consists of an infrared Radiance 1 camera manufactured by Amber Engineering with a 256×256 element InSb (indium antimonide) focal plane array. The FPA spectral response is $\approx 3.8\mu$m to 5.1μm (MWIR) The optical portion of the sensor is a Cassegrain telescope with focal length = 1.19m, and effective $f/\# = 3.9$. Thus the sensor has a field of view = 4.49×4.49 milliradians ($\approx .484° \times .484°$), and an instantaneous field of view = 33×33 microradians for each detector element; however the blur spot for the optics was ≈ 60 microradians.

The IR source is an industrial panel heater positioned on a mobile shuttle on a tower. The shuttle moves on a two minute cycle of vertical motion on the tower, ascending for 40 sec from a bottom position $z_{bottom} = 1.6$m above sea surface to a top position $z_{top} = 10.5$m, resting at top for 20 sec, descending for 40 sec, and resting at bottom for 20 sec. The tower is mounted on a 60-foot fishing boat which travels radially outbound from a point on the river near the sensor. The position of the boat and the sensor is measured with GPS receivers.

The video output from the sensor is processed digitally through a point source detection algorithm. Detections are thresholded, and the pixel location of the exceedence centroid is time-tagged and recorded. The camera has a 30 Hz frame rate, and the detection rate is 4 Hz. Since the Amber Radiance camera is mounted on a stepper motor platform with a fixed angular elevation, the elevation corresponding to each pixel row of the FPA can easily be determined. Thus each intensity detection of an image in the focal plane can be recorded along with simultaneous range and height data for the source.

A typical set of data from the September 19 field test is shown in fig. 1. The height and range data is saved and plotted *only when a detection was made at the sensor.* Hence when the source disappears below the horizon, no detection is made and no height-range point is plotted in fig. 1.

5 Comparison of field test data and model data

Fig. 2 displays a typical data set for subrefractive conditions (the air-sea temperature difference is negative). This is the same temperature profile used in fig. 1. There are two sets of data overlaid in fig. 2. The field test data is plotted with small "+" symbols. This dataset show the source detections made by the IRP sensor as the source made an outbound run. As the source ascends and descends, at the near range (5 km to 8 km) a single image is detected at the sensor. Near the 10 km point, a second mirage image appears at lower elevation. As the upper image ascends, the lower image descends, and vice versa.

Near the 14 km point, the two images are seen to merge and disappear for a portion of the source cycle. Between 22 km and 23 km the source disappears over the horizon. Note that this corresponds in fig. 1 to the zig-zag source path being entirely outside the ray-trace envelope. Note also that the ray-trace envelope is separated from the zero-refraction horizon line: in sub-refractive conditions, the horizon moves in closer to the sensor.

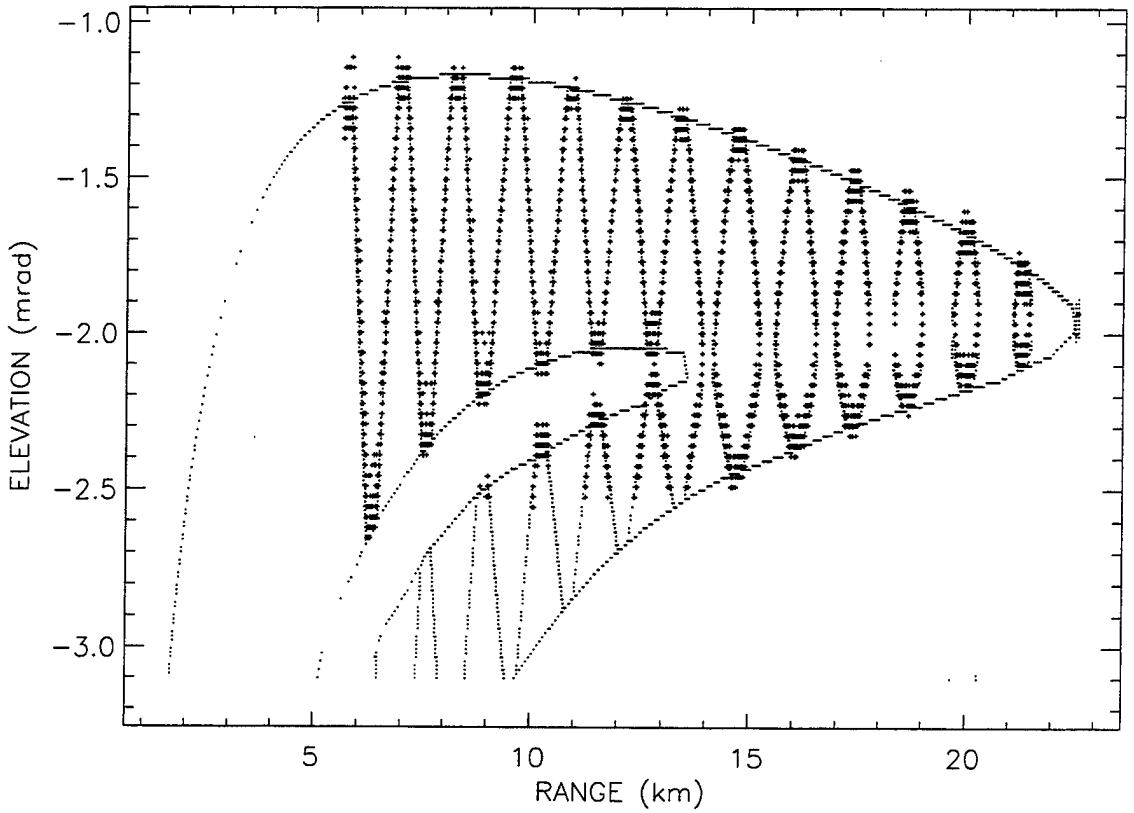

Figure 2: A detection dataset for the September 19 field test. The small "+" symbol shows sensor detections of the source at the angular elevation shown on the vertical axis. As the source moves downrange (to the right), note that a single detection "curve" is joined by a second image detection set at roughly the 10 kilometer point.

The field data overlies a second set of points that are plotted as dots. These are the simulated detections generated by IRWarp, using as input the height and range data from the field test. The apparent elevation at the sensor is generated by the point of intersection of the ray-trace surface with the height-range point.

The set of rays tracing the propagation path generates a surface. This surface has an intersection structure with the set of *isomet* surfaces (isomet surface ≡ surface of constant height). In fig. 1 there are two isomets shown at 1.6 m and 10.5 m, delimiting the upper and lower height extent of the boat-borne source. The intersection structure induces a transformation of the isomets. The result of the transformation is shown in fig. 2; the image of the isomets clearly defines an inner and an outer envelope for the detection set displayed between them.

To generate more detailed information about this transformation, the ray-trace envelope can be intersected with a family of isomet surfaces. In figure 3, the same temperature profile

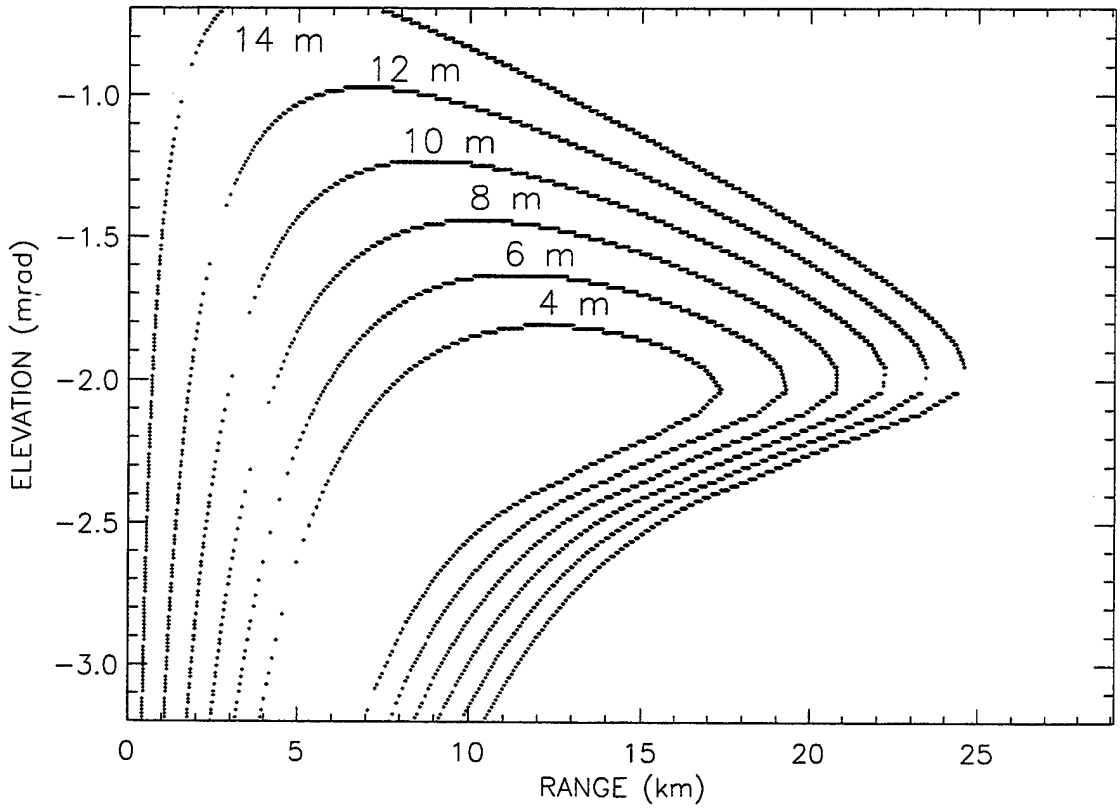

Figure 3: A series of isomets at the heights of $4, 6, 8, 10, 12$, and 14 meters.

and ray-trace of fig. 1 is used to calculate the intersection set between the ray-trace envelope and a set of isomets at heights of $4, 6, 8, 10, 12$, and 14 meters. I will let isomet refer to the contour curves representing the intersection set between an isomet surface and the ray-trace envelope (shown in fig. 3). Each of the isomets in the figure displays a similar form. This can be interpreted by imagining a source confined to one of the isomet surfaces (say the 14 meter isomet) and moving toward the sensor from the 30 km range. At $\approx$ 24 km, the source appears over the horizon, and immediately starts to split into two images. One image descends, and the upper image ascends, as the source moves closer in range. At $\approx$ 11 km, the bottom image has been descending rapidly and disappears beneath the lowest edge of the sensor focal plane. The (now solitary) upper image continues to rise, and disappears briefly above the upper edge of the sensor field-of-view. It finally reappears and rapidly moves from above the top edge to below the bottom edge.

This form for the 14 m isomet is characteristic of all the isomet contours for surfaces of height less than the sensor height. When the isomet surface height is greater than sensor height, an inbound upper image disappears across the upper boundary, and never re-crosses from top to bottom.

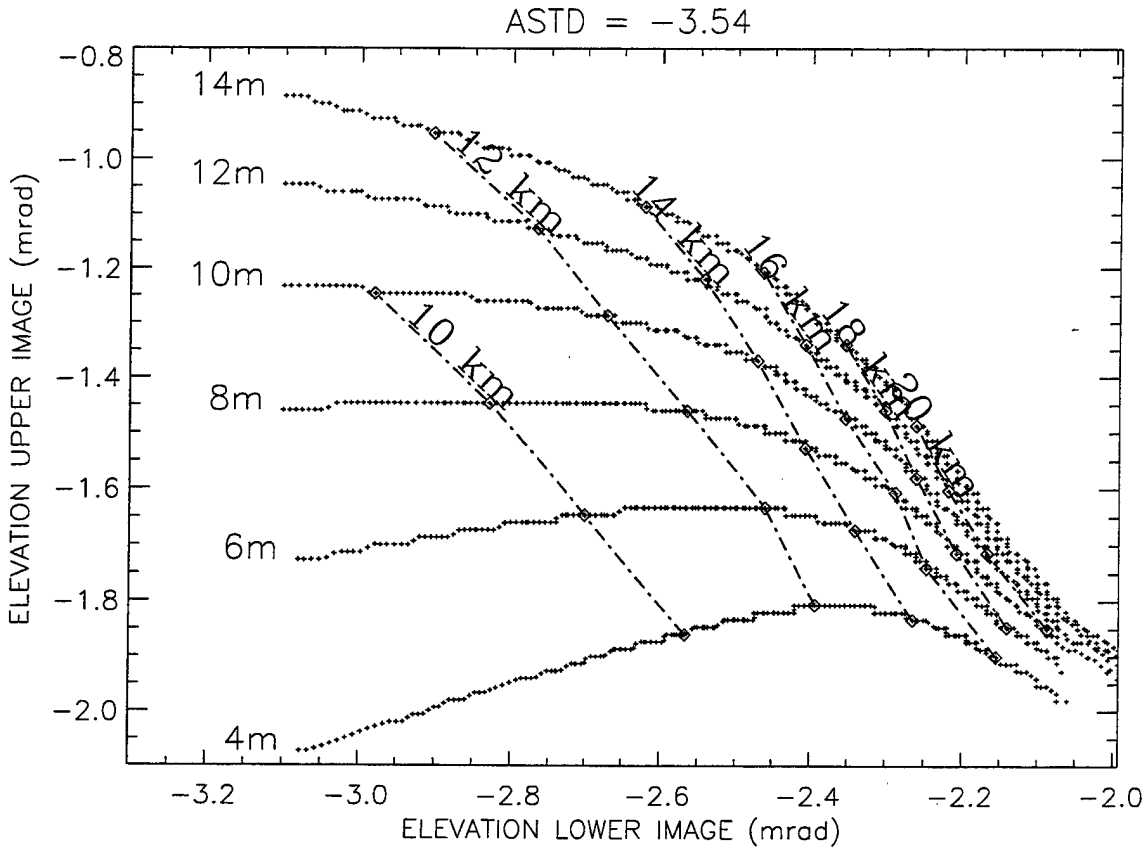

Figure 4: Elevation of lower image vs elevation of upper image for each of the isomets of height 4–14 m.

6 Objective: Assess Range-Finding Capabilities

The central result from this paper is fig. 4. When two images are detected by a sensor, the elevations of the lower and upper images can be plotted as a point in fig. 4, and the height and range of that point can be read from the inner coordinate system. To say it differently, the figure contains the transformation which takes two elevation measurements as input, and generates as output both height and range of the source or target. In terms of coordinate systems, the rectilinear lower elevation vs upper elevation coordinate system is transformed to the distorted, curvilinear height vs range coordinate system.

To summarize: when subrefractive atmospheric conditions occur, it is possible to utilize the two images of an object to determine range and height of that object. This is done by means of a transformation from angular elevation measurements to target range and target height data.

As can be seen in fig. 3, for a given range value, each isomet defines either $0, 1$, or 2 corresponding elevation values. Consider the subset of range values which correspond to 2 elevation values. Within this subset, a particular range value maps to a lower elevation

value and a distinct upper elevation value. The entire subset generates upper elevation as a function of lower elevation.

The graph of upper elevation vs lower elevation is shown in fig. 4. Each point on the curve corresponds to a range value. In the figure, a coarse set of range values is shown for each isomet. The range values encompass most of the usable range: from 10 to 20 km.

This example indicates the potential for range-finding. For a source between 10 km and 20 km, the sensor will detect two images. The elevation of each is found, and the transformation portrayed in fig. 4 provides the corresponding range and height of the source.

Note that the range limits for effective range-finding are determined by the intensity of the sub-refractive conditions. As the air-sea temperature difference becomes more negative, the refractive potential for two images moves closer to the sensor, reducing the lower bound on the ranging domain. In contrast, height limitations are primarily determined by the field of view and look-angle of the sensor.

It is clear that work must be done to make the demonstration contained here rigorous. It is necessary to define the limits of applicability for the method. It is necessary to establish a mathematical foundation for assumptions I have made concerning the behavior of surfaces and the intersections between them. Furthermore, the method utilizes an implicit assumption of homogeneity: the full propagation range is characterized by one vertical profile. This appears to be a reasonable assumption for the sub-refractive case, but this also must be carefully examined.

7 Acknowledgments

I thank the Office of Naval Research and Dr. William Stachnik for support of this work. Mr. J. W. Trahan is responsible for the initial concept and studies of range-finding in sub-refractive conditions. Mr. H. Rivera designed and assembled the IRP test facility to collect high-quality data. Both Mr. Trahan and Mr. Rivera collected the data examined within this paper.

References

[1] S. Hammel and N. Platt, *Topological description of mirage effects*, Proceedings of the Vision Geometry conference, SPIE **2573**, 398-406, (1995).

[2] N. Platt, S. Hammel, J. Trahan, H. Rivera, *Mirages in the marine boundary layer – comparison of experiment with model*, Proc. IRIS Passive Sensors, Monterey, CA, vol. 2, 195-210 (1996).

[3] Lehn, W., *Appl. Math. Model.* **9**, 447, (1985).

[4] Hill, R., Clifford, S., and Lawrence, R., *J. Opt. Soc. Am.* **70**, 1192 (1980).

[5] Davidson, K., Schacher, G., Fairall, C., and Goroch, A., *Applied Optics* **20,** 2919 (1981).

[6] Trahan, J., and Rivera, H. "Mid-wave infrared low elevation propagation experiment on the Potomac River, Summer 1995", Technical Report NSWCDD/TR-96/23 (Sept. 1996).

Mesoscale Simulation of Electromagnetic Refractivity in Surface and Elevated Ducts during the VOCAR Experiment

Robert T. Williams[1], Nelson L. Seaman*, David R. Stauffer and John C. Wyngaard

Department of Meteorology
The Pennsylvania State University
University Park, PA 16802

[1]Current affiliation: USAF, Offutt AFB, NB 68113-4039

Abstract

Refraction of propagating electromagnetic (EM) waves in the atmosphere is an important source of signal degradation that causes severe problems for marine communications. In the present study, the Penn State/NCAR mesoscale model, MM5, was run with resolutions ranging from 108 km to 12 km to simulate conditions for the week of August 24-31, 1993. The goals were to identify key physical processes responsible for modulation of summertime ducting conditions off the CA coast and to evaluate the ability of a model to reproduce the marine atmospheric boundary layer (MABL) and the inversion-layer structures associated with wave ducting. Special data confirm that the MM5 simulates the synoptic and mesoscale variability in the MABL depth and the trapping-layer intensity in a continuous seven-day simulation. Over time scales of several days, MABL characteristics are shown to be a function primarily of the intensity of synoptic-scale subsidence in the East Pacific Ridge and surface fluxes from the ocean surface. At the mesoscale, diurnal variations in the vertical velocity field due to the mesoscale coastal sea-breeze are found to have a significant impact on the MABL depth at San Nicolas Island (about 120 km offshore). Mid-tropospheric moisture flowing outward from Tropical Storm Hilary produced a complex vertical moisture structure in the California Bight that contributed to a strong surface-based ducting layer on August 26-27. Finally, MM5 developed gravity waves in the MABL as the regional flow encountered the coastal mountains of southern CA.

1. Introduction

Refraction of microwave and radar transmissions can affect marine communications and coastal defense systems by bending these waves away from a straight-line path. Atmospheric EM refractivity is primarily a function of the vertical structure of temperature and water vapor. For a standard lapse rate, horizontally emitted EM waves are bent upwards away from the earth's surface. However, in very stably stratified conditions, a *trapping layer* is formed, in which horizontally emitted EM waves are bent downward. If the base of the trapping layer is above the surface, so that waves below the layer can propagate upward, then the waves alternate between upward and downward propagation inside a wave *duct*.

To simplify interpretation of the refractivity, a "modified refractivity", M, can be defined such that the effect of the earth's curvature is removed (Burk and Thompson 1997). That is, M = 1 describes the refractivity condition for which a horizontally emitted wave bends downward just enough to remain at the same altitude above a spherically curved earth. When M increases (decreases) with height, EM

*Corresponding author address: Nelson L. Seaman, Pennsylvania State Univ., Dept. of Meteorology, 503 Walker Bldg., University Park, PA 16802; email: seaman@psumeteo.psu.edu

waves are bent upward (downward) relative to the earth. Figure 1 shows the relationship between the temperature and moisture profiles of the MABL and the M-structure for a typical case at San Nicolas Is. (120 km southwest of Los Angeles). The figure shows that an *elevated duct* exists (i.e., base of the duct is above the surface) from 60 to 460 m. The trapping layer is the upper part of the duct (400 to 460 m), where $dM/dz < 0$. If the base of the duct is at the ground (ocean), so that there exists a level h where M(h) is less than all M(z) below h, then a *surface-based duct* is said to exist.

Ducting conditions are found in many marine environments where large oceanic anti-cyclones produce dry mid-tropospheric conditions through subsidence, while surface fluxes generate moist, thermally neutral or slightly unstable marine boundary layers. Neiberger et al. (1961) analyzed soundings over the eastern North Pacific Ocean and developed a summertime climatology of the MABL structure. Their climatology showed that MABL depth is fairly well correlated with sea-surface temperature (TSS). Near the CA coast, upwelling of deep ocean water causes cold TSSs and the MABL becomes quite shallow, (only 400 - 600 m). It is the strong climatological signal of these summertime features that make ducting conditions frequent, although not continual, over coastal regions of western North America and western coasts of other land masses at similar latitudes.

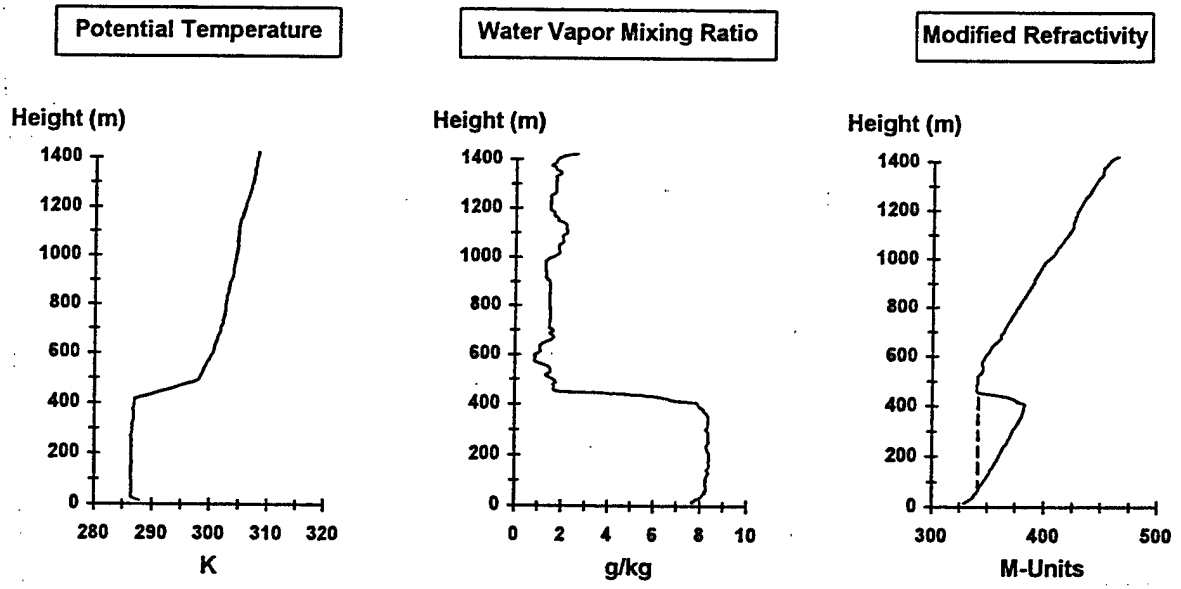

Figure 1. Sounding at San Nicolas Is. for 1200 UTC, 24 August 1993. The elevated duct on the M-profile is shown to the right of the dashed line.

Traditionally, estimations of refractivity conditions have been made using intermittent radiosondes or dropsondes, which are then assumed to represent horizontally homogenous and steady-state propagation conditions over the range of transmission. This approach has met with only limited success. Consequently, it is appropriate to consider data-assimilating mesoscale models would be the best approach to describe and forecast refractive conditions. However, accurate numerical prediction of ducting layers is a challenging problem because of sparse observations for model initialization and inadequate representation of the physical processes in and above the MABL. In addition limited computational resources have made it difficult, until recently, to apply 3-D models with sufficient vertical and horizontal resolution to represent the strong stratification found in the data.

Burk and Thompson (1997) applied the Navy Operational Regional Atmospheric Prediction System

(NORAPS) at 20-km resolution and with 30 layers to simulate M-field evolution during the Variability of Coastal Atmospheric Refractivity (VOCAR) experiment. In this notable recent study, a sequence of 12 - 24 h simulations was composited to cover the period from 24 August - 3 September 1993. They found that NORAPS performed well for representing the dominant trends in the trapping-layer height. However, fairly short model simulations such as these often retain many details from their initial states. If the physical processes most important for modulating the height of the MABL inversion (i.e., the trapping layer) act on time scales of several days, then this approach cannot correctly reveal the role of those processes or determine if the model physics and dynamics represent them accurately. Furthermore, Burk and Thompson focused primarily on describing the model's MABL structure and some diurnal cycles found in that structure. Their study was far less concerned with identifying the processes that determine its evolution.

In the present study, the Penn State/NCAR mesoscale model MM5 was run for the week of 24 - 31 August 1993 during VOCAR. The *objectives* were (1) to evaluate model physics and physics necessary for improved mesoscale predictions of the MABL and the inversion layer, which define the trapping and ducting layers, and (2) to identify the importance of synoptic-scale and mesoscale processes which can contribute to the evolution of the MABL and ducting characteristics. This work is a preliminary step in the development of multi-scale model predictions covering the full range of scales controlling refractivity and EM propagation, from the mesoscale to the turbulence scales.

2. Model Description

The MM5 is a non-hydrostatic mesoscale model with a terrain-following sigma vertical coordinate (non-dimensionalized pressure). A full description of the model equations and numerics is given by Grell et al. (1994). In this study three nested grids were used. A continental-scale 108-km grid covered most of North America and the eastern North Pacific Ocean to about 160 W. Nested within the outer grid, a 36-km mesoalpha-scale grid covered the western U.S. and Baja CA, while a 12-km mesobeta-scale grid covered a region of 936 X 864 km (79 X 73 points) centered on the CA Bight. All domains had 53 layers (lowest calculation level at 20 m). The vertical resolution was 40 m from the surface to 600 m AGL, with 24 layers below 1500 m. The top of the model was at 100 mb. The MM5 was configured for this case with explicit cloud and precipitation microphysics and a column radiation scheme (Dudhia 1989), which helps to maintain the inversion by longwave cooling from the top of stratus clouds in the upper part of the MABL. A Blackadar boundary layer scheme is used to represent surface fluxes and turbulence processes (Grell et al. 1994).

3. Experiment Design

Initial and lateral boundary conditions were derived at 12-h intervals from the National Centers for Atmospheric Prediction's (NCEP) spectral analyses. Analyses for temperature, wind and mixing ratio also were blended into MM5's solutions on the 108-km and 36-km domains throughout the study period using four-dimensional data assimilation (FDDA). No data assimilation, however, was performed on the 12-km domain. Limiting the FDDA to the two outer domains provided the inner domain with accurate boundary conditions, while allowing the model's physical processes to develop the 12-km solutions without artificial forcing. Finally, a 12-h dynamic initialization, based on the Marine Boundary Layer Initialization (MBLI) of Leidner and Stauffer (1996), was used to impose a realistic MABL structure early in the study period. The MBLI assimilates the climatology of Neiberger et al. (1961) for the summertime MABL and inversion structure from CA to Hawaii. The dynamic

initialization ceases after 12 h, at 0000 UTC, 25 August.

4. Case Description

The VOCAR study was conducted during summer of 1993 in the CA Bight to investigate conditions responsible for the variability of atmospheric refractivity commonly observed in marine environments, especially in coastal regions. The period from 1200 UTC, August 24, to 1200 UTC, August 31, was chosen for simulation because it exhibited short and long term variations in refractivity that may be related to mesoscale and synoptic-scale variability.

A moderate 500-mb ridge was quasi-stationary over the eastern Pacific during the period (not shown). Meanwhile, surface analyses showed that the semi-permanent East Pacific Ridge dominated the region, with mostly northwesterly flow along the CA coast. Analyzed 500-mb heights in the VOCAR area rose by 34 m from 25 to 27 August, before falling about 50 m by 30 August. Heights slowly began to recover on 31 August. This implies that subsidence in the East Pacific Ridge may have strengthened early in the period as the upper ridge intensified, but weakened later on. Near the middle of the same week, the near-climatological conditions in the coastal regions of southern CA and the Baja peninsula were disrupted by the remnants of Tropical Storm Hilary. This storm traveled northward from the tip of Baja on 24 August to the mouth of the Colorado River on 27 August (Figure 2). Although Hilary weakened steadily as it progressed northward, the mid-level outflow ahead of it caused the 850-mb wind to become southeasterly over the CA Bight on 25-27 August, while the surface winds remained mostly northwesterly.

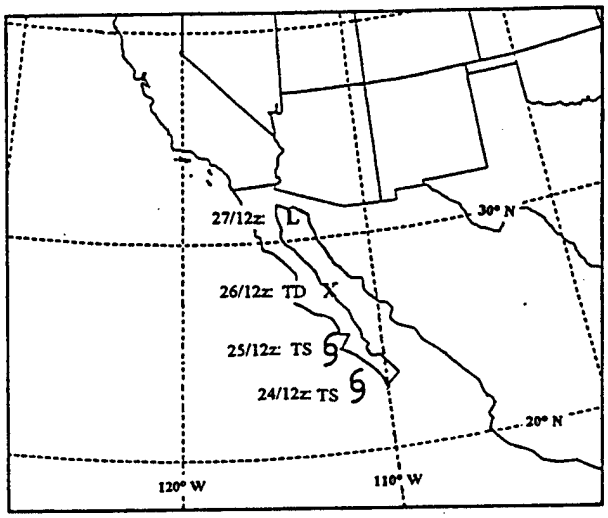

Figure 2. Storm track for Tropical Storm Hilary, 24 - 27 August 1993.

5. Results

5.1 Synoptic-Scale Influences

Evaluation of the 7-day MM5 simulation focused on the 12-km fields, comparing results to VOCAR observations. First, the relationship between synoptic-scale forcing and the MABL depth was investigated. The dominant synoptic influences controlling the marine mixed layer and the height of the capping inversion are hypothesized to be the surface heat flux, which tends to raise the inversion, and synoptic-scale subsidence, which lowers it. The SSTs, however, evolve very slowly and therefore are unlikely to control changes in the regional mean MABL depth on time scales as short as several days. Thus, attention was focused on the evolution of the subsidence associated with the East Pacific Ridge.

Examination of the modified refractivity structure (M) observed at San Nicolas Is., based on frequent radiosonde measurements, shows that the inversion height (trapping layer) fell steadily from 25 to 27 August (Figure 3). This coincides well with the period when both observed and simulated 500-mb heights off CA were rising rapidly (Figure 4). Later, the inversion heights rose from 27 to 30

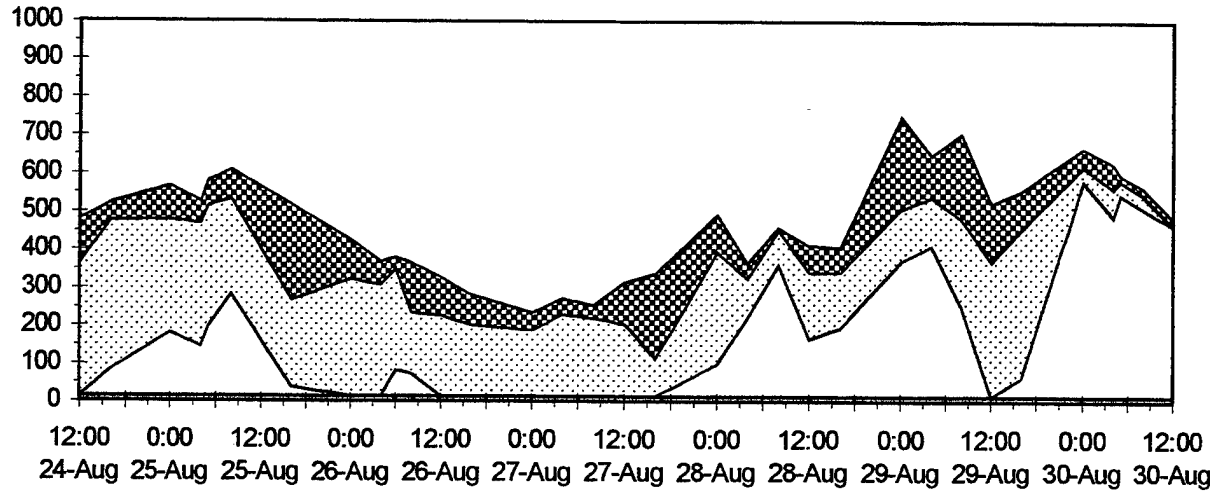

Figure 3. Evolution of the observed refractive structure at San Nicolas Is. for 25-31 August 1993. Ordinate is in m MSL. Solid line indicates top of the trapping layer (inversion top), while the dotted line is the bottom of the trapping layer (inversion base). The dashed line denotes the base of the ducting layer, revealing a surface duct on 26-27 August.

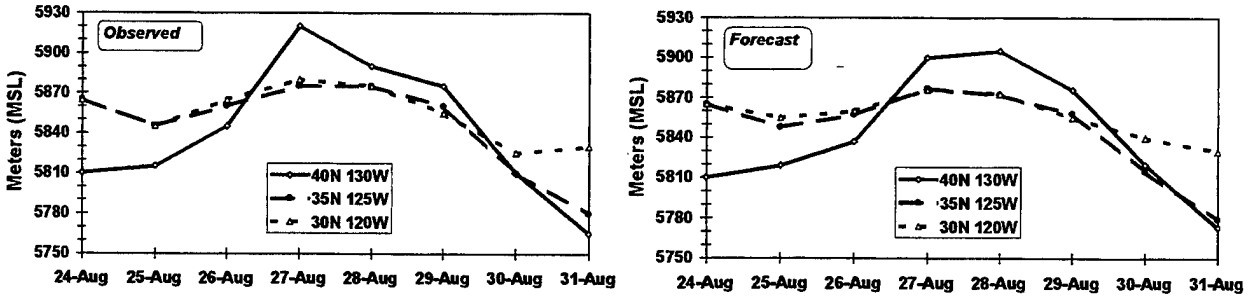

Figure 4. Evolution of the observed and MM5-simulated 500-mb heights (m) for three points off the coast of CA during the VOCAR period of 24-31 August 1993.

August before reversing slightly on 31 August (Figure 3). Again, this pattern matches exactly that of falling 500-mb heights in Figure 4. Next, Figure 5 shows the profiles of the MM5-simulated vertical velocity from the surface to 6 km MSL for three days near the middle of the study period. The figure reveals deep subsidence in the ridge throughout the period, with maximum sinking on 27 August, when the 500-mb ridge approached maximum strength. The MM5-simulated M structure at San Nicolas Is. for the same period is shown in Figure 6. The pattern is remarkably similar to the observed pattern for the first four days (compare to Figure 3), although the trapping layer and duct lift from the surface a bit too slowly during the last three days. Notice that the simulated sinking motion is almost as strong on the 28th as on the 27th (Figure 5). This may explain why the trapping layer in the model failed to rise as rapidly as observed (Figs. 3 and 6). Finally, comparison of displacement rates for the observed and model-simulated inversion base indicated very close agreement with the vertical velocity at the height of the inversion. Thus, the observational and model-derived evidence confirm that subsidence in the East Pacific Ridge is the primary synoptic-scale influence controlling the inversion height during this episode. Also, the model-simulated M-structure and vertical velocity profiles further indicate that, given adequate vertical resolution and physics for radiation and surface fluxes, a model can simulate the multi-day trend in the evolution of the trapping layer, including the synoptic-scale processes associated with ridging.

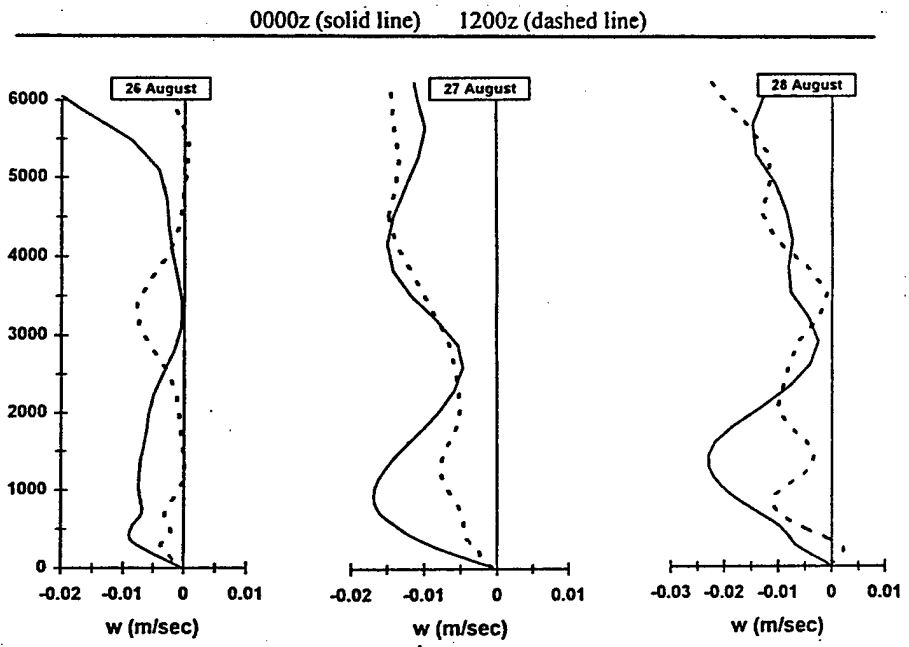

Figure 5. MM5-simulated vertical velocity (m s^{-1}) versus height (m) averaged over a 120 X 120 km area centered on San Nicolas Is. during August 1993. Solid lines at 0000 UTC, dashed lines at 1200 UTC.

5.2 Mesoscale Influences

Figure 5 also gives insight into mesoscale influence on the refractivity structure. Clearly, the sinking motion near 1 km MSL is considerably stronger in afternoons (0000 UTC) than in the mornings (1200 UTC). Examination of the model's coastal circulations indicated that this pattern is due to enhanced late-afternoon sinking induced by the return branch of the mesoscale sea breeze and mountain-valley wind in the LA Basin and other nearby areas of Southern CA. The onshore surface winds associated

with these circulations also have their maximum about 0000 UTC. Careful examination of the M-

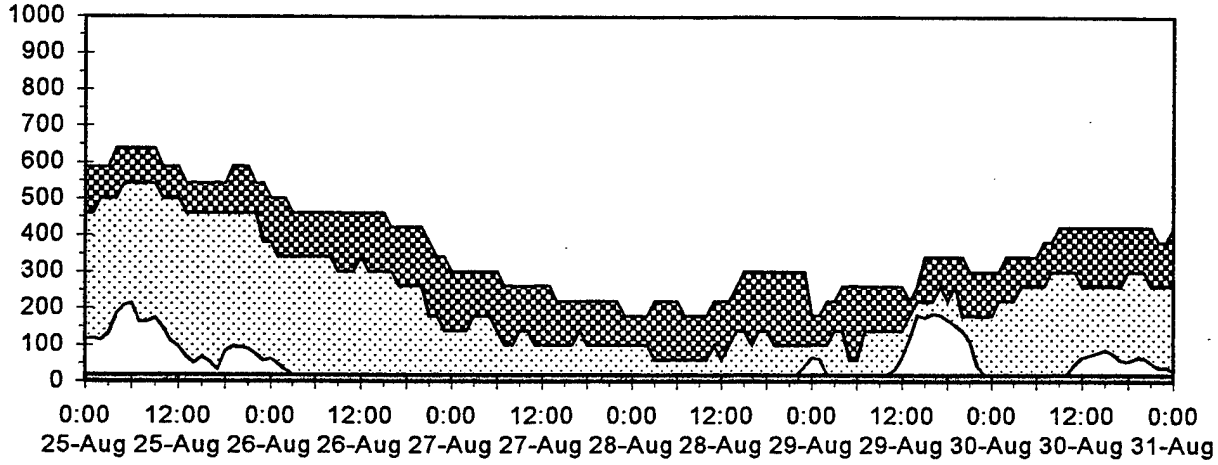

Figure 6. Same as Figure 4, except that the MM5 12-km simulated refractive structure (M) is shown.

structure in Figure 6 shows that the inversion top often tends to be suppressed by about 50 m at 0000 UTC, compared to 3 h earlier and later. Thus, the mesoscale circulations of the CA Bight can have a strong impact on ducting and refractivity over the coastal region at least to 120 km offshore.

A more unusual mesoscale feature in this case is related to the passage of Tropical Storm Hilary nearby (Figure 2). Early in the period (24 - 25 August), radiosondes revealed that the troposphere above the MABL was very dry (not shown). This is normal for the Bight in summer when strong ridging and deep subsidence persist for long periods. The approach of Hilary, however, brought a mid-level moist outflow over the CA Bight on 26 - 27 August. Beginning on 26 August, this moist layer was observed between 850 mb and 675 mb (not shown). Since the moist MABL was only 350 m deep (below 975 mb) at that time, a dry layer (minimum mixing ratio of 2 g kg^{-1}) became isolated between

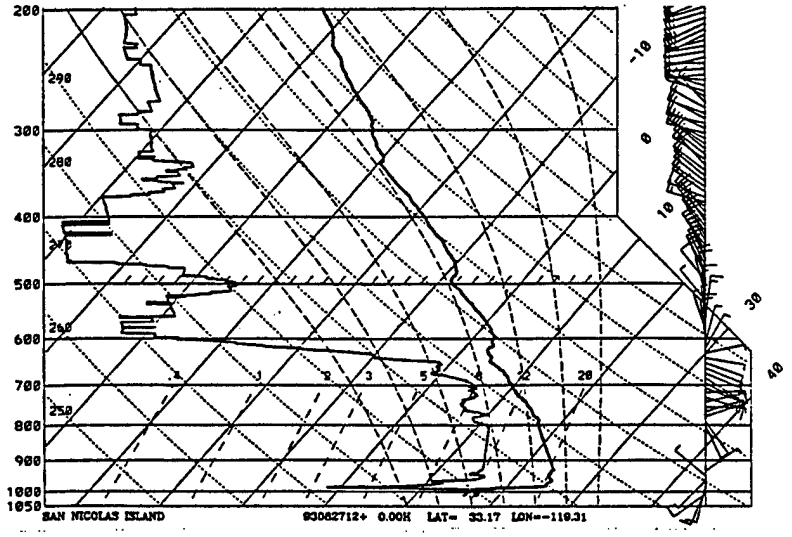

Figure 7. Observed sounding (Skew-T, log-p) at San Nicolas Is. at 1200 UTC, 27 August 1993.

850 mb and 975 mb. As Hilary continued to pump moisture northwest, both the synoptic-scale and

mesoscale subsidence acted on the column. Thus, the moist air slowly was advected downward, squeezing the isolated dry layer until it became extremely thin by 1200 UTC, 27 August (Figure 7).

The 12-km MM5 captured these processes in progress 24 h earlier on 26 August. Figure 8 shows mixing ratio in a north-south cross section along 119.6 W from Santa Barbara southward through San Nicolas Is. to 30 N. The moist outflow from Hilary dominates from about 700 mb down to 890 mb, except at the northern extreme near the Santa Inez Mts. Maximum mixing ratios aloft are about 10 g kg^{-1}. The extreme moisture gradient at the top of the MABL is evident near 970 mb, with moist air below (10-12 g kg^{-1}). Notice that the dry air from 890 mb to 960 mb is being trapped in between, with a minimum mixing ratio of 2.5 g kg^{-1}. This is consistent with the observed San Nicolas sounding at the same time, while vertical velocity was downward practically everywhere in the cross section (not shown).

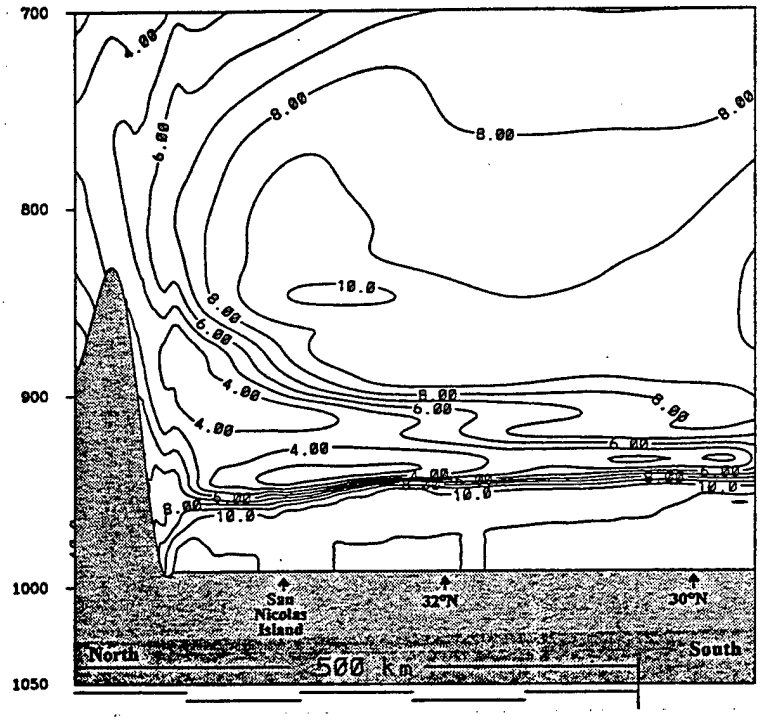

Figure 8. MM5 12-km simulation of mixing ratio in a north-south vertical cross section through San Nicolas Is. at 1200 UTC, 26 August 1993.

As moist advection from Hilary and the synoptic-scale subsidence continued, the model-predicted sounding at 1200 UTC, 27 August, also developed an isolated, very thin dry layer (Figure 9), which matches the observed sounding remarkably well (compare to Figure 7).

The impact of mesoscale influences from the tropical storm on the modified refractivity structure in the CA Bight is revealed in Figure 10, which compares observed and simulated M profiles at San Nicolas Is. on three successive mornings. The model has clearly done very well in reproducing the height and strength of the trapping layer (where $dM/dz < 0$). It has also done very well in simulating the mean slopes above and below the trapping layer, although it cannot be expected to capture some of the finer scale features. Thus, the combination of model physics, multi-scale dynamics and fine resolution has proved mostly successful in simulating the evolution of the M-profile structure due to

mesoscale processes.

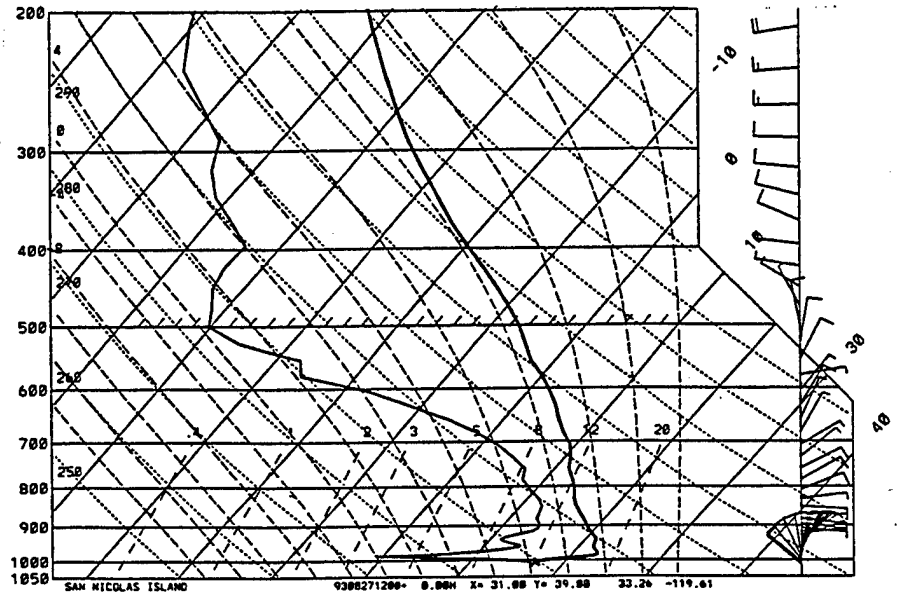

Figure 9. MM5-simulated sounding (Skew-T, log-p) at San Nicolas Is. at 1200 UTC, 27 August 1993.

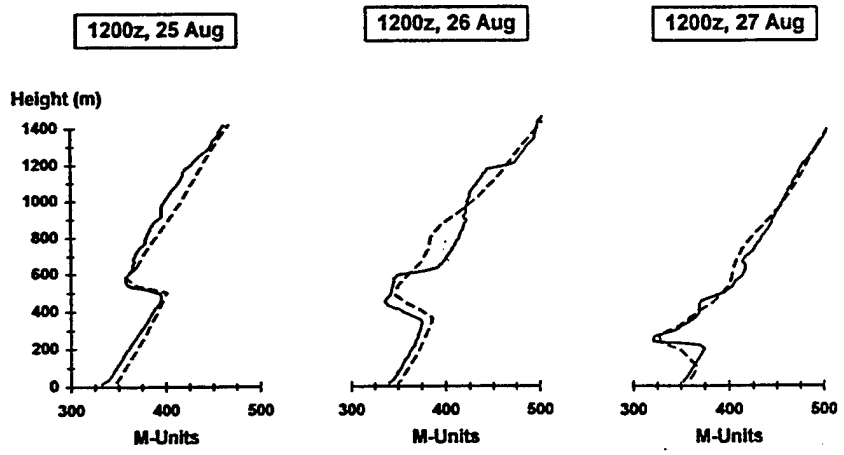

Figure 10. Observed (solid) and MM5 12-km simulated (dashed) M-profiles at San Nicolas Is. for 1200 UTC, 26 - 28 August 1993.

Finally, the simulated M-field was examined in vertical cross sections through the CA Bight, before and during the tropical storm's influence in the area (not shown). Series of gravity waves were found in the M field (near or in the trapping layer) and emanating from the vicinity of the coastal mountain ranges. The largest of these waves distorted the trapping layer by about 100 m and in some regions the vertical gradient of refractivity was intensified as the waves passed. These gravity waves had a phase speed of about 15 m s^{-1} and a period of about 3 h. Such distortions of the trapping layer height and strength may change the refractivity and EM wave propagation through this region.

6. **Summary**

The MM5 model was applied with 12-km resolution, 53 layers, modified physics, dynamic initialization and coarse-grid FDDA to simulate a week during the VOCAR study. The model reproduced most aspects of the thermal, moisture and refractivity structure for the period. Synoptic-scale subsidence was found to control the depth of the mixed layer on time scales of a week. Important mesoscale influences included the return branch of the CA sea breeze and mountain valley winds, plus an outflow of moist air from nearby Tropical Storm Hilary. In addition there is evidence of mesoscale gravity waves in the model solutions, which may further modulate the trapping-layer structure on time scales of a few hours.

7. **Acknowledgments**

This research was funded by the Office of Naval Research Grant N00014-92-J-1688 and U.S. Navy Contract N00039-92-C-0100. Computing was conducted at Penn State's Earth System Science Center. Mr. Glenn Hunter of Penn State provided valuable assistance in support of the MM5 modeling experiments and visualization.

8. **References**

Burk, S.D. and W.T. Thompson, 1997: Mesoscale modeling of summertime refractive conditions in the Southern California Bight. *J. Appl. Meteor.*, **36**, 22-31.

Dudhia, J., 1989: Numerical study of convection observed during the winter monsoon experiment using a mesoscale two-dimensional model. *J. Atmos. Sci.*, **46**, 3077-3107.

Grell, G.A., J. Dudhia and D.R. Stauffer, 1994: A description of the fifth-generation Penn State/NCAR mesoscale model (MM5). NCAR Technical Note, NCAR/TN-398+STR, 122 pp.

Leidner, S.M. and D.R. Stauffer, 1996: Improving California coastal-zone forecasting by initialization of the marine boundary layer. 11th Conf. on Num. Wea. Pred., Norfolk, VA, 19-23 Aug., 177-179.

Neiburger, M., D. Johnson and C. Chien, 1961: Studies of the structure of the atmosphere over the eastern Pacific Ocean in summer: I Inversion over the eastern North Pacific Ocean. U. Calif. Publ. Meteor., **1**, No. 1, 94 pp.

Estimation of the E-2 Overland Height Finding Capabilities

L. M. Zurk
MIT Lincoln Laboratory
244 Wood St.
Lexington, MA 01720
zurk@ll.mit.edu

1. Introduction

Many surveillance platforms, such the Navy's E-2, have radars with insufficient elevation beamwidths to determine target height. One technique to provide this information is to infer target height from the characteristics of multipath propagation such as the time difference of arrival (TDOA) between the direct and ground bounce paths. The E-2 uses the observed TDOA to estimate target heights over the water where the reflecting surface is fairly smooth. However, it is uncertain whether this technique is applicable over land where the surface is more variable. To extend this technique to an overland situation, two criteria have to be satisfied: 1) a detectable ground bounce must be observable and 2) an algorithm must be present to invert the TDOA into a height estimate.

To investigate the first criteria, MIT Lincoln Laboratory engaged on an airborne data collection campaign in fall, 1996. The mission involved two airborne platforms equipped with VHF and UHF antennas that transmitted and received a 3 MHz pulsed-CW signal. The complex propagation data was collected over a variety of terrains to statistically address the relationship between the terrain type and the multipath characteristics. The data showed that a detectable ground reflection was observed for a wide variety of terrain types and that the characteristics of this reflection are directly related to the properties of the terrain. Details of the data collection and comparison of the results with wideband propagation simulations can be found in [1,2].

In this paper we will address the second criteria - how to utilize time domain data from overland multipath to yield an accurate height estimate. We consider two methods. The first method is to combine the observed TDOA with the spherical earth formula to produce a height estimate. The second method is to apply a Matched Field Processing (MFP) algorithm. This paper shows results of both algorithms applied to the VHF and UHF propagation data. The results show that acceptable height estimates can be produced from both techniques, with a more accurate estimate resulting from the MFP algorithm. For terrain that is not overly rough (RMS terrain slope < 0.05) target height estimates with errors on the order of 1000 ft can be achieved. The error for both methods increase for more severe terrain.

2. Multipath Characteristics from Data

The introduction briefly described a propagation experiment which provided direct observation of the multipath environment for a variety of terrain types. The flights were designed so that the 3 MHz-pulsed CW pulse arriving via a direct path and that reflected from the ground are separated in time. An example of the VHF data from White Sands Missile Range (WSMR) is shown in Figure 1. The three plots show the time domain signature for three different receiver altitudes with the direct pulse arriving at t=0. The terrain at the reflection point grows successively rougher as the receiving platform drops in altitude from the top to the bottom plot. As the figure shows, the multipath response changes in strength and in the time delay relative to the direct in response to the changing terrain. Further details of the data collection and a comparison with propagation simulations can be found in [1,2].

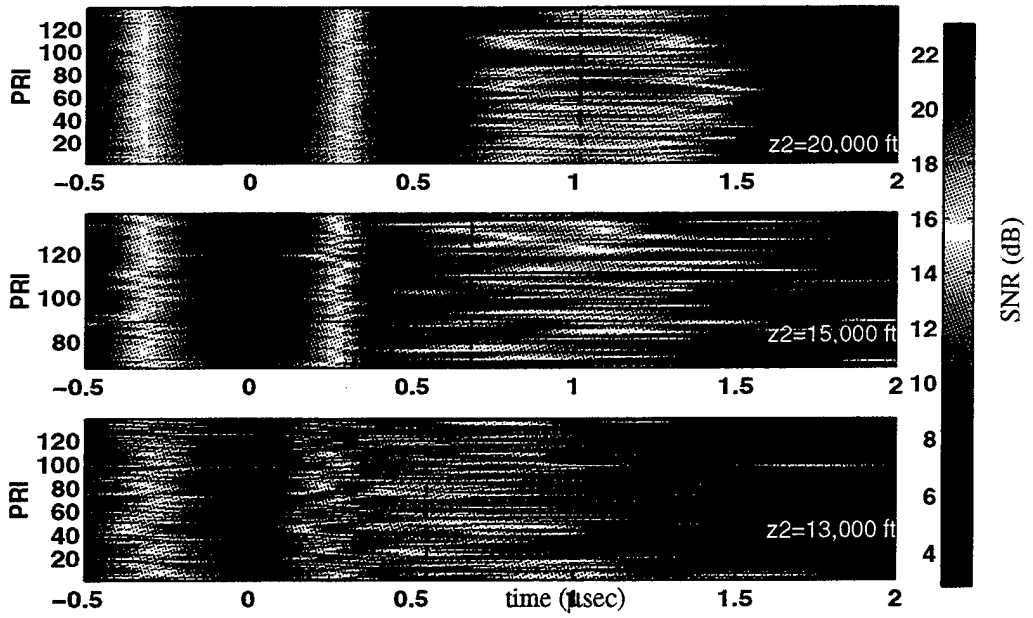

Figure 1. VHF H-pol data from a flight on 9/22/97 at White Sands Missile Range, NM. Each plot is one data group consisting of 138 pulses obtained at a 2 Hz PRF rate. The transmitter was at 20,000 ft at a range of 130 km from the receiver. In the last two plots the reflection point was over rough terrain producing a reflection that was lower in power and more variable in TDOA. The dashed lines show the spherical earth prediction

The propagation experiment provided information on how the strength of the multipath response varies with terrain type. Multipath height finding is only feasible for the situations where this response is strong enough to be detected and used. Figure 2 shows the average power level of the ground bounce term relative to the direct path signal for two-way propagation. (A monostatic radar will experience a 6 dB enhancement for the ground bounce term due to the existence of two coherent reflected ray paths). As expected, the strength of the response decreases with increasing terrain roughness since the roughness serves to diminish the coherent specular return.

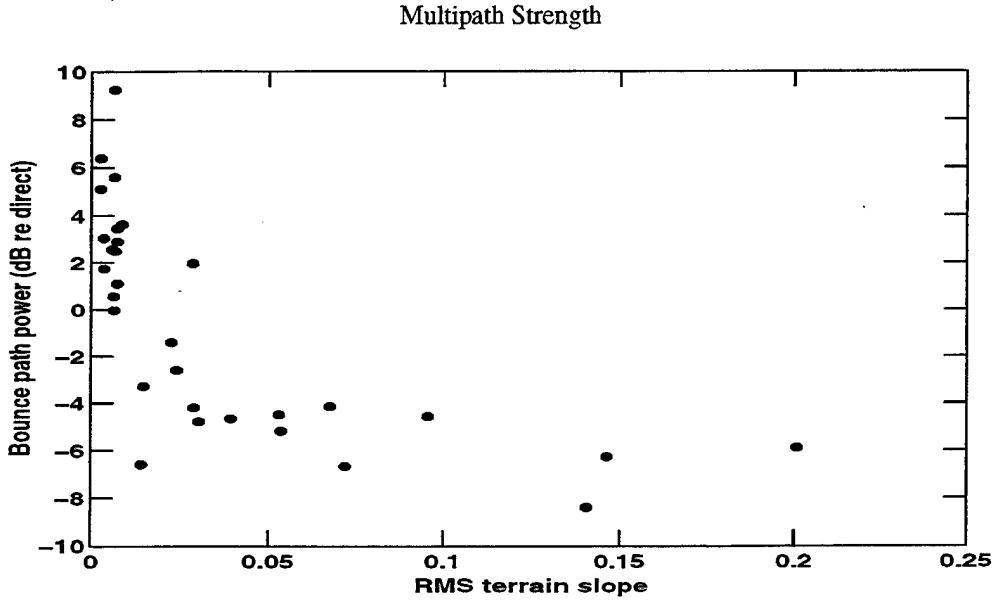

Figure 2. Power of the ground reflected pulse in dB relative to the direct pulse. Values are from experimental observation extended to a two-way propagation scenario.

3. TDOA Height Estimates

In this section we briefly describe the process used to obtain a height estimate from the TDOA observed in the data with the spherical earth formula. The spherical earth formula can be used to relate the observed TDOA, Δr, to the target height through [3]:

$$z_2' = \frac{\Delta r r}{2 z_1'} \qquad (1)$$

The error in the above estimate due to uncertainties in target range and platform height can be computed. For overland height finding, the dominant source of error can be due to the variation of land cover from the spherical earth model. It should be possible to compute the error from variations in the terrain if the statistical nature of the ground cover is known. This is a topic of future research.

When processing the propagation data, the presence of a ground reflected pulse and the determination of Δr was determined by a correlation analysis. A Gaussian pulse representing the transmitted pulse was shifted by a time delay of t_s and correlated with the time domain response in each PRI of the measured data. A pulse at some delay t_s was considered to be present if it was at least 3 dB above the noise floor and had a SNR that was no lower than 13 dB below the direct pulse. If multiple ground reflections were detected in any one PRI, only the characteristics of the earliest arrival were considered for a height estimate. Once a value of Δr was determined for a PRI the target height was computed using equation 1.

4. MFP Height Estimates

For complicated propagation scenarios - such as over terrain - a technique which has proved useful for source localization is Matched Field Processing (MFP). The rationale of MFP is to use a sophisticated forward propagation model to propagate energy from a source at a hypothetical location to the receiver. This process is repeated for sources at all possible locations and then the resulting "replica" fields are compared or "matched" to those actually observed at the receiver to determine the most likely source location. The power of the MFP algorithm is that instead of ignoring the complicated environment, it exploits our knowledge of the physics of the propagation and it brings it to bear on the localization problem. The MFP algorithm originated in the acoustics community [4] but is recently receiving attention for application to the tropospheric propagation [5,6].

Unlike conventional MFP, in this work we perform the pulse matching in the time domain to exploit the time domain signature of the pulses (i.e., coherent MFP). The process is as follows. For each PRI we generate a family of approximately 100 pulses that are the output of a wideband pulse synthesis model [1,2] using a SEKE propagation model [7] fed with the appropriate terrain elevation data and variable target heights. We then calculate the least square error between each of the replica pulses and the actual pulse. The height corresponding to the replica pulse which minimizes the error is chosen as the target height estimate. In some of the data the multipath response was either too weak or the noise is too strong such that there is no meaningful information. We filter out these pulses by applying a threshold for the minimum error relative to the maximum error. For those pulses which do not have a true minimum no height estimate is made.

5. Height Estimates from Data

The accuracy of the height estimate for both of the methods depends on the terrain type, in particular on the terrain roughness. To illustrate this point we present height estimates obtained for VHF H-pol flights over a smooth, desert terrain and over a rough, mountainous terrain. Each histogram shows the distribution of the height estimates across a single CPI consisting of 138 pulses obtained over a 69 second interval. The 2 Hz PRF rate was designed so that the plane's motion in the 0.5 seconds between pulses resulted in a collection of statistically independent samples of each terrain type.

Figure 3 shows the estimates obtained for the flight where the ground reflection was on smooth, desert terrain. The top histogram shows the height estimates obtained using the observed TDOA was used in conjunction with equation 2. The bottom histogram shows the estimates when a MFP algorithm is used. Both techniques provide estimates that are fairly good and have a mean estimate within 1000 ft of the actual

height (target height of 17.5 kft is indicated with the arrow). In addition, the variance of the estimates is relatively small with 80% of the estimates falling within of the 1000 ft of the mean. The physical significance of this result is that smooth terrain is well approximated by a spherical earth formula and it can be used to produce acceptable height estimates or the more sophisticated MFP algorithm can be used. It is interesting to note that since the specular ray is the shortest path from target to radar, inversion using the spherical earth formula tends to overestimate target height. That is, any deviations that are present in the terrain tend to produce rays that arrive at the receiver later in time than expected and hence produce target heights estimates that are too large.

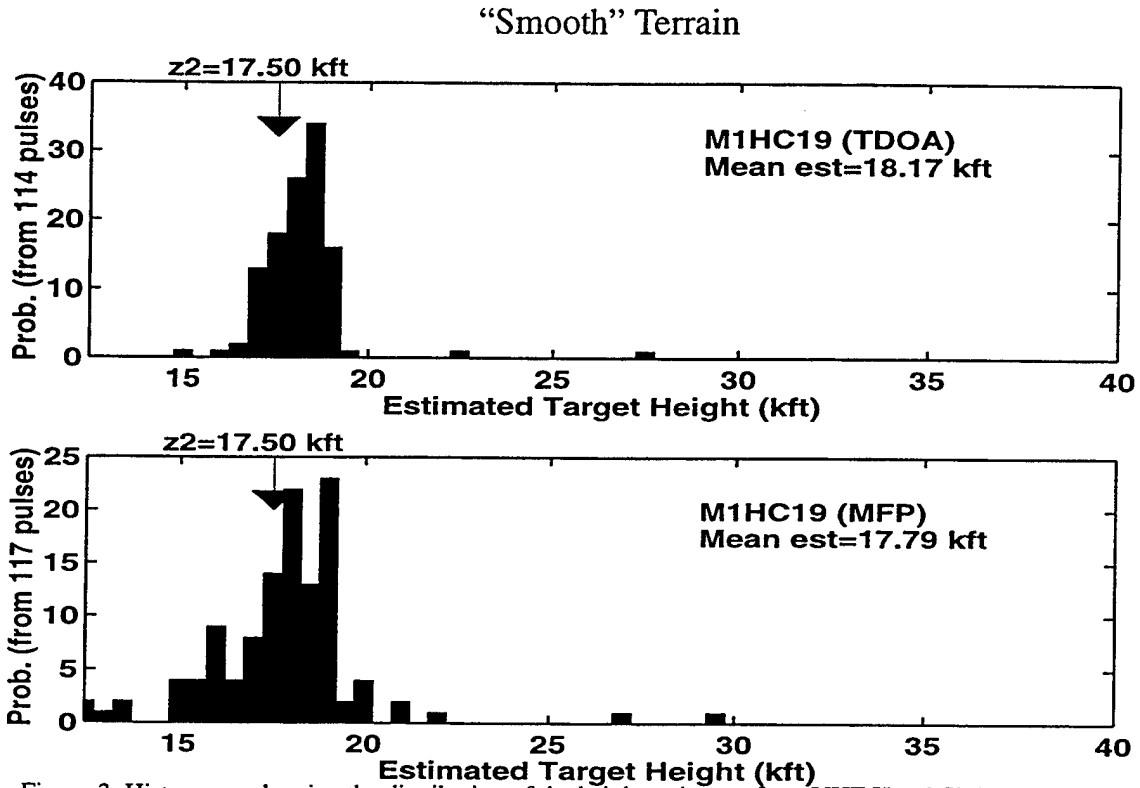

Figure 3. Histograms showing the distribution of the height estimates for a VHF H-pol flight over smooth desert terrain. The top plot is produced using the observed TDOA with a spherical earth formula; the bottom plot is from MFP. The transmitter was at 15 kft in altitude and 100 km from the target.

Figure 4 shows the height estimates for a flight when the reflection point lay on rough, mountainous terrain. In contrast to the smooth terrain case, the histograms show a much greater variance in the height estimates. The top histogram has been produced using the TDOA with the spherical earth formula. The errors in the estimates for this case are due to the inadequacy of the spherical earth model to account for the terrain features. The physical interpretation is that the variation in the earth's surface relative to a smooth spherical earth is incorrectly interpreted as a variation in target height. The mean height estimate for the rough terrain using the MFP algorithm has improved by a factor of 12.5% relative to that from the TDOA estimate but the estimates show greater variation than those for the smooth terrain. The increase in accuracy is due to the fact that the underlying propagation model for the MFP processing is more sophisticated than a spherical earth model and takes into account the variations in the terrain.

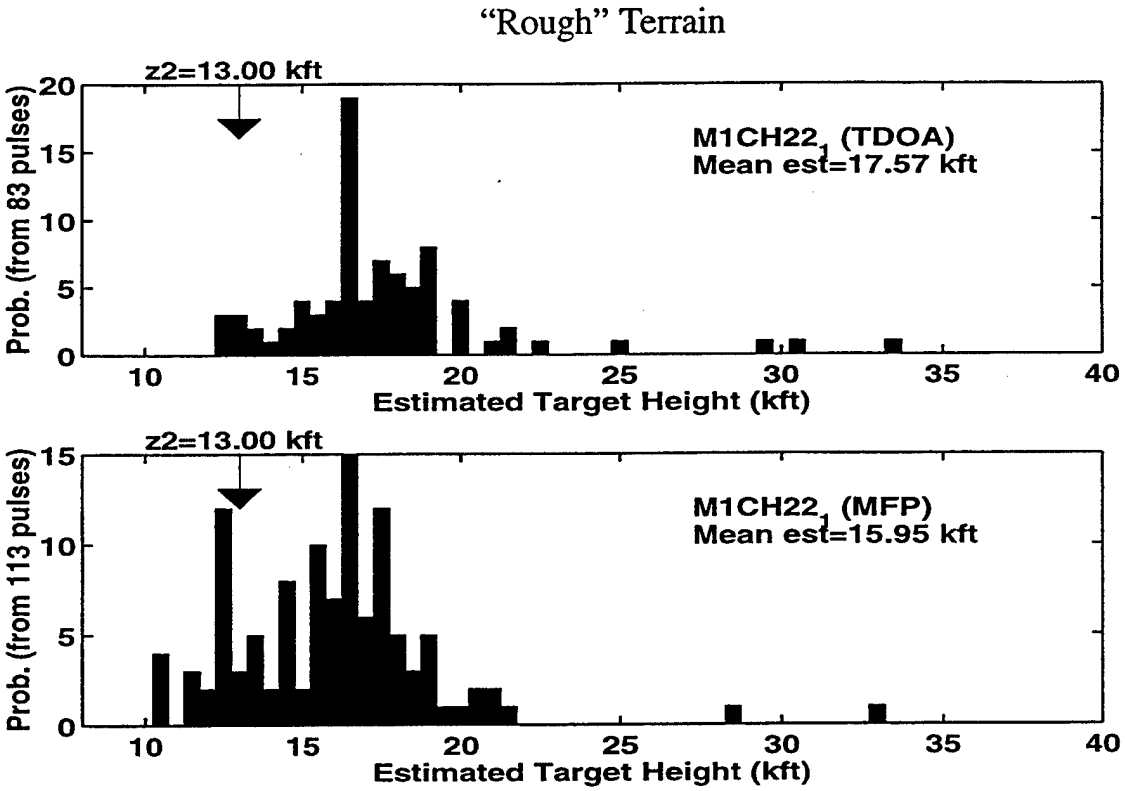

Figure 4. Histograms showing the distribution of the height estimates for a VHF H-pol flight over rough, mountainous terrain. The top plot is produced using the observed TDOA with a spherical earth formula; the bottom plot is from MFP. The transmitter was at 20 kft in altitude and 130 km from the target.

There are limitations to how well the model underlying the MFP algorithm can predict the nature of the multipath. One of these limitations is the approximations inherent in whatever propagation model is utilized (in this case SEKE was used with a wide-band pulse synthesis method [1,2]). A greater source of error is the lack of sufficient information about the propagation environment, notably the terrain features. The DMA data used to characterize the terrain is given on a 96 m grid spacing. The coarseness of this specification relative to a wavelength indicates that the wave will respond to terrain features not available to the propagation model. Examples and further discussion of this effect are given in [2].

The TDOA and MFP processing was repeated for each of the 31 VHF and UHF data groups obtained during the Propagation Experiment. The error in the mean estimates derived from this process are shown in Figure 5 and are plotted as a function of terrain type. As the figure shows, the maximum error in the estimate is less than 6000 ft with estimates for the smoother terrain having errors on the order of a couple thousand feet. In the plot, the results from TDOA processing are shown as open circles and the linear fit shown as a dashed line. The asterisks indicate the results of the MFP processing. It can be seen that the MFP processing performs better than the TDOA estimates. Although this improvement seems to be less for the rougher terrains there are too few data points in this region to make a conclusion.

It is worthwhile to note the computational overhead involved in producing the height estimates in Figure 5. The 31 data points on the plot represent the mean of 138 pulses each. For the TDOA processing this entails calculating the linear relationship in equation 1 a total of 4278 times. For the MFP results, each estimate is based on matching the observation with100 replicas generated from a wideband propagation model. Thus, to produce the data in Figure 5, SEKE was run a total of 427,800 times with geometry specific terrain information. A more sophisticated propagation model would substantially increase the compu-

tational overhead of this process, as would the extension of the search space for multi-parameter estimation

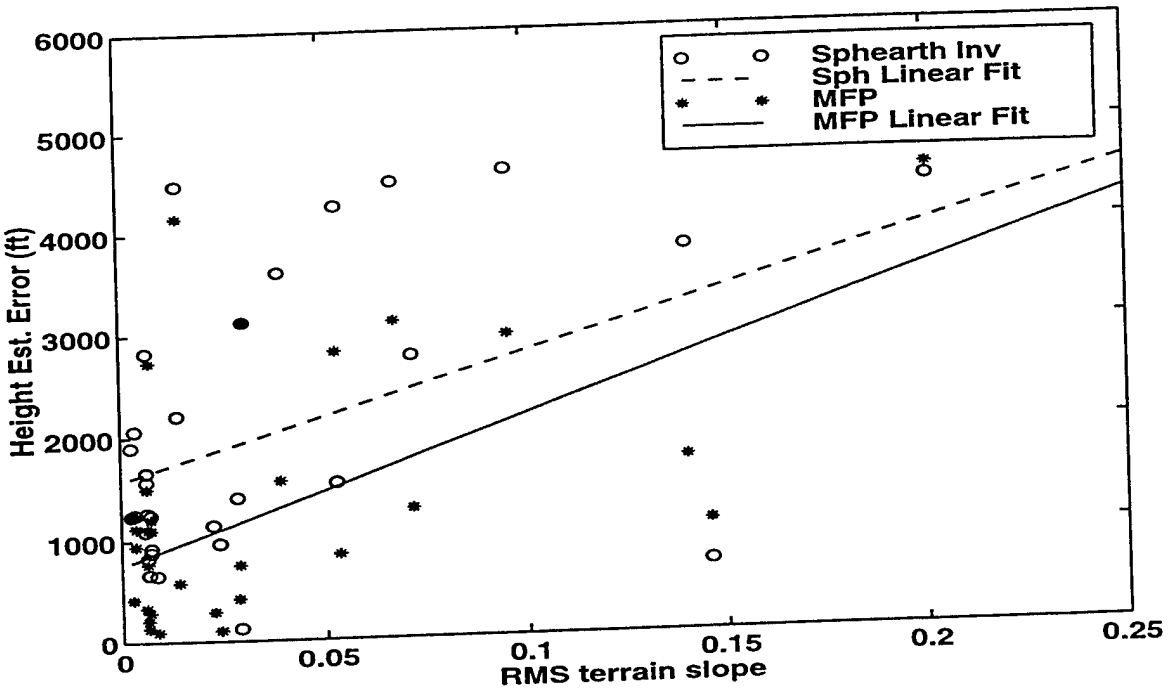

Figure 5. Error in the mean height estimates obtained using VHF and UHF propagation data. Results using observed TDOA with spherical earth are shown as open circles with the linear fit is a dashed line; results from MFP are shown as asterisks with the linear fit as a solid line.

The terrain roughness in Figure 5 is quantified by the dimensionless RMS slope that is measured along the great circle path between the transmitter and receiver and calculated in the region falling in the first Fresnel zone. In order to give an indication of the physical significance of these numbers, Figures 6 and 7 show two regions of the world with color coding corresponding to the RMS terrain slope. Figure 6 shows the Middle East where the terrain is fairly smooth; in this region RMS terrain slopes are approximately 0.025, and from Figure 5 one could expect height finding errors on the order of 1000 ft if a MFP algorithm is used. Figure 7 shows North Korea which quite mountainous. Height estimates obtained from overland height finding in this area of the world would have considerably more error.

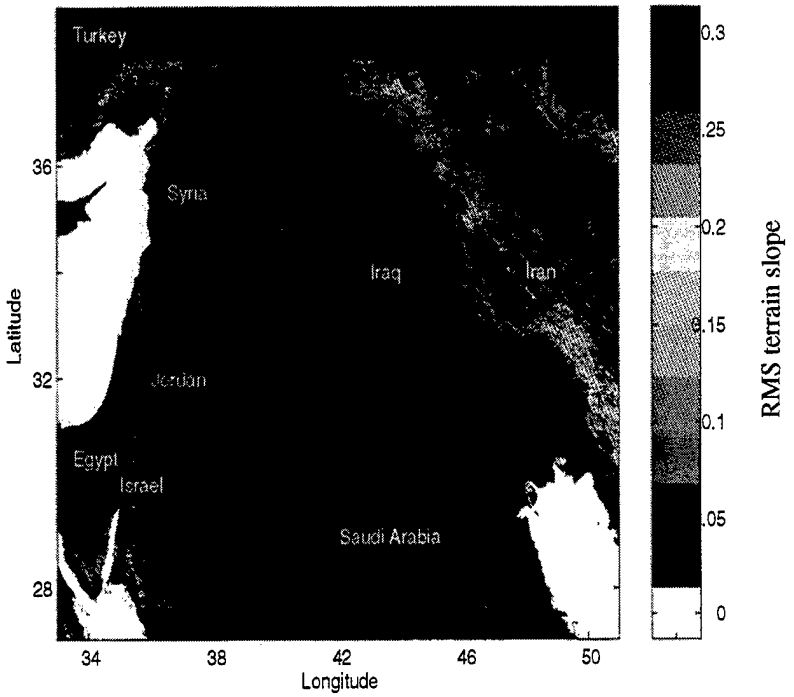

Figure 6. Color coded map of the Middle East showing the average terrain slope.

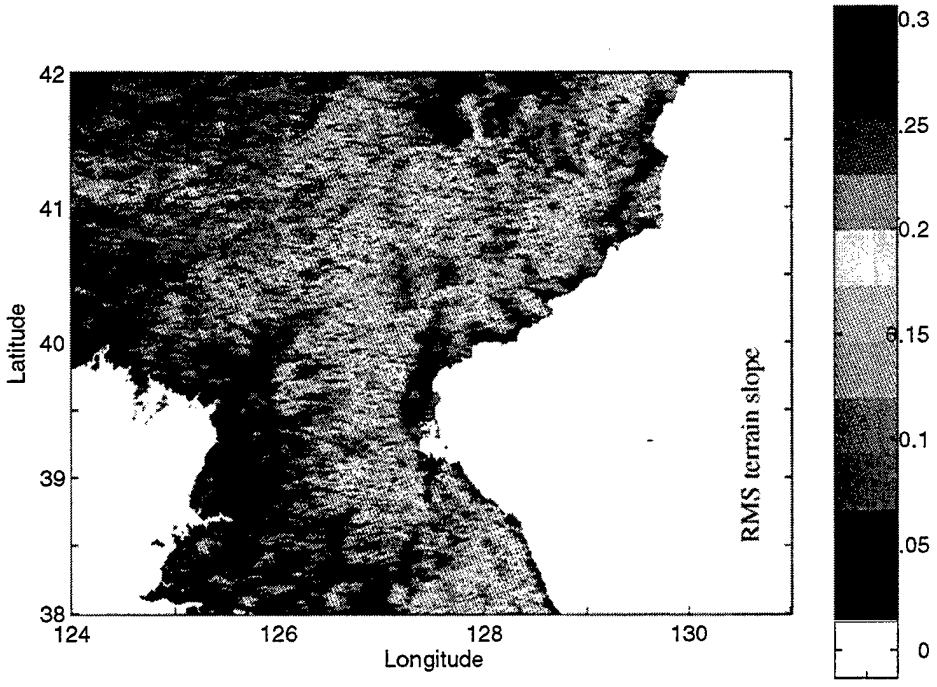

Figure 7. Color coded map of North Korea showing the average terrain slope.

6. Conclusions

In this paper we have presented height estimates derived from VHF and UHF propagation data to illustrate the viability of overland height finding techniques. For smooth terrain these height estimates differ from the true target height by a 1000 ft or so. This error grows for more severe terrain and the strength of the multipath response decreases as well.

We present two methods of obtaining a height estimate. The first method entails combining the observed TDOA with spherical earth formula and it is applicable when the terrain is reasonably smooth. The second method is a Matched Field Processing (MFP) algorithm which compares the results of a propagation model with the observed response. The MFP algorithm produces more accurate results than using a spherical earth formula but still gives less accurate estimates for very rough terrain due to the lack of sufficiently detailed terrain data. There is also a substantial computational overhead in generating the replica pulses.

This work was sponsored by DARPA under Air Force Contract F19628-95-C0002. Opinions, interpretations, conclusions and recommendations are those of the author and are not necessarily endorsed by the United States Air Force.

7. References

[1] Zurk, L.M., and S. Coutts, "Electromagnetic Pulse Propagation and Scattering from Terrain: Experimental Observation and Comparison with Theory", 1997 IEEE AP-S International Symposium and URSI Radio Science Meeting, Seattle, Montreal, Canada, July 1997

[2] Zurk, L.M., "Experimental Observation and Statistics of Multipath from Terrain with Application to Overland Height Finding", submitted for publication to IEEE Trans. Ants. and Prop., August 1997

[3] Kerr, Donald E., "Propagation of Short Radio Waves", McGraw-Hill, New York, 1951

[4] A. B. Baggeroer, W. A. Kuperman, and P. N. Mikhalevsky, "An Overview of Matched Field Methods in Ocean Acoustics", IEEE Jour. of Oceanic Eng., Vol 18, No 4, Oct. 1993

[5] Jao, Jen King, A Matched Array Beamforming Technique for Low Angle Radar Tracking in Multipath, IEEE National Radar Conference, pp 171-176, 1994

[6] Donald F. Gingras, Peter Gerstoft, and Neil L. Gerr, "Electromagnetic Matched-Field Processing: Basic Concepts and Tropospheric Simulations", IEEE Trans. Ant. and Prop., Vol. 45, No 10, Oct., 1997

[7]Ayasli, S. and Carlson, M.B., "SEKE: A Computer Model for Low-Altitude Radar Propagation over Irregular Terrain", 70, (May 1 1985)

Modeling the atmospheric refractivity structure for the EM inverse medium problem

L. Ted Rogers
Propagation Division
Space and Naval Warfare Systems Center
Code D883
San Diego, CA 92152-7385

1 Introduction

The problem of inferring atmospheric refractivity from measurements of the electromagnetic (EM) field is the inverse problem in EM propagation. The "conventional" method [*Cheney,* [1997] for solving the EM inverse problem is as follows: Let $M(z)$ be the "true" modified refractivity profile, where z is the height, and and let d_{obs} (for "observed data") be the measurements of the EM field. The solution is found by changing a modeled refractivity parameter vector θ, thus a modeled refractivity profile $\hat{M}(z;\theta)$, and computing the goodness of fit between d_{obs} and $G(\hat{M}(z;\theta))$ where G is the "forward" model (an EM propagation model such as the Radio Physical Optics (RPO) model [*Hitney,* 1993]). The set of refractivity parameters that maximizes the goodness of fit is θ^*.

If no statistical constraints are imposed on θ, then the number of elements of θ must be fewer than that of d_{obs} for the problem to have the potential for a unique solution. Since G is non-linear for EM propagation, being underdetermined does not guarantee uniqueness. The experience in ocean acoustic matched field processing is telling in this regard; typically, the acoustic propagation environment is described using less than 10 parameters, while d_{obs} (in this instance, the vector of measurements of the acoustic pressure field) may consist of tens to a few hundreds of measurements (see, for example, *Gerstoft,* [1994]).

The heuristic tri-linear refractivity model illustrated in Figure 1 is often used to model the refractivity structure associated with capping inversion of the marine atmospheric boundary layer (MABL). The tri-linear model has been implemented in the inverse problem by *Hitney,* [1992] and *Gingras, Gerstoft and Gerr,* [1997], and by the author in *Rogers,* [1997]. In the author's paper, it was found that during strong ducting conditions, refractivity profiles inferred from measured propagation were quite close to measured profiles. During weak ducting though, the inversion algorithm tended to overestimate the strength of the inversion (the M-deficit in figure 1). The reason for the overestimation of the M-deficit was hypothesized to be that the smooth segments of the tri-linear profile did not account for fluctuations in refractivity profiles that are observed in measured profiles that lead to scattering that may be the dominant mechanism for beyond-line-of-sight propagation with weak ducting.

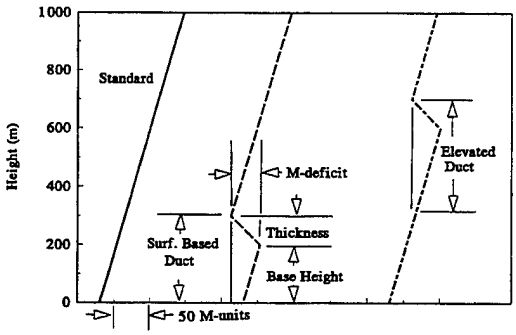

Figure 1: Standard profile (left), surface based duct profile (center) and elevated duct profile (right). The three parameters used to define the tri-linear profile, base-height, M-deficit, and thickness, are also shown.

Based on the hypothesized weakness of the tri-linear model, an effort was undertaken to develop an improved refractivity model. This report on that effort will:

1. Describe the data used for the analysis.
2. Quantify the differences between propagation calculations made using measured refractivity profiles and those made using the tri-linear model.

3. Describe an alternative model for the refractivity structure associated with the capping inversion of the MABL profiles that is based on shifted empirical orthogonal functions (SEOFs).

4. Provide a quantitative discussion of the performance of the SEOF model in forward calculations.

5. Provide a qualitative discussion of performance of the SEOF model in the inverse problem.

6. Summarize results.

Before proceeding further it is noted that no improvement was noted when the "improved" model was implemented for refractivity inversions on the same data set as used in the author's paper (above). That said, forward modeling results indicate that:

1. The tri-linear model is a biased model for predicting propagation loss while the alternate parameterizations based on shifted empirical orthogonal functions (SEOFs) appears to be an unbiased model.

2. The SEOF model achieves the same accuracy as high resolution radiosondes when used for estimation of propagation loss; that degree of accuracy is essentially the limiting accuracy for a fading channel as described in *Rogers,* [1996]. Additionally, that degree of accuracy is achieved using only two deterministic parameters, and characterizing the rest statistically.

The second result is more important than is immediately obvious and will be discussed in the summary.

2 Variability of Coastal Atmospheric Refractivity (VOCAR) experimental data.

All of the data used for this analysis were from the Variability of Coastal Atmospheric Refractivity (VOCAR) experiment. The VOCAR data set is one of very few available where propagation data are accompanied by time series of high resolution soundings (a vertical sampling interval of 10 meters or less) on the propagation path. An overview of VOCAR is given in *Paulus,* [1994]. Radio data from VOCAR are from transmission links at 143, 263, and 375 MHz that were operated on a path from San Clemente Island to Point Mugu (Path A) and a path from San Clemente Island to San Diego (Path B). The radio data were recorded from June 1, 1993, to September 5, 1993. The VOCAR data set includes an intensive observation period (IOP) of two week's duration that began on August 23, 1993. In addition to the transmission data recorded during this period, radiosondes were launched from numerous locations in the southern California bight, including San Clemente Island (the seaward endpoint of Path A), from the Research Vessel Point Sur that was located at the mid-point of Path A, and from Point Mugu (the land endpoint of Path A). The radiosondes were launched at roughly 4 hour intervals.

Only data from path A will be used for the work described in this paper. The transmission path geometry parameters for Path A include a) transmitting antenna heights of 18.4 meters above mean sea level (MSL), b) receiving antenna height of 30.5 meters (MSL), and c) the path length was 132.6 km.

A detailed picture of the evolution of the meteorology over the IOP is given in *Burk and Thompson,* [1996]. Analysis by the author in *Rogers,* [1996] demonstrated that propagation estimates calculated using the VOCAR radiosondes taken at San Clemente Island and from the path mid-point achieved very close to the limiting performance for estimating propagation in a fading channel. Consequently, the VOCAR soundings are viewed as a suitable basis for development of an empirical parameterizations, and the VOCAR propagation data are view as suitable validation data testing them.

3 Comparison of measured profiles to their tri-linear approximations

Two refractivity profiles from the VOCAR experiment are plotted in the left and right boxes in Figure 2 using solid lines. Their respective tri-linear approximations are plotted using dashed lines. In the pair on the left, the tri-linear approximation provides a good fit. On the right though, the profile has numerous fluctuations in it; it is not clear what constitutes a trapping layer in the profile. The obvious question is whether or not the poor fit (with weak ducting) is significant in propagation.

Propagation estimates calculated using the full profiles are now compared to those calculated using the tri-linear approximation. As described in section 2, the soundings from San Clemente Island and the Path A mid-point provided highly accurate propagation es-

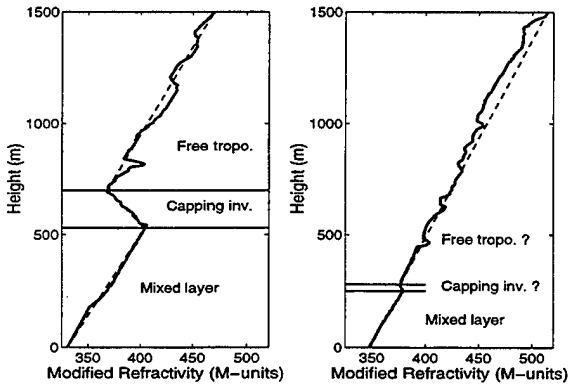

Figure 2: Examples of measured refractivity profiles (solid line) with corresponding tri-linear extreme-value fit (dashed line). The left and right soundings are from San Clemente Island at 1612 Pacific Standard Time (PST), August 24, 1993, and 0402 PST, September 1, 1993, respectively.

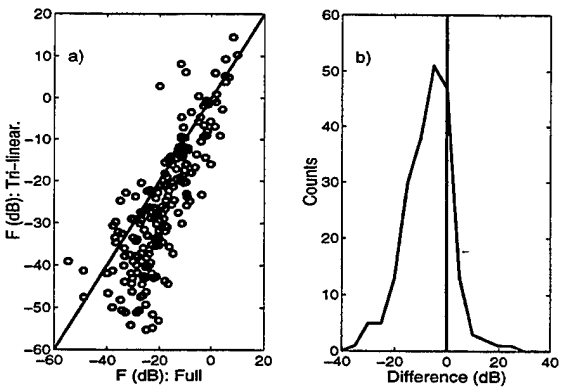

Figure 3: (Left) Scatter plot of propagation estimates for 262 MHz VOCAR transmission link calculated using full profiles and tri-linear approximations. (Right) Histogram of difference between the estimates calculated using full profiles and those calculated using the tri-linear approximation.

timates. Therefore, all of those soundings (43 from San Clemente Island and 27 from the path mid-point) are used in this analysis. Each of the soundings was used to calculate propagation at 143, 263, and 375 MHz for a path geometry corresponding to the VOCAR path A transmission links, using the Terrain Parabolic Equation Model (TPEM) [*Barrios,* 1994]. The propagation calculations were repeated using the tri-linear approximations in place of the soundings. The results are displayed in figure 3. It is clear from the scatter plot (on the left) that when propagation factors calculated using the full sounding are -20 or greater, there is no systematic difference apparent between the full soundings and their tri-linear approximations. On the other hand, when the propagation factors calculated using the full sounding are around -30 or less, the propagation estimates calculated using the tri-linear approximations are observed to have a negative bias on the order of 12 dB. A histogram of the differences between the propagation estimates calculated using the full profiles and those calculated using the tri-linear approximations appears on the right plot of the figure. It is observed that there is roughly a 7 dB bias (over all of the data points) between the two. This analysis has established that there is a systematic difference between the full profiles and the tri-linear approximations.

4 The shifted empirical orthogonal function (SEOF) refractivity model

Let $u_k(z)$ be a column vector that represents the k'th refractivity profile where z is the height. The set of N soundings form the columns of the matrix U. Knowing the inversion base height in each of the soundings (the $z_{I,k}$'s), we can shift each of the soundings using $u_k^S(z) = u_k^S(z - z_{I,k})$ to develop a matrix of shifted soundings (U^S). The Karhunen-Loeve (KL) transform (see, *Jain,* [1989]), can be used to develop a set of "shifted empirical orthogonal functions" from U^S.

The KL procedure is implemented as follows:

1. Let there be N refractivity profiles where each profile is a column vector $u^S(z)$, of length P. [Note: It is understood that the $z's$ are actually discrete.] The mean profile $u(\bar{z})$ and the covariance matrix R_u are calculated:

$$\begin{aligned} \bar{u}(z) &= \langle u(z) \rangle \\ R_u &= \langle (u - \bar{u})(u - \bar{u})^T \rangle \end{aligned}$$

   R_u is a $P \times P$ matrix. The $<>$ is used to indicate the expected value and T indicates the transpose.

2. The eigenvectors and eigenvalues of R_m are computed and stored in the $P \times P$ matrix Φ and

diagonal matrix Λ respectively. Each ϕ_i (a column of Φ) is an eigenvector, and any refractivity profile in the data set used to calculate $m(z)$ can be exactly expressed as

$$\begin{aligned} u^S(z) &= \bar{u}^S(z) + \sum_{i=1}^{i=P} c_i \phi_i(z) \\ &= \bar{u}^S(z) + \Phi c \end{aligned}$$

where Φ is the inverse KL transform matrix and c is the column vector of c_i's . The KL transform matrix is Φ^H, where "H" denotes the Hermitian transpose. The relationship between the KL transform of the data and the data is $c = \Phi^H m$. Two important properties are:

(a) Let the eigenvalues and corresponding eigenvectors be arranged in the order $\lambda_1 > \lambda_2 > \ldots > \lambda_P$. Using the first K eigenvectors to represent the $m(z)$'s will result in the minimum mean squared error in that representation possible using a linear combination of K orthogonal functions.

(b) Each λ_i, is the variance of the coefficient of its associated eigenvector over the set of u's. A consequence of Λ being diagonal is that the c_i's are statistically independent.

3. In a deterministic application, only the first K of P parameters (c_i's) are used, and the remaining parameters are assumed to be zero. In the SEOF application, z_I is an explicit parameter, so the parameter arguments for a given SEOF would be $z_I, c_1, c_2, \ldots c_K$:

$$u^S(z; z_I, c_1, c_2, \ldots c_K) = \bar{u}(z - z_I) + \sum_{i=1}^{i=K} c_i \phi_i(z - z_I)$$

where $K << P$. When implemented in an inverse problem, an optimization algorithm will vary the values of z_I and the c_i's to change $u(z)$, which results in a different modeled EM field to match to a measured field.

4. A Monte-Carlo realization approach can also be utilized. A realizations of the c_i's can be generating by multiplying a vector $\vec{n}$ of length P consisting of unit-variance, independent, random numbers, by the eigenvalue matrix $\sqrt{\Lambda}$:

$$c = \sqrt{\Lambda}\vec{n}. \qquad (1)$$

where c is the column vector containing the c_i's. Refractivity realizations may then generated *ad nauseum,* until one having the desired property (or properties) is found. An example may clarify this: Say it is desired to generate a refractivity profile where the base height is 370 meters and the M-deficit is 35 M-units. In the SEOF model, z_I is an explicit parameter, so the only problem is generating one with the right M-deficit. So realizations are generated until one having an M-deficit between $35 - \delta$ and $35 + \delta$ is generated, where δ is a reasonably small number, with $\delta = 1/2$ used for the work presented here. The advantage of this formulation is that all scales of fluctuations present in U^S are present in the synthesized soundings, with the same density as in U^S.

5 Forward modeling performance

As described in section 2, both meteorology and propagation data are available from the VOCAR IOP; that data set is now used to test forward modeling performance. Propagation estimates at the three VOCAR frequencies are calculated using: a) measured refractivity profiles, b) tri-linear approximations to the measured profiles, and c) SEOFs conditioned on the base heights and M-deficits from the measured profiles, for the geometry of VOCAR path A. The propagation estimates are compared to measured propagation and the respective error histograms are shown in figure 4.

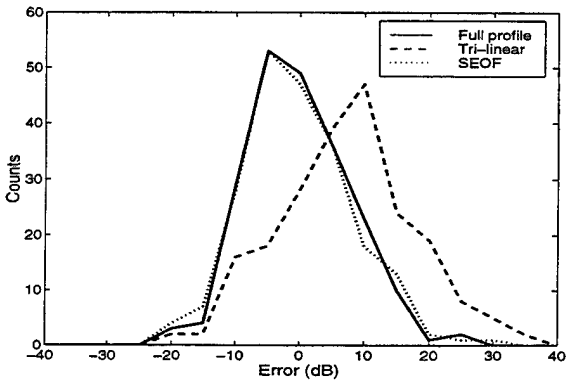

Figure 4: Distribution of errors for estimating propagation factor on the VOCAR path A links.

In figure 4, the plot for estimation errors using the

measured profiles lies under the plot associated with the SEOFs. In *Rogers,*[1996], it was demonstrated that propagation estimates calculated from the measured refractivity profiles from VOCAR taken from San Clemente Island and from the path mid-point achieved very close to the limiting error for estimating propagation in a fading channel. Since the histogram of the SEOF errors lies essentially on top of that for the measured profiles, it can be assumed that the SEOFs achieve the limiting error. It is observed that both of the histograms are roughly centered about zero, meaning the errors associated with both the measured profiles and the SEOFs are unbiased. On the other hand, the histogram associated with the tri-linear profiles is observed to lie significantly to the right of zero, appearing to indicate a bias of roughly 7 dB.

This forward modeling provides experimental validation for two items:

1. Not including the fine structure in refractivity profiles negatively biases results.
2. Very good propagation estimation results can be obtained even when only two parameters are known explicitly.

The latter item is of importance in improving propagation estimation in general and will be further addressed in the summary.

6 Inverse problem performance

The SEOF model was implemented for performing refractivity inversions from the VOCAR path A transmission data, the same data used in *Rogers,*[1997]. A detailed description of the inversion algorithm is given in that paper and it will not repeated here. Measured inversion base heights and M-deficits and those inferred using the tri-linear model and the SEOFs are shown in figure 5. It is observed that there is no clear difference in the quality of the inversion results between the tri-linear and the SEOF results. By and large, both perform well until day 243.0. After that date, the inferred base heights for both the tri-linear and SEOF model exhibit a positive bias, and the inferred M-deficits also exhibit a positive bias. It is clear that the use of the SEOF model has not improved inversion results.

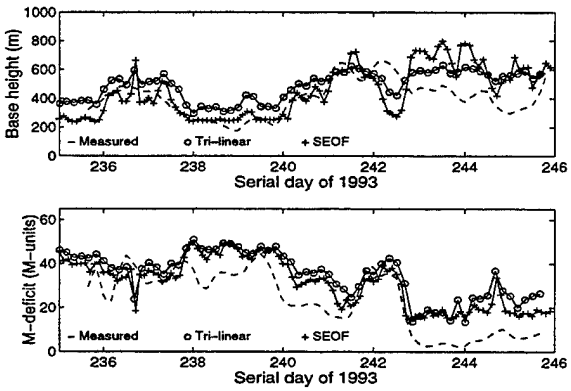

Figure 5: Time series of measured, inferred using tri-linear model, and inferred using SEOF model, base height and M-deficit.

7 Summary

The overall objective of this effort has been to develop an improved parameterization for the EM inverse problem. Forward modeling results indicate that the "improved" model based on shifted empirical orthogonal functions (SEOFs) is superior to the tri-linear model particularly where there is weak ducting. As described in Sections 6 though, there is no evidence that the model based on shifted empirical orthogonal functions performed any better than the commonly-used, heuristic, tri-linear model.

7.1 Impact on data fusion

As described in *Richter,* [1994], the long term solution for the assessment of refractivity is a system that merges the outputs of direct and remote sensors with that of the mesoscale model for estimation of atmospheric refractivity. A key element of developing an efficient parameterization for *fusing* model and sensor outputs is determining what needs to be known deterministically, what can be considered statistically, and what doesn't need to be known at all, to achieve a desired level of accuracy in propagation estimation. It has been demonstrated here that (provided other parameters are considered statistically) as few a two refractivity parameters need be considered deterministically for very good propagation estimates. It is conjectured by the author that it may (for data fusion purposes) be possible to replace the vertical grid representation of refractivity (as from a mesoscale model or from a radiosonde) with a parameterized representation, thereby transform the refractivity data fusion

problem from a 3-D into a 2-D problem. While this is far too limited a study to say just what does and does not need to be considered deterministically and statistically in propagation estimation, it is a step in the right direction.

7.2 Future work

The fluctuations in the refractivity profile characterized using the SEOF model are the result of turbulence. There is a considerable body of literature devoted to turbulence and the resulting fluctuations in refractivity profiles. A goal of future work in this area is tying the empirical work reported here with the historical work reported in *Gossard and Strauch,*[1983] and with the multi-scale modeling effort that is underway at Penn State University (see *Khanna and Wyngaard,* [1996]).

Acknowledgements

The San Clemente Island and Point Mugu radiosondes were provided courtesy of the Naval Air Warfare Center, Point Mugu, CA. The radiosondes from the mid-path location were provided courtesy of the Naval Postgraduate School, Monterey, CA. The VOCAR data collection effort was funded from Office of Naval Research (ONR) code 322. This analysis was funded by ONR 313 and 321.

Much of the work presented here has been inspired by the authors close association with Dr.'s Seaman, Wyngaard, Stauffer, and Gilbert of the Meteorology Department at Penn State University and Dr.'s Krolik and Tabrikian of the Electrical Engineering Department at Duke University

References

[1] Barrios, A.E., A terrain parabolic equation model for propagation in the troposphere, *IEEE Trans. Antennas and Propagation,* vol. 42, no. 1, pp. 90-98, Jan., 1994

[2] Burk, S.D. and W.T. Thompson, Mesoscale modeling of summertime refractive conditions in the southern California bight, *Journal of Applied Meteorology,* Vol. 36, pp. 22-31, 1996

[3] Cheney, M., Inverse boundary-value problems, *American Scientist,* vol. 85, pp. 448-455, Sep.-Oct., 1997

[4] Gerstoft, P., Inversion of seismoacoustic data using genetic algorithms and a posteriori probability distributions, *J. of Accoustical Society of America,* vol. 95, no 2, pp 770-782, Feb., 1994

[5] Gingras, D.F., P. Gerstoft and N.L. Gerr, Electromagnetic matched field processing: Basic concepts and tropospheric simulations, *IEEE Trans. Antennas and Propagation,* vol. 42, no. 6, pp. 1305-1306, Oct., 1997

[6] Gossard, E.E. and R.G. Strauch, Radar observations of clear air and clouds, Elsevier, 1983

[7] Hitney, H.V., Hybrid ray optics and parabolic equation methods for radar propagation modeling, *Proc. of IEE Radar '92 Conference,* pp. 58-61, 1993

[8] Hitney, H.V., Remote sensing of refractivity structure by direct radio measurements at UHF, *Proc. of AGARD SPP symposium on "Remote sensing of the propagation environment",* held in Cesme, Turkey, 30 Sep. - 4 Oct., 1991, Feb., 1992

[9] Jain, A.K., Fundamentals of digital image processing, Prentice-Hall, 1989

[10] Khanna, S. and J.C. Wyngaard, Local refractive index structure-function parameter and its application to wave propagation. *Proceedings of the 1996 Battlespace Atmospherics Conference, December 3-5, 1996,* J.H. Richter and K.D. Anderson, Eds., NRad Tech. Doc. 2938, 1996

[11] Paulus, R.A., VOCAR: An experiment in the variability of coastal atmospheric refractivity, *Proc. of International Geoscience and Remote Sensing Symposium, California Institute of Technology, Pasadena, CA, August 8-12, 1994,* vol. I, pp. 386-388, 1994

[12] Richter, J.H., Sensing of radio refractivity and aerosol extinction, *AGARD Lecture Series 196,* Advisory Group for Aerospace Research and Development, 7 Rue Ancelle, 92200 Neuilly-Sur-Seine, France, pp. 3.1-3.17, Sep., 1994

[13] Rogers, L.T., Effects of the variability of atmospheric refractivity on propagation estimates, *IEEE Trans. on Antennas and Propagation,* vol. 44, no. 4, pp. 460-465, April, 1996

[14] Rogers, L.T., Likelihood estimation of tropospheric refractivity parameters, *Radio Science,* Jan. - Feb., 1997

Tropospheric Refractivity Estimation using Radar Clutter from the Sea Surface

Jeffrey L. Krolik and Joseph Tabrikian
Department of Electrical and Computer Engineering,
Duke University, Durham, NC 27708-0291, USA
jk@ee.duke.edu

February 19, 1998

Abstract

The refractivity profile in coastal regions to a large extent determines the performance of radar and communication systems. The purpose of this paper is to present a new estimation technique for microwave remote sensing of refractivity using radar clutter returns from the sea surface. A maximum *a posteriori* method using a fast dynamic programming technique is developed in order to jointly estimate the unknown refractivity parameters and the uncertain, spatially varying sea surface backscatter cross section. The estimator is evaluated using computer simulations and results show that given a sufficient clutter-to-noise ratio, the base height of the refractivity profile can be estimated with relatively small mean square error.

1 Introduction

The vertical and horizontal refractivity profile in the coastal regions determines, to a large extent, the performance of shipboard radar and communications systems. If the atmospheric conditions, particularly the water vapor spatial distribution, were known, numerical propagation models could be used for such purposes as predicting detection ranges, correcting altitude estimates, and estimating surface backscatter strength. The effect of the variability of atmospheric refractivity on propagation estimates using real data profiles has been investigated in [1]. Since direct measurement of atmospheric conditions is difficult and expensive, remote sensing by multiple point-to-point propagation loss measurements at multiple frequencies has been proposed as a means of synoptic monitoring of tropospheric refractivity [2]. While this approach has yielded some promising results, it suffers from the need for many receiver-transmitter pairs in

order to get an adequate reconstruction of the 3D refractivity profile over the surveillance region of the radar.

In this paper, a method for estimating refractivity from clutter (RFC) is presented. The advantage of estimating RFC is that the radar itself is used as the refractivity remote sensing device and thus no additional transmitters or receivers are necessary. A maximum *a posteriori* (MAP) approach is developed here for estimating the refractivity profile in the presence of an uncertain range dependent backscatter cross section. The remainder of the paper is organized as follows. In the next section, the measurement model and the basic assumptions are presented. In Section 3, a MAP estimator is derived for jointly estimating the refractivity profile parameters and backscatter cross section. In the fourth section, the estimator performance is evaluated by Monte-Carlo computer simulations.

2 Problem formulation

The problem of estimating refractivity from clutter is in many respects similar to that of coherent imaging in the presence of so-called "speckle noise". Speckle is produced by the interference of returns produced when narrowband radiation is scattered from a surface whose roughness is on the order of a wavelength. This produces a multiplicative noise which is Rayleigh distributed in magnitude. In the RFC problem, this multiplicative noise is produced by backscatter from the sea-surface. The radar clutter return, $f(x)$, in radar "slant" range x, is given by:

$$f(x) = \int_{x'} \int_{y'} H(x; x', y') b(x', y') dx' dy' + \eta(x) \tag{1}$$

where $b(x', y')$ is the complex coefficient of the sea-surface, and the impulse response of the radar, $H(x; x', y')$, defines the output at slant coordinates x due to a point source at true coordinates (x', y') on the ocean surface. Note that $H(x; x', y')$ is a function of both radar parameters such as the beamformer weights and pulse shape, as well as propagation model parameters such as refractivity. Because of surface roughness, $b(x, y)$ maybe modeled as a complex zero-mean random process. Additive noise at the receiver is denoted by $\eta(x)$ and is modeled as complex zero-mean Gaussian distributed and uncorrelated with $b(x, y)$. Assume the impulse response, $H(x; x', y')$, is approximately zero outside some resolution cell, $\Omega(x, y)$, and further express $H(x; x', y') \approx L(x; \mathbf{g}) h(x; x', y')$ within the cell, where $L(x; \mathbf{g})$ is the two-way propagation loss which depends on unknown refractivity profile vector parameter, $\mathbf{g}$, and $h(x; x', y')$ is the impulse response determined assuming propagation through a standard troposphere and using the radar's beam and pulse width. Substituting into Eq. (1) gives:

$$f(x) = L(x; \mathbf{g}) a(x) + \eta(x) \tag{2}$$

where

$$a(x) \triangleq \int \int_{\Omega} h(x; x', y') b(x', y') dx' dy' \tag{3}$$

is a stochastic integral. Assuming the correlation length of $b(x', y')$ is smaller than Ω, the Central Limit Theorem suggests that $a(x)$, the radar clutter, is approximately zero-mean complex Gaussian distributed with variance, $\sigma_a^2(x) = E\left(|a(x)|^2\right)$.

The clutter return intensity is sampled at range bins x_n, and the measurement model is:

$$f(x_n) = L(x_n; \mathbf{g}) a(x_n) + \eta(x_n) \tag{4}$$

where the additive noise, $\eta(x_1), \cdots, \eta(x_N)$, is assumed to be i.i.d. with variance σ_η^2. The radar clutter, $a(x_n)$, is a random process whose statistics depend on the sea surface roughness and known radar parameters. The backscatter cross section is assumed to be unknown, but modeled as a first order Markov random sequence with conditional transition probabilities $p\left(\sigma_n | \sigma_{n-1}\right)$ and prior $p\left(\sigma_1\right)$, where $\sigma_n \triangleq \sigma_a(x_n)$, $n = 1, \cdots, N$. Letting Σ denote the vector of backscatter cross sections at the N range bins, $\Sigma \triangleq (\sigma_1, \cdots, \sigma_N)^T$. The objective is to estimate the refractivity profile vector parameter, $\mathbf{g}$, and the nuisance parameters, Σ, given N samples of the clutter intensity, $\mathbf{f} \triangleq (f(x_1), \cdots, f(x_N))^T$, in the presence of both multiplicative and additive random processes.

3 Refractivity estimation

In this section the MAP estimator for the problem stated in the previous section is developed. Since the elements of $\mathbf{f}$ are independent, the conditional probability distribution function (pdf), is

$$p(\mathbf{f} | \Sigma, \mathbf{g}) = \prod_{n=1}^{N} p\left(f(x_n) | \sigma_n, \mathbf{g}\right) \tag{5}$$

where

$$p(f(x_n) | \sigma_n, \mathbf{g}) = \frac{1}{\pi \sigma_{fn}^2} exp\left(-\frac{|f(x_n)|^2}{\sigma_{fn}^2}\right) \tag{6}$$

and the variance of $f(x_n)$, σ_{fn}^2, is given by

$$\sigma_{fn}^2 = L^2(x_n; \mathbf{g}) \sigma_n^2 + \sigma_\eta^2, \quad n = 1, \cdots, N. \tag{7}$$

The MAP estimator of the parameters $\mathbf{g}$ and Σ is obtained by maximizing the joint probability distribution of the measurements $\{f(x_n)\}_{n=1}^N$ and the unknown random vector parameter Σ:

$$\left(\hat{\mathbf{g}}, \hat{\Sigma}\right)_{MAP} = \arg \max_{\mathbf{g}, \Sigma} p\left(\mathbf{f}, \Sigma | \mathbf{g}\right). \tag{8}$$

The vector Σ does not depend on $\mathbf{g}$. Therefore,

$$p(\mathbf{f}, \Sigma|\mathbf{g}) = p(\mathbf{f}|\Sigma, \mathbf{g})\, p(\Sigma)\,. \tag{9}$$

The backscatter cross section is assumed to be a first order Markov sequence:

$$p(\Sigma) = \prod_{n=2}^{N} p(\sigma_n|\sigma_{n-1}) p(\sigma_1) \tag{10}$$

Note that the MAP estimator does not depend on the measurement phase, but depends on the clutter intensity, $|f(x_n)|^2$. By substitution of (9) into (8), using (7) and (10), and taking logarithm, one obtains:

$$\left(\hat{\mathbf{g}}, \hat{\Sigma}\right)_{MAP} = \arg\max_{\mathbf{g},\Sigma} \left[\sum_{n=1}^{N} \log f(x_n|\sigma_n, \mathbf{g}) + \sum_{n=1}^{N} \log p(\sigma_n|\sigma_{n-1})\right], \tag{11}$$

where $p(\sigma_1|\sigma_0) = p(\sigma_1)$. Assuming that the unknown random parameter vector, Σ is discrete on a given pre-determined grid, the MAP estimator in (11) can be realized using a fast recursive dynamic programming technique known as the Viterbi algorithm [3]. For each hypothesized value of $\mathbf{g}$, maximization can be performed with respect to Σ using the Viterbi algorithm. Consider the following definitions:

$$V_i(\mathbf{g}, n) \triangleq \log f(x_n|\sigma_n = s_i, \mathbf{g}), \quad n = 1, \cdots, N,\ i = 1, \cdots, K,$$

$$B_{j,i}(n) \triangleq \log p(\sigma_n = s_i|\sigma_{n-1} = s_j), \quad n = 1, \cdots, N,\ i, j = 1, \cdots, K,$$

where K is the number of points on the grid of σ_n. Then maximization with respect to Σ for each $\mathbf{g}$ consists of calculating $W_i(\mathbf{g}, N)$ defined by the following recursive equation for $n = 1, \cdots, N$:

$$W_i(\mathbf{g}, n) = \max_j \left(W_j(\mathbf{g}, n-1) + B_{j,i}(n)\right) + V_i(\mathbf{g}, n). \tag{12}$$

Then the MAP estimator of $\mathbf{g}$ is given by:

$$\hat{\mathbf{g}}_{MAP} = \arg\max_{\mathbf{g}} W_i(\mathbf{g}, N), \tag{13}$$

where $W_i(\mathbf{g}, N)$ can be calculated by the recursive equation from (12). The estimator assumes knowledge of the transition probabilities $p(\sigma_n|\sigma_{n-1})$ and the additive noise variance, σ_η^2. For mathematical simplicity, the above discussion assumed that the backscatter cross section can vary between consequent range bins in a straight-forward manner. The estimator can be easily modified for the case where the backscatter cross-section is constant over a group of range bins, x_n, but varies between the groups.

4 Simulations

In this section the MAP estimator for RFC is evaluated using computer simulations. The refractivity profile, depicted in Fig. 1, is assumed to be tri-linear where its base height is assumed to be the unknown non-random parameter, g_o. The two-way propagation loss, assuming base height of $g_o = 30$ m, is illustrated in Fig. 2. The propagation loss is calculated using Radio Physical Optics (RPO) code. The backscatter cross section is assumed to be a Markov sequence when $20\log\sigma_1$ is uniformly distributed on -10 and +10dB, and $20\log\left(\frac{\sigma_n}{\sigma_{n-1}}\right)$ is uniformly distributed between -3dB and 3dB. The backscatter cross section is assumed constant over 2 km intervals and the clutter intensity, $|f(x_n)|^2$, is available every 50 m. A typical realization of the radar clutter return from the sea surface and the two-way propagation loss for a minimum clutter-to-noise ratio (CNR) of -30 dB are shown in Fig. 3. The CNR is defined as $CNR \triangleq \frac{\min_x L^2(x;g_o)}{\sigma_\eta^2}$ where the minimum is taken over the range extent of the dwell.

The RFC estimator has been applied on the scenario described above. Fig. 4 shows backscatter cross section estimation for a single realization at a CNR of -30 dB. It can be observed that the estimates follow the changes in the true value of the backscatter cross section except the ranges between 10-30 km which can be explained by the fact that the clutter return at these ranges is well below the noise level (see Fig. 3). The performance of the estimator is evaluated as a function of CNR using Monte-Carlo simulations. Fig. 5 illustrates the estimator performance, based on 100 independent realizations for the case where σ_n is an unknown Markov sequence as described above versus the clairvoyant situation where σ_n is known and range-independent. This figure shows that above a threshold CNR, the refractivity profile can be estimated with a root mean-square error of less than 0.5 m. The price paid for uncertainty in the backscatter cross-section is evidenced by the fact that the threshold CNR is 8 dB higher in the unknown range-varying σ_n case versus when σ_n is a known constant.

5 Conclusions

In this paper an algorithm for estimation of refractivity from clutter has been presented and evaluated. A fast dynamic programming technique facilitates joint maximization of the objective function with respect to parameters of the refractivity and the clutter statistics. It has been shown that given sufficiently high CNR, the refractivity profile can be estimated using backscatter from the sea surface even when its roughness is unknown and spatially variable.

Acknowledgment

This work was supported by SPAWAR systems center and ONR.

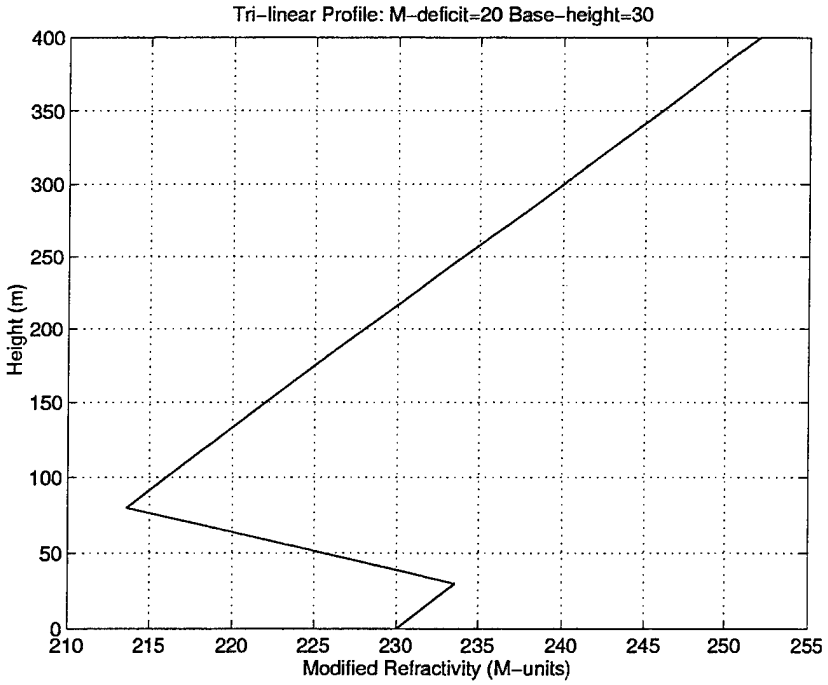

Figure 1: The tri-linear refractivity profile

References

[1] T. Rogers, "Effects of the variability of Atmospheric refractivity on propagation estimates," *IEEE Trans. Antennas Propagat.*, vol. AP-44, pp. 460-465, Apr. 1996.

[2] J. Tabrikian and J. L. Krolik, "Theoretical Performance Limits on Tropospheric Refractivity Estimation using Point-to-Point Microwave Measurements," submitted for publication in *IEEE Trans. on Antennas and Propag.*, January 1998.

[3] C. W. Therrien, *"Discrete random signals and statistical signal processing,"* Prentice Hall, 1992.

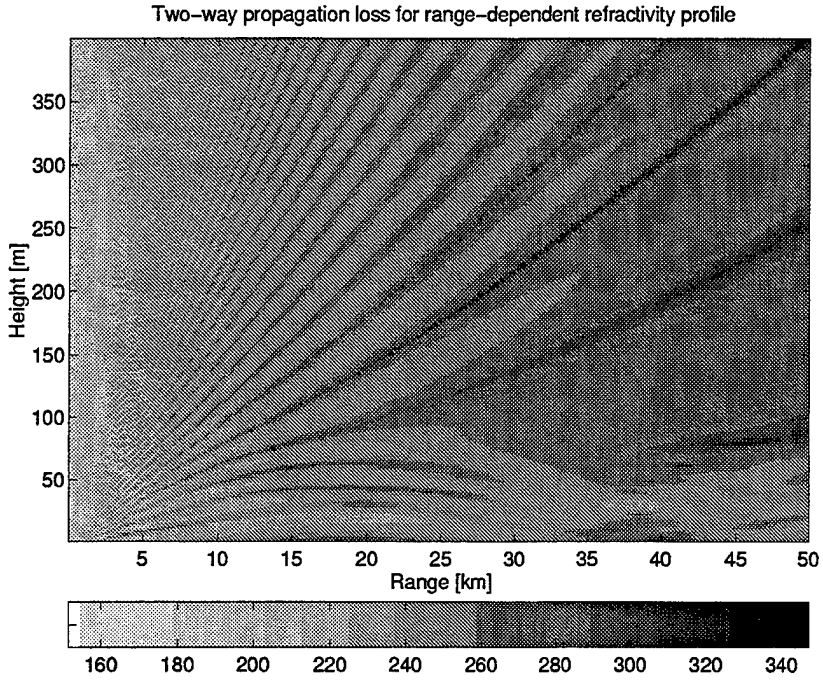

Figure 2: The two-way propagation loss, assuming base height of 30 m

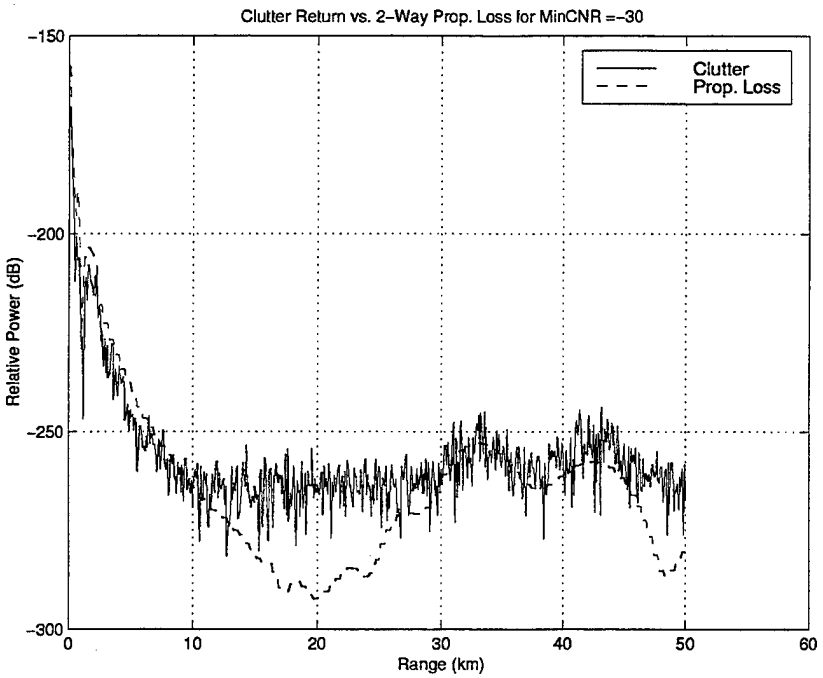

Figure 3: Typical realization of the radar clutter return and the two-way propagation loss at CNR of -30 dB

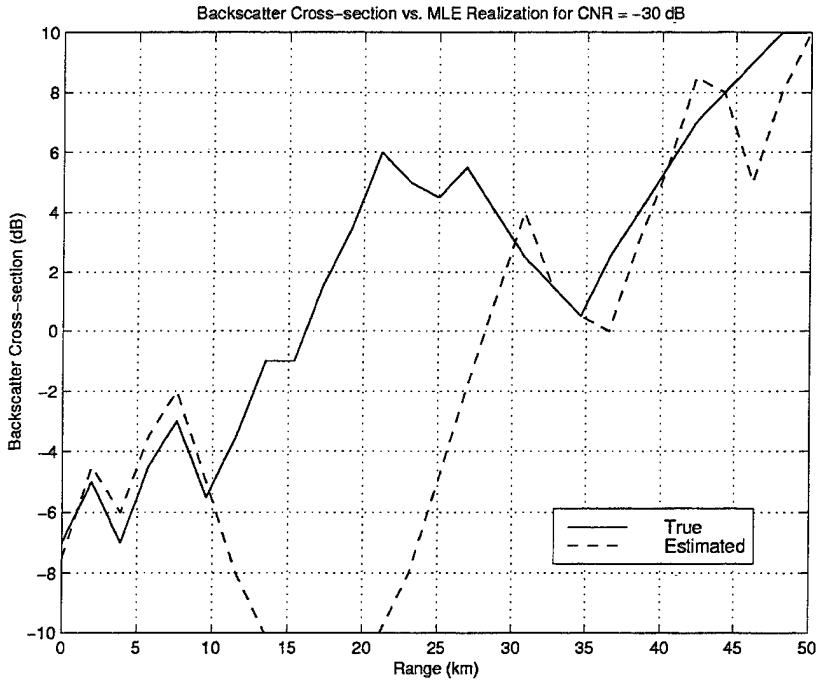

Figure 4: Backscatter cross section versus MAP estimator realization at a CNR of -30 dB

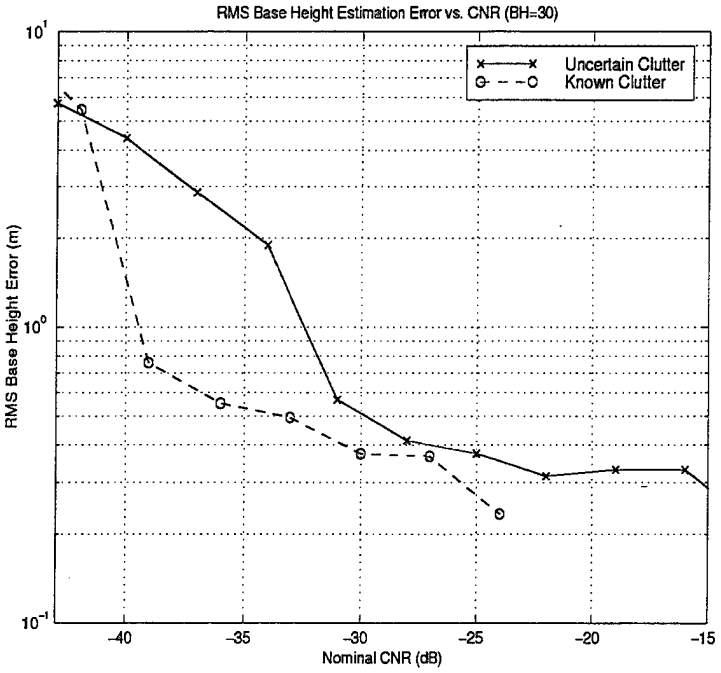

Figure 5: RMS base height error versus CNR for base height of 30 m

Shore-to-Ship Automated Support for Characterizing the Battle Space Environment

J. Rosenthal, LCDR D. Ruth, M. McGovern, B. Cohenour, R. Helvey,
P. Greiman & L. Eddington
Geophysics Branch
Naval Air Warfare Center Weapons Division, Point Mugu, CA
J. Peak, R. Nagle
Computer Sciences Corporation (CSC)
L. Phegley, J. Cook
Naval Research Laboratory (NRL), Monterey, CA

Abstract

With the rapid change to Internet Web-Site methodology for transferring meteorology and oceanography (METOC) products to the warrior, several demonstrations of this technology have taken place and are in progress from the Naval Air Warfare Center Weapons Division (NAWCWPNS) Battle Management Interoperability Center (BMIC) at Point Mugu, California. These efforts include the fusion of satellite and operational geometry information, and transmission to ship and regional METOC centers via an upgraded SIPRNET connection from BMIC. Using IR-duct and other algorithms developed at NAWCWPNS for estimating radio/radar propagation conditions from METOC satellite data, statistical properties are being extracted which will be included in upgrades to EXPERDUCT software, that describes refractive conditions over ocean and coastal regions where they apply. Methods for short term predictions of cloud features, using satellite data and advection techniques, are also being developed to address strike warfare and EO assessment requirements. To demonstrate the feasibility of running a high-resolution three-dimensional forecast model aboard ship, a test was jointly conducted with Naval Research Laboratory (NRL) Monterey and the USS NIMITZ, whereby global forecast fields were sent from Fleet Numerical Meteorology & Oceanography Center (FNMOC) via SIPRNET to BMIC, which was emulating a regional METOC center. From BMIC, this data was merged with local observations then sent via SIPRNET to USS NIMITZ, where 36-hour high resolution forecasts were produced using the NRL-developed Shipboard Tactical Atmospheric Forecast Capability (STAFC) which hosted the Coupled Ocean/Atmosphere Mesoscale Prediction System (COAMPS) model. These forecast outputs were then transferred to Point Mugu and displayed in BMIC using the MOSAIC Web Browser for potential access by operational users anywhere. Additionally, COAMPS (run at NRL Monterey and received at Point Mugu on the Home Page) output were used to calculate and display air trajectories for selected source regions as part of a CNO-sponsored study and participation in the multi-agency Southern California Ozone Study (SCOS-97)/North American Research Strategy for Tropospheric Ozone (NARSTO).

1. Introduction

Current planning for joint military exercises, to successfully implement rules of engagement, require rapid characterization of the meteorological and oceanographic (METOC) battlespace to optimize weapons and sensor performance. At sea, and in the air, operational response and decision making timelines are short, and resources to make comprehensive atmospheric measurements throughout the battlespace may be limited. Much of this burden can be eliminated with the implementation of IT-21 technology using centralized internet web sites, so that the necessary data can be quickly distributed and accessed by fleet users as needed. Proof-of-concept demonstrations of the feasibility of these techniques are being carried out in the Naval Air Warfare Center Weapons Division (NAWCWPNS) Battle Management Interoperability Center (BMIC) at Point Mugu under the sponsorship of the Navy's METOC Systems Program Office at SPAWAR (PMW-185). This paper describes some of the tests conducted, and the potential for exploiting these web site capabilities for the warrior.

2. Some Early Successes

During the Joint Task Force Exercise JTFEX 97-1, METOC forecasts, upper-air sounding data, climatological (statistical planning) data and other information was placed on a dedicated section of the NAWCWPNS Geophysics home page. From BMIC, serving as a regional METOC center, the products were accessible via SIPRNET by the Naval Pacific METOC Facility San Diego home page, operating the Fleet's Central host or anchor web site for the fleet exercise. Fleet combatants operating within the Southern California operating area then selected products tailored for their mission support roles. Another internet capability demonstrated during this exercise was the use of Internet-Chat. In this mode, participants at San Diego, afloat on ships, and in BMIC discussed METOC observations and forecast products in an interactive real-time mode earning the approval of VADM Browne for demonstration of IT-21 technology.

Other recent exercises in BMIC also demonstrated the fusion of satellite, grid-point, tactical display and operational route data into one overlay which were sent via SIPRNET to other home page sites. Examples of their use of internet technology included Tomahawk Strike planning displays in JWID-95 which were sent to CINCPACFLT, Camp Pendleton and missile launching platforms afloat, and enroute and target area weather depictions installed on the TESS Remote Workstation (TRWS) for use in supporting JSOW test operations (figure 1)

3. Recent Propagation Applications

Fusion of satellite data, derived quantities and operational routing information has also been initiated recently to estimate the variability of elevated duct height along some specified horizontal path. Using the satellite IR-duct height technique developed by NAWCWPNS, estimates of duct height over low cloud-covered areas of the sub-tropical Pacific Ocean were calculated at selected points from infrared (IR) imagery and displayed atop concurrent visible satellite imagery. An overlay of a horizontal route, to simulate a planned ship or aircraft route was created, and all merged on a single product displayed on the TRWS (figure 2). Once there, SIPRNET can be used to transfer the product to a home page installed on another TRWS anywhere afloat or ashore. In figure 2, the route was constructed to show the diversion necessary

from a straight route due to a tropical cyclone, with duct heights along the final route useful for planning expected radar propagation and detection conditions from initial point to destination (assuming static conditions). The estimates of duct height can also be used as input to Experduct, a new PC-based expert system under development to estimate radar propagation conditions from a blend of climatology, synoptic parameters and satellite data (figure 3). The duct height data can also be used potentially as input to RPOT, the NRaD-developed range-dependent radar/radio propagation assessment program to anticipate the actual effects expected on systems performance.

4. Use and Transfer of Geostationary Data

Most past use of satellite data on the TRWS involved imagery from polar-orbiting DMSP or NOAA satellites pulled down into the TESS architecture using the SMQ-11 satellite ingest system. Using the DSAT system (and subsequently the Navy's Geostationary Satellite Display System, NSDS-E), geostationary imagery can be exploited to highlight time-varying cloud and precipitation features so that estimates can be made of such quantities as cold front or thunderstorm arrival, and stratus dissipation (or reformation) etc. Using the DSAT system in BMIC, transfer of geostationary imagery to the NPMOF NAVPACMETOCFAC San Diego and NAVEURMETOCCEN in Rota, Spain was done to demonstrate the use of SIPRNET in sending geostationary data in near real time from a 'regional' center to any other METOC facility ashore or afloat. This bypasses the previous antennae-related obstacles to receiving high-resolution satellite imagery aboard ship.

5. Transfer of First Shipboard of 3-D Forecasts

During June 1997, the Naval Research Laboratory (NRL) in Monterey conducted the first successful test of the Shipboard Tactical Atmospheric Forecast Capability (STAFC) onboard the USS NIMITZ during a transit along the U. S. West Coast. Global NOGAPS forecast grids were received in BMIC from FNMOC in Monterey. These files were sectorized and together with local observations, were sent via SIPRNET to the NIMITZ. The grids were used to produce the first shipboard processing of the Navy's high-resolution Coupled Ocean and Atmospheric Prediction System (COAMPS) 3-D model run on a TAC-4. The 12, 24 and 36 hour forecast outputs of wind, pressure and other parameters were then relayed via SIPRNET back to BMIC at Point Mugu where they were able to be displayed on the BMIC system using the MOSAIC Web Browser, as well as transferred back up to the Monterey web site. Figure 4 shows the connectivity and communication paths used for this exercise. The COAMPS forecast product displayed in BMIC is shown in figure 5.

6. Air Mass Transport and Pollution Trajectories on Web Site

During summer 1997, another application of COAMPS resulted in data displayed on web sites at Point Mugu and NRL to address the forecast or expected trajectories of polluted air. This was accomplished in support of the Southern California Ozone Study - North American Research Strategy For Tropospheric Ozone (SCOS-97/NARSTO) in which the U. S. Navy played a key role in coastal and offshore measurements and meteorological analyses. This was the largest air

pollution field measurement program ever undertaken, and involved a number of federal, state, and local government agencies and academic institutions.

An important element in the study was a daily decision-making process in which present and upcoming potential for smog transport was discussed as the basis for initiating intensive-mode measurement efforts involving 6 aircraft, 7 ozonesonde stations, 12 radiosonde stations, 26 profilers and hundreds of other surface weather, air quality and aerosol measurements. These were coordinated with the Navy's EOPACE program. An air trajectory graphical display derived from hourly COAMPS forecasts was developed at NAWCWPNS and displayed atop the COAMPS forecast at verification time. This product, shown in figure 6, was used by NAWCWPNS and was also displayed on the NRL home page.

7. Short-Term Forecasts of Satellite-Observed Cloud Cover

The final application of internet technology to be discussed is the display of forecast satellite cloud pictures or animations. These are being developed under NAWCWPNS and SPAWAR sponsorship by R. Nagle at NRL Monterey. Termed the Nagle Cloud Advection Model (NCAM), the technique involves the displacement of actual satellite-observed cloud features and systems by the physics inherent in the Navy's NOGAPS global model. The resulting animations are forecasts out to about 24 hours of the synoptic features responsible for precipitation and other weather and sea conditions that limit operational decision-making and tactical operations. These short-term forecasts, which are currently displayed for several areas on the NRL home page, are critically needed for the Joint Mission Planning System (JMPS) and other strike planning aids once the technique is updated, validated, and approved for operational use. An example is shown in figure 7.

8. Conclusions and Follow-On Plans

A variety of METOC products which provide real-time and forecast depictions of cloud cover, precipitation, winds, seas, aerosol transport, radar propagation conditions, and other parameters needed for GO/NO GO decision-making are able to be displayed on home page, web-sites and transferred to operational decision-makers ashore or afloat. This is accomplished via SIPRNET, and existing and upcoming METOC architectures. Intended for use with JMPS, TAMPS, MDS, APS, and other mission planning systems, the displays are fused with quantitative data, operational routes and tactical displays so that meaningful assessments of weather impacts on operations or systems performance can be made. The BMIC at Point Mugu is being used for proof-of-concept testing and demonstration of many of these concepts and will be a key in helping to mature the operational use of IT-21 technology.

9. References

(1). LCDR D. Ruth & J. Cook (NRL Monterey), "First Test of STAFC Afloat Succeeds", Naval Meteorology & Oceanography Command News (CNMOC News), Oct-Nov 1997.

(2). Rosenthal, J., R. A. Helvey, M. McGovern, P. Greiman, B. Cohenour,

D. Ruth, "Battlespace Weather and EM/EO Conditions for Joint Strike Support," Proceedings of SPIE Conference 'Propagation and Imaging through the Atmosphere', 29-31 July 1997.

(3). Rosenthal, J. and M. McGovern, "Battlespace Weather Conditions for Joint Strike Support," Navy Battlespace Assessment Conference, San Diego, 1996.

(4). P. Greiman, J. Rosenthal and R. Helvey, "Synoptic Variability Revealed by Satellite and Equivalent Altitude," NATO AGARD CP582, pp 47.1-47.12, 1996.

(5). R. Helvey, J. Rosenthal, L. Eddington, P. Greiman and C. Fisk, "Use of Satellite Imagery and Other Indicators to Assess Variability and Climatology of Oceanic Elevated Ducts", NATO AGARD CP-567, pp 33.1-33.13, 1994.

Figure 1. TRWS satellite product for JSOW combining cloud cover, temperature, and operational geometry.

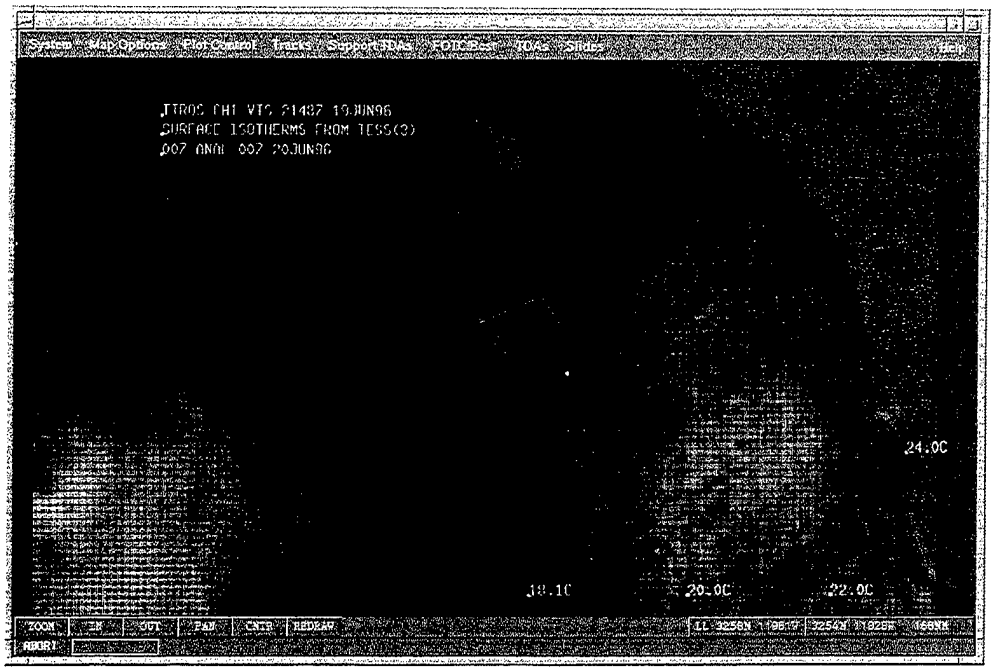

Figure 2. Satellite imagery superimposed by estimates of duct height and by routes of operational interest fused into one display.

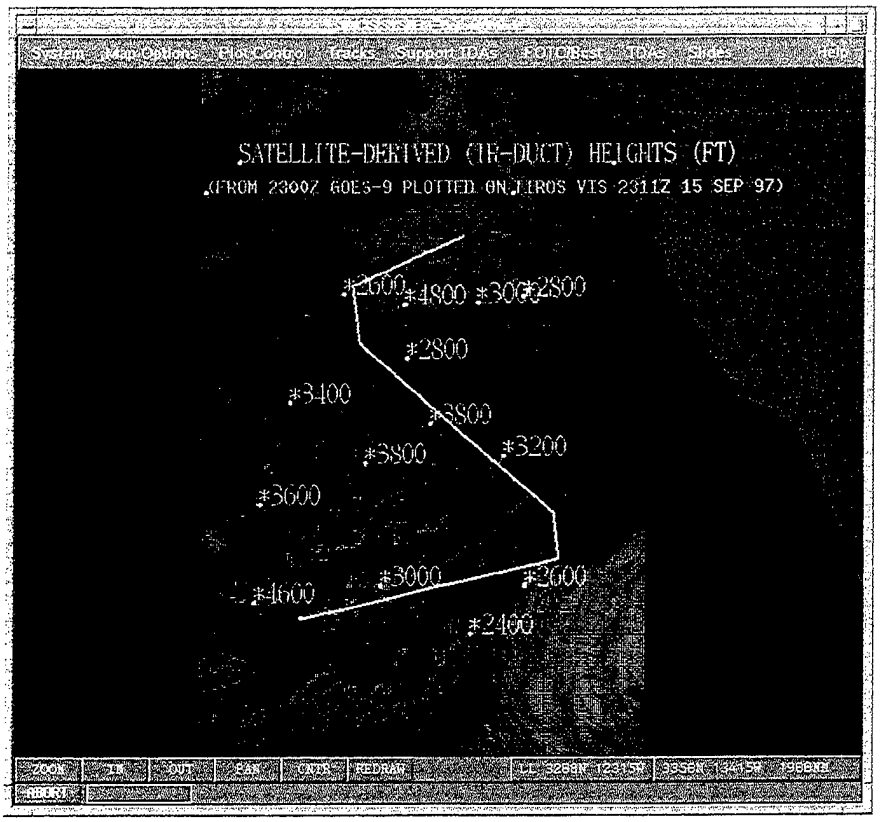

Figure 3. Sample screen from Experduct blending synoptic, satellite and climatological data.

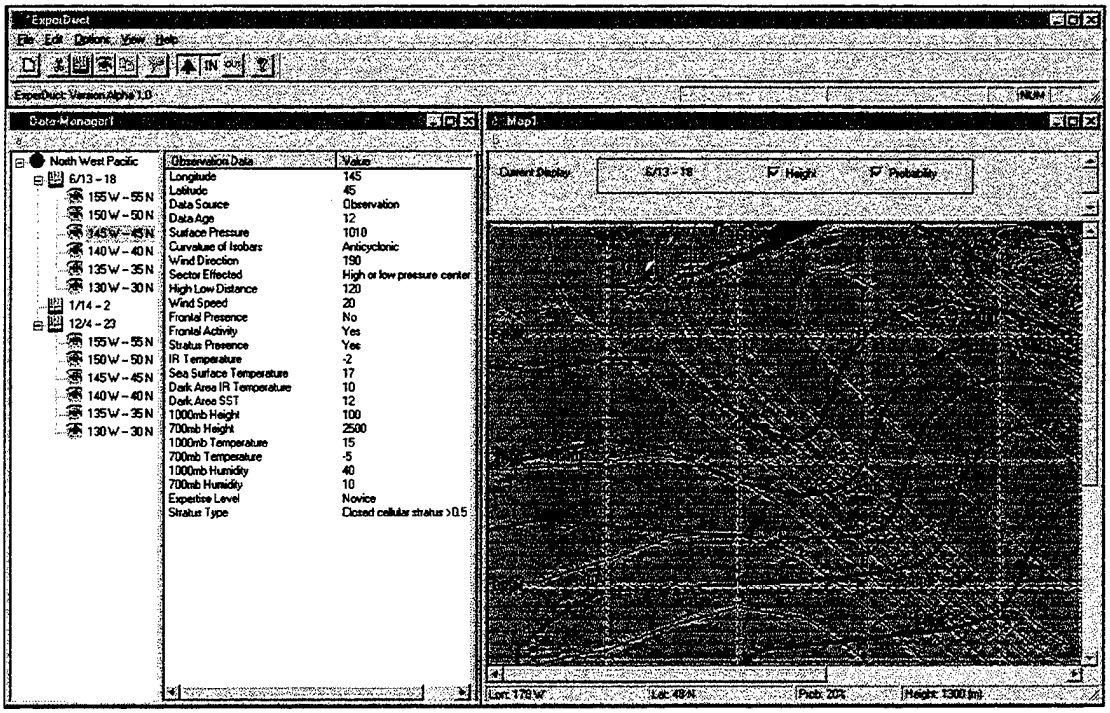

Figure 4. Communication paths used during STAFC test.

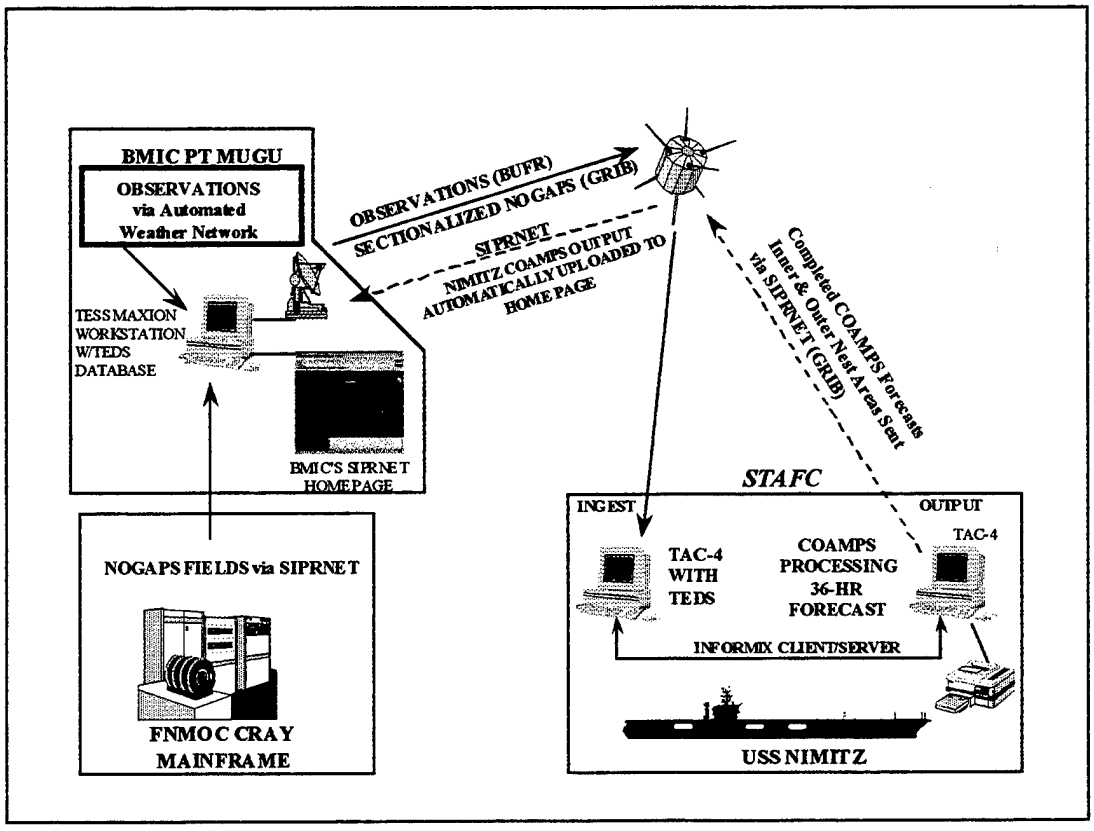

Figure 5. COAMPS output from NIMITZ

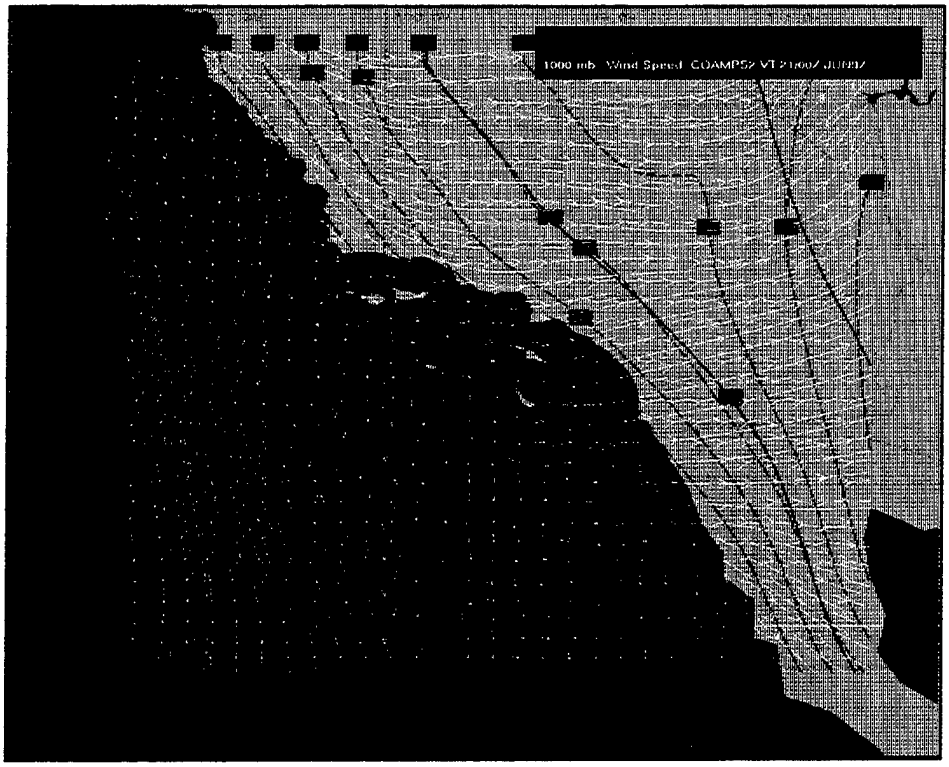

Figure 6. Air trajectories as function of time using COAMPS high resolution wind forecast.

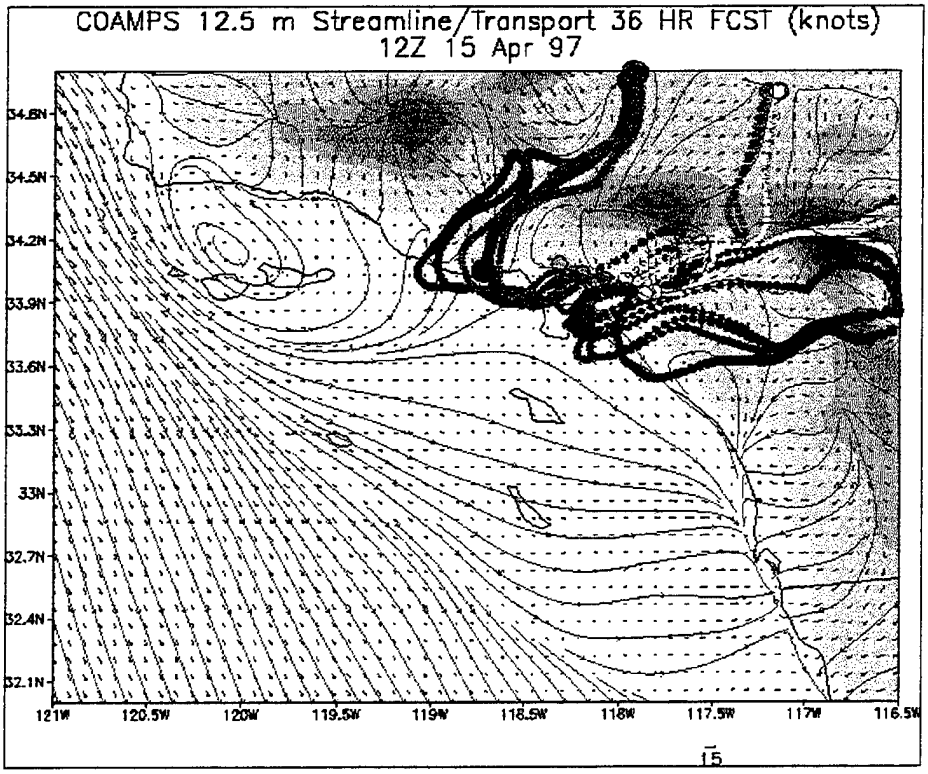

Figure 7. Forecast satellite cloud depiction.

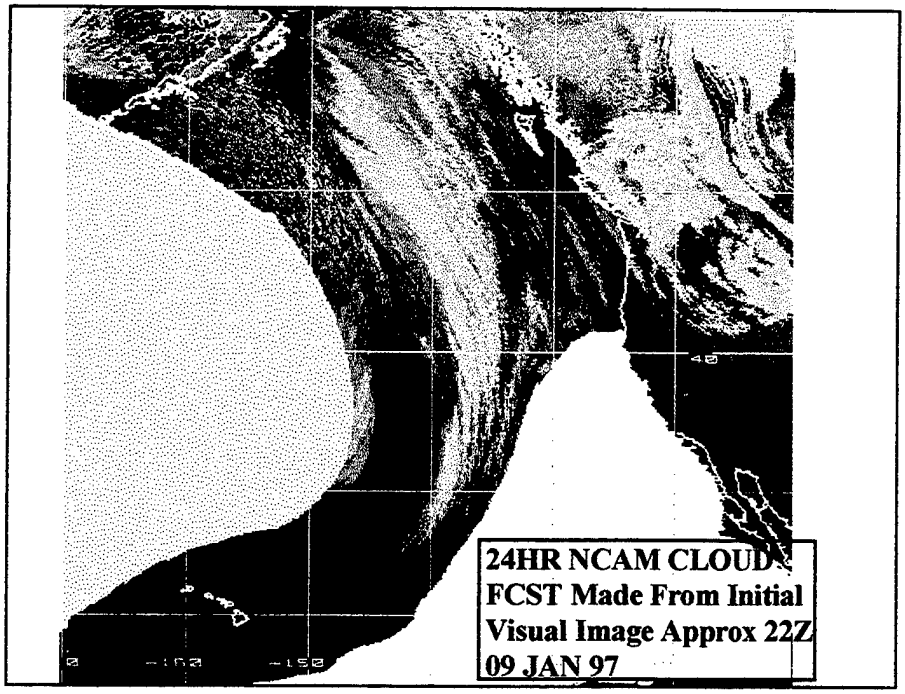

INTEGRATION OF WEATHER EFFECTS MODELS WITH REAL-TIME PHYSIOLOGICAL MEASUREMENTS IN THE DISMOUNTED INFANTRY BATTLESPACE

William T. Matthew, Reed W. Hoyt, Tammy J. Doherty, and Mark Buller
U.S. Army Research Institute of Environmental Medicine
Natick, MA 01760-5007

ABSTRACT

Dismounted soldiers can experience extraordinary combined stresses from local weather and mission requirements such as chemical protective encapsulation and movement over terrain with heavy loads. In real-time training and operational settings, the ability of command and control elements to assess health risks requires integration of physiologically based mathematical models with weather, terrain, and mission information resources. Currently, the lack of individual-specific data necessitates significant assumptions or generalizations about initial physiological state and anthropometric characteristics for predictive model input. Consequently, confidence limits for predicted group-average responses are wide, and the inherent uncertainties for individuals get worse in continuous or sustained operations scenarios. From our analysis of 30-second interval, body core temperature measurements from 10 Ranger students during 96 hours of swamp-phase training in February 1997, we conclude that an automated capability to initialize and run short-term prediction models "on the fly" for individual soldiers is needed to effectively identify those at risk. To accomplish this and as part of a broad technical effort to enable real-time physiological monitoring of individual soldiers in the dismounted infantry battlespace, we have developed a preliminary architecture to merge predictive models with individual soldier physiological measurements and real-time weather and terrain data resources. The approach employs a directory tree data archive structure, standard TCP/IP communications links, and the Unix-based MERCURY Test Bed as the prototype computation and display environment.

1. INTRODUCTION

The Dismounted Infantry Battlespace. Dismounted infantry soldiers are exposed to extraordinary combined thermal stresses from local weather and mission requirements such as chemical protective encapsulation and movement over terrain with heavy loads. The ability of command and control elements to assess the current and projected physiological status of these soldiers in real-time operational settings would significantly enhance soldier system situational awareness in critical force management decisions.

MERCURY and population-based predictive models. Using data from several fixed site weather stations, the Unix-based MERCURY system spreads weather data across a battle scale region of up to 200 x 200 kilometers (Fields et al., 1992) . The 1 km gridded weather parameters and terrain database provide a spatial context relevant to dismounted infantry operations, and a computational platform for physiologically-related predictive models and algorithms (Gagge and

Gonzalez, 1996; Pandolf et al., 1986; Tikuisius, 1995). Since June of 1996, a MERCURY Test Bed system at Eglin Air Force Base, Florida, has been used to automate the integration of real-time weather data from seven stations in the Range Automated Weather Stations (RAWS) system at Eglin with thermal strain prediction models (Matthew et al., 1996). With generalized inputs for workload, acclimatization status, hydration state, nutritional status and anthropometric characteristics this system can provide reasonable estimates of current thermal injury risk for a dismounted infantry unit. This is a totally non-intrusive command and control capability to assess time and mission-specific heat or cold injury risks on a *generic* group basis. Nevertheless, it is understood that some individuals will be hotter or colder, and at greater or lesser risk of injury because of their own variations from the generalized input values and from a host of contributing factors that may include recent thermal stress exposure history or predisposing illness. In reality, individual thermal strain responses are distributed about the population average response at any given time and this technology does not provide a means for leadership to identify those specific individuals in the *risk tails* of the response frequency distribution curve.

Why direct measures are needed. There are compelling reasons for technology investments in a direct physiological status monitoring capability for training or operational settings. These include a force management capability to intervene before a particular soldier becomes a casualty, and a medical casualty management capability to assess physiological status should an individual enter the medical care chain. It is now recognized that development of an individual warfighter physiological status monitoring capability is a desirable goal for Force XXI (Army Science and Technology Master Plan, 1997). The intended operational platform for validated physiological status monitoring capabilities has been identified as the Land Warrior System.

Why a technology push is needed for both the sensor and the data management systems. The dismounted infantry battlespace imposes severe technical constraints on physiological sensor systems. Ruggedness, maintainability, size, weight, and power requirements will ultimately determine the practical feasibility of wearable components. Equally challenging is the development of viable methods to manage the potentially massive streams of heterogeneous data these sensors will generate. A test-bed platform to evaluate the suitability of various user interface, display, and data archive resource options in a real-time command and control context that includes mission scenario, weather, and terrain is crucial to the development process. This paper describes our initial efforts to develop a test-bed system that leverages the existing predictive model based weather effects computation and data archive resources of MERCURY.

2. OBJECTIVES AND SCOPE

The primary objectives of this paper are to provide a brief illustration of a relevant physiological data set and to present a preliminary description of an adaptable, open test-bed platform to support fusion of real-time weather and warfighter physiological data with predictive models. Scope is limited to proposed output, process, and archive features for weather and physiological data streams that would arrive at the test-bed as data file elements over Internet resources.

3. MEASURED THERMAL RESPONSES

The emergence of physiological sensor technologies that allow unencumbered measurements on free moving soldiers provide an unprecedented view of the dynamic nature of physiological parameters in the field. The USARIEM Body Core Temperature Monitor (BCTM) temperature pill system provides a direct measure of a crucial physiological parameter. (O'Brien et al., 1996). In February 1997, using the BCTM system, we monitored the body core temperature responses of 10 Army Rangers during 4 days of routine training at Camp Rudder, Eglin AFB, Florida (Hoyt et al., 1997). These data illustrate the magnitude and extraordinarily dynamic nature of thermal responses of dismounted soldiers to weather and operational scenario. It is generally accepted that serious hypothermia risk begins as body core temperatures fall below 35.5 ° C (Hoyt et al., 1997) and that hyperthermia risks are associated with body core temperatures above 38.5 ° C (Sawka et al., 1992). Figure 1 shows that group average responses, during "mild" winter weather at Camp Rudder, came within roughly 0.5 ° C of both the heat and cold injury risk thresholds over the course of a single 24 hour period on 27/28 February.

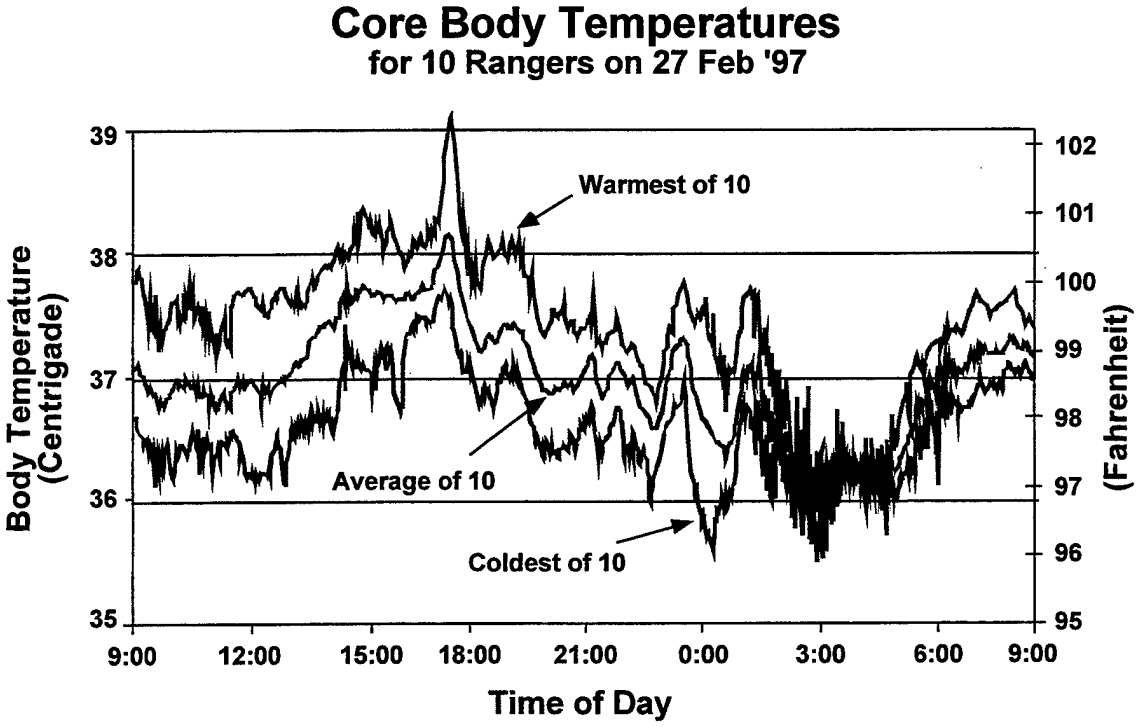

Figure 1. Body core temperatures of ten Army Rangers during routine training on 27/28 February 1997.

Moreover, these data show that the warmest individual reached a body core temperature in excess of 39 ° C at about 1730 local time (Air temp. 23 ° C) and the coldest soldier was at or near the 35.5 ° C threshold at midnight (Air temp. 21 ° C) and again at 0300 (Air temp. 21 ° C) on 28 February. These responses illustrate the need for an adaptable, open test-bed platform to evaluate strategies for handling physiological data streams that will include time and location-

stamped body core temperature data, as well as heart rate, expended energy, and other related physiological sensor data.

4. TECHNICAL APPROACH

Our approach is to leverage existing systems and infrastructure, minimize proprietary encapsulation of component technologies, and to focus primarily on a command and control oriented prototyping capability. The MERCURY system currently uses real-time weather data and mathematical thermal strain models to predict and display physiological impacts as map overlays on a geospatial scale relevant to dismounted infantry operations. It is a command and control computer "node" on a global network, with automated links to a weather data "node". It has the basic resources to support processing and archiving of physiological data streams coming from individual soldier nodes and its current weather information management and display structures are generally analogous to, and synergistic with those needed for physiological data. Figure 2 is a schematic overview of MERCURY with the addition of links to a consolidated soldier node, models, and physiological data archive.

Figure 2. Schematic overview of MERCURY integration with a soldier node, models, and physiological data archive.

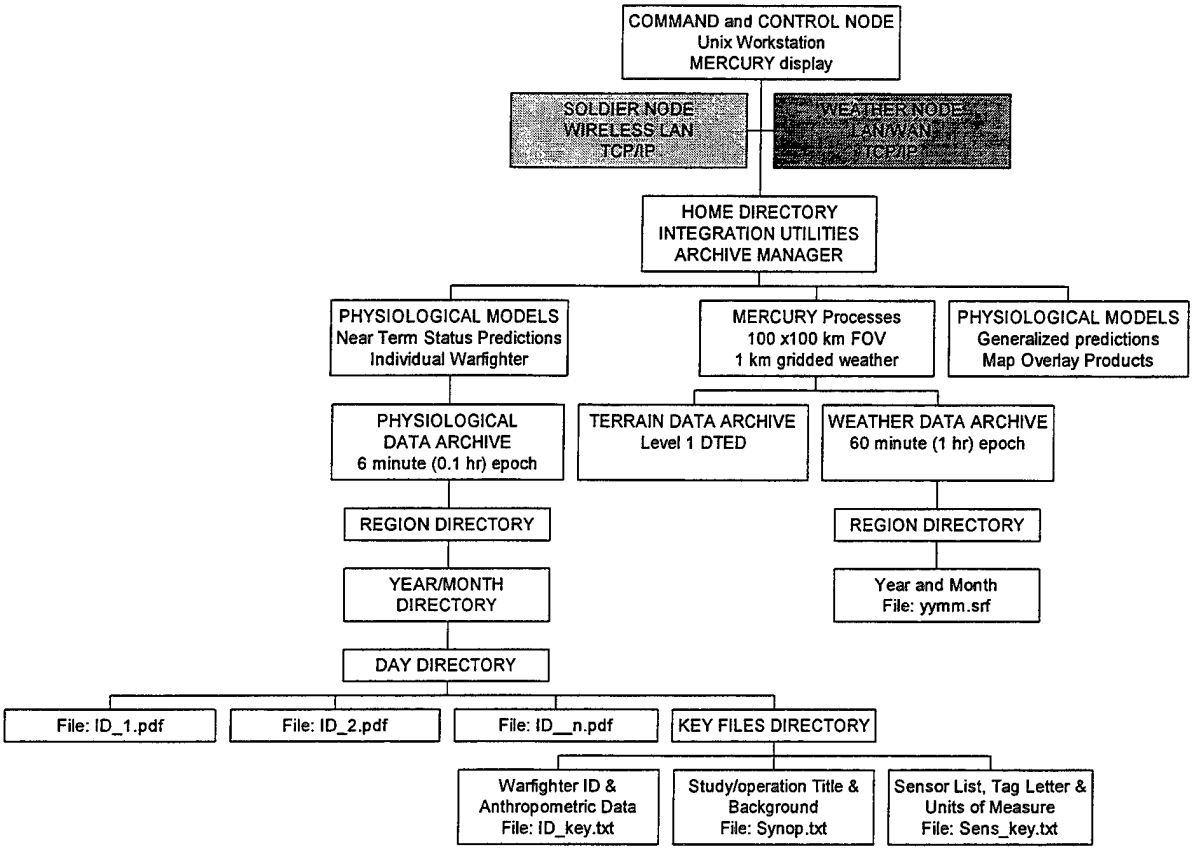

5. PHYSIOLOGICAL DATA ARCHIVE

The PPDU: The basic building block within the physiological data file archive will be the *Physiological Protocol Data Unit (PPDU)*. A PPDU, generated at the soldier node at rates of one or more per minute, is a line of time and geo-location stamped data with space delimited fields containing the individual warfighter's personal identification code and the measured physiological data elements. Initially, these may be received from the soldier node in blocks or "epochs" of six minutes in order to minimize File Transfer Protocol (FTP) connection loads . System flexibility and robustness in terms of missing data tolerance are viewed as a critical requirements. The proposed PPDU format anticipates occasional data losses from the sensors and places an alpha character tag as a prefix to each data field to specifically identify that parameter.

Physiological Data File (PDF): The Physiological Data File (PDF) will be a simple ASCII text file built from a concatenation of the PPDU records. The PDF file name will incorporate the date and soldier identification code and the file will "grow" until the date changes. At the date change, a new file will begin. Figure 3 shows a conceptual fragment of the proposed PDF that is in many ways analogous to a MERCURY weather data file.

Figure 3. Conceptual physiological data file fragment.

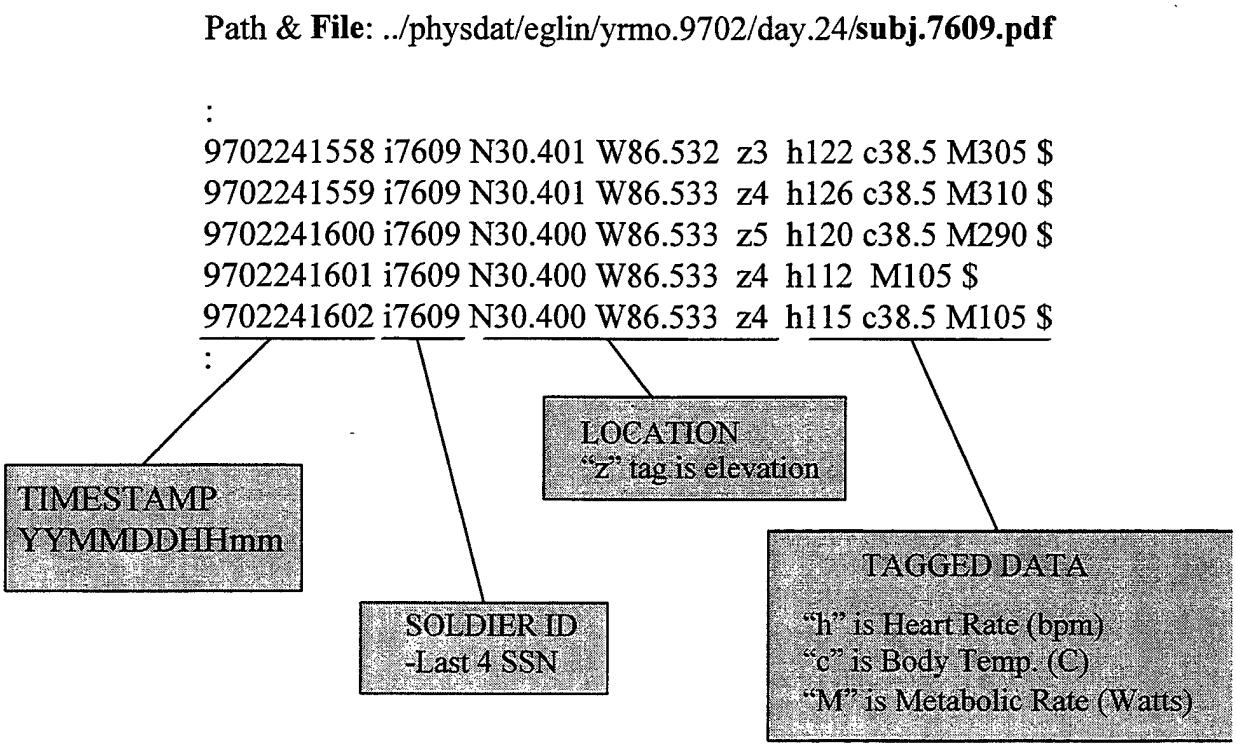

Related Files: An ASCII text " key" file relating each character tag to its respective sensor and units of measure will reside within each physiological data file directory. Another "key" file with ID codes as well as anthropometric and related information on each individual will be linked to each PDF. The physiological data file directory will also contain a catalog file giving a brief synopsis of the study or mission scenario, key personnel, and relevant background information.

Directory Structure: The directory structure for the physiological data archive, Figure 2, is organized first by geographic region, and then by year, month and day. Our intent is to employ a simple directory tree structure with a consistent and visible path architecture similar to that seen in the Internet's World Wide Web Universal Resource Locator (URL) notation. This test-bed directory structure should allow for a high degree of flexibility in evaluating data fusion strategies needed for real-time modeling and display. It will also provide a highly automated, Internet- accessible database for model validation and verification.

6. REAL-TIME PHYSIOLOGICAL STATUS AND SHORT TERM PROGNOSES

Real-time display of multiple physiological parameters from multiple soldier nodes would have limited value to military command and control echelons. The practical utilization of these data streams is critically dependant on the automation of those processes required to interpret the physiological measurements in a context that includes recent status history, mission demands for physical effort, and weather effects. Our intent is to develop a model, or suite of models, incorporating these elements and running continuously as background processes to provide concise, operationally useful information about an individual warfighter's current and predicted status either on user request or autonomously when physiological limits are approached.

Figure 4a. Conceptual Physiological Status Report.

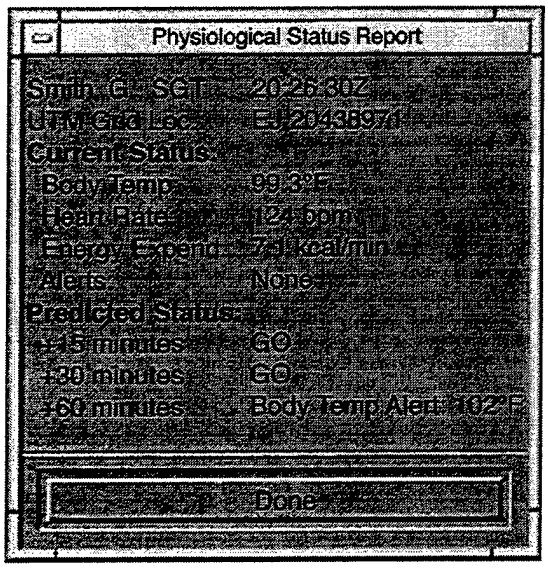

Although existing mathematical models may be adaptable to a real-time measure and predict forward capability for individual warfighters, it is very likely that a neural network approach will be required.

Figures 4a and 4b depict a conceptual warfighter physiological status report and how it might appear on the MERCURY Test bed display screen. This type of pop-up report would be programmed to automatically appear as a result of the hyperthermia state predicted for the + 60 minutes status for this individual. Other individual status reports could be viewed by clicking on the triangular soldier icons shown in Figure 4b.

Figure 4b. Physiological Status Report on MERCURY display screen.

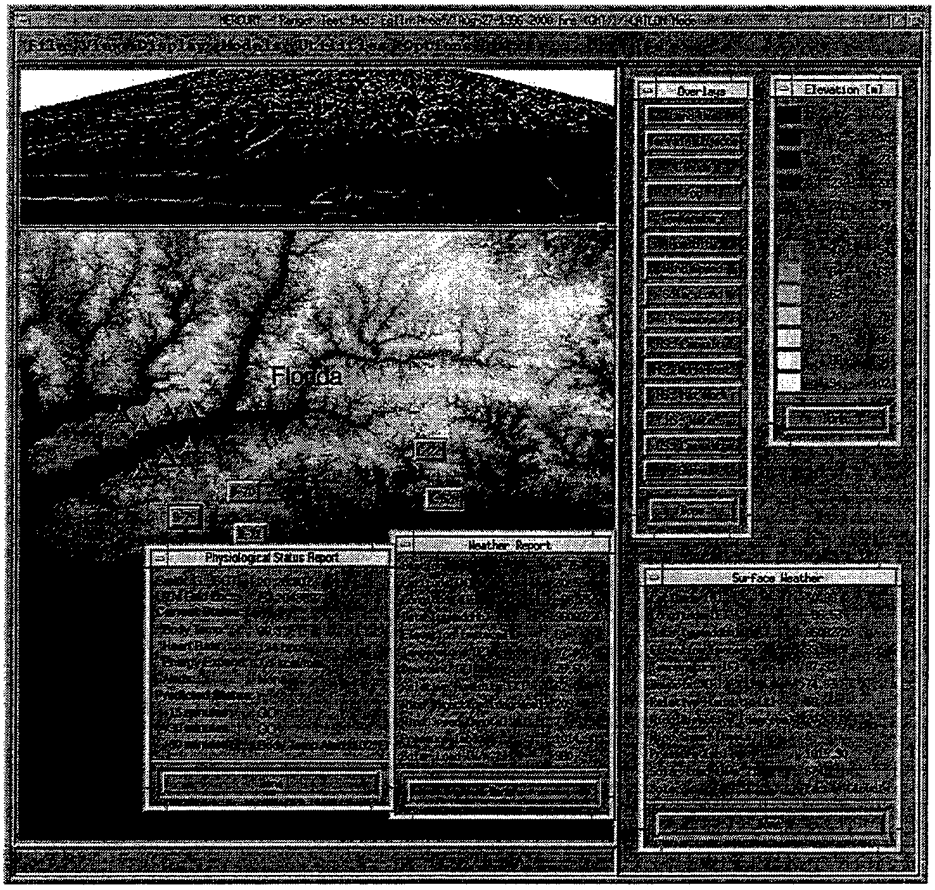

7. SUMMARY

There is a need for a rapid test and prototype capability to support the development of those technologies needed to bring warfighter physiological status monitoring capabilities to the dismounted infantry battlespace. We have a multi-process, multi-user computational platform with resources to support the integration of weather and terrain data with real-time individual warfighter physiological measurements in a context relevant to the dismounted infantry battlespace. Based on standard Transmission Control Protocol/ Internet Protocol (TCP/IP) communications links and a simple directory tree data archive structure, this system leverages the existing MERCURY Test Bed resources at Eglin Air Force Base, but could be used in real-time at any location with an Internet-accessible weather data node.

REFERENCES

Fields, C.A., J.E. Newberry, H.D. Pfeiffer, C.A. Soderlund, S.F. Kirby, and G.B. McWilliams, 1992: MERCURY: A heterogeneous system for spatial extrapolation of mesoscale meteorological data. *International Journal of Man-Machine Studies*, **36**, 309-326, 1992.

Gagge, A.P. and R.R. Gonzalez. Chapter 4. Mechanisms of Heat Exchange:Biophysics and Physiology, 1996. In: Handbook on Adaptation to the Environment. Part I, The Thermal Environment. M.J.Fregly and C.M. Blatteis (Eds.). American Physiological Society. Rockville, MD. pp45-84, 1996.

Hoyt, R.W., A.J. Young, W.T. Matthew, J.E. Kain, and M. Buller, 1997. Warfighter Physiological Status Monitoring (WPSM): Body Core Temperatures During 96 H of Swamp Phase Ranger Training. USARIEM Technical Report No. T97-4, 1997.

Matthew, W.T. , W.R. Santee, R.W. Hoyt, P. Tikuisis, E.S. Barnes, G.B. McWilliams, H.D. Pfeiffer, and J. Furlong, 1996. Automated Thermal Injury Risk Assessment in the Dismounted Infantry Battlespace. In Proceedings of the 1996 Battlespace Atmospherics Conference, NRAD, San Diego, California, pp 579-586, December 1996.

O'Brien, C., R.W. Hoyt, M.J. Buller, J.W. Castellani, and A.J. Young, 1997. Telemetry pill measurement of core temperature during active heating and cooling. USARIEM Technical Report No. T97-8, 1997.

Pandolf, K.B., L.A. Stroschein, L.L. Drolet, R.R. Gonzalez, and M.N. Sawka, 1986: Prediction modeling of physiological responses and human performance in the heat. *Computers in Biology and Medicine*, **16**, 319-329, 1986.

Sawka, M.N., A.J. Young,W.A. Latzka, P.D. Neufer, M.D. Quigley, and K.B. Pandolf, 1992. Human tolerance to heat during exercise: influence of hydration. *Journal of Applied Physiology*, **73**, 368-375, 1992.

Tikuisis, P., 1995: Predicting survival time for cold exposure. *International Journal of Biometeorology* **39**, 94-102, 1995.

A Refractive Index Structure Parameter Model

Arnold D. Tunick

U.S. Army Research Laboratory, Information Science and Technology Directorate
Battlefield Environment Division, 2800 Powder Mill Road, Adelphi, Md. 20783-1197

Abstract

The CN2 model is a semi-empirical algorithm that makes a quantitative assessment of atmospheric optical turbulence. The algorithm uses surface layer gradient assumptions applied to two levels of discrete vertical profile data to calculate the refractive index structure parameter. Model results can be obtained for unstable, stable, and near-neutral atmospheric conditions. The CN2 model has been benchmarked on data from the REBAL '92 field study. The model will shortly be added to the Electro-Optics Atmospheric Effects Library (EOSAEL). This paper contains technical and user's guide information on the CN2 model.

1. Introduction

Atmospheric optical turbulence is a problem for most electro-optical (EO) systems. The image distortion it promotes can drastically reduce system and sensor performance. A means of assessing the levels of optical turbulence, relying on calculations that require a minimum of atmospheric data, could be an advantage to those in the field of EO system design and application. This paper introduces the CN2 model, a semi-empirical algorithm developed by the Army Research Laboratory (ARL) for inclusion into the Electro-Optics Atmospheric Effects Library (EOSAEL), which addresses the atmospheric optical turbulence problem. This paper gives a mathematical outline of the CN2 model and provides some user's guide information on this new module intended for the EOSAEL.

The propagation of a light beam through the atmosphere is affected by random fluctuations in the refractive index of air (Kunkel et al., 1981). These fluctuations or discontinuities cause *optical turbulence*—variations in the speed at which the wavefront propagates. The refractive index structure parameter (C_n^2) is a quantitative measure of optical turbulence.

The value of C_n^2 has been generally observed to range from about 10^{-12} to 10^{-16} $m^{-2/3}$. High values of C_n^2, 10^{-12} $m^{-2/3}$ or greater, even over nominal distances, usually indicate turbulent atmospheres wherein considerable visual blurring or image distortion would be present (as if one were looking out over a hot paved road, over an airport runway, or, in an extreme case, through the exhaust behind a jet engine). At lower values of C_n^2, 10^{-16} to 10^{-15} $m^{-2/3}$, atmospheric optical turbulence would generally be considered negligible. (However, there could be other image-degrading effects arising from other factors, such as precipitation, fog, or smoke.)

Many simulation models have been developed that address optical turbulence in the atmospheric surface layer (Kunkel et al., 1981; Andreas, 1988; Miller and Ricklin, 1990; Tunick and Rachele, 1991; Sadot and Kopeika, 1992; Tofsted, 1993; and Rachele and Tunick, 1994); these models vary both in mathematical complexity and in the amounts and types of inputs and computer capabilities required. The CN2 model reported on here is a refractive index structure parameter model that makes a quantitative assessment of atmospheric optical turbulence given two levels of wind, temperature, and humidity profile data as input. It contains a surface layer profile structure algorithm derived by Rachele et al. (1991, 1995, 1996a) that makes estimates of C_n^2 obtainable for unstable, stable, and near-neutral atmospheric conditions. CN2 also computes the surface heat and moisture flux.

2. Mathematical Description of CN2 Model

The proposal to include CN2 in the EOSAEL was drafted only recently. The model itself, however, is based on a combination of concepts and algorithms that had been developed and partially validated over a number of years, such as those documented in Rachele et al. (1991, 1995, 1996ab), Tunick and Rachele (1991), Rachele and Tunick (1992, 1994), and Tunick et al. (1994). The motivation for these studies was principally to develop and verify a set of equations for the atmospheric stability portion of the calculations needed to evaluate an expression for C_n^2, such as the one given in Tatarski (1961), which can be written as

$$C_n^2(z) = b\frac{K_H}{\varepsilon^{1/3}}\left(\frac{\partial n}{\partial z}\right)^2 , \tag{1}$$

where b is equal to 3.2 and is called the Obukhov-Corrsin constant, K_H is the turbulent exchange coefficient for heat diffusion, ε is the energy dissipation rate (Panofsky, 1968), and $\partial n/\partial z$ is the vertical gradient of the index of refraction n. For visible and IR wavelengths, the expression for $\partial n/\partial z$, as presented in Tunick and Rachele (1991), is based on work reported by Andreas (1988). For the visible region and near-infrared wavelengths (0.36 to 3 μm) and for IR wavelengths (7.8 to 19 μm) in the range from –40.0 to +40.0 °C, the index of refraction gradient is determined as a function of wavelength (in micrometers), atmospheric pressure P (in millibars), and the partial derivatives with respect to height of potential temperature, $\partial\theta/\partial z$ (where θ is in kelvins) and specific humidity, $\partial q/\partial z$ (where q is in grams of water content per total grams of water and dry air combined). The surface layer algorithm called MARIAH (Rachele et al., 1991, 1995, 1996ab) is used to obtain a noniterative solution for the temperature and moisture partial derivatives. The MARIAH algorithm is based on a series of concepts more commonly known as similarity theory (as defined by the earlier efforts discussed in Obukhov (1946), Monin and Obukhov (1954), Businger et al. (1971), and Busch (1973)).

As similarity theory prescribes, the partial derivatives of wind speed, temperature, and moisture with respect to height can be written as

$$\frac{\partial V}{\partial z} = \frac{u_*}{kz}\phi_m , \quad \frac{\partial \theta}{\partial z} = \frac{\theta_*}{kz}\phi_H , \quad \frac{\partial q}{\partial z} = \frac{q_*}{kz}\phi_q , \tag{2}$$

where V is wind speed (m/s), u_* is the friction velocity (m/s), θ_* is the potential temperature scaling constant (K), q_* is the specific humidity scaling constant (g/g), z is height above ground, k is Karman's constant (0.4), and ϕ_m, ϕ_H, and ϕ_q are the dimensionless wind shear, dimensionless temperature lapse rate, and dimensionless humidity lapse rate, respectively. The MARIAH algorithm suggests that the scaling constants in Eq. (2) can be expressed as

$$u_* = \frac{k\Delta V}{\phi_m \Delta \ln z}, \quad \theta_* = \frac{k\Delta \theta}{\phi_H \Delta \ln z}, \quad q_* = \frac{k\Delta q}{\phi_H \Delta \ln z}, \tag{3}$$

where the Δ operator refers to the difference in data taken from one tower level to another (i.e., $V_2 - V_1$). Here, the dimensionless term for humidity is assumed equal to the dimensionless temperature lapse (i.e., $\phi_q = \phi_H$), even though field observations have shown that atmospheric gradients of temperature do not always behave similarly to those of moisture. The relationships in Eq. (3) can be solved in a straightforward manner, given expressions for the dimensionless shear and lapse rate terms. Following Dyer (1974) and Hicks (1976), we use

$$\phi_m = [1 - 15(z/L)]^{-1/4} \text{ and } \phi_H [1 - 15(z/L)]^{-1/2}, \tag{4}$$

for unstable atmospheric conditions, and from Webb (1970), we use

$$\phi_m = \phi_H = 1 + 5(z/L)], \tag{5}$$

for stable atmospheric conditions. Busch (1973) defines the Monin-Obukhov (M-O) scaling ratio as

$$\frac{z}{L} = k \frac{g}{\theta_v} \frac{\theta_{v*}}{u_*^2} z, \tag{6}$$

where $\theta_v = \theta(1 + 0.61q)$ is the virtual potential temperature, and $\theta_{v*} = \theta_* + 0.61\theta q_*$ is the virtual potential temperature scaling constant. (This equation for the M-O scaling ratio, which reflects atmospheric stability in terms of the scaling constants in Eq. (3), includes the effects of water (vapor) content by considering the dry or virtual atmosphere. The virtual temperature is the temperature that dry air must have for its density to equal that of moist air at the same pressure (Stull, 1988).) Therefore, from Eqs. (3) and (6), the expression for the Obukhov length L in Eqs. (4) and (5) can be formulated as

$$L = \frac{1}{\Delta \ln z} \frac{\theta_v}{g} \frac{(\Delta V)^2 \phi_H}{[\Delta\theta + 0.61\theta\Delta q]\phi_m^2}, \tag{7}$$

so that for unstable atmospheric conditions,

$$L = \frac{1}{\Delta \ln z} \frac{\theta_v}{g} \frac{(\Delta V)^2}{\Delta\theta + 0.61\theta\Delta q}. \tag{8}$$

For stable atmospheric conditions, it can be expressed as

$$L\phi_m = \frac{1}{\Delta \ln z} \frac{\theta_v}{g} \frac{(\Delta V)^2}{\Delta\theta + 0.61\theta\Delta q}. \tag{9}$$

Note that the surface layer gradients referred to by the expressions in Eq. (2) should be taken to mean those tangent to the indicated profiles at $z = z^*$, where $z^* = \Delta z/(\Delta \ln z)$, instead of $z^* = (z_1 \cdot z_2)^{1/2}$, the geometric mean, which is almost always assumed (Rachele

and Tunick, 1991; Rachele et al., 1991). The relationships for profiles of C_n^2 that are generally accepted for $z \leq |L|$ can be expressed as

$$C_n^2(z) = C_n^2(z^*) \cdot \left(\frac{z}{z^*}\right)^{-4/3} \quad \text{and} \quad C_n^2(z) = C_n^2(z^*) \cdot \left(\frac{z}{z^*}\right)^{-2/3} \quad , \tag{10}$$

for unstable and stable or near-neutral atmospheric conditions, respectively, where the –4/3 and –2/3 behavior were indicated by experimental surface layer data (as discussed in somewhat more detail by Wyngaard, 1973, and Wyngaard and LeMone, 1980).

3. Verification

The CN2 model was benchmarked on data collected during the field study entitled "Radiation Energy Balance Experiment for Imagery and EM Propagation" (REBAL '92). REBAL '92 (Tunick et al., 1994) was conducted during May and July 1992 at Bushland, TX (35°N latitude, 102°W longitude, 1170-m elevation above mean sea level), by the Army Research Laboratory (ARL) and the Conservation and Production Research Laboratory (CPRL) of the USDA Agricultural Research Service (ARS). (The Bushland test site is approximately 16 km due west of Amarillo.) Diurnal measurements of sky and emitted radiation, soil heat flux, soil temperature and volumetric water content, evaporation, optical turbulence (from a scintillometer*), near- and far-field infrared imager data, and micrometeorological profile data were collected over wet and dry bare soil for clear and cloudy sky conditions.

The micrometeorological profiles of wind speed, temperature, and relative humidity were measured on an 8-m tower centered in the test area (at 0.5, 1, 2, 4, and 8 m above the surface). A 0.94-μm scintillometer (Lockheed Engineering & Management IV-L†) source module was mounted 2 m above ground on a tripod at the north end of the test area and was aligned and focused down-field (i.e., to the south) over a path of approximately 450 m.

Figure 1 shows time series from CN2 model results compared to time series of the observed data. Each plot reflects conditions during the same collection interval (i.e., 8 July 1992, 1230 local time (LT), to 9 July 1992, 2100 LT), except that the wind speed, temperature, and relative humidity input data (15-min averaged) are taken from different heights above ground (that is, 1 and 4 m, 2 and 4 m, and 4 and 8 m above ground, respectively).

Overall, the C_n^2 estimates appear to be in line with the observations. However, there are several instances when the CN2 model results are in extreme contrast to the scintillometer data. These occur numerically when the computed temperature gradients are very, very small: small enough to cause singularities in the model calculations. They occur physi-

---

* Scintillometers are ground-based, remote-sensing instruments designed to measure optical turbulence intensity along a line-of-sight path established between a transmitter and a downrange receiver. Scintillometer operation is based on the principle that scintillations or light intensity variations occur as atmospheric density discontinuities create refraction effects in light propagating along a path (Clifford et al., 1974). The refractive index structure parameter, C_n^2, is related to the intensity of these refraction effects.

† The use of company or corporation names with regard to instrumentation and equipment does not constitute an endorsement by either the U.S. Army or the USDA-ARS.

cally during periods, however brief, of near-neutral or neutral atmospheric stability. Figure 2 is a time series of temperature data, measured at four heights above ground level. Segments of the data (indicated on the figure by arrows) illustrate where differences in temperature from one level to the next (i.e., the gradients) are slight and nearly impossible to distinguish. Apparently, the CN2 model's "local-gradient" approach tends to exaggerate the near zero- and zero-gradient situations. Future studies using more complex sets of equations for the atmosphere may help to improve upon turbulence assessments at these times.

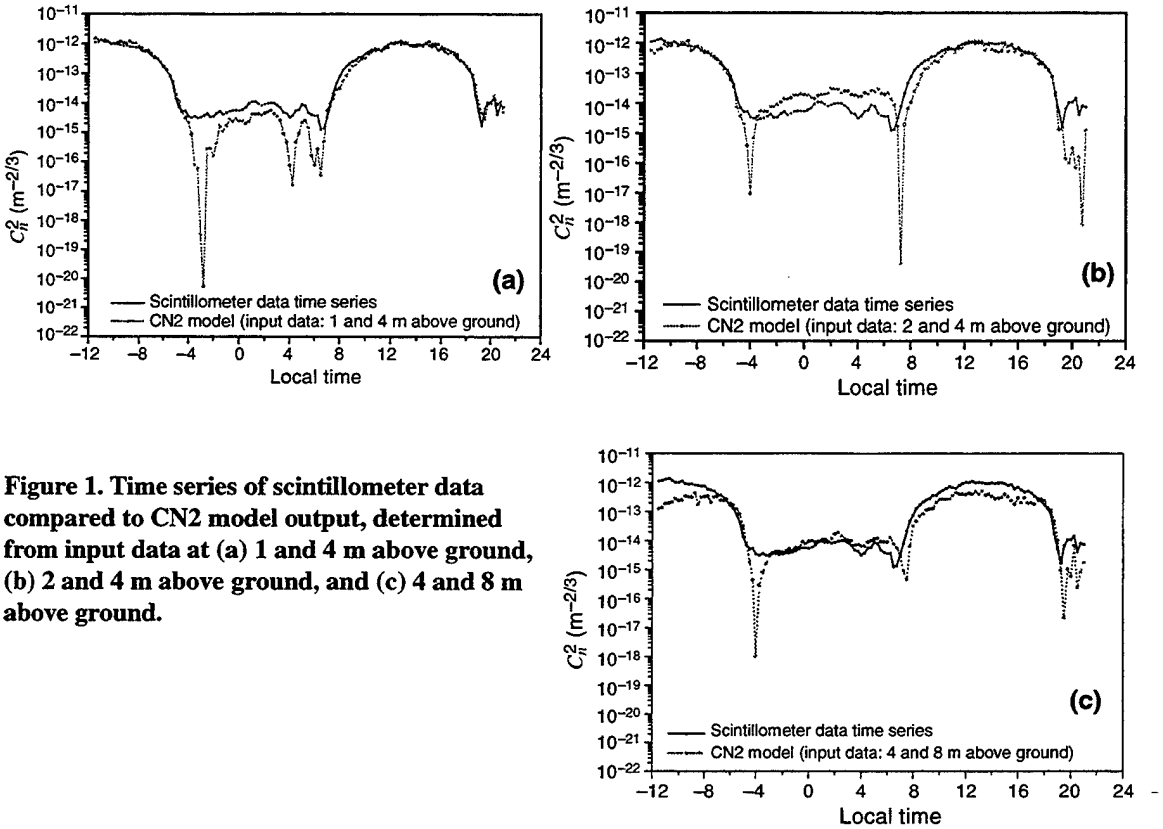

Figure 1. Time series of scintillometer data compared to CN2 model output, determined from input data at (a) 1 and 4 m above ground, (b) 2 and 4 m above ground, and (c) 4 and 8 m above ground.

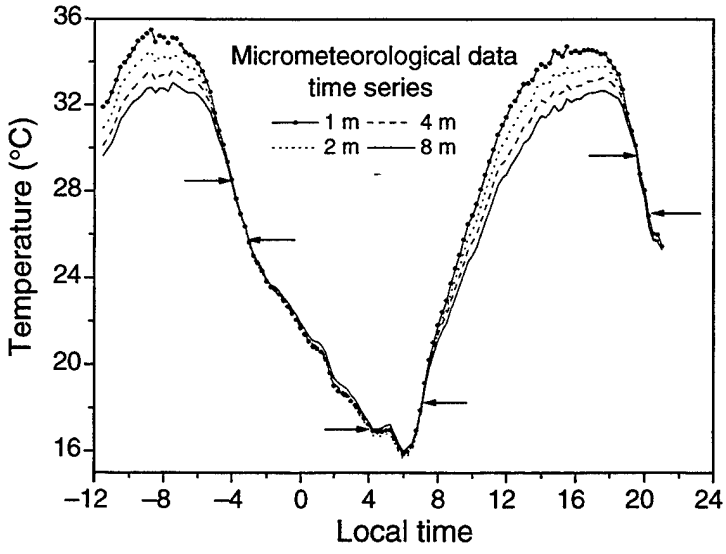

Figure 2. Time series of temperature data collected during REBAL '92 field study, 8–9 July 1992.

Finally, the time series analysis of temperature gradients shown in figure 3 implies that the most unstable gradients were described by data closer to the ground (resulting in higher estimates of optical turbulence during daytime hours). However, these data did not describe the greater stable gradients. An unexpected result from this study (as indicated in the figure by the solid squares) was that the greater stable gradients (and estimates of C_n^2) for much of the nighttime hours were described by data from 2 and 4 m.

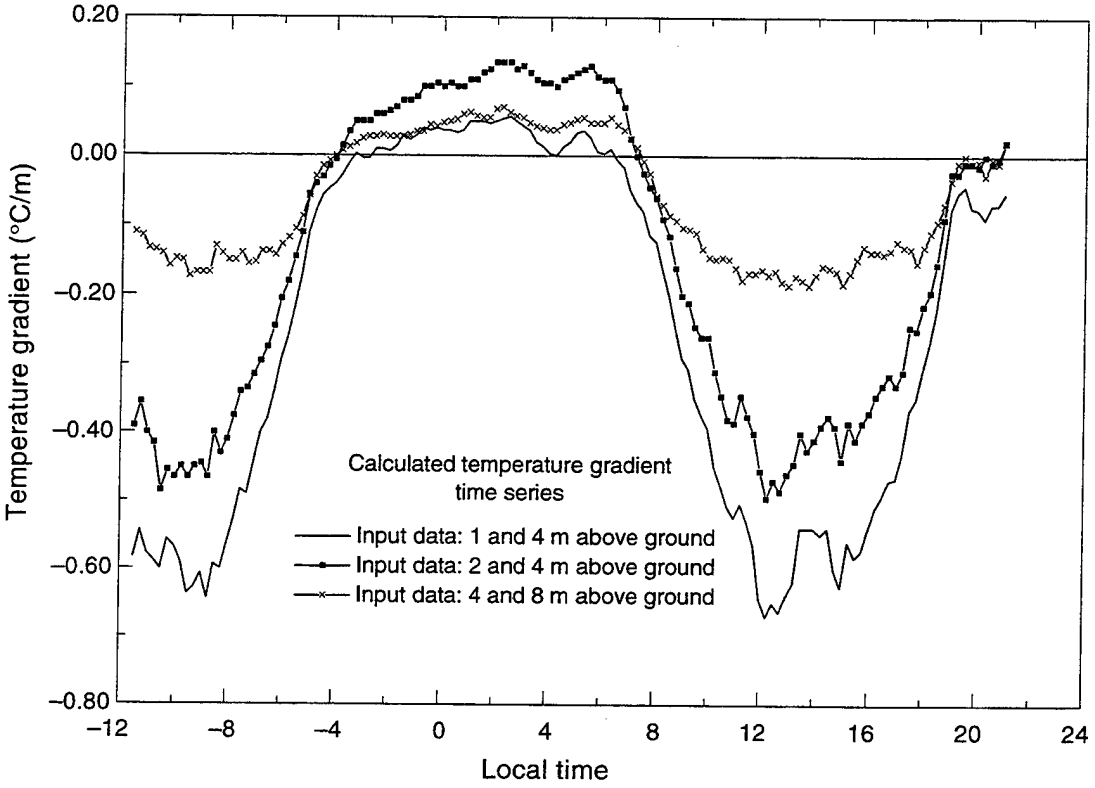

Figure 3. Time series of calculated temperature gradients from data collected during REBAL '92 field study, 8–9 July 1992.

4. CN2 Model User's Information

CN2 is one of several new modules that ARL is developing for inclusion into the EOSAEL. This state-of-the-art computer library comprises fast-running, theoretical, semiempirical, and empirical computer programs that mathematically describe aspects of electromagnetic propagation in battlefield environments. The modules are connected through an executive routine, but are often exercised individually (Wetmore et al., 1997 (this volume)).

There are four input file records (referred to as "input cards") that contain the wavelength and meteorological data for the CN2 model calculations. Two additional cards (not shown) control program execution. Table 1 gives descriptions of the CN2 model input cards, along with range restrictions recommended for the parameters that these cards control.

Table 1. CN2 model input cards and parameter range restrictions.

Card	Identifier	Variable	Description	Recommended range restrictions
1	WAVE	WV	Wavelength (μm)	Visible: 0.36 μm ≤ WV ≤ 3.0 μm IR: 7.8 μm ≤ WV ≤ 19.0 μm
2	DATM	PR	Atmospheric pressure (mb) (at surface or either measurement height)	700 mb ≤ PR ≤ 1060 mb
3	LVL1	HGHT1	Height (m) above ground level, level 1 data	HGHT1 ≤ HGHT2 ≤ 20 m HGHT1 ≠ HGHT2 HGHT1 ≥ 0.5 m HGHT2 ≥ 1.0 m 0.5 m ≤ HGHT2 – HGHT1 ≤ 18.0 m
		TEMP1	Temperature (°C) at HGHT1	TEMP1 ≠ TEMP2 –40.0 °C ≤ (TEMP1, TEMP2) ≤ +40.0 °C
		WSPD1	Wind speed (m/s) at HGHT1	WSPD1 < WSPD2 0.0 m/s ≤ WSPD1 ≤ 18.0 m/s 1.0 m/s ≤ WSPD2 ≤ 18.0 m/s
		RHUM1	Relative humidity (%) at HGHT1	0% ≤ (RHUM1, RHUM2) ≤ 100%
4	LVL2	HGHT2 TEMP2 WSPD2 RHUM2	(parallel to LVL1 variables above)	(see above)

5. Output Examples

In this section, I present examples of the output produced by the CN2 model for the three general categories of atmospheric conditions: unstable, stable, and near-neutral atmospheric conditions.

5.1 Calculation for Unstable Atmospheric Conditions

Example 1 takes meteorological data from the REBAL '92 field study for 9 July 1992 at 1330 LT. The input data are representative of typical mid-afternoon, clear sky, unstable atmospheric conditions. The surface heat and moisture flux calculations reflect intense gradients of surface layer temperature and specific humidity. The computed C_n^2 at 2 m is on the order of 10^{-12}.

```
WAVELENGTH                    .94   MICRONS

ATMOSPHERIC PRESSURE       891.60   MB

LEVEL1 METEOROLOGY AT        1.00   METERS
AIR TEMPERATURE             33.44   C
WINDSPEED                    5.39   M/S
RELATIVE HUMIDITY           30.20   %

LEVEL2 METEOROLOGY AT        4.00   METERS
AIR TEMPERATURE             31.42   C
WINDSPEED                    6.35   M/S
RELATIVE HUMIDITY           32.90   %

SURFACE HEAT FLUX           468.01   W/M^2
SURFACE MOISTURE FLUX       209.46   W/M^2

"UNSTABLE ATMOSPHERE"
TEMPERATURE GRADIENT    -.6635E+00   DEGK/M
MOISTURE GRADIENT       -.1188E-03   G/G/M
```

```
 REFRACTIVE INDEX STRUCTURE PARAMETER = CN^2   M^(-2/3)
-------------------------------------------------------------
   Z=1       Z=2       Z=5       Z=10      Z=15      Z=20
-------------------------------------------------------------
3.843E-12 1.525E-12 4.495E-13 1.784E-13 1.039E-13 7.079E-14
-------------------------------------------------------------
```

5.2 Calculation for Stable Atmospheric Conditions

Example 2 takes meteorological data from the REBAL '92 field study for 9 July 1992 at 0200 LT. The input data are representative of typical nighttime atmospheric conditions under mostly cloudless skies. The calculated heat flux reflects a slight surface inversion in temperature within this weakly stable layer. The computed C_n^2 at 2 m is on the order of 10^{-14}.

```
    WAVELENGTH                    .94   MICRONS

    ATMOSPHERIC PRESSURE       893.50   MB

    LEVEL1 METEOROLOGY AT        1.00   METERS
    AIR TEMPERATURE             18.73   C
    WINDSPEED                    2.77   M/S
    RELATIVE HUMIDITY           64.00   %

    LEVEL2 METEOROLOGY AT        4.00   METERS
    AIR TEMPERATURE             19.06   C
    WINDSPEED                    3.80   M/S
    RELATIVE HUMIDITY           64.60   %

    SURFACE HEAT FLUX           -20.07   W/M^2
    SURFACE MOISTURE FLUX       -42.07   W/M^2

    "STABLE ATMOSPHERE"
    TEMPERATURE GRADIENT      .1198E+00  DEGK/M
    MOISTURE GRADIENT         .1005E-03  G/G/M
```

```
 REFRACTIVE INDEX STRUCTURE PARAMETER = CN^2   M^(-2/3)
-------------------------------------------------------------
   Z=1       Z=2       Z=5       Z=10      Z=15      Z=20
-------------------------------------------------------------
3.619E-14 2.280E-14 1.238E-14 7.798E-15 5.951E-15 4.912E-15
-------------------------------------------------------------
```

5.3 Calculation for Near-Neutral Atmospheric Conditions

Example 3 takes meteorological data from the REBAL '92 field study for 9 July 1992 at 0630 LT. The input data are representative of typical atmospheric conditions that tend to occur daily within an hour after sunrise. During this interval of time, there is almost always at least one instance of a near-neutral lapse in temperature as the ground warms with increasing amounts of incident solar radiation that begins to break up the nighttime inversion. The calculated surface fluxes at this time are small. The computed C_n^2 at 2 m is on the order of 10^{-17}.

```
    WAVELENGTH                    .94   MICRONS

    ATMOSPHERIC PRESSURE       893.00   MB

    LEVEL1 METEOROLOGY AT        1.00   METERS
```

```
AIR TEMPERATURE              16.25   C
WINDSPEED                     2.88   M/S
RELATIVE HUMIDITY            74.04   %

LEVEL2 METEOROLOGY AT         4.00   METERS
AIR TEMPERATURE              16.20   C
WINDSPEED                     3.72   M/S
RELATIVE HUMIDITY            75.05   %

SURFACE HEAT FLUX              1.45   W/M^2
SURFACE MOISTURE FLUX        -17.62   W/M^2

"NEAR-NEUTRAL ATMOSPHERE"
TEMPERATURE GRADIENT     -.6866E-02   DEGK/M
MOISTURE GRADIENT         .3327E-04   G/G/M
```

REFRACTIVE INDEX STRUCTURE PARAMETER = CN^2 M^(-2/3)

Z=1	Z=2	Z=5	Z=10	Z=15	Z=20
5.856E-17	3.689E-17	2.003E-17	1.262E-17	9.628E-18	7.948E-18

6. Summary

The CN2 model will shortly be added to the Electro-Optics Atmospheric Effects Library (EOSAEL). By applying surface layer gradient assumptions for two levels of wind, temperature, and humidity profile data to the calculation of the refractive index structure parameter C_n^2, the CN2 model makes a quantitative assessment of atmospheric optical turbulence. The model was benchmarked on REBAL '92 field study data. CN2 will be made available to U.S. Government agencies, specified allied organizations, and their authorized contractors through ARL's EOSAEL point of contact, Alan Wetmore.

References

Andreas, E. L., 1988: "Estimating C_n^2 over Snow and Sea Ice from Meteorological Data," *J. Opt. Soc. Am.* **5** (4), 481–495.

Busch, N. E., 1973: "On the Mechanics of Atmospheric Turbulence," *Workshop on Micrometeorology,* D. A. Haugen (ed.), American Meteorological Society, Boston, MA, pp 1–65.

Businger, J. A., J. C. Wyngaard, Y. Izumi, and E. F. Bradley, 1971: "Flux-Profile Relationships in the Atmospheric Surface Layer," *J. Atmos. Sci.* **28**, 181–189.

Clifford, S. F., G. R. Ochs, and R. S. Lawrence, 1974: "Saturation of Optical Scintillation by Strong Turbulence," *J. Opt. Soc. Am.* **64**, 148–154.

Dyer, A. J., 1974: "A Review of Flux-Profile Relationships," *Bound.-Layer Meteorol.* **7**, 363–372.

Hicks, B. B., 1976: "Wind Profile Relationships from the Wangara Experiment," *Q. J. R. Meteorol. Soc.* **102**, 535–551.

Kunkel, K. E., D. L. Walters, and G. A. Ely, 1981: "Behavior of the Temperature Structure Parameter in a Desert Basin," *J. Appl. Meteorol.* **20**, 130–136.

Miller, W. B., and J. C. Ricklin, 1990: *A Module for Imaging Through Optical Turbulence: IMTURB*, Atmospheric Sciences Laboratory, ASL-TR-0221-27 (available from Army Research Laboratory, 2800 Powder Mill Road, Adelphi, MD 20783-1197).

Monin, A. S., and A. M. Obukhov, 1954: "Basic Regularity in Turbulent Mixing in the Surface Layer of the Atmosphere," *Trans. Geophys. Inst. (Trudy) Acad. Sci. USSR* **24**, 163–187.

Obukhov, A. M., 1946: "Turbulence in an Atmosphere of Non-Homogeneous Temperature," *Trans. Inst. Theor. Geophys. USSR* **1**, 95–115.

Panofsky, H. A., 1968: "The Structure Constant for the Index of Refraction in Relation to the Gradient of the Index of Refraction in the Surface Layer," *J. Geophys. Res.* **73**, 6047–6049.

Rachele, H., and A. Tunick, 1991: *On the Subject of Geometric Spacing of Meteorological Sensors,* Atmospheric Sciences Laboratory, ASL-TMR-0011 (available from Army Research Laboratory, 2800 Powder Mill Road, Adelphi, MD 20783-1197).

Rachele, H., A. Tunick, and F. V. Hansen, 1991: *A Method for Estimating Similarity Scaling and Obukhov Lengths from Discrete Vertical Profile Data,* Atmospheric Sciences Laboratory, ASL-TR-0303 (available from Army Research Laboratory, 2800 Powder Mill Road, Adelphi, MD 20783-1197).

Rachele, H., and A. Tunick, 1992: *Sensitivity of C_n^2 to Random Variations of Windspeed, Sensible Heat Flux, and Latent Heat Flux,* Atmospheric Sciences Laboratory, ASL-TR-0308 (available from Army Research Laboratory, 2800 Powder Mill Road, Adelphi, MD 20783-1197).

Rachele, H., and A. Tunick, 1994: "Energy Balance Model for Imagery and Electromagnetic Propagation," *J. Appl. Meteorol.* **33**, 964–976.

Rachele, H., A. Tunick, and F. V. Hansen, 1995: "MARIAH—A Similarity Based Method for Determining Wind, Temperature, and Humidity Profile Structure in the Atmospheric Surface Layer," *J. Appl. Meteorol.* **34**, 1000–1005.

Rachele, H., A. Tunick, and F. V. Hansen, 1996a: "Reply," *J. Appl. Meteorol.* **35** (4), 613–614. (Reply to Arya, S. P., 1996: "Comments on 'MARIAH—A Similarity Based Method for Determining Wind, Temperature, and Humidity Profile Structure in the Atmospheric Surface Layer,' " *J. Appl. Meteorol.* **35** (4), 610–612.)

Rachele, H., A. Tunick, L. Kordova, and Y. Mahrer, 1996b: "A Radiation and Energy Balance Model for the Microscale-Surface Layer Environment," *Proc. 22nd Conf. Agri. Forest Meteorol.*, 28 January–2 February, Atlanta, American Meteorological Society, Boston.

Sadaot, D., and N. S. Kopeika, 1992: "Forecasting Optical Turbulence Strength on the Basis of Macroscale Meteorology and Aerosols: Model and Validation," *Opt. Eng.* **31** (2), 200–212.

Stull, R. B., 1988: *An Introduction to Boundary Layer Meteorology*, Kluwer Academic Publishers.

Tatarski, V. I., 1961: *Wave Propagation in a Turbulent Medium,* McGraw-Hill.

Tofsted, D. H., 1993: *A Surface Energy Budget Model Modifying Heat Flow by Foliage Effects,* Army Research Laboratory, ARL-TR-60.

Tunick, A., 1995: "ARL Professional Exchange Program (APEX) to Israel," *Proc. Battlefield Atmospherics Conference*, 28–30 November, White Sands Missile Range, NM (available from Army Research Laboratory, 2800 Powder Mill Road, Adelphi, MD 20783-1197).

Tunick, A., and H. Rachele, 1991: "Estimating the Effects of Temperature and Moisture on C_n^2 in the Damp Unstable Boundary Layer for Visible, Infrared, Radio, and Millimeter Wavelengths," *Proc. Battlefield Atmospherics Conference*, 3–6 December, Fort Bliss, TX (available from Army Research Laboratory, 2800 Powder Mill Road, Adelphi, MD 20783-1197).

Tunick, A., H. Rachele, F. V. Hansen, T. A. Howell, J. L. Steiner, A. D. Schneider, and S. R. Evett, 1994: "REBAL '92—A Cooperative Radiation and Energy Balance Field Study for Imagery and EM Propagation," *Bull. Am. Meteorol. Soc.* **75**, 421–430.

Webb, W. K., 1970: "Profile Relationships: The Log-Linear Range, and Extension to Strong Stability," *Q. J. R. Meteorol. Soc.* **96**, 67–90.

Wetmore, A., P. Gillespie, A. McCann, and J. Schroeder, 1997: "EOSAEL—Current Work and Future Directions," *Proc. Battlespace Atmospherics Conference*, 2–4 December, San Diego, CA.

Wyngaard, J. C., 1973: "On Surface-Layer Turbulence," *Workshop on Micrometeorology*, D. A. Haugen (ed.), American Meteorological Society, Boston, MA, pp 101–149.

Wyngaard, J. C., and M. A. LeMone, 1980: "Behavior of the Refractive Index Structure Parameter in the Entraining Convective Boundary Layer," *J. Atmos. Sci.* **37** (3), 1573–1585.

Passive Radar Observation of the Battlespace Environment

Mr. Robert J. Farrell Jr. and Capt Robert D. Duncomb Jr.
Air Force Research Laboratory Information Directorate
AFRL/IFO-WE, Acquisition Meteorology Office
26 Electronic Parkway, Rome, NY 13441
(315) 330-3085, we@rl.af.mil

Mr. Paul F. Gilgallon
Air Force Research Laboratory Sensors Directorate
AFRL/SNRD, Surveillance Radar Technology
26 Electronic Parkway, Rome, NY 13441
(315) 330-4409, gilgallonp@rl.af.mil

ABSTRACT

Throughout history, weather has dramatically impacted man's ability to wage war. Many military campaigns have failed because of inadequate planning or respect for inclement weather. Joint Vision 2010's dependence on Precision Guided Munitions (PGMs) to reach our national objectives requires an increased emphasis on weather conditions at the target site. Knowing the weather at time-over-target is critical to mission success since inclement weather dramatically hinders or prevents PGMs from hitting their designated targets.

A limiting factor in our ability to provide accurate weather awareness, however, is the almost complete lack of weather observations over hostile territory. A Scientific Advisory Board Quick-Look Study concluded that such observations are essential to Combat Weather fulfilling its potential. They identified many possible solutions but overlooked the option of using passive radar. The Air Force Research Laboratory Sensors Directorate has a viable passive radar solution that, in addition to their shared radar concepts, could extend coverage beyond what the Tactical Weather Radar will be providing.

Passive Radar Observation of the Battlespace Environment (PROBE) exploits electromagnetic emissions from a variety of cooperative and, more importantly, non-cooperative transmitters to provide surveillance of the surrounding area. The covert nature of the technology allows it to be placed in the near-target environment without being detected. A single PROBE can process received signals to provide air defense, traffic control, and weather information. Hence, systems (and costs) will be shared among many functional groups. Because of its low per-unit-cost and versatility, many systems can be deployed to fill in gaps in coverage. It is versatile enough to be employed from both the air and the ground. On the ground, it could be carried in by a soldier or mounted on a HMMWV, perhaps with the IMETS. In the air, it could be employed on any of several airborne platforms including Global Hawk, Dark Star, RC-135s, JSTARS, AWACS, airborne command posts, and others.

Weather radar information would include standard reflectivity and velocity measurements. These measurements would dramatically improve modeling of such things as transmissivity, trafficability, and NBC dispersion. This information can then be used to assist in strike planning and troop movements, as well as allowing for improved bomb damage assessment (BDA). Clearly, one of the most important areas where this sensor can have a value-added impact is in support of PGMs. In Desert Storm, roughly 40% of the sorties were adversely affected by the weather. That translated into putting aircrews and high-value weapon systems into harms way with no beneficial payoff. With high resolution observations enhanced by a network of PROBEs, the resulting better battlespace awareness and improved model forecasts will result in more intelligent PGM employment decisions, maximizing the efficiency of the weapon while minimizing the threat to aircrews. This paper describes how such a sensor would be employed and how it could be used to augment the battlespace data cube.

PROBLEM

The now infamous[1], and recently declassified, GAO Report, *"Operation Desert Storm: Evaluation of the Air Campaign,"* is full of examples of weather adversely impacting the air campaign. The report concludes that 8% of all sorties aborted or canceled because of adverse weather[2]. Assuming for a moment that proper Combat Weather support could have eliminated this problem, the strategic air campaign could have been 4 days further into their plan; we would have saved $400M in sortie costs; and $490M in munitions-costs wasted on weather-related misses[3].

The USAF Scientific Advisory Board Quick-Look Study on *"Weather Monitoring and Forecasting In Theater,"* also makes a strong case that weather impacts modern combat.[4] They show that in the Persian Gulf War, the mean lost-bomb-fraction related to weather obscurations was 18% overall, and losses greater than 50% were encountered on several days[5] (and this in a climate that is one of the statistically best in the world for PGM-employment[6]). With Joint Vision 2010's increased reliance on Precision Guided Munitions (PGMs) to accomplish our national objectives, our military forces will be especially dependent on high-quality battlespace weather-awareness. Unfortunately, as the SAB report goes on to establish, there is a critical lack of battlespace weather observations. Hence, our ability to globally engage is significantly hampered.

As the Air Force Weather (AFW) Mission Support Plan (MSP) states:

> The amount and quality of basic meteorological data available to characterize the environment in not sufficient for operations or climatology.
>
> Frequent, high-density observations of winds, temperature, pressure, and moisture form the foundation of [Combat Weather's] capability to specify and predict the environment. Present day collection systems do not have sufficient horizontal, vertical, and temporal resolution or coverage to adequately provide the detail and accuracy needed for planning and executing [military] operations[7]

The AFW MSP goes on to say that, *"In areas where friendly forces are not in control, the situation is worse and* [indeed] *it is in these locations where the level of interest is often greatest."*.[8] Presently, most observing is done by humans who read instruments, look at the clouds, precipitation, and visibility, and then manually input this information into their weather

---

[1] There have been many recent attacks by special interest groups on the GAO's analysis (see Aerospace America article, Oct 97 issue)

[2] GAO Report, GAO/NSIAD-97-134, "Operation Desert Storm: Evaluation of the Air Campaign," June 1997, p. 132.

[3] GAO Report, See Appendix for cost analysis.

[4] USAF Scientific Advisory Board (SAB) Study Report on *"Weather Monitoring and Forecasting In Theater,"* SAB-TR-96-04, Aug 97.

[5] SAB, slide 4.

[6] USAF Environmental Tactical Application Center, Southwest Asia-Northeast Africa Climatological Study, 1991

[7] Air Force Weather Mission Support Plan, 10 Oct 97, Data Collection Deficiency DC1, p 2-7.

[8] AFW MSP, p. 2-7

systems where it eventually ends up in the global database. Some observations are taken in hostile territory, but most are taken at friendly airfields and on our side of the Forward Line Of Troops (FLOT). The observations on our side do little to help define en route and target area weather; the weather most important for getting bombs on target.

The SAB report points out that the weather that impacted Desert Storm PGMs existed over the target at take-off time in almost all cases[9]. Hence, a weather observation at the target would have significantly improved their bombs-on-target ratios. Having a weather radar picture over the target would go a long way toward enabling Joint Vision 2010's Precision Engagement concept.

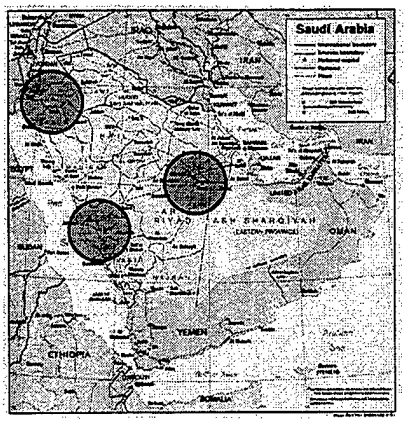

Figure 1. TWR coverage (minimum detectable altitude ≥10kft beyond circle)

In light of these deficiencies, HQ USAF approved the Operational Requirements Document for the Tactical Weather Radar (TWR).[10] The TWR will give Combat Weather a mission-critical view into the battlespace. This will enable Combat Weather to provide the resource protection and flight safety support that forward-based airbases need for aircraft launching, recovering, and re-generating. However, due to concerns specified in the Air Defense Plan and Emissions Control Plan, the TWR, as specified in the ORD, will not be allowed to operate further forward than the air base, typically located 300nm from the FLOT. This is too far away from potential target areas to provide useful target weather information since its range may be as low as 180 nm (precipitation)/50 nm (velocities). Hence, it will not help us with en route or target area weather; the weather most important to ensuring mission success, especially when using PGMs. Indeed, the TWR will only be able to support 5 of the 19 missions (Tables 1 and 2) listed in the ORD; and two of those five only some of the time.[11]

Table 1. Air Component Mission Areas Needing Support	
⊙ Counter Air	⊙ Electronic Combat, Surveillance, and Reconnaissance
⊙ Strategic Attack	⊙ Special Operations
⊙ Interdiction	O Base Operability and Defense
⊙ Close Air Support	◎ Logistics
O Strategic Airlift	⊙ Combat Support
◎ Aerial Refueling	O Aeromedical Evacuation
⊙ Denotes activity that takes place along the FLOT and into hostile territory ◎ Denotes activity that takes place in friendly and enemy territory (i.e., some inside and some outside of TWR range)	

[9] SAB, slide 4.
[10] Operational Requirements Document for Tactical Weather Radar (TWR), HQ USAF (CAF) ORD 301-92-I/II, approved by AF/CV on 12 June 1997.
[11] TWR ORD, para 1.1.1

Table 2. Land Component Mission Areas Needing Support	
⊙ Aviation	⊙ Land Combat Engineering Support
⊙ Air Defense	⊙ Fire Support, Biological, and Chemical
⊙ Combat Maneuver	⊙ Special Operations
⊙ Close Combat (Heavy & Light)	
⊙ Denotes activity that takes place along the FLOT and into hostile territory	

Clearly, to fulfill the requirements laid out in the TWR ORD, we need a constellation of assorted radars to fill in the complete battlespace picture. We definitely need the quality of information the TWR will provide at our operating bases, but we must look to the existing radar assets that are covering the FLOT and beyond, and to other radar technologies that will allow us to see within hostile territory.

SOLUTION

The solution to the radar coverage problem is really three-fold. First, we have to acquire the TWR for flight safety coverage of our airbases. Second, we have to be more aggressive in extracting weather information from non-weather radars already in-theater. Third, we have to incorporate passive sensors into our sensing strategy if we ever hope to get observations over the target.

One way to extend coverage into hostile territory is to extract weather information from existing non-weather radars. Many refer to this as data mining. Radars like the TPS-75, the Air Force's primary aircraft surveillance radar, can provide us useful weather information deep into hostile territory. A weather data extractor has already been developed, demonstrated, and deployed in SOUTHCOM where they're getting weather pictures from their older TPS-43. AFRL/SNRD has demonstrated the capability for the newer TPS-75. The Navy is doing the same thing with their Aegis Cruiser SPY-1 surveillance radar. The beauty of this capability is that the signals are processed off board so does not interfere with the primary mission of the radar. Indeed, Lockheed Martin has demonstrated that weather processing can make due with whatever scan strategy is being used, although some are obviously better than others.[12]

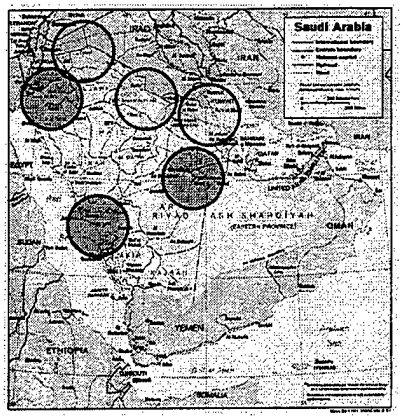

Figure 2. Added coverage from TPS-75 (mda ≥10kft outside of circles)

Data mining saves money in two ways: 1) it makes full use of existing assets instead of developing new radar systems for unique applications, and 2) it allows us to mitigate the deployment footprint by just adding a signal processor to the existing suite of equipment instead of a whole new system (antenna, processor, power plant, trailer, etc.) . This is a capability that

[12] SPY-1 Weather Experiment Final Report, Lockheed Martin Corp., Oct 1997

can be inexpensively added to existing radars, but also as new radars are developed, they must be designed with multi-users in mind. The scan strategies, wave-forms, and frequencies must be dynamically controlled to optimize sharing by multiple users (e.g., air traffic control, air defense, close air support, and weather). For example, a new radar with photonic phasing of its phased array, and the latest in signal-processing will be able to use scan strategies and wave forms optimized for low observable target ID and then once every 15 minutes or so automatically change the scan strategy to get an optimized weather picture. But even this capability is limited in it's ability to acquire boundary layer target weather information because surface-based radars are usually about 100 nm from the FLOT putting their minimum detection altitude, at range, at about 7,000 feet. Therefore, neither the TWR nor data mining will extend the coverage to the boundary layer over the target. Hence, we need still another solution that will get us even closer to the action.

Any solution to extend the coverage deep into hostile territory must consider the associated threats of being placed within hostile territory. A transmitting radar in this region would immediately become a hot target blaring its location to even unsophisticated enemies. Hence, equipment and attending personnel would be unacceptably vulnerable. Ideally, we want a system that is undetectable and yet gives us a clear operational picture of what is happening. PROBE offers a passive radar capability. It is a silent listener that intercepts radio-frequency-emissions from any illuminator of opportunity whether it be friendly or hostile and produces the weather and air traffic pictures.

The idea is for PROBE to be a portable gap-filler in both friendly and hostile territory. The system is portable and lightweight enough to be carried in by Army, Marine, or Special Forces ground units, but it could also be mounted on a HMMWV, UAV, or any other mobile platform. Its versatility and affordability means that we are free to use it whenever and wherever we want. The economy of deploying passive receivers is much less expensive than deploying enough transmitters to fill the battlespace. For example: If the few TWRs a Commander JTF is given end up too far apart to sense low-level weather in friendly territory, deploy PROBEs in between them. If the TPS-75s are placed too far from enemy targets to observe target weather, deploy PROBEs. When Special Operations Forces are in hostile territory and want an air and weather picture, their own PROBE will give it to them. If anomalous propagation causes severe ducting which takes out our coverage over a certain region, deploy PROBEs. The extended coverage gained from the fused efforts of all three of these efforts (TWR, data mining, and PROBEs) will help us significantly improve our awareness of the battlespace, thereby making a significant positive impact on the war effort. But, what type of weather information can we expect to get from a PROBE?

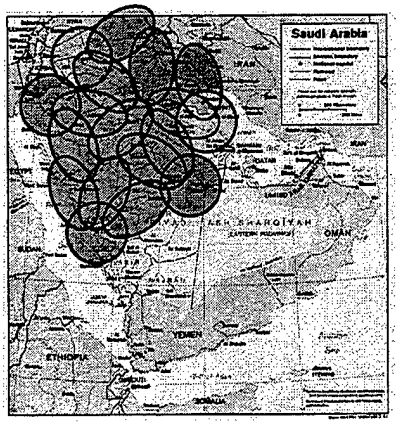

Figure 3. Added coverage from PROBEs

Most weather radars operate in the S-band because that has proven to be the optimum frequency, but there is useful weather information to be gained at other frequencies. The

amount of exploitable information is only restricted by what frequencies are available to intercept. The good news is that a broad range of frequencies can provide us a wealth of weather information. Typically, the battlespace will be illuminated by radars doing long-range air surveillance (S-band), air traffic control (L-band), and tactical air and ground surveillance (C- and X-bands). You can see from Table 3 that any or all of these would help us immensely in building our battlespace awareness. The PROBE will sense what frequencies, wave-forms, and scan strategies are available to intercept and choose the optimum one for each of its mission areas (i.e., air traffic control, air defense, and weather). It then will alternate among transmitters as it does each separate function. With the weather function, we can expect to get standard reflectivity and doppler data. There is a good chance it will also be able to glean polarization data. Hence, there is no reason why it will not be able to mimic any and all NEXRAD functionalities.

Table 3. Weather information with different frequency bands (adapted from Rinehart 1991)

Band designation	Frequency Range	Wavelength	Info
HF	3-30 MHz	100-10 m	refractive index
VHF	30-300 MHz	10-1 m	ref. index, winds
UHF	300-1000 MHz	1-.3 m	ref. index, winds
L	1-2 GHz	30-15 cm	precip., winds
S	2-4 GHz	15-8 cm	precip., winds
C	4-8 GHz	8-4 cm	precip.
X	8-12 GHz	4-2.5 cm	precip., cloud drops
K_u	12-18 GHz	2.5-1.7 cm	precip., cloud drops
K	18-27 GHz	1.7-1.2 cm	cloud drops
K_a	27-40 GHz	1.2-.75 cm	cloud drops
mm	40-300 GHz	7.5-1 mm	cloud particles

To get the full benefit of having so many sensors, we have to fuse together the individual pictures to get one comprehensive picture of the entire battlespace. The data could be fused at the Control and Reporting Center (CRC) to produce a radar mosaic. The lack of reliable secure communications in theater to bring this data together is another problem that needs to be solved. This data will help us describe the battlespace weather picture including trafficability, NBC dispersion, and transmissivity. Perhaps the biggest advantage of all of having such inexpensive and portable sensors is that it allows us to view the same volume of space with multiple sensors thereby giving us three-dimensional winds with no assumptions necessary. This capability alone will reap spectacular improvement in meso-scale model forecasts. This in turn will enhance Combat Weather's ability to contribute to the war effort. But, what do we do with all this information to have a positive impact on the war effort?

WARFIGHTER IMPACT

It is clear that high resolution weather data throughout the battlespace would benefit the warfighter in many ways. Just to list a few:

- Aircrew safety is enhanced by helping aircrews avoid identified hazards.
- Dynamic replanning helps us avoid wasting resources by not flying where we know the weather will keep us from doing what we want to do.
- Trafficability assessment will help ground units avoid trouble spots, anticipate enemy actions, and use the terrain as a force-multiplier.
- Air defenses will be enhanced by knowing where the propagation gaps are occurring and allowing air defense planners to compensate accordingly.
- Airborne Laser performance predictions will help us better assess its capabilities.
- Bomb Damage Assessment (BDA) will be aided by allowing planners to schedule intelligence, surveillance, and reconnaissance (ISR) assets to collect during cloud-free windows of opportunity.
- Precision Guided Munitions will be chosen so that the right weapon, is on the right target, at the right time and thus avoiding the 18% bomb miss/no-drop rate due to weather experienced in Desert Storm.[13]

Combat METOC is here to help the warfighter *"choose the weather for battle."* In lieu of the SAB report, many good things are happening. The TWR is coming on line, and several efforts are demonstrating that we can indeed use non-weather radars (data mining). AFRL/SNRD has just started an in-house effort to synergize multistatic radar weather signal processing algorithms with USAF state-of-the-art passive radar technologies to develop a device that will be an inexpensive gap-filler. PROBE will contribute mightily. With these observations, Combat METOC will be ready and able to advise the decision-maker making the difference that makes the victory.

[13] SAB, slide 4

References

Air Force Weather Mission Support Plan, HQ AF/XOW, 10 Oct 97.

Dorr, R., *"GAO Takes On High-Tech Weapons"*, Aerospace America, Oct 97, pp 32-36.

GAO Report, GAO/NSIAD-97-134, *"Operation Desert Storm: Evaluation of the Air Campaign,"* June 1997.

Gilgallon, P., Farrell, R., Duncomb, R., 1997: Development of a Passive Sensor for Battlefield Weather Surveillance, *Proceedings of the 43rd Tri-Service Radar Symposium (SECRET),* Boulder, CO, June, 1997.

Operational Requirements Document for Tactical Weather Radar (TWR), HQ USAF (CAF) ORD 301-92-I/II, approved by AF/CV on 12 June 1997.

Mazarr, Michael J., Don M. Snider, and James A. Blackwell, Jr., Desert Storm, The Gulf War and What We Learned, Center for Strategic and International Studies, Boulder CO, Westview Press, 1993.

Rinehart, R.E., 1991: Radar for Meteorologists, Knight Printing Co., 334 pp.

SPY-1 Weather Experiment Final Report, NS-L-TWR-T-2004, Lockheed Martin Corporation, Government Electronic Systems, Moorestown, NJ, Oct 97.

USAF Environmental Tactical Application Center, Southwest Asia-Northeast Africa Climatological Study, Feb 91.

USAF Scientific Advisory Board (SAB) Study Report on *"Weather Monitoring and Forecasting In Theater,"* SAB-TR-96-04, Aug 97.

Wurman, J., 1994: Vector Winds from a Single Transmitter Bistatic Dual-Doppler Radar Network, *Bulletin of the American Meteorological Society,* **75**, pp 983-994

Appendix

Here is an analysis of savings that Combat Weather Support might have made if it had been integrated within the Desert Storm JFACC decision-making process. We get our numbers from the GAO Report (1997), Leydon (1997), and the SAB Quick-Look Study Report (1997). There could very well be reports detailing what we are reporting here, but we have not found them. To glean weather impact from what we do have, we had to do a bit of deductive reasoning.

Leydon (1997) reports that the Air Force and Navy have a different total of sorties for the 43 days of the air war and recommends that 109,876 is the best number. The GAO reports that the average sortie cost was $17,000 (GAO, 1997: p. 166). Hence, that makes the total sortie cost for Desert Storm $1.8B.

The GAO reports that the total munitions cost was $2.7B (GAO, 1997: p. 178). Thus, the total cost of the air campaign was $4.5B. This is a gross underestimation because it does not include most of the support costs. $4.5B divided by the 43 days of the air war is approximately $100M per day.

A footnote on page 132 of the GAO Report says that 8% of all sorties were aborted or canceled due to adverse weather. Note that this does not include sorties having to go on to a secondary target or diverting because of

adverse weather. Most sources report that up to 40% of all combat sorties were adversely affected by the weather.[14] 8% of 109,876 is 8790. That equates to approximately 4 days worth of sorties. Four days is 9% of the total air war.

The SAB reports that 18% of the total expended munitions missed their target or were not released because of adverse weather (SAB, 1997: Slide 4). 18% of the total $2.7B is $490M.

Hence, integrated Combat Weather support could have saved the Coalition 4 days in the strategic air campaign, $400M in sortie costs, and $490M in munitions cost.

[14] Mazarr, et al., 1993, pp. 102-103.

Monte Carlo Modeling of the Propagation of Solarblind UV Radiation in the Lower Atmosphere

C.M. Cully and D.L. Hutt

252 Parkglen Cres. SE, Calgary, Alberta, Canada. T2J 4M2.
Tel: (403) 271 5806, email: cmcully@acs.ucalgary.ca or ascully@canuck.com

Defence Research Establishment Valcartier
2459 Pie XI Blvd., North, Val-Belair, Quebec, G3J 1X5, Canada
Tel: (902) 426 3100, FAX: (902) 426 9654, email: daniel.hutt@drea.dnd.ca

Abstract

The high Rayleigh scattering coefficient in the solarblind UV waveband (240 to 280 nm) gives rise to a strong scattered radiation field arriving at a detector from off the source-detector axis. In order to accurately predict signals from commonly used wide field of view detectors, this scattered signal must be accounted for. Exact solutions cannot be found, however, for realistic atmospheres. A Monte Carlo method for simulating the radiative transfer of solarblind UV radiation is outlined and compared to both an existing model and to experimental data. The simulation allows for detectors of an arbitrary field of view looking in arbitrary directions in a standard atmosphere. Multiple detectors can be simultaneously calculated, decreasing the calculation time for data at multiple ranges or from horizontal flight paths. The effect of the ground, the effect of pressure variation with altitude and the effect of anisotropic scattering are considered. Model predictions are found to be in good agreement with a variety of experimental data.

Introduction

The ozone layer acts as an extremely effective filter of UV radiation in the region between 240 and 280 nm. So little radiation in this waveband reaches the Earth's surface that a sensitive photomultiplier tube limited to this waveband may be pointed directly at the noon sun and record little more than dark current. In effect, it is always "night" in this waveband, and the band is termed the solarblind ultraviolet (SBUV).

This near-complete absence of background radiation is currently being exploited for use in missile approach warning systems (MAWS). Prediction and modeling of system performance is made difficult, however, by the high degree of Rayleigh scattering associated with the SBUV band. Any model, particularly for wide field-of-view detectors such as the ones commonly used in MAWS, must take into account the scattered contributions to the total signal. To complicate matters, at optical depths of interest, a significant portion of the signal may come from photons that have been scattered more than once, or "multiply scattered".

The inclusion in the model of a ground plane, anisotropic scatterers and atmospheric density variation with altitude makes for little symmetry in the problem. Unfortunately, most analytic approaches require stronger symmetry. Davison (Ref. 1) gives a result for infinite homogeneous atmospheres, while Elliot (Ref. 2) includes a ground plane under certain conditions. Although the techniques used are extremely powerful, the results are valid only when large simplifying assumptions are made. It was therefore decided that a numerical approach was justified. Specifically, a Monte Carlo approach was pursued.

The Monte Carlo Method in Radiative Transfer

A common alternative to the finite element transport methods such as the Zachor model (Ref. 3) or OSIC (Ref. 4) is the Monte Carlo method. Monte Carlo approaches use random number generators to numerically simulate the radiative transfer process. The basic technique is to randomly simulate "photons" traveling along possible paths from source to receiver. Photons are represented as discrete units of energy with an associated direction. The energy does not, in general, correspond to the energy of an actual photon of the given wavelength, but is simply the energy emitted by the source divided by the number of photons simulated. Each process (emission, scattering, absorption) is simulated in such a manner as to follow the probability distribution function physically observed for that process. For example, when a scattering event is simulated, the direction the photon continues in after the event is statistically governed by the scattering phase function, an experimentally determined function that gives the likelihood of scattering in any given solid angle.

There is a statistical fluctuation associated with the technique, since the problem is simulated one "photon" at a time, and the path is randomly chosen. However, each path is intrinsically statistically weighted by the simulation process. Therefore, after a large number of photons (typically $\sim 10^6$), the accumulated results converge to a physically meaningful solution. Although the signal to noise ratio improves as the square root of the number of photons simulated, it should be noted that there is always some statistical fluctuation involved in the Monte Carlo technique.

Examining the simulation event by event, the first event is the emission of a photon, which is simulated at a random angle from the point source. The free path length is then chosen from the sample population of possible free path lengths. The photon proceeds for this distance and is then either absorbed or scattered. If it is scattered, the probability that it is scattered into the receiver is calculated and added to the total signal at that angle. The photon proceeds like this until it is either absorbed or reaches a predetermined maximum radius from the source.

As the method is quite general, a relatively descriptive model of the atmosphere may be used. In particular, a ground plane may be easily added, as can an exponential decrease in particle density with altitude. In addition, the particles need not be confined to scattering isotropically, but can scatter according to any arbitrary phase function. In principle, any suitably discretized change in atmospheric conditions may be incorporated.

Finally, the signal at multiple detectors may be calculated from the same scattering points. In this way, there is little loss of computational speed incurred by including more than one detector.

Atmospheric Model

There are two distinct types of scattering that are accounted for: Rayleigh scattering and Mie scattering. Rayleigh scattering results from the scattering of photons by molecules such as N_2, O_2 or CO_2. These molecules are much smaller than the wavelength of incident light. The second type of scattering, Mie scattering, is used for aerosol particles which are much larger than the wavelength of the incident photon.

Each scattering event is described by an extinction coefficient and a (normalized) scattering phase function. The extinction coefficient α is defined as the fraction of monochromatic light lost per unit length of medium to the given process. It has dimensions of length^{-1}. There is an extinction coefficient associated with each of 4 different processes: Rayleigh scattering (α_R), Mie scattering (α_M), absorption by ozone (α_{O3}) and absorption by aerosols (α_A). The total extinction coefficient α is the sum of the four contributions.

The phase function determines the angular dependence of the scattering; that is, it is more likely that a given type of scattering will scatter in certain directions than in others. The value of the

normalized phase function, integrated over a given solid angle, gives the probability that a scattering event will scatter in that solid angle. The integral over all solid angles is equal to 1.

The Rayleigh extinction coefficient can be calculated based on commonly available atmospheric quantities. From Penndorf (Ref. 5), we find for unpolarized light:

$$\alpha_R = \frac{8\pi^3\left(n_s^2 - 1\right)^2}{3\lambda^4 N_s^2}\left(\frac{6+3\rho_N}{6-7\rho_N}\right)N \tag{1}$$

where n_s is the refractive index for standard air at 15 °C, λ is the wavelength, N is the number density of particles, N_s is the number density of particles for standard air at 15 °C and ρ_N is the depolarization factor, equal to 0.035 (Ref. 5). Since n_s is not a commonly measured quantity, it is found in the code by using the following equation from Penndorf (Ref. 5):

$$\left(n_s - 1\right)\text{x}10^{-8} = 6432.8 + \frac{2949810}{146 - 1/\lambda^2} + \frac{25540}{41 - 1/\lambda^2} \tag{2}$$

Also, N is found from the pressure and temperature using the ideal gas law. The Rayleigh scattering extinction coefficient can thus be found based only on the temperature and pressure at the scattering volume and the wavelength of incident light. Typical values in the SBUV are about 0.3 km^{-1}.

For the Mie scattering coefficient, observation can be made somewhat more directly. Visibility (and hence, the total extinction coefficient) at 550 nm is a commonly measured quantity. Of the 4 effects of Rayleigh scattering, Mie scattering, O_3 absorption and aerosol absorption, Mie scattering dominates at this wavelength. Thus, this measurement functions to essentially measure the Mie scattering extinction coefficient at 550 nm. The extinction coefficient in the SBUV is then estimated by multiplying this value by 1.35 for haze or 0.98 for fog (defined as visible extinction greater than 1.5 km^{-1}) (Ref. 6). Typical values for a clear day are about 0.06 km^{-1}.

The normalized Rayleigh scattering phase function is dependent upon the polarization of the incident radiation. The polarization of each photon is not, however, tracked during the simulation. Thus the unpolarized scattering phase function is used. For unpolarized light, the Rayleigh scattering phase function $P_M(\beta)$is given as:

$$P_M\left(\beta\right) = 0.7629\left(1 + 0.932\cos^2\beta\right) \tag{3}$$

where β is the scattering angle (Ref. 5). $P_M(\beta)$ is plotted in figure 1a.

The Mie scattering phase function depends in a complex way on the size distribution and refractive index of the aerosols, which are generally unknown. For modeling purposes, generic phase functions have been developed that are characteristic of different environments and visibility levels. The Monte Carlo code uses phase functions supplied with the OSIC model developed by Scitec Inc. (Ref. 4). The OSIC aerosol types include continental, desert, maritime and fog with variations for high and low extinction levels. Figure 1b shows the phase function for continental aerosols (high extinction). Note that a logarithmic scale is used.

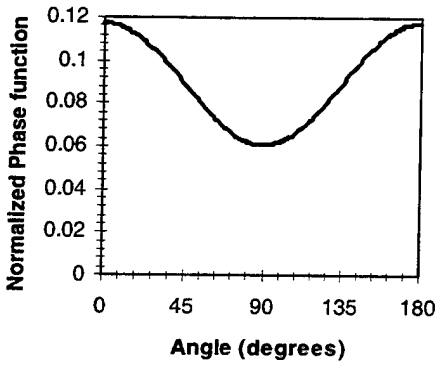

Fig 1a. Rayleigh scattering phase function.

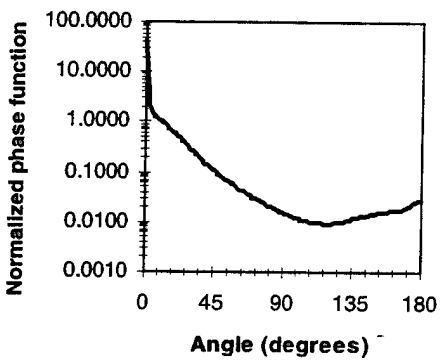

Fig 1b. Mie scattering phase function.

Aerosols can both scatter and absorb photons. Absorption in the solarblind UV is typically much less significant than scattering. For both fog and haze, the aerosol absorption coefficient is on the order of 10^{-4} smaller than the scattering coefficient.

The primary atmospheric gases that absorb in the UV are O_3, O_2, SO_2 and nitrogen oxides. However, the experimental data uses an extremely narrow band at 253.7 nm (a mercury emission line). For a narrow band at this wavelength, the absorption cross-section for ozone is so much larger than the cross-sections for the other gases that they may safely be ignored (Ref. 7). Wide-band calculations would necessitate inclusion of other gases in the model, notably O_2. At 253.7 nm and STP, the extinction coefficient due to ozone absorption is 30 $km^{-1}ppm^{-1}$ (Ref. 4). Thus, for a typical concentration near 30 ppb, the absorption coefficient due to molecular absorption is 0.90 km^{-1}.

Following the (1962) U.S. Standard Atmosphere (Ref. 8), density in the region of interest is allowed to decrease exponentially with height according to the isothermal approximation. Although the temperature also decreases with height so that this approximation is not strictly true, the derived density gradient is a good approximation to measured density gradients. Under this approximation, the exponential rate of decay of the number density of particles is equal to Mg/RT, where M is the average molecular weight (taken as 70% N_2, 30% O_2), g is the acceleration due to gravity (assumed constant), R is the gas constant and T is the temperature of the isothermal column, taken to be the ground-level temperature. Typical values for the decay constant are near 0.1 km^{-1}. The change in the number density of particles is assumed to affect all four extinction coefficients in the same manner.

Modeling of the receiver

The simulation should be able to handle arbitrary receiver geometries. In general, a receiver may be specified by its field of view, response curve for light arriving off-axis and aperture size. The orientation of the sensor must also be accounted for. One common way that this is done is to multiply each photon that hits the detector by the response of the detector at the angle of incidence. However, this adds overhead to the main loops and forces re-calculation of the simulation if the type of detector is changed.

These problems are circumvented by pulling all sensor characteristics outside the loop. Inside the loop, the detector is assumed to be a sphere that presents unit cross-sectional area. The sphere is divided into 200 rings of equal surface area, each of which is again subdivided into 200 equal-area segments. The axis of the rings points towards the source. Information about the angle of incidence of the photon is stored by determining into which of the 40 000 angular bins the photon falls.

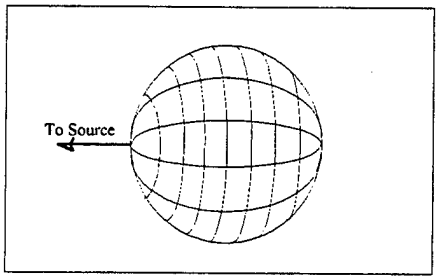

Figure 2. Receiver used in loops.

Outside the loops, the "real" detector is specified by a certain vector orientation, field of view and response curve within that field of view. For example, an ideal flat detector would have a cosine response curve within a 180° field of view. The product of the signal at a given angular element on the sphere and the response of the detector at the angle made between that element and the receiver axis gives the contribution to the "real" total signal. Integrating over all 40 000 elements gives the total number of photons seen by a 1 m^2 receiver with the specified characteristics. Detector aperture is then compensated for by multiplying by the area of the aperture.

Free path simulation

In a homogeneous atmosphere, the probability distribution for the free path length is simply an exponential distribution. In an atmosphere that varies continuously with altitude, however, the distribution is more complicated, and depends on the altitude and direction of propagation of the photon. In general, letting $\tau(\ell)$ be the optical depth, $e^{-\tau(l)}$ is the probability that a photon will traverse the path without being scattered or absorbed (Ref. 9). Letting a be the z component of the direction of propagation, Z_o be the starting altitude with extinction coefficient α_o and β be the density decay constant Mg/RT, the optical depth $\tau(\ell)$ in the presence of the atmospheric density gradient may be written as:

$$\tau(l) = \int_0^l \alpha(\vec{r}(s))ds \tag{4}$$

$$\tau(l) = -\frac{\alpha_o e^{-\beta Z_o}}{\beta a}\left(e^{-\beta a l} - 1\right) \tag{5}$$

This expression satisfies the necessary limit that as ℓ approaches 0, so does $\tau(\ell)$. In addition, as β approaches 0, $\tau(\ell)$ approaches its value in a homogenous space, $-\alpha_o\ell$.

The free path is then chosen by first generating a value for $\tau(\ell)$ that obeys the necessary exponential distribution (since $e^{-\tau(l)}$ is the probability that a photon will traverse the path without being scattered or absorbed). The free-path length ℓ is then found from there. That is, if γ is uniformly distributed on the interval (0,1], we let

$$-\ln\gamma = \tau(l) \tag{6}$$

(Ref. 8). Substitution of equation 5 gives:

$$l = -\frac{\ln\left|\frac{\beta a}{\alpha_o e^{-\beta z_o}} \ln \gamma + 1\right|}{\beta a} \tag{7}$$

Equation 7 allows the free path length to be simulated from a number γ uniformly distributed on the interval (0,1], the slant of the path (which is known from the unit vector describing the direction of motion of the photon) and atmospheric parameters. Special cases are used for α_o, β or a equal to 0.

Experimental Comparison

Reference 10 details experimental measurements performed over the course of the summer of 1997. Comparisons will be made with two of the experiments described therein.

The first experiment measured the radiant field at a sensor as a function of sensor angle with a narrow field of view. An isotropic source was placed at a range of 538m from the sensor. The sensor field of view was limited to 8°. The sensor initially was placed looking directly at the source and a measurement made. The elevation was then increased in steps through 190 degrees, measuring at each step. In this manner, the field arriving at the location of the detector was determined in the y-z plane as a function of elevation angle. The conditions on the day of the measurements were as follows:

- Ozone concentration: 30 ppb
- Temperature: 28 °C
- Pressure: 998 mb
- Visible extinction at 550 nm: 0.04 km^{-1}
    - Aerosol extinction at 254 nm: 0.054 km^{-1} (calculated from above)
    - Aerosol absorption at 254 nm: 5.4×10^{-6} km^{-1} (calculated from above)
- Continental aerosol scattering phase function assumed
- Source-detector range: 538 m
- Height of source above ground: 4m
- Height of receiver above ground: 9m

Using these same parameters, the Monte Carlo code was used to simulate the experiment. Figure 3 compares the experimental data to the simulated points. The signal received has been normalized to one at 0 degrees elevation to make the results independent of source intensity and receiver sensitivity. The point at 190 degrees came out in the simulation as exactly zero. Since this value cannot be plotted on a logarithmic scale, it was plotted at the lowest value shown. Figure 3 shows that the agreement between the measured radiant field profile and the Monte Carlo simulation is very good.

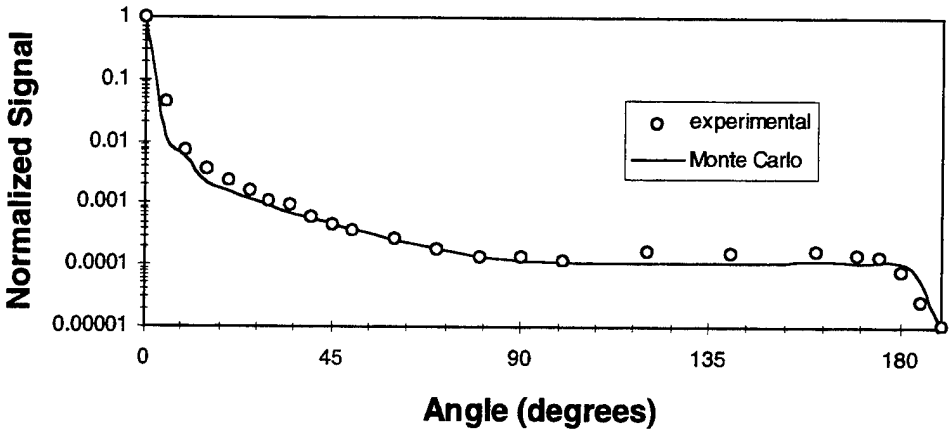

Figure 3. Comparison with experimental results for elevation scan.

In a second experiment, 3 sensors with acceptance angles of 120 ° were placed along 3 different axes. One faced the source, one faced directly away from the source and one was at 90 degrees elevation relative to the source. The signals received at all 3 sensors were recorded for a wide variety of atmospheric conditions and the ratios of signals from the off-axis sensors and the sensor pointing at the source were calculated. The ratios were also simulated under the same conditions. The angular sensitivity of the sensors was modeled as a cosine curve truncated at ± 60°. Ozone is treated as the independent variable. The conditions were similar to those of the first comparison, except that ozone concentration ranged from 17 to 110 ppb. Figure 4 compares the experimental data to the simulated points. The ratios have been expressed as percentages.

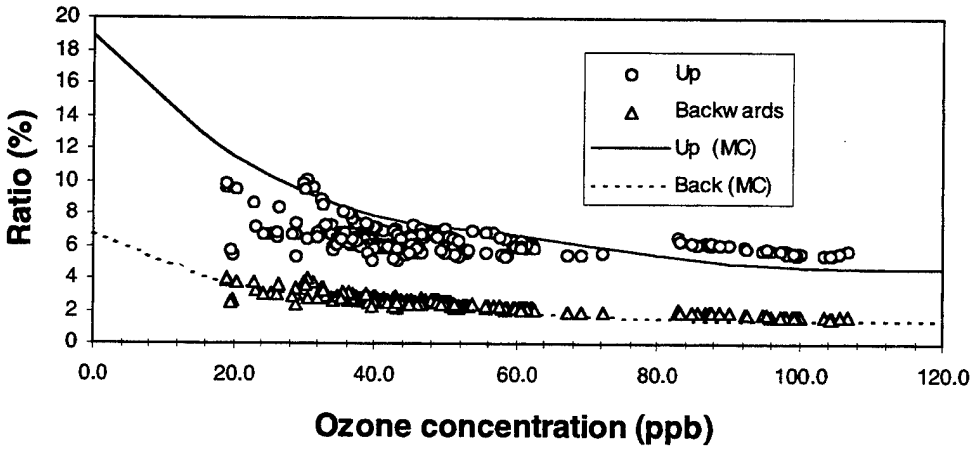

Figure 4. Comparison with experimental results for directional ratios.

Again, the Monte Carlo results are in good agreement with the measured ratios. As with the angular radiant field measurement, the signal ratios of figure 4 are independent of source intensity and receiver sensitivity. Some of the scatter in the data of figure 4 is due to different aerosol extinctions encountered during the series of measurements. Also, the ozone concentration measurement is a local measurement made at the receiver end of the path and may not be representative of the ozone along the entire path, thus contributing to scatter in the measured data of figure 4.

Comparison with an existing model

Results from the Monte Carlo simulation were also compared to an existing model called OSIC (Ref. 4), which uses a finite element transport method.

The comparison was made under the following conditions, based on a default setting in OSIC:

- Ozone concentration: 10 ppb and 50 ppb
- Temperature: 28 °C
- Pressure: 1013 mb
- Aerosol extinction at 254 nm: 0.166 km^{-1}
- Aerosol absorption at 254 nm: 0.01 km^{-1}
- Continental aerosol scattering phase function
- Source-detector range: 100 m to 10 km
- Height of source above ground: 1m
- Height of receiver above ground: 1m
- Sensor field of view: 180 degrees, cosine response
- Sensor orientation: toward source

The comparison between the two models is shown below as figure 5. The signal received at the detector has been normalized by the unscattered signal so that a linear scale can be used for the comparison and so that absolute source intensity can be neglected. Figure 5 shows that the Monte Carlo and OSIC simulations are in fairly good agreement with a maximum difference of only 20% between them. This is remarkable considering that the calculations span a range of optical depths from near zero to 15. The difference between results from the two models depends to some extent on the geometry of the simulation and the choice of atmospheric parameters. When combined with experimental results, comparisons such as those shown in figure 5 provide a means of evaluating the relative benefit of different models.

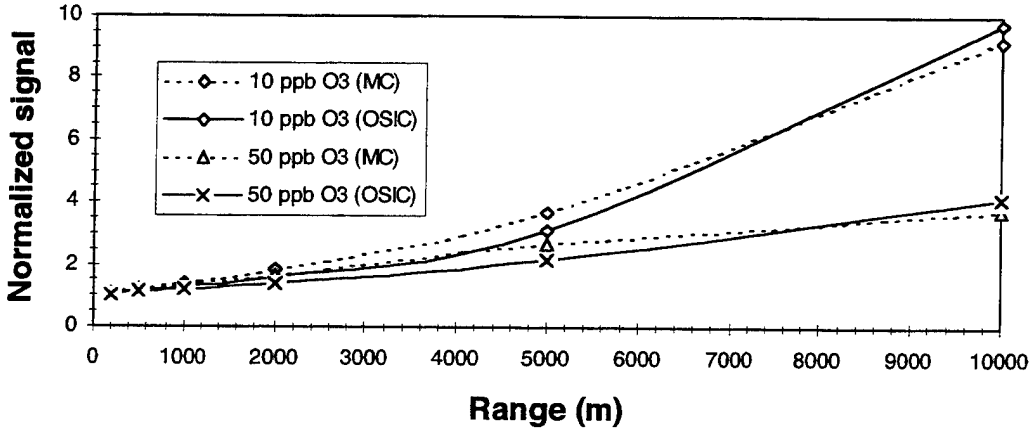

Figure 5. Comparison with OSIC model. Signal has been normalized by unscattered contribution.

Numerical comparison of different simplifying assumptions

The Monte Carlo code can be used as a tool for evaluating the validity of certain approximations. Various simplifying assumptions are compared in figure 6 under the following conditions:

- Ozone concentration: 30 ppb
- Temperature: 15 °C
- Pressure: 1013 mb
- Aerosol extinction at 254 nm: 0.166 km^{-1}
- Aerosol absorption at 254 nm: 0.01 km^{-1}
- Continental aerosol scattering phase function
- Source-detector range: 100 m to 10 km
- Height of source above ground: 1m
- Height of receiver above ground: 5m
- Sensor field of view: 180 degrees
- Sensor orientation: toward source

The four different situations of simplifying assumptions used are:

a) ground plane included, atmospheric density gradient included, anisotropic scattering
b) no ground plane, no atmospheric density gradient, isotropic scattering
c) ground plane included, no atmospheric density gradient, isotropic scattering
d) ground plane included, atmospheric density gradient included, isotropic scattering

Figure 6 gives the ratio of cases b, c and d to case a. Case a is the most realistic. Surprisingly, the least sophisticated approximation proves to be the most accurate in this case. However, the ratios of figure 6 depend on the geometry and particular atmospheric parameters chosen, and other geometries or choices of parameters may change the relative accuracy of any given approximation.

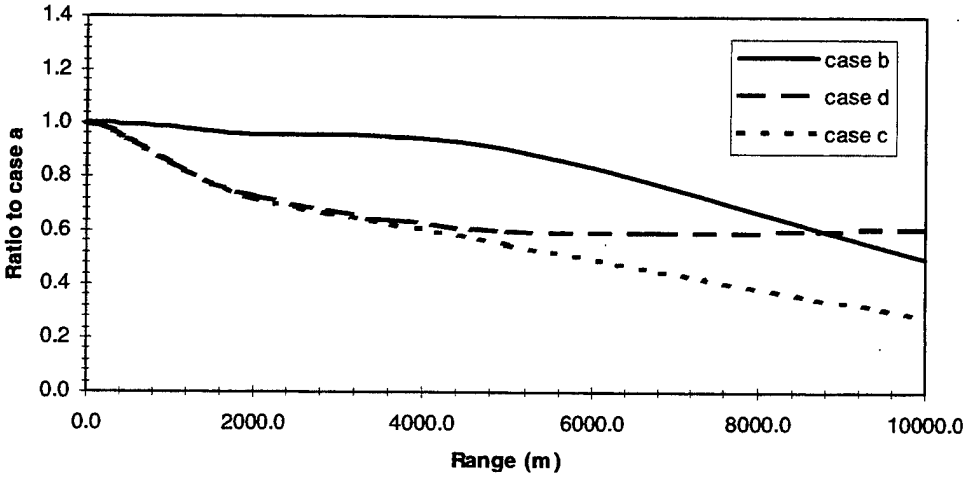

Figure 6. Comparison of simplifying assumptions.

Conclusion

We have applied the Monte Carlo technique to the problem of modeling the propagation of UV radiation from an isotropic point source through the atmosphere to a wide field of view receiver. The Monte Carlo approach was chosen because it requires a minimal number of simplifying assumptions and approximations to be made about the geometry of the simulation and the optical properties of the atmosphere. The model can take into account the presence of a ground plane, arbitrary source and receiver heights, arbitrary receiver pointing angle, an atmosphere with height dependent characteristics, arbitrary absorption and scattering coefficients and arbitrary aerosol scattering phase functions. Due to

the generality of the model, real experimental situations can be closely represented allowing model results to be compared to experimental data. Calculations with the Monte Carlo model were compared to measurements of the angular profile of received UV radiation and to the ratios of signals measured with receivers pointing directly toward a UV source (0°), at 90° elevation relative to the source and directly away from the source (180°). Good agreement was obtained between the model and measurements. The Monte Carlo model was also compared to a finite element transport model with good agreement. The flexibility and generality of the Monte Carlo model makes it a useful tool for analysis of UV propagation experiments, modeling atmospheric effects on UV system performance and for evaluating other models.

Acknowledgments

The authors would like to thank Dr. David J. Fry for his help and encouragement.

References

1. Davison, B. Neutron Transport Theory. Oxford University Press, Toronto. 1958.

2. Elliot, J. P. Milne's problem with a point-source. Proceedings of the Royal Society A. Volume 228. Page 424. 1955.

3. Zachor, Alexander S. Aureole radiance field about a source in a scattering-absorbing medium. Applied Optics. Vol. 17, no. 12. Page 1911. June 1978.

4. Crow, K. OSIC: Model description and user's manual. SciTec technical report, SciTec Inc. Princton, NJ. 1995.

5. Penndorf, Rudolf. Tables of the refractive index for standard air and the Rayleigh scattering coefficient for the spectral region between 0.2 and 20.0 μ and their application to atmospheric optics. Journal of the Optical Society of America. February, 1957.

6. Shettle, E.P. and Fenn, R. Models for the aerosols of the lower atmosphere and the effects of humidity variations on their optical properties. Air Force Geophysics Laboratory, AFGL-TR-79-0214. 1979.

7. Patterson, Edward M. and Gillespie, James B. Simplified ultraviolet and visible wavelength atmospheric propagation model. Applied Optics. Vol. 28, no. 3. Page 425. February 1989.

8. Valley, Shea L. Handbook of Geophysics and Space Environments. McGraw-Hill Book Company, New York. 1965.

9. Marchuk, G.I., Mikhailov, G.A., Nazaraliev, M.A., Darbinjan, R.A., Kargin, B.A. and Elepov, B.S. The Monte Carlo Methods in Atmospheric Optics. Springer-Verlag, Toronto. 1980.

10. . D. L. Hutt and C. Cully. Measurements of scattering and propagation of solarblind ultraviolet radiation through the atmosphere. Proceedings of the 1997 Battlespace Atmospherics Conference 2-4 December, Eds. K.D. Anderson and J.H. Richter, Space and Naval Warfare Systems Center Technical Document 2989, December 1997.

REPORT DOCUMENTATION PAGE

Form Approved
OMB No. 0704-0188

1. AGENCY USE ONLY *(Leave blank)*	2. REPORT DATE	3. REPORT TYPE AND DATES COVERED
	March 1998	Final

4. TITLE AND SUBTITLE

PROCEEDINGS OF THE 1997 BATTLESPACE ATMOSPHERICS CONFERENCE 2–4 DECEMBER 1997

5. FUNDING NUMBERS

PE: 0602435N
AN: DN302214
WU: R3532

6. AUTHOR(S)

Editors: K. D. Anderson, J. H. Richter

7. PERFORMING ORGANIZATION NAME(S) AND ADDRESS(ES)

Space and Naval Warfare (SPAWAR) Systems Center
San Diego, CA 92152–5001

8. PERFORMING ORGANIZATION REPORT NUMBER

TD 2989

9. SPONSORING/MONITORING AGENCY NAME(S) AND ADDRESS(ES)

Office of Naval Research
800 North Quincy Street
Arlington, VA 22217

10. SPONSORING/MONITORING AGENCY REPORT NUMBER

11. SUPPLEMENTARY NOTES

12a. DISTRIBUTION/AVAILABILITY STATEMENT

Approved for public release; distribution is unlimited.

12b. DISTRIBUTION CODE

13. ABSTRACT *(Maximum 200 words)*

The 1997 Battlespace Atmospherics Conference was held 2–4 December 1997 at the Space and Naval Warfare (SPAWAR) Systems Center, San Diego (SSC San Diego). The conference objective is to enhance cooperation and coordination in all aspects of atmospheric effects assessment between the U. S. military services, the civilian community, and other nations. The conference proceedings cover a broad range of atmospheric sciences including model development, experiments, sensor and sensing technique development, modeling and simulation, tactical decision aids, and operational issues.

14. SUBJECT TERMS

Mission Area: Command, Control, and Communications
electromagnetics
propagation
atmosphere

15. NUMBER OF PAGES

710

16. PRICE CODE

17. SECURITY CLASSIFICATION OF REPORT	18. SECURITY CLASSIFICATION OF THIS PAGE	19. SECURITY CLASSIFICATION OF ABSTRACT	20. LIMITATION OF ABSTRACT
UNCLASSIFIED	UNCLASSIFIED	UNCLASSIFIED	SAME AS REPORT

21a. NAME OF RESPONSIBLE INDIVIDUAL	21b. TELEPHONE *(include Area Code)*	21c. OFFICE SYMBOL
J. H. Richter	(619) 553–3053 e–mail: richter@spawar.navy.mil	Code D88

INITIAL DISTRIBUTION

Code D0012	Patent Counsel	(1)
Code D0271	Archive/Stock	(6)
Code D0274	Library	(2)
Code D027	M. E. Cathcart	(1)
Code D0271	D. Richter	(1)
Code D88	J. H. Richter	(30)
Code D883	K. D. Anderson	(31)
Code D883	A. E. Barrios	(1)
Code D883	C. P. Hattan	(1)
Code D883	H. V. Hitney	(1)
Code D883	D. R. Jensen	(1)
Code D883	K. M. Littfin	(1)
Code D883	C. P. McGrath	(1)
Code D883	W. L. Patterson	(1)
Code D883	R. A. Paulus	(1)
Code D883	L. T. Rogers	(1)

Defense Technical Information Center
Fort Belvoir, VA 22060–6218 (4)

SPAWARSYSCEN Liaison Office
Arlington, VA 22202–4804

Center for Naval Analyses
Alexandria, VA 22302–0268

Navy Acquisition, Research and Development
Information Center (NARDIC)
Arlington, VA 22244–5114

GIDEP Operations Center
Corona, CA 91718–8000

84th Radar Evaluation Squadron
Gilbert J. Estebo
Hill AFB, UT 84056–3920

AFRL
Dr. Dana M. Madsen
Hanscomo AFB, MA 01731

AFRL/VSB
Gail P. Anderson
Hanscom AFB, MA 01731–3010

Airtouch Cellular
Brian D. Sherwood
Irvine, CA 92614

AMT Fur Wehrgeophysik/WI Mont Royal
Harold Weber
Traben–Trarbach, Germany

Applied Research Laboratory
Pennsylvania State University
Christophe F. Bas
University Park, PA 16802

Applied Research Laboratory
Pennysylvania State University
Jason N. Bode
Dr. Stephen A. Fast
Dr. Kenneth E. Gilbert
Rodney R. Korte
Dr. C. Russell Philbrick
State College, PA 16804–0030

CDMA, Meteo–France
Dominique Chaupin
Rene Dufoulon
Toulouse Cedex, France

Chief of Naval Operations
CDR Randy J. Scanlon, USN
Washington, DC 20392

CIRA/Colorado State University
Dr. Mahmood R. Azimi
Kenneth E. Eis
John Hair
Dr. Thomas H. Vonder Haar
Fort Collins, CO 80523–1375

COLSA Corporation
Dr. Edwin Nunez
Huntsville, AL 35806

Computer Sciences Corporation
Steven B. Dreksler
Monterey, CA 93940

DAMI–POB
Leander Page, III
Washington, DC 20310–1067

Defense Information Systems Agency
LCDR Frank Baker
Falls Church, VA 22041

Defence Research Establishment
Dr. J. Luc Forand
Quebec, Canada

Defence Research Establishment Atlantic
Dr. Daniel L. Hutt
Dartmouth, Nova Scotia

DERA
Dr. Rupert M. J. Watson
Worcs, United Kingdom

DERA
James Branson
Dr. Don Manson
Fareham, United Kingdom

DRI–ASC
Dr. William P. Arnott
Reno, NV 89506

Duke University
Dr. Jeffery L. Krolink
Durham, NC 27708

EORD
Dr. Ami Ben–Shalom
Haifa, Israel

EPSHOM
Michel Aidonidis
Brest, Cedex, France

FGAN Forschungs Institut Fuer Optik
Dr. Dieter Clement
Tuebingen, Germany

German Military Geophysical Office
Gernot Grosz
Traben–Trarbach, Germany

Imperial College
Prof. J. C. Dainty
London, United Kingdom

Johns Hopkins University
Applied Physics Laboratory
G. Daniel Dockery
Peter Econ
Michael H. Newkirk
Laurel, MD 20723–6099

Lockheed Martin Corporation
Henry S. Owen
James W. Stephans
Dr. Harry Urkowitz
Moorestown, NJ 08057

MIT
Dr. F. Wesley Wilson
Dr. Lisa M. Zurk
Lexington, MA 02173–9185

Naval Postgraduate School
Paul A. Frederickson
Dr. Philip L. Walker
Dr. Chuck Wash
Monterey, CA 93943–5502

Naval Research Laboratory
Dr. Stephen D. Burk
B. John Cook
Dr. Andreas Goroch
Ms. Tracy Haack
Dr. Richard M. Hodur
Thomas Lee
Dr. Jerome M. Schmidt
Monterey, CA 93943–5502

Naval Research Laboratory
CDR David G. Markham
Washington, DC 20375

NAWCWPNS
Jay Rosenthal
Point Mugu, CA 93042–5001

NCAR/RAP
Dr. Arthur Schantz
Boulder, CO 80301

NIRSL/UMASS
Brian D. Pollard
Amherst, MA 01003

New Mexico State University
Dr. Vladimir E. Ostashev
Las Cruces, NM 88003–8001

Norwegian Defence Research Establishment
Espen Stark
Kjeller, Norway

Office of Naval Research
Dr. Ronald J. Ferek
Dr. Scott Sandgathe
Arlington, VA 22217–5660

Ontar Corporation
Dr. John Schroeder
North Andover, MA 01845–4532

OSD/DDR&E (ST)
COL Al Shaffer
Washington, DC 20301–3080

Pennsylvania State University
Dr. Nelson L. Seaman
University Park, PA 16802

Phillips Lab Geophysics Directorate
CAPT Gail M. Weaver, USAF
Ft. Campbell, KY 42223–5000

Photon Research Associates
Dr. Wayne H. Wilson
San Diego, CA 92121

Planning Systems Incorporated
Dr. Robert L. Martin
Stennis SP CTR, MS 39529–5005

RAL, Radio Com. Res. U.
Dr. Mireille Levy
Oxon, United Kingdom

Rocketdyne Div., Boeing–North American
David Nahrstedt
Canoga Park, CA 91303

Rome Laboratory USAF (RL/WE)
Robert J. Farrell, Jr.
Rome, NY 13441–4514

Royal Military College of Canada
Dr. William S. Andrews
Ontario, Canada

Science Applications International
Corporation
Dr. Robert E. Turner
Monterey, CA 93940

Science Applications International
Corporation
Gregory A. Vayda
Monterey, CA 93940

Science & Technology Corporation
Dr. Adarsh Deepak
Hampton, VA 23666

Scripps Institution of Oceanography
Dr. David P. Rogers
La Jolla, CA 92093–0230

Sonalysts, Incorporated
Patrick R. Kelly
San Diego, CA 92123

Space and Naval Warfare Systems Command
Dr. Edward J. Harrison, PMW 185
San Diego, CA 92110–3127

STC/GWEX
Dr. Paul F. Twitchell
Silver Spring, MD 20910

TASC, Incorporated
Dr. Peter S. Dailey
Reading, MA 01867

United States Air Force
CAPT Peter J. Cohen, USAF
CDR Timothy K. Cummings
Scott AFB, IL 62225–5116

United States Air Force
Research Laboratory
Paul Tattelman
Hanscom AFB, MA 01731–3010

USARIEM
William T. Matthew
Natick, MA 01760–5007

U.S. Army National Ground
Intelligence Center
Jan D. Breeden
Charlottesville, VA 22901

U. S. Army Research Laboratory
David I. Knapp
Las Cruces, NM 88011–8041

U. S. Army Research Laboratory
Dr. James L. Cogan
Robert E. Dumais, Jr.
Dr. Donald W. Hoock
Dr. Edward M. Measure
David Sauter
Dr. Richard C. Shirkey
Dr. Robert A. Sutherland
Richard J. Szymber
David H. Tofsted
Mario Torres
White Sands Missile Range, NM 88002–5501

U. S. Army Research Laboratory
Ronald M. Cionco
Dr. James Gillespie
Arnold D. Tunick
Dr. Alan E. Wetmore
Timothy J. White
Dr. David K. Wilson
Adelphi, MD 20783–1197

U. S. Army Reseach Laboratory, Information
Science & Technology Directorate
Dr. Jagdish Chandra
Adelphi, MD 20783–1197

U. S. Army Research Office
Dr. Walter D. Bach, Jr.
Research Triangle Park, NC 27709

U. S. Army Waterways Experiment Station
Jeff Jorgeson
Vicksburg, MS 39180

U. S. Department of Commerce
Dr. Steven F. Clifford
Boulder, CO 80303–3328

U. S. Special Operations Command
Greg A. Eisman
MacDill AFB, FL 33621–5323

University of Alabama in Huntsville
Dr. Oskar Essenwanger
Huntsville, AL 35803–1630

University of Colorado
Dr. Rod G. Frehlich
Boulder, CO 80309

University of Massachusetts, Knowles
Dr. Stephen J. Frasier
Amherst, MA 01003

University of Mississippi
Dr. Henry E. Bass
University, MS 38677

University of Washington
Applied Physics Laboratory
Dr. Andrew T. Jessup
Dr. Pierre D. Mourad
Dr. Jeffrey A. Nystuen
Dr. Dale Winebrenner
Seattle, WA 98105

VPI&SU
Dr. Gary S. Brown
Blacksburg, VA 24061–0111